CRYSTALLIZATION TECHNOLOGY HANDBOOK

Second Edition

Revised and Expanded

edited by

A. Mersmann

CRYSTALLIZATION TECHNOLOGY HANDBOOK

Second Edition
Revised and Expanded

edited by
A. Mersmann
Technical University of Munich
Garching, Germany

MARCEL DEKKER, INC. NEW YORK • BASEL

ISBN: 0-8247-0528-9

This book is printed on acid-free paper

Headquarters
Marcel Dekker, Inc.
270 Madison Avenue, New York, NY 10016
tel: 212–696-9000; fax: 212-685-4540

Eastern Hemisphere Distribution
Marcel Dekker AG
Hutgasse 4, Postfach 812, CH-4001 Basel, Switzerland
tel: 41-61-261-8482; fax: 41-61-261 8896

World Wide Web
http://www.dekker.com

The publisher offers discounts on this book when ordered in bulk quantities. For more information, write to Special Sales/Professional Marketing at the headquarters address above.

Current printing (last digit):
10 9 8 7 6 5 4 3 2 1

PRINTED IN THE UNITED STATES OF AMERICA

Preface

The aim of this book is to provide reliable information not only on the science of crystallization from solution and from melt but also on the basic design methods for laboratory and especially industrial crystallizers. Up to now the niche between scientific results and practical design and operation of large-scale crystallizers has scarcely been filled. A work devoted to this objective has to take into account relevant crystallization phenomena as well as chemical engineering processes such as fluid dynamics, multiphase flow, and heat and mass transfer. In the design of crystallizers, experiments are initially performed on laboratory crystallizers to obtain kinetic data. In this book, information is given on reliable scale-up of such crystallizers. The selection, design, and operation of large-scale industrial crystallizers based on fundamentals is the most significant objective of this work. To this end, an appendix listing important physical properties of a large number of crystallization systems is included. A selection of design data valid for industrial crystallizers with volumes up to several hundred cubic meters demonstrates the applicability of the design and scale-up rules.

To date, the design of crystallizers has not been achievable from first principles. The reason is very simple: a complex variety of different processes occur in crystallizers, such as nucleation, crystal growth, attrition and agglomeration of crystals, fluid dynamics, and heat and mass transfer. Some of these processes are not yet well understood although the design and operation of large-scale crystallizers require reliable knowledge of the most essential processes. The book presents a survey of the state of the art and stresses the interrelationships of the essential mechanisms in such an apparatus. Furthermore, with respect to nucleation and crystal growth, general approaches have been developed to predict the kinetic rates that are needed for chemical engineering design and a new chapter on agglomeration has been added.

Supersaturation is the decisive driving force with respect to the kinetics of crystallization. Optimal supersaturation is a prerequisite for the economical production of crystals with a desired size, shape, and purity. The book offers information on the most suitable supersaturation requirements in laboratory and industrial crystallizers. Not only are aspects of cooling and evaporative crystallization considered, but drowning-out and reaction crystallization are also described in detail. In dealing with precipitation the complex interrelationships between mixing and product quality are discussed. A special segment is devoted to the problem of how the process components of an entire crystallization process can be economically fitted together. The aspects stressed are always those of production quality; size distribution, coefficient of variation, crystal shapes and purity, and the problem of encrustation are considered. One chapter is devoted to the control of crystallizers and another deals with the role of additives and impurities present in the solution. Crystallization from the melt is described in full detail, and information is given on how to design and operate the corresponding crystallizers. The book describes the most significant devices for crystallization from the melt and solidification processes. Process development such as high-pressure crystallization and freezing are considered and in this second edition new results on direct contact cooling crystallization have been added.

My goal has been to edit a work as homogeneous and practical as possible. The book is therefore not a mere collection of independent articles written by several contributors but a coordinated handbook with a single list of symbols and a unified bibliography. It is divided into 15 chapters to make it easier to find points of interest. Only simple derivations and equations absolutely necessary for understanding and for calculation are presented.

The book is based on literature that is available worldwide (especially references from the United States, Europe, and Japan) and on the direct experience of the contributors. Some of the contributors work in the indus-

trial sector, and nearly all have spent some time in industrial plants. A few fundamental chapters were written by scientific researchers at universities. Because this volume addresses the theory and practice of crystallization, it should be valuable in both academia and industry.

A. Mersmann

Contents

Contributors

B. BRAUND Technische Universität München, Garching, Germany

R. DAVID Ecole des Mines d'Albi-Carmaux-CNRS, Albi, France

A. EBLE Technische Universität München, Garching, Germany

C. HEYER Technische Universität München, Garching, Germany

I. HIRASAWA Waseda University, Tokyo, Japan

J. KLEIN Université Claude Bernard-CNRS, Villeurbanne, France

M. LAHAV The Weizmann Institute of Science, Rehovot, Israel

L. LEISEROWITZ The Weizmann Institute of Science, Rehovot, Israel

A. MERSMANN Technische Universität München, Garching, Germany

F. W. RENNIE Du Pont de Nemours & Co., Wilmington, Delaware

S. ROHANI The University of Western Ontario, London, Ontario, Canada

K. TOYOKURA Waseda University, Tokyo, Japan

I. WEISSBUCH The Weizmann Institute of Science, Rehovot, Israel

G. WELLINGHOFF BASF AG, Ludwigshafen, Germany

K. WINTERMANTEL BASF AG, Ludwigshafen, Germany

2
Activated Nucleation

A. MERSMANN, C. HEYER, AND A. EBLE Technische Universität München, Garching, Germany

Crystals are created when nuclei are formed and then grow. The kinetic processes of nucleation and crystal growth require supersaturation, which can generally be obtained by a change in temperature (cooling in the case of a positive gradient $dC^*/d\vartheta$ of the solubility curve or heating in the case of a negative gradient), by removing the solvent (usually by evaporation), or by adding a drowning-out agent or reaction partners. The system then attempts to achieve thermodynamic equilibrium through nucleation and the growth of nuclei. If a solution contains neither solid foreign particles nor crystals of its own type, nuclei can be formed only by *homogeneous nucleation*. If foreign particles are present, nucleation is facilitated and the process is known as *heterogeneous nucleation*. Both homogeneous and heterogeneous nucleation take place in the absence of solution-own crystals and are collectively known as *primary nucleation*. This occurs when a specific supersaturation, known as the *metastable supersaturation* ΔC_{met}, is obtained in the system. However, in semicommercial and industrial crystallizers, it has often been observed that nuclei occur even at a very low supersaturation $\Delta C < \Delta C_{\text{met}}$ when solution-own crystals are present (e.g., in the form of attrition

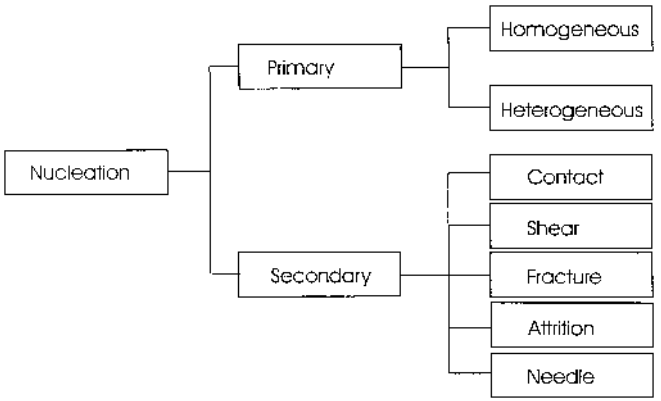

Figure 0.1. Various kinds of nucleation. (From Ref. 0.1.)

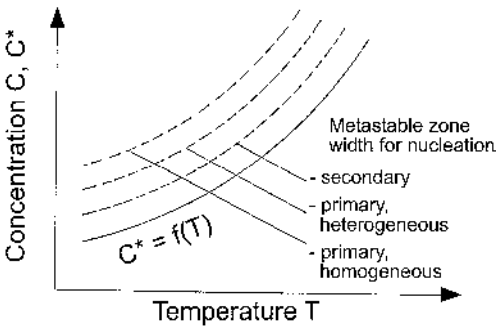

Figure 0.2. Metastable supersaturation against temperature for several types of nucleation process.

fragments or added seed crystals). Such nuclei are known as *secondary nuclei*. However, it should be noted that a distinction is made between nucleation resulting from contact, shearing action, breakage, abrasion, and needle fraction (see Fig. 0.1). Figure 0.2 illustrates the dependence of supersaturation on several types of nucleation process plotted against solubility.

In the following sections, the three mechanisms of activated nucleation will be discussed in more detail: homogeneous, heterogeneous, and activated secondary nucleation. All these mechanisms have in common the fact that a free-energy barrier must be passed in order to form clusters of a critical size, beyond which the new phase grows spontaneously. The height of this barrier

or, equivalently, the extent of penetration into the metastable zone is different for each process due to different physical mechanisms. Homogeneous nucleation is treated in Sec. 1, including discussions on classical theory (Sec. 1.1) and kinetic theory (Sec. 1.2), and rules for industrial application are given in Sec. 1.3. In Secs. 2 and 3, heterogeneous and secondary nucleation are presented, and, finally, all three mechanisms are compared in Sec. 4.

1. HOMOGENEOUS NUCLEATION

1.1. Classical Theory

The classical nucleation theory dates back to the work of Volmer and Weber [1.1, 1.2], who were the first to argue that the nucleation rate should depend exponentially on the reversible work of the formation of a critical cluster and was later extended by authors such as Becker and Döring [1.3], Farkas [1.4], Zeldovich [1.5], Frenkel [1.6], and others [1.7]. In order for a new phase to appear, an interface must be formed, which (in the absence of impurities or suspended foreign material) occurs by small embryos in the new phase being formed within the bulk metastable phase. These embryos are formed due to spontaneous density or composition fluctuations, which may also result in the spontaneous destruction of such an embryo. The creation of nuclei can, therefore, be described by a successive addition of units A according to the formation scheme

$$A_1 + A = A_2; \qquad A_2 + A = A_3; \ldots; A_n + A \underset{k_D}{\overset{k_A}{\Leftrightarrow}} A_{n+1} \tag{1.1}$$

Here, it is assumed that there is no molecular association in the metastable solution and that the concentration of embryos is small. Under these conditions, embryos can only grow or shrink as a result of single-molecule events, which can be described by the rate constants k_A and k_D. The value k_A is the rate constant of addition and k_D that of decay of units from a cluster. Because addition is a random process—if supersaturation is sufficiently high—more and more elementary units can join together and create increasingly large nuclei known as *clusters*. The reversible work necessary to form such a cluster is given by a balance of the free enthalpy ΔG_V, that is gained (being proportional to the condensed matter and, thus, to the volume of the cluster) and the free-surface enthalpy ΔG_A needed to build the new surface. The change in positive free-surface enthalpy ΔG_A increases with the interfacial tension γ_{CL} between the solid crystal surface and the surrounding solution, as well as with the surface of the nucleus. The enthalpy change is to be added to the system and is therefore positive. On the other hand, the change in free-volume enthalpy ΔG_V during solid phase formation is set free

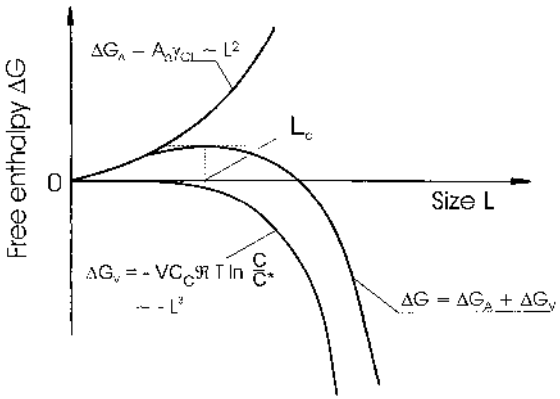

Figure 1.1. Free enthalpy ΔG against nucleus size L.

and is thus negative. The magnitude ΔG_V of this enthalpy is proportional to the volume of the nucleus and increases with increasing energy $\Re T \ln S$, where $S = a/a^*$ or in ideal systems, $S = C/C^*$, when the concentration C of the elementary units changes to the lower equilibrium concentration $C^* = C - \Delta C$.

According to Figure 1.1, in which the free enthalpies ΔG_A and ΔG_V and the total enthalpy $\Delta G = \Delta G_A + \Delta G_V$ are plotted against the nucleus radius, the following is obtained with nucleus surface A_n, nucleus volume V_n, the degree of dissociation α, and the number of ions ν:

$$\Delta G = \Delta G_A + \Delta G_V = A_n\gamma_{CL} - (1 - \alpha + \nu\nu)V_nC_c\Re T \ln S \tag{1.2}$$

The change in total enthalpy ΔG with respect to the nucleus size L passes through a maximum value. This is because the free-volume enthalpy ΔG_V is a function of the volume of a cluster and therefore

$$\Delta G_V \sim V_n \sim L^3 \tag{1.3}$$

whereas the free-surface enthalpy ΔG_A is related to the size of the nucleus in the following manner:

$$\Delta G_A \sim A_n \sim L^2 \tag{1.4}$$

A thermodynamically stable nucleus exists when the total enthalpy ΔG does not change when elementary units are added or removed; in other words, for the case of

$$\frac{\partial \Delta G}{\partial L} = 0 \tag{1.5}$$

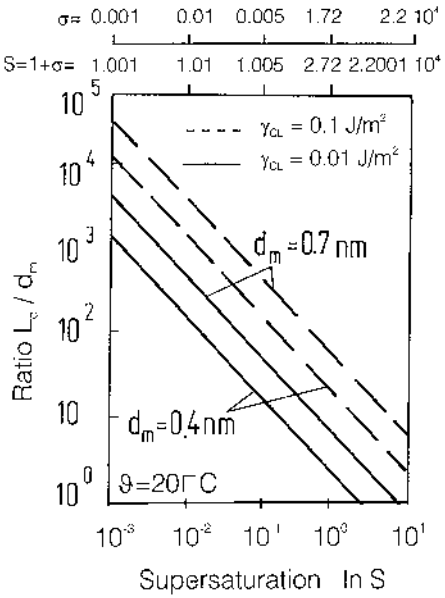

Figure 1.2. Ratio L_c/d_m with respect to the natural logarithm of supersaturation S for different interfacial tensions and molecule diameters.

In the case of such nuclei, the rate constant k_A of addition is as great as that of decay k_D. Therefore, neither growth nor decomposition takes place. The last four equations yield the following relationship for the critical nucleus diameter L^*_{crit} in the case of spherical nuclei:

$$L^*_{\text{crit}} = \frac{4\gamma_{CL}}{(1-\alpha+\nu\alpha)\Re T C_C \ln S} \tag{1.6}$$

With the Boltzmann constant $k = \Re/N_A$ and

$$V_m = \frac{1}{C_C N_A} = \frac{\tilde{M}}{\rho_C N_A} \tag{1.7}$$

we obtain for $\alpha = 0$ and $\nu = 1$ (i.e., molecules)

$$L_c = \frac{4\gamma_{CL}}{kT \ln S} V_m \tag{1.8}$$

Because the free enthalpy ΔG for nucleus sizes $L > L_c$ decreases with the nucleus size, the addition reaction takes place by itself due to the laws for disturbed equilibria (i.e., the nucleus can continue growing). On the other hand, in the range $L < L_c$, the change in free enthalpy increases with

increasing nucleus size. This means that the rate constant of decay is greater than that of growth, and the nucleus disintegrates.

The rate of primary homogeneous nucleation according to the classical nucleation theory can be obtained by calculating the number of critical clusters that cross the nucleation barrier described earlier and is then given by

$$B_{\text{hom}} = kn_c Z \tag{1.9}$$

It can be seen that the rate is a product of three factors:

- n_c, the number concentration of critical clusters
- k, the rate at which clusters cross the barrier
- Z, the imbalance factor

all of which will be explained in more detail.

Assuming that the cluster size distribution n_i is caused by random collisions of molecules and can be described by a Boltzmann distribution, we obtain

$$n_i = n_0 \exp\left(-\frac{\Delta G_i}{kT}\right) \tag{1.10}$$

or for critical clusters,

$$n_c = n_0 \exp\left(-\frac{\Delta G_c}{kT}\right) \tag{1.11}$$

where n_0 is the number concentration of monomers in the supersaturated solution.

The value ΔG_c in equation (1.11) is the free-nucleation enthalpy of a critical cluster. According to Volmer and Weber [1.1], this enthalpy is given by

$$\Delta G_c = \tfrac{1}{3} A_c \gamma_{CL} \tag{1.12}$$

which can be achieved by inserting L_c [Eq. (1.8)] into the expression for ΔG [Eq. (1.2)]. Equation (1.6) for the critical cluster diameter $L_c = \sqrt{A_c/\pi}$ gives the following expression for the distribution of critical clusters with $\alpha = 1$:

$$n_c = n_0 \exp\left[-\frac{16}{3}\pi\left(\frac{\gamma_{CL}}{kT}\right)^3\left(\frac{1}{C_C N_A}\right)^2 \frac{1}{(\nu \ln S)^2}\right] \tag{1.13}$$

Having determined the number of critical clusters, it is now necessary to obtain the rate at which they cross the nucleation barrier (i.e., grow by one monomer).

For nucleation from the gas phase, the rate at which monomers impinge successfully on the surface of a nucleus of size L is given by

$$k = Anq\frac{w}{4} \tag{1.14}$$

Here, A is the surface area of a nucleus, n is the number concentration of monomers, w is the mean velocity of monomers, and q the "condensation" coefficient, which is the fraction of monomers hitting the surface that actually stick. Assuming that every monomer that hits the surface is incorporated (i.e., $q = 1$) and that the number concentration of monomers is hardly not reduced by the nucleation process, for an ideal gas

$$k = A_c n_0 \sqrt{\frac{kT}{2\pi m_1}} \tag{1.15}$$

is obtained, where m_1 is the mass of a monomer.

Using the same assumptions as above, the following form of the impact coefficient k was derived by Kind and Mersmann [1.8, 1.9] for nucleation in condensed fluids:

$$k = \tfrac{3}{4} n_0^{4/3} D_{AB} A_c \tag{1.16}$$

So far, all these calculations have been made assuming an equilibrium. In order to relate the number of critical nuclei in the equilibrium distribution to the number in the steady-state distribution, the Zeldovic factor is introduced. It is given by

$$Z = \sqrt{\frac{Q}{2\pi kT}} \tag{1.17}$$

where

$$Q \equiv -\left[\frac{\partial^2 \Delta G}{\partial i^2}\right]_{i_c} \tag{1.18}$$

is the second derivative of the free energy with respect to cluster number i at the top of the barrier. Using the expression of the classical nucleation theory [Eq. (1.2)] for ΔG and assuming that the nucleation process is volume conserving, leading to

$$i_c = \frac{\pi}{6} L_c^3 C_C N_A \tag{1.19}$$

as the number of elementary units of a cluster with diameter L_c, for the imbalance factor Z

$$Z = \sqrt{\frac{\Delta G_c}{3\pi k T i_c^2}} = \frac{2}{\pi C_C N_A L_c^2}\sqrt{\frac{\gamma_{CL}}{kT}} \tag{1.20}$$

is obtained. Inserting the values of n_c [Eq. (1.13)], Z [Eq. (1.20)], and k [Eq. (1.16)] into the expression for B_{hom} [Eq. (1.9)] finally gives the following form of B_{hom}:

$$B_{\text{hom}} = 1.5 D_{AB}(CN_A)^{7/3}\sqrt{\frac{\gamma_{CL}}{kT}}\frac{1}{C_C N_A} \times \exp\left[-\frac{16}{3}\pi\left(\frac{\gamma_{CL}}{kT}\right)^3\left(\frac{1}{C_C N_A}\right)^2\frac{1}{(\nu \ln S)^2}\right] \tag{1.21}$$

This equation provides a simple way of predicting nucleation rates, especially because only easily accessible substance properties are needed: the diffusion coefficient D_{AB}, the actual and equilibrium concentrations, C and C^*, or activities, a and a^*, the molar density of the solid C_C and the surface tension, γ_{CL}, which can be calculated according to Mersmann [1.10] in the following manner:

$$\frac{\gamma_{CL}}{kT} = K(C_C N_A)^{2/3}\ln\left(\frac{C_C}{C^*}\right) \tag{1.22}$$

The derivation of this surface tension and especially of the factor K are elucidated in Chapter 1.

It should be noted that for the derivation of the enthalpy of a critical nucleus according to equations (1.2) and (1.12) and thus for the rate of homogeneous nucleation, it was assumed that the nucleus consists of only one component and that no solvent molecules are incorporated into the lattice; that is, the solvent is insoluble in the solid phase. This, however, is not necessarily the case in every nucleation process and there might be some two-component or multicomponent nucleating systems. Although it is beyond the scope of this book to go into more detail with regard to these special processes, we wish to draw the reader's attention to the fact that there are some differences for multicomponent systems. The main difference is the evaluation of the free enthalpy of formation because one has to take into account the ratio in which the different molecules are incorporated into the cluster and how they may affect each other. In addition, the preexponential term of the rate of homogeneous nucleation may be altered due to changes in the diffusivities of the different types of molecules, which not only act on each other within the solid phase but also in the solution.

Besides the nucleation of multicomponent systems, the classical nucleation theory presented is strictly speaking not valid for the case of nucleation in the presence of temperature changes, because its derivation is based on an

isothermal process. For its practical application, this, however, is usually no hindrance. Most processes take place under isothermal conditions, and in the few cases in which high temperature changes occur (e.g., due to the heat of mixing in acid pasting processes), the equations can at least be used for the estimation of a range of possible nucleation rates by using the highest and lowest temperatures occurring. In this way, it is possible to obtain an idea about the nucleation rates a priori and to control the process.

It should also be noted that the classical nucleation theory is based on two approximations:

- The treatment of small embryos as though they have bulk properties
- The need to invoke an equilibrium distribution of embryos in order to calculate k_D, the dissociation or decay coefficient in equation (1.1)

The first approximation, also known as the capillarity approximation, circumvents statistical mechanics in favor of heuristics, whereas the latter transforms a kinetic theory into a thermodynamic one. The first-principle treatments of energetics in nucleation, such as the idea of a physically consistent cluster according to Reiss et al. [1.11–1.19] or the application of density functional theory to nucleation according to Oxtoby [1.20–1.27], require extensive computer simulations, and they are, therefore, not discussed any further here. For more information on these topics, the reader is referred to the articles by Reiss and Oxtoby. The kinetic approach for determining nucleation rates, however, seems to be a promising, straightforward idea, and will be explained in more detail.

1.2. Kinetic Approach

The aim of nucleation theory is to predict a priori the rate at which nuclei are formed, pass a critical threshold size, and grow spontaneously. So far, this task has been treated merely thermodynamically. The reason for this was that the dissociation constant K_D in equation (1.1) is not known at all, whereas the arrival rate k_A can be obtained more easily. Therefore, k_D was expressed in terms of k_A by applying equilibrium conditions and using detailed balancing. The main problem to be solved was then the calculation of the equilibrium nuclei distribution or the energy of formation of critical nuclei, respectively.

A purely kinetic approach to nucleation in liquids was proposed for the first time in 1989 by Ruckenstein et al. [1.28–1.31]. They avoided the assumption of equilibrium and calculated the rate $\alpha(n)$ at which single molecules left a cluster of n molecules. This was done assuming that a molecule that moves in a thin layer surrounding the cluster leaves this cluster when it acquires enough energy to overcome the potential energy

barrier due to the cluster and its surrounding fluid. Using the mean dissociation time $\overline{\tau(n)}$, the rate at which molecules abandon the cluster can be written

$$\alpha = \frac{N_s(n)}{\overline{\tau(n)}} \tag{1.23}$$

where N_s is the number of molecules in the surface layer (i.e., within a distance $R < r < R + d_m$ of the center of the cluster). Here, R is the radius of the cluster and d_m is the diameter of a molecule. If $r > R + d_m$, the molecule dissociates from the cluster.

If the cluster is a uniform spherical solid, the number of molecules within it is given by

$$i = \tfrac{4}{3}\pi R^3 C_C N_A \tag{1.24}$$

which is equivalent to equation (1.19). The number of surface molecules is then, according to Ruckenstein and Nowakowski [1.30],

$$N_s = 4\pi R^2 d_m C_C N_A \left[1 + \frac{d_m}{R} - \frac{1}{3}\left(\frac{d_m}{R}\right)^2\right] \tag{1.25}$$

Here, it should be noted that N_s is proportional to the surface of the cluster only for large particles.

$\bar{\tau}$ is the mean dissociation time averaged over all initial positions of a molecule within the surface layer. It is, therefore, a function of the mean dissociation rate of one molecule initially at a certain point ξ in the surface layer integrated over the initial distribution function of surface molecules. Because the derivation of this expression would be beyond the scope of this textbook, the interested reader is referred to an article by Ruckenstein and Nowasowski [1.30] and we will discuss only the results of this kinetic nucleation theory. Ruckenstein and Nowasowski showed that the rate α is only a function of the intermolecular potential and the size of the cluster. Using a supersaturation-dependent rate of condensation, β, they obtained the following equation for the nucleation rate:

$$B_{\text{hom,kin}} = \frac{\beta(1) n_0}{2\displaystyle\int_0^\infty \exp[-2w(g)]\, dg}, \qquad w(g) = \int_0^g \frac{\beta(g) - \alpha(g)}{\beta(g) + \alpha(g)} dg \tag{1.26}$$

where $\beta(1)$ is the rate of single-molecule coagulation. Equation (1.26) can be evaluated by the method of steepest descent, because the function $w(g)$ exhibits a fairly sharp minimum at the critical cluster size g^*. The nucleation rate, $B_{\text{hom,kin}}$, can then be expressed by

$$B_{\text{hom,kin}} = (0.5)\beta(1)n_0\left(\frac{w''(g^*)}{\pi}\right)^{0.5}\exp[2w(g^*)] \tag{1.27}$$

which looks similar in structure to the result of the classical nucleation theory; see equation (1.21). However, this approach has the advantage that it does not rely on the assumption of an equilibrium or on the application of continuum thermodynamics to very small objects. Although there are still some disadvantages, such as the following:

- Numerical calculations are needed in order to estimate α and therefore $w(g)$
- Accurate knowledge of the intermolecular potential is essential

the work of Ruckenstein et al. provides an important step toward the development of a kinetic theory of homogeneous nucleation. There is now a need for calculations using realistic intermolecular potential and for the evaluation of those results, not only in comparison with classical theory but also using experimental data.

1.3. Industrial Application

So far, the theoretical background of homogeneous nucleation has been discussed. In industrial crystallizers, however, homogeneous nucleation is usually not desired at all, and for the production of large crystals in particular, it has to be avoided. Only for the crystallization of very fine or even nano-sized materials may this mechanism be useful. In each case, it is essential to know the supersaturation $\Delta C_{\text{met,hom}}$ that must be obtained in order to produce a certain number of homogeneous nuclei. This supersaturation $\Delta C_{\text{met,hom}}$ is known as the *metastable zone width* in homogeneous nucleation. Although homogeneous nuclei are not formed in the Ostwald–Miers range of $0 < \Delta C < \Delta C_{\text{met,hom}}$, crystals can grow at $\Delta C > 0$. The curve $C^* + \Delta C_{\text{met,hom}}$ as a function of temperature ϑ is known as the supersolubility curve and depends on substance values and generally on the concentration C. Relationship (1.21) can be used to calculate the metastable supersaturation $\Delta C_{\text{met,hom}}$ for given nucleation rates. Combining equations (1.21) and (1.22) leads to

$$\begin{aligned}\frac{B_{\text{hom}}}{D_{AB}(C_C N_A)^{5/3}} &= 1.5\left(\frac{C}{C_C}\right)^{7/3}\sqrt{K\ln\left(\frac{C_C}{C^*}\right)} \\ &\quad\times\exp\left\{-\frac{16\pi}{3}\left[K\ln\left(\frac{C_C}{C^*}\right)\right]^3\left(\frac{1}{\nu\ln S}\right)^2\right\}\end{aligned} \tag{1.28}$$

or, in general,

$$\frac{\Delta C}{C_C} = g\left(\frac{C^*}{C_C}; \frac{B_{\text{hom}}}{D_{AB}(C_C N_A)^{5/3}}; \nu\right) \tag{1.29}$$

The value C^*/C_C now represents dimensionless solubility and the expression $B^*_{\text{hom}} = B_{\text{hom}}/D_{AB}(N_A C_C)^{5/3}$ is the dimensionless rate of primary, homogeneous nucleation. If a certain dimensionless rate B^*_{hom} is given, the dimensionless metastable supersaturation $(\Delta C_{\text{met}})/C_C$ of homogeneous primary nucleation can be calculated for a system with C^*/C_C:

$$\frac{\Delta C_{\text{met}}}{C_C} = g_1\left(\frac{C^*}{C_C}; \nu; \underbrace{\frac{B_{\text{hom}}}{D_{AB}(C_C N_A)^{5/3}}}_{B^*_{\text{hom}}}\right) \tag{1.30}$$

Figure 1.3 illustrates this dimensionless metastable supersaturation $\Delta C_{\text{met}}/C_C$ against the dimensionless solubility C^*/C_C for various rates of homogeneous primary nucleation, which are valid for $K = 0.414$. The curves are valid for $D_{AB} = 1 \times 10^{-9}\,\text{m}^2/\text{s}$ and $C_C = 13.3\,\text{kmol/m}^3$. These are mean

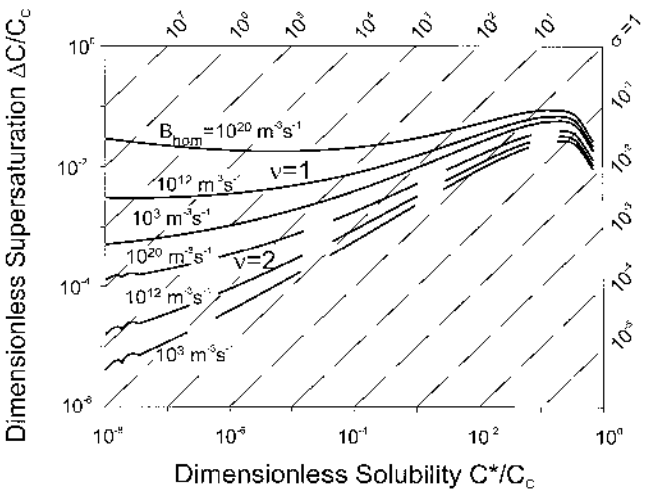

Figure 1.3. Dimensionless metastable supersaturation against dimensionless solubility for homogeneous nucleation for $\nu = 1$ (molecules) and $\nu = 2$.

values for C_C and D_{AB}. Note the strong influence of the stoichiometric coefficient ν for sparingly soluble systems [1.32].

It is somewhat surprising that all curves pass through a maximum for a dimensionless solubility of approximately $C^*/C_C \approx 0.16$. The reason for this may be that equation (1.22) is a simplified version of the general equation (see Ref. 1.10):

$$\gamma_{CL} = KkT(C_C N_A)^{2/3}\left[\ln\left(\frac{C_C}{C^*}\right) + \int_{\gamma_i^L}^{\gamma_i^C} \frac{d\gamma_i}{\gamma_i}\right] + \gamma_{CL}^0 \tag{1.31}$$

Unfortunately, neither the activity coefficient γ_i of the dissolved substance nor the integration constant γ_{CL}^0 is known [1.10]. It is assumed that both γ_{CL}^0 and the term $0.414kT(C_C N_A)^{2/3}\ln(\bar{\gamma}_i^c/\bar{\gamma}_i^L)$ are small compared to γ_{CL}. The values $\bar{\gamma}_i^c$ and $\bar{\gamma}_i^L$ are the activity coefficients (determined by means of the concentration) of the dissolved substance i in the crystalline or liquid phase. The greater the solubility C^* of a substance in a solvent, the greater the activity coefficient depends on the concentration and the less accurately the interfacial tension γ_{CL} can be calculated according to the simplified equation (1.22). The metastable zone width $\Delta C_{\text{met}}/C_C$ of homogeneous primary nucleation depends on the nucleation rate and the dimensionless solubility C^*/C_C. The following simplified equations can be given (compare Fig. 1.3) for a dimensionless nucleation rate of 10^{-26} (valid for $\nu = 1$):

For $C^*/C_C < 10^{-5}$

$$\frac{\Delta C_{\text{met}}}{C_C} \approx 0.02\left(\frac{C^*}{C_C}\right)^{1/8} \tag{1.32}$$

for $10^{-5} < C^*/C_C < 1$

$$\frac{\Delta C_{\text{met}}}{C_C} \approx 0.1\left(\frac{C^*}{C_C}\right)^{1/4} \tag{1.33}$$

However, these relationships are valid only when the solution is absolutely free of foreign particles, which is never the case in industrial crystallizers. Moreover, heterogeneous nucleation of all apparatus and machine parts wetted by the solution must also be avoided, which is very difficult and, again, not the case in practice. Besides, one also has to keep in mind that other effects such as mixing might have a huge influence on nucleation rates in industrial crystallizers. So far, mixing has not been considered at all,

because, theoretically, it should not influence the physical mechanism of nucleation. However, the buildup of supersaturation can be influenced considerably by the mixing process; hence, the nucleation rate changes and, thus, the emerging particle size distribution may be altered significantly. For the application of the equations of homogeneous nucleation rates deduced, it is therefore absolutely necessary to know the correct local supersaturation that can only be achieved if the local composition and therefore mixing are well understood, which is, unfortunately, not the case for most types of apparatus.

The last descriptions already suggest why it is so difficult to verify the theory of nucleation and why experimentally determined nucleation rates differ so strongly from theoretically predicted ones. In addition to the problems stated, it must be borne in mind that in order to determine nucleation rates experimentally, a number of particles are needed that are produced in a specific volume over a certain amount of time. As long as it is not possible to count particles in the nanometer or even smaller size range in-line, there will always be certain assumptions to get to the desired rate: The time is not known exactly, the actual supersaturation usually cannot be monitored in-line and particle sizes have to be measured off-line and recalculated to particle numbers. Therefore, it is not surprising that all nucleation rates measured so far are much lower than the theoretically predicted ones. With improving measurement devices and standard sampling methods, this should be strongly improved and it is expected that measured values approach theoretically predicted ones in the near future.

2. HETEROGENEOUS NUCLEATION

2.1. Theoretical Approach

Up to now, it has been assumed that collisions between units in a solution lead to clusters of varying size and that nuclei result from the fact that clusters above the critical nucleus size L^*_{crit} can continue growing into crystals, assuming that the original solution is entirely pure (i.e., free of solid particles). In reality, it is impossible to remove completely all solid matter from a solvent or solution. In bidistilled water, many SiO_2 particles in the size range of only a few nanometers can be found. Schubert [2.1] came to the conclusion that the volumetric surface of these foreign particles is approximately $a_{for} \approx 2.5 \times 10^3\ m^2/m^3$; but how do such small foreign particles (such as sand, rust, etc.) affect nucleation? This is illustrated in Figure 2.1, which shows a foreign particle in a supersaturated solution. According to Blander and Katz [2.2] and also Schubert [2.1], the rate of heterogeneous nucleation is proportional to the volumetric surface a_{for} of

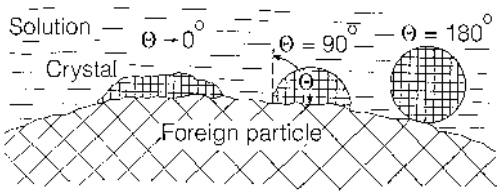

Figure 2.1. Nucleation on a foreign particle for different wetting angles.

foreign particles and not to the number of those particles. The model proposed by Schubert [2.1] describes the rate of heterogeneous nucleation B_{het} as a product of the volumetric surface a_{for} of foreign particles and the rate $B_{\text{het,surf}}$ of heterogeneous nucleation based on the surface of foreign particles according to equation (2.1):

$$B_{\text{het}} = a_{\text{for}} B_{\text{het,surf}} \tag{2.1}$$

The rate $B_{\text{het,surf}}$ can be described as being equivalent to the rate of homogeneous nucleation by

$$B_{\text{het,surf}} = k n_c Z \tag{2.2}$$

Again, the factor Z takes into account the difference between the equilibrium and stationary state, having the same definition as in homogeneous nucleation [see Eqs. (1.17) and (1.18)]. The number of critical nuclei, n_c, is now based on the surface of foreign particles and not on the volume, as in homogeneous nucleation, and the rate at which clusters cross the barrier, k, takes into account not only impingements from the volume but also those from molecules adsorbed on the surface of the foreign particle. Because the two factors in equation (2.2), k and n_c, are different than those in classical homogeneous nucleation theory, they will be discussed in more detail.

The number n_c of critical clusters depends on the number of molecules $C_{\text{ad}} N_A$ adsorbed on the foreign surface and the nucleation energy $\Delta G_{c,\text{het}}$ of heterogeneous nucleation according to a Boltzmann distribution:

$$n_c = C_{\text{ad}} N_A \exp\left(-\frac{\Delta G_{c,\text{het}}}{kT}\right) \tag{2.3}$$

Assuming now that the thickness of the adsorption layer does not exceed the diameter d_m of a molecule, which is valid for precipitation because of very low concentrations in the solution, the surface-based concentration C_{ad} can be expressed in terms of the volume-related concentration $C_{\text{ad},v}$ by

$$C_{\text{ad}} = C_{\text{ad},v} d_m \tag{2.4}$$

Taking into consideration the fact that the adsorption isotherm, which describes the relation between the concentration $C_{\mathrm{ad},v}$ of units adsorbed on the foreign surface and the concentration C of these units in the bulk of the solution, can be described by a linear relationship due to the low concentrations, expression

$$C_{\mathrm{ad},v} = \mathrm{He}_{\mathrm{ad}} C \tag{2.5}$$

is obtained, with the adsorption constant $\mathrm{He}_{\mathrm{ad}}$. The surface-based concentration C_{ad} can then be expressed in terms of the bulk concentration C and the adsorption constant $\mathrm{He}_{\mathrm{ad}}$:

$$C_{\mathrm{ad}} = \mathrm{He}_{\mathrm{ad}} C d_m \tag{2.6}$$

The free-nucleation enthalpy of heterogeneous nucleation, $\Delta G_{c,\mathrm{het}}$, is smaller than the nucleation enthalpy needed for homogeneous nucleation and is given by

$$\Delta G_{c,\mathrm{het}} = f \Delta G_{c,\mathrm{hom}} = f\left(\frac{16}{3}\right)\pi\left(\frac{\gamma_{CL}}{kT}\right)^3 V_m^2 \left(\frac{1}{\nu \ln S_a}\right)^2 kT \tag{2.7}$$

Here, f is a geometric correction factor, which is the ratio of the volume of the truncated nucleus to that of a sphere with the same radius. Thus, it depends on the wetting or contact angle θ as follows, assuming a flat foreign surface:

$$f = \frac{(2 + \cos\theta)(1 - \cos\theta)^2}{4} \tag{2.8}$$

If the foreign surface is not flat, as in the case of nano-sized foreign particles, the size of the foreign material has to be taken into account too, because it influences the ratio of the truncated nucleus volume to that of a sphere of equal size.

In Figure 2.2, the factor f is plotted against the angle θ for the case of a smooth, flat foreign surface. This angle ranges from 0° to 180°, depending on the "wetting" of the foreign particle by the units. A contact angle of 180° (point contact) corresponds to nonwettability or homogeneous nucleation with $f = 1$. When the angle θ is between 0° and 180°, the nucleation work is reduced by the "wetting" surface of the foreign particle. If $\theta \to 0^\circ$, the foreign particle is completely wetted and both the nucleation work and the formation of heterogeneous nuclei tend toward zero. This shows that the better the wetting, the smaller the volume of the truncated nucleus and the smaller the free-energy cost associated with its formation.

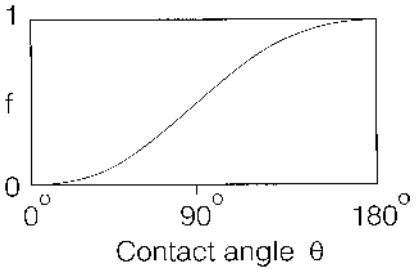

Figure 2.2. Factor f as a function of the contact angle.

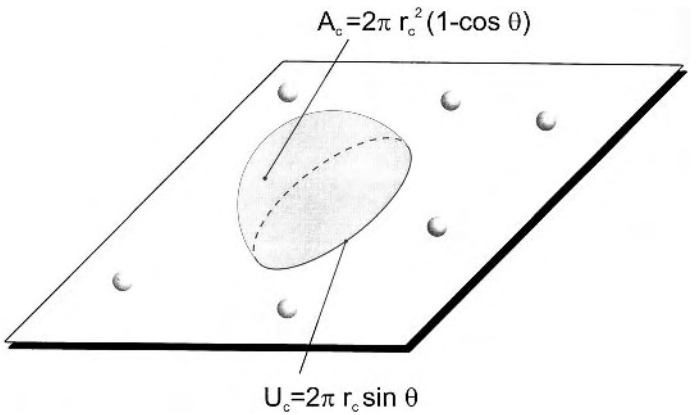

Figure 2.3. Schematic diagram of a nucleus on a solid surface.

The impact coefficient k in heterogeneous nucleation has to account for impingements from the bulk of the solution, which are proportional to the surface of the nucleus, A, as well as for impingements of units already adsorbed on the foreign surface, which increase with the circumference U_{surf} of the nucleus; see Figure 2.3. The total number of impacts is

$$k = U_{\text{surf}}\dot{n}_{\text{surf}} + A\dot{n}_v \tag{2.9}$$

The impact rate of units arriving from the volume can be described by a model already presented for units hitting a homogeneous nucleus:

$$\dot{n}_v = \tfrac{3}{4} D_{AB}(CN_A)^{4/3} \tag{2.10}$$

This rate is proportional to the diffusivity D_{AB} of units in the volume. On the other hand, surface diffusion is the decisive transport mechanism for units that arrive from the surface of the foreign particle, and the impact rate

$\dot{n}_{\text{surf}}$ can be derived from the laws of statistical thermodynamics for a two-dimensional problem [2.1]:

$$\dot{n}_{\text{surf}} = \frac{D_{\text{surf}}}{2\pi}(C_{\text{ad}}N_A)^{3/2} \tag{2.11}$$

In this equation, D_{surf} is the surface-diffusion coefficient of units moving on the foreign surface. According to Suzuki [2.3] and Schubert [2.1], it is given by

$$D_{\text{surf}} = \frac{1}{4d_m C_{\text{ad}} N_A}\sqrt{\frac{\pi k T N_A}{2\tilde{M}}} \tag{2.12}$$

Although this equation predicts physically impossible, nonfinite values of the surface diffusion for $C_{\text{ad}} \to 0$, it gives plausible results for common values of C_{ad}.

Next, expressions are needed for the surface A_c and the circumference U_c of a critical nucleus with radius r_c and the contact angle θ. The different geometries are depicted in Figure 2.3. The surface A_c of a critical nucleus can be calculated to be

$$A_c = 2\pi r_c^2(1-\cos\theta) = 2\pi\left(\frac{2\tilde{M}\gamma_{CL}}{\rho_C \nu R T \ln S_a}\right)^2(1-\cos\theta) \tag{2.13}$$

and the circumference U_c of such a nucleus can be expressed by

$$U_c = 2\pi r_c \sin\theta = 2\pi\left(\frac{2\tilde{M}\gamma_{CL}}{\rho_C \nu R T \ln S_a}\right)\sin\theta \tag{2.14}$$

Combining equations (2.1)–(2.3), (2.6), and (2.9)–(2.14) leads to the following expression for the rate of heterogeneous nucleation:

$$\begin{aligned} B_{\text{het}} = {} & \frac{1}{2\pi} a_{\text{for}} d_m \,\text{He}_{\text{ad}}(CN_A)^{7/3}\sqrt{\frac{f\gamma_{CL}}{kT}}V_m \\ & \times\left(\frac{(\sin\theta)D_{\text{surf}}}{r_c}\text{He}_{\text{ad}}d_m^{3/2}(CN_A)^{1/6} + 3\pi D_{AB}(1-\cos\theta)\right) \\ & \times\exp\left[-f\left(\frac{4}{3}\right)\pi\frac{\gamma_{CL}}{kT}r_c^2\right] \end{aligned} \tag{2.15}$$

The preexponential term can be divided into a contribution of impacts coming from the volume and another contribution that describes the impacts from the surface of the foreign particle on the circumference of the nucleus. The higher the concentration C, the more dominant is the volume contribution in comparison to that coming from the surface. This

is also the case if the adsorption constant He_{ad} or the surface diffusion coefficient D_{surf} is small.

The rate of heterogeneous nucleation depends on the same parameters as the rate of homogeneous nucleation (i.e., the supersaturation S_a, the concentration C, the surface tension γ_{CL}, the diffusivity D_{AB}, the equilibrium concentration C^*, and the molar density C_C) and also on the following, additional parameters:

- The volumetric surface a_{for} of foreign particles present in the solution
- The adsorption constant He_{ad}
- The contact angle θ or the factor f, which is a function of the contact angle
- The surface diffusion coefficient D_{surf}

We are not yet able to predict the contact angle θ and the adsorption constant He_{ad}, but some experiments have shown that the contact angle in aqueous systems is often in the range $40^\circ < \theta < 53^\circ$ or $0.038 < f < 0.1$, respectively. Schubert [2.1] carried out precipitation experiments with the reactants $Ba(OH)_2$ and H_2SO_4 in the presence of SiO_2, Al_2O_3, and TiO_2 in the nanometer range. The particles were added in order to investigate their influence on the rate of heterogeneous nucleation. The volumetric surface a_{for} of the foreign particles was varied between 5×10^3 and $2.5 \times 10^5\ m^2/m^3$. In all cases, the rate of heterogeneous nucleation was proportional to the surface a_{for} of foreign particles. When a_{for} is smaller than $10^4\ m^2/m^3$, it is necessary to take into account the basic level of SiO_2 particles that is always present, even in ultrapure water ($a_{for} \approx 2500\ m^2/m^3$). It is important to mention that it is not the number of foreign particles but their volumetric surface a_{for} that is the decisive parameter for heterogeneous nucleation.

2.2. Application

In Sec. 2.1, the theoretical background of heterogeneous nucleation was discussed. Comparison with experimental results is a good tool not only for evaluating this theory but also for providing a set of rules on how to control nucleation and, therefore, the final product quality.

When carrying out nucleation experiments, it is expedient to plot the nucleation rate against $1/(\ln S_a)^2$. In Figure 2.4, the rate of heterogeneous nucleation, B_{het}, is plotted versus $1/(\ln S_a)^2$ for $BaSO_4$ and SiO_2 particles (Fig. 2.4a), TiO_2 particles (Fig. 2.4b), and Al_2O_3 particles (Fig. 2.4c). In all cases, the volumetric surface of the added foreign particles was $a_{for} = 1.5 \times 10^5\ m^2/m^3$. Additional experiments were carried out without the addition of foreign particles. The figures show that the nucleation rate increases with the surface a_{for} for a given supersaturation. When the critical

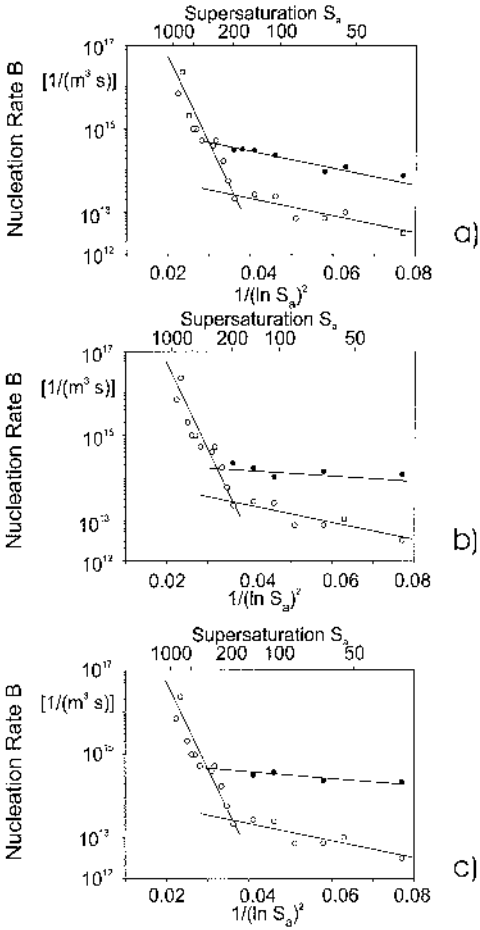

Figure 2.4. Experimentally determined rate of heterogeneous nucleation for $BaSO_4$ and SiO_2 (a), TiO_2 (b), and Al_2O_3 (c). o = without the addition of foreign particles.

supersaturation $S_{a,\mathrm{crit}}$ is exceeded, the rate of homogeneous nucleation is higher than the rate of the heterogeneous nucleation mechanism. This critical supersaturation depends *inter alia* on the volumetric surface a_{for} of foreign particles. In Table 2.1, results of the parameter f, θ, and $S_{a,\mathrm{crit}}$ are given for different substances of the foreign particles. The adsorption constant of $BaSO_4$ on SiO_2 was determined to be $\mathrm{He_{ad}} = 1.1 \times 10^{-8}$ at 25°C. This constant decreases with increasing temperature, as can be seen in Figure 2.5, in which $\mathrm{He_{ad}}$ is plotted against the temperature.

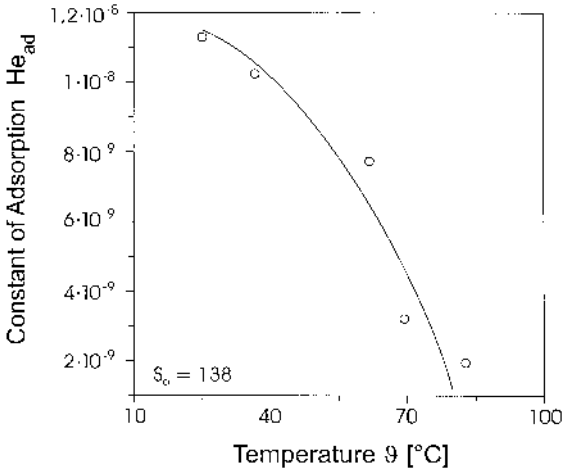

Figure 2.5. Experimentally determined adsorption constant of $BaSO_4$ on SiO_2 as a function of temperature.

Table 2.1. Experimentally Determined Values of the Parameters f, θ, and $S_{a,\text{crit}}$

Solid substance	f	θ	$S_{a,\text{crit}}$
SiO_2	0.102	52.83°	322
TiO_2	0.034	38.85°	263
Al_2O_3	0.041	40.88°	330

It has been shown that the rate of heterogeneous nucleation depends on the following heterogenity parameters:

- Volumetric surface a_{for} of foreign particles
- Contact angle θ or the factor f
- Adsorption constant He_{ad}

In Figures 2.6, 2.7, and 2.8 the supersaturation $\Delta C/C_c$ is plotted against the dimensionless solubility for a certain set of parameters: Whereas in Figure 2.6, the volumetric surface area is varied, Figure 2.7 shows plots for different adsorption constants, and in Figure 2.8, one may see a variation of the f factor (i.e., a change in contact angle). All figures are valid for the stoichiometric factor $\nu = 1$.

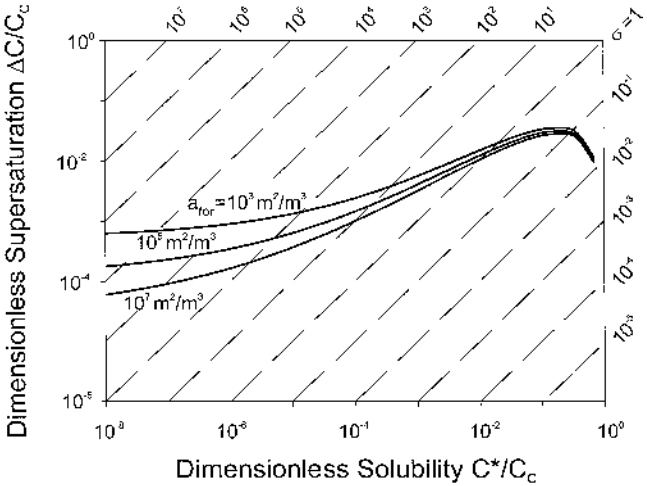

Figure 2.6. Metastable zone width of heterogeneous nucleation, valid for $B_{het} = 10^{12}\,m^{-3}s^{-1}$, $f = 0.1$, $He_{ad} = 10^{-9}$, $a_{for} = 10^3$, 10^5, and $10^7\,m^2/m^3$.

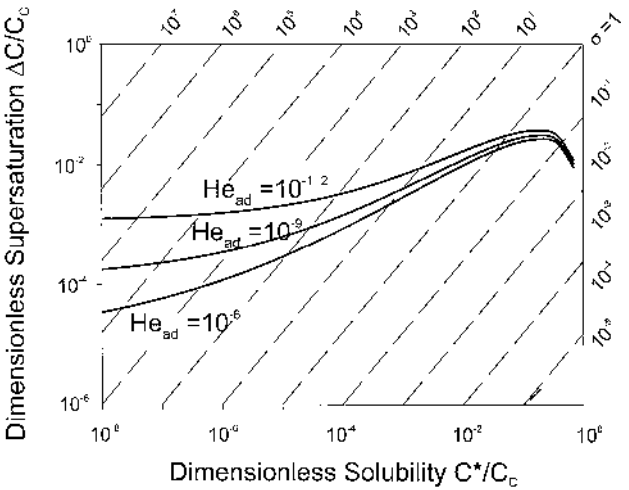

Figure 2.7. Metastable zone width of heterogeneous nucleation, valid for $B_{het} = 10^{12}\,m^{-3}s^{-1}$, $f = 0.1$, $a_{for} = 10^5\,m^2/m^3$, $He_{ad} = 10^{-6}$, 10^{-9}, and 10^{-12}.

In the range of high solubility ($C^*/C_C > 0.01$), the metastable zone width for the rate $B_{het} = 10^{12}\,m^{-3}s^{-1}$ is scarcely affected by the parameter a_{for} and He_{ad}. The smaller the factor f or the contact angle θ, the more the metastable zone width is reduced. With sparingly soluble substances

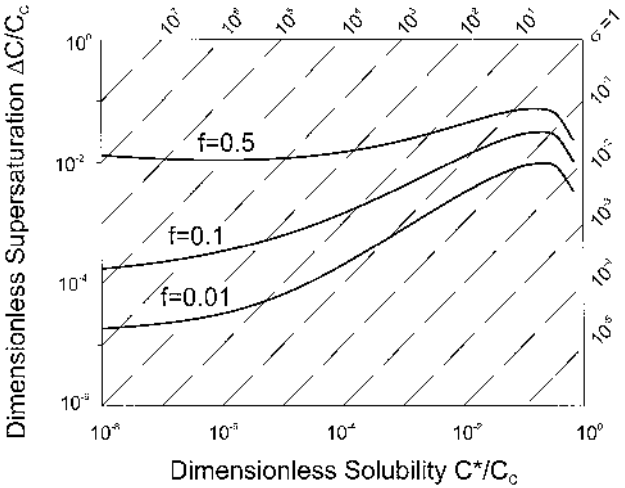

Figure 2.8. Metastable zone width of heterogeneous nucleation, valid for $B_{het} = 10^{12}\,m^{-3}s^{-1}$, $a_{for} = 10^{5}\,m^2/m^3$, $He_{ad} = 10^{-9}$, $f = 0.5$, 0.1, and 0.01.

($C^*/C_C < 10^{-5}$), the parameters a_{for}, He_{ad}, and θ have a strong influence on $\Delta C_{met,het}/C_C$. For the nucleation rate $B_{het} = 10^{12}\,m^{-3}s^{-1}$, the metastable zone width decrease with increasing values of a_{for} and He_{ad} but decreasing factors f or contact angle θ. Because these parameters are not known for a real solution, the metastable zone width is unpredictable for substances with a very low solubility. On the other hand, the equations may be useful for the seeding of solutions in order to obtain controlled nucleation. This can be done by the addition of foreign particles which can be characterized by the parameters a_{for}, He_{ad}, and f. When these added foreign particles are dominant with respect to nucleation in comparison to particles that are already in the solution, the nucleation process can be controlled. In combination with controlled growth, it would be possible to produce crystals with a desired specification.

3. SURFACE NUCLEATION ON CRYSTALS

In seeded batch crystallizers and in continuously operated crystallizers, a great number of crystals with the volumetric surface a_C[m^2 crystal surface/m^3 crystals] are present. The surface of such crystals is very smooth in molecular terms if the supersaturation is low ($\sigma < 0.01$) and the crystals are small in size in the absence of particle collisions. With increasing

supersaturation the probability of surface nucleation rises. There is some evidence in the literature that secondary nuclei that are not attrition fragments are formed either as preordered species or as clusters in the immediate solution vicinity of the crystal surface or on the crystal surface by dendritic growth and dendritic coarsening [3.1–3.8]. These mechanisms can lead to the formation of nuclei and/or the detachment of small dendrites from the crystal surface without any fluid dynamics or mechanical shear [3.1–3.4].

Surface nuclei are formed when the relative supersaturation $S_{\text{met},s}$ is exceeded. According to Nielsen [3.9], this supersaturation depends on the edge energy, γ_e, and the maximum difference in the free energy, $\Delta G_{\max,s}$:

$$\nu \ln S_{\text{met},s} = \pi \frac{\gamma_e^2 a^2}{kT \Delta G_{\max,s}} \tag{3.1}$$

With the approximation $a \approx d_m \approx (C_C N_A)^{-1/3}$ and the interfacial energy $\gamma_{CL} \approx \gamma_e / d_m$, the following equation is obtained:

$$\frac{\Delta G_{\max,s}}{kT} = \pi \frac{\gamma_{CL}^2 d_m^4}{(kT)^2 \nu \ln S_{\text{met},s}} \tag{3.2}$$

Again, the expression

$$\frac{\gamma_{CL} d_m^2}{kT} = K \ln\left(\frac{C_C}{C^*}\right) \tag{3.3}$$

is introduced for the interfacial tension γ_{CL}. Combining the last two equations gives

$$\frac{\Delta G_{\max,s}}{kT} \approx \pi \frac{[K \ln(C_C/C^*)]^2}{\nu \ln S_{\text{met},s}} \tag{3.4}$$

The rate of surface nucleation, B_s, in nuclei per square meter crystal surface and per second depends on the diffusivity, D_{AB}, and the nucleation energy, $\Delta G_{\max,s}$, according to [3.9, 3.10] (compare with page 73)

$$B_s = \frac{D_{AB}}{d_m^4} \exp\left(-\frac{\Delta G_{\max,s}}{kT}\right) \tag{3.5}$$

or

$$B_s \approx \frac{D_{AB}}{d_m^4} \exp\left(-\pi \frac{[K \ln (C_C/C^*)]^2}{\nu \ln S_{\text{met},s}}\right) \tag{3.6}$$

In general, the following relationship is obtained:

$$\frac{B_s d_m^4}{D_{AB}} = f\left(\frac{C^*}{C_C}, \sigma_{\text{met},s} = \frac{\Delta C_{\text{met},s}}{C^*} = S_{\text{met},s} - 1, \nu\right) \tag{3.7}$$

With increasing supersaturation S, the number of surface nucleation events rises rapidly with the consequence that the surface gets rougher and rougher. This roughening is accompanied by another effect that supports this process—the decrease in the critical radius r_s^* of surface nucleation according to

$$\frac{r_s^*}{d_m} = \frac{\gamma_{CL} d_m^2}{kTv \ln S} = K\left(\frac{\ln(C_C/C^*)}{\nu \ln S}\right) \tag{3.8}$$

With increasing supersaturation, the number of surface nuclei increases and the radius of a nucleus decreases. The probability that a nucleus is formed on another nucleus (nucleus above nucleus) is very high and this effect leads to polynuclear growth, which can be derived from the rate of surface nucleation. According to Nielsen [3.9; see also Ref. 3.10], the rate of polynuclear growth, v_{PN}, is given by

$$\begin{aligned} v_{\text{PN}} &= \frac{D_{AB}}{3d_m}\left(\frac{\Delta C}{C_C}\right)^{2/3} \exp\left(-\frac{\Delta G_{\max,s}}{kT}\right) \\ &= \frac{D_{AB}}{3d_m}\left(\frac{\Delta C}{C_C}\right)^{2/3} \exp\left(-\pi \frac{[K \ln(C_C/C^*)]^2}{\nu \ln S}\right) \end{aligned} \tag{3.9}$$

It is important to mention that the rate v_{PN} increases rapidly with supersaturation because this growth is an activated process. This rapid growth is described in the literature as broomlike, spikelike, skeletal, or dendritic [3.5, 3.6]. Other authors speak of growth instability and the formation of step bunches that grow together. Dendrites that grow very fast at the top can be dissolved at the bottom with respect to the concentration field. Tiny needles can be detached from the crystal surface and can act as secondary nuclei in the supersaturated solution. Some authors speak of catalytic secondary nucleation. The exact mechanisms are not known and it is, therefore, difficult to develop a quantitative treatment. However, it is possible to derive a relatively narrow range of supersaturation in which surface nucleation and polynuclear growth become very fast and the radius r_s^* of a stable surface nucleus is only 5–10 times the unit diameter d_m. In Figure 3.1, the metastable zone width $\Delta C_{\text{met},s}/C_C$ based on the molar density C_C of the crystal is plotted against the dimensionless solubility, C^*/C_C, for different rates of surface nucleation. The curves are valid for the following:

- Molecules ($\nu = 1$) with
- Diameter $d_m = 5 \times 10^{-10}$ m and
- Diffusivity $D_{AB} = 10^{-9}$ m^2/s

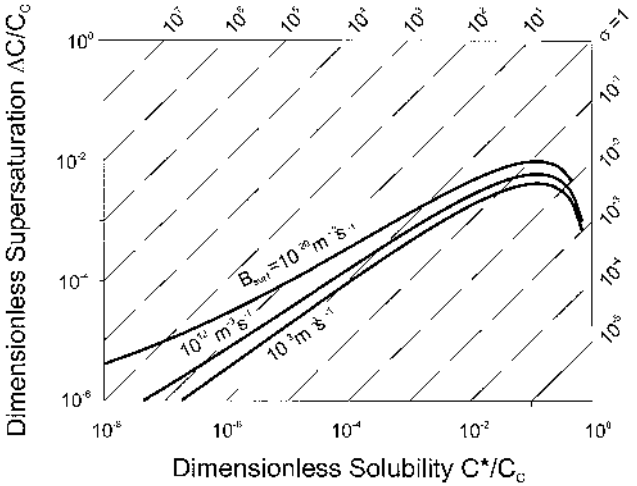

Figure 3.1. Dimensionless metastable supersaturation as a function of dimensionless solubility for secondary nucleation.

This diffusivity is a mean value for small molecules in solutions of low viscosity ($\eta_L = 1\,\text{mPa} \cdot \text{s}$). All calculations are carried out with concentrations C and the activity coefficient $\gamma = 1$. The curves are valid for $K = 0.414$. As can be seen, the rate of surface nucleation rises rapidly with increasing supersaturation. Figure 3.2 shows the same kind of diagram, in which the dimensionless supersaturation $\Delta C/C_C$ is plotted against the dimensionless solubility, C^*/C_C. Curves are depicted for the ratio $2r_s^*/d_m$ of the diameter $2r_s^*$ of a stable nucleus based on the molecule diameter d_m. All these curves make it possible to define a borderline between an area of solubility and supersaturation, where activated nucleation is dominant, and the area below, where activated nucleation is so weak that new nuclei are formed only as attrition fragments; see Chapter 5. The importance of this statement for the mean crystal size in industrial crystallizers will be shown later. In any case, at $\Delta C > \Delta C_{\text{met},s}$, a large number of nuclei are formed, either by cluster formation or dendrite detachment. If a certain portion E of surface nuclei is detached to become volume nuclei, the volumetric rate of surface nucleation, B_{surf}, in nuclei/(m^3 s), should be proportional to B_s and the volumetric area a_c (a_c is the surface of all crystals divided by the volume of the suspension). In this case, the following is obtained with the efficiency factor E ($0 < E < 1$):

$$B_{\text{surf}} = EB_s a_c \tag{3.10}$$

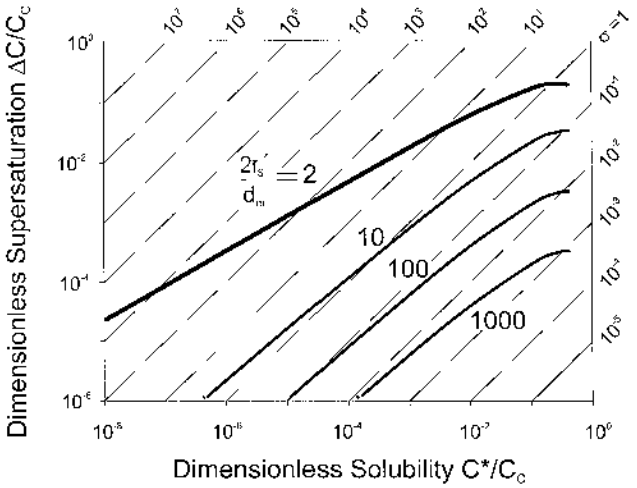

Figure 3.2. Dimensionless supersaturation against the dimensionless solubility with curves of constant ratios of the radius r_s^* of a surface nucleus and the molecule diameter d_m.

or with the Sauter mean diameter of crystals, L_{32}, and the crystal holdup φ_T,

$$B_{\text{surf}} = E\frac{6\varphi_T}{L_{32}}B_s \tag{3.11}$$

With coarse crystalline products ($0.1 < L < 1$ mm), the volumetric area $a_c = 6\varphi_T/L_{32}$ is of the order of magnitude of about $10^3\,\text{m}^2/\text{m}^3$–$10^4\,\text{m}^2/\text{m}^3$. This means that the volumetric area a_c does not have a strong influence on the metastable zone width $\Delta C_{\text{met},s}$.

4. COMPARISON OF NUCLEATION RATES

In general, rates of activated nucleation, B_{hom}, B_{het}, and B_{surf} or, in general, B, can be described by

$$B = FE \tag{4.1}$$

where F is the preexponential factor and E is an exponential term, originating from the physical derivations described in the above sections. In an attempt to compare the three mechanisms of activated nucleation, let us first consider the exponential term E, which can be written as

$$E = \exp\left[-f\frac{4\pi}{3}\frac{\gamma_{CL}d_m^2}{kT}\left(\frac{r_c^*}{d_m}\right)^a\right] \tag{4.2}$$

In the case of three-dimensional nucleation (homogeneous and heterogeneous nucleation), the exponent a is $a = 2$. With the corresponding equation for the radius r_c^* of a critical nucleus, we obtain

$$E = \exp\left(-f\frac{4\pi}{3}\frac{(\gamma_{CL}d_m/kT)^2}{(\nu \ln S_a)^2}\right) \tag{4.3}$$

or using $\gamma_{CL}d_m^2/kT = K\ln(C_C/C^*)$, we get

$$E = \exp\left(-f\frac{4\pi}{3}\frac{[K\ln(C_C/C^*)]^3}{(\nu \ln S_a)^2}\right) \tag{4.4}$$

For homogeneous nucleation, $f = 1$. The factor $f \approx 0.058$, which is valid for $\theta = 45^\circ$, may be an approximate value at high supersaturation for heterogeneous nucleation in order to begin to estimate nucleation rates.

Surface nucleation leads to two-dimensional nuclei with a height of only one unit. With $a = 1$ in equation (4.2) and after some adjustment of the factor $4\pi/3$, which is necessary because surface nuclei are assumed to be of cylindrical and not spherical shape, we obtain, according to Sec. 3,

$$E = \exp\left(-\pi\frac{(\gamma_{CL}d_m^2/kT)^2}{\nu \ln S_a}\right) = \exp\left(-\pi\frac{[K\ln(C_C/C^*)]^2}{\nu \ln S_a}\right) \tag{4.5}$$

It can be seen that for three-dimensional nucleation, the exponential term E is a much stronger function of supersaturation than it is for two-dimensional nucleation. It should be noted that the exponent of the denominator is 2 in the case of three-dimensional nucleation and only 1 for the two-dimensional case. The exponents of the expression $K\ln(C_C/C^*)$ are also different (3 for three-dimensional and 2 for two-dimensional nucleation).

The preexponential factor F according to Schubert, using the expression of Kind for the impingements from the volume, is given by

$$\begin{aligned} F = {} & \frac{3}{4}\frac{D_{AB}}{d_m^5}\left(\frac{C}{C_C}\right)^{7/3}\sqrt{\frac{f\gamma_{CL}d_m^2}{kT}}(a_{\text{for}}d_m)(1-\cos\theta)\text{He}_{\text{ad}} \\ & \times\left(1+\frac{2}{3\pi r_c}\frac{\sin\theta}{1-\cos\theta}\frac{D_{\text{surf}}}{D_{AB}}(\text{He}_{\text{ad}}d_m)^{3/2}(CN_A)^{1/6}\right) \end{aligned} \tag{4.6}$$

or, using the expression of Söhnel and Garside [4.1] combined with the result of Schubert, F can be written in the following manner:

$$F = \frac{3}{4}\frac{D_{AB}}{d_m^5}\sqrt{\frac{4\Delta G^*_{\text{hom}}}{3\pi k T i_c^{*2}}}(a_{\text{for}}d_m)(1-\cos\theta)\text{He}_{\text{ad}} \times \left(1+\frac{2}{3\pi r_c}\frac{\sin\theta}{1-\cos\theta}\frac{D_{\text{surf}}}{D_{AB}}(\text{He}_{\text{ad}}d_m)^{3/2}(CN_A)^{1/6}\right) \tag{4.7}$$

Whereas the term for impingements from the foreign surface to the cluster is the same in equations (4.7) and (4.6), it should be noted that the expressions for the impingements from the volume differ by a factor of $(C/C_C)^{7/3}$. This is due to the fact that Söhnel and Garside used the expression of Nielsen for the determination of the homogeneous nucleation rate, who used a one-dimensional diffusion, which equalled the mean displacement with the size of one ion diameter and interpreted the reciprocal of the time with a unimolecular reaction rate constant to yield the following form of k:

$$k = 2\frac{D_{AB}}{d_m^5} \tag{4.8}$$

which does not take into account the amount of material in the solution. Although this result is for fairly high soluble systems in surprisingly good accordance with the results obtained using the expression containing the concentration of monomers in the solution, it has to be noted that for sparingly soluble substances, the preexponential factor may vary several orders of magnitude depending on whether the expression of Nielsen or Kind is used for the rate of impingements.

Considering that the preexponential term is the product of the impact coefficient, the Zeldovic factor, and the number concentration of monomers [see Eqs. (1.9) and (2.2)] and, in the cases of heterogeneous and activated secondary nucleation, also of the amount of surface area of solid matter within the solution, the general expression of F given for heterogeneous nucleation in equations (4.6) and (4.7) can be transformed into the factors for homogeneous and activated secondary nucleation under certain assumptions.

In the case of homogeneous nucleation the contact angle is $\theta = 180^\circ$. This means that $\sin\theta = 0$, $\cos\theta = -1$, and $f = 1$. With the following assumptions:

- $a_{\text{for}} = 1/d_m$ (all molecular units represent the "volumetric area") or $a_{\text{for}}d_m = 1$
- $\text{He}_{\text{ad}} = 1$ (there is no longer an interfacial area between a solid and a liquid phase, adsorption loses its physical significance and He_{ad} can, therefore, be omitted)

the factor F for homogeneous nucleation becomes

$$F = \frac{3}{2}\frac{D_{AB}}{d_m^5}\left(\frac{C}{C_C}\right)^{7/3}\sqrt{\frac{\gamma_{CL}d_m^2}{kT}} = \frac{3}{2}\frac{D_{AB}}{d_m^5}\left(\frac{C}{C_C}\right)^{7/3}\sqrt{K\ln(C_C/C^*)} \tag{4.9}$$

according to Kind [1.9] or

$$F = \frac{D_{AB}}{d_m^5}\frac{2}{3.32}\frac{(\nu\ln S_a)^2}{[K\ln(C_C/C^*)]^{3/2}} \tag{4.10}$$

according to Söhnel and Garside [4.1].

In the case of surface nucleation, units impinging on the surface of a crystal present in the system are decisive for nucleation, and the deviation from equilibrium of the size distribution of the embryos in the solution no longer plays a role. When the factor Z is omitted (or $Z = 1$), the preexponential factor F becomes

$$F = \frac{3}{2}\frac{D_{AB}}{d_m^4}a_c E = \frac{3}{2}\frac{D_{AB}}{d_m^4}\frac{6\varphi_T}{L_{32}}E \tag{4.11}$$

or

$$F = 9E\frac{D_{AB}}{d_m^4 L_{32}}\varphi_T \tag{4.12}$$

So far, the analogy of the nucleation rates has been discussed. For practical applications, however, it is not only interesting to see the equalities but also to know under which process conditions which nucleation mechanism dominates. This is especially necessary if one tries to influence the product quality by adding foreign particles to the solution, thus attempting to control the nucleation event. In this case, it is useful to know whether the homogeneous nucleation rate is dominant (i.e., higher than the rate of heterogeneous nucleation at a given amount of foreign surface). Using equations (2.15) and (1.21), for the ratio of heterogeneous to homogeneous nucleation

$$\begin{aligned}\frac{B_{\text{het}}}{B_{\text{hom}}} &= 0.5\sqrt{f}a_{\text{for}}d_m(1-\cos\theta)\\ &\times \text{He}_{\text{ad}}\left(1+\frac{D_{\text{surf}}}{D_{AB}}\frac{\sin\theta}{1-\cos\theta}\frac{2(\text{He}_{\text{ad}}d_m)^{3/2}}{3\pi r_c}(CN_A)^{1/6}\right)\\ &\times \exp\left[(1-f)\frac{16}{3}\pi\left(\frac{\gamma_{CL}}{kT}\right)^3 V_m^2\frac{1}{(\nu\ln S)^2}\right]\end{aligned} \tag{4.13}$$

In Figure 4.1, the ratio of heterogeneous to homogeneous nucleation is plotted as a function of dimensionless supersaturation and dimensionless

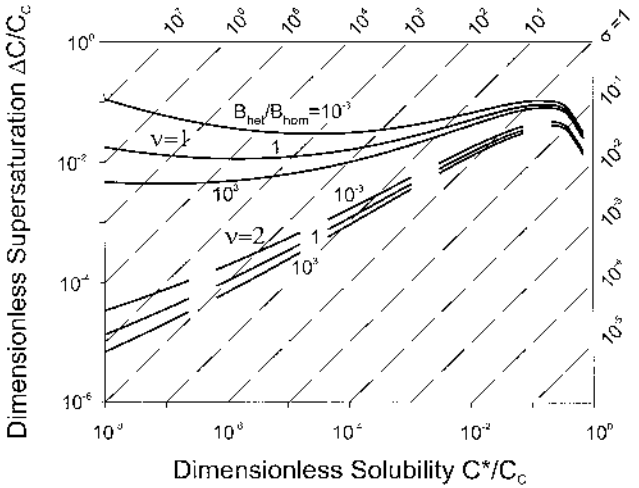

Figure 4.1. Ratios of heterogeneous to homogeneous nucleation rates.

solubility for the case of a volumetric surface area of $a_{for} = 10^5\,m^2/m^3$ and an adsorption constant of $He_{ad} = 10^{-9}$. It can be seen that in the case of molecular substances (i.e., $\nu = 1$), the dimensionless supersaturation has to be much higher than for dissociated systems in order to obtain an equality between homogeneous and heterogeneous nucleation. On the other hand, it can also be seen that for $\nu = 2$, the range in which the change between heterogeneously and homogeneously dominated nucleation occurs is fairly small compared to the same range at the same dimensionless solubility for $\nu = 1$. This means that for substances that dissociate, it is much more difficult to control the process exactly.

The fact that it is possible to compare nucleation rates facilitates the selective control of the nucleation event and, therefore, the final product quality. A simple map as shown in Figure 4.1 makes it possible to readily estimate the operation condition needed either to force homogeneous nucleation, which may be desired for the production of very fine materials, or to prevent, in particular, this mechanism of nucleation, which can make the whole of an industrial crystallizer oscillate and therefore cause it to become out of control, with the effect that the final product does not meet the requirements at all. Nevertheless, the event of nucleation cannot be viewed separately, because for an industrial product, the final quality (e.g., purity, shape, and, most importantly, particle size and size distribution) is decisive (see Chapter 7). Therefore, it is always necessary to take the three mechanisms

- Nucleation
- Agglomeration, and
- Growth

into account at one time and usually also at one place within the crystallizer, especially when supersaturation is high. In this case, nucleation often occurs according to the homogeneous mechanism, growth is usually diffusion controlled and, because of the very small particles agglomeration, follows a perikinetic law. It is important to stress that in this case, the rate of all three mechanisms is determined by the diffusion process and that it will be hard to distinguish among them easily. However, only by controlling the first step within a crystallization process—the nucleation event—which can be achieved by correctly controlling the driving force (i.e., supersaturation) can the final product quality be achieved.

REFERENCES

[0.1] P. Nore and A. Mersmann, Batch precipitation of barium carbonate, *Chem. Eng. Sci.*, *48*(17): 3083 (1993).

[1.1] M. Volmer and A. Weber, Keimbildung in übersättigten Lösungen, *Z. Phys. Chem.*, *119*: 277 (1926).

[1.2] M. Volmer, *Kinetik der Phasenbildung*, Steinkopf, Dresden (1939).

[1.3] R. Becker and W. Döring, Kinetische Behandlung der Keimbildung in übersättigten Dämpfen, *Ann. Phys.*, *24*(5): 719 (1935).

[1.4] L. Farkas, Keimbildungsgeschwindigkeit in übersättigten Dämpfen, *Z. Phys. Chem.*, *A125*: 236 (1927).

[1.5] Y. B. Zeldovich, On the theory of new phase formation: Cavitation, *Zhur. Eksper. Teor. Fiz.*, *12*: 525 (1942); translated in *Selected Works of Yakov Borisovich Zeldovich, Volume I, Chemical Physics and Hydrodynamics* (J. P. Osterik, G. I. Barenblatt, and R. A. Sunayev, eds.), Princeton University Press, Princeton, NJ (1992).

[1.6] J. Frenkel, *Kinetic Theory of Liquids*, Dover; New York, Chap. 7. (1955).

[1.7] R. Lacmann, Volmersche Keimbildungstheorie, in *Kinetik metallurgischer Vorgänge bei der Stahlherstellung* (W. Dah., ed.), Verlag Stahleisen, Düsseldorf (1972).

[1.8] M. Kind and A. Mersmann, Methoden zur Berechnung der homogenen Keimbildung aus wässrigen Lösungen, *Chem. Ing. Techn.*, *55*: 270 (1983).

[1.9] M. Kind, Über die Übersättigung während der Kornkristallisation aus Lösungen, Thesis, Technical University of Munich (1989).
[1.10] A. Mersmann, Calculation of interfacial tensions, *J. Cryst. Growth*, *102*: 841 (1990).
[1.11] H. Reiss, The treatment of droplike clusters by means of the classical phase integral in nucleation theory, *J. Statist. Phys.*, *2*: 83 (1970).
[1.12] H. Reiss and J. L. Katz, Resolution of the translation-rotation paradox in the theory of irreversible condensation, *J. Chem. Phys.*, *46*: 2496 (1967).
[1.13] H. Reiss and M. Shugard, On the composition of nuclei in binary Systems, *J. Chem. Phys.*, *65*: 5280 (1976).
[1.14] H. Reiss, J. L. Katz, and E. R. Cohen, Translation–rotation paradox in the theory of nucleation, *J. Chem Phys.*, *48*: 5553 (1968).
[1.15] H. Reiss, A. Tabazadeh, and J. Talbot, Molecular theory of vapor phase nucleation: The physically consistent cluster, *J. Chem. Phys.*, *92*: 1266 (1990).
[1.16] H. M. Ellberly, C. L. Weakliem, and H. Reiss, Towards a molecular theory of vapor phase nucleation. I. Identification of the average embryo, *J. Chem. Phys.*, *95*: 9209 (1991).
[1.17] H. M. Ellberly and H. Reiss, Towards a molecular theory of vapor-phase nucleation. II. Fundamental treatment of the cluster distribution, *J. Chem. Phys.*, *97*: 5766 (1992).
[1.18] C. L. Weakliem and H. Reiss, Towards a molecular theory of vapor phase nucleation. III. Thermodynamic properties of argon clusters from Monte Carlo simulations and a modified liquid drop theory, *J. Chem. Phys.*, *99*: 5374 (1993).
[1.19] C. L. Weakliem and H. Reiss, Towards a molecular theory of vapor phase nucleation. IV. Rate theory using the modified liquid drop model, *J. Chem. Phys.*, *101*: 2398 (1994).
[1.20] P. Harrowell and D. W. Oxtoby, A molecular theory of crystal nucleation from the melt, *J. Chem. Phys.*, *80*: 1639 (1984).
[1.21] D. W. Oxtoby and R. Evans, Nonclassical nucleation theory for the gas–liquid transition, *J. Chem. Phys.*, *89*: 7521 (1988).
[1.22] X. C. Zeng and D. W. Oxtoby, Gas–liquid nucleation in Lennard–Jones fluids, *J. Chem. Phys.*, *94*: 4472 (1991).
[1.23] X. C. Zeng and D. W. Oxtoby, Binary homogeneous nucleation theory for the gas–liquid transition: A nonclassical approach, *J. Chem. Phys.*, *94*: 5940 (1991).
[1.24] D. W. Oxtoby, Homogeneous nucleation: Theory and experiment, *J. Phys. Cond. Matter*, *4*: 7627 (1992).
[1.25] V. Talanquer and D. W. Oxtoby, Dynamic density functional theory of gas–liquid nucleation, *J. Chem. Phys.*, *100*: 5190 (1994).

[1.26] V. Talanquer and D. W. Oxtoby, Nucleation of bubbles in binary fluids, *J. Chem. Phys.*, *102*: 2156 (1995).
[1.27] A. Laaksonen and D. W. Oxtoby, Gas–liquid nucleation of nonideal binary mixtures. I. A density funtional study, *J. Chem. Phys.*, *102*: 5803 (1995).
[1.28] G. Narisihman and E. Ruckenstein, A new approach for the prediction of the rate of nucleation in liquids, *J. Colloid Interf. Sci.*, *128*: 549 (1989).
[1.29] B. Nowakowski and E. Rukenstein, Rate of nucleation in liquids for FCC and icosahedral clusters, *J. Colloid Interf. Sci.*, *139*: 500 (1990).
[1.30] E. Ruckenstein and B. Nowakowski, A kinetic theory of nucleation in liquids, *J. Colloid Interf. Sci.*, 137: 583 (1990).
[1.31] B. Nowakowski and E. Ruckenstein, A kinetic approach to the theory of nucleation in gases, *J.Chem. Phys.*, *94*: 1397 (1991).
[1.32] M. Angerhöfer, Untersuchungen zur Fällungskristallisation von Bariumsulfat, Thesis, TU Munich (1993).
[2.1] H. Schubert, Keimbildung bei der Kristallisation schwerlöslicher Stoffsysteme, Dissertation, *TU München* (1998).
[2.2] M. Blander and J. L. Katz, Bubble nucleation in liquids, *AICHE J.*, *21*: 833 (1975).
[2.3] M. Suzuki, Adsorption Enginering, *Chemical Engineering Monographs*, Vol. 25, Elsevier, Amsterdam (1990).
[2.4] A. S. Myerson, P. Y. Lo, Y. C. Kim, and R. Ginde, Diffusion, viscosity and cluster formation in metastable solutions, In *Proc. 11th Symp. on Industrial Cristallization* (A. Mersmann, ed.), pp. 847–852 (1990).
[2.5] J. J. P. Valeton, Wachstum und Auflösung der Kristalle, *Z. Kristallogr.*, *59*: 135, 335 (1923); *60*: 1 (1924).
[2.6] D. E. Temkin, *Crystallization Processes*, Consultants Bureau, New York, p. 15 (1964).
[2.7] P. Bennema, J. Boon, C. van Leeuwen, and G. H. Gilmer, Confrontation of the BCF theory and computer simulation experiments with measured (R/σ) curves, *Krist. Technol.*, *8*: 659 (1973).
[2.8] G. H. Gilmer and P. Bennema, Simulation of crystal growth with surface diffusion, *J. Appl. Phys.*, *43*: 1347 (1972).
[2.9] A. Pakter, A. Alleem, P. Chauhan, and S. C. Uppalandini, The precipitation of sparingly soluble metal salts from aqueous solution: Heterogeneous nucleation numbers at low to intermediate supersaturation, *Cryst. Res. Technol.*, *16*: 1419 (1981).
[3.1] E. G. Denk, Fundamental studies in secondary nucleation, Ph.D. thesis, Tufts University, Medford, USA (1970).

[3.2] E. G. Denk and G. D. Botsaris, Fundamental studies in secondary nucleation from solution, *ICC6-3* (1971).
[3.3] M. G. Kilya, *Sov. Phys. Cryst.*, 1: 456 (1956).
[3.4] D. D. Saratovkin, *Dentritic Crystallization*, Consultants Bureau, p. 64 (1959).
[3.5] E. G. Cooke, The influence of added impurities on the growth and nucleation of sodiumchloride, *Kristall und Technik*, 1: 119 (1966).
[3.6] R. F. Strickland-Constable, *Kinetics and Mechanisms of Crystallization*, Academic Press, London (1968).
[3.7] N. A. Clontz and W. L. McCabe, *Chem. Eng. Prog., Symp. Ser.*, 118 (1972).
[3.8] M. H. Kind, Über die Übersättigung während der Kornkristallisation aus Lösungen, Ph.D. thesis, Technische Universität München (1989).
[3.9] A. E. Nielsen, *Pure Appl. Chem.*, *53*: 2025 (1981).
[3.10] J. A. Dirksen and T. A. Ring, Fundamentals of Crystallisation-kinetic effects on particle size distribution and morphology, *Chem. Eng. Sci.*, *46*: 2389 (1991).
[4.1] Söhnel and J. Garside, *Precipitation: Basic Principles and Applications*, Butterworth–Heinemann, Boston (1992).

3
Crystal Growth

A. MERSMANN, A. EBLE, AND C. HEYER Technische Universität München, Garching, Germany

The growth of crystals in a supersaturated solution is a very complex process that has not been well understood up to now. The reason for this is that many subsequent steps have to take place before a growth unit from the bulk solution is incorporated into the crystal lattice. Only a few of these steps are sufficiently understood to allow a predictive calculation of growth rates. Moreover, a variety of growth units (atoms, molecules, ions, hydrated solute molecules, dimers, trimers, polymers, clusters, etc.) exists depending on the crystallizing system and the solvent, which complicates the situation even more. When dealing with crystal growth of an ionizing solute, the following steps can be distinguished according to Mullin [0.1]:

1. Bulk diffusion of solvated ions through the diffusion boundary layer
2. Bulk diffusion of solvated ions through the adsorption layer
3. Surface diffusion of solvated or unsolvated ions
4. Partial or total desolvation of ions
5. Integration of ions into the lattice
6. Counterdiffusion through the adsorption layer of the water released
7. Counterdiffusion of water through the boundary layer

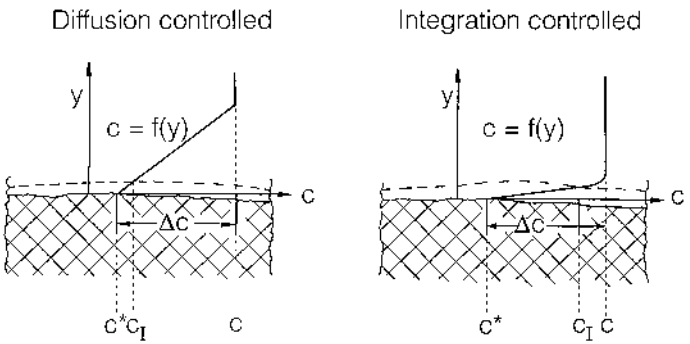

Figure 0.1. Concentration profiles for growth that is limited by diffusion or integration.

In accordance with this list, diffusion and reaction steps, such as dissociation and integration in a kink or at a step, play a certain role. The slowest of these subsequent steps are rate determining. In the more universal model of Berthoud [0.2] and Valeton [0.3], a crystal surface grows in such a way that units (atoms, molecules, ions) in a supersaturated solution (or generally in a supersaturated fluid) are first transported by diffusion and convection and then built into the surface of the crystal by integration or an integration reaction, with the supersaturation, ΔC or Δc, being the driving force. Depending on the system, state of flow, and supersaturation, the first or second step can determine the entire process, or both steps can control growth to different extents. This is demonstrated by Figure 0.1, in which a crystal surface and a continuous solution are represented with concentration profiles of the solute.

Accordingly, the entire concentration gradient, $\Delta c = c - c^*$, is divided into two parts. The first part, $c - c_I$, within a diffusive–convective layer causes diffusive–convective transport, whereas the second, $c_I - c^*$ (I is the interface), is decisive for the integration reaction within a reaction boundary layer. For growth that is completely determined by diffusion and convection, $c_I - c^* \ll c - c_I$ or $(c_I - c^*)/(c - c_I) \ll 1$. On the other hand, $(c - c_I)/(c_I - c^*) \ll 1$, when crystal growth is controlled by the integration reaction. The mass flux density, $\dot{m}$, directed toward the crystal surface is

$$\dot{m} = k_d(c - c_I) = k_r(c_I - c^*)^r \tag{0.1}$$

Here, k_d is the mass transfer coefficient, k_r is the reaction rate constant, and r is the order of the integration reaction. The temperature dependency of the

reaction rate constant is generally described according to the Arrhenius formulation:

$$k_r = k_{r0} \exp\left(-\frac{\Delta E_r}{RT}\right) \tag{0.2}$$

where k_{r0} is the reaction constant and ΔE_r is the activation energy.

Instead of describing crystal growth by mass flux density, $\dot{m}$ (with dimensions of kg/m^{2}s), it can be described by the displacement rate, v, of a crystal surface [referred to as v_{hkl} for surfaces indexed with (*hkl*), etc.] or the overall crystal growth rate, $G = dL/dt$ (both with dimensions of m/s). The overall linear crystal growth rate, G, refers, in principle, to any characteristic length, L, where a diameter of the crystal is generally used. When r is the radius and $L = 2r$, the diameter of a sphere corresponding to geometrically similar crystals with the volume shape factor $\alpha = V_p/L^3$ and the surface shape factor $\beta = A_p/L^2$, the following conversion is obtained between the mass flux density, $\dot{m}$, the mean displacement rate, $\bar{v}$, of the crystal surfaces, and the crystal growth rate $G = 2\bar{v}$:

$$\dot{m} = \frac{1}{A_p}\frac{dM}{dt} = \frac{6\alpha}{\beta}\rho_C \frac{dr}{dt} = \frac{6\alpha}{\beta}\rho_C \bar{v} = \frac{3\alpha}{\beta}\rho_C G \tag{0.3}$$

Each of the given definitions is useful for a different approach to crystal growth, such as from a mass balance, an observation of the crystal size distribution with time, or a focus on the crystal shape. To calculate the growth rate a priori, the concentration profile according to Figure 0.1 and the corresponding coefficients would have to be known, which is not the case. Before reflecting on the general case of a superposition of mass transport and integration mechanisms, two special regimes should be considered first: the control of crystal growth by diffusion/convection or by the integration reaction.

1. DIFFUSION-CONTROLLED CRYSTAL GROWTH

When the integration reaction is indefinitely fast, in other words, $k_r \to \infty$, crystal growth is determined by the diffusive–convective transport of units. In this case, $c - c_I \approx c - c^* = \Delta c$ and the following is obtained when the mass flux density is low:

$$\dot{m} = k_d \Delta c \tag{1.1}$$

or

$$G = \frac{\beta}{3\alpha} k_d \frac{\Delta c}{\rho_C} \tag{1.2}$$

For the mass transfer coefficients k_d provided in the literature and the equations given for them, it must be determined whether they concern equimolar diffusion or mass transfer to a semipermeable interface. Moreover, it is necessary to find out whether transport is merely diffusive or both diffusive and convective. The difference increases with mass flux density and can be considerable if the substances are highly soluble. If k_d is used to denote purely diffusive or true mass transfer coefficients and $k_{d,s}$ the mass transfer coefficients at a semipermeable interface, which is generally the case in crystal growth, the following applies:

$$k_{d,s} = \frac{k_d}{1 - w_i} \tag{1.3}$$

If the mass fraction, w_i, tends toward zero, $w_i \to 0$, then $k_{d,s} = k_d$.

The mass transfer coefficient determining the slope of the linear relationship of the growth rate and supersaturation [see Eq. (1.2)] may be related to the Sherwood number, $\mathrm{Sh} = k_d L / D_{AB}$, and therefore to fluid dynamics, particle size, diffusivity, and viscosity. Diffusivity in liquids depends on the volume of the diffusion species or its diameter, on the viscosity η_L of the solution and on the kinetic energy kT. Figure 1.1 gives a sketch of some principle dependencies of diffusion-controlled growth on operating conditions. The dashed lines for minor levels of supersaturation indicate the initial limitation by integration reactions. It should be noted that the growth

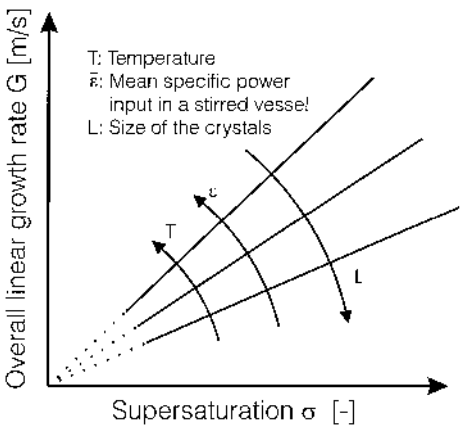

Figure 1.1. Influence of some principal operating conditions on diffusion-controlled growth.

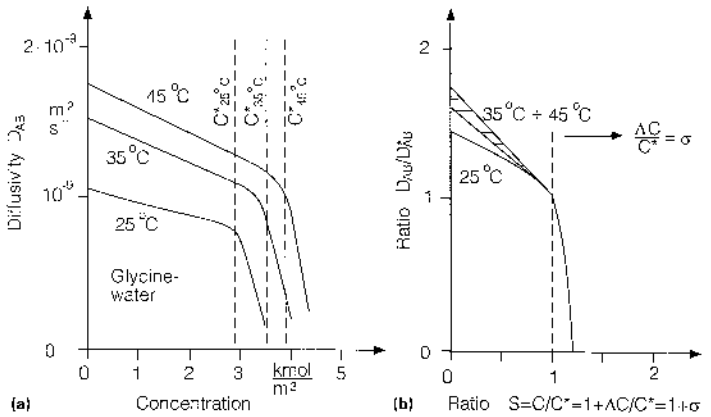

Figure 1.2. (a) Diffusivities D_{AB} of glycine in water against concentration; (b) ratio of diffusivities D_{AB}/D^*_{AB} against supersaturation. (From Ref. 1.4.)

rate calculated from equation (1.2) always gives the maximum growth rate, as no growth unit may be integrated into the crystal lattice that was not first transported from the bulk solution.

Some particular features of diffusivity may arise due to the complexes, oligomers, and clusters that may be formed by the growth units in solution depending on their concentration. Both Larson [1.1] and Chang and Myerson [1.2] have shown that such structures and clusters exist and that diffusivities are strongly influenced by these phenomena. Myerson et al. [1.3] have examined a number of solutions, both electrolytes and nonelectrolytes, to determine the diffusion coefficients of the solutes. The solutes studied include urea, glycine, valine, sodium chloride, and potassium chloride. Diffusivities tend rapidly toward zero as the spinodal is reached. This corresponds to a concentration close to the metastable limit of the supersaturated region. Figure 1.2a shows the diffusivities of glycine in water. In Figure 1.2b, the ratio of the diffusivities D_{AB}/D^*_{AB} (i.e., the concentration-dependent diffusion coefficient D_{AB} based on the value D^*_{AB} at saturation) is plotted against the ratio $S = C/C^*$ for glycine according to Myerson et al. [1.3] and Chang and Myerson [1.4]. Linear extrapolation of diffusivities in the supersaturation range $1 < S < S_{\text{met,hom}}$ is recommended. Generally speaking, diffusivities depend not only on temperature but also on concentration.

Another special feature of diffusivity arises for dissociating molecules. Here, each component exhibits a diffusion coefficient in solution, where the differences become significant with increasing difference in molecular mass

of the dissociated species. Generally, the smaller and, thus, more mobile species will migrate to the surface faster, forming an excess concentration. The growth rate will not depend on this excess forming species but on the slower migrating species. Hence, in the case of two or more components that are necessary to form a lattice molecule, the smallest diffusion coefficient determines the rate. For ions, the situation is somewhat different, as the excess forming ion will set up a charge on the crystal surface, causing the counterion to migrate faster through the electrostatic attraction. In this case, an apparent diffusion coefficient, D_{AB}, can be composed from the harmonic mean of the single-ion diffusion coefficients, D_A and D_B, with the charges of the ions, z_A and z_B, respectively [1.5]:

$$D_{AB} = \frac{(z_A + z_B)D_A D_B}{z_A D_A + z_B D_B} \tag{1.4}$$

2. INTEGRATION-CONTROLLED CRYSTAL GROWTH

When the diffusive/convective transport of units takes place rapidly [i.e., mass transfer coefficient $k_d \to \infty$ or the integration reaction takes place very slowly ($k_r \to 0$)], crystal growth is determined by the integration reaction occurring on the crystal surface. The individual processes involved can be diverse and complex and therefore are difficult to understand. A possible integration inhibition may consist, for example, of foreign particles or impurities being adsorbed on the crystal surface. The particles must then be desorbed or overgrown, which are processes that sometimes occur only at a higher supersaturation of the crystallizing substance. Large integration units of, for example, organic substances are transported very slowly by surface diffusion to the crystal surface and must revolve around the integration site until they are in a suitable position for integration.

2.1. Energetically Favorable Integration Sites

Despite the complexity of the integration of a growth unit into the crystal lattice, there has not been a lack of attempts to describe crystal growth theoretically. The structure of the crystal–solution interface (topology) must be taken into account here. As soon as a unit collides with the crystal and does not immediately rebound but is adsorbed, it diffuses on the surface. The chemical bonds of the unit to a plane face of the crystal are strong enough for the sorption, but not strong enough to hold it tightly at one place of the lattice. Hence, the growth unit must find an energetically favorable

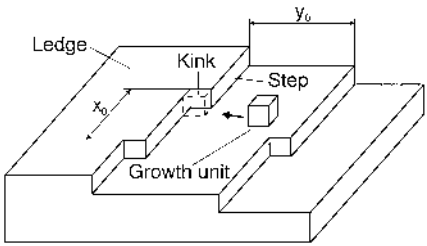

Figure 2.1. Energetically favorable sites for integration.

site, into which it becomes permanently integrated; otherwise, the growth unit will return to the solution after a certain diffusion distance. Such favorable integration sites arise from the topology of the crystal surface, in other words from the molecular crystal surface structure, and can be classified into kinks and steps (see Fig. 2.1).

If, in molecular terms, the surface is rough and has many kink sites, "continuous growth" may occur, provided that thermodynamic barriers do not impede it. After a short distance of surface diffusion, each growth unit reaching the surface in a supersaturated solution is integrated into the crystal lattice. If the crystal surface, on a molecular scale, becomes smoother, growth becomes considerably more difficult, as energetically favorable sites are limited. Different sources for kink and step sites, such as surface nucleation and screw dislocations, have to be taken into account in order to quantitatively describe growth rates in this case.

Generally speaking, the mechanism of crystal growth on the crystal surface can be described by the dimensionless driving force $\Delta\mu^* = \Delta\mu/kT$ and the surface energy ϕ^*. The parameter ϕ^* is a thermodynamic surface energy parameter introduced by Temkin [2.1] and Jackson [2.2] and defined for a (001) surface of a Kossel crystal by the following equation:

$$\Delta\phi^* = \frac{4\phi_{CL} - 2(\phi_{CC} + \phi_{LL})}{kT} \tag{2.1}$$

The energies ϕ_{CL}, ϕ_{CC}, and ϕ_{LL} represent the binding energy of a first-neighboring solid–liquid bond (index CL), a first neighboring solid–solid bond (index CC), or a first-neighboring liquid–liquid bond (index LL), respectively.

As the energy gain $\Delta\phi$ in the formation of a solid–liquid bond is

$$\Delta\phi = \phi_{CL} = \tfrac{1}{2}(\phi_{CC} + \phi_{LL}) \tag{2.2}$$

the following is obtained:

$$\Delta\phi^* = \frac{4\Delta\phi}{kT} = \frac{4}{kT}[\phi_{CL} - \tfrac{1}{2}(\phi_{CC} + \phi_{LL})] \tag{2.3}$$

Low values of $\Delta\phi^*$ generally yield a rough surface with integration sites covering the entire surface so that "continuous" growth occurs. As $\Delta\phi^*$ increases, a smoother surface is formed, and above a critical value of $\Delta\phi^*$, the surface can be considered even (i.e., it is smooth on a molecular scale). Computer simulations of crystal growth have shown that continuous growth takes place at $\Delta\phi^* < 3.2$, that two-dimensional nucleus growth must take place at a $\Delta\phi^*$ of 3.2–5.0 so that energetically favorable sites for growth units are created, and that the presence of steps on the crystal surface at $\Delta\phi^* > 5$ is required for growth to start [2.3, 2.4].

Bourne and Davey [2.5] have shown that $\Delta\phi^*$ can be approximated by $\Delta\phi^* \approx 4\gamma_{CL}d_m^2/kT$, so when $\gamma_{CL}d_m^2/kT$ is replaced by $K\ln(C_C/C^*)$, we obtain $\Delta\phi^* = 1.66\ln(C_C/C^*)$ with $K = 0.414$. This means that the surfaces of systems with $C^*/C_C > 0.145$ are rough on a molecular scale and systems with $C^*/C_C < 0.049$ exhibit very smooth surfaces.

In practice, it is very difficult to determine $\Delta\phi^*$ accurately enough to be able to use the relationships mentioned above. Bourne and Davey [2.5] examined the growth of hexamethylene tetramine from aqueous and ethanol solutions as well as from the gaseous phase. With the estimated $\Delta\phi^*$ values that result from interactions of varying degrees between the solvent and the dissolved substance, growth from the aqueous solution should be continuous, from the alcohol solution by mechanisms of nucleation and step growth and from the gaseous phase by flaw mechanisms. Experimental results seem to confirm this. In the case of growth from solutions, a nucleation mechanism or a continuous-step growth mechanism usually seems to confirm the experimental result best. Thus, these models should be discussed in more detail.

2.2. Screw Dislocation Mechanisms

As mentioned earlier, a crystal surface is, in particular for high surface energies, absolutely smooth and thus does not provide any integration site for an arriving growth unit. In practice, crystals have lattice imperfections preventing such ideally smooth surfaces. Frank [2.6] assumes that the presence of spiral dislocations, which end somewhere on the crystal surface, create steps, and are thus a continuous source of favorable integration sites. Burton, Cabrera, and Frank (BCF) [2.7] designed a step model for crystal growth in which the crystal surfaces grow by the addition of growth units to kink sites on an endless series of steps an equal distance apart.

These spiral steps are characterized by the average distance, y_0, between neighboring turns and by the average distance, x_0, between neighboring kinks in the steps. These distances can be described by the equations ([2.8]; see also Ref. 2.9)

$$\frac{x_0}{d_m} = \exp\left(\frac{\gamma_{CL} d_m^2}{kT}\right)\frac{1}{\sqrt{S}} \approx \frac{(C_C/C^*)^K}{\sqrt{S}} \tag{2.4}$$

and

$$\frac{y_0}{d_m} = 19\frac{r_s^*}{d_m} = 19\frac{\gamma_{CL} d_m^2}{kT\nu \ln S} \approx 19\frac{K \ln (C_C/C^*)}{\nu \ln S} \tag{2.5}$$

where ν is the number of ions dissociating from a molecule, and with the expression

$$\frac{\gamma_{CL} d_m^2}{kT} \approx K \ln\left(\frac{C_C}{C^*}\right) = 0.414 \ln\left(\frac{C_C}{C^*}\right) \tag{2.6}$$

introduced earlier (cf. Sec. 8 in Chapter 1). For high levels of supersaturation, equation (2.5) has to be corrected by a factor to give [2.10]

$$\frac{y_0}{d_m} = \frac{1 + 3S^{-1/2}}{1 + 3^{-1/2}}\left(19\frac{\gamma_{CL} d_m^2}{kT\nu \ln S}\right) \approx \frac{1 + 3S^{-1/2}}{1 + 3^{-1/2}}\left(19\frac{K \ln(C_C/C^*)}{\nu \ln S}\right) \tag{2.7}$$

The average distance between steps, y_0, and kinks along a step, x_0 (see Fig. 2.1), together denote reciprocally the average density of surface sites on a crystal face. In Figure 2.2, the dimensionless supersaturation $\Delta C/C_C$ is plotted against the dimensionless solubility C^*/C_C, and lines of constant x_0/d_m and y_0/d_m are depicted. As can be seen, the distances x_0 and y_0 decrease with increasing supersaturation. The lower the solubility C^*, the higher must be the supersaturation S to obtain the same x_0 and y_0 values.

Spiral dislocations are regarded as the source of these steps, and the steps, which are remote from the centers of these spiral dislocations, are considered to be parallel to each other and the same distance apart from each other. Regarding the surface-diffusion process, which can be expressed by Fick's law, Burton et al. (BCF) derived equations that describe this surface diffusion. They show that the linear growth rate of a crystal surface from the vapor phase is given by the following type of equation:

$$v_{\mathrm{BCF}} = \beta' x_s f \frac{kT}{2\pi\gamma}\exp\left(-\frac{W}{kT}\right)(\nu \ln S)\sigma \tanh\left(\frac{2\pi\gamma a}{x_s kT}\frac{1}{\nu \ln S}\right) \tag{2.8}$$

With $\ln S \approx \sigma$ valid for $\sigma < 0.5$, we obtain

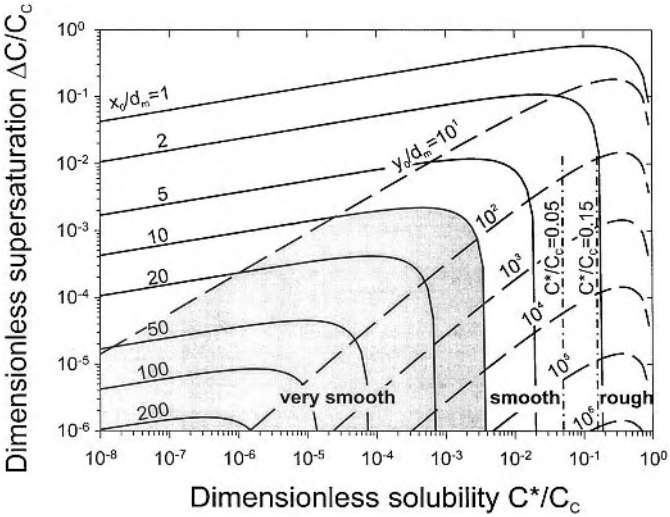

Figure 2.2. Lines of constant kink spacing x_0/d_m (solid) and lines of constant step spacing y_0/d_m (dashed) in a plot of dimensionless supersaturation $\Delta C/C_C$ against the dimensionless solubility C^*/C_C; shaded areas relate to rough, smooth, and very smooth surfaces of crystals (assuming that there are no collisions between crystals).

$$v_{\mathrm{BCF}} = \beta' x_s f \frac{kT}{2\pi\gamma} \exp\left(-\frac{W}{kT}\right) \nu\sigma^2 \tanh\left(\frac{2\pi\gamma a}{x_s kT} \frac{1}{\nu\sigma}\right) \tag{2.9}$$

In these equations, β' is a correction factor ($\beta' \approx 1$ or $\beta' < 1$), f is a frequency of the order of the atomic frequency of vibration, W is the total energy of evaporation, x_s is the mean displacement of adsorbed units, γ is the edge energy and a is the distance between two neighboring equilibrium points on the crystal surface or the intermolecular distance. For low supersaturations $\sigma \ll \sigma_c \equiv 2\pi\gamma a/x_s kT\nu$, a parabolic law

$$v_{\mathrm{BCF}} \sim \sigma^2 \tag{2.10a}$$

is obtained, but for high supersaturations $\sigma \gg \sigma_c$, the linear law

$$v_{\mathrm{BCF}} \sim \sigma \tag{2.10b}$$

is valid. This general relationship has been confirmed experimentally by numerous authors.

Ohara and Reid [2.20] replaced the edge energy γ with the interfacial tension $\gamma_{CL} \sim \gamma/a^2$. With the surface-diffusion coefficient D_{surf} according to

$$D_{\text{surf}} = a^2 f \exp\left(-\frac{U_s}{kT}\right) \tag{2.11}$$

where U_s is the activation energy between two neighboring equilibrium points on the surface, and some other minor modificaitons ($V_m \sim a^3$ and $\beta' \approx 1$), the BCF equation can be written more generally enclosing crystallization from solution as

$$v_{\text{BCF}} = \frac{2kT\Gamma^* D_{\text{surf}}}{19 x_s \gamma_{CL}} (\nu \ln S)\sigma \tanh\left(\frac{19 V_m \gamma_{CL}}{2 x_s kT} \frac{1}{\nu \ln S}\right) \tag{2.12}$$

For low supersaturation ($\sigma < 0.5$), equation (2.12) simplifies to

$$v_{\text{BCF}} = \frac{2kT\Gamma^* D_{\text{surf}}}{19 x_s \gamma_{CL}} \nu\sigma^2 \tanh\left(\frac{19 V_m \gamma_{CL}}{2 x_s kT} \frac{1}{\nu\sigma}\right) \tag{2.13}$$

with V_m the volume of a unit and Γ^* the equilibrium concentration of surface adsorbed units or molecules (molecules per unit area) at the temperature in question if the bulk supersaturation were unity. Again, if $\sigma \ll \sigma_c$ ($\sigma_c \equiv 19 V_m \gamma_{CL}/2 x_s kT\nu$), $\tanh(\sigma_c/\sigma)$ assumes unity, resulting in a parabolic law, whereas for $\sigma \gg \sigma_c$ the hyperbolic tangent collapses to the argument, resulting in a linear dependency on supersaturation.

In the case of a group of s overlapping dislocations, the average distance between neighboring turns reduces to $y_{0,s} = y_0/s$. With respect to $v_{\text{BCF}} = (v_{\text{step}} a)/y_{0,s}$, crystal growth will be enhanced. Sometimes, crystals do not grow at all. According to Burton et al. this could possibly be interpreted as being due to the absence of dislocation on the surface ($s = 0$) [another explanation is the presence of impurities (cf. Chap. 5), or deformations caused by stress (cf. Chap. 5)].

In equations (2.8) and (2.12), surface diffusion to the step is assumed as rate controlling. There is some evidence that volume diffusion in the immediate vicinity of a step and not surface diffusion becomes decisive when dealing with crystal growth from solution. Regarding this, the authors themselves modified the BCF equation for growth from solution to give

$$v_{\text{BCF,dif}} = \frac{kTV_m C^* N_A D_{AB}}{2x_0 \gamma} [\sigma(x_0, y_0)]^2 \sim \frac{kTaC^* N_A D_{AB}}{2x_0 \gamma_{CL}} [\sigma(x_0, y_0)]^2 \tag{2.14}$$

Herein, x_0 and y_0 denote the average distance between two kinks in a step and two steps on a ledge, respectively. With this equation the semicylindrical mass fluxes around a step and the hemispherical mass fluxes around a kink (both described with volume-diffusion coefficient D_{AB}) are assumed to be rate controlling. Thus, in analogy to equations (2.8) and (2.12), the growth rate increases with increasing kink density expressed as $1/x_0 y_0$. This, again,

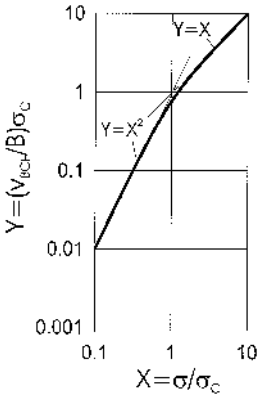

Figure 2.3. Dimensionless growth rate against dimensionless supersaturation for the BCF model.

makes it clear that the surface microstructure plays an important role in crystal growth.

Equations (2.8) and (2.12) can also be written in the dimensionless form

$$Y = X^2 \tanh\left(\frac{1}{X}\right) \tag{2.15}$$

with $Y \equiv (v_{\mathrm{BCF}}/A)\sigma_c$ and $X \equiv \sigma/\sigma_c$. Figure 2.3 represents the change from the parabolic law $Y = X^2$ for $\sigma \ll \sigma_c$ to the linear law $Y = X$ for $\sigma \gg \sigma_c$. Both curves representing these two marginal cases meet at $X = 1$, where $\sigma = \sigma_c$. The transformation from a parabolic to a linear law results from the effects of the steps on the surface. It is possible to illustrate that half the distance, $y_0/2$, between parallel steps is connected by the following relationship with supersaturation when surface diffusion is decisive:

$$\frac{y_0/2}{x_s} = \frac{\sigma_c}{\sigma} \tag{2.16}$$

In the case of low levels of supersaturation, $\sigma \ll \sigma_c$ and $x_s \ll y_0$, all growth units that reach the surface within a distance x_s from a step are integrated into this step. Diffusion fields of the neighboring steps do not affect this integration. As the linear spreading rate of a step and the step density are proportional to σ, the crystal growth rate is proportional to the square of relative supersaturation, σ^2. High levels of supersaturation, $\sigma \gg \sigma_c$, result in $x_s \gg y_0$. This has a strong influence on diffusion fields that are caused by the steps. Growth units on the surface can now be integrated into several steps. The linear spreading rate of a step then becomes independent of σ and the

growth rate is proportional to relative supersaturation. The parameter σ_c is thus a measure of the influence of diffusion fields, and its value determines the shape of the curve for the growth rate against supersaturation. In the case of growth from solutions, values for σ_c are expected in the range of $10^{-2} < \sigma_c < 10^{-1}$ [2.18].

Bennema and Gilmer [2.3, 2.11, 2.12] revised the BCF theory with regard to growth from solutions, and their calculations confirm the role played by surface diffusion. At very low supersaturation, the integration of growth units from the solution directly into kink sites seems to be a very complex process. Some authors have been very critical of the assumptions of the BCF theory. As a result, deviations arise when the length of the crystal junction is much greater than the radius of the critical nucleus. In this way, many ends of spiral dislocations remain within the length of the crystal junction. This gives a linear law. If the distance between neighboring dislocations is smaller than $9.5r_s^*$ (r_s^* is the radius of the critical surface nucleus), a group of spirals can act together to form a greater source of steps. This results in a large number of overlapping spirals [2.13]. Deviations from the parabolic law could occur if the predicted linear relationship between step density and supersaturation changes notably with the distance from the source of the steps (i.e., the dislocation). Other effects that have already been examined include the influence of surface diffusion on the step distance [2.14], differences in the integration resistance in a step from one side to the other [2.15–2.17] and deviations and flaws in the steps with respect to their equidistant positions [2.13, 2.16]. It can generally be said that improving the BCF equation by integrating all these modifications into the main statement does not change very much.

2.3. Surface Nucleation Mechanisms

Although the screw-dislocation mechanism already causes a certain roughening of the crystal surface, the density of energetically favorable surface sites is still small and the increase in the growth rate with increasing supersaturation in a parabolic law is still moderate. With rising supersaturation, there is a possible change in growth mechanisms and surface nucleation becomes a source of much higher densities of kink sites, which contrasts with an exponential dependency on supersaturation. It is thus considered that adsorbed growth units collide with each other and form clusters and, finally, nuclei, in accordance with the considerations given in Section 2. For a two-dimensional cluster to be stable (i.e., larger than the critical nucleus diameter), sufficient growth units must join together to form a nucleus of critical size on the crystal surface. Once this has been achieved, other growth

units can join onto the corners of the nucleus so that crystal growth takes place over the entire surface area. Various assumptions about the spreading rate of this type of nucleus form the basis of theoretical considerations. Growth depends on the ratio of the spreading rate to the time required for another nucleus to be formed on the smooth surface. The number of growth units required to form a critical nucleus can also vary considerably [2.18, 2.19].

Ohara and Reid [2.20] introduced three models, all denoting the relationship between the growth rate v and the supersaturaiton σ as follows:

$$\mathrm{v} = A'\sigma^{p} \exp\left(-\frac{B'}{\sigma}\right) \tag{2.17}$$

A borderline case is the so-called mononuclear model, whereas the spreading rate of this layer is very rapid compared to the surface nucleation rate and $p = \frac{1}{2}$. The other extreme configuration is the polynuclear mechanism, where the spreading rate of this layer is slow compared to always new nuclei formed; in this case, $p = -3/2$. In between these two borderline cases is the *birth and spread* (B + S) *model* with $p \approx \frac{5}{6}$, considered for the first time by Hilling [2.21] and also known as the *nuclei-above-nuclei* (NAN) *model* (see also Ref. 2.8). With the assumptions of nuclei possibly borne on incomplete layers and growing at a constant step advancement, v_{step}, independently from each other (i.e., nuclei may slip over the edge of other nuclei), the growth rate of this B + S mechanism rate $v_{\mathrm{B+S}}$ is given by

$$\mathrm{v}_{\mathrm{B+S}} = h\mathrm{v}_{\mathrm{step}}^{2/3} B_{\mathrm{surf}}^{1/3} \tag{2.18}$$

where B_{surf} and h refer to the two-dimensional nucleation rate and to the height of the nuclei, respectively. With assumed rate-controlling surface diffusion, the step advancement, reads

$$\mathrm{v}_{\mathrm{step}} = \beta' \frac{2V_m \Gamma^* D_{\mathrm{surf}}}{x_s h}\sigma \tag{2.19}$$

In this equation, β' is a correction factor, as was that introduced with equation (2.8) ($\beta' \approx 1$ or $\beta' < 1$), x_s is the mean displacement of adsorbed units, D_{surf} is the surface-diffusion coefficient [cf. Eq. (2.11)], V_m is the volume of a unit, and Γ^* is the equilibrium concentration of surface-adsorbed units or molecules (molecules per unit area) at the temperature in question if the bulk supersaturation were unity. The two-dimensional nucleation rate derives analogous to the considerations in Chapter 2 from a number concentration of nuclei with an impinging rate of units from the surface and the Zeldovich factor [2.20]:

$$B_{\text{surf}} = \frac{2}{\pi}(\Gamma N_A)^2 \overline{v}\left(\frac{V_m}{h}\nu \ln S\right)^{1/2} \exp\left(\frac{-\Delta G^S_{\max}}{kT}\right) \tag{2.20}$$

A combination of equations (2.18)–(2.20) while replacing the mean surface-diffusion velocity of units, $\overline{v}$, with $\overline{v} = 2D_{\text{surf}}\sqrt{\Gamma N_A}$ [2.22] and assuming a step-height equivalent to one molecule diameter $h \approx a$ finally leads to

$$\text{v}_{\text{B+S}} = A\sigma^{2/3}(\nu \ln S)^{1/6} \exp\left(-\frac{B}{\nu \ln S}\right) \tag{2.21}$$

with

$$A = \left(\frac{16}{\pi}\right)^{1/3} a^{1/6} D_{\text{surf}} (V_m \Gamma N_A)^{5/6} \left(\frac{\beta' \Gamma^*}{x_s}\right)^{2/3} \tag{2.21a}$$

$$B = \frac{\pi}{3} V_m a \left(\frac{\gamma_{CL}}{kT}\right)^2 \approx \frac{\pi}{3}\left[K \ln\left(\frac{C_C}{C^*}\right)\right]^2 \tag{2.21b}$$

With $\ln S \approx \sigma$, equation (2.21) can be written in terms of dimensionless numbers according to

$$\frac{\text{v}_{\text{B+S}}}{AB^{5/6}} = \left(\frac{\sigma}{B}\right)^{5/6} \exp\left(-\frac{B}{\sigma}\right) \tag{2.22}$$

or with $Y \equiv v_{\text{B+S}}/AB^{5/6}$ and $X \equiv \sigma/B$, as

$$Y = X^{5/6} \exp\left(-\frac{1}{X}\right) \tag{2.23}$$

Equation (2.23) is illustrated in Figure 2.4. $\sigma \ll B$ results in very low growth rates because two-dimensional nucleation formation is inhibited in this range; $\sigma \gg B$ yields $Y = X^{5/6}$.

Equation (2.21) still seems to produce good results even when surface diffusion is integrated into the simulation process of growth [2.23], provided that the value of $\Delta\phi^*$ is smaller than the critical value at which the surface becomes noticeably smooth. On the other hand, for systems with low interfacial energies or slow surface diffusion, the activation term in equation (2.21) is dominant, so the influence of the spreading of the surface nuclei on the growth rate diminishes and, accordingly, growth becomes dominated by a polynuclear mechanism.

This *polynuclear* (PN) or activated growth mechanism exhibits a very strong dependency of growth on supersaturation, because with increasing supersaturation, the time elapsing between two nucleation events decreases rapidly. For a distinct range of small supersaturation, almost no growth appears, and when supersaturation rises above a critical value, the growth increases rapidly to the domain of limiting bulk diffusion. The rate v_{PN}

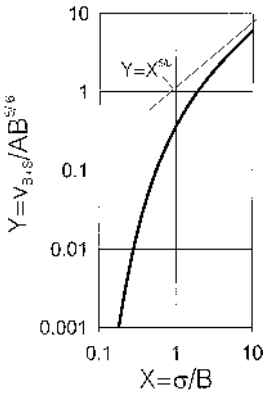

Figure 2.4. Dimensionless growth rate against dimensionless supersaturation for the B + S model.

can be derived from the rate of surface nucleation and can be described by [2.24]

$$v_{PN} = \frac{D_{AB} d_m}{3} (N_A C^*)^{2/3} \sigma^{2/3} \exp\left(-\frac{\Delta G^S_{\max}}{kT}\right) \tag{2.24}$$

In the case of cylindrical surface nuclei, the ratio of the surface nucleation energy $\Delta G^S_{\max}$ and kT can be written as [2.8]

$$\frac{\Delta G^S_{\max}}{kT} = \pi \left(\frac{\gamma_{CL} d_m^2}{kT}\right)^2 \frac{1}{\nu \ln S} \tag{2.25}$$

For squares instead of cylinders, the factor π must be replaced by 4. Together with equation (2.6), combining the last two equations leads to

$$v_{PN} = \frac{D_{AB}}{3 d_m} \left(\frac{\Delta C}{C_C}\right)^{2/3} \exp\left(-\pi \frac{[K \ln(C_C/C^*)]^2}{\nu \ln S}\right) \tag{2.26}$$

With the rapid increase of the growth rate with supersaturation assumed from equation (2.26), it is possible to make a general prediction concerning the intersection of the two different regimes of integration-controlled and diffusion-controlled growth. Equating v_{PN} with the growth rate calculated from diffusion-controlled growth [cf. Eq. (1.2)] allows a critical supersaturation to be calculated at which the change from a smooth surface to a rough surface appears. Below this supersaturation, the growth rate follows the BCF and B + S mechanisms, whereas above it, the linear relationship of

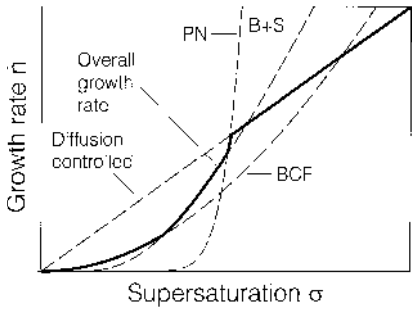

Figure 2.5. Scheme of competing growth regimes with rising supersaturation.

equation (1.2) is valid (cf. Sec. 3.2). Note that due to the strain of the crystals and/or impurities, the growth rate in the domain of integtration limitation may be reduced, essentially even down to zero. In this case, growth is attainable only with a supersaturation sufficiently high for a surface roughening through equation (2.26).

Polynuclear growth was found for a number of highly soluble materials [2.18] as well as for sparingly soluble substances [2.25]. For example, for $BaSO_4$ with the maximum supersaturation $S < 10$, the growth rates were described by equation (2.26) with $K = 0.296$ for cylindrical nuclei, with π in the exponential term.

To summarize the considerations so far, the growth rate, in principle, follows the scheme presented in Figure 2.5. Viewed on a molecular scale, crystal growth preferably takes place at energetically favorable surface sites. For very low supersaturations, only the omnipresent imperfections at the crystal surface, such as screw dislocations, act as possible sources for integration sites. With rising supersaturation, the formation of surface nuclei from adsorbed growth units becomes more probable and new sources for integration sites are possibly created by a birth and spread mechanism. Generally, the surface nucleation mechanisms exhibit a very strong dependency of the growth rate on supersaturation. By further increasing the supersaturation, the spreading of the nuclei loses ground compared to new nuclei continuously roughening the surface (polynuclear mechanism) and thus forming numerous energetically favorable integration sites. With a rough surface providing enough favorable sites for approaching growth units, the course of the growth rate with supersaturation continues to be controlled solely by bulk diffusion.

3. ESTIMATION OF CRYSTAL GROWTH RATES

Although the models presented earlier give a good insight into the physics of crystal growth, they imply many parameters such as surface-diffusion coefficients and kink densities that are difficult or even impossible to determine or predict, and even though this might be possible one day, it would lead to a single-face growth rate of an ideal crystal rather than to an overall growth rate of a crystal collective in an industrial crystallizer. Thus, usually the application of these models is restricted to accompanying experimental studies of growth rates in order to determine the missing parameters. For a predictive estimation of growth rates, further-reaching assumptions are necessary, where the crucial question is to predict the different regimes of the integration-controlled and diffusion-controlled growth mechanisms.

3.1. Analogy to Diffusion-Reaction Theory

As suggested in the preceding sections, there is a variety of mechanisms of crystal growth, which take place in competition and lead to different growth regimes. Table 3.1 provides a summary of these growth models. In addition to the B + S (birth and spread) model, the BCF (Burton–Cabrera–Frank) model, and the diffusion-integration model with the special cases of a reaction order r of $r = 1$ and $r = 2$, the following very simple equation for the overall molar flux density, $\dot{n}$, is often used:

$$\dot{n} = k_g(\Delta C)^g \tag{3.1}$$

The results of these relationships coincide with the two borderline cases of the BCF theory, where $g = 2$ at low supersaturations and $g = 1$ at high supersaturations. If both the diffusive–convection step and the integration step determine growth, the concentration C_I at the interface according to Figure 0.1 must be used in the models mentioned. For example, the decisive factor in the BCF equation is the supersaturation $\sigma_I = (C - C_I)/C^*$ at the interface between the surface diffusion or adsorption layer and the volume-diffusion layer. This also applies to equations that describe only the integration step.

In reaction kinetics, the relationship between the diffusion and reaction rates is commonly described by characteristic numbers (e.g., the Damköhler number Da [3.2], the Hatta number [3.3] for chemical adsorption, or the catalytic efficiency or Thiele module for chemical catalysis). Accordingly, an effectiveness factor η was also introduced by Garside [3.4] for crystal growth according to

Table 3.1. Growth-Rate Models

Total growth rate	Mass transport	$\dot{n} = k_g(C - C^*)^g$ with $C - C^* = \Delta C$	(3.1)
Physicochemical models	Only convection + diffusion	$\dot{n} = k_d(C - C_I)$	(3.4)
	Only surface integration	$\dot{n} = k_r(C_I - C^*)^r$ with $k_r = k_{r0}\exp\left(-\frac{\Delta E_r}{RT}\right)$	(3.5)
	Elimination of C_I	$\dot{n} = k_r\left(\Delta C - \frac{\dot{n}}{k_d}\right)^r$	(3.8)
	Special case $r = 1$	$\dot{n} = \frac{\Delta C}{1/k_d + 1/k_r}$	(3.9)
	Special case $r = 2$	$\dot{n} = k_d\Delta C + \frac{k_d^2}{2k_r} - \sqrt{\frac{k_d^4}{4k_r^2} + \frac{k_d^3\Delta C}{k_r}}$	(3.10)
Surface-integration models	B + S model	$v_{\mathrm{B+S}} = K_{\mathrm{B+S}}\left(\frac{\Delta C}{C^*}\right)^{5/6}\exp\left(-\frac{K'_{\mathrm{B+S}}}{T}\frac{C^*}{\Delta C}\right)$	(2.21)
	BCF model	$v_{\mathrm{BCF}} = K_{\mathrm{BCF}}T\left(\frac{\Delta C}{C^*}\right)^2\tanh\left(\frac{K''_{\mathrm{BCF}}}{T}\frac{C^*}{\Delta C}\right)$	(2.13)
	PN model	$v_{\mathrm{PN}} = \frac{D_{AB}}{3d_m}\left(\frac{\Delta C}{C_C}\right)^{2/3}\exp\left(-\pi\frac{K\ln(C_C/C^*)]^2}{\nu\ln S}\right)$ with $v = \frac{\dot{n}\tilde{M}}{\rho_C}$	(2.26)

Source: Ref. 3.1.

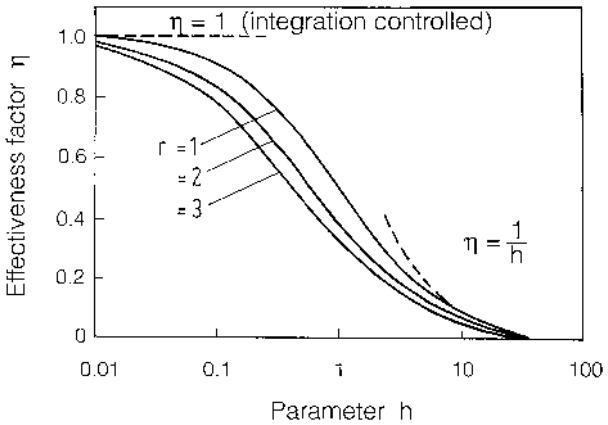

Figure 3.1. Curve for the effectiveness factor against parameter h.

$$\eta = \frac{G_{\text{exp}}}{G_{\text{int}}} \tag{3.2}$$

where G_{exp} is the experimentally determined growth rate and G_{int} the growth rate at an indefinitely fast and, thus, negligible volume diffusion.

When the physical mass transfer coefficients become very large ($k_d \to \infty$) or the integration reaction is very slow compared to the diffusive–convective transport of the crystal components, we obtain $\eta \to 1$. In this case, crystal growth is controlled by the reaction and can be described by equations (2.8) and (2.21) alone, where $\Delta C = C_I - C^* \approx C - C^*$, and in the BCF equation, $\sigma_I = (C_I - C^*)/C^* \approx (C - C^*)/C^*$ must be used. On the other hand, when the integration reaction is indefinitely fast ($k_r \to \infty$) and thus negligible, or diffusive–convective transport is very slow (e.g., when the solution is highly viscous) compared to integration, we obtain $\eta \to 0$. In Figure 3.1, the effectiveness factor η is plotted against the ratio h:

$$h = \frac{\text{Mass flow density at compl. integration limitation}}{\text{Mass flow density at compl. diffusion limitation}}$$

The parameter h can be formulated for the integration reaction as follows:

$$h = \frac{k_r(C - C^*)^r}{k_d(C - C^*)} \tag{3.3}$$

If the parameter h is very small ($0 < h \ll 1$), crystal growth is completely controlled by the reaction ($\eta = 1$). If parameter h is large ($1 \ll h < \infty$), crystal growth is increasingly limited ($\eta \to 0$) by diffusion.

As the reaction rate constant k_r generally increases more quickly with temperature than the mass transfer coefficient k_d, the abscissa value increases with increasing temperature. The effectiveness factor tends toward zero and growth finally becomes completely limited by diffusion. This has been proven, for example, for potash alum [3.5], magnesium sulfate heptahydrate [3.6], and ammonium sulfate [3.7] in the range $5°C < \vartheta < 60°C$. However, it must be noted that impurities and additives can have a considerable influence on crystal growth. As the temperature increases, the crystal surface generally becomes less covered with foreign molecules (i.e., its adsorptive coverage decreases). Unfortunately, adsorption isotherms of impurities, admixtures, and additives are usually not known in solution–crystal systems. If the crystal growth rate increases with temperature, it is essential to check whether this is due to an increase in the reaction-rate constants (e.g., according to Arrhenius's formulation) in the "pure" system or due to the desorption of foreign particles in the real system.

It must be emphasized that it is difficult to divide systems into those that are limited by diffusion and those that are limited by integration with respect to crystal growth. First, the growth limitation depends on supersaturation. Furthermore, small crystals under 100 μm often grow under integration limitation, whereas the growth of large crystals of the same system can be described by the assumption of a purely diffusive–convective resistance and an indefinitely fast integration reaction. This behavior can be explained, for example, by the BCF equation, according to which the growth rate depends on the number of dislocations s on the crystal. Therefore, it can be assumed that large crystals exhibit sufficient dislocations and, therefore, sufficient integration sites so that growth will not be limited by the integration reaction. On the other hand, it is precisely the integration reaction that can limit the growth of small crystals if these have only a few dislocations and are largely "smooth." It is also possible for layers of units on the surface of the crystal to be so deformed that absolutely no growth takes place at all, at least at low supersaturation. Such a crystal may be stimulated to grow (i.e., activated) only at relatively high supersaturation by the growth of surface nuclei. This explains why crystals of the same size in completely the same environment (supersaturation, fluid dynamics, temperature, concentration of impurities) grow at different rates. Such effects are observed and described by the term *growth dispersion* and will be considered in Section 3.3.

3.2. General Prediction of Mean Growth Rates

In the literature, experimentally determined growth rates can be found for more than 50 systems. In most cases, the system studied was an aqueous solution of inorganic solutes, but measurements carried out with organic components, such as solvents or solutes, do not show major differences. Moreover, all theoretical derivations are based on the physical properties of the materials under discussion and do not distinguish between organic and inorganic substances. The growth-rate measurements of the 50 systems mentioned earlier refer to a wide range of supersaturations and temperatures. If supersaturation is too high, the quality of products is inferior because of the excessive nucleation rate. In addition, admixtures and impurities are incorporated into the crystal lattices with rising supersaturation (cf. Chapter 7). If supersaturation is too low, however, the crystallization process is not economical because of the low crystal growth rate. A comparison of the supersaturation and growth rates published in a great number of articles shows that the most suitable, and probably the most economical growth rates are usually limited by bulk diffusion and integration. Therefore, when dealing with crystallization technology, there is tremendous interest in deriving, with tolerable accuracy, equations that describe mean crystal growth rates for any system in the transition range of diffusion–integration. Due to growth-rate dispersion, these equations should be based on a large number of crystals (as in the case of MSMPR crystallizers; see Section 4) and provide statistically mean values rather than be derived from single-crystal experiments. The multitude of experimental results for a variety of systems has enabled us to develop such a relationship. The overall molar flux density $\dot{n} = \bar{v}C_C$ is given by

$$\dot{n} = k_g(\Delta C)^g \tag{3.1}$$

with the exponent $1 < g < 2$ in most cases. Growth that is limited only by convection of the solution and bulk diffusion can be described by

$$\dot{n}_{\text{dif}} = k_d(C - C_I) \tag{3.4}$$

[cf. Eq. (1.1)]. If growth is limited only by integration, the molar flux density $\dot{n}_{\text{int}}$ is expressed as

$$\dot{n}_{\text{int}} = k_r(C_I - C^*)^r \tag{3.5}$$

As mentioned at the very beginning of this section, the entire concentration gradient $\Delta C = C - C^*$ is thus—with the concentration at the interface C_I—divided into two parts. It is difficult to predict C_I, which alters with the supersaturation ΔC. Therefore, as a first approach for a material with unknown growth kinetics, it is interesting to know at what level of super-

saturation the superposition of transport limitation and limitation by integration has to be taken into account; in other words, the range of supersaturation in which the growth rate might be described in a good approximation solely by transport limitation (i.e., $C - C_I \approx C - C^* = \Delta C$) or solely by integration limitation (i.e., $C_I - C^* \approx C - C^* = \Delta C$). To demarcate these two regimes, the parameter h as introduced in equation (3.3) can be set to unity, assuming that growth is completely controlled by integration up to the specific supersaturation $\Delta C_{h=1}$ or $\sigma_{h=1}$ and completely controlled by mass transport above this level:

$$1 = h = \frac{k_r \Delta C_{h=1}^r}{k_d \Delta C_{h=1}} = \frac{k_r \sigma_{h=1}^r}{k_d \sigma_{h=1}} C^{*(r-1)} \tag{3.6}$$

The polynuclear growth mechanism can be considered as a borderline case between integration-controlled and diffusion-controlled growth (see Fig. 2.5), because with the strong dependency on supersaturation, the number of energetically favorable integration sites increases dramatically. Thus, by combining equations (2.26) and (3.6) with $1/(1 - w) \approx 1$, we gain a relation denoting the maximum supersaturation $\sigma_{h=1}$ for the regime of integration-controlled growth:

$$1 = \frac{D_{AB}}{3 d_m k_d} \left(\frac{C^*}{C_C} \sigma_{h=1} \right)^{-1/3} \exp\left(- \frac{\pi K^2}{\nu} \frac{[\ln(C_C/C^*)]^2}{\ln(1 + \sigma_{h=1})} \right) \tag{3.7}$$

Unfortunately, equation (3.7) cannot be solved for $\sigma_{h=1}$. The predictive character of this equation for the demarcation of the integration-controlled and diffusion-controlled growth regimes has been compared with experimental data for growth rates of different materials with dimensionless solubilities C^*/C_C varying over five decades and stoichiometric coefficients between $\nu = 1$ and $\nu = 3$ [3.10]. The comparison shows that the course of the predicted specific supersaturations with the dimensionless solubilities is in good agreement with experimental findings, where the predicted values are always about three times higher than the experimentally determined values. This can be explained by the fact that equation (3.7) denotes the maximum value of $\sigma_{h=1}$, where the diffusion-limited range may be found for smaller values, when the resistance of the other integration mechanisms (e.g., BCF, B + S) is low. Another explanation for this deviation arises from the assumption of complete dissociation of the ions assumed for the experimental data. Values of $\sigma_{h=1}$ calculated for different solubilities and stoichiometric coefficients are plotted in Figure 3.2. Note that the diagram is given in concentrations. It is also valid for the more general case with respect to nonideal behavior of the thermodynamic driving force, when replacing the concentrations with activities, if ideal behavior of the solid crystal and

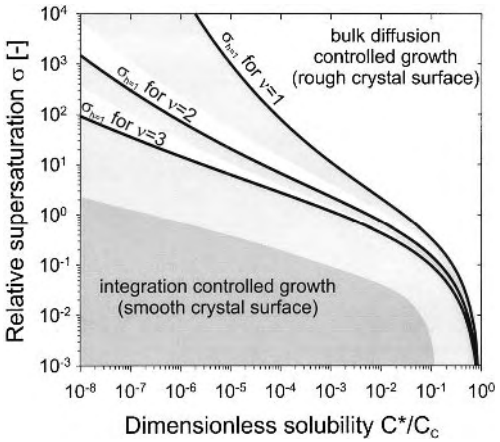

Figure 3.2. Calculated borderline cases [see Eq. (3.7)] for the transition of smooth growth faces to rough growth faces with the dimensionless solubility for different degrees completely dissociating ($\nu = 2$, $\nu = 3$) materials (valid for $D_{AB} = 10^{-9}\,\mathrm{m^2/s}$, $d_m = 5 \times 10^{-10}\,\mathrm{m}$, $k_d = 10^{-4}\,\mathrm{m/s}$, and $K = 0.414$).

the interfacial tension can be assumed. Thus, especially for the sparingly soluble substances with high supersaturations, the dimensionless quantities should be replaced by $(\gamma C - \gamma^* C^*)/C_C$ and $\gamma^* C^*/C_C$. In comparison with the experimental data, it can be concluded that in a good approximation, the growth rate can be assumed to be completely diffusion controlled for $\sigma > \sigma_{h=1}$. For $\sigma < \sigma_{h=1}$ the superposition of both regimes has to be taken into account, and for $\sigma \ll \sigma_{h=1}$, the integration step limits the growth rate.

In order to describe the transition range of diffusion and integration limitation, the overall mass flow rate has to be stated more generally as $\dot{n} = \dot{n}_{\mathrm{dif}} = \dot{n}_{\mathrm{int}}$. Together with equations (3.4) and (3.5), this leads to

$$\dot{n} = k_r \left(\Delta C - \frac{\dot{n}}{k_d} \right)^r \tag{3.8}$$

and for $r = 1$, to

$$\dot{n} = \frac{\Delta C}{1/k_d + 1/k_r} \tag{3.9}$$

whereas for $r = 2$, we obtain

$$\dot{n} = k_d \Delta C + \frac{k_d^2}{2k_r} - \sqrt{\frac{k_d^4}{4k_r^2} + \frac{k_d^3 \Delta C}{k_r}} \tag{3.10}$$

or with $\dot{n} = \bar{v}C_C = (G/2)C_C$, assuming $\beta/3\alpha = 2$ (valid for spheres and cubes),

$$\frac{\bar{\nabla}}{k_d} \equiv \frac{G}{2k_d} = \frac{\Delta C}{C_C} + \frac{k_d}{2k_r C_C} - \sqrt{\frac{k_d^2}{4k_r^2 C_C^2} + \frac{k_d}{k_r C}\frac{\Delta C}{C_C}} \tag{3.11}$$

where $C_C = \rho_C/\tilde{M}$.

Theoretical considerations and experimental results have shown that the growth rate $\bar{\nabla}_{\text{int}}$, which is limited only by integration, can generally be described by [3.11]

$$\begin{aligned}\frac{\bar{\nabla}_{\text{int}}}{k_d} &= 2.25 \times 10^{-3} \nu^2 \frac{D_{AB}(C_C/C^*)^{2/3}}{d_m k_d \ln(C_C/C^*)} \left(\frac{\Delta C}{C_C}\right)^2 \\ &= \frac{2.25 \times 10^{-3}}{P_{\text{dif}}} \left(\frac{\Delta C}{C_C}\right)^2\end{aligned} \tag{3.12}$$

where ν is the number of ions dissociating from a molecule, and P_{dif} the crystallization parameter according to

$$P_{\text{dif}} \equiv \frac{1}{\nu^2}\frac{d_m k_d}{D_{AB}} \left(\frac{C^*}{C_C}\right)^{2/3} \ln\left(\frac{C_C}{C^*}\right) \tag{3.13}$$

Alternatively, equation (3.12), with $\sigma^2 = (\Delta C/C^*)^2 = (\Delta C/C_C)^2 (C_C/C^*)^2$, becomes

$$\bar{\nabla}_{\text{int}} = 2.25 \times 10^{-3} \nu^2 \frac{D_{AB}}{d_m} \frac{(C^*/C_C)^{4/3}}{\ln(C_C/C^*)} \sigma^2 \tag{3.14}$$

With equation (3.12), the general relationship (3.11) can be formulated as follows [3.11, 3.12]:

$$\frac{\bar{\nabla}}{k_d} \equiv \frac{G}{2k_d} = \frac{\Delta C}{C_C} + 200 P_{\text{dif}} - \sqrt{(200 P_{\text{dif}})^2 + 400 P_{\text{dif}} \frac{\Delta C}{C_C}} \tag{3.15}$$

In Figure 3.3, the dimensionless growth rate $G/2k_d$ is plotted against dimensionless supersaturation $\Delta C/C_C$ for various lines of the crystallization parameter P_{dif}. The shaded area shows crystal growth limited by integration ($G < 0, 1 G_{\text{dif}}$). In contrast to bulk diffusion and convection, the crystal growth is reduced by the integration step with an increasing crystallization parameter P_{dif} and with decreasing dimensionless supersaturation $\Delta C/C_C$.

Finally, it will be mentioned here that an equation similar to equation (3.11) with the kinetic coefficient k_g' according to $\bar{\nabla}_{\text{int}} = k_g' \sigma^2$ can be derived [3.12]:

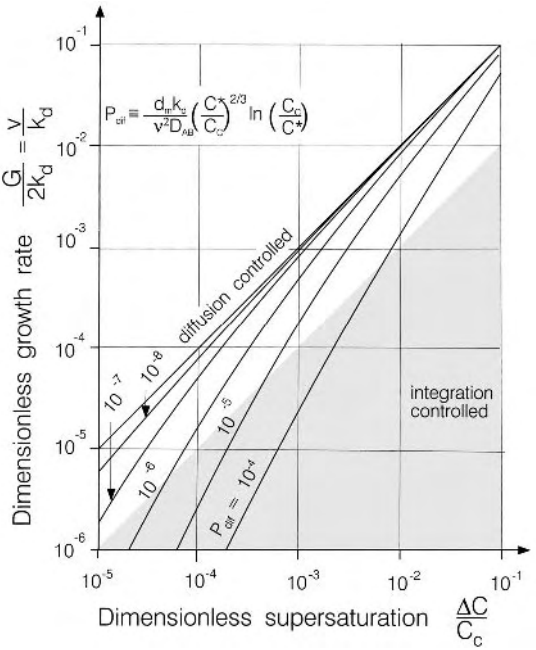

Figure 3.3. Dimensionless growth rate against dimensionless supersaturation for any system with $\tilde{M} <\approx 500$ kg/kmol and $\approx 25°C$.

$$\frac{\bar{v}}{k_d} = \frac{\Delta C}{C_C} + \frac{k_d}{2k_g'}\left(\frac{C^*}{C_C}\right)^2 - \sqrt{\left(\frac{k_d}{2k_g'}\right)^2\left(\frac{C^*}{C_C}\right)^4 + \frac{k_d}{k_g'}\left(\frac{C^*}{C_C}\right)^2 \frac{\Delta C}{C_C}} \tag{3.16}$$

with

$$k_g' = 2.25 \times 10^{-3} \nu^2 \frac{D_{AB}}{d_m} \frac{(C^*/C_C)^{4/3}}{\ln(C_C/C^*)}$$

This growth coefficient constant 2.25×10^{-3} is based on experimental results obtained at a temperature of approximately 25°C. Growth experiments carried out at higher temperatures have shown that the growth coefficient increases with rising temperature. This is to be expected because the diffusion coefficient, D_{AB}, also rises with temperature, and this increase is often described by an Arrhenius term. Therefore, it is reasonable to plot a correction factor, f_T, against the reciprocal of the absolute temperature, T; see Figure 3.4. In this diagram, the temperature correction factor, f_T, is set as $f_T = 1$ for 25°C according to many experimental results. In the diagram, straight lines are drawn for the activation energies of 50 and 100 kJ/mol.

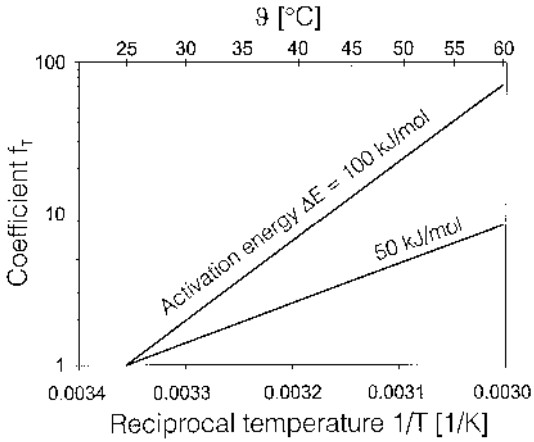

Figure 3.4. Arrhenius plot of the temperature correction factor, f_T, against the temperature.

Experimentally determined activation energies can be found in this range; for example, Wang [3.13] found an activation energy of $\Delta E = 92.7\,\text{kJ/mol}$ for KNO_3. The growth behavior of this substance has been studied between 20°C and 45°C. Angerhöfer [3.14] investigated the growth of $BaSO_4$ in the temperature range between 20°C and 50°C. Virtually no influence of temperature has been observed between 20°C and 30°C, and in the range between 30°C and 50°C, the experimental results can be described with an activation energy of $\Delta E = 87.5\,\text{kJ/mol}$.

A general plot of predicted mean crystal growth rates (valid at approximately 25°C) can be summarized from a combination of the above considerations [Eqs. (3.7) and (3.15)] as a function of dimensionless supersaturation $\Delta C/C_C$ and dimensionless solubility C^*/C_C, with the relative supersaturation σ as a parameter; see Figs. 3.5 and 3.6. The growth rates in these diagrams refer to the following parameters, which are valid in good approximation for the majority of crystallizing systems:

Diffusivity	$D_{AB} = 10^{-9}\,\text{m}^2/\text{s}$
Molecule diameter	$d_m = 5 \times 10^{-10}\,\text{m}$
Mass transfer coefficient	$k_d = 10^{-4}\,\text{m/s}$
Complete dissociating molecules	$\nu = 2$
or nondissociating molecules	$\nu = 1$

The borderline case between diffusion-controlled and integration-controlled growth, which is, of course, a steady transition rather than an immediate

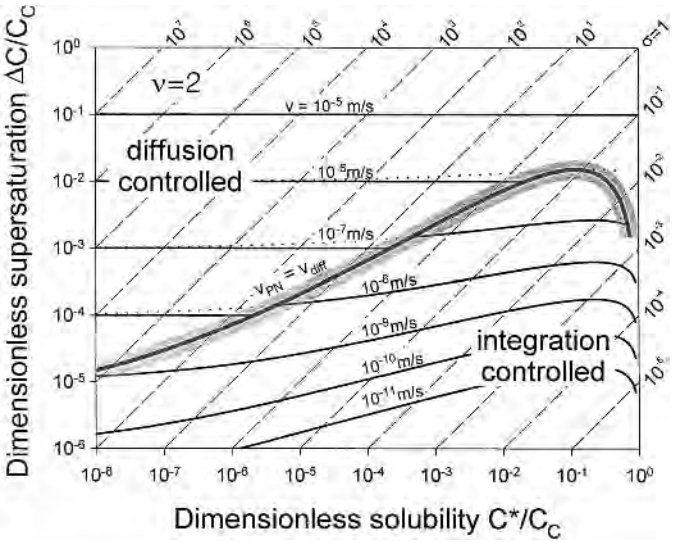

Figure 3.5. General plot of predicted mean crystal growth rates for dissociating materials as a function of dimensionless supersaturation and dimensionless solubility (valid for $D_{AB} = 10^{-9}\,\mathrm{m^2/s}$, $d_m = 5 \times 10^{-10}\,\mathrm{m}$, $k_d = 10^{-4}\,\mathrm{m/s}$, $K = 0.414$, and $\nu = 2$).

change, is obtained from equation (3.7), assuming that the polynuclear growth mechanism increases the number of integration sites dramatically. Above this bold printed curve, the crystal rate is solely diffusion controlled and the growth rate is given by

$$\frac{\overline{v}}{k_d} = \frac{\Delta C}{C_C} \tag{3.17}$$

The area below this borderline can be subdivided into a field where diffusion and integration play a role in crystal growth and into a field at the bottom of the diagram where crystal growth is solely controlled by the integration step. The curves were calculated from equation (3.15). It should again be noted that the diagram is given in concentrations, but it is more generally valid for the thermodynamic driving force expressed in activities when the ideal behavior of the solid crystal is assumed. Therefore, the dimensionless quantities should again be replaced by $(\gamma C - \gamma^* C^*)/C_C$ and $\gamma^* C^*/C_C$, especially for the sparingly soluble substances with high supersaturations. Each material is represented in this diagram with its dimensionless solubility with a parallel line to the ordinate $C^*/C_C = \text{const.}$, and the prevailing

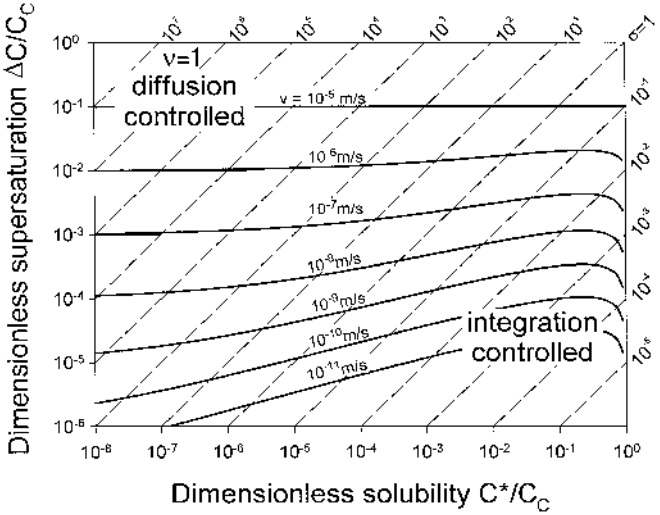

Figure 3.6. General plot of predicted mean crystal growth rates for non-dissociating materials as a function of dimensionless supersaturation and dimensionless solubility (valid for $D_{AB} = 10^{-9}\,\mathrm{m}^2/\mathrm{s}$, $d_m = 5 \times 10^{-10}\,\mathrm{m}$, $k_d = 10^{-4}\,\mathrm{m/s}$, $K = 0.414$, and $\nu = 1$).

growth rate can be read dependent on the prevailing supersaturation. In the "Integration Controlled" area, the crystal surface is very smooth (cf Fig. 2.2) and screw dislocation is the decisive mechanism. With increasing supersaturation, more and more units hitting the surface can be integrated into kinks because the kink density rises. Just below the borderline (represented by the polynuclear mechanism), the kink density is so high that the impingement rate of units is no longer rate controlling because their diffusive transport to the immediate crystal surface is not sufficient. Therefore, growth is controlled by diffusion and integration and depends on the impingement rate of units, their diffusivity, and the kink density of the crystal surface. When the supersaturation of a given system is further increased, the borderline will be crossed and the polynuclear mechanism will lead to a strong roughening of the crystal surfaces by which each arriving unit is promptly integrated. However, the units must first be transported by diffusion from the bulk of the solution to the immediate vicinity of the crystal surface and mass transfer is now decisive for crystal growth. The curves are only valid for the parameters given earlier, whereas the qualitative behavior will remain for other values of D_{AB}, d_m, and k_d.

3.3. Size-Dependent Growth and Growth-Rate Dispersion

In 1929, McCabe showed that all geometrically similar crystals of different sizes but the same solute grow at the same growth rate (delta L law, or ΔL law). However, the experimental results of several authors indicate that the crystal growth of several substances is a function of crystal size; experimental results have been obtained for potash alum [3.9], potassium sulfate [3.15], nickel sulfate [3.16], and potassium dichromate [3.17]. The crystal size L lies within the range 0.4–4 mm. Janse and de Jong [3.17] suspect that such effects occur when crystals of the same size exhibit growth-rate distribution under the same conditions. Results of experiments in which an initially narrow crystal size distribution broadened were published for the first time by White and Wright [3.18] and Janse and de Jong. Another example is shown in Figure 3.7 with the growth behavior of individual citric acid crystals [3.8]; each crystal has an individual growth rate that can remain constant during the course of growth. Natal'ina and Treivus [3.19] published growth rates of individual KDP crystals that exhibited significant growth dispersion. This is probably due to differences in the surface structure and perfection, indicated by Bennema [2.13]. In practice, however, it is very difficult to evaluate the influence of such phenomena quantitatively from growth rates obtained in polydisperse systems. A distinction can hardly be made between growth dispersion and size-dependent growth. Janse and de Jong [3.17] showed that when growth dispersion occurs, the mass of crystals having a high growth rate increases to a greater extent than the mass of crystals that grow slowly. Because the fast-growing crystals make a larger contribution

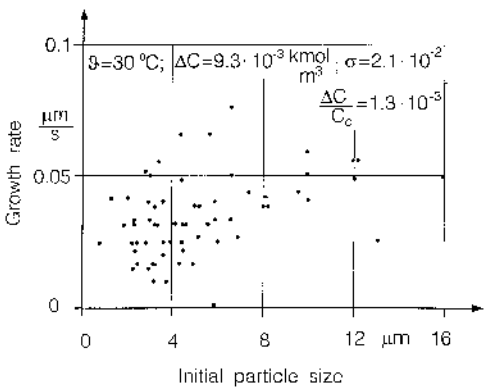

Figure 3.7. Growth rates of individual citric acid crystals by subcooling to 3 K against initial particle size.

to the total mass than other crystals, their mass increase is even greater than it would be on the basis of an average growth rate. Presumably, the growth rate will be found to increase with crystal size. Subsequently, sieve analysis separates the large, fast-growing crystals from the small, slow-growing crystals, which, in turn, show false size-dependent growth if they are then used for growth measurement.

Two models [the random fluctuation (RF) model and constant crystal growth (CCG) model] have been developed in order to interpret and describe growth-rate dispersion (GRD). According to the RF model, random fluctuations of the growth rate of a definite crystal occur [3.18, 3.20]. The spread of growth rates is described by a coefficient of dispersion analogously to Taylor dispersion of fluid dynamics [3.21]. On the other hand, the CCG model [3.17] assumes constant crystal growth of an individual crystal independent of time as long as the surroundings (supersaturation, relative velocity) are unchanged. This model was confirmed experimentally by various authors [3.8, 3.16, 3.22]. However, different crystals and even different crystal faces can exhibit growth rates that differ by a factor of one order of magnitude or more. Furthermore, studies have shown that the growth rate of an individual crystal at a certain level of supersaturation can be changed after a period of increased or decreased supersaturation [2.5]. Therefore, it is necessary to take into account the molecular surface structure and impurity-adsorption layer of the crystal and its deformation state in order to gain a better understanding.

3.4. Crystal Growth and Heat Effects

The heat of crystallization generated at the crystal–solution interface creates a temperature field in this area. The supersaturation that is decisive for crystal growth is now different than that which was calculated on the basis of the equilibrium concentration in an isothermal field. The intensity and resulting significance of this temperature effect have been calculated by Ohara and Reid [2.20].

In the case of an exothermic specific heat of crystallization Δh^*, the generation of heat at the crystal surface is given by the relationship

$$\Delta h^* \frac{G}{2} \rho_C = h(\vartheta_I - \vartheta) \tag{3.18}$$

where h is the heat transfer coefficient. The bulk temperature and bulk concentration are represented by ϑ and c, respectively, and the equilibrium concentration at the temperature ϑ is referred to as c^*. The corresponding

parameters at the crystal–solution interface are denoted as ϑ_I, c_I, and c_I^*. Within a small temperature range, the following equation can be written

$$c_I - c^* = (\vartheta_I - \vartheta)\frac{dc^*}{d\vartheta} \tag{3.19}$$

where $dc^*/d\vartheta$ is the slope of the solubility curve. If the heat transfer coefficient h is described by the Nusselt number [$\mathrm{Nu} = h(L/\lambda_L)$] and equations (3.18) and (3.19) are combined, the following is obtained:

$$c_I - c^* = \frac{G\rho_C L\Delta h^*}{(2\mathrm{Nu})\lambda_L}\frac{dc^*}{d\vartheta} \tag{3.20}$$

Limitation of the growth rate by volume diffusion alone results in the greatest amount of growth and generation of heat possible. The growth rate can be expressed by

$$\frac{G}{2}\rho_C = k_d(c - c_I) = k_d[(c - c^*) - (c_I - c^*)] \tag{3.21}$$

If the mass transfer coefficient k_d is expressed by the Sherwood number $\mathrm{Sh} = k_d(L/D_{AB})$, $c - c_I$ can be eliminated from equations (3.20) and (3.21), giving

$$G\left(1 + \frac{D_{AB}}{\lambda_L}\Delta h^*\frac{dc^*}{d\vartheta}\frac{\mathrm{Sh}}{\mathrm{Nu}}\right) = 2k_d\frac{c - c^*}{\rho_C} \tag{3.22}$$

or with the bulk supersaturation σ,

$$G = \frac{2k_d}{1 + \Psi(\mathrm{Sh}/\mathrm{Nu})}\frac{c^*}{\rho_C}\sigma = \frac{2k_d}{1 + \Psi(\mathrm{Sh}/\mathrm{Nu})}\frac{\Delta c}{\rho_C} \tag{3.23}$$

where

$$\Psi = \frac{D_{AB}}{\lambda_L}\Delta h^*\frac{dc^*}{d\vartheta} \tag{3.24}$$

Equation (3.23), derived in a slightly different way by Ohara and Reid, describes the growth rate with respect to supersaturation. If equation (3.23) is rewritten for mass-transport-controlled growth and isothermal conditions, the following is obtained:

$$G = 2k_d\frac{c^*}{\rho_C}\sigma = 2k_d\frac{\Delta c}{\rho_C} \tag{3.25}$$

Deviations of the $\Psi(\mathrm{Sh}/\mathrm{Nu})$ term from 0 determine whether the heat of crystallization Δh^* affects the isothermics of the system and should thus be taken into account. For growth in a still liquid, in which mass and heat transport take place by molecular transport, $\mathrm{Sh} = \mathrm{Nu}$ and the correc-

tion term is simplified to $1 + \Psi$. In the case of forced convection, Sh and Nu are given by the following types of relationship:

$$\mathrm{Sh\,(or\,Nu)} = a\,\mathrm{Re}^{1/2}[\mathrm{Sc\,(or\,Pr)}]^{1/3} \tag{3.26}$$

or

$$\frac{\mathrm{Sh}}{\mathrm{Nu}} = \left(\frac{\mathrm{Sc}}{\mathrm{Pr}}\right)^{1/3} = \mathrm{Le}^{1/3} \tag{3.27}$$

where $\mathrm{Le} = \lambda_L/\rho_L c_p D_{AB}$ is the Lewis number. The correction factor in this case is $1 + \Psi(\mathrm{Le}^{1/3})]$. For growth from aqueous solutions at low temperatures, the heat of crystallization Δh^* should be approximately equal to 400 kJ/kg. If $D_{AB} \cong 10^{-9}\,\mathrm{m^2/s}$, $\lambda_L \cong 0.6\,\mathrm{W/m\,K}$ is assumed for a system having a steep solubility curve ($dc^*/d\vartheta \cong 10\,\mathrm{kg/m^3\,K}$), values for Ψ of approximately 7×10^{-3} are obtained. Ohara and Reid [2.20] did, in fact, determine values of 2.2×10^{-3} and 4.4×10^{-4} for potassium chloride and potassium alum, respectively, for aqueous solutions at about 300 K, $\mathrm{Sh} \cong 10^3$ and $\mathrm{Pr} \cong 7$, which gives $\mathrm{Le}^{1/3}5$ and $\Psi(\mathrm{Le}^{1/3}) \cong 0.035$.

These values result in a very small error, due to the thermal effects being neglected. An isothermal calculation of crystal growth is thus exact enough when substances crystallize out of aqueous solutions at room temperature. The effects of heat could play a significant role in crystallization from a melt. In this case, it is necessary to consider the effects of heat.

4. GROWTH IN MULTICOMPONENT SYSTEMS AND SOLVENT EFFECTS

When crystallization is started from solution, the solvent already represents a second component to the system and may influence the kinetics significantly. As crystallization is commonly used not only as a solidification but also as a separation process, at least two components exist. Thus, in general, industrial crystallization takes place in multicomponent systems from which one component or a mixture of components is crystallized. Despite this fact, only a few systematic investigations have been carried out on the growth kinetics in the presence of admixtures or in dependence on solvent properties.

4.1. Multicomponent Systems

According to Mullin and Garside [4.1], additional components can (a) change the solution properties, such as density, viscosity, the diffusion coef-

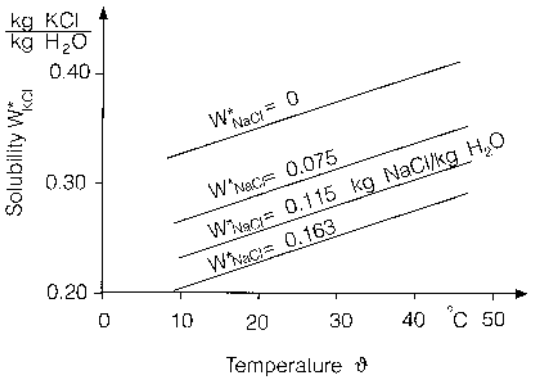

Figure 4.1. Solubility of KCl in the ternary KCl–NaCl–water system.

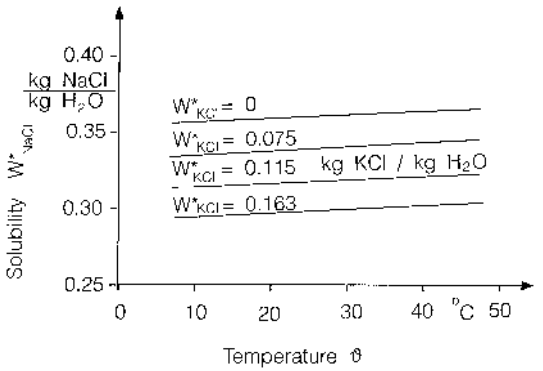

Figure 4.2. Solubility of NaCl in the ternary KCl–NaCl–water system.

ficient, the structure of the solution, and so on, or (b) be adsorbed on certain faces of the crystals, thus altering the crystal surface (change of surface roughness or blocking of steps or kinks) or modifying the habit.

Information on habit modifiers and adsorption phenomena is given in Sec. 5 and Chapter 12, respectively. First, some experimental results obtained for the ternary system KCl–NaCl–H_2O by König et al. [4.2] and Farelo et al. [4.3] will be presented. In Figures 4.1 and 4.2, the solubility of KCl and NaCl in ternary KCl–NaCl–H_2O systems is plotted against temperature. In all cases, the solubility of the aqueous KCl or NaCl solution is reduced in the presence of a third component. The solubility of ternary systems can best be shown in special diagrams (see Fig. 4.3). In the triangular diagram, ternary mass fractions w of the three components according to the definitions

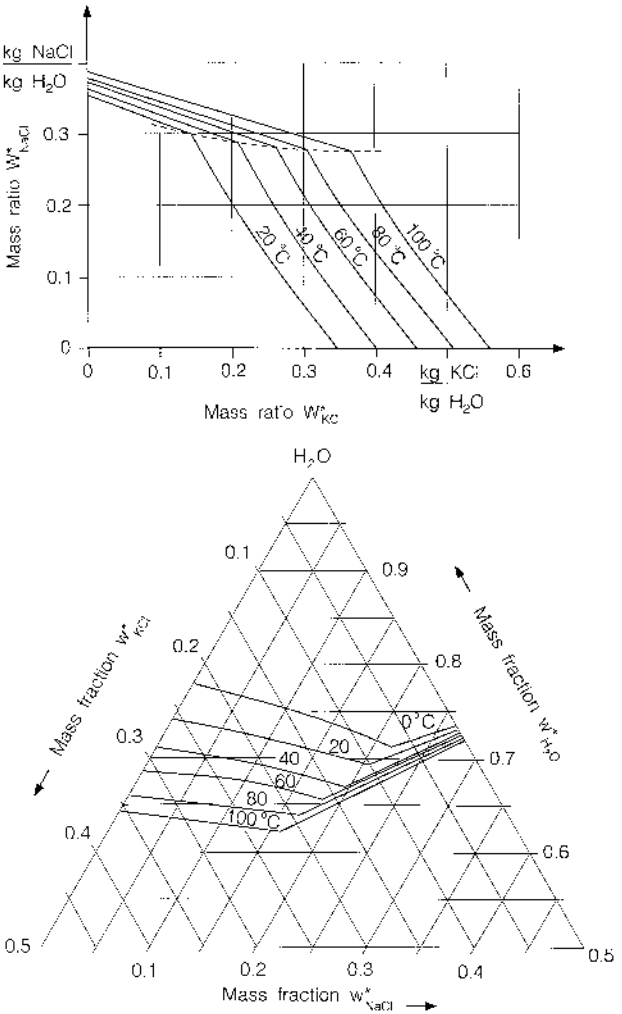

Figure 4.3. Solubility of the ternary KCl–NaCl–water system: (a) w^*_{NaCl} against w^*_{KCl}; (b) triangular diagram.

$$w_{KCl} = \frac{\text{Mass of KCl}}{\text{Mass of KCl} + \text{mass of NaCl} + \text{mass of } H_2O}$$

$$w_{NaCl} = \frac{\text{Mass of NaCl}}{\text{Mass of KCl} + \text{mass of NaCl} + \text{mass of } H_2O}$$

$$w_{H_2O} = \frac{\text{Mass of } H_2O}{\text{Mass of KCl} + \text{mass of NaCl} + \text{mass of } H_2O}$$

are used, as concentration with $w_{KCl} + w_{NaCl} + w_{H_2O} = 1$. The solubilities w^* for 0°C, 10°C, 20°C, and 30°C are taken from the literature [4.4]. The driving force for crystallization kinetics is given for component i by

$$\frac{\Delta\mu_i}{RT} = \nu_i \ln\left(\frac{a_i}{a_i^*}\right) = \nu_i \ln\left(\frac{\gamma_i y_i}{\gamma_i^* y_i^*}\right) \tag{4.1}$$

with activity a_i as the product of the activity coefficient γ_i and the ternary mole fraction y_i. The asterisk denotes equilibrium, and ν_i is the number of ions in which a molecule dissociates. Because $y_i = (\tilde{M}_{ABC}/\tilde{M}_i)w_i$, equation (4.1) can also be written

$$\frac{\Delta\mu_i}{RT} = \nu_i \ln\left(\frac{\gamma_i w_i}{\gamma_i^* w_i^*}\right) = \nu_i S_a = \nu_i(1 + \sigma_a) \tag{4.2}$$

Because the activity coefficients γ_i and γ_i^* are approximately equal ($\gamma_i = \gamma_i^*$) and if the degree of dissociation is small, the driving force can be expressed as

$$S = \ln\left(\frac{w_i}{w_i^*}\right) \tag{4.3}$$

or

$$\sigma \approx \frac{\Delta w_i}{w_i^*} \quad \text{for } \sigma < 0.5 \tag{4.4}$$

Therefore, many authors use the simplified driving force $\sigma_w = \Delta w_i / w_i^*$ or $\sigma_c = \Delta c_i / c_i^*$, instead of the thermodynamically correct expression of equation (4.1).

In Figure 4.4, the growth rate of KCl, and in Figure 4.5 the growth rate of NaCl in binary and ternary solutions is plotted against supersaturation. In the original literature, information is given on dissolution experiments. Assuming that dissolution is limited only by bulk diffusion, it is possible to calculate mass transfer coefficients k_d. The growth experiments have shown that the mass transfer coefficients obtained for dissolution are nearly the same for growth, but that the integration resistance for NaCl increases in the presence of KCl. When dealing with the growth of KCl, this effect was far less pronounced.

4.2. Solvent Effects

Besides admixtures, additives, and impurities, the solvent itself plays an important role in crystal growth. Parameters such as the type of liquid and its structure and the degree of dissociation can affect the growth rate. It is necessary to take into account not only the microstructure (roughness in

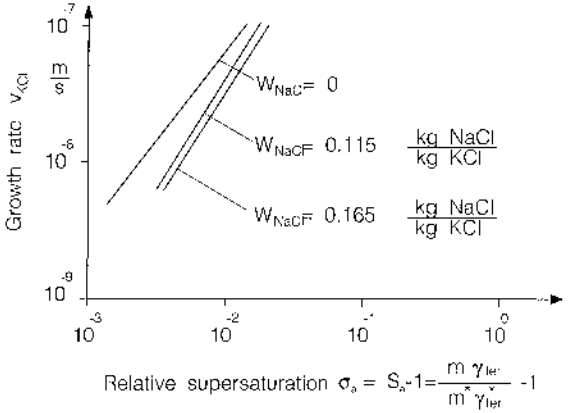

Figure 4.4. Growth rate of KCl against supersaturation.

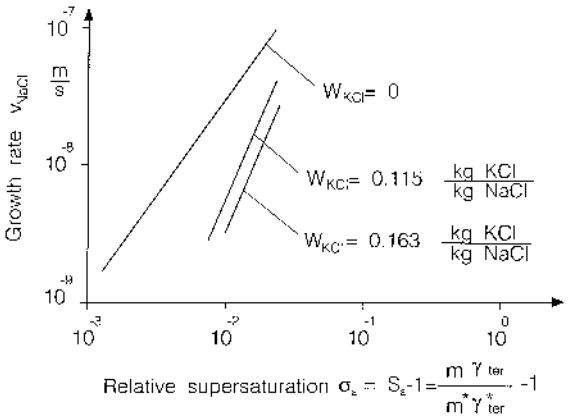

Figure 4.5. Growth rate of NaCl against supersaturation.

a molecular sense) of the crystal surface but also any kind of adsorbed species.

In particular, in the case of electrolyte solutions, the solvent affects crystallization kinetics significantly. As the water molecule itself dissociates into H^+ and OH^-, usually at least a five-component system is in contact with the ionic crystal surface. The dissociated ions are hydrated to specific hydration numbers with a specific hydration enthalpy depending on the valency and the reciprocal ionic radius [4.5]. As this hydrate layer has to be removed during the growth process to a certain degree, any change in the structure of

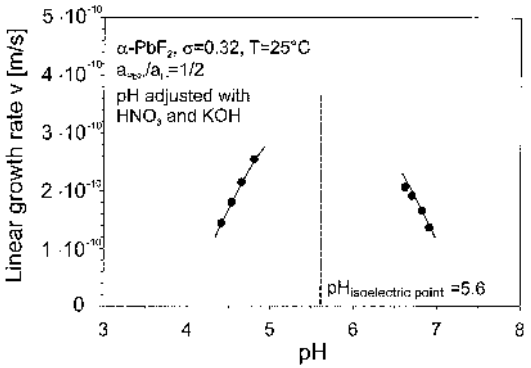

Figure 4.6. Linear growth rate of α-PbF_2 at 25°C from acidic $pH^\circ = 3.5$ and alkaline $pH^\circ = 7.1$ (at positive and negative surface charge, respectively) supersaturated solution as a function of pH, Pb^{2+}, and F^- activity ratio $R = \frac{1}{2}$. (Data from Ref. 4.7.)

the solvated ions affects growth kinetics too. For example, metal ions tend to form different complex species, depending on the pH, which contain hydroxide or hydronium ions, respectively, thus changing the charge of the complex and affecting the hydration enthalpy. On the other hand, the crystal surface itself has a hydrate layer, which changes with pH and results in a surface charge on the crystal. There is a great deal of experimental evidence for the importance of solution conditions such as pH and ionic strength in the literature, which points to a distinct dependence of growth rates on these parameters.

Let us present some examples. Stubicar et al. [4.6, 4.7] found that the growth rate of lead fluoride depends significantly on the solution pH, ionic strength, and the composition of the mother liquor (i.e., the molar ratio between the lead and the fluoride ion). Figure 4.6 represents their findings on the dependence on pH. It is difficult to extract these findings from theory due to the interplay of multiple effects. Both ionic species form various hydrate complexes in the pH range considered, and the surface charge of the crystal surface varies; it is not being clear whether this is because of excess adsorption of one lattice ion or because of the adsorption of hydronium/hydroxide.

Similar strong dependencies on pH, but with an inverse effect, have been found for potassium dihydrogen phosphate [4.8]. When changing the solution composition to an excess of P_2O_5 or to an excess of K_2O, the growth rate is unequivocally increased the further the composition deviates from the stoichiometric case (see Fig. 4.7). Again, the link to theoretical considerations is not straightforward, as at the same time both the solution composi-

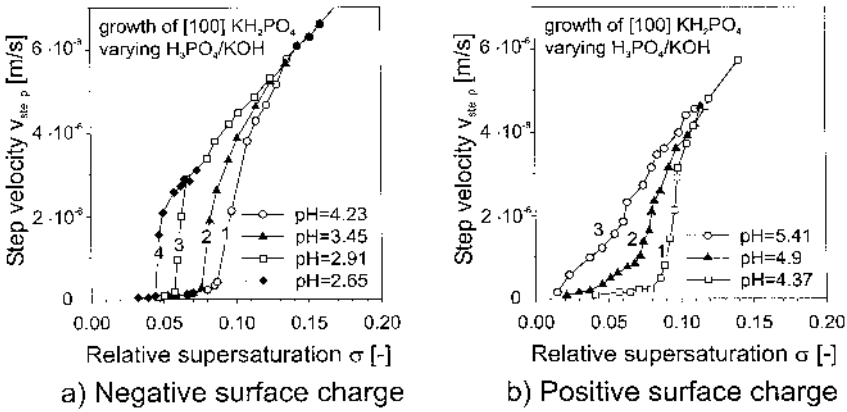

Figure 4.7. Influence of supersaturation on the step velocity on prismatic faces in solutions of varying acidity. (a) Acidic conditions. The values of pH and the concentration of P_2O_5 in the solvent (g/100 g of the solvent): (1) 4.23, 0; (2) 3.45, 0.778; (3) 2.91, 5.12; (4) 2.65, 7.40. (b) Alkalic conditions. The values of pH and the concentration of K_2O in the solvent (g/100 g of the solvent): (1) 4.37, 0; (2) 4.9, 0.37; (3) 5.41, 1.00. (Data from Ref. 4.8.)

tion (i.e., pH, ionic strength, and relative concentration of the reactants) and the surface charge change. With increasing deviation from the stoichiometric composition, the excessive species takes on the role of an admixture with comparable impact on growth, as described earlier. Comparable results were found for barium sulfate [4.9–4.11] and for potassium chloride [4.12].

Despite the difficulties in considering these solvent effects theoretically, their potential importance should always be borne in mind. In general, it is necessary to take into account not only the crystallizing solute but also the solvent conditions and latent components.

5. INFLUENCE OF ADDITIVES AND IMPURITIES

The crystal growth rate is exposed to the influence of any trace component in the solution. The trace components are said to be additives if they are used intentionally for a specific purpose (e.g., to optimize the crystal habit) and are known as impurities if the effects are unintentional. However, there is no distinction in terms of the impact on crystallization kinetics. The decisive mechanisms for the action of these additives and impurities on growth take place when they are adsorbed on the crystal faces. This line of thinking is supported by the facts that the additives and

impurities may influence the kinetics of different crystal faces specifically and that even very small amounts in the range of several ppm bring about significant changes in the growth rate. Thus, when giving a structure to the influence of additives and impurities on crystal growth, there may be a separation into the physicochemistry of adsorption and the question as to where and how these adsorbed species affect the growth rate. Both steps also have to be taken into account when looking for a "tailor-made" additive, a systematic search for an additive using an approach from stereochemistry (see Chapter 12).

5.1. Adsorption on Crystal Faces

Additives and impurities form a wide field of substances with the adsorbate on the crystal varying from ions, atoms, molecules, and macromolecules to clusters, so a detailed description of the underlying physicochemistry would be beyond the scope of this chapter. Nevertheless, adsorption is an important step to be mentioned when dealing with additives or the inevitable impurities. Some fundamental and particular features are therefore now given.

For nonionic impurities, the adsorption equilibrium may be described using the Langmuir isotherm; the loading, θ (i.e., the number of adsorbed units based on the total number of adsorption sites), depends on the Henry coefficient, He_{im}, of the additive or impurity and its mole fraction, y^*_{im}, in the mother liquor:

$$\theta = \frac{(He_{im})y^*_{im}}{1 + (He_{im})y^*_{im}} \tag{5.1}$$

or

$$\frac{\theta}{1-\theta} = (He_{im})y^*_{im} \tag{5.2}$$

If the loading, θ, is very small, equation (5.2) may be simplified to give a direct proportionality of the loading to the concentration, y^*_{im}.

Care has to be taken with respect to the total number of surface sites referred to by the loading. In general, a crystal face is inhomogeneous, as are the surface sites available for adsorption of the additive. As mentioned in Chap. 2.1, beside the plane surface, there are kinks and steps exposed to the interface, which are energetically favorable not only for the incorporation of new growth units but also for the adsorption of any substance (see Fig. 5.1). There is experimental evidence for the existence of such distinct levels of free energy of adsorption ΔG_{im} [e.g., for Cd^{2+} on NaCl, with -46.9 kJ/mol, -36.4 kJ/mol, and -26 kJ/mol for the adsorption on kinks, steps, and a ledge (plane face), respectively]

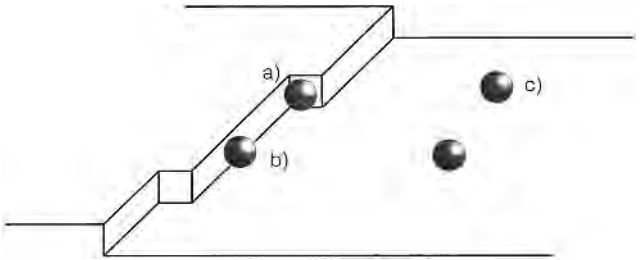

Figure 5.1. Distinct adsorption sites for additives and impurities: (a) kink, (b) step, (c) ledge.

[5.1, 5.2]. With equation (5.3) denoting the dependence of the Henry coefficient on temperature and the free energy of adsorption, ΔG_{im}, this leads to a single isotherm for each category of surface site:

$$\mathrm{He}_{\mathrm{im}} = \exp\left(-\frac{\Delta G_{\mathrm{im}}}{kT}\right) \tag{5.3}$$

Although this seems complicated at first, it encourages the development of quantitative models for the influence of additives and impurities on crystal growth, because the mechanism of disturbance also depends on the location where the additive is adsorbed. Generally, there is little literature available on additives and impurities where the adsorption isotherms have been determined. Davey [5.2] has summarized and recalculated data for several organic and inorganic additives on a variety of crystals, pointing out the different adsorption locations and disturbances of growth kinetics. A compilation of various free adsorption energies is given in Table 5.1. In addition to being able to quantitatively describe the disturbance of growth kinetics, benefit from accurately determining the adsorption equilibria can also be gained in the search for the right additive. For example, the affinity of adsorption in a homologous series of adsorbates increases with increasing molecular mass, due to the rule of Traub, which was also found to be reflected in the impact of carboxylic acids and polyols on the growth rate [5.4, 5.5].

Ionic additives and impurities present a special case, because two additional obstacles to adsorption have to be taken into account. As already mentioned in Sec. 4.2, a crystal surface in an electrolytic solution is charged when the pH or the stoichiometry of the lattice ions is varied. For a detailed description of these effects, reference is made to the literature on adsorption of ions [5.6, 5.7]. At a glance, with the multicomponent adsorption of H^+, OH^-, and the surplus lattice ion, there is a positively or negatively charged crystal face depending on the solution conditions and an electrical double layer is formed. When an ionic

Table 5.1. Free-Adsorption Energies

Adsorbent	Adsorbate	Crystal face	Adsorption site[a]	ΔG_{im} [kJ/mol]	Ref.
NaCl	Cd^{2+}	(100)	K	−46.9	5.1
		(100)	S	−36.4	5.1
		(100)	L	−26.0	5.1
$(NH_4)H_2PO_4$	Fe^{3+}	[001]	L	−15.9	5.2
		[010]	L	−16.3	5.2
	Al^{3+}	[001]	L	−15.5	5.2
		[010]	L	−16.7	5.2
KBr	HCOOH	{100}	K	−17.33	5.4
	CH_3COOH	{100}	K	−25.04	5.4
	C_2H_5COOH	{100}	K	−30.8	5.4
	C_3H_7COOH	{100}	K	−36.6	5.4
	Phenol	{100}	L	−10.9	5.4
NaCl	Pb^{2+}	{111}	K	−41.4	5.2
KCl	Pb^{2+}	{111}	K	−41.4	5.2

[a] Adsorption site: K: kink; S: step; L: ledge (cf. Fig. 5.1).

additive is approached against such a charged interface, additional reversible work due to the electrostatic repulsion or attraction has to be overcome. On the other hand, metal ions, in particular, tend to form differently charged complexes in electrolytic solutions, depending on the pH. The valence of the prevailing complex and not of the ionic additive then has to be taken into account for the adsorption equilibria with a charged surface. Additionally, if there are several coexisting complexes with the same total amount of the additive, the activity of the adsorbing complex varies with pH. The importance of the above considerations is emphasized by experimentally determined adsorption isotherms for several metal ions with pH [5.8, 5.9] and, of course, the experimental findings concerning the extent to which the impact of ionic additives on the growth rate depends on the pH and composition of the mother liquor [5.10–5.12].

5.2. Impact on Growth Kinetics

The effect of an adsorbed additive or impurity on crystal growth may be principally divided into thermodynamic effects and kinetic effects on the

growth models described in Chap. 2 [5.13]. Because the adsorption and crystal growth are both highly specific to the single faces of a crystal, the impact of an additive has to be seen as face-specific, too. Generally, as explained below, an additive or impurity might accelerate, decrease, or totally suppress the growth of a crystal face. In addition, the mechanism of growth might be changed by the effect of the additive. The answer to the important question as to which of these contrary effects predominates has to be found from the consideration as to which of the thermodynamic and kinetic effects prevails. Beyond these direct effects of additives or impurities on crystallization kinetics, attention has to be paid for continuously operated industrial crystallizers to the interdependence of these effects with supersaturation from a mass-balance point of view [5.14].

5.2.1. *Thermodynamic Effects*

The important thermodynamic parameter in the BCF, B + S, and PN model [see Eqs. (2.13), (2.24), and (2.26), respectively], which is altered notably through the adsorption of an impurity, is the interfacial energy, γ_{CL}. Setting up the Gibbs adsorption equation in such a way that the excess of the solvent is zero, the effect of the adsorbing species on the interfacial energy $\gamma_{CL,\mathrm{im}}$, with the coverage Γ in moles per unit area of the surface, reads

$$\gamma_{CL,\mathrm{im}} = \gamma_{CL,0} - \int \Gamma_{\mathrm{im}}\, d\mu_{\mathrm{im}} \tag{5.4}$$

When the Langmuir adsorption isotherm [Eq. (5.2)] is applied with the maximum coverage of impurities, $\Gamma_{\max}$, equation (5.4) becomes

$$\gamma_{CL,\mathrm{im}} = \gamma_{CL,0} - \Re T\, \Gamma_{\max} \ln\left(\frac{1}{1-\theta}\right) \tag{5.5a}$$

and for an ionic impurity of valence, z, adsorbing on a face with the surface charge density, σ, it becomes

$$\gamma_{CL,\mathrm{im}} = \gamma_{CL,0} - \Re T\, \Gamma_{\max} \ln\left(\frac{1}{1-\theta}\right) - \frac{8\Re TI}{z\kappa}\left[\sqrt{1+\left(\frac{\kappa\sigma}{4FI}\right)^2} - 1\right] \tag{5.5b}$$

For the latter equation, a simple diffuse-layer model for the electrical double layer was assumed with the ionic strength I, the reciprocal Debye length κ, and the Faraday constant F (cf. Chapter 6) [5.15]. The above equations generally lead to a decrease in the interfacial energy with increasing adsorption of the additive and, thus, to an increase in the growth kinetics, whichever one of the growth mechanisms mentioned above prevails. The reduction in the interfacial energy brings about a reduction in the Gibbs free enthalpy to form nuclei, so that at a given supersaturation, the number

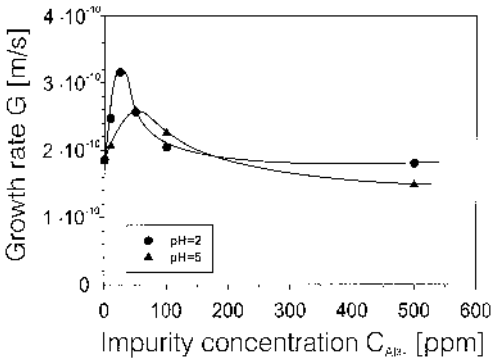

Figure 5.2. Interrelation of thermodynamic (accelerating) and kinetic (retarding) effects of Al^{3+} on $(NH_4)_2SO_4$ for two different pHs. (Data from Ref. 5.12.)

of nuclei in the polynuclear and birth + spread models increases. The kink spacing, x_0, and also the step spacing, y_0, are reduced, which, in turn, causes the steps to advance faster. It should be noted that equations (5.5a) and (5.5b) are face-specific, as the interfacial energy, $\gamma_{CL,0}$, the maximum coverage, Γ_{max}, the surface charge density, σ, and the loading, θ, are face-specific, too. Single faces will, therefore, be accelerated faster than others. Based on this thermodynamic effect, Knacke and Stranski [5.16] and, later, Lacmann and Stranski [5.17] developed a model for the equilibrium shape of crystals under the influence of additives.

Experimental evidence for this accelerating effect of additives on growth kinetics has been given, for example, by Blisnakov and Kirkova [5.18] for small amounts of Methylene Blue on lead nitrate. For higher additive concentrations, the growth kinetics decrease as a consequence of superposing retarding effects (i.e., kinetic effects), as mentioned below. Comparable results are shown in Figure 5.2 for the influence of Al^{3+} on ammonium sulfate at two different pH values [5.12], whereas there is an interplay of accelerating effects due to possibly simultaneous changes in the supersaturation. Generally, the extent to which an additive leads to an acceleration of growth kinetics also depends on the prevailing supersaturation. When, in the case of an underlying screw-dislocation mechanism, the supersaturation is $\sigma > 19V_n\gamma_{CL}/2kT\nu x_s$ [see Eq. (2.13)], the growth is not limited by the spacing of the kinks and steps. A further decrease in the kink and step spacing through a decrease in γ_{CL} will not, therefore, accelerate growth. Growth retardation resulting from the kinetic effects of the adsorbed impurity mentioned below will prevail. A similar consideration can be found for

the birth and spread mechanism: If the supersaturation is $\sigma > (\pi/3)V_m^{4/3}(\gamma_{CL}/kT)^2$ [see Eq. (2.24)], the growth is not limited by surface nucleation, and a further increase in surface nuclei due to the lower interfacial energy will not result in faster growth. In contrast, if the supersaturation is below the critical values given above, adsorption of an additive will increase growth kinetics, in principle, for both growth mechanisms, whereas experimental evidence for this was found for B + S only [5.2]. Note that beside the effects on crystal growth mentioned, the decrease in the interfacial energy has an even stronger impact on nucleation kinetics and, thus, on the metastable zone width, as recently shown in experimental studies [5.19].

5.2.2. *Kinetic Effects*

When sufficient sites for the integration of growth units are available and bulk diffusion is still not limiting, the growth rate is bound to the advancement of the steps on the crystal surface, whether the source of the steps are spiral dislocations or nuclei, as in the birth and spread model. Any impact of the adsorbed impurity on this advancement of steps is summarized here as kinetic effects. Depending on the location of the adsorbed additive or impurity, different models describe the kinetic effects that result in an impeded step velocity. For the reversible adsorption on kink sites, Blisnakow and Kirkova [5.18] have given a simple model for the growth velocity of a crystal face:

$$v_{imp} = v_0(1 - \theta_k) + v_{imp,\infty}\theta_k \tag{5.6}$$

with θ_k the loading of the impurity on available kink sites and v_{imp}, v_0, and $v_{imp,\infty}$ the face growth rate in the presence, in the absence, and in the case of complete coverage with the impurity, respectively. Comparable equations can be found for the reversible adsorption at a step and on a ledge [5.2, 5.3]. The physical meaning of the impeded velocity is that the impurity has to desorb before a new growth unit is incorporated into the lattice in the case of kink-site adsorption, that the effective length along which kink sites may form is reduced in the case of step-site adsorption, and that the surface diffusion of the growth units is reduced in the case of adsorption on a ledge.

It being assumed that the additive is adsorbed irreversibly on the smooth face, the Cabrera–Vermileya model [5.20] considers the adsorbed units to be stumbling blocks for the advancement of the steps. The advancing step is predicted to divide at these adsorbed units and to continue growing between two neighboring adsorbed units with a radius of curvature r (see Fig. 5.3) and thus growing at a slower rate than with infinite radius according to the BCF theory [2.7, 2.20]. If the radius of curvature is smaller than the critical value ($r < r_c$), the advancement of the step is stopped and the growth of the

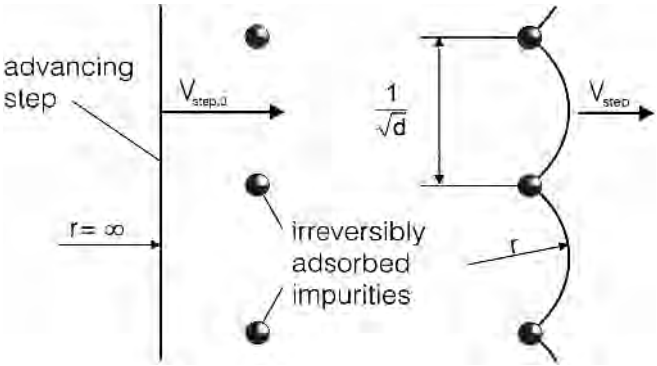

Figure 5.3. Impeded step velocity with irreversibly adsorbed impurities (r: radius of curvature; d: average density of impurities).

crystal face is blocked. The impeded step velocity, $v_{step,imp}$ is hence related to the velocity in the absence of impurities $v_{step,0}$ and to the average density of adsorbed impurities, d,

$$\frac{v_{step,imp}}{v_{step,0}} = (1 - 2r_c\sqrt{d})^{1/2} \tag{5.7}$$

with the critical radius of curvature,

$$r_c = \frac{\gamma_{CL} V_m}{kTv \ln S} \quad \text{(cf Eq. (2.5))} \tag{5.8}$$

The models given above form the basis for various extended or modified models, which can be found in the literature (e.g., Refs. 2.20 and 5.21); the general distinction can be made that models based on equation (5.7) predict zero growth below a minimum supersaturation, whereas models assuming reversible adsorption describe a nonzero growth behavior. It should be noted that according to the considerations in Sec. 5.1, kink positions form an energetically more favorable site for adsorption than a step or a ledge, so that with increasing concentration of the impurity, the underlying mechanism might change (e.g., when all kink positions are filled and the impurity starts to adsorb on the step [5.22]). The Cabrera–Vermileya model will generally be valid, if the additive is incorporated into the crystal lattice, as is the case especially for "tailor-made" additives (cf. Chapter 12) or if the mobility on the surface decreases with rising molecular mass of the adsorbate. In Figure 5.4, an example of the behavior of single-face growth rates with increasing concentration of the impurity is given for reversible adsorption (Fig. 5.4a) irreversible adsorption (Fig. 5.4b). Whereas in Figure 5.4a, the decrease in the growth rate is already strong with small amounts of the

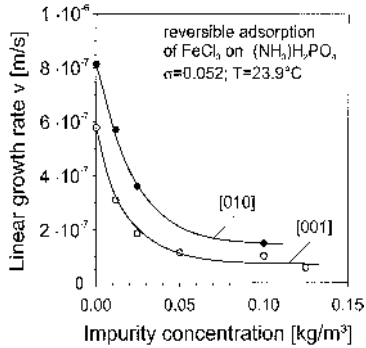

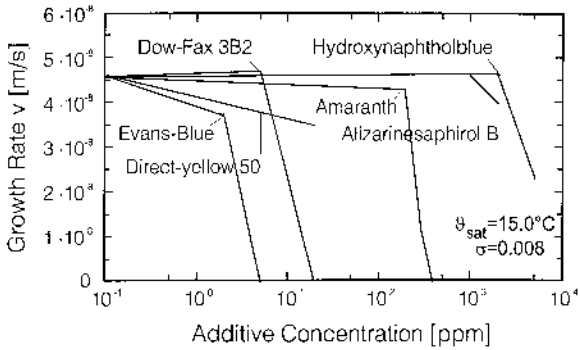

Figure 5.4. Nonzero and zero growth behavior as a consequence of reversible and irreversible adsorption of impurities. (a) Reversible adsorption of $FeCl_3$ and $AlCl_3$ on the [001] and [010] directions for the {100} faces of $(NH_3)H_2PO_4$ [5.3]; (b) irreversible adsorption of various additives on the {110} face of KNO_3 [5.23].

impurity and tends asymptotically toward a lower but nonzero growth rate with full coverage of the adsorption sites, in Figure 5.4b, the growth rate remains almost unaffected up to a specific adsorption density at which the mean distance between neighboring adsorbates is smaller than the critical radius and thus the growth is steeply reduced to zero.

6. METASTABLE ZONE, RECOMMENDED SUPERSATURATION

In Chapter 5, it will be shown that besides activated or catalytic secondary nucleation, secondary nucleation can be caused by collision, contact, and

shear stress. In general, we are currently not in a position to predict with sufficient accuracy the nucleation rates depending on the mechanical impact, such as forces or stress, and on supersaturation as the driving force for this kinetic parameter. Furthermore, the microstructure and roughness of the parent crystal surface play a role, the extent of which is influenced by supersaturation. It must always be kept in mind that the detectable number of crystalline species growing in a supersaturated solution depends on the device used for measuring the crystal size distribution. The smaller the detectable particle, the larger the number of particles registered by the analyzer. Consequently, it is difficult to define a rate of nucleation because the exact number of solid particles and their change with time is not known. With respect to a crystalline material produced in a crystallizer, it is the crystal size distribution in a certain size range which is important, not the total number of all species. This size distribution depends primarily on the growth rates of all effective nuclei. Therefore, it is reasonable to define rates of nucleation and growth with respect to the design the scale-up of crystallizers rather than in a more physical sense.

The sections on the metastable zone width for homogeneous primary nucleation and on the recommended supersaturation $\Delta C < \Delta C_{\text{met}}$ have made it clear that in industrial crystallizers, homogeneous nucleation can occur only at points of very high supersaturation (i.e., heat transfer areas, feedpoint of solution, etc.). When dealing with unseeded batch crystallizers, $\Delta C > \Delta C_{\text{met}}$ can occur at the beginning of the batch for a short period, especially in the case of natural cooling or a constant cooling rate or evaporation rate, because no crystal surface is available. As a rule, heterogeneous nucleation takes place and the number of heterogeneous nuclei can be reduced by a suitable preparation of the solution (i.e., removal of the dust particles by filtration). Seed crystals may be covered by crystalline dust, which can be removed by washing them with an undersaturated solution. However, when dealing with industrial brines, it is not possible to predict the rate of heterogeneous nucleation B_{het} because neither the particle size distribution of the dust nor the contact angle θ between foreign particles and solute nuclei are known (cf. Sec. 2 in Chapter 2). Furthermore, agglomeration can play an important role. For this reason, crystallization experiments with an industrial brine must be carried out in the laboratory, especially for systems with medium or low solubility.

Things are slightly easier for relatively pure systems with a high solubility ($C^*/C_C > 0.01$) crystallized at a low relative supersaturation ($\sigma < 0.01$). There is experimental evidence that in this case, the rate of activated or catalytic nucleation due to the removal of preordered species and/or clusters from the crystals present in the crystallizer is small in comparison to the rate of secondary nucleation caused mainly by crystal–crystal and crystal–rotor

collisions. However, the situation may change when supersaturation is increased, and it is necessary to give some information on the metastable zone width $\Delta C_{\mathrm{met,sec}}$ for secondary nucleation. Mullin [0.1] and Nyvlt et al. [6.1], in particular, measured this zone width for constant cooling rates in the presence of parent crystals for a total of more than 20 systems. Kind and Mersmann [6.2] measured the increase of particles with time at a constant relative supersaturation for two systems with low solubility and two others with medium solubility. As a rule, agitation was not provided during these experiments, which prevented collisions of crystals with other crystals or with a rotor. After a certain induction time t_{ind} at a constant cooling rate $d\vartheta/dt$, a shower of visible nuclei was observed. The original literature gives the subcooling temperature $\Delta\vartheta_{\mathrm{met}}$ at which the shower occurred. This temperature difference $\Delta\vartheta_{\mathrm{met}}$ can be expressed by supersaturation $\Delta C_{\mathrm{met,sec}}$ according to

$$\Delta C_{\mathrm{met,sec}} = \frac{dC^*}{d\vartheta}\,\Delta\vartheta_{\mathrm{met,sec}} \tag{6.1}$$

or as the relative metastable supersaturation

$$\sigma_{\mathrm{met,sec}} = \frac{\Delta C_{\mathrm{met,sec}}}{C^*} = \frac{d(\ln C^*)}{d\vartheta}\,\Delta\vartheta_{\mathrm{met,sec}} \tag{6.2}$$

Table 6.1 contains metastable zone widths $\Delta\vartheta_{\mathrm{met}}$ and ΔC_{met} of aqueous systems according to the measurements of Nyvlt et al. [6.1]. Because pure systems were investigated and collisions of parent or seed crystals did not take place, it must be assumed that clusters of size $L_c \geq L^*$ are the source of these nuclei. Here, L^* is the size of a nucleus that is just stable at relative supersaturation σ (cf. Sec. 1 of Chapter 2). The nuclei of minimum size L^* will grow in the supersaturated solution during the induction time to size L, which is sensitive for the particle analyzer or for the crystal size distribution of the product under discussion. This growth can be controlled by diffusion according to

$$\frac{\overline{v}_{\mathrm{dif}}}{k_d} = \frac{\Delta C}{C_C} \tag{6.3}$$

and by integration according to

$$\frac{\overline{v}_{\mathrm{int}}}{k_g'} = \left(\frac{\Delta C}{C^*}\right)^r \tag{6.4}$$

With the simple assumption that $2\overline{v}t_{\mathrm{ind}} = L - L^*$, we obtain

Table 6.1. Metastable Zone Widths

System	$\Delta\vartheta_{met}$ [K]	C^* Hyd. (25°C) [kmol/m^3]	C_c [kmol/m^3]	C^*/C_C	ΔC_{met} [kmol/m^3]	$\Delta C_{met}/C_C$ [$\times 10^3$]	$\Delta C_{met}/C^*$ [$\times 10^3$]
$NH_4Al(SO_4)_2$	3	0.18	3.62	0.049	0.018	4.92	99.70
NH_4Cl	0.7	5.65	28.55	0.198	0.028	0.97	4.93
NH_4NO_3	0.6	11.21	21.55	0.520	0.057	2.65	5.10
$(NH_4)_2SO_4$	1.8	4.09	13.39	0.306	0.016	1.21	3.95
$NH_4H_2PO_4$	2.5	2.94	15.67	0.187	0.126	8.04	42.91
$CuSO_4$	1.4	1.37	9.16	0.150	0.032	3.54	23.66
$FeSO_4$	0.5	1.87	6.83	0.273	0.020	2.95	10.81
$MgSO_4$	1	2.90	6.82	0.425	0.043	6.23	14.65
$NiSO_4$	4	2.57	6.94	0.371	0.136	19.52	52.63
NaCl	1	5.43	37.01	0.147	0.001[a]	0.02[a]	0.12[a]
$Na_2B_4O_7$	3	0.16	4.44	0.035	0.021	4.66	131.81
Na_2HPO_4	0.4	0.81	4.24	0.192	0.040	9.47	49.42
$NaNO_3$	0.9	7.80	26.55	0.294	0.042	1.60	5.43
Na_2SO_4	0.3	1.87	4.56	0.411	0.040	8.84	21.54
$Na_2S_2O_3$	1	3.85	7.08	0.544	0.066	9.38	17.24
$KAl(SO_4)_2$	4	0.27	3.70	0.072	0.036	9.60	134.21
KCl	1.1	4.15	26.68	0.155	0.031	1.18	7.56
KH_2PO_4	9	1.70	17.26	0.099	0.285	16.48	167.85
K_2SO_4	6	0.67	15.28	0.044	0.059	3.87	88.72

[a]Probably too small. *Source*: Ref. 6.1.

$$\frac{\Delta C_{\text{met,sec}}}{C_C} = \frac{L - L^*}{2t_{\text{ind}}k_d} \tag{6.5}$$

$$\sigma_{\text{met,sec}} = \frac{\Delta C_{\text{met,sec}}}{C^*} \approx \left(\frac{L - L^*}{2t_{\text{ind}}k_g'}\right)^{1/r} \tag{6.6}$$

When dealing with systems of high solubility and large median crystal sizes ($L_{50} > 100\,\mu\text{m}$), we can assume $L^* \ll L$ or

$$\frac{\Delta C_{\text{met,sec}}}{C_C} \approx \frac{L}{2t_{\text{ind}}k_d} \tag{6.7}$$

$$\sigma_{\text{met,sec}} = \frac{\Delta C_{\text{met,sec}}}{C^*} \approx \left(\frac{L}{2t_{\text{ind}}k_g'}\right)^{1/r} \tag{6.8}$$

In the case of diffusion-controlled growth (which applied to high $\Delta C/C_C$ values for systems with a given dimensionless solubility C^*/C_C), the dimensionless metastable zone width $\Delta C_{\text{met,sec}}/C_C$ decreases with long induction times t_{ind}. According to Kind and Mersmann [6.2], the mean residence time τ or the batch time τ_{batch} should be smaller than the induction time period t_{ind}. For this reason, $\Delta C_{\text{met,sec}}/C_C$ is low. With $\frac{1}{2}L = 10^{-4}$ m, $k_d = 10^{-4}$ m/s, and $t_{\text{ind}} = 10^3$ s, we obtain $\Delta C_{\text{met,sec}}/C_C = 10^{-3}$. Reducing the dimensionless supersaturation $\Delta C/C_C$ leads to growth, which is now controlled to a greater extent by integration (cf. Fig. 3.3). From equation (6.8), we can see that the metastable zone width, now better expressed as the relative metastable supersaturation $\sigma_{\text{met,sec}}$, increases with a decreasing growth coefficient k_g'. In addition, the metastable zone width always depends on the induction time period t_{ind} and on the detectable particle size L_{det}. This can be explained by a model derived for predicting the metastable zone width when catalytic secondary nucleation (no attrition) and integration-controlled growth are the decisive mechanisms [6.3]. The definition of the metastable supersaturation should be based on a certain nucleation rate. Because measured data for this rate are not available, a seeded solution is cooled at a constant cooling rate, which leads to a continuous increase of supersaturation with time. After a certain induction time, the supersaturation passes through a maximum, which can be interpreted as the metastable zone width $\Delta C_{\text{met,sec}}$ for secondary nucleation.

Metastable zone widths have been measured for many substances by Mullin [0.1] and Nyvlt et al. [6.1]; see Tables 6.2 and 6.3. These experimental $\Delta C_{\text{met,sec}}$ (data of 28 aqueous systems in total) were compared with values calculated from the model. The accuracy is not very good but sufficient for industrial crystallization. The advantage of the model is that it allows metastable zone widths to be predicted from the solubility parameter $d(\ln C^*)/d(\ln T)$ and the cooling rate $dT/dt = \dot{T}$; however, extensive

Table 6.2. Metastable Zone Widths for a Cooling Rate of 5 K/h (Solvent: H_2O)

Solute	Dimensionless solubility C^*/C_C	Solubility parameter $\frac{d(\ln C^*)}{d(\ln T)}$	Maximum detectable subcooling $\Delta T_{met,exp}$ in K for $dT/dt = 5\,K/h$ according to Mullin [0.1]
Ammonium alum	0.08	15.0	3.0
Ammonium chloride	0.20	2.1	0.7
Ammonium nitrate	0.52	2.5	0.6
Ammonium sulfate	0.31	0.7	1.8
Ammonium dihydrogenphosphate	0.19	5.1	2.5
Copper sulfate	0.15	5.0	1.4
Ferrous sulfate	0.27	6.4	0.5
Magnesium sulfate	0.43	4.4	1.0
Nickel sulfate	0.37	3.9	4.0
Sodium tetraborate	0.04	12.7	3.0
Sodium dihydrogen-phosphate	0.19	20.0	0.4
Sodium nitrate	0.29	1.8	0.9
Sodium sulfate	0.43	20.3	0.3
Sodium thiosulfate	0.55	5.1	1.0
Potassium aluminum sulfate	0.07	9.9	4.0
Potassium chloride	0.16	2.0	1.1
Potassium dihydrogen-phosphate	0.10	5.7	9.0
Potassium sulfate	0.04	4.4	6.0
Calcium nitrate	0.71	2.0	0.7
Boric acid	0.04	7.9	1.9
Potassium bromide	0.20	1.4	1.6
Potassium iodide	0.33	0.6	0.8
Potassium nitrite	0.62	0.3	1.2
Potassium nitrate	0.18	7.0	0.5
Sodium sulfite	0.39	6.6	0.6
Sodium bromide	0.48	1.2	1.4
Sodium iodide	0.64	0.7	1.4
Sodium nitrite	0.29	0.7	1.4

Table 6.3. Metastable Zone Widths for Cooling Rates of 2, 5, and 20 K/h (Solvent: H_2O)

Solute	Dimensionless solubility C^*/C_C	Solubility parameter $\frac{d(\ln C^*)}{d(\ln T)}$	Maximum detectable subcooling $\Delta T_{\text{met,exp}}$ in K for $dT/dt =$		
			2 K/h	5 K/h	20 K/h
Calcium nitrate	0.71	2.0	0.6	0.9	1.5
Boric acid	0.04	7.9	1.3	1.9	3.1
Potassium bromide	0.20	1.4	1.1	1.6	2.7
Potassium iodide	0.33	0.6	0.6	0.8	1.2
Potassium nitrite	0.62	0.3	0.9	1.2	1.8
Potassium nitrate	0.18	7.0	0.4	0.5	0.7
Sodium sulfite	0.39	6.6	0.56	0.6	0.7
Sodium bromide	0.48	1.2	1.0	1.4	2.3
Sodium iodide	0.64	0.7	1.2	1.4	2.0
Sodium nitrite	0.29	1.2	1.4	1.8	2.6

Source: Ref. 6.1.

calculations are necessary. Therefore, an even more simplified model was derived with the following assumptions:

- The nucleation step is so fast that it is not rate controlling for the prediction of $\Delta C_{\text{met,sec}}$.
- The increase in size of the nuclei according to growth is decisive for the occurrence of a shower of nuclei; see Ref. 6.4.
- With respect to the low level of supersaturation at the beginning of the cooling, the growth is controlled by the integration step.
- The metastable zone width $\Delta C_{\text{met,sec}}$ is observed when the nuclei have grown to a mean detectable size $L_{\text{det}} = 10\,\mu\text{m}$ and the crystal holdup φ_T has assumed values between 10^{-4} and 10^{-3}.

The metastable zone width is then given by

$$\frac{\Delta C_{\text{met,sec}}}{C_C} = 12\left[\frac{d(\ln C^*)}{d(\ln T)}\left(\frac{C^*}{C_C}\right)^{5/3}\ln\left(\frac{C_C}{C^*}\right)\frac{\dot{T}}{T}\frac{d_m L_{\text{det}}}{D_{AB}}\right]^{1/3} \tag{6.9a}$$

or

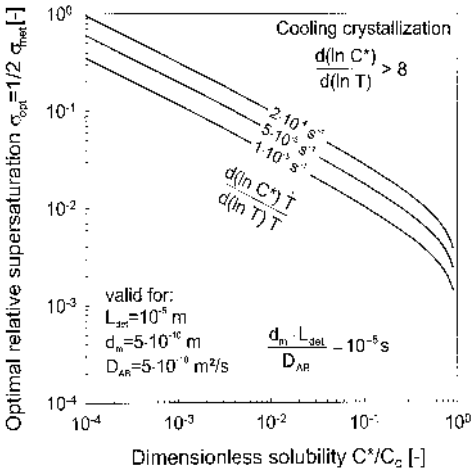

Figure 6.1. Metastable and optimal supersaturation versus the dimensionless solubility for various cooling rates $[d\ln C^*/d(\ln T)](\dot{T}/T)$ of cooling crystallization.

$$\sigma_{\mathrm{met,sec}} = 12\left[\frac{d(\ln C^*)}{d(\ln T)}\left(\frac{C_C}{C^*}\right)^{4/3}\ln\left(\frac{C_C}{C^*}\right)\frac{\dot{T}}{T}\frac{d_m L_{\mathrm{det}}}{D_{AB}}\right]^{1/3} \tag{6.9b}$$

This equation is illustrated in Figure 6.1.

Cooling crystallization is only profitable when the slope $d(\ln C^*)/d(\ln T)$ is greater than approximately 8. When the solubility versus temperature curve is flat $[d(\ln C^*)/d(\ln T) < 1]$, evaporative crystallization is applied. In this case, the equations for the metastable zone widths can be formulated with the evaporation rate instead of the cooling rate $\dot{T}/T$. With the assumption made earlier, the following equations can be derived:

$$\frac{\Delta C_{\mathrm{met,sec}}}{C_C} = 12\left[\left(\frac{C^*}{C_C}\right)^{5/3}\ln\left(\frac{C_C}{C^*}\right)\frac{\Delta\dot{L}^\circ}{L_\alpha^\circ}\frac{d_m L_{\mathrm{det}}}{D_{AB}}\right]^{1/3} \tag{6.10a}$$

or

$$\Delta C_{\mathrm{met,sec}} = 12\left[\left(\frac{C_C}{C^*}\right)^{4/3}\ln\left(\frac{C_C}{C^*}\right)\frac{\Delta\dot{L}^\circ}{L_\alpha^\circ}\frac{d_m L_{\mathrm{det}}}{D_{AB}}\right]^{1/3} \tag{6.10b}$$

In these equations, $\Delta\dot{L}^\circ$ is the mass flow rate of the solvent evaporated from the solution and L_α° is the mass of the solvent in the crystallizer at the beginning of the batch. As can be seen, the expression $[d(\ln C^*)/d(\ln T)] \times (\dot{T}/T)$ of cooling crystallization is replaced by the mass flow rate $\dot{L}^\circ$ of the

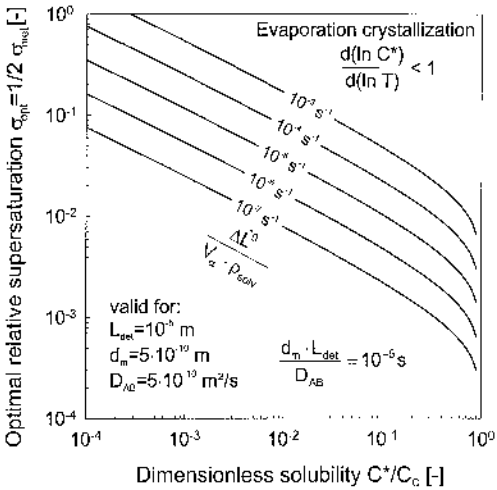

Figure 6.2. Metastable and optimal supersaturation versus the dimensionless solubility for various evaporation rates $\Delta\dot{L}^{\circ}/(V_{\alpha}\rho_{\mathrm{solv}})$ of evaporation crystallization.

solvent based on the initial mass L_{α}° of the solvent. However, if the contents of the evaporation crystallizer are not well mixed, the actual mass L_{act}° is smaller than L_{α}° because only the solution in a certain layer below the boiling liquid surface is supersaturated. Because it is difficult to predict the field of supersaturation in a large evaporative crystallizer, the equations for the metastable zone widths are problematic but give an initial rough estimate. In Figure 6.2, the optimal relative supersaturation $\sigma_{\mathrm{opt}} = 0.5\sigma_{\mathrm{met,sec}}$ is plotted against the dimensionless solubility for different rates of evaporated solvent based on the initial solvent mass.

The median crystal size and the crystal size distribution depend on the kinetics (nucleation and growth) being the result of supersaturation. In industrial crystallizers, the relative supersaturation σ can be in the range from $\sigma = 10^{-4}$ to $\sigma < 10^{8}$ for systems with $10^{-8} < C^*/C_C < 1$. A crystalline product with a certain specification requires an optimal supersaturation that leads to the product properties via nucleation and growth. The diagrams shown in Figures 6.1 and 6.2 can give a first estimate of this optimal supersaturation with respect to nucleation. Further information can be drawn from diagrams in which crystal growth rates are depicted (cf. Fig. 3.5). It has been shown that at low supersaturation, the kink density is very low and the crystals' faces are smooth insomuch as growth is appreciably enhanced only by surface nucleation and polynuclear growth. The kink density and the

number of collisions of units determine the growth rate, which will change from a parabolic law ($G \sim \sigma^2$) to an exponential law with increasing supersaturation. For even higher supersaturation, the crystal surface is rough on a molecular scale (i.e., the kink density is high) so that volume diffusion is now the controlling mechanism ($G \sim \sigma$).

It is difficult to predict the controlling step for crystal growth in general. The maximum possible growth rates are described by equations (3.9) and (3.10), which represent a superposition of the growth rates of volume diffusion, v_{dif}, and of the integration step v_{int}. In the diagram in Figure 3.5, lines for $v_{dif} = v_{int}$ and also for $v_{dif} \ll v_{int}$ and for $v_{dif} \gg v_{int}$ are drawn according to the corresponding equations. The growth rate v_{int} increases approximately with $(C^*)^{4/3}$ for a given supersaturation σ. The supersaturation must be much higher for sparingly soluble substances in order to obtain an industrially advantageous growth rate of $10^{-9} < G < 10^{-7}$ m/s. When new crystals are formed by primary nucleation at low levels of supersaturation ($S < 10$), the nuclei are smooth and appreciable growth is gained only by the polynuclear growth mechanism with the characteristic strong increase in the growth rate with supersaturation. This has been observed for $BaSO_4$ [3.14]. In contrast, nuclei produced in the range $20 < S < 100$ exhibit molecular rough surfaces and their growth can be described by the superposition of v_{int} and v_{dif}. With respect to industrial crystallization, the following conclusions can be reached:

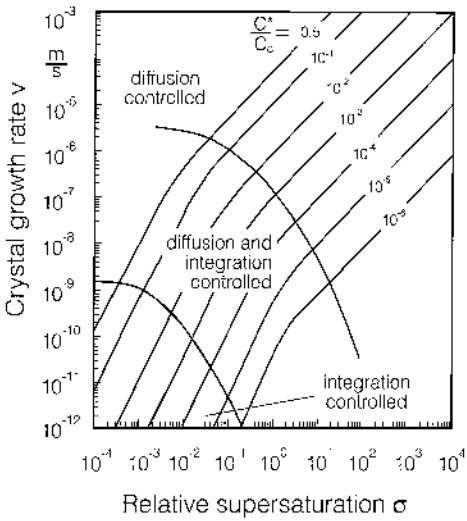

Figure 6.3. Crystal growth rate, v, versus supersaturation, σ (valid for $k_d = 10^{-4}$ m/s and $D_{AB} = 10^{-9}$m^2/s).

- The growth rate of systems with a low solubility ($C^*/C_C < 10^{-7}$) is diffusion controlled for $\sigma > 10$ and $\nu = 1$.
- This is also true of systems with $C^*/C_C < 10^{-4}$ for the relative supersaturation $\sigma > 1$.
- In general, both mechanisms, volume diffusion and integration, contribute to growth when $0.1 < C^*/C_C < 10^{-4}$ and $10^{-3} < \sigma < 0.1$.
- The integration of units is the decisive step for crystal growth in the ranges $C^*/C_C < 10^{-4}$ and $\sigma < 0.1$ with $v_{\text{int}} < 10^{-9}$ m/s.

This information can also be drawn from Figure 6.3, in which the growth rate, v, is plotted against the relative supersaturation, σ, for various ratios of C^*/C_C. Growth is either controlled by diffusion or by both mechanisms (diffusion and integration) in order to obtain optimal growth rates. Polynuclear growth can be important to roughen a smooth surface and to start growth, but the mechanism is not decisive in industrial crystallizers, which should be operated without appreciable fluctuations in supersaturation in order to obtain good product quality. The optimal supersaturation can be determined by supersaturation sensors [6.5; 6.6]

REFERENCES

[0.1] J. W. Mullin, *Crystallization*, 3rd ed., Butterworth, Oxford (1993).

[0.2] A. Berthoud, Théorie de la formation des faces d'un crystal, *J. Chim. Phys.*, *10*: 624 (1912).

[0.3] J. J. P. Valeton, Wachstum und Auflösung der Kristalle, *Z. Kristallogr.*, *59*: 135, 335 (1923); *60*: 1 (1924).

[1.1] M. A. Larson, Solute clustering in concentrated and supersaturated solutions, in *Proc. 11th Symp. on Industrial Crystallization* (A. Mersmann, ed.), pp. 841–846 (1990).

[1.2] Y. C. Chang and A. S. Myerson, The diffusivity of glycine in concentrated saturated and supersaturated solutions, *AIChE J.*, *32*: 1747 (1986).

[1.3] A. S. Myerson, P. Y. Lo, Y. C. Kim, and R. Ginde, Diffusion, viscosity and cluster formation in metastable solutions, in *Proc, 11th Symp. on Industrial Crystallization* (A. Mersmann, ed.), pp. 847–852 (1999).

[1.4] Y. C. Chang and A. S. Myerson, Diffusion coefficients in supersaturated solutions, in *Industrial Crystallization '84* (S. J. Jancic and E. J. de Jong, eds.), Elsevier, Amsterdam (1984).

[1.5] A. E. Nielsen, Transport control in crystal growth from solution, *Croatica Chem. Acta*, *53*(2): 255 (1980).

[2.1] D. E. Temkin, *Crystallization Processes*, Consultants Bureau, New York, p. 15 (1964).
[2.2] K. A. Jackson, *Liquid Metals and Solidification*, American Society for Metals, Cleveland, OH, p. 174 (1958).
[2.3] P. Bennema and G. H. Gilmer, in *Crystal Growth: An Introduction* (P. Hartman, ed.), North-Holland, Amsterdam, p. 263 (1973).
[2.4] P. Bennema, Crystal growth from solution: Theory and experiment, *J Cryst. Growth*, *24/25*: 76 (1974).
[2.5] J. R. Bourne and R. J. Davey, Solvent effects in the growth of hexamethylene tetramine crystals, in *Industrial Crystallization* (J. W. Mullin, ed.), Plenum Press, New York (1974).
[2.6] F. C. Frank, The influence of dislocations on crystal growth, *Discuss. Faraday Soc.*, *5*: 48 (1949).
[2.7] W. K. Burton, N. Cabrera, and F. C. Frank, The growth of crystals and the equilibrium structure of their surface, *Phil. Trans. Roy. Soc. London*, *243*: 299 (1951).
[2.8] A. E. Nielsen, Electrolyte crystal growth mechanisms, *J. Cryst. Growth, 67*: 289 (1984).
[2.9] A. Mersmann, General prediction of statistically mean growth rates of a crystal collective, *J. Cryst. Growth, 147*: 181 (1995).
[2.10] A. E. Nielsen, Theory of electrolyte crystal growth, *Pure Appl. Chem.*, *53*: 2025 (1981).
[2.11] P. Bennema, Analysis of crystal growth models for slightly supersaturated solutions, *J. Cryst. Growth, 1*: 278 (1967).
[2.12] P. Bennema, The importance of surface diffusion for crystal growth from solution, *J. Cryst. Growth, 5*: 29 (1969).
[2.13] P. Bennema, Theory and experiment for crystal growth from solution: Implications for industrial crystallization, in *Industrial Crystallization* (J. W. Mullin, ed.), Plenum Press, New York (1976).
[2.14] N. Cabrera and R. V. Coleman, *The Art and Science of Growing Crystals*, John Wiley & Sons, New York (1963).
[2.15] C. van Leeuwen, G. Janssen-van Rosmalen, and P. Bennema, Simulation of step motion on crystal surfaces, *Surf. Sci.*, *44*: 213 (1974).
[2.16] R. Janssen-van Rosmalen and P. Bennema, Simulation of perturbations in trains of steps on crystal surfaces, *J. Cryst. Growth, 32*: 293 (1976).
[2.17] R. L. Schwoebel, Step motion on crystal surfaces, II, *J. Appl. Phys.*, *40*: 614 (1969).
[2.18] P. Bennema, J. Boon, C. van Leeuwen, and G. H. Gilmer, Confrontation of the BCF theory and computer simulation

experiments with measured (R, σ) curves, *Krist. Technol.*, *8*: 659 (1973).
[2.19] J. C. Brice, *The Growth of Crystals from Liquids*, North-Holland, Amsterdam (1973).
[2.20] M. Ohara and R. C. Reid, *Modeling Crystal Growth Rates from Solution*, Prentice-Hall, Englewood Cliffs, NJ (1973).
[2.21] W. B. Hilling, A derivation of classical two-dimensional nucleation kinetics associated crystal growth laws, *Acta Metallurgica*, *14*: 1868 (1966).
[2.22] H. Schubert, *Keimbildung bei der Kristallisation schwerlöslicher Stoffsysteme*, Thesis, Technische Universität München (1998).
[2.23] G. H. Gilmer and P. Bennema, Simulation of crystal growth with surface diffusion, *J. Appl. Phys.*, *43*: 1347 (1972).
[2.24] J. A. Dirksen and T. A. Ring, Fundamentals of crystallization: Kinetic effects on particle size distribution and morphology, *Chem. Eng. Sci., 46*(10): 2389 (1991).
[2.25] A. E. Nielsen and J. M. Toft, Electrolyte crystal growth kinetics, *J. Cryst. Growth.*, *67*: 278 (1984).
[3.1] A. Mersmann, Design of Crystallizers, in *Proc. 10th Symp. on Industrial Crystallization* (J. Nyvlt and S. Zacek, eds.), Elsevier, Amsterdam (1989).
[3.2] G. Damköhler, Einflüsse der Strömung, Diffusion und des Wärmeüberganges auf die Leistung von Reaktionsöfen, *Z. Elektrochem. Angew. Phys. Chem.*, *42*: 846 (1936).
[3.3] S. Hatta, On the absorption of gases by liquids, II. Theoretical considerations of gas absorption due to chemical reaction, *Tech. Rep. Tohoku Imperial Univ.*, *10*: 613 (1931).
[3.4] J. Garside, Effectiveness factors in crystal growth, *Chem. Eng. Sci.*, *26*: 1425 (1971).
[3.5] J. Garside and J. W. Mullin, *Trans. Inst. Chem. Eng.*, *46*: T11/18 (1969).
[3.6] C. Y. Liu, H. S. Tseui, and G. R. Youngquist, Crystal growth from solution, *Chem. Eng. Prog. Symp. Ser.*, *110*(67): 43 (1970).
[3.7] T. Tengler and A. Mersmann, Einfluss von Temperatur, Übersättigung und Anströmgeschwindigkeit auf das Kristallwachstum aus Lösungen, *Chem. Ing. Techn.*, *55* (9): 730 (1983).
[3.8] K. A. Berglund and M. A. Larson, Growth of contact nuclei of citric acid monohydrate, *AIChE Symp. Ser.*, *78*: 215 (1982).
[3.9] J. Garside and J. W. Mullin, The crystalliaztion of aluminium potassium sulphate: A study in the assessment of crystalizer design data. III. Growth and dissolution rates, *Trans. Inst. Chem. Eng.*, *46*: 11 (1968).

[3.10] A. Mersmann, K. Bartosch, B. Braun, A. Eble, and C. Heyer, Möglichkeiten einer vorhersagenden Abschätzung der Kristallisationskinetik, *Chem. Ing. Techn.*, *72*(1/2): 17 (2000).
[3.11] A. Mersmann, M. Angerhöfer, T. Gutwald, R. Sangl, and S. Wang, General prediction of median crystal sizes, *Separ. Technol.*, *2*: 85 (1992).
[3.12] A. Mersmann, General prediction of statistically mean growth rates of a crystal collective, *J. Cryst. Growth.*, *147*: 181 (1995).
[3.13] Wang, *Größenabhängige Wachstumsdispersion von Abriebsteilchen und die Relevanz zur effektiven sekundären Keimbildung*, Thesis, Technische Universität München (1992).
[3.14] M. Angerhöfer, *Untersuchungen zur Kinetik der Fällungskristallisation von Bariumsulfat*, Thesis, Technische Univetsität München (1994).
[3.15] J. Garside, J. W. Mullin, and S. N. Das, Growth and dissolution kinetics of potassium sulphate crystals in an agitated vessel, *Ind. Eng. Chem. Fundam.*, *13*(4): 299 (1974).
[3.16] V. R. Phillips and N. Epstein, Growth of nickel sulphate in a laboratory-scale fluidized-bed crystallizer, *AIChE J.*, *20*(4): 678 (1974).
[3.17] A. H. Janse and E. J. de Jong, The occurence of growth dispersion and its consequences, in *Industrial Crystallization* (J. W. Mullin, ed.), Plenum Press, New York (1976).
[3.18] E. T. White and P. G. Wright, Magnitude of size dispersion effects in crystallizers, *Chem. Eng. Prog. Symp. Ser.*, *67*(110): 81 (1971).
[3.19] L. N. Natal'ina and E. B. Treivus, Growth rate variations for KDP crystals, *Sov. Phys. Crystallogr.*, *19*: 389 (1974).
[3.20] E. T. White and P. G. Wright, *Proc. Queensland Society of Sugar Cane Technology*, *36th Conf.*, p. 299 (1969).
[3.21] A. D. Randolph and E. T. Wright, Modeling size dispersion in the prediction of crystal size distribution, *Chem. Eng. Sci.*, *32*: 1067 (1977).
[3.22] J. Garside and M. A. Larson, Direct observation of secondary nuclei production, *J. Cryst. Growth*, *43*: 694 (1978).
[3.23] S. J. Jancic, G. M. van Rosmalen, and J. P. Peeters, Growth dispersion on nearly monosize crystal populations, in *Industrial Crystallization '84* (S. J. Jancic and E. J. de Jong, eds.), Elsevier, Amsterdam (1984).
[4.1] J. W. Mullin and J. Garside, Crystallization in the presence of impurities, *Chem. Eng.*, 402 (1974).
[4.2] A. König, H. H. Emons, and J. Nyvlt, The influence of sodium chloride on the driving force of the crystallization of potassium chloride from aqueous solutions, *Cryst. Res. Technol.*, *22*: 13 (1987).

[4.3] F. Farelo, G. von Brachel, and H. Offermann, Growth kinetics of NaC1 and KC1 crystals in ternary aqueous systems, in *Proc. 11th Symp. on Industrial Crystallization* (A. Mersmann, ed.), p. 459 (1990).
[4.4] A. Seidell and W. F. Linke, *Solubilities of Inorganic and Metal Organic Compunds*, 4th ed., Van Nostrand, New York, Vols. 1 and 2 (1958); W. F. Linke, American Chemical Society, Washington, D.C. (1965).
[4.5] J. N. Murrell and A. D. Jenkins, *Properties of Liquids and Solutions*, John Wiley & Sons, Chichester (1994).
[4.6] N. Stubicar, M. Scrbak, and M. Stubicar, Crystal growth of lead flouride using the constant composition method. II. The effect of Pb/F activity ratio on the kinetics of crystal growth, *J. Cryst. Growth*, *100*: 261 (1990).
[4.7] N. Stubicar, B. Markovic, A. Tonejc, and M. Stubicar, Crystal growth of lead fluoride phases using the constant composition method. III. The effect of pH and ionic strength, *J. Cryst. Growth*, *130*: 300 (1993).
[4.8] L. N. Rashkovich and G. T. Moldazhanova, Growth kinetics and morphology of potassium dihydrogen phosphate crystal faces in solutions of varying acidity, *J. Cryst. Growth*, *151*: 145 (1995).
[4.9] M. Aoun, E. Plasari, R. David, and J. Villermaux, Are barium sulphate kinetics sufficiently known for testing precipitation reactor models? *Chem. Eng. Sci.*, *51*(10): 2449 (1996).
[4.10] W. J. Benton, I. R. Collins, I. M. Grimsey, G. M. Parkinson, and S. A. Rodger, Nucleation, growth and inhibition of barium sulfate-controlled modification with organic and inorganic additives, *Faraday Discuss.*, *95*: 281 (1993).
[4.11] R. B. Fischer and T. B. Rhinehammer, *Rapid precipitation of barium sulfate*, Department of Chemistry, Indiana University, Bloomington, IN, p. 586 (1953).
[4.12] H. A. Mohamed and J. Ulrich, Influence of the pH-value on the growth and dissolution rate of potassium chloride, *Cryst. Res. Technol.*, *31*(1): 27 (1996).
[5.1] M. Mathieu, B. Simon, and R. Boistelle, *Compt. Rend (Paris)*, *C274*: 473 (1972).
[5.2] R. J. Davey, The effect of impurity adsorption on the kinetics of crystal growth from solution, *J. Cryst. Growth.*, *34*: 109 (1976).
[5.3] R. J. Davey and J. W. Mullin, Growth of the {100} faces of ammonium dihydrogen phosphate crystals in the presence of ionic species, *J. Cryst. Growth*, 26: 45 (1974).

[5.4] G. Bliznakow and R. Nikolaeva, Über den Einfluβ der aliphatischen Carbonsäuren auf die Wachstumsgeschwindigkeit von KBr-Kristallen, *Kristall Technik*, *2*(2): 161 (1967).
[5.5] P. G. Smith, H. R. Watling, and P. Crew, The effects of model organic compounds on gibbsite crystallization from alkaline aluminate solutions: polyols, *Colloids Surf. A.*, *111*: 119 (1996).
[5.6] M. A. Anderson and A. J. Rubin, *Adsorption of Inorganics at Solid–Liquid Interfaces*, Ann Arbor Science Publishers, Ann Arbor, MI, (1981).
[5.7] R. J. Hunter, *Foundations of Colloid Science*, *Vol. I*, Claredon Press, Oxford (1995).
[5.8] P. W. Schindler, B. Fuerst, R. Dick, and P. Wolf, Ligand properties of surface silanol groups. I. Surface complex formation with Fe^{3+}, Cu^{2+}, Cd^{2+}, and Pb^{2+}, *J. Collid Interf. Sci.*, *55*: 469 (1976).
[5.9] W. Stumm, H. Hohl, and F. Dalamg, Interaction of metal ions with hydrous oxide surfaces, *Croatica Chem. Acta*, *48*: 491 (1976).
[5.10] D. Seifert, Untersuchung der Kristallisation von Kaliumchlorid aus wässriger Lösung, Thesis, Technische Universität München (1977).
[5.11] N. Kubota, J. Fukazawa, H. Yashiro, and J. W. Mullin, Impurity effect of chromium(III) on the growth and dissolution rates of potassium sulfate crystals, *J. Cryst. Growth.*, *149*: 113 (1995).
[5.12] S. Kuch, Die Fremdstoffbeinflussung der Massenkristallisation von Ammoniumsulfat, Diploma-Thesis, Technische Universität Braunschweig (1994).
[5.13] R. J. Davey, The control of crystal habit, in *Industrial Crystallization '78* (S. J. Jancic and E. J. de Jong, eds.), North-Holland, Amsterdam, p. 169 (1979).
[5.14] M. Rauls, K. Bartosch, M. Kind, S. Kuch, R. Lacmann, and A. Mersmann, The influences of impurities on crystallization kinetics—A case study on the crystallization of ammonium sulfate, *J. Cryst. Growth*, *213(1/2)*:116(2000).
[5.15a] A. Eble and A. Mersmann, Interaction of kinetics governing the precipitation of nanoparticles, in *Proc 14th Int. Symp. Industrial Crystallization* (J. Garside and M. Hounslow, eds.), IChemE, Rugby, UK (1999).
[5.15b] A. Eble, *Precipitation of nanoscale crystals with particular reference to interfacial energy*, Thesis, Technische Universität München, Shaker-Verlag (2000).
[5.16] O. Knacke and I. N. Stranski, Kristalltracht und Absorption, *Z. Electrochem. 60*: 816 (1956).
[5.17] R. Lacmann and I. N. Stranski, The effect of adsorption of impurities on the equilibrium and growth forms of crystals, in *Growth and*

Perfection of Crystals (R. H. Doremus, B. W. Roberts, and D. Turnbull, eds.), John Wiley & Sons, London, pp. 427–440 (1958).
[5.18] G. Blisnakov and E. Kirkova, Der Einfluβ der Adsorption auf das Kristallwachstum, Z. *Phys. Chem.*, *206*: 271 (1957).
[5.19] M. C. van der Leeden, D. Kashchiev, and G. M. van Rosmalen, Effect of additives on nucleation rate, crystal growth rate and induction time in preciptiation, *J. Cryst. Growth*, *130*: 221 (1993).
[5.20] N. Cabrera and D. A. Vermilyea, The growth of crystals from solution, In: *Growth and Perfection of Crystals* (R. H. Doremus, B. W. Roberts, and D. Turnbull, eds.), John Wiley & Sons, London, pp. 393–410 (1958).
[5.21] N. Kubota, M. Yokota, and J. W. Mullin, Supersaturation dependence of crystal growth in solutions in the presence of impurity, *J. Cryst. Growth*, *182*: 86 (1997).
[5.22] K. Sangwal, Effect of impurities on the process of crystal growth, *J. Cryst. Growth*, *128*: 1236 (1993).
[5.23] J. Rolfs, Untersuchung zum Wachstum von KNO_3-Einkristrallen in wäßriger Lösung mit und ohne Fremdstoff, Thesis, Technische Universität Braunschweig (1992).
[6.1] J. Nyvlt, R. Rychly, J. Gottfried, and J. Wurzelova, Metastable zone width of some aqueous solutions, *J. Cryst. Growth.*, *6*: 151 (1970).
[6.2] M. Kind and A. Mersmann, On the width of the metastable zone of solutions, in *Proc. 10th Symp. on Industrial Crystallization* (J. Nyvlt and S. Zacek, eds.), Elsevier, Amsterdam (1989).
[6.3] A. Mersmann and K. Bartosch, How to predict the metastable zone width, *J. Cryst. Growth*, *183*: 240 (1998).
[6.4] M. Kind, Über die Übersättigung während der Kornkristallisation aus Lösungen, Thesis, Technische Universität München (1989).
[6.4] M. Kühberger, Neue Sensoren zur Messung und Regelung der Übersättigung in Kristallisatoren, Thesis, Technische Üniversität München (1999).
[6.5] A. Mersmann and M. Löffelmann, Crystallization and Precipitation: The Optimal Supersaturation, *Chem. Ing. Techn. 71*: 1240–1244 (1999).

4

Particle Size Distribution and Population Balance

A. MERSMANN Technische Universität München, Garching, Germany

In addition to purity and crystal shape, the crystal size distribution of a crystalline product is an important criterion for assessing the properties and quality of a product.

1. PARTICLE SIZE DISTRIBUTION

The simplest way of representing a crystal size distribution (CSD) consists of representing the partial masses M_i of a grain size interval or, in general, of a dispersion size interval in dependence on the dispersion size L. If the partial mass M_i is applied to the total mass M, the percentage by mass M_i/M is obtained. In Figure 1.1, the percentages by mass of a particle group are plotted against the crystal size L in the form of a histogram.

The sum of the partial masses $\sum M_i$ is equal to the total mass M:

$$\sum M_i = M \tag{1.1}$$

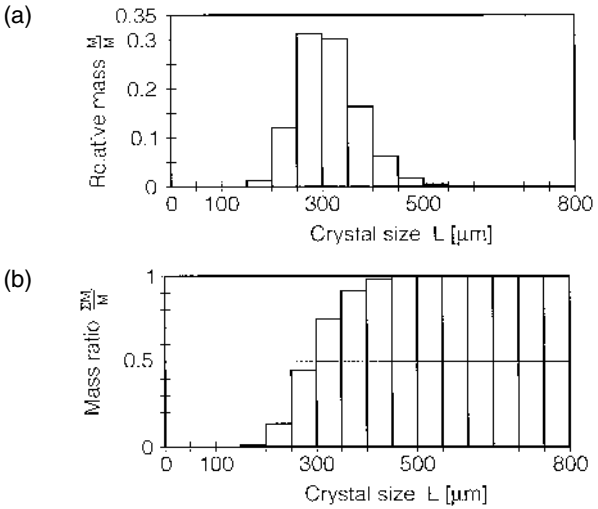

Figure 1.1. Histogram and cumulative mass of crystal size distribution.

A partial number N_i of an interval ΔL of size L can be chosen instead of the partial mass of an interval. Here, it is also advisable to apply the partial number N_i to the total number of particles. The value N_i/N represents a specific or relative number. At the same time, the sum of the total numbers $\sum N_i$ is naturally equal to the total number N_T:

$$\sum N_i = N_T \tag{1.2}$$

However, the relative distribution is less suitable for characterizing particle systems than the density of a distribution or distribution density, which is obtained by dividing the relative distribution by the interval width. In addition to the dispersion characteristics, number, and mass, it is sometimes also interesting to consider the characteristic length, area, and volume of the particles. If the distribution density is represented by q and the dispersion characteristics by the indices $r = 0$ for number, $r = 1$ for length, $r = 2$ for area, $r = 3$ for volume, and $r = 3^*$ for mass, the density distributions presented in Table 1.1 arise.

If the crystal density ρ_C is the same for all particles, the volume density and mass distribution densities are equal:

$$q_3(L) = q_3^*(L) \tag{1.8}$$

If the interval width is taken to be zero, continuous curves generally arise. In this case, the distribution sum is defined by the integral

Table 1.1. Distributions and Type of Quantity

Parameter	Dimension	Distribution density	
Number	$[L^0]r = 0$	$q_0(L_i) = \frac{N_i}{\sum N_i}\frac{1}{\Delta L_i}$	(1.3)
Length	$[L^1]r = 1$	$q_1(L_i) = \frac{L_i N_i}{\sum L_i N_i}\frac{1}{\Delta L_i}$	(1.4)
Area	$[L^2]r = 2$	$q_2(L_i) = \frac{L_i^2 N_i}{\sum L_i^2 N_i}\frac{1}{\Delta L_i}$	(1.5)
Volume	$[L^3]r = 3$	$q_3(L_i) = \frac{L_i^3 N_i}{\sum L_i^3 N_i}\frac{1}{\Delta L_i}$	(1.6)
Mass	$[\rho_C L^3]r = 3^*$	$q_3^*(L_i) = \frac{\rho_C L_i^3 N_i}{\sum \rho_C L_i^3 N_i}\frac{1}{\Delta L_i}$	(1.7)

$$Q_r(L) = \int_0^L q_r(L)\,dL \tag{1.9}$$

Figure 1.2 shows the cumulative undersize against crystal size L. For reasons of standardization, the specific integral over all particles is 1:

$$Q_r(L \to \infty) = \int_0^\infty q_r(L)\,dL = 1 \tag{1.10}$$

It is helpful to imagine a sieve with mesh size L_s, where particles having a separation size of up to L_s "fall through" and particles of size $L > L_s$ remain on the sieve as residue, $R(L)$. This leads to the following definitions and relationships:

$$Q_3(L) = \int_0^{L_s} q_3(L)\,dL \tag{1.11}$$

$$R(L) = 1 - Q_3(L) = \int_{L_s}^\infty q_3(L)\,dL \tag{1.12}$$

$$q_3(L) = \frac{dQ_3(L)}{dL} = -\frac{d}{dL}[1 - Q_3(L)] \tag{1.13}$$

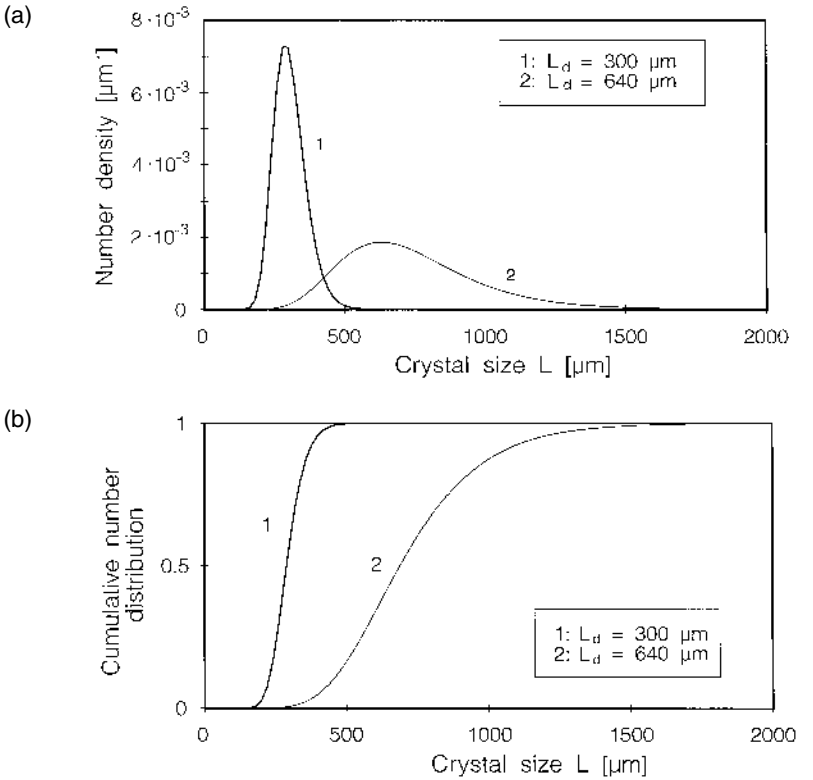

Figure 1.2. Density (population and mass) and cumulative undersize population and mass against crystal size L.

Equation (1.13) naturally applies only if the distribution sum curves are continuous. It should also be noted that depending on the measuring techniques for the dispersion parameter L, not only are the length, area, volume, and mass used but also other physical parameters, such as the settling rate of the particles in a fluid.

There are several mathematical functions for approximately describing measured distribution sum curves. The most common functions are the Gaussian distribution, Gaussian logarithmic distribution, RRSB distribution according to Rosin, Rammler, Sperling, and Bennet, and exponential distribution. Table 1.2 contains the corresponding expressions for mass distribution sums and densities.

Generally, however, none of these functions can be expected to exactly

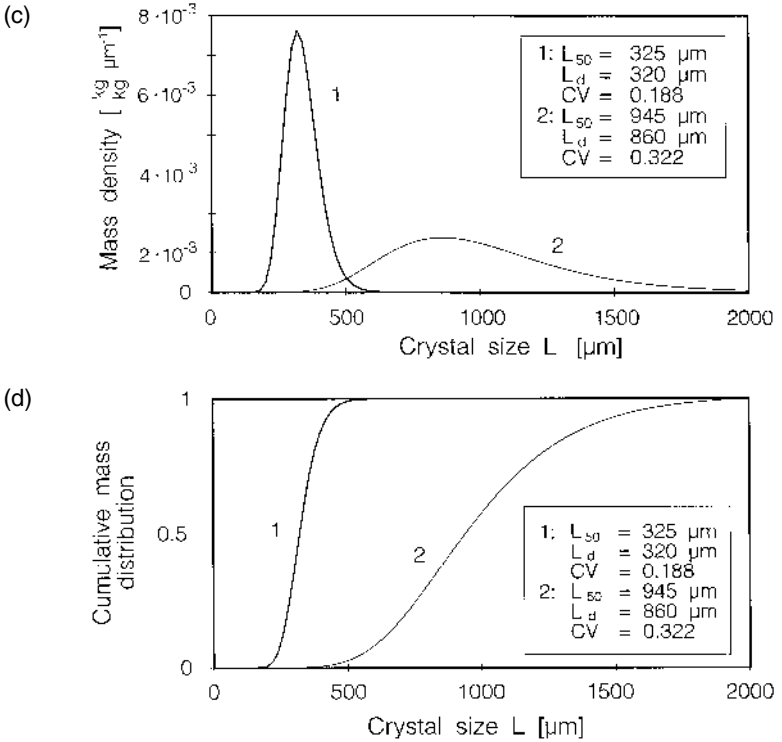

Figure 1.2. (*continued*)

describe the particle size distribution of a crystalline product. The RRSB distribution is of empirical nature and was proposed in particular, for granular products resulting from comminution. If crystals are subjected to a certain amount of mechanical stress during mechanical liquid separation in centrifuges and filters or during the subsequent drying process, the grain size distribution of dried products can often be described well according to RRSB. This does not apply to products that are directly removed from a crystallizer that treats the crystals gently.

A further drawback of the relationships for grain size distribution listed in Table 1.2 is the fact that the so-called population parameters (e.g., the standard deviation σ and the mean value of distribution of Normal distributions or the uniformity coefficient n' and the characteristic grain size L' for aperture $1/e = 0.368$) provide no information on the kinetic parameters involved in crystallization.

Table 1.2. Distribution Functions in Particle Measuring Techniques

Designation	Function	Position parameter	Dispersion parameter
Exponential distribution	$Q_3(L) = \left(\frac{L}{L_{\max}}\right)^m$	$L_{\max}$	m
RRSB distribution	$1 - Q_3(L) = \exp\left[-\left(\frac{L}{L'}\right)^{n'}\right]$	L'	n'
Normal distribution	$Q_r^*(z) = \int_{-\infty}^{z} q_r^*(\xi)\, d\xi$		
	$q_r^*(z) = \frac{1}{\sqrt{2\pi}\sigma} \exp\left(-\frac{z^2}{2}\right)$		
Linear abscissa	$z = \frac{L - L_{50,r}}{\sigma}$	$L_{50,r}$	σ
Logarithmic abscissa	$z = \frac{\log(L/L_{50,r})}{\log \sigma_g}$	$L_{50,r}$	$\sigma_g = \exp(\sigma)$
	e.g., $z = \frac{\ln(L/L_{50,r})}{\sigma}$	$L_{50,r}$	σ

Crystal size distribution can only be predicted when a particle number balance is formulated for a crystallizer. Although energy, mass, or material balances can be used to specify which crystalline mass precipitated out of the supersaturated solution, they provide no information on the number and size of the particles over which this crystal mass is distributed. If these questions are to be answered, a number balance must also be formulated in addition to the mass and energy balances.

2. POPULATION BALANCE

Population balances were introduced by Hulburt and Katz [2.1] and later formulated in full detail for crystallization processes by Randolph and Larson [2.2]. The formulation of the number balance is based on the number distribution density $n(L)$, which is derived from the number of particles per unit volume N (e.g., cubic meters of suspension). The number density n is then derived as the limiting value of the number of particles per unit volume in the crystal size interval ΔL:

$$n = \lim_{\Delta L \to 0} \frac{\Delta N}{\Delta L} = \frac{dN}{dL} \tag{2.1}$$

In practice, the number density is calculated from the relationship

$$n = \frac{N_T}{V \Delta L_i} = \frac{M_i}{M_p V \Delta L_i} = \frac{M_i}{\alpha \rho_C \overline{L_i}^3 V \Delta L_i} \tag{2.2}$$

where M_i is the mass of the sieve residue on the sieve i, M_p is the mean particle mass, $\overline{L_i}$ is the mean crystal size of a particle in the grain size interval between $\overline{L_i} - \Delta L_i/2$ and $\overline{L_i} + \Delta L_i/2$, and V is the volume of the suspension sample or, if applied to the entire crystallizer, its total suspension volume.

The number density balance in a differential form arises by examining the particle numbers in a differential crystal size interval dL. This is explained in Figure 2.1. This interval can be entered by crystals that are in the feed. Of course, this contribution does not apply if the flow entering the crystallizer is a clear solution free of any crystals. In the case of a batch crystallizer, the crystal number of the interval is not reduced by particle removal when the entire suspension is withdrawn as a product after the batch process. In continuously operated crystallizers, on the other hand, crytals that are continually removed by product flows must be taken into account. In a differential period of time, crystals that are smaller than L can grow into the size interval to $L + dL$, and crystals ranging from L to $L + dL$ can grow out of the interval. Finally, in real crystallizers, effects such as crystal abrasion, breakage, agglomeration, and dissolution occur. For example, if a crystal in the to $L + dL$ interval breaks down into several fragments of roughly the same size, the original particle disappears or is eliminated from the interval. This is known as the *death rate*, $D(L)$. This effect can also occur when several crystals agglomerate. Upon breakage, however, the fragments populate small crystal size intervals, whereas the agglomerate that has been

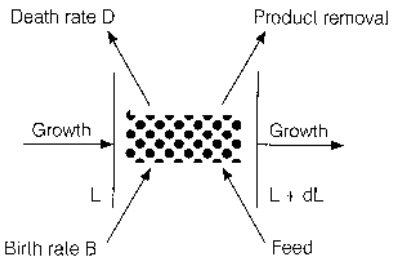

Figure 2.1. Change in the number of crystals per unit volume in the crystal size range of L and $L + dL$.

formed belongs to a large particle size interval. If crystals that are slightly larger than $L + dL$ are abraded, they may enter the interval in question and cause what is generally known as a *birth rate*, $B(L)$. If crystals in a range of small crystal sizes are completely dissolved in an undersaturated area, they disappear from the interval concerned and no longer reappear in any other grain size interval. All these effects can be considered in connection with a birth rate $B(L)$ and a death rate $D(L)$ for the interval concerned. The number of particles that exist in a differential interval and in an infinitely small volume dV at time t is given by

$$dN = n\,dV \tag{2.3}$$

The total number of particles in volume V is then

$$N_T(V) = \int_V n\,d\mathrm{V} \tag{2.4}$$

The number density balance of particles in a specific volume can thus generally be described by the relationship Particle density = Particle inflow − Particle outflow + Net number of births. When this is expressed mathematically for volume V, we obtain

$$\frac{d}{dt}\int_V n\,dV = \int_V [B(L) - D(L)]\,dV \tag{2.5}$$

The substantial derivation on the left-hand side can be described by a locally unsteady term and a convective term. When the vector $\mathbf{v}$ is written for the derivation dL/dt, the equation reads

$$\int_V \left(\frac{\partial n}{\partial t} + \nabla(\mathbf{v}\cdot n)\right) dV = \int_V [B(L) - D(L)]\,dV \tag{2.6}$$

The vector $\mathbf{v}$ comprises an internal part $\mathbf{v}_i$ and an external part $\mathbf{v}_e$: $\mathbf{v} = \mathbf{v}_e + \mathbf{v}_i$. The vector $\mathbf{v}_e$ is given by the external particle velocity in an external coordinate system (reference system, e.g., the crystallizer) and can be determined using a force balance of the individual particle. The internal velocity $\mathbf{v}_i$ orientates itself along an internal coordinate system (reference system, e.g., the particle). In a supersaturated solution, for example, the linear growth rate $G = dL/dt$ of a crystal yields the most important factor for internal velocity. However, this also includes the negative linear rate for internal abrasion $G_a = -dL/dt$ of a crystal of size L or, in undersaturated areas.

Equation (2.6) completely describes the formation and dynamics of a particle size distribution in space by taking into account the energy, mass, and material balances. It can also be written as

$$\int_V \left(\frac{\partial n}{\partial t} + \nabla \mathbf{v}_e \cdot n + \nabla \mathbf{v}_i \cdot n + D(L) - B(L) \right) dV = 0 \tag{2.7}$$

In a crystallizer, well-mixed volumetric zones occur frequently, resulting in the fact that roughly the same particle size distribution is found throughout the entire volume. Small laboratory crystallizers can often be operated in such a way as to obtain virtually ideal mixing. This means that the terms in equation (2.7) no longer differ from area to area (i.e., they are independent of the volume element concerned). In equation (2.7), therefore, the parameters n, $B(L)$, and $D(L)$ are only functions of time, not of position. The second term can be considered a surface integral of the system:

$$\int_V \nabla \mathbf{v}_e \cdot n \, dV = \int_S \mathbf{v}_n \cdot n \, dS \tag{2.8}$$

Here, the vector $\mathbf{v}_n$ describes the mean particle velocity perpendicular to the surface. The parameter S denotes the sum of all moving surfaces of the system and is composed of three parts:

1. The inflow and outflow of a totals of k particle flows $\dot{V}_i$:

$$\int_{S_m} \mathbf{v}_n \cdot n \, dS = \sum_k \dot{V}_i n_i \tag{2.9}$$

2. The change in the solid-free systems volume (e.g., in evaporative crystallization):

$$\int_{S_s} \mathbf{v}_n \cdot n \, dS = n \frac{dV_s}{dt} \tag{2.10}$$

3. The change in aperture volume due to suspended particles:

$$\int_{S_e} \mathbf{v}_n \cdot n \, dS = -n \frac{dV_e}{dt} \tag{2.11}$$

In these equations, S_s represents the free surface of the liquid, V_s is the solid-free volume of the liquid, S_e is the total solid–liquid phase boundary, and V_e is the total particle volume. Parts 2 and 3 can also be combined as the complete change in solid-free volume:

$$\int_{S_e} \mathbf{v}_n \cdot n \, dS + \int_{S_s} \mathbf{v}_n \cdot n \, dS = n \frac{dV}{dt} \tag{2.12}$$

We then obtain

$$\int_V \nabla \mathbf{v}_e \cdot n \, dV = \sum_k \dot{V}_i n_i + n \frac{dV}{dt} \tag{2.13}$$

By applying this equation to the number density balance and integrating and dividing by volume V, we finally obtain

$$\frac{\partial n}{\partial t} + \nabla \mathbf{v}_i \cdot n + n\frac{\partial V}{V\partial t} + D(L) - B(L) + \sum_k \frac{\dot{V}_i n_i}{V} = 0 \tag{2.14}$$

If the linear growth rate G contributes only to the internal velocity, the following is obtained:

$$\nabla \mathbf{v}_i \cdot n = \frac{\partial (Gn)}{\partial L} \tag{2.15}$$

The general equation for the number density balance of a crystallizer having volume V is then

$$\frac{\partial n}{\partial t} + \frac{\partial (Gn)}{\partial L} + n\frac{\partial V}{V\partial t} + D(L) - B(L) + \sum_k \frac{\dot{V}_i n_i}{V} = 0 \tag{2.16}$$

The term $\partial n/\partial t$ gives the change in number density with respect to time in the batch crystallizer and disappears in the case of a continuously operated, steady-state apparatus. The expression $\partial(Gn)/\partial L$ describes the difference between crystals growing into and out of a crystal size interval dL due to the crystal growth rate $G = dL/dt$. The term $n(\partial V/V\partial t)$ takes into account changes in crystal volume with respect to time (e.g., the decrease in volume in batch-operated evaporative crystallizers due to the evaporation of the solvent). The parameters $D(L)$ and $B(L)$ represent the death rate and birth rate, respectively, which arise due to the agglomeration of crystals or their attrition and breakage. If, for example, two large crystals join together, they disappear from their interval and the twin then populates a different interval. On the other hand, if a crystal undergoes a considerable amount of attrition or even breaks into fragments, the attrition particles or fragments will appear in intervals of smaller mean diameter. Finally, the term $\sum_k (\dot{V}_i n_i/V)$ gives the sum of all particle flows entering and leaving the crystallizer.

Equation (2.16) is difficult to solve because the birth rate $B(L)$ and death rate $D(L)$ cannot be formulated in a general way for any case, as processes such as crystal breakage and attrition are brought about by mechanical and fluid dynamic processes and are initially not influenced by the kinetics of crystallization. However, if the fragments and attrition particles exist in a supersaturated solution, they can grow. Their growth ability and growth rate are then greatly influenced by supersaturation. The complex interaction of mechanical and kinetic effects leads to the difficult problem of describing the birth and death rates in a general way. In the laboratory, crystallization

experiments can often be performed so that crystal breakage and attrition hardly occur. Moreover, if the same supersaturation occurs throughout the crystallizer due to good mixing, no crystals will dissolve and they will grow at approximately the same rate. In moderately supersaturated solutions, agglomeration of crystals $L > 10\,\mu m$ should hardly take place if the suspension density is low.

If all these requirements are fulfilled, the terms $B(L)$ and $D(L)$ can sometimes be neglected in the number-density balance. In the case of a continuously operated cooling crystallizer without fluctuations with respect to time, the terms $\partial n/\partial t$ and

$$n\frac{\partial V}{V\partial t} = n\frac{\partial(\ln V)}{\partial t}$$

both equal zero. The number density balance is then simplified to

$$\frac{\partial(Gn)}{\partial L} + \sum_k \frac{n_i \dot{V}_i}{V} = 0 \tag{2.17}$$

The solution fed into continuously operated crystallizers is often free of crystals, and only one volume flow $\dot{V}$ is continuously removed. In this case, the number density balance is simplified even further to

$$\frac{\partial(Gn)}{\partial L} + n\frac{\dot{V}}{V} = 0 \tag{2.18}$$

As the ratio $V/\dot{V}$ between the volume V and flow rate $\dot{V}$ equals the mean residence/retention time τ of the suspension that is assumed to be ideally mixed, we finally obtain with $\tau = V/\dot{V}$,

$$\frac{\partial(Gn)}{\partial L} + \frac{n}{\tau} = 0 \tag{2.19}$$

In this equation, it is assumed that the solution and the crystals have the same mean residence time τ in the crystallizer. In principle, the crystal growth rate G can depend on particle size, especially the growth of small crystals. This is connected, among other things, to the fact that the mass transfer coefficient of particles in the grain size area of $100\,\mu m < L < 2000\,\mu m$ is slightly influenced by particle size in the case of diffusion-limited growth. If growth is limited by integration and the supersaturation is not excessively low, the crystal growth rate is also only slightly affected by the size of the crystals. If the parameter G (which is, in reality, a mean growth rate) is not a function of the crystal size L, it can be placed in front of the differential in equation (2.19), giving

$$G\frac{dn}{dL}+\frac{n}{\tau}=0 \tag{2.20}$$

This greatly simplified relationship for the differential number density balance of the crystal size interval dL applies only to MSMPR (mixed suspension, mixed product removal) crystallizers. The relationship can be integrated with the integration constant n_0 as the number density for crystal size $L = 0$:

$$n = n_0 \exp\left(-\frac{L}{G\tau}\right) \quad \text{or} \quad \ln\left(\frac{n}{n_0}\right) = -\frac{L}{G\tau} \tag{2.21}$$

If the logarithm of the number density n is plotted against the crystal size L, a straight line is produced with the negative slope $-(1/G\tau)$. The moments of the number density distribution can be used to calculate important parameters such as the total number of crystals, their surface, volume, and mass, each per unit volume of suspension.

The zeroth moment gives the volume-related total number of crystals (index T):

$$N_T = \int_0^\infty L^0 n_0 \exp\left(-\frac{L}{G\tau}\right)dL = n_0 G\tau \quad \left[\frac{\text{particles}}{\text{m}^3_{\text{suspension}}}\right] \tag{2.22}$$

The volume-related surface a_T of all crystals plays an important role in mass transfer; it can be calculated from the second moment of the number density distribution:

$$a_T = \beta \int_0^\infty L^2 n_0 \exp\left(-\frac{L}{G\tau}\right)dL = 2\beta n_0 (G\tau)^3 \tag{2.23}$$

where a_T has dimension $m^2_{\text{crystal surface}}/m^3_{\text{suspension}}$. The third moment gives the crystal volume (i.e., the volumetric holdup of crystals φ_T with respect to the suspension volume):

$$\varphi_T = \alpha \int_0^\infty L^3 n_0 \exp\left(-\frac{L}{G\tau}\right)dL = 6\alpha n_0 (G\tau)^4 \quad \left[\frac{\text{m}^3_{\text{crystals}}}{\text{m}^3_{\text{suspension}}}\right] \tag{2.24}$$

If the volumetric holdup φ_T is multiplied by the solid density ρ_C of the compact crystal, we obtain the suspension density m_T (i.e., the mass of crystals per unit volume of suspension):

$$m_T = \varphi_T \rho_C \quad \left[\frac{\text{kg}_{\text{crystals}}}{\text{m}^3_{\text{suspension}}}\right] \tag{2.25}$$

Table 2.1 gives a summary of the individual moments.

Table 2.1. Moments of Distribution

Moments	Meaning: Basic	Meaning: MSMPR	
$m_0 = \int_0^\infty n(L)dL$	Total number $N_T = m_0$	$N_T = n_0 G\tau$	(2.26)
$m_1 = \int_0^\infty Ln(L)dL$			
$m_2 = \int_0^\infty L^2 n(L)dL$	Total surface $a_T = \beta m_2$	$a_T = 2\beta n_0 (G\tau)^3$	(2.27)
$m_3 = \int_0^\infty L^3 n(L)dL$	Solid volume fraction $\varphi_T = \alpha m_3$	$\varphi_T = \frac{m_T}{\rho_C} - 6\alpha n_0 (G\tau)^4$	(2.28)

The average particle size $L_{r,r'}$ (moments r and r') is $L_{r,r'} = \left(\frac{m_r}{m_{r'}}\right)^{1/(r-r')}$

The median crystal size L_{50} occurring at a cumulative mass undersize of 0.5 (see Fig. 1.2) can be determined from

$$\frac{\int_0^{L_{50}} L^3 n_0 \exp(-L/G\tau)\, dL}{\int_0^\infty L^3 n_0 \exp(-L/G\tau)\, dL} = 0.5 \tag{2.29}$$

Evaluation of this equation gives

$$L_{50} = 3.67 G\tau \tag{2.30}$$

Similarly, the maximum of mass distribution density $q_3^*(L)$ (cf. Fig. 1.2) or the dominant size L_d can be shown to occur at a crystal size of

$$L_d = 3G\tau \tag{2.31}$$

In primary nucleation, newly formed nuclei are very small and lie in the nanometer range (i.e., $L \to 0$). With the intercept of the ordinate n_0 for $L = 0$, we obtain the following for the nucleation rate B_0:

$$B_0 = \frac{dN_0}{dt} = \frac{dN_0}{dL}\frac{dL}{dt} = n_0 G \tag{2.32}$$

The slope $-(1/G\tau)$ and the intercept of the ordinate n_0 of the straight line in the number-density diagram can thus be used to determine the two kinetic parameters: nucleation rate B_0 and growth rate G. These parameters determine the median value L_{50} of crystal size distribution.

A combination of the equations (2.29)–(2.32) gives the following relationship for the nucleation rate B_0/φ_T based on the volumetric holdup φ_T:

$$\frac{B_0}{\varphi_T} = \frac{1}{6\alpha G^3 \tau^4} = \frac{(3.67)^3}{6\alpha L_{50}^3 \tau} = \frac{(3.67)^4 G}{6\alpha L_{50}^4} \tag{2.33}$$

or for the median crystal size L_{50}:

$$L_{50} = 3.67 \sqrt[4]{\frac{G}{6\alpha(B_0/\varphi_T)}} \tag{2.34}$$

The median crystal size in a crystallizer increases with an increasing growth rate G and a decreasing nucleation rate B_0 in relation to the volumetric holdup φ_T.

Equation (2.33) is illustrated in Figure 2.2. The nucleation rate B_0 that is related to the volumetric crystal content $\varphi_T = m_T/\rho_C$ is shown against the mean growth rate G of all crystals having the median crystal size L_{50}. The mean residence time τ can then be plotted as another parameter according to the relationship (2.33).

The great advantage of number density diagrams over diagrams based on the relationship for mass distribution densities and sums listed in Table 1.1 is that only the diagrams shown in Figures 2.4 and 2.5 can be interpreted on a kinetic basis. This is shown by a comparison of diagrams in Figure 2.3. Figure 2.3 shows the number density distributions of potassium chloride at 20°C and for suspension densities $m_T = 30\,\mathrm{kg/m^3}$ and $200\,\mathrm{kg/m^3}$ and for two different residence times. The residence time $\tau = 30\,\mathrm{min}$ results in a growth rate of $G = 6.7 \times 10^{-8}\,\mathrm{m/s}$ (curve 1) whereas a residence time of $\tau = 90\,\mathrm{min}$ gives only $G = 3.3 \times 10^{-8}\,\mathrm{m/s}$. This is connected with the fact that the supersaturation of the solution decreases to a greater extent the longer the residence time, and the decreased supersaturation also leads to a lower growth rate. The higher the suspension density m_T or the volumetric crystal holdup $\varphi_T = m_T/\rho_C$, the higher the straight lines, whose slopes, however, depend only on the residence time τ and the crystal growth rate. The straight lines of the number density diagram (known as straight MSMPR lines) have been transferred to an RRSB diagram in Figure 2.3. Here the curves are arched and can no longer be interpreted on a kinetic basis. The growth rate and nucleation rate cannot be determined from these curves without further calculations. Straight $n = f(L)$ lines having the same slope $-(1/G\tau)$ but different suspension densities are parallel to each other and are given by

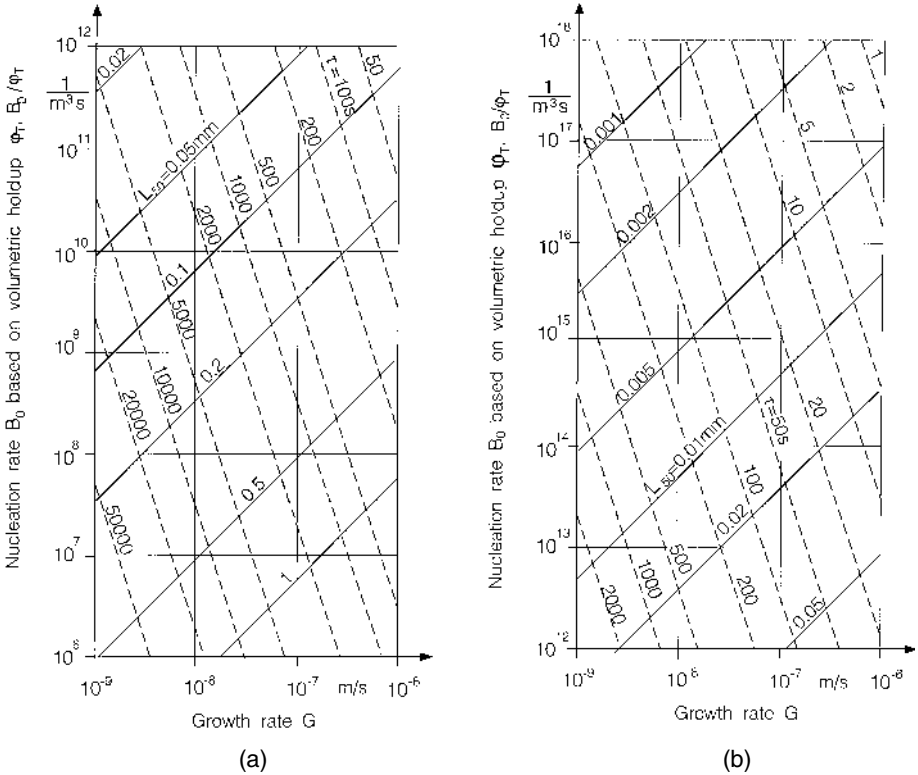

Figure 2.2. Nucleation rate based on volumetric holdup versus crystal growth rate and median crystal size and mean residence time as parameter.

arched curves in the RRSB networks. Figure 2.3 illustrates the effects of the residence time τ and the suspension density m_T on the number density distribution. It should be emphasized once more that the population parameters L' and n' of the RRSB distribution cannot be interpreted kinetically (i.e., the crystal growth rate G and the rate B_0 of nucleation cannot be derived from these parameters). The population parameters, such as the most frequently occurring crystal size and the mean of the standard deviations σ of Normal distributions, are not suitable for calculating the growth and nucleation rates, either. On the other hand, the semilogarithmic population-density diagram yields the mean crystal growth rate G and the nucleation rate B_0 directly from the slope of the straight lines and from their ordinate intercepts at $L \to 0$. The position of such straight lines depends

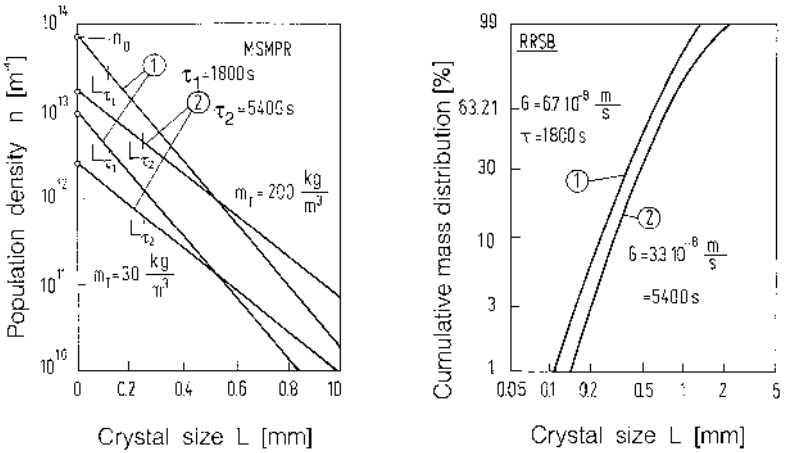

Figure 2.3. Comparison of size distributions according to population density and RRSB.

on the mean residence time τ, which is strongly interrelated with supersaturation ΔC.

Actually, number density distributions which have been determined experimentally in small, continuously operated crystallizers can often be described well by equation (2.21), provided that certain operating conditions were observed, as shown in Figures 2.4 and 2.5 using the examples of ammonium sulfate and calcium carbonate [2.3]. In these figures, the number density $n(L)$ is illustrated as a logarithm against the crystal size L in a semilogarithmic network. Because the slope of the straight line is $-(1/G\tau)$ and the residence time $\tau = V/\dot{V}$ is known, the mean crystal growth rate G of all crystals can be determined from the slope of the straight line in the number density diagram $\ln(n) = f(L)$. As will be shown in more detail later, the following operating conditions must be fulfilled to avoid severe attrition and to obtain roughly straight lines in such number density diagrams for $L_{50} > 100\,\mu m$: specific power $\bar{\varepsilon} < 0.5\,W/kg$, suspension density $m_T < 50\,kg/m^3$, volume fraction of the crystal phase $\varphi_T < 0.02$, and residence time $\tau < 5000\,s$.

Crystal attrition and breakage can be so great, especially in the case of high specific power input, long residence times, and high suspension densities, that straight lines no longer result. Moreover, large industrial crystallizers cannot be operated to allow ideal mixing. The fact that the suspension does segregate when the product is continuously removed [i.e., separation

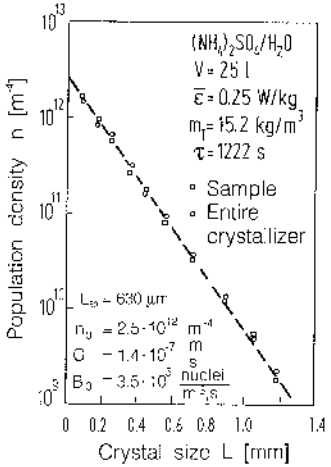

Figure 2.4. Population density versus the crystal size for the ammonium sulfate–water system.

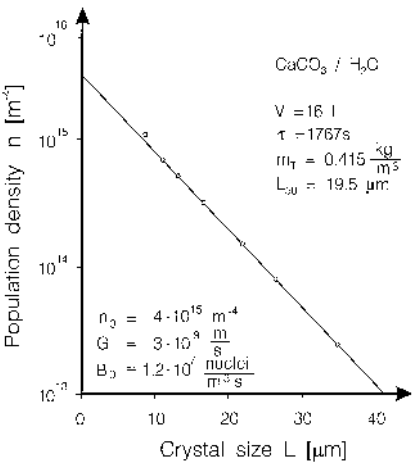

Figure 2.5. Population density versus the crystal size for the calcium carbonate–water system.

effects cannot occur to meet the requirements of equation (2.16)], is a great problem. This means that the crystals and solution must be removed isokinetically, which causes problems, because slippage takes place between the solid and the liquid in every suspension flow. The requirements of equation

(2.16) are met only when the entire suspension is ideally mixed and an ideally mixed suspension is removed isokinetically for both phases. Crystallizers operated in this way are known as MSMPR (mixed suspension, mixed product removal) crystallizers. They are remarkably suitable for determining the two important kinetic parameters, the growth rate G and the rate B_0 of nucleation. Crystallization experiments are performed at different residence times τ. The crystal size distribution of the crystal product is then determined, for example, by wet sieving or with the aid of particle size analyzers. If necessary, the mass distribution density is then converted to the number density, which is then plotted logarithmically against the crystal size L. If this type of diagram gives a straight line, the linear, mean crystal growth rate G can be calculated for a known residence time τ directly from the slope $d(\ln n)/dL = -1/G\tau$, or

$$G = -\frac{1}{\tau[d(\ln n)/dL]} \tag{2.35}$$

and the nucleation rate B_0 by applying equation (2.32), where N_0 is the number of nuclei formed per unit volume, assuming that they are formed only at nucleus size $L \to 0$. This means that the nucleation rate B_0 can be determined from the intercept of the ordinate n_0 and the slope of the straight line in such population-density plots.

Both G and B_0 increase with supersaturation. In the case of low and medium supersaturations, G often increases with ΔC faster than B_0, resulting in a coarser crystal product. When the supersaturation is very high, the nucleation rate can increase so greatly compared to the growth rate that the product becomes finer. If experiments are performed in an MSMPR crystallizer to determine these kinetic parameters, different residence times produce different supersaturations and, thus, different growth rates G and nucleation rates B_0/φ_T. This is explained in more detail later.

By varying the residence time τ in experiments with MSMPR crystallizers, pairs of B_0/φ_T and G are obtained. In a diagram, these pairs lead to a kinetic whose exact position, among other things, is determined by attrition. This type of curve can often be obtained roughly in the double logarithmic network by a straight line having slope i, which can be interpreted kinetically according to

$$B_0 \sim (\Delta C)^n \tag{2.36}$$

and

$$G \sim (\Delta C)^g \tag{2.37}$$

which results in

$$B_0 \sim G^i \tag{2.38}$$

with $i = n/g$.

In Figure 2.6a, experimental results of B_0/φ_T of KCl and, in Figure 2.6b, results of $KAl(SO_4)_2 \cdot 12H_2O$ are plotted against the mean growth rate G. In both cases, the exponent i is approximately 2. As a rule, this exponent is < 2 in the range of small supersaturation and growth rates. Figure 2.6c shows the nucleation rate B_0/φ_T based on volumetric holdup against the mean growth rate G for KNO_3. A long residence time τ (ΔC and G small) and a high specific power input $\bar{\varepsilon}$ lead to $i < 1$ (e.g., the median crystal size decreases with increasing residence time). Further experimental results obtained for potash alum and ammonium sulfate crystallized in stirred vessels and fluidized beds are shown in Figure 2.6d. As can be seen from the experimentally determined curves, the exponent i depends (besides other parameters) on the mean specific power input and on the residence time.

If one assumes that increasing growth-rate values are related to an increase in supersaturation ΔC and a decrease in residence time τ, the following results are obtained:

1. If $i > 1$, the median crystal size increases with increasing residence time τ.
2. If $i = 1$, the median crystal size does not change with the residence time.
3. If $i < 1$, the median crystal size decreases with increasing residence time. This is due to large crystals being substantially abraded. The combination of $B_0/\varphi_T \sim 1/L_{50}^3\tau \sim G^i$ and $L_{50} \sim G\tau$ leads to the proportionality

$$L_{50} \sim \tau^{(i-1)(i+3)} \tag{2.39}$$

It can be observed that under certain conditions, $i \approx 2$ often applies, which means that $L_{50} \sim \tau^{0.2}$ [2.4]. Generally, $1 < i < 2$ gives the relationship $L_{50} \sim \tau^0 = \text{constant}$ up to $L_{50} \sim \tau^{0.2}$. This means that the median crystal size increases with the residence time τ only to a relatively small extent. Accordingly, a coarse crystal product requires a crystallizer of a large volume for a given production rate.

However, in the case of a crystal product with particles roughly over 100 µm, the exact position of the kinetic curve depends not only on supersaturation and thus kinetics but also on mechanics and fluid dynamics, due to crystal attrition and breakage, because attrition particles can act as secondary nuclei and therefore influence crystal size distribution considerably. The exponent i tends to zero ($i \to 0$) for crystals prone to attrition when the residence time is long. More information on "secondary nucleation" is provided in Chapter 5, where it will be shown that strong deviations from straight lines in a semilogarithmic $\ln n$, L diagram can occur.

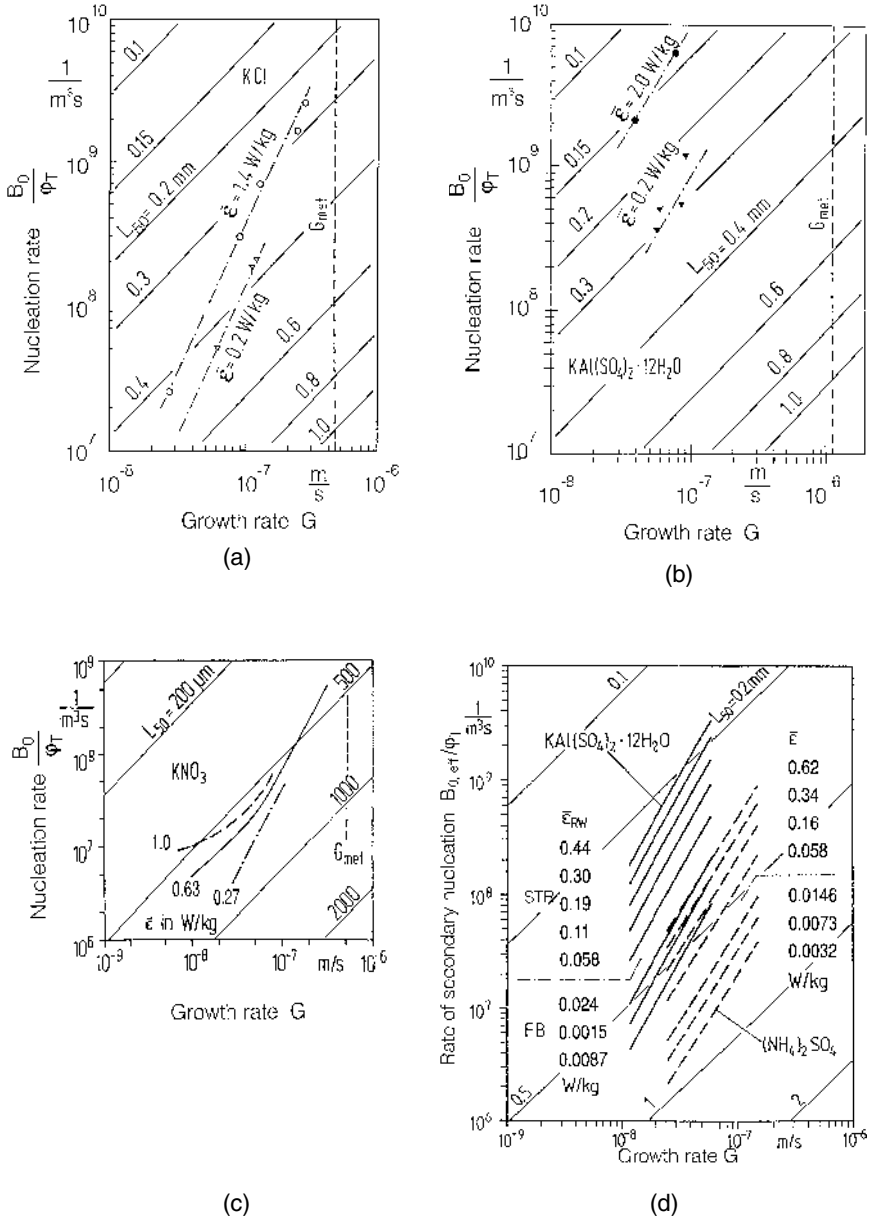

Figure 2.6. Nucleation rate based on volumetric holdup against crystal growth rate; experimental results for KCl (a), $KAl(SO_4)_2$ (b), KNO_3 (c), and for $KAl(SO_4)_2$ and $(NH_4)_2SO_4$ in stirred vessels and fluidized beds (d).

3. CLEAR-LIQUOR ADVANCE (GROWTH-TYPE CRYSTALLIZERS)

Generally speaking, the median crystal size of a crystalline product can be increased by (a) a decrease of the number of nuclei and (b) an increase of the growth period of crystals present in a crystallizer operated at optimum supersaturation. Therefore, a clear-liquor advance is favorable for crystal size distribution (CSD) because the residence times of the clear overflow mother liquor and of the crystals can be separated. The larger the clear-liquor flow for a given feed flow, the longer is the residence time of the crystals in the product stream. As a rule, there is an additional positive effect. In reality, the so-called "clear"-liquor advance contains a large number of small particles (attrition fragments, foreign particles, clusters) which can be activated in a supersaturated solution and become crystals, which lead to a finer product.

The effect of clear-liquor overflow on CSD can best be explained by a comparison of MSMPR- and growth-type crystallizers. An MSMPR crystallizer (index 1) is shown in Figure 3.1a and growth-type crystallizers (index 2) are shown in Figures 3.1b and 3.1c. With respect to the operating modes, the advanced liquor may be recycled separately, with the result that the suspension density of the product stream is high. Figure 3.1c shows the double draw-off on the right-hand side. Because the production rate is the same as in the MSMPR crystallizer for a given desupersaturation, the suspension density m_T in the unified streams is also equal to the value of the MSMPR crystallizer. However, the double draw-off operating mode with clear overflow is not very realistic because small particles cannot be separated completely. The realistic case of separation at a size L_F is explained in Sec. 4.

According to the literature, the fines removal rate R is defined by

$$R = \frac{\text{Feed flow}}{\text{Product flow}} \tag{3.1}$$

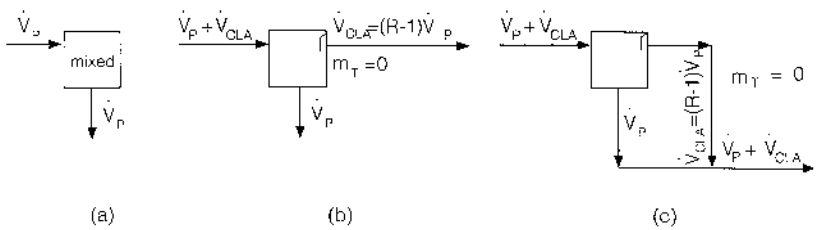

Figure 3.1. (a) MSMPR crystallizer; (b) crystallizer with clear-liquor advance (CLA); (c) double draw-off (DDO) crystallizer.

or

$$R = \frac{\text{Product flow} + \text{fines (or liquor) removal flow}}{\text{Product flow}} \tag{3.2}$$

or with the flows in Figure 3.1,

$$R = \frac{\dot{V}_P + \dot{V}_{CLA}}{\dot{V}_P} = 1 + \frac{\dot{V}_{CLA}}{\dot{V}_P} \tag{3.3}$$

For an ideally mixed crystallizer without clear-liquor advance (CLA) we obtain $R = 1$ valid for the MSMPR crystallizer. Under certain operating conditions of growth-type crystallizers, the yield as well as the median crystal size are improved. A further advantage can be the reduction of fouling [2.4].

Because the production rates in the MSMPR crystallizer and the growth-type crystallizer are the same, the following equations can be derived (see Fig. 3.2):

$$\dot{V}_P(G_1\tau_1)^4 n_{0,1} = (\dot{V}_P - \dot{V}_{CLA})(G_2\tau_2)^4 n_{0,2} \tag{3.4}$$

and

$$\dot{V}_P m_{T1} = (\dot{V}_P - \dot{V}_{CLA}) m_{T2} \tag{3.5}$$

For a constant specific power input $\bar{\varepsilon}$, equation (2.38) is valid (see also Chapter 5):

$$n_0 = \frac{B_0}{G} = K_n G^{i-1} m_T^l \tag{3.6}$$

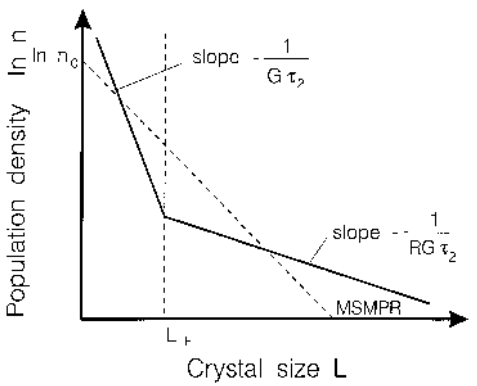

Figure 3.2. Population density versus crystal size for clear-liquor advance.

Because the dominant crystal size L_d is proportional to the product of crystal growth rate G and the residence time τ of the crystals, further calculations lead to

$$\frac{L_{d2}}{L_{d1}} = \left(\frac{\dot{V}_P + \dot{V}_{CLA}}{\dot{V}_P}\right)^{(i-1)(i+3)} = R^{(i-1)(i+3)} \tag{3.7}$$

Dealing with highly soluble substances, $i \approx 2$ and $l \approx 1$ may be realistic exponents for $\varphi_T < 0.05$ and a certain distance of the supersaturation ΔC from the metastable value $\Delta C_{\text{met}}(\Delta C < 0.5\Delta C_{\text{met}})$ is needed (see Chapter 3). For this case, we obtain

$$\frac{L_{d2}}{L_{d1}} = \left(\frac{\dot{V}_P + \dot{V}_{CLA}}{\dot{V}_P}\right)^{0.2} = R^{0.2} \tag{3.8}$$

Removal of 50% of the feed stream as advanced clear-liquor flow $\dot{V}_{CLA}$ results in an increase of only 15% of the dominant crystal size. Sometimes, a certain improvement of the median crystal size has been observed in industrial crystallizers, even better than according to equation (3.7). This can be due to fines removal, as it is very difficult to separate all small attrition fragments and foreign particles.

Let us assume that all particles with $L < L_F$ are withdrawn by the clear-liquor advanced flow $\dot{V}_{CLA}$ and that they grow at growth rate G_2 during retention time τ_2. The larger the ratio R or the clear-liquor removal flow, the longer is the retention time of the product crystals. Therefore, the slope of the logarithm of the population density versus crystal growth rate is

$$-\frac{1}{G\tau_2} \qquad \text{for } L < L_F \tag{3.9}$$

and

$$-\frac{1}{RG\tau_2} \qquad \text{for } L > L_F \tag{3.10}$$

(see Fig. 3.2) [3.1]. Sometimes, the fines removal flow is not separately recovered but heated for fines dissolving and recycling into the crystallizer.

4. FINES DESTRUCTION WITH SOLUTE RECYCLE

An MSMPR crystallizer is shown in Figure 4.1a, and crystallizers with fines destruction and solute recycle are depicted and Figures 4.1b and 4.1c. Fines can be withdrawn at a very small size, and the suspension density of the overflow $\dot{V}_0$ is very small (Fig. 4.1b). Another operating mode is shown on

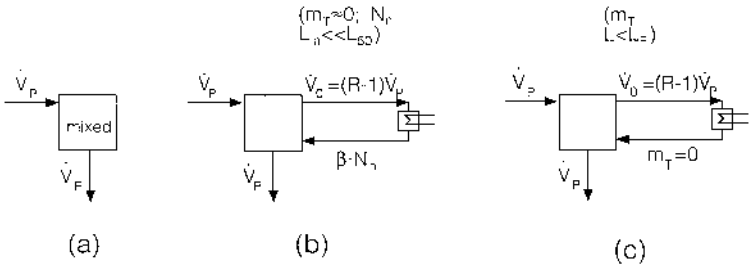

Figure 4.1. (a) MSMPR crystallizer; (b) crystallizer with clear-liquor overflow and fines destruction; (c) crystallizer with overflow and fines destruction.

the right-hand side of this figure: The advanced stream is classified at the size L_F and all particles $L < L_F$ are dissolved in the dissolver. At first, the concept of a point fines trap will be discussed. Fines are removed at a size that is negligibly small compared to product size crystals. In this case, the size improvement ratio L_{d2}/L_{d1} is given by [2.2]

$$\frac{L_{d2}}{L_{d1}} = \left(\frac{1}{\beta}\right)^{1/(i+3)} \tag{4.1}$$

where L_{d2} is the dominant size with destruction and L_{d1} is the size without this treatment, and β stands for the fraction of nuclei that survive in the fines destruction system. According to equation (4.1), the size improvement is appreciable if (a) the kinetic exponent i is small and (b) the fraction β of surviving nuclei is also small.

Because only $i > 1$ results in an increase of the median crystal size L_{50} with the residence time τ of a MSMPR crystallizer and the exponent i decreases with the mean specific power input $\bar{\varepsilon}$ but increases with supersaturation ΔC and growth rate G, good results of product coarsening can be obtained in crystallizers operated at a small power input $\bar{\varepsilon}$ and optimum residence time τ. It is essential to choose the residence time such that the mean supersaturation ΔC has a certain distance from the metastable zone width ΔC_{met} ($\Delta C \leq 0.5\Delta C_{\text{met}}$).

The efficiency of fines destruction depends on the undersaturation $-(C - C^*)$ in the destruction system and the residence time, which must exceed the dissolution time of nuclei. For the complete dissolution of small crystals, the dissolution time t_{dis} is given by

$$t_{\text{dis}} = \frac{L_n^2 \rho_C}{8cD_{AB}\ \ln[c/(c - c^*)]} = \frac{L_n^2 C_C}{8CD_{AB}\ \ln[C/(C - C^*)]} \tag{4.2}$$

where L_n is the initial size of the nucleus to be dissolved, D_{AB} stands for the diffusivity, C or c is the concentration of the solution, and C^* or c^* its solubility. In the case of small driving forces $-(C - C^*)$ for dissolution, the time t_{dis} may be quite long. Therefore, the fines destruction system must be designed carefully to obtain an appreciable size improvement.

Modeling the effect of fines destruction when the removed particles are not negligibly small compared to product size cystals is more complicated (see [2.2]). According to Figure 4.1, the drawdown times τ_F of the fines and τ_P of the product are

$$\tau_F = \frac{V}{\dot{V}_P + \dot{V}_0} = \frac{V}{R\dot{V}_P} \quad \text{for } L > L_F \tag{4.3}$$

and

$$\tau_P = \frac{V}{\dot{V}_P} \qquad \text{for } L > L_F \tag{4.4}$$

The ratio R of the drawdown times is

$$R = \frac{\tau_P}{\tau_F} = \frac{\dot{V}_P + \dot{V}_0}{\dot{V}_P} \tag{4.5}$$

It is assumed that the population densities n_0 of nuclei at size $L = 0$ are the same for the MSMPR crystallizer and the crystallizer with the fines destruction system. Because the drawdown time of the product is almost the same in both cases, it must be concluded that the growth rate G_2 of the crystallizer with fines removal is larger than for the MSMPR crystallizer. Therefore, the slopes in the density population plots are different in the ranges $0 < L < L_F$ and $L_F < L < \infty$. It also can be concluded that

$$\frac{R}{G_2\tau} > \frac{1}{G_1\tau} > \frac{1}{G_2\tau} \tag{4.6}$$

Because $G_2 > G_1$, it must also be concluded that the supersaturation $(\Delta C)_2$ in the crystallizer with fines destruction is larger than $(\Delta C)_1$ in the MSMPR crystallizer. This means that more attrition fragments will be activated, with the result that the nucleation rate increases according to $B_0 = n_0 G$ with $G = f(\Delta C)$. In Figure 4.2, the population density of crystallizers with fines destruction is shown. The population density n is given by [2.2]

$$n = n_0 \exp\left(-\frac{RL_F}{G_2\tau}\right) \exp\left(-\frac{L - L_F}{G_2\tau}\right) \tag{4.7}$$

Because $R > 1$, the slope of the straight line in the fines range $L < L_F$ is larger than the slope of the product crystals.

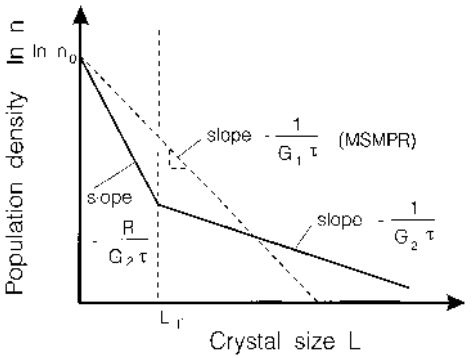

Figure 4.2. Population density versus crystal size for fines destruction.

Accelerated fines removal can result in bimodal weight distribution of the product crystals. The condition for such a mass peak in a small size range is given by [2.2]

$$\frac{3GV}{L_F(\dot{V}_0 - \dot{V}_P)} < 1 \tag{4.8}$$

where L_F is the fines classification, $\dot{V}_0$ is the volumetric fines removal rate or overflow rate of the crystallizer, and $\dot{V}_P$ is the mixed-product underflow rate. For a given crystallizer with the volume V operated at the supersaturation ΔC which results in the growth rate G, a bimodal size distribution occurs in the case of large L_F sizes and large overflow rates $\dot{V}_0$. On the other hand, fines destruction leads to a higher level of supersaturation and growth and to larger median crystal sizes, L_{50} having less total surface area [2.2].

5. CLASSIFIED PRODUCT REMOVAL WITH FINES DESTRUCTION

In Figure 5.1, a crystallizer equipped with devices for product classification and fines destruction is shown. The flow rate $(R-1)\dot{V}_P$ (compare Fig. 4.1) is withdrawn and split up in the overflow rate $\dot{V}_0$ and in the flow rate $R\dot{V}_P - \dot{V}_{\text{feed}} = (R-1)\dot{V}_P - \dot{V}_0$, which is passed through the fines destruction system. Only crystals with $L < L_F$ are destroyed. Additionally, the stream $z\dot{V}_P$ is separated in the classification device in the product flow rate $\dot{V}_P$ and in the recycle flow $(z-1)\dot{V}_P$. Again, we assume a sharp size cut at L_c in the classifier. The objective of this arrangement is to compensate

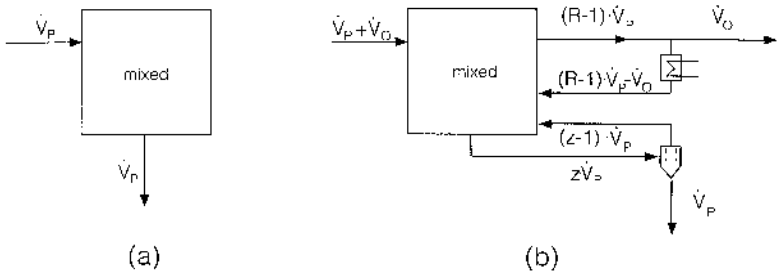

Figure 5.1. (a) MSMPR crystallizer; (b) crystallizer with overflow, fines destruction, and classified product removal.

the increase of nuclei caused by higher supersaturation with respect to classification by a dissolution of fines in the heat exchanger. Therefore, a coarse product with a narrow size distribution can be expected, of course, at the expense of higher investment cost. In Figure 5.2a, the population density as a function of crystal size is shown with the three segments. The slopes of these segments are

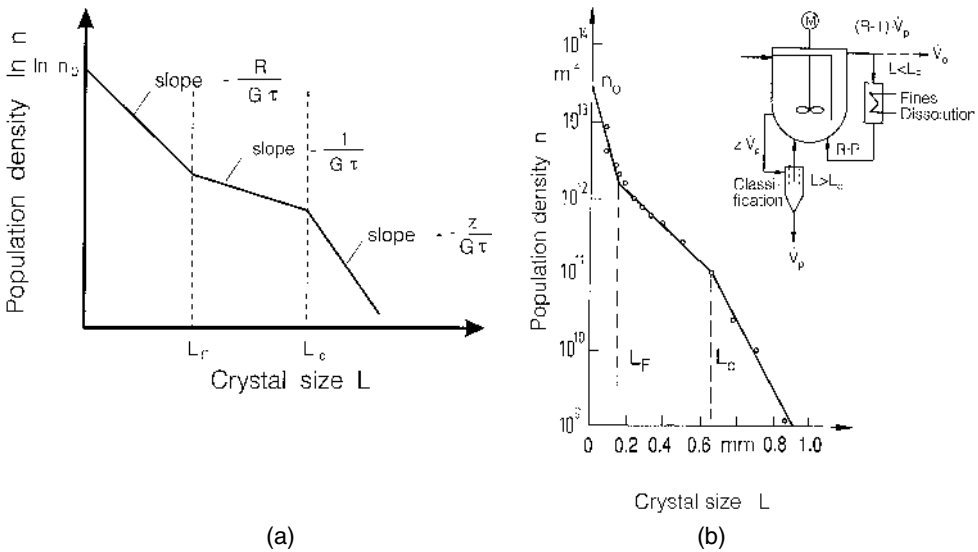

Figure 5.2. Population density versus crystal size for fines destruction and classified product removal: (a) principal; (b) experimental.

$$-\frac{R}{G\tau} \quad \text{for } L < L_F \tag{5.1}$$

$$-\frac{1}{G\tau} \quad \text{for } L_F < L < L_c \tag{5.2}$$

and

$$-\frac{z}{G\tau} \quad \text{for } L > L_c \tag{5.3}$$

Without fines withdrawal [$\dot{V}_P(R-1)=0$] and classification [$\dot{V}_P(z-1)=0$] or $R=1$ and $z=1$, the arrangement corresponds to an MSMPR crystallizer. The deviations from the MSMPR straight line in the population-density plot increase with increasing values for R and z or withdrawal of fines or recycle from the classifier, respectively.

Juzaszek and Larson [3.1] applied the Rz model to describe the crystallization of potassium nitrate in a crystallizer equipped with fines destruction and classification (see Fig. 5.2b). The relationship for the population density can be derived according to the different size ranges:

$$n = n_0 \exp\left(-\frac{RL}{G\tau}\right) \quad \text{for } L < L_F \tag{5.4}$$

$$n = n_0 \exp\left(-(R-1)\frac{L_F}{G\tau}\right)\exp\left(-\frac{L}{G\tau}\right) \quad \text{for } L_F \le L \le L_c \tag{5.5}$$

and

$$n = n_0 \exp\left((z-1)\frac{L_c}{G\tau} - (R-1)\frac{L_F}{G\tau}\right)\exp\left(-\frac{zL}{G\tau}\right) \quad \text{for } L > L_c \tag{5.6}$$

Of course, such straight lines are obtained only in the absence of attrition and agglomeration (e.g., the MSMPR conditions described earlier must be fulfilled).

6. CLASSIFIED PRODUCT REMOVAL

Figure 6.1 shows an MSMPR crystallizer and a crystallizer with classified product removal. The classification device may be a hydrocyclone (see Fig. 6.1), a classifier, a wet screen, a fluidized bed, or a separating centrifuge. It is assumed that this device separates the flow $z\dot{V}_P$ withdrawn from the mixed crystallizer at a size cut L_c. The product flow $\dot{V}_P$ is removed and the stream $(z-1)\dot{V}_P$ is recycled into the crystallizer. In the case of a sharp classification at size L_c, the drawdown times are defined as

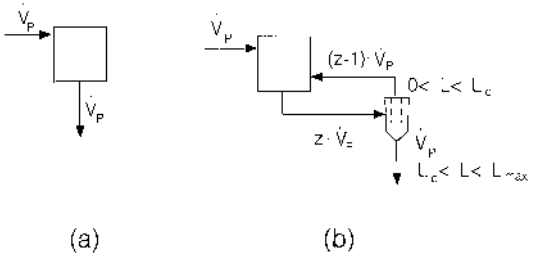

Figure 6.1. (a) MSMPR crystallizer; (b) crystallizer with classified product removal.

$$\tau_c = \frac{V}{\dot{V}_P} = \tau \qquad \text{for } L < L_c \tag{6.1}$$

and

$$\tau_P = \frac{V}{z\dot{V}_P} = \frac{\tau}{z} \qquad \text{for } L > L_c \tag{6.2}$$

$z > 1$ leads to a circulation flow from the classification device back to the crystallizer, and by this, the retention time of the coarse product crystals is reduced. Therefore, classification results in products with a smaller median crystal size but narrow CSD. The limiting case $z = 1$ corresponds to the MSMPR crystallizer.

Solving the population density leads to

$$n_2 = k_2 \exp\left(-\frac{L}{G_2\tau}\right) \qquad \text{for } L < L_c \tag{6.3}$$

and

$$n_2' = k_2' \exp\left(-\frac{zL}{G_2\tau}\right) \qquad \text{for } L > L_c \tag{6.4}$$

With respect to continuity, the condition

$$n_2(L_c) = n_2'(L_c) \tag{6.5}$$

is given. Because $z > 1$, the straight line of the population density $n_2' = f(L)$ in the coarse particle range is steeper than for the small crystals (see Fig. 6.2). As the slurry density is reduced by the preferential removal of oversize crystals, the volumetric holdup φ_T, which is proportional to the integral $\int L^3 dL$ over the entire distribution, is less for classification than in the MSMPR crystallizer. However, the specific area $a_T = 6\varphi_T/L_{32}$ is increased

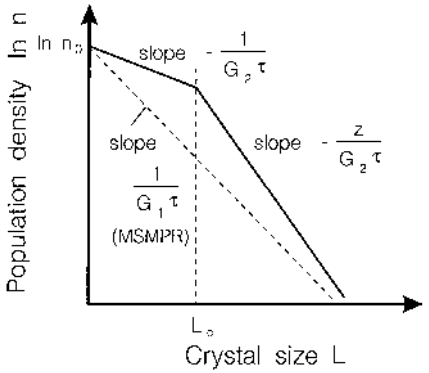

Figure 6.2. Population density versus crystal size for classified product removal.

with respect to a finer distribution. The total crystal surface can increase (significant decrease of mean crystal size and small increase of volumetric holdup φ_T) or decrease. In the latter case, the supersaturation $(\Delta C)_2$ and the growth rate G_2 are larger than for the MSMPR crystallizer. However, an increase in supersaturation increases the nucleation rate, with the result that the median crystal size is reduced. Therefore, classified crystallizers are often equipped with a fines destruction system to reduce the number of activated nuclei.

7. DEVIATIONS FROM THE MSMPR CONCEPT

The term *ideal MSMPR model* refers to a model in which all previously named assumptions and conditions are fulfilled so that the equations mentioned up to now apply and the measured distributions can be represented by straight lines in a semilogarithmic number-density diagram. In laboratory crystallizers, deviations occur only under certain circumstances (not ideally mixed, undesirable or desirable product classification removal, fines dissolution, agglomeration, size-dependent growth and growth dispersion, and, above all, high specific power input, suspension densities, and residence times that lead to attrition and breakage). In industrial crystallizers, such deviations always exist. Figure 7.1 shows a stirred-vessel crystallizer in which the above-mentioned effect may arise. Figures 7.2 and 7.3 illustrate the effects on crystal size distribution. Particularly strong attrition leads to the fact that the maximum crystal size $L_{\max}$ is not exceeded because the positive kinetic growth rate is equal to the negative linear attrition rate

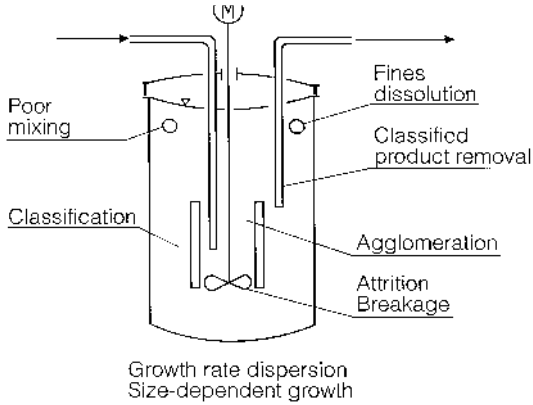

Figure 7.1. Effects in a nonideal MSMPR crystallizer.

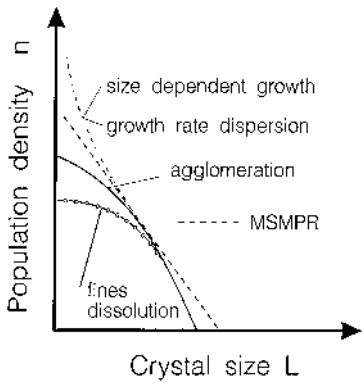

Figure 7.2. Deviation from the straight line due to kinetic effects.

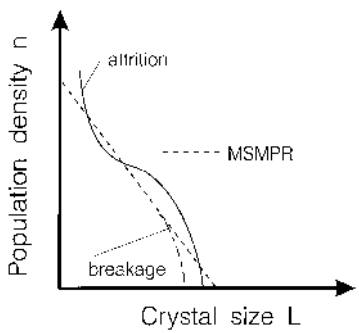

Figure 7.3. Deviation from the straight line due to mechanical effects (fluid shear and solid attrition effects).

G_a (see Fig. 7.4). In Figure 7.4, it is assumed that the growth rate does not depend on the crystal size but that the attrition rate increases quadratically with the crystal size, depending on the probability of large crystals colliding with the circulating device (cf. Chapter 5). Such attrition rates G_a have been determined experimentally for KNO_3, which is very prone to attrition [7.1].

The attrition of large crystals causes the median crystal size L_{50} plotted against the residence time τ to pass through a maximum value. This applies, for example, to potassium nitrate, which tends to abrade easily (see Fig. 7.5) but not to abrasion-resistant ammonium sulfate (Fig. 7.6). In the area to the right of the maximum value (i.e., at long residence times), supersaturation and therefore the kinetic growth rate G are very low, resulting in the mechanical attrition rate G_a being larger than G. The greater the mean specific power input in the crystallizer, the higher the attrition rate, especially for crystal products that tend to abrade easily, and the smaller the residence time τ at which the maximum value occurs. The effects of classifying removal, fines dissolution, size-dependent growth, and growth dispersion should be dealt with in more detail.

The most common operational cause of the deviation from the "ideal" straight line is classified product removal, which can take place in two ways:

1. *Broad-range classification* over large crystal size ranges characterized by narrow selectivity. The reasons for this are usually a poorly chosen site for product removal and unsuitable product removal conditions, such as insufficient flow rates in the discharge duct. The effects on product crystal distribution and the mathematical modeling of this type of screening are described in Ref. 2.2. The curve of population density

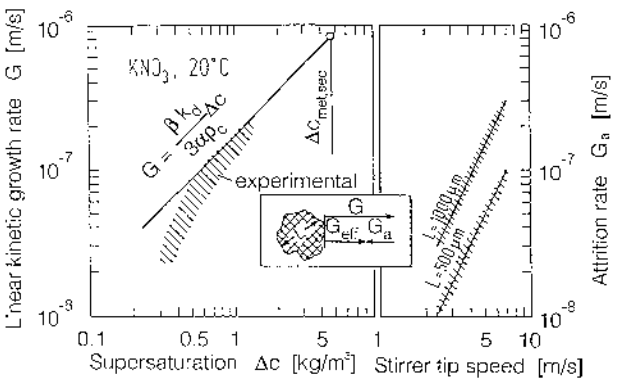

Figure 7.4. Kinetic growth rate versus supersaturation (left); attrition rate versus stirrer tip speed (right).

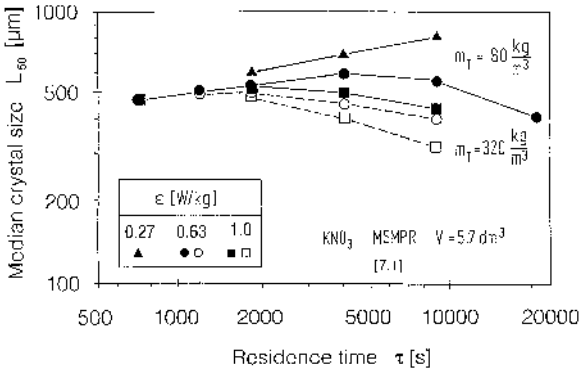

Figure 7.5. Median crystal size of potassium nitrate in the stirred vessel.

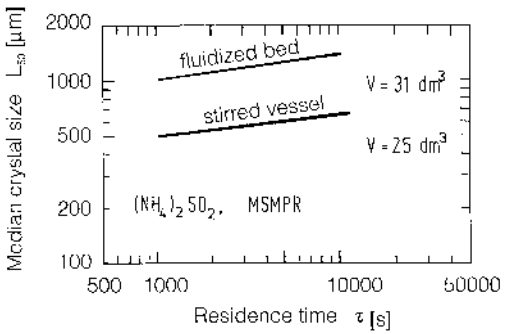

Figure 7.6. Median crystal size of ammonium sulfate in the stirred vessel and fluidized bed.

distribution varies greatly depending on the classification function. Figure 7.7 provides two examples, which differ only in the stirrer speed. The dependency of classification on crystal size is determined by an empirical classification function which must be determined experimentally in washing-out experiments. This type of product classification is generally undesirable for the experimental determination of kinetic data based on the MSMPR principle and should be avoided by selecting suitable removal conditions [7.3].

2. *Narrow-range classification* occurs frequently in industrial crystallizers. In this case, industrial features include product removal via salt sacks, the distribution of the crystallizer volume over nucleation and growth zones, removal of fines or fines dissolution, or the increase of the crystal residence time due to clear-liquid overflow.

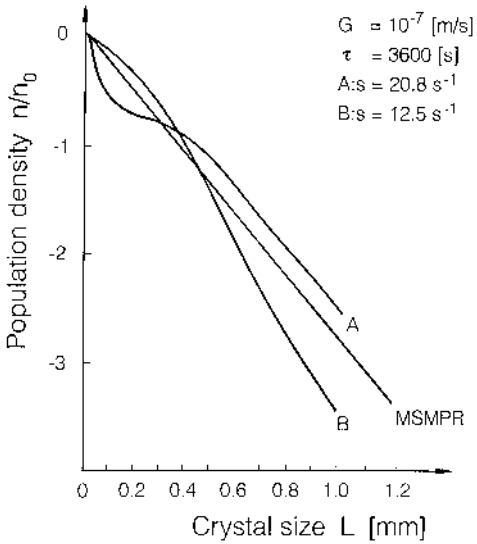

Figure 7.7. Effects of broad-range classification on the population density distribution; experimental results for potash alum. (From Ref. 7.2.)

Another reason for deviations from the ideal, straight MSMPR lines is size-dependent growth. The term *size-dependent growth* should be understood according to the information provided in Chapter 3. It is difficult to distinguish between size-dependent growth and growth dispersion. Based on the present level of knowledge, *size dependency* basically conceals two reasons for making one believe that growth is faster: effects of growth dispersion and agglomeration processes. Moreover, true size-dependent growth of attrition fragments can take place in a crystallizer; see Chapter 5. The ASL (Abegg–Stephan–Larson) model [7.4] is often used according to the following equation to describe size-dependent growth generally:

$$G = G_0\left(1 + \frac{L}{G_0\tau}\right)^b \tag{7.1}$$

G_0 is the growth rate of very small crystals ($L < 100\,\mu m$), which is often lower than that of large crystals ($L > 100\,\mu m$). The crystal size dependency is described by exponent b. The differential equation for the number density balance in this case is

$$\frac{d[G_0(1 + L/G_0\tau)^b n]}{dL} + \frac{n}{\tau} = 0 \tag{7.2}$$

The number density distribution is then

$$n = n_0\left(1 + \frac{L}{G_0\tau}\right)^{-b} \exp\left(\frac{1-(1+L/G_0\tau)^{1-b}}{1-b}\right) \tag{7.3}$$

Figure 7.8 illustrates the number density distributions for different values of b. When $b = 0$, no size-dependent growth occurs. The suspension density can again be calculated with the third distribution moment:

$$m_T = \alpha\rho_C \int_0^\infty L^3 n(L)\, dL \tag{7.4}$$

This gives a complex expression for suspension density that can only be solved numerically. However, it can be rewritten in such a way that the influence of b can be represented in the form of an independent function $c(b)$ [7.4]:

$$m_T = c_1(b)\beta\rho_C n_0 (G_0\tau)^4 \tag{7.5}$$

The maximum value of mass density distribution can be considered the same way:

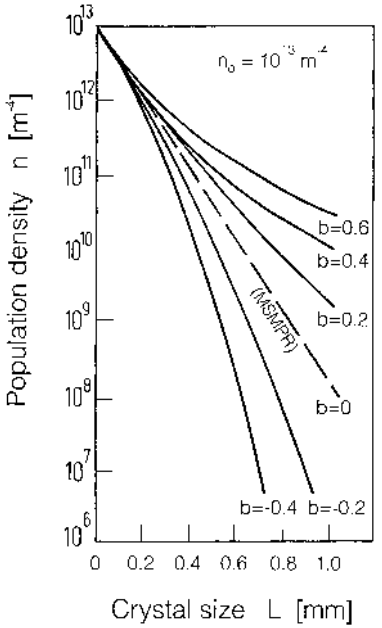

Figure 7.8. Number density versus the crystal size for different values of b.

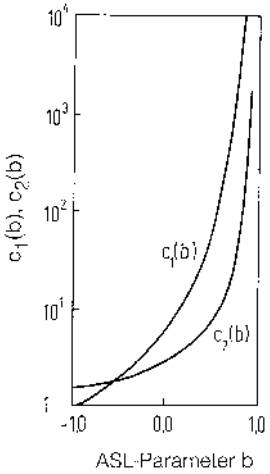

Figure 7.9. Parameters $c_1(b)$ and $c_2(b)$ defined by equations (7.5) and (7.6), respectively.

$$L_{\max} = c_2(b) G_0 \tau \tag{7.6}$$

The parameters $c_1(b)$ and $c_2(b)$ are obtained from Figure 7.9. Analysis of experimental results produced $b = 0.4$ to 0.6 for the drowning-out crystallization of aqueous sodium sulfate solutions with methanol [7.5] and $b = 0.43$ to 0.62 for potassium carbonate [7.6]. However, these values for b have been obtained from experimental results, and it should be stressed that there is no way of predicting such values in advance. This is understandable with respect to the more empirical feature of the ASL model, which comprises summary processes such as size-dependent growth, growth dispersion, and agglomeration. Agglomeration is considered in more detail in Chapter 6.

The number of crystals in a crystallizer is altered not only by attrition, agglomeration, poor mixing, and nonrepresentative withdrawal of the product but also by seeding. In Figure 7.10, the crystal size distribution of $K_2Cr_2O_7$ crystals is shown. As can be seen from the diagrams, deviation from the straight lines according to MSMPR conditions occur due to seeding. Furthermore, the mass and size distribution of the seed play a role for the population density, at least during the first residence times after the addition of the seed.

The ideal MSMPR concept can be extended by treating common procedures such as seeding, product classification, and fines dissolution in a theoretical manner. These measures for influencing the crystal size distribution

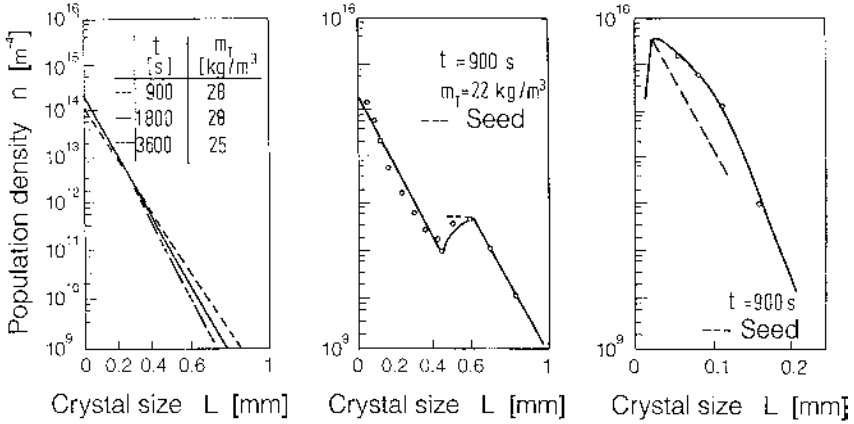

Figure 7.10. Crystal size distributions of $K_2Cr_2O_7$–water in a continuously operated cooling crystallizer (from Ref. 7.8); influence of residence time and seeding.

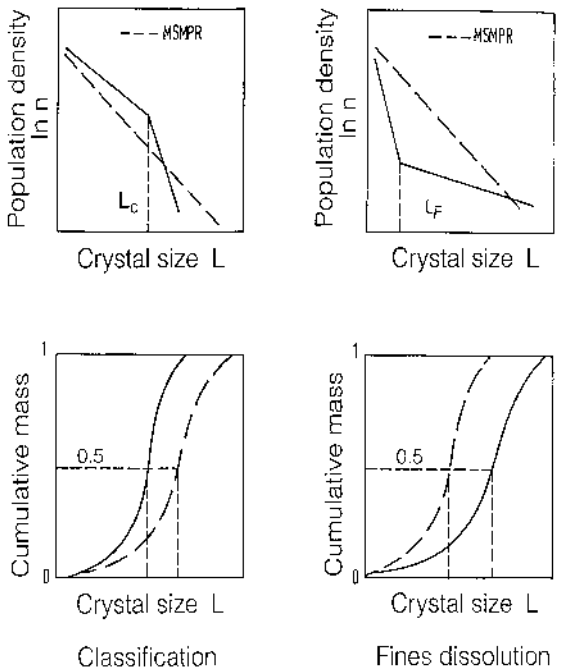

Figure 7.11. Effects of classified removal and fines dissolution.

lead to mean crystal sizes, as shown qualitatively in Figure 7.11 [7.7]. The two diagrams on the left apply to classified removal, and the two diagrams on the right describe the effects of fines dissolution. The upper diagrams show the number densities and the lower diagrams the cumulative undersize or the aperture against the crystal size L. The dashed curves represent results expected to be obtained under ideal MSMPR conditions. In the case of classified removal, a more narrow crystal size distribution is obtained but with a smaller mean particle diameter. Exactly the opposite applies in the case of fines dissolution, where a larger median diameter L_{50} is obtained.

8. POPULATION BALANCE IN VOLUME COORDINATES

The rates of nucleation and crystal growth decide on the final CSD; however, it is difficult to define and to measure nucleation rates because the term "nucleus" is used for a variety of solid species present in a solution. The smaller the particles, the more difficult it is to measure their size. As a rule, the nucleation rate B is defined as the total number of particles N_T generated in a certain volume ΔV of constant supersaturation in a certain time Δt:

$$B = \frac{N_T}{\Delta V \Delta t} \tag{8.1}$$

or according to the MSMPR concept,

$$B_0(L \to 0) = \frac{N_T}{\Delta V \Delta t} = n_0 G \tag{8.2}$$

The MSMPR modeling assumes that nuclei are born at $L \to 0$, which is not true in reality. Later, it will be shown that in crystallizers operated at $\sigma < 0.1$, many attrition fragments are formed in the size range between 1 and 150 µm, with the consequence that the population density $n(L)$ in a semilogarithmic plot is often not a straight line. Therefore, the ordinate intersection n_0 as well as the slope $1/(G\tau)$ and also the nucleation rate $B_0 = n_0 G$ lose their physical significance. In the size range between 1 and 10 µm, a huge number of attrition fragments is present in the slurry; however, nearly all of them do not grow at all. These particles are not active nuclei and do not play a role for the CSD as long as the supersaturation remains constant and they stay inert. Up to a value for the relative supersaturation of $\sigma < 0.1$, activated nucleation can be neglected. This will change for $\sigma > 0.5$. With increasing supersaturation, the rates of activated nucleation rise rapidly; see Chapter 2. Such nuclei grow in a supersaturated solution, and the CSD depends on the rates of nucleation and growth. However, when the supersaturation assumes values above $\Delta C/C_C > 0.1$ or $\sigma > 0.1(C_C/C^*)$ the rate of collisions $(dN/dt)_{\text{col}}$ is higher than the rate

B_{hom} of homogeneous primary nucleation. This will be demonstrated in more detail later. With respect to the very rapid agglomeration, it is not possible to measure real nuclei. Many particle size analyzers are only able to count the number of the aggregates. In this case, the nucleation rate is only an apparent value and may be expressed by the number N_{agg} of aggregates based on a certain volume ΔV and a certain time Δt:

$$B_{\text{app}} = \frac{N_{\text{agg}}}{\Delta V \Delta t} \tag{8.3}$$

These examples show that the simplified MSMPR modeling does not exactly describe the reality in crystallizers. However, the concept can often be used as a first approximation under the following conditions:

- When the supersaturation is smaller than $\sigma = 0.1$ and the median crystal size is approximately $L_{50} = 100 = 500\,\mu\text{m}$, it can be useful to introduce the rate $B_{0,\text{eff}}$ of effective nucleation according to $B_{0,\text{eff}} = n_o G$ and to apply the equations for the MSMPR modeling.
- When the relative supersaturation is in the range $0.5 < \sigma < 0.1(C_C/C^*)$ and crystals in the range $1 < L < 100\,\mu\text{m}$ are produced, the MSMPR modeling gives often useful results.
- When the relative supersaturation assumes values of $\sigma > 0.1(C_C/C^*)$, a very rapid agglomeration takes place and aggregates instead of real nuclei will be measured. In this case, the MSMPR modeling based on the number of aggregates instead of real nuclei calculated from the equations of activated nucleation can lead to reasonable results for the prediction of the median crystal size.

In an industrial crystallizer, there is a huge variety of real, effective, and apparent nuclei with quite different growth behavior and of crystals which grow either fast or retarded or do not grow at all. Moreover, the behavior of particles depends on supersaturation which can vary with the local position and time. We have also seen that supersaturation can occur in the range $10^{-4} < \sigma < C_C/C^*$, depending on the solubility of the solute under discussion.

These considerations show that the population balance based on numbers can be a less appropriate tool to model CSD. Especially for the processes of breakage and agglomeration in the absence of supersaturation, the volume of the solid matter remains constant. A population balance equation in volume coordinates can take these processes into account. The population density n_v expressed in volume coordinates is given by

$$n_v = \frac{\text{Number of particles}}{(\text{m}^3 \text{ suspension})(\text{m}^3 \text{ particle volume})} \tag{8.4}$$

Desupersaturation results in nucleation (i.e., the formation of particles with the smallest measurable volume) and leads to an increase of the particle volume per unit time according to the growth rate G_v (in m^3/s). In a certain volume interval du of the crystal volume u, particles can appear either by aggregation with the rate B_{agg} or by disruption with the rate B_{dis}. At the same time, particles of this interval du can disappear according to death rates. The death rate D_{agg} describes the death rate by aggregation and the death rate D_{dis} denotes the number of particles in the interval du which disappear by disruption. In the general case of an instationary crystallizer with a changing volume (evaporation), the population balance is given by

$$\frac{\partial n_v}{\partial t} + \frac{\partial (n_v G_v)}{\partial u} + \frac{\partial (n_v V)}{V \partial t} + \frac{n_{vp} n_{vf}}{\tau} = B_{agg} - D_{agg} + B_{dis} - D_{dis} + B_u \delta(u - u_0) \tag{8.5}$$

The difference $B_{agg} - D_{agg}$ represents the net formation of particles of volumetric size u by aggregation. Corresponding to this, the difference $B_{dis} - D_{dis}$ describes the net formation of particles formed by disruption. The source function B_u is the birth rate of particles at the lowest measurable size u_0, accounting for the growth and agglomeration of particles into the measurable range of the particle volume. The combination of two particles of size u and $v - u$ to form a particle size v can be written as

$$B_{agg} = \frac{1}{2} \int_0^v \beta(u, v - u) n_v(u, t) n_v(v - u, t)\, du \tag{8.6}$$

and

$$D_{agg} = n_v(v, t) \int_0^\infty \beta(u, v) n_v(u, t)\, du \tag{8.7}$$

Here, B_{agg} is the rate at which particles of volume v appear (or are born) through particles of volume $v - u$. β (in m^3/s) is the aggregation rate constant or the aggregation kernel which depends on the frequency of collision between particles. The factor $\frac{1}{2}$ prevents each aggregation event from being counted twice. Further information on agglomeration will be presented in Chapter 6.

REFERENCES

[2.1] H. M. Hulburt and S. Katz, Some problems in particle technology, *Chem. Eng. Sci.*, *19*: 555 (1964).

[2.2] A. D. Randolph and M. A. Larson, *Theory of Particulate Processes*, 2nd ed., Academic Press, San Diego, CA (1988).

[2.3] R. W. Peters, P. H. Chen, and T. K. Chang, $CaCO_3$ precipitation under MSMPR conditions, in *Industrial Crystallization '84* (S. J. Jancic and E. J. de Jong, eds.), North-Holland, Amsterdam, 309 (1984).
[2.4] A. Mersmann, Design of crystallizers, *Chem. Eng. Process.*, *23*: 213 (1988).
[3.1] P. Juzaszek and M. A. Larson, Influence of fines dissolving in crystal size distribution in an MSMPR-crystallizer, *AIChE J.*, *23*: 460 (1977).
[7.1] J. Pohlisch and A. Mersmann, The influence of stress and attrition on crystal size distribution, *Chem. Eng. Technol.*, *11*: 40 (1988).
[7.2] J. Garside, A. Mersmann, and J. Nyvlt, *Measurement of Crystal Growth Rates*, European Federation of Chemical Engineering, Munich (1990).
[7.3] J. R. Bourne, Hydrodynamics of crystallizers with special reference to classification, in *Industrial Crystallization '78* (E. J. de Jong and S. J. Jancic, eds.), North-Holland, Amsterdam (1979).
[7.4] B. F. Abegg, J. D. Stevens, and M. A Larson. Crystal size distributions in continuous crystallizers when growth rate is size dependent, *AIChE J.*, *14*: 118 (1968).
[7.5] W. Fleischmann and A. Mersmann, Drowning-out crystallization of sodium sulphate using methanol, in *Proc. 9th Symp. on Industrial Crystallization* (S. J. Jancic and E. J. de Jong, eds.), Elsevier, Amsterdam (1984).
[7.6] D. Skrtic, R. Stangl, M. Kind, and A. Mersmann, Continuous crystallization of potassium carbonate, *Chem. Eng. Technol.*, *12*: 345 (1989).
[7.7] B. J. Asselbergs and E. J. de Jong, Integral design of crystallizer as illustrated by the design of a continuous stirred-tank cooling crystallizer, in *Industrial Crystallization* (J. W. Mullin, ed.), Plenum Press, New York (1976).
[7.8] R. M. Desai, J. W. Rachow, and D. C. Timm, Collision breeding: A function of crystal moments and degree of mixing, *AIChE J.*, *20*: 43 (1974).

5

Attrition and Attrition-Controlled Secondary Nucleation

A. MERSMANN Technische Universität München, Garching, Germany

Generally speaking, the rates of agglomeration, attrition, fines dissolving, nucleation, and crystal growth determine crystal size distribution (CSD). The attrition of crystals is important when designing and operating crystallizers for two reasons:

- The linear mechanical attrition rate $G_a = -dL/dt$ of a crystal is in inverse proportion to the kinetic crystal growth rate G. This means that a crystal can only grow at the effective rate $G_{\text{eff}} = G - G_a$.
- When attrition fragments grow in a supersaturated solution, they are secondary nuclei and influence the population balance and, ultimately, the CSD and the median crystal size.

In order to have a clear understanding of the two effects, the following parameters must be known:

- The volume V_a abraded from one crystal after a collision, or the volumetric attrition rate $dV_a/dt = \dot{V}_a$ from which the linear attrition rate can be derived according to $G_a = (1/A)(dV_a/dt) = (1/3\alpha L_{\text{par}}^2)(dV_a/dt) =$

$V_a/3\alpha L_{\text{par}}^2 = 2\dot{V}_a/\beta L_{\text{par}}^2$, where $A = \beta L_{\text{par}}^2$ is the parent particle surface (valid for spheres where $3\alpha = \beta/2$).

- The number of attrition fragments formed in a particle size interval per unit time.

When a stirrer rotates in a suspension, attrition by the stirrer, according to Ref. 0.1, is a function of dynamic pressure $\rho_C u_{\text{tip}}^2/2$, which increases the square of the circumferential velocity u_{tip} of the stirrer and the density ρ_C of the particle. Some models for the attrition of crystals assume that the attrition rate is proportional to the contact energy w_{col}^2 and the crystal density ρ_C. The parameter w_{col}^2 is the square of the collision velocity w_{col} and represents the specific contact energy (e.g., in J/kg). If this energy is multiplied by the collision frequency $f_{\text{col}} \sim s$, we obtain the specific contact power input (e.g., in W/kg). It can be shown that this frequency (collisions of crystals with the rotor) in stirred suspension is approximately proportional to the circulated volumetric flow of the suspension and, thus, to the stirrer speed. This means that the attrition rate should be proporational to the mean specific power input $\bar{\varepsilon}_C$ of the crystalline solid (e.g., in W/kg solid). If it is also assumed that the specific power input in a stirred-vessel crystallizer is proportional to the mean specific power input $\bar{\varepsilon}_C$ for a certain crystal volumetric holdup φ_T, we obtain

$$\frac{d\text{Va}}{dt} = G_a A \sim w_{\text{col}}^2 s \sim \overline{\varepsilon_C} \sim \bar{\varepsilon} \tag{0.1}$$

Botsaris [0.2] assumes that the effective rate $B_{0,\text{eff}}$ of secondary nucleation is proportional to this attrition rate, which, however, is multiplied by the factors f_1 and f_2 to take into account the number f_1 of attrition fragments formed per collision and the percentage f_2 of growing attrition particles capable of surviving. Botsaris then arrives at

$$B_{0,\text{eff}} \sim f_1 f_2 \bar{\varepsilon} \tag{0.2}$$

According to its physical meaning, parameter f_1 depends on the mechanical processes (and the properties of the solid), whereas parameter f_2 is influenced in particular by supersaturation (i.e., by kinetics). Moreover, it can be shown that the effective nucleation rate in the case of crystal–rotor collisions is proportional to the volumetric holdup φ_T, and in the case of crystal–crystal collisions, it is proportional to the square of the volumetric holdup φ_T^2 [0.3]. This gives the following relationship:

$$B_{0,\text{eff}} \sim f_1(\text{mechanics}) f_2(\Delta c) \bar{\varepsilon} \varphi_T^m \tag{0.3a}$$

where $m = 1$ for crystal–rotor collisions and $m = 2$ for crystal–crystal collisions.

Although the proportionality $B_{0,\text{eff}} \sim \bar{\varepsilon}$ has in some cases (high mean specific power input $\bar{\varepsilon} > 1$ W/kg and crystals prone to attrition) been verified approximately on an experimental basis [0.3], numerous experiments have led to the result

$$B_{0,\text{eff}} \sim (\bar{\varepsilon})^r \tag{0.3b}$$

where $0.5 < r < 0.8$ [0.4–0.8]. For this reason, other formulations for attrition have been proposed with which many experimental results can be described more efficiently.

When secondary nuclei are formed just from growing attrition fragments during contact nucleation, the following parameters must be known in order to calculate the rate of secondary nucleation:

1. The volumetric attrition rate $\dot{V}_a$ abraded from one crystal
2. The size distribution of the fragments
3. The growth behavior of attrition fragments with respect to supersaturation
4. The total number of growing attrition fragments produced per unit time

1. ATTRITION AND BREAKAGE OF CRYSTALS

Let us assume that a single crystal of size L sinks in a solution with density ρ_L. When $\Delta\rho = \rho_C - \rho_L$ is the density difference between the crystal and the solution, the volumetric energy $(v'_{\text{eff}})^2 \rho_L/2$ must be transferred from the liquid to the particle in order to compensate the loss $L\Delta\rho g$ of potential energy. This leads to

$$(v'_{\text{eff}})^2 = 2L\frac{\Delta\rho}{\rho_L}g \tag{1.1}$$

In systems with rotors (for instance, a stirred vessel), the fluctuating velocity v'_{eff} is proportional to the tip speed, u_{tip}, of the rotor:

$$v'_{\text{eff}} \sim u_{\text{tip}} \tag{1.2}$$

Therefore, the tip speed of a rotor must increase with the crystal size L and the density difference $\Delta\rho$ in order to prevent the settling of particles in the gravitational field with the acceleration g. Let us consider a stirred vessel (see Fig. 1.1). The target efficiency $\eta_t \sim y/D_t$ determines whether or not a parent crystal collides with the rotor and is defined by the ratio number of colliding parent crystals in the projection area of the rotor and the total number of crystals in this area. $\eta_t = 1$ means that all crystals arriving in the projection area impinge either on the edge or on the breadth of the stirrer. On the other hand, if there are no or only negligible collisions, $\eta_t = 0$.

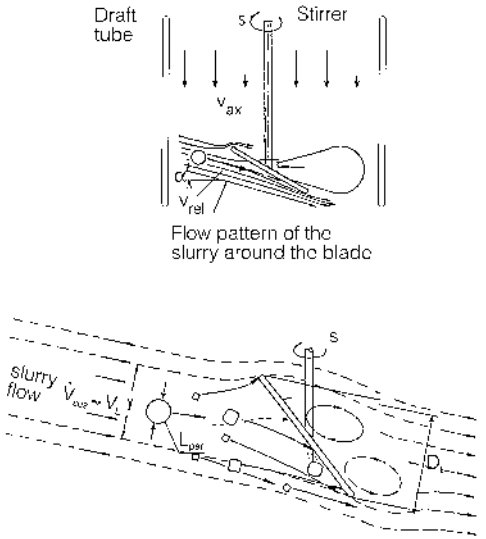

Figure 1.1. Definition of target efficiency.

Generally speaking, the target efficiency depends on the Stokes number St [1.1] (see Fig. 1.2). The diagram is valid for any system and may be useful for evaluating the operating conditions of impingement collectors [1.2]. In Figure 1.3, the target efficiency of particles impinging on a stirrer is plotted against the particle size L for three different collision velocities w_{col} and for the specific conditions given in the figure. As can be seen, the target efficiency is less than 0.1 for small particles ($L < 100\,\mu\mathrm{m}$) but is approximately $\eta_t = 1$ for parent crystals where $L > 500\,\mu\mathrm{m}$ when collision velocities are greater than 5 m/s. The collision velocities w_{col} occurring in stirred vessels of different geometries and sizes can be calculated from the fluid dynamics in such vessels (see, e.g., Ref. 1.3).

The intensity and frequency of the crystal–rotor collisions depend on the following:

- Geometry parameters, such as the volume V of the crystallizer or the tank diameter T, the diameter D of the rotor, and the number a of the blades
- Operating parameters, such as the speed s and the pumping capacity N_V of the rotor
- Physical properties of the solid–liquid system, such as the size L of the particles, their volumetric holdup φ_T, the particle density ρ_C, the density ρ_L, and the viscosity η_L of the liquid.

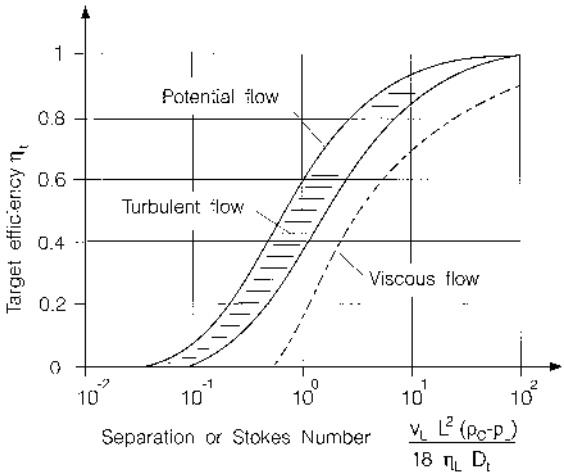

Figure 1.2. Target efficiency versus the Stokes number.

High collision velocities w_{col} occur in small crystallizers equipped with a high-speed rotor, especially when large crystals with a large $\Delta\rho$ are suspended in a solution of low viscosity.

In small and medium-sized stirred vessels, off-bottom lifting of particles is the decisive criterion for scale-up. This means that the tip speed must be the same in stirred vessels of different sizes; Chapter 8.

The collision velocity w_{col} between a crystal and a rotor is smaller than the tip speed but increases with u_{tip}. The square of the collision velocity, w_{col}^2, is a specific energy that can be transferred to the crystal to a certain extent. If this energy and the resulting strain in the particle are high enough, a small volume V_a of the particle is abraded and distintegrates into a large number of attrition fragments. Because such fragments can grow in a supersaturated solution and can become attrition-induced secondary nuclei, the answers to the following questions are very important for the modeling of secondary nucleation at low levels of supersaturation ($\sigma < 0.1$) when activated nucleation is negligible:

- What is the volume V_a abraded from a parent crystal with the size L_{par}?
- What is the size distribution of the attrition fragments?
- What are the most important material properties for attrition?
- What is the growth behavior of attrition fragments in a supersaturated solution?

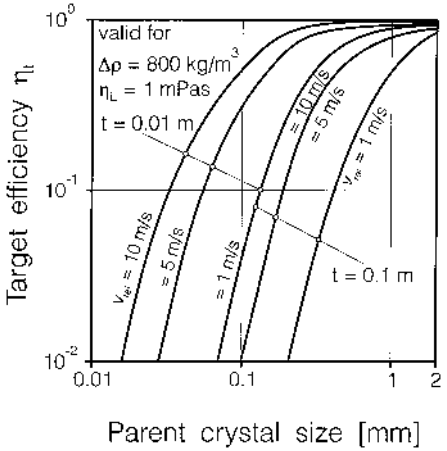

Figure 1.3. Target efficiency against the parent crystal size for the velocities 1, 5, and 10 m/s and the target dimensions $t = 0.01$ m and 0.1 m. (From Ref. 1.4.)

- What is the influence of the liquid surrounding a crystal on attrition phenomena (saturated or supersaturated solution)?
- Is it advantageous to study the attrition phenomena of crystals surrounded by air and to apply the results to crystals surrounded by a supersaturated solution?

Let us consider a crystal that is subject to an indentation test (see Fig. 1.4). In the zone of radius a_r or in the hydrostatic core, plastic deformation

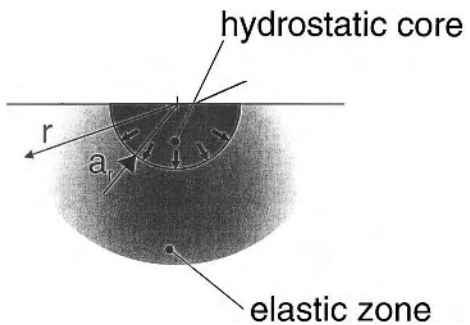

Figure 1.4. Simplified stress field created by a plastic–elastic induction. (From Ref. 1.9.)

takes place. Outside this zone, the mean volume–related strain energy w_V (which is proportional to the specific energy $e = w_V/\rho_C$) depends on the Vickers' hardness H_V and the shear modulus μ according to Refs. 1.4–1.6 (cf. Chapter 1):

$$w_V = \frac{3}{16}\frac{H_V^2}{\mu}\left(\frac{a_r}{r}\right)^4 \tag{1.3}$$

The ratio H_V/μ determines the amount of collision energy that is converted into elastic strain energy. If H_V/μ is less than 0.1 (which applies almost to all organic and inorganic crystals), the collision energy is almost completely converted into plastic deformation work W_{pl}:

$$W_{\text{pl}} = \frac{\pi}{8} H_V a_r^3 \tag{1.4}$$

Cracks are induced by the volume-related strain energy with the result that the surface area and the fracture surface energy known as fracture resistance Γ are increased. For an atttrition fragment of size L_a, the following energy balance can be formulated with the volumetric energy w_V [1.15]:

$$w_V = \frac{2}{L_a}\left(\frac{\Gamma}{K}\right) \tag{1.5}$$

In this equation, K is an efficiency factor that has to be determined experimentally. Combining equations (1.3)–(1.5), the following equation for an attrition fragment of size L_a is obtained:

$$L_a = \frac{3\mu}{(W_{\text{pl}})^{4/3} H_V^{2/3}}\left(\frac{\Gamma}{K}\right) r^4 \tag{1.6}$$

According to this equation, which is illustrated in Figure 1.5, the fragments are smallest in the contact zone ($r \to a$) and their size increases rapidly with the radius r. For a given plastic deformation work W_{pl}, the size L_a increases with increasing fracture resistance (Γ/K) but decreases as the hardness of the solid material increases. For attrition fragments ranging in size between $L_{a,\min}$ and $L_{a,\max}$ and with a number–density distribution $q_0(L_a)$, the volume V_a abraded in the elastic deformation zone is

$$V_a = \alpha N_a \int_{L_{a,\min}}^{L_{a,\max}} L_a^3 q_0(L_a)\, dL \tag{1.7}$$

Here, N_a is the number of all attrition fragments. By combining equation (1.7) with

$$\frac{dV_a}{dL} = \alpha N_a L_a^3 q_0(L_a) \tag{1.8}$$

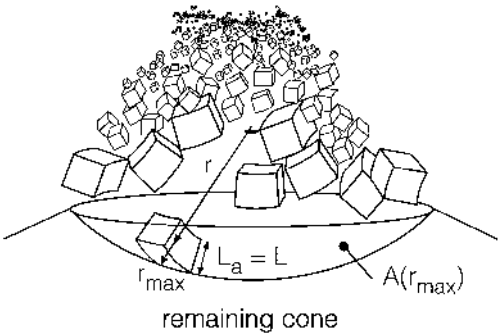

Figure 1.5. Representation of a theoretical attrition process. (From Ref. 1.5.)

and

$$\frac{dV_a}{dr} = \pi r^2 \tag{1.9}$$

the equation

$$\alpha N_a q_0(L) = \frac{\pi}{9} \frac{W_{\text{pl}} H_V^{1/2}}{\mu^{3/4}} \left(\frac{K}{\Gamma}\right)^{3/4} L^{-(3,25)} \tag{1.10}$$

can be derived: With the integral

$$\int_{L_{a,\min}}^{L_{a,\max}} q_0(L_a)\, dL_a = 1 \tag{1.11}$$

the number density results in

$$q_0(L_a) = \frac{2.25}{L_{a,\min}^{-2.25} - L_{a,\max}^{-2.25}} L_a^{-3.25} \tag{1.12}$$

and the total number N_a of fragments can be calculated from

$$N_a = \frac{\pi}{21\alpha} \frac{W_{\text{pl}} H_V^{1/2}}{\mu^{3/4}} \left(\frac{K}{\Gamma}\right)^{3/4} \left(\frac{1}{L_{a,\min}^{2.25}} - \frac{1}{L_{a,\max}^{2.25}}\right) \tag{1.13}$$

It should be noted that the total number of fragments mainly depends on the size $L_{a,\min}$ of the smallest fragments. Combining the equations presented here leads to the following expression for $L_{a,\min}$:

$$L_{a,\min} = \frac{32}{3} \frac{\mu}{H_V^2} \left(\frac{\Gamma}{K}\right) \tag{1.14}$$

The minimum fragment size increases with the shear modulus μ and the fracture resistance (Γ/K). The harder the crystal, the smaller the minimum size $L_{a,\min}$. Because $L_{a,\min} \ll L_{a,\max}$, combining equations (1.13) and (1.14) leads to the following equation for the total number N_a of fragments:

$$N_a = 7 \times 10^{-4} \frac{W_{\text{pl}} H_V^5}{\alpha \mu^3} \left(\frac{K}{\Gamma}\right)^3 \tag{1.15}$$

The total number of fragments is proportional to the plastic deformation work W_{pl} for a given crystal with the properties H_V, μ, and Γ/K. Therefore, theoretical considerations based on Rittinger's law [see Eq. (1.5)] and some calculations lead to the volume V_a abraded from one parent crystal after the transfer of the energy W_{pl}:

$$V_a = \frac{2}{3} \frac{H_V^{2/3}}{\mu} \left(\frac{K}{\Gamma}\right) (W_{\text{pl}})^{4/3} \tag{1.16}$$

The size $L_{a,\max}$ of the largest fragments is given by

$$L_{a,\max} = \frac{1}{2} \frac{H_V^{2/9}}{\mu^{1/3}} \left(\frac{K}{\Gamma}\right)^{1/3} (W_{\text{pl}})^{4/9} \tag{1.17}$$

The main result of this modeling, which is based on the fundamentals of physics, is that the attrition parameters V_a, $L_{a,\min}$, $L_{a,\max}$, and N_a depend on the material properties H_V, μ, and Γ/K and on the plastic deformation work W_{pl}. The shear modulus μ can be expressed by Young's modulus E and the Poisson ratio ν_c according to

$$E = 2\mu(1 + \nu_c) \tag{1.18}$$

Table 1.1 gives an overview of all these equations. This will be compared with modeling that is based on the assumption that crystals are homogenous spheres.

In the first edition of this book, a very simple model based on the theory of Hertz [1.7] and Huber [1.8] was presented for predicting the abraded volume V_a. This model, which was developed for modeling the abrasion from one parent crystal, assumes a homogeneous sphere with density ρ_C and modulus of elasticity E. When a sphere collides with a plate, longitudinal waves with the velocity of sound, c_s, run through the solid body. The maximum values of the normal strain and the shear strain determine the abraded volume. For spherical, isentropic, and homogeneous particles, the abraded volume V_a is proportional to the third power of the radius r_a of the contact circle: $V_a = 0.73 r_a^3$ with the radius r_a according to

Table 1.1. Survey of Equations Relevant to Attrition

Estimation of the fracture resistance (indentation)	$\frac{\Gamma}{K} = \frac{1}{10}\frac{W_{\text{crit}}^{1/3} H_V^{5/3}}{\mu}$
Estimation of the fracture resistance (Orowan)	$\frac{\Gamma}{K} = 1,7El_0; \quad l_0 = \left(\frac{\tilde{M}}{\rho_c n N_A}\right)^{1/3}$
Volume abrade from one particle	$V_a = CW^{4/3}$
Attrition coefficient C	$C = \frac{2}{3}\frac{H_V^{2/3}}{\mu}\left(\frac{\Gamma}{K}\right)$
Minimum energy for the production of attrition fragments	$W_{\min} = 64\frac{\mu^3}{H_V^5}\left(\frac{\Gamma}{K}\right)^3$
Minimum size of fragments	$L_{\min} = \frac{32}{3}\frac{\mu}{H_V^2}\left(\frac{\Gamma}{K}\right)$
Maximum size of fragments	$L_{\max} = \frac{1}{2}\left(\frac{H_V^{2/3} K}{\mu\Gamma}\right)^{1/3} W_{pl}^{4/9}$
Size distribution (number)	$q_0(L) = \frac{2.25}{L_{\min}^{-2.25} - L_{\max}^{-2.25}} L^{-3.25}$
Total number of fragments	$N_a = \frac{\pi}{21}\frac{H_V^{1/2}}{\alpha\mu^{3/4}}\left(\frac{K}{\Gamma}\right)^{3/4}\left(\frac{1}{L_{\min}^{2.25}} - \frac{1}{L_{\max}^{2.25}}\right) W_{pl}$
Total number for $L_{\min} \ll L_{\max}$	$N_a = 7 \times 10^{-4}\frac{H_V^5}{\alpha\mu^3}\left(\frac{K}{\Gamma}\right)^3 W_{pl}$

Source: Ref. 1.5.

$$r_a = 1.32\frac{L_{\text{par}}}{2}\left[\frac{(1+\kappa)(1-\nu_c)^2}{1-2\nu_c}\left(\frac{w_{\text{col}}}{c_s}\right)^2\right]^{0.2} \tag{1.19}$$

κ is related to the elastic properties of the plate (index p, rotor, wall) and of the crystal (index C) as follows:

$$\kappa = \frac{1 - \nu_p^2 E_C}{1 - \nu_c^2 E_p} \tag{1.20}$$

and the velocity c_s can be expressed by the modulus E or the shear modulus μ according to

$$c_s = \sqrt{\frac{1 - \nu_c}{(1 + \nu_c)(1 - 2\nu_c)}}\sqrt{\frac{E}{\rho_C}} = \sqrt{\frac{2(1 - \nu_c)}{1 - 2\nu_c}}\sqrt{\frac{\mu}{\rho_C}} \tag{1.21}$$

This leads to the following equation for the radius r_a:

$$r_a = 1.32\frac{L_{\text{par}}}{2}\left(\frac{(1 + \kappa)(1 - \nu_c)}{2}\frac{\rho_C w_{\text{col}}^2}{\mu}\right)^{0.2} \tag{1.22}$$

and the volume V_a is

$$V_a = 0.482 L_{\text{par}}^3\left(\frac{(1 + \kappa)(1 - \nu_c)}{2}\frac{\rho_C w_{\text{col}}^2}{\mu}\right)^{0.6} \tag{1.23}$$

Let us compare the results of the two models for the volume V_a abraded from one crystal to show the differences. This comparison will be carried out for potassium nitrate with the properties

$\rho_C = 2109\ \text{kg/m}^3$
$H_V = 0.265 \times 10^9\ \text{J/m}^3$
$\mu = 7.17 \times 10^9\ \text{J/m}^3$
$\Gamma/K = 2.8\ \text{J/m}^2$

The results are shown in Figure 1.6 where the relative abraded volume, $V_a/\alpha L_{\text{par}}^3$, is plotted against the collision velocity w_{col}. As can be seen, the increase in the ratio $V_a/\alpha L_{\text{par}}^3$ or the relative abraded volume with increasing collision velocity is much more pronounced in the model developed by Gahn [1.4] than in the former model, which does not take into account the dependency on the size of the parent crystal. An encouraging result is the fact that for collision velocities between 1 and 5 m/s, which are relevant for industrial crystallizers and for large parent crystals 1 mm in size, the order of magnitude of the dimensionless abraded volume is the same.

In order to check the validity of his model, Gahn carried out attrition experiments with crystals of nine different inorganic and organic materials. In Figure 1.7, the volume V_a abraded from potash alum crystals is plotted against the collision energy W_{col} according to

$$W_{\text{col}} = \alpha L_{\text{par}}^3 \rho_C \frac{w_{\text{col}}^2}{2} \tag{1.24}$$

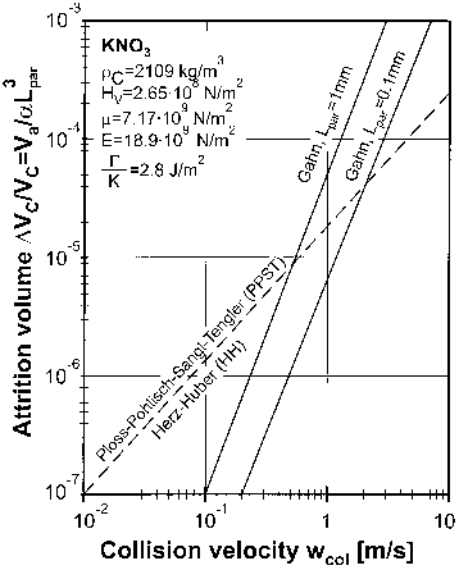

Figure 1.6. Volume removed by attrition as a function of impact energy. (Data from Refs. 0.6–0.8 and 1.4.)

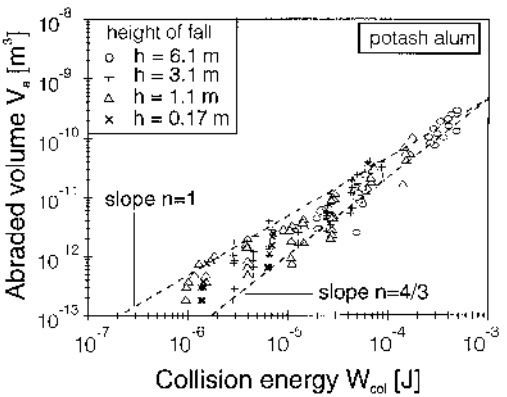

Figure 1.7. Volume of attrition fragments as a function of impact energy. (From Ref. 1.4.)

and Figure 1.8 shows results for potassium nitrate, magnesium sulfate, tartaric acid, ammonium sulfate, calcium sulfate, and citric acid. It is rather surprising that the attrition behavior of all these systems does not differ greatly, but this can be explained by the narrow ranges of the material

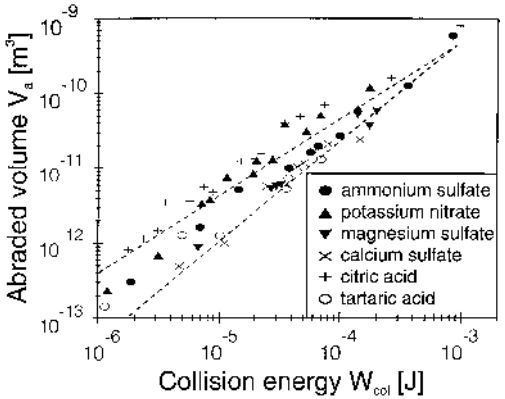

Figure 1.8. The average volume of fragments produced from six repeated impacts as a function of impact energy. (From Ref. 1.4.)

properties H_V, μ, and Γ/K. Because of the difficulties in carrying out measurements, the different shapes of the crystals and the inner heterogeneity of the polycrystals, the accuracy of the data is not very high (see Figs 1.7 and 1.8). This is especially true of brittle materials such as potassium nitrate, citric acid, and potassium alum. Additional experiments have been carried out with more ductile crystals such as potassium chloride and sodium chloride, with the result that the abraded volume V_a is smaller than predicted for low collision energies $W_{\text{col}} \ll 5 \times 10^{-5}$ J. Some time ago, Engelhardt and Haussühl [1.11] carried out abrasion experiments with crystals of more than 50 different materials. Their results show that Gahn's model predicts the volume V_a abraded from crystals very accurately when the ratio of Young's modulus and the hardness is in the range $15 < E/H_V < 100$. Thus, the assumptions made for Gahn's model are sufficiently valid. The abraded volume is smaller than predicted when the hardness is either very high [SiO_2,$Be_3Al_2(Si_6O_{18})$, $Al_2SiO_4(FOH)_2$] or very low, as for soft ionic materials (AgCl, KCl, KF, LiCl, LiBr, NaBr, NaCl, NaJ). Therefore, the equations presented here allow the maximum volumes abraded from one crystal after a collision with a resistance to be calculated.

Next, the particle size distribution predicted by the model will be compared with experimental results obtained in a small stirred vessel, in which parent crystals in the size range between 1 and 1.4 mm were suspended in a saturated solution. The experiments were carried out in such a way that it was always possible to distinguish clearly between parent crystals and attrition fragments. In Figures 1.9 and 1.10, the number density $q_0(L_a)$ of attri-

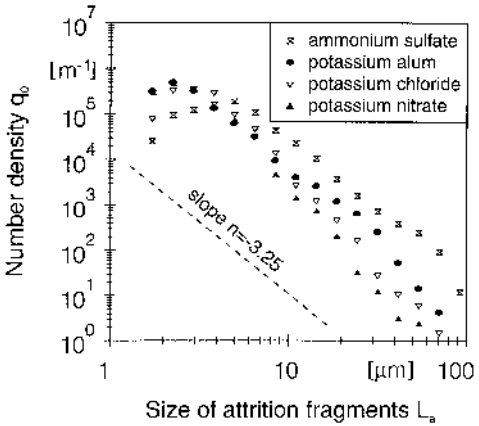

Figure 1.9. The number–density distribution of fragments generated. (From Ref. 1.16.)

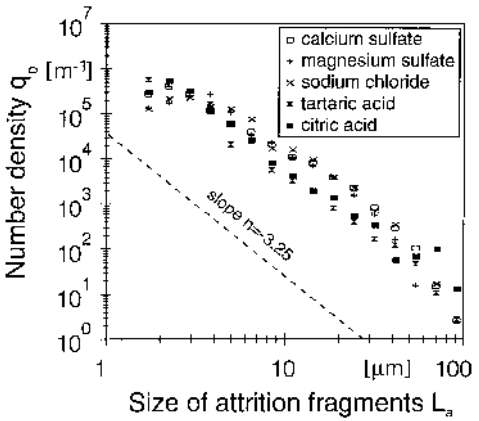

Figure 1.10. The number–density distribution of fragments generated. (From Ref. 1.16.)

tion fragments is plotted against their size for the seven substances mentioned earlier. As can be seen, the slope $n = -3.25$ of the model is confirmed by the experimental results in the size range between a few microns and approximately 100 µm. The curves of the number density of abrasion-resistant substances such as ammonium sulfate, potassium sulfate, magnesium sulfate, and tartaric acid are close together and their number density in the

size range between 50 and 100 μm is much greater than for materials prone to attrition such as potassium alum and, in particular, potassium nitrate.

It can be seen that a huge number of attrition fragments smaller than 10 μm are formed but that the number of large fragments above 50 μm is fairly small. The number–density distribution $q_0(L_a)$ depends on the minimum and maximum size of attrition fragments. In Figure 1.11, the minimum size $L_{a,\min}$ is plotted against the expression $\mu(\Gamma/K)$ for the materials mentioned earlier. With the exception of thiourea, all the minimum sizes are between 1 and 3 μm. The maximum size $L_{a,\max}$ depends on the collision energy. In Figure 1.12, the ratio $L_{a,\max}/L_{\text{par}}$ is plotted against the collision velocity using the expression $[(H_V^{2/3}/\mu)(K/\Gamma)]^{1/3}$ as the parameter. The

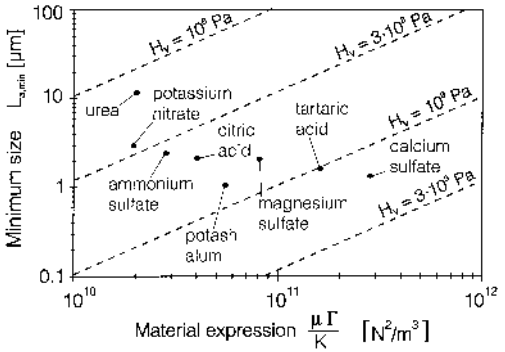

Figure 1.11. Theoretical minimum size of attrition fragments. (From Ref. 1.16.)

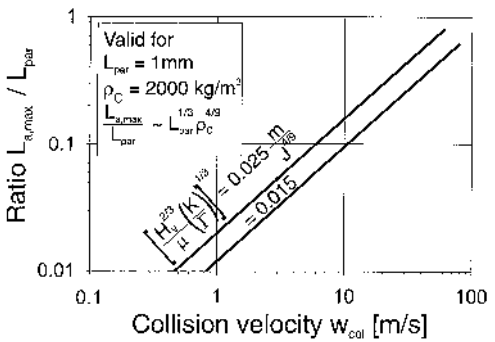

Figure 1.12. Theoretical maximum size of attrition fragments. (From Ref. 1.16.)

curves are valid for $L_{par} = 1\,mm$ and $\rho_C = 2000\,kg/m^3$. The ratio $L_{a,max}/L_{par}$ is proportional to $L_{par}^{1/3}(\rho_C)^{4/9}$. The decisive material properties H_V, μ, and Γ/K are in the range $0.015 < [(H_V^{2/3}/\mu)(K/\Gamma)]^{1/3} < 0.025\,m/J^{4/9}$ for the many organic and inorganic substances.

As can be seen, a collision velocity of 1 m/s is necessary in order to obtain attrition fragments larger than 10 μm, and with collision velocities above 10 m/s, the largest fragments are approximately 100 μm in size. Provided that $L_{a,max} \ll L_{par}$, the terms *attrition* and *abrasion* are used. If the collision velocity is much higher than 10 m/s, breakage of crystals take place. This means that the parent crystal loses its identity and distintegrates. This can be seen in Figure 1.13, where the breakage probability of glass particles of different sizes is plotted against the collision velocity. Crystalline substances ($CaCO_3$, sugar) have also been investigated and the results are similar. The smaller the size of the particle, the higher the collision velocity necessary to initiate breakage. As will be shown later, it is advantageous to restrict the tip speed of rotors to $u_{tip} < 10\,m/s$ in order to avoid breakage and the production of attrition fragments.

The attrition model described here can also be applied to crystals suspended in a fluidized bed. In such a bed, the collision velocity w_{col} depends mainly on the specific power input ε and the size of the parent crystal. According to Levich [1.12] and Ottens [1.14], the root-mean-square value of the fluctuating velocity between a turbulent liquid and a particle is given by

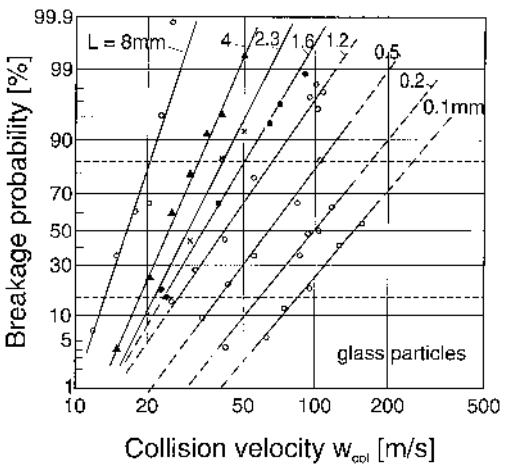

Figure 1.13. Breakage probability of glass particles of different sizes. (From Ref. 1.17.)

$$\overline{v'_{\text{rel}}} = \frac{1.43}{c_w^{1/3}} \left(\frac{\rho_C - \rho_L}{\rho_C} \right)^{1/2} \left(\frac{\rho_C}{\rho_L} \right)^{1/3} (\varepsilon L_{\text{par}})^{1/3} \tag{1.25}$$

where c_w is the drag coefficient of the particles and ε denotes the local specific power input. It is assumed that there are no great differences between the maximum values of the fluctuating velocities v'_{eff}, the fluid/particle relative velocities and the collision velocity w_{col} of two crystals. This collision velocity increases with the third root of the specific power input and the size of the parent crystal. With $c_w = 0.5$, $\rho_C = 2000\,\text{kg/m}^3$, and $\rho_L = 1000\,\text{kg/m}^3$, we obtain

$$\overline{v'_{\text{rel}}} \approx w_{\text{col}} \approx 1.66(\varepsilon L_{\text{par}})^{1/3} \tag{1.26}$$

Information on the local and mean specific power inputs in crystallizers is given in Chapter 8. The mean specific power input $\bar{\varepsilon}$ of fluidized beds with a small crystal holdup $\varphi_T < 0.05$ is approximately $\bar{\varepsilon} \approx w_s(g\Delta\rho/\rho_L)$. With $w_s = 0.2\,\text{m/s}$, $\Delta\rho/\rho_L = 1$, and $L_{\text{par}} = 1\,\text{mm}$, the collision velocity is $w_{\text{col}} = 0.21\,\text{m/s}$, which is one order of magnitude smaller than in crystallizers with rotors.

So far, it has been assumed that the crystals have a more or less spherical shape. This is only true of crystals exposed to high collision intensities and frequencies, not of crystals after a certain undisturbed growth period. Experiments have shown that at the beginning of an attrition run, the total volume removed increases strongly with the impact energy. After the crystals have repeatedly come into contact with a rotor, the volume V_a abraded after one collision is significantly lower. In Figure 1.14, the top

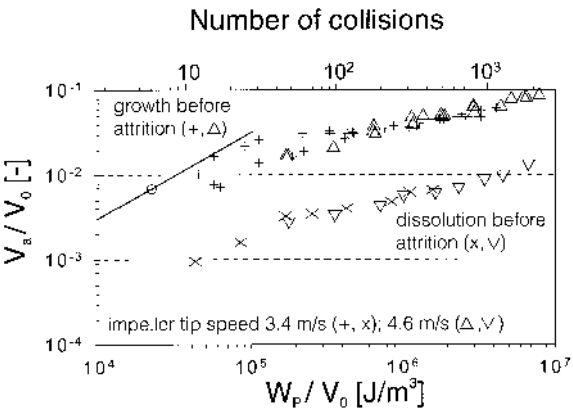

Figure 1.14. Relative volume of fragments removed as a function of the number of impacts. (From Ref. 1.13.)

abscissa indicates the number of impeller impacts that a particle 0.5 mm in size experienced when it was suspended at the impeller tip speed $u_{tip} = 3.4\,m/s$ [1.13]. The relative volume of fragments is plotted against the volumetric impact energy and the number of impacts. It can be seen that the relative attrition volume is approximately one order of magnitude smaller for crystals after many impacts than for crystals with well-developed faces during a growth period. Therefore, under growth conditions, high attrition can be expected when the crystals redevelop their edges and corners. This is usually the case when the increase in the volume of the crystal due to growth is much higher than the decrease according to attrition.

2. GROWTH OF ATTRITION FRAGMENTS

Most of the attrition experiments described in the preceding section were carried out with parent crystals surrounded by air or a saturated solution. Wang and Mersmann [2.1] investigated whether these results can be applied to parent crystals in a supersaturated solution; see also Ref. 2.2.

Attrition fragments formed in a supersaturated solution were separated from the parent crystals and transferred to a growth vessel in which constant supersaturation was maintained. Experiments were carried out with potassium nitrate and potash alum. Wang came to two important conclusions:

- Attrition fragments produced in supersaturated solutions are in the size range between a few micrometers and approximately 100 μm, as predicted by the model.
- The particle size distribution of newly formed attrition fragments is obviously not dependent on the surroundings of the parental crystal.

In Figure 2.1a, the number density $q_0(L_a)$ of attrition fragments of KNO_3 formed in supersaturated solution is plotted against the size L_a of these attrition fragments, and Figure 2.1b shows experimental results for $KAl(SO_4)_2 \cdot 12H_2O$. Both materials are very prone to attrition. As can be seen, the size distribution of these attrition fragments produced in supersaturated solutions is approximately the same as fragments generated in saturated solutions or fragments abraded from parent crystals surrounded by air. The slope of the distribution lines in the double logarithmic diagram is approximately -3 and is slightly different from the -3.25 predicted by the physical modeling. It can be concluded that measurements of attrition phenomena carried out with crystals not surrounded by a supersaturated solution can give important indications about the mechanism of attrition. Figure 2.1 shows additional size distributions for these attrition fragments after certain growth periods when these fragments have become crystals.

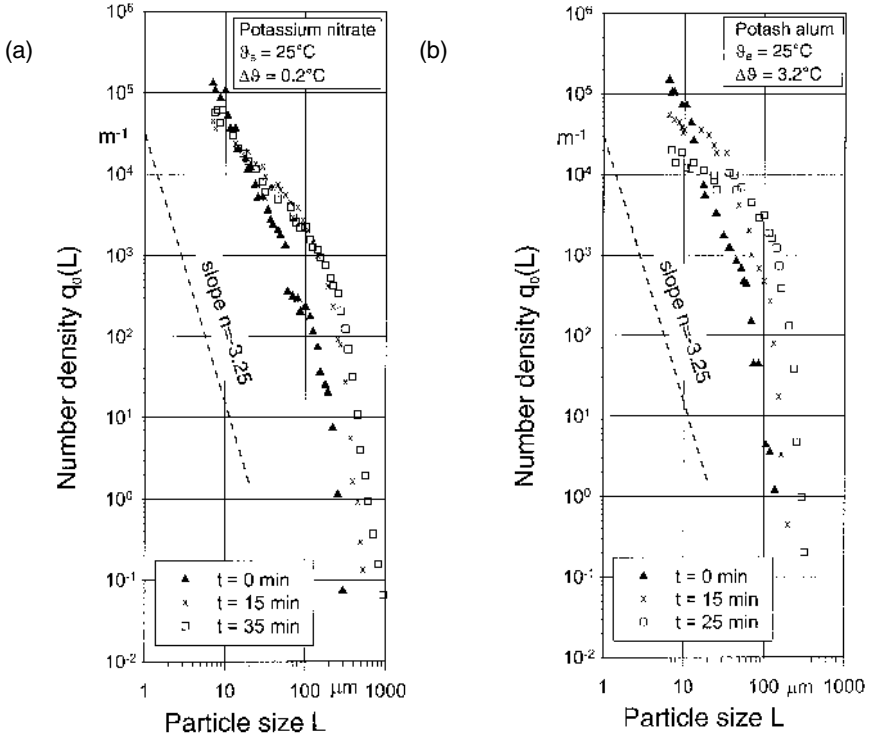

Figure 2.1. Formation and growth of attrition fragments.

Broadening of the size distributions can be clearly observed. Obviously, the mean growth rate increases with increased fragment size. Small fragments take up more energy per unit volume than large fragments.

The chemical potential of attrition fragments and their solubility c^*_{eff} is increased, which leads to a reduction in the relative supersaturation σ_{eff}:

$$\sigma_{\text{eff}} = \frac{c - c^*_{\text{eff}}}{c^*_{\text{eff}}} = \frac{\mu_L - (\mu_0 + W)}{RT} = \sigma - \frac{W}{RT} \tag{2.1}$$

In this equation, μ_0 is the chemical potential of an ideal crystal and W is the elastic strain energy. In Figure 2.2, the solubilities for an ideal crystal and for a real crystal are shown. Ristic et al. [2.3] and Sherwood et al. [2.4] stressed the role of dislocations and mechanical deformation in growth-rate dispersion, Van der Heijden [2.5] and Zacher and Mersmann [2.2] showed how the deformation energy depends on dislocations, small-angle boundaries and stacking faults. In Figure 2.3, the mosaic structure of two

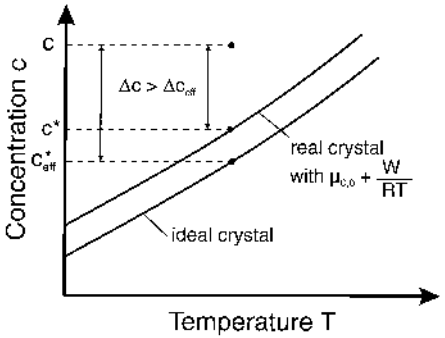

Figure 2.2. Solubility of an ideal and real (strained) crystal. (From Ref. 2.6.)

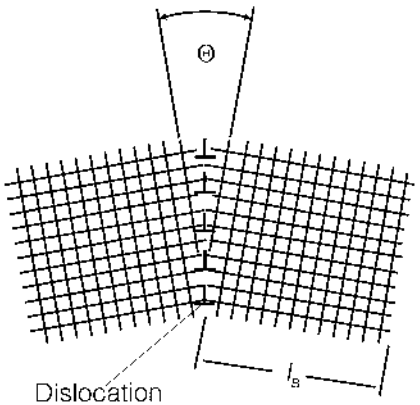

Figure 2.3. Schematic representation of a grain boundary. (From Ref. 2.6.)

blocks of size l_B and small angle θ is depicted. The energy per unit grain-boundary area is given by [2.6]

$$\gamma_B = \frac{\mu a}{4\pi(1-\nu_c)}\theta\left(1+\ln\left(\frac{b}{2\pi r_0}\right)-\ln\theta\right) \tag{2.2}$$

In this equation, a is the lattice constant, b is the length of the Burgers vector, and r_0 is the radius of the dislocation nucleus. The mosaic spread can be described by

$$\eta \approx \theta \sqrt{\frac{L}{l_B}} \tag{2.3}$$

The total area of the grain boundaries is approximately

$$A_B \approx 3\frac{L^3}{l_B} \tag{2.4}$$

when $l_B \ll L$. The energy $\gamma_B A_B$ induced by all the boundaries in the crystal of size L has to be differentiated to the molar quantity of substance in order to obtain the molar elastic strain energy

$$W = \frac{0.24\mu a}{(1-\nu_c)C_C}\frac{\eta}{\sqrt{L_a l_B}}\ln\left(\frac{0.43b}{r_0\eta}\sqrt{\frac{L_a}{l_B}}\right) \tag{2.5}$$

Combining the above equation with equation (2.1) results in

$$\sigma_{\text{eff}} = \sigma - \frac{0.24\mu a}{(1-\nu_c)\Re TC_C}\frac{\eta}{\sqrt{L_a l_B}}\ln\left(\frac{0.43b}{r_0\eta}\sqrt{\frac{L_a}{l_B}}\right) \tag{2.6}$$

The main conclusions that can be drawn from this modeling are as follows:

- The smaller the size L_a of an attrition fragment, the greater the reduction in supersaturation σ.
- The reduction in σ increases with growing mosaic spread η or with increasing deviation from ideal crystals.
- Small mosaic blocks of size l_B and large angles θ, in particular, lead to low effective supersaturation.

In general, the growth rate G of attrition fragments can be described by

$$G = k_g\sigma_{\text{eff}}^g = k_g\left[\sigma - \frac{0.24\mu a}{(1-\nu_c)\Re TC_C}\frac{\eta}{\sqrt{L_a l_B}}\ln\left(\frac{0.43b}{r_0\eta}\sqrt{\frac{L_a}{l_B}}\right)\right]^g \tag{2.7}$$

The kinetic coefficient k_g depends on the volume and surface diffusion and on the surface structure of the particle in the molecular range (microstructure), and the effective supersaturation σ_{eff} is a function of the inner state of a particle (volume effect) which can be characterized by grain boundaries, defects, and the mosaic structure (η, l_B). The model has been verified by experiments with potash alum carried out in a stirred vessel [2.6]. Table 2.1 gives characteristic data for this substance.

In Figure 2.4, the number density is plotted against the crystal size L for potash alum crystallized in a MSMPR (mixed suspension, mixed product removal) crystallizer at a mean specific power input of $\bar{\varepsilon} = 0.20\,\text{W/kg}$. Figure 2.4a is valid for the long residence time $\tau = 111\,\text{min}$ and the relative

Table 2.1. Characteristic Data of Potash Alum

Lattice constant	$a = 1.22\,\text{nm}$
Molar crystal density	$C_C = 3.70\,\text{kmol/m}^3$
Young's modulus	$E = 1.80 \times 10^{10}\,\text{J/m}^3$
Shear modulus	$\mu = 6.7 \times 10^9\,\text{J/m}^3$
Poisson's ratio	$\nu_c = 0.33$
Size of a mosaic block	$l_B = 200\,\text{nm}$

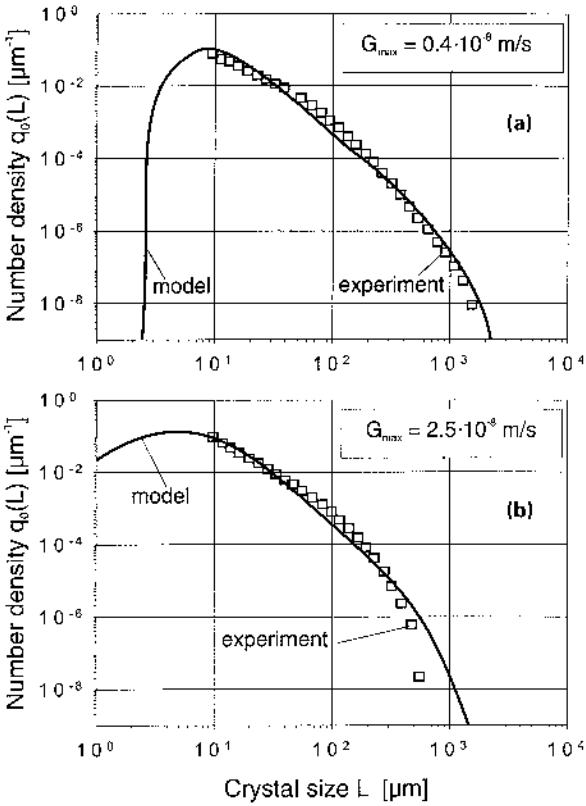

Figure 2.4. Theoretical and experimental number–density distributions from MSMPR experiments. (From Ref. 2.6.)

supersaturation $\sigma = 0.02$. Figure 2.4b shows results for the much higher relative supersaturation $\sigma = 0.092$, which was measured for the short residence time $\tau = 9$ min. These results show not only that the mean growth rate but also the growth-rate distribution increases with rising supersaturation. This can be explained by the fact that more and more small attrition fragments are stimulated to grow at different rates when the supersaturation is increased.

It is important to note that an individual attrition fragment has taken up an individual amount of deformation energy. Therefore, individual fragments are exposed to different effective supersaturations and possess individual growth rates, at least for a certain growth period. This is shown in Figure 2.5, where the growth rates of 356 KNO_3 attrition fragments are plotted against their critical size. Figure 2.6 depicts the growth behavior of 39 potash alum fragments according to measurements [2.1, 2.7]. In both cases, the fragments are in the size range between 5 and 100 µm.

Fragments of both systems exhibit a strong growth-rate dispersion (GRD) with the tendency that the mean growth rate of a size interval increases with increasing fragment size. Many of the $KAl(SO_4)_2$ fragments below 15 µm and of the KNO_3 fragments smaller than 30 µm do not grow at all. This can be explained by a strong deformation of the small attrition fragments in particular. A local high specific deformation work w_V leads to a small attrition fragment size L_a generated from crystals with a given fracture resistance (Γ/K) according to [2.8]

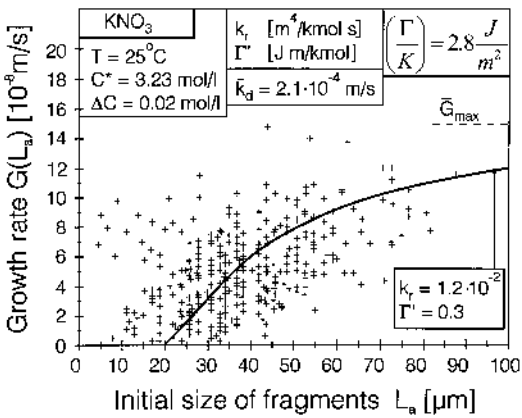

Figure 2.5. Growth rate of 356 KNO_3 attrition fragments against their initial size. (Compare Refs. 2.1 and 2.7.)

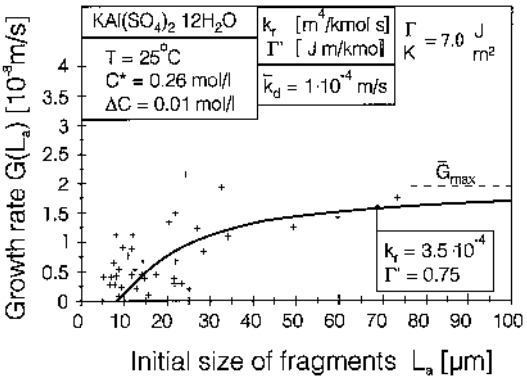

Figure 2.6. Growth rate of 39 potash alum fragments against their critical size. (Compare Refs. 1.16, 2.6, and 2.7.)

$$L_a = \frac{2}{w_V}\left(\frac{\Gamma}{K}\right) \tag{2.8}$$

The increase of the mean growth rate as a result of the increase of the effective supersaturation $\Delta C_{\text{eff}}(L_a)$ according to [1.16]

$$\Delta C_{\text{eff}}(L) = C - C^* \exp\left[\frac{1}{\Re T L_a C_c}\left(\frac{\Gamma}{K}\right)\right] \tag{2.9}$$

can be explained with Gahn's model described earlier.

3. IMPACT OF ATTRITION ON THE CRYSTAL SIZE DISTRIBUTION

The attrition of crytals can have a strong influence on the median crystal size and CSD. This is especially true of materials prone to attrition, for instance KNO_3. In Figure 3.1, the median crystal size L_{50} of KNO_3 is plotted against the residence time τ of a continuously operated stirred vessel ($V_{\text{sus}} = 5.7\,\text{dm}^3$) and of a forced circulation (FC) crystallizer ($V_{\text{sus}} = 70\,\text{dm}^3$). The FC crystallizer was equipped with a radial-flow pump with a rotor diameter of 0.17 m. The diameter of the stirrer was $D = 0.1$ m. The mean specific power input $\bar{\varepsilon}$ was varied between 0.27 and 1.7 W/kg. In all cases, the volumetric crystal holdup was $\varphi_T < 0.05$ [3.1, 3.2].

As can be seen from Figure 3.1, the relationship

$$L_{50} \sim \tau^{(i-1)/(i+3)} \quad \text{with } 0 < i < 2 \text{ (compare Chapter 4)} \tag{3.1}$$

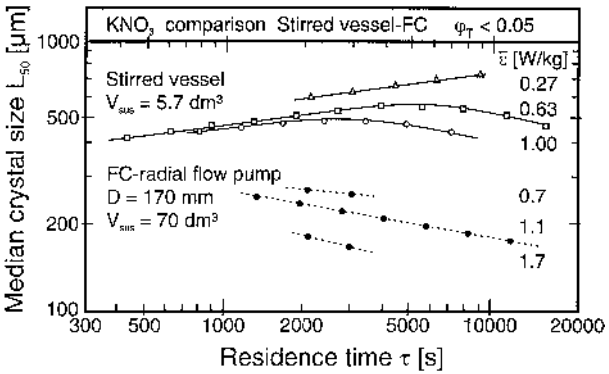

Figure 3.1. Median crystal size of KNO_3 obtained from different crystallizers. (From 3.1.)

was found. The exponent $i \approx 2$ can be expected for an MSMPR crystallizer. The exponent $i = 0$, however, indicates that the median crystal size is attrition controlled.

Figure 3.2 shows results that are valid for a residence time of 1 h. The median crystal size is again plotted against the mean specific power input for stirred vessles of different volumes ($V_{sus} = 5.7$; 10 and 63 dm^3) and the FC crystallizer $V_{sus} = 70\,dm^3$. Besides the specific power input, the geometry and the size of the impellers are important parameters for the median

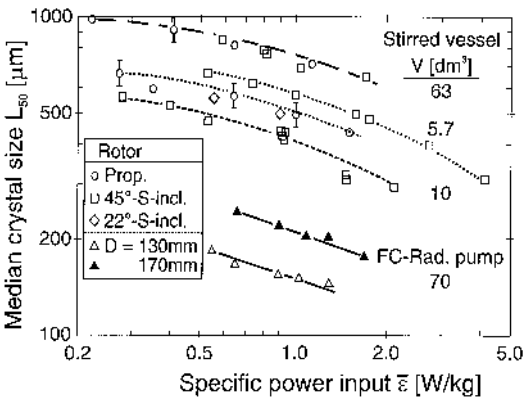

Figure 3.2. Median crystal size versus the mean specific power input for stirred-vessel and FC crystallizers. (From Ref. 3.1.)

size. The final size and the distribution of a crystalline product can be controlled by the following:

- Supersaturation when attrition rates of the crystals are small for a given growth period (small crystals, small collision velocities or small specific power input, for instance in fluidized beds)
- Attrition when large crystals at low supersaturation are produced in crystallizers equipped with a high-speed rotor which leads to high collision velocities

The ratio G/G_a of the kinetic growth rate G with $G = f(\Delta C)$ to the attrition $G_a = -dL_{\text{par}}/dt$ is the crucial mechanism which determines crystal size.

It has been shown that the largest particles are most prone to attrition. The volumetric attrition rate $\dot{V}_a = dV_a/dt$ of a single crystal is given by

$$\frac{dV_a}{dt} = \frac{\beta}{2} G_a L_{\text{par}}^2 \quad \text{or} \quad G_a = \frac{2\alpha L_{\text{par}}\, dV_a}{\beta V_a\, dt} \tag{3.2}$$

Assusming that the parent crystals are monosized, the number of parent crystals is $V_{\text{sus}}\varphi_T/\alpha L_{\text{par}}^3$). The total volumetric attrition rate based on the volume $V_{\text{sus}}\varphi_T$ of all the parent crystals is the product of $\dot{V}_a$ valid for one crystal and the number of all-parent crystals:

$$\frac{dV_{a,T}}{V_{\text{sus}}\varphi_T\, dt} = \frac{\beta\, G_a}{2\alpha L_{\text{par}}} \left[\frac{\text{m}^3 \text{ abraded volume}}{\text{m}^3 \text{ parent crystals } s} \right] \tag{3.3}$$

In Figure 3.3, the attrition rate G_a valid for crystals with a size of 0.5 mm is plotted against the mean specific power input $\bar{\varepsilon}$ for the stirred vessels of different sizes and the FC crystallizer. The figure shows that attrition phenomena are not sufficiently described by the mean specific power input alone.

A simple model is now presented that allows the attrition rate G_a, which reduces the size of the crystals, to be evaluated. Let us consider the volume V_a abraded from *one* crystal after *one* collision with a rotor which has the speed s and the tip speed u_{tip}. This volume V_a is given by

$$V_a = C \left(\frac{\alpha L^3}{2} \rho_C w_{\text{col}}^2 \right)^{4/3} \quad \text{with } C = \frac{2H_V^{2/3}}{3\mu} \left(\frac{K}{\Gamma} \right) \tag{3.4}$$

The linear attrition rate G_a is the volumetric attrition rate $\dot{V}_a$ divided by the surface of the parent crystal:

$$G_a = 2 \frac{\dot{V}_a}{\beta L_{\text{par}}^2} \tag{3.5}$$

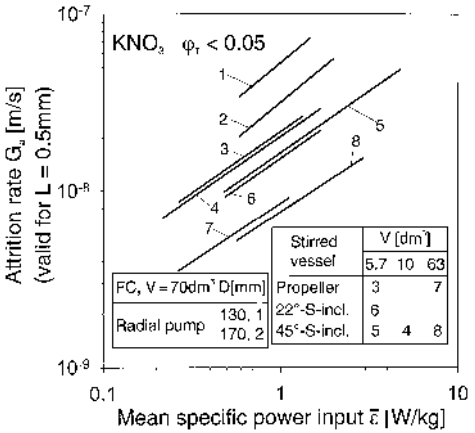

Figure 3.3. Attrition rate (valid for $L = 0.5\,\text{mm}$) against the mean specific power input for stirred-vessel and FC crystallizers.

The frequency of collisions, f_{col}, is proportional to the stirrer speed s multiplied by a geometrical target efficiency η_g. The factor η_g depends on the thickness e, the breadth b, and the angle β (angle of inclination) of the blades of the stirrer (see Fig. 3.4). The volumetric flow $\dot{V}$ through the horizontal plane described by the stirrer is proportional to the flow number or the pumping capacity N_V, the stirrer speed s, and the stirrer diameter D to the third power:

$$\dot{V} = N_V s D^3 \tag{3.6}$$

The angle between the direction of the main flow and the horizontal plane is α, which can differ from the blade angle β. It is assumed that only collisions between the crystals and the blades lead to attrition of crystals due to high collision velocities.

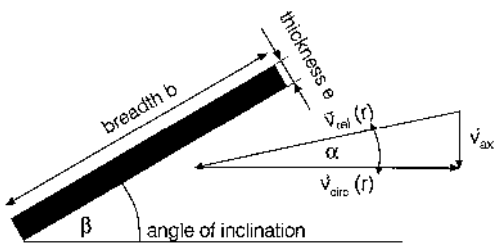

Figure 3.4. Breadth b, thickness e, and angle β of an inclined blade.

All the crystals present in the projection plane $(e + b)(D/2)$ can hit either the edge (e) or the breadth (b) of the stirrer blade. When a is the number of blades, the ratio g_e of the projection area of the blade based on the area $D^2\pi/4$ is given by

$$g_e = \frac{ae(D/2)}{D^2\pi/4} = \frac{2ae}{\pi D} \tag{3.7}$$

and the ratio g_b of the projection area of the breadth of the blade and the area $D^2\pi/4$ results in

$$g_b = \frac{ab(D/2)}{D^2\pi/4} = \frac{2ab}{\pi D} \tag{3.8}$$

The angle α can be calculated from the volumetric flow $\dot{V}$ and the tip speed of the stirrer:

$$\tan\alpha = \frac{6}{\pi^2} N_V \approx 0.6 N_V \tag{3.9}$$

The fraction g_e must be multiplied by f_e when the angles α and β differ. This must also be done for the breadth b. Geometrical considerations lead to the equations

$$f_e = [\cos\beta(1 + \tan\alpha\tan\beta)]^2 \tag{3.10a}$$

$$f_b = \left[\sin\beta\left(1 - \frac{\tan\alpha}{\tan\beta}\right)\right]^2 \tag{3.10b}$$

In Figure 3.5, the factor f_e is plotted against the pumping capacity N_V for different angles β, and Figure 3.6 shows the relationship for the factor f_b. It can be seen that crystals mainly hit the edge when the blade angle β is small and the pumping capacity is high. In this case, the frequency at which the crystals hit the breadth of the stirrer is low. The flow rate $\dot{V}$ must be multiplied by the factor η_g with

$$\eta_g = (g_e f_e + g_b f_b) = \left[\frac{2ae}{\pi D} f_e + \frac{2ab}{\pi D} f_b\right] \tag{3.11}$$

in order to take into account the fact that only some of the crystals in the suspension hit the blades, rather than all of them. It should be stressed here that this simplified modeling cannot precisely take into account the complex suspension flow; however, many experimental results obtained for a marine-type propeller and inclined stirrers have shown that the real flow conditions are modeled satisfactorily. It has been observed that only part of the breadth of the blades is hit by the crystals. Therefore, it is recommended that only part of the breadth is taken into account rather than the full breadth. This is

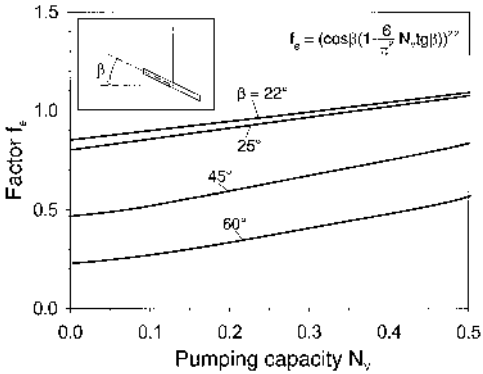

Figure 3.5. Factor f_e versus the pumping capacity N_V.

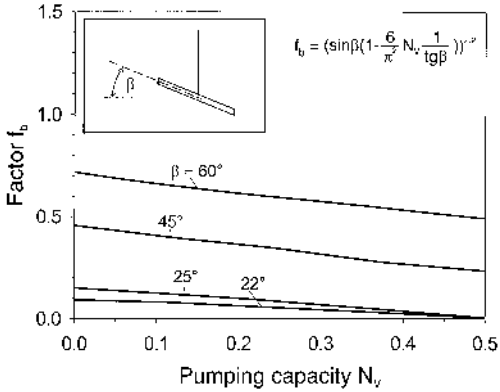

Figure 3.6. Factor f_b versus the pumping capacity N_V.

not a great disadvantage of the model because at small angles ($\beta \approx 25^\circ$), the contribution due to the edge is much greater than the contribution from the breadth.

The target efficiency of velocity $\eta_w (0 < \eta_w < 1)$ can be approximated by

$$\eta_w = \frac{w_{\mathrm{col}}}{u_{\mathrm{tip}}} \tag{3.12}$$

With the rotor flow number N_V according to

$$N_V = \frac{\dot{V}}{sD^3} \tag{3.13}$$

and $\dot{V}$ as the internal circulation flow rate, the frequency of collisions, f_{col}, is proportional to the ratio $s(D^3/V_{\text{sus}})$ with V_{sus} as the suspension volume:

$$f_{\text{col}} = \eta_g \eta_w \frac{N_V s D^3}{V_{\text{sus}}} \tag{3.14}$$

The target efficiency η_g is determined by the geometry, whereas the target efficiency η_w depends on fluid dynamics.

The volumetric rate $\dot{V}_a$ abraded from one crystal is obtained when the volume V_a abraded from a crystal after one collision is multiplied by the frequency of collisions:

$$\dot{V}_a = C\left(\frac{\alpha}{2}\right)^{4/3} L_{\text{par}}^4 \rho_C^{4/3} w_{\text{col}}^{8/3} s \frac{D^3}{D_{\text{sus}}} N_V \eta_g \eta_w \tag{3.15}$$

Combining equation (3.15) with equation (3.5) leads to

$$G_a = \frac{C}{\beta}\left(\frac{\alpha}{2}\right)^{4/3} L_{\text{par}}^2 \rho_C^{4/3} \frac{D^3}{V_{\text{sus}}} N_V \eta_g \eta_w^{11/3} s u_{\text{tip}}^{8/3} \tag{3.16}$$

This equation predicts an increase in the attrition rate with the square of the crystal size and the power 8/3 of the collision velocity. Large crystals are most prone to abrasion, with the consequence that their maximum size is limited when the kinetic growth rate is equal to the attrition rate: $G = G_a = -dL_{\text{par}}/dt$. This has been confirmed experimentally by Pohlisch and Mersmann [3.1, 3.2], who carried out crystallization experiments in stirred vessels and FC.

In Figure 3.7, the linear attrition rate G_a is plotted against the parent crystal size L_{par} for different speeds in a stirred vessel and in an FC crystallizer. The relationship

$$G_a \sim L_{\text{par}}^2 \tag{3.17}$$

is confirmed. In order to verify whether the model also takes into account the other parameters, calculations have been carried out for KNO_3 crystals. The results obtained for this substance are valid for the following parameters:

Attrition coefficient $C = 2 \times 10^{-5}\,\text{m}^3/\text{J}^{4/3}$
Density of the crystals $\rho_C = 2109\,\text{kg/m}^3$
Diameter of the marine-type propeller $D = 0.1\,\text{m}$
Volume of the stirred vessel $V_{\text{sus}} = 5.7 \times 10^{-3}\,\text{m}^3$
Target efficiency (velocity) $\eta_w = 1$
Target efficiency (geometry) $\eta_g = 0.03$
Pumping capacity $N_V = 0.3$
Volume shape factor $\alpha = \pi/6$
Surface shape factor $\beta = \pi$

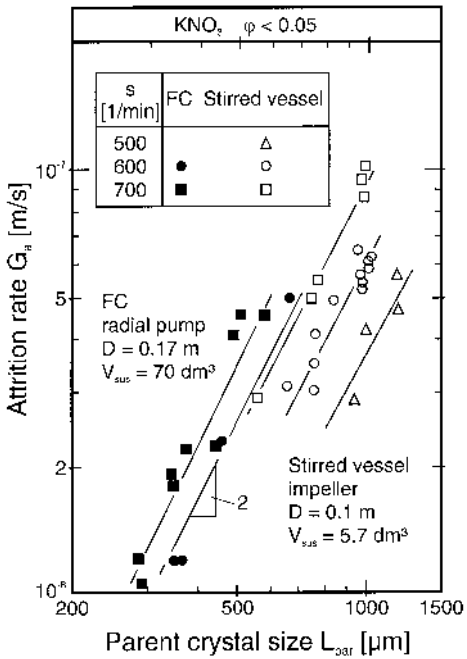

Figure 3.7. The linear attrition rate G_a as a function of crystal size and impeller speed. (From Ref. 3.1.)

In Figure 3.8, the attrition rate G_a is plotted against the parent particle size L_{par} for the speeds $s = 8.33\,\text{s}^{-1}$, $s = 10\,\text{s}^{-1}$ and $s = 11.66\,\text{s}^{-1}$ applied during the experiments. These results fully agree with the experimental results obtained for a volumetric crystal holdup of $\varphi_T \approx 0.05$. The model takes into account all the decisive parameters for monosized parent crystals but does not sufficiently consider the interaction of the crystals at high suspension densities. It is advantageous to plot the kinetic growth rate G and the attrition rate G_a in the same diagram in order to show the effective growth rate according to

$$G_{\text{eff}} = G - G_a \tag{3.18}$$

as a function of the parent crystal size and the collision velocity. In Figure 3.9, the experimentally determined attrition rates G_a for KNO_3 are again plotted against the size of the parent crystal. The growth of KNO_3 is diffusion controlled and the growth rate G can be calculated from

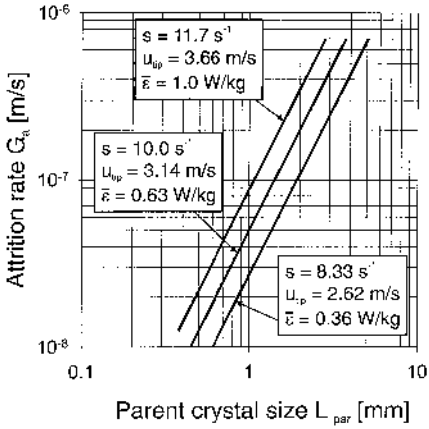

Figure 3.8. Theoretical attrition rates according to equation (3.16).

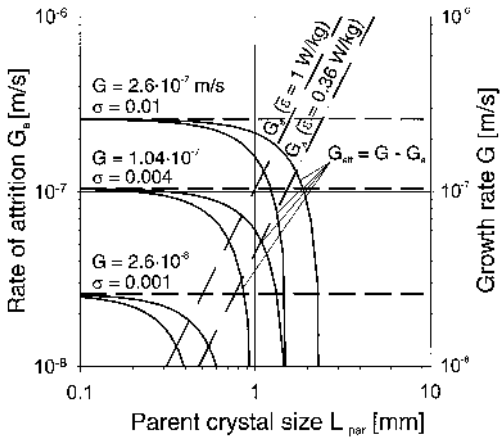

Figure 3.9. Rates of growth and attrition valid for KNO_3. (From Ref. 3.1.)

$$G = k_d \frac{\Delta C}{C_C} = k_d \frac{\Delta C}{C^*} \frac{C^*}{C_C} = k_d \frac{C^*}{C_C} \sigma \tag{3.19}$$

With $k_d = 2 \times 10^{-4}$ m/s and $C^*/C_C = 0.13$, we obtain

$G = 2.6 \times 10^{-8}$ m/s for $\sigma = 0.001$
$G = 1.04 \times 10^{-7}$ m/s for $\sigma = 0.004$
$G = 2.6 \times 10^{-7}$ m/s for $\sigma = 0.01$

(see Fig. 3.9).

Figure 3.9 shows that the maximum crystal size is large at high rates of supersaturation and growth but at small specific power inputs. If, however, the level of supersaturation is low in the presence of high attrition rates, the maximum size is small with the consequence that the crystal size distribution is attrition controlled. On the other hand, crystal growth is the decisive mechanism for small crystals (less than 300 µm). The maximum size of the parent crystals is controlled by both the kinetic growth rate G and the attrition rate G_a and is determined by the condition $G = G_a$. This can also be seen in the diagram, in which the logarithm of the number density n is plotted against the crystal size (see Fig. 3.10).

The results are valid for KNO_3 that was crystallized in a 5.7-dm^3 stirred vessel at the mean specific power inputs $\bar{\varepsilon} = 0.36\,W/kg$ and $\bar{\varepsilon} = 1.75\,W/kg$. The maximum sizes are $L_{par,\,max} \approx 950\,\mu m$ and $L_{par,\,max} \approx 700\,\mu m$, respectively [3.1, 3.3].

The population-density distribution $n(L)$ can be written

$$n(L) = n_0 \frac{[1 - (L/L_{par,\,max})]\,[(L_{par,\,max}/2G\tau) - 1]}{[1 + (L/L_{par,\,max})]\,[(L_{par,\,max}/2G\tau) + 1]} \tag{3.20}$$

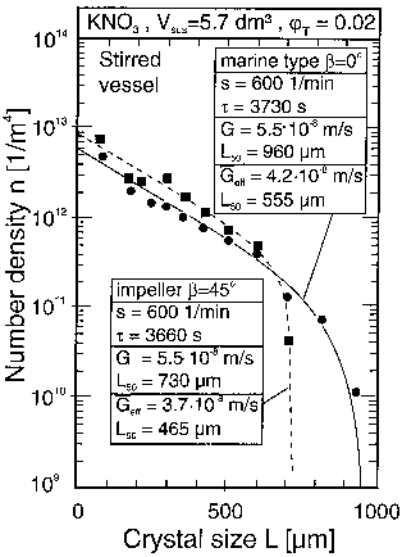

Figure 3.10. Number-density distributions of KNO_3 obtained in a continuously operated crystallizer.

This equation shows that the population density in the entire size range is the result of a complicated interplay between the growth rate G, which is controlled via supersaturation by kinetics, and the attrition rate G_a, which is mainly controlled via attrition by the properties of the crystal ($\rho_C, H_V, \mu, \Gamma/K$) and the fluid dynamics (u_{tip} or $\bar{\varepsilon}, N_V$, Power number, η_g, η_w).

Summarizing the effects of attrition, the following can be seen:

- Attrition fragments in the size range between 1 and 100 μm are formed (and not of size $L \to 0$).
- It is mostly large parent crystals that are abraded, with the result that the maximum size $L_{\text{par, max}}$ cannot be exceeded.

Therefore, the simplified or ideal MSMPR concept is not able to describe exactly the experimental CSD of the crystalline products in industrial crystallizers when $L_{,\max}$ and $\Delta\rho$ are large, and straight lines cannot be expected in a $\log n(L) = f(L)$ diagram. This will now be shown in more detail.

In Figures 3.11 and 3.12, the cumulative undersize mass distribution is plotted against the crystal size L for attrition-resistant KCl [0.7] and attrition-prone KNO_3 [0.6], respectively, according to experimental results obtained in MSMPR stirred vessels. As can be seen, the maximum crystal size $L_{\max}$ of KNO_3 decreases remarkably with the mean specific power input ($\bar{\varepsilon}$). This effect is more pronounced in crystallizers operating at long residence times τ because the supersaturation Δc and growth rate G are low in comparison with the attrition rate G_a.

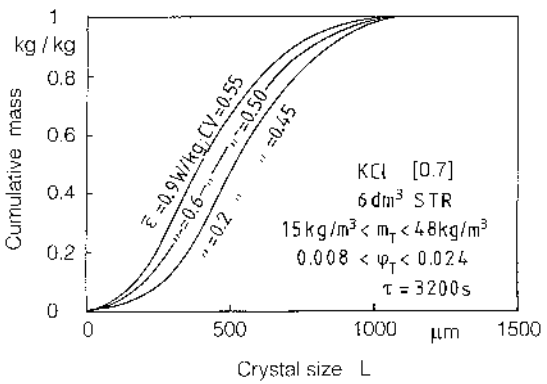

Figure 3.11. Cumulative undersize mass versus crystal size of attrition-resistant potassium chloride.

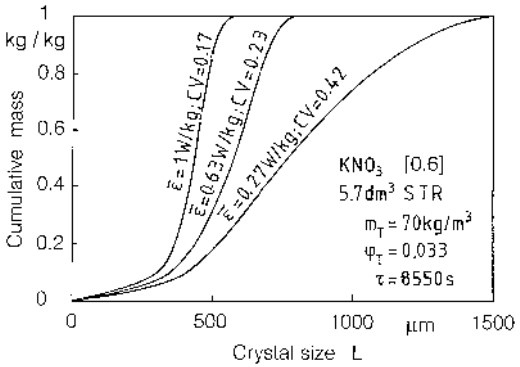

Figure 3.12. Cumulative undersize mass versus crystal size of attrition-prone potassium nitrate.

In a population-density plot (log n versus L), deviations occur from the straight line expected for ideal MSMPR crystallizers (see Figs. 3.13 and 3.14). Here, the population density $n(L)$ is again plotted against the crystal size for the materials KCl and KNO_3. When residence times are very long, a maximum crystal size L_{max} cannot be exceeded because of the condition $G = G_a$. The curve in the population-density plot is then vertical. This occurs with attrition-prone KNO_3 after only 1–2 h, but after several hours with attrition-resistant KCl. These statements can be generalized for inorganic and organic products. As a rule, a reduction in the maximum crystal size L_{max} is always accompanied by a decrease in the coefficient of variation (CV).

The CV is influenced only slightly by the suspension density m_T or the volumetric holdup φ_T. In all cases, the median crystal size L_{50} decreases with increasing power input $\bar{\varepsilon}$. There is no dramatic change in the coefficient of variation for KCl, which is resistant to attrition (see Fig. 3.11). However, the median size L_{50} of attrition-prone KNO_3 crystals is greatly reduced as the specific power input increases. This behavior is more pronounced in the case of long residence times because supersaturation and, consequently, the kinetic growth rate are low and the attrition rate is high. This leads to an attrition-controlled cystalline product with small coefficients of variation. It has been shown that KNO_3 is strongly abraded [in a similar way to $KAl(SO_4)_2 \cdot 12H_2O$, citric acid, and thiourea], whereas KCl [and also $(NH_4)_2SO_4$ and tartaric acid] exhibits only a low degree of attrition. Therefore, the statements given above may be generalized to a certain extent [3.4].

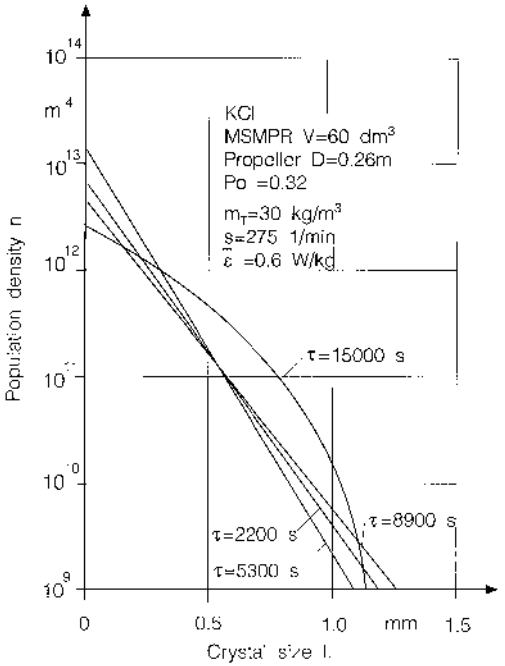

Figure 3.13. Population density versus crystal size of attrition-resistant potassium chloride.

The CSD of products obtained in the presence of high attrition rates can be described by the Rosin–Rammler–Sperling–Bennet (RRSB) distribution which was originally proposed for materials processed by communition in the size range between a few micrometers and 1 mm. It is not surprising that after transportation, solid–liquid separation, and drying, a crystalline product often complies with RRSB.

Information on the log-normal distribution, the RRSB distribution, and the population density distribution has been presented in Chapter 4. With industrial crystallizers operating at a high suspension density and high specific power input, the CSD cannot be described with great accuracy using these equations. However, these models are helpful for specifying product quality and how it varies when the operating conditions of such crystallizers and the scale of the apparatus are changed. Both the CSD and CV depend on (a) the type, geometry, and scale of the crystallizer, (b) the operating conditions $[m_T, (\bar{\varepsilon}), \tau, \Delta\rho$, etc.], (c) the properties of the solution (ρ_L, η_L), and (d) the properties of the solid (shape, structure, E, ν_c, H_V, μ). More information is given in Chapter 7.

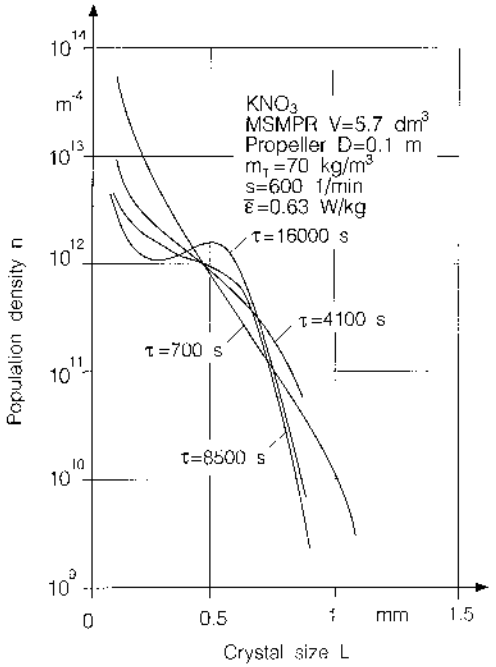

Figure 3.14. Population density versus crystal size of attrition-prone potassium nitrate.

4. ESTIMATION OF ATTRITION-INDUCED RATES OF SECONDARY NUCLEATION

It is not possible to predict the rate of secondary nucleation exactly; however, the decisive processes are now well understood. It is assumed in this section that the relative supersaturation is always $\sigma < 0.1$. In Chapter 2, it was shown that the rates of activated nucleation are extremely low for $S < 1.1$. Industrial crystallizers for the production of coarse crystals cannot be operated under conditions of activated nucleation because a small increase in supersaturation leads to the formation of a huge number of nuclei, which significantly reduces the median crystal size. The means that activated attrition fragments are the main source of nuclei for $\sigma < 0.1$.

A simplified model will now be presented with the objective of evaluating rates of secondary nucleation controlled by attrition. This model takes into account only crystal–rotor collisions because the collision velocities for this mechanism are approximately one order of magnitude greater than the

collision velocities for crystal–crystal contacts. The number of new attrition-induced and active nuclei depends on the following:

- The number of parent crystals which hit the rotor
- The collision frequency of such parent crystals
- The total number of active attrition fragments abraded from only one parent crystal after only one collision
- The percentage of active fragments

The number of growing attrition fragments is smaller than the total number of atttition fragments and increases with supersaturation because small fragments will be stimulated to grow. The model describes the situation occurring in a stirred vessel equipped with an inclined stirrer or marine-type impeller, it being relatively easy to model the fluid dynamics valid for this geometry. However, it should be noted that the model can be extended to cover other conditions of the suspension flow. In order to avoid or reduce the attrition of large crystals, it is advantageous to equip the stirred vessel with a rotor which has a low flow resistance. Marine-type propellers and stirrers with inclined blades have Power numbers in the range $0.3 < \mathrm{Po} < 1$. The exact value of Po depends on the inclination angle β of the blade (blade angle). This angle and also the thickness e and the breadth b of the blades determine whether or not a crytal hits the blade. The probability of collisions will again be described by a target efficiency η_g. Let us consider a blade with thickness e, breadth b, an angle β (see Fig. 3.4). The volumetric flow $\dot{V}$ through the horizontal plane described by the stirrer is proportional to the flow number or pumping capacity N_V, the stirrer speed s, and the third power of the stirrer diameter D:

$$\dot{V} = N_V s D^3 \tag{4.1}$$

The angle between the direction of the main flow and the horizontal plane is α, which can differ from the blade angle β. All parent crystals moving in the flow at the volumetric flow rate $\dot{V}\eta_g = N_V s D^3 \eta_g$ hit the blades when it is assumed that $\eta_w \approx 1$. The maximum collision velocity is proportional to the stirrer tip speed u_{tip}, which can be expressed by the Power number of the stirrer and the mean specific power input $\bar{\varepsilon}$:

$$u_{\mathrm{tip}} = \left(\frac{\pi^3 \bar{\varepsilon} V_{\mathrm{sus}}}{\mathrm{Po} D^2} \right)^{1/3} \tag{4.2}$$

The collision velocity is the result of the addition of the circumferential velocity and the axial velocity; see Fig. 3.4.

It has been shown that the approximate collision velocity is $w_{\mathrm{col}} = \eta_w u_{\mathrm{tip}}$, with $\eta_w < 1$. Let us first consider the collision of a single parent crystal which hits the blade with the collision velocity w_{col}.

The total number $N_{a,\mathrm{tot}}$ of attrition fragments resulting from this parent crystal which gains the collision energy W_{col} is

$$N_{a,\mathrm{tot}} = 7 \times 10^{-4} \frac{H_V^5}{\alpha \mu^3} \left(\frac{K}{\Gamma}\right)^3 W_{\mathrm{col}} \tag{4.3}$$

or with the collision energy W_{col} according to

$$W_{\mathrm{col}} = \alpha L_{\mathrm{par}}^3 \rho_C \frac{w_{\mathrm{col}}^3}{2} \tag{4.4}$$

we obtain

$$N_{a,\mathrm{tot}} = 7 \times 10^{-4} \frac{H_V^5}{\mu^3} \left(\frac{K}{\Gamma}\right)^3 L_{\mathrm{par}}^3 \frac{\rho_C w_{\mathrm{col}}^2}{2} \tag{4.5}$$

It has been shown that nearly all small attrition fragments possess an increased chemical potential (or elevated solubility) due to deformation. They either do not grow at all or only grow slowly at a low supersaturation $\sigma < 0.1$. Therefore, it is not the total number $N_{a,\mathrm{tot}}$ of fragments but the number $N_{a,\mathrm{eff}}$ of effective attrition fragments that is decisive for the rate of secondary nucleation. The effectiveness of attrition fragments has been investigated by Wang and Mersmann [2.1], Zacher and Mersmann [2.2], and Gahn and Mersmann [3.4]. In Figure 4.1, the number density $q_0(L_a)$ and the cumulative number distribution Q_0 according to

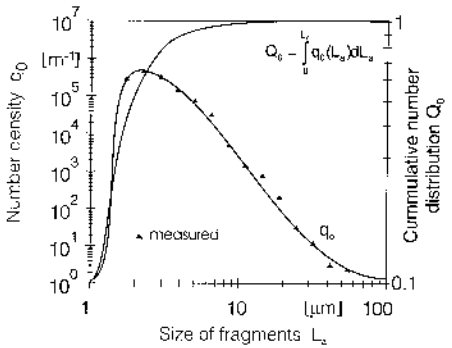

Figure 4.1. Number density and cumulative number distribution of KNO_3 attrition fragments.

$$Q_0 = \int_0^{L_a} q_0(L_a)\, dL_a \tag{4.6}$$

are plotted against the size L_a of KNO_3 attrition fragments. It has been shown that only fragments with $L_a > L_{a,\text{eff}}$ possess such a high statistically mean growth rate that they are effective fragments or secondary nuclei. The ratio $N_{a,\text{eff}}/N_{a,\text{tot}}$ of effective fragments to the total number of fragments is given by

$$\frac{N_{a,\text{eff}}}{N_{a,\text{tot}}} = \int_{L_{a,\text{eff}}}^{\infty} q_0(L_a)\, dL_a = 1 - \int_0^{L_{a,\text{eff}}} q_0(L_a)\, dL_a \tag{4.7}$$

The number-density distribution $q_0(L_a)$ can be approximated by

$$q_0(L_a) = \frac{2.25 L_a^{-3.25}}{L_{a,\min}^{-2.25} - L_{a,\max}^{-2.25}} \approx \frac{2.25 L_a^{-3.25}}{L_{a,\min}^{-2.25}} \approx 2.25 \left(\frac{32}{3} \frac{\mu}{H_V^2} \left(\frac{\Gamma}{K}\right)\right)^{2.25} L_a^{-3.25} \tag{4.8}$$

In Figure 4.2, the ratio $N_{a,\text{eff}}/N_{a,\text{tot}}$ is shown for substances characterized by $L_{a,\min}$. The decisive fragment size $L_{a,\text{eff}}$ depends on supersaturation because the mean growth rate of a size interval increases with supersaturation. In

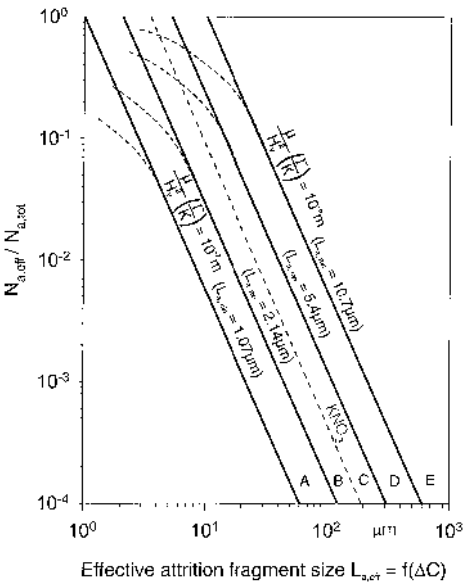

Figure 4.2. The ratio of effectively growing fragments as a function of their mechanical material properties and size.

Figure 2.6, it has been shown that only fragments larger than $L_{a,\mathrm{eff}} \approx 25\,\mu\mathrm{m}$ contribute significantly to growth [$G(L_a) > 0.1\bar{G}_{\max}$]. This effective size $L_{a,\mathrm{eff}}$ is smaller when supersaturation is higher and vice versa.

A very simplified model is now presented in order to estimate the effective rate of attrition-controlled secondary nucleation. With the mean specific power input

$$\bar{\varepsilon} = \frac{\mathrm{Po} D^2 u_{\mathrm{tip}}^3}{\pi^3 V_{\mathrm{sus}}} \tag{4.9}$$

the collision velocity

$$w_{\mathrm{col}} = \eta_w u_{\mathrm{tip}} \tag{4.10}$$

and the frequency of contacts, f_{col}, of a parent crystal with a rotor

$$f_{\mathrm{col}} \approx \eta_g \eta_w \frac{N_V s D^3}{V_{\mathrm{sus}}} \tag{4.11}$$

equation (4.3) can be written

$$\frac{f_{\mathrm{col}} N_{a,\mathrm{tot}}}{V_{\mathrm{sus}}} = 7 \times 10^{-4} \frac{H_V^5}{\mu^3} \left(\frac{K}{\Gamma}\right)^3 \frac{\pi^2 \rho_C \bar{\varepsilon} N_V L_{\mathrm{par}}^3}{2\mathrm{Po} V_{\mathrm{sus}}} \eta_w^3 \eta_g \tag{4.12}$$

This equation describes the total number of fragments abraded from parent crystals of size L_{par} per unit volume suspension and per unit time. In reality, there is a size distribution of parent crystals; however, it has been shown that the attrition rate rises with the second power of the parent crystal size. Therefore, it is assumed that the parent crystals are monosized and have the median size L_{par} with $L_{50} < L_{\mathrm{par}} < L_{\max}$. The right-hand side of equation (4.12) has to be multiplied by the factor $N_{a,\mathrm{eff}}/N_{a,\mathrm{tot}}$ and by the total number of parent crystals, which amounts to

$$N_{\mathrm{par,tot}} \approx \frac{V_{\mathrm{sus}} \varphi_T}{\alpha L_{\mathrm{par}}^3} \tag{4.13}$$

which is valid for the monodispersed parent crystals. This leads to the effective rate of secondary nucleation based on the volumetric crystal holdup φ_T:

$$\frac{B_{0,\mathrm{eff}}}{\varphi_T} = 7 \times 10^{-4} \frac{H_V^5}{\mu^3} \left(\frac{K}{\Gamma}\right)^3 \frac{\pi^2 \rho_C \bar{\varepsilon} N_V}{2\alpha^3 \mathrm{Po}} \frac{N_{a,\mathrm{eff}}}{N_{a,\mathrm{tot}}} \eta_w^3 \eta_g \tag{4.14}$$

As can be seen, the parent crystal size L_{par} is canceled. Because the target efficiencies η_w and η_g are functions of the fluid velocities and therefore also depend on the mean specific power input $\bar{\varepsilon}$, the relationship $B_{0,\mathrm{eff}} \sim \varepsilon^r$ with $0.5 < r < 0.8$ has often been found in experiments. With

$H_V = 2.68 \times 10^8\,\mathrm{J/m^3}$
$\mu = 7.17 \times 10^9\,\mathrm{J/m^3}$
$\Gamma/K = 2.8\,\mathrm{J/m^2}$
$\rho_C = 2109\,\mathrm{kg/m^3}$
$\bar{\varepsilon} = 0.27\,\mathrm{W/kg}$ [3.1]
Po = 0.36 [3.1]
$N_V = 0.30$ [3.1]
$\eta_w = 0.80$ [3.1]
$\eta_g = 0.03$ estimation according to Refs. 0.7, 1.16, and 4.1
$N_{a,\mathrm{eff}}/N_{a,\mathrm{tot}} = 0.017$ (see Fig. 4.2)

the result is $B_{0,\mathrm{eff}}/\varphi_T = 7.4 \times 10^7 \mathrm{nuclei/m^3 s}$, valid for KNO_3.

Pohlisch [3.1] determined the effective rate of secondary nucleation of KNO_3 in a stirred vessel with $V_{\mathrm{sus}} = 5.7 \times 10^{-3}\mathrm{m^3}$ for these conditions, and he obtained the experimental result

$$\frac{B_{0,\mathrm{eff}}}{\varphi_T} \approx 5 \times 10^7 \tag{4.15}$$

up to $6 \times 10^7 \mathrm{nuclei/m^3\,s}$ for two different calculation procedures.

The model produces useful results and describes the decisive processes in a simple way, but there are some weak points which will be discussed shortly. The effective fragment size $L_{a,\mathrm{eff}}$ and the ratio $N_{a,\mathrm{eff}}/N_{a,\mathrm{tot}}$ can only be determined experimentally for a certain supersaturation and both parameters increase with rising supersaturation. Due to the extreme growth rate dispersion, which is also size dependent, it is impossible to predict the growth behavior of a single fragment. Only statistically mean growth rates give an insight into the important processes and this requires a great deal of experimental work. On the other hand, many investigations carried out on different substances have shown that the effective size $L_{a,\mathrm{eff}}$ is often in the range between 20 and 40 µm. This means that only approximately 1% of all attrition fragments are effective, but they represent most of the volume abraded from the parent crystals.

With respect to the design and operation of industrial crystallizers, many parameter which influence atttrition are unknown and difficult to determine experimentally or to predict. The parameter pumping capacity N_V and the target efficiencies η_w and η_g depend not only on the geometry of the crystallizer but also on the fluid dynamics regimes. The properties of the solid crystal as the hardness H_V, the shear modul μ, and the fracture resistance (Γ/K) can be easily determined by an indentation test; see Chapter 1. It is reasonable to simplify equation (4.14) to

$$\frac{B_{0,\text{eff}}}{\varphi_T} = K_a \left[\frac{H_V^5}{\mu^3} \left(\frac{K}{\Gamma} \right)^3 \right] \rho_C \bar{\varepsilon} \tag{4.16}$$

The results shown in Figure 4.3 are valid for $KAl(SO_4)_2 \cdot 12H_2O$ and $(NH_4)_2 \cdot SO_4$ crystallized in a stirred vessel and fluidized bed and can be described by $K_a = f(G)$; see Figure 4.4. The coefficient K_a is proportional to $N_{a,\text{eff}}/N_{a,\text{tot}}$ and a function of supersaturation. Because the relationship $N_{a,\text{eff}}/N_{a,\text{tot}} = f(\Delta C)$ or the size of the effective attrition fragment, $L_{a,\text{eff}}$, are not known, the coefficient K_a is plotted versus the mean growth rate of the crystals. It is important to note that the coefficient K_a is valid for a regime in which the median crystal size is controlled by the crystallization kinetics and not solely by attrition, which occurs at very low supersaturation. This requires minimum specific power input, which is sufficient for the suspension of crystals.

The model gives some important advice on how to design and operate crystallizers in order to obtain coarse products. The tip speed u_{tip} of the rotor or the mean specific power input $\bar{\varepsilon}$ according to

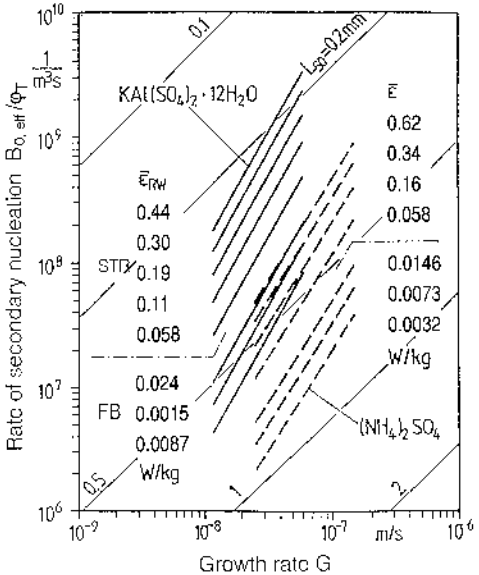

Figure 4.3. Rate of secondary nucleation based on φ_T versus the mean growth rate for $KAl(SO_4)_2$ and $(NH_4)_2SO_4$ crystallized in stirred tanks and fluidized.

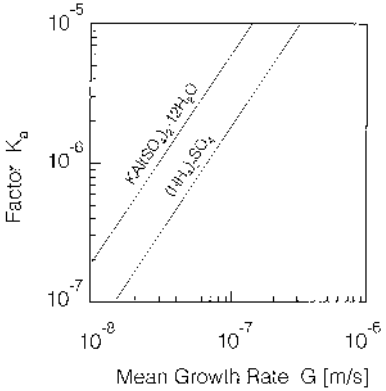

Figure 4.4. Factor K_a against the mean growth rate (results from Fig. 4.3).

$$\bar{\varepsilon} \sim \frac{u_{\text{tip}}^3}{T} \tag{4.17}$$

should be as low as possible in order to reduce the nucleation rate and to increase the mean particle size. However, the minimum tip speed increases with the size of the largest crystals $L_{\text{par,max}}$ and the density difference $\Delta\rho$:

$$u_{\text{tip,min}} \sim \sqrt{L_{\text{par,max}} \frac{\Delta\rho}{\rho_L} g} \tag{4.18}$$

and such particles are most prone to attrition. There is a self-regulating effect with the consequence that it is not possible to produce crystals above a certain size in crystallizers equipped with rotors (stirred vessel, forced cirulation). Coarse crystals can be obtained in fluidized-bed (FB) crystallizers when the flow of solution through the circulating pump is either free of crystals or contains only very tiny particles. Because the collision velocities in FB crystallizers are at least one order of magnitude smaller than in STR and FC crystallizers the product is much coarser. However, with increasing crystal size, the specific power input

$$\bar{\varepsilon} \sim \sqrt{L\left(\frac{\Delta\rho}{\rho_L} g\right)^3} \tag{4.19}$$

rises, resulting in higher rates of attrition and secondary nucleation. Again, the self-regulating effect limits the maximum size, but the product is coarser in FB than with STR and FC.

REFERENCES

[0.1] E. P. K. Ottens and E. J. de Jong, A model for secondary nucleation in a stirred vessel cooling crystalllizer, *Ind. Eng. Chem. Fundam.*, *12*: 179 (1973).

[0.2] G. D. Botsaris, Secondary nucleation: A review, in *Industrial Crystallization* (J. W. Mullin, ed.), Plenum Press, New York, pp. 3–22 (1976).

[0.3] E. P. K. Ottens, Nucleation in continuous agitated crystallizers, Thesis, Technical University of Delft (1973).

[0.4] W. F. Beer, Untersuchungen zur Maβstabsvergrösserung der Chargenkühlungskristallisation von Kaliumchlorid in Leitrohrkristallisatoren, Thesis, Technische Universität München (1981).

[0.5] W. Fleischmann, Unterschungen zur Verdrängungskristallisation von Natriumsulfat aus wässriger Lösung mit Methanol, Thesis, Technische Universität München (1986).

[0.6] J. Pohlisch, Einfluss von mechanischer Beeinflussung und Abrieb auf die Korngrössenverteilung in Kühlungskristallisatoren, Thesis, Technische Universität München (1987).

[0.7] R. Ploss, Modell zur Kontaktkeimbildung durch Rührer/*Kristall-Kollisionen in Leitrohrkristallisatoren*, Thesis, Technische Universität München (1990).

[0.8] T. Tengler, Wachstum und Keimbildung bei der Kühlungskristallisation von Ammoniumsulfat, Thesis, Technische Universität München (1990).

[1.1] U. Riebel, U. Zitzmann, and F. Löffer, Mechanische Beanspruchung suspendierender Teilchen am Leitroher-Propellerrührer, *Chem. Ing. Techn.*, *59*: 436 (1987).

[1.2] R. H. Perry and C. H. Chilton (eds.), *Perry's Chemical Engineers' Handbook*, 5th ed., McGraw-Hill, New York, pp. 20–80 (1973).

[1.3] A. Mersmann and R. K. Geisler, Determination of the local turbulent energy dissipation rates in stirred vessels and its significance for different mixing tasks, *Proc. 4th World Congress of Chemical Engineering* (1991).

[1.4] C. Gahn and A. Mersmann, Theoretical prediction and experimental determination of attrition rates, *Trans. IChemE*, *75A*: 125 (1997).

[1.5] A. E. H. Love, *A Treatise on the Mathematical Theory of Elasticity*, 2nd ed., Cambridge University Press, Cambridge (1906).

[1.6] J. H. Mitchell, Some elementary distribution of stress in three dimensions, *London Math. Soc. Proc.*, *32*: 23 (1900).

[1.7] H. Hertz, Über die Berührung fester elastischer Körper, *J. reine Angew. Math. Leipzig*, *92*(2): 156 (1881).
[1.8] M. T. Huber, Zur Theorie der Berührung fester elastischer Körper, *Ann. Phys.*, *14*: 153 (1904).
[1.9] C. Gahn and A. Mersmann, The brittleness of substances crystallized in industrial processes, *Powder Technol.*, *85*(1): 71 (1996).
[1.10] D. M Marsch, Plastic flow in glass, *Proc. Roy. Soc. London Ser. A.*, *279*: 420 (1964).
[1.11] W. Engelhardt and S. Haussühl, Festigkeit und Härte von Kristallen, *Fortschr. Mineral.*, *42*: 5 (1964).
[1.12] V. G. Levich, *Physiochemical Hydrodynamics*, Prentice-Hall, Englewood Cliffs, NJ, p. 179 (1962).
[1.13] C. Gahn, J. Krey, and A. Mersmann, The effect of impact energy and the shape of crystals on their attrition, *J. Cryst. Growth*, *166*: 1058 (1996).
[1.14] E. P. K. Ottens, *Nucleation in continuous agitated crystallizers*, Thesis, Technical University of Delft, Delft (1973).
[1.15] C. Gahn and A. Mersmann, Brittle fracture in crystallization processes, Part A, Attrition and abrasion of brittle solids, *Chem. Eng. Sci.*, *54*: 1273 (1999).
[1.16] C. Gahn, Die Festigkeit von Kristallen und ihr Einfluβ auf die Kinetik in Suspensionskristallisatoren, Thesis, Technische Universität München (1997).
[1.17] H. Rumpf, Die Einzelkornzerkleinerung als Grundlage einer technischen Zerkleinerungswissenschaft, *Chem. Ing. Techn.*, *37*(3): 187 (1965).
[2.1] S. Wang and A. Mersmann, The initial size-dependant growth rate of attrition fragments and secondary nuclei, *Chem. Eng. Sci.*, *47*: 1365 (1992).
[2.2] U. Zacher and A. Mersmann, The influence of internal crystal perfection on growth rate dispersion in a continous suspension crystallizer, *J. Crystal Growth.*, *147*: 172 (1995).
[2.3] R. L. Ristic, J. N. Sherwood, and T. Shripathi, The role of dislocations and mechanical deformation in growth rate dispersion in potash alum, in *Advances in Industrial Crystallization* (J. Garside, R. J. Davey, and A. G. Jones, eds.), Butterworth–Heinemann, Oxford, pp. 77–91 (1991).
[2.4] J. N. Sherwood, R. L. Ristic, and T. Shripathi, The influence of mechanical deformation and fracture on crystal growth: A potential cause for growth rate dispersion, in *Proceedings of the 11th Symposium on Industrial Crystallization* (A. Mersmann, ed.) Garmisch-Partenkirchen, Germany, pp. 349–353 (1990).

[2.5] A. E. D. M. van der Heijden, Secondary nucleation and crystallization kinetics, Thesis, University of Nijmegen, Nijmegen (1992).
[2.6] U. Zacher, Die Kristallwachstumsdispersion in einem kontinuierlichen Suspensionskristallisator, Thesis, Technische Universität München (1995).
[2.7] S. Wang, Großenabhängige Wachstumsdispersion von Abriebsteilchen und die Relevanz zur effecktiven sekundären Keimbildung, Thesis, Technische Universität München (1992).
[2.8] C. Gahn and A. Mersmann, Brittle fracture in crystallization processes, Part B: Growth of fragments and scale-up of suspension crystallizers, *Chem. Eng. Sci.*, *54*: 1283 (1999).
[3.1] R. J. Pohlisch, Einfluß von mechanischer Beeinflussung und Abrieb auf die Korngrößenverteilung in Kühlungskristallisatoren, Thesis, Technische Universität München (1987).
[3.2] R. J. Pohlisch and A. Mersmann, The influence of stress and attrition in crystal size distribution, *Chem. Eng. Technol.*, *11*: 40 (1989).
[3.3] J. Garside, A. Mersmann, and J. Nyvlt, *Measurement of Crystal Growth Rates*, European Federation of Chemical Engineering, Working Party on Crystallization, Munich (1990).
[3.4] C. Gahn and A. Mersmann. Theoretical prediction and experimental determination of attrition rates, *Trans. IChemE*, *75A*: 125 (1997).
[4.1] R. Sangl and A. Mersmann, Attrition and secondary nucleation in crystallizers, in *Proceedings of the 11th Symposium on Industrial Crystallization* (A. Mersmann ed.), Garmisch-Partenkirchen, Germany, pp. 59–64 (1990).
[4.2] L. Hedström, Secondary nucleation of pentaerythritol and citric acid monohydrate, Thesis, University of Stockholm (1994).
[4.3] A. Chianese, R. Sangl, and A. Mersmann, On the size distribution of fragments generated by crystal collisions, *Chem. Eng. Commun.*, *146*: 1 (1996).

6
Agglomeration

A. MERSMANN AND B. BRAUN Technische Universität München, Garching, Germany

At the end of Chapter 2, it has been shown that it is sometimes difficult to distinguish among the following processes:

- Nucleation
- Growth
- Agglomeration (perikinetic and orthokinetic)

This is especially true for all solid particles in the nanometer range. The unification of a 500-nm particle with a critical cluster of 5 nm can be interpreted as an agglomeration, growth, or even nucleation event. It has also been shown that processes of particles in the nanometer range are mostly diffusion controlled and should be described in a common way as diffusion-driven collision processes which take place in a multiparticle system. In doing so, it is necessary to take into consideration the unification probability of every collision and, therefore, the interparticle forces. Because an agglomerate can be destroyed by fluid shear, intraparticle forces of such species must be considered also. Collision shear rates and shear stresses are induced by fluid dynamics, which, in general, plays an important role in

all crystallization processes. This is especially valid for particles in the micrometer range. In Chapter 5, it has been demonstrated that attrition fragments are the main source of nuclei in systems with a low supersaturation and that such fragments have a size range between 2 µm and 150 µm. Therefore, the assumption of nuclei born at $L \rightarrow 0$ is not true and the effective nucleation rate $B_{0,\mathrm{eff}}$ for mixed suspension, mixed product removal (MSMPR) crystallizers is physically not correct but can be helpful in chemical engineering. Attrition fragments can also be the subject of (orthokinetic) agglomeration, and again, it can be difficult to separate the processes of nucleation and agglomeration. Because a common and general description of agglomeration, nucleation, and growth is not yet possible, a separate treatment of these processes is justified, but it is absolutely necessary to consider the entire range of particle size from a few nanometers up to several millimeters.

With respect to the real crystal size distribution (CSD) in a crystallizer, we must always keep in mind the fact that the complete population balance includes a birth rate $B(L)$ and a death rate $D(L)$. These rates are caused by attrition and breakage, on the one hand, and, on the other hand, by agglomeration. Furthermore, clusters in the solution, preordered species removed from the crystals, and/or foreign particles can contribute to an interval of size. Our knowledge of size distribution of any solid matter in a supersaturated solution is poor, which can be demonstrated by Figure 0.1. In this figure, the population density $n(L)$ of $KAl(SO_4)_2 \cdot 12H_2O$ [0.1] and of KCl [0.2] is plotted against the size L of condensed species for (a) clusters in a saturated and a supersaturated aqueous solution of KCl and $BaSO_4$ according to results calculated on the basis of the classical nucleation theory (cf.

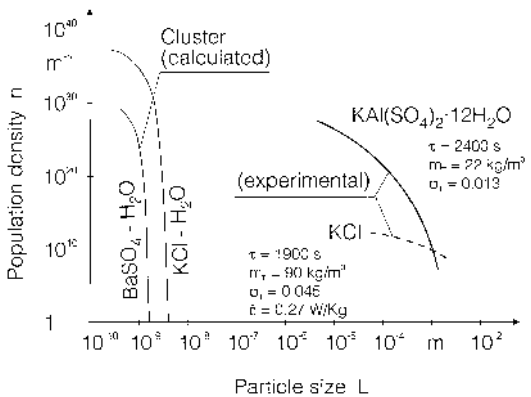

Figure 0.1. Population density versus particle size.

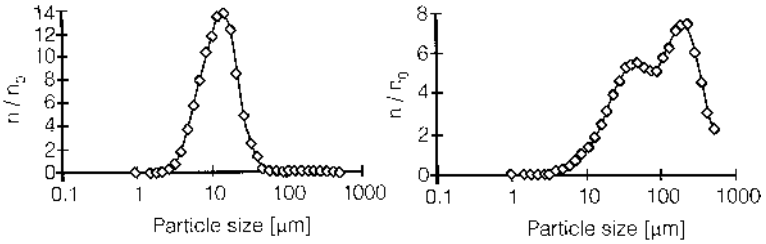

Figure 0.2. Number density versus particle size for SiO_2 precipitated from $NaO(SiO_2)_{rm}$ by the addition of sulfuric acid. (From [0.4].) With (left) and without (right) ultrasonic treatment.

Chapter 2) in the range $L < 5 \times 10^{-9}$ m [0.3] and (b) crystals produced in an MSMPR crystallizer in the range $10^{-4} < L < 2 \times 10^{-3}$ m.

In Figure 0.2, the number density n is plotted against the particle size for SiO_2, which was precipitated from $NaO(SiO_2)_{rm}$ by the addition of sulfuric acid [0.4]. After nucleation, which resulted in a very high population density, the final size distribution stabilized after several minutes at a mean crystal size of approximatley 50–100 nm.

It is assumed that particles ranging in size between 10^{-9} and 10^{-4} m are present in a crystallizer. However, their population density is not well known due to the difficulty in measuring their size and number. Consequently, we are not in a position to trace back the origin of crystals present in a crystallizer. Because agglomeration can influence the CSD, it is essential to predict the importance of this process occurring in industrial crystallizers. Moreover, it is important but at the same time difficult to distinguish among (a) agglomeration, (b) aggregation, and (c) flocculation of particles.

According to [0.5], agglomeration is the unification of primary particles that are cemented afterward by chemical forces (e.g., by a crystalline bridge between two or more crystals). The formation of this bridge requires crystal growth, for which supersaturation is an essential prerequisite. When dealing with aggregation and flocculation, the bonding forces, such as van der Waals forces, are quite weak [0.6]. A flocculate is a group of particles that consists of primary particles connected by weak cohesive forces. In the case of aggregates, the strength of the bonding forces is intermediate to agglomerates and flocculates. Aggregates and flocculates can occur in saturated or undersaturated solutions and can readily be destroyed. However, strong agglomerates are generated only in supersaturated solutions. Information on the bonding forces is given in Figure 0.3, in which the tensile strength is plotted against the particle diameter L for different kinds of force.

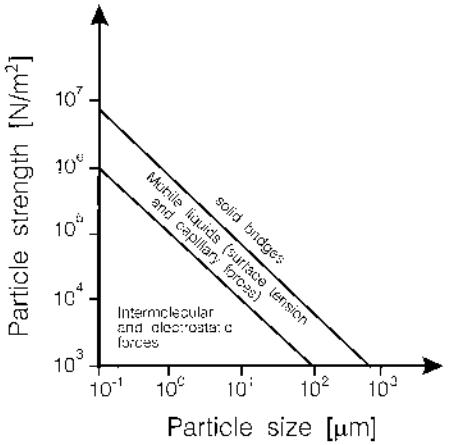

Figure 0.3. Particle strength versus particle size.

A distinction can be made between two types of crystal agglomeration: (a) primary agglomeration as a result of malgrowth of crystals (polycrystals, dendrites, and twins) and (b) secondary agglomeration as a consequence of crystal–crystal collisions in supersaturated solutions. It is often difficult to distinguish between the different origins of particles by microscopic observation. Secondary agglomeration (from now on referred to simply as agglomeration) takes place in suspended particle systems and depends on (a) mechanical and fluid dynamic processes, such as the movement of primary particles and liquid, and on particle collisions, (b) kinetic processes, mainly crystal growth in supersaturated solutions, and (c) particle properties. Agglomeration is dominant in the submicron and micron ranges of primary species and it is less important or negligible for particles larger than 50 μm.

According to survey papers [0.7, 0.8], agglomeration in crystallizers does not occur with particles above a certain critical size. This critical size depends on the suspension density m_T, crystal growth rate G, and specific power input $\bar{\varepsilon}$, and ranges from 10 to 30 μm for aluminum trihydrate [0.9]. In [0.10], it is assumed that for particles smaller than the critical size, a fraction (independent of size) will be converted to agglomerates, the fraction depending on the crystal residence time τ, the growth rate G, and the time necessary to join the loosely agglomerated particles together.

As a rule, agglomeration takes place after small primary particles have been formed by primary nucleation [0.11]. At the beginning of crystallization, the rate of homogeneous or heterogeneous primary nucleation deter-

mines the number of primary particles generated in a supersaturated solution. An approximate idea of the importance of homogeneous and heterogeneous nucleation can be obtained from the figures in Chapter 2. According to [0.12], the early stage of precipitation appears to be governed by the classical mechanism of attachment of ions to nuclei rather than by the agglomeration of either molecular aggregates present in the solution or of nuclei that have already been formed. At the end of the induction period, crystals are present primarily as individual entities of narrow size distribution ranging from 1 to 3 μm. Consequently, agglomeration is negligible during the induction period of a few seconds. However, after approximately 1 min of agglomeration, agglomerates ranging between 20 and 30 μm have been observed.

These results confirm the statements published in the literature that agglomeration is complete when the agglomerates have reached a size of more than 10–30 μm, which depends on fluid dynamics, the suspension density, and the growth rate. The degree of agglomeration Z, defined as the number of individual crystals per unit volume based on the number of separate particles per unit volume according to $Z = N_0/N(t)$, is a function of time and increases greatly with the initial concentration of reactants in the case of precipitation, or with supersaturation. For example, maximum values of $Z = 80$ have been observed for $SrMoO_4$ [0.12]. The modeling of agglomeration is based on material and population balances, interparticle forces, and crystallization kinetics.

1. POPULATION BALANCE

The population balance based on a particle-size interval has already been derived in Chapter 4. This balance for the size interval dL is given by

$$\begin{pmatrix}\text{Particles}\\ \text{entering}\\ \text{the reactor}\end{pmatrix} + \begin{pmatrix}\text{Particles}\\ \text{formed by}\\ \text{nucleation}\end{pmatrix} + \begin{pmatrix}\text{Particles}\\ \text{formed by}\\ \text{birth/death}\end{pmatrix} + \begin{pmatrix}\text{Particles of}\\ \text{size } L - dL\\ \text{growing to}\\ \text{size } L\end{pmatrix}$$
$$= \begin{pmatrix}\text{Particles}\\ \text{leaving}\\ \text{the reactor}\end{pmatrix} + \begin{pmatrix}\text{Particles of}\\ \text{size } L \text{ growing}\\ \text{to size } L + dL\end{pmatrix} + \begin{pmatrix}\text{Particles of}\\ \text{size } L \text{ lost by}\\ \text{birth/death}\end{pmatrix}$$
$$+ \begin{pmatrix}\text{Particles}\\ \text{accumulating during}\\ dt \text{ in the reactor}\end{pmatrix} \tag{1.1}$$

The general equation for the number density n (in m^{-4}) of a crystallizer having the volume V is

$$\frac{\partial n}{\partial t} + \frac{\partial (Gn)}{\partial L} + n\frac{\partial V}{V\,\partial t} + D(L) - B(L) + \sum_k \frac{\dot{V}_i n_i}{V} = 0 \tag{1.2}$$

with the population density n according to

$$n = \frac{\text{Number of particles}}{(\text{m}^3 \text{ suspension})(\text{m size interval})}$$

and the mean growth rate G (in m/s). The birth rate $B(L)$ and the death rate $D(L)$ (both measured in m^{-4}/s) are controlled by processes of agglomeration, attrition, and breakage or disruption of particles present in the suspension. It is assumed that nuclei are formed by activated nucleation at the size $L \to 0$ and that this process can be described by the nucleation rate $B_{0,\text{eff}}$ (in nuclei/m^3 s) according to

$$B_{0,\text{eff}} = n_0 G \tag{1.3}$$

It has been shown in Chapter 5 that the introduction of the effective nucleation rate $B_{0,\text{eff}}$ is very helpful for engineering modeling of products of several hundred micrometers in size. Strong agglomeration only takes place in the size range up to 30 µm. In this case, it is advantageous to use the population density n_v according to

$$n_v = \frac{\text{Number of particles}}{(\text{m}^3 \text{ suspension})(\text{m}^3 \text{ particle volume interval})}$$

because the mass and, with $\rho_C = \text{const.}$, also the volume of the solid matter remain constant. Desupersaturation of the solution leads to nucleation (i.e., the formation of particles with the smallest volume that can be measured) and to an increase in the particle volume according to the growth rate G_v (in m^3/s). The general form of the population balance equation expressed in volume coordinates for an MSMPR crystallizer in the presence of agglomeration and disruption of agglomerates is given by

$$\frac{\partial n_v}{\partial t} + \frac{\partial (n_v G_v)}{\partial u} + n_v\frac{\partial V}{V\,\partial t} + \frac{n_{vp} - n_{vf}}{\tau} = B_{\text{agg}}(V) - D_{\text{agg}}(V) + B_{\text{dis}}(V) - D_{\text{dis}}(V) + B_u\delta(u - u_0) \tag{1.4}$$

where n_v (number/m^6) is the population density defined on a crystal volume basis, G_v is the volumetric growth rate (in m^3/s), and $B_{\text{agg}} - D_{\text{agg}}$ and $B_{\text{dis}} - D_{\text{dis}}$ represent the net formation of particles of volumetric size u by

aggregation (agg) and disruption (dis), respectively. The source (or nucleation) function B_u is the birth rate of particles at the lowest measurable size u_0, accounting for the growth and agglomeration of particles into a measurable size range. The combination of two particles of volume u and $v-u$ to form particle size v can be written

$$B_{\text{agg}}(V) = \frac{1}{2}\int_0^v \beta(u, v-u)n_v(u, t)n_v(v-u, t)\,du \tag{1.5}$$

and

$$D_{\text{agg}}(V) = n_v(v, t)\int_0^\infty \beta(u, v)n_v(u, t)\,du \tag{1.6}$$

Here, B_{agg} is the rate at which particles of volume v appear due to particles of volume u agglomerating with particles of volume $v-u$. β (in m^3/s) is the agglomeration rate constant or the aggregation kernel, which depends on the frequency and the efficiency of collisions between the particles. The factor $\frac{1}{2}$ prevents each agglomeration event from being counted twice. The tensile strength of agglomerates can be weak (electrostatic forces) or high (crystalline bridges). The events of the disruption of agglomerates are described by disruption functions. As a rule, the disruption of agglomerates is physically different from the attrition of polycrystals described in Chapter 5.

As the simplest case, it is assumed that one large agglomerate breaks into two smaller pieces, each half of the original volume. For this case, it follows that [1.1]

$$B_{\text{dis}} = 2D_{\text{dis}}(2v) \tag{1.7}$$

In literature [1.2], it is proposed that the disruption term D_{dis} is proportional to the volume of the disrupting agglomerates and the population density n_v at that volume. In this case, the disruption functions become

$$D_{\text{dis}} = K'_{\text{dis}}n_v(v) \tag{1.8}$$

and

$$B_{\text{dis}} = 4K_{\text{dis}}vn_v(2v) \tag{1.9}$$

In these equations, K_{dis} (in $1/\text{m}^3$ s) and K'_{dis} (in 1/s) are disruption parameters that are expected to increase with the shear rate in the agglomerator. In addition, the disruption parameter depends on the tensile strength of the agglomerates. The disruption functions may be negligible if the shear rate is small and agglomerates are cemented by crystalline material. On the other hand, submicron particles show strong agglomeration rates in the presence

of a high particle concentration N (in particles/m^3) and the absence of repulsive interparticle forces.

Let us first consider the process of agglomeration in more detail. The formulation of the aggregation kernel β is chosen to correspond to the particular mechanism and to account for the physicochemical and fluid dynamic forces. It will be shown that it is very difficult to predict the rates of B_{agg} in a general way because these rates depend on the physicochemical properties of the solution and of the primary particles and also on the fluid dynamics caused by gravitational or turbulent forces. At the moment, some simplifying models are available that allow a certain quantitative approach. Let us begin with a simple chemical reaction by which the precipitation process is often initiated. When a species A and a species B react by addition to a product P, the kinetics of this reaction can often be described by

$$\frac{dC_P}{dt} = kC_AC_B \tag{1.10}$$

with C as the molar concentration (in kmol/m^3) or $N = CN_A$ (in molecules/m^3) as the number of units per unit volume. The rate constant k is given in m^3/(kmol s) or m^3/(molecules s). The molecule or particle unification rate for the reaction A + B $\leftrightarrow$ P is proportional to the square of the particle number per unit volume for an equimolar reaction. Von Smoluchowski [1.3] was the first to describe the change in the number concentration N with respect to time. The description of such a process of particle unification is easy when only monosized particles are considered.

This mechanism can be governed by (a) perikinetic agglomeration caused by Brownian motion of monodisperse, submicron primary particles that are subjected to collisions (diffusion controlled) in a solution at rest, (b) orthokinetic agglomeration induced by fluid-mechanical forces acting on particles (shear rate controlled) in a solution in motion, or (c) differential settling by gravitational or centrifugal forces. Von Smoluchowski has derived equations for these two agglomeration mechanisms (see Table 1.1). N_0 is the starting number of crystals per unit volume after nucleation, A_{agg} is an attachment factor, and $\dot{\gamma}$ represents the shear rate, which is proportional to the stirrer speed s in a stirred vessel or to the expression w_L/D in pipes with diameter D. According to these equations, a plot of $N_0/N(t)$ against time t yields a straight line in the case of perikinetic agglomeration. When dealing with orthokinetic agglomeration, the logarithm of $N_0/N(t)$ is proportional to time.

For orthokinetic agglomeration in a plot of $\ln L^3(t)$ against t, a straight

Table 1.1. Perikinetic and Orthokinetic Agglomeration

Perikinetic agglomeration

$$\frac{dN(t)}{dt} = -4\pi D_{AB} L N^2 \quad \text{or} \quad \frac{d(1/N)}{dt} = 4\pi D_{AB} L \tag{1.11}$$

$$\frac{dZ}{dt} = \frac{d}{dt}\left(\frac{N_0}{N(t)}\right) = 4\pi D_{AB} L N_0 \tag{1.12}$$

$$Z \equiv \frac{N_0}{N(t)} = 1 + 4\pi D_{AB} L N_0 t \tag{1.13}$$

$$N(t) = \frac{N_0}{1 + 4\pi D_{AB} L N_0 t} \tag{1.14}$$

Orthokinetic agglomeration

$$\frac{dN(t)}{dt} = -\frac{2}{3} A_{\text{agg}} \dot{\gamma} L^3(t) N^2(t) \quad \text{or with volumetric holdup}$$

$$\varphi_T = \alpha L^3(t) N(t) \neq f(t) \tag{1.15}$$

$$\frac{dN(t)}{dt} = -\frac{2}{3\alpha} A_{\text{agg}} \dot{\gamma} \varphi_T N(t) \tag{1.16}$$

$$Z \equiv \frac{N_0}{N(t)} = \exp\left(\frac{2A_{\text{agg}} \dot{\gamma} \varphi_T t}{3\alpha}\right) \tag{1.17}$$

$$N(t) = \frac{N_0}{\exp(2A_{\text{agg}} \dot{\gamma} \varphi_T t / 3\alpha)} = \frac{\varphi_T}{\alpha L^3(t)} \tag{1.18}$$

line is obtained, the slope of which should increase with increasing agitation (stirrer speed $s \sim \dot{\gamma}$) and concentration:

$$\ln\left[\frac{\alpha}{\varphi_T} N_0 L^3(t)\right] = \frac{2A_{\text{agg}} \dot{\gamma} \varphi_T}{3\alpha} t \tag{1.19}$$

The equations of von Smoluchowski have been confirmed experimentally by various authors who carried out experiments in small laboratory crystallizers under given conditions. According to these relationships, the collision rate depends on the motion of the primary particles, that is (a) the Brownian or diffusional motion in the case of very small particles in a motionless

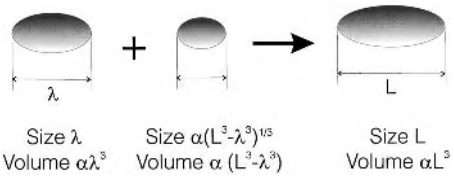

Figure 1.1. Aggregation of two particles, $L - \lambda$ and λ in diameter, forming a particle of size L.

liquid, (b) the shear rate $\dot{\gamma}$ for larger particles, and (c) the differential settling.

The agglomeration rate dN/dt is proportional to the square of the number of primary particles N per unit volume for the case of monodispersed particle size distributions. With respect to high shear rates, especially in the vicinity of rotors in industrial crystallizers, and large crystals, orthokinetic agglomeration is important for crystallization technology.

Let us now consider agglomeration processes in systems with particle size distributions. In the simplest case, a particle with size λ and volume $\alpha\lambda^3$ combines with another particle to give an agglomerate with the size L and the volume αL^3; see Figure 1.1. When the number density of particles of size λ in a certain interval is N_λ and the number density of particles termed $L - \lambda$ is $N_{L-\lambda}$, the birth rate in this interval due to agglomeration is proportional to the agglomeration kernel β and the product $N_\lambda N_{L-\lambda}$. In the case of a size distribution, the contributions of the various intervals must be added according to

$$\left(\frac{dN_L}{dt}\right)_{\text{birth}} = \frac{1}{2}\sum_{\lambda=0}^{L-\lambda} \beta(\lambda, L-\lambda) N_\lambda N_{L-\lambda} \tag{1.20}$$

At the same time, particles of this interval will disappear because they agglomerate with others and leave the interval. This death rate is proportional to the number density N_L and depends on the aggregation kernel β and the number density N_λ.

The change in the number density N_L of particles of size λ with respect to time or the net rate of agglomeration of these particles by birth and death events is then given by

$$\frac{dN_L}{dt} = \frac{1}{2}\sum_{\lambda=0}^{L-\lambda} \beta(\lambda, L-\lambda) N_\lambda N_{L-\lambda} - N_L \sum_{\lambda=0}^{\infty} \beta(L, \lambda) N_\lambda \tag{1.21}$$

Later it will be shown how this balance equation reads when it is formulated with population densities either based on length or volume.

When the size of the particles is in the molecular range (or the particles are ions, atoms, molecules, dimers, or trimers), the aggregation kernel is given by

$$\beta(L,\lambda) = \frac{2kT}{3\eta_L}\frac{(L+\lambda)^2}{L\lambda} = \beta_0\frac{(L+\lambda)^2}{L\lambda} \tag{1.22}$$

with $\beta_0 = 2D_{AB}d_m$. Here, η_L is the dynamic viscosity of the liquid and D_{AB} is the diffusivity of units with a molecular size d_m. The aggregation rate $dN_\lambda/dt = \dot{N}_\lambda$ is proportional to the expression $N_\lambda N_{L-\lambda}$ or to N^2 for particles of equal size. Therefore, aggregation is always very strong for small particles with a high diffusivity at high particle concentrations N. The aggregation kernel then assumes the highest values. With $\eta_L = 1\,\text{mPa·s}$ and $T = 300\,\text{K}$, a maximum value of $\beta_0 = 2.76 \times 10^{-18}\,\text{m}^3/\text{s}$ can be calculated for diffusion-controlled or perikinetic aggregation.

Let us return to the equimolar chemical rection of the species A and B. With $\beta_0 = 2.76 \times 10^{-18}\,\text{m}^3/\text{s}$ and the concentrations $C_A N_A$ and $C_B N_A$ (both measured in m^{-3}), the maximum aggregation rate $\dot{N}_{\text{agg}}$ is given for a concentration C of 1 mol/L by

$$\dot{N}_{\text{agg}} = \beta_0 C_A N_A C_B N_A = 1.66 \times 10^{35}\,\text{m}^{-3}/\text{s} \tag{1.23}$$

Such very high aggregation rates (the order of magnitude is comparable to the highest rates of homogeneous nucleation at $\Delta C/C_C > 0.1$; see Chapter 2) lead to rapid aggregation, with the result that aggregates in the size range of nanometers are very quickly formed.

The number of aggregates and their diffusivity decreases with increasing size of the aggregates and the aggregation rate $\dot{N}_{\text{agg}}$ slows down. Soon there is a continuous size distribution of particles, the size of which increases with time, rather than discrete distributions of monosized particles. Large agglomerates can disrupt in a shear field or after collision with a rotor. The rate $r_{\text{agg}}(L)$ of particles of size L is defined as the difference between the birth rate $B_{\text{agg}}(L)$ of aggregation of particles of size L and the death rate $D_{\text{agg}}(L)$ of particles that disappear due to aggregation (here based on size coordinates):

$$r_{\text{agg}}(L) = B_{\text{agg}}(L) - D_{\text{agg}}(L) \tag{1.24}$$

In the case of a discrete population, the terms $B_{\text{agg}}(L)$ and $D_{\text{agg}}(L)$ can be written

$$B_{\text{agg}}(L) = \frac{1}{2}\sum_{i=1}^{L-1} J(L, \lambda - L) \tag{1.25}$$

and

$$D_{\text{agg}}(L) = \sum_{i=1}^{\infty} J(L, \lambda) \tag{1.26}$$

Here, J is the frequency of particle collisions per unit volume suspension and interval size in number of collisions/m^4 s, or m^{-4}/s.

When the size distribution is continuous, the equations must be written with integrals instead of sums. This will now be derived for a population balance that is based on particle volume with n_v (in m^{-6}) according to

$$n_v = \frac{\text{Particles}}{(\text{m}^3 \text{ suspension})(\text{m}^3 \text{ crystal volume})} = \frac{\text{Particles}}{\text{m}^6}$$

The corresponding equations for the volume-based rate $r_{\text{agg}}(V)$ of particles of size L are given by

$$r_{\text{agg}}(V) = B_{\text{agg}}(V) - D_{\text{agg}}(V) \tag{1.27}$$

with

$$B_{\text{agg}}(V) = \frac{1}{2}\int_0^v \beta(u, v-u) n_v(u) n_v(v-u)\, du \tag{1.28}$$

and

$$D_{\text{agg}}(V) = n_v(v) \int_0^{\infty} \beta(u, v) n_v(u)\, du \tag{1.29}$$

Here, the terms $B_{\text{agg}}(V)$ and $D_{\text{agg}}(V)$ are frequencies (in m^{-6}/s) of successful collisions per unit time, unit suspension volume, and unit crystalline matter in the entire suspension volume. The aggregation kernel β is a measure of the frequency of collisions between particles of volumes u and v that are successful in producing an agglomerate of volume $v + u$.

Hounslow [1.4] has shown that the rates $B_{\text{agg}}(V)$ and $D_{\text{agg}}(V)$ can be expressed in the forms $B_{\text{agg}}(L)$ and $D_{\text{agg}}(L)$ based on the size L of particles. This is advantageous because the growth rate in the population balance is expressed as the change in particle size L with time. The number of particles per unit suspension volume and time that are formed by aggregation in the volume interval $[\alpha L^3, \alpha L^3 + d(\alpha L^3)]$ is the same as the number of particles generated in the size interval $[L, L + dL]$. This identity can be expressed by

$$n_v(\alpha L^3)\, d(\alpha L^3) = n(L)\, dL \tag{1.30}$$

and

$$B_{\text{agg}}(V)\, d(\alpha L^3) = B_{\text{agg}}(L)\, dL \tag{1.31}$$

In this way, the following equations can be derived:

$$B_{\text{agg}}(L) = \tfrac{3}{2}\alpha L^2 \left[\int_0^L \beta(\lambda, (\alpha L^3 - \alpha\lambda^3)^{1/3}) \frac{n(\lambda) n((\alpha L^3 - \alpha\lambda^3)^{1/3})}{3\alpha(L^3 - \lambda^3)^{2/3} 3\alpha\lambda^2} 3\alpha\lambda^2 \, d\lambda \right] \tag{1.32}$$

$$D_{\text{agg}}(L) = \tfrac{3}{2}\alpha L^2 \left[\int_0^\infty \beta(L, \lambda) \frac{n(L) n(\lambda)}{3\alpha L^2 (3\alpha\lambda^2)} 3\alpha\lambda^2 \, d\lambda \right] \tag{1.33}$$

or

$$B_{\text{agg}}(L) = \frac{L^2}{2} \left[\int_0^L \beta(\lambda, (\alpha L^3 - \alpha\lambda^3)^{1/3}) \frac{n(\lambda) n((\alpha L^3 - \alpha\lambda^3)^{1/3})}{(\alpha L^3 - \alpha\lambda^3)^{2/3}} \, d\lambda \right] \tag{1.34}$$

$$D_{\text{agg}}(L) = n(L) \int_0^\infty \beta(L, \lambda) n(\lambda) \, d\lambda \tag{1.35}$$

When aggregates that are larger than approximately 100 μm are exposed to collisions with a rotor or to a strong shear of high-turbulence flow, there is a danger of disruption. Disruption occurs in particular with aggregates that have a low tensile strength. The process of disruption can be modeled in a manner similar to that for aggregation. The rate of disruption, $r_{\text{dis}}(V)$, is the net rate or the difference between the birth rate $B_{\text{dis}}(V)$ of particles with volume V that are generated by disruption and the rate $D_{\text{dis}}(V)$ of such particles that disappear:

$$r_{\text{dis}}(V) = B_{\text{dis}}(V) - D_{\text{dis}}(V) \tag{1.36}$$

Again, these rates are based on particle volume.

When the particle size distribution is continuous, the rates $B_{\text{dis}}(V)$ and $D_{\text{dis}}(V)$ can be formulated according to Villermaux [1.5]:

$$B_{\text{dis}}(V) = \int_{\alpha L^3}^\infty \Gamma(\alpha\lambda^3) \nu(\alpha\lambda^3) p(\alpha\lambda^3, \alpha L^3) n(\alpha\lambda^3) \, d(\alpha\lambda^3) \tag{1.37}$$

$$D_{\text{dis}}(V) = \Gamma(\alpha L^3) n_v(\alpha L^3) \tag{1.38}$$

Here, the expression $\Gamma(\alpha L^3)$ represents the frequency of disruption (in 1/s) or the fraction of particles with volume αL^3 that disrupt per unit time. The term $p(\alpha\lambda^3, \alpha L^3)$ denotes the probability that particles in the volume range αL^3 and $\alpha L^3 + d(\alpha L^3)$ will disrupt. Finally, $\nu(\alpha\lambda^3)$ is the mean number of particles born as a result of disruption from a particle with the volume αL^3. As a rule, the functions $p(\alpha\lambda^3, \alpha L^3)$ and $\nu(\alpha\lambda^3)$ are unknown and difficult to predict.

The modeling of attrition presented in Chapter 5 might be helpful with respect to the largest attrition fragments if the agglomerates exhibit strong tensile strength. Let us explain the difference between the disruption of

aggregates and the attrition of polycrystals in more detail. Aggregates are composed of a certain number of primary particles that are strongly cemented together when the aggregate has been exposed to a high supersaturation for a long period. Such aggregates have a low probability of disruption. However, at very high supersaturation, $\Delta C/C_c = \sigma(C^*/C_c) > 0.1$, the rate of homogeneous primary nucleation can be so high that $B_{\text{hom}} > \dot{N}_{\text{agg}}$ and supersaturation is rapidly consumed by nucleation, with the consequence that the primary particles agglomerate at a very low supersaturation. This results in aggregates that can easily be disintegrated due to their weak tensile strength. Unlike disruption, attrition is predominant in crystallization of large crystals with $L > 100\,\mu\text{m}$ that are produced in systems with a high solubility. Here, the supersaturation is low (approximately $\sigma < 0.1$) in order to avoid activated nucleation. As has been shown in Chapter 5, the attrition rate increases with the collision velocity and the size of parent crystals, and crystals with a high settling velocity (large L_{par} and large $\Delta\rho$) are most prone to attrition. The attrition fragments in the size range between $2\,\mu\text{m}$ and $150\,\mu\text{m}$ are partly attached to large crystals and may contribute to their growth to a certain degree. However, such mechanisms play a minor role and aggregation may be neglected in suspensions with crystals larger than $100\,\mu\text{m}$. On the other hand, in precipitation of systems with a low solubility, primary particles that are formed by activated nucleation have a strong tendency to agglomerate and the final particle size distribution is often controlled by agglomeration.

Attractive and repulsive forces of the primary particles decide on the progress and the rates of aggregation. The unification of two particles requires the following:

- First, the collision that depends on the collision frequency J as a function of fluid dynamics, particle size and interparticle forces
- Their cohesion, which is a function of the tensile strength of the aggregates and the collision and/or shear forces coming from a rotor and/or fluid dynamics

The population balances can only be solved when the total interplay of attractive and repulsive forces of small primary particles, the tensile strength of aggregates, and the forces acting on aggregates are known. Some information on this topic will be given in the following section.

2. INTERPARTICLE FORCES

Interactions between atoms, molecules, and macroscopic particles cause forces that can be repulsive or attractive in nature. In principle, all kinds of interactions can be derived from the Schrödinger equation to obtain

electron density maps and the intermolecular energies. However, although this has been done for simple molecules, such as NaCl, in practice the intermolecular energy is represented by a sum of different contributions:

$$\begin{aligned} E_{ij} = &\text{ Charge transfer intractions} \\ &+ \text{Electrical multipole–electrical multipole intractions} \\ &+ \text{Electrical multipole–induced multipiole interactions} \\ &+ \text{Dispersion interactions} \\ &+ \text{Overlap interactions} \end{aligned} \tag{2.1}$$

Charge transfer interactions are determined by the exchanging or sharing of electrons between atoms (covalent bonds, ionic bonds). They are important in the organization of crystalline structures, very short ranged (0.1–0.2 nm), and highly directional. Like overlap interactions, charge transfer interactions are quantum mechanical in nature. Overlap interactions, also known as exchange or steric interaction, are repulsive due to the Pauli exclusion principle. They balance the attractive forces in the range of interatomic distances and are usually described by the power law for the interparticle energy E:

$$E = \left(\frac{\sigma}{D}\right)^n \tag{2.2}$$

where D is the separation distance and σ a constant related to the size of the molecule; n is an integer usually taken to be between 9 and 16.

As already mentioned, both quantum-mechanical forces act over very short distances. Because our goal in this chapter is to describe the interaction of macroscopic particles where the forces are long ranged (compared to interatomic distances), we will not discuss these forces any further and refer to the literature.

Electrical multipole–electrical multipole interactions can be described by classical electrostatics. They include ion–ion, ion-dipole, and dipole–dipole interactions. The latter two energies lead to polarization forces from the dipole moments induced in atoms and molecules by the electric field and nearby charges and permanent dipoles. In the following sections, we will formulate expressions for these forces and interactions to answer the following two questions:

1. When does aggregation occur in disperse systems and how fast is this aggregation step?
2. Which measures can be taken into consideration to promote or to prevent aggregation?

In the first subsection, we will consider DLVO interactions.

2.1. DLVO Theory

The DLVO theory was independently developed by Derjaguin and Landau [2.1] in 1941 and by Vervey and Overbeek [2.2] in 1948. It gives a very successful mathematical approach on the basis of only two acting forces, which, in practice, dominate in many systems. We will start with the attractive force and then discuss the electrostatic repulsion.

2.1.1. Van der Waals forces

In our attempt to calculate the van der Waals force, we will confine this approach to the London theory and give just a short summary of the general van der Waals interaction. Three forces contribute to the van der Waals force, namely, the Keesom orientation force, the Debye inductive force, and the London dispersion force. The first, $E_k(D)$, is of purely electrostatic origin and describes the interaction between two dipole molecules. It is calculated from

$$E_k(D) = -\frac{u_1^2 u_2^2}{3(4\pi\varepsilon_0\varepsilon_r)^2 kTD^6} \tag{2.3}$$

where u_i $(i = 1, 2)$ represents the dipole moments of molecule 1 and 2, ε_0 is the electrical field constant, and ε_r is the electrical permittivity. D denotes the distance between two particles. The induction of a dipole moment in one molecule by a dipole molecule can be described by the Debye interaction:

$$E_D(D) = -\frac{(u_1^2\alpha_{02} + u_2^2\alpha_{01})}{(4\pi\varepsilon_0\varepsilon_r)^2 D^6} \tag{2.4}$$

where α_{0i} $(i = 1, 2)$ is the polarizability of molecules 1 and 2, respectively.

The contribution of van der Waals forces that is usually most important is presented by the dispersion forces, also known as London, electrodynamic, or charge fluctuation forces. Their origin is quantum chemical, although the result seems to be electrostatic. The dispersion forces can be understood by the following argument. Although the time-averaged dipole moment is 0 for molecules without a dipole, there exists at any time a finite value. An electromagnetic field emanates from this dipole moment and induces a dipole in a nearby molecule. Thus, it is easy to see that dispersion forces, like gravitational forces, must be ubiquitous. As will be seen later, they are always attractive in vacuum and between like particles. However, they can become repulsive under certain conditions between unlike particles in a dispersion medium.

A mathematical approach was made by London [2.3]. The derivation of London's theory would be far beyond the scope of this book. Therefore, we will summarize the final results. Like the Keesom and Debye interaction, the London interaction varies with D^{-6} for molecules:

$$E_L = -\frac{3\alpha_0^2 h\nu}{(4\pi\varepsilon_0)^2 D^6} \tag{2.5}$$

Here, h is Planck's constant and ν denotes the frequency. Equation (2.5) is generally known as the London equation. More rigorous solutions are available in the literature.

We have given a short summary of van der Waals forces between molecules, which can be so strong that solids just held together by dispersion forces are formed. Examples include higher alkanes (e.g., hexane). Now, we will introduce the Hamaker theory, which assumes the pairwise summation of molecular forces to obtain van der Waals forces for macrobodies. Figure 2.1 summarizes the van der Waals interaction for different geometries. It should be noted that E_{vdW} is a long-range interaction since it varies with D^{-1}, e.g. for two spheres:

$$E_{vdw} = -\frac{A}{6D}\left(\frac{R_1 R_2}{R_1 + R_2}\right) \tag{2.6}$$

with A representing the Hamaker constant defined in a conventional manner by

$$A = \pi C N_{\mathrm{at},1} N_{\mathrm{at},2} \tag{2.7}$$

Here $N_{\mathrm{at},1}$ and $N_{\mathrm{at},2}$ are the number of atoms per unit volume and C is the coefficient in the atom–atom pair potential, according to

$$C = -\frac{3\alpha_0^2 h\nu}{(4\pi\varepsilon_0)^2} \tag{2.8}$$

The Hamaker theory has two serious shortcomings. First, as already mentioned, the pairwise additivity of forces is assumed, and second, the retardation effect is neglected. The latter comes into being for distances between particles over 50 nm. Because the electromagnetic field travels only with the speed of light, the response from a nearby molecule coincides with another fluctuation of the first molecule. The major consequence of this effect is that the range of macroscopic van der Waals forces is limited.

These problems are entirely avoided in the Lifshitz theory. In contrast to the Hamaker approach, Lifshitz treated the particles as continuous objects.

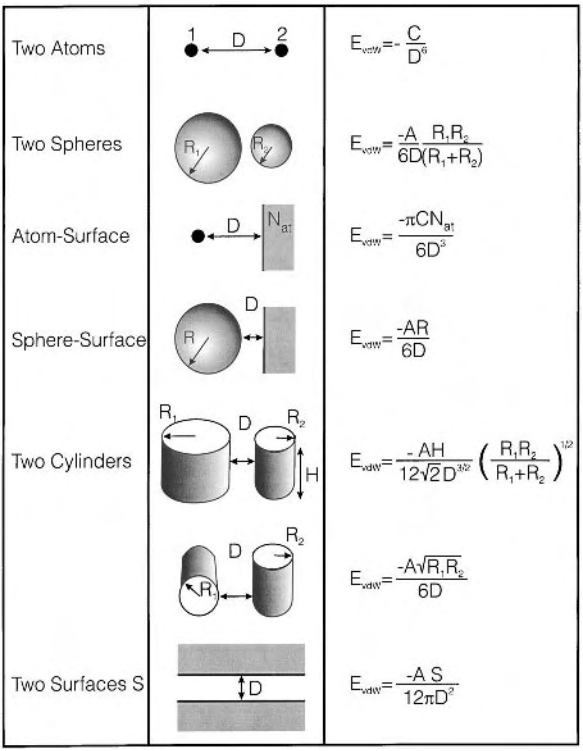

Figure 2.1. Van der Waals interaction energies for different geometries using the Hamaker theory.

However, because all the results given earlier remain valid, we will concentrate on the Hamaker constant, which is derived in terms of dielectric constants and refractive indices of the three media, as has been shown in equations (2.9) and (2.10):

$$A \approx \frac{3}{2}kT\left(\frac{\varepsilon_1 - \varepsilon_3}{\varepsilon_1 + \varepsilon_3}\right)^2\left(\frac{\varepsilon_2 - \varepsilon_3}{\varepsilon_2 + \varepsilon_3}\right)^2 + \frac{3h}{4\pi}\int_{\nu_1}^{\infty}\left(\frac{\varepsilon_1(i\nu) - \varepsilon_3(i\nu)}{\varepsilon_1(i\nu) + \varepsilon_3(i\nu)}\right)\left(\frac{\varepsilon_1(i\nu) - \varepsilon_3(i\nu)}{\varepsilon_1(i\nu) + \varepsilon_3(i\nu)}\right)d\nu \tag{2.9}$$

$$A = \frac{3}{4}kT\left(\frac{\varepsilon_1 - \varepsilon_3}{\varepsilon_1 + \varepsilon_3}\right)^2 + \frac{3h\nu_e}{16\sqrt{2}}\frac{(n_1^2 - n_3^2)}{(n_1^2 + n_3^2)^{3/2}} \tag{2.10}$$

Here, ε is the dielectric constant, n is the refractive index of the particles, ν_e is the absorption frequency, and h is Planck's constant. The $\varepsilon(i\nu)$ are the values of ε at imaginary frequencies. Neither equation gives an exact solution. In equation (2.9), only the first two terms of an infinite summation are given. This is justified by the fact that all other terms rarely contribute more than 5%. Equation (2.10) is just a crude estimation but is very easy to calculate. For the computation of A according to equation (2.9), reference is made to Israelachvili [2.4] and Hunter [2.5]. It should be noted that Hamaker's approach is only valid between particles in a vacuum, whereas the theory of Lifshitz remains accurate when a disperse medium exists but fails in the case of molecular dimensions.

It has been shown that there are at least two ways to calculate Hamaker's constant. Other possibilities include experimental determination and the application of mixing rules analogous to the calculation of interaction parameters in fluid-phase equilibria:

$$A_{12} = \sqrt{A_{11}A_{22}} \tag{2.11}$$

This equation describes the Hamaker constant between two different kinds of particles in a vacuum in terms of Hamaker constants between identical particles. When a medium (3) is involved the following equation can be used:

$$A_{132} = (\sqrt{A_{11}} - \sqrt{A_{33}})(\sqrt{A_{22}} - \sqrt{A_{33}}) \tag{2.12}$$

In the case of like particles, the following equation is recommended:

$$A_{131} = (\sqrt{A_{11}} - \sqrt{A_{33}})^2 \tag{2.13}$$

It should be noted that the Hamaker constant of a dispersion medium that is intermediate to the media 1 and 2 becomes negative and, therefore, the van der Waals force is repulsive. This is, for example, the case for the system (1)quartz–(2)water–(3)air.

We can conclude that the van der Waals interaction is difficult to manipulate because it depends mostly on particle properties ($\eta, \varepsilon, \alpha_0, u, n$). Another force that is much more sensitive to changes in the environmental conditions is the repulsive electrostatic force, which we shall discuss in the following subsubsection.

2.1.2. Electrostatic repulsive force

Electrostatic forces in disperse systems arise when charged particles or interfaces are present. The charging of the surface usually occurs due to one of three mechanisms [2.5]:

- Ionization and dissociation of surface groups
- Ion adsorption from solution
- Crystal lattice defects

In a suspension of clay particles in water, for example, the clay surface loses positively charged ions and continues to have a negative charge. Because the surface possesses a negative charge, the nearest environment in the solution must contain more positive (counterions) than negative (co-ions) ions. In the bulk solution, both kinds are equally distributed.

The mathematical description of the charge distribution from the particle surface to the bulk solution was successfully implemented by Guoy and Chapman in 1910 using the Poisson–Boltzmann equation:

$$\nabla^2\psi = -\frac{1}{\varepsilon_0\varepsilon_r}\sum N_i^0 z_i e \exp\left(-\frac{z_i e\psi}{kT}\right) \tag{2.14}$$

where ψ is the electrostatic potential, z_i is the valency, e is the elementary electrical charge, and N_i^0 is the bulk concentration of ions of type i (in m^{-3}). A complete solution gives values for the potential and charge at any distance from the surface and on the surface itself. Figure 2.2 shows how the potential varies with the distance for different electrolyte concentrations and ion valencies. A very simple solution for the Poisson–Boltzmann equation is given for low electrolyte concentrations ($|z_i e\psi| < kT$) with the Debye–Hückel equation:

$$\psi = \psi_0 \exp(-\kappa z) \tag{2.15}$$

In this equation, the decay length $1/\kappa$, also known as the Debye–Hückel parameter or the Debye screening length, is encountered for the first time. From equation (2.14), it is simple to derive κ as

$$\frac{1}{\kappa} = \sqrt{\frac{\varepsilon_r\varepsilon_0 kT}{\sum (z_i e)^2 N_i^0}} \tag{2.16}$$

Often $1/\kappa$ is described as the distance at which the particles can "see" each other or, in other words, the Debye length is a measure of the thickness of the diffuse Guoy–Chapman layer. It is important to note that $1/\kappa$ depends only on solution properties and not on any particle properties. For a sodium chloride solution with the concentration C_{NaCl} (in mol/L), we can calculate $1/\kappa$, for example, by

$$\frac{1}{\kappa} = \frac{0.304}{\sqrt{C_{NaCl}}}\,\text{nm (at 25°C)} \tag{2.17}$$

In pure water (pH 7; i.e., $C_{H_3O^+} = C_{OH^-} = 10^{-7}$ mol/L), the Debye length is

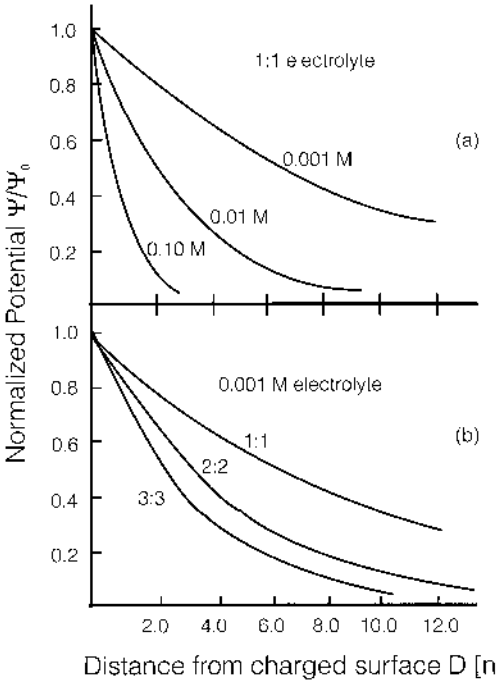

Figure 2.2. Decay in the potential in the double layer as a function of distance from a charged surface according to the limiting form of the Guoy–Chapman equation. (a) Curves are drawn for a 1:1 electrolyte of different concentrations. (b) Curves are drawn for different 0.001*M* symmetrical electrolytes. (From [2.6].)

approximately 1 μm. However, if we add just 1 m*M* NaCl, $1/\kappa$ drops to 9.6 nm, which is a remarkable effect.

A more complete solution of the Poisson–Boltzmann equation gives

$$\psi(z) = \frac{2kT}{ze} \ln\left(\frac{1 + \Gamma_0 \exp(-\kappa z)}{1 - \Gamma_0 \exp(-\kappa z)}\right) \tag{2.18}$$

with Γ_0 containing the surface potential ψ_0,

$$\Gamma_0 = \frac{\exp(ze\psi_0/2kT) - 1}{\exp(ze\psi_0/2kT) + 1} \tag{2.19}$$

Although the Guoy–Chapman theory has several shortcomings, it is remarkably accurate. This results mostly from the fact that the neglected forces tend to balance out each other.

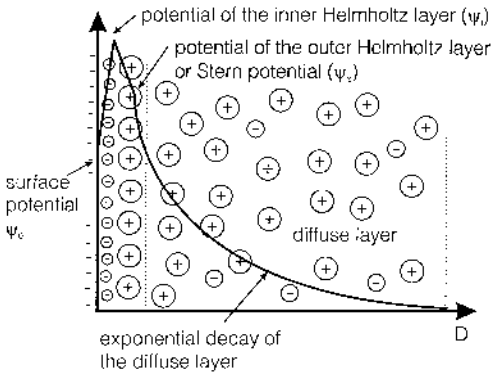

Figure 2.3. Electrostatic potential as a function of distance; an adsorbed layer leads to a maximum at the inner Helmholtz plane followed by a linear decrease to the Stern potential. The decay in the double layer obeys the Guoy–Chapman equation.

A more accurate theory uses the model shown in Figure 2.3. It takes into account an adsorbed layer, called the Stern or Helmholtz layer, between the surface and the diffuse layer where the Poisson–Boltzmann equation is valid. More general theories, which include potential determining ions (e.g., AgI, where the Ag^+ ions have a higher affinity to adsorb on the surface) and other effects, are available in the literature (e.g., [2.5]).

After showing the connection between the potential and the distance between two particles, we can calculate the repulsive force and interaction energy, respectively. Israelachvili gives the following equation for the repulsive force F_{rep} between two spheres:

$$F_{\text{rep}} = 2\pi r\varepsilon_r\varepsilon_0\kappa\psi_0^2 \exp(-\kappa D) = 2\pi r\sigma^2 \frac{\exp(-\kappa D)}{\kappa\varepsilon_r\varepsilon_0} \tag{2.20}$$

where r is the radius of the two spheres, D is the distance between them, and ψ_0 is the surface potential that is related to the electrical charge σ by

$$\sigma = \varepsilon_r\varepsilon_0\kappa\psi_0 \tag{2.21}$$

By integrating equation (2.20), we obtain the interaction energy E_{rep}

$$E_{\text{rep}} = 2\pi r\varepsilon_r\varepsilon_0\psi_0^2 \exp(-\kappa D) \tag{2.22}$$

Both equations are only valid for low surface potentials (<25 mV) and the general equation is

$$E_{\text{rep}} = \frac{64\pi r N_i^0 kT\Gamma_0^2}{\kappa^2} \exp(-\kappa D) \tag{2.23}$$

Now, we can give the solution of the DLVO theory, which is simply the sum of the attractive van der Waals forces and the repulsive electrostatic forces:

$$E_{\mathrm{DLVO}} = E_{vdW} + E_{\mathrm{rep}} \tag{2.24}$$

and results in

$$E_{\mathrm{DLVO}} = \pi r\left(-\frac{A_{131}}{12\pi D} + \frac{64N_i^0 kT\Gamma_0^2 \exp(-\kappa D)}{\kappa^2}\right) \tag{2.25}$$

for two identical spheres.

The result of the addition of these two interactions is shown in Figure 2.4. Israelachvili distinguishes five different regimes:

1. Highly charged surface; dilute electrolyte gives long-range repulsion.
2. At higher electrolyte concentrations a secondary minimum (>3 nm) appears. Particles can aggregate and form a kinetically stable colloid or stay dispersed in the solution. They cannot reach the primary minimum.
3. With decreasing charge density, the energy barrier will be lower, leading to slow coagulation.
4. When the maximum interaction energy reaches zero at the critical coagulation concentration, rapid coagulation takes place.
5. The net van der Waals attraction dominates when the surface charge or the potential reaches zero.

2.2. Non-DLVO Forces

The DLVO theory, with its various approximations and assumptions, is very successful in the description of many disperse systems. However, it is important to note that the DLVO theory does not take into account all the mechanisms and forces that can play a role in suspensions. Moreover, when the particles are in the size range of a few nanometers, the continuum theory breaks down. Additional forces overlap with DLVO forces. These forces can be monotonic, oscillatory, repulsive, or attractive and are not normally additive to each other or to DLVO forces. We will mention only three kinds of non-DLVO forces:

- Solvation forces
- Structural forces
- Hydration forces

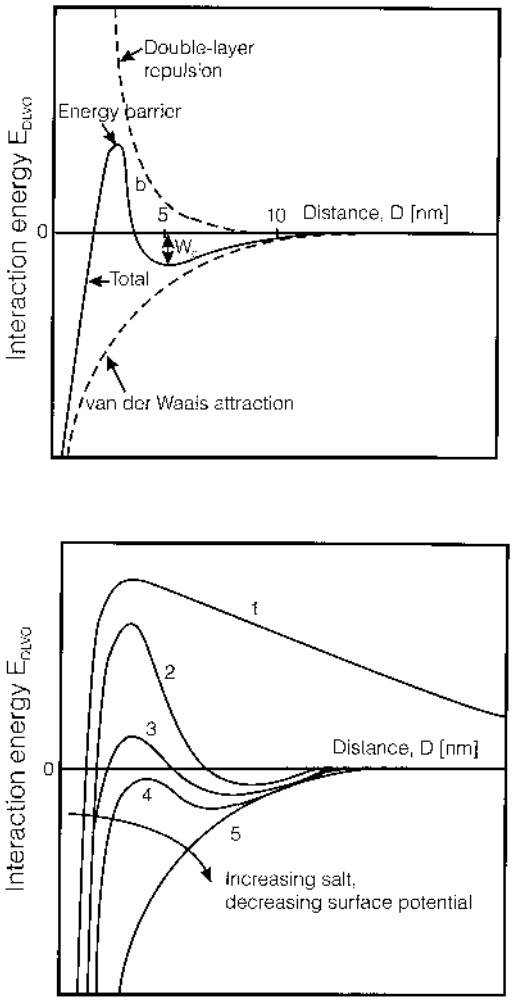

Figure 2.4. Interaction energy E_{DLVO} versus distance. E_{DLVO} is calculated as the sum of the electrostatic repulsion and attractive van der Waals energy.

Solvation forces exist due to surface–solvent interactions. When a second surface approaches the first, the solvent molecules are ordered and properties such as the density or the dielectric permittivity differ from the bulk values. The solvation force is strongly dependent on the geometry of both the particle surface and the solvent molecules; for example, for spherical molecules between two hard, smooth surfaces, it is usually an oscillatory

function. However, solvation forces can also be monotonic (e.g., for asymmetric molecules), repulsive, or attractive. Intuitively, they may be understood as van der Waals forces at separations of several angstroms to a few nanometers when the change in the ordering of the molecules is considered.

When we talk of aqueous systems, solvation forces are often referred to as repulsive hydration or attractive hydrophobic forces. In the first case, water molecules are bound to the surface and influence adjacent water molecules so that the resulting particle–particle interaction is repulsive over a distance range of about 5 nm. A steric hydration force caused by the overlapping of surface groups must be considered if the distance decreases to 1–2 nm. Attractive forces usually exist between hydrophobic surfaces. A well-known example is the micellization of tensides, but spherical agglomeration, which is based on different solubilities of particles in two solvents, can also be explained using solvation forces.

Both repulsive hydration and attractive hydrophobic interactions can be quantified using an exponential approach. The repulsion energy is given by

$$w_s = w_{s0} \exp\left(-\frac{D}{\lambda_0}\right) \tag{2.26}$$

where w_{s0} and λ_0 must be determined experimentally. Pashley [2.7] found $\lambda_0 = 0.6$ to 1.1 nm for 1:1 electrolytes. The surface energy w_{s0} depends on the hydration of the surface and is usually below 3–30 $\mathrm{mJ/m^2}$. The surface energy w_s according to the attractive force is given by

$$w_s = -2\gamma_i \exp\left(-\frac{D}{\lambda_0}\right) \tag{2.27}$$

where $\gamma_i = 10 - 50\,\mathrm{mJ/m^2}$ and $\lambda_0 = 1$–2 nm.

The solvation forces in aqueous systems are very important; however, they are not well understood.

Another class of forces must be considered for surfaces that are rough in molecular terms. One example of a rough surface is coverage with polymers. Figure 2.5 shows that the particles cannot decrease the distance between them any further because the adsorbed polymer molecules act as a steric obstacle.

At the end of this chapter, a summary of some important properties of interactions between particles in solution will be given. In many cases, it is sufficient to consider only two forces: the attractive and ubiquitous van der Waals force and the repulsive electrostatic force. The DLVO theory assumes additivity of both forces and is theoretically well justified. It breaks down for very small distances when the continuous approach is no longer valid. Other forces such as solvation forces must be taken into account for such small

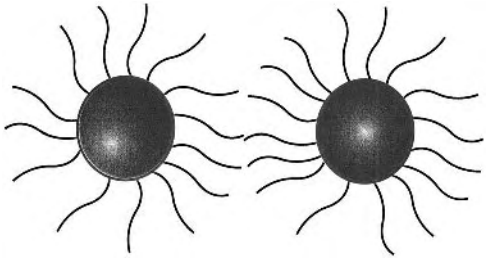

Figure 2.5. Steric repulsion due to polymer-covered surfaces.

separations and sometimes over a wide range of distances too. In aqueous systems in particular, when hydrogen-bonding is strong, colloidal particles attract or repel each other by a variety of forces that are not well understood at present. These forces and interactions are not additive, although they sometimes tend to erase each other so that one or two forces play a dominant role and almost all of the others can be neglected. A much more extensive study of interparticle and also of intermolecular forces is given by Israelachvili [2.4].

After the introduction of agglomeration expressions, based on length- or volume-related population balance, interparticle forces have been discussed. These forces decide whether particles can touch each other, which may result in an agglomeration event. In the following section agglomeration rates will be presented with the objective how such rates can be predicted in a general way.

3. AGGLOMERATION RATES

The aggregation kinetics is difficult to describe, mainly because it depends on many different parameters such as the hydrodynamic conditions, the properties (e.g., size, shape, and density) of the particles, and the interactions between two particles or a particle with the solvent.

For this reason, there is no fundamental theoretical approach. On the contrary, many different models of aggregation kinetics are presented in the literature. Over the last 10 years in particular, there has been rapid development in this area. However, most authors refer to the early work of von Smoluchowski [1.3] who described the kinetics using the simple equation

$$-\frac{dN}{dt} = \beta N^2 \tag{3.1}$$

where N is the total number of particles per unit volume suspension and β is the agglomeration kernel. Considering one size L, we obtain

$$\frac{dN_L}{dt} = \frac{1}{2}\sum_{\lambda=0}^{L-\lambda} \beta(\lambda, L-\lambda) N_\lambda N_{L-\lambda} - N_L \sum_{\lambda=0}^{\infty} \beta(L, \lambda) N_\lambda \tag{3.2}$$

with $\beta(L, \lambda)$ as a size-dependent agglomeration kernel. These kernels have been subject to intensive studies. Therefore, we will compare experimental data with results derived by theoretical equations.

First, we should mention that the agglomeration kernel is usually divided into three independent terms:

$$\beta = W_{\text{eff}} \beta_{\text{col}} \beta^*(\lambda, L) \tag{3.3}$$

Here, β_{col} is the collision frequency determined by hydrodynamic conditions as will be described in Section 5. The collision efficiency W_{eff} is a measure of the number of successful collisions that actually lead to an aggregate. Zeichner and Schowalter [3.1] define a stability ratio W_{eff} as

$$W_{\text{eff}} = \frac{\text{Actual number of collisions}}{\text{No. collisions without hydrodynamic and colloidal forces}} \tag{3.4}$$

The inverse of the stability ratio is called the capture efficiency [3.2] and has values between zero and one. Fuchs presented a formalism used in industrial applications even though slight variations are applied [3.3]:

$$W_{\text{eff}} = 2R \int_{2R}^{\infty} \frac{1}{r^2} \exp\left(\frac{\varphi(r)}{kT}\right) dr \tag{3.5}$$

R is the radius of the particle and r is the distance between two particles. $\varphi(r)$ describes the interaction potential and can be calculated, for example, according to the DLVO theory.

Finally, a size-dependent term is introduced. Over 30 different approaches can be found in the literature. Many of them are empirical formulations. Again, von Smoluchowski was the first to derive the size dependency from theoretical considerations, arriving at

$$\beta^*(\lambda, L) = \left(\frac{1}{\lambda} + \frac{1}{L}\right)(\lambda + L) \tag{3.6}$$

Considering all three terms of the kernel, von Smoluchowski derived the following equation:

$$\beta = \frac{2kT}{3\eta W_{\text{eff}}}(R_1 + R_2)\left(\frac{1}{R_1} + \frac{1}{R_2}\right) \tag{3.7}$$

If we assume that there are spherical particles with $R_1 = R_2$, the size-dependent term is 4. Therefore, we obtain

$$\beta = \frac{8kT}{3\eta} \quad \text{for } W_{\text{eff}} = 1 \tag{3.8}$$

Using equations (3.7) and (3.8), we can calculate a theoretical value for diffusion-limited aggregation, for instance, in water. At 20°C, the dynamic viscosity of water is 1.012 mPa·s. If the efficiency factor is unity ($W_{\text{eff}} = 1$) (i.e., no repulsive or attractive forces are present), we obtain $\beta = 1.07 \times 10^{-17}\,\text{m}^3/\text{s}$. Herrington and Midmore [3.4] confirmed this maximum value experimentally. They used monodispersed and spherical polystyrene lattices ranging from 121 to 623 nm. The experimentally determined aggregation rates have been found in the range $\beta = (1.5\text{–}3) \times 10^{-18}\,\text{m}^3/\text{s}$. Similar results were obtained for TiO_2, 260 nm in diameter, ($\beta = 6 \times 10^{-18}\,\text{m}^3/\text{s}$) and AgI having a diameter of 53 nm and 73 nm, respectively, and an aggregation kernel of $\beta = 5.89 \times 10^{-18}\text{m}^3/\text{s}$ and $\beta = 5.94 \times 10^{-18}\,\text{m}^3/\text{s}$, respectively.

Gardner and Theis [3.5, 3.6] derived the collision efficiency from experiments with hematite in an aqueous solution. The results were numerically evaluated and an efficiency $W_{\text{exp}} = 0.0001$ was determined (i.e., $\beta = 1.07 \times 10^{-21}\,\text{m}^3/\text{s}$). A system with a much lower efficiency was investigated by Grabenbauer and Glatz [3.7]. An aggregation kernel of $\beta = 2.0 \times 10^{-23}\,\text{m}^3/\text{s}$ was observed for a soy protein.

All these experimentally determined β values are smaller than data calculated according to von Smoluchowski for Brownian diffusion. However, for larger particles, the agglomeration mechanism changes from the perikinetic (Brownian motion) to the orthokinetic mechanism where the flow conditions must be considered.

First, the agglomeration behavior of SiO_2 will be discussed. Schaer [0.4] investigated the nucleation and agglomeration behavior of this system in a T-mixer. The suspension was released in a stirred vessel in which the nuclei were grown to a size of at least 5 nm in order to measure their volumetric number and size. The temperature in the T-mixer was 25°C while the temperature in the stirred vessel was 80°C.

SiO_2 was precipitated from $Na_2O(SiO_2)_{\text{rm}}$ by the addition of sulfuric acid:

$$Na_2O(SiO_2)_{\text{rm}} + H_2SO_4 \leftrightarrow \text{rm}SiO_2 + Na_2SO_4 + H_2O$$

Oligomers are formed by the condensation of monomers $Si(OH)_4$ after nucleation. In a basic milieu, the particles are negatively charged. The repulsive forces avoid aggregation of the particles that grow in a supersaturated solution. However, when the electrolyte concentration is between 0.2 and

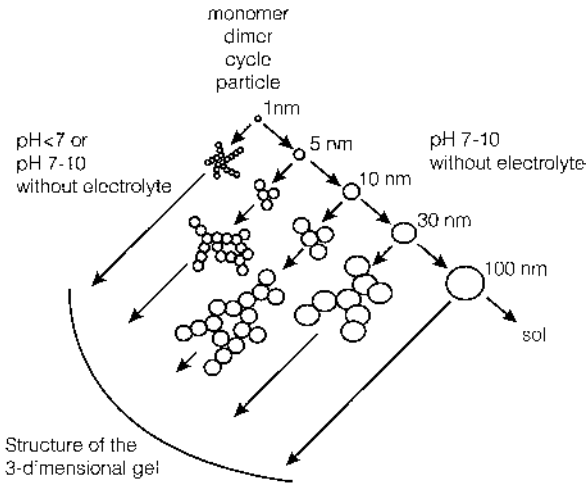

Figure 3.1. Precipitation of silicon particles. (From [0.4].)

$0.3\,\mathrm{mol/dm^3}$, the surface charges are compensated and aggregation will start. In an acid milieu, the repulsive forces are so weak that rapid aggregation takes place.

This behavior is illustrated in Figure 3.1, which shows the structure and development of the aggregates. If the attractive van der Waals forces are larger than the repulsive electrostatic forces at pH < 7, the aggregation starts with two particles on which OH^- ions are adsorbed coming into contact with each other. The monosilicon acid will rapidly cement the two particles together. The critical concentration of coagulation depends on the concentration of SiO_2 and on the temperature; see Figure 3.2.

In Figure 3.3, the particle concentration is plotted against time and Figure 3.4 shows the mean particle size L_{50} as a function of time. As can be seen, the influence of the stirrer speed is always very weak. Calculations of the perikinetic and the orthokinetic aggregation lead to the following results. In the first 5 min, slow perikinetic aggregation takes place. The agglomeration rate is much smaller than would be expected for diffusion-controlled perikinetic aggregation. The reason for this is probably hindrance by electrostatic forces due to the low molar concentration of Na^+ ions ($0.6\,\mathrm{mol/dm^3}$). When this concentration is increased to $0.8\,\mathrm{mol/dm^3}$, the particle concentration of $N = 10^{12}\,\mathrm{m^{-3}}$ is obtained after 180 s instead of $N = 10^{20}\,\mathrm{m^{-3}}$ for $C_{Na^+} = 0.6\,\mathrm{mol/dm^3}$. This rapid decrease can be described by diffusion-controlled perikinetic aggregation; however, it is necessary to take into account the increasing size of the particles and the decreasing

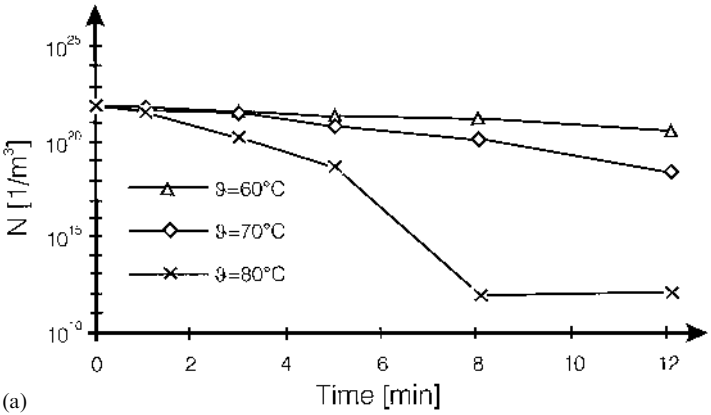

(a)

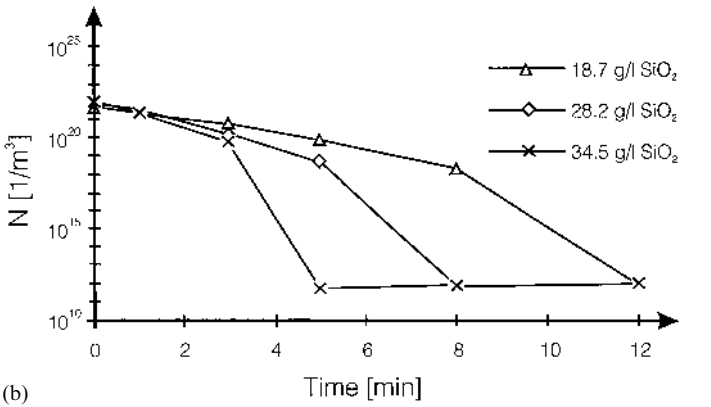

(b)

Figure 3.2. Number of particles per cubic meter suspension versus time; (a) influence of temperature, (b) influence of SiO_2 concentration. (From [0.4].)

diffusivity. After approximately 300 s, a particle size of 0.25 μm is reached, which leads to a change from perikinetic to orthokinetic aggregation.

According to the experimental results, an aggregation kernel of $\beta = 2.48 \times 10^{-14}\,\mathrm{m^3/s}$ was found, which can be compared with a value calculated from [1.3]:

$$\beta = \frac{\dot{\gamma}}{6}(L + \lambda)^3 \tag{3.9}$$

where the shear rate is approximately $\dot{\gamma} = 10\,\mathrm{s^{-1}}$. Using the assumption $L = \lambda = 10\,\mu\mathrm{m}$, the value $\beta = 2.48 \times 10^{-14}\,\mathrm{m^3/s}$ is obtained. The assumed size of 10 μm corresponds well with the values found experimentally; that is,

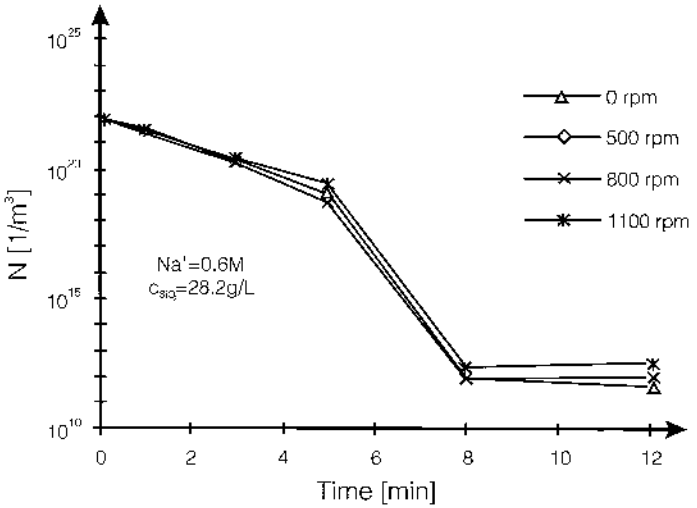

Figure 3.3. Number of particles per volume N against time; influence of stirrer speed. (From [0.4].)

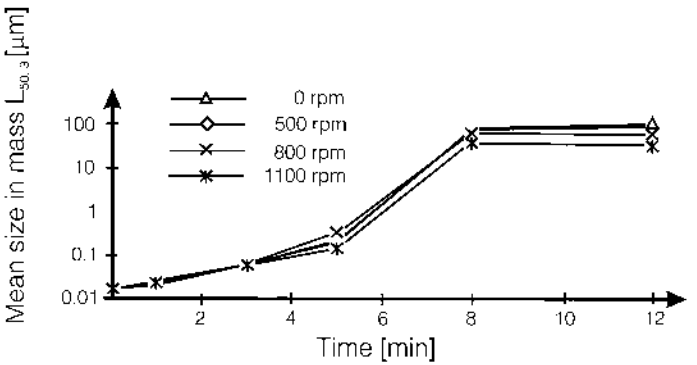

Figure 3.4. Mean particle size L_{50} as a function of time; influence of stirrer speed. (From [0.4].)

it is possible to describe the aggregation mechanism quantitatively. However, it is important to note that a change in the concentration of the feed solution or the stoichiometry can alter the situation completely.

The agglomeration behavior of calcium oxalate in a Couette flow aggregator was studied by Hartel et al. [0.5, 3.8]. The rotational speed of the inner

Table 3.1. Aggregation Kernels of Calcium Oxalate According to [1.2]

Sizes λ, L	β (in m^3/s) for [Ox] < 1 mM and 150 rpm
$\lambda = 5\,\mu m$ $L = 13\,\mu m$	2.75×10^{-13}
$\lambda = 5\,\mu m$ $L = 22\,\mu m$	1.37×10^{-12}
$\lambda = 11\,\mu m$ $L = 17\,\mu m$	2.75×10^{-13}
$\lambda = 11\,\mu m$ $L = 24\,\mu m$	1.37×10^{-12}

cylinder of this apparatus was varied between 1.33 and $4.17\,s^{-1}$. In addition to fluid dynamics, the influence of physicochemical properties was investigated by varying the initial equivalent concentration of calcium and oxalate in the range from 0.6 to 1.8 mM. The authors came to the conclusion that the aggregation kernel could be best described for a turbulent aggregation mechanism due to inertial collisions. At the low oxalate concentration of 0.6 mM, no influence of fluid dynamics has been observed. The authors carried out calculations of the aggregation kernels β for particle sizes between 2 and 30 nm. Aggregation kernels between zero and $\beta = 10^{-12}\,m^3/s$ can be calculated. Some experimental results are listed in Table 3.1. According to equation (3.9), the aggregation kernel increases with the shear rate $\dot{\gamma}$. This shear rate can be described for a system with a fixed and a rotating cylinder and is proportional to its rotational speed [3.9, 3.10]:

$$\dot{\gamma} = 4\pi s \tag{3.10}$$

Assuming that $s = 3\,s^{-1}$, an aggregation kernel $\beta = 1.69 \times 10^{-13}\,m^3/s$ can be calculated for $L = 5\,\mu m$ and $\lambda = 25\,\mu m$. For the sizes $L = 5\,\mu m$ and $\lambda = 13\,\mu m$, $\beta = 3.6 \times 10^{-14}\,m^3/s$ is calculated.

A similar experimental result was found by Skrtic et al. [3.11]. They investigated the aggregation behavior of calcium oxalate trihydrate in a batch crystallizer at 25°C. Applying a shear rate $\dot{\gamma} = 5\,s^{-1}$, they obtained an aggregation kernel $\beta = (3.9 \pm 0.6) \times 10^{-14}\,m^3/s$, which corresponds well with the maximum value found by Hartel et al. [0.5, 1.2]. Similar results will be obtained using the more complex equations given in Table 5.1 for

turbulent flow, whereas the perikinetic aggregation mechanism fails to yield reasonable results.

The authors also found that at higher oxalate concentrations which result in higher supersaturation, the crystal growth rate and the bonding between crystals are enhanced. In addition, the oxalate ions added alter the surface charge and compress the electrical double layer of the crystal, therefore reducing the electrostatic forces.

The disruption of agglomerates has also been studied by these authors. The disruption parameter increased with the speed of the inner cylinder but decreased with the oxalate concentration in the aggregator.

The precipitation of $BaSO_4$ in a 2.4-L MSMPR crystallizer with clear-liquor advance was investigated by Beckman and Farmer [3.12]. The authors found a bimodal crystal size distribution with a median crystal size of 16 μm. Agglomeration is a predominant factor for crystals smaller than 5 μm according to an agglomerative growth mechanism. Typical agglomerates consisted of a number of planar dendritic crystallites cemented together, in particular, at high supersaturation. For complete modeling of size-dependent agglomeration, it is necessary to take into account the fluid dynamics and the chemical environment.

All simplifying calculations show that it is possible to evaluate realistic orders of magnitude of aggregation kernels.

Finally, we will discuss two empirical approaches in which the aggregation kernel β is presented as a function of important variables in crystallization such as the supersaturation or the growth rate. In Figure 3.5, the aggregation kernel β is plotted against the suspension density m_T with the stirrer speed s as parameter according to experimental results obtained from Tavare et al. [3.13].

For the agglomeration of nickel ammonium sulfate in an MSMPR crystallizer according to [3.13], experiments were performed in a 5-L agitated vessel at 25°C with stoichiometric amounts of nickel sulfate and ammonium sulfate solutions. The aggregation kernel found empirically showed that both the growth rate and the nucleation rate, and therefore the supersaturation, have a significant influence on agglomeration. Tavare et al. explained the fact that β decreases with increasing magma density m_T, with the breakage of aggregates, due to higher collision rates and energies.

In Figure 3.6, the aggregation kernel β is plotted against the suspension density of calcite based on experiments carried out by Tai and Chen [3.14]. The experiments were performed in a 2.7-L crystallizer at 30°C and 800 rpm. Unfortunately, the stirrer speed was not varied. In contrast to the findings of Tavare et al., the aggregation rate β increases with the suspension density m_T. Scanning electron micrographs of calcite showed agglomerates of small-

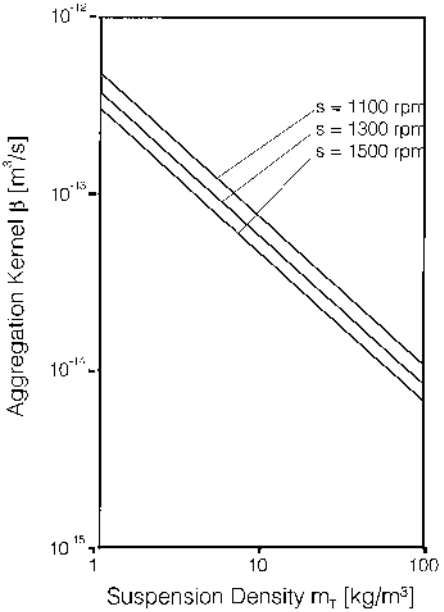

Figure 3.5. Aggregation kernel β versus suspension density m_T with the stirrer speed s as parameter; agglomeration of nickel ammonium sulfate was performed in an MSMPR crystallizer. (From [3.13].)

sized crystals, indicating a long contact time and, therefore, the building of strong agglomerates due to interparticular growth.

4. AVOIDANCE AND PROMOTION OF AGGLOMERATION

The experimental results presented in the last section have clearly shown that the population balance, in combination with appropriate aggregation kernels that are valid for actual disruption functions, is an excellent tool for modeling the process of agglomeration with respect to industrial precipitators. However, it is sometimes difficult to estimate the physico-chemical conditions and the interparticle forces and to determine the appropriate aggregation kernel. It is not easy to predict the efficiency of collisions. The most difficult task is perhaps the prediction of the tensile strength of agglomerates and the modeling of disruption. Aggregation occurs when two or more particles collide and adhere. Simultaneous

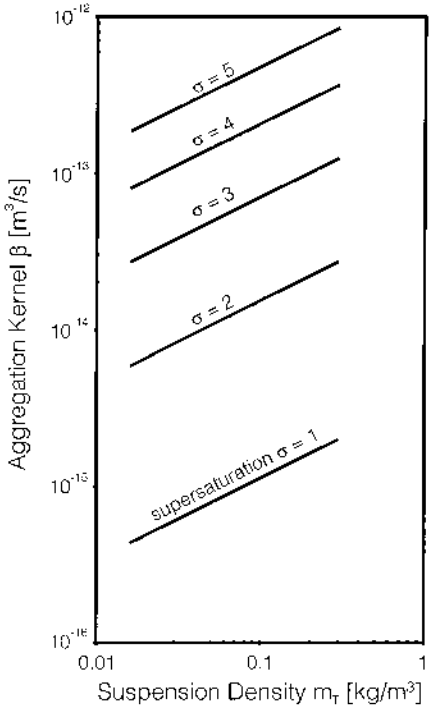

Figure 3.6. Aggregation kernel β versus suspension density m_T of calcite with the supersaturation σ as parameter. (From [3.14].)

encounters between three or more particles are unlikely to occur and can be neglected. Before two particles aggregate, they must first be brought close together by diffusion and/or convection. When the repulsive forces are dominant, the particles will not attach, with the result that the suspension is stable without aggregation. When attractive forces prevail, the particles remain attached to each other after a collision and their growth is controlled by supersaturation. When supersaturation is high and the primary particles of the aggregate remain attached for a certain period of time, crystalline bridges will be formed with the result that the tensile strength is high. In this way, large agglomerates can be formed. The contrary is true when the aggregation takes place at a lower supersaturation in a turbulent flow field with strong shear stresses $\tau \sim \rho_L(v'_{\text{eff}})^2$. In this case, it is necessary to take into consideration the disruption of aggregates and the modeling of this process when formulating the population balance.

In Table 4.1, a summary of all important mechanisms and parameters is given. The purpose of this survey is to give hints to the chemical engineer on how to avoid or at least reduce aggregation that is not desired and on how to promote aggregation that is desired. In order to avoid agglomeration, it is necessary to change the physicochemical conditions of the suspension in such a way that the interparticle repulsive forces are stronger than the attractive forces. The example of the precipitation of SiO_2 has shown that aggregation starts at $pH < 7$. The aggregation is very low for a low concentration of Na^+ ions ($0.4M$) or low temperature ($\vartheta = 60°C$). On the other hand, aggregation was significantly enhanced at a concentration of Na^+ ions of $0.8M$ and at a temperature of $\vartheta = 80°C$. An increase in the SiO_2 concentration from 18.7 to 34.5 kg/m^3 also resulted in more rapid aggregation.

As a rule, the process of aggregation can be promoted by the following:

- Elevated temperature
- Low viscosities
- Small particle sizes
- High particle concentration
- High diffusivities

if the physicochemical conditions allow rapid aggregation. Increasing turbulence or fluctuating velocities v'_{eff}, shear rates $\dot{\gamma}$ ($\dot{\gamma} \sim s$ or $\dot{\gamma} \sim \sqrt{\varepsilon/\nu_L}$), shear stress τ [$\tau = \eta_L \dot{\gamma}$ or $\tau \sim \rho_L (v'_{\text{eff}})^2$] and local specific power input ε [$\varepsilon = (v'_{\text{eff}})^3/\Lambda$] favor the collision frequency and aggregation. However, due to increasing shear stresses, the disruption of weakly bonded aggregates becomes stronger. It has often been observed that aggregation is first promoted with increasing shear or turbulence but then reduced. Therefore, the aggregation rate passes through a maximum with increasing shear and the diameter of the aggregates is limited to a maximum size.

Up to now, it has been assumed that every collision leads to an aggregation event, but this is not the case. If there are weak repulsive interactions between particles (electrostatic double-layer repulsion and/or steric effects), the aggregation kernel has to be multiplied with an efficiency factor between 0 and 1. As a rule, this will be a fitting factor obtained from experiments because the real mechanisms are complex and difficult to describe.

It has been shown that the process of agglomeration is induced by interparticle collisions and that the collision frequency in multiparticle systems is a very important parameter which depends on shear rates and on fluctuating velocities in a turbulent flow. For this reason, a short review on fluid dynamics in agglomerators will be given.

Table 4.1. Summary of Mechanisms Influencing the Aggregation of Particles in Solution

	Interparticle forces	Properties of: Particles	Properties of: Solution	Fluid dynamics
Parameter	van der Waals force: Hamaker constant A electric permittivity ε_r refractive index n Electrostatic repulsion force: ionic strength I pH Solvation forces: attractive: hydrophobic force repulsive: hydration force Steric repulsive forces Osmotic force	Diffusivity D_{AB} Particle size L, λ Particle concentration ζ-Potential ζ (surface potential ψ_0) Tensile strength σ_t Young's modulus E Fracture resistance Γ	Temperature T Density ρ_L Viscosity η_L Surface tension γ_{LG} Supersaturation σ Ionic strength I pH Electric permittivity ε_r Refractive index n Velocity of the bulk solution relative to the interface v_0	Fluctuating velocity u' Shear rate $\dot{\gamma} \sim s$ or $\dot{\gamma} \sim \sqrt{\varepsilon/\nu}$ Shear stress $\tau = \eta_L \dot{\gamma}$ $\tau \sim \varphi(v'_{\text{eff}})^2$ Local specific power $\varepsilon = (v'_{\text{eff}})^3/\Lambda$ Mean specific power $\bar{\varepsilon} \sim s^3 D^2$ Ratio $\varepsilon/\bar{\varepsilon}$
Comments	Addition of hydrophobic adsorptives favors aggregation		Elevated temperature, high diffusivities, small particles, high volumetric particle numbers, low viscosity, high supersaturation and strong bonding forces favor aggregation	Fluid dynamics bivalent: Increase in v', $\dot{\gamma}$, τ, ε, $\bar{\varepsilon}$ leads to increase of collision frequency → promotion of aggregation Increase of disruption → avoidance of aggregation

5. COLLISIONS IN MULTIPARTICLE SYSTEMS

The frequency and the intensity of collisions depend on the fluid dynamics in the agglomerator which can be a stirred vessel with the stirrer tip speed u_{tip}, a fluidized bed with the superficial velocity $\dot{v}_L$, or a Couette flow apparatus.

Let us begin with the stirred vessel, which is widely used in industry (cf. Chapter 5). The movements of particles depend on the mean velocity $\bar{v}$ and the mean fluctuating velocity v'_{eff} of a turbulent flow with $0 < \bar{v} < u_{tip}$ and $v'_{eff,min} < v'_{eff} < v'_{eff,max}$. The mean velocity and the mean fluctuating velocities are proportional to the tip speed of the stirrer with

$$\bar{v} \sim u_{tip} \tag{5.1}$$

and

$$v'_{eff} \sim u_{tip} \tag{5.2}$$

with $v'_{eff} = \sqrt{\overline{(v')^2}}$ (see Chapter 9) and depend on the Power number Po of the stirrer with the definition

$$\mathrm{Po} = \frac{P}{\rho_{sus} s^3 D^5} \tag{5.3}$$

Here, P is the power consumption of the stirrer. Information on the Power number is given in Chapters 5 and 8. The maximum fluctuating velocity $v'_{eff,max}$ is given by [5.1]

$$v'_{eff,max} = 0.18\mathrm{Po}^{7/18} u_{tip} \tag{5.4}$$

and the minimum fluctuating velocity $v'_{eff,min}$ can be calculated from

$$v'_{eff,min} = 0.088\mathrm{Po}^{7/18} \left(\frac{D}{T}\right)^{3/2} u_{tip} \tag{5.5}$$

In Figure 5.1, the cumulative number distribution of the fluctuating velocities is plotted against the ratio v'_{eff}/u_{tip} for different ratios D/T of the diameters D (stirrer) and T (tank). The larger the D/T ratio, the more uniform is the distribution of the fluctuating velocities.

The local specific power input ε is given by

$$\varepsilon = \frac{(v'_{eff})^3}{\Lambda} \tag{5.6}$$

with Λ as the macroscale of turbulence. As a rough estimate [3.10],

$$\Lambda = 0.15\mathrm{Po}_{turb}^{5/9} \frac{u_{tip}}{v'_{eff}} D \tag{5.7}$$

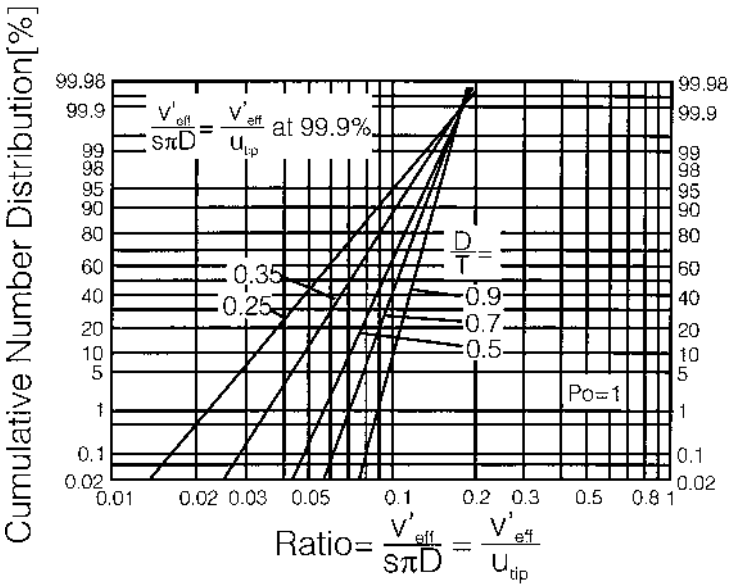

Figure 5.1. Integral $\int dV/V_{\text{tot}}$ as a function of the ratio $v'_{\text{eff}}/u_{\text{tip}}$ in a logarithmic probability plot.

is valid. The microscale of turbulence, λ_k, and the characteristic time scale, τ_k, of turbulence are defined as

$$\lambda_k = \left(\frac{\nu_L^3}{\varepsilon}\right)^{1/4} \tag{5.8}$$

and

$$\tau_k = \left(\frac{\nu_L}{\varepsilon}\right)^{1/2} \tag{5.9}$$

respectively. The mean specific power input, $\bar{\varepsilon}$, can be calculated from

$$\bar{\varepsilon} = \frac{4\text{Po}}{\pi}\frac{s^3 D^5}{T^3} \quad \text{for } H = T \tag{5.10}$$

or

$$\bar{\varepsilon} = \frac{4\text{Po}}{\pi^4}\left(\frac{D}{T}\right)^2 \frac{(u_{\text{tip}})^3}{H} \tag{5.11}$$

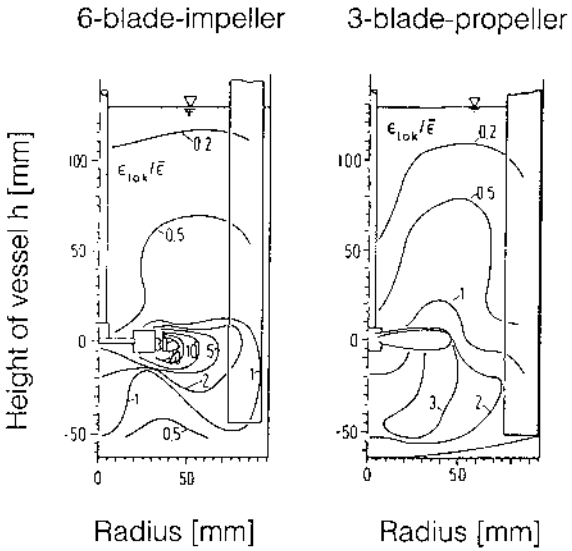

Figure 5.2. Lines of constant energy dissipation $\varepsilon/\bar{\varepsilon}$ for different stirrers in water. (From [3.10].)

with H as the filling height of the stirred vessel. The ratio $\varepsilon/\bar{\varepsilon}$ has been determined for different stirrers and does not depend on the size of the vessel when the geometry is similar and the stirrer Reynolds number is

$$\mathrm{Re} = \frac{sD^2}{\nu_L} > 10^4 \tag{5.12}$$

In Figures 5.2 and 5.3, lines of constant $\varepsilon/\bar{\varepsilon}$ values are drawn. These data allow the local specific power input and the local fluctuating velocities to be predicted at any point in the vessel for $\mathrm{Re} > 10^4$. The mean shear rate, $\bar{\dot{\gamma}}$, in a stirred vessel with a rotating cylinder as stirrer can be calculated from

$$\bar{\dot{\gamma}} = 4\pi s \tag{5.13}$$

and for other stirrers, we obtain approximately [5.1]

$$\bar{\dot{\gamma}} \approx 50 \frac{D}{T} \left(\frac{D}{H}\right)^{1/2} s \tag{5.14}$$

The difference $\Delta v'_{\mathrm{eff}}$ between two local fluctuating velocities at two points in the vessel at a distance Δr from each other depends on the local specific power input ε and the viscosity ν_L when the microscale of turbulence λ_k is

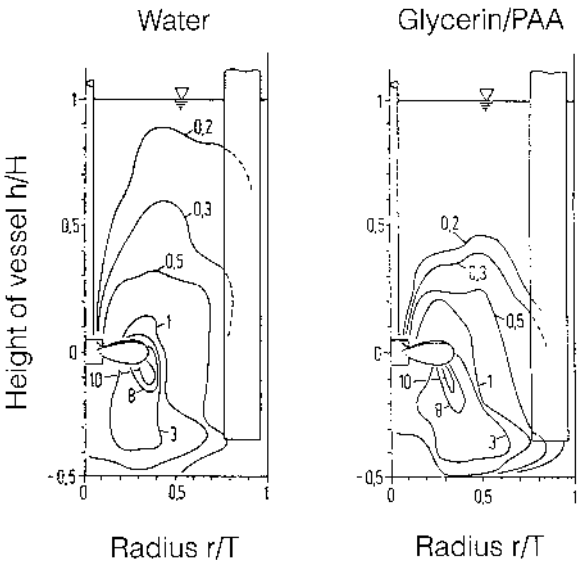

Figure 5.3. Lines of constant energy dissipation $\varepsilon/\bar{\varepsilon}$ in water and a non-Newtonian solution of glycerin and PAA. (From [5.1].)

large in comparison to the distance Δr. The mean difference $\Delta v'_{\text{eff}}$ is then given by [5.3]

$$\Delta v'_{\text{eff}} = 0.0676\left(\frac{\varepsilon(\Delta r)^2}{\nu_L}\right)^{1/2} \quad \text{for } 0 < \Delta r < 5\lambda_k \tag{5.15}$$

When, however, the microscale of turbulence is small in comparison to Δr, the difference $\Delta v'_{\text{eff}}$ is no longer dependent on the liquid viscosity and is only a function of the local specific power input ε (compare equation 5.1.26):

$$\Delta v'_{\text{eff}} = 1.9(\varepsilon \Delta r)^{1/3} \quad \text{for } 20\lambda_k < \Delta r < 0.05\Lambda \tag{5.16}$$

It is important to note that the ratio $\Delta v'_{\text{eff}}/\Delta r$ is a frequency and the aggregation kernel is the product of a collision frequency and a volume provided by the particles. Equation (5.16) can be rewritten in the simple form

$$\frac{\Delta v'_{\text{eff}}}{\Delta r} = 0.0676\left(\frac{\varepsilon}{\nu_L}\right)^{1/2} \tag{5.17}$$

and equation (5.17) correspondingly reads

Table 5.1. Collision Kernel β_{col} in Laminar, Turbulent, and Gravitational Shear Fields

Mechanism	Collision frequency	Restrictions	Ref.
	$\beta_{col} = \frac{4}{3}\bar{\dot{\gamma}}(R_1 + R_2)^3$ with $\bar{\dot{\gamma}} = \left(\frac{\varepsilon}{\nu_L}\right)^{1/2}$ or $\beta_{col} = \sqrt{\frac{8\pi}{15}}\left(\frac{\varepsilon}{\nu}\right)^{1/2}(R_1 + R_2)^3$ with $R_i = \frac{L_i}{2}$	• Particles follow fluid motion completely • $R_1 + R_2$ is small compared with smallest eddies $\Rightarrow L$, $\lambda < (\nu^3/\varepsilon)^{1/4}$ • Relaxation time $\ll$ period of small-scale motion of fluid $\tau = \frac{2R_i^2\rho_C}{9\eta_L} < \tau_k = \left(\frac{\nu_L}{\varepsilon}\right)^{1/4}$ $\Rightarrow \varepsilon \approx 0.1\,\mathrm{W/kg}$ and $L \approx 50\,\mu\mathrm{m}$ in water	5.4, 5.5
Turbulent flow	$\beta_{col} = \sqrt{8\pi}(R_1 + R_2)^2(\bar{U}_1^2 + \bar{U}_2^2)^{1/2}$ $\bar{U}$ is the mean squared velocity deviation of the flux [5.6]	High energy dissipation or large particles ($L \geq 100\,\mu\mathrm{m}$ in water), $L^2 > \frac{15\eta_L\bar{U}^2}{\rho_C\varepsilon}$	5.6
	$\beta_{col} = \sqrt{\frac{8\pi}{3}}(R_1 + R_2)^2\sqrt{w_{accel}^2}$ w_{accel} is the relative velocity between the particles and the suspending fluid [5.5, 5.7]	$\sqrt{\Theta_1\Theta_2} < 0.1$ and $\sqrt{\Theta_1\Theta_2} > 10$; θ_i dimensionless particle relaxation time $\Rightarrow L < 85\,\mu\mathrm{m} + L > 270\,\mu\mathrm{m}$ in water for $\rho_C = 2500\,\mathrm{kg/m^3}$	5.7
	$\beta_{col} = \sqrt{\frac{8\pi}{3}} \cdot (R_1 + R_2)^{7/3} \cdot \varepsilon^{1/3}$	$L \approx \lambda_k = \left(\frac{\nu_L^3}{\varepsilon}\right)^{1/4}$	5.8

Perikinetic agglomeration: Brownian motion or diffusion	$\beta_{\text{col}} = \dfrac{2kT}{3\eta_L}\left(\dfrac{1}{R_1}+\dfrac{1}{R_2}\right)(R_1+R_2)$ $\beta_{\text{col}} = \dfrac{8kT}{3\eta_L}$ if $R_1 = R_2$	$R_i < 0.5\,\mu\text{m}$ (submicron particles)	1.3
Orthokinetic agglomeration: laminar shear	$\beta_{\text{col}} = \frac{4}{3}\dot{\gamma}(R_1+R_2)^3$	$L, \lambda \approx 1, \ldots, 100\,\mu\text{m}$	1.3
Gravity	$\beta_{\text{col}} = \pi g(R_1+R_2)^2\left(1-\dfrac{\rho_C}{\rho_L}\right)\lvert\tau_1-\tau_2\rvert$ with $\tau_i = \dfrac{2R_i^2\rho_C}{9\eta_L}$ valid for $\text{Re}_P < 1$		5.5
Turbulent flow and gravity	$\beta_{\text{col}} = \sqrt{8\pi}(R_1+R_2)^2\left[\left(1-\dfrac{\rho_C}{\rho_L}\right)(\tau_1-\tau_2)^2(\bar{a}^2+\frac{1}{3}g^2)+\dfrac{(R_1+R_2)}{9}\dfrac{\varepsilon}{\nu_L}\right]^{1/2}$ with $\bar{a}^2 = 1.3\left(\dfrac{\varepsilon^3}{\nu_L}\right)^{1/2}$		5.5

$$\frac{\Delta v'_{\text{eff}}}{\Delta r} = 1.9\left(\frac{\varepsilon}{\Delta r^2}\right)^{1/3} \tag{5.18}$$

It should be recalled that the effective value of the fluctuating velocity, v'_{eff}, is proportional to the mean flow velocity v and that the ratio of any velocity and a distance can be interpreted as a frequency. This is the background of equations for the aggregation kernels listed in Table 5.1. These kernels have the dimension volume per time and the unit is cubic meter per second. The two kernels according to von Smoluchowski have already been explained. The other kernels can be divided into two groups: When the fluctuating velocities v'_{eff} and the local specific power input $\varepsilon \approx 5(v'_{\text{eff}})^3/D$ are high and the settling velocity w_s of the particles is small (small L and $\Delta\rho$), forces of the turbulent flow are dominant. In this case, the aggregation kernels are dependent on the ratio λ_k/L. Furthermore, the fluctuating velocities v'_{eff}, the local specific power input, and, for $L > \lambda_k$, the viscosity play a role. In the case of gravitational settling in the laminar region, the ratio $w_s/\Delta r$ of the settling velocity w_s and the distance Δr is proportional to the frequency $\Delta r \Delta\rho g/\eta_L$, which can be found in the corresponding equations. If forces caused by the turbulent flow and gravity play a role, the aggregration kernel can be composed of the two contributions.

After a certain number of successful unification events, an aggregate approaches a size so that it is influenced by shear forces in a way that may lead to a disruption event. The probability of such an event depends on the interparticle forces that are acting between the primary particles of an aggregate. Let us have a brief look at the nature and order of magnitude of these forces.

6. TENSILE STRENGTH OF AGGREGATES

Let us consider an aggregate which consists of two particles connected by a bridge; see Figure 6.1. The tensile strength of such an aggregate depends on the geometry and the physical properties of the bridge, which can consist of

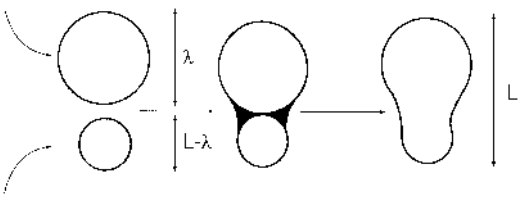

Figure 6.1. Crystals forming a crystalline bridge after agglomeration.

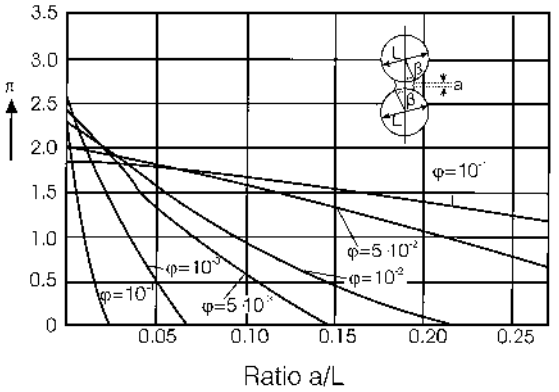

Figure 6.2. Force of adherence π against the dimensionless distance a/L with the liquid holdup φ as the parameter. (From [6.1].)

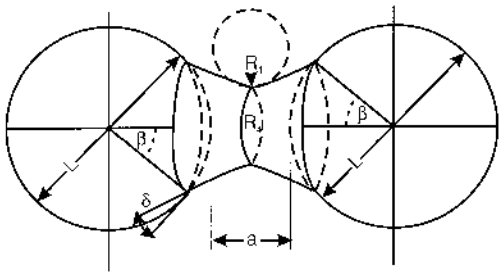

Figure 6.3. Geometry of liquid bridge described by angle β.

a liquid, a suspension, or crystalline solid material. Liquid bridges have been thoroughly investigated by Schubert [6.1]. According to this author, the force of adherence, F_{adh}, is plotted against the dimensionless distance a/L with the liquid holdup $\varphi = V_L/2V_C$ as the parameter in Figure 6.2. Here, V_L denotes the liquid volume of the bridge and V_C is the volume of a crystal.

The maximum dimensionless tensile strength π is given by

$$\pi = \frac{F_{\max}}{\gamma_{\text{LG}} L} \tag{6.1}$$

The smaller the volumetric holdup φ of the liquid within the aggregate, the smaller is the tensile strength. The geometry of the liquid bridge can be described by the angle β, which is explained in Figure 6.3. As the distance

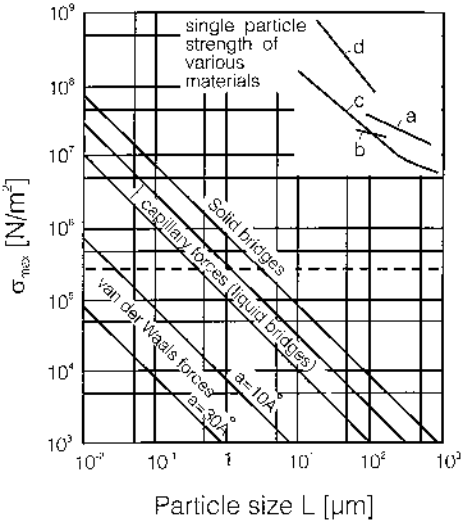

Figure 6.4. General graph of maximum transmissible tensile stresses for different types of bonding in relation to primary grain size of agglomerates.

between the two particles increases, the tensile force is reduced. Because this force is proportional to the particle size L, the tensile strength $\sigma \sim F/L^2 \sim \gamma_{LG}L/L^2 \sim \gamma_{LG}/L$ is inversely proportional to the particle size L. This can be seen in Figure 6.4, in which the maximum tensile strength σ_{max} is plotted against the size of two spherical particles.

Aggregates are composed of many particles between which the porosity ε remains. Investigations have shown that the strength of aggregates increases with the number of contacts between the particles within an aggregate and that this number is proportional to π/ε. This leads to the following basic equation for the tensile strength σ:

$$\sigma = \frac{(1-\varepsilon)}{\varepsilon}\frac{F}{L_{12}^2} \sim \frac{(1-\varepsilon)}{\varepsilon}\frac{\gamma_{LG}}{L} \tag{6.2}$$

High tensile strengths can be expected for aggregates composed of small particles, which lead to a small porosity ε of the agglomerate. As a rule, aggregates of particles with a favorable size distribution ($\varepsilon \to 0$) are stronger than aggregates of monodisperse particles.

Let us now consider aggregates formed by precipitation or crystallization. When the aggregates are not generated at very high supersaturation ($S < 0.1C_C/C^*$), a crystalline bridge will form between the primary crystals

due to crystal growth. The tensile strength of such real polycrystals is the decisive material property. In Chapter 5, the equation of Orowan [6.2]

$$\frac{\Gamma}{K} \approx 1.7E\left(\frac{1}{nC_C N_A}\right)^{1/3} \tag{6.3}$$

was presented for the fracture resistance, which is now the decisive material property rather than the surface tension γ_{LG}. The fracture resistance is approximately two orders of magnitude higher than the surface tension. In Chapter 5, (Γ/K) data between 5 and 15 J m^{-2} can be found. (The surface tension of water/air is $\gamma_{LG} = 0.072\,\text{J/m}^2$ at 20°C.) Consequently, the tensile strength of aggregates formed after crystallization is approximately two orders of magnitude higher than for aggregates with liquid bridges. It is not surprising that large crystals produced by crystallization at low supersaturation ($S < 1.1$) exhibit the highest tensile strength σ_{max}, which can be evaluated from

$$\sigma_{max} \approx 0.005E \tag{6.4}$$

With Young's modulus $E \approx 2 \times 10^{10}\,\text{N/m}^2 = 2 \times 10^{10}\,\text{J/m}^3$, tensile strength of the order of magnitude of $\sigma = 10^8\,\text{N/m}^2$ can be expected for 1-mm polycrystals. Again, the strength σ of real polycrystals with $L < 100\,\mu\text{m}$ is inversely proportional to their size. The geometry of the crystalline bridge depends on the supersaturation and the growth period. The equations presented here allow the prediction of the order of magnitude of particle strength.

REFERENCES

[0.1] S. Jancic and J. Garside, A new technique for accurate crystal size distribution analysis in a MSMPR crystallizer, in *Industrial Crystallization* (J. W. Mullin, ed.), Plenum Press, New York (1976).

[0.2] R. Ploss, Modell zur Kontaktkeimbildung durch Rührer/Kristall-Kollisionen in Leitrohrkristallisatoren, Thesis, Technische Universität München (1990).

[0.3] I. T. Rusli and M. A. Larson, Nucleation by cluster coalescence, in *Proc. 10th Symp. on Industrial Crystallization* (J. Nyvlt and S. Zacek, eds.), Elsevier, Amsterdam (1989).

[0.4] E. Schaer, Conception d'un procédé pour la production de microparticules filtrables et redispersables, Thesis, Institut Nationale Polytechnique de Lorraine Ensic (1996).

[0.5] R. W. Hartel, B. E. Gottung, A. D. Randolph, and G. W. Drach, Mechanisms and kinetic modeling of calcium oxalate crystal aggrega-

tion in a urinelike liquor. I. Mechanisms, *AIChE J.*, *32*(7): 1176 (1986).
[0.6] H. Schubert, Principles of agglomeration, *Int. Chem. Eng.*, *21*: 363 (1981).
[0.7] A. G. Jones, Agglomeration during crystallization and precipitation from solution, *IChemE 5th Int. Symp. on Agglomeration* (1989).
[0.8] R. J. Batterham, M. Cross, and J. A. Thurlby, A review of modelling in agglomeration systems, *IChemME 5th Int. Symp. on Agglomeration* (1989).
[0.9] P. J. Cresswell and T. Nguyen, *Proc. International Alumina Quality Workshop*, pp. 231–239 (1988).
[0.10] M. L. Steemson, E. T. White, and R. J. Marshall, Mathematical model of the precipitation of a Bayer plant, *Light Metals*, 237 (1984).
[0.11] H. Ooshima, G. Sazaki, and Y. Harano, Effects of lysozyme and some amino acids on precipitation of thermolysin, in *Proc. 11th Symp. on Industrial Crystallization* (A. Mersmann, ed.), pp. 285–290 (1990).
[0.12] O. Söhnel, J. W. Mullin, and A. G. Jones, Crystallization and agglomeration kinetics in a batch precipitation of strontium molybdate, *Ind. Eng. Chem. Res.*, *27*(9): 1721 (1988).
[1.1] A. D. Randolph and M. A. Larson, *Theory of Particulate Processes*, 2nd ed., Academic Press, San Diego, CA (1988).
[1.2] R. W. Hartel and A. D. Randolph, Mechanisms and kinetic modeling of calcium oxalate crystal aggregation in a urinelike liquor. II. Kinetic modeling, *AIChE J.*, *32*(7): 1186 (1986).
[1.3] M. von Smoluchowski, Versuch einer mathematischen Theorie der Koagulationskinetik kolloider Lösungen, *Zeitschr. Phys. Chem.*, *92*: 129 (1917).
[1.4] M. J. Hounslow, Nucleation, growth, and aggregation rates from steady-state experimental data, *AIChE J.*, *36*: 1748 (1990).
[1.5] J. Villermaux, *Génie de la réaction chimique—Conception et fonctionnement des réacteurs*, 2nd ed., Tec & Doc-Lavoisier (1993).
[2.1] B. V. Derjaguin and L. Landau, Theory of the stability of strongly charged lyophobic sols and of the adhesion of strongly charged particles in solutions of electrolytes, *Acta Physicochim. URSS*, *14*: 633–662 (1941).
[2.2] E. J. W. Verwey and J. T. G. Overbeek, *Theory of Stability of Lyophobic Colloids*, Elsevier, Amsterdam (1948).
[2.3] F. London, The general theory of molecular forces, *Trans. Faraday Soc.*, *33*: 8 (1937).
[2.4] J. Israelachvili, *Intermolecular & Surface Forces*, 2nd ed., Academic Press, London (1991).

[2.5] R. J. Hunter, *Foundations of Colloid Science Volume I*, Clarendon Press, Oxford (1987).
[2.6] P. C. Hiemenz, *Principles of Colloid and Surface Chemistry*, 2nd ed., Marcel Dekker, Inc. New York, p. 695 (1986).
[2.7] R. M. Pashley, Hydration forces between mica surfaces in electrolyte solutions, *Adv. Colloid Interf. Sci.*, *16*: 57 (1982).
[3.1] G. R. Zeichner and W. R. Schowalter, Use of trajectory analysis to study stability of colloidal dispersions in flow fields, *AIChE J.*, *23*: 243 (1977).
[3.2] T. G. M. van de Ven and S. G. Mason, The microrheology of colloidal dispersions. VII. Orthokinetic doublet formation of spheres, *Colloid Polym. Sci*, *255*: 468 (1977).
[3.3] N. Fuchs, Über die Stabilität und Aufladung der Aerosole, *Zeitschr. Phys.*, *89*: 736 (1934).
[3.4] T. M. Herrington and B. R. Midmore, Determination of rate constants for the rapid coagulation of polystyrene microspheres using photon correlation spectroscopy, *J. Chem. Soc. Faraday Trans.*, *85*: 3529 (1989).
[3.5] K. H. Gardner and T. L. Theis, Colloid aggregation: Numerical solution and measurements, *Colloids Surfaces A: Physicochem. Eng. Aspects*, *141*: 237 (1998).
[3.6] K. H. Gardner and T. L Theis, A unified model for particle aggregation, *J. Colloid Interf. Sci.*, *180*: 162 (1996).
[3.7] G. C. Grabenbauer and C. E. Glatz, Protein precipitation–Analysis of particle size distribution and kinetics, *Chem. Eng. Commun.*, *12*: 203 (1981).
[3.8] R. W. Hartel, B. E. Gottung, A. D. Randolph, and G. W. Drach, Mechanisms and kinetic modeling of calcium oxalate crystal aggregation in a urinlike liquor—Part I: Mechanisms, *AIChE J.*, *32*: 1176 (1986).
[3.9] R. Zeppenfeld, *Verfahrenstechnik der Polysaccharidfermentation im Rührreaktor*, Thesis, Technische Universität München (1988).
[3.10] F. C. Werner, *Über die Turbulenz in gerührten newtonschen und nichtnewtonschen Fluiden*, Thesis, Technische Universität München (1997).
[3.11] D. Skrtic, M. Markovic, and H. Furedi-Milhofer, Orthokinetic aggregation of calcium oxalate trihydrate, *Ind. Crystall.*, *84*: 421 (1984).
[3.12] J. R. Beckman and R. W. Farmer, Bimodal CSD barite due to agglomeration in an MSMPR crystallizer, *AIChE Symp. Series, 253*(83): 85 (1987).

[3.13] N. S. Tavare, M. B. Shaw, and J. Garside, Crystallization and agglomeration kinetics of nickel ammonium sulphate in an MSMPR crystallizer, *Powder Technol.*, *44*: 13 (1985).
[3.14] C. Y. Tai and P. C. Chen, Nucleation, agglomeration and crystal-morphology of calcium carbonate, *AIChE J.*, *41*: 68 (1995).
[5.1] A. B. Mersmann, F. C. Werner, S. Maurer, and K. Bartosch, Theoretical prediction of the minimum stirrer speed in mechanically agitated suspensions, *Chem. Eng. Proc.*, *37*: 503 (1998).
[5.2] R. K. Geisler, *Fluiddynamik und Leistungseintrag in turbulent gerührten Suspensionen*, Thesis, Technische Universität München (1991).
[5.3] J. O. Hinze, *Turbulence*, 2nd ed., McGraw-Hill, New York (1975).
[5.4] T. R. Camp and P. C. Stein, Velocity gradients and internal work in fluid motion, *J. Boston Soc. Civil Eng.*, *30*: 219–237 (1943).
[5.5] P. G. Saffman and J. S. Turner, On the collision of drops in turbulent clouds, *J. Fluid Mech.*, *1*: 16–30 (1956).
[5.6] J. Abrahamson, Collision rates of small particles in a vigorously turbulent fluid, *Chem. Eng. Sci.*, *30*: 1371–1379 (1975).
[5.7] F. E. Kruis, K. A. Kusters, The collision rate of particles in turbulent flow, *Chem. Eng. Commun.*, *158*: 201–230 (1997).
[5.8] R. Kuboi, I. Komasawa, and T. Otake, Behavior of dispersed particles in turbulent liquid flow, *J. Chem. Eng. Japan, 5*: 349–355 (1972).
[6.1] H. Schubert, Principles of agglomeration, *Int. Chem. Eng.*, *21*: 363–377 (1981).
[6.2] E. Orowan, Fracture and strength of solids, *Rep. Prog. Phys.*, *12*: 185 (1949).

7
Quality of Crystalline Products

A. MERSMANN Technische Universität München, Garching, Germany

In addition to the median crystal size, important quality parameters include the crystal size distribution (CSD) and the coefficient of variation (CV). Furthermore, the shape of crystals and their purity play an important role in commercial products. The rates of nucleation, growth, agglomeration, and attrition determine the size distribution and median size L_{50} of crystals produced in batch or continuously operated crystallizers. For the sake of simplicity, let us consider an (MSMPR) mixed suspension, mixed product removal crystallizer for which the median crystal size L_{50} depends on the growth rate G, the nucleation rate B, and the volumetric holdup φ_T [see equation (4.2.34)]:

$$L_{50} = 3.67\sqrt[4]{\frac{G}{6\alpha B_0}\varphi_T} \tag{0.1}$$

The previous chapters have shown that despite the general occurrence of growth-rate dispersions for primary and secondary nuclei as well as for large crystals, some general statements can be made concerning a large number of

crystals growing in a solution free of impurities and additives. This is not the case with respect to the rates of nucleation because the origin of the nuclei can differ greatly. In general, the rate of nucleation is the sum of the rates of homogeneous (B_{hom}), heterogeneous (B_{het}), and secondary (B_{sec}) nucleation:

$$B_0 = B_{\text{hom}} + B_{\text{het}} + B_{\text{sec}} \quad \text{with } B_{\text{sec}} = B_a + B_{\text{surf}} \tag{0.2}$$

The rate of secondary nucleation may be subdivided according to various mechanisms, such as cluster detachment, shear stress, fracture, attrition, and needle breaking, or according to the different types of collision, such as crystal–crystal collision and crystal–rotor collision. It is presumed that secondary nucleation dominates in systems of high solubility due to the fact that a coarse product is usually obtained.

On the other hand, the relative supersaturation σ in systems of low solubility is greater than in highly soluble systems. Therefore, nuclei are generated (mainly by primary nucleation) to such an extent that the median crystal size is greatly reduced, with the result that secondary nucleation no longer plays an important role. However, it is often necessary to take into account both agglomeration, especially at high levels of supersaturation, and the disruption of large agglomerates in the vicinity of rotors with a high local specific stress. Despite the variety of all these parameters, it is possible to make some general remarks about the median crystal size to be expected for a certain system crystallized in an apparatus under specific operating conditions.

1. MEDIAN CRYSTAL SIZE

In this section, a more general method for predicting median crystal sizes is introduced, depending on (a) the type and geometry of the crystallizer, (b) the operating conditions of the crystallizer, and (c) the physical properties of the supersaturated solution and of the crystals. When operating a crystallizer continuously, it is important to choose the maximum permitted, most economical, or optimal supersaturation ΔC for the corresponding residence time $\tau = V_{\text{sus}}/\dot{V}$ as well as the mean specific power input ($\bar{\varepsilon}$) and suspension density m_T. Here, V_{sus} represents the suspension volume of the crystallizer and $\dot{V}$ stands for the volumetric feed rate of a cooling crytallizer.

Information on the metastable zone width and the optimal supersaturation has been given at the end of Chapter 3. Let us repeat the basic idea and demonstrate how the most economical supersaturation can be estimated.

Because the increase in the nucleation rate B with supersaturation ΔC is greater than with the growth rate G, the median crystal size L_{50} passes through a maximum at optimum supersaturation $(\Delta C)_{\text{opt}}$. At

$\Delta C > (\Delta C)_{\text{opt}}$, many small attrition fragments or foreign particles, which are always in suspension, grow into the product range, with the result that the median size L_{50} is reduced. For example, let us assume that a huge number of attrition fragments of size $L_a \approx 10\,\mu\text{m}$ is present in the slurry of an industrial crystallizer. As shown earlier, the mass transfer coefficient k_d is approximately $k_d \approx 10^{-4}\,\text{m/s}$ for crystals where $L > 100\,\mu\text{m}$ in solutions of low viscosity in crystallizers operating at $0.1\,\text{W/kg} < \bar{\varepsilon} > 0.5\,\text{W/kg}$. The metastable zone width $\Delta C_{\text{met,sec}}/C_c$ or $\sigma_{\text{met,sec}}$ for secondary nucleation can be calculated with the equation (see Sec. 3.6):

$$\frac{\Delta C_{\text{met,sec}}}{C_c} = \frac{L - L_a}{2t_{\text{ind}}k_d} \tag{1.1}$$

for diffusion-controlled growth and from the equation

$$\sigma_{\text{met,sec}} \approx \left(\frac{L - L_a}{2t_{\text{ind}}k_g'}\right)^{1/g} \tag{1.2}$$

for integration-controlled growth. Assuming that the order of growth is $g = 2$, the latter equation becomes

$$\sigma_{\text{met,sec}} \approx \left(\frac{L - L_a}{2t_{\text{ind}}k_g'}\right)^{1/2} \tag{1.3}$$

It can be seen that the metastable zone width depends on (a) the kinetic coefficient k_d or k_g', (b) the induction time period t_{ind}, and (c) the size L of outgrown attrition fragments.

With coarse crystalline products ($L_{50} \geq 500\,\mu\text{m}$), the size $L/2 \approx 100\,\mu\text{m}$ may be sensitive to CSD. If a large number of attrition fragments of the size $L_a \ll L$ grew during the residence time $\tau = t_{\text{ind}}$ to a size of $L/2 = 100\,\mu\text{m}$, the median size of the crystalline product would be greatly reduced. An induction time t_{ind} of the order of magnitude of $t_{\text{ind}} = 10^3\text{s}$ is feasible with respect to a mean residence time $\tau = 1\,\text{h}$ of crystals in a cooling or evaporative crystallizer. Using these data, it is possible to evaluate the metastable zone width $\Delta C_{\text{met,sec}}$ in order to get some idea of the optimal supersaturation $\Delta C_{\text{opt}} < \Delta C_{\text{met,sec}}$.

In the case of diffusion-controlled growth, we obtain

$$\frac{\Delta C_{\text{met,sec}}}{C_c} \approx \frac{L}{2t_{\text{ind}}k_d} \approx \frac{10^{-4}\text{m}}{10^3\text{s} \times 10^{-4}\text{m/s}} \approx 10^{-3} \tag{1.4}$$

Furthermore, equation (1.3) gives an initial estimate of the metastable relative supersaturation $\sigma_{\text{met, sec}}$, again for the induction time $t_{\text{ind}} = 10^3\,\text{s}$. Equation (3.16), 2.72c of Chapter 3 allows the kinetic growth coefficient k_g' to be evaluated. With $C^*/C_c = 0.01$, $D_{AB} = 10^{-9}\text{m}^2/\text{s}$, and $d_m = 5 \times 10^{-10}\text{m}$,

we obtain $k_g' \approx 10^{-5}$ m/s. If growth is purely integration controlled, the metastable zone width is of the following order of magnitude:

$$\sigma_{\text{met, sec}} \approx \left(\frac{L}{2t_{\text{ind}}k_g'}\right)^{1/2} \approx \left(\frac{10^{-4}\,\text{m}}{10^3\,\text{s} \times 10^{-5}\,\text{m/s}}\right)^{1/2} = 0.1 \tag{1.5}$$

or $\sigma_{\text{met, sec}} \approx 0.032$ for $t_{\text{ind}} = 10^4$ s.

All of these considerations are valid only if attrition fragments are the main source of nuclei. With increasing supersaturation, the number of nuclei generated by heterogeneous nucleation and/or surface nucleation via dendrite coarsening will increase and attrition fragments may be negligible. However, detached clusters and activated foreign particles also have to grow over a certain period of time in order to influence the CSD under discussion.

There is some experimental confirmation of these ideas by experimental results. As can be seen, the experimentally determined metastable zone widths according to Tables 6.1–6.3 of Chapter 3 are in the ranges

$$10^{-3} < \frac{\Delta C_{\text{met, sec}}}{C_c} < 2 \times 10^{-2}$$

and

$$4 \times 10^{-3} < \sigma_{\text{met, sec}} < 0.16$$

The metastable zone width depends on the growth behavior of nuclei and/or fragments. In Figure 1.1, the maximum permitted crystal growth rate G is plotted against the induction time period for four inorganic and organic aqueous systems investigated by Kind and Mersmann [1.1]. In any case, supersaturation has to be limited to avoid the production and outgrowth of too many nuclei; otherwise, it is not possible to obtain a certain median crystal size L_{50} [1.2]. According to these considerations, in Figure 1.2 the maximum permissible crystal growth rate $G_{\text{met}} \sim \Delta C_{\text{met}}/C_c$ (for constant k_d) is plotted against the induction time period t_{ind}, which is necessary for excessive secondary nucleation. The mean residence time must be less than t_{ind}. The hatched area corresponds to crystal sizes $G_{\text{met}}t_{\text{ind}}$ between 100 and 200 μm, which is valid for most systems listed in Chapter 3 [1.1].

According to experiments and theoretical considerations, the most economical residence time τ for continuously operated crystallizers depends on the tendency toward attrition because in the case of attrition-prone products, the median crystal size L_{50} passes through a maximum with increasing τ. This τ is short for crystals of KNO_3, $KAl(SO_4)_2{\cdot}12H_2O$, thiourea, and citric acid but much longer for attrition-resistant products such as $(NH_4)_2SO_4$, KCl, and NaCl [1.3]. According to $L_{50} \sim \tau^{0.15}$ up to $\tau^{0.25}$, a

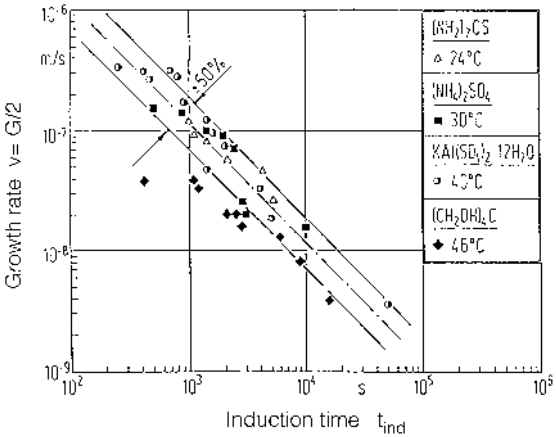

Figure 1.1. Maximum crystal growth rate permitted for various systems of high solubility ($C^*/C_C > 10^{-3}$) versus induction time.

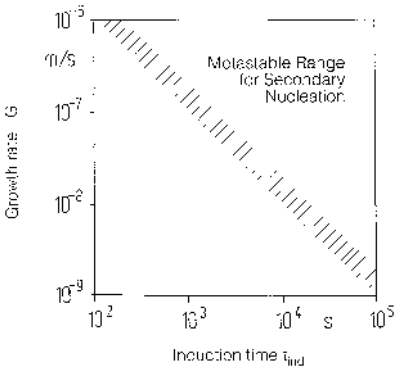

Figure 1.2. Maximum crystal growth rate permitted versus the induction time period for highly soluble systems.

longer residence time leads to an increase in the median size L_{50} (cf. Figures 7.5 and 7.6 in Chapter 4). However, this behavior occurs only if the kinetic growth rate G is much larger than the attrition rate G_a. The most economical residence time τ and, consequently, the most economical supersaturation $\Delta C = f(\tau)$ can be chosen only when information on the attrition behavior of the crystal is available.

In Chapter 5, a model for predicting of nucleation rates that are mainly controlled by attrition is presented. Crystallizers for systems with high solubilities ($C^*/C_C > 10^{-3}$) are operated at supersaturations in the range

$0.001 < \sigma < 0.1$, in which activated nucleation can be ignored and growth is controlled by both integration and bulk diffusion. The maximum possible growth rate is given by the simple equation

$$G_{\max} = \frac{k_d}{2}\frac{\Delta C}{C_C} \tag{1.6}$$

Let us assume the operation of an MSMPR crystallizer for which the median crystal size can also be drawn from the simple equation

$$L_{50} = 3.67\left[\frac{G}{6\alpha}\left(\frac{\varphi_T}{B_0}\right)\right]^{1/4} \tag{1.7}$$

Combining of the last two equations with the relationship for the attrition-controlled nucleation rate $B_{0,\text{eff}}/\varphi_T$ results in the proportionality (see Chapter 5)

$$L_{50,\max} \sim \left[\frac{\mu^3}{\rho_C H_V^5}\left(\frac{\Gamma}{K}\right)^3 \frac{(\text{Po})(k_d)}{N_V \eta_w^3 \eta_g \bar{\varepsilon}}\left(\frac{N_{\text{a, tot}}\Delta C}{N_{\text{a, eff}} C_C}\right)\right]^{1/4} \tag{1.8}$$

As can be seen, the maximum median size decreases with increasing mean specific power input $\bar{\varepsilon}$ [$L_{50,\max} \sim (\bar{\varepsilon})^{-1/4}$] and depends on the material properties ρ_C, H_V, μ, and Γ/K. The influence of the supersaturation ΔC is ambiguous. It should be noted that the ratio $N_{a,\text{eff}}/N_{a,\text{tot}}$ increases with rising supersaturation. With $G \sim \Delta C$ and $L_{50} \sim G\tau$, the size increases but the number of effective attrition fragments also increases with ΔC. Therefore, the size L_{50} is not proportional to $(\Delta C)^{1/4}$ but can be independent of supersaturation at high attrition rates. Operation at the minimum mean specific power input is recommended in order to produce coarse crystals.

The situation is different when the solubility is low ($C^*/C_C < 10^{-3}$) and the supersaturation is high ($\sigma > 1$). Because the median size is $L_{50} < 100$ mm, nucleation is no longer controlled by attrition. Besides the growth rate G, the nucleation rate B is also necessary for calculating the median crystal size. Because foreign particles are always present in real brines, it can be assumed that heterogenous primary nucleation is the decisive nucleation mechanism, perhaps in combination with surface nucleation. In Chapter 2, it has been shown that besides the reduction of the nucleation work by the factor f, the rate of heterogeneous nucleation, B_{het}, is proportional to the heterogenity factor

$$(a_{\text{for}} d_m)(1 - \cos\theta)\text{He}_{\text{ad}}$$

where a_{for} is the volumetric surface area of foreign particles, θ is the contact angle, and He_{ad} is the adsorption constant. Let us again combine the equa-

tions for the median crystal size, L_{50}, and for the rate, B_{het}, of heterogeneous nucleation with the equations valid for surface integration-controlled crystal growth:

$$G_{\text{int}} = 4.5 \times 10^{-3} \nu^2 \frac{D_{AB}}{d_m} \frac{(C_C/C^*)^{2/3}}{\ln(C_C/C^*)} \left(\frac{\Delta C}{C_C}\right)^2 \tag{1.9}$$

and

$$G_{\text{dif}} = \frac{k_d}{2} \frac{\Delta C}{C_C} \tag{1.10}$$

which is valid for bulk-diffusion-limited growth.

Combining the equations for L_{50}, B_{het}, and G_{int} and equations for γ_{CL} and d_m (see Chapter 1) results in

$$L_{50} \approx d_m \left\{ \nu^2 \varphi_T (1 + S_a)^2 \exp\left(\frac{16\pi f}{3} \frac{[K \ln(C_C/C^*)]^3}{(\nu \ln S_a)^2}\right) \times \left[\alpha \left(\frac{C^*}{C_C}\right) \left[K \ln\left(\frac{C_C}{C^*}\right)\right]^{3/2} S_a^{7/3} (a_{\text{for}} d_m)(1 - \cos\theta)\text{He}_{\text{ad}}\right]^{-1} \right\}^{1/4} \tag{1.11}$$

For G_{dif} instead of G_{int}, we obtain

$$L_{50} \approx d_m \left\{ \beta \varphi_T \left(\frac{k_d d_m}{D_{AB}}\right) \left(\frac{\Delta C}{C_C}\right) \exp\left(\frac{16\pi f}{3} \frac{[K \ln(C_C/C^*)]^3}{(\nu \ln S_a)^2}\right) \times \left[\alpha^2 \left(\frac{C^*}{C_C}\right)^{7/3} \left[K \ln\left(\frac{C_C}{C^*}\right)\right]^{1/2} S_a^{7/3} (a_{\text{for}} d_m)(1 - \cos\theta)\text{He}_{\text{ad}}\right]^{-1} \right\}^{1/4} \tag{1.12}$$

A number of calculations will be carried out below in order to give an idea of the importance of the various parameters.

For the sake of simplicity, we will assume $D_{AB} = 10^{-9}\ \text{m}^2/\text{s}$, $d_m = 5 \times 10^{-10}\ \text{m}$, $\alpha = \beta = \nu = 1$, $\varphi_T = 0.05$, $K = 0.414$, $a_{\text{for}} = 10^5\ \text{m}^2/\text{m}^3$, $\theta = 45^\circ$, $1 - \cos\theta = 0.293$, and $f = 0.058$. When all of these parameters are constant, the median crystal size L_{50} is only a function of the supersaturation S_a, the dimensionless solubility C^*/C_C, and the adsorption constant He_{ad}. In Figure 1.3, the median crystal size L_{50} is plotted against the supersaturation σ for different values fo C^*/C_C and $\text{He}_{\text{ad}} = 10^{-9}$. It is

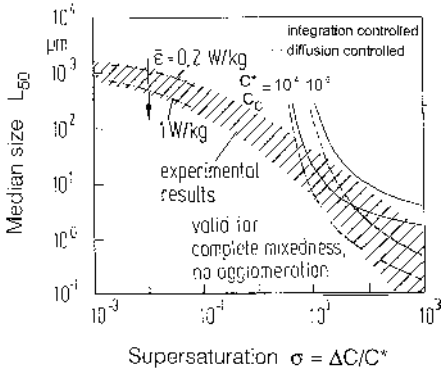

Figure 1.3. Median crystal size versus relative supersaturation according to experimental results and calculations.

important to mention that the curves are only valid if the following conditions are fulfilled:

- Complete mixing
- No aggregation
- No attrition
- Other MSMPR conditions
- Validity of equations (1.7), (1.9), and (1.10).

The second condition is violated when the supersaturation is high, because the particle concentration N also increases, due to rapid activated nucleation and subsequent agglomeration. Nevertheless, the curves clearly show a trend: With increasing supersaturation σ and increasing dimensionless solubility C^*/C_C, the median crystal size decreases rapidly and enters the submicron range, in which, however, strong aggregation is expected. This can be seen in Figure 1.4, where the volume fraction of boehmite [1.4] and quinacridone [1.5], respectively, are plotted against the particle size. When the repulsive interparticle forces for $L_{50} < 1\,\mu m$ are not predominant, the primary nanoparticles will quickly aggregate to form secondary particles in the size range of a few micrometers in which the number concentration N_{agg} is so low that aggregation can be neglected. Such aggregates have often been interpreted as nuclei ($N_{agg} \approx 10^{12}$ particles/m^3 and $B \approx 10^{16} \div 10^{20}$ nuclei/m^3 s), but in reality, they are agglomerates which will be termed "apparent nuclei." Nanoparticles are only stable if the interparticle repulsive forces are stronger than the attractive forces. When agglomeration takes place at high levels of supersaturation and high particle concentration N, two conditions can be distinguished:

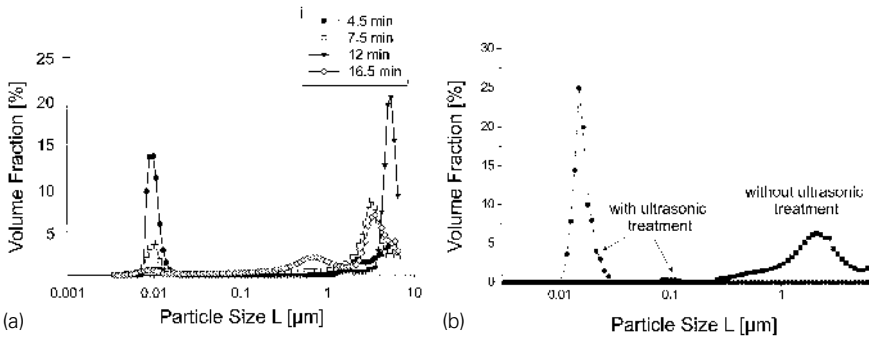

Figure 1.4. Measure particle size distribution of boehmite (a) and quinacridone (b).

- At medium supersaturation ($\Delta C/C_C < 0.1$), the primary particles aggregate in the presence of supersaturation and due to interparticle crystalline bridges or cemented aggregates, it is very difficult to destroy them.
- At very high supersaturation ($\Delta C/C_C > 0.1$ or $S > 0.1C_C/C^*$), the homogeneous primary nucleation can be so fast that supersaturation is rapidly consumed by nucleation, with the result that aggregation can take place in an almost desupersaturated solution. This leads to weakly bonded aggregates, which can be destroyed by ultrasound.

The median particle size of several hundred micrometers of a common product of systems with a high solubility [see Eq. (1.8)] will be considered in more detail below. Because the ratio $N_{a,\,\mathrm{eff}}/N_{a,\,\mathrm{tot}}$ increases strongly with supernaturation [$N_{a,\mathrm{eff}}/N_{a,\mathrm{tot}} \sim (\Delta C)^n$, where $n > 1$], the median crystal size drops slightly with increasing supersaturation. We are now in a position to put together the puzzle which allows a crude estimate of the median particle sizes to be expected. In Figure 1.5, ranges of mean crystal sizes are given in the diagram, with the supersaturation $\Delta C/C_C$ as the ordinate and the solubility C^*/C_C as the abscissa. Please note that the median crystal sizes are only a crude estimate, which, however, is based on experimental data and theoretical considerations. Additional information is given in Figure 1.6. These diagrams show approximate borderlines between activated/attrition-controlled nucleation, diffusion/integration-controlled growth, and the "attrition corner" below and the "agglomeration corner," and also the "gel-corner" at the top. The dotted diagonal lines represent lines of constant

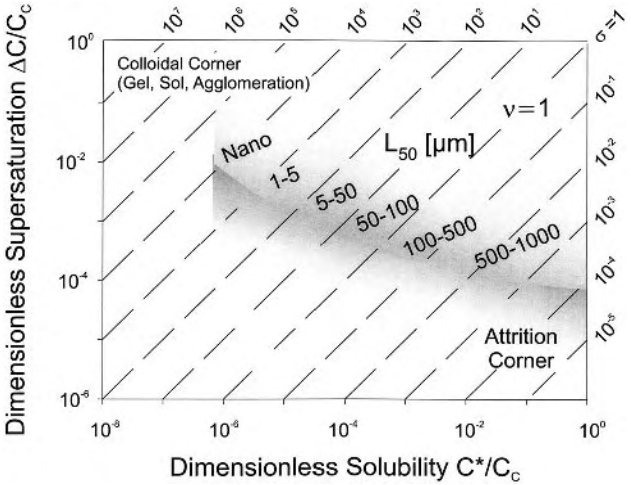

Figure 1.5. Ranges of median crystal size in a $\Delta C/C_C = f(C^*/C_C)$ plot.

supersaturation σ or $S \approx \sigma$ for $\sigma > 10$. The entire diagram can be subdivided according to

$$\frac{\Delta C}{C_C} > 0.05\left(\frac{C^*}{C_C}\right)^{0.45} \quad \text{or} \quad \sigma > 0.05\left(\frac{C^*}{C_C}\right)^{-0.55} \tag{1.13}$$

in an upper area in which the crystals possess rough surfaces caused by surface nucleation, and growth is controlled by bulk diffusion, and a lower area. In this region,

$$\frac{\Delta C}{C_C} < 0.01\left(\frac{C^*}{C_C}\right)^{0.45} \quad \text{or} \quad \sigma < 0.01\left(\frac{C^*}{C_C}\right)^{-0.55} \tag{1.14}$$

activated nucleation can be neglected and nucleation is controlled by attrition. The crystal sufaces are smooth with the result that a parabolic relationship according to the BCF equation valid for solutions can be expected. Because more and more attrition fragments are stimulated to grow with increasing supersaturation, the median crystal size decreases.

Considering again Figure 1.5, at very low supersaturation σ we obtain a low growth rate that is approximately the same as the negative attrition rate G_a so that only the maximum crystal size $L_{\max}$ can be obtained and the crystals are rounded. This is especially true of crystals with a high settling

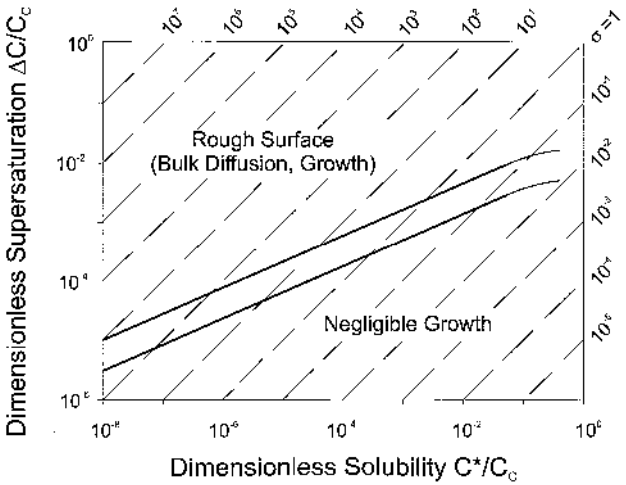

Figure 1.6. Dimensionless supersaturation versus dimensionless solubility with ranges of dominant kinetics.

velocity, which has to be compensated by a certain stirrer tip speed. In the lower area of the diagram, the median crystal size is mainly controlled by attrition and attrition rates, which are discussed in Chapter 5 in more detail, and both activated nucleation and aggregation can be neglected. In the upper part of the diagram, activated nucleation (surface, heterogeneous, and homogeneous nucleation with increasing supersaturation) and aggregation are the decisive parameters for the median crystal size. The growth of crystals with a rough surface is controlled by bulk diffusion and will be increasingly accompanied by aggregation as supersaturation increases. At $\Delta C/C_C > 0.1$ or $\sigma > 0.1(C_c/C^*)$, the aggregation can be so fast that a bimodal size distribution is obtained with nanoparticles agglomerating and with aggregates a few micrometers in size. Real nucleation rates with $B \approx 10^{30}$ nuclei/m^3 s and nanoparticles can only be measured if aggregation is avoided by strong repulsive forces of nuclei.

In the "gel corner" above the range of $L_{50} = 10$ to 100 nm, a transient or permanent gel exists [1.6]. The higher the supersaturation, the more stable the gel can be. The transformation process of such an amorphous material in a crystalline system can be very slow. The maximum possible increase of the volume αL_c^3 of a crystallite with the size L_c is controlled by diffusion according to [1.7]:

$$\frac{d(L_c^3)}{dt} = \frac{8D_{AB}\gamma_{CL}V_m^2C^*}{9\nu\Re T} = \frac{8D_{AB}d_m}{9\nu}\left(\frac{\gamma_{CL}d_m^2}{kT}\right)\frac{C^*}{C_C} \tag{1.15}$$

This equation shows that the rate of transformation is reduced by the following:

- Decreasing solubility C^*
- Decreasing diffusivity D_{AB}
- Decreasing interfacial tension γ_{CL}

In addition to gel transformation and Ostwald ripening, other processes can occur [1.8]:

- Transformation of metastable crystals into polymorphs with a greater stability according to dissolution and recrystallization
- Transformation of dendrites and platelets into more isomorphic crystals induced by surface diffusion
- Aggregation and agglomeration

Up to now, it is very difficult to predict the structure of precipitates and the size and shapes of crystallites when the solubility is very low but the supersaturation very high.

The median crystal sizes given in Figure 1.5 are partly calculated from the equations discussed earlier and partly drawn from experimental data published in the literature. Due to the manifold and complex mechanisms during the generation of a solid matter (it should be noted that rates of activated nucleation rise very rapidly with supersaturation and rates of agglomeration are difficult to predict; see Chapter 3), only an initial estimate can be obtained. This might be helpful when only the solubility of a new solute to be crystallized is known.

2. CRYSTAL SIZE DISTRIBUTION

When operating an MSMPR crystallizer, the size distribution can be described by the slope $-1/(G\tau)$ in a semilogarithmic diagam in which the population density n is plotted against the crystal size L (see Figure 2.3 in Chapter 4). The line for the residence time $\tau = 1800$ s is much steeper than for $\tau = 5400$ s because the mean supersaturation in the crystallizer drops with the residence time τ (cf. Fig. 2.1) which shows the mean crystal growth rate as a function of τ. Because the growth rate of KCl is bulk diffusion controlled, it is possible to calculate a second ordinate with $\Delta C/C_C$ instead of G. According to the residence time distribution of crystals in an MSMPR

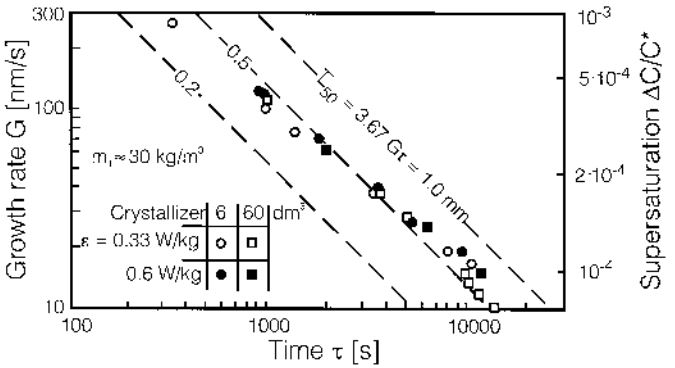

Figure 2.1. Mean growth rate of KCl and dimensionless supersaturation versus the residence time.

crystallizer, the distribution of the sizes $L = Gt$ becomes broader with increasing mean residence time τ.

The residence time distribution of crystals in a crystallizer can deviate from distributions valid for MSMPR conditions and can be determined by a washout experiment. The particle size distribution in the crystallizer while the particles are being washed out, with no additional particles being added to the feed stream, is measured as a function of time. The residence time of different particle sizes can then be estimated for an ideally mixed stirred vessel:

$$\frac{M(L,t)}{M_\alpha(L)} = \exp\left(-\frac{t}{\tau(L)}\right) \tag{2.1}$$

Here, $M_\alpha(L)$ is the mass of particles of size L at the time $t = 0$. The slopes of lines in a semilogarithmic plot give the residence times of each particle size class. The broader the residence time distribution of suspension elements in the crystallizer, the broader the size distribution, due to the greatly varying times for growth. Figure 2.2 shows the cumulative mass of KCl as a function of size for the mean residence times $\tau = 1800\,\text{s}$ and $\tau = 5400\,\text{s}$. The coefficient of variation (CV) increases slightly with the residence time. In the case of batch crystallizers, the coefficient of variation is small; however, the CSD will become broader with increasing batch time due to growth-rate dispersion.

Much stronger impacts on the coefficient of variation come from attrition phenomena, as has been demonstrated in Chapter 5. This is especially true of crystals prone to attrition. In Chapter 5, it has been shown that for

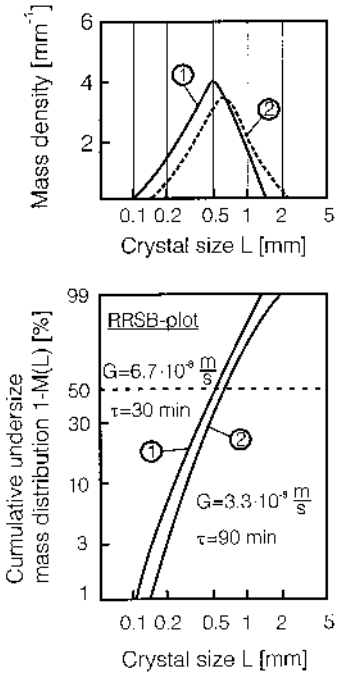

Figure 2.2. Cumulative undersize distribution of KCl in a Rosin–Rammler–Sperling–Bennet (RRSB) net.

attrition-resistant KCl, the coefficient of variation CV is 0.55 in the range of the mean specific power input between $\bar{\varepsilon} = 0.2\,\mathrm{W/kg}$ and $\bar{\varepsilon} = 0.9\,\mathrm{W/kg}$. However, in the case of KNO_3, which is very prone to attrition, the coefficient of variation decreased from $CV = 0.42$, which is valid for $\bar{\varepsilon} = 0.27\,\mathrm{W/kg}$ to $CV = 0.17$ at $\bar{\varepsilon} = 1\,\mathrm{W/kg}$. This is because large particles will be abraded, with the result that the size distribution becomes very narrow. Strongly abraded crystals can often be described using a Rosin–Rammler–Sperling–Bennet (RRSB) distribution and its uniformity coefficient. When discussing the coefficient of variation or, in general, the broadness of a crystal size distribution, it is possible to distinguish among different influences:

- Influence of residence time distribution of a poorly mixed crystallizer
- Influence of growth dispersion according to different chemical potentials of crystals of equal size in the identical surroundings (cf. Chapter 5)
- Influence of attrition caused by high collision velocity

When large crystals which are prone to attrition are produced, their high settling velocity must be compensated by a high tip speed of the stirrer in a vessel, and high collision velocities lead to rounded parent crystals and a variety of attrition fragments in the size range between 1 and 150 μm. These attrition fragments exhibit a broad distribution of growth rates or growth-rate dispersion, which leads to a broad size distribution even for crystals of the same size with an identical residence time in the crystallizer. However, when the specific power input is increased, the collision velocities will increase too, and this leads to an abrasion of the largest crystals down to L_{max} for which $G = G_a$ (see Chapter 5). The coefficient of variation CV may at first increase with the specific power input, but then decreases. A general prediction of CV is difficult and measurements are therefore recommended. There may be a possibility of estimating the tendency of the CV as a function of the operating parameters.

3. CRYSTAL SHAPE

It is extremely difficult to predict the shape of crystals due to the vast variety of different parameters. The shape of crystals in industrial crystallizers can be influenced by the following:

1. Properties of the crystalline solid (size, lattice, modification, morphology, interfacial tension, hardness. Young's modulus, fracture resistance, tensile strength, brittle or ductile behavior, resistance to attrition, etc.)
2. Properties of the solution (pressure, temperature, density, viscosity, concentration, additives and impurities, supersaturation, ionic strength, pH, tendency to aggregate, etc.)
3. Type and geometry of the crystallizer (DTB, STR, fluidized bed, forced circulation, etc.)
4. Operating mode (cooling, evaporation, drowning out, reaction) and conditions (specific power input, tip speed of rotors, suspension density, residence or batch time, feed time, feed ratio of reactants, feed point, premixed feed, seeded feed, etc.)

Therefore, it is advisable to determine the best combination of these parameters in the laboratory and to operate the industrial crystallizer under the optimum operating conditions.

The shape of large crystals above 0.5 mm in size is mostly determined by the mechanics of collision and the shear stresses. The crystals are more or less rounded as the result of attrition. The shape depends on the frequency and intensity of collisions and on the material properties of the crystals. This

has been described in more detail in Chapter 5. The higher the intensity of strain (which can be quantified by the collision velocity or by operating parameters such as the stirrer tip speed, the shear stress, or the specific power input), the more rounded the crystals. This is especially true of materials prone to attrition. As an example, Figure 3.1 shows crystals of attrition-resistant KCl and in Figure 3.2 crystals of attrition-prone KNO_3 are depicted. Figure 3.3 gives some information about the importance of the parameter supersaturation ΔC or growth $[G = f(\Delta C)]$, suspension density m_T or volumetric crystal holdup φ_T, and the specific power input ε. Only in the case of a crystallizer operated at a very low attrition intensity (fluidized bed or stirred vessel at $\bar{\varepsilon} < 0.1\,\mathrm{W/kg}$, crystals with a small sedimentation velocity $w_s < 0.03\,\mathrm{m/s}$) can we expect distinct crystalline shapes, which are controlled by the different growth rates of the faces according to the overlapping principle (see Fig. 3.4). There are fast-growing faces that will disappear after a certain growth period, and slow-growing faces that will survive leading to the crystal habit changing with time. Each face always moves parallel to its original position according to the "principle of the parallel displacement of the faces." It is important to mention that the differences in growth rates of the various faces can be very great (see Chapter 3).

Let us now concentrate on the influence of thermodynamics and kinetics, which often determine the habit of small crystals ($L < 0.5\,\mathrm{mm}$) in fluidized beds, stirred vessels at low specific power input, or a single large crystal suspended by an upward flow. Such influences can be best studied with freely suspended single crystals. Such a procedure is far removed from the situation in an industrial crystallizer, but can give important information about the crystal shape, which is controlled by the crystallization kinetics. The shape can be influenced by the following:

1. The different growth rates of the crystal faces, $v_{h,k,l}$
2. The reduction or even blockage of growth of certain faces due to the adsorption of impurities, admixtures, and additives (see Chapter 3)
3. The type and intensity of agglomeration

The crystal habit depends on the ratio of the growth rates $v_{h,k,l}$ of the faces, as can be seen in Figure 3.5 (only two-dimensional here) starting from the nucleus; the growth rates of all faces are equal until crystal I is obtained. The growth rates of the various faces then vary (possibly due to the incorporation of impurities present in the solution or habit modifiers added to the solution), with the result that the crystal habit changes (see habits II and III). The direction of the normals on the faces, however, remains constant, as do the angles between the different faces (this has been known since 1669). The final habit of the crystal is determined by the faces having the

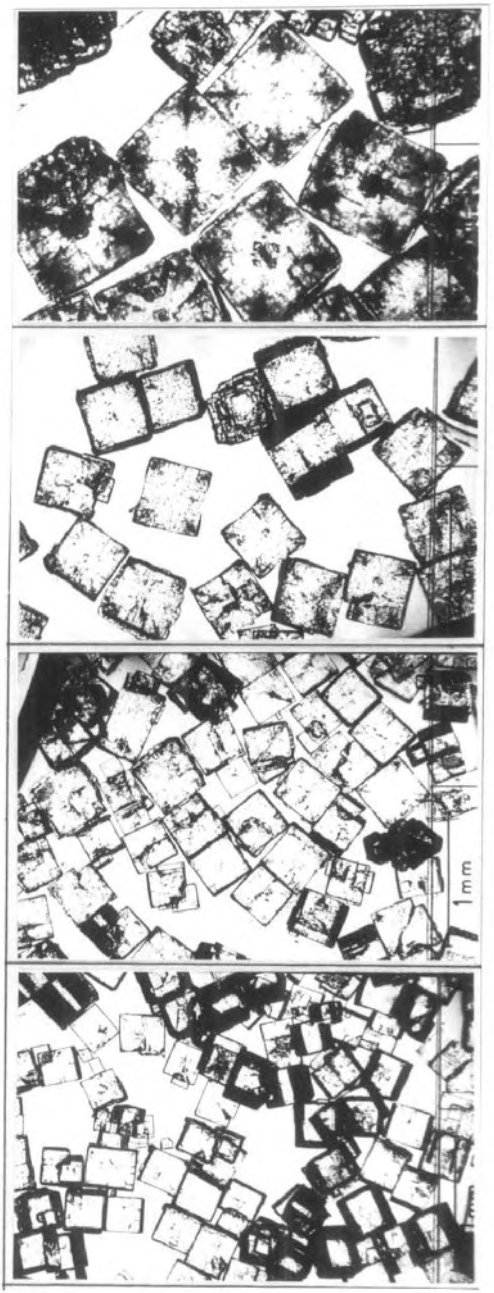

Figure 3.1. Photograph of attrition-resistant potassium chloride crystals.

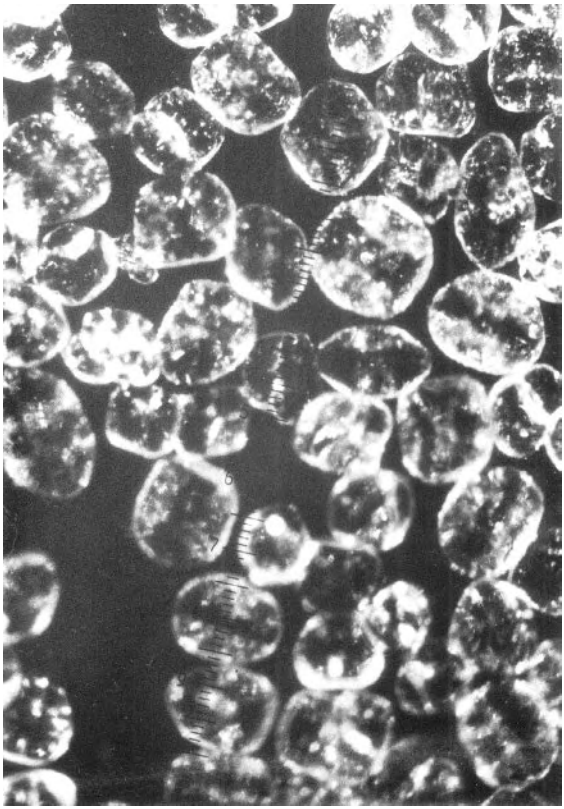

Figure 3.2. Photograph of potassium nitrate crystals prone to attrition.

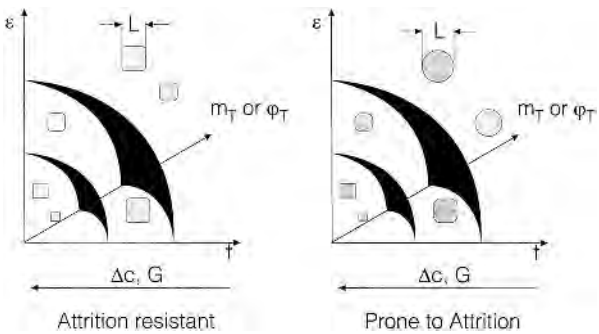

Figure 3.3. Information on the importance of several parameters for the crystal shape.

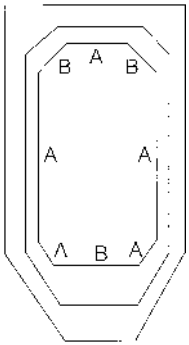

Figure 3.4. Overlapping principle of growing crystals: A, slow-growing faces; B, fast-growing faces.

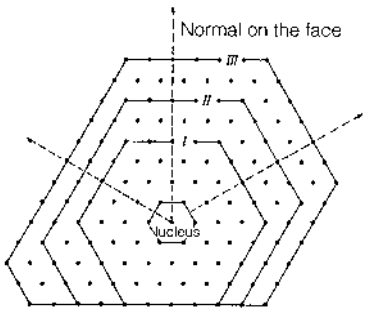

Figure 3.5. Habit of crystals depending on the growth of the various faces.

lowest growth rate. As a rule, these are faces with a high density of units and low indication numbers. High-index faces grow faster than low-index faces. This growth behavior can be used to explain the three fundamental types of crystal habit: isometric, planar, and prismatic or needlelike (cf. Chapter 1). Even if the crystals have a typical habit, they cannot be expected to have an ideal lattice without defects. Such defects were described in Chapter 1. The higher the growth rate and the concentration of foreign substances in the solution, the larger the deviations from the ideal crystals. Real crystals often show a mosaic structure and are composed of aggregated crystal blocks that form a polycrystal; compare Chapter 5.

When dealing with crystalline products obtained by precipitation, the prediction of crystal shapes is even more difficult due to additional parameters, such as ionic strength, pH, and so on, which can have an influence

on the habit. As an example, let us consider the precipitation of β-BaF_2 from solutions of $Ba(C_2H_3O_2)_2{\cdot}2H_2O$ (acetate) and NH_4F according to the experimental results of Kolar et al. [3.1]. Precipitates were prepared by quickly pouring 25 cm^3 of a 0.3 M ammonium fluoride solution into a 100-cm^3 vessel containing 25 cm^3 of a 0.15 M barium acetate solution at 50°C. After mixing, the suspension was kept at a precipitation temperature of 1°C to 80°C for 1800 s (aging time) in order to study the influence of temperature on the size and habit of crystals. In Figure 3.6, the median crystal size is plotted against the precipitation temperature. A distinct maximum size of 4.2 µm occurred at 50°C, and the crystals exhibited a cubelike morphology with {100} faces, which grow most slowly under the conditions mentioned above. At low temperatures, the crystals exhibited face-centered plateaus, as can be seen in Figure 3.7a for crystals that formed at 1°C. At 50°C, the crystals appear to be completely smooth (see Fig. 3.7b).

As another example, the precipitation of $BaSO_4$ was investigated by van der Leeden and van Rosmalen under a wide range of temperatures and pH values [3.2]. Barium sulfate was produced by the dropwise addition of 0.01 M H_2SO_4 to an equal amount of 0.01 M solution of $BaCl_2$, both containing 0.01M HCl. At 25°C and pH 2, lenticular, slightly agglomerated crystals were formed (see Fig. 3.8a) with a median size of $L_{50} \approx 20$ µm. A rise in temperature to 73°C at the same pH 2 led to well-shaped blocklike crystals, bounded by {001}, {210}, and less frequently by {211} faces (see Fig. 3.8b). Agglomeration of the crystals of $L_{50} \approx 65$ µm was not observed at this temperature. Experiments were also carried out at pH 7 and 25°C, which again led to the formation of lenticular-shaped crystals of a size similar to those formed at pH 2 and 25°C. However, due to increased

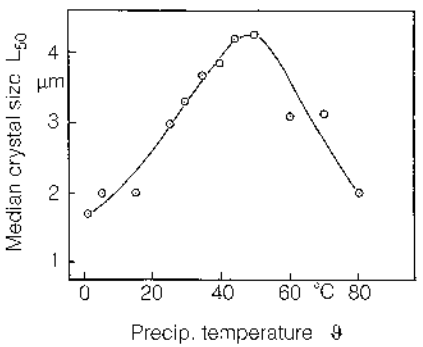

Figure 3.6. Median crystal size versus precipitation temperature of barium fluoride.

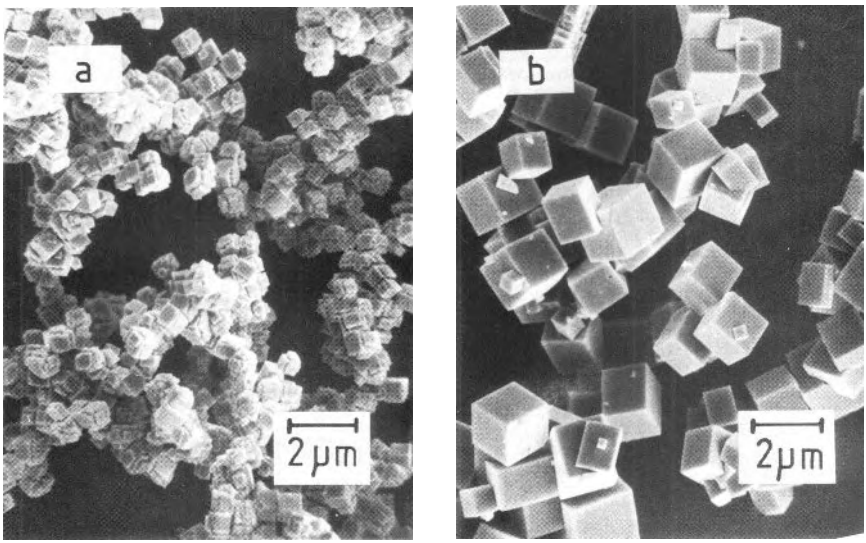

Figure 3.7. (a) Crystals of barium fluoride with face-centered plateaus; (b) completely smooth crystals of barium fluoride.

agglomeration, the median particle size was approximately $L_{50} \approx 10\,\mu m$. At pH7 and 73°C, blocklike crystals or lenses with partly developed {120} faces were formed (see Fig. 3.8c).

In general, the habit of crystals smaller than 100 µm is determined by the growth kinetics, by the structure of the lattice or by both. In the past, many authors have tried to predict the morphology by considering the crystalline structure and thermodynamic properties as the interfacial tension and/or the heat of sublimation. Bravais [3.3], Friedel [3.4], and, later, Donnay and Harker [3.5] considered the package of units in a lattice and their distances in different directions (see Fig. 3.9). According to these authors, a face (*hkl*) becomes more and more dominant when the distance between the lattice elements increases, and the importance of morphology (IM) is proportional to the distance d of the elements in this plane: $IM \sim d$.

This means that the most commonly occurring faces will be those which belong to planes with a high density of elements or with a high reticular density. As a rule, the surface tension of a plane increases with the density of the elements. Therefore, Wulff quickly came to the conclusion that a face is developed to a higher degree when its surface tension is low or $IM \sim 1/\gamma_{CL}$. According to Gibbs' thermodynamics, the volume free energy per unit

(a)

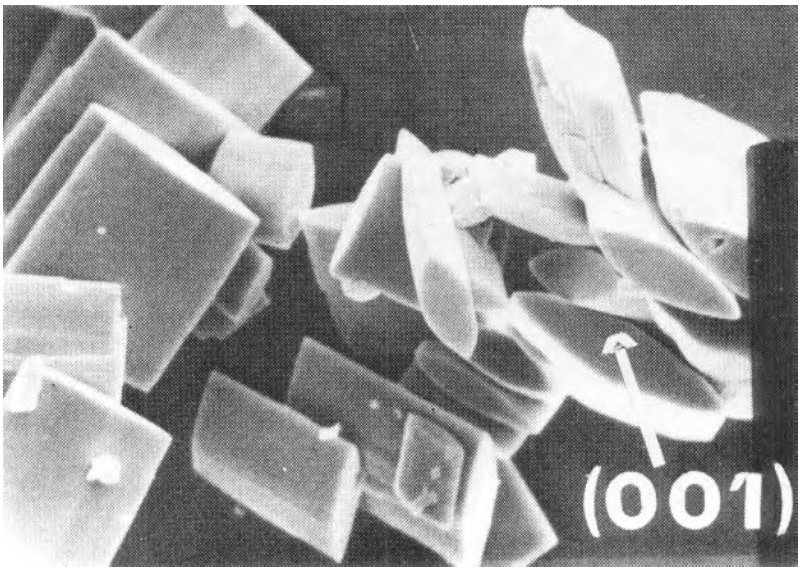

(b)

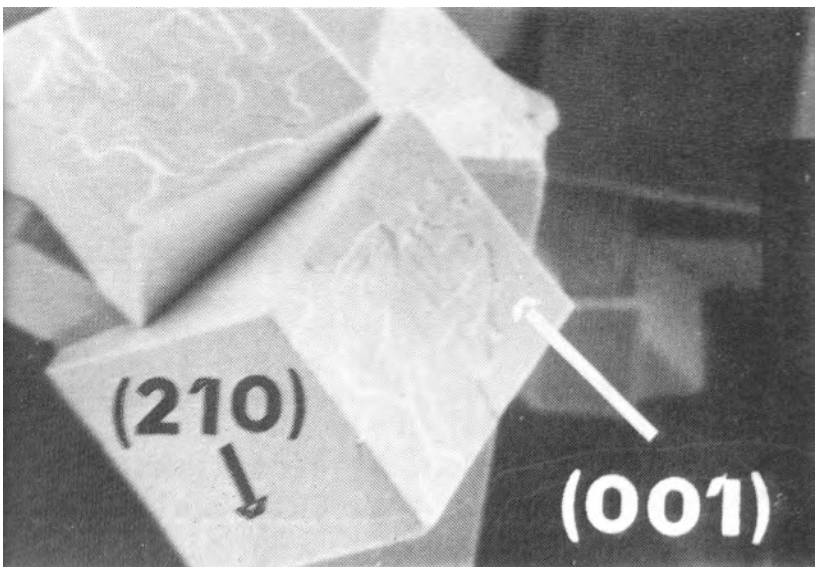

(c)

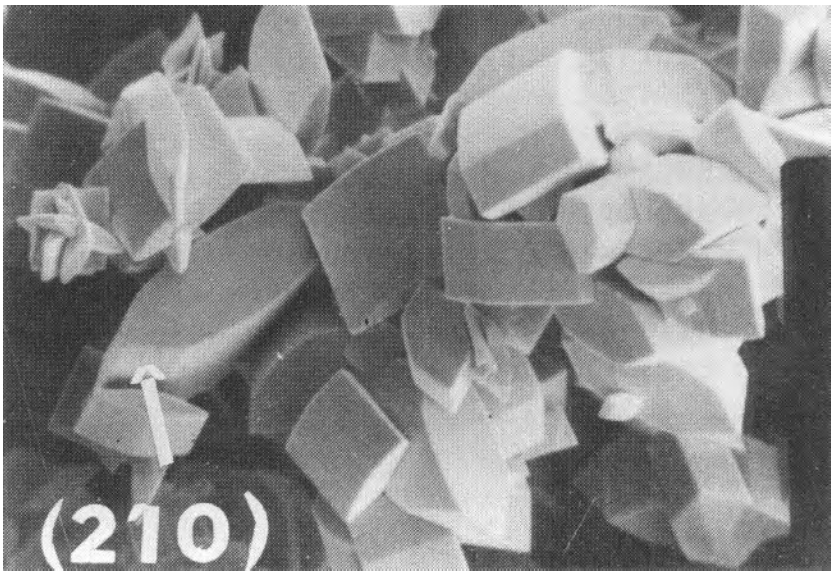

Figure 3.8. (a) Lenticular slightly agglomerated crystals of barium sulfate; (b) blocklike crystals of barium sulfate; (c) lenselike crystals of barium sulfate.

volume should be constant throughout the crystal, which results in the minimum value of energy

$$\sum_i A_i \gamma_{\mathrm{CL},i}$$

where A_i is the area of the ith face and $\gamma_{\mathrm{CL},i}$ its surface tension. Consequently, the equilibrium shape depends on the surface energies per unit area of the different faces. This is known as Wulff's hypothesis and has been confirmed experimentally. When a crystal maintains its geometric pattern during growth, it is called invariant. However, as a rule, crystals do not maintain geometric similarity and exhibit overlapping.

Another approach developed by Hartman and Bennema [3.7] considers the attachment energy to be an important parameter for the shape of crystals. The energy E_{CC} of a crystal is the sum of the interaction energies of a lattice unit with the other surrounding units (see Fig. 3.10). When a unit in a kink is considered, the energy $E_{CC,k}$ is less than E_{CC} because there are only three interactions:

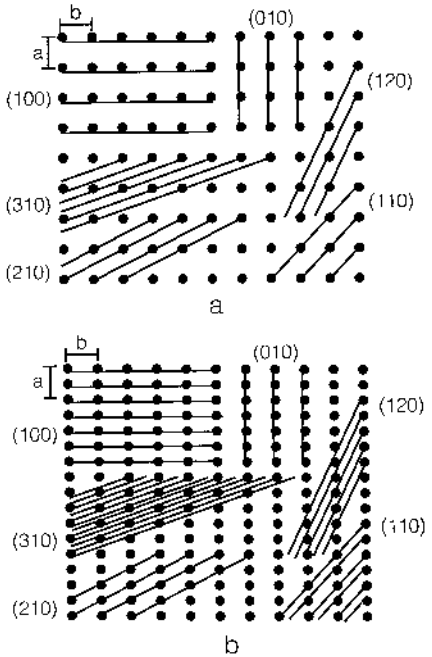

Figure 3.9. Systematic extinctions and lattice distances. The order of importance is the following: $\{100\} = \{010\} > \{110\} > \{210\} > \{120\} > \{310\}$ in (a) and $\{010\} > \{100\} > \{210\} > \{110\} > \{120\} > \{310\}$ in (b). (From [3.6].)

- Interaction with the plane of the terrace
- Interaction with the units on the left
- Interaction with the unit behind

When the crystal is surrounded by a vapor phase and the interactions of its nearest neighbors are equal, the following simple equation is valid:

$$|E_{CC}| = 2|E_{CC,k}| = 2\Delta H_{SG} \tag{3.1}$$

Here ΔH_{SG} is the energy of sublimation which can be measured by a calorimeter or calculated from the vapor pressure versus temperature. In order to determine the energy of attachment, it is assumed that a slice with a thickness of one unit is separated from the crystal; see Fig. 3.11. After separation, the slice has the energy $E_{CC,sl}$ and the two pieces have gained the attachment energy E_{att}:

$$E_{CC} = E_{CC,sl} + 2E_{att} \tag{3.2}$$

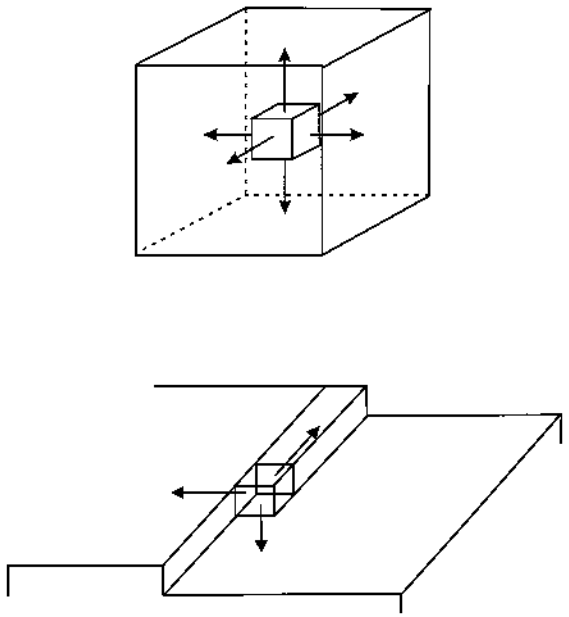

Figure 3.10. Top: E_{CC}; bottom: $E_{CC,k.}$

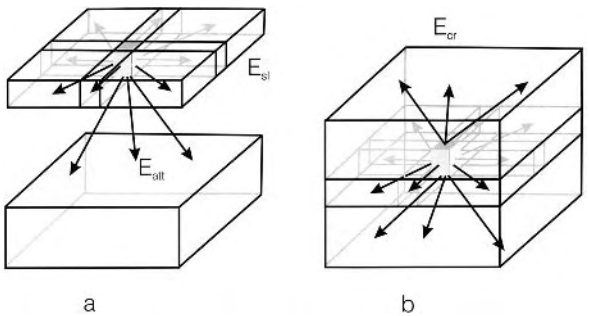

Figure 3.11. Definition of the attachment energy E_{att}.

or

$$E_{\text{att}} = \Delta H_{\text{SG}} - \frac{E_{CC,sl}}{2} \tag{3.3}$$

This model leads to the following prediction: The smaller the attachment

energy of a certain face, the more this face is expected to develop (IM $\sim 1/E_{att}$).

The models discussed here have been used to predict the morphology of crystals at low supersaturation [3.6]. Molecular modeling based on the thermodynamic equilibrium has produced good results for adipic acid and succinic acid in the vapor phase, but the agreement between the theoretical prediction and the habit found experimentally was poor for the growth in solution. It is necessary to take into account the properties of the solvent. Besides the two diacids, other organic compounds [$C_{14}H_{10}$, $(C_6H_5)_2CO$, $C_9H_{10}ON_2Cl_2$, $C_{19}H_{11}O_2N_2F_5$, and $C_{18}H_{13}F_3NO_2$] have been investigated. The results have shown that it is only possible to predict crystal habits to a limited degree (no interaction with the surroundings of the crystal as in desublimation).

4. PURITY OF CRYSTALS

It is difficult to predict the purity of crystals because this property depends on a variety of thermodynamical, kinetic, mechanical, and fluid dynamic parameters. In the case of crystallization from the melt, it is known that the level of impurity is mostly governed by the impure melt adhering to the crystals, but this can also be true of crystals obtained from solution. This phenomenon will be discussed later. As a rule, the interior of crystals grown at a very low growth rate is very pure, which is the advantage of the unit operation crystallization. According to the thermodynamic equilibrium, very few impurities are incorporated as units that do not desorb and diffuse back into the bulk of the solution fast enough or melt when crystal growth rates reach economically reasonable values. Burton et al. [4.1] developed a model that predicts the effective distribution coefficient k_{diff}, which is defined by the equation

$$k_{diff} = \frac{C_{im,C}}{C_{im,L}} \frac{\rho_L}{\rho_C} = \frac{c_{im,C}}{c_{im,L}} \frac{\rho_L}{\rho_C} \tag{4.1}$$

In this equation, $C_{im,C}$ is the concentration of the impurity in the crystal and $C_{im,L}$ is its concentration in the bulk liquid. It is important to note that k_{diff} is a differential and, above all, an effective distribution coefficient and not a thermodynamic or equilibrium coefficient. The authors [4.1] assumed a kinetic boundary layer model and took into account two kinetic parameters: the crystal growth rate G and the mass transfer coefficient k_d. In general, the differential distribution coefficient k_{diff} is a function of the parameters G and

k_d and depends on the impurity concentration $C_{\mathrm{im},L}$ in the liquid and the densities ρ_C and ρ_L of the two phases:

$$k_{\mathrm{diff}} = f\left\{\frac{c_{\mathrm{im},L}}{\rho_L - c_{\mathrm{im},L}}\left[\exp\left(\frac{G\rho_C}{k_d\rho_L}\right) - 1\right]\right\} \tag{4.2}$$

This equation clearly shows that very pure crystals can only be obtained when the crystal growth rate (and also the supersaturation) is low and the mass transfer coefficient is high. Therefore, a turbulent flow of a liquid of low viscosity and a low supersaturation (or crystal growth rate) are advantageous for obtaining a high-purity product. The higher the concentration $C_{\mathrm{im},L}$ in the liquid, the more impure the crystals. At low crystal growth rates, compact crystals with low porosity are produced, with the result that virtually no solvent or impurities are entrapped. Burton et al.'s model can explain the effect of kinetics on the purity of well-grown compact crystals, but at high levels of supersaturation things are more complicated.

Principally speaking, the purity of crystals generated in solution depends on (a) thermodynamics, or the equilibrium distribution of impurities, admixtures, and additives (inclusion), (b) kinetics, or uptake of these materials by the crystal during nucleation and, in particular, crystal growth (inclusion), and (c) the quantity of adhering mother liquor and its concentration of impurities, admixtures, and additives (occlusion). As a rule, the purity of crystals that are in equilibrium with the solution is very high (often $>99.9\%$ by mass) because the distribution coefficient of the individual impurities K_{im} according to

$$K_{\mathrm{im}} = \frac{C^*_{\mathrm{im},C}}{C_{\mathrm{im,L}}} \tag{4.3}$$

is very small, especially at low temperatures. However, the distribution coefficient may vary with temperature. It is very difficult to determine such coefficients because this only is possible at very low supersaturation and growth rates. An increase in supersaturation and growth lead to a buildup of impurities and of impure mother liquor. The higher the growth rate, the larger the amount of impurities built up.

Supersaturation may have to be restricted to achieve the product purity desired by the customer. In the literature, little information is given on the relationship between supersaturation ΔC and the growth rate G, on the one hand, and on the purity of crystals on the other. Molecules of impurities, admixtures, and additives are present in the immediate vicinity of the crystal surface and are adsorbed on the surface according to adsorption isotherms. The greater the bulk concentration, the higher the surface loading or surface coverage. In the case of growing crystals, these foreign molecules must be

desorbed and then transported by bulk diffusion into the solution against the arriving solute molecules. Consequently, the purity of crystals is influenced by the following processes:

1. Equilibrium adsorption loading due to the isotherms of impurities
2. Kinetics of desorption of foreign components from the crystal surface into the bulk of the solution on the one hand, and
3. Volume diffusion of the solute
4. Impingement of solute units on the crystal surface
5. Surface diffusion of solute units at the surface
6. Integration of these units at a kink or step

on the other.

Furthermore, processes such as the association and dissociation of solvent molecules in the crystalline lattice or of the molecules of solute and/or foreign components can play a role. Because of the variety of limiting steps, we are not in a position to predict the purity of crystals of arbitrary systems. However, the decisive process can sometimes be found by performing relatively simple experiments in the laboratory. When dealing with industrial products, the purity of the final products is often determined by the adhering mother liquid and its concentration. The total amount M_{im} of the various impurities (index im) a, b, c, ... is given by

$$M_{\text{im}} = V_{\text{adh}}(c_{\text{im},a} + c_{\text{im},b} + c_{\text{im},c} + \cdots) \tag{4.4}$$

where V_{adh} is the liquor volume adhering to the crystals and $c_{\text{im},i}$ is the concentration of the impurity i under discussion. It is important to keep in mind that the concentration of foreign material c_{im} will increase in an evaporative crystallizer according to

$$c_{\text{im},i} = \frac{c_{\text{im},i,\alpha}}{ER} \quad \text{(batch)} \tag{4.5}$$

or

$$c_{\text{im},i} = \frac{c_{\text{im},i,0}}{ER} \quad \text{(continuous)} \tag{4.6}$$

The expression ER is the evaporation ratio defined as

$$\text{ER} = \frac{\text{solvent } \Delta L^{\circ} \text{ evaporated}}{\text{Starting brine } L_{\alpha} \text{ or } L_0} \tag{4.7}$$

A small volume V_{adh} of adhering liquor is obtained for isometric crystals with a large median size L_{50} and with a small coefficient of variation after a long separation time in a batch or continuously operated separation device such as a centrifuge or filter.

In Figure 4.1, the volume of the adhering mother liquor V_{adh} based on the voidage volume ψV_{cake} of the crystal cake with the thickness s (ψ is the voidage of the cake) is plotted against the dimensionless separation time

$$\tau^*_{sep} = \frac{L_{50}^2 \psi^2 \rho_L g z}{(1-\psi)^2 s \eta_L} \tau_{sep} \tag{4.8}$$

with the ratio

$$\frac{We}{Fr} \equiv \frac{L_{50} \psi s \rho_L g z}{(1-\psi)\gamma_{LG}}$$

as parameter [4.2]. We is the Weber number and Fr is the Froude number. τ_{sep} is the separation time, γ_{LG} is the surface tension of the mother liquor, and

$$z = \frac{w_{circ}^2}{rg} = \frac{\omega_{circ}^2 r}{g}$$

is the multiple of acceleration due to gravity, where w_{circ} is the circumferential velocity, ω_{circ} is the angular velocity of the centrifuge rotor, and r is its radius. The diagram shows very clearly that a small volume of adhering mother liquor can only be obtained for coarse products (L_{50} high) in liquids of low viscosity at high centrifugal speeds after a minimum separation time τ_{sep}. The diagram is valid for monosized crystals. When the particle size distribution is broad, the volume of the adhering mother liquid is greater. Again, it is very important to reduce nucleation in the crystallizer in order to obtain a pure product. This also applies to filter cakes.

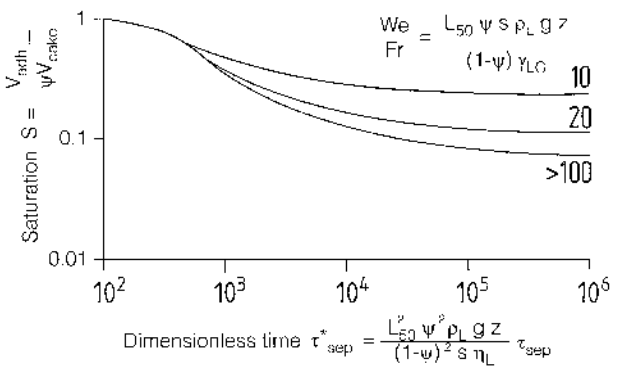

Figure 4.1. Residual adhering liquor versus the dimensionless separation time of a centrifuge.

Sometimes, the cake is washed with an undersaturated clean mother liquor, or a washing liquid is applied in order to remove the adhering liquor with its impurities. This removal can be carried out by (a) mechanical displacement of the fixed-bed crystal cake or (b) mixing and suspending the crystals and the washing agent. In fixed-bed filter cakes, the liquid may channel, especially in the case of fine materials, with the result that large parts of the cake are not cleansed. Removal of the impurities can be controlled by (a) displacement of the mother liquor or (b) diffusion of the impurities from the adhering film around the crystals into the bulk of the washing agent.

As a rule, the purity of the final crystals increases with the ratio $\dot{L}^{\circ}/\dot{M}_C$ of the mass flow $\dot{L}^{\circ}$ of the washing liquor based on the crystal mass flow $\dot{M}_C$. When the washing process is carried out in a suspension-stirred vessel, all the crystals should be suspended, and a certain mixing time is necessary for blending and for diffusing foreign components from the crystal surface into the bulk of the liquid. When the crystals are inorganic and hydrophilic and water is used as the solvent, washing with an organic, hydrophobic liquid with a low viscosity and low solubility for crystals and water but high solubilities for the impurities can be very effective.

Another problem is the removal of the solvent or of foreign components which are adsorbed on the outer surface of compact crystals and on the inner surface of agglomerates, which can be very important for ultrapure substances. Two steps are involved in desorbing these impurities: (a) desorption of the molecules from the surface and (b) diffusion through the microspores and macropores of the agglomerates and the concentration film around the particles. As a rule, the first desorption step does not control the rate of desorption, and diffusion in the porous solid material may be decisive for the purity of the final product.

The residual moisture or residuals of the solvent can only be removed completely during drying in an atmosphere where the partial pressure of these components is zero. If this is not the case, residual loading of the crystals may cause caking, especially when water is used as the solvent.

As a rule, caking of the crystals occurs if the the atmospheric humidity exceeds certain values at a given temperature (see Table 4.1). The relative saturation or humidity depends on the crystalline product under discussion and on the temperature and must be determined experimentally. It is important to keep in mind that this humidity in the atmosphere surrounding packaged crystals can be increased by (a) release of vapor due to insufficient drying, (b) release of vapor caused by breakage of crystals and subsequent evaporation of water inclusions trapped in the crystals, and (c) cooling of the crystals in the bag or container.

Table 4.1. Caking of Crystals

System	Temp. (°C)	Humidity p_i (Pa)	Vapor pressure p° (Pa)	Saturation φ
$CaCl_2 \cdot 6H_2O$	15	544	1701	0.32
NaCl	15	1327	1701	0.78
$Na_2SO_4 \cdot 10H_2O$	15	1582	1701	0.93

Caking becomes more severe when there are a large number of contact points between the crystals. Small crystals with a broad CSD therefore have a stronger tendency to cake than large isometric and especially spherical crystals. Sometimes, crystals are coated with a thin layer that is a barrier to water vapor diffusion and may even serve as a water adsorbent.

5. FLOWABILITY OF DRIED CRYSTALS AND CAKING

The flowability of dry crystals depends on many parameters such as the following:

- Crystal density
- Crystal size distribution
- Median crystal size
- Shape of the crystals
- Voidage fraction of the solids
- Degree of mixedness
- Inner voidage of the crystals
- Residual moisture content
- Concentration of adsorbed vapors and gases

It is common practice to describe the flow behavior of crystals using flow indexes. Flow indexes are classified according to the state of powders consisting of particles mainly above 100 μm [5.1]:

- Powders that are slightly consolidated at storage with a voidage fraction below 0.4. Cohesion due to their weight is the most important parameter for overcoming the onset of motion.
- Powders that are loosely packed solids, which are able to move at low shear rates because the interparticle friction forces are weak. As a rule, the voidage fraction is in the range between 0.4 and 0.43.

- Powders that are in a fluidized state with a voidage fraction above 0.45. The main source of momentum transfer and the main factor in determining flowability is the effect of interparticle collisions.

The smaller the particles and the more they deviate from spheres, the stronger the friction and cohesion forces are, with the result that the flowability is reduced. This is especially true of platelets and needlelike crystals. The flowability of solid material depends on its lifetime because important parameters such as the voidage fraction, interparticle forces and crystalline bridges, adsorbates, and so forth change with time. Material leaving a fluidized-bed dryer is in the fluidized state with a variety of large and small gas bubbles incorporated in the bulk. Such a material can have excellent flowability. However, during transport and storage, first the gas bubbles and then the interstitial gas leave, with the result that the voidage fraction decreases and flowability worsens (Fig. 5.1). With increasing deaeration, small particles enter the interstices between the large ones and the voidage fraction decreases more and more, especially in the lower part of the layer. Cohesion progresses due to the weight of the crystals. The solid material is exposed to an atmosphere which sometimes contains various adsorptives, especially vapor. The onset of adsorption processes changes the surface behavior of crystals and influences the cohesion of particles. Caking of crystals is very common, especially during relatively long storage periods.

In the following it is assumed that caking will not significantly influence the flowability of crystalline solids and that friction forces determine this property of particulate systems. A simple method of characterizing solid

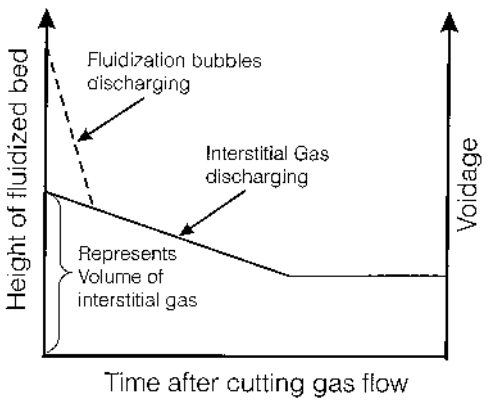

Figure 5.1. Height of fluidized bed versus time after cutting gas flow.

material is to measure the loosely packed bulk density, $\rho_{\text{bulk, loosely packed}}$, and the tapped bulk density, $\rho_{\text{bulk, tapped}}$ (see Fig. 5.2). The so-called Hausner ratio HR [5.9] is defined as

$$\text{HR} = \frac{\rho_{\text{bulk, tapped}}}{\rho_{\text{bulk, loosely packed}}} \tag{5.1}$$

The Hausner ratio correlates well with fluidizability because the loosely packed state is sometimes brought about in a fluidized bed after deaeration and settling of the particles.

The static and dynamic angle of repose can also give useful information for characterizing the flowability of a powder. The static angle of repose is the angle with the horizontal made by a pile of solid particles (see Fig. 5.3a). The dynamic angle of repose or the tilting angle of repose is explained in Figure 5.3b and gives information on the behavior of powders in slow motion. One decisive parameter that influences the angle of repose is the ratio of a mean interparticle cohesive force and the force of gravity. Angles above 30° indicate cohesive forces, which are explained in more detail in Chapter 6. Methods for measuring these angles are standardized and described in ISO 3923/1 and ISO 3923/2; see also [5.9].

In addition to the consolidation test by tapping (which might be problematic with respect to the attrition and breakage of crystals) and the measurement of the angle of repose, the flow factor (FF) is an excellent index for determining the flowability of powders and designing storage bins. The factor FF is based on the measurement of shear stress in a powder as a function of the pressure within it. It should be noted that the hydrostatic pressure in a bin or layer is proportional to the height of solids above a

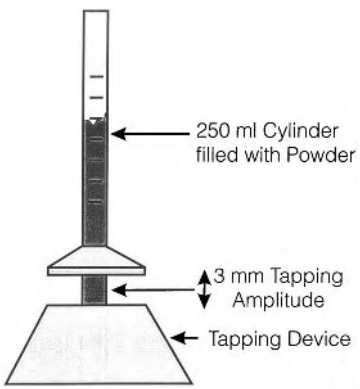

Figure 5.2. Apparatus for measuring the Hausner ratio.

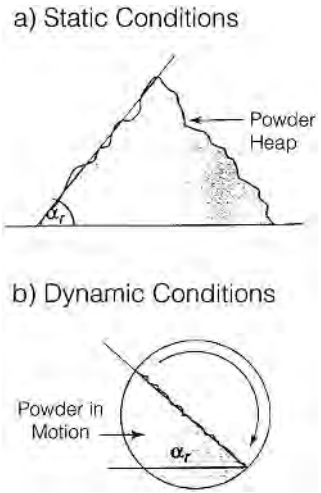

Figure 5.3. The angle of repose as a widely used measure of flowability of loosely packed powders: (a) static conditions; (b) dynamic conditions.

certain volume element. In Figure 5.4a, a powder element in general is shown with the major and minor principal stresses or normal stresses (σ_1 and σ_2, respectively) which are perpendicular to the planes of the element. Let us now consider a plane which forms the angle α with the vertical. Where $\alpha = 0^\circ$, there is no shear stress in the plane; this also applies where $\alpha = 90^\circ$. If the powder is on a free surface (see Fig. 5.4b), only the normal stresses σ_1 are effective. In both cases, the shear stress τ_s is a function of the normal stress σ. If the shear stress τ_s of any inclined plane exceeds a given value which depends on σ, an onset of flow will take place. The shear stress τ_s is measured in dependence on normal stresses or pressure by means of a suitable device. Jenike et al. [5.6] was the first to determine this relationship using a shear cell. Such cells have been improved, and biaxial and triaxial shear cells [5.7, 5.8] as well as ring shear cells are now used. The experimentally determined shear stresses τ_s are plotted against the normal stress σ for a given solid material (see Fig. 5.5). The data points measured lie on the so-called yield locus. The angle of the yield locus with the σ axis is called the angle of internal friction. In the case of zero yield stress ($\tau_s = 0$), the yield locus gives the tensile strength T of the powder. If there is no normal stress σ at all ($\sigma = 0$), the point C gives the shear stress for the onset of flow for this condition. Important information on the flow behavior of the solid can be obtained from the so-called Mohr circles, which are drawn below the yield

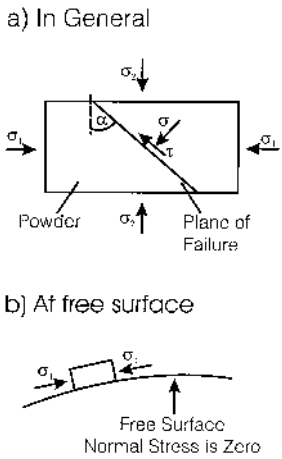

Figure 5.4. States of stress in a powder.

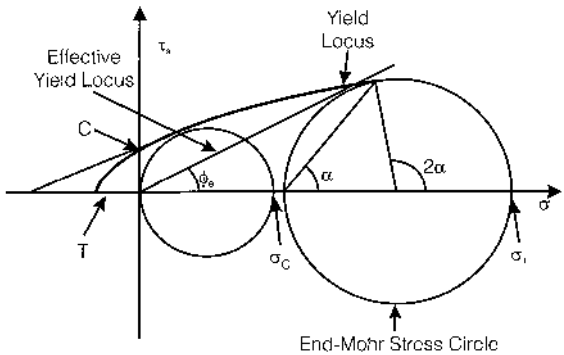

Figure 5.5. Mohr diagram shows the conditions of failure under various values of the principal stresses, shown as a yield locus.

locus in such a way that the circles touch the yield locus tangentially. The first circle in the region $\sigma > 0$ gives the stress σ_c as the intersection point with the σ axis, and the ratio σ_1/σ_c is the flow function FF and a measure of the flow behavior:

$$\mathrm{FF} = \frac{\sigma_1}{\sigma_c} \tag{5.2}$$

Here, σ_1 is the consolidation pressure, which depends on the position in a layer, storage silo, or hopper. The shape of the yield locus curve can be described by the Warren Spring equation [5.6]:

$$\left(\frac{\tau}{C}\right)^n = 1 + \frac{\sigma}{T} \tag{5.3}$$

The flowability index n is unity for a free-flowing powder and higher for a cohesive powder. The exponent n assumes the value 2 for a nonflowing powder.

In Table 5.1, the different flow behaviors in relation to various flowability indexes are given. It is important to note that these indexes as a whole give useful information about the flowability, but they correspond to each other only to a certain degree. Aging can be a major problem with crystalline material, because consolidation and adsorption/desorption of water will always take place. For instance, the release of water, which may lead to caking, can only be avoided if the crystals are dried under zero humidity and always kept under these conditions in the storage container.

Let us briefly discuss the interrelationship between the flowability indexes (HR ratio, angle of repose, flow function FF) and the properties of the crystalline material (density ρ_C, CSD, L_{50}, shape, purity, etc.). There is so far no way predicting this; however, some hints can be given.

Density ρ_C: The higher the density of the crystals, the higher the hydrostatic pressure for a given voidage of a layer and the more preconsolidated the powder. According to $\tau_s = f(\sigma)$ and increased cohesive contacts, the flowability of the solid is reduced with rising ρ_C.

CSD, percentage of fines: The flowability of a crystalline product can be expected to worsen with increasing fines (below 100 µm) because the voidage fraction will decrease and the number of interparticle contacts

Table 5.1. Flow Behavior in Relation to Various Indexes

	FF[a]	HR[b]	$\alpha_{r'}^{c}$
Nonflowing	< 2	> 1.4	> 60
Cohesive	2–4	> 1.4	> 60
Fairly free-flowing	4–10	1.25–1.4	45–60
Free-flowing	> 10	1–1.25	30–45
Excellent flowing	> 10	1–1.25	10–30
Aerated	> 10	1–1.25	< 10

[a] Flow factor, dimensionless. [b] Hausner ratio, dimensionless. [c] Static angle of repose.

per unit volume will increase. According to interparticle cohesive and friction forces, the onset of movement is hindered.

Shape: The more the shape of crystals deviates from spheres, the more the flowability is reduced. It is expected that needlelike and flat crystals will exhibit poor flowability. Attrition will always lead to rounded crystals, which move better, but this process leads to fines with increased friction or to dust problems during the transport and storage of crystals.

Purity: Crystals with more or less purity are adsorbents for any kind of gaseous adsorptives present in the surrounding gas. The interparticle forces are dependent on the amount and kind of adsorbed species, and the adsorption isotherm for a distinct adsorption can be influenced by impurities present in the surface of crystals. Because it is not possible to predict the quality and quantity of interparticle forces in a general way, it is difficult to establish relationships between purity and flowability of crystalline material.

REFERENCES

[1.1] M. Kind and A. Mersmann, On the width of metastable zone of solutions, in *Proc. 10th Conf. on Industrial Crystallization* (J. Nyvlt and S. Zacek, eds.), Elsevier, Amsterdam (1989).

[1.2] A. Mersmann, Bei welcher Übersättigung soll man kristallisieren? *Chem. Ing. Tech.*, *64*: 991 (1992).

[1.3] A. Mersmann, M. Angerhöfer, T. Gutwald, R. Sangl, and S. Wang, General prediction of median crystal sizes, *Sep. Technol.*, *2*: 85 (1992).

[1.4] A. Eble, Precipitation of nanoscale crystals with particular reference to interfacial energy, Thesis, Technische Universität München (2000).

[1.5] C. Heyer, Production of nano-sized particles by drowning-out precipitation, Thesis, Technische Universität München (2000).

[1.6] W. Gösele, Precipitation to obtain easily separated solids, *Chem. Eng. Sci.*, *48*(2): 295–303 (1993).

[1.7] M. Kahlweit, Ostwald ripening of precipitates, *Adv. Colloid Interf. Sci.*, *5*: 1–35 (1975).

[1.8] J. Nyvlt, O. Söhnel, M. Matuchova, and M. Broul, *The Kinetics of Industrial Crystallization*, Chemical Engineering Monographs Vol. 19, Elsevier, Amsterdam (1985).

[3.1] Z. Kolar, J. J. M. Binsma, and B. Subotic, The influence of temperature and the concentration of the precipitating components on the formation and the properties of β-BaF_2 microcrystals, in *Proc. 9th Conf. on Industrial Crystallization* (S. J. Jancic and E. J. de Jong, eds.), Elsevier, Amsterdam (1984).

[3.2] M. C. van der Leeden and G. M. van Rosmalen, The role of additives in the agglomeration of barium sulfate, in *Proc. 9th Conf. on Industrial Crystallization* (S. J. Jancic and E. J. de Jong, eds.), Elsevier, Amsterdam (1984).
[3.3] A. Bravais, *Etudes cristallographiques*, Gauthier-Villars, Paris (1866).
[3.4] G. Friedel, *Bull. Soc. Fr. Mineral.*, *30*: 326 (1907).
[3.5] J. D. H. Donnay and D. Harker, A new law of crystal morphology extending the law of Bravais, *Am. Mineral.*, *22*: 446 (1937).
[3.6] G. Pfefer, Méthodologie d'étude du changement de la morphologie et du faciès cristallin, Thèse, université Marseillle (1996).
[3.7] P. Hartman and P. Bennema, *J. Cryst. Growth.*, *49*: 145 (1980).
[4.1] J. A. Burton, R. C. Prim, and W. P. Slichter, The distribution of solute grown from the melt Part I. *Theoret. J. Chem. Phys.*, *21*(11): 1987 (1953).
[4.2] A. Mersmann and J. Franke, Thermal analysis of solid production processes, *Chem. Eng. Technol.*, *16*: 75 (1993).
[5.1] J. A. H. de Jong, A. C. Hoffman, and H. J. Finkers, Properly determine powder flowability to maximise plant output, *Chem. Eng. Prog.*, *95*: 25 (1999).
[5.2] D. Geldart, N. Harnby, and A. C. Wong, Fluidization of cohesive powders, *Powder Technol.*, *37*: 25 (1984).
[5.3] N. Harnby, A. E. Hawkins, and D. Vandame, The use of bulk density determination as a means of typifying the flow characteristics of loosely compacted powders under conditions of variable relative humidity, *Chem. Eng. Sci.*, *42*: 879 (1987).
[5.4] J. Schwedes, *Fliessverhalten von Schüttgütern in Bunkern*, Verlag Chemie, Weinheim (1968).
[5.5] D. Geldart, M. F. Mallet, and N. Rolfe, Assessing the flowability of powders using angle of repose, *Powder Handling Proc.*, *2*: 341 (1990).
[5.6] A. W. Jenike, P. J. Elsey, and R. H. Woolley, Flow properties of bulk solids, *Proc. Am. Soc. Testing Mater.*, *60*: 1168 (1960).
[5.7] J. Schwedes and D. Schulze, Measurement of flow properties of bulk solids, *Powder Technol.*, *61*: 59 (1990).
[5.8] F. J. Carr and D. M. Walker, An annular cell for granular materials, *Powder Technol.*, *1*: 369 (1967/1968).
[5.9] M. D. Ashton, D. C.-H. Cheng, R. Farley, and F. H. H. Valentin, Some investigation into the strength and flow properties of powders, *Rheol. Acta*, *4*(3): 206–218 (1965).

8
Design of Crystallizers

A. MERSMANN Technische Universität München, Garching, Germany

The selection and design of a crystallizer depend on the type of supersaturation to be produced (cooling, evaporative, drowning out, chemical reaction), the mode of operation (continuously fed or batch), the desired crystal size distribution and median crystal size, and the purity of the product. It is generally possible to "cultivate" practically any crystal size distribution, but this is a complex procedure with respect to apparatus (crystallizer volume) and operation (e.g., classifying crystallization, fines dissolution, seeding the solution, precise control over supersaturation, switching between several crystallizers, etc.). The following designs are based on single-step continuously operated stirred cooling crystallizers; however, information on other types of apparatus and operating modes is also provided. In the crystallizer, the desired optimum supersaturation should occur evenly throughout the growth zone, the solution should be as well mixed as possible, and all crystals should be in suspension.

Optimum supersaturation, at which existing crystals grow at the maximum rate permitted (e.g., the desired grain shape is obtained without mother liquor or impurity inclusions) and at which a certain number of

crystals is not exceeded, must be determined experimentally. Useful approximate values for systems of high solubility lie roughly within the range $0.01 < \Delta C < 0.1\,\mathrm{kmol/m^3}$ (cf. Chapter 3) and can be given by a certain safe distance from the metastable supersaturation $\Delta C_{\mathrm{met,hom}}$ for primary homogeneous nucleation. This statement is generally applicable; that is, it applies to cooling, evaporative, drowning-out, and reaction crystallization.

The flow and, above all, the volumetric flow circulated in loop-type crystallizers (stirred-vessel crystallizers with a draft tube and forced-circulation crystallizers) should be set in such way that all crystals are evenly distributed throughout the apparatus and are all subject to optimum supersaturation. Moreover, the metastable zone ΔC_{met} should not be exceeded anywhere, if possible. This requires the rotors (stirrer or pump impeller of diameter D) to have a specific rotational speed s and a specific peripheral speed $s\pi D$, leading to a certain minimum specific power input $(\bar{\varepsilon})_{\mathrm{min}}$ in the crystallizer.

1. CRYSTALLIZATION APPARATUS

The choice and design of the crystallization apparatus depends, among other things, on the properties of the phases involved and the flow required for mixing and suspension. Generally, a distinction can be made between crystallization from solution and crystallization from a melt in order to choose the correct type of crystallization apparatus. Melt crystallizaiton can be subdivided into two groups with respect to the process principles involved:

1. Processes in which connected crystal layers are usually discontinuously deposited from a melt onto cooled surfaces so that the remaining solution can be separated from the crystal layers without a further separation step in the process.
2. Processes in which the entire melt is usually converted continuously to a crystal suspension by being cooled. The suspension is then separated into a solid and the remaining melt in a separate process, which is often mechanical liquid separation.

1.1. Crystallization from Solutions

When crystals are generated out of a solution in a crystallizer, the suspension must be mixed and deposition avoided. It must generally be determined as to whether the entire suspension, including coarse crystals, or only that part of the flow containing crystals larger than approximately 100 μm is to

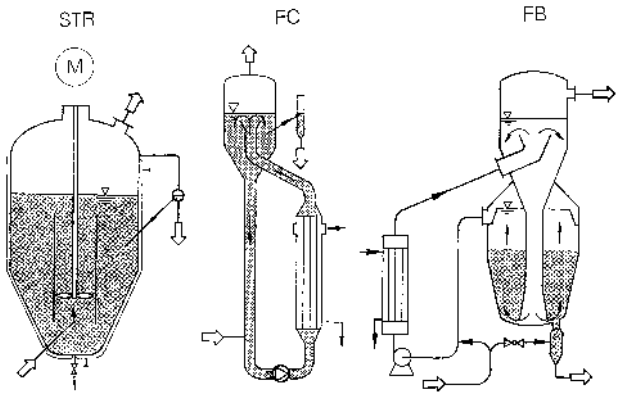

Figure 1.1. Typical industrial crystallizers.

be circulated by a circulating device (stirrer or axial/radial pump). In the former case, relatively strong attrition occurs, especially of large crystals. As attrition fragments can act as effective secondary crystal nuclei (cf. Chapter 5), the crystal size distribution of a crystalline product and thus the mean crystal size are often determined by attrition processes. The fluidized-bed crystallizer differs from the typical industrial crystallizers [1.1] illustrated in Figure 1.1 by the fact that a suspension flow containing only small crystals (e.g., under 100 μm) is conducted by the circulation device (pump). For this reason, fluidized-bed (FB) crystallizers generally yield a coarser product than stirred vessels and forced-circulation (FC) crystallizers. FC and FB crystallizers have the advantage over stirred vessels that the ratio of the heat-exchange surface to the crystallizer volume can be maintained due to the external heat exchanger when scaling up the crystallizer.

The preceding statement is explained in Figure 1.2 and 1.3 with reference to fluidized-bed crystallizers. This type of crystallizer is a classifying crystallizer with external circulation of the solution in order to attain spatial separation of supersaturation and growth. The solution is supersaturated in a virtually crystal-free zone, whereas supersaturation in the growth zone is given over to the crystallizer. The growth zone is designed in such a way that a fluidized bed is created by the upward flow. The crystals remain at certain levels, depending on their size.

Figure 1.2 shows a cooling crystallizer with an external heat exchanger. Despite the minimal temperature differences allowed (usually under 2 K) between the circulated solution and the solvent, high heat flux densities can be obtained. A small flow of warm, concentrated inlet solution is added directly to the much larger circulating flow upstream of the heat

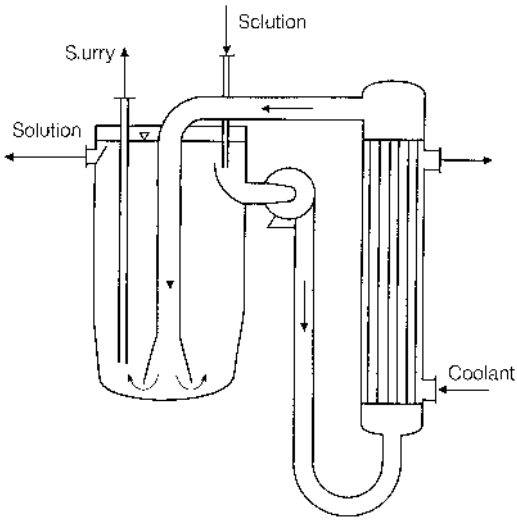

Figure 1.2. Cooling crystallizer with a circulating pump and an external cooler.

exchanger. The solution supersaturated in the heat exchanger enters the crystallization chamber at the bottom of the crystallizer and suspends the crystals. By enlarging the flow cross section, the solid is separated. The growing crystals sink to lower levels according to their rate of sedimentation until they finally reach the product outlet.

Figure 1.3 illustrates this type of crystallizer in the form of an evaporative crystallizer. The evaporation and crystallization parts are joined directly to each other. The crystallization vessel is connected to the heat exchanger by the circulation pump and the fresh solution is fed into the circulation flow.

The vacuum crystallizer illustrated in Figure 1.4 does not have a heat exchanger in the crystallization flow. This figure shows the open model, in which the crystallization part is under atmospheric pressure. The difference in pressure to the vacuum part is compensated by the hydrostatic pressure of the liquid.

Figure 1.5 shows a vacuum crystallizer with upward flow in the tube and agitator baffles. This type of crystallizer yields the degree of growth required for the production of coarse crystals. Instead of a circulation pump as in Figure 1.1, a circulating device is built into the lower part of the draft tube. The holding sheets of the tube serve as agitator baffles. Fresh solution is fed directly into the tube. The crystals enter the vicinity of the vaporizing

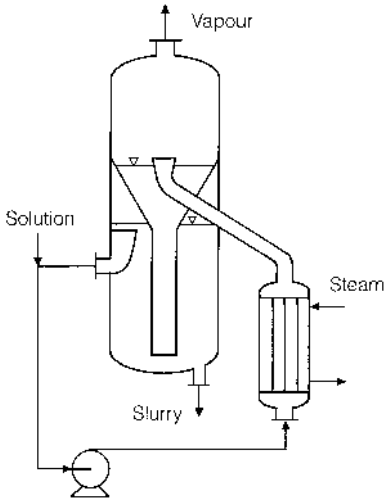

Figure 1.3. Evaporative crystallizer with an external boiler.

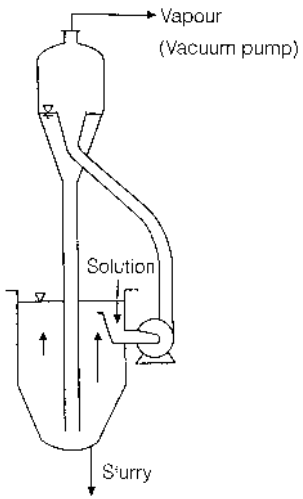

Figure 1.4. Vacuum crystallizer with separate crystallization and evaporative chambers.

surface, where supersaturation is at its peak. Fines can be removed by an overflow in the ring chamber. The coarse part of a narrow crystal size distribution is separated by a screening tube at the lower end of the crystallizer.

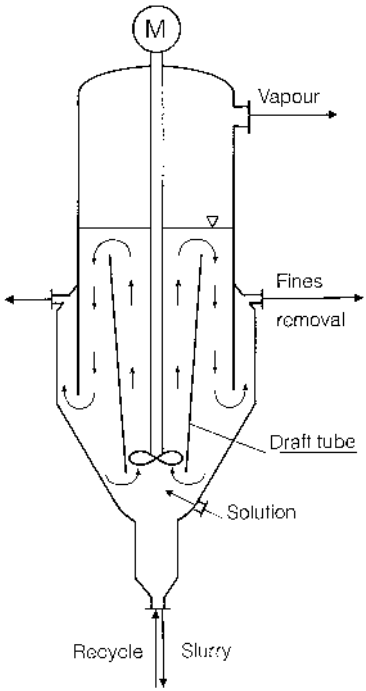

Figure 1.5. Continuously operated vacuum crystallizer with a circulating device.

There are two suspension circulation flows in the fluidized-bed crystallizer illustrated in Figure 1.6, which has two concentric tubes, a bottom tube with a circulating device and an external ejection tube and a continuous gap around the crystallizer. A fine product exists primarily in the inner circulation, which has a fast upward flow in the inner tube and a high supersaturation value at the evaporation surface. An external circulation with a classifying zone is created above the ejector in the lower chamber of the casing by the downflowing solution in the ring chamber. In this external chamber, a classifying fluidized bed is formed in which coarse crystals tend to exist; fine crystals are carried away and drawn into the inner circulation via the ejector gap. The crystal contents can be influenced by a solution overflow above the classifying zone. Fresh solution is fed directly into the tube. The product is withdrawn from the classifying zone. The crystallizer can be operated in many ways by a number of control options (e.g., stirrer revolution, solution overflow, and ejector adjustment).

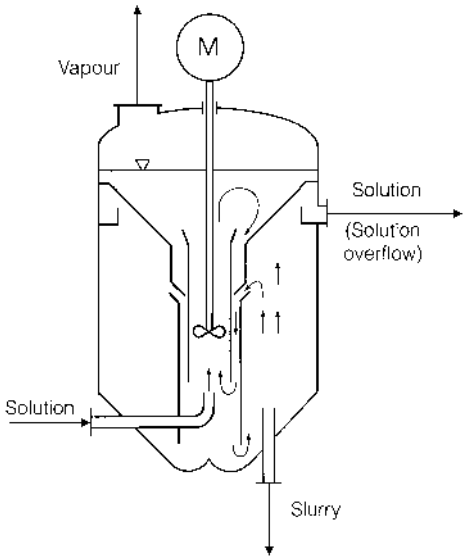

Figure 1.6. Vacuum crystallizer with a circulating device in a tube.

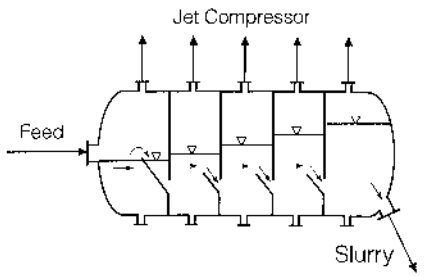

Figure 1.7. Horizontal five-stage vacuum crystallizer.

Figure 1.7 shows a multistage crystallizer in a horizontal position without moving parts. This type of crystallizer is suitable for vacuum-cooling crystallization. The evaporation chambers are separated from each other by several partitions; the solution chambers are thus connected to each other so that the suspension flows from stage to stage. Fresh solution is fed in at the first stage and is cooled continuously from stage to stage. The product is withdrawn at the last stage, which has the lowest pressure. Steam jets maintain the various low pressures. In many cases, the liquid is brought into motion in the individual stages by bubbling gas (air).

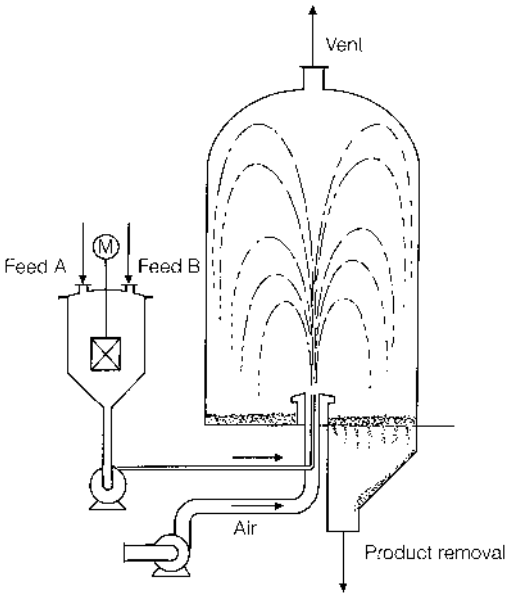

Figure 1.8. Prilling tower for producing calcium nitrate.

In many crystallizers, cooling air cools the solution and causes the solvents to evaporate. Figure 1.8 shows a diagrammatic view of a prilling tower for calcium nitrate. Cooling air sucked in from a ventilator sprays the solution of calcium nitrate and ammonium nitrate from the reservoir through the spray nozzle. The salt in the solution crystallizes out after the liquid has cooled and lost part of the solvent through evaporation. The solid crystals drop to the floor of the prilling tower, from where they are mechanically transported to a cooling drum.

1.2. Crystallizing Out Layers from the Melt

Tubular, wetted-wall, and bubble-column crystallizers are used for crystallizing out layers (see Fig. 1.9). In the tubular apparatus, the molten mixture to be separated is conveyed through cooled pipes. As soon as a certain amount of solid has grown as a crust on the pipe wall from the component or components that are more difficult to melt, the melt remaining in the pipe core is withdrawn via a foot valve. This is usually followed by the process of sweating; the crystalline layer is slowly heated so that only the

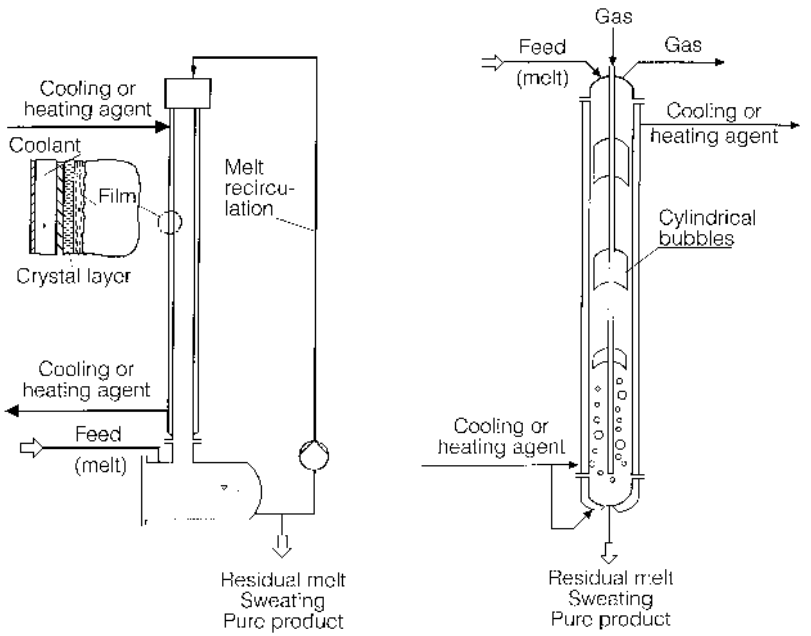

(a) (b)

Figure 1.9. (a) Wetted-wall crystallizer (Sulzer-MWB); (b) bubble-column crystallizer (Rütgerswerke).

component(s) that are more difficult to melt remain. Eventually, these can be obtained in a very pure form.

In the wetted-wall crystallizer, the molten mixture to be separated is fed into the top end of a cooled pipe or pipe bundle as trickling film and is circulated by a pump. When a continuous layer of a certain thickness has been formed, any impurities in the crystals and, finally, the pure crystals can be obtained by controlled heating and partial melting [1.3]. The bubble-column crystallizer is characterized by the fact that the crystal layers are formed in jacket-cooled pipes, with bubbles of an inert gas rising through the melt to enhance heat and mass transfer [1.4].

1.3. Crystallizing Out Suspensions from the Melt

If the crystal product crystallizing from a melt is granular, it is separated from the melt either by mechanical liquid separation (centrifuging, filtering,

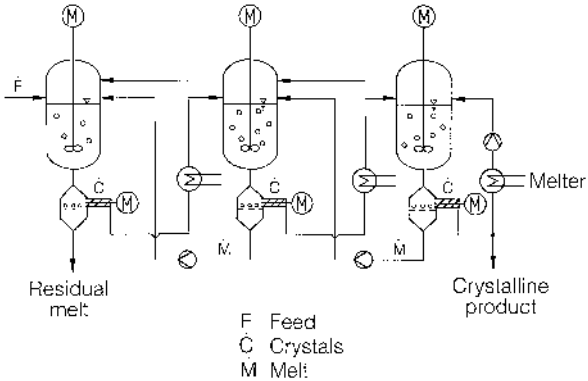

Figure 1.10. Three-stage countercurrent separating device for melt crystallization.

compressing) or by remelting it (sometimes only after it has been washed). The choice of apparatus depends strongly on whether only one or several separating procedures are required in order to obtain products of the desired purity. If this can be achieved in one theoretical separating stage (e.g., for the simple eutectic system), stirring devices, fluidized beds, three-phase beds operated with an inert cooling gas [1.5, 1.6], and even special apparatus such as scraped-surface heat exchangers, disk condensers, and cooling belts are frequently used as crystallizers. Selecting the apparatus generally becomes more difficult when the separation of substances involves more than one stage. One possibility is to switch the single-step apparatus to countercurrent flow (see Fig. 1.10). Although this does not pose any great problems with respect to operating safety and scale-up, it involves relatively high investment costs. In view of this, countercurrent flow crystallization columns are more economical but their scale-up is often problematic.

Figure 1.11 provides some possible apparatus options: the Brodie purifier with horizontal transport, the Kureha column with vertical mechanical forced conveying by double-lead screws, and the vertically arranged Phillips pressure crystallization column. The Brodie purifier (see Fig. 1.11a) consists of horizontally installed scraped-surface heat exchangers connected in tandem and a vertical purification column. In the Kureha column (see Fig. 1.11b), a crystal product which has mainly been freed from the remaining melt is fed in at the bottom and transported to the column head by means of a double-lead screw. After the crystals have been completely melted, part of the purified melt is withdrawn as the end

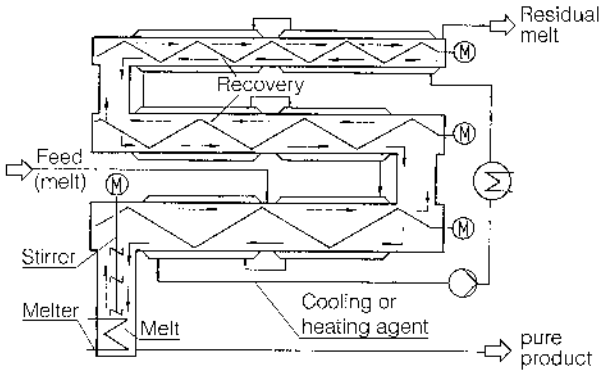

(a)

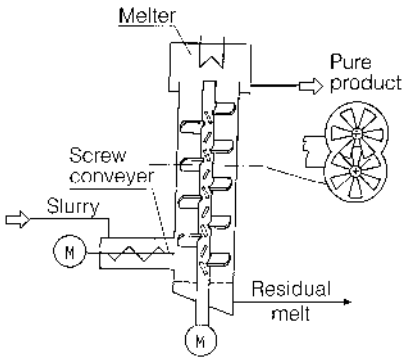

(b)

Figure 1.11. (a) Brodie purifier; (b) crystallization column with mechanical transport.

product while the other part flows as reflux in the opposite direction to the crystals, which are being transported upward.

The Phillips pressure column (see Fig. 1.11c) is characterized by the fact that the mixture to be purified is fed into the column under pressure via a scraped-surface heat exchanger. While the crystals in the column flow downward and are melted at the bottom, a large part of the liquid phase is pressed out of the column via a filter embedded in the wall. The purified product leaves the column while the rest flows in the opposite direction to the crystal suspension as reflux. By using special pumps, the suspension column can be pulsated to improve mass transfer between the crystals and the remaining melt.

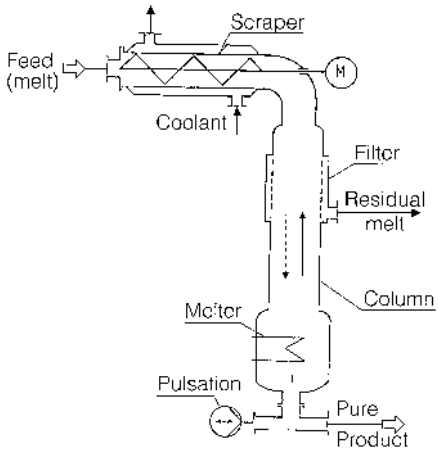

(c)

Figure 1.11. (c) Pressure crystallization column (Phillips).

2. OPERATING MODES

Depending on the creation of supersaturation, a distinction is generally made between the following types of crystallization from solutions: (a) cooling crystallization, (b) evaporative crystallization, (c) drowning-out crystallization, and (d) reaction crystallization. Vacuum crystallization combines cooling and evaporative crystallization. Sometimes, an increase in temperature combined with a great increase in pressure causes the solution to become supersaturated, as in the case with aqueous saccharose and magnesium sulfate solutions. The boundaries between drowning-out and reaction crystallization may be fluent depending on whether and to what extent a third substance added to the solution reacts with one or a number of solution components. Crystallization can thus occur when a strong electrolyte and an organic solution are mixed in a process known as salting-out. The term *precipitation crystallization* is frequently used in the literature for a very rapid crystallization process that can often be controlled to only a small extent and in which a large number of crystal nuclei are formed.

This section will focus on the design of apparatus for cooling and evaporative crystallization, which is suitable for the production of coarse crystals. Information on fine crystals in the micrometer and nanometer ranges can also be found in Chapter 9. The mode of crystallization and the final median crystal size for a given growth period depend mainly on the following system parameters:

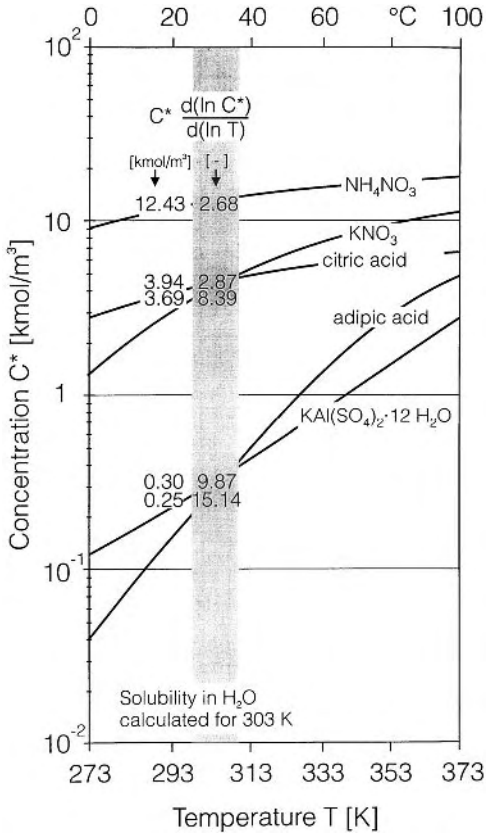

Figure 2.1. Solubility curves and steepness $d(\ln C^*)/d(\ln T)$ of different inorganic and organic systems.

- Solubility C^*
- Slope of the solubility curve $dC^*/d\vartheta$ or dC^*/dT with $T = 273 + \vartheta$
- Supersaturation

In Chapter 1, it has been shown that the heat of crystallization in ideal systems is proportional to $d(\ln C^*)/d(\ln T)$. In this case, the solubility C^* versus the temperature T is a straight line in a double-logarithmic plot. In Figure 2.1, the solubility C^* of aqueous systems is plotted against the absolute temperature T for some organic and inorganic solutes. The smallest slope at a temperature of 30°C has NH_4NO_3 where $d(\ln C^*)/d(\ln T) = 2.68$ and the solubility curve of adipic acid is very steep where

$d(\ln C^*)/(\ln T) = 15.1$. A rough guide for the crystallization mode may be as follows:

$$\frac{d(\ln C^*)}{d(\ln T)} = \frac{T}{C^*}\frac{dC^*}{dT} > 8 \quad \text{Cooling crystallization}$$

$$\frac{d(\ln C^*)}{d(\ln T)} = \frac{T}{C^*}\frac{dC^*}{dT} < 1 \quad \text{Evaporative crystallization}$$

Vacuum crystallization (cooling and evaporation) is often used in systems with moderate slopes of the solubility curve. Evaporative flash crystallization has the great advantage that the encrustation of cooling or heating surfaces can be avoided. With respect to the third parameter, supersaturation, it is important to avoid activated nucleation and to operate the crystallizer at the appropriate rate of attrition-controlled secondary nucleation. A rough guide for the maximum allowable supersaturation is given in Figure 2.2, in which σ is plotted against the dimensionless solubility C^*/ρ_C; see also Sec. 3.4. Below the curve, which approximately separates the ranges of activated and attrition-controlled nucleation, optimum supersaturations

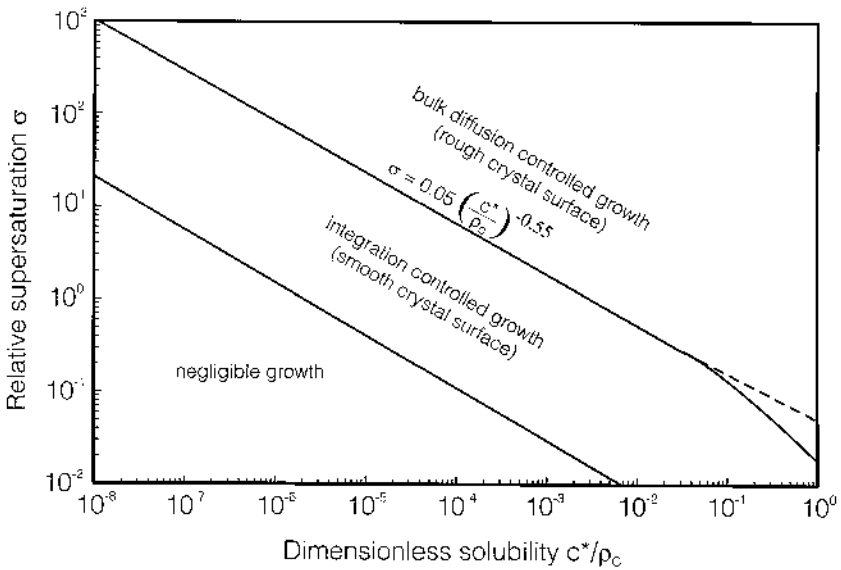

Figure 2.2. σ against c^*/ρ_C. Area below the curve: attrition controlled nucleation and integration controlled growth are dominant; area above the curve: activated nucleation and diffusion-controlled growth are dominant.

Δc_{opt} can be found. Further information on this topic has already been presented in Chapter 3.

2.1. Cooling Crystallization

The process of cooling crystallization can be used when the solubility of the substance to be crystallized greatly increases with temperatures (see Figs. 2.3 and 2.4). Typical examples of this are the aqueous solutions of potassium, sodium, and ammonium nitrate as well as copper sulfate. The undersatu-

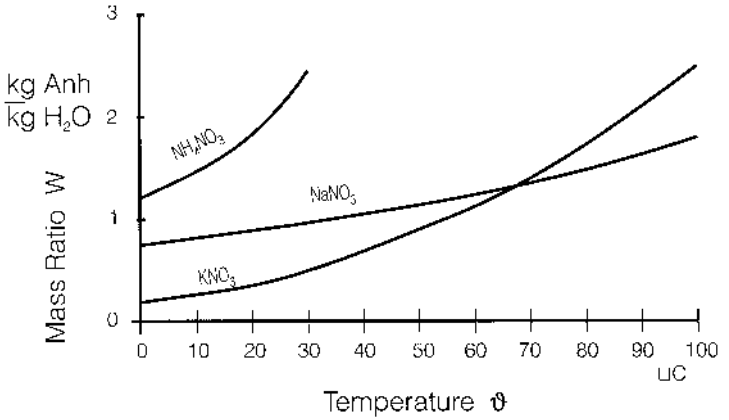

Figure 2.3. Solubility of inorganic systems ($dW^*/d\vartheta$ large).

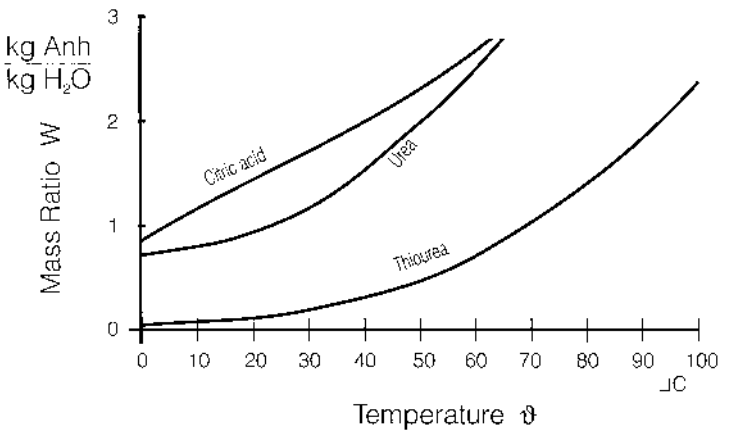

Figure 2.4. Solubility of organic systems ($dW^*/d\vartheta$ large).

rated solution is fed into the crystallizer and cooled either via an external jacket or a cooler inside the crystallizer. Continuous operation of this apparatus is aimed at obtaining an optimum supersaturation Δc_{opt}, yielding a growth rate as high as possible while keeping the rate of nucleation low enough for a sufficiently coarse crystal product to be formed. In small production plants, crystallizers are usually operated in a batch mode. A simple operating method consists in cooling the solution at a constant cooling rate. However, this is not ideal because at the beginning of cooling, no seed surface or, after seeding, only a small seed surface is available, creating very high levels of supersaturation followed by extensive nucleation. At the end of the cooling process, the crystal product may have a large surface, but it still grows very slowly due to the low supersaturations. Therefore, it is beneficial to set the cooling rate so that supersaturation remains almost constant during the cooling period. When the crystallizer contents are well mixed and the heat is withdrawn uniformly with respect to space, approximately the same optimum supersaturation and crystal size distribution exist throughout the crystallizer.

2.2. Evaporative Crystallization

Evaporative crystallization is useful when solubility increases only slightly, remains almost constant, or even decreases with temperature (see Figs. 2.5

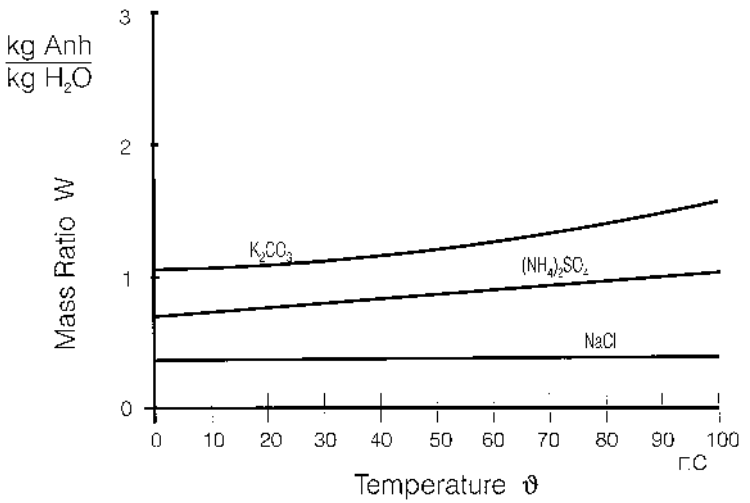

Figure 2.5. Solubility of inorganic systems ($dW^*/d\vartheta$ small).

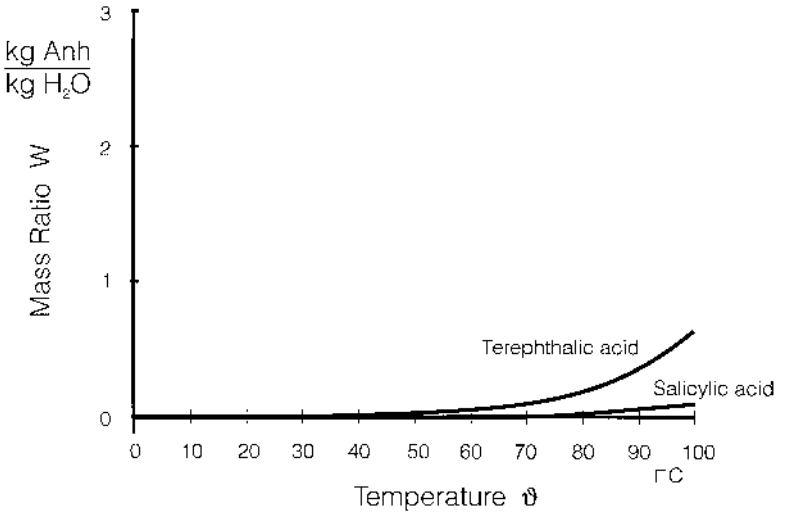

Figure 2.6. Solubility of organic systems ($dW^*/d\vartheta$ small).

and 2.6). Typical systems are aqueous solutions of sodium chloride, ammonium sulfate, and potassium sulfate, as well as methanol solutions of terephthalic acid. The undersaturated solution is fed into the crystallizer and heated to the boiling point of the solution so that the solvent evaporates. Because the boiling point of the solution is a function of pressure, boiling tends to take place at the surface of the liquid, which can lead to high levels of supersaturation. In continuous crystallizers, the supersaturation occurring in the middle depends on the rate of evaporation. In batch crystallizers, the same occurs as in cooling crystallization. At a constant rate of evaporation, supersaturation at the beginning of the operation is unfavorably high, and toward the end, it is uneconomically low. In this case, it is also beneficial to set the rate of evaporation in relation to time so that supersaturation remains approximately constant and has an optimum value for crystal size distribution.

2.3. Vacuum Crystallization

In vacuum crystallization, the solution is evaporated and cooled simultaneously by decreasing the pressure and temperature. The vacuum is often created and maintained by steam jet compressors in up to six steps. Because the enthalpy of vaporization is withdrawn from the solution, it will cool

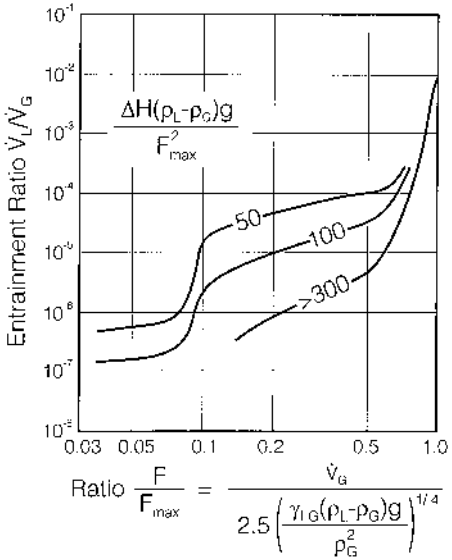

Figure 2.7. Entrainment ratio versus the ratio $F/F_{\max}$ for different heights ΔH above the liquid surface.

down. As a result, it is often possible to dispense with having to use cooling surfaces, which involves the risk of encrustation. Nevertheless, the vapor leaving the surface of the liquid entrains highly supersaturated droplets which are sprayed onto the walls, where they reevaporate, leading to heterogeneous nucleation and, finally, encrustation. To counteract this problem, rinsing the walls of the apparatus with solvent or undersaturated solution is recommended. Moreover, the droplets are entrained to a limited extent when an F factor known from gas–liquid columns is not exceeded [2.1]:

$$F \equiv w_G\sqrt{\rho_G}\ [\text{Pa}] < 0.017\,[\text{m/s}]\sqrt{\rho_L - \rho_G}\ [\text{kg/m}^3] \tag{2.1}$$

In addition, the size of the droplets depends on the surface tension γ_{LG} of the solution. In Figure 2.7, the ratio $\dot{V}_L/\dot{V}_G$ of the liquid $\dot{V}_L$ entrained by the vapor flow rate $\dot{V}_G$ is plotted against the ratio [2.2]

$$\frac{F}{F_{\max}} \quad \text{with } F_{\max} \approx 2.5\ [\gamma_{LG}(\rho_L - \rho_G)g]^{1/4} \tag{2.2}$$

As some solutions require a pressure of only a few hundred pascals, the flange of the crystallizer must be designed accordingly (e.g., with a groove and spring or an O-ring).

2.4. Drowning-out, Pressure, and Reaction Crystallization

Drowning-out crystallization of inorganic salts from aqueous solutions with the aid of organic substances may offer the advantage over other processes of reducing energy consumption, as the enthalpy of vaporization of drowning-out agents is usually considerably smaller than that for water. However, drowning-out crystallization then competes against multistage evaporative crystallization or methods involving thermocompression or a combination of other processes that enable energy to be saved during crystallization. Drowning-out crystallization of sodium sulfate and potash alum from aqueous solutions by methanol, ammonium alum, and potassium chloride with the aid of ethanol has already been examined scientifically [2.3–2.5].

In Figure 2.8, the solubility of the three-component Na_2SO_4–H_2O–CH_3OH system at 40°C is illustrated in a triangular diagram. Sodium sulfate is formed above a temperature of 32.5°C. Supersaturation can easily be determined by drawing a straight line from the composition of the binary

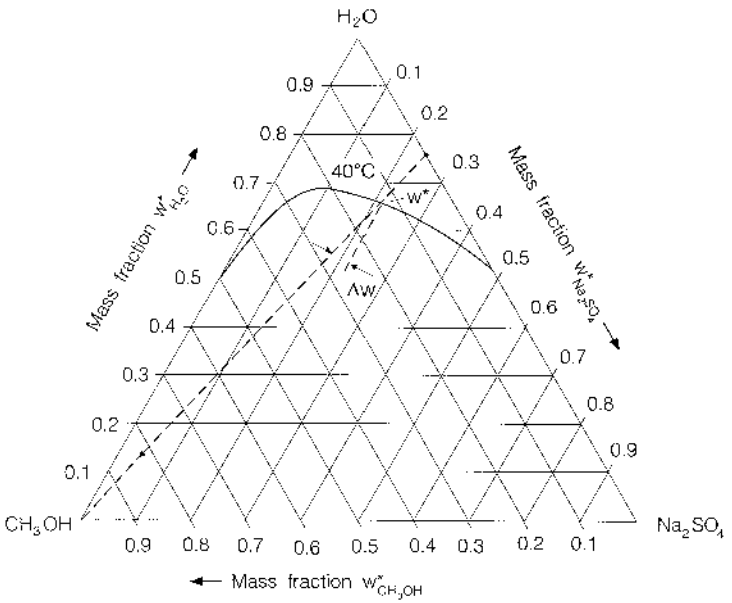

Figure 2.8. Solubility of three-component Na_2SO_4–H_2O–CH_3OH system at 40°C.

Na_2SO_4–H_2O system to the methanol corner. The amount of drowning-out agent added determines the supersaturation $\Delta w = w - w^*$ or $\sigma = \Delta w / w^*$, where w^* denotes the equilibrium concentration of the saturated ternary system and Δw denotes the excess of Na_2SO_4 that is salted out. As in cooling and evaporative crystallization, the mean crystal size depends *inter alia* on supersaturation.

There are several sulfites and sulfates for which the solubility increases with temperature, passes through a maximum, and then decreases again. This applies to $Fe(II)SO_4 \cdot H_2O$, $MgSO_4 \cdot H_2O$, $Na_2CO_3 \cdot H_2O$, Na_2SO_4, Na_2SO_3, and $ZnSO_4 \cdot H_2O$ at temperatures ranging from 32.5°C for Na_2SO_3 to 67°C for $MgSO_4 \cdot H_2O$. When the aqueous solutions of these salts are placed under pressure to avoid evaporation and are heated above the temperature of their maximum solubility, nuclei form and grow due to supersaturation. Although the compression of the liquid solution and the pressure crystallizer involve additional costs, the solvent does not have to be evaporated. Because nucleation takes place in the bulk of the solution, encrustation can be reduced.

In homogeneous reaction crystallization, one or more reactants react with one or more components in a liquid phase. In the case of heterogeneous reaction, a reactant is often added in gas or vapor form. The technological aspects of reaction crystallization, such as the process of macromixing and micromixing and the addition of reactants as well as the type and place of addition, are described in Chapter 9. In a homogeneous chemical reaction, the reactants or educts must first be macromixed and then micromixed on a molecularly disperse basis (the micromixing time is generally shorter than the macromixing time; see Chapter 9. In very fast reactions, the reaction rate and, thus, the product formation rate depend on the mixing time and they depend on the reaction time in very slow reactions. The product concentration forming in the crystallizer and the supersaturation for a given solubility are determined by (a) the product formation rate and (b) the desupersaturation of the solution by nucleation and crystal growth.

Heterogeneous gas–liquid reactions involve additional transport resistance in the gas and liquid phases, causing the product concentration (and also the supersaturation and mean particle size) to depend on the following processes:

1. Mass transfer in the vapor phase
2. Mass transfer in the liquid phase
3. Product formation rate by the chemical reaction
4. Desupersaturation of the solution by nucleation and growth

2.5. Approximate Operating Conditions

In the following, some operating conditions of crystallizers used for systems with high solubilities ($c^*/\rho_C > 0.01$) will be presented. Industrial crystallizers are mainly stirred-vessel [STR = stirred tank reactor or DTB = draft tube baffled), forced circulation (FC), and fluidized-bed (FB)] crystallizers, presented here according to their importance in industry. Mullin [2.6] has given a representative overview of these three basic types of continuous crystallizer (see Fig. 2.9), of mixed suspension crystallizers (see Fig. 2.10), and of simplified flow patterns in agitated vessels (see Fig. 2.11). The heat exchanger in each case may be either a heater or a cooler, and the apparatus may be operated as a cooling, evaporative, or vacuum crystallizer. In the total-discharge mixed suspension, mixed product reactor (MSMPR) crystallizer, the crystal and liquor residence times are identical. In the case of a clear-liquor overflow, the crystal and liquor retention times become independent of one another, which makes it possible to control the suspension density. Classification of the product can be obtained in MSCPR crystallizers (see Chapter 4).

When dealing with agitated vessels, a vertical flow from the stirrer to the bottom is recommended and a draft tube (DT) is favorable in order to

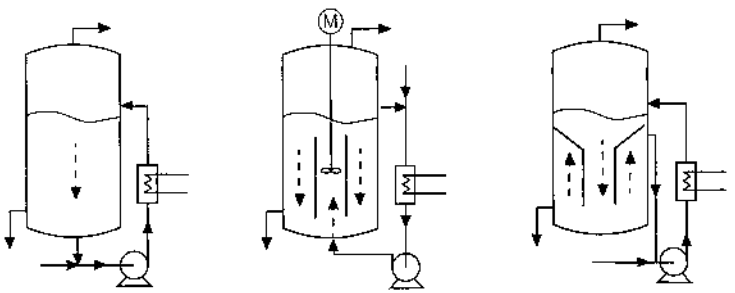

Figure 2.9. Basic types of continuous crystallizer.

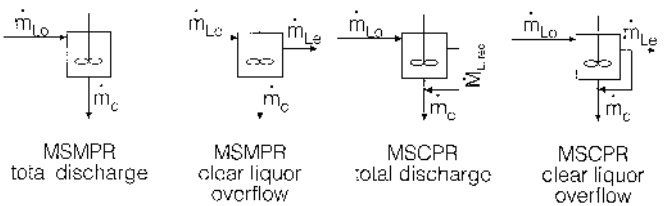

Figure 2.10. Mixed suspension crystallizers.

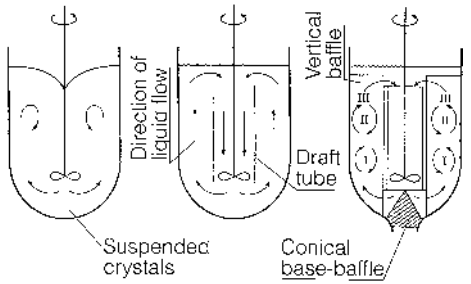

Figure 2.11. Simplified flow pattern in an agitated vessel.

operate the crystallizer with the minimum specific power input $(\bar{\varepsilon})_{\min}$, which is smaller than in a vessel without this tube. Baffles (or heat exchanger coils) are necessary in order to avoid a deep vortex at a high stirrer Reynolds number $\mathrm{Re} = sD^2/\nu_L$, >1000 and an insurge of the gas phase.

The product capacity $\dot{m}_{Cv}$ based on the crystallizer volume V is given by

$$\dot{m}_{Cv} \equiv \frac{\dot{M}_C}{V} = \tfrac{1}{2} a_T G \rho_C = \frac{3\varphi_T}{L_{32}} G \rho_C \tag{2.3}$$

With the growth rate

$$G = \frac{\beta}{3\alpha} k_d \frac{\Delta c}{\rho_C} \quad \text{(diffusion controlled)} \tag{2.4}$$

or

$$G = \frac{2\beta}{3\alpha} k_g' \sigma^g \quad \text{(integration controlled)} \tag{2.5}$$

we obtain the separation intensity

$$\mathrm{SI} \equiv \dot{m}_{Cv} L_{32} = \frac{\beta}{\alpha} \varphi_T k_d \Delta c \tag{2.6}$$

or

$$\mathrm{SI} \equiv \dot{m}_{Cv} L_{32} = \frac{2\beta}{\alpha} \varphi_T k_g' \rho_C \sigma^g \tag{2.7}$$

The product $\dot{m}_{Cv} L_{32}$, known as the separation intensity (SI) [2.7], ranges from 100 to 200 $\mathrm{kg/m^3\,h} \times \mathrm{mm}$ but depends on the volumetric holdup φ_T, the supersaturation Δc or σ, and the mass transfer coefficient k_d (diffusion controlled) or the kinetic growth coefficient k_g'. In the case of very small

Table 2.1. Approximate Operating Conditions of Crystallizers

	m_T [kg/m^3]	φ_T [m$_C^3$/m$_{sus}$]	τ [h]	$(\bar{\varepsilon})$ [W/kg]	$\frac{\Delta c}{\rho_C}$	L_{50} [mm]
FC	200–300	0.1–0.15	1–2	0.2–0.5	10^{-4}–10^{-2}	0.2–0.5
DTB	200–400	0.1–0.2	3–4	0.1–0.5	10^{-4}–10^{-2}	0.5–1.2
FB	400–600	0.2–0.3	2–4	0.01–0.5	10^{-4}–10^{-2}	1–5(10)

Note: Conditions valid for systems with $c^*/\rho_C > 0.01$

values of k_g' occurring in systems of low solubility, the separation intensity decreases.

Approximate operating conditions of crystallizers such as the suspension density m_T, the volumetric holdup φ_T, the mean residence time τ, the mean specific power input $\bar{\varepsilon}$, the dimensionless supersaturation $\Delta c/\rho_C$, and the median crystal size L_{50} are presented in Table 2.1. A coarse crystalline product can be produced in fluidized beds, but the median size L_{50} of crystals obtained from forced-circulation crystallizers is fairly small. With small crystallizers, the minimum specific power input depends on the suspension of crystals because particles have the tendency to settle and to form layers on the bottom. However, in large-scale industrial crystallizers for the production of crystals with a high solubility, circulation and macromixing may be critical.

3. MASS BALANCE

The design of crystallizers is first based on mass and energy balances. In this section, the formulation of balances for cooling and evaporative crystallization apparatus are given, taking the stirred-vessel crystallizer as an example. As the aim is to yield not only a sufficiently pure product but also a product exhibiting a specific crystal size distribution, mean crystal size, and a desired crystal shape, it is necessary to limit the number of newly formed crystal nuclei and, thus, the number of crystals.

Mass balances will be formulated for continuously operated and batch crystallizers. It will be shown how the uptake of solvent into the crystal can be taken into account and how the triangular diagram can be used favorably in the case of the two solutes.

3.1. Mass Balance of Continuously Operated Crystallizers

In addition to mass fractions and mass ratios, the mass concentration c (in kg/m^3) is also commonly used in crystallization technology. Figure 3.1 illustrates a stirred-vessel crystallizer. The mass flow $\dot{L}_0$ of solution entering the crystallizer with concentration c_0 is equal to the sum of the mass flows of vapor $\Delta\dot{L}^\circ$ (superscript stands for pure solvent) and the suspension flow $\dot{M}_{\text{sus}}$:

$$\dot{L}_0 = \Delta\dot{L}^\circ + \dot{M}_{\text{sus}} \tag{3.1}$$

In this example, it is assumed that the vapor does not contain any solute or droplets of solution. The outflowing suspension consists of solution with a concentration of c_1 and crystals whose suspension density m_T is taken to be in kilograms of crystals per cubic meter of suspension. The mass balance of the solute is [3.1]

$$\dot{V}_0 c_0 = \dot{V}_{\text{sus}}(1-\varphi_T)c_1 + \dot{V}_{\text{sus}}\varphi_T\rho_C$$

or with $\varphi_T = m_T/\rho_C$ and ρ_L as the density of the feed solution:

$$\frac{\dot{L}_0}{\rho_L}c_0 = \frac{\dot{M}_{\text{sus}}}{\rho_{\text{sus}}}[(1-\varphi_T)c_1 + m_T] \tag{3.2}$$

where ρ_C is the density of the compact crystals (i.e., the density of the solid). If the suspension density m_T is much smaller than the density of the suspension ρ_{sus} (in industrial crystallizers, m_T is often $<200\,\text{kg/m}^2$) or $\varphi_T \ll 1$, and if the densities ρ_L and ρ_{sus} of the flowing/outgoing solution and of the suspension are identical, combining equations (3.1) and (3.2) gives

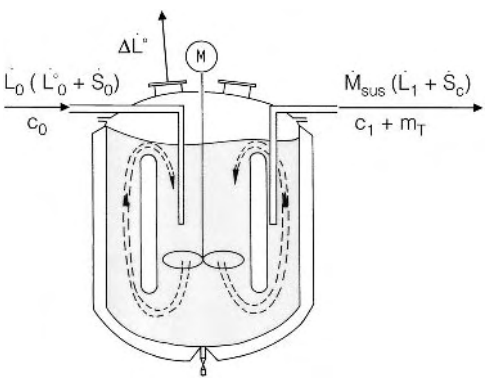

Figure 3.1. Mass balance of continuously operated crystallizer.

$$\frac{c_0}{1-\Delta\dot{L}^{\circ}/\dot{L}_0} - c_1 - m_T = 0 \tag{3.3}$$

where $\Delta\dot{L}^{\circ}/\dot{L}_0$ is the evaporation ratio, which is equal to zero in cooling crystallizers. In this specific case, the following applies:

$$c_0 - c_1 - m_T = 0 \tag{3.4}$$

Therefore, if the density ρ_L of the solution in cooling crystallizers is constant and $\varphi_T \ll 1$, the concentration difference $c_0 - c_1$ is the volume-related amount of crystals m_T: $m_T = c_0 - c_1$. (In the case of batch-operated cooling crystallizers, the suspension density $m_T = c_\alpha - c_\omega$ would be obtained where c_α is the initial concentration and c_ω is the final concentration which will be discussed later.) The difference $\Delta c_0 = c_0/(1 - \Delta\dot{L}^{\circ}/\dot{L}_0) - c^*$ is a theoretical supersaturation that would exist throughout an ideally mixed crystallizer in the absence of nucleation and growth. In reality, an ideally mixed apparatus has a supersaturation of only $\Delta c < \Delta c_0$, the magnitude of which is determined by nucleation and growth kinetics.

In continuously operated crystallizers, Δc should be as constant and as optimal as possible with respect to time and space. According to the solubility curve $c^* = f(\vartheta)$, the saturation concentration c^* depends on the temperature ϑ, whose value can be determined from the energy balance. The supersaturation which actually exists, Δc, is the driving force for crystal growth. It can be determined for a known solubility curve $c^* = f(\vartheta)$ from the difference in temperature $\Delta\vartheta$ between the actual temperature and the supersaturation temperature belonging to the concentration $c = c^* + \Delta c$:

$$\Delta c = \frac{dc^*}{d\vartheta}\Delta\vartheta \tag{3.5}$$

If the system has a high crystal growth rate, the remaining supersaturation $\Delta c = c_1 - c^*$ is often much lower than the suspension density m_T. In this particular case, m_T is approximately equal to the theoretical inflowing supersaturation Δc_0:

$$m_T = \Delta c_0 = \frac{c_0}{1-\Delta\dot{L}^{\circ}/\dot{L}_0} - c^* \tag{3.6}$$

3.2. Mass Balance of Batch Crystallizers

In a batch crystallizer, $c_\omega \approx c_\omega^*(\Delta c_\omega \to 0)$ would finally give the suspension density

$$m_{T,\omega} = \frac{c_\alpha}{1-\Delta L^{\circ}/L_\alpha} - c_\omega^* \tag{3.7}$$

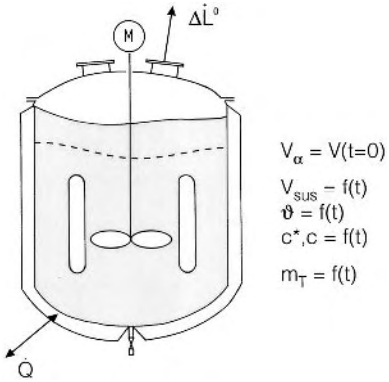

Figure 3.2. Mass balance of a batch crystallizer.

where L_α represents the initial amount of solution and ΔL° represents the amount of vapor evaporated. However, this equation is valid only if the above-given conditions are approximately fulfilled.

The variation of the suspension density m_T with time can easily be derived for seeded batch crystallizers with a negligible nucleation rate. Figure 3.2 shows a batch crystallizer with the active suspension volume V_{sus}. Heat is removed in the case of a cooling crystallizer but added if the apparatus is used as an evaporative crystallizer which evaporates the mass flow rate $\Delta \dot{L}^\circ$ of the solvent. The material balance of solute states that a change in the concentration c results in a change in the mass of crystals per unit volume m_T or suspension density. The exact derivation, given in Table 3.1, is rather complicated with respect to changes in the suspension volume. Simplified equations for the mass balance will now be presented.

Because maximum supersaturation must be $\Delta c < \Delta c_{\text{met}}$ and $\Delta c_{\text{met}} < 0.01\rho_C$ for $c^*/\rho_C > 10^{-2}$, the balance

$$\frac{dc}{dt} + \frac{dm_T}{(1-\varphi_T)\,dt} = \frac{dc^* + \Delta c}{dt} + \frac{dm_T}{(1-\varphi_T)\,dt} = 0 \tag{3.8}$$

can be simplified for $\Delta c \ll c^*$ to

$$\frac{dc^*}{dt} + \frac{dm_T}{(1-\varphi_T)\,dt} \approx 0 \tag{3.9}$$

This equation corresponds to equation (3.13b) in Table 3.1 for a cooling crystallizer ($\Delta \dot{L}^\circ = 0$ and $dV_{\text{sus}}/dt = 0$).

With $dc^*/dt = -(dc^*/d\vartheta)(d\vartheta/dt)$, the cooling rate $d\vartheta/dt$ can be written as

$$\frac{d\vartheta}{dt} \approx \frac{1}{(dc^*/d\vartheta)}\frac{dm_T}{(1-\varphi_T)\,dt} \tag{3.10}$$

with the slope $dc^*/d\vartheta$ of the solubility curve. With an evaporation crystallizer ($\vartheta = \text{const.}$) equation (3.13b) can be simplified again for the restriction $c^* \ll \rho_C$ or $c^*/\rho_C \ll 1$ to

$$\frac{dV_{\text{sus}}}{dt} = -\left(\frac{1}{1+\varphi_T\rho_C/c^*}\right)\frac{V_{\text{sus}}}{c^*}\frac{dm_T}{dt} \tag{3.11a}$$

or

$$\frac{\Delta\dot{L}^\circ c_i^*}{M_{\text{sus}}} \approx \frac{1}{1+\varphi_T\rho_C/c^*}\frac{dm_T}{dt} \tag{3.11b}$$

Assuming that the crystallizer is seeded with a mass m_S per unit volume of seed crystals of uniform size L_S at the beginning of the charge and that it is operated at a negligible nucleation rate at a constant growth rate G, the influence of time on the volume-based mass m_T of the crystals can be expressed as follows (see Table 3.1):

$$\frac{dm_T}{dt} = 3m_S\frac{G}{L_S}\left(\frac{Gt}{L_S}+1\right)^2 \tag{3.12a}$$

or in the integrated form

$$m_T(t) = m_S\left(\frac{Gt}{L_S}+1\right)^3 \tag{3.12b}$$

Combining equations (3.10) with (3.13a) in Table 3.1 gives $\Delta\dot{L}^\circ = 0$ and $\varphi_T \to 0$ for a cooling crystallizer:

$$\frac{d\vartheta}{dt} \approx -\frac{3m_SG}{(dc^*/d\vartheta)L_S}\left(\frac{Gt}{L_S}+1\right)^2 \tag{3.17a}$$

Correspondingly, for an evaporative process $d\vartheta/dt = 0$ or $\vartheta = \text{const.}$, equation (3.16b) in Table 3.1 can be simplified again for $\varphi_T \to 0$ to

$$\frac{\Delta\dot{L}^\circ c_i^*}{M_{\text{sus},\alpha}} \approx 3m_S\frac{G}{L_S}\left(\frac{Gt}{L_S}+1\right)^2 \tag{3.17b}$$

It can be seen from these two equations that the cooling or evaporation rate must increase as the batch operation time progresses in order to obtain the assumed constant growth rate. At the beginning ($t = 0$), only low rates can be permitted in order to restrict supersaturation and the resulting growth rate.

Table 3.1. Mass Balance of a Batch Crystallizer

Definitions:

$$\frac{V_C}{V_{\text{sus}}} = \frac{m_T}{k_C}; \quad 1 - \varphi_T = \frac{V_{\text{sol}}}{V_{\text{sus}}}; \quad M_{\text{sus}} = V_{\text{sus}}\rho_{\text{sus}} = V_{\text{sus}}[(1-\varphi_T)\rho_L + \varphi_T\rho_C], \text{ component } i$$

$$\frac{dM_{i,\text{sol}}}{dt} + \frac{dM_{i,C}}{dt} = 0 \tag{3.13a}$$

$$M_{i,\text{sol}} = (c_i^* + \Delta c_i)V_{\text{sol}} = (c_i^* + \Delta c_i)(1-\varphi_T)V_{\text{sus}}$$

If $\Delta c_i \ll c_i$:

$$\frac{dM_{i,\text{sol}}}{dt} = (1-\varphi_T)V_{\text{sus}}\frac{dc_i^*}{dt} - c_i^* V_{\text{sus}}\frac{d\varphi_T}{dt} + c_i^*(1-\varphi_T)\frac{V_{\text{sus}}}{dt}$$

$$M_{i,C} = m_T V_{\text{sus}}; \qquad \frac{dM_{i,C}}{dt} = V_{\text{sus}}\frac{dm_T}{dt} + m_T\frac{dV_{\text{sus}}}{dt}$$

$$\boxed{(1-\varphi_T)V_{\text{sus}}\left(\frac{dc_i^*}{d\vartheta}\right)\left(\frac{d\vartheta}{dt}\right) + V_{\text{sus}}\left(1 - \frac{c_i^*}{\rho_{i,C}}\right)\frac{dm_T}{dt} + [\varphi_T\rho_{i,C} + (1-\varphi_T)c_i^*]\frac{dV_{\text{sus}}}{dt} = 0} \tag{3.13b}$$

Cooling crystallizer:

$$m_S = \frac{N_S\alpha L_S^3\rho_{i,C}}{V_{\text{sus}}}; \quad m_T = \frac{N_S\alpha L^3\rho_{i,C}}{V_{\text{sus}}}; \quad \frac{dm_T}{dt} = \frac{1}{V_{\text{sus}}}\left(\frac{dV_C}{dL}\right)\left(\frac{dL\rho_{i,C}}{dt}\right)$$

$$= \frac{3N\alpha\rho_C}{V_{\text{sus}}}L^2\rho_{i,C}\frac{dL}{dt} = \frac{3N\alpha}{V_{\text{sus}}}\rho_{i,C}(L_S + Gt)^2 G$$

With $N = N_S = \text{const}$: $\boxed{m_T = m_S\left(1 + \frac{Gt}{L_s}\right)^3}$ (3.14a) $\qquad \boxed{\frac{dm_T}{dt} = \frac{3Gm_S}{L_S}\left(1 + \frac{Gt}{L_S}\right)^2}$ (3.14b)

Evaporation crystallizer:

$$V_{\text{sus}}\rho_{\text{sus}} + \Delta L^{\circ} = \text{const.}; \quad \frac{d(\Delta L^{\circ})}{dt} = \Delta \dot{L}^{\circ} = -\rho_{\text{sus}}\frac{dV_{\text{sus}}}{dt} - \underbrace{V_{\text{sus}}\frac{d\rho_{\text{sus}}}{dt}}_{\text{very small}} \tag{3.15}$$

Cooling crystallizer $\left[\dfrac{d(\Delta L^{\circ})}{dt} = \Delta \dot{L}^{\circ} = 0\right]$

$$\boxed{\frac{d\vartheta}{dt} = -\left(\frac{1 - c_i^*/\rho_{i,C}}{1 - (m_S/\rho_C)(1 + Gt/L_S)^3}\right)\frac{3Gm_S}{(dc_i^*/d\vartheta)L_S}\left(1 + \frac{Gt}{L_S}\right)^2} \tag{3.16a}$$

Evaporation crystallizer $\left(\dfrac{d\vartheta}{dt} = 0 \text{ or } \vartheta = \text{const.}\right)$

$$\boxed{\frac{\Delta \dot{L}^{\circ} dc_i^*}{M_{\text{sus},\alpha}} = \left(1 - \frac{c_i^*}{\rho_{i,C}}\right)\frac{3Gm_S}{L_S}\left(1 + \frac{Gt}{L_S}\right)^2} \tag{3.16b}$$

As already mentioned, the above equations are valid only in the case of a constant number of crystals (i.e., at a negligible nucleation rate). This condition is not fulfilled in crystallizers that produce a crystalline material with a mean size $L_{50} > 100\,\mu m$ (see Chapter 5).

3.3. Mass Balance of Crystals with Built-in Solvents

A certain problem in the formulation of mass balances occurs when solvent molecules are integrated into the crystal lattice. This applies particularly to aqueous solutions which yield crystals in the form of hydrates. A hydrate is the crystal product, including the associated solvent (i.e., the water of crystallization in the case of aqueous solutions). If S_{hyd} is taken to be the mass of the hydrate, the anhydrate mass S_C can be calculated by taking into account the molar mass $\tilde{M}$ of the substance containing no water of crystallization and that of the hydrate $\tilde{M}_{hyd}$:

$$S_C = S_{hyd} \frac{\tilde{M}}{\tilde{M}_{hyd}} \tag{3.18}$$

The following still applies:

$$\tilde{M}_{hyd} - \tilde{M} = \frac{\text{kg solvent in crystal}}{\text{kmol solvent-free crystals}}$$

This means that $\tilde{M}_{hyd} - \tilde{M}$ kilograms of solvent in the crystal exist per kilomole of solvent-free crystals. This gives

$$\frac{\tilde{M}_{hyd} - \tilde{M}}{\tilde{M}} = \frac{\text{kg solvent in crystal}}{\text{kg solvent-free crystals}}$$

According to Figure 3.3, a mass balance of the solute yields

$$\dot{S}_0 = \dot{S}_1 - \dot{S}_C \tag{3.19}$$

or, with the mass ratio W (in kg solute/kg solvent),

$$\dot{S}_0 = \dot{S}_1 - \dot{S}_C = W_0 \dot{L}_0^\circ - W_1 \dot{L}_1^\circ \tag{3.20}$$

The index $^\circ$ is intended to specify that the solvent is pure. A solvent balance gives

$$\dot{L}_0^\circ = \dot{L}_1^\circ - \Delta \dot{L}^\circ + \dot{S}_C \left(\frac{\tilde{M}_{hyd}}{\tilde{M}} - 1 \right) \tag{3.21}$$

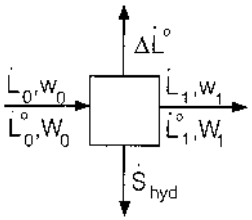

Figure 3.3. Mass balance of a crystallizer for crystals with built-in solvents.

Finally, we obtain the following results, which can be formulated both with mass ratios W (kg solute/kg solvent) and mass fractions w (kg solute/kg solution):

$$\dot{S}_C = \dot{L}_0^\circ \frac{W_0 - W_1(1 - \Delta\dot{L}_0/\dot{L}_0^\circ)}{1 - W_1[(\tilde{M}_{\text{hyd}}/\tilde{M}) - 1]} = \frac{\dot{L}_0(w_0 - w_1) + \Delta\dot{L}^\circ w_1}{1 - w_1(\tilde{M}_{\text{hyd}}/\tilde{M})} \tag{3.22}$$

The mass of crystals (for aqueous solutions, hydrate) containing solvent can be calculated as

$$\dot{S}_{\text{hyd}} = \dot{S}_C \frac{\tilde{M}_{\text{hyd}}}{\tilde{M}} \tag{3.23}$$

The maximum crystal mass is obtained when the outflowing solution leaves the crystallizer with an equilibrium concentration of c_1^* or equilibrium ratio of W_1^* or equilibrium mass fraction of w_1^*; in other words, when

$$c_1 = c_1^* \quad \text{or} \quad W_1 = W_1^* \quad \text{or} \quad w_1 = w_1^*$$

In the specific case of cooling crystallization ($\Delta\dot{L}^\circ = 0$) and a solvent-free product ($\tilde{M}_{\text{hyd}}/\tilde{M} = 1$), the mass balance for the solute is simplified to

$$\dot{S}_C = \dot{L}_0^\circ(W_0 - W_1) = \dot{L}_0 \frac{w_0 - w_1}{1 - w_1} \tag{3.24}$$

3.4. Mass Balance of Systems Containing Two Solutes

If two substances are dissolved in a solvent, the triangular coordinate network can be used to represent the crystallization process. The yield and composition of the crystals can be determined from the law of mixtures as explained by the triangular diagram in Figure 3.4. There is an undersaturation area at the top of this triangular network. The two-phase *CDG* and

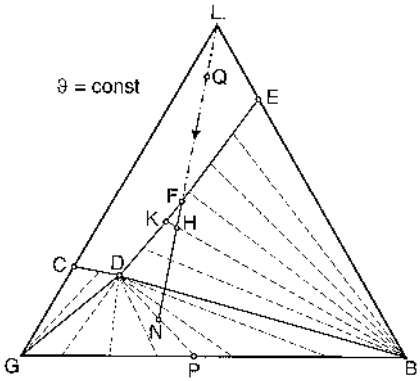

Figure 3.4. Crystallization process in a triangular diagram.

BDE areas contain a solution and a solid in equilibrium. The three-phase *BDG* area shows the presence of a solution that corresponds to point *D* as well as two solid crystals from components *B* and *G*.

The crystallization process is described for an evaporative crystallizer. If, for example, a solution corresponding to point Q exists and is evaporated, it changes according to a conjugation line through points L_r, Q, and F. At point F, the first crystals that consist of substance B precipitate. When point H is reached, more crystals have precipitated and the solution is depleted of B according to the change from F to K. When the connecting line BD is finally exceeded, we enter the three-phase area, where crystals of substance G precipitate. The percentage of crystal types B and G and of the solution corresponding to point D can be determined for each point in the three-phase area by applying the law of mixtures or the balance principle twice. Point N, for example, is divided into solution D and a mixture corresponding to point P. According to the balance principle, this mixture can, in turn, be divided into the two crystals B and G. If the law of mixtures is applied to the points of the conjugation line, it is possible to determine the amount of evaporated solvent in relation to the solution or crystals. Diagrams of the system KCl–NaCl–H_2O and Na_2CO_3–Na_2SO_4–H_2O are presented in Chapter 3.

4. ENERGY BALANCE

Figure 4.1 illustrates a crystallizer where the mass flow $\dot{L}_0$ of the solution flows in and the mass flow $\dot{L}_1$ flows out. In cooling crystallization, the heat

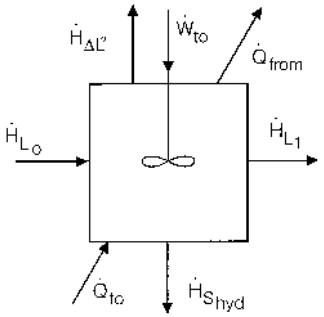

Figure 4.1. Energy balance of a continuously operated crystallizer.

flow $\dot{Q}_{\text{from}} = \dot{L}_0 c_{L0} \Delta\vartheta$ is removed, and in evaporative crystallization, the heat flow $\dot{Q}_{\text{to}} = \Delta\dot{L}^{\circ} \Delta h_{\text{LG}}$ is added. In the latter case, the mass flow $\Delta\dot{L}^{\circ}$ of the evaporated solvent to which the enthalpy flow $\dot{H}_{\Delta L^{\circ}}$ belongs leaves the crystallizer.

Finally, energy can be added via the circulating device and when this is operated nonadiabatically, heat can be exchanged with the atmosphere. If the crystallizer is operated in the steady-state mode, the following energy balance is obtained around the crystallizer:

$$\underset{\text{added heat flow}}{\dot{Q}_{\text{to}}} + \underset{\substack{\text{enthalpy of}\\ \text{inflowing solution}}}{\dot{H}_{L0}} + \underset{\text{added work}}{\dot{W}_{\text{to}}}$$

$$= \underset{\substack{\text{removed}\\ \text{heat flow}}}{\dot{Q}_{\text{from}}} + \underset{\substack{\text{enthalpy of}\\ \text{outflowing solution}}}{\dot{H}_{L1}} + \underset{\substack{\text{enthalpy of}\\ \text{crystals}}}{\dot{H}_{S_{\text{hyd}}}} + \underset{\substack{\text{enthalpy of}\\ \text{vapor}}}{\dot{H}_{\Delta L^{\circ}}} \tag{4.1}$$

The heat of crystallization is the amount of heat to be added or removed at a constant temperature during crystallization and is equal to the negative value of the heat of solution that applies when crystals dissolve in (the proximity of) a saturated solution. The heat of crystallization is included in the enthalpy parameters. Processes occurring in crystallizers can be easily followed when an enthalpy–concentration diagram exists for the system concerned (cf. Chapter 1). In contrast to real mixtures, only pure components have an enthalpy of zero at the reference temperature. The balance principle or law of mixtures can be used in such diagrams, as shown by the calcium chloride–water system. Figure 4.2 shows the specific enthalpy with respect to mass fractions for this system.

In cooling crystallization (1–2), heat is removed and the enthalpy decreases from point 1 to point 2. Point 2 is in a two-phase area in which the solution and a hexahydrate exist in equilibrium. The paths $\overline{22''}$ and $\overline{2'2}$

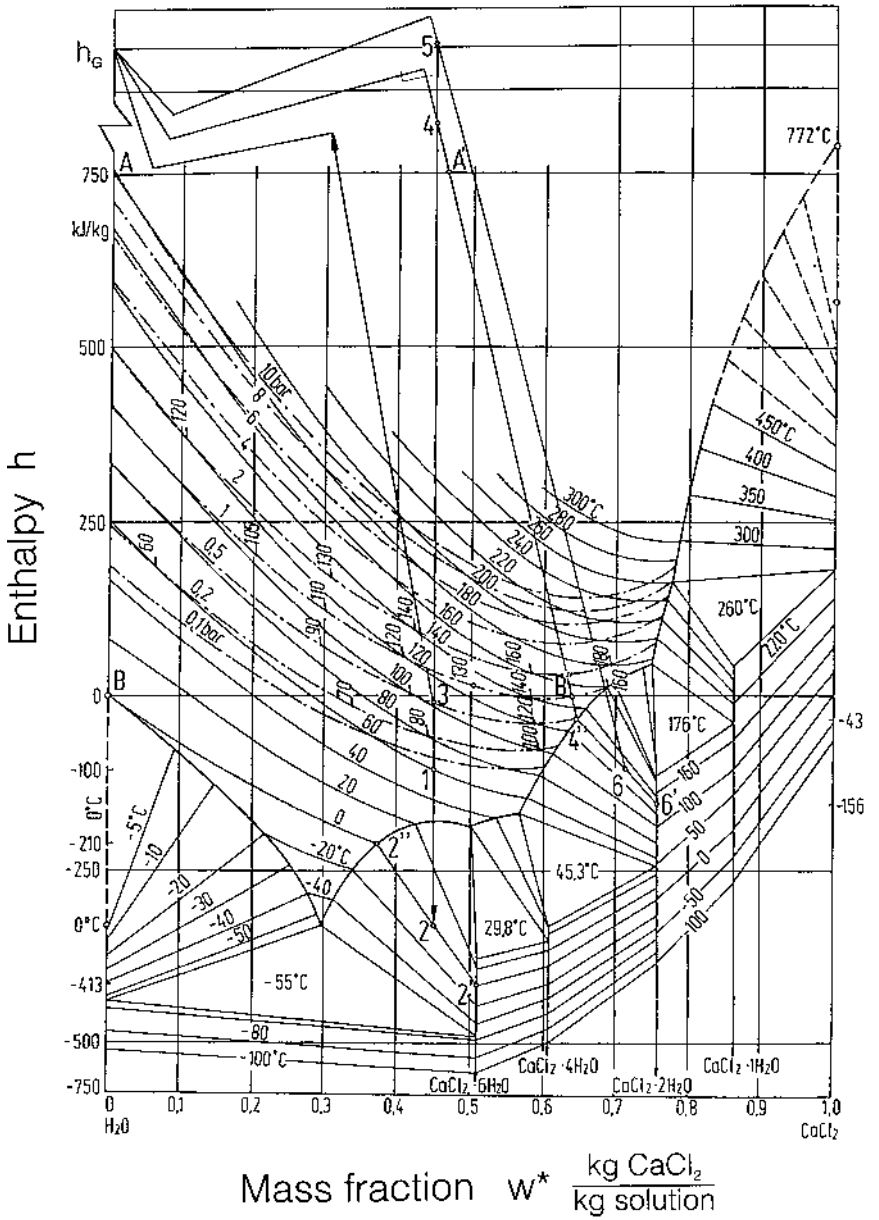

Figure 4.2. Diagram of enthalpy against concentration for the $CaCl_2$–water system with dew point isotherms; a process of cooling crystallization (1–2) and of evaporative crystallizaiton (1–3–4–5) is shown.

are in the same ratio as the amount of hexahydrate to the amount of solution. The diagram also shows evaporative crystallization processes in a vacuum at 0.5 bar. When the final solution is heated ($y = 0.45$, $\vartheta = 60°C$, point 1), the boiling point is attained at approximately 105°C (point 3). The solution is then in equilibrium with steam free of salt (point h_G, point of intersection between the dew point isotherms and the ordinate $y = 0$). If more heat is added [e.g., $\Delta h = 830\,\text{kJ/kg}$ (point 4)], the system forms a vapor phase (point h_G) and a liquid phase (point $4''$). The vapor and the solution have a temperature of 125°C. The solution is just saturated. The addition of even more heat leads to the formation of crystals $CaCl_2 \cdot H_2O$ ($6'$), a saturated solution ($4''$), and overheated vapor (point h_G).

5. FLUIDIZED BED

Chapter 5 deals with fluidized-bed crystallizers, because it is possible to derive basic equations for the suspension of crystals. Problems with circulation and macromixing are discussed in Sec. 6. It is emphasized that a general description of mixing and suspension is presented in order to obtain a general relationship regardless of the particular crystallizer under discussion.

Figure 5.1 shows a cooling crystallizer and Figure 5.2 shows an evaporative crystallizer. In both crystallizers, the crystals are suspended by an upward flow of solution that will be desupersaturated when flowing through the voidage of the fluidized bed. With respect to fluid dynamics, it is very important to avoid the settling of large particles; otherwise, the crystallizer may become plugged and subsequently inoperable.

The largest crystals of size $L_{\max}$ ($L_{\max} \approx 1.5$ up to $2 \times L_{50}$) show the highest settling velocity w_{ss} for hindered settling in a fluidized bed. With respect to the homogeneity of such beds, it is known that the fluidized suspension is fairly homogeneous for $\rho_C/\rho_L < 2$ and Archimedes number

$$\text{Ar} = \frac{L^3 g(\rho_C - \rho_L)}{\nu_L^2 \rho_L} < 10^2 \tag{5.1}$$

In this case, the minimum superficial volumetric flow density $\dot{v}_L$ must be equal to the settling velocity w_{ss} and can be read from Figure 5.3, in which the dimensionless flow density

$$\dot{v}_L^* \equiv \dot{v}_L \left(\frac{\rho_L}{\nu_L(\rho_C - \rho_L)g} \right)^{1/3} \qquad \text{with } w_{ss} \approx \dot{v}_L \tag{5.2}$$

is plotted against the dimensionless crystal size

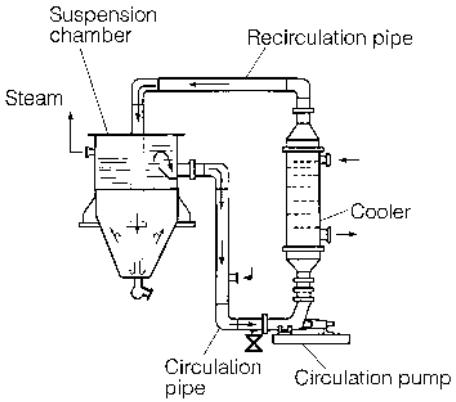

Figure 5.1. Fluidized-bed cooling crystallizer.

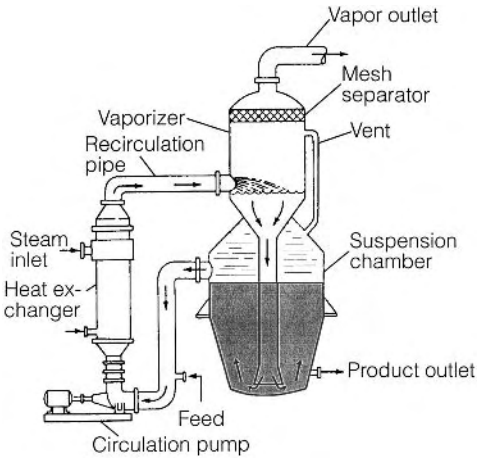

Figure 5.2. Fluidized-bed evaporative crystallizer.

$$L^* = L\left(\frac{(\rho_C - \rho_L)g}{\nu_L^2 \rho_L}\right)^{1/3} \tag{5.3}$$

for different values of volumetric crystal holdups φ_T. (When dealing with suspensions, it is always reasonable to apply the volumetric holdup and not a mass holdup $\varphi_m = \varphi_T \rho_C / \rho_{\text{sus}}$ with the mean density ρ_{sus} of the slurry because the calculation procedure is rather general.) Furthermore, in

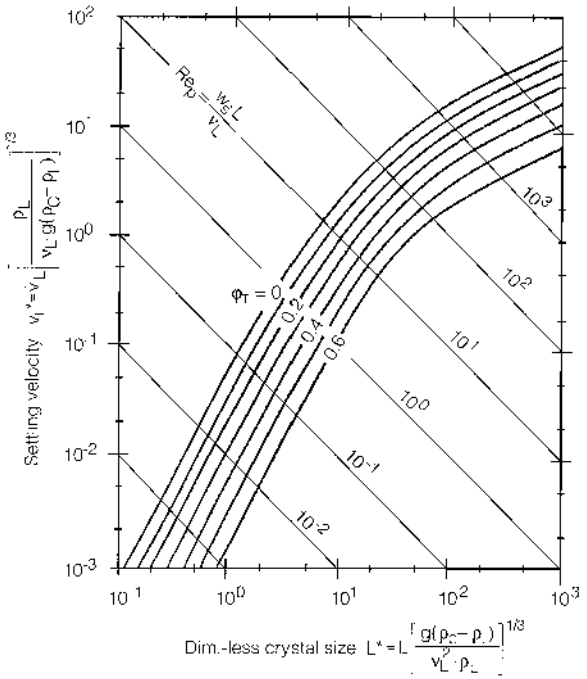

Figure 5.3. Dimensionless settling velocity versus dimensionless particle diameter for homogeneous fluidized beds.

Figure 5.3, straight lines for equal particle Reynolds numbers $\mathrm{Re}_P = Lw_s/\nu_L$ are drawn with the settling velocity w_s of a single particle in a solution of density ρ_L and kinematic viscosity ν_L. It is important to keep in mind that this diagram is valid only for cylindrical fluidized beds in which a homogeneous suspension of monosized particles is suspended by a liquid flowing evenly throughout the entire cross-sectional area. In this case, the minimum specific power input $\bar{\varepsilon}_{\min}$ necessary for the avoidance of settling is given by

$$\bar{\varepsilon}_{\min} = \varphi_T \frac{g(\rho_C - \rho_L)}{\rho_L} w_{ss} \left(\frac{w_{ss,\mathrm{turb}}}{w_{ss}} \right) \tag{5.4}$$

The ratio $w_{ss,\mathrm{turb}}/w_{ss}$ of the settling velocity of crystals in a turbulent liquid based on the velocity w_{ss} in a quiescent liquid is not known precisely and varies between 0.5 and 1 [5.1]. On the other hand, the mean specific power input necessary to suspend particles in a small conical fluidized bed may be two to four times larger than the values calculated from equation (5.4) for

$w_{ss,\text{turb}}/w_{ss} = 1$. This can be caused by the lack of homogeneity in heterogeneous fluidized beds containing particles with a high Archimedes number. As a rule, crystalline products exhibit a size distribution that usually increases with decreasing specific power input because large crystals undergo less attrition compared with the smaller ones in the upper section. This classification may be desirable in order to be able to withdraw a fraction of large crystals as a product. On the other hand, blending of the entire bed contents may be improved at higher superficial liquid velocities. The mean density of the slurry

$$\rho_{\text{sus}} = \varphi_T \rho_C + (1 - \varphi_T)\rho_L \tag{5.5}$$

decreases with increasing bed height because the volumetric holdup decreases. A sharp decline of ρ_{sus} may take place and the crystal size distribution is narrower. It is sometimes desirable to withdraw solution containing only a few small particles from the top of the fluidized bed because the liquid is recirculated by a centrifugal pump, and attrition of large crystals is caused by crystal–impeller contact (cf. Chapter 5). Figure 5.3 can be applied to determine the settling velocity w_s of single crystals of any size at $\varphi_T \to 0$. According to the target efficiency diagram in Figure 1.2 of Chapter 5, the probability of crystal–impeller contact and the volume V_a abraded from a parent crystal are both very low with the result that contact secondary nucleation is small. Therefore, fluidized-bed crystallizers are operated if a very coarse product is desired. It is thus possible to produce crystals of $L_{50} = 5$ to 10 mm with a narrow partricle-size-distribution range. The drawback of such a plant is a large crystallizer volume combined with high investment costs and problems in the event of power failures.

6. STIRRED VESSEL (STR)

In stirred-vessel crystallizers with or without a draft tube, a stirrer or pump circulates a volumetric flow. This circulated volumetric flow must be determined in such a way that the supersaturation Δc of the solution is not greatly reduced during a cycle. If supersaturation decreased too soon, crystal growth would not take place due to the lack of supersaturation, and it would not be possible to operate the crystallizer economically.

In the case of a stirred-vessel crystallizer with a draft tube (stirred vessel with a diameter ratio stirrer/tank of $D/T = 1/3$, apparatus height H with a ratio of $H/T = 1$, marine-type propeller), the required minimum speed $s_{\min}$ of the rotor can be determined from the following equation [6.1]:

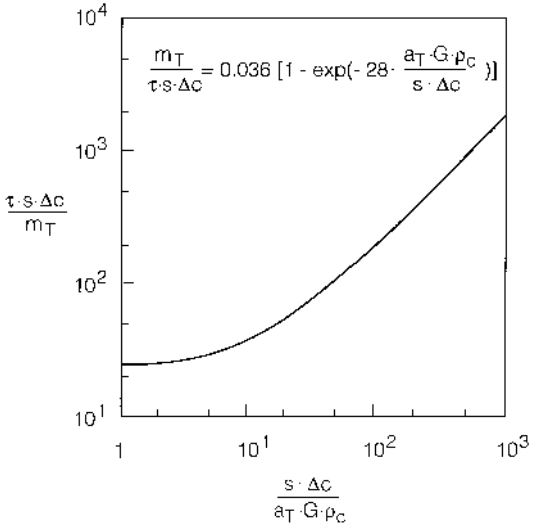

Figure 6.1. Information on the minimum stirrer speed for macromixing.

$$\frac{m_T}{\tau s \Delta c} = 0.036\left[1 - \exp\left(-28\frac{a_T G \rho_C}{s\Delta c}\right)\right] \tag{6.1}$$

In Figure 6.1, the expression $s\tau\Delta c/m_T$ is plotted against $s\Delta c/a_T G\rho_C$. The curve for both $s\Delta c/a_T G\rho_C < 2$ and $s\Delta c/a_T G\rho_C > 50$ leads to the same simple equation:

$$s = 28\frac{m_T}{\tau\Delta c} = 28\frac{\varphi_T \rho_C}{\tau\Delta c} \tag{6.2}$$

In the case of highly soluble systems, crystallization occurs at a low dimensionless supersaturation $\Delta c/\rho_C < \Delta c_{\text{met}}/\rho_C$, to avoid excessive nucleation, and also frequently at high suspension densities m_T or volumetric holdup φ_T. This means that scale-up should be performed at approximately $s\tau = \text{const.}$ (i.e., at a constant rotor speed s for a specific system that crystallizes at the optimum residence time τ). Such a scale-up is ruled out for economic reasons, as the mean specific power input ($\bar{\varepsilon}$) increases according to

$$\bar{\varepsilon} \sim s^3 D^2 \tag{6.3}$$

with the square of the rotor diameter D. This would result in an unfavorably large mean specific power input which is not required for crystal suspension and is detrimental to crystal size. Later, it will be shown that the minimum

mean specific power input required for suspension by no means increases with the scale-up factor, but, instead, decreases and remains constant in very large stirred vessels. This leads to the simple statement that although the solution in small crystallizers is well mixed, the crystals are not readily suspended. In large stirred vessels, on the other hand, crystals are readily suspended, but mixing is difficult. This is why the statement on the minimum speed according to equation (6.2) is very important for large apparatus.

With the volume-related production rate $\dot{m}_{Cv}$ [in kg crystals/(m^3 suspension s)] and the volume-related crystallizing volumetric flow $\dot{v}_{Cv}$ [in m^3 crystals/(m^3 suspension s)] according to

$$\dot{m}_{Cv} = \dot{v}_{Cv}\rho_C = \frac{m_T}{\tau} \tag{6.4}$$

equation (6.2) can be written as

$$s_{\min} \approx 28\frac{\dot{m}_{Cv}}{\Delta c} \approx 28\frac{\dot{m}_{Cv}}{\rho_C}\frac{\rho_C}{\Delta c} \approx 28\dot{v}_{Cv}\frac{\rho_C}{\Delta c} \tag{6.5}$$

The smaller the dimensionless supersaturation $\Delta c/\rho_C$, the higher the minimum rotational speed $s_{\min}$ required for mixing. According to the explanations given in Chapter 3, the lowest dimensionless metastable supersaturations $\Delta c_{\text{met}}/\rho_C$ must be assumed [i.e., the highest values of $\rho_C/\Delta c_{\text{met}}$ in the case of highly soluble substances of $0.1 < c^*/\rho_C < 1$, such as NaCl, KCl, $NaNO_3$, KNO_3, $(NH_4)SO_4$, NH_4BO_3, urea, and sugar]. In the crystallization processes of these products, circulation is a problem in large crystallizers and should be studied carefully. On the other hand, even the suspension of large crystals in a stirred vessel does not present a problem provided that the optimum geometric configuration is chosen for both the stirred vessel and the stirrer, as will be demonstrated later.

For practical reasons, it is necessary to take a closer look at the flow in a stirred vessel with regard to processes such as the mixing, suspension, abrasion, and agglomeration of crystals, the destruction of agglomerates, mass transfer between crystals and the solution, and heat transfer between the suspension and the heating/cooling surface (double jacket and cooling coils).

6.1. Flow and Shear Stress

With the stirrer diameter D and speed s, the circulated volumetric flow $\dot{V}_{\text{circ}}$ is given by

$$\dot{V}_{\text{circ}} = N_V s D^3 \tag{6.6}$$

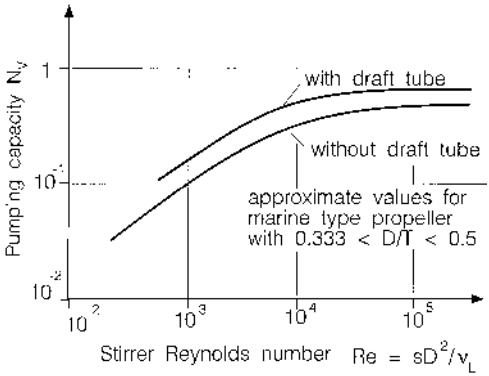

Figure 6.2. Pumping capacity versus stirrer Reynolds number.

Figure 6.2 illustrates values of the pumping capacity N_V. The mean volumetric flow density or the mean velocity $\bar{v}$ in the stirred vessel of diameter T results in

$$\bar{v} \sim s\frac{D^2}{V^{1/3}} \sim sD\frac{D}{T} \tag{6.7}$$

When crystals and crystal agglomerates are subject to shear stress, the decisive factor is the fluctuating velocity of the liquid. The maximum value $v'_{\text{eff,max}}$ of the fluctuating velocity

$$v'_{\text{eff}} = \sqrt{\frac{1}{k}\sum_k (v'_{\text{eff}})^2} = \sqrt{\overline{(v'_{\text{eff}})^2}}$$

of a turbulent stirred vessel flow ($\text{Re} \equiv sD^2/\nu_L > 10^4$) can be estimated from the peripheral speed $s\pi D$ and geometric configuration of the stirrer. At identical speeds s, stirrers that are favorable for flow (e.g., marine-type propellers and pitched-blade impellers) require much less driving power than stirrers that are unfavorable for flow (e.g., multiblade flat turbines and leaf impellers). The power P is given by

$$P = (\text{Po})\rho_{\text{sus}} s^3 D^5 \tag{6.8}$$

Figure 6.3 provides information on the power number Po. The maximum fluctuating velocity $v'_{\text{eff,max}}$ occurs directly in the stirrer outflow zone and can be estimated according to the following relationship, which is valid for liquids and suspensions [6.2]:

$$\frac{v'_{\text{eff,max}}}{s\pi D} \approx 0.18\text{Po}^{7/18} \tag{6.9}$$

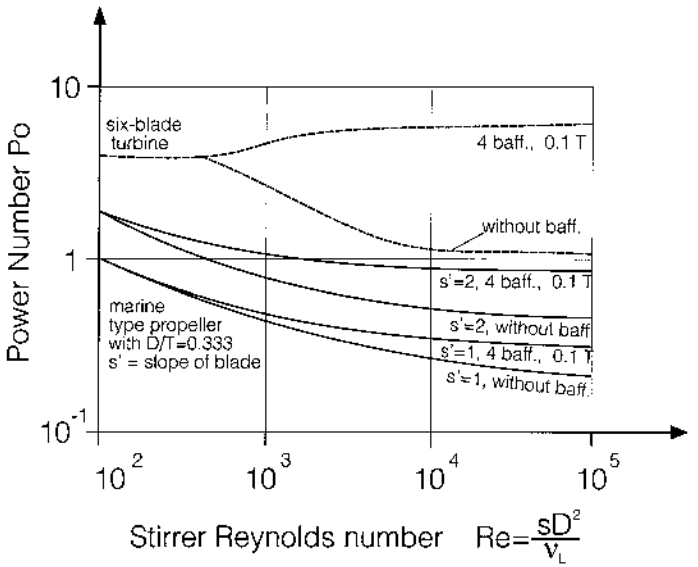

Figure 6.3. Power number versus Reynolds number of the stirrer for several agitators.

According to this equation, the value $v'_{\text{eff,max}}$ is independent of the geometric configuration of the stirred vessel and the D/T ratio provided that $\text{Re} > 10^4$; see Figure 2.11 in Chapter 5. In stirred-vessel crystallizers, the local and mean specific power inputs, ε and $\bar{\varepsilon}$ respectively, often differ greatly. The value $\bar{\varepsilon}$, with height H of the stirred vessel, is equal to

$$\bar{\varepsilon} \equiv \frac{P}{\rho_{\text{sus}} V} = \frac{4\text{Po}}{\pi} s^3 D^2 \left(\frac{D}{T}\right)^2 \frac{D}{H} \tag{6.10}$$

The effective fluctuating value $\bar{v}'_{\text{rel}}$ between a particle and a turbulent liquid, which is the decisive value for shear stress, is given by [6.2]

$$\frac{\bar{v}'_{\text{rel}}}{s\pi D} = 0.32\text{Po}^{1/3} \left(\frac{\rho_C - \rho_L}{\rho_L}\right)^{1/2} \left(\frac{\rho_C}{\rho_L}\right)^{1/3} \left(\frac{L}{D}\right)^{1/3} \frac{D}{T} \left(\frac{T}{H}\right)^{1/3} \left(\frac{\varepsilon}{\bar{\varepsilon}}\right)^{1/3} \tag{6.11}$$

or, for the same crystal suspension in geometrically similar stirred vessels,

$$\bar{v}'_{\text{rel}} \sim (\bar{\varepsilon} T)^{1/3} \left(\frac{\varepsilon}{\bar{\varepsilon}}\right)^{1/3} \tag{6.12}$$

To calculate v'_{rel}, the ratio $\varepsilon/\bar{\varepsilon}$ of the local power input to the mean specific power input must be known. Figure 6.4 shows this ratio for some stirrers according to laser–doppler–anemometric measurements. These isoenergetic

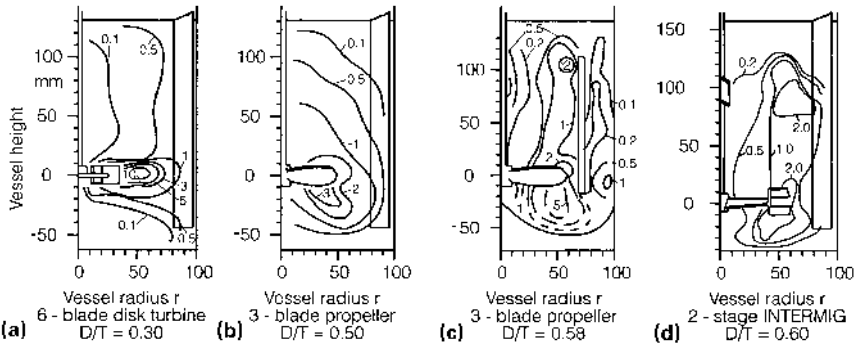

Figure 6.4. Local specific power input based on the mean value, $\bar{\varepsilon}$, for several stirrers.

lines remain unchanged for the geometrically similar scale-up in the case of a fully turbulent stirred vessel flow of $\mathrm{Re} = sD^2/\nu_L > 10^4$. The diagrams clearly show that the highest local specific power and thus the highest values of v'_{rel} occur in the discharge area of the axial or radial stirrers. This is also where the greatest amount of attrition takes place, the largest crystals and agglomerates being subject to attrition. Favorable stirrers with respect to attrition are those with a small power number Po and a large pumping capacity N_V, that can be operated at the minimum specific suspension power $\bar{\varepsilon}_{\min}$ with respect to mixing and suspending. A large difference between the crystal and the solution densities $\rho_C - \rho_L$ is unfavorable because it causes high fluctuating velocities.

Relatively loose agglomerates can be destroyed by the shear stress τ_s of the flow. The theoretically permissible shear stress of compact crystals and agglomerates can be estimated from Figure 6.5, where the tensile strength of solid crystals and agglomerates is plotted against the size of such particles. The stress depends on whether the agglomerate is held together by solid bridges, capillary forces, or intermolecular and electrostatic forces (cf. Chapter 6). The agglomerate breaks when the shear stress τ_s of the liquid exceeds the permitted shear stress of the agglomerate. The shear stress $\tau_{s,\mathrm{turb}}$ for turbulent stirred-vessel flow ($\mathrm{Re} > 10^4$) can be estimated from the relationship [6.3]

$$\frac{\tau_{s,\mathrm{turb}}}{\rho_{\mathrm{sus}}(s\pi D)^2} \approx \left(\frac{\mathrm{Po}_{\mathrm{turb}}}{2\pi^4}\right)^{2/3} \frac{D}{T}\frac{H}{T}\left(\frac{\varepsilon}{\bar{\varepsilon}}\right)^{2/3} \tag{6.13}$$

In Figure 6.6, lines of identical shear stress are plotted for different stirrers. The maximum shear stress naturally occurs in the stirrer outflow area and

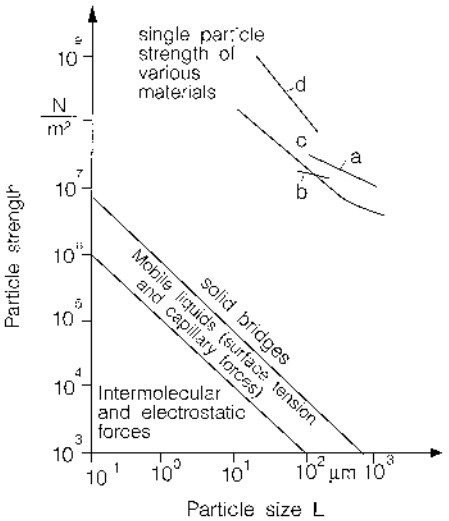

Figure 6.5. Tensile particle strength of agglomerates and solid crystals versus their size: (a) cane sugar; (b) potash salts; (c) limestone; (d) boron carbide.

can be estimated from the following equation for different stirrers with a varying ratio of stirrer diameter to vessel diameter D/T [6.4]:

$$\frac{\tau_{s,\text{turb}}}{\rho_{\text{sus}}(s\pi D)^2} \approx 0.03\text{Po}_{\text{turb}} \tag{6.14}$$

Marine-type impellers that are favorable for flow are recommendable for gentle circulation of the crystal suspension. The larger the stirred vessel and the greater the ratio D/T, the more a certain mean specific power dissipated in the vessel contents will be converted to a desirable large volumetric circulation flow $\dot{V}_{\text{circ}}$ and the less it will be converted to an undesirable mean shear stress τ_s [6.5]:

$$\frac{\dot{V}_{\text{circ}}}{\tau_s} \sim \frac{1}{\rho_{\text{sus}}}\left(\frac{D^5}{\bar{\varepsilon}}\right)^{1/3}\frac{D}{T} \tag{6.15}$$

This is why it is recommended to integrate the specific power required for mixing and suspension in a stirred vessel as large as possible, and not in several small apparatus, and to equip this large crystallizer with a marine-type propeller of $D/T \geq 0.5$, which is favorable for flow. However, it must be noted that the intermixture of the crystal

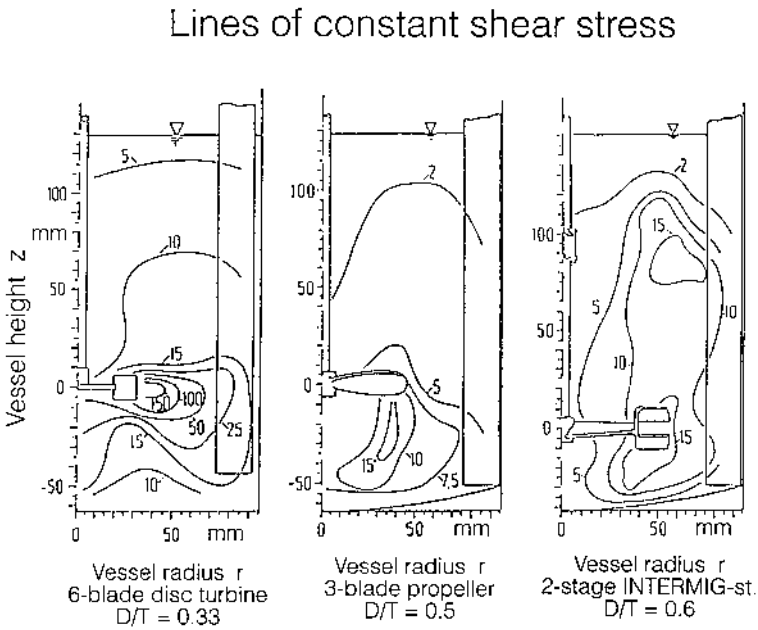

Figure 6.6. Local shear stress based on the maximum value for several stirrers $[\tau_{s,\mathrm{turb}}/\rho_{\mathrm{sus}}(s\pi D)^2 \times 10^3]$.

suspension decreases with increasing vessel size. As has been mentioned earlier, the constant-mixing quality would require the same speed in the model and in the industrial-scale crystallizer. In other words, according to $\bar{\varepsilon} \sim s^3 D^2$, the mean specific power input $\bar{\varepsilon}$ would increase with the square of the stirred vessel diameter ($\bar{\varepsilon} \sim T^2$) with the geometric configuration remaining identical ($D/T = \text{const.}$). Such a large specific power is not only uneconomical but also causes a large amount of crystal abrasion.

6.2. Mixing

With respect to the intermixture of the stirred-vessel contents, it must be noted that the minimum macromixing time t_{macro} increases with vessel diameter T and decreases with increasing mean specific power $\bar{\varepsilon}$ in the case of turbulent flow ($\mathrm{Re} = sD^2/\nu_L > 10^4$) [6.6]:

$$t_{\text{macro}} \approx 5\left(\frac{T^2}{\bar{\varepsilon}}\right)^{1/3} \tag{6.16}$$

This relationship is valid for liquids and should also yield useful values for suspensions. The macromixing time lies often in range of a few seconds but may be considerably longer in the transition range ($10 < \text{Re} < 10^4$), especially in the laminar-flow area of the stirrer ($\text{Re} < 10$). The following applies to a helical ribbon impeller $D/T = 0.9$ and $H/T = 1$ in the range of $\text{Re} < 10$ [6.6]:

$$t_{\text{macro}} \approx 50\sqrt{\frac{\nu_L}{\bar{\varepsilon}}}\ln(\text{Sc}) \tag{6.17}$$

where Sc is the Schmidt number. It must be emphasized, however, that macromixing is intended to compensate for local differences in certain parameters (e.g., temperature, concentration, supersaturation, suspension density). However, the relationship between the macromixing time t_{macro} and the magnitude of these differences is not generally known.

With respect to the design and operation of reaction crystallizers, the micromixing time t_{micro} may have a considerable effect on the progress of the chemical reaction, the concentration and supersaturation of the product formed, and the crystal size distribution [6.7, 6.8]. This applies, above all, when the relative supersaturation is in the range $\sigma > 1$ and leads to primary nucleation in the case of fast chemical reactions (e.g., ionic reactions with short or very short reaction times). Various models for calculating the micromixing time are described in the literature. Based on the models of Brodkey [6.9], Corrsin [6.10], and Costa and Trevissoi [6.11], the following relationship can be derived between the micromixing time t_{micro}, the degree of segregation I_s, and the local specific power input ε:

$$I_s = \frac{1}{1 + 2\sqrt{\varepsilon/\nu_L}\,t_{\text{micro}}/[0.88 + \ln(\text{Sc})]} \tag{6.18}$$

If $I_s < 0.1$ (which is to be strived for) and $\text{Sc} > 10^3$, which is valid for liquids, the following is sufficiently accurate:

$$t_{\text{micro}} \approx 5\sqrt{\frac{\nu_L}{\varepsilon}}\ln(\text{Sc}) \tag{6.19}$$

It should be noted that the micromixing time t_{micro} is inversely proportional to the micromixing parameter E in Figure 3.4 of Chapter 2.

The local specific power input ε is given by

$$\varepsilon = \frac{(v'_{\text{eff}})^3}{\Lambda} \tag{6.20}$$

with

$$\Lambda = 0.15\mathrm{Po}_{\mathrm{turb}}^{5/9}\left(\frac{u_{\mathrm{tip}}}{v'_{\mathrm{eff}}}\right)D \tag{6.20a}$$

see Chapter 6, or approximately by

$$\varepsilon = 6\frac{(v'_{\mathrm{eff}})^3}{D} \tag{6.21}$$

where the fluctuating velocity v'_{eff} of the liquid of a turbulent stirred-vessel flow is proportional to the stirrer peripheral speed $s\pi D$. Reference should be made to Figure 6.4 for values of the local fluctuating velocity v'_{eff} and of the local specific power input. Note that with increasing fluid viscosity ν_L and increasing Schmidt number $\mathrm{Sc} = \nu_L/D_{AB}$, the local micromixing time becomes equal to the mean macromixing time t_{macro} for $\mathrm{Re} < 10$ and $I_s = 0.01$.

6.3. Suspension of Crystals in Stirred Vessels

The impeller in a stirred vessel has the task not only of mixing but also of suspending the crystals that have a difference in density of $\rho_C - \rho_L$ compared to the solution. With respect to the state of suspension in stirred vessels, a distinction is made among (a) incomplete, (b) complete, and (c) homogeneous suspensions.

Incomplete suspension: In this case, part of the solid phase is deposited on the bottom of the vessel or carries out a rolling movement on the bottom surface. In flat-bottomed tanks in particular, the solid phase has a tendency to build up corner deposits or layered zones at the edges of the vessel or at the center of the vessel bottom, where only a stagnant fluid flow exists. In this case, off-bottom lifting is the decisive process, and it can be modeled by a simple energy balance according to

$$(v'_{\mathrm{eff}})^2 = \sqrt{3c_w Lg\frac{\rho_C - \rho_L}{\rho_L}}w_s \tag{6.22}$$

In this equation, $(v'_{\mathrm{eff}})^2$ is the square of the effective fluctuating velocity or the specific energy of the fluid at the bottom, which is necessary to prevent the settling of a crystal of size L and settling velocity w_s in the gravitational field with the acceleration g. ρ_C and ρ_L are the densities of the crystal or the liquid, respectively, and c_w stands for the drag coefficient of the particle. Because the fluctuating velocity at every point in the vessel is proportional to the tip speed u_{tip} of the stirrer, the scale-up criterion for the "off-bottom lifting" process is simply

$$u_{\text{tip}} = \text{const.} \quad \text{or} \quad \bar{\varepsilon} \sim \frac{u_{\text{tip}}^3}{T} \sim \frac{(\text{const.})^3}{T}$$

for a given suspension. This means that the mean specific power input $\bar{\varepsilon}$ is inversely proportional to the diameter T of the vessel for geometrically similar vessels.

Complete suspension: A suspension is complete when no particles remain on the vessel bottom for more than 1–2 s [6.12]. Under this condition, the total surface area of crystals is suspended in the solution and is available for crystal growth. However, the crystals are not distributed homogeneously throughout the entire vessel. Because the energy balance $(v'_{\text{eff}})^2 = 2Lg[(\rho_C - \rho_L)/\rho_L]$ is valid everywhere most of the crystals are in the vicinity of the stirrer where high fluctuating velocities exist. In the region below the liquid surface at the top, crystals settle because of the small velocities and the crystal holdup is small.

Homogeneous suspension: A homogeneous suspension exists when the local particle concentration in the vessel and, for a specific range of particle sizes, the particle size distribution is constant throughout the entire contents of the vessel. In the case of large particles, density differences $(\rho_C - \rho_L)$, and small viscosities of the solution, it is difficult, indeed virtually impossible, to obtain a homogeneous suspension, even at a very high specific power input. The higher the density ratio ρ_C/ρ_L and the Archimedes number, the greater the gravitational and centrifugal forces, with the result that the suspension becomes increasingly heterogeneous. This can be compensated by higher specific power input [6.13].

An approximate guide is given by

$$\text{Ar} < 10 \,\text{and}\, \frac{\rho_C}{\rho_L} < 2 \quad \text{(fairly homogeneous suspension)}$$

$$\text{Ar} > 10^4 \,\text{and}\, \frac{\rho_C}{\rho_L} > 5 \quad \text{(more heterogeneous suspension)}$$

A minimum fluctuating velocity v'_{eff} or specific fluid energy $(v'_{\text{eff}})^2$ is necessary for the off-bottom lifting of particles. In particular, in small stirred vessels characterized by a high Stokes number (St) with

$$\text{St} = \left(\frac{L}{T}\right) \frac{L\dot{v}_L(\rho_C - \rho_L)}{18\eta_L} \tag{6.23}$$

with

$$\dot{v}_L \approx \frac{4N_V}{\pi} sD \tag{6.24}$$

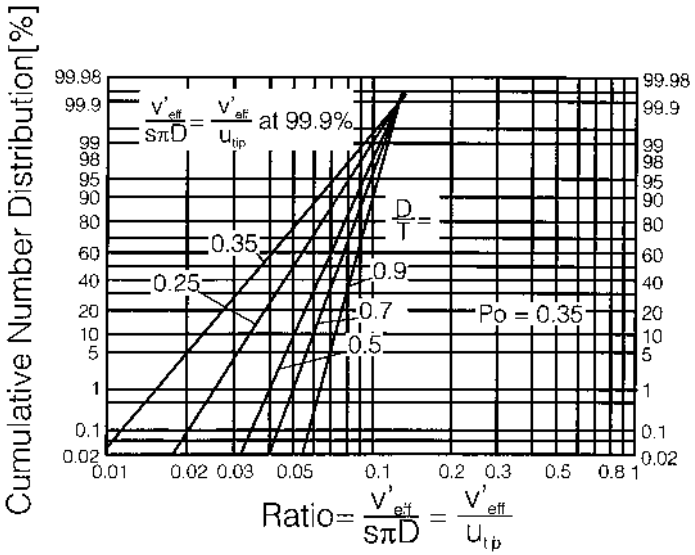

Figure 6.7. Cumulative number distribution versus the ratio $v'_{\text{eff}}/u_{\text{tip}}$ valid for Po = 0.35.

crystals impinge on the bottom of the vessel and must be transported and lifted by the specific energy $(v'_{\text{eff}})^2$. The fluctuating velocity v' has been derived from theoretical considerations supported by experimental results. In Figure 6.7, the cumulative number distribution is plotted against the ratio $v'_{\text{eff}}/u_{\text{tip}}$ for different ratios D/T of the stirrer diameter D based on the tank diameter T. As can be seen, the distribution of the fluctuating velocity is narrow for large D/T ratios. Therefore, such stirrers lead to high fluctuating velocities at the bottom of the vessel for a given tip speed u_{tip} and can be recommended for stirred-vessel crystallizers. The minimum fluctuating velocity $v'_{\text{eff,min}}$ necessary for off-bottom lifting is given by [6.14]

$$v'_{\text{eff,min}} = 0.088\text{Po}^{7/18} u_{\text{tip}} \left(\frac{D}{T}\right)^{3/2} \tag{6.25}$$

This relationship can be transformed into the following equation for the calculation of the minimum tip speed necessary for off-bottom lifting:

$$0.088\text{Po}^{7/18} u_{\text{tip}} \left(\frac{D}{T}\right)^{3/2} = (3c_w L w_s \varepsilon_{ss})^{1/4} \tag{6.26}$$

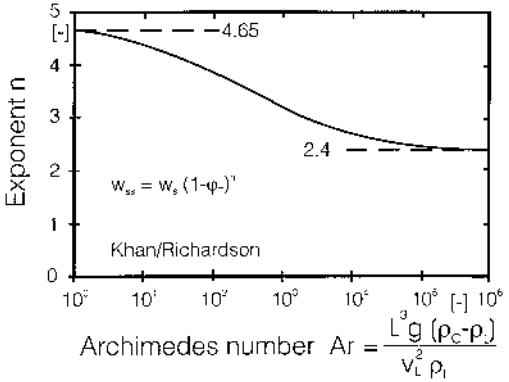

Figure 6.8. Exponent n as function of the Archimedes number.

with ε_{ss} as the specific power of settling crystals with the volumetric holdup φ_T according to

$$\varepsilon_{ss} = \varphi_T(1-\varphi_T)^n w_s g \frac{\rho_C - \rho_L}{\rho_L} \tag{6.27}$$

The exponent n depends on the Archimedes number (cf. Fig. 6.8), which shows the exponent n for particular fluidization as a function of the Archimedes number.

The specific settling power ε_{ss} of particles in a swarm can be derived from a power balance P_{sett} according to

$$P_{\text{sett}} = V_{\text{sus}}\varphi_T(\rho_C - \rho_L)g w_{ss} = V_{\text{sus}}\varphi_T \Delta\rho g w_{ss} \tag{6.28}$$

divided by the mass $V_{\text{sus}}\rho_{\text{sus}} \approx V_{\text{sus}}\rho_L$ of the suspension:

$$\varepsilon_{ss} = \frac{P_{\text{sett}}}{V_{\text{sus}}\rho_L} = \varphi_T(1-\varphi_T)^n w_s g \frac{(\rho_C - \rho_L)}{\rho_L} \tag{6.27}$$

All these equations clearly show that the tip speed u_{tip} necessary for suspension increases with the settling velocity of the crystals. Therefore, crystals with a high settling velocity are most prone to attribution because the attrition rate increases strongly with the collision velocity between a crystal and a rotor (see Chapter 5).

The specific settling power ε_{ss} of the particles in the suspension must be balanced by the mean specific power input $\bar{\varepsilon}$ provided by the stirrer according to

$$\bar{\varepsilon} = \frac{4\mathrm{Po}}{\pi^4}\left(\frac{D}{T}\right)^2\left(\frac{T}{H}\right)\frac{u_{\mathrm{tip}}^3}{T} \tag{6.29}$$

in order to avoid settling. Therefore, besides the criterion "off-bottom lifting," the second criterion "avoidance of settling" (AS) must be fulfilled. The specific power ε_{ss} depends only on the properties of the suspension and not on the geometry and operating conditions of the stirred vessel. It has been shown that "off-bottom lifting" (BL) requires a minimum tip speed u_{tip} for a certain geometry of the vessel and given properties of the suspension. However, for a constant tip speed of a stirred vessel with $\mathrm{Po} = \text{const.}$, $D/T = \text{const.}$, and $T/H = \text{const.}$, the mean specific power input $\bar{\varepsilon}$ becomes smaller as the vessel size T increases and can fall below ε_{ss} in a large vessel. A general relationship can be obtained when the mean specific power input $\bar{\varepsilon}_{\mathrm{AS}} = \varepsilon_{ss}$ for the "avoidance of settling" is added to the specific power input $\bar{\varepsilon}_{\mathrm{BL}}$ necessary for "off-bottom lifting":

$$\bar{\varepsilon} = \bar{\varepsilon}_{\mathrm{BL}} + \bar{\varepsilon}_{\mathrm{AS}} \tag{6.30}$$

In small vessels, $\bar{\varepsilon}_{\mathrm{BL}}$ is dominant, but $\bar{\varepsilon}_{\mathrm{AS}}$ can be the decisive parameter in very large vessels. The specific power inputs $\bar{\varepsilon}_{\mathrm{BL}}$ and $\bar{\varepsilon}_{\mathrm{AS}}$ can be expressed by the properties of the suspension ($\mathrm{Ar} = L^3 g \Delta\rho/\nu_L^2\rho_L$ and φ_T) and the geometry of the vessel:

$$\bar{\varepsilon}_{\mathrm{BL}} \approx 200\mathrm{Ar}^{1/2}[\varphi_T(1-\varphi_T)^n]^{3/4}\,\frac{\nu_L g \Delta\rho}{H\rho_L}\left(\frac{T}{D}\right)^{5/2} \tag{6.31}$$

and

$$\bar{\varepsilon}_{\mathrm{AS}} \approx 0.4\mathrm{Ar}^{1/8}[\varphi_T(1-\varphi_T)^n]\sqrt{L\left(\frac{\Delta\rho g}{\rho_L}\right)^3} \tag{6.32}$$

These equations show that the specific power input $\bar{\varepsilon}_{\mathrm{BL}}$ is inversely proportional to the size of the vessel and the specific power $\bar{\varepsilon}_{\mathrm{AS}}$ depends only on the properties of the suspension. When scaling up a stirred vessel containing a suspension, the specific power input can be reduced and remains constant when ε_{ss} is reached in order to obtain the same suspension quality. With respect to macromixing, however, the scale-up rule is quite different. The same homogeneity of the solution is obtained for a constant impeller speed s, which would result in an increasing specific power input $\bar{\varepsilon}$ according to

$$\bar{\varepsilon} = s^3 D^2 \tag{6.33}$$

with increasing scale-up factors. To balance the different requirements for adequate suspensions ($\bar{\varepsilon} \sim 1/T$ for $D/T = \text{const.}$ or $\bar{\varepsilon} = \text{const.}$ in large

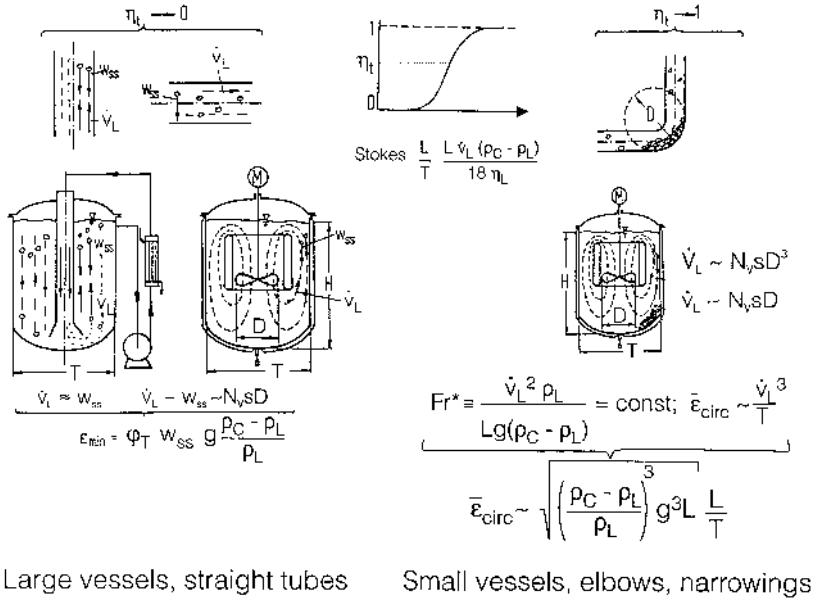

Figure 6.9. General information on the suspension of particles.

vessels) and macromixing ($\bar{\varepsilon} \sim D^2$), a constant specific power input $\bar{\varepsilon}$ is recommended and often employed in practice for crystallizer scale-up.

Further suspension problems occur in horizontal and vertical tubes, elbows, and all kinds of fluidized bed. The minimum fluid velocity $\dot{v}_{L,\min}$ required for suspending solid particles can be determined approximately according to Figure 6.9. The most simple relationships are those valid for large tubelike stirred vessels inside which a flow-favorable propeller circulates a volumetric flow in such a way that an upward flow is achieved, as in a fluidized bed. The settling power of the crystals $P_{\text{sett}} = V_{\text{sus}}\varphi_T(\rho_C - \rho_L)gw_{ss}$ must, in any case, be compensated by the stirrer power $P_{\min} = (\text{Po})\rho_{\text{sus}}s^3D^5$. In a fluidized bed, the mean fluid velocity $\dot{v}_L$ must simply be as high as the settling velocity w_{ss} of crystals in a swarm. This means that the circumferential velocity $D\pi s$ of a rotor must remain constant. The target efficiency, which depends on the Stokes number determines whether the crystal will impinge on the bottom of a vessel or the wall of an elbow tube.

The calculation procedure of a two-phase flow is recommended if the volumetric holdup of particles of $L > 0.2\,\text{mm}$ is smaller than $\varphi_T = 0.05$. With increasing holdup φ_T, according to

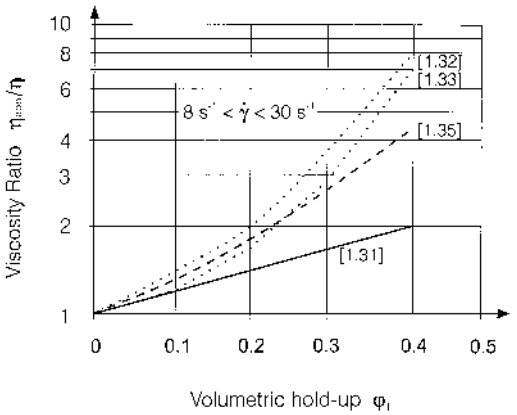

Figure 6.10. Ratio η_{app}/η_L versus the volumetric holdup φ_T.

$$\varphi_T = \frac{\text{Volume of crystals}}{\text{Volume of slurry}} = \varphi_m \frac{\rho_{\text{sus}}}{\rho_C} = \frac{m_T}{\rho_C} = \frac{\varphi_m \rho_L}{\rho_C - \varphi_m(\rho_C - \rho_L)} \tag{6.34a}$$

or

$$\varphi_m = \frac{\text{Mass of crystals}}{\text{Mass of slurry}} = \frac{\varphi_m \rho_C}{\rho_L + \varphi_T(\rho_C - \rho_L)} \tag{6.34b}$$

the rheological behavior changes to non-Newtonian fluids to which the law of Ostwald–de Waele can be applied:

$$\tau_s = K\dot{\gamma}^n = \eta_{\text{app}}(ks) \tag{6.35}$$

and

$$\eta_{\text{app}} = K\dot{\gamma}^{n-1} = K(ks)^{n-1} \tag{6.36}$$

The shear stress τ_s depends on the shear rate $\dot{\gamma}$ or the speed s and on the fluidity K and flow index n, which have to be determined experimentally by means of a rotational viscosity meter. The constant k known from many experiments is approximately $k \approx 10$; compare Chapter 6. In Figure 6.10, the apparent viscosity η_{app} based on the dynamic viscosity η_L of the solid-free solution is plotted against the volumetric holdup of the crystals according to the theoretical and experimental results of various authors [6.15–6.19].

For the vertical and lateral hydraulic transport of suspensions, the mean fluid rate $\dot{v}_{\text{sus}}$ must generally be larger than the settling rate of the particles in the swarm ($\dot{v}_{\text{sus}}/w_{ss} > 3$). Deposits in wide horizontal tubes can be avoided when a Froude number, derived with the particle diameter L,

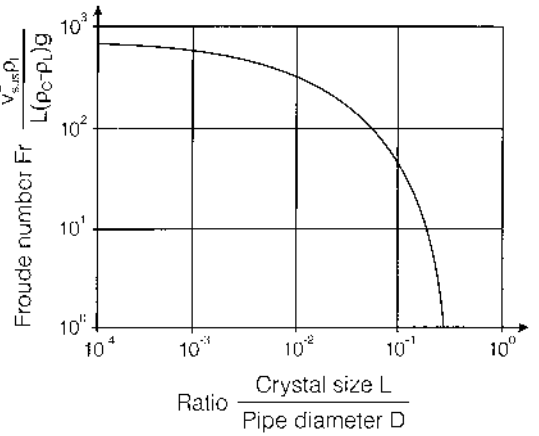

Figure 6.11. Froude number necessary for the suspension of particles in horizontal pipes versus the ratio L/D.

$\mathrm{Fr} = \dot{v}_{\mathrm{sus}}^2 \rho_L / gL(\rho_C - \rho_L)$, is larger than 700 [6.20]. This Froude number usually depends on the L/D ratio (see Fig. 6.11). Deposits in supersaturated solutions lead to the formation of crusts because the particles deposited grow and finally join together. It should be noted that a certain settling velocity w_{ss} of the suspension in the tube requires a corresponding fluid rate $\dot{v}_{\mathrm{sus}}$ of the suspension in the tube, where $\dot{v}_{\mathrm{sus}}$ should be approximately three to five times greater than w_{ss}. The relationship for the mean specific power input $\bar{\varepsilon}$ in tubes according to

$$\bar{\varepsilon} = \frac{\lambda}{2} \frac{\dot{v}_{\mathrm{sus}}^3}{D} \tag{6.37}$$

leads, in turn, to the relationship $\bar{\varepsilon} \sim 1/D$ (cf. Fig. 6.9). In this equation, D is the diameter of the tube and λ is the coefficient of friction. However, it must also be noted that for $D/L < 700$, the deposition of particles, in turn, depends on the ratio D/L itself [6.20].

In vertical hydraulic transport, a reliable suspension flow is obtained when the transport rate $\dot{v}_{\mathrm{sus}}$ is at least three times the swarm settling rate w_{ss} of particles having the mean value L_{50} and the range of crystal size distribution is not very wide. Otherwise, it is advisable to operate according to the settling rate of the largest crystals.

The mean specific power input ($\bar{\varepsilon}$) for flow through the mountings, elbows, and narrowings is given by the following equation, where the greatest suspension rate $\dot{v}_{\mathrm{sus}}$ occurs in the narrowest cross-sectional area A of such a resistance, the volume V_{el}, and the friction coefficient ξ:

$$\bar{\varepsilon} = \frac{\xi}{2} \dot{v}_{\text{sus}}^3 \frac{A}{V_{\text{el}}} \tag{6.38}$$

7. FORCED CIRCULATION

In forced-circulation (FC) crystallizers, the slurry is circulated by a pump through the heat exchanger, the tubes, and the separation chamber (see Fig. 7.1). The circulation flow rate $\dot{v}_{\text{sus}}$ of the suspension or the suspension velocity $\dot{v}_{\text{sus}}$ in the tubes must guarantee (a) sufficient macromixing in the entire loop (cf. Fig. 6.1), (b) sufficient suspension of crystals, especially of coarse crystals of $L_{\max} \approx 2L_{50}$ in the upward flow, and (c) moderate attrition and breakage of crystals. The second condition can be fulfilled with $\dot{v}_{\text{sus}} \approx 3w_{ss}$, and the settling velocity of a swarm of crystals w_{ss} can be obtained from Figure 5.3. This calculation procedure is recommended in the event of a small volumetric holdup; the slurry increasingly adopts the behavior of a non-Newtonian liquid to which the Ostwald–de Waele law applies in describing the shear stress as a function of the shear rate $\dot{\gamma}$, the stirrer speed s, and the fluidity constant (see Sec. 6).

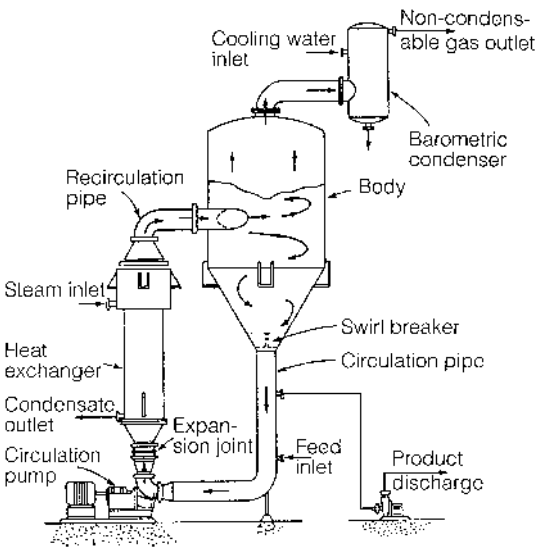

Figure 7.1. Forced-circulation crystallizer.

As a rule, centrifugal pumps are used to circulate the slurry. The volumetric flow rate of such pumps is proportional to the impeller speed s and the third power of the impeller diameter D according to equation (6.6):

$$\dot{V}_{\text{sus}} = N_{V,\text{sus}} s D^3$$

The total pressure drop Δp_T of the slurry in the entire loop consists of individual pressure drops caused by the tubes, the valves, and the hydrostatic pressures $\sum H \rho_{\text{sus}} g$ and is proportional to the total head H_T and the slurry density ρ_{sus}:

$$\Delta p_T \equiv H_T \rho_{\text{sus}} g = \underbrace{\sum \lambda \frac{L \dot{v}_{\text{sus}}^2 \rho_{\text{sus}}}{2D}}_{\text{tubes}} + \underbrace{\sum \xi \frac{\dot{v}_{\text{sus}}^2 \rho_{\text{sus}}}{2}}_{\text{valves}} + \underbrace{\sum H \rho_{\text{sus}} g}_{\text{hydrostatic}} \tag{7.1}$$

Attrition of crystals in the pump increases with the peripheral velocity $s\pi D$ of the impeller. Therefore, it is recommended that this velocity should be chosen to be as low as possible but sufficiently high to overcome the friction and hydrostatic losses of the circulating slurry. With small crystallizers, it is difficult to select an appropriate centrifugal pump because the minimum suspension flow rate is approximately $\dot{V}_{\text{sus}} \approx 5\,\text{m}^3/\text{h}$. The efficiency η of such pumps is low and severe attrition may occur. On the other hand, large FC crystallizers may be poorly mixed because of a limitation of the peripheral velocity of the impeller to $s\pi D = 15\,\text{m/s}$, which may cause crystal breakage (see Chapter 5).

The minimum power of the pump is proportional to the minimum suspension flow rate $\dot{V}_{\text{sus}}$ necessary for macromixing and the total pressure drop Δp_T:

$$P_{\text{min}} = \dot{V}_{\text{sus}} \Delta p_T \tag{7.2}$$

The minimum specific power input $\bar{\varepsilon}_{\text{min}}$ is given by

$$\bar{\varepsilon}_{\text{min}} \equiv \frac{P_{\text{min}}}{V \rho_{\text{sus}}} = \frac{P_{\text{eff}} \eta}{V \rho_{\text{sus}}} = \frac{\dot{V}_{\text{sus}} \Delta p_T}{V \rho_{\text{sus}}} \tag{7.3}$$

It is recommended to operate the pump at the point of maximum efficiency $\eta = P_{\text{min}}/P_{\text{eff}}$ to minimize the effective power P_{eff} and the mean specific power input in the entire suspension loop in order to avoid the attrition of crystals. Lines of constant efficiencies can be read from the diagrams in which the total head is plotted against the discharge flow $\dot{V}_{\text{sus}}$ for different impeller speeds s (see Fig. 7.2). An appropriate design of the entire arrangement with respect to fluid dynamics in a prequisite for optimal operating conditions to produce coarse crystals.

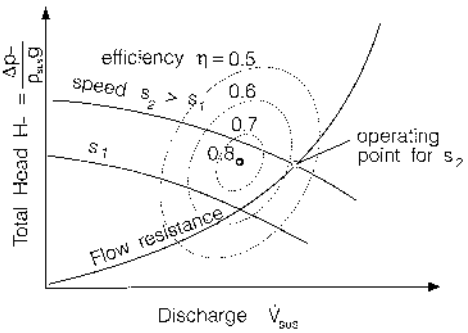

Figure 7.2. Total head versus the discharge of a centrifugal pump.

8. HEAT TRANSFER

At first, some theory-based equations for heat transfer coefficients will be presented. Such coefficients are very high for evaporation and condensation, and not representative for the design of crystallizers. In such an apparatus, the heat transfer is often limited by the slow flow of a sometimes viscous slurry. Therefore, at the end of this section some overall heat transfer coefficients suitable for the design of crystallizers will be presented.

The heat transfer coefficient h is defined by the equation

$$h = \frac{\dot{Q}}{A\Delta\vartheta} = \frac{\dot{q}}{\Delta\vartheta} \tag{8.1}$$

with heat flow rate $\dot{Q}$, heat transfer area A, and the temperature difference $\Delta\vartheta = (\vartheta_W - \vartheta_B)$ between the wall with the temperature ϑ_W and the bulk liquid (temperature ϑ_B). The maximum permissible heat flux density $\dot{q}_{\max}$ with respect to the metastable zone width Δc_{met} is given by

$$\dot{q}_{\max} = h(\Delta\vartheta)_{\text{met}} = h\Delta c_{\text{met}}\left(\frac{dc^*}{d\vartheta}\right)^{-1} \tag{8.2}$$

The Nusselt number $\text{Nu} = hT/\lambda_L$ (i.e., the dimensionless heat transfer coefficient), depends on the Reynolds number $\text{Re} = sD^2/\nu_L$ of the stirrer and on the Prandtl number $\text{Pr} = \nu_L/a_L$ of the liquid with the kinematic viscosity ν_L and the thermal diffusivity a_L. Crystals in the solution exhibit only a small influence on coefficient h. In Table 8.1, equations for the prediction of heat transfer coefficients are presented for the transitional and turbulent flow range or the liquid in the vessel. It is possible to derive these relationships from equations that are valid for a fluid flowing over a flat plate by forced

Table 8.1. Fluid Dynamics, Heat, and Mass Transfer in Stirred Vessels

Fluid dynamics	Flow rate, $\dot{V}_{\text{circ}}$	$\dot{V}_{\text{circ}} = N_V s D^3$
	Mean velocity, $\bar{v}$	$\bar{v} \sim sD^2/V^{1/3} \sim sD\dfrac{D}{T}$
	Mean fluctuating velocity, v'_{eff}	$v'_{\text{eff}} \sim sD\dfrac{D}{T}$
	Shear rate, $\dot{\gamma}$	$\dot{\gamma} \sim s$
	Shear stress, $\tau_{s,\text{turb}}$	$\tau_{s,\text{turb}} \sim \rho_{\text{sus}}(v'_{\text{eff}})^2 \sim \rho_{\text{sus}}(sD)^2\left(\dfrac{D}{T}\right)^2$
	Power consumption, P	$P = (\text{Po})\rho_{\text{sus}} s^3 D^5$
	Specific power input, ε	$\bar{\varepsilon} = \dfrac{4}{\pi}(\text{Po}) s^3 D^2 \left(\dfrac{D}{T}\right)^2 \dfrac{D}{H}$
	Ratio $\dot{V}_{\text{circ}}/\tau_{s,\text{turb}}$	$\dfrac{\dot{V}_{\text{circ}}}{\tau_{s,\text{turb}}} \sim \left(\dfrac{D^5}{\bar{\varepsilon}}\right)^{1/3} \dfrac{D}{T}\dfrac{1}{\rho_{\text{sus}}}$
Mixing	Macromixing time, $t_{\text{macro,turb}}$	$t_{\text{macro,turb}} \approx 5\left(\dfrac{T^2}{\bar{\varepsilon}}\right)^{1/3}$
	Macromixing time, $t_{\text{macro,lam}}$	$t_{\text{macro,lam}} \approx 5\left(\dfrac{\nu_L}{\varepsilon}\right)^{1/2} \ln(\text{Sc})$
	Micromixing time, t_{micro}	$t_{\text{micro}} \approx 5\left(\dfrac{\nu_L}{\varepsilon}\right)^{1/2} \ln(\text{Sc})$

Suspension	Suspension criterion, $T/L_{50} > 10^5$	$\overline{\varepsilon_{\min}} = \varphi_T w_{ss} g \dfrac{\rho_C - \rho_L}{\rho_L}$
	Suspension criterion, $T/L_{50} < 10^4$	$\bar{\varepsilon} \sim \dfrac{(\mathrm{Po})(sD)^3}{D}$ with $sD = f(\mathrm{Ar})$
Breakup of gas	Specific interfacial area, a_G	$a_G = \dfrac{6\varphi_G}{d_{32}}$ with $\varphi_G \approx \left(2 + \dfrac{w_B}{\dot{v}_G}\right)^{-1}$
	Gas bubble velocity, w_B	$w_B = 1.55\left(\dfrac{\gamma_{\mathrm{LG}}(\rho_L - \rho_G)g}{\rho_L^2}\right)^{1/4}$
	Sauter mean diameter, d_{32}	$d_{32} = (1 + \varphi_G)\gamma_{LG}^{0.6}(\rho_L^{0.6}\bar{\varepsilon}^{0.4})^{-1}$
Heat transfer	Heat transfer coefficient h, $10^4 < \mathrm{Re} < 10^6$	$h = 0.8\dfrac{\lambda_L}{T}\left(\dfrac{\bar{\varepsilon}D^4}{(\mathrm{Po})\nu_L^3}\right)^{2/9}\left(\dfrac{T}{D}\right)^{4/9}\left(\dfrac{H}{T}\right)^{2/9}\left(\dfrac{\nu_L}{a_L}\right)^{1/3}\left(\dfrac{\eta_L}{\eta_{Lw}}\right)^{0.14}$
	Heat transfer coefficient h, $\mathrm{Re} > 10^6$	$h = 0.072\dfrac{\lambda_L}{T}\left(\dfrac{\bar{\varepsilon}D^4}{(\mathrm{Po})\nu_L^3}\right)^{1/4}\left(\dfrac{T}{D}\right)^{3/4}\left(\dfrac{H}{T}\right)^{1/4}\left(\dfrac{\nu_L}{a_L}\right)^{5/12}$
Mass transfer	Mass transfer coefficient k_L (bubbles)	$k_L = (0.2 \div 0.4)\left(\dfrac{D_{AB}^2\bar{\varepsilon}}{\nu_L}\right)^{1/4}$
	Mass transfer coefficient k_d (wall), $10^4 < \mathrm{Re} < 10^6$	$k_d = 0.8\dfrac{D_{\mathrm{AB}}}{T}\left(\dfrac{\bar{\varepsilon}D^4}{(\mathrm{Po})\nu_L^3}\right)^{1/4}\left(\dfrac{T}{D}\right)^{4/9}\left(\dfrac{H}{T}\right)^{2/9}\left(\dfrac{\nu_L}{D_{AB}}\right)^{1/3}$
	Mass transfer coefficient k_d (crystal)	$k_d = \dfrac{D_{AB}}{L}\left[0.8\left(\dfrac{\bar{\varepsilon}L^4}{\nu_L^3}\right)^{1/5}\left(\dfrac{\nu_L}{D_{AB}}\right)^{1/3} + 2\right]$

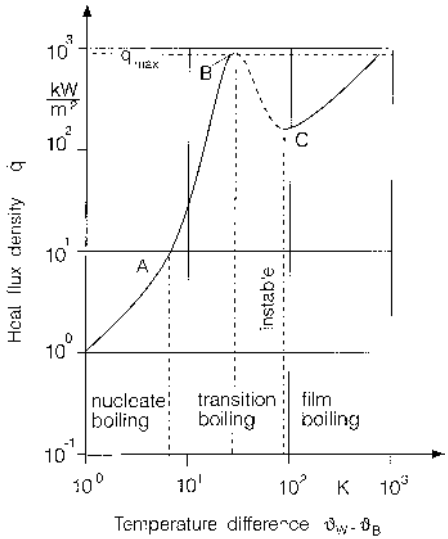

Figure 8.1. Heat flux density versus the temperature difference when water boils at 1 bar.

convection [8.1]. The Reynolds number can be expressed as the dimensionless power number $\bar{\varepsilon}D^4/(\mathrm{Po})\nu_L^3$ in the case of turbulent flow. Equations for the heat transfer coefficient with this power group are listed in Table 8.1. The heat transfer coefficients of evaporation crystallizers are much more difficult to predict.

In heat transfer from a heating surface to a boiling liquid, heat is transferred by convection when the difference between the surface temperature of the heating surface and that of the liquid is small; this is known as *convective boiling*. When a specific temperature difference is exceeded, more and more vapor bubbles are formed, leading to enhanced heat transfer due to the stirring effect of these bubbles; this is known as *nucleate boiling*. When the temperature difference is even greater, the bubbles formed on the heating surface may be so close to one another that they grow together to form a film of vapor; this is known as *film boiling*.

The three stages can be represented in a diagram in which the heat flux density is plotted against the difference between the wall temperature and the boiling point. In Figures 8.1 and 8.2, the heat flux density and heat transfer coefficient, respectively, are plotted against the temperature difference valid for water at 1 bar. In the range of nucleate boiling, the heat flux density and the heat transfer coefficient both increase with the temperature

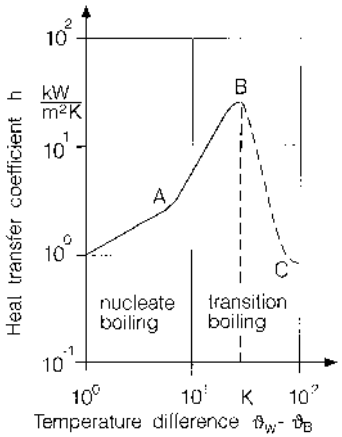

Figure 8.2. Heat transfer coefficient versus the temperature difference when water boils at 1 bar.

difference. The heat transfer coefficient can be calculated according to the relationships for free or forced convection.

In the zone of transition boiling, the heat flow density $\dot{q}$ and the heat transfer coefficient h increase to a greater extent than for convective boiling. At the peak of the curve, the maximum heat flux density of 900 kW/m^2 is obtained at a temperature difference of approximately 30 K. When the temperature difference increases even further, the driving temperature gradient must be increased considerably (in this case to 800 K) in order for the heat flux density to continue increasing. In the unstable zone, the heating surface often burns out due to overheating.

In Figure 8.3, the heat transfer coefficient is plotted against the heat flux density for water and various organic liquids. From this graph, it can be determined that the maximum heat flow density of organic liquids has a value of approximately 300 kW/m^2. For all pressures and temperatures, the greatest temperature difference $\vartheta_W - \vartheta_B$ in nucleate boiling is roughly three to four times higher than the value at the beginning of nucleate boiling.

In the nucleate boiling range, the heat transfer coefficient h_B depends on pressure in the case of still liquids. For practical purposes, this relationship is determined with the aid of reduced pressure. The heat transfer coefficient for reduced pressure $p_r = p^0/p_c$ is given by the equation [7.1]:

$$\frac{h_B d_A}{\lambda_L} = c\left(\frac{\dot{q} d_A}{\lambda_L T_b}\right)^{n_1}\left(\frac{d_A T_b \lambda_L}{\nu_L \gamma_{LG}}\right)^{n_2}\left(\frac{R_P \rho_G \Delta h_{LG}}{(f d_A)^2 d_A \rho_L}\right)^{0.133} \tag{8.3}$$

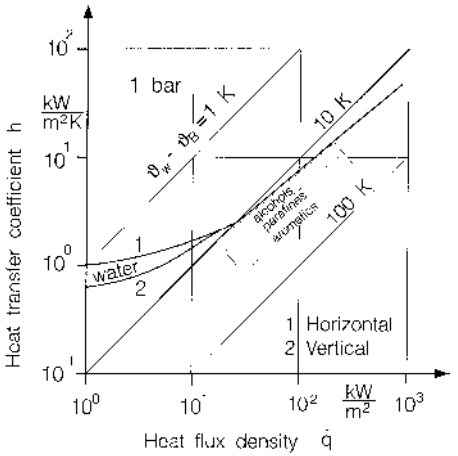

Figure 8.3. Heat transfer coefficient versus heat flux density for water and organic liquids.

Table 8.2. Magnitude of Constant and Exponents During Boiling Processes

	c	n_1	n_2
Horizontal flat plate	0.013	0.8	0.4
Horizontal tube	0.071	0.7	0.3

where d_A is the bubble diameter, which can be calculated as follows [7.1]:

$$d_A = 0.0144\beta_R\sqrt{\frac{2\gamma_{\mathrm{LG}}}{(\rho_L - \rho_G)g}} \tag{8.4}$$

The wetting angle β_R is 45° for water and 35° for refrigerants. The product of the square of the bubble-detaching diameter was determined empirically as $f^2 d_A = 3.06\,\mathrm{m/s^2}$. The smoothing depth R_P of the heating surface is given by DIN 4762. Table 8.2 provides information on the magnitudes of constant c and exponents n_1 and n_2 during boiling processes on horizontal flat plates and horizontal tubes. The effects of pressure can be determined with the following equation [7.1]:

$$h_B = h_{B_{(p^0, p_c, 0.03)}}\left[0.70\frac{p^0}{p_c}\left(8 + \frac{2}{1 - p^0/p_c}\right)\right] \tag{8.5}$$

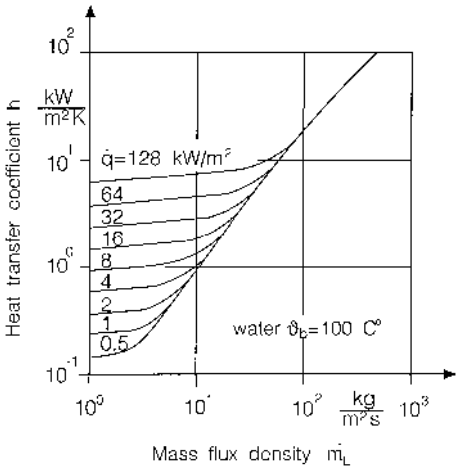

Figure 8.4. Mean heat transfer coefficient versus mass flux density when water boils at 1 bar.

If the boiling process concerned is advanced nucleate boiling, liquid subcooling has no particular effect on the heat transfer coefficient.

The maximum heat flow density $\dot{q}_{\max}$ is given by the following equation [7.1]:

$$\dot{q}_{\max} = 0.14 \Delta h_{LG} \sqrt{\rho_G} \sqrt[4]{\gamma_{LG}(\rho_L - \rho_G)g} \tag{8.6}$$

This limitation results from the fact that above a certain volumetric flow density of the vapor, the liquid on the heating surface is dragged along against gravity so that a vapor film is formed.

Many apparatuses used in the field of crystallization technology contain vertical evaporator tubes in which a certain mass flow density of vapor and liquid arises. Heat transfer improves with increasing mass flux density $\dot{m}_L$ of the liquid, as shown for water in Figure 8.4. If the value of the mass flux density is still moderate and if the liquid has become saturated, the heat transfer coefficient in a tube with then diameter D can be calculated from the following equation:

$$h = h_B \left[29 \left(\frac{\eta_L}{\dot{m}_L D(1-\varphi_G)} \right)^{0.3} \left(\frac{\dot{m}_L^2 (1-\varphi_G)^2}{D \rho_L^2 g} \right)^{0.2} \right. \tag{8.7}$$

where h_B is the value according to the equations specified for nucleate boiling [see Eq. (8.3)]. The transfer coefficient thus depends both on mass flux density $\dot{m}_L$ and vapor contents φ_G. If an evaporator tube is operated at

forced convection, the mass flow density is determined by the circulating element. However, in the case of a natural circulation evaporator, circulation must be determined by the fact that the difference in hydrostatic pressure must overcome the flow resistance of circulation due to the lower density of the liquid–vapor mixture in the evaporator tube.

When a solution with condensing water vapor is vaporized in a vertical tubular evaporator with natural or forced convection, the overall heat transfer coefficient k, where

$$k = \frac{\dot{Q}}{A(\vartheta_{HC} - \vartheta_B)} \quad \text{with } \frac{1}{k} = \frac{1}{h_i} + \frac{s}{\lambda_s} + \frac{1}{h_a} \tag{8.8}$$

depends, above all, on the mass flow density in the tube and on the viscosity and thermal conductivity of the solution.

8.1. Overall Heat Transfer Coefficients

In the case of natural convection, it can be assumed that $k = 300$ to $900\,W/m^2\,K$ for viscous solutions and $k = 900$ to $1800\,W/m^2\,K$ for less viscous liquids. Even greater heat transfer coefficients of $k = 900$ to $2700\,W/m^2\,K$ can be obtained with forced convection of solutions of low viscosity. Approximate overall heat transfer coefficients are of the order of magnitude of $100\,W/m^2\,K$ (organics, low-specific-power input) up to $1000\,W/m^2\,K$ (aqueous systems, high-specific-power input) in draft tube baffled crystallizers [6.5].

9. MASS TRANSFER

When dealing with cooling and evaporative crystallizers, the mass transfer coefficient k_d between the crystals and the surrounding solution is decisive for diffusion-controlled crystal growth. In heterogeneous gas–liquid reaction crystallization, mass also has to be transferred from the gas phase to the liquid.

9.1. Mass Transfer in Solid–Liquid Systems

Growing crystals in a supersaturated solution can be (a) fixed in a channel on a rod or on a plate, (b) suspended in a stirred vessel or fluidized bed, or (c) transported in a concurrent flow in a FC crystallizer. Sometimes, the crystal growth rate of single fixed crystals is determined in a tube with the diameter D. The Sherwood number $Sh = k_d L/D_{AB}$ depends on the

Reynolds number $\mathrm{Re} = w_L L/\nu_L$ of the solution flow and on the Schmidt number $\mathrm{Sc} = \nu_L/D_{\mathrm{AB}}$ of the solution and is given for $10 < \mathrm{Re} < 10^3$ by [9.1]:

$$\mathrm{Sh} = 2 + 0.8(\mathrm{Re})^{1/2}(\mathrm{Sc})^{1/3} \tag{9.1}$$

or, with equation (6.37),

$$\frac{k_d L}{D_{AB}} = 2 + 0.8\left(\frac{2DL^3}{\lambda \nu_L^3}\bar{\varepsilon}\right)^{1/6}(\mathrm{Sc})^{1/3} \tag{9.2}$$

The mass transfer coefficient depends on specific input ($k_d \sim (\bar{\varepsilon})^{1/6}$) to only a small extent and is inversely proportional to the square root of the crystal size L. In general, we obtain

$$\mathrm{Re} = \frac{w_L L}{\nu_L} < 1: \quad k_d \sim L^{-1} \tag{9.3}$$

$$10 < \mathrm{Re} < 10^3: \quad k_d \sim L^{-0.5} \tag{9.4}$$

$$\mathrm{Re} > 10^5: \quad k_d \sim L^{-0.2} \tag{9.5}$$

Because the variation in crystal size L for substances with high dimensionless solubility $c^*/\rho_C > 10^{-3}$ is fairly small, the mass transfer coefficient k_d depends primarily on diffusivity D_{AB}($k_d \sim D_{AB}^{2/3}$).

When dealing with crystals suspended or transported in a crystallizer, mass transfer no longer depends on the tube diameter D or vessel diameter T but only on the crystal size L. The equation

$$\mathrm{Sh} = \frac{k_d L}{D_{AB}} = 2 + 0.8\left(\frac{L^4\bar{\varepsilon}}{\nu_L^3}\right)^{1/5}(\mathrm{Sc})^{1/3} \tag{9.6}$$

applies to stirred-vessel and fluidized-bed crystallizers [9.2]. Because mass transfer is greatly limited by bulk diffusion in the immediate vicinity of the crystals, it is again very important to know the diffusivities D_{AB} in supersaturated solutions. This is currently the most severe drawback when predicting of exact and reliable mass transfer coefficients k_d. With regard to this aspect, equation (9.6) can generally be recommended for the calculation of mass transfer coefficients for crystals in arbitrary crystallizers. In Figure 9.1, the mass transfer coefficient k_d valid for $\mathrm{Sc} = 10^3$, $\nu_L = 10^{-6}$, and $D_{AB} = 10^{-9}\ \mathrm{m^2/s}$ is plotted against the crystal size L with the specific power input $\bar{\varepsilon}$ as parameter.

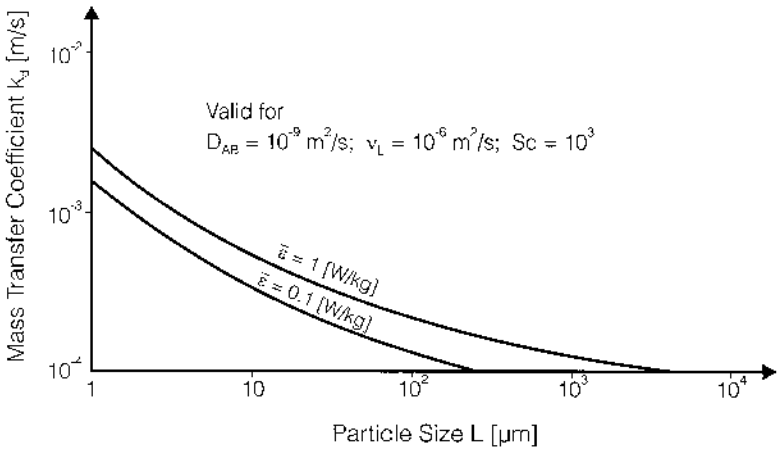

Figure 9.1. Mass transfer coefficient k_d versus the particle size L (valid for certain values of ν_L and D_{AB}).

9.2. Mass Transfer in Gas–Liquid Systems

Sometimes, precipitates are produced by a heterogeneous gas–liquid reaction (see Chapter 11). A gas (SO_2, CO_2, HCl, NH_3, etc.) reacts with a caustic to form a product P, which will be dissolved in the solution. When the solubility in this liquid is exceeded, this component will be crystallized by nucleation and crystal growth in the supersaturated solution. With respect to the gaseous reactant i, the following steps may control the rate of reaction (see Fig. 9.2):

1. Mass transfer $N_{G,i} = k_{G,i} a_G \Delta p_{G,i} / \Re T$ in the gas phase
2. Mass transfer $N_{L,i} = k_{L,i} a_G \Delta c_{L,i}$ in the liquid phase
3. Chemical reaction of the dissolved gas component with the reactant in the liquid:

$$\frac{dN_i}{dt} = -k_0 \exp\left(-\frac{E}{\Re T}\right) c_i^{\alpha} c_j^{\beta} \tag{9.7}$$

4. Nucleation rate of the product (primary or secondary)
5. Growth rate of the product controlled by diffusion and/or integration, due to the supersaturation $\Delta c_P = c_P - c_P^*$ or $\sigma_P = \Delta c_P / c_P^*$

It is important to distinguish among the different driving forces for various steps. When dealing with a gaseous reactant that is highly concentrated in the gas phase but only slightly dissolved in the liquid phase, mass transfer

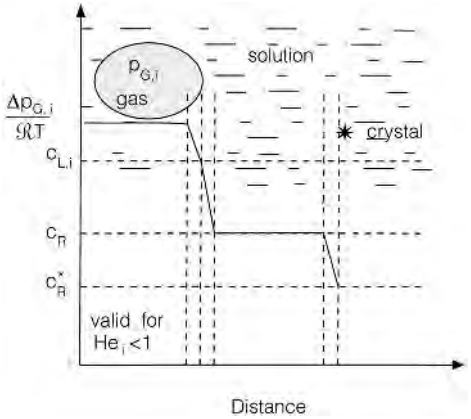

Figure 9.2. Concentration profile in a gas–liquid–solid system of a precipitation crystallizer due to a heterogeneous chemical reaction.

from the gas–liquid interface to the bulk of the liquid controls the rate of fast chemical reactions with a high reaction rate constant k_0 and/or a small activation energy E, especially at high temperatures T. The concentration c_P of the product then depends on the gas–liquid mass transfer coefficient $k_{L,i}$ of the gas component i, the interfacial area a_G between the liquid and the gas phase according to

$$a_G = \frac{6\varphi_G}{d_{32}} \tag{9.8}$$

and on the concentration difference $\Delta c_{L,i}$ (see Fig. 9.2). If the partial gas pressure $p_{G,i}$ in the gas is known, the interfacial concentration $c_{L,i}$ of the component can be calculated by Henry's law ($He_i = y^*_{G,i}/x_i$), with y^*_i and x_i as the mole fraction of the component i in the gas or the liquid phase, respectively:

$$c_{L,i} = He_i \frac{p_{G,i}}{\Re T} \tag{9.9}$$

The gas holdup φ_G and the specific interfacial area a_G can be obtained from Table 8.1, which applies to stirred vessels equipped with Rushton turbines, which are recommended for the breakup of gases to produce small bubbles with the Sauter mean diameter d_{32}. The mass transfer coefficient k_L in the liquid phase can be calculated by

$$k_L = (0.2 \div 0.4)\left(\frac{D_{AB}^2 \bar{\varepsilon}}{\nu_L}\right)^{1/4} \tag{9.10}$$

where $\bar{\varepsilon}$ is the mean specific power input, D_{AB} is the diffusivity of the diffusing component in the liquid, and ν_L is its kinematic viscosity.

REFERENCES

[1.1] W. Wöhlk and G. Hofmann, Types of crystallizers, *Int. Chem. Eng.*, *24*: 419–431 (1984).

[1.2] S. J. Jancic, Fractional crystallization, in *Proc. 10th Symp. Industrial Crystallization* (J. Nyvlt and S. Zadek, eds.), Elsevier, Amsterdam (1989).

[1.3] M. Matsuoka, M. Ohishi, and S. Kasama, Purification of *p*-dichlorobenzene and *m*-chloronitrobenzene crystalline particles by sweating, *J. Chem. Eng. Jpn.*, *19*(3): 181–185 (1986).

[1.4] K. Stolzenberg, Der Blasensäulenkristaller, *Chem. Ing. Tech.*, *55*(1): 45–46 (1983).

[1.5] K. -J. Kim and A. Mersmann, Melt crystallization with direct contact cooling techniques, *Trans. IChemE Part A.*, *75*: 176–182 (1997).

[1.6] K. Bartosch and A. Mersmann, Design of a continuously operating melt crystallizer based on direct contact cooling techniques, *Proceedings 14th International Sympsoium on Industrial Crystallization* (1999).

[2.1] A. G. Toussaint and J. M. H. Fortuin, Design criteria for DTB vacuum crystallizers, In *Industrial Crystallization* (J. W. Mullin, ed.), Plenum Press, New York, pp. 311–318 (1976).

[2.2] A. Mersmann, *Thermische Verfahrenstechnik*, Springer-Verlag, Berlin, p. 225 (1980).

[2.3] W. Fleischmann and A. Mersmann, Drowning-out crystallization of sodium sulphate using methanol, in *Proc. 9th Symp. on Industrial Crytsallization* (S. J. Jancic and E. J. de Jong, eds.), Elsevier, Amsterdam (1984).

[2.4] H. P. Wirges, Beeinflussung der Korngrössenverteilung bei Fällungskristallisationen, *Chem. Ing. Tech.*, *58*(7) 586–587 (1986).

[2.5] I. Liszi and J. Liszi, Salting out crystallization in KC1-water-methanol system, in *Proc. 11th Symp. on Industrial Crystallization* (A. Mersmann, ed.), pp. 515–520 (1990).

[2.6] J. W. Mullin, Crystallizer deisgn and operation, in *Industrial Crystallization* (J. W. Mullin, ed.), Plenum Press, New York (1976).

[2.7] H. Griffiths, Mechanical crystallization, *Trans. J. Soc. Chem. Ind.*, *44*(2): 7T–18T (1925).
[3.1] A. Mersmann and M. Kind, Design principles of mass crystallizers, *Ger. Chem. Eng.*, *8*: 394–405 (1985).
[5.1] H. G. Schwartzberg and R. E. Treybal, Fluid and particle motion in turbulent stirred tanks, *Ind. Eng. Chem. Fundam.*, *7*(1): 6–12 (1968).
[6.1] A. Mersmann and M. Kind, Design principles of mass crystallizers, *Ger. Chem. Eng.*, *8*: 394–405 (1985).
[6.2] R. Geisler, Fluiddynamik und Leistungseintrag in turbulent gerührten Suspensionen, Thesis, Technische Universität München, Munich (1991).
[6.3] A. Mersmann and R. Geisler, Determination of the local turbulent energy dissipation rates in stirred vessels and its significance for different mixing tasks, in *Proc. 4th World Congress of Chemical Engineering*, (1991).
[6.4] A. Mersmann, G. Schneider, H. Voit, and E. Wenzig, Selection and design of aerobic bioreactors, *Chem. Eng. Technol.*, *13*: 357–370 (1990).
[6.5] R. H. Perry and D. Green (eds.), *Perry's Chemical Engineers' Handbook*, 6th ed., McGraw-Hill, New York, p. 19 (1984).
[6.6] R. Geisler, A. Mersmann, and H. Voit, Macro- and micromixing in stirred tanks, *Int. Chem. Eng.*, *31*(4): 642–653 (1991).
[6.7] J. Garside and S. N. Tavare, Mixing reaction and precipitation: Limits of micromixing in a MSMPR crystallizer, *Chem. Eng. Sci.*, *40*(8): 1085–1093 (1985).
[6.8] N. S. Tavare and J. Garside, Simulation of reactive precipitation in a semi-batch crystallizer, *Trans. Inst. Chem. Eng.*, *68A*: 115–122 (1990).
[6.9] R. S. Brodkey, Fundamentals of turbulant motion, mixing and kinetics, *Chem. Eng. Commun.*, *8*: 1–23 (1981).
[6.10] S. Corrsin, The isotropic turbulent mixer. II. Arbitrary Schmidt number, *AIChE J.*, *10*(10): 870–877 (1964).
[6.11] P. Costa and C. Trevissoi, Some kinetic and thermodynamic features of reactions between partiallly segregated fluids, *Chem. Eng. Sci.*, *27*: 653–668 (1972).
[6.12] T. N. Zwietering, Suspending of solid particles in liquid by agitators, *Chem. Eng. Sci.*, *8*: 244–253 (1958).
[6.13] F. Magelli, D. Fajner, M. Nocenti, and G. Pasquali, Solid distribution in slurry reactors stirred vessels with multiple axial impellers, *Chem. Eng. Proc.*, *29*: 27 (1991).
[6.14] A. Mersmann, F. Werner, S. Maurer, and K. Bartosch, Theoretical prediction of the minimum stirrer speed in mechanically agitated suspensions, *Chem. Eng. Process.*, *37*: 503–510 (1998).

[6.15] A. Einstein, Eine neue Bestimmung der Moleküldinesionen, *Ann. Phys.*, *19*: 289–306 (1906).
[6.16] H. Eilers, Die Viskosität von Emulsionen hochviskoser Stoffe als Funktion der Konzentration, *Kolloid Z.*, *97*(3): 313–323 (1941).
[6.17] K. Magnusson, Rührwerke für viskose Flüssigkeiten und Zweiphasensysteme, *Deut. Farben Z.*, *7*(2): 39–44 (1953).
[6.18] A. B. Metzner and R. E. Otto, Agitation of non-Newtonian fluids, *AIChE J.*, *38*: 328–342 (1992).
[6.19] P. M. Weinspach, Hydrodynamisches Verhalten von Suspensionen in Rührgefässen, *Chem. Eng. Technol.*, *41*: 260–265 (1969).
[6.20] H. Brauer, *Grundlagen der Einphasen- und Mehrphasenströmung*, Sauerländer, Franfurt (1971).
[7.1] A. Mersmann, *Thermische Verfahrenstechnik*, Springer-Verlag, Berlin (1980).
[8.1] F. Kneule, *Rühren (Stirring)*, Dechema, Frankfurt am Main (1986).
[9.1] A. Mersmann, *Stoffübertragung*, Springer-Verlag, Berlin (1986).
[9.2] J. Garside, A. Mersmann, and J. Nyvlt, *Measurement of Crystal Growth Rates*, European Federation of Chemical Engineering, Working Party on Crystallization, Munich (1990).

9
Operation of Crystallizers

A. MERSMANN Technische Universität München, Garching, Germany

F. W. RENNIE Du Pont de Nemours & Co., Wilmington, Delaware

Industrial crystallizers can be operated continuously or batchwise. Crystallizers are run continuously when they are integrated in a large production plant that is also operated continuously. Encrustation, however, can result in short operation times with the consequence of frequent shutdowns. The advantage of continuous operation over the batch process is then lost. The advantages and drawbacks of the various modes of operation will be discussed in more detail.

1. CONTINUOUSLY OPERATED CRYSTALLIZERS*

The most important advantage of continuously operated crystallizers is the fact that the mean supersaturation is a function of the mean residence time $\tau = V_{\text{sus}}/\dot{V}_R$, where V_{sus} is the suspension volume and $\dot{V}_R$ is the volumetric flow of the product suspension removed from the crystallizers. This means that the optimal supersaturation ΔC_{opt} can be easily maintained by a certain flow $\dot{V}_R$ for a given volume V_{sus}.

*By A. Mersmann.

At optimum supersaturation, the median crystal size passes through a maximum, which can be explained by the counteractions of supersaturation and residence time because the mean supersaturation decreases with increasing residence time. Macromixing determines the question as to whether there are differences between mean (and possibly time independent) and local supersaturation. It is important to keep the local supersaturation within the metastable zone width in order to avoid activated nucleation, which would lead to a large number of nuclei and to a reduction in the median crystal size. Such peaks of supersaturation can occur in the mixing zone of an inlet stream or in the surface boiling layer of an evaporation crystallizer. The local supersaturation also depends on the presence of crystals according to the desupersaturation caused by crystal growth. It is very important, however, to keep in mind that the desupersaturation process by growth is very slow in comparison to nucleation. Therefore, a huge crystal surface area (high suspension density of fine crystals) must be present in the zone of high supersaturation to avoid excessive nucleation. On the other hand, it is important to fulfill requirements resulting from the population balance. If activated nucleation is to be avoided, it is necessary to produce as many active attrition fragments as crystals are withdrawn from the crystallizer; otherwise, the number of growing crystals and their volumetric surface $a_T = 6\varphi_T/L_{32}$ can become so small that supersaturation increases with time. This can ultimately lead to a nucleation burst with a sudden breakdown of the supersaturation. Large crystallizers, in particular, have a tendency to oscillate: This means that the mean supersaturation, the suspension density, and, in particular, the crystal size distribution (CSD) oscillate. As a rule, oscillation is most pronounced at a supersaturation close to the metastable zone limit. One important result of this undesired operating condition may be the lack of active attrition fragments, the rate of which is given by (cf. Chapter 5)

$$\frac{B_a}{\varphi_T} \approx 7 \times 10^{-4} \frac{H_V^5}{\mu^3} \left(\frac{K}{\Gamma}\right)^3 \frac{\pi^2 \rho_C \bar{\varepsilon} N_V}{2\alpha^3(\mathrm{Po})} \frac{N_{a,\mathrm{eff}}}{N_{a,\mathrm{tot}}} \eta_w^3 \eta_g \tag{1.1}$$

In Chapter 5, it has been shown that the scale-up rule $u_{\mathrm{tip}} \sim (\bar{\varepsilon}T)^{1/3} = \mathrm{const.}$ is sufficient to suspend the crystals, or $\bar{\varepsilon} \sim 1/T$. Furthermore, the target efficiencies η_w and η_g decrease as the size of the crystallizer increases. When insufficient attrition fragments are generated in a large industrial crystallizer to replace the number of product crystals and the volumetric crystal surface becomes too small, supersaturation starts to increase. Finally, the metastable supersaturation limit is reached, which results in a shower of nuclei produced by activated nucleation. After a rapid decrease in the mean supersaturation, this driving force starts to rise

again, and during this period, the newly generated nuclei (which are not attrition fragments) grow to such an extent that the median crystal size decreases. It should be noted here that the attrition rate G_a and the target efficiencies η_w and η_g are dependent on the crystal size. As has been shown, the oscillation of crystallizers is a complex process. According to Chapter 5, the production of attrition fragments depends on a variety of material ($H_V, \mu, \Gamma/K$) and operating ($s, u_{\text{tip}}, \bar{\varepsilon}$) parameters. The production or destruction of fines is a suitable tool for avoiding or minimizing the oscillation of crystallizers.

1.1. Fines Dissolution

The crystal size distribution of a crystalline material is determined by (a) the net rate of particles (nuclei, crystals, attrition fragments, agglomerates) produced in batch or continuously operated crystallizers and (b) the growth behavior of these particles in supersaturated solution. An increase in supersaturation leads to a larger median crystal size due to a higher growth rate G for the same batch or retention time and to a reduction in the median crystal size because more particles (nuclei, attrition fragments) are generated and stimulated to grow, with the result that the solute is deposited on more particles. As a consequence, it is very important to choose the optimum retention time τ_{opt} (which is connected with supersaturation) for continuously operated crystallizers or the optimum supersaturation ΔC_{opt} for batch crystallizers ($\Delta C_{\text{opt}} = \text{const.}$). Generally speaking, the possibilities of changing the crystal size distribution and the median crystal size are rather limited, with the exception of fines destruction or removal. The effects of clear-liquor advance, fines destruction, and classified product removal have been discussed in Chapter 4. Reducing the number of fine particles is very efficient provided that particles which grow to a product-relevant size during the batch or retention time are substantially removed.

In the literature, various methods are described for fines destruction. Sometimes, cycling of the operating conditions (flow, cooling, heating, temperature, concentration, super/undersaturation) is applied with the objective of dissolving or agglomerating fine particles during periods of changed supersaturation [1.1]. The most efficient tool, however, is the withdrawal of fine particles and the dissolution in a separate loop (see Fig. 1.1). The maximum size of the particles removed depends on their settling velocity w_{ss} and can be chosen by the condition $w_{ss} = \dot{v}_{\text{sus}}$ for turbulent flow with superficial suspension velocity in the tube (when dealing with laminar flow, $\text{Re} = \dot{v}_{\text{sus}} D/\eta_{\text{sus}} < 2300$, particles of $w_{ss} = 2\dot{v}_{\text{sus}}$ are

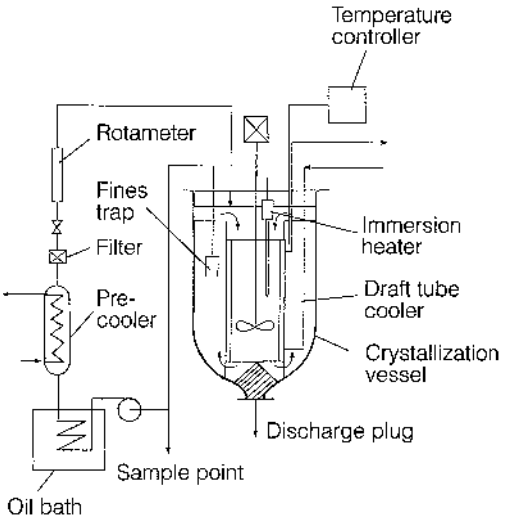

Figure 1.1. Crystallizer with a fines dissolution loop.

withdrawn). The percentage β of dissolved particles (see Eq. (4.4.1)) depends mainly on (a) the degree of undersaturation, $-\Delta c$, and (b) the retention time t of particles in the undersaturated solution. Where the size reduction $L_\alpha - L$ is small, the dissolution time t_{dis} is a function of the mass transfer coefficient k_d [1.2]:

$$t_{\text{dis}} = \frac{(L_\alpha - L)\rho_L}{2k_d(-\Delta c)} \tag{1.2}$$

with undersaturation $-\Delta c = -(c - c^*) = c^* - c$. The mass transfer coefficient can be obtained from equations presented in Chapter 8.

When dealing with greater changes in particle size L and undersaturation, $-\Delta c$, the dependence of mass transfer on the operating conditions has to be taken into consideration. In the tube of the heat exchanger, particles can settle on the tube wall. Dissolution can then be controlled by diffusion ($\text{Sh} = k_d L/D_{AB} = 2$; Sh = Sherwood number). The reduction from size L_α to L as a function of the dissolution time is given by

$$L = \sqrt{L_\alpha^2 - \frac{8cD_{AB}}{\rho_C}\ln\left(\frac{c}{c - c^*}\right)t} \tag{1.3}$$

The time for complete dissolution ($L = 0$) is

$$t = \frac{L_\alpha^2 \rho_C}{8 c D_{AB} \ln[c/(c - c^*)]} \tag{1.4}$$

As a rule, a reduction to $L = 10\,\mu m$ is sufficient, because at low supersaturation, only a few attrition fragments with weak growth ability are generated. Figure 2.1 provides an example of the coarsening of a product by fines particle dissolution [1.3].

As has been shown in Chapter 4, classified product removal leads to a reduction in the median crystal size and the coefficient of variation. The separation size L_c of a classifying device (elutriator) can be found by the condition $w_{ss}(L_c) = \dot{v}_{sus}$. As a rule, however, no sharp size cut can be expected due to turbulent multiphase flow.

1.2. Crystallizers with Classification Equipment

Crystallizers are sometimes equipped with classification devices such as the following:

- Fluidized beds
- Hydrocyclones
- Centrifuges
- (Wet) screens

These apparatuses can be employed to produce more narrowly distributed crystals while reducing the average size of the crystals in the crystallizer (cf. Chapter 4). Information on the design and operations of some of these devices is given in Sec. 7.3. It should be noted that the operation of all of the equipment can be troublesome and cause attrition and breakage. The smaller the collision velocity w_{col} or, in general, the smaller the pressure drop or volumetric energy (batch) or the specific power input (continuous), the smaller the attrition rates are (cf. Chapter 5).

Fluidized beds are more favorable with respect to attrition than hydroclones and centrifuges. Another important parameter is the efficiency of separation or the overlapping particle size range of the two separated streams. Wet sieving and hydrocyclones are usually superior to elutriation and fluidized beds. However, the sharpness of separation depends mainly on the load of the suspension stream per unit area perpendicular to the flow direction. As a rule, the oversize is withdrawn as the product stream. The undersize can be recycled with or without all the crystals being dissolved. The mode of operation is decisive for the entire population balance of the process and especially for the CSD.

1.3. Crystallizer Cascades

Despite increased investment, a crystallizer cascade can offer economical advantages over a single-body crystallizer of the same volume V [1.4]. Figure 1.2 shows a cascade of eight countercurrent crystallizers with a total volume of 2800 m^3 for the production at 140,000 kg/h of coarse KCl crystals [1.5].

The main reason for the cascade is the limitation of the mean supersaturation to $\Delta c \approx 2\,kg/m^3$ in each crystallizer. Consequently, the total temperature decrease of $82^\circ C - 30^\circ C = 52\,K$ is divided into a temperature span of approximately 6.5 K in each stage to avoid excessive local supersaturation. Twenty-seven percent of the feed mass flow is withdrawn from the last stage as fines removal to reduce the number of nuclei. The stream leaving a crystallizer passes through a classification zone in the next crystallizer to classify the slurry that is withdrawn from the bottom of the crystallizer. Because 8.6% of the feed stream is evaporated from the eight bodies, a final slurry flow that represents 64.4% of the feed is removed from the cascade. In addition to the advantage of the large temperature span, there is another reason for choosing a cascade instead of a single body. In Chapter 8, it has been shown that the recirculation flow necessary to avoid local

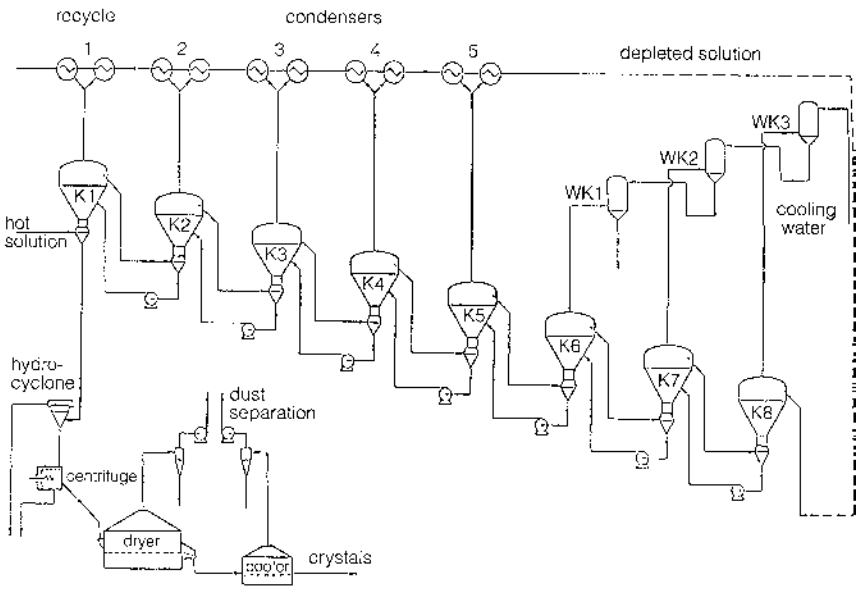

Figure 1.2. Cascade of eight industrial crystallizers.

desupersaturation can be critical in very large crystallizers. The modeling of crystallizer cascades is based on the balances of mass and number and on the crystallization kinetics of each crystallizer, which can differ from one to the next with respect to volume and operating conditions such as supersaturation, suspension density, and specific power input. Consequently, the crystallization kinetics may alter from stage to stage. Let us assume a cascade of four crystallizers with the same volume (see Fig. 1.3). If nucleation only takes place in the first crystallizer (the second, third, and fourth crystallizers may be fluidized beds operating at a very low specific power input), the cumulative weight fraction can be derived as a function of the dimensionless size $L/G\tau$ for multitank operation (see Fig. 1.4) [1.6]. τ is the reference drawdown time. As can be seen from Fig. 1.4, the median crystal size L_{50} increases with the number k of crystallizers operating in series. However, in cascades of stirred vessels, nucleation will take place in each crystallizer and the increase in the median crystal size L_{50} with extended residence time in the cascade competes with an increase in the nucleation rate caused by

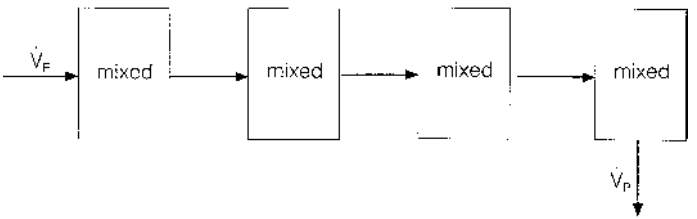

Figure 1.3. Cascade of four crystallizers.

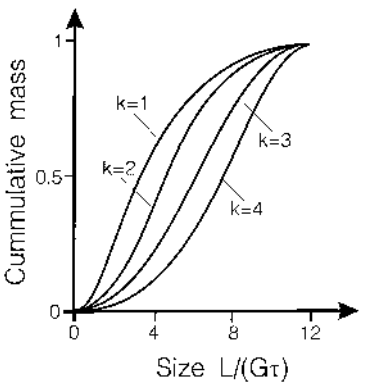

Figure 1.4. Cumulative mass versus dimensionless size.

impeller–crystal and crystal–crystal collisions for an optimum supersaturation and growth rate. As a rule, the dominant crystal size is reduced in multistage tanks, compared to a large single-stage crystallizer with the same volume as the cascade.

2. BATCH CRYSTALLIZERS*

Because a wide variety of crystalline products is obtained in small and medium amounts, many more batch crystallizers than continuous crystallizers are used in industry. The main drawback with batch crystallizers is the difficulty in operating them at constant supersaturation, which is common in continuous crystallizers and favorable for the product quality and economic aspect of the crystallization process. With continuous crystallizers, it is possible to maintain optimum supersaturation ΔC_{opt}, resulting in a moderate nucleation rate and favorable growth rate by selecting an advantageous retention time in combination with a constant cooling or evaporation rate. In principle, this is also possible with batch crystallizers, as has been shown in the laboratory [2.1]. Kinetic data, such as the nucleation and growth rates, can be obtained by batch experiments, which are less expensive and less time-consuming, and these data can be applied to the design and operation of different types of both batch and continuous crystallizers. In industry, however, batch crystallizers are not usually operated at constant supersaturation because the programmed cooling or evaporation process is too expensive and not sufficiently reliable. The main problem is the lack of inexpensive and robust sensors for measuring the level of supersaturation, which may be very low for systems of high solubility (see Chapters 2 and 3).

Because temperatures can readily be measured at an early stage, a 'programmed'' cooling process has been proposed for controlling nucleation at a constant rate in a seeded crystallizer. The first attempts to establish a general theory for calculating ''optimum'' cooling curves in order to improve the product crystal size distribution were made by Mullin and Nyvlt [2.2] (see also [2.3]). Such cooling curves show that the temperature should be reduced slowly in the early stages and more rapidly at the end of the batch. In the case of evaporative crystallizers, it is necessary to start with a very small vapor mass flow, which can then be increased. This is because only a small surface area of the seed crystals or nuclei is available initially, but the crystal surface increases with time. Jones and Mullin [2.3, 2.4] developed the theory of programmed cooling, recognizing that secondary nucleation can occur in seeded solutions even at very low supersaturation. The authors distinguish among natural cooling, linear cooling, and controlled cooling and assume

*By A. Mersmann.

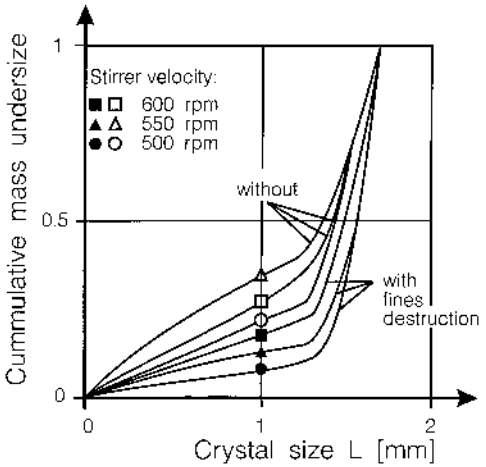

Figure 2.1. Increase in the crystal size due to fines dissolution.

that the nucleation rate depends on supersaturation and not on suspension density and fluid dynamics.

The basic equations are the mass conservation and population balance equations (see Table 2.1). The mass balances of a batch crystallizer have already been derived in Chapter 8. This problem is discussed in more detail with respect to different cooling modes and nucleation conditions. According to the mass balance, desupersaturation of the solution dW/dt is converted into growth of the seed (index S), growth of newly formed nuclei (index n), and new nuclei generated at size L_n. The material balance equation can be transformed into a desupersaturation equation. The population equation is written with population density p (instead of n), which is based on 1 kg of solvent.

Solving these basic equations leads to expressions in which either the cooling rate $d\vartheta/dt$ can be calculated for a given mass m_S of seed crystals of size L_S in a system with slope $dc^*/d\vartheta$ of the solubility curve, or in which the temperature $\vartheta(t)$ can be obtained as a function of time (Table 2.2). The relationship between temperature and time is very simple for a linear solubility curve if the growth rate is constant in the absence of nucleation ($\Delta c < \Delta c_{\text{met, sec}}$).

For $G \neq f(t) = \text{const.}$ and $d(\Delta c)/dt = 0$ (i.e., $\Delta c = \text{const.}$ during the entire cooling period) equation (3.17a) in Chapter 8 can be written

$$\frac{d\vartheta}{dt} = -\frac{3m_S L_S^2(t) G}{L_S^3 (dc^*/d\vartheta)} \tag{2.1}$$

Table 2.1. Modeling of Batch Crystallizers (Basic Equations)

Mass balance	$\frac{dW}{dt} = -\frac{3m_S^\circ}{\rho_{L^\circ} L_S^3} L_S^2(t) G_S(L,t) + \alpha\rho_C \left[3\int_0^\infty p_n(L,t) G_n N(L,t) L_n^2(t) dL + B(t) L_{n0}^3 \right]$	(2.3)
	$m_T(t) = m_S \left(\frac{Gt}{L_S} + 1 \right)^3$	(2.4)
Supersaturation balance	$\frac{d(\Delta W)}{dt} = -\frac{d\vartheta}{dt}(\vartheta, t) \frac{dW}{d\vartheta}(t) + \frac{3m_S^\circ}{\rho_{L^\circ} L_S^3} L_S^2(t) G_S(L,t) + \alpha\rho_C \left[3\int_0^\infty p_n(L,t) G_n N(L,t) L_n^2(t) dL + B(t) L_{n0}^3 \right]$	(2.5)
Population balance	$\frac{\partial p}{\partial t} + G\left(\frac{\partial p}{\partial L}\right) = B^\circ$	(2.6)
Kinetics	$B = k_n \sigma^n$	(2.7)
	$G = 2k_g' \sigma^g$	(2.8)

Source: Ref. 2.4.

Table 2.2. Modeling of Batch Crystallizers (Temperature Versus Time)

$$\frac{d\vartheta}{dt} = -\frac{3m_S L_S^2(t) G_S(t)}{L_S^3[d(\Delta c)/d\vartheta + dc^*/d\vartheta} = -\frac{3N_S \alpha \rho_C L_S^2(t) G_S(t)}{d(\Delta c).d\vartheta + dc^*/d\vartheta} \tag{2.9}$$

valid for metastable controlled cooling and no nucleation

$$\vartheta(t) = -\int_0^\tau \frac{3N_S \alpha \rho_C L_S^2(t) G_S(t)}{dc^*/d\vartheta} dt \tag{2.10}$$

valid for no nucleation and $\Delta c \neq f(t)$ ($\Delta c = \text{const.}$)

$$\vartheta(t) = \vartheta_0 - \frac{3m_S}{dc^*/d\vartheta} \frac{(L_S(\tau) - L_S)}{L_S} \frac{t}{\tau} \times \left(1 + \frac{L_S(\tau) - L_S}{L_S} \frac{t}{\tau} + \frac{L_S(\tau) - L_S}{L_S} \frac{t^2}{3\tau^2}\right) \tag{2.11}$$

valid for $dc^*/d\vartheta = \text{const.}$ and $G \neq f(\Delta c)$

$$\vartheta(t) = \vartheta_0 - \frac{N_S \alpha \rho_C G^3}{dc^*/d\vartheta} t^3 \tag{2.12}$$

$$\vartheta(t) = \vartheta_0 - \frac{\vartheta_0 - \vartheta f}{\tau^3} t^3 \tag{2.13}$$

valid for $dc^*/d\vartheta = \text{const.}$, $G \neq f(\Delta c)$, $L_S \ll L$, and no nucleation

For a seed of constant size L_S, the cooling rate is given by

$$\frac{d\vartheta}{dt} \approx -\frac{3m_S G}{L_S(dc^*/d\vartheta)} \left(1 + \frac{Gt}{L_S}\right)^2 \tag{2.2}$$

or, after integration,

$$\vartheta_\alpha - \vartheta(t) = -\frac{3m_S G}{L_S(dc^*/d\vartheta)} \left[1 + \frac{Gt}{L_S} + \frac{1}{3}\left(\frac{Gt}{L_S}\right)^2\right] \tag{2.14}$$

A corresponding equation for evaporative crystallization can be derived in a similar way. Instead of the cooling rate $d\vartheta/dt$, the evaporation rate (i.e., the mass flow rate of solvent $\Delta \dot{L}^\circ$, based on the mass $M_{\text{sus},\alpha}$ of the suspension in the crystallizer) is now decisive for the batch process (see Chapter 8):

$$\frac{\Delta \dot{L}^{\circ} c^{*}}{M_{\mathrm{sus},\alpha}} \approx \frac{3 m_S G}{L_S} \left(\frac{Gt}{L_S} + 1 \right)^2 \tag{2.15}$$

In both cases, the rates of cooling and evaporation increase with the square of time t; this leads to low rates at the beginning and rapid cooling or evaporation at the end of the batch.

The change in suspension density with time $m_T = f(t)$ can be obtained from the mass equation [see Eq. (2.4)]. Assuming that the crystallizer is seeded with a mass m_S of seed crystals of uniform size L_S at the beginning of the batch and that the crystallizer is operated at a negligible nucleation rate and at a constant growth rate G at $\Delta c_{\mathrm{opt}} < \Delta c_{\mathrm{met,\,sec}}$, the change in suspension density m_T with time t is given by

$$\frac{dm_T}{dt} = \frac{3 m_S G}{L_S} \left(\frac{Gt}{L_S} + 1 \right)^2 \tag{2.16}$$

or, after integration,

$$m_T(t) = m_S \left(\frac{Gt}{L_S} + 1 \right)^3 \quad (\text{cf. Table 2.1}) \tag{2.17}$$

As can be seen, the suspension density greatly increases with time.

It is important to keep in mind that all these equations are valid only for systems with negligible nucleation. When dealing with systems of high solubility and corresponding median crystal sizes $L_{50} > 100\,\mu\mathrm{m}$, however, a large number of attrition fragments are generated, especially at high suspension densities and mean specific power input. Chapter 5 demonstrates that the rate of secondary nucleation $B_{0,\mathrm{sec}}$ is proportional to the volumetric crystal holdup φ_T for $\varphi_T < 0.1$. Therefore, the rate $B_{0,\mathrm{sec}}/\varphi_T$ (i.e., the nucleation rate based on φ_T) is approximately constant during the entire batch time for a constant mean specific power input. This was experimentally verified for potassium alum and ammonium sulfate [2.1]. In Figure 2.2, the suspension density m_T of $KAl(SO_4)_2 \cdot 12H_2O$ is plotted against the cooling time for crystals produced in a stirred vessel and in a fluidized bed at a growth rate of $G = 3 \times 10^{-8}$ m/s. The curves are valid for a volumetric mass $m_S = 0.21\,\mathrm{kg.m^3}$ of seed crystals having a size of $L_S = 142\,\mu\mathrm{m}$.

The greater the specific power input, the higher the rate $B_{0,\mathrm{sec}}/\varphi_T$ of secondary nucleation and the shorter the batch time required to obtain a certain suspension density. This is understandable because an additional crystal surface is created by attrition fragments and, consequently, the cooling rate must be increased to avoid a reduction in supersaturation. It is now necessary to take into account growing attrition fragments, which are generated during the entire batch time T.

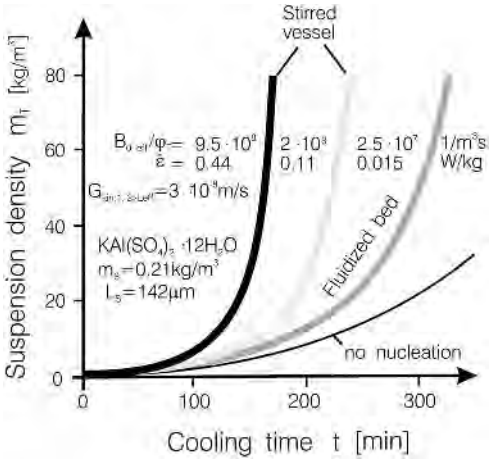

Figure 2.2. Suspension density of potassium alum against the cooling time of a batch crystallizer (stirred vessel and fluidized bed) operated at constant supersaturation.

By the end of the batch time T, fragments produced at the beginning $t = 0$ of the process have grown to the size $L = GT$ for a constant growth rate G (according to $\Delta c = \text{const.}$). Fragments generated at any time t, however, have their size $L = -G(t - T)$. The specific surface area $a_T(T)$ of all crystals is given by

$$a_T(T) = \beta \int_0^T (L^2(t) B_{0,\text{eff}}(t)\, dt = \beta G^2 \int_0^T (t - T)^2 B_{0,\text{eff}}(t)\, dt \tag{2.18}$$

The total specific surface area of seed (index S) and nuclei (index n) is composed of these two contributions:

$$a_T(T) = a_{T,S}(T) + a_{T,n}(T) = \beta N_S L^2 + \beta G^2 \int_0^T (t - T)^2 B_{0,\text{eff}}(t)\, dt \tag{2.19}$$

Let us assume a monosized seed of size L_S which has grown to

$$L = L_S + GT \tag{2.20}$$

after the batch time T.

The mass balance can be written as the volumetric crystal rate $\dot{V}_{CV}(t)$, which represents the volumetric rate of crystalline material based on the volume of the suspension:

$$\dot{V}_{CV}(t) = a_{C,\mathrm{tot}}(T)\frac{G}{2} \tag{2.21}$$

This balance can also be expressed as the volumetric holdup $\varphi_T(t)$ as a function of time:

$$\varphi_T(t) = \int_0^t \dot{V}_{CV}\, dt \tag{2.22}$$

It is now assumed that the effective rate of secondary nucleation based on the volumetric holdup

$$\frac{B_{0,\mathrm{eff}}(t)}{\varphi_T(t)} \equiv \bar{B}_\varphi \tag{2.23}$$

remains constant throughout the entire batch process. The volumetric holdup $\varphi_T(t)$ is then given by

$$\varphi_T(t) = \int_0^t a_T(T)\frac{G}{2}\, dt \tag{2.24}$$

or, for $\Delta c = \text{const.}$ and $G = \text{const.}$,

$$\varphi_T(t) = \frac{\beta G}{2}\left[G^2 \int_0^t \int_0^T (t-T)^2 \varphi_T(t)\bar{B}_{\varphi T}\, dt\, dt + N_S \int_0^t (L_S + GT)^2\, dt\right] \tag{2.25}$$

Solving this integral equation leads to a homogeneous differential equation of fourth order with constant coefficients. Besides the trivial solution described previously, the dependence of volumetric holdup $\varphi_T(t)$ on time is given by

$$\frac{\varphi_T(t)}{\varphi_{T,S}} = A\cosh t^* + \left(\frac{1}{2}\sqrt{\frac{\alpha_S}{\beta_S}}(A-1)^{3/2} + \frac{1}{4}\sqrt{\frac{\beta_S}{\alpha_S}}(A-1)^{1/4}\right)\sinh t^*$$
$$+ (1-A)\cos t^* + \left(\frac{1}{2}\sqrt{\frac{\alpha_S}{\beta_S}}(A-1)^{3/2} + \frac{1}{4}\sqrt{\frac{\beta_S}{\alpha_S}}(A-1)^{1/4}\right)\sin t^* \tag{2.26}$$

with

$$A = 1 + \alpha_S\left(\frac{\beta_S G}{(\alpha_S L_S)^4 \bar{B}_\varphi}\right)^{1/2} = 1 + \frac{\sqrt{\beta_S}}{\alpha_S}\left(\frac{G}{L_S^4 \bar{B}_\varphi}\right)^{1/2} \tag{2.27}$$

and

$$t^* = (\beta G^3 \bar{B}_\varphi)^{1/4} t \tag{2.28}$$

Figure 2.3 illustrates equation (2.26). The choice of supersaturation Δc determines the kinetic parameters G and $\bar{B}_\varphi$ because both depend on Δc, and $\bar{B}_\varphi$ is additionally influenced by the mean specific power input. These parameters are given by

$$G = \frac{2\beta}{3\alpha} k_g' \left(\frac{\Delta c}{c^*} \right)^g$$

and

$$\bar{B}_\varphi \equiv \frac{B_{0,\text{eff}}}{\varphi_T} = f_1(\Delta c, \bar{\varepsilon}) = f_2(G, \bar{\varepsilon}) \tag{2.29}$$

On the left of Figure 2.4, the development of the suspension density of a seeded batch crystallizer in the absence of any attrition is shown, whereas on the right, the case of a seeded batch crystallizer is demonstrated when attrition and the production of secondary nuclei coming from activated attrition fragments take place. In both diagrams, the ratio $m_T(t)/m_S = \varphi_T(t)/\varphi_{T,S}$ is plotted against the dimensionless time, which is proportional to the size Gt of crystals grown from seed, from attrition fragments, or both. If no attrition occurs, the time needed to obtain a certain ratio $m_T(t)/m_S$, say 100, is

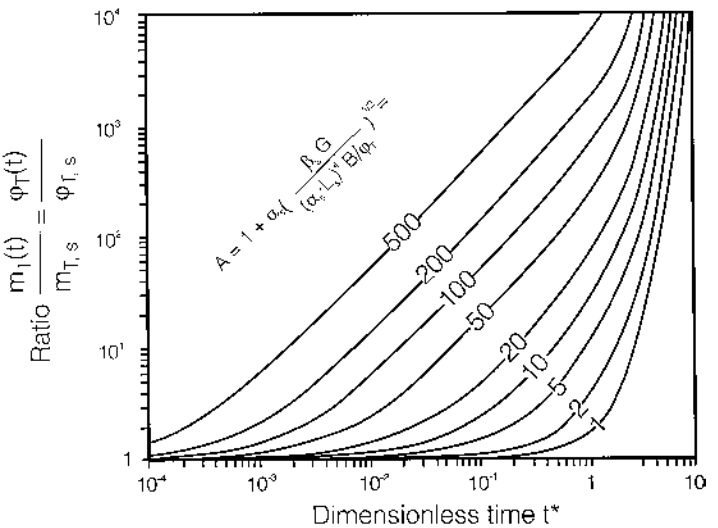

Figure 2.3. Dimensionless volumetric holdup versus dimensionless batch time according to equation (2.26).

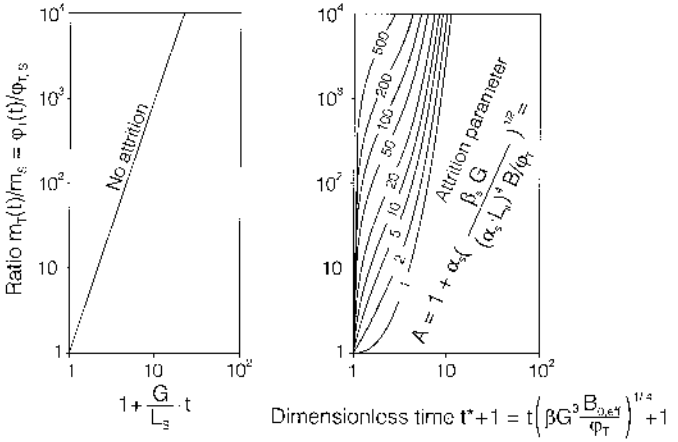

Figure 2.4. Dimensionless volumetric holdup versus dimensionless batch time according to equation (2.26).

short when the seed size is small and the supersaturation and growth rate G are high. In the case of a seeded batch crystallizer with attrition-controlled secondary nucleation, the batch time for $m_T(t)/m_S = \text{const.}$ can be reduced if the suspension density m_T and the stirrer speed are high, which leads to high attrition-induced rates, $B_{0,\text{eff}}/\varphi_T$, of secondary nucleation. This can be expected at the end of the batch. When a batch crystallizer is seeded with fine seed (say, $L_S \approx 100\,\mu\text{m}$) and a small seed mass m_S per unit volume (say, $m_S \approx 1\,\text{kg/m}^3$), the attrition rate and the attrition-induced rate of secondary nucleation are small. The crystallizer behaves like a seeded batch crystallizer without attrition and the increase in $m_T(t)/m_S$ as a function of time can be read from the diagram on the left. With increasing crystal size and suspension density, the effect of attrition becomes more and more pronounced. The diagram on the right takes into account the additional seed produced by attrition. When the supersaturation Δc and the kinetic parameters $B_{0,\text{eff}}$ and G (approximation) are kept constant, the suspension density m_T is a linear function of time. This is the case up to $t^* \approx 0.5$. The maximum slope of a curve $m_T = f(t)$ is 3 ($m_T(t)/m_S \sim (Gt/L_S)^3 \sim t^3$) for a long batch time ($Gt/L_S \gg 1$) and a seeded crystallizer without attrition. In the presence of attrition, the exponent of e of the relationship $m_T \sim (t)^e$ is $e > 3$ for long batch times ($t* \equiv (\beta B_{0,\text{eff}}/\varphi_T G)^{1/4} Gt > 3$). This means that for $t^* > 3$, the batch time is strongly reduced by attrition in comparison to a crystallizer without attrition. The following relationships can be derived for seeded batch crystallizers in the presence of attrition for $\Delta c = \text{const.}$:

$t^* < 0.5$:

$$\frac{\varphi_T(t)}{\varphi_{T,S}} \sim (t)^1$$

$0.5 < t^* < 3$:

$$\frac{\varphi_T(t)}{\varphi_{T,S}} \sim (t)^e \quad \text{with} \quad 1 < e < 3$$

$t^* > 3$:

$$\frac{\varphi_T(t)}{\varphi_{T,S}} \sim (t)^e \quad \text{with} \quad e > 3$$

It is advisable to operate the crystallizer at optimum supersaturation Δc_{opt} (cf. Chapter 3). It has been shown that in most cases, the relationship between $B_{0,\text{eff}}/\varphi_T$ and G is given by $B_{0,\text{eff}}/\varphi_T \sim G$ (attrition-controlled regime) up to $B_{0,\text{eff}}/\varphi_T \sim G^2$ (controlled by the crystallization kinetics). This means that in the attrition-controlled regime at the end of the batch, the parameter A in Figure 2.4 remains constant ($G\varphi_T/B_{0,\text{eff}} = \text{const.}$) and the suspension density rises very sharply with the time t or with the product size $L \sim Gt$.

What are the consequences when a batch crystallizer is operated at optimum supersaturation ($\Delta c_{\text{opt}} = \text{const.}$, $G = \text{const.}$) but the specific power $\bar{\varepsilon}$ is increased? As a first approach, the relationship $B_{0,\text{eff}} \sim \bar{\varepsilon}$ is valid. Let us assume that a certain ratio $m_T(t)/m_S$ should be obtained. Because the parameter A decreases, the operating point moves to the right into an area where the slopes of the curves are steeper. This means that the batch crystallizer enters the operation range earlier where additional seed is produced by attrition, with the result, however, that the batch time is reduced at the expense of the maximum crystal size.

To obtain a constant product quality when using batch crystallizers, it is recommended that the same starting conditions be created at the beginning of crystallization through constant seeding. It is important but difficult to add the seed at the right moment when the solution is just saturated. Addition in an undersaturated solution could result in dissolution of the seed, and if the solution is already too supersaturated, a shower or primary nuclei can occur, with the result that the rate of nucleation changes from batch to batch. Another important factor is the seed mass per unit volume m_S and its size and size distribution. In order to obtain a large surface area of the seed, a small mass of small seed particles is more advantageous than a large mass of coarse seed. Fine seed particles, however, dissolve more readily than coarse crystals. According to Figure 2.3, the batch time can be

considerably reduced by applying a fine seed of a small size L_S at a given supersaturation $\Delta c \approx \Delta c_{\text{opt}}$, which would lead to an optimum growth rate $G = f(\Delta c_{\text{opt}})$ and a certain rate $\overline{B_\varphi} \equiv \bar{B}_0/\varphi_T = f(\Delta c_{\text{opt}})$ of secondary nucleation.

3. SEEDING*

The origin of crystals after a growth period can be traced back to the following:

- Nuclei generated by activated nucleation
- Growth-activated attrition fragments abraded from parent crystals
- Seed crystals added to the crystallizer

The rate of activated nucleation increases strongly with supersaturation and the rate of attrition-controlled secondary nucleation depends on the process of attrition and on supersaturation. Only when seed crystals are added are the mass and size distribution of the seed either known or can be determined experimentally. Therefore, adding seed is an appropriate way of starting the crystallization process under reproducible operating conditions and of avoiding primary nucleation, which is difficult to control. The time of addition of the seed and the location of the seed feed are important operating parameters. Seed should be added when the supersaturation is in the range $0 < \Delta c < \Delta c_{\text{met}}$ in order to avoid dissolution of the seed. The mass and its size distribution, on the one hand, and the time of addition at a certain supersaturation in the crystallizer, on the other hand, must be chosen in such a way that spontaneous nucleation can be avoided. When the seed is added to the feed stream, the supersaturation in the mixing zone can be decreased. In addition to other parameters, the efficiency of seeding depends on the growth ability of the seed crystals. It is known that the milling of crystals for the production of seed can increase or reduce the growth rates of seed crystals at a given supersaturation. The origin, the purity, the temperature, and the morphology of the seeds are important material parameters. Systems with conglomerates and dendrites require perfect seed crystals. Systems with stereochiral isomers, optical isomers, and enantiomers are very sensitive with respect to seeding. The preparation of a pure seed with a rough surface in the molecular sense and a minimum amount of lattice deformation are prerequisites for increasing the selectivity of crystallization processes. The addition of seed has been successfully applied to the crystallization of asparagine, theomin, phosphinothrine, and glutamic acid [3.1]. The separation of acetylglutamic acid has been achieved by seeding with

*By A. Mersmann.

large crystals from one enantiomer and small crystals from the other enantiomer. Additional information can be found in [3.2].

In practice, the reproducibility of the seed is a great problem when zero variation of the product from batch to batch is desired. The control of the mass, the size distribution, the temperature, and the purity are not sufficient because adhering dust may provide additional nuclei. After milling or drying, the seed should be washed and slightly dissolved in order to remove dust particles. In the case of fine seed, there is always a tendency toward aggregation with the result that the specific surface of a given mass of seed changes. Deagglomeration without destruction of the primary particles is recommended. Sometimes, the seed is stored in an organic liquid (for instance, sugar seed in propylalcohol) to avoid aggregation and the crystallizer is seeded with a certain mass of the slurry.

The mass of the seed and its size distribution will now be discussed in more detail. The main objective of seeding is to avoid spontaneous nucleation which occurs at ΔC_{met}. At higher supersaturation, growth is mostly controlled by diffusion and the maximum allowable growth rate $G_{\max} = G_{\text{met}}$ is given by

$$G_{\max} = \frac{2k_d}{\rho_C} \Delta c_{\text{met}} \tag{3.1}$$

The cooling rate $dT/dt = \dot{T}$ for cooling crystallization and the evaporation rate $\dot{M}_{\text{solv}}$ of the solvent for evaporation crystallization determine the progress of supersaturation. Equations for the calculation of the mass M_S of the seed with the median size L_S have been derived by Gutwald and Mersmann [3.3]. The seed mass necessary for cooling crystallization is given by

$$M_S = -\frac{2\alpha_S}{\beta_S} \left(\frac{dW^*}{dT}\right) M_{\text{solv}} \frac{\dot{T} L_S}{G_{\text{met}}} \left(1 + \frac{1}{2} \frac{G_{\text{met}} \Delta T_{\text{met}}}{\dot{T} L_S}\right)^{-2} \tag{3.2}$$

and for evaporation crystallization, this equation reads

$$M_S = -\frac{2\alpha_S}{\beta_S} W^* \frac{\dot{M}_{\text{solv}} L_S}{G_{\text{met}}} \left(1 + \frac{1}{2} \frac{G_{\text{met}} t_{\max}}{L_S}\right)^{-2} \tag{3.3}$$

In these equations, W^* is the solubility in kilograms of solute per kilogram of solvent, dW^*/dT is the slope of the solubility curve, and M_{solv} is the mass of solvent in the crystallizer. In the case of cooling crystallization, the seed mass M_S is proportional to the mass M_{solv} of the solvent and to the cooling rate $\dot{T}$. The steeper the solubility curve, the more seed is necessary to avoid spontaneous nucleation. The seed mass is high when the median size of the seed crystals is large and the growth rate G_{met} is low according to a narrow

metastable zone width. This is also true of evaporation crystallization for which the seed mass is proportional to the mass rate $\dot{M}_{\text{solv}}$ of the evaporated solvent. The time $t_{\max}$ is the ratio of the maximum allowable undercooling ΔT_{met} and the cooling rate $\dot{T}$:

$$t_{\max} = \frac{\Delta T_{\text{met}}}{\dot{T}} \tag{3.4}$$

If the median size L_S of the seed is not very small ($L_S > 100\,\mu\text{m}$), the factor $[1 + \frac{1}{2}(G_{\text{met}} t_{\max}/L_S]$ in equation (3.3) is not very far from unity and can be omitted in order to obtain simple equations for the seed mass.

Let us assume that a potassium alum solution at 40°C should be cooled down at a cooling rate of $5\,\text{K/h} = 1.39 \times 10^{-3}\,\text{K/s}$. The metastable zone width, expressed as maximum undercooling, is $\Delta T_{\text{met}} = 4K$ and the slope of the solubility curve $dW^*/dT \approx 0.05$ [kg solute/(kg water K)]. With the metastable undercooling $\Delta T_{\text{met}} = 4\,\text{K}$ of potassium alum, the metastable zone width can be calculated from

$$\Delta W_{\text{met}} = \frac{dW*}{dT} \Delta T_{\text{met}} = 0.020 \frac{\text{kg solute}}{\text{kg water}} \tag{3.5}$$

The order of magnitude of the diffusion-controlled metastable growth rate G_{met} is

$$G_{\text{met}} \approx k_d \frac{\Delta c_{\text{met}}}{\rho_C} \approx 10^{-4} \left(\frac{17.5}{1757} \right) \approx 10^{-6} \frac{\text{m}}{\text{s}} \tag{3.6}$$

Assuming a seed size $L_S = 100\,\mu\text{m}$ or $10^{-4}\,\text{m}$, a seed mass of $2.4 \times 10^{-4}\,\text{kg}$ seed/kg water or approximately $m_S \approx M_S/V_{\text{solv}} = 0.24\,\text{kg}$ seed/m^3 solution can be calculated from equation (3.2).

This corresponds to a volumetric surface of the seed crystals of $8\,\text{m}^2$ surface/m^3 suspension. In general, 1 kg seed/m^3 suspension or 1% of the final suspension density may be an appropriate value for systems which exhibit metastable undercooling in the range $0.5 < \Delta T_{\text{met}} < 5\,\text{K}$.

The median crystal size of crystals produced in batch crystallizers depends on the following:

- Cooling rate
- Presence or absence of seed
- Mass of the seed
- Size distribution and the median size of the seed

This has been demonstrated by Gutwald and Mersmann [3.4] with attrition-resistant $(NH_4)_2SO_4$ and $KAl(SO_4)_2{\cdot}12H_2O$, which is prone to attrition.

In Figure 3.1, the supersaturation ΔW (in kg solute/kg water) is plotted versus the cooling time for different cooling rates and for seeded and unseeded runs. The experiments were carried out in a 6-dm^3 stirred vessel operating at a low mean specific power input of $\bar{\varepsilon} = 0.143$ W/kg. The cooling rate was varied in the range $3 < dT/dt < 7$ K/h and the suspension density of the seed was in all cases but one, $m_S = 0.21$ kg/m^3. The metastable zone width of $(NH_4)_2SO_4$, here expressed in mass fraction w, is $\Delta W_{\text{met}} \approx 0.003$ kg solute/kg water. Very rapid (uncontrolled) cooling results in a maximum supersaturation of $\Delta W_{\max} = 0.018$ or $\Delta W_{\max} = 6\Delta W_{\text{met}}$ and a small median crystal size of $L_{50} = 470\,\mu$m. As can be seen from the diagram, the peak of supersaturation can be reduced by a reduction of the cooling rate and the addition of seed. Only the low cooling rate of 3K/h and the addition of seed with $m_S = 0.21$ kg/m^3 resulted in a maximum supersaturation equal to the metastable zone width. The positive effects of appropriate cooling and seeding can be seen in Figure 3.2, in which the median crystal size is plotted against the maximum supersaturation measured. The smaller the maximum supersaturation, the larger the median crystal size. Further experiments carried out with potassium alum produced the same result: All measures that reduce the maximum supersaturation during a batch lead to an increase in the median crystal size.

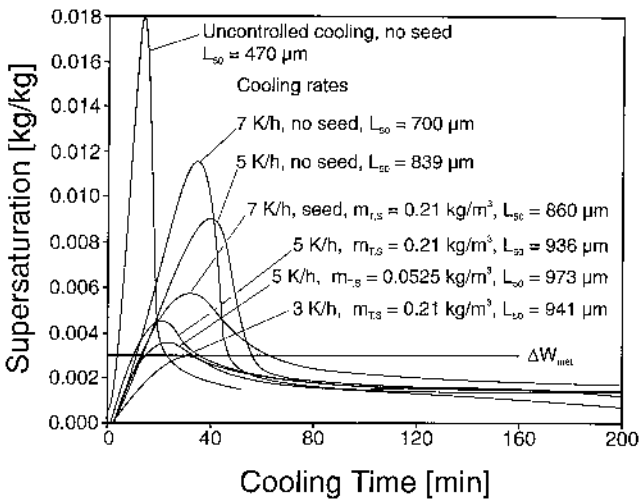

Figure 3.1. Supersaturation versus the time for different operating conditions $[(NH_4)_2SO_4]$.

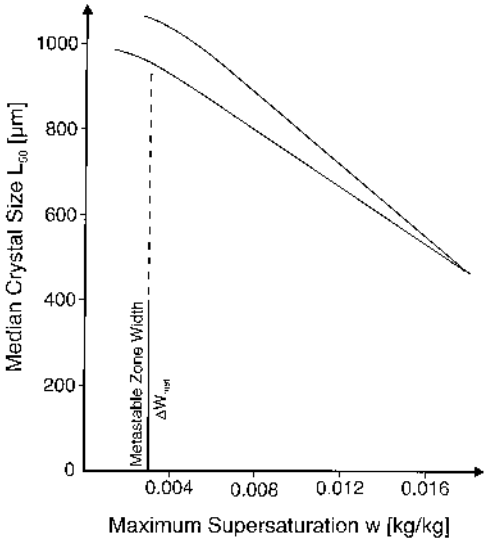

Figure 3.2. Median crystal size as a function of the maximum supersaturation.

4. CRYSTALLIZERS FOR DROWNING-OUT AND PRECIPITATION*

In reaction crystallization, two or more reactants are transformed in a product P, which precipitates because it is supersaturated. The reactants can be a liquid or gas. In Table 4.1, some equations of reaction crystallization processes are given.

In crystallizers for precipitation and drowning-out (see also Chapter 11), the addition of at least one reactant or drowning-out agent is necessary. In principle, such crystallizers can be operated batchwise or continuously. In batch crystallizers, a reactant is sometimes fed into the vessel, which already contains the other reactant or solution. It is also possible to add both reactants simultaneously. This is usually the mode of operation in continuous crystallizers, with either a mixed product or classified product removal. Unlike in cooling and evaporative crystallizers, supersaturation is not induced by the removal or addition of heat. Therefore, heat transfer areas are necessary only to maintain approximately isothermal conditions. If the reaction enthalpy is released in a huge liquid volume, especially in the case of a diluted solution, the change in temperature is often small, and although heat transfer is not a problem, mixing is important. This is why, as a rule,

*By A. Mersmann.

Table 4.1. Rate Equations for Reaction and Crystallization Kinetics and Mixing

	Kinetics
Chemical reaction	$A + B \overset{k_r}{\rightleftharpoons} P + R$
	$-\frac{dc_A}{dt} = k_0 \exp\left(-\frac{E}{\Re T}\right) c_A^{\alpha} c_B^{\beta} \ldots$ for $\alpha = 1$ and $c_B \gg c_A$
	$-\frac{dS}{dt} = k_r \frac{c_A}{c_p^*}$
	with $k_r = k_0 \exp\left(-\frac{E}{\Re T}\right)$
Crystallization kinetics	$B_0 = k_n S^n \qquad G = k_g'(S-1)^g$
	Relevant times
Residence	$\tau = \frac{V}{\dot{V}_A + \dot{V}_B}$
Reaction	$\tau_{\text{reac}} \sim \frac{1}{k_r}$
Induction	$t_{\text{ind}} \approx \frac{80 d_m^2}{D_{AB} \ln S}$
Macromixing	$t_{\text{macro}} \approx 5\left(\frac{T^2}{\bar{\varepsilon}}\right)^{1/3}$
Micromixing	$t_{\text{micro}} \approx 5\left(\frac{\nu_L}{\varepsilon}\right)^{1/2} \ln Sc$

stirred vessels are used as crystallizers for precipitation and drowning-out. Crystallization is often carried out at medium or high values of relative supersaturation, which results in products where $L_{50} < 100\,\mu\text{m}$. According to the statements in Chapter 8, only a small specific power input is necessary in order to suspend particles, especially in large vessels. The median crystal size depends primarily on the nucleation rate, which increases strongly with supersaturation; the mean and local levels of supersaturation depend on mixing in the arrangement.

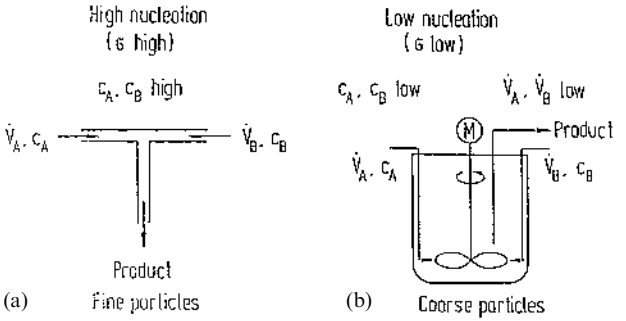

Figure 4.1. (a) T-mixer; (b) stirred-vessel precipitation crystallizer.

In Figure 4.1, a T-mixer (a) and a mixed suspension, mixed product reactor (MSMPR) precipitation crystallizer (b) are shown. The feed stream $\dot{V}_A$ with the reactant A and the feed stream $\dot{V}_B$ with the reactant B are fed into the reactor, where the main product P and the side product R are produced (see Table 4.1, in which important equations for the reaction and crystallization kinetics and for mixing processes are listed). The reactants must first be blended by macromixing and micromixing. In a stirred vessel, the macromixing time t_{macro} depends mainly on the impeller speed, whereas the process of micromixing is strongly dependent on the local specific power input. After mixing on a molecular scale, the chemical reaction takes place. The reaction time is inversely proportional to the reaction rate constant k_r. The supersaturation $S = c_p/c_p^*$ of the product is the driving force for nucleation and crystal growth. The maximum possible supersaturation $\sigma_{\max}$ is given in a T-mixer, assuming that the chemical reaction has finished but that nucleation has not yet taken place. With a stirred vessel, the initial supersaturation σ_0 can be calculated on the assumption that the chemical reaction is instantaneous and that the reactants are completely blended with the entire vessel contents without nucleation. This supersaturation may be in the range $10 < \sigma_0 < 100$, but the maximum supersaturation $\sigma_{\max}$ can be up to $\sigma_{\max} = 1000$ and above. $\sigma_{\max}$ and σ_0 are theoretical supersaturations. The real supersaturation is smaller because the process of primary nucleation is very fast and the solution is rapidly desupersaturated, especially in the case of high σ values. It is important to note that the fast nucleation proces depends on the local supersaturation. In contrast, the process of crystal growth takes minutes rather than just milliseconds, which is the timescale for primary nucleation. Therefore, the mean supersaturation is decisive for growth. Furthermore, the relative supersaturation $\sigma = \Delta c_p/c_p^*$ depends on the solubility c_p^* of the precipitation product P, which is a function of the temperature and of the concentration of the side product R. If the chemical reaction is very fast, the conversion of the

reactants A and B to the product P is controlled by mixing, and the processes of macromixing and micromixing determine the local concentration c_P (or the supersaturation σ in an isothermal system) as a function of the position in the crystallizer and of time. The mean residence time τ in continuously operated crystallizers or the time t of batch crystallizers, on the one hand, and the times necessary for macromixing and micromixing, on the other hand, are decisive for the process of desupersaturation by nucleation and growth.

Let us define a dimensionless time t^* according to

$$t^* = \frac{1}{t_{\text{macro}}}\left(\frac{V_{\text{sus}}}{\dot{V}_A + \dot{V}_B}\right) = \frac{\tau}{t_{\text{macro}}} \tag{4.1}$$

for continuously operated crystallizers and to

$$t^* = \left(\frac{\dot{V}_A + \dot{V}_B}{V_{\text{sus}}}\right)t \tag{4.2}$$

for batch crystallizers. The degree of mixing increases with the dimensionless time t^*. Let us assume that the addition time $V_{\text{sus}}/(\dot{V}_A + \dot{V}_B)$ of a batch reaction crystallizer is very short compared to the total batch time. If the micromixing time of the liquid mixture with the viscosity ν_L for a segregation degree of 0.1 according to

$$t_{\text{micro}} \approx 5\ln(\text{Sc})\frac{\nu_L^{1/2}}{\varepsilon^{1/2}} \tag{4.3}$$

is very short [$t_{\text{micro}} \ll t_{\text{macro}}$ or $(t_{\text{macro}}/t_{\text{micro}}) \to \infty$], the maximum possible supersaturation $S_{\max}$ is obtained after a short time (batch crystallizers) or a short residence time (continuously operated crystallizers) (see point A in Fig. 4.2). The supersaturation decreases very rapidly as increases t^*. The

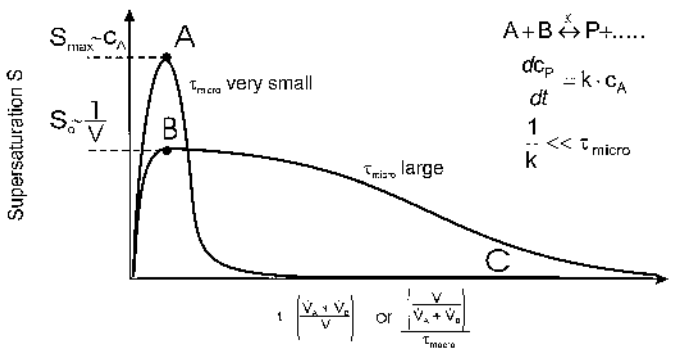

Figure 4.2. Supersaturation versus the dimensionless time for different mixing conditions.

shorter the micromixing time t_{micro} is in comparison to the macromixing time t_{macro}, the higher the supersaturation for a given t^*. Consequently, the nucleation rate increases, resulting in a decreasing median crystal size. Therefore, a T- or Y-mixer with small volume V_{sus} operated continuously at a very high level of specific power input $\varepsilon \approx (\lambda/2)(w^3/D)$ (where for $\lambda = 0.02$, $w = 10\,\text{m/s}$, and $D = 1\,\text{mm}$, we obtain $\varepsilon = 10^4\,\text{W/kg}$) is an excellent tool for producing very small crystals in the micrometer or even nanometer range. With respect to high number densities N, a strong agglomeration can take place (see Chapter 6). When growth of the tiny particles is not desired, the outflow from the T-mixer can be conveyed into a stirred vessel containing a very small or zero supersaturation. This combination of a T- or Y-mixer and a stirred vessel may be an effective tool for producing nanoparticles. If large crystals produced at a lower supersaturation are desired, it is advantageous to omit the T-mixer and to operate the stirred vessel continuously. When the feed points of the reactants A and B are not close together and the volume of the vessel is large, the effect of dilution will lead to moderate supersaturation and rates of activated nucleation. The actual local concentration and supersaturation can be influenced by the following processes:

- Dilution ($\sigma \sim 1/V_{sus}$) (see point B in Fig. 4.2)
- Macromixing ($\sigma \sim 1/S$ or $\sigma \sim (\bar{\varepsilon})^{-1/3}$)
- Micromixing $\sigma \sim \varepsilon^{-1/2}$

The prediction of the median crystal size therefore requires the mixing phenomena to be predicted and the local concentration and supersaturation profiles to be calculated.

Because local supersaturation is decisive for the maximum local rate of nucleation, there is a strong relationship between the median crystal size L_{50} and the micromixing time. Therefore, the stirrer speed is chosen with respect to mixing.

Garside and Tavare [4.1] have shown that crystal size distribution is strongly influenced by the process of micromixing. The authors investigated two models: Model I assumes maximum species and age mixing, and model II is based on the assumption of maximum species but minimum age mixing (see Fig. 4.3). Aslund and Rasmuson [4.2] have shown experimentally that the median crystal size and CSD depend strongly on process variables such as mixing, reactant feed rate, and concentration.

The field of supersaturation is decisive for nucleation and depends on (a) the concentration and stochiometry of the reactants, (b) the mode of feed, (c) the location of the feed, (d) the fluid dynamics (circulation rate and specific power input), and (e) the presence of seed or recirculated slurry. As a rule, the reaction rate increases strongly with the temperature in the

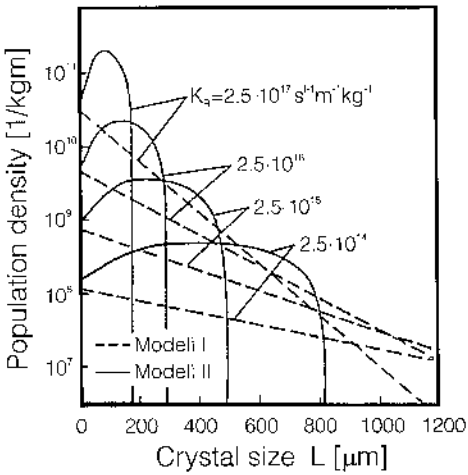

Figure 4.3. Calculated population density versus crystal size (according to [4.1]).

precipitator. This temperature change combined with the variation in concentration, especially of the by-product, results in changed values of solubility c_p^* of the product. If the local concentrations c_p of this product and the local values of solubility c_p^* are known, it is possible to calculate the local supersaturation. The points of constant local concentration and supersaturation, however, depend on mixing processes. In very slow chemical reactions, the system is reaction-controlled in a well-mixed precipitator. On the other hand, in rapid chemical reactions of ions, the rate constant k_r is very high. In this case, the progress of the reaction is controlled by mixing [4.3].

With regard to mixing, it is necessary to distinguish between the macromixing within the entire reactor and the local micromixing based on a molecular scale. The times necessary for macromixing and micromixing depend on the mean specific power input and the local specific power input, $\bar{\varepsilon}$ and ε, respectively. In Figure 6.4 in Chapter 8 information is given on the values of the local specific power input ε and the mean specific power input $\bar{\varepsilon}$. These data are valid only for fully turbulent flow (i.e., the stirrer Reynolds number exceeds 10^4). In this figure, isoenergetic lines are drawn for a Rushton turbine, a marine propeller in a vessel with and without a draft tube, and the Intermig stirrer. As can be seen from this figure, the local specific power input can be higher than the mean value in the discharge region of the stirrer by a factor up to 10 or more.

With batch precipitators, it is possible first to add the solvent and, subsequently, to introduce the two reactants simultaneously (see Figs. 4.4a and

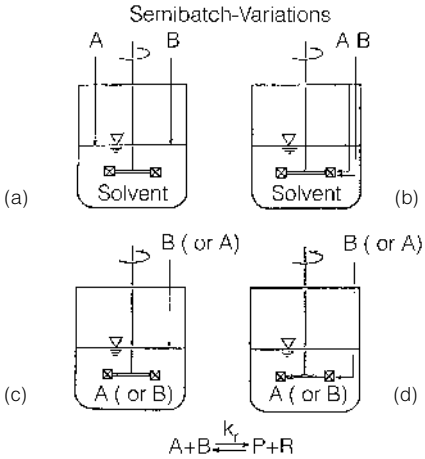

Figure 4.4. Operating modes of batch-precipitation crystallizers.

4.4b). Another operating mode could involve one of the reactants being precharged to the precipitator and the other reactant then being added. This is shown in Figs. 4.4c and 4.4d. The reactants can be fed in with feed points far apart from each other at the surface (Fig. 4.4a) or close together in the discharge region of the stirrer (Fig. 4.4b).

In the case of continuously operated crystallizers (see Fig. 4.5), the two reactants A and B are fed in continuously and simultaneously and the suspension is withdrawn continuously. Stirred vessels equipped with an agitator with a large D/T are advantageous because the reactants are macromixed and diluted rapidly, and high supersaturation can thus be avoided (left-hand side). This is the case, in particular, for stirrers operating at high Reynolds numbers $\mathrm{Re} > 1000$ and high mean specific power inputs. Contrary to this, other operating modes of the vessels are depicted on the right-hand side. The reactants are added to the stirrer discharge region and the feed points are close together. High local specific power inputs may lead to supersaturation peaks and high local nucleation rates.

The resulting processes, especially the median crystal size, depend on a variety of different times, which will now be explained (see Table 4.1). The mean residence time is given by the equation

$$\tau = \frac{V}{\dot{V}_A + \dot{V}_B} \tag{4.4}$$

This time depends on the volume V of the crystallizer and on the volumetric flow rates $\dot{V}_A$ and $\dot{V}_B$ of the reactants A and B. The reaction time t_{reac} is inversely proportional to the rate constant of the chemical reaction:

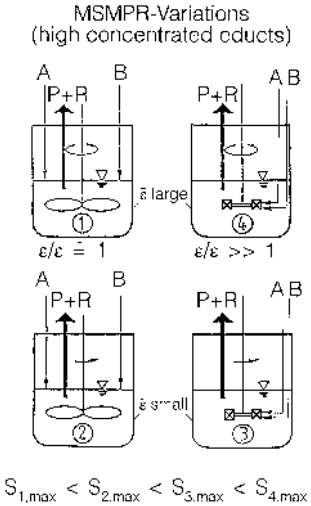

Figure 4.5. Operating modes of continuous-precipitation crystallizers.

$$t_{\text{reac}} \sim \frac{1}{k_r} \tag{4.5}$$

As soon as a certain level of supersaturation is exceeded, the induction time of nucleation is given by [4.4]

$$t_{\text{ind}} \approx \frac{80 d_m^2}{D_{AB} \ln S} \tag{4.6}$$

For solutions with a low viscosity, the induction time is very brief compared to the mean residence time. Therefore, in most cases, this induction time is not relevant for the process of precipitation. The field of product concentration and supersaturation depend on the mixing process. The minimum time t_{macro} necessary for macromixing that is valid for the optimum stirrer Reynolds number is given by [4.5]

$$t_{\text{macro, min}} \approx 5 \left(\sqrt[3]{\frac{T^2}{\bar{\varepsilon}}} \right) \tag{4.7}$$

The macromixing time increases with the two-thirds power of the tank diameter T but is inversely proportional to the third root of the mean specific power input $\bar{\varepsilon}$. The entire reaction contents are well macromixed if the time for macromixing, t_{macro}, is very short in comparison to the mean residence time τ ($t_{\text{macro}} \ll \tau$). In this case, the reactants added to the reactor

quickly become blended with the total contents, and this leads to a dilution effect that consequently lowers the concentration c_p of the product. Because the induction time is very brief, nucleation is expected to take place very soon after the addition of the reactants. The rate of nucleation depends on the local supersaturation, which is strongly influenced by micromixing. If, at the moment of addition of the reactants, the local micromixing is very intensive but macromixing is very poor throughout the entire vessel, extremely high local supersaturation may occur, which leads to high rates of primary nucleation. The duration of micromixing depends on the Schmidt number $\mathrm{Sc} = \nu_L / D_{AB}$ and on the kinematic viscosity ν_L of the liquid.

With reference to this fact, adding two reactants to be added to the discharge region of the impeller is not recommended. Rushton turbines with a small stirrer diameter D compared to the tank diameter T, in particular, produce very high local specific power inputs in the discharge region. However, their circulation rate is low and, therefore, the time for macromixing is high. If both reactants are fed into the discharge region, very high local specific power inputs and, consequently, high supersaturation may occur, leading to elevated rates of nucleation and small median crystal sizes. Therefore, the feed points of the two reactants should be far apart from each other in a region where a low specific power input occurs. It is also important to choose and operate the stirrer with a high flow number N_V according to

$$\dot{V}_{\mathrm{circ}} = N_V s D^3 \tag{4.8}$$

and a large circulation flow $\dot{V}_{\mathrm{circ}}$ to obtain short macromixing times. This would lead to dilution of the two educts and would lower the concentration of the product and the supersaturation, which determines the rate of nucleation.

These statements are based on the assumption that very high local supersaturation leads to high nucleation rates, which are usually responsible for a small median crystal size. It is important to keep in mind that the nucleation process of primary nucleation is extremely rapid and that local supersaturation may be decisive. On the other hand, growth is a slow process, and mean supersaturation rather than local specific power or local supersaturation is responsible for the mean growth rate. According to these considerations, it is possible to draw some conclusions about the relationship between the median crystal size and the mean specific power input. In Figure 4.6, the median crystal size is plotted against the mean specific power input $\bar{\varepsilon}$ for very slow chemical reactions. The progress of precipitation is controlled by the chemical reaction, not by the mixing process. Therefore, the median crystal size is independent of the specific power inputs. The higher the concentration of the reactants, the higher the concentration of the product and,

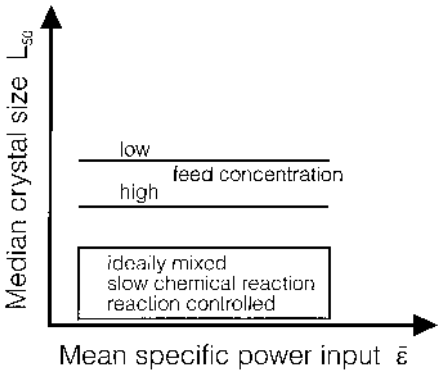

Figure 4.6. Median crystal size versus specific power input (slow chemical reaction).

consequently, of supersaturation. Therefore, the median crystal size can be expected to increase as the concentration of the feed decreases.

The situation is quite different in the case of a very rapid chemical reaction where the processes of macromixing and micromixing determine the field of supersaturation. If the feed points of the two reactants are close together and located in the discharge flow of a stirrer with an extremely high local specific power input (Rushton turbine) and very short micromixing times and if the macromixing is extremely poor, very high local supersaturation may occur. This leads to an extremely high nucleation rate and a small crystal size. The higher the speed of the stirrer, the higher the local specific power input and the shorter the time span of macromixing. In this case, a decrease in the median crystal size is expected with an increase in the stirrer speed and the mean specific power input (see Fig. 4.7). The contrary may be true for other geometrical and operational conditions. Let us assume that the feed points of the reactants are far away from each other in a region with a low local specific power input and that the circulation rate of the stirrer is very high, which results in short macromixing times. The incoming reactants are quickly blended with the entire contents of the vessel and diluted. This dilution leads to a lower concentration of the product and to lower supersaturation at a given solubility. Consequently, the rate of primary nucleation is lower and the median crystal size should be larger. The higher the speed of the stirrer, the more the incoming reactants will be diluted with the solvent. Therefore, it is expected that the median crystal size increases with the mean specific power input. However, if the crystals grow even larger and if they are predisposed to

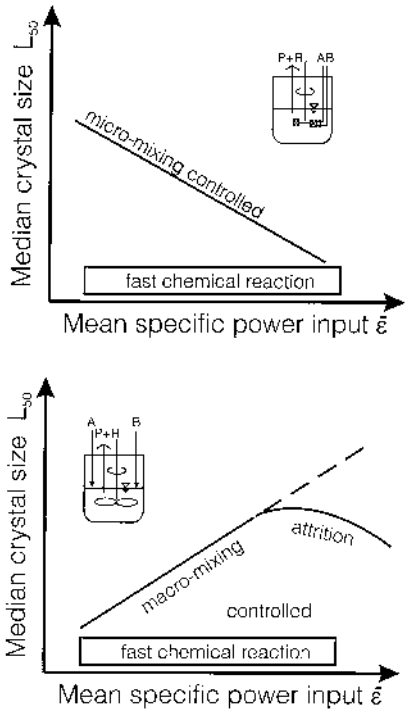

Figure 4.7. Median crystal size versus specific power input (fast chemical raction).

fracturing (i.e., needles or platelets), attrition or breakage may occur when the stirrer speed and mean specific power input exceed a certain value. For this reason, the median crystal size as a function of the mean specific power input may surpass a maximum.

In order to obtain a coarse precipitate, it is recommended to limit the mean and, in particular, the maximum supersaturation by (a) thorough macromixing of the entire vessel contents but poor micromixing of feed streams located in the immediate vicinity of the feed point, (b) vigorous seeding, especially at the feed point of the reactants, (c) high circulation rates of slurry with a high suspension density, and (d) low concentration of the reactants. These objects can best be met in a stirred vessel that is operated continuously at the optimum Reynolds number of the stirrer with the minimum number of revolutions st_{macro} for macromixing (see Fig. 4.8). The reactants are fed to a suspension with a high suspension density in order to obtain a large specific crystal surface area a_T according to

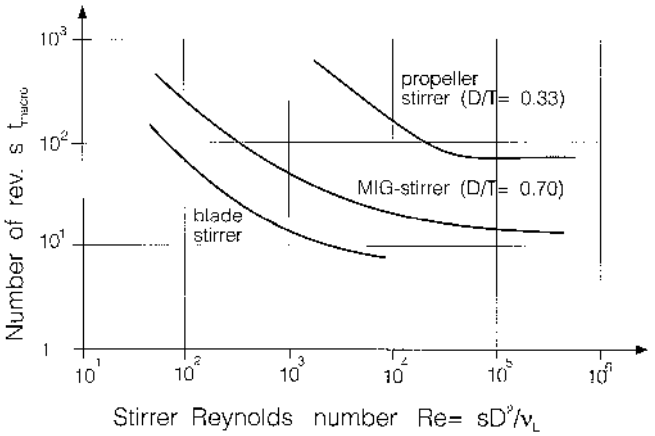

Figure 4.8. Number of revolutions versus Reynolds number of the stirrer.

$$a_T = \frac{6\varphi_T}{L_{32}} \tag{4.9}$$

with L_{32} as the Sauter mean diameter of crystals. The desupersaturation rate dc_P/dt for growth only can be derived from a mass balance of the reaction product P in a volume element ΔV:

$$(1-\varphi_T)\Delta V \frac{dc_P}{dt} = \frac{1}{2}\Delta V a_T \rho_C G \tag{4.10}$$

At high supersaturation Δc_P, the growth rate G is diffusion controlled:

$$G = 2k_d \frac{\Delta c_P}{\rho_C} \tag{4.11}$$

Combining these equations leads to

$$\frac{d(c_P^* + \Delta c_P)}{dt} = -\frac{6\varphi_T}{1-\varphi_T}\frac{k_d}{L_{32}}\Delta c_P \tag{4.12}$$

Where the solubility c_P^* is independent of time, equation (4.12) can easily be integrated:

$$\ln\frac{\Delta c_P}{\Delta c_{P,0}} = \ln\left(\frac{\sigma}{\sigma_0}\right) = -\frac{6\varphi_T k_d t}{(1-\varphi_T)L_{32}} \quad \text{for} \quad c_P^* \neq f(t) \tag{4.13}$$

In this equation, $\Delta c_{P,0}$ is the maximum initial supersaturation in the volume element. For a given desupersaturation ratio σ/σ_0, the time t for this desupersaturation is inversely proportional to the crystal holdup φ_T but

decreases with the mean crystal size L_{32}. As a rule, the volumetric holdup φ_T is small if no slurry recirculation takes place. Therefore, it is recommended that large slurry rates be recirculated to maintain a large crystal holdup φ_T in the inlet region of the feed. Fast desupersaturation by crystal growth can thereby be obtained, which results in low nucleation rates and large median crystal sizes. Consequently, the throughput of slurry-separating devices such as centrifuges or filters is improved remarkably. Furthermore, the purity of the precipitate is high because less residual mother liquor remains in the filter cake, which can also be washed more efficiently.

5. SAMPLING AND SIZE CHARACTERIZATION*

To ensure high product quality, the operation of a crystallizer requires sampling and particle characterization. Sampling has to be carried out representatively in order to obtain an overall picture of the operating conditions of the crystallizer and to avoid misleading results [5.1]. The sample mass necessary for measurement depends on the method of analysis and the particular instrument to be employed, the average size of the particles, and their size spread. Size characterization includes the measurement of CSD, median crystal sizes, and the shape factors that are most suitable for describing the variety of shapes and crystals (cf. Sec. 3 of Chapter 7).

5.1. Sampling

To characterize the size distribution of a suspension product, a representative sample of the slurry has to be measured. There are various ways of measuring particle size:

1. *In-line*: continuous isochronic measurements inside the crystallizer
2. *On-line*: continuous quasi-isochronic measurements outside the crystallizer
3. *Off-line*: nonisochronic measurements outside the crystallizer

In-line measurement requires no special preparation of the sample, and the sensor is placed inside the crystallizer. When applying this method, the location of the sensor has to be chosen carefully. In a large crystallizer in particular, there is an inhomogeneous field with respect to suspension density and particle size distribution. Therefore, it is difficult to find a location with a particle size distribution that is representative of the entire crystallizer volume.

*By A. Mersmann.

Until now, only a few techniques for in-line analysis have been available: light-scattering and ultrasonic measurements. The application of in-line methods is limited because industrial crystallizers are often operated at high suspension densities, and diluting the suspension is expensive and can be tedious. As a result, on-line and off-line measurements are predominantly employed for describing the crystal size distribution. In these cases, a representative sample has to be removed from the crystallizer and prepared according to the standards of the applied measuring technique (wet or dry sieving, Fraunhofer diffraction, image analysis, etc.).

To remove a characteristic sample flow from the crystallizer continuously, isokinetic withdrawal is necessary [5.2]. This means that the flow velocity in the withdrawal tube v_T has to be equal to the velocity of the suspension, $\dot{v}_{\text{sus}}$, at this point in the crystallizer. When there is a significant difference between the velocities two cases can be distinguished (see Fig. 5.1).

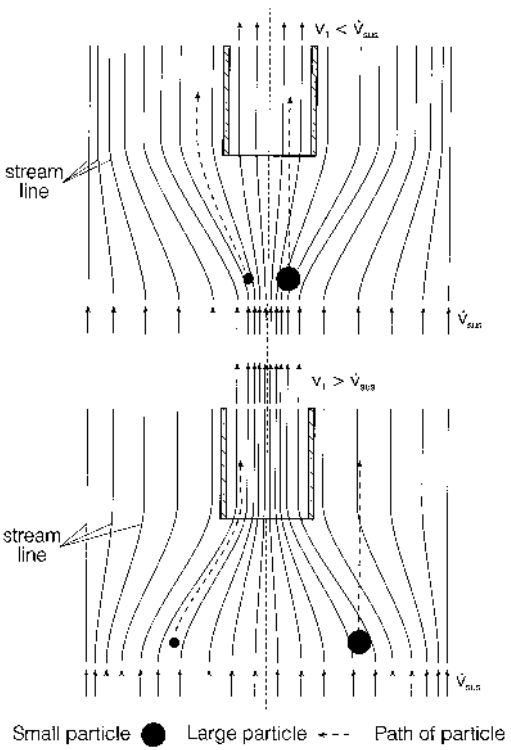

Figure 5.1. Streamlines around a suspension withdrawal tube for $v_T < \dot{v}_{\text{sus}}$ (top) and $v_T > \dot{v}_{\text{sus}}$ (bottom).

For $v_T > \dot{v}_{sus}$, the mean particle size of the sample will be smaller than the mean crystal size, which is representative of the true suspension. In contrast, the measured mean value will be larger if $v_T < \dot{v}_{sus}$ (see Fig. 5.2). These considerations are valid if the wall thickness of the suction tube is very small. Experiments have shown that the best results are obtained when the velocity in the tube is up to 20% higher than the velocity in the crystallizer in order to compensate for the loss of velocity due to the flow resistance caused by the wall thickness of the suction tube. Remarkable deviations from the true CSD can occur, especially in the case of large particles and crystal densities.

After the sample has been withdrawn from the crystallizer, it must be prepared according to the requirements of the measuring technique used. For on-line analysis, it is not necessary to separate the solids from the liquid. The suspension is transported through the cuvette of the particle size analyzer employed for the measurement. In most cases, the optical density of the suspension does not allow direct measurements. The use of Fraunhofer diffraction measurements and laser scanning methods is therefore restricted primarily to low suspension densities (20–50 kg/m^3). As a rule, the suspension density in industrial crystallizers is much higher. In this case, on-line dilution of the sample stream is necessary. Figure 5.3 shows a possible setup. The arrangement with two peristaltic pumps guarantees isokinetic removal from the crystallizer (pump 1), on the one hand, and a variable dilution ratio can be realized (pump 2), on the other. It is possible to choose the dilution ratio by the speed of pump 2 and by the diamter ratio of the flexible tubes in

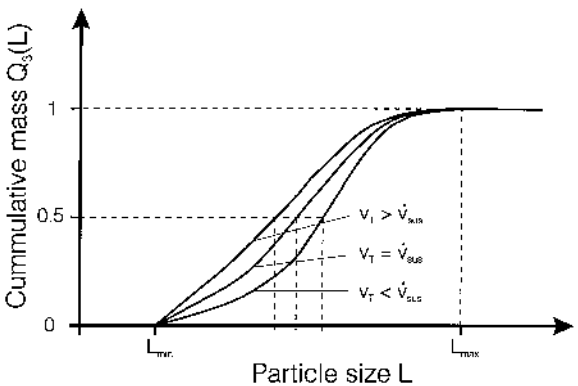

Figure 5.2. Cumulative mass distribution versus particle size for three different suction velocities v_T; $\dot{v}_{sus}$ is the velocity of the undisturbed suspension flow.

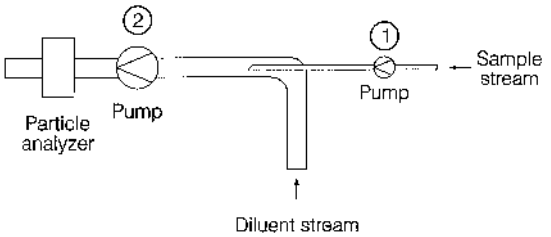

Figure 5.3. Device for diluting suspension in connection with a particle analyzer.

pumps 1 and 2. The use of centrifugal pumps is not recommended in order to avoid attrition and fracture of crystals. Peristaltic pumps can be operated reliably at a constant flow rate provided that the presure in the suction line is constant. With the arrangement shown in Figure 5.3, the suspension can be diluted according to the requirements necessary for the analysis [5.3–5.5].

Saturated solution, clear solution from the crystallizer, or pure solvent can be used as the diluent. A hydrocyclone is a suitable device for separating solution from a slurry. To minimize changes in particle size distribution by growth or dissolution while diluted flow is being withdrawn, the distance between the removal point in the crystallizer and the cuvette of the particle analyzer should be as small as possible.

In off-line analysis, the crystals must be separated from the mother liquor. This separation process has to take place over a very short period of time in order to avoid further crystal growth. A sufficient amount of pure or diluted suspension is first filtered by vacuum or pressure filtration; the filter is then filled with an inert immiscible fluid, which can be an organic liquid for an aqueous crystallizing system. Solution still adhering to the crystal surface is displaced by the filtration of this fluid through the filter cake. Afterward, the crystal cake can be washed with an inert fluid (e.g., hexane) and dried. If the particles of the crystal cake stick together, an ultrasonic bath is a suitable separating device. This method can also be applied to separate agglomerates.

5.2. Size Characterization

In crystallization processes, the crystals must be characterized with respect to CSD and shape. Size distribution measurements are always difficult when the crystals exhibit an irregular and nonisometric shape such as platelets or needles. The modern approach is to relate all particle sizes to either the

equivalent volume diameter or the equivalent surface diameter. Irregular crystals can be characterized by maximum and minimum diameters. In particle size measurement, Feret's and Martin's diameters are known. Feret's diameter is the perpendicular projection, for a given direction, of the tangents to the extremities of the crystal profile. Martin's diameter is defined as the line, parallel to the fixed direction, that divides the particle profile into two equal areas.

The range of particle sizes in industrial practice covers more than five to six orders of magnitude, with the critical nuclei as the smallest particle sizes. The measurement of CSD is feasible only if a representative sample can be taken from the bulk material. The sample mass necessary for measurement depends on the method of analysis and the particular instrument, the average size of the particles, and their size spread (see Fig. 5.4).

The analysis of crystal size above 1 μm can be based on different principles (see Fig. 5.4) [5.6, 5.7]:

1. Light diffraction and light scattering
2. Microscope methods (image analysis)
3. Counting methods (light, ultrasonic, or electrical sensing zone)
4. Sedimentation methods
5. Classification methods (sieving, elutriation)

These methods are used either to measure individual particles or to classify particles according to their properties (as in sieving and sedimentation). With regard to the size characterization of crystal suspensions, a problem may arise when the solution is not saturated or cools down. Crystallization or dissolution of crystals during measurement leads to a change in CSD.

5.2.1. Sedimentation methods

Single particles settle in a quiescent liquid under the influence of gravity or centrifugal forces, with a constant velocity after a short sedimentation time. The settling velocity can be taken to calculate the size of a sphere that has the same settling velocity as the particle.

The methods used in sedimentation analysis can be subdivided into two groups, which apply to both gravity and centrifugal fields (see Fig. 5.5):

1. *Suspension techniques*: The particles are suspended homogeneously throughout the entire liquid volume.
2. *Superimposed layer technique*: The suspension containing the particles to be analyzed is superimposed by a thin layer on top of a solid free liquid volume.

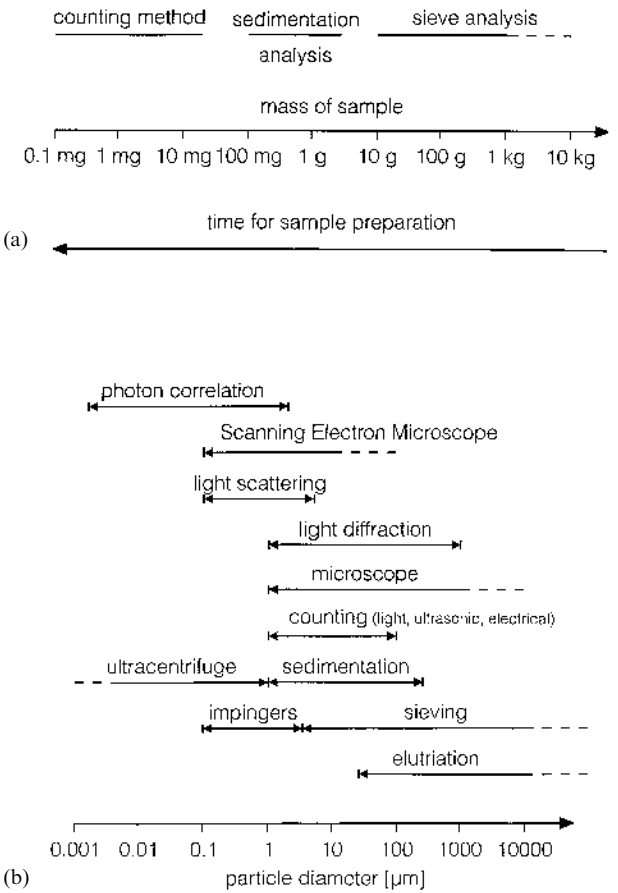

Figure 5.4. (a) Comparison of counting, sedimentation, and sieving with respect to mass and preparation time of the sample; (b) analysis methods.

The choice of fluid in which the particles are dispersed depends on the following factors:

1. The liquid used should not affect the particles either physically or chemically.
2. Reagglomeration must be avoided.
3. The density of the liquid must be lower than the solids density.
4. To carry out the analysis in a reasonable amount of time, the viscosity of the fluid should be in an appropriate range.

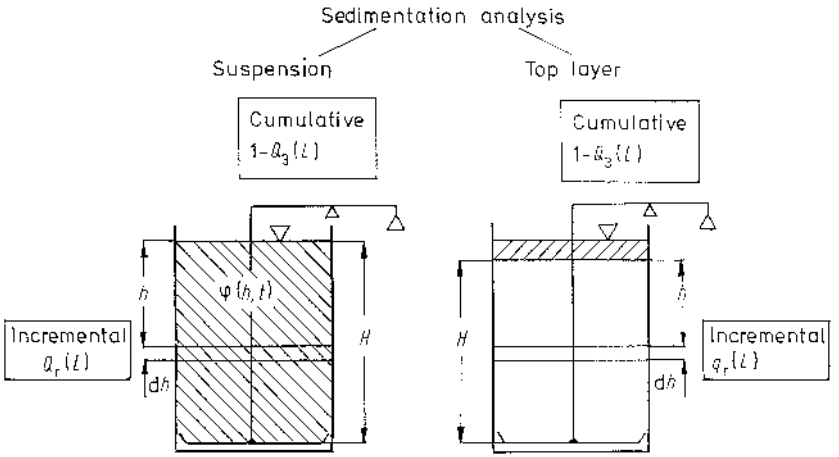

Figure 5.5. Comparison of suspension and top layer sedimentation analysis.

The individual settling velocity of a particle depends on the particle size, shape, and density. The relationship between the stationary settling rate and the diameter according to Stokes' law is valid only for a single spherical particle and laminar flow. When applying this law to a particle swarm, it is necessary to ensure that the particles do not influence each other during settling. Therefore, the solid volume concentration should be kept smaller than 2×10^{-3} vol%. Temperature changes have to be small (≤ 0.01 K/min) to avoid convective flow. The physical method used is the change of the suspension with time. The local suspension density is registered as a function of height and time, and different instruments can be employed to measure the change in suspension properties. Sedimentation analysis is applicable for size distributions with particles in the range of 2–100 μm. Centrifugal methods are used for particles smaller than about 5 μm.

Sedimentation balances or photosedimentometers are the most common devices used at present. A sedimentation balance determines the cumulative mass of solids collected on a submerged balance pan at the lower end of the suspension column. Undersized mass distribution can be obtained by graphical or numerical differentiation. Photosedimentometers measure the attenuation of an incident beam of either white light or of γ-rays by the particles. Besides the analysis based on the Lambert–Beer law, it is possible to calculate the size distribution if the extinction coefficient is known.

5.2.2. Classification methods

All classification methods separate suspension samples into at least two fractions: one comprising particles smaller and the other larger than a separation size. Sieve analysis and air classification are generally used.

Sieve analysis uses several sieves, one on top of the other, with an adequate decrease in successive sieve openings from top to bottom. The sieve column is vibrated mechanically or electromechanically so that particles move horizontally and vertically. Only if there is relative motion of the particles on the sieve cloth, which can be attained either by motion of the sieve cloth itself or by the transport of the particles with air or liquid flow over the sieve, can the particles pass through the opening of the sieve.

The time and intensity of shaking are always a compromise between the requirements of effective classification and minimal attrition of the crystals. At the end, the number of particles on each sieve can be calculated (see Chapter 4). The sieve cloths are standardized and the range of sieve openings varies from 5.5 μm (electroformed sieves) to 1250 μm (woven-wire sieves).

The sieving process depends on various parameters, such as the intensity and frequency of relative motion, sieving aids, effective width distribution, solid loading, particle shape and size, attrition and fracture of crystals, tendency to clog the sieve openings, tendency to agglomerate, and moisture content of the material. In the case of continuously operated laboratory crystallizers, the sample volume depends on the volume of the crystallizer and should be no more than one-tenth of the crystallizer volume.

5.2.3. Elutriation method

Particles are separated according to their terminal settling velocity. However, this method is fairly crude because the velocity profile across the column with the upward-moving fluid is parabolic for small pipe Reynolds numbers. At higher velocities, eddies occur and the separation is not sharp.

5.2.4. Counting methods

All counting methods determine the total number of crystals. The density distributions can be obtained by measuring the size of each particle. The physical properties used to analyze the size are (a) characteristic dimensions such as circumference or the area of projected particles, (b) particle volume, and (c) distribution of an electromagnetic field or of a light beam.

Generally speaking, both direct and indirect counting methods are possible. Direct counting is performed with the particle itself, whereas the

second method is based on the image of the particle. For proper analysis, each particle must be detectable in the measuring zone of the instrument. This can only be achieved at low-volume solids concentration.

As a rule, particle analyzers are videocamera devices focused on a microscope stage or photograph. Such instruments and the computer for data reduction are expensive. An image analysis such as indirect counting methods yields the most definite size and sharp description, depending on the method used; however, it is one of the most time-consuming and labor-intensive methods in use.

The sample has to be prepared so that single particles are distributed without agglomeration. In crystallizing systems, the particles must generally be filtered with special handling to avoid difficulties when focusing in the microscope and further crystallization during the drying process. A very large number of particles should be measured to achieve statistical significance.

5.2.5. Sensing-zone methods or stream methods

The particles to be measured are examined individually in a suspension flow. As the (diluted) slurry passes through a sensing zone, the presence of particles is detected by perturbation. This can be achieved by using light beams, ultrasonic waves, or electrical resistance measurements. The electrical sensing-zone method (e.g., Coulter counting method) determines the number and size of particles suspended in an electrolyte by causing them to pass through a small orifice where electrodes are placed on both sides (see Fig. 5.6). The changes in electrical resistance when particles pass through the aperture generate voltage pulses whose amplitudes are proportional to volumes of the particles. The pulses are amplified, sized, and counted, and the size distribution of the suspended phase can be determined from the data obtained. This method is typically used for particles between 1 and 100 μm. However, each measuring cell aperture has a dynamic range of only 1:15, and larger particles may clog the orifice. Because analysis can be carried out rapidly with good reproducibility, this method has become popular in a very wide range of industrial processes.

5.2.6. Measurement by light scattering or absorption

Small particles scatter and absorb electromagnetic radiation. Scattering represents the deflection of a light beam by refraction, reflection, and diffraction, and absorption prevents the transmission of light by converting it into different kinds of energy.

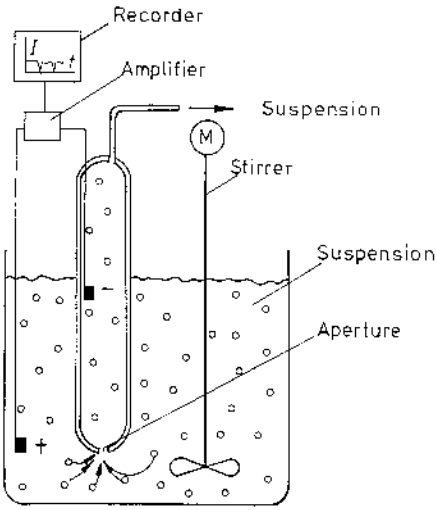

Figure 5.6. Schematic of a counting device (sensing-zone technique).

5.2.7. Optical photon correlation spectroscopy

In optical photon correlation spectroscopy, particle size is determined by detecting and evaluating pulses when light is reemitted by the particles. For particles that are large compared with the radiation wavelength, interference between the radiation reemitted by the individual electrons results in an angular dependence of the scattering intensity characteristic of the particle geometry. Small particles are measured by evaluating a series of pulses in the circuit of the photomultiplier. This is possible because the light scattered by individual particles diffusing into and out of the measured part of the volume due to Brownian motion combines to produce a temporally varying net scattered intensity. These fluctuations in scattered-light intensity contain information about the diffusivity of the scattering particles, which, in turn, depend on the size of the particles and on the forces acting upon them in solution. Standard data analysis techniques relate the correlations in measured intensity fluctuation to the apparent diffusion coefficient of the scattering particles.

A schematic setup used for scattered-light methods is shown in Figure 5.7. The measuring device may be in line with the light beam or at any angle to the incident light beam. Such analysis methods may be used for particle sizes down to 3 nm. By using lenses with various focal lengths, the range of the instrument may cover a wide size distribution. The dynamic range for the shadowing device can be more than 1:100. Unfortunately, particle

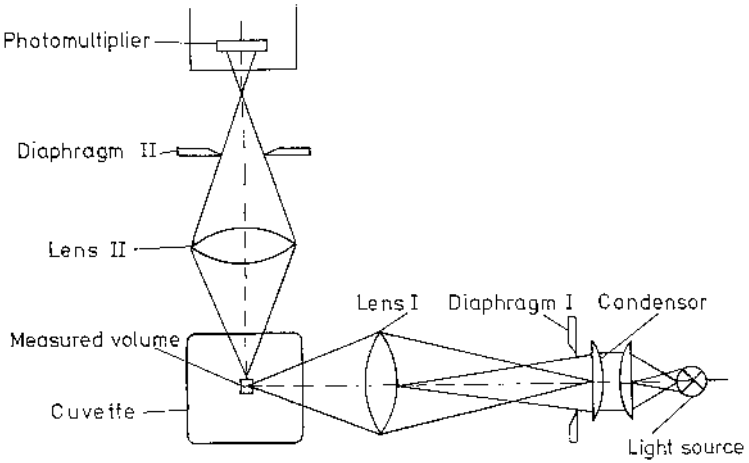

Figure 5.7. Optical setup for scattered-light measuring.

concentration is limited depending on the actual size distribution. This is due to the fact that this method estimates the Brownian motion of particles, which depends in the case of dilute solutions only on solution viscosity, temperature, and particle size, but as concentration increases, interparticle and hydrodynamic forces have to be taken into account, making the data analysis very hard or even impossible. For spherical particles, the mathematical process for this method of analysis works straightforward and satisfactorily. However, crystalline materials often have different shapes and rough surfaces, which can significantly influence the distribution of scattered light and therefore complicate the analysis.

5.2.8. Fraunhofer diffraction

A Fraunhofer diffraction analyzer employs forward scattering of laser light (see Fig. 5.8). A monochromatic light beam is expanded by optimal means and passes through the measuring zone. Spherical particles create a radially symmetrical diffraction pattern, which consists of an extremely bright central spot with coaxial dark and bright rings. Smaller crystals will diffract the laser beam at a larger angle than coarse particles. The energy level at any point varies with the concentration. The diffraction pattern is sensed by a photodetector at a series of radial points from the beam axis to define the energy-level distribution. Calculations are performed digitally by the analyzer microprocessor based on the first-order, first-kind integral equation. The particle size range that can be measured by this optical setup lies between 1 and 100 μm. Flow rates up to 1 dm^3/min can be used without difficulty.

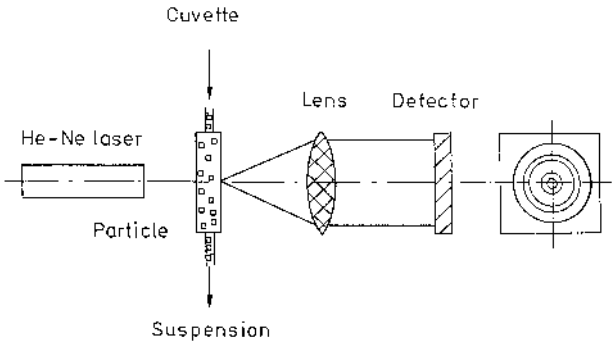

Figure 5.8. Fraunhofer diffraction analyzer.

6. INCRUSTATION*

The operation time of crystallizers is often limited by severe encrustation, and the cleaning time depends on the thickness and structure of the crust. With regard to encrustation, all relationships between the rates of nucleation, growth, and agglomeration, on the one hand, and the supersaturation present in the crystallizer, on the other hand, remain valid because encrustation is a quite natural but unwanted process driven by supersaturation. During the early stage of encrustation, either crystals settle and rest on a surface without reentrainment by fluid dynamics, or heterogeneous nuclei are generated on a solid surface. In the presence of supersaturation, these particles or nuclei will grow until, finally, a hard crust is formed on the surface. In evaporative and vacuum crystallizers, the vapor released from the boiling zone entrains droplets which will be splashed against the wall of the headroom. After a certain amount of solvent has evaporated from these droplets, heterogeneous nuclei will be formed on the wall due to the supersaturated solution. Finally, the crystals adhering to the wall will grow together and form a crust.

The most severe problem is the detachment of crystalline lumps which fall off, and plugging of tubes, clearances, or pumps may occur, which can result in shutdowns. This is not only detrimental to the running time of a crystallizer but also costly with respect to the energy consumption necessary for the hot water needed to dissolve the crusts [6.1, 6.2].

Generally speaking, two cases can be distinguished: (a) crystallizers without heat transfer surfaces such as true vacuum and flash evaporation crystallizers and (b) cooling or evaporative crystallizers with heat transfer surfaces. For both types of crystallizers, encrustation can

*By A. Mersmann.

be induced by settling crystals and/or foreign particles. Therefore, the local slurry velocity throughout the crystallizer should exceed a minimum velocity at which settling of particles will start [6.3]. In the previous chapters, information has been given on settling velocities and the minimum slurry velocities necessary for the avoidance of settling. As has been shown in Chapter 8, $\dot{v}_{\text{sus}} \approx 5w_{ss}$ is recommended for the design of transportation tubes, where w_{ss} is the swarm settling velocity of the coarsest crystals. The adherence of crystals, nuclei, and foreign particles to a solid surface depends *inter alia* on the type and smoothness of the surface. Glass, glass-lined material, and polished stainless steel are more favorable than regular steel. The pipes and ducts should be as flat and even as possible without traps, which catch any type of solid material.

In short, the local slurry velocity should be as high as is necessary to avoid settling in a turbulent flow, but the opposite is true for the superficial vapor velocity in the headroom of vacuum crystallizers [6.4]. The entrainment rate and, especially, the size of the largest droplets depend on the density of the vapor and the superficial velocity (cf. Sec. 2 of Chapter 8).

Severe splashing of liquid can be avoided by a low superficial velocity w_G of the vapor according to [6.5].

$$w_G \leq 0.1 \sqrt[4]{\frac{\gamma_{\text{LG}}(\rho_L - \rho_G)g}{\rho_G^2}} \tag{6.1}$$

Unfortunately, low vapor velocities at low pressures result in voluminous headrooms. Washing the endangered surface with warm solvent or undersaturated solution can help to counteract fouling. However, it is difficult to ensure sufficient spreading of this washing solution all over the wall and to obtain a closed liquid film.

As a general strategy, it is recommended that a certain degree of supersaturation be avoided on all surfaces exposed to the solution. Energy can be added or removed by means of a heating or cooling agent such as air, evaporating refrigerants, or liquids that are not soluble in the crystallizing solution. For aqueous solutions, hydrocarbons or fluorocarbons are appropriate liquid or evaporating coolants, whereas for organic solutions, the choice of coolants is often limited only to water. Air or nitrogen can also be used very well as gas coolants. Gases have a low heat capacity, but to improve the efficiency of the coolant, the process can be carried out under pressurized conditions. If gas coolants are introduced from below, in a bubble column, no stirrer is needed, because the introduced coolant supplies enough mixing.

By applying direct cooling with cold air or a cold organic liquid, supersaturation occurs only on the surface of the bubbles or drops, and heat transfer areas prone to encrustation are not necessary. The volumetric flow density of coolants is in the range from 10^{-6} to $10^{-4}\,m^3/m^2s$ for liquid and evaporating coolants and from 0.01 to $0.1\,m^3/m^2s$ for gas coolants. Surface-based heat transfer coefficients between solution and dispersed phase are general very high (up to $1000\,W/m^2\,K$ for gas coolants and up to $3000\,W/m^2\,K$ for liquid and evaporating coolants). Volumetric heat transfer coefficients are controlled by particle size of coolant and holdup of coolant and can reach values up to $10^3\,kW/m^3\,K$ for aqueous systems, if the coolant is dispersed effectively into the solution.

The use of direct contact cooling techniques in crystallization has been investigated intensively in the 1960s for the desalination of seawater. New efforts have been made to use direct contact cooling in the field of melt crystallization; see Chapter 13.

In the case of evaporative crystallization, the undersaturated solution can be heated under pressure without evaporation or encrustation. Supersaturation is created by depressurization and flash evaporation. It is important that the decisive pressure drop takes place in the free space, far away from solid surfaces, to avoid encrustation.

With the heat transfer coefficient h and the temperature difference $\Delta\vartheta_W$ at the wall, supersaturation Δc_W at the wall can be expressed by the heat flux density $\dot{q}_W$ and the slope $dc^*/d\vartheta$ of the solubility curve:

$$\Delta c_W = \left(\frac{dc^*}{d\vartheta}\right)\Delta\vartheta_W = \left(\frac{dc^*}{d\vartheta}\right)\frac{\dot{q}_W}{h} \tag{6.2}$$

The higher the heat flux density for a given transfer coefficient h, the higher the supersaturation Δc_W at the wall of the heat exchange tube, especially for systems with a steep solubility versus temperature curve. An increase in the heat transfer coefficient h due to an increase in the fluid velocity is favorable with respect to wall supersaturation but less advantageous for secondary nucleation. Sometimes, solutions are heated under normal or elevated pressure, thus avoiding evaporation and crystallization, and the preheated solution is then flash-evaporated into a crystallizer operating at reduced pressure or in a vacuum. Flash evaporation and supersaturation take place in the upper part of the bulk of the solution, thus avoiding encrustation of the walls because heat transfer areas are not necessary in the crystallizer. In adiabatic evaporative-cooling crystallizers, the preheated solution is fed into the loop where the product suspension has been withdrawn from the liquid surface as far as possible in order to create moderate supersaturation in the entire active volume of the crystallizer.

6.1. Limitation of Heat Flux Densities

Drawbacks of flash evaporation include the high preheating temperature, which may be detrimental, or the very low operating pressure of the crystallizer and the operating costs of evacuation. Heat must then be added (heating or evaporation for negative or small positive $dc^*/d\vartheta$ slopes of the solubility–temperature curve) or removed for cooling crystallization. The following considerations are valid if there is only a deposition process on the wall and removal processes such as erosion and dissolution of deposited material do not take place. As a rule, dense encrustation layers with strong bonding forces to the wall are formed at relatively low supersaturation at the wall and high liquid velocities. With respect to encrustation, it is recommended that the temperature, concentration, and supersaturation profiles be calculated in the immediate vicinity of all the walls. This will be demonstrated for the horizontal tube on a heat exchanger that is operated as a cooler or evaporator [6.6]. In Figure 6.1, the solubility concentration c^* is plotted against the temperature ϑ. In Figures 6.2 and 6.3, the temperature profile ϑ and concentration profile c are shown for cooling and evaporative crystallization. The temperature profiles can be obtained by simultaneously solving the conservation laws of momentum and energy. The local differences in temperature between the bulk (ϑ_B) and wall (ϑ_W) is given by $\dot{q}_W/h$. The saturation concentration profile c^* results from the local temperature and the solubility curve. It is presumed that there are no radial concentration profiles $c \neq f(r)$ of the intrinsic concentration c with respect to turbulent flow. In Figure 6.2, the bulk solution is either undersaturated ($c < c^*$) or supersaturated ($c > c^*$). However, in both cases, the solution at the wall is

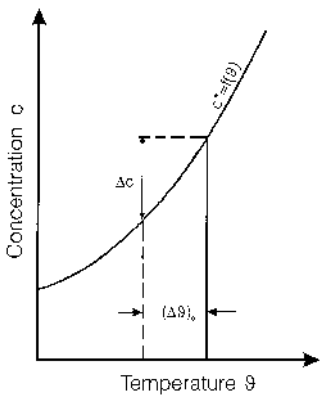

Figure 6.1. Solubility concentration versus temperature.

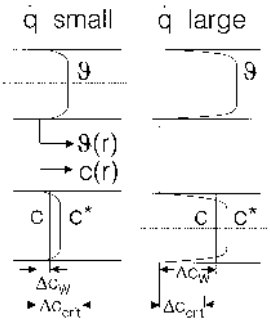

Figure 6.2. Temperature and concentration profiles in tubes of a cooling crystallizer.

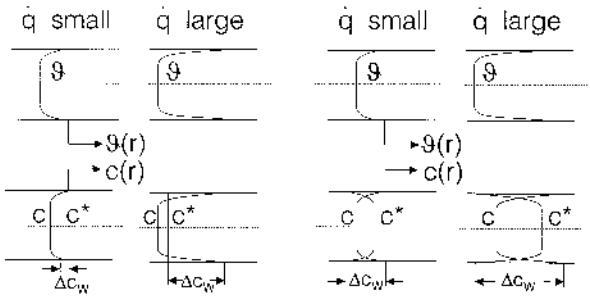

Figure 6.3. Temperature and concentration profiles in tubes of an evaporation crystallizer.

supersaturated, either only slightly ($\Delta c_W < \Delta c_{\text{met}}$) or considerably ($\Delta c_W > \Delta c_{\text{met}}$). It is understandable that even for solutions undersaturated in the bulk flow, encrustation can occur in cold areas of the crystallizer system and the heat flux density $\dot{q}_W$ is the most important encrustation parameter. This is also true for heating or evaporative crystallization (see right-hand side of Fig. 6.3). Again, two different cases of a low (left) and a high (right) heat flux density are shown. The wall temperature ϑ_W is now higher than the bulk temperature ($\vartheta_W > \vartheta_B$) and the vector of heat flow density $\dot{q}_W$ is directed into the tube. However, in the case of encrustation, the vector of the mass flow density is perpendicular to the inner wall surface with its crust layer. Contrary to cooling crystallization, the concentration c_W is higher than the bulk concentration c_B with respect to boiling at the wall.

The temperature, concentration, and supersaturation profiles can only be obtained from the calculation programs described elsewhere in the litera-

ture. Restriction of the heat flow density $\dot{q}_W$ and proper insulation of the entire piece of equipment in combination with a reduction in splashed solution are in any case suitable measures for reducing encrustation and obtaining extended operating times.

The economics of the entire crystallization process ultimately determine the heat flux density $\dot{q}$ and the temperature difference $\Delta\vartheta$, which are the main parameters influencing encrustation. It must be established whether a high heat flux density and short operating period or a small heat flux density with a low temperature $\Delta\vartheta$ (which results in large heat transfer areas and investment costs but long periods of operation) is more economical. Sometimes, dual-surface installation is the most economical solution. When the crust-laden surfaces are cleansed, production can be continued with the aid of the second heat exchanger. As a rule, only one cooler or evaporator equipped with smooth tubes and operated at low heat flux density under appropriate slurry velocities is most economical. To obtain long operating periods, the following measures are recommended [6.7–6.9]:

1. Optimal surface of the solid surface and appropriate fluid dynamics and turbulence
2. Optimum temperature difference between the wall surface and the bulk of the suspension
3. Detachment of crystals and crusts by ultrasonic vibration
4. Addition of additives

These possibilities are discussed in more detail below.

6.2. Optimal Surface and Appropriate Fluid Dynamics

At the beginning of encrustation in crystallizers, heterogeneous nuclei are generated or settled crystals start to grow on the surface. The nucleation rate B_{het} depends on the nucleation energy ΔG according to

$$B_{\text{het}} \sim \exp\left(-\frac{\Delta G_{\text{het}}}{kT}\right) \tag{6.3}$$

with

$$\Delta G_{\text{het}} = G_{\text{hom}} f = G_{\text{hom}} \frac{(2+\cos\theta)(1-\cos\theta)^2}{4} \tag{6.4}$$

where θ is the contact angle between the nucleus and the wall (cf. Sec. 2 in Chapter 2). The nucleation energy is dependent on the interfacial tension γ_{CL} for three-dimensional nuclei and of the edge energy δ_e for two-dimensional nuclei:

$$\Delta G_{3\text{dim}} = \frac{16\pi\gamma_{\text{CL}}^3 V_m^2}{3(\Delta\mu)^2} = \frac{16\pi d_m^6 \gamma_{\text{CL}}^3}{3(\Delta\mu)^2} \tag{6.5}$$

and

$$\Delta G_{2\text{dim}} = \frac{\pi d_m^2 \delta_e^2}{\Delta\mu} \tag{6.6}$$

$\Delta\mu = \nu\Re T \ln(a/a^*) \approx \nu\Re T \ln(c/c^*) \approx \nu\Re T \ln S$ is the difference in the chemical potential of the solute in the nucleus and in the solution. According to this theoretical model, the probability of heterogeneous nuclei occurring is high when (a) the interfacial or edge energy is low, (b) the contact angle is small, and (c) the driving force $\Delta\mu$ is high.

The higher the solubility of a system, the smaller the interfacial and edge energy. Consequently, highly soluble systems are more prone to encrustation than sparingly soluble solutes. The contact angle depends on the affinity of the crystals, the solid material of construction, and the molecular roughness of the solid surface. Experiments have shown that the rate of heterogeneous nucleation can be reduced considerably if the surface is very smooth and has a low affinity to the crystalline material. Glass and glass-lined surfaces are superior to all metal surfaces even when the latter are electropolished. The affinity between crystals and walls can be reduced by coating materials on the surfaces. Generally speaking, a monomolecular layer of coating is sufficient to change the contact angle completely. However, one drawback of this method can be that the long-term stability of such coatings is not sufficient. Many experiments have shown that the induction time of heterogeneous nucleation can be extended for smooth and/or coated surfaces, but it was not possible to avoid encrustation for very long periods [6.10]. Therefore, from the theoretical standpoint, only the third possibility remains (e.g., the reduction in chemical potential or supersaturation).

The role of fluid dynamics and turbulence is ambiguous: loosely bonded nuclei and crystals can be detached by high fluid velocities and degrees of turbulence. The wall shear stress, $\tau_{s,W}$, induced by suspension flow is given by

$$\tau_{s,W} = \frac{\lambda}{8}\rho_{\text{sus}}\dot{v}_{\text{sus}}^2 = \frac{\bar{\varepsilon}\rho_{\text{sus}} D}{4\dot{v}_{\text{sus}}} \tag{6.7}$$

High wall shear stresses are advantageous for removing heterogeneous nuclei and crystals fixed on the wall. The success depends on the bonding force between the particles and the wall. However, if the particles are strongly bonded, high fluid velocities lead to a high mass transfer coefficient, with the result that first the particles and then the entire crust grow quickly according to diffusion-controlled growth, which ocurs at high supersatura-

tion. Again, it can be seen that it is necessary to limit supersaturation not only in the bulk of slurry but especially on the walls that are prone to encrustation.

6.3. Application of Ultrasonic Vibration

The influence of ultrasonic vibration on encrustation has been investigated by various authors [6.9, 6.11, 6.12]. The objective of such a measure is to avoid nucleation and remove or reduce attached crystals and crusts. In [6.8], the encrustation of potassium nitrate and potassium sulfate was investigated and the authors came to the conclusion that vibration of the heat exchanger is more advantageous than the vibration of the solution. Turbulence in the solution induced by vibration tends to reduce the settling of particles, which may trigger encrustation. According to [6.11], heat exchanger surfaces remain free of deposits when exposed to ultrasonic vibrations in the range from 10 to 100 kHz. Ashley [6.12] reports that applying vibration is an economical measure with respect to encrustation and cleaning. Of course, the scale-up of vibrators necessary for large-scale crystallizers is problematic and literature reports are ambiguous. Some authors claim that encrustation of laboratory crystallizers can be reduced or even avoided for a certain operating time by ultrasonic vibrations. However, it is not possible to operate industrial crystallizers over a long period without any encrustation. Goldmann and Spott [6.9] compared the progress of encrustation on cooling surfaces at rest and surfaces exposed to mechanical vibration and ultrasonic vibration. The experiments were carried out with potassium nitrate ($3 < \Delta c < 30\,\mathrm{kg/m^3}$) and adipic acid ($2 < \Delta c < 10\,\mathrm{kg/m^3}$). In all cases, encrustation was retarded by vibration. However, after a crust with a certain thickness was formed, there was no longer any difference in encrustation progress.

6.4. Addition of Additives

Encrustation can be influenced by additives present in the solution according to the following mechanisms:

1. Adsorption on the wall prone to encrustation
2. Adsorption on heterogeneous and secondary nuclei that come into contact with the wall
3. Alteration of the surface structure of nuclei and crystals

Additives should (a) increase the metastable zone width, (b) reduce the affinity between nuclei and solid surfaces, (c) increase the growth rate of crystals, and (d) decrease the rate of nucleation and the growth rate of nuclei.

Detailed information on the variety of the fundamental mechanisms is presented in Sec. 5 in Chapter 3; however, little is known about the general relationship between additives and encrustation. Wijnen and van Rosmalen [6.13] report that the use of polyelectrolytes is recommended to reduce scaling of anionic surfactants such as the sodium salts of butyl ester of oleic acid (SEO). This has resulted in a reduction of fines production [6.14]. Therefore, the encrustation of sodium perborate in the presence of SEO has been investigated by Chianese et al. [6.15]. Glass and steel were employed as the construction material for the baffles and rods exposed to a supersaturated solution of sodium perborate, but the encrustation process was not influenced significantly by the type of material. As expected, the mass flux density $\dot{m}$ to the crust increases with supersaturation Δw [$\dot{m} \sim (\Delta w)^{1.5}$ up to $(\Delta w)^{1.6}$]. The most remarkable result of the experiments is that the encrustation rate is reduced by more than one order of magnitude. The encrustation rate of rods already encrusted is much higher than that of clean rods. It is difficult to deduce general and quantitative rules about the progress of encrustation in crystallizers because few experimental results are known, which does not make it possible to develop a predictive relationship.

6.5. Process of Fouling

This chapter deals with fouling in the heat exchanger in more detail. According to equation (6.8), the overall heat transfer coefficient k for clean surfaces is given by

$$k = \frac{\dot{Q}}{A(\vartheta_W - \vartheta_B)} \tag{6.8}$$

For a constant temperature of the heat transfer medium (cooling water, refrigerant, steam), temperature profiles are obtained, such as those shown in Figure 6.4, for clean (left) and fouled (right) heat transfer surfaces [6.10]. In the presence of a fouling layer with a thickness δ_f and thermal conductivity λ_f, the overall heat transfer coefficient is only $k_f < k$ due to the additional heat transfer resistance $1/k_f = \delta_f/\lambda_f$. This additional resistance is called the fouling factor R_f:

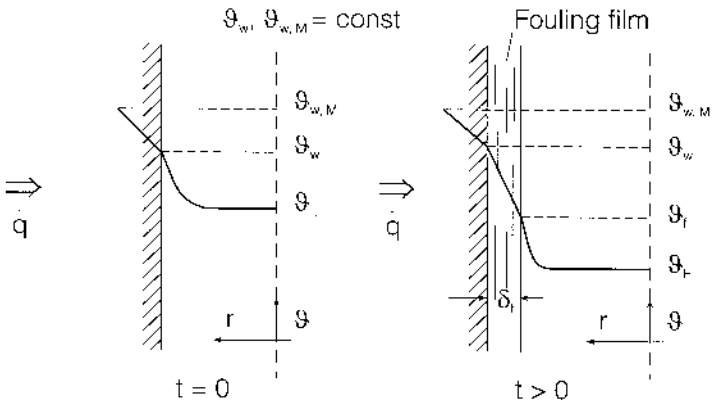

Figure 6.4. Temperature profile in a fouled heat transfer wall.

$$R_f \equiv \frac{\delta_f}{\lambda_f} = \frac{1}{k_f} - \frac{1}{k} \tag{6.9}$$

The fouling factor, R_f, is the difference in the resistance to heat transfer between the fouled and clean heat transfer surfaces.

The amount of solid deposited per unit surface is given by

$$m_f = \rho_f \delta_f = \rho_f R_f \lambda_f \tag{6.10}$$

For constant values of ρ_f and λ_f, the fouling factor is directly proportional to the mass of solid, m_f, deposited per unit area, which can be a function of the operating time t. In the vast majority of cases of fouling studied so far, the deposition process (index d) is accompanied by a removal process (index r). The rate $\dot{m}_f = dm_f/dt$ is given by

$$\frac{dm_f}{dt} = \dot{m}_d - \dot{m}_r \tag{6.11}$$

Figure 6.5 illustrates various deposition and removal processes caused not only by crystallization and dissolution but also by sedimentation and erosion [6.10]. In Figure 6.6, different fouling curves are shown where three different cases may be distinguished:

1. Linear rate of growth of scale mass per unit area, or fouling factor. This behavior is observed primarily for very tough and hard scales with strong bonding forces to the heat-exchanger wall.
2. A decreasing rate of growth of scale with increasing scale thickness is found for deposits of small mechanical strength. The shearing forces of flow cause solids to be removed.

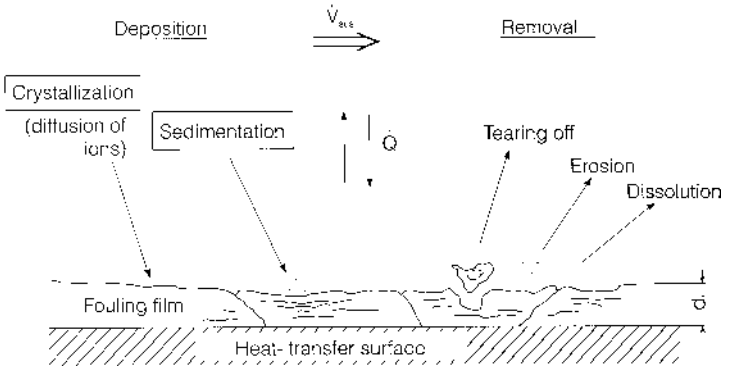

Figure 6.5. Deposition and removal processes.

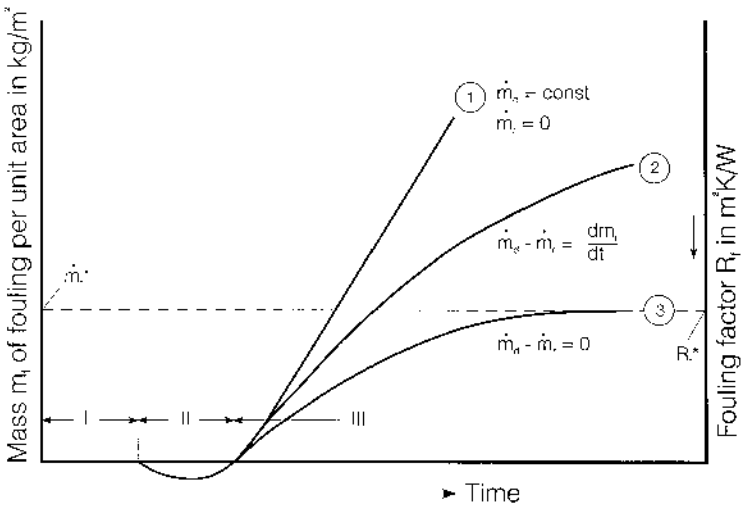

Figure 6.6. Fouling curves: I, induction; II, transition; III, fouling. (1) Rate of growth is constant; (2) rate of growth decreases with time; (3) rate of growth decreases with time and approaches zero.

3. At the end of the fouling process, the rate of solids removed per unit time and unit area is equal to the rate of deposition of solids per unit area. Here, the mass per unit area of the fouling deposit, and thus the fouling factor, reaches limiting values m_f^* and R_f^*, respectively.

Sometimes, three time periods can be defined, such as induction (I), transition (II), and fouling time (III). The induction and transition times may not exist, depending on various operating parameters.

The induction time in particular can be extended considerably by the following measures:

1. Low heat flux density and wall temperature difference
2. Optimal slurry velocity
3. Smooth and/or coated tubes
4. Ultrasonic vibration of tubes
5. Presence of additives that act as fouling inhibitors

However, after a certain period of time, encrustation will start, and after the transition period, fouling takes place, which is then independent of the roughness of the tubes. Because of this behavior, contradictory literature reports on the role of tube roughness are understandable. The induction time can be very short for water-hardness-causing substances, for which the solubility decreases with increasing temperature. This is referred to as *inverse solubility dependence*. Such substances are $CaSO_4$, $CaCO_3$, $Ca_3(PO_4)_2$, $CaSiO_3$, $Ca(OH)_2$, $Mg(OH)_2$, $MgSiO_3$, Na_2SO_4, Li_2SO_4, and Li_2CO_3. The scaling of gypsum, in particular, has been investigated by various authors [6.8, 6.16]. Krause [6.10] measured the fouling velocity w_L (see Fig. 6.7). In this diagram, the fouling factor R_f is plotted against the running time for $\Delta\vartheta = 40\,\mathrm{K}$, which is the difference between the surface temperature of the fouling layer and the average liquid temperature. As can be seen, the fouling factor is much higher and the induction time is much shorter for the liquid velocity $w_L = 0.5\,\mathrm{m/s}$ than for $w_L = 1.3\,\mathrm{m/s}$. As a result of the high liquid velocity, the heat flux density is also high. The relationship between the fouling factor and the heat flux density is therefore ambiguous and depends, among other parameters, on the presence of removal or erosion processes and on the temperature, concentration, and supersaturation profiles in the immediae vicinity of the fouling surface. A better approach to fouling is always to plot the rate of deposited mass and corresponding fouling factor against the supersaturation. Figure 6.8 shows the fouling factor R_f as a function of the supersaturation Δc of aqueous $CaSO_4$ solutions for the liquid velocities $w_L = 0.5\,\mathrm{m/s}$ and $w_L = 1.3\,\mathrm{m/s}$. The fouling factor increases with supersaturation because the growth rate of the fouling layer increases with Δc. The higher the liquid velocity, the more deposit is removed, on the one hand, and of course, the greater the mass transfer coefficient between the bulk flow and the crust. Section 9 of Chapter 8 shows that it is difficult to present general prediction rules and that it is necessary to consider each case separately.

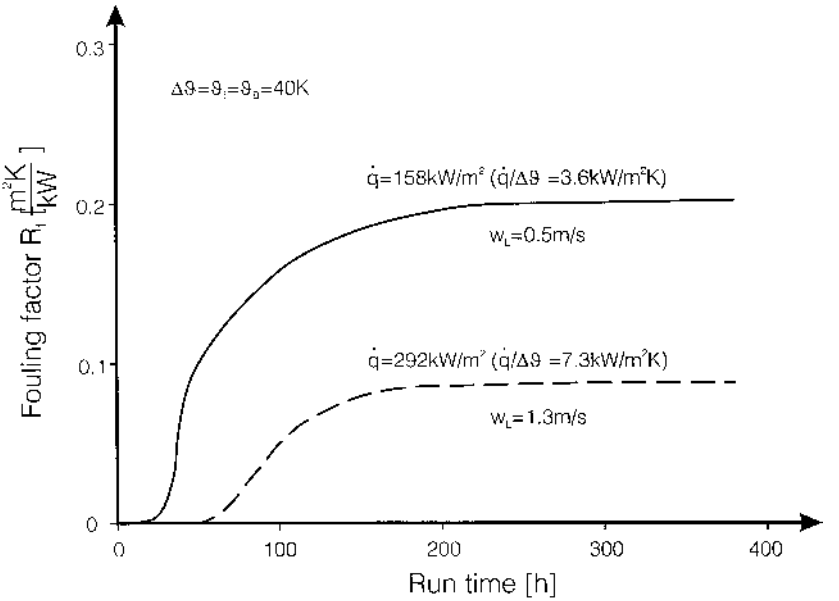

Figure 6.7. Fouling factor R_f versus run time for $CaSO_4$.

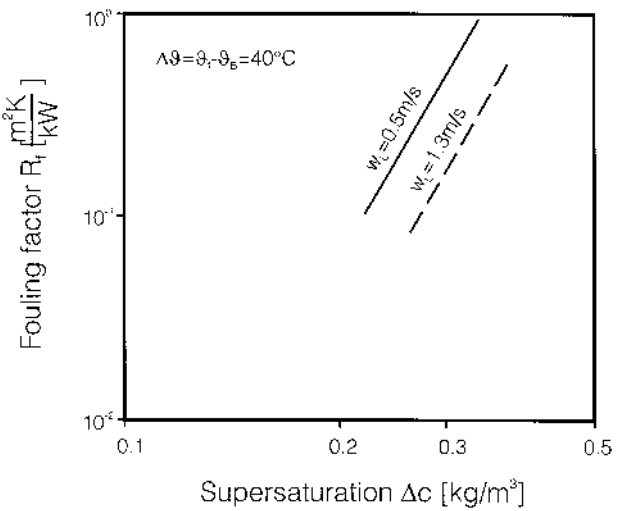

Figure 6.8. Fouling factor R_f versus supersaturation for two different liquid velocities.

7. FITTING THE PROCESS PARTS TOGETHER*

This section deals with the handling and separation of slurries. In chemical processes, crystallization does not stand alone. Indeed, the crystallization process itself can be expected to require only a small part of the total investment in an operating plant and in its operating costs. This is the result of a series of operations whose requirements interact with the crystallizer to produce the desired overall result. The results and limitations of the crystallization process define the requirements for subsequent process operations. When the product from the crystallizer is not satisfactory, the crystallization step must be altered or additional operations performed on the crystals. Such operations increase the cost and frequently generate side streams that involve even greater costs.

In this section, we will discuss some questions of detail to be resolved from a chemical engineer's point of view in order for a successful process to be developed and operated. Once these questions have been solved, a good mechanical design is possible. The basic understanding of a crystallization process requires knowledge of the kinetics of crystal formation and growth, the fluid dynamics of the crystallizer, slurry transport lines, heat transfer, and the effect of crystallizer operation on associated equipment: solid separation equipment, dryers, solvent recovery systems, and so on. Often, these other operations will control what is to be done in the crystallizer.

Controlling of the process is determined by the desired properties of the final product: good size distribution, dust-free, high purity, free flowing, and so on. For existing products, the market has already set the requirements. For new products, the requirement should be set carefully with a view to realistic needs and possible future market developments. Too stringent a specification can lead to substantially greater and perhaps unnecessary costs. For example, a requirement of 99.99% purity is substantially greater than 99.9% and, frequently, considerably more expensive, and expecting very large crystals of sparingly soluble materials could be asking the impossible.

The discussion is based on over 30 years of engineering experience in solid–liquid processing, the latter half of which included crystallization processes. The author's intent was to label the items that are opinion, and those that can be sources, not necessarily the original ones.

A number of situations can arise:

1. *All properties are satisfactory*. The subsequent processes must not alter the desirable properties.

*By F. W. Rennie.

2. *The purity is not satisfactory*. Recrystallization and sometimes staged crystallization will correct this.
3. *The morphology is not satisfactory*. Alteration of the crystallization itself by addition or deletion of other components occurs. Sometimes, agglomeration, grinding, or pelletizing processes are used downstream of the crystallizer. A different solvent may change the morphology.
4. *The size is not satisfactory*. Changes in the crystallization process or some of the processes noted earlier must be used.
5. *A combination of problems*. For example, both morphology and purity are often related to the concentration of other dissolved components.

Some possible ways of resolving these situations will be discussed below.

7.1. Defining the Process

Proper process design requires a complete material and energy balance, which accounts for every gram of material and joule of energy. Consider the various streams shown in Figure 7.1. These are in addition to the normal vents found on most equipment, which may also contain materials detrimental to the environment.

In general, some operations will need to be performed on the crystallizer product before the desired material is produced. Consider one of the simpler

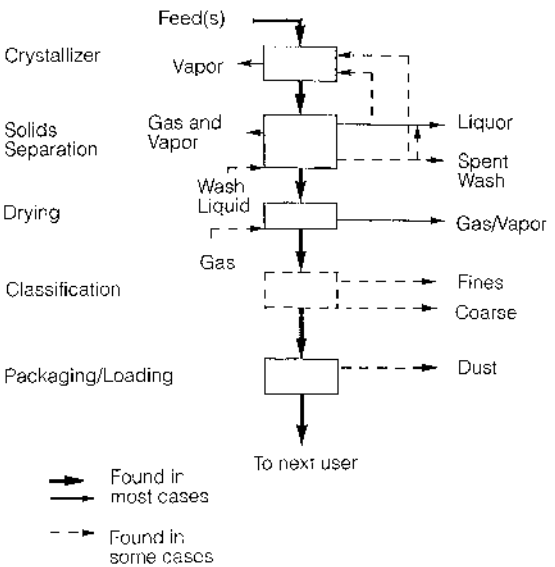

Figure 7.1. Various streams in a crystallization process.

process sequences: crystallizer, centrifuge, dryer, packing. For the centrifuge to separate the crystals, there must be a liquid effluent stream. In addition, there could be a spent wash stream and an inert-gas purge flow. The dryer will produce a vapor stream from the solvent, perhaps mixed with an inert gas.

Handling the crystals in the process outlined above can lead to a considerable reduction in particle size. For example, in one organic crystal process known to the author, the particle size distribution was reduced by about 15% in each case in the following processes: feeding the centrifuge, centrifuging, drying, and pneumatic conveyance to the product storage bin. Thus, even in this simple process, each step requires consideration.

7.1.1. Transporting the slurry

The slurry of crystals needs to be transported from the crystallizer to the crystal-separating device. For batch systems, this is often a two-step process from the crystallizer to holding in the feed tank and then to the separator. For continuous systems, the feed tank is often eliminated. In essence, the slurry must be transported so as to overcome the differences in pressure and elevation between the crystallizer and the separator. In addition, the flow control system will require a pressure drop (this is discussed in more detail below).

If a hold tank is included, there may be a vent that must be considered as a possible environmental problem. Such a tank must be agitated sufficiently well in order to permit a relatively constant composition of feed to the separator, with regard to both slurry concentration and size distribution. A poorly agitated system will make a batch centrifuge difficult to operate, as the particle sizes and concentration reaching the centrifuge change due to classification in the feed tank.

7.1.2. Filtrate stream

In many operations, the filtrate can be recycled to the crystallizer. This is particularly useful for giving a pumpable slurry concentration and good yield. Care should be taken to ensure that a recycle stream does not furnish an undue amount of nuclei, which result from failure to separate small crystals in the centrifuge or from cooling of the filtrate. Heating the recycle stream or adding solvent can avoid this at the expense of cooling capacity or evaporation load in the crystallizer.

It should be noted that a purge of liquor is usually required in order to avoid an accumulation of impurities that do not crystallize. Otherwise, the impurities will accumulate until the concentration reaches such a level that the material balance is met by impurity in the wet cake or the impurity itself

crystallizes. Obviously, this will not be satisfactory if one of the purposes of the crystallization was to purify the product. Nevertheless, such a process is often acceptable when the sole purpose of the crystallizer is to make crystals. In other cases, increased concentration of the impurity may change the morphology and/or crystal size. In some processes, only a small purge of liquor will maintain the impurity concentration at an acceptable level.

If the crystallizer is to purify the product, part or all of the filtrate stream must be processed further. These processes include another crystallization step to recover the product, various waste disposal processes, and solvent recovery. In a few instances, the stream may be recycled back to the preceding step, such as a reactor, where the impurity is converted into the product.

For systems in which a solvent other than water is used, solvent recovery usually becomes an economic necessity. The expected results of this process will be a reusable solvent and an impurity-laden stream to be processed further. In some processes, such a stream can be sold as a product.

When all these considerations are met, the economically optimum solvent is not necessarily also the best for the overall crystallization process. Rather, the price of the solvent, its ease of recovery, and the cost of its disposal will enter into the final selection of the solvent.

7.1.3. Spent wash stream

Most of the considerations for the filtrate also apply to the spent wash stream. However, the impurity concentrations in this stream frequently allow recycling to the crystallizer. It is often mixed with the filtrate in the solid–liquid separation equipment, either deliberately or as a result of the choice of separator.

7.1.4. Vent stream from the separator

The vent stream from the separator will probably be saturated with the solvent. It may also contain other materials from the entrainment of liquid or due to the vapor pressure of the solids. The stream is rarely large but must be considered from an environmental point of view.

7.1.5. Drying step and packaging

Considerations similar to those discussed above must be applied to the dryer, particularly when the solvent needs to be recovered. The vapor stream may contain dust, which must be separated and processed in some manner. The dust may be a product in itself, which is dissolved and recycled to the crystallizer, or it may require a disposal process.

The major part of the heat load for a dryer comes from the evaporation of the solvent from the wet solids. This becomes a particular problem if the crystals are heat sensitive. As a result, solids with less solvents are more economical. In addition, the dustiness of the dried product may be of concern, in which case an operation such as sieving or elutriation may be needed to remove the fines. This will produce a stream of fines that may be treated as above for the dust in the vapor.

7.2. Some Solutions

The way in which problems are solved often determines the difference between optimum operating processes producing good quality products and poorly operating ones with marginally acceptable products. Product chemical quality and particle morphology are set in the crystallizer. Chemical purity will change little in downstream processes, but particle size is subject to considerable size reduction in the equipment. As a result, much discussion is concerned with minimizing particle damage.

7.2.1. Choice of pumping systems

Only when pump choice is considered as a whole can a good slurry transporting system be developed. The pump is only part of the problem; this is an area in which opinions differ widely and comparative data are nearly nonexistent. Pumps that have been used include diaphragm, moving capacity, centrifugal, recessed impeller, and piston pumps. Each type of pump is said to be advantageous in some operations, but comparative data are rarely offered.

Centrifugal pumps are employed in many plants. These pumps are not very sensitive to sedimentation and plugging of crystals, but there is a relatively high mean specific power input $\bar{\varepsilon}$ in the casing of the pump. According to the simple laws of similarity and scale-up of such pumps, the minimum mean specific power input is given by

$$\bar{\varepsilon}_{\min} = 2\pi^3 s^3 D^2 = \frac{2(s\pi D)^3}{D} \tag{7.1}$$

The mean specific power input increases with the third power of the peripheral rotor velocity $s\pi D$ and is inversely proportional to the rotor diameter D. With $s\pi D = 10\,\text{m/s}$ and $D = 0.5\,\text{m}$, a minimum specific power input $\bar{\varepsilon} = 4000\,\text{W/kg}$ is obtained. This value is some orders of magnitude larger than the highest values in the vicinity of a stirrer (see Fig. 8.6.4). Therefore, the choice of pump and its operating conditions is very important in order to avoid excessive attrition and breakage (cf. Chapter 5).

If slurry is to be pumped from a vacuum crystallizer to a separator operating at atmospheric pressure and at a different, usually higher, elevation, the pressure must be raised to atmospheric and the head furnished for the change in levels. To do this, the pump also provides additional energy for the following:

1. Losses in the pump (the efficiency may be as low as 20%; cf. Chapter 8
2. Friction losses in the pipelines
3. Pressure drop in the flow control system

The effects here can be analyzed in many ways. In the pump, turbulence, crystal-to-crystal collisions, crystal-to-impeller collisions, and crystal-to-stationary pump parts can be expected to cause attrition and crystal breakage. In control valves, the energy is lost in a similar way, but at greater turbulence in a smaller volume. One way of examining such effects would be to consider the energy loss per unit volume or pressure drop in the pump or valve system, as is often done in crystallizers for nucleation considerations (cf. Eq. (5.4.14)). When this is done, breakage in control systems become striking because the loss occurs in a small volume within the valve and immediately downstream of the valve.

This author has definite preferences for slurry transfer, which are not wholly supported by firm data. However, an examination of a system is perhaps in order. Consider that a pumping rate of 6 L/s is needed to move the slurry from a crystallizer under 6 kPa absolute pressure to a separator whose feed points are at atmospheric pressure and 10 m above the level in the crystallizer (see Fig. 7.2). The entire volume of the circulation loop is approximately 0.04 m^3. If one were to consider this as a liquid system, the instrument engineer might require a 30-kPa pressure drop across the control system. A quick analysis of the flow rate would indicate that the pressure loss in the piping is about 4 kPa.

A typical pump for such a system is a centrifugal pump running at 1400–3600 rpm, developing 129 kPa total head for water and requiring about 1.6 kW input power. Pumping efficiency is about 50%. Thus, the distribution of power is as follows:

Elevation of 6 L/s to 10 m and raising to atmospheric pressure	585 W
Pipeline loss	24 W
Control valve	180 W
Loss in pump (50% efficiency)	789 W
Total	1579 W

The intensity of the power loss in the pump will vary with the pump size from 200 to 2400 W/L, smaller pumps requiring higher speeds. The intensity of the energy loss in the control system is many times that in the pump

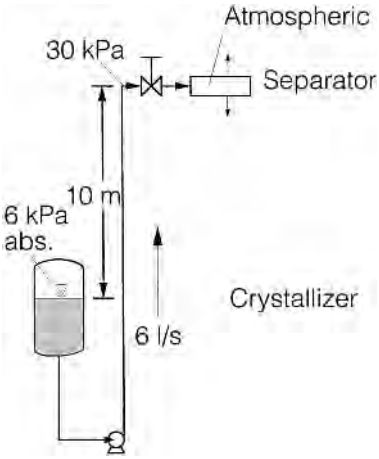

Figure 7.2. Slurry transportation system.

because the volume in which the loss occurs is very small. This is far beyond the intensity used to agitated tanks, which is seldom more than 50 W/L of volume swept by the agitator.

Only rarely will such a system be used for slurries. A large turndown ratio must be met by providing a very high pipeline velocity so as to avoid settling in the lines at the lowest flow rates. A more typical system is shown in Figure 7.3. As the feed to the separator increases, the flow through the recirculation line increases and the total flow decreases. The control valve in the recycle loop keeps the pressure at the level required. The pressure drop in the return lines is not usually sufficient to provide this pressure, with the result that this valve sees a greater pressure drop than the one serving the separator. The power necessary for the process is as follows:

Elevation of 6 L/s to 10 m and raising to atmospheric pressure	585 W
Pipeline loss	24 W
Feed control valve loss	180 W
Recirculation system, 6 L/s	
Pipeline loss	24 W
Recycle valve loss	765 W
Pump loss (50% efficiency)	1579 W
Total	3156 W

This system would seem to be one of the least advantageous, yet it is frequently used.

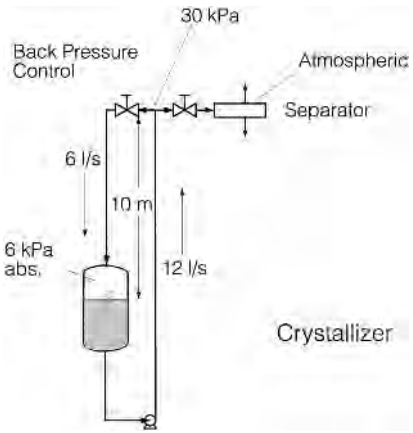

Figure 7.3. Slurry transportation system with recirculation line.

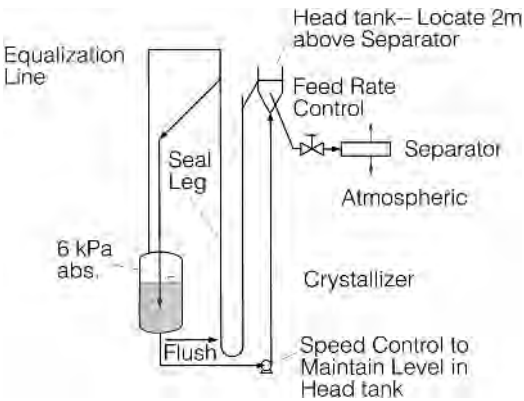

Figure 7.4. Slurry transportation system with change of the pump speed.

Figure 7.4 describes a much gentler system that is controlled by changing the speed of the pump rather than throttling the flow, thereby eliminating the high-intensity loss in the control valve. The speed may be controlled in many ways, but current technology points to a variable-frequency control of the motor. When centrifugal pumps are used, a relatively large-diameter pump should be used so that the speed may be reduced. Frequently, this pump will have a higher efficiency as well. Turndown is limited to the velocity at which particles will start to salt out in the pipelines. When the lowest allowable pump speed is reached, the head tank will overflow to the

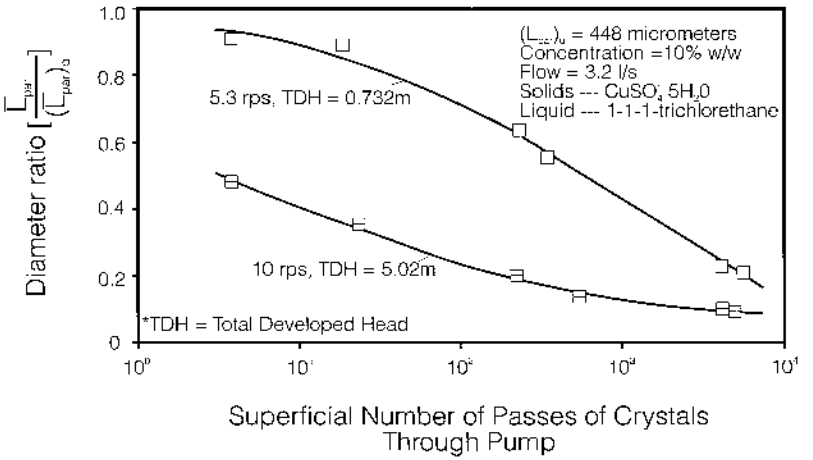

Figure 7.5. Attrition in an open-impeller centrifugal pump loop.

crystallizer. The energy situation for Figure 7.4 is as follows:

Elevation of 6 L/s to 10 m and raising to atmospheric pressure	585 W
Pipeline loss	24 W
Control valve loss (2 m)	117 W
Pump loss (50% efficiency)	26 W
Total	1452 W

Over 40% of the energy is now used to do the necessary work.

The last choice is based on somewhat limited data. A typical set of data is shown in Figure 7.5. The tests were run by adjusting a pinch valve and the pump speed to achieve the desired head and flow. These data are not entirely satisfactory, because the heads developed do not extend to the amount frequently needed, and the agitator power is not known. However, the difference in the two curves is clearly that for pumping through a throttled valve. Recessed impeller pumps were slightly better; diaphragm pumps were considerably better. Later test results with a screw centrifugal (e.g., Hidrostal) pump were considerably better than all the test results except those for the diaphragm pump. However, operating experience with diaphragm pumps has not been satisfactory.

7.2.2. Slurry flow rates

Several approaches to the slurry flow rate are reported in the literature, one of which (by Spells) is available in *Perry's Chemical Engineers' Handbook*

[7.1]. It should be noted that the problem is in horizontal piping. Flow upward or downward can be accomplished with less velocity than for horizontal piping and can be justified by examining the terminal velocity of a settling particle. Spell's equation is

$$\frac{\dot{v}_L \rho_L}{L(\rho_C - \rho_L)g} = 0.074\left(\frac{\dot{v}_L D}{\nu_L}\right)^{0.775} \tag{7.2a}$$

This was developed for sand, ash, and lime particles suspended in water pipes from 50 to 300 mm in diameter. This flow allows a turndown to a little less than half the rate before saltation predominates. As a result, a velocity somewhat greater than that calculated would be used if a greater turndown is expected.

Spell's equation can be rearranged to

$$\frac{\dot{v}_L^2 \rho_L}{L(\rho_C - \rho_L)g} \approx 0.155\mathrm{Ar}^{0.6}\left(\frac{L}{D}\right)^{-1.2} \tag{7.2b}$$

with the Archimedes number $\mathrm{Ar} = L^3(\rho_C - \rho_L)g/\nu_L^2\rho_L$. In Figure 7.6, results according to equation (7.2b) are compared with statements of Figure 8.6.11. Both coincide for $\mathrm{Ar} \approx 10 \div 100$.

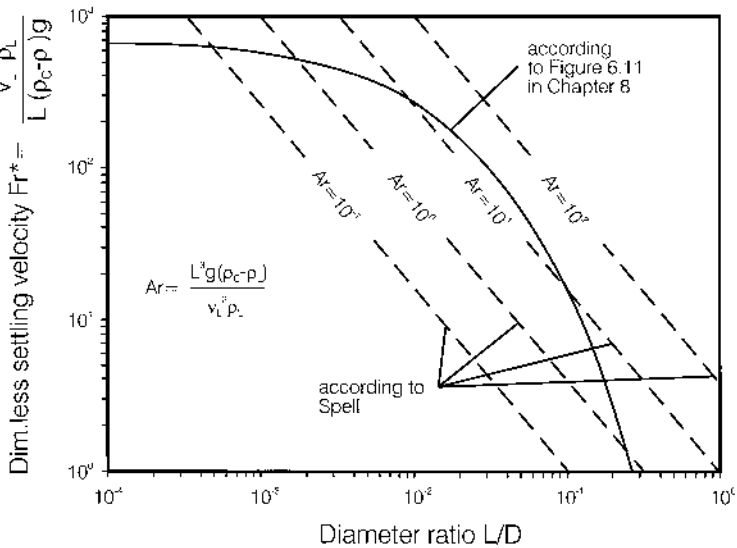

Figure 7.6. Froude number versus ratio L/D.

7.2.3. Choice of pumps

The choice of pumps becomes considerably less important if the best of the systems described above is used. Few comparative data are available concerning attrition in pumps. It should be noted, however, that if one considers the power loss per unit volume of a pump, a large centrifugal pump should be chosen with a full-size impeller operated at only sufficient speed to provide the necessary head; see equation (7.1). Such pumps are reasonable in size if care is taken to avoid unnecessary head development.

7.2.4. Effect of particle size on separators

The effect of particle size on separation is well known. Carman-Kozeny developed a relationship for packed beds or particles, as well as for filter cake, which shows that the flow rate $\dot{v}_L$ of a fluid through the bed is proportional to

$$\dot{v}_L \sim (\beta L)^2 \frac{\Psi^3}{(1-\Psi)^2} \tag{7.3a}$$

where L is the particle diameter, β accounts for nonsphericity, and Ψ is the volume fraction not occupied by solids. The pressure drop Δp of the fluid passing through a particle bed with the height H is given by

$$\Delta p \approx 180 H \dot{v}_L \frac{\eta_L}{(\beta L)^2} \frac{(1-\Psi)^2}{\Psi^3} \tag{7.3b}$$

This equation is valid for $\dot{v}_L L \rho_L/(1-\Psi)\eta_L < 10$ and clearly indicates that the larger the particle size, the greater the filtration rate. Indeed, there is a still greater effect. If the particles are large enough, centrifuges such as pushers can be used, which have the advantage of very large capacity in a single machine and a relatively dry cake. One also expects that irregular particles will form a filter cake with a larger pore fraction, Ψ.

Similarly, devices that rely on sedimentation will have greater capacity for large particles. This is clearly shown by the gravity sedimentation equations for single particles, Stokes' and Newton's laws. Stokes' law is valid for terminal velocities when the particle Reynolds number is less than about 0.1 and with a reasonable accuracy to a particle Reynolds number of 2:

$$w_s = \frac{L^2 g(\rho_C - \rho_L)}{18\eta_L} \tag{7.4}$$

This implies particles smaller than about 160 μm in a gravity field or 1–10 μm in a centrifugal field of 4000 g for solids of density 2000 kg/m^3 in

water. For Reynolds numbers between about 10^3 and 10^6, Newton's law applies:

$$w_s = 1.73\left(gL\frac{\rho_C - \rho_L}{\rho_L}\right)^{0.5} \tag{7.5}$$

An intermediate relationship may be fitted for Reynolds numbers between 0.1 and 1000 or can be read from Figure 8.5.3 for $\varphi_T = 0$. In concentrations so great that particles interfere with one another, the effect is still as large. The situation can then be compared to a fluid flowing through a bed of solids, with the volume rate of liquor equivalent to the volume rate of solids settling.

Few data have been published about the effect on retained liquor. However, if one considers that most of the liquor can be held either on the wetted surface or at the contact points between particles, the obvious conclusion is that larger particles should retain less liquor on separation (cf. fig. 7.4.1). This still leaves room for considerable variation. A separation force is necessary, which varies from equipment to equipment. One would expect that the greater the force, the greater the amount of liquor removed from the particles and this is borne out in practice. A thesis by Han [7.2] supports this conclusion (see Fig. 7.7). This was developed using almost

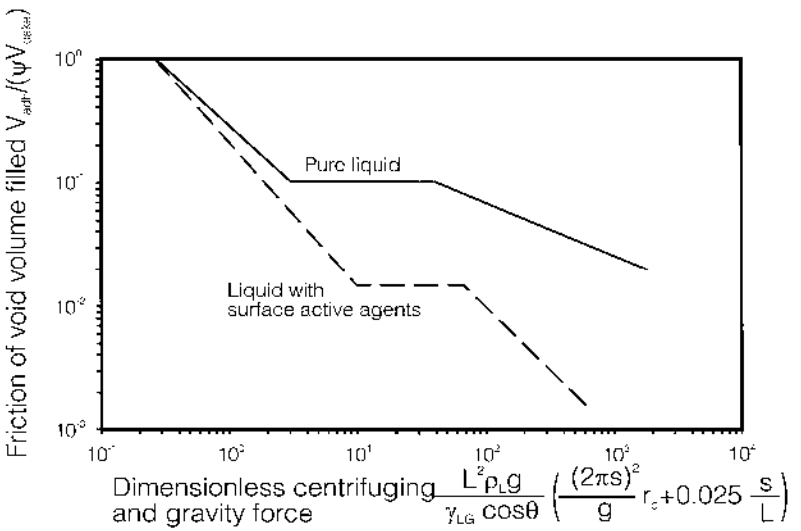

Figure 7.7. Fraction of adhering liquor versus the drainage force. (Redrawn from [7.2].)

monodisperse particles and does not include the effect of blowing gas through a cake, as can be done on a filter.

7.3. Improving the Morphology

This is a complex problem stemming from fundamental aspects of crystallization. The morphology will be affected by the conditions of crystallization: crystal growth rate, purity of solution from which the crystals are formed, temperature in some cases, choice of solvent, and concentration of the slurry. The morphology may be altered by changing one or more of these. In Chapter 12, additives and impurities are discussed. The purity of the crystal and its morphology are frequently related.

7.3.1. Improving the crystal size and size distributions

Care should be taken to ensure that the expectation for size and distribution is reasonable. The crystal size that can be obtained in customary systems is principally a function of solubility, the diffusivity, and the rate at which production must be obtained. Reference should be made to Mersmann et al. [7.3] for size prediction.

The size distribution for an MSMPR crystallizer with size-independent growth rate can be predicted from the mass median crystal size

$$L_{50} = 3.67G\tau \tag{7.6}$$

or for all sizes (after Nyvlt et al. [7.4]),

$$L_i = z_i G\tau \tag{7.7}$$

The cumulative mass undersize $Q_3(L)$ can be described by

$$Q_3(L) = 1 - \frac{1 + z_i + z_i^2/2 + z_i^3/6}{e^{zi}} \tag{7.8}$$

In Figure 7.8, the expression $Q_3(L)$ is plotted against the dimensionless retention time $z_i = L_i/G\tau$. For this distribution, $Q_{3,15} = 0.556Q_{3,50}$ and $Q_{3,85} = 1.638Q_{3,50}$. If this distribution is not satisfactory, one of two general actions can be taken: (a) the product can be screened to separate the proper size distribution or (b) the crystallization can be changed to a classifying design. In the first of these actions, two unsatisfactory materials may be generated: the undersize or fines and the oversize or coarse product. If possible and economical, either of these products may be sold as an additional grade of material. The fines might be compacted or granulated to form a larger size and recycled to the screener. The coarse product may be

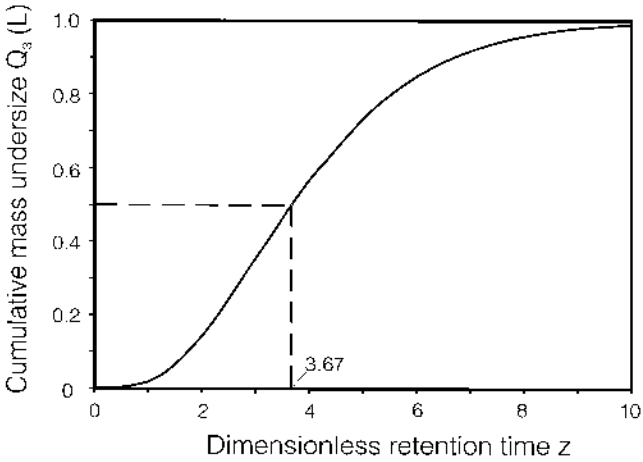

Figure 7.8. Expression $Q_3(L)$ over the dimensionless retention time z_i.

ground and recycled to the screener. Usually, the coarse grinder will also produce fines.

Alternative crystallizer designs that may produce narrow size distributions include fluidized-bed designs (Figures 8.1.1 and 8.1.2) and classifier designs using fines removal and classified product removal (see Chapter 4). Classified product can produce larger, more narrowly distributed product while reducing the average size remaining in the crystallizer. Fines removal can also enlarge the crystal size in both the crystallizer and the product.

We shall consider fines separation and coarse product separation separately. Fines removal in the form of fines advance is particularly useful for increasing the particle size of sparingly soluble materials. In one process of the author's design, gypsum was enlarged from 35 μm average in the MSMPR operation to 140 μm with a fines removal system that increased the product hold from 2 to 15 h by increasing the slurry concentration from about 2.3% to 17%. The fines advance was mixed with the feed and sent to a filter already in use in another part of the process. In general, because fines removal also produces crystals, some means of disposal is required, such as destruction and recycling to the crystallizer by heating or solvent addition, mixing with the coarse product before separation, or recycling to an earlier step in the process.

Coarse product removal is rarely used by itself because the product stream does not usually contain enough liquor to meet the material balance. As a result, a clear-liquor advance system that removes virtually solids-free

liquor is needed. The latter usually has very small particles, thereby becoming a fines removal process as well.

When operating classified product systems, provision must be made for all crystal sizes being removed. If the middle size range is not removed, the concentration of these particles in the crystallizer will increase until a sufficient number grows into the coarse product removal range.

7.3.2. Classification equipment

Classification devices generally used for crystallization operations rely on the relative settling rate of crystals on different sizes. Elutriation in a gravity vessel is the most common, and hydrocyclones can also be used.

7.3.3. Elutriation approaches for product removal

Elutriation devices work in a region of fluid–solids flow known as *fluidization*. In this regime, the solids are suspended in a bed by the relative flow of fluid past the solid particles. The result is a bed of solids that has some of the properties of fluids. There is an increasingly large amount of literature concerning gas fluidization, but little on liquid fluidization. However, the equations for gas as a fluid tend to be satisfactory for liquids.

For fluidization, the friction of a fluid flowing through a bed of solids must be sufficient to support the solids; as a result, there is a minimal flow rate. There are many relationships in the literature. However, this author prefers to use one by Leva [7.5]. Let us consider the situation for which the flow rate upward in a bed of particles is sufficient to support the bed, but no greater. By equating the force necessary to support the bed and relationship for the flow through packed beds, a new relationship can be developed. Such equations require knowledge of the fractional volume occupied by fluid. Leva reduced this by using an experimental relationship with particle size and shape:

$$\dot{v}_L^3 \frac{\rho_L}{g(\rho_C - \rho_L)\nu_L} = 10^{-9}\mathrm{Ar}^{1.82} \tag{7.9a}$$

or

$$\dot{v}_L \left(\frac{\rho_L}{g(\rho_C - \rho_L)\nu_L} \right)^{1/3} = 10^{-3}\mathrm{Ar}^{0.606} \tag{7.9b}$$

(cf. Fig. 8.5.3). When this equation is reduced, the following results for the minimum mass flow density of liquid:

$$(\dot{m}_L)_{\mathrm{mf}} \equiv (\dot{v}_L \rho_L)_{\mathrm{mf}} = \frac{L_c^{1.82}[g\rho_L(\rho_C - \rho_L)]^{0.94}}{919\eta_L^{0.88}} \tag{7.10a}$$

The form of the equation (7.9b) shows the effect of physical variables. In the development of this equation, there is an implied relationship with the fluid fraction Ψ, the particle shape factor β, and the Reynolds number $\mathrm{Re} = \dot{m}_L L/\eta_L$:

$$\frac{\Psi_{\mathrm{mf}}^3 \beta^2}{1 - \Psi_{\mathrm{mf}}} = \frac{0.14}{\mathrm{Re}^{0.063}} \tag{7.10b}$$

This might be used to estimate the void fraction.

In the operation of a continuous liquid elutriation device, the particles are fed to the top of the bed and the solids are withdrawn to maintain the bed height. The resulting motion of the solids downward in the bed also contributes to the relationship; that is, the equations above define the relative velocity of the solids and the liquid. If the solids move, the liquid rate must be reduced to maintain the same bed conditions. This author has found that operation near the minimum fluidization condition does not permit much classification. As the relative velocity increases, so does the void fraction. Leva cites data such that in the laminar flow region one can expect

$$\frac{\dot{v}_L}{(\dot{v}_L)_{\mathrm{mf}}} = \left(\frac{1 - \Psi}{\Psi^3}\right)_{\mathrm{mf}} \frac{\Psi^3}{1 - \Psi} \tag{7.11}$$

Thus, for a moving fluidized bed,

$$\left(\frac{\dot{m}_e}{\dot{m}_{\mathrm{mf}}}\right) \frac{\dot{m}_{\mathrm{mf},L}}{\rho_L \Psi_e} = \frac{\dot{m}_{m,e,L}}{\rho_L \Psi_e} + \frac{\dot{m}_{m,e,L}}{\rho_C (1 - \Psi_e)} \tag{7.12}$$

The author believes that for elutriation to take place at a sufficient rate, the value of $\dot{m}_e/\dot{m}_{\mathrm{mf}}$ should be 5 or somewhat greater. These equations can be considered sufficiently accurate for $\mathrm{Re} < 5$ and $\Psi < 0.8$; they would not be expected to apply to long needlelike crystals or to very thin platelets. The equations will assist in the design of product classifiers such as those indicated in Figure 8.5.3.

For product classifiers, one can also expect a wash effect when displacing crystallizer liquor with a cleaner liquor for fluidization. However, displacement of liquor with a cleaner liquor is more effective in the $\dot{m}_e/\dot{m}_{\mathrm{mf}}$ region 2–3. In such circumstances, the displacement can be over 99% effective. However, because the purpose of the operation is classification, the displacement effect is much smaller, say 50–60%. A need for a greater wash effect would indicate subsequent operation. This approach can lead to the accumulation of smaller or midsize crystals in the crystallizer; a reduced elutriation flow or a separate draw-off for those particles could thus be required. Such systems can be added to existing crystallizers as separate

vessels. To do this effectively, a large flow is sent to stimulate the internal circulation of a crystallizer and the excess is returned to the crystallizer.

7.3.4. Elutriation approaches for fines removal

The approach here is to provide an upward velocity that will carry some of the particles that are smaller than an arbitrary size, called a cut point, from the crystallization zone. Usually, this is done by using a single particle-settling calculation. A particle moving by gravity in a fluid is acted upon by three forces: the buoyant force due to displacement of the fluid, gravitational forces, and a resistance to movement. When these are balanced, the particle cannot accelerate and a constant velocity is reached. This occurs quickly. Lapple and Shepherd [7.6, 7.7] show the relationship valid for spheres as follows:

$$w_s = \left[\frac{4}{3c_W}\frac{L(\rho_C - \rho_L)g}{\rho_L}\right]^{0.5} \tag{7.13}$$

For spheres when $\mathrm{Re} \equiv w_s L/v_L < 1$, this reduces with $c_W = 24/\mathrm{Re}$ to equation (7.4) (Stokes' law).

When this velocity is coupled with the required fines removal rate, the cross section of the removal zone can be calculated. The calculation is not sufficiently precise, nor is the expected requirement sufficiently precise to meet all operating conditions. As a result, the separating zone is usually divided by vertical baffles into a section with separate exits. These allow the cut point to be increased by withdrawal at the same total rate using fewer sections or by keeping the same cut point at lower withdrawal rates in fewer sections.

The withdrawal rate results from one of two considerations: (a) classified product withdrawal does not withdraw sufficient liquor or (b) the fines are to be removed for crystal size adjustment. First, a convenient cut point may be selected and the necessary flow withdrawn. Because this flow will be mixed with the product, a small cut point is indicated. For the second case, both the cut point and the flow rate need to be selected carefully.

Just how this is to be done depends on the disposal of the fines flow. If this is to be returned to the crystallizer with the crystals dissolved, the amount of material dissolved will be recrystallized, thereby increasing the crystal production rate. At the same time, the surface area for growth will be reduced. Both of these effects lead to a higher supersaturation and, possibly, a higher nucleation rate. Therefore, both the cut point and the flow rate must be chosen carefully. It should be noted that to double the number-average crystal size, one must reduce the number of crystals allowed to grow to product size by $(2^3 - 1)/2^3$, or 87.5% of the crystals nucleate; that is, the

fines removal flow must contain 87.5% of the crystals nucleated with the rate B.

With the arbitrary factor F_F, the flow rate $\dot{V}_F$ of the fines withdrawal for a volume V is

$$\dot{V}_F = F_F \frac{VB}{\int_0^{L_F} n_F dL} \tag{7.14}$$

The cut point and fines flow rate are related. A higher cut point leads to a lower flow rate, but calculations will show a larger mass of crystals removed. Thus, a balance must be achieved.

7.3.5. Hydrocyclones for classification

At first glance, hydrocyclones appear to be ideal for classification operations because they are inexpensive. However, several factors must be considered. For operation, hydrocyclones require pressure drops of about 30–600 Pa, the larger cyclones operating in the low-pressure drop end of this range. One would expect some crystal breakage and attrition. Once a cut point and hydrocyclone size have been selected, and flow rate through the cyclone is fixed by the properties of the system, densities, liquor viscosity, and slurry concentration. As a result, several cyclones must be used when the necessary flow rate is greater. This can be an advantage in that the cut point may be held with changing flows by removing or adding cyclones. Cut points can be affected by no more than about 50% by changing the flow rate to each cyclone and by about 40% in the operating ranges recommended.

Hydrocyclones are necessarily external to the crystallizer. Thus, they may be added to an existing crystallizer in order to improve the operation. The size and number of cyclones should be the result of a joint study by the designer of the crystallizer and the cyclone manufacturer. Hydrocyclones operate most successfully when the ratio of underflow to feed is set by the hydrocyclone design. Attempts to force other distributions by throttling the flows will be at the expense of greater pressure drops and the resulting grinding and attrition; see also the notes on the underflow concentration below.

7.3.6. Hydrocyclones for fines removal

Figure 7.9 shows a hydrocyclone for fines removal. The material balance around the cyclone must be developed carefully. The cyclone underflow $\dot{V}_u$ will be more concentrated in crystals than the feed $\dot{V}_f$ by a factor of nearly $\dot{V}_f/\dot{V}_u$. This concentration must remain below that value which will plug the

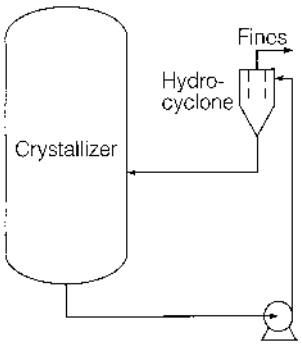

Figure 7.9. Hydrocyclone for separation operation.

system. The concentration is a function of the particle size distribution, the particle shape, the liquor viscosity, and, to some extent, the equipment configuration. A maximum operating value may be determined approximately by measuring the concentration that will settle so as to leave about 20% of the volume as supernatant liquid.

7.3.7. Hydrocyclones for product classification

The considerations are similar to those for fines removal. However, the product will now be the concentrated stream (see Fig. 7.10); this means that the liquor is not removed as fast as the crystals. No problem results if any remaining solvent is to be evaporated in the crystallizer. It should be

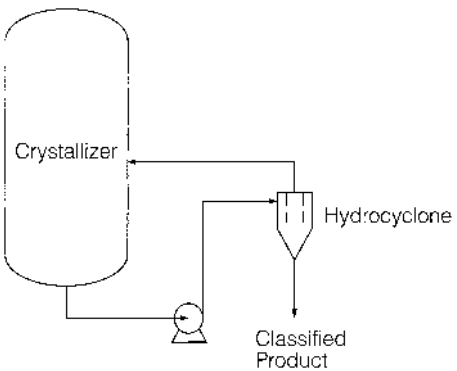

Figure 7.10. Hydrocyclone for classified product removal.

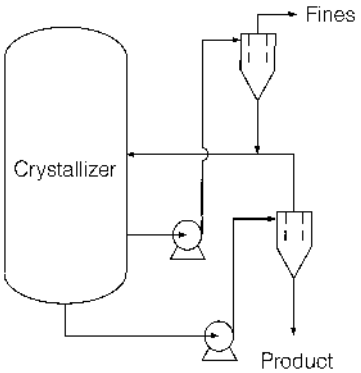

Figure 7.11. Hydrocyclone for fines and product removal.

noted that this will increase the concentration of impurities in the liquor and possibly within the crystals. Otherwise, a fines removal system must be added. Note also that the underflow product stream necessarily contains the full range of particles in the crystallizer, thereby removing all sizes. In Figure 7.11, hydrocyclones for combined classifications are shown. The pumping of a combined classification system will probably require two different pumps, because the product hydrocyclones may not require as great a pressure drop as the fines hydroclyclones.

7.3.8. Particle-size control in downstream equipment

The choice of equipment plays an important part in the ability to maintain the particle size distribution in the crystallizer product. As in the pumping systems described above, attention must be paid to the application of energy to the particles. Continuous centrifuges such as decanters, pushers, and conical screens will attrite and break crystals more than filters. Basket centrifuges have been used to avoid the breakage of needlelike materials (author's experience). Similar considerations apply to dryers and conveyors; those that apply mechanical or fluid energy directly to the particles, such as pneumatic conveyers and dryers, have a tendency to break crystals.

Centrifuges and dryers are usually sized from operation of prototypic equipment. The types that are likely to damage the particles usually offer a significant economic advantage. Therefore, in assessing the application, breakage and attrition should be measured. If the results are satisfactory, such equipment is a good choice.

7.4. Crystallizers Product Is Not Sufficiently Pure

When there is a thermodynamic distribution of impurity between the liquor and the crystals, the amount of impurity in the crystal depends on the way in which the crystallization operation is performed. The ratio of impurity to product is lowest in the feed material. For batch crystallization as the product crystallizes, the ratio of impurity to product in the liquor increases because the liquor is being depleted of product faster than of impurity. As a result, a batch crystallizer will produce crystals with the lowest impurity that can be achieved from the feed material.

A continuous crystallizer will operate at the ratio of impurity to product in the liquor with the effect of having a high ratio of impurity to product. This effect can be reduced with staged crystallization. For the situation in Figure 7.12, the following data results:

Batch crystallization, 50–30°C, continuous	32.5 ppm
Two-stage, 40 and 30°C	41.4 ppm
One-stage, 30°C	57.3 ppm

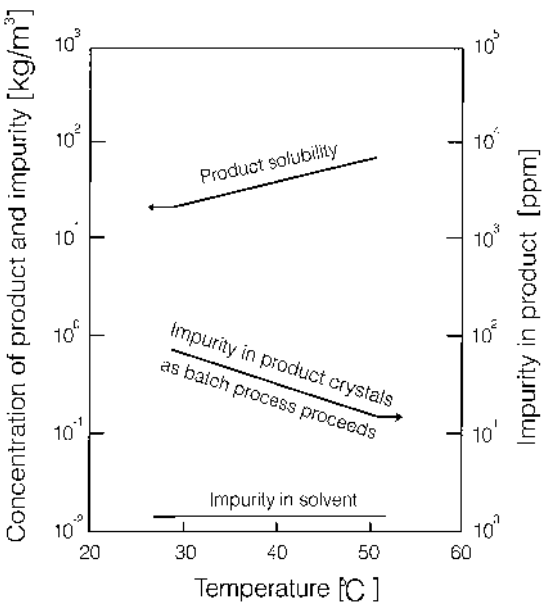

Figure 7.12. Product solubility, impurity in solvent, and impurity in product crystals as batch process proceeds against the temperature.

The more stages used, the nearer to batch impurity level the product will be.

If the impurity level cannot be reached by a single crystallization stage and mechanical separation of the liquor, a further step is needed. Such steps include dissolving/crystallization/mechanical separation, distillation, and washing in countercurrent-moving beds of crystals and clean liquid. The latter can achieve liquor removal efficiencies as high as 99.9% and will sometimes leach impurity from the crystals. Usually, however, the impurity that is cocrystallized will be removed only partially in washing operations.

7.5. Summary

It is quite clear that crystallization is only the first step toward an industrial product. The following steps must be analyzed as part of the overall process to ensure a successful economic process, which becomes part of the crystallizer optimization. The same is true of solvent recovery, purge systems, and water disposal.

REFERENCES

[1.1] A. D. Randolph, J. R. Beckman, and Z. I. Kraljevich, Crystal size distribution dynamics in a classified crystallizer. I. Experimental and theoretical study of cycling in a potassium chloride crystallizer, *AIChE J.*, *23*: 500 (1977).

[1.2] A. Mersmann, *Stoffübertragung*, Springer-Verlag, Berlin (1986).

[1.3] A. G. Jones, A. Chianese, and J. W. Mullin, Effetcs of fines destruction on batch cooling crystallization of potassium sulphate solutions, in *Proc. 9th Symp. on Industrial Crystallization* (S. J. Jancic and E. J. de Jong, eds.), Elsevier, Amsterdam, p. 191 (1984).

[1.4] J.-S. Wey and J. P. Terwillinger, Design consideration for a multistage cascade crystallizer, *Ind. Eng. Chem. Process. Des. Dev.*, *15*(3): 467 (1976).

[1.5] H. Domning, Die Grobkorn-Kristallisationsanlage des Werks Wintershall, *Kali Steinsalz*, *7*(4): 155 (1977).

[1.6] A. D. Randolph and M. A. Larson, Transient and steady state size distributions in a continuous mixed suspension crystallizer, *AIChE J.*, *8*(5): 639 (1962).

[2.1] T. Gutwald, *Über die Bestimmung kinetischer Parameter bei der diskontinuierlichen Kristallisation aus Lösungen*, Thesis, Technische Universität München (1991).

[2.2] J. Mullin and J. Nyvlt, Programmed cooling of batch crystallizers, *Chem. Eng. Sci.*, *26*: 369 (1971).
[2.3] A. G. Jones and J. W. Mullin, Programmed cooling crystallization of potassium sulphate solutions, *Chem. Eng. Sci.*, *29*: 105 (1974).
[2.4] A. G. Jones, Optimal operation of a batch cooling crystallizer, *Chem. Eng. Sci.*, *29*: 1075 (1974).
[3.1] J. Jaques, A. Collet, and S. H. Wilen, *Enantiomers, Racemates and Resolutions*, John Wiley & Sons, New York, p. 222 (1981).
[3.2] W. R. Brode and I. J. Wernert, The resolutions β-ethoxyamines, *J. Am. Chem. Soc.*, *55*: 1685 (1993).
[3.3] T. Gutwald and A. Mersmann, Evaluation of kinetic parameters of crystallization from batch and continuous experiments, *Separ. Technol.*, *4*: 2 (1994).
[3.4] T. Gutwald and A. Mersmann, Batch cooling crystallization at constant supersaturation: Technique and experimental results, *Chem. Eng. Technol.*, *13*: 229 (1990).
[4.1] J. Garside and S. N. Tavare, Mixing reaction and precipitation: Limits of micromixing in a MSMPR crystallizer, *Chem. Eng. Sci.*, *40*(8): 1085 (1985).
[4.2] B. Aslund and A. C. Rasmuson, Semibatch reaction crystallization of benzoic acid, *AIChE J.*, *38*: 328 (1992).
[4.3] A. Mersmann, M. Angerhöfer, and J. Franke, Controlled precipitation, *Chem. Eng. Technol.*, *17*: 1 (1994).
[4.4] A. E. Nielsen, *Kinetics of Precipitation*, Pergamon Press, Oxford (1964).
[4.5] R. Geisler, A. Mersmann, and H. Voit, Macro- and micromixing in stirred tanks, *Int. Chem. Eng.*, *31*(4): 642 (1991).
[5.1] C. Bernhardt, Preparation of suspensions for particle size analysis. Methodical recommendations. Liquids and dispersing agents, *Adv. Colloid Inter. of Sci.*, *29*: 79 (1988).
[5.2] J. Garside, A. Mersmann, and J. Nyvlt, *Measurement of Crystal Growth Rates*, European Federation of Chemical Engineering, Working Party on Crystallization (1990).
[5.3] D. J. Brown and K. Alexander, On-line measurement of crystal growth using a sample dilution method, in *Proc. 11th Symp. on Industrial Crystallization* (A. Mersmann, ed.), Garmisch-Partenkirchen, Germany p. 553 (1990).
[5.4] J. Jager, S. de Wolf, W. Kapwijk, and E. J. de Jong, A new design for on-line CSD-measurements in product slurries, in *Proc. 10th Symp. on Industrial Crystallization* (J. Nyvlt and S. Zacek, eds.), Elsevier, Amsterdam (1989).

[5.5] J. Jager, S. de Wolf, H. J. M. Kramer, and E. J. de Jong, On-line crystal size measurement in dense slurries, in *Proc. 11th Symp. on Industrial Crystallization* (A. Mersmann, ed.), Garmisch-Partenkirchen, Germany (1990).
[5.6] K. Leschonski, Particle size analysis and characterization of a classification process, in *Ullman's Encyclopedia of Industrial Chemistry*, Vol. B2 (B. Elvers and W. Gerhartz, eds.), VCH, Weinheim, pp. 2.1–2.33 (1988).
[5.7] R. Clift, Inertial, sedimentation, image analysis and electrozone methods of particle size analysis, in *Particle Size Analysis 1988* (*Proceedings of the 6th Particle Size Conference*) (P. J. Lloyd, ed.), John Wiley & Sons, London (1988).
[6.1] L. A. van Wijk, Incrustation in crystallizers, in *Proc. 7th Symp. on Industrial Crystallization* (E. J. de Jong and S. J. Jancic, eds.), North-Holland, Amsterdam (1979).
[6.2] L. A. van Wijk and B. G. Wienk, Incrustation prevention in industrial crystallizers, in *Proc. 8th Symp. on Industrial Crystallization* (S. J. Jancic and E. J. de Jong, eds.), North-Holland, Amsterdam (1982).
[6.3] J. L. Chandler: Effects of supersaturation and flow conditions on the initiation of scale formation, *Trans. Inst. Chem. Eng.*, *42*: 24 (1964).
[6.4] S. K. Heffels, L. J. Kuijvenhoven, and E. J. de Jong, Incrustation above the liquid level in sucrose crystallizers, in *Proc. 9th Symp. on Industrial Crystallization* (S. J. Jancic and E. J. de Jong, eds.), Elsevier, Amsterdam (1984).
[6.5] A. Mersmann, *Thermische Verfahrenstechnik*, Springer-Verlag, Berlin (1980).
[6.6] A. Mersmann, Verkrustungsprobleme – Ursachen, *Chem. Ing. Tech.*, *52*(7): 576 (1980).
[6.7] D. Hasson and J. Zahavi, Mechanism of calcium sulphate scale deposition on heat-transfer surfaces, *Ind. Eng. Chem. Fund.*, *9*: 1 (1970).
[6.8] P. Butler, Ultrasonics stops the fouling in a copper sulphate crystallizer, *Process. Eng.*, *10*: 100 (1974).
[6.9] G. Goldman and G. Spott, Krustenbildung in Kristallisationsanlagen, *Chem. Ing. Tech.*, *55*: 214 (1983).
[6.10] S. Krause, Fouling of heat-transfer surfaces by crystallization and sedimentation, *Int. Chem. Eng.*, *33*: 355 (1993).
[6.11] A. G. Duncan and C. D. West, Prevention of encrustation on crystallizer heat exchanger surfaces by ultrasonic vibrations, *U. K. AERE Harwell Research*, Report R64812 (1970).
[6.12] M. J. Ashley, Preventing deposition on heat exchange surface with ultrasound, *Ultrasonic*, *9*: 215 (1974).

[6.13] M. P. C. Wijnen and G. M. van Rosmalen, The influence of various polyelectrolytes on the precipitation of gypsum, *Desalination*, *54*: 239 (1985).
[6.14] J. Duga and B. Simon, Crystallization of sodium from aqueous solution II. Growth kinetics, *J. Cryst Growth*, *44*: 280 (1978).
[6.15] A. Chianese, S. di Cave, and B. Mazzarotta, Incrustation throughout sodium perborate crystallization, in *Proc. 11th Symp. on Industrial Crystallization* (A. Mersmann, ed.), Garmisch-Partenkirchen, Germany (1990)
[6.16] K. J. Schmid-Schönbein, Konvektive Wärme- und Stoffübertragung bei kristalliner Verkrustung von Heizflächen, *Chem. Ing. Tech.*, *48*: 1205 (1979).
[7.1] B. C. Sakiadis, Particle dynamics, in *Perry's Chemical Engineers' Handbook*, 6th ed. (R. H. Perry and D. W. Green, eds.), McGraw-Hill, New York (1984).
[7.2] C. D. Han. *Retention and washing of liquids retained by granular solids*, Thesis, MIT, Cambridge, MA (1964).
[7.3] A. Mersmann, M. Angerhöfer, T. Gutwald. R. Sangl, and S. Wang, General prediction of median crystal sizes, *Separ. Technol.*, *2*: 85 (1992).
[7.4] J. Nyvlt, O. Söhnel, M. Matuchova, and M. Browl, *The Kinetics of Crystallization*, Elsevier, Amsterdam (1985).
[7.5] M. Leva, *Fluidization*, McGraw-Hill, New York, (1959).
[7.6] C. E. Lapple, *Fluid and Particle Mechanics*, University of Delaware Press, Newark, p. 277 (1951).
[7.7] C. E. Lapple and C. B. Shepherd, Calculation of particle trajectories, *Ind. Eng. Chem.*, *22*: 605 (1959).

10

Challenges in and an Overview of the Control of Crystallizers

S. ROHANI The University of Western Ontario, London, Ontario, Canada

1. INTRODUCTION

The objective in the operation of a crystallization process is to meet product specifications: (a) a narrow crystal size distribution (CSD), (b) maximum crystal purity, (c) high yield, and (d) acceptable crystal morphology. Moreover, the manufacturer's requirements for economic and trouble-free operation should be met. Depending on the type of the product, one of the above objectives may be critical. For example, in the production of fertilizers, less significance is ascribed to product purity, whereas in the manufacture of pharmaceuticals, product purity is of utmost importance. A narrow CSD is always required; however, the desirable mean crystal size varies depending on the type of the product. Maximum yield with a given driving force is to be achieved under all circumstances subject to constraints on crystal quality. Finally, well-formed crystals with uniform morphology not susceptible to breakage are desirable.

It has been demonstrated that a generalized theory for the analysis and prediction of the CSD is available; however, the birth and death rates in the

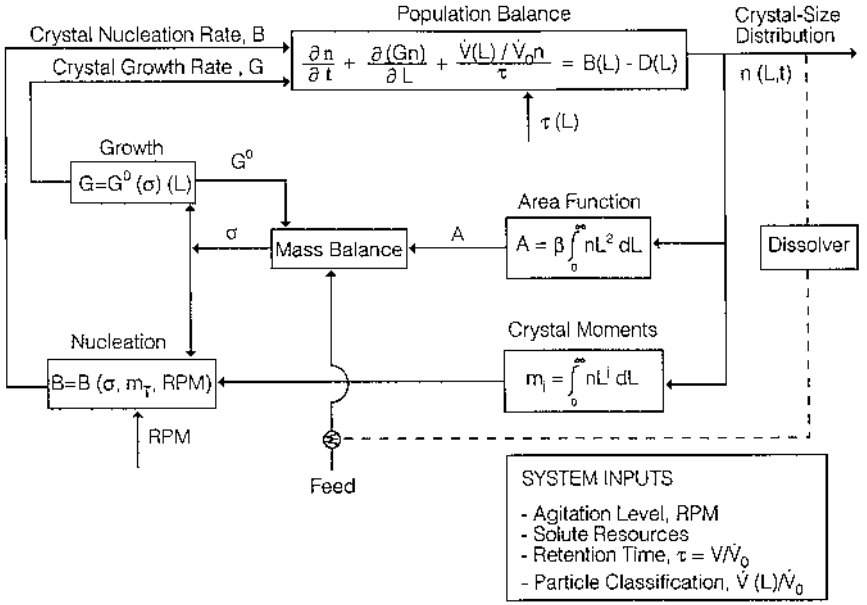

Figure 1.1. Information flow diagram of a crystallization process.

population equation are poorly understood. The principal reason for this is that presently we are unable to make a general prediction of agglomeration, attrition, and breakage rates. This is also true for the rates of nucleation. As a rule, the true supersaturation in the crystallizer is not known and can oscillate even in continuous crystallizers.

Furthermore, the process interrelations that determine the CSD in mixed-magma crystallizers are extremely complicated (see Fig. 1.1). In this information flow diagram according to Ref. [1.1], the population balance is the central equation with reference to the CSD. Besides agglomeration and attrition, the rates of nucleation and growth are the main kinetic parameters that determine the size distribution. These kinetic parameters depend strongly on supersaturation and impurities present in the solution. The true supersaturation is influenced not only by the balances of mass and energy but also by the kinetics of the crystallization process. The picture becomes even more complicated if such processes as clear-liquor advance, fines destruction, and classified product removal are taken into account. According to Fig. 1.1, the main system inputs are the agitation level, solute resources, retention time, and particle classification.

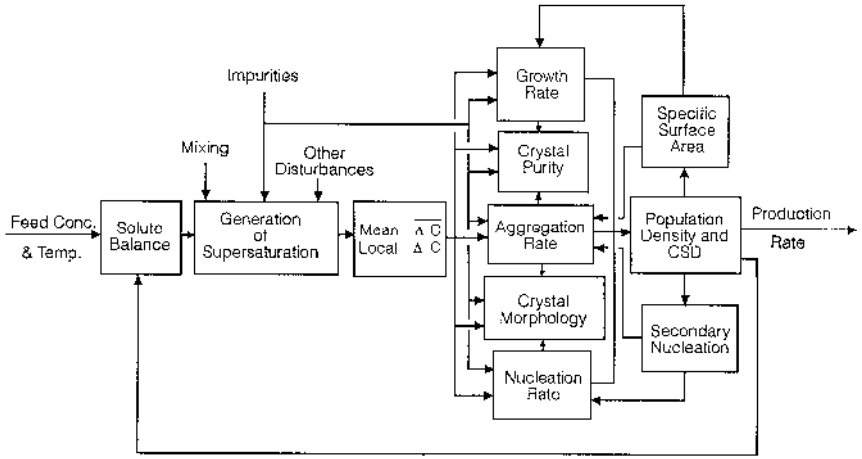

Figure 1.2. Dependence of the properties of a crystalline material on supersaturation. The interaction among variables in a crystallization process.

As discussion in earlier sections, crystallization from solution can be brought about by various mechanisms, such as cooling, evaporation, salting out, and reaction using a batch or continuous mode of operation. The common feature among these is the existence of the crystallization driving force (i.e., supersaturation). The method by which supersaturation is generated and various factors affecting its "local" and "average" values have a strong influence on all properties of a crystalline material. Figure 1.2 is a pictorial presentation of the influence of supersaturation on crystal properties and the interdependence of crystal properties. Note that the local and average values of supersaturation affect growth, nucleation, and aggregation rates, which, in turn, determine population density and the CSD. The crystal size distribution, on the other hand, determines specific surface area and magma density, which strongly affect growth rate, rate of secondary nucleation, aggregation rate, and solute mass balance in a feedback fashion. Irrespective of the mechanism of generation of supersaturation, impurities exert a strong effect on the width of the metastable zone. Impurities also influence crystallization kinetics, crystal purity, crystal morphology, and aggregation rate. Other disturbances affecting crystal properties are the intensity of mixing, heat losses from the crystallizer, variations in the crystallizer head pressure, and feed temperature and composition.

Any attempt to control a crystallization process to meet the above-mentioned product qualities should be directed toward generating and maintaining a mild and homogeneous supersaturation in the crystallizing magma at the local and average levels; see Sec. 6 in Chapter 3. This favors growth rate and prevents spontaneous nucleation. In industrial crystallizers, this objective is achieved by improving the design of crystallizers as well as controlling some of the easily measurable process variables, like temperature, pressure, level, and flow rates. Such an approach is not sensitive to frequent variations in the feed composition, feed temperature, impurities, and local degree of mixedness. Consequently, in the presence of disturbances, off-specification product is to be expected. Improvement in product quality can be assured if advanced control algorithms incorporating sophisticated sensors for on-line measurement or inference of product properties using state estimators (the extended Kalman filter) are employed. The control algorithm should have knowledge of the prevailing local and average supersaturation. If supersaturation is generated in regions where a sufficient crystal surface area does not exist, the available supersaturation will be relieved in primary nucleation and/or leads to encrustation and fouling. Moreover, the likelihood of capturing impurities either in the lattice or in the form of mother liquor inclusion is increased.

Control over crystal morphology is a very complex process. It can be realized either by a controlled growth rate through proper adjustment of supersaturation or by the addition of certain habit modifiers. The habit modifiers are either surface-active agents that adhere to a specific crystal surface retarding its growth rate or are tailor-made additives that would be incorporated in the crystal lattice at one end and slow down further growth at their other end (see Chapter 12). There is growing interest in the design and manufacture of habit modifiers, which are often product dependent [1.2–1.5].

Accordingly, in this section, the main emphasis is placed on the control of the CSD, crystal purity, and crystal yield from a suspension. Moreover, control strategies used in melt crystallization will not be considered. Conventional control strategies utilized in industrial crystallizers and recent advances in academic research to improve the CSD and product purity for batch and continuous operations are summarized. It should be borne in mind that product quality in industrial crystallizers is affected not only by the crystallizer but also by the upstream and especially downstream processes (i.e., dewatering, filtration, and drying steps). Discussion on the nature and extent of such effects, however, is beyond the scope of this chapter. Conventional sensors used in the existing control strategies are explained briefly.

2. DYNAMIC MODELING OF CRYSTALLIZATION PROCESSES

2.1. Mechanistic Modeling

Crystallization takes place in a multiphase, multicomponent system. It is concerned with particulate solids whose size and size distribution vary with time. The solution can fluctuate between a metastable and a labile state. The nucleation and growth rates can be strongly influenced by minute amounts of impurities. Therefore, for a complete description of the CSD, it is necessary to quantify the nucleation and growth rates and to apply the three conservation principles of mass, energy, and crystal population.

2.1.1. A continuous MSMPR crystallizer

The mixed suspension, mixed product removal (MSMPR) crystallizer is the analog of the continuous stirred-tank reactor (CSTR) in chemical reaction engineering. Similar to a CSTR at *steady state*, which has an exponential residence time distribution, an MSMPR operating at *steady state* has an exponential crystal size distribution. In this section, however, we present the transient behavior of an MSMPR expressed by solute and solvent dynamic mass balances and the dynamic crystal population density. The dynamic energy balance is redundant if we assume that the MSMPR is operated isothermally. The isothermal operation, in practice, can be realized using an independent tight temperature controller.

Let us consider an MSMPR crystallizer. Crystal-free feed enters at solvent mass flow rate $\dot{M}_i$ (kg/s) and a temperature ϑ_i (K) and dissolved solute concentration of W_i (kg anhydrous solute/kg solvent). The crystallizer has a working volume of V (m^3) with a solvent capacity of M° (kg), operated at a constant temperature ϑ (K). The solute concentration is W (kg anhydrous solute/kg solvent) and the crystal suspension density or magma density is m_T° (kg anhydrous crystals/kg solvent). The assumption of MSMPR implies that the magma density in the crystallizer is homogeneous and it is the same as in the product line. Therefore, the product is withdrawn at a solvent mass flow rate of $\dot{M}_C$ at a temperature ϑ and solute concentration W with a suspension density m_T° (see Fig. 2.1 for the schematic of a complex continous crystallizer).

Solvent balance

Note that although the crystallizer working volume is assumed to be constant by an independent level controller, the solvent capacity, M°, inside the vessel may undergo transient changes due to the variations in m_T° with time. Therefore, we have

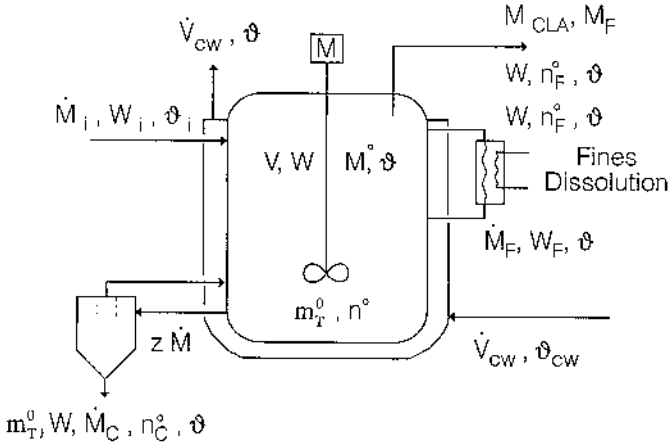

Figure 2.1. Schematic of a continuous crystallizer with fines dissolution, clear-liquor advance, and product classification.

$$\frac{dM^\circ(t)}{dt} = \dot{M}_i(t) - \dot{M}_C(t) \tag{2.1}$$

with the initial condition $M^\circ(0) = M_0^\circ$ which is the solvent capacity at $t = 0$.

Component mass balance

The crystallizing solute mass balance can be written as

$$\frac{d\{M^\circ(t)[W(t) + m_T^\circ(t)]\}}{dt} = \dot{M}_i(t)W_i(t) - \dot{M}_C(t)[W(t) + m_T^\circ(t) \tag{2.2}$$

The initial condition, $W(0) = W_0$, represents the crystallizing solute concentration at $t = 0$. For a multicomponent system in which only one component crystallizes, similar equations may be written for all components, excluding the terms which account for the solid-phase formation.

Crystal population density balance

Assuming a crystal-free feed stream, no crystal breakage and agglomeration, homogeneous magma density, representation product removal, and uniform crystal shape, the population balance can be written as

$$\frac{\partial[M^\circ(t)n^\circ(L, t)]}{\partial t} = -M^\circ(t)G(t)\frac{\partial n^\circ(L, t)}{\partial L} - \dot{M}_C(t)n^\circ(L, t) \tag{2.3}$$

Note that equation (2.3) at steady state results in an exponential crystal population density. The initial condition of equation (2.3) represents the crystal population density in the crystallizer at $t = 0$, which can be taken

either as a *steady-state* crystal size distribution or as zero corresponding to a clear liquor start-up condition. The boundary condition is the ratio of the nucleation rate to growth rate:

$$n(0, t) = \left[\frac{dN}{dL}\right]_{L\to 0} = \left[\frac{dN}{dt}\right]_{L\to 0} \frac{dt}{dL} = \frac{B_0(0, t)}{G(0, t)} \tag{2.4}$$

The above equations on solute and solvent mass balances and crystal population density balance with their initial and boundary conditions (nucleation and growth rates) render a complete description of the transient behavior of an MSMPR crystallizer.

The moments equations

Further equations on the moments of the crystal population density may be developed by defining the jth moment of the population density as

$$m_j(t) = \int_0^\infty L^j n^\circ(L, t)\, dL \tag{2.5}$$

The zeroth moment represents the number of crystals per unit mass of solvent, the first moment is the total length of all crystals (placed side by side) per unit mass of solvent, the second moment is related to the area of crystals per unit mass of solvent through the area shape factor, and the third moment is related to the volume of crystals per unit mass of solvent. The magma density can be defined in terms of the third moment by

$$m_T^\circ(t) = \rho_c k_v m_3(t) \tag{2.6}$$

The moments equations can be obtained by multiplying both sides of equation (2.3) by $L^j\, dL$ and integrating over the entire crystal size range:

$$\frac{d[M^\circ(t)m_j(t)]}{dt} = 0^j B_0 M^\circ(t) + j m_{j-1}(t) G(t) M^\circ(t) - \dot{M}_C(t) m_j(t) \tag{2.7}$$

Solution of the population balance along with the mass and energy balances will render the complete description of the CSD. This requires extensive computational effort for the solution of a partial differential equation and a set of ordinary differential equations. On the other hand, solving the moments equations with the mass and energy balances involves only ordinary differential equations at the expense of losing detailed information on the CSD. There are, however, two terms which describe the CSD; the mean crystal size and the coefficient of variation (CV), which can be obtained from the moments of the crystal population density.

2.1.2. A continuous complex crystallizer (Fig. 2.1)

In the case of a complex crystallizer equipped with clear-liquor advance, fines dissolution, and product classification, the last term in the population balance [Eq. (2.3)] must be multiplied by a product withdrawal function given by

$$\gamma(L) = \begin{cases} \dfrac{\dot{M}_F + \dot{M}_C + \dot{M}_{\mathrm{CLA}}}{\dot{M}_C} = R, & 0 < L \le L_F \\ 1, & L_F < L \le L_P \\ z, & L_P < L \end{cases} \tag{2.8}$$

The material and energy balances will not change significantly.

Because industrial continuous crystallizers are very large (each stage has a volume of 150–200 m^3), there will be inhomogeneous distribution of supersaturation and solids in each effect. Therefore, in modeling of such systems, each effect is divided into several compartments that can be assumed approximately homogeneous, with the pertinent conservation laws of mass, energy, and crystal population. Appropriate internal [in draft tube baffled (DTB) crystallizers] and external (in Oslo crystallizers) circulation rates should be selected. This technique has been applied [2.1] to an evaporative KCl–NaCl–H_2O pilot plant 1-m^3 crystallizer and a two-stage DTB industrial crystallizer circuit. In Ref. [2.1], internal and external fines dissolution have been adopted. Moreover, crystallization and dissolution rates of both KCl and NaCl are considered.

2.1.3. Multiple-effect evaporative/cooling industrial crystallizers

In order to save energy, it is customary to use multistage evaporative/cooling crystallizers in series. Four to six crystallizers are placed in each circuit. Saturated feed is charged to the first effect, which is held at a pressure slightly lower than atmospheric pressure. The overflow from each effect, often after fines dissolution, is fed to the subsequent effect, which is held at a lower pressure and temperature. The product slurry can be withdrawn from all effects or only from the last stage. The extension of the above-presented modeling approach to multieffect crystallizers has been discussed by Rohani [2.2, 2.3].

2.1.4. A batch crystallizer

A batch crystallizer is often seeded with a narrow size distribution of solute crystals. The time of addition of seeds and the amount and their size distribution are among factors which influence the CSD. Therefore, in model-

ing a batch crystallizer, it is necessary to write down the crystal population balance both for the seed crystals and the newly generated nuclei by primary and secondary nucleation. Such an approach results in a bimodal CSD. For modeling of a seeded cooling batch crystallizer, equipped with fines dissolution, refer to Ref. [4.14].

2.2. Process Identification, the Blackbox Modeling

2.2.1. Linear modeling using time series analysis

Apart from the physical modeling of a crystallization process discussed earlier, process identification and parameter estimation methods have also been used to identify both linear [state space and autoregressive exogenous [ARX)] and nonlinear neural networks models for batch [2.4, 2.5, 4.14] and continuous [2.6–2.8] crystallizers. A general ARX model of a MIMO (multi-input, multi-output) system can be written as

$$Y(z) = G(z)U(z) \tag{2.9}$$

where $G(z)$ is the pulse transfer matrix and $U(z)$ and $Y(z)$ are the input and output vectors. The input vector consists of the manipulated variables and the output vector consists of the controlled variables. Each element of $G(z)$, $g_{ik}(z)$, can be obtained by time series analysis in terms of the ratio of two polynomials $A_{ik}(z)$ and $D_{ik}(z)$ and a time delay term d_{ik} between input k and output i:

$$g_{ik}(z) = \frac{A_{ik}(z)}{D_{ik}(z)} z^{-d_{ik}} \tag{2.10}$$

Based on the visual inspection of the dynamic response curves between the inputs and the outputs, the order of the polynomials is usually chosen as 1 or 2.

The choice of the optimal input signal is critical in an identification experiment. The input signal must be uncorrelated with the process noise, it must have the proper frequency content (as a general rule, this is around the break frequency of the process), and sufficient amplitude of excitation. Two types of input signals are used in process identification. The first is a pseudorandom binary signal (PRBS) whose switching interval is the main design parameter. In general, this should be chosen between half to one effective time constant of the process. The second type of the input signal is a random-magnitude random-interval (RMRI) signal which covers a larger range of frequency spectrum. This technique has been applied [2.6] to a continuous crystallizer with three inputs and three outputs.

2.2.2. Nonlinear modeling using neural networks

A nonlinear model for dynamic systems with sampled input and output data can be expressed as

$$Y_m(t) = f\{\hat{Y}(t-1), \ldots, \hat{Y}(t-k_y), U(t-1), \ldots, U(t-k_u)\} \tag{2.11}$$

where $Y_m(t)$ is the model output vector at time t, f is a nonlinear function, U is the input vector, $\hat{Y}$ is the process output vector, and the k's are integers indicating the model orders. Many procedures have been suggested to identify (determine) the function f using the input–output process data. One approach is to use artificial neural networks. The artificial neural networks are able to generate nonlinear mapping between input and output data. Neural networks can be considered as functional expansions to equation (2.11), in which the expansion is based on nonlinear functions employed in neural units. Both recurrent and feedforward neural networks were employed in Ref. [2.6] to identify a continuous crystallizer. Training of the networks was achieved by minimizing the performance index $J(w, w_0)$ defined as

$$J(w, w_0) + \frac{1}{2}\sum_{\Omega}(\hat{Y} - Y_m)^2 \tag{2.12}$$

where w and w_0 are the networks weights and Ω is the entire domain of samples used to train the network.

Linear modeling provided simple structures. Neural-network-based nonlinear modeling, on the other hand, resulted in complicated model structures but resulted in better accuracy both for steady-state and dynamic conditions. A comprehensive comparison of the results is available in Ref. [2.6].

3. INSTRUMENTATION IN CRYSTALLIZATION CONTROL

3.1. Conventional Instrumentation

The major process variables that describe the state of a crystallizer-crystal size distribution, fines suspension density, supersaturation, and crystal purity cannot be measured on-line with sufficient accuracy using the existing instrumentation in the market. Consequently, measurements of secondary variables, such as temperature, pressure, level, and flow rate, are used to infer the primary variables. The sensors used for measurement of the secondary variables in a crystallization process are basically the same as for other processes, with the exception that their location in the crystallizer

must be carefully selected to minimize solids deposition. Any encrustation grown on the surface of a sensor will result in erroneous measurement and an increase in the time constant of the sensor, which necessitate frequent tuning of the controller and eventual instability of the control loop. For example, it would be preferable to install the temperature sensor in the crystallizer headspace instead of immersing it in the bulk solution. A noncontract flow meter such as a magnetic flow meter, ultrasonic-level transmitter, or radiation sensor for measurement of the magma density (as opposed to a differential pressure sensor) would work better. Frequent solvent flush of the instrumentation is necessary for smooth operation.

3.2. Particle-Size Measurement

Several instruments have been used for the on-line measurement of the CSD. Rovang and Randolph [3.1] used an electronic zone-sensing particle analyzer, a Coulter® counter, for the on-line measurement of the CSD. Numerous problems, such as excessive electrical noise and frequent plugging of the orifice, were encountered. In a subsequent attempt, Randolph et al. [3.2] used the Microtran® particle-size analyzer, based on forward low-angle laser-light-scattering technique. This instrument allowed measurement of particles in an ideally conditioned sample cell, in the size range 2–170 μm, which was subsequently extended to 0.7–700 μm at solids concentrations up to about 0.1% by volume. Some of the operational difficulties encountered with the Coulter counter were overcome at the expense of poor precision. Multiple scattering at high solids concentration, high background noise, and window cell fouling were additional problems. The Brinkmann® particle-size analyzer, based on the measurement of the time of travel of a laser beam across a particle and the rotational speed of a wedge prism, is expensive and suffers from the problems mentioned earlier. Other reasonably priced forward laser-scattering probes are now available in the market which can be used for both size and shape characterization.

Lasentec® has introduced an in-line laser sensor based on focused beam reflectance measurement (FBRM®) technique which measures the chord-length distribution in terms of a 4–20 mA signal. The major advantage of this instrument is its reproducibility and that it can work at high solids concentration of up to 30 vol%. Another advantage of this sensor over the other particle-size analyzers is the fact that it can be located in the crystallization magma and withdrawal of a representative sample is no longer needed. The probe tip is, however, susceptible to occasional fouling and attachment of small air bubbles. The other difficulty is that the meas-

urements are in terms of the chord-length distributions and not the size; that is, one gets a Normal distribution of the chord length even for mono-sized spherical particles. Inference of the CSD from the measured chord-length distribution has been discussed in Ref. [3.3] for spherical and ellipsoidal particles. The resolution of the probe has been improved in the most recent version of the probe which is capable of reporting the chord-length distribution from 0 to 1000 μm over 4000 channels.

Ultrasound spectroscopy provides another possibility for the size measurement of larger particles at high solids concentration of up to 50 vol%. The major disadvantage of this technique is its sensitivity to temperature changes which requires careful calibration.

Interference from the air bubbles and insoluble foreign particles is common to all the instruments described earlier. The withdrawal of representative samples from the crystallizer is difficult and would have to be performed isokinetically and with extreme care; see Sec. 5 of Chapter 9. Crystallization or dissolution in the sample line should be prevented. The particle-size analyzer should be placed as close as possible to the crystallizer, which may not always be convenient.

3.3. Supersaturation Measurement

On-line estimation of supersaturation is a very difficult task. Various methods have been suggested in the literature, including the measurement of the density of the clear liquor. One instrument capable of such a measurement is the Anton Paar® DPR 407 YE measuring cell in conjunction with the mPDS 2000 evaluation unit density meter. Another sensor for estimation of the supersaturation is shown in Figure 3.1. This sensor is the modified version of the fines suspension density transmitter (FSDT) developed by Rohani and Paine [4.15]. A clear-liquor sample is withdrawn from the crystallizer. The sample is cooled by circulating water through the jacket of the sample cell. The temperature, ϑ_1, at which the percent transmittance of an infrared light beam passing through the sample cell drops sharply (the onset of spontaneous nucleation) and the crystallizer temperature, ϑ_2, yield a temperature difference, $\Delta\vartheta_s = \vartheta_2 - \vartheta_1$, which is related to the supersaturation. Withdrawal of a clear-liquor sample from the crystallizer could be achieved using an inverted cylinder bent away from the suspension flow. A more precise method for the determination of supersaturation is the Raman and Fourier-transform infrared (FTIR) spectroscopy.

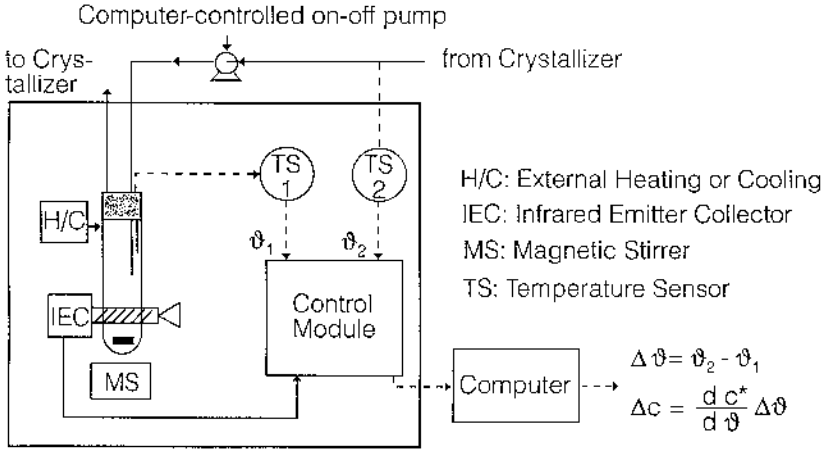

Figure 3.1. Schematic of a sensor for the on-line estimation of supersaturation or fines suspension density in terms of $\Delta\vartheta$.

3.4. Measurement of Fines Suspension Density

On-line estimation of fines suspension is achieved by collecting a representative slurry sample containing fine crystals from a quiescent zone within the crystallizer. The sample is stirred vigorously and heated by a heating element while the percent transmittance of an infrared light beam through the sample cell and the sample temperature are measured. The temperature at which the percent transmittance reaches a plateau, ϑ_1, and the crystallizer temperature, ϑ_2, provide a temperature difference, $\Delta\vartheta_F = \vartheta_1 - \vartheta_2$, which is related to the fines suspension density. A modified version of this instrument based on the Beer–Lambert's law was developed by Tadayyon et al. [3.4]. The modified sensor is capable of on-line measurement of the solids concentration, m°, or the mean particle size, $L_{4,3}$ using the measured turbidity of the slurry, τ, at a given wavelength λ:

$$\tau(\lambda) = \alpha L_{4,3}^{\nu} m^\circ \tag{3.1}$$

The constants α and ν are obtained by calibration. In order to account for the insoluble background particles, the same sensor was employed using two infrared detectors [3.4].

3.5. Particle Shape Characterization and Classification

Shape characterization of crystals can be performed by image analysis. Off-line image analysis from pictures taken by an optical or scanning electron microscopy has advanced tremendously. Mathematical morphology and

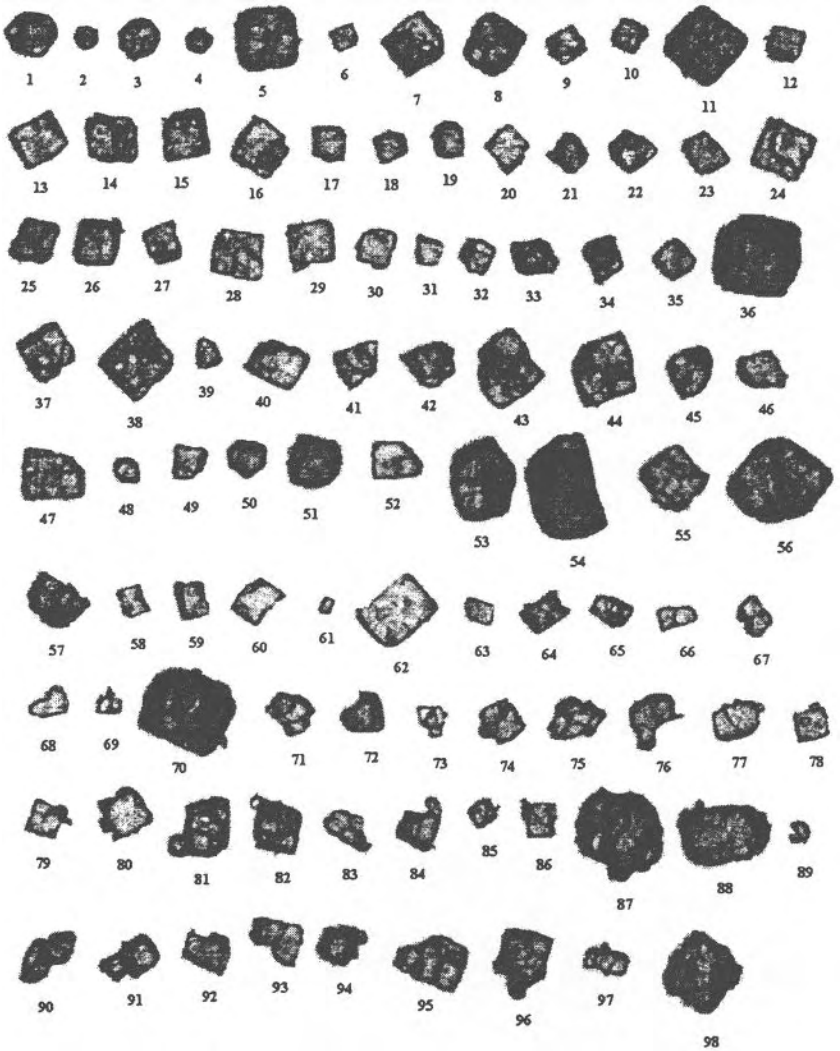

Figure 3.2. Total population of 98 KCl crystals characterized by Fourier descriptors and geometric/morphological parameters.

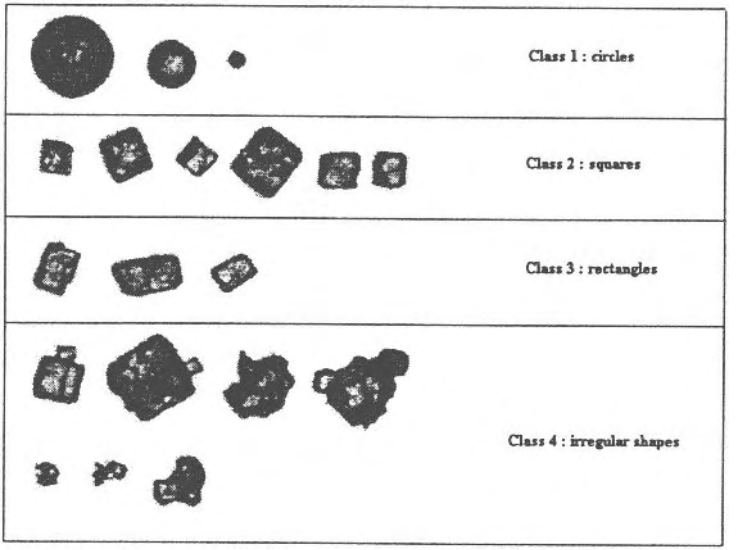

Figure 3.3. Various shape classes of KCl crystals for the training of the neural networks and the discriminant factorial analysis to classify crystals shown in Fig. 3.2.

Fourier descriptors have been used [3.5, 3.6] for shape characterization. Figure 3.2 shows a population of crystals whose shape (or the individual crystals and/or of the entire population) is to be characterized in terms of various categories depicted in Figure 3.3. A number indicating the shape of a crystal or the shape of the entire population of the crystals can be assigned by the principal component analysis or feedforward neural networks [3.5, 3.6] for shape classification. On-line crystal shape characterization/classification using fiber optics is the leading technology. However, enhanced computational power and automated focusing will have to advance before making this a reality.

3.6. Characterization of Polymorphism

Polymorphism and crystal structure can be determined using the x-ray diffraction method, atomic force microscopy, or the synchrotron light source. All these techniques require substantial capital costs but offer great potential in the manufacture of pharmaceutical and specialty chemicals in the years to come.

3.7. The Final Control Element

The final control elements, such as control valves and variable-speed pumps, can present potential problems for line plugging, crystal attrition, and secondary nucleation. The flow rate in the lines should be maintained above a minimum to prevent plugging due to solids settling. Control valves that do not create a cavity, such as pinch valves, are more suitable. Low-head positive-displacement variable-speed pumps minimize attrition and are recommended. Facilities for line flush should be provided in the case of line plugging.

4. CONTROL OF CRYSTALLIZATION PROCESSES

Industrial crystallizers combine improved equipment design and process variables manipulation to achieve satisfactory control of crystal properties. Economical operation calls for heat integration and multiple-effect continuous crystallizers (see Chapter 15). Such measures, however, introduce further interactions among process variables and complicate the control effort. In what follows, a brief description of control principles used in the operation of industrial batch and continuous crystallizers is presented. Reference is also made to recent research on the subject. This description is not comprehensive and is meant to provide an introduction to the subject.

4.1. Batch Operation

Batch crystallizers are used primarily for reactive precipitation and crystallization in the production of fine chemicals, pharmaceuticals, dyestuffs, and other specialty chemicals. They handle a relatively small volume of materials, ranging from 0.02 to 20 m^3. They operate in a transient manner; therefore, supersaturation and other process variables vary significantly in an uncontrolled batch operation, resulting in excessive nucleation and undesirable product quality. Figure 4.1 shows a typical glass-lined jacketed vessel equipped with a variable-speed agitator and a baffle assembly to provide mixing. In the case of vacuum crystallizers, a condenser is also installed to provide a partial vacuum. Figure 4.2 shows a forced-circulation DTB batch crystallizer with external cooling.

In batch crystallizers, control is achieved using (a) improved mixing at the macroscale and molecular level in the case of reactive precipitation processes, which often have a very short reaction time in the order of a few milliseconds, (b) optimal cooling or reactant addition rate to generate

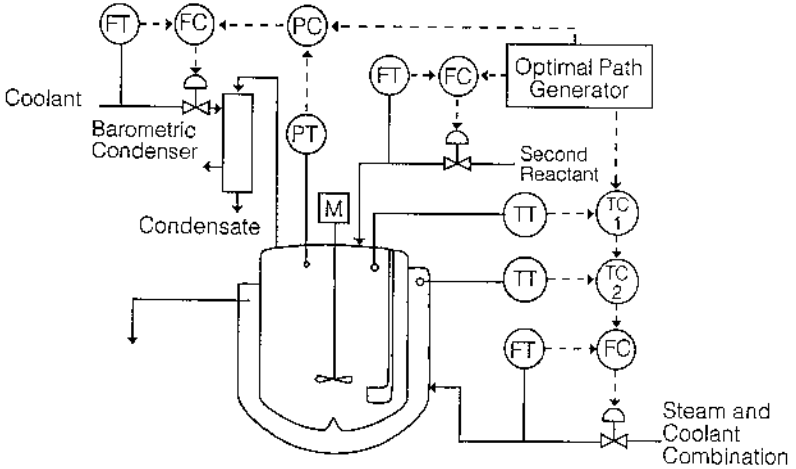

Figure 4.1. Schematic of a surface-cooled batch crystallizer with the associated instrumentation.

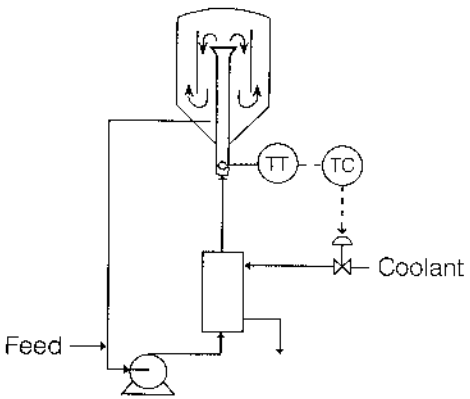

Figure 4.2. Forced-circulation DTB batch crystallizer.

constant supersaturation during a batch or semibatch operation, (c) seeding with a narrow distribution of product crystals, and (d) fines dissolution.

4.1.1. Mixing

It is important to generate a uniform and mild supersaturation within the crystallization magma (i.e., a uniform distribution of solute molecules or

ions and negligible temperature gradient at the macro-scale and molecular level) during the course of crystallization. Moreover, a uniform solids suspension density provides homogeneous distribution of crystal area for growth within the bulk solution. If the local supersaturation is high where there is a deficiency of crystal surface area for growth, spontaneous nucleation will initiate and lead to a small mean crystal size and a broad CSD. At very high local supersaturation, excessive nucleation occurs even in the presence of crystals. Good bulk mixing can be provided by improving the crystallizer configuration (e.g., by inserting baffles and draft tubes, by appropriate selection of the location of the feed pipes, and by increasing the agitation rate and using high efficiency impellers with high pumping capacity). The resulting increase in the secondary nucleation rate due to the high shear rate is less than the increase in spontaneous nucleation due to poor mixing in the regions of high supersaturation at feed entries in reactive crystallization or close to the cooling surfaces in cooling crystallizers (compare Sec. 1.2 of Chapter 3). In semibatch operation, gradual addition of a nonsolvent diluent or the second reactant for reactive precipitation processes in the impeller region, where the intensity of turbulence is maximum, is another method of generating uniform supersaturation. In a reactive precipitation process involving fast reactions, the time constants of bulk mixing, micromixing, reaction, nucleation, and growth should be estimated. The relative magnitude of these time constants will determine the significance of mixing at macro- and micro-scales on the crystal properties. If micromixing proves to be important, special care should be exercised in the design of the feed pipe diameter (to prevent backmixing), the feed entry location, the reactant addition rate, and the rate of energy dissipation per unit mass by the stirrer. Gradual increase in the magma suspension density and continuous addition of one of the reactants causes a steady increase in the volume of the crystallizer, which calls for increasing agitator speed toward the end of batch to provide good mixing. The effect of mixing on the CSD in reactive precipitation has been investigated by many workers [4.1–4.5].

The feed location of the second reactant and adjustment of the agitator speed must be controlled carefully to ensure good mixing of the solute molecules, negligible temperature gradients, and uniform solids suspension leading to sufficient crystal surface area for growth in the bulk solution. Control can be realized by improving the crystallizer configuration and by manipulation of the stirrer speed and proper selection of the feed pipe location. Manipulation of the agitator speed can be performed by a controller if automation of this variable proves to be economically feasible.

4.1.2. Optimal cooling rate, evaporation rate, or reactant addition rate

Generation of supersaturation depends mainly on the cooling rate in cooling crystallization, on the solvent removal rate in evaporative crystallizaiton, and on the rate of reactant addition in reactive precipitation. Significant improvement in the product CSD has been observed using an optimal cooling rate in comparison with a linear cooling rate or a natural cooling rate (compare Sec. 2 in Chapter 9). In natural cooling, a constant-temperature coolant is used throughout the batch. Accordingly, at the beginning, when the temperature difference between the coolant and the bulk solution is the largest, supersaturation will exceed the metastable limit and spontaneous nucleation and wall fouling result, leading to undesirable CSD, loss of product, and increased cycle time for cleaning. In optimal cooling, however, the cooling profile to ensure optimization of a performance index is sought after. The performance index could be defined as constant supersaturation throughout the batch [4.6, 4.7] or minimization of the squared deviations of the mean size from a desired value [2.4, 2.5, 4.8]. These methods involve simultaneous solution of population density balance, energy balance, and solute balance in a batch crystallizer linked to an optimization algorithm. Rohani and Bourne [4.9] have proposed a simple numerical method to determine the optimal cooling policies to generate constant supersaturation and constant nucleation rate without resorting to optimization algorithms. Mayrhofer and Nyvlt [4.10] have derived an analytical expression for the optimal temperature profile of a seeded and an unseeded batch crystallizer:

$$\frac{\vartheta_a - \vartheta}{\vartheta_a - \vartheta_w} = \left[1 - K\left(1 - \frac{t}{t_w}\right)\right]\left(\frac{t}{t_w}\right)^3 \tag{4.1}$$

were ϑ is the crystallizer temperature, ϑ_a and ϑ_w are the initial and final temperatures, t is the time, t_w is the total batch time, and $\mathrm{K} = (1 + 4N_s^\circ / B_0 t_w)^{-1}$ is a parameter ranging between 0 (negligible nucleation) and 1 (unseeded batch). N_s° is the number of seed crystals per unit volume of solvent, and B_0 is the nucleation rate per unit volume of solvent.

The optimal cooling, evaporation, and reactant addition rates are implemented on the crystallizer using low-level controllers in a supervisory control fashion; that is, the optimal trajectories are sent as set points to the flow, temperature, or pressure controllers to force the crystallizer to follow an optimal path. Figure 4.1 shows the hierarchy of control algorithms in which the calculated optimal cooling rate, evaporation rate, or reactant addition rate are sent to temperature, pressure, and flow controllers, respectively. Often, to achieve better and faster control, cascade control is used to eliminate disturbances within the inner temperature and flow loops. Temperature control is achieved by throttling the flow rate of

steam–water mix to the crystallizer jacket. To increase the operational temperature range, a heat transfer oil may be used. Under certain circumstances when large cooling rates are required, a refrigeration system may be necessary. If spontaneous nucleation is to be avoided, the maximum temperature difference between the cooling surface and the bulk solution should not exceed the metastable limit. Higher cooling rates can be achieved by adiabatic evaporation without the wall fouling encountered in surface cooling. An optimal evaporation rate can be achieved by adjusting the vacuum source, which may be a vacuum pump, a barometric condenser, a steam ejector, or a combination thereof. An optimal reactant addition rate or nonsolvent diluent addition rate can be achieved by flow control of these streams. All three modes of generating supersaturation (i.e., cooling, evaporation, and reactant/nonsolvent addition) may be combined for higher efficiencies at the expense of requiring advanced controller design to deal with possible interactions among these modes.

Miller and Rawlings [2.5] have used on-line parameter estimation technique, based on the measurement of clear-liquor density and light transmittance through a slurry sample to determine the kinetic parameters in a cooling batch crystallizer. The estimated kinetic parameters were combined with a model predictive control approach to improve the terminal product crystal size in the batch crystallizer. They observed an increase in the terminal mean crystal size compared to a natural cooling run.

Recently, a nonlinear geometric control algorithm including an extended Kalman filter (EKF) for state estimation has been applied to maintain supersaturation at a prespecified level during the operation of a batch crystallizer [4.11]. The supersaturation as well as the first four leading moments of the population density function were estimated by the EKF using the measured crystallizer temperature and the clear-liquor density collected by an in-line density meter (see Fig. 4.3). The required inlet cooling water to the cooling jacket to maintain the supersaturation at a set-point is calculated by the non-linear geometric controller (NGC). The inlet jacket temperature is manipulated by a split-range controller shown in Figure 4.3. In order to avoid a bimodal distribution in the potash alum batch cooling crystallizer, the supersaturation set point toward the end of batch was reduced as shown in Figure 4.4. The mean crystal size was increased by 11% and the coefficient of variation was reduced by 42% compared to the linear cooling mode.

4.1.3. Seeding

Seeding with a narrow distribution of product crystals prevents spontaneous nucleation and results in an improved CSD. Seeding is often performed

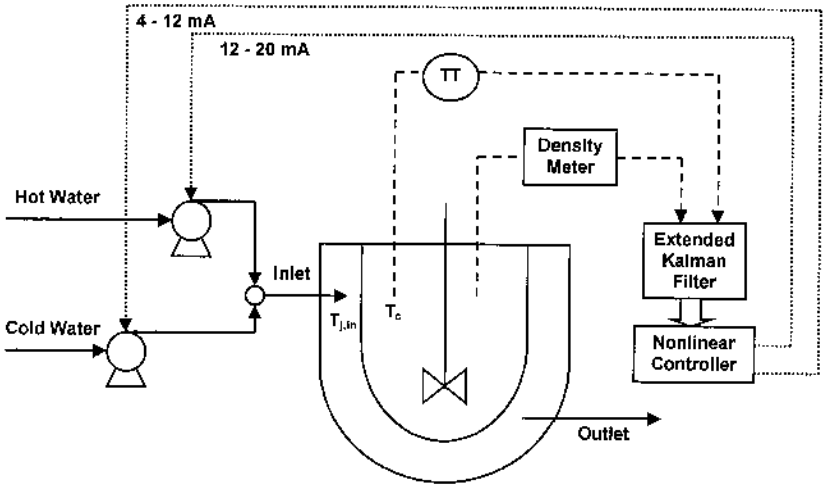

Figure 4.3. The piping and instrumentation diagram of the EKF NGC used for the control of supersaturation in a cooling batch crystallization of potash alum.

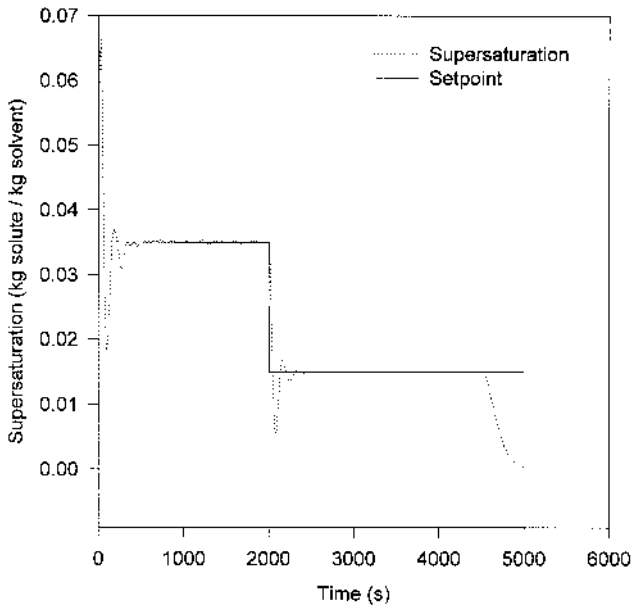

Figure 4.4. The set point and the actual supersaturation profiles during cooling batch crystallization of potash alum using the EKF-based nonlinear geometric controller.

manually. The time of addition of seed crystals is very critical and should be at the start of the operation to avoid spontaneous nucleation (compare Sec. 2 in Chapter 9). Breeding due to the adherence of small crystals to the surface of seed crystals should be avoided completely by prewashing the seed crystals with the mother liquor. If proper and sufficient seeding is utilized, spontaneous nucleation may be avoided even when a natural cooling policy is employed, leading to a unimodal distribution of the final crystal mass.

4.1.4. Fines dissolution

Fines dissolution is not commonly practiced in industry for batch crystallizers; however, it has been used by academic researchers to improve the product CSD in both an open-loop manner [4.12] and in a feedback control configuration [4.13, 4.14]. Excessive fines, generated during periods of high supersaturation, can be withdrawn from the quiescent zone of the crystallizer, dissolved by the addition of either solvent or heat and returned to the crystallizer. The advantage of this technique over optimal control of batch crystallizers discussed earlier is that it is sensitive to random disturbances, which may cause excessive fines generation. The off-line optimal control is basically an open-loop policy that minimizes fines generation; it is incapable of responding to the disturbances that may produce the fines. Jones and Chianese [4.12] have shown that although optimal operation of batch crystallizers improves the product CSD, some fines will be formed even at low levels of mean supersaturation. Fines destruction at a constant rate was shown to be capable of improving the CSD under these conditions. Rohani et al. [4.13] proposed a feedback scheme for the control of the CSD. The algorithm was based on the on-line measurement of fines suspension density and manipulation of the fines dissolution rate. Measurement of fines suspension density was performed by the on-line measuring device developed by Rohani and Paine [4.15]. A proportional-integral controller was used and significant improvement in the product CSD was achieved. Rohani and Bourne [4.14] in a numerical simulation of a potash alum batch cooling crystallizer, used a self-tuning regulator for the feedback control of the CSD. They showed that fines dissolution was more effective than controlled cooling operation in increasing the product mean size and the product yield and in decreasing the spread of the crystal size distribution. The objective was to demonstrate that the feedback control scheme based on indirect measurement of fines suspension density and regulation of fines dissolving rate is superior to the conventional schemes using controlled cooling or seeding policies. This control scheme is a closed-loop system and hence has regulatory and command-following capabilities. The

performance of a minimum-variance self-tuning controller (MVSTC) for the CSD control in a batch crystallizer was compared with a PI controller in terms of its ability to improve the product mean size and its coefficient of variation. The experimental and simulation results of the implementation of the scheme on a batch cooling crystallizer were compared. The manipulated variable was $F(k)$, the volumetric flow rate of suspension in the fines loop, and the controlled variable was a temperature difference $\Delta\vartheta$ representing the fines suspension density. For the minimum variance controller, a single-input single-output model was used to describe the process:

$$\Delta\vartheta_F(z) = \frac{A(z^{-1})}{D(z^{-1})}F(z) + \frac{1}{D(z^{-1})}\xi(z^{-1}) \tag{4.2}$$

$$A(z^{-1}) = 1 + a_1 z^{-1} + a_2 Z^{-2} + \cdots + a_{n_A} a_{n_A} z^{-n_A} \tag{4.3}$$

$$D(z^{-1}) = d_0 + d_1 z^{-1} + d_2 z^{-2} + \cdots + d_{n_D} z^{-n_D} \tag{4.4}$$

where $\xi(z^{-1})$ is a zero mean random white noise, and $a_1, \ldots, a_{nA}, d_0, \ldots, d_{nD}$ are process model parameters to be determined. Let us define the measured input/output vector, $\phi(k)$, and the parameter vector, $\eta(k)$ by

$$\phi^T(k) = [-\Delta\vartheta_F(k), \ldots, -\Delta\vartheta_F(k - n_A + 1), \\ d_0 F(k - k_d - 1), \ldots, d_0 F(k - n_D - k_d)] \tag{4.5}$$

$$\eta^T(k) = \lfloor a_1, \ldots, a_{n_A}, d_0, \ldots, d_{n_D} \rfloor \tag{4.6}$$

where k_d is the integer multiple of sampling/control interval in the process time delay. The minimum variance controller at the kth control interval is

$$F(k) = -\frac{\phi^T(k)\hat{\eta}(k)}{d_0} \tag{4.7}$$

where $\hat{\eta}(k)$ is the least squares estimate of the parameter vector. A recursive least squares parameter estimation technique with a variable forgetting factor was used for the estimation of the parameter vector in a recursive manner. The proposed control scheme was compared with the traditional control strategies using optimal cooling policies and was found to be superior in improving the product CSD.

Although fines dissolution provides a powerful means for the control of the CSD in crystallization processes in which the expected mean crystal size is over a few hundred micrometers, it cannot be used for reactive precipitation, where the mean particle size is in the micrometer or submicron range. Improved mixing and optimal control would be more effective in reactive precipitation processes (compare Sec. 4 in Chapter 9).

4.2. Continuous Operation

Continuous crystallizers are used for the separation of bulk commodities such as fertilizers and salts (see Figs. 4.5–4.8). The operational capacity of these units may be as high as 40 tons per day. To reduce the possibility of wall fouling encountered in surface-cooling crystallizers, evaporative crystallizers are often employed. Heat integration and multiple-effect crystallizers are used to reduce the utilities cost, which introduce further complications in the control of such units. Moreover, due to their large scales, achieving uniform distribution of solute, temperature, and solids within the bulk solution is not possible. In order to prevent excessive nucleation, sufficient crystal surface area should be made available in the regions where supersaturation is high. The control of industrial continuous crystallizers is often achieved by improved equipment design such as draft-tube-baffled (DTB), forced-circulation evaporative, and surface-cooled crystallizers, and growth-type crystallizers, shown in Figs. 4.5–4.8, respectively. In addition to the conventional process variables (temperature, flow rate, pressure, and the intensity of mixing), other variables may also be used. These include the residence time of different size ranges of crystals, the total volume of the crystallizer magma, and the volumetric ratio of the clear-liquor advance to the product removal rate. Product classification, fines destruction, and double draw-off configuration are various methods used to improve the product CSD in continuous crystallizers. However, in industrial crystallizers, feedback control for the adjustment of these variables is not commonly practiced. In the DTB configuration shown in Figure 4.5, the fines are withdrawn at a constant rate and dissolved in an external

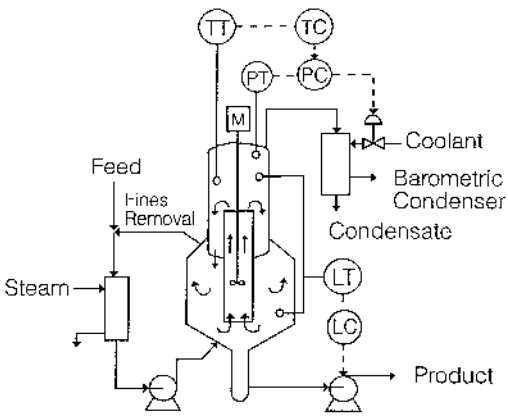

Figure 4.5. Draft-tube-baffled continuous crystallizer.

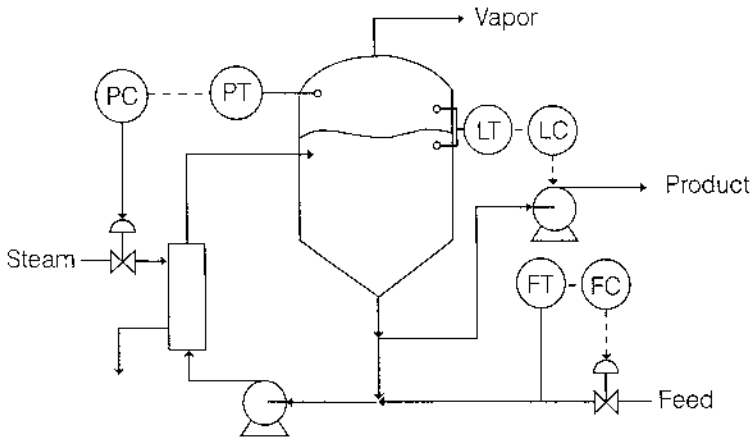

Figure 4.6. Single-effect forced-circulation evaporative continuous crystallizer.

heat exchanger. The feed flow rate can be controlled by an independent-flow control loop. The product removal rate is the difference between the feed flow rate and the rate of evaporation for constant volume operation. The rate of evaporation can be controlled by the steam flow rate to the heat exchanger in evaporative crystallizers, or the coolant flow rate to a barometric condenser, or the suction side of the vacuum source in vacuum crystallizers. The addition of an elutriation leg allows withdrawal of larger crystals in the product stream. The feed should be introduced in a way to avoid solvent flashing and excessive nucleation. The product removal rate may be used to control suspension holdup in the crystallizer. Crystal buildup on the walls is prevented by frequent solvent flush.

The forced-circulation evaporative crystallizers are often used in multiple-effect circuits. A typical single-effect evaporative crystallizer is shown in Figure 4.6. In multiple-effect operation, maximum purity is achieved in countercurrent-flow configuration between the feed and product streams. Feed is introduced to the first effect and the crystalline product is recycled from the last to the first effect through all crystallizers in series and withdrawn from the first effect, where the impurity concentration of the mother liquor is lowest (compare Sec. 1.3 in Chapter 9). Larger mean crystal size is obtained in cocurrent-flow configuration, where feed and product are introduced and withdrawn to and from each effect independently. The evaporation rates in different effects are coupled and cannot be set independently. Pressure in the first effect is controlled by adjusting the steam flow

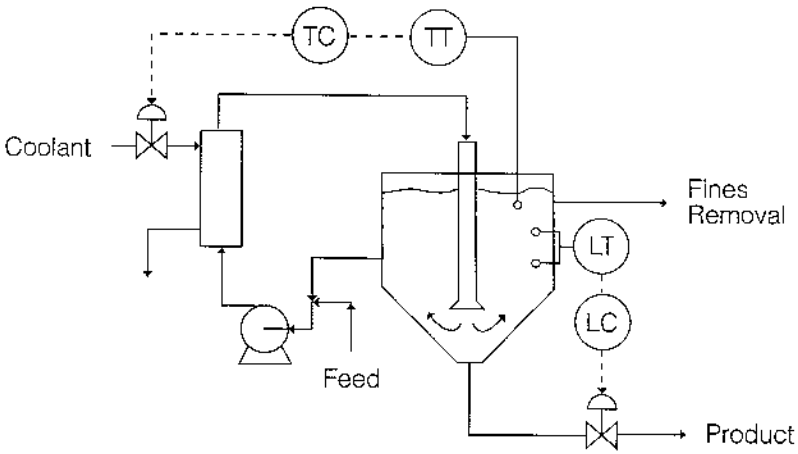

Figure 4.7. Forced-circulation surface-cooled continuous crystallizer.

rate. Feed flow rate is controlled independently, and level control is achieved through adjustment of the product withdrawal rate. In the forced-circulation surface-cooled configuration shown in Figure 4.7, the flow rate of the coolant can be adjusted to control the operating temperature. The temperature difference between the coolant and the bulk solution should not exceed the metastable zone width. The coolant temperature is controlled by blending fresh and recirculating coolant.

In the growth-type crystallizer shown in Figure 4.8, crystal attrition and secondary nucleation are reduced by fluidizing the crystals. Adiabatic evaporation takes place at the liquid free surface in the evaporation chamber. Level control in the upper chamber is achieved through clear-liquor advance and in the suspension chamber by the product removal rate. The double draw-off configuration results in a bimodal distribution that is detrimental to the filtration efficiency (see Sec. 4 in Chapter 4).

It has been shown that continuous industrial crystallizers, in the presence of size classification, show sustained limit cycling even in the absence of external disturbances. This is attributed to the existence of an inherent feedback between the supersaturation and the CSD.

Similar to the batch crystallizers, crystal properties in continuous crystallizers are affected by the crystallizer geometry, the intensity of mixing at bulk and molecular levels, location and diameter of feed and recirculation pipes, the rate of solvent evaporation, mother liquor and solids residence times, recirculation and clear-liquor advance flow rates, seeding, and feedback control by fines dissolution. The comments made concerning the effect

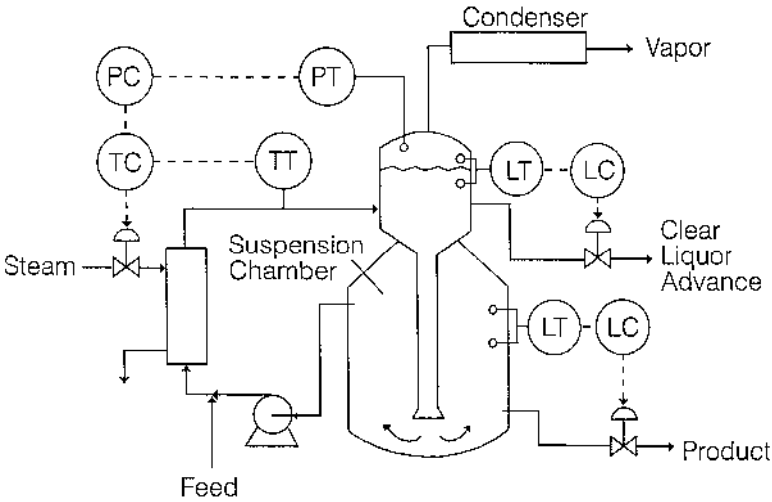

Figure 4.8. Schematic of an Oslo growth-type continuous crystallizer.

of various process variables on the crystal properties in batch crystallizers remain valid here. The key issue is to make sure that regions of high local supersaturation are avoided. Homogeneous mild supersaturation promotes growth rate over the nucleation rate and improves crystal habit and purity. Good and sound design of crystallizers (dimensions of the vessel; feed point and recirculation pipe locations; the type, speed, and material of construction of the stirrer; recirculation and feed pumps; the diameter and the height of the draft tube; etc.), as well as proper selection of process variables (pressure, temperature, the evaporation rate, the seeding rate, etc.) are the essential prerequisites to ensure acceptable crystal properties. Once these prerequisites are met, further refinement on the crystal properties and rejection of outside disturbances can be achieved by exerting feedback control on the crystal properties.

Feedback and feedforward control of CSD in continuous crystallizers have been studied by many researchers [4.16–4.27]. Randolph et al. [4.18] suggested that the nuclei density in the fines destruction loop should be measured and controlled through adjustment of the fines destruction rate for effective CSD control. Nuclei density was calculated as the ratio of the estimated nucleation rate to the growth rate. The on-line estimation of the kinetics was performed by the measurement of the CSD with a Coulter counter and a laser-light-scattering particle-size analyzer [4.18–4.20]. Until a reliable instrument is available for the on-line measurement of the CSD in

the presence of foreign particles and entrained air bubbles, the usefulness of this scheme remains in question. De Jong and his co-workers have published extensively on the control and parameter estimation of industrial crystallizers [4.21, 4.22]. Experimental measurements clearly indicate a pronounced difference in the dynamic behavior of continuous crystallizers with different sizes. The differences in circulation time $t_{circ} \sim 1/s$ (s is the stirrer speed) lead to different supersaturation profiles. If crystallizers are scaled up at a constant mean specific power input $\bar{\varepsilon} \sim s^3 D^2$, the speed decreases with the scale-up factor and the circulation time increases. Therefore, the desupersaturation is enhanced in large industrial crystallizers, and the supersaturation at the feed point is more pronounced than in laboratory crystallizers. This may be the main reason for the oscillation of large units. Additional information is provided in Sec. 7 in Chapter 9. In any case, cycling of crystallizers happens if the local supersaturation in the crystallizer is close to the metastable supersaturation. Therefore, a small circulation time and good macromixing are prerequisites to limit supersaturation peaks and avoid excessive nucleation.

Rohani [4.23] suggested that the fines suspension density in the fines loop has dynamics similar to those of nuclei density. It was shown that feedback control of fines suspension density was an effective means for the CSD control. Rohani and Paine [4.15] proposed a fines suspension density device which is insensitive to the presence of foreign insoluble particles and entrained air bubbles. The proposed sensor was used to control the CSD in a continuous-cooling laboratory [4.24] and a 1-m^3 pilot plant KCl [4.25] crystallizer. Figure 4.9 depicts the schematics of the fully instrumented pilot plant crystallizer circuit. The crystallizer is equipped with an on-line density meter, a Partec-100® model particle-size analyzer, a double-sensor infrared turbidity meter [3.4], in addition to conventional temperature, flow, pressure, and level sensors. Significant increase in the mean crystal size and decrease in the spread of the distribution were observed in both the laboratory and pilot plant crystallizers under the proposed control scheme in comparison with uncontrolled runs. Both internal and external fines dissolution were attempted to improve the CSD (Fig. 4.10). Internal fines dissolution was accomplished by adding water (and, in some cases, steam) to the quiescent zone in the crystallizer while the external fines dissolution was carried out with the help of a heat exchanger and a dissolution tank. The internal fines dissolution is advantageous with respect to lower capital costs, faster response, and ability to help maintain the system away from the cosaturation region (in the KCl–NaCl–H_2O system) which leads to the possible generation of impure crystals. However, the main drawback of internal fines dissolution as opposed to the external is the lack of selectivity (i.e., the added solvent will dissolve the crystals irrespective of their size).

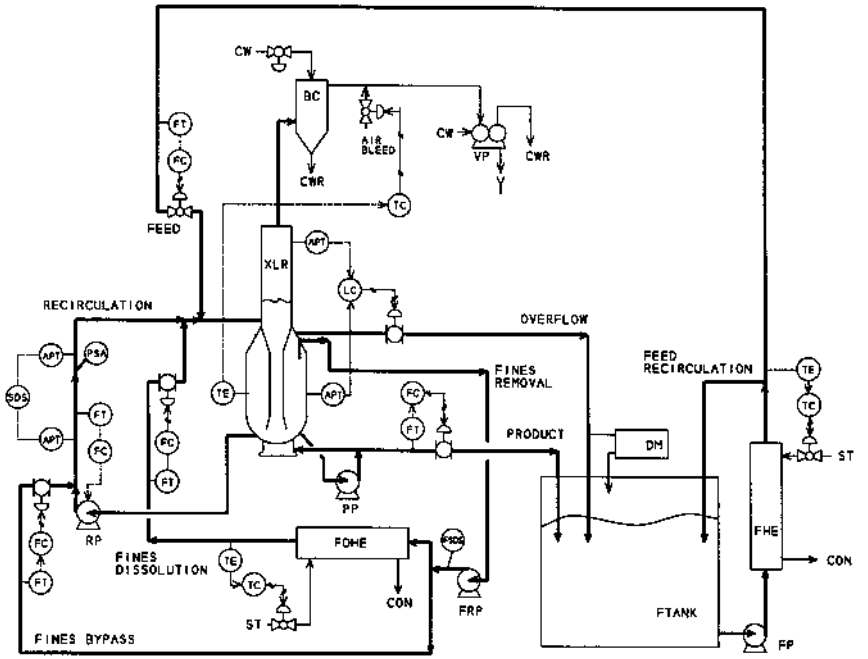

Figure 4.9. Schematic of the 1-m^3 continuous-cooling KCl crystallizer. APT: pressure transmitter, BC: barometric condenser, CON: condensate, CW: cooling water, DM: Anton Paar on-line density meter for the estimation of supersaturation, PSA: Partec 100 FBRM particle-size analyzer, FC: flow controller, FDHE: fines-dissolution heat exchanger, FRP: fines-removal pump, FT: flow transmitter, LC: level controller, PP: product pump, RP: recirculation pump, SDS: fines suspension density sensor, ST: steam, TC: temperature controller, TE: temperature element, VP: vacuum pump, XLR: crystallizer.

In a more recent study [4.26], a detailed experimental study was carried out in a 1.5-L continuous cooling KCl crystallizer to compare the efficacy of the FBRM and transmittance probes to control the total particle count in the crystallizer and the infrared transmittance in the fines removal stream for the control of fines suspension density and the CSD. Figure 4.11 illustrates the schematic diagram of the crystallizer circuit and the position of the probes in the crystallizer and the fines loop.

There are a few theoretical studies dealing with the MIMO control of continuous crystallizers. There is extensive interaction among the control

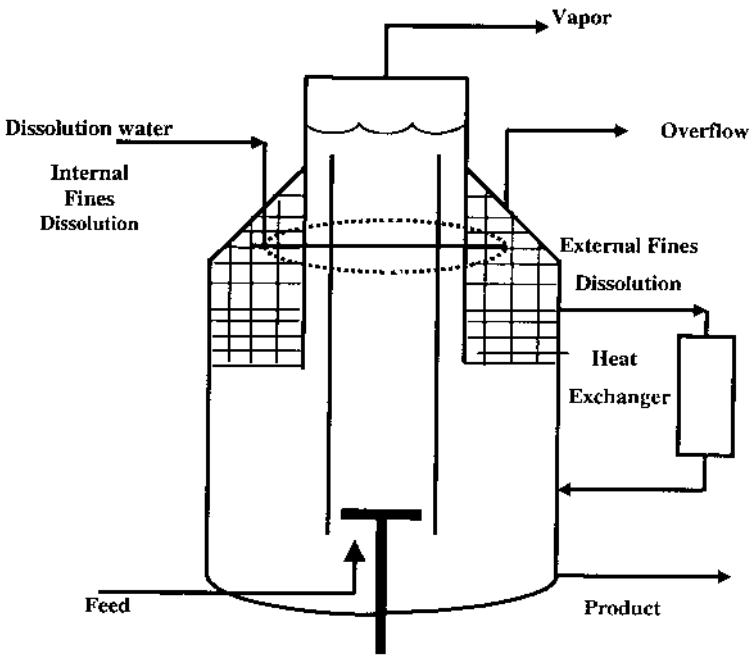

Dimensions (m)

Crystallizer body diameter:	0.92
Crystallizer body height:	1.90
Draft tube height :	1.65
Draft tube diameter:	0.22
Baffle diameter:	0.46
Baffle height:	0.67
Mixer diameters:	0.15

Figure 4.10. Schematic of the 1-m^3 pilot plant continuous KCl crystallizer equipped with internal and external fines dissolution.

objectives in a crystallization process. For example, crystal habit, the CSD, and crystal purity are influenced by the degree of aggregation. On the other hand, the CSD affects crystal purity and production rate. All of these properties are strongly influenced by nucleation, growth, and breakage processes, which, in turn, are affected by many operating conditions, such as the type and concentration of impurities, solids, and mother liquor residence times, the operating and feed temperatures, the crystallizer configuration and mode of operation, the stirrer type, and the intensity of mixing. Some of these variables, such as the type and concentration of

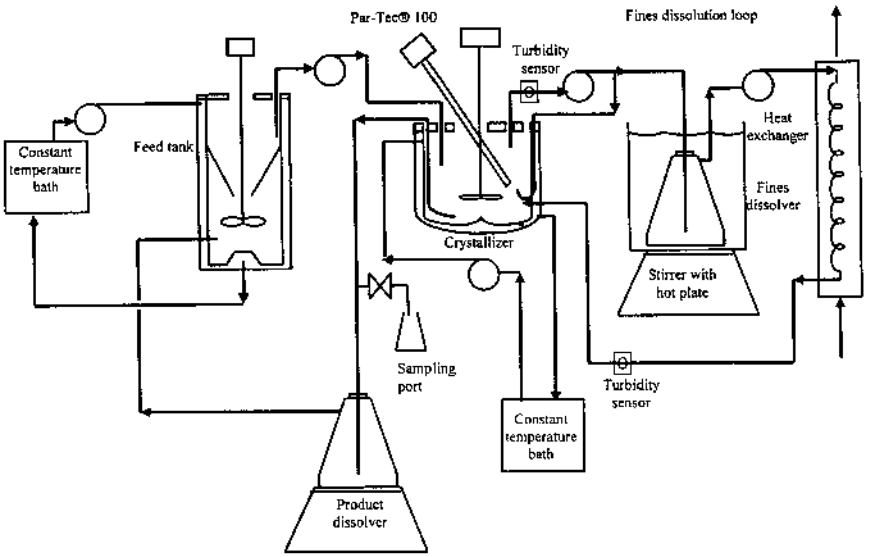

Figure 4.11. Schematic of the 1.5-L continuos crystallizer equipped with the infrared transmission and the FBRM probes.

impurities, degree of mixing, feed temperature, and solute concentration, act as disturbances to a crystallization process. Selection of the most appropriate controlled, measured, and manipulated variables and their subsequent pairing in a logical control configuration require careful analysis of the crystallization process. The nonavailability of reliable on-line sensors is a serious limitation in the design of an overall control strategy for crystallization processes.

In Ref. [4.27], linear and nonlinear MIMO model predictive control (MPC) using ARX and nonlinear neural networks has been used for the control of the CSD, crystal purity, and production rate. The proposed multivariable control scheme is based on the indirect measurement of fines suspension density, supersaturation, and product suspension density. The manipulated variables can be selected from among the fines dissolution rate, feed rate, crystallizer pressure, and clear-liquor advance flow rate. The steady-state and transient responses of the crystallizer demonstrated that the system is multivariable with significant interactions among its input (fines dissolution rate, crystallizer temperature, and the clear liquor or overflow rate) and output variables ($\Delta\vartheta_F$ representing the fines suspension density for the indirect control of the CSD, $\Delta\vartheta_S$ representing the supersaturation for indirect control of crystal purity, and m_T° the magma density in the product

line for the control of production rate) variables. The system dynamics included time delay, nonminimum phase behavior, and steady-state and dynamical nonlinearities. In what follows, a brief review on the implementation of the MIMO MPC on the crystallizer using linear ARX and nonlinear neural networks models will be presented [4.27].

The future optimal moves of the inputs are calculated by minimization of

$$\min_{\Delta U} J = \frac{1}{2}\sum_{k=1}^{3}\sum_{i=1}^{\text{oh}} P_y(k,i)[r_t(k,t+i) - y_m(k,t+i) - d(k,t)]^2 + \frac{1}{2}\sum_{j=1}^{3}\sum_{i=1}^{\text{ih}} P_u(j,i)[\Delta U(j,t+1)]^2 \tag{4.8}$$

with

$$\Delta U = [\Delta u(1,t), \ldots, \Delta u(1,t+\text{ih}), \Delta u(2,t), \ldots, \Delta u(2,t+\text{ih}), \Delta u(3,t), \ldots, \Delta u(3,t+\text{ih})] \tag{4.9}$$

where $r_k(k,t+i)$ is the desired output, y_m is the measured output, d is the disturbance, ih and oh are the input and output prediction and control horizons, P_u and P_y are the penalty matrices on the input and output, and ΔU is the incremental input (control) vector.

Optimization is an important step in the solution of the model predictive controllers. The sequential quadratic programming (SQP) can be expressed as

$$\begin{aligned} &\min F(s) = s^T(X) + \tfrac{1}{2}s^T H s \\ &\text{s.t.} \quad h_j(X) + s^T \nabla h_j(X) = 0, \quad \forall j = 1, \ldots, m \\ &\qquad g_j(X) + s^T \nabla g_j(X) \le 0, \quad \forall j = m+1, \ldots, p \end{aligned} \tag{4.10}$$

where s is the search direction and H is a positive definite approximation of the Hessian of the Lagrange function. A serious shortcoming with the SQP approach is that there is no guarantee that the solution in each iteration step, X_k, will satisfy the constraints. The feasible sequential quadratic programming (FSQP) approach deals with this shortcoming by ensuring that the solution in each iteration is a feasible approximation while the full step move of Newton's method, required for superlinear convergence near the solution, is applicable. More details on the FSQP algorithm are given in Bonnans et al. [4.28], Panier and Tits [4.29], and Zhou and Tits [4.30].

In a recent attempt [4.31], multivariable control of the same 1-m^3 KCl continuous-cooling crystallizer was studied using an extended quadratic dynamic matrix control (EQDMC). Figure 4.12 shows the block diagram

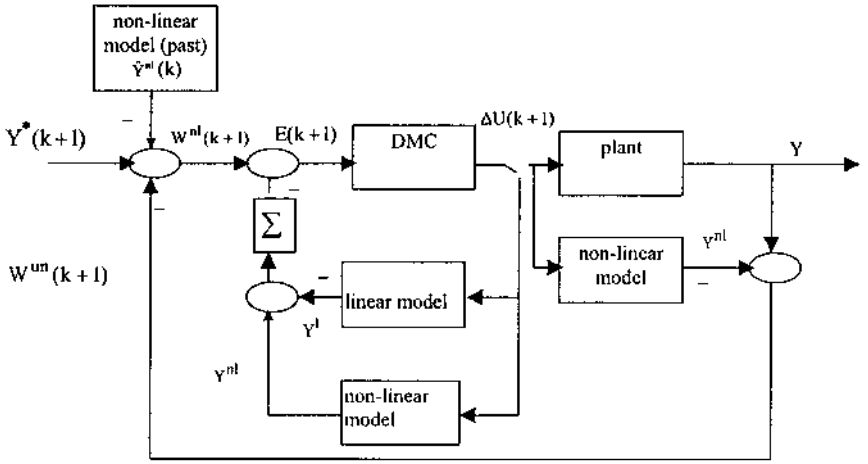

Figure 4.12. Block diagram of the nonlinear quadratic dynamic matrix controller for the control of the 1-m^3 crystallizer. K: sampling interval, Y: process output, Y^l: output of the linear model, Y^{nl}: output of the nonlinear model, E: the error signal, Y*: the set point, $W = Y - Y^{nl}$.

of the proposed algorith. A step-response model was used as the linear model and a feedforward neural network as the nonlinear model. Iterations were carried out in the inner loop until the output of the linear and nonlinear models matched. The controller was able to maintain all three controlled variables in the presence of noise and in the event of simultaneous step changes in the controller set points (see Fig. 4.13).

Supersaturation measurements and control using a density meter [4.32, 4.33] for the control of crystal purity in a laboratory-scale cooling KCl crystallizer have shown some success. Other workers have used refractive index as the means for supersaturation measurement with less success.

No studies have yet been reported on the feedback control of crystal shape. Although image analysis offers a powerful tool for the shape characterization of crystals, due to the lack of automatic focusing devices, especially for the very small crystals, and the heavy computational loads necessary for image grabbing and analysis, feedback control of crystal shape using image analysis remains to be a formidable task. There have been a great number of studies to determine the effect of various tailor-made additives, the method of feeding, the intensity of mixing, and impurities on the crystal shape. The results of such studies are often case-specific.

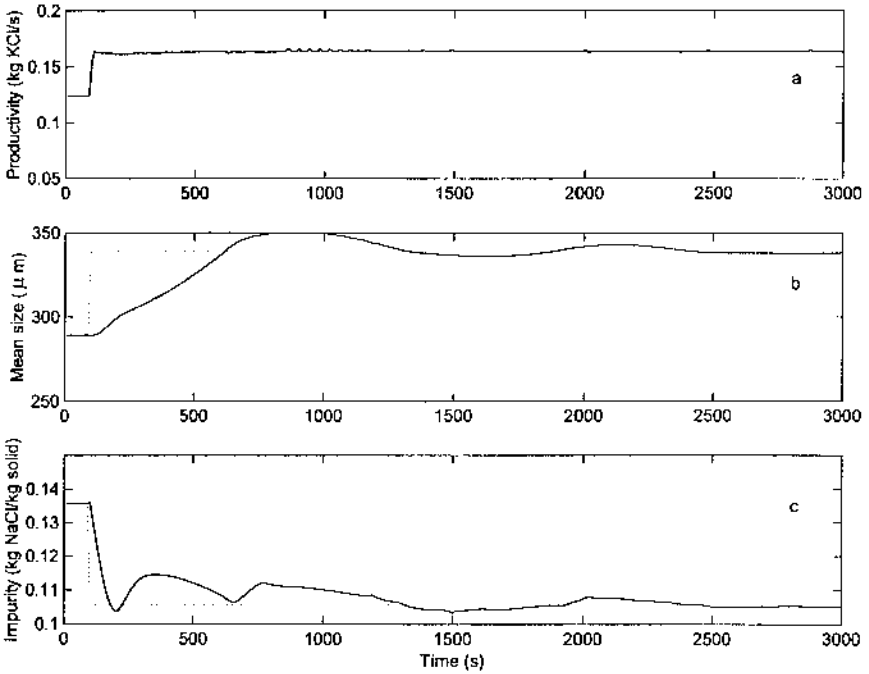

Figure 4.13. Servo response of the 1-m^3 continuous crystallizer under the nonlinear quadratic dynamic matrix controller.

5. CONCLUSION

The effective control of crystallizers which can compensate the adverse effects of major disturbances must be based on variable regulation as well as improved equipment design. Such control schemes, however, require on-line measurement of crystal properties like the CSD, supersaturation, and crystal purity. On-line measurement of these variables with the existing sensors is either not feasible or extremely difficult. Any improvement in crystallization control depends heavily on the advent of new robust on-line measurement techniques. In the meantime, measurement of secondary variables such as turbidity, density of the clear-liquor solution, fines suspension density, and supersaturation offer great potential.

Based on previous work on the feedback control of the CSD in our group, a simple and yet effective control configuration is proposed. The measured variable must be the fines suspension density using a double transmittance sensor and the manipulated variable be the fines-dissolution

rate implemented either internally (by adding solvent or installing a heating ring in the quiet zone of the crystallizer) or externally (by withdrawing the fines slurry and circulating it through a heat exchanger) [2.2, 3.4, 4.26]. Note that the fines suspension density sensor must be installed on an independent constant-flow-rate loop to minimize noise as a result of fluctuations in the flow rate.

REFERENCES

[1.1] C. G. Moyers and A. D. Randolph, Crystal size distribution and its interaction with crystallizer design, *AIChE J.*, *19*: 1089–1103 (1973).

[1.2] R. J. Davy, Looking into crystal chemistry, *Chem. Eng.*, 24 (December 1987).

[1.3] I. Weissbuch, D. Zbaida, L. Leiserowitz, and M. Lahav, Design of polymeric inhibition for the control of polymorphism: Induced enantiomeric resolution at racemic histidine by crystallization at 25°C, *J. Am. Chem. Soc.*, *109*: 1869 (1987).

[1.4] M. Matsuoka, N. Kanekuni, and H. Tanaka, Growth rates and compositions of organic solid solution crystals from binary melts: experimental study, *J. Crystal Growth*, *73*: 563 (1985).

[1.5] R. C. Zumstein and R. W. Rousseau, The influence of surfactants on the crystallization of Lisoleucine, *Ind. Eng. Chem. Res.*, *28*: 334 (1989).

[2.1] A. Tadayyon and S. Rohani, Dynamic modeling of a continuous evaporative cooling KC1–NaCl crystallizers, *Can. J. Chem. Eng.*, *77*: 1195–1204 (1999).

[2.2] S. Rohani, Crystallization, kinetics, modeling, and control: A review, *Trends Chem. Eng.*, *5*: 173–193 (1998).

[2.3] S. Rohani, *Modelisation et commande en cristillisation*, Hermes, Paris, 2000.

[2.4] J. B. Rawlings, S. M. Miller, and W. R. Witkowski, Model identification and control of solution crystallization processes, a review, *Ind. Eng. Chem. Res.*, *32*: 1275–1296 (1993).

[2.5] S. M. Miller and J. B. Rawlings, Model identification and control strategies for batch cooling crystallizers, *AIChE J.*, *40*(8): 1312–1327 (1994).

[2.6] S. Rohani, M. Haeri, and H. C. Wood, Modeling and control of a continuous crystallization process, Part 1: Linear and non-linear modeling, *Compt. Chem. Eng.*, *23*: 263–277 (1999).

[2.7] S. de Wolf, J. Jager, H. J. M. Kramer, R. Eek, and O. H. Bosgra, Derivation of state space model of continuous crystallizers, in *Proc.*

IFAC Symp. on Dynamics and Control of Chemical Reactors, Distillation Columns and Batch Processes (1989).

[2.8] R. A. Eek, Control and dynamic modeling of industrial crystallizers, Ph.D. thesis, Delft University of Technology (1995).

[3.1] R. D. Rovang and A. D. Randolph, On-line particle size analysis in the fines loop of a KCl crystallizer, *AIChE Symp. Ser.*, *76*: 18 (1980).

[3.2] A. D. Randolph, E. T. White, and C.-C. D. Low, On-line measurement of fine crystal response to crystallizer disturbances, *Ind. Eng. Chem. Process Design Develop.*, *20*: 496 (1981).

[3.3] A. Tadayyon and S. Rohani, Determination of PSD by ParTec 100: Modeling and experimental results, *Part. Part. Syst. Charact.*, *15*: 127–135 (1998).

[3.4] A. Tadayyon, S. Rohani, and M. N. Pons, On-line measurement of solids concentration or the mean particle size in a saturated slurry containing background particles using turbidity method, *Part. Part. Syst. Charact.*, *14*: 138–141 (1998).

[3.5] H. S. Hundal, S. Rohani, H. C. Wood, and M. N. Pons, Particle shape characterization using image analysis and neural networks, *Powder Technol.*, *91*: 217–227 (1997).

[3.6] B. Bernard-Michel, S. Rohani, M. N. Pons, H. Vivier, and H. S. Hundal, Classification of crystal shape using Fourier descriptors and mathematical morphology, *Part. Part. Syst. Charact.*, *14* (1997).

[4.1] R. Pohorecki and J. Baldyga, The influence of intensity of mixing on the rate of precipitation, in *Industrial Crystallization*, '79 (E. J. de Jong and S. J. Jancic, eds.), North-Holland, Amsterdam (1979).

[4.2] R. Pohorecki and J. Baldyga, The use of a new model of micromixing for determination of crystal size in precipitation, *Chem. Eng. Sci.*, *38*(1): 79 (1983).

[4.3] N. S. Tavare and J. Garside, Mixing, reaction and precipitation: Limits of macromixing in an MSMPR crystallizer, *Chem. Eng. Sci.*, *40*(8): 1485 (1985).

[4.4] N. S. Tavare and J. Garside, Micromixing limits in an MSMPR crystallizer, *Chem. Eng. Technol.*, *12*: 1 (1989).

[4.5] R. Philips, S. Rohani, and J. Baldyga, Micromixing in a single-feed semi-batch precipitation process, *AIChE J.*, *45*(1), 82–92 (1999).

[4.6] A. G. Jones, Optimal operation of batch cooling crystallizer, *Chem. Eng. Sci.*, *29*: 1075 (1974).

[4.7] A. G. Jones and J. W. Mullin, Programmed cooling crystallization of potassium sulphate solutions, *Chem. Eng. Sci.*, *29*: 105 (1974).

[4.8] M. Morari, Some comments on the optimal operation of batch crystallizers, *Chem. Eng. Commun.*, *4*: 167 (1980).

[4.9] S. Rohani and J. R. Bourne, A simplified approach to the operation of a batch crystallizer, *Can. J. Chem. Eng.*, *68*: 799 (1990).
[4.10] B. Mayrhofer and J. Nyvlt, Programmed cooling of batch crystallizers, *Chem. Eng. Process.*, *24*: 217 (1988).
[4.11] W. Xie and S. Rohani, Nonlinear control of a batch crystallizer, *Chem. Eng. Commun.* (in press).
[4.12] A. G. Jones and A. Chianese, Fines destruction during batch crystallization, *Chem. Eng. Commun.*, *62*: 5 (1987).
[4.13] S. Rohani, N. S. Tavare, and J. Garside, Control of crystal size distribution in a batch cooling crystallizer, *Can. J. Chem. Eng.*, *68*: 260 (1990).
[4.14] S. Rohani and J. R. Bourne, Self-tuning control of crystal size distribution in a cooling batch crystallizer, *Chem. Eng. Sci.*, *45*: 3457 (1990).
[4.15] S. Rohani and K. Paine, Measurement of solids concentration of a soluble compound in a saturated slurry, *Can. J. Chem. Eng.*, *65*: 163 (1987).
[4.16] W. C. Saeman, Crystal size distribution in mixed suspension, *AIChE J.*, *2*: 107 (1956).
[4.17] M. B. Sherwin, R. Shinnar, and S. Katz, Dynamic behavior of the well-mixed isothermal crystallizers, *AIChE J.*, *13*: 1141 (1967).
[4.18] A. D. Randolph, J. R. Beckman, and Z. I. Kraljevich, Crystal size distribution in a classified crystallizer. I. Experimental and theoretical studies of cycling in a KCl crystallizer, *AIChE J.*, *23*: 500 (1977).
[4.19] A. D. Randolph and C.-C. D. Low, Some aspects of CSD control utilizing on-line measurement of nucleation rate, in *Industrial Crystallization*, *'81* (S. J. Jancic and E. J. de Jong, eds.), North-Holland, Amsterdam, p. 29 (1982).
[4.20] A. D. Randolph, L. Chen, and A. Tavana, Feedback control of CSD in a KCl crystallizer with a fines dissolver, *AIChE J.*, *33*: 383 (1987).
[4.21] J. Jager, H. J. M. Kramer, B. Scarlett, E. J. de Jong, and S. de Wolf, Effect of scale of operation on crystal size distribution in evaporative crystallizers, *AIChE J.*, *37*(2): 182 (1991).
[4.22] J. Jager et al., Control of industrial crystallizers, *Powder Technol.*, *69*(1): 11 (1992).
[4.23] S. Rohani, Dynamic studies and control of crystal size distribution in a KCl crystallizer, *Can. J. Chem. Eng.*, *64*: 112 (1986).
[4.24] S. Rohani and K. Paine, Feedback control of crystal size distribution in a continuous cooling crystallizer, *Can. J. Chem. Eng.*, *69*: 165 (1991).

[4.25] T. P. Redman, S. Rohani, and G. Strathdee, Control of crystal mean size in a pilot plant potash crystallizer, *I.Chem.E. Trans.*, *75A*, 183–192 (1997).
[4.26] A. Tadayyon and S. Rohani, Control of fines suspension density in the fines loop of a continuous KCl crystallizer using transmittance and an FBRM® probes, *Can. J. Chem. Eng.*, *78(4)*, 663–673 (2000).
[4.27] S. Rohani, M. Haeri, and H. C. Wood, Modeling and control of a continuous crystallization process, part 2: Model predictive control, *Compt. Chem. Eng.*, *23*, 279–286 (1999).
[4.28] J. F. Bonnans, E. R. Panier, A. L. Tits, and J. L. Zhou, Avoiding the maratos effect by means of non-monotone line search II. Inequality constrained problems, feasible iteration. *SIAM J. Num. Anal.*, *29*(4), 1187–1202 (1992).
[4.29] E. R. Panier and A. L. Tits, On combining feasibility, descent and super-linear convergence in inequality constrained optimization. *Math. Program.*, *59*, 261–276 (1993).
[4.30] J. L. Zhou and A. L. Tits, *User's Guide for FSQP Version 3.0b*, Electrical Engineering Department, University of Maryland, College Park (1992).
[4.31] A. Tadayyon and S. Rohani, Nonlinear model predictive control of a continuous KCl–NaCl crystallizer, *Particle Sci. Tech. J.* (in press).
[4.32] T. P. Redman and S. Rohani, On-line determination of supersaturation of a KCl–NaCl aqueous solution based on density measurement, *Can. J. Chem. Eng.*, *71*, 64–71 (1994).
[4.33] T. P. Redman, S. Rohani, and G. Strathdee, On-line control of supersaturation in a continuous cooling KCl crystallizer, *Can. J. Chem. Eng.*, *73*, 725–733 (1995).

11
Reaction Crystallization

R. DAVID Laboratoire de Génie des Procédés des Solides Divisés, Ecole des Mines d'Albi-Carmaux-CNRS, Albï, France

J. P. KLEIN Laboratoire d'Automatique et de Génie des Procédés, Université Claude Bérnard-CNRS, Villeurbanne, France

1. INTRODUCTION

Reaction crystallization, also called precipitation, is an area for which crystallization as well as reaction engineering aspects are important. Classically, crystals are obtained from a solution by (a) cooling, (b) increasing the concentration of the solute through solvent evaporation, (c) combining these two processes when the solvent evaporation is used both for cooling and for concentrating, or (d) by salting or drowning-out with the help of a cosolvent.

Precipitation differs from these classicial processes in that the supersaturation, which is required for the crystallization, no longer results from an action on the physical properties of the solution. It is obtained by a chemical reaction between two soluble components leading to a less soluble product which crystallizes. The reactants can be molecules or ions. The reaction crystallization may proceed via a third intermediate, a dissolved molecule, which becomes solid afterwards. Alternatively, the reactants can directly lead to a very sparingly soluble precipitate. The generated solids can be

crystalline or amorphous. Reticulation of the suspended, solid particles may take place, and the suspension is then called a gel.

In both cases, the reaction and the crystallization occur simultaneously and have their own kinetics. Both have to be taken into account. Thus, it will be necessary to consider the crystallizer as a chemical reactor with complex kinetics and to apply the chemical reaction engineering methodology for its design and characterization. Reaction and crystallization kinetics have to be measured in ideal laboratory reactors. In addition, mixing effects have to be considered in two ways: (a) the global or partial homogeneity of the vessel (also called macromixing), which is a general problem also for classical crystallizers, and (b) the local mixing effects (also called micromixing), particularly near the feed point of the reactants. At this point, in the case of fast reaction kinetics, the supersaturation may be very high and thus high nucleation rates can be observed. Then, reaction and crystallization kinetic rates are faster or in the same order of magnitude than the mixing processes rates, resulting in a competition among mixing, reaction, and nucleation. The mixing kinetics will have a high effect on the yielded crystals, especially on the number concentration of crystals formed and on their size.

Hence, the study of reaction crystallization is more difficult than that of classical crystallization, because the crystal generation depends on several processes, which all have their own kinetics (e.g., chemical reaction, crystallization, and mixing). The competition between these three steps generally results in (a) rapid crystallization and especially nucleation, which is very problematic to keep under control, and (b) multiple zones in the apparatus showing different mixing conditions and, consequently, very different crystallization and reaction conditions. Therefore, it is necessary to split the reactor into ideal zones, each zone having given mixing parameters, global reaction crystallization kinetics, and subsequent mechanisms influenced by mixing. As an example, in a stirred, single-jet, semibatch vessel, one can distinguish the input zone and the agitator zone, which have very different mixing and concentrations levels than those of the remainder of the reactor. These considerations are a classical approach used in chemical reaction engineering. This approach has, for instance, successfully been applied to fast chemical kinetics, leading to a solute which crystallizes afterward (salicyclic acid precipitation by chemical reaction between sodium salicylate and sulfuric acid [1.1]), and to the direct precipitation of a sparingly soluble salt after a chemical reaction (sodium perborate crystallization [1.2]). To obtain a rational optimal approach of the development of precipitation processes, it seems to be necessary to go on in this direction and to improve this methodology, which is described in detail in the following pages.

Due to the complexity of the reaction crystallization, the following steps are to be studied:

1. The kinetics of the chemical reaction leading to the supersaturation. These kinetics are often very fast, especially when combining ionic species or for acid–base reactions, leading, in turn, to high local supersaturation. In some cases, these kinetics can be complex, for gas–liquid reactions or for organic reactions between molecules, for example.
2. The kinetics of crystallization, including primary and secondary nucleation, growth, agglomeration and Ostwald ripening, which can be considered as important mechanisms during the precipitation of very small particles. The species are often ionic components and, as an example, growth can be considered as a rather complicated step, because one has to take into account the surface integration and the diffusion of two ions. Chiang and Donohue have proposed pertinent models for the growth of crystals from ionic solutions [1.3].
3. The kinetics of mixing, which can have a high effect on both reaction and crystallization kinetic rates if they are of the same order of magnitude. Both macromixing and micromixing have to be considered in this case.

A modeling of the precipitator needs to consider all of these phenomena and their interactions. It is especially important to take into account the mixing models if crystallization and/or reaction kinetics is fast. Then, the vesesel can no longer be considered as a perfect mixed reactor.

2. DRIVING FORCE OF REACTION CRYSTALLIZATION

2.1. Solubility

Two possibilities are to be considered, and we will find this duality in all our discussions:

1. The chemical reaction leads to a more or less soluble molecule P, which then crystallizes. This is the case for many compounds (e.g., salicyclic acid precipitation from sodium salicylate and sulfuric acid).

   $$A + B \rightleftharpoons P \rightleftharpoons S\,(\text{solid})$$

   The first reaction can either be at equilibrium or with finite rates in both directions. For such problems, the solubility of component P can be described as the molar concentration of P in the solution at the thermodynamic solid–liquid equilibrium. This concentration is a function of temperature (see Chapters 1 and 8).

2. The chemical reaction does not lead to any intermediate soluble species, and the solid crystallizes directly from the reactants. This is the case of many ionic reactions, leading to a sparingly soluble salt, between a cation and an anion.

$$x\mathrm{A}^{z+} + y\mathrm{B}^{z'-} \leftrightarrow \mathrm{A}_x\mathrm{B}_y \text{ (solid)}$$

with the electroneutrality condition

$$xz = yz'$$

In case 2, the thermodynamic equilibrium will be described by the solubility product, which is a function of temperature, and is defined by

$$k_a = a_{Ae}^x a_{Be}^y \tag{2.1}$$

where a_{Ae} is the activity of the cation A^{z+} and a_{Be} is the activity of the anion $B^{z'-}$ at equilibrium, given by

$$a_{Ae} = f_z[\mathrm{A}^{z+}]_e \tag{2.2a}$$

$$a_{Be} = f_{z'}[\mathrm{B}^{z'-}]_e \tag{2.2b}$$

$[\mathrm{A}^{z+}]_e$ and $[\mathrm{B}^{z'-}]_e$ are the molar concentrations of the two ions at equilibrium conditions. f_z and $f_{z'}$ are the activity coefficients of ions A^{z+} and $\mathrm{B}^{z'-}$. The solubility of the electrolyte $\mathrm{A}_x\mathrm{B}_y$ can be expressed by a concentration C^* at thermodynamic equilibrium, calculated from

$$C^* = \frac{[\mathrm{A}^{z+}]_e}{x} = \frac{[\mathrm{B}^{z'-}]_e}{y} \tag{2.3}$$

The representation of this concentration as a function of temperature is the solubility curve and generally solubility increases with temperature (see Fig. 2.1). The use of the mean ionic activity $a_\pm$ is defined with respect to mean ionic concentration C (C^* at equilibrium) and the mean ionic activity coefficient $f_\pm$ by

$$a_\pm = (x^x y^y)^{1/(x+y)} C f_\pm \tag{2.4}$$

with

$$f_\pm = (f_z^x f_{z'}^y)^{1/(x+y)}$$

The activity coefficients f_z and $f_{z'}$ can be calculated with help of very sophisticated models [2.1] in the general case. For dilute solutions, a rather good precision can be obtained from the well-known Debye and Hückel equation:

$$\log_{10}(f_\pm) = -A_{\mathrm{DH}} z z' I^{0.5} \tag{2.5}$$

where I is the ionic force of the solution (mol/L) given by

$$I = \frac{1}{2}\sum_i C_i z_i^2 \tag{2.6}$$

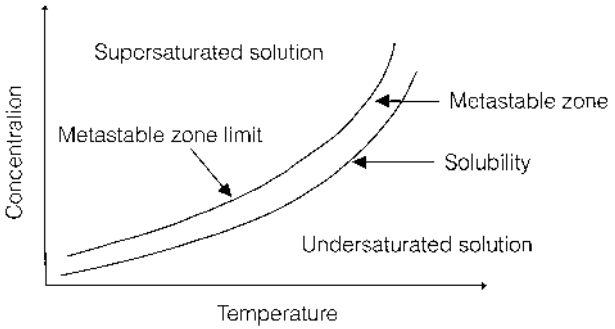

Figure 2.1. Solubility and metastable zone.

C_i is the concentration of ion i and z_i is its valency.

A_{DH} is a constant for a given temperature: 0.5 at 15°C, 0.509 at 25°C, and 0.553 at 65°C (see Appendix A1). In many cases and particularly for $I \leq 0.02$ mol/L, the application of this very simple law allows one to obtain a precise enough value of $f_{\pm}$. For other cases, one will find useful information in Ref. [2.2]. The solubility product becomes

$$K_a = f_z^x f_{z'}^y [A^{z+}]_e^x [B^{z'-}]_e^y = f_{\pm}^{x+y} [A^{z+}]_e^x [B^{z'-}]_e^y \tag{2.7}$$

It enables one to calculate the concentration product at equilibrium

$$K_c = \frac{K_a}{f_z^x f_{z'}^y}$$

and the equilibrium concentration C^*

$$C^* = \left(\frac{K_c}{x^x y^y}\right)^{1/(x+y)} \tag{2.8}$$

For very sparingly soluble salts, solubility concentrations are very low and $f_{\pm}$ becomes close to 1. In this case, $K_a = K_c$.

At last, Ostwald and Freundlich have shown that solubility depends on particle size: It increases if the particle size decreases. The obtained effect is important only for very small particles, as the one crystallized in a precipitation process. For particles that are supposed to be spherical with diameter L, the solubility may be written

$$C^*(L) = C^*(L \to \infty) \exp\left(\frac{4\tilde{M}_S \gamma_{CL}}{\nu \rho_C \Re T L}\right) \tag{2.9}$$

The variations resulting from equation (2.9) are only perceptible for very small crystal (< 1 μm). The consequences of this phenomenon are generally

negligible, but not for crystals obtained by reaction crystallization at high rates.

2.2. Supersaturation

Supersaturation has been defined in a general way in Chapter 1. In the case of precipitation of molecular components, it can be defined in the same way as is done for classical crystallization processes:

$$S = \frac{C}{C^*} \tag{2.10}$$

or

$$\sigma = \frac{C}{C^*} - 1 = S - 1 \tag{2.11}$$

where C is the concentration of the solute in the solution and C^* its solubility.

The relative supersaturation will be preferred for primary nucleation occurring at the first moments of the crystallization at sometimes a very high supersaturation. This is particularly important during precipitation for which local effects at the reactants feed points and high chemical reaction kinetics (ionic reactions for example) may lead to very high local supersaturations, then followed by locally very rapid primary nucleation.

The driving force of the crystallization is, in reality, the difference between the chemical potentials of the solute in the liquid phase and on the solid. At equilibrium conditions, these two chemical potentials are equal. The chemical potential of the solute on the crystals may then be expressed as the potential in the solution at equilibrium. The general expression of the chemical potential in a solution is

$$\mu = \mu_0 + \Re T \ln a \tag{2.12}$$

where μ_0 is the standard chemical potential of the crystallizing product and a is its activity in the solution. The theoretical value of the supersaturation then is

$$\mu - \mu^* = \Re T \ln\left(\frac{a}{a^*}\right) \tag{2.13}$$

where μ^* and a^* are the chemical potential and the activity of the solute in the solution at equilibrium, respectively. In the case of an ionic solid, one has to consider the two ions, with the following stoichiometry:

$$x\mathrm{A}^{z+} + y\mathrm{B}^{z'-} \leftrightarrow \mathrm{A}_x\mathrm{B}_y\,(\text{solid})$$

and the chemical potential to be used can be written

$$\mu = x\mu_A + y\mu_B \tag{2.14}$$

where

$$\mu_A = \mu_{A0} + \Re T \ln(a_A) \tag{2.15a}$$

$$\mu_B = \mu_{B0} + \Re T \ln(a_B) \tag{2.15b}$$

are the chemical potentials of ions A^{z+} and $B^{z'-}$, respectively. The driving force of the crystallization is, in this case,

$$\Delta\mu = x(\mu_A - \mu_A^*) + y(\mu_B - \mu_B^*) = \Re T \ln\left(\frac{a_A^x a_B^y}{a_A^{*x} a_B^{*y}}\right) \tag{2.16}$$

Equation (2.16) can be written

$$\Delta\mu = \Re T \ln\left(\frac{a_A^x a_B^y}{K_a}\right) \tag{2.17}$$

In this expression, $\Delta\mu$ is the difference of chemical potential for one molecule A_xB_y, and the supersaturation can be defined as [2.3]

$$S_a = \frac{a_X^x a_B^y}{K_a} \tag{2.18}$$

In a different way, the reference can be chosen as the variation of a unit ion in the solution [2.4]. Equation (2.17) becomes

$$\Delta\mu = (x + y)\Re T \ln S' \tag{2.19}$$

and the supersaturation is then defined by

$$S_a' = (S_a)^{1/(x+y)} \tag{2.20}$$

For classical crystallization processes, all the phenomena occur in the metastable zone at sufficiently reasonable supersaturation to allow the activity coefficients to be looked upon as constants. In this case, S can be expressed by

$$S = \frac{C_A^x C_B^y}{K_c} \tag{2.21a}$$

or by

$$S' = \left(\frac{C_A^x C_B^y}{K_c}\right)^{1/(x+y)} \tag{2.21b}$$

For precipitation processes, the supersaturation can reach very high local values, particularly at the introduction points of reactants if the reaction kinetics are fast. Equations (2.21a) and (2.21b) can then no longer be

applied and equations (2.18) or (2.20) have to be used in the expressions of the kinetic rates of primary nucleation and of the growth of the formed nuclei. This high supersaturation explains one among the main differences between precipitation and classical crystallization and the obtained effects of mixing on crystal size. A high complexity level and difficulties of modeling of the obtained phenomena result.

3. REACTION CRYSTALLIZATION KINETICS

As noted earlier, kinetics of the solid generation result from two processes which have each their own kinetics: (a) the chemical reaction and (b) the crystallization with its own elementary processes such as nucleation, ripening, growth, agglomeration, and breakage. It is necessary to define and to separate these two types of kinetics.

3.1. Reaction Kinetics

The chemical reaction leading to the insoluble compound P is generally represented by a stoichiometric equation

$$\nu_A A + \nu_B B \rightarrow \nu_P P + \nu_R R$$

A and B are initial reactants, P is the sparingly soluble product, and R may be a soluble coproduct. The kinetics of such a reaction may be described by using the so-called generalized reaction extent ζ [2.4], defined in a batch reactor by

$$n_A = n_{A0} - \nu_A \zeta \tag{3.1a}$$

$$n_B = n_{B0} - \nu_B \zeta \tag{3.1b}$$

$$n_P = n_{P0} + \nu_P \zeta \tag{3.1c}$$

$$n_R = n_{R0} + \nu_R \zeta \tag{3.1d}$$

n_i is the number of moles of component i in the reactor at time t and n_{i0} the initial number of moles of component i charged in the reactor. The reaction rate r is then the variation of ζ per unit time and per unit volume of the reactor. The disappearance rate of A and B may be written with these notations:

$$r_A = \nu_A r \tag{3.2a}$$

$$r_B = \nu_B r \tag{3.2b}$$

The reaction kinetics of P and R can be written in the same way:

$$r_P = \nu_P r \tag{3.3a}$$

$$r_R = \nu_R r \tag{3.3b}$$

In a homogeneous volume, r is constant at all points of the considered volume at time t and can generally be written as a sole function of temperature and concentrations. In the general case,

$$r = k_r C_A^{\alpha} C_B^{\beta} \tag{3.4}$$

In this equation, k_r is a function of temperature, called the Arrhenius law:

$$k_r = k_0 \exp\left(-\frac{E}{\Re T}\right) \tag{3.5}$$

Exponents α and β are the partial reaction orders, k_r is the reaction rate constant, and E is the activation energy of the reaction. α, β, and k_r are obtained from experiments in ideal, perfect mixed-batch, semibatch, or continuous reactors at a given temperature. Different values of k_r measured at different temperatures are necessary to obtain the activation energy of the reaction.

In some cases, complex reaction mechanisms may lead to more complicated expressions of the reaction rate than the one given by equation (3.4). Each of these cases has to be considered individually, and the reaction rate expression has to be deduced from the reaction mechanisms involved. In other cases, one has to consider the reaction with mass transfer, and transfer limitations have to be taken into account. Developments of such mechanisms and the resulting expressions of the reaction rates can be found in the literature [3.1, 3.2].

These considerations allow one to write mass balances for ideal reactors and to calculate the reaction extent, the concentration of all the reactants, and, consequently, the supersaturation in the case of reaction crystallization in which we are interested. All of these properties are obtained as functions of time for reactors that are run in non-steady-state conditions.

3.2. Crystallization Kinetics

Crystallization kinetics have previously been described in detail in Chapters 2 and 3. Here, we shall only consider the important specificities of reaction crystallization.

3.2.1. Nucleation

Three mechanisms of crystal nucleation are generally acknowledged: (a) the primary homogeneous nucleation, (b) the primary heterogeneous nucleation, (c) the secondary nucleation.

Primary nucleation is described as a preorganization of the solute in the solution to obtain clusters. These clusters become solids if their size is sufficient to create stable nuclei, which are able to grow afterward. The kinetics of this homogeneous process are developed in Chapter 2 and the corresponding rate expression can be written according to

$$B_{\text{hom}} = A_{\text{hom}} \exp\left(\frac{-K_{\text{hom}}}{(\nu \ln S)^2}\right) \tag{3.6}$$

K_{hom} is generally given for spherical nuclei:

$$K_{\text{hom}} = \frac{16\pi\gamma_{\text{CL}}^3}{3(C_C N_A)^2 (kT)^3} \tag{3.7}$$

Primary homogeneous nucleation is highly nonlinear. Its kinetics are very low for small values of the supersaturation S. They become very high for values of S higher than a critical one, $S_{\text{crit, hom}}$, corresponding to the metastable zone limit for homogeneous nucleation.

For crystallization processes, the supersaturation is obtained smoothly by cooling or solvent evaporation. Primary nucleation is generated at $S_{\text{crit, hom}}$ and S cannot exceed $S_{\text{crit, hom}}$. One of the fundamental differences presented by reaction crystallization in the case of a rapid reaction is that very high local supersaturations can be observed, especially in the first moments of mixing the reactants. These values of supersaturation can thus substantially exceed $S_{\text{crit, hom}}$ and result in very high, local, primary nucleation kinetics. Therefore, it is necessary to take into account local effects when modeling of the precipitation in order to obtain the particle size distribution. The influence of mixing thus explains the high sensitivity of reaction crystallization to hydrodynamics on both macroscopic (macromixing) and microscopic (micromixing) levels.

In industrial practice, primary nucleation cannot be considered as homogeneous, but it arises essentially from a heterogeneous mechanism on various foreign surfaces (dust particles, solid impurities, agitator, crystallizer wall, etc.). In this case, even at lower supersaturation than $S_{\text{crit, hom}}$, heterogeneous nucleation is observed and the width of the metastable zone is reduced, as shown in Sec. 2 of Chapter 2:

$$B_{\text{het}} = A_{\text{het}} \exp\left(-\frac{fK_{\text{hom}}}{(\nu \ln S)^2}\right) \tag{3.8}$$

The correction factor f is given by

$$f = \frac{(2 + \cos\theta)(1 - \cos\theta)^2}{4} \tag{3.9}$$

θ is the contact angle between the nuclei and the solid–liquid interface on which the heterogeneous nucleation occurs.

Regarding these expressions, the following problems appear:

1. In industrial crystallizers, it is very difficult to know the part played by the homogeneous and heterogenous mechanisms in the globally observed primary nucleation process. This point can certainly explain why it is rather difficult to scale-up and to foresee the primary nucleation kinetics in industrial crystallizers from laboratory experiments. For reaction crystallization with high chemical kinetic rates and sparingly soluble components, the high local supersaturation levels that are obtained probably lead more to homogeneous mechanisms than in the case of classical crystallization.
2. The contact angles depend on temperature, and f may be a rather complicated function of temperature.

Secondary nucleation arises at low supersaturations and explains the steady-state running of continuous crystallizers. It takes also place for reaction crystallization, but it becomes predominant at low supersaturations only, especially in continuous precipitators. The proposed mechanisms result from collisions between two crystals or between one crystal and a part of the crystallizer, generally the stirrer. Kinetics are described by an empirical expression of the type

$$B_{\text{sec}} = A_{\text{sec}} \sigma^n m_T^l \varepsilon^r \tag{3.10}$$

where σ is the relative supersaturation.

As secondary nucleation generally is not as important a process in the case of reaction crystallization as primary nucleation, the precision of empirical equation (3.10) is sufficient. For theoretical developments, one should refer to Chapter 5.

3.2.2. Ostwald ripening [3.3–3.5]

As discussed earlier, solubility is in reality a function of the particle size, given for spherical particles of diameter L by the expression

$$C^*(L) = C^*(L \to \infty) \exp\left(\frac{4\gamma_{\text{CL}} \tilde{M}_S}{\nu \rho_C \Re T L}\right)$$

In this expression, it is common to introduce the Ostwald diameter [3.4]:

$$\lambda = \frac{4\gamma_{CL}\tilde{M}_S}{v\rho_C \Re T} \tag{3.11}$$

to obtain

$$C^*(L) = C^*(L \to \infty)\exp\left(\frac{\lambda}{L}\right) \tag{3.12}$$

λ is only a function of the crystallizing solvent–solute system. In the crystallizer, if the solute concentration is C, we can define the supersaturation for a particle of size L:

$$S_L = \frac{C}{C^*(L)} = \frac{C}{C^*(L \to \infty)}\exp\left(-\frac{\lambda}{L}\right) \tag{3.13}$$

The commonly used supersaturation S is C/C^* and we can write

$$S = S_L \exp\left(-\frac{\lambda}{L}\right) \tag{3.14}$$

The actual supersaturation for a given crystal is thus a decreasing function of its size. For given crystallization conditions, the supersaturation is consequently lower for small particles, which grow more slowly than larger particles. The current values of λ are in the order of magnitude of 10^{-9}–10^{-8} m.

As an example, if we consider a value of λ of 5×10^{-9} m, $C^*(L)/C^*$ is equal to 1.051 for particles of 0.1 μm, to 1.005 for 1-μ m particles, and to 1.0005 for 10-μm particles. Sensible differences in solubilities are thus obtained only for small particles below 1 μm. These differences are rather important in the case of reaction crystallization where small particles are obtained, but do not have any incidence when crystallized particles are above 10 μm: Their solubility can be considered as constant. One of the phenomena resulting directly from these solubility variations with the particle size is the so-called isothermal Ostwald ripening.

At the end of the crystallization, the solute concentration in the solution returns to equilibrium with the largest particles obtained. Then, the solution is undersaturated with respect to the smallest crystals that dissolve. Again, the dissolved matter leads to supersaturation for the largest particles that will grow. The overall observed effect is the disappearance of the small particles and the subsequent growth of the large crystals. As seen earlier, the disappearance rate is only important for small crystals, but it can be particularly efficient during reaction crystallization, for which the generated particles are generally very small.

General models for crystallization including Ostwald ripening have been developed by Matz [3.4] and by Muhr and co-workers [3.6, 3.7]. They use

growth-rate equations combined with external diffusion for the small particles and the larger ones as well. For every particle size, supersaturation is calculated using its own solubility from equation (3.14). The mass transfer equations written for each size are then able to represent the dissolution of the small crystals and the simultaneous growth of the larger ones.

3.2.3. Growth

Chapter 3 shows currently used models for crystal growth, which apply also in the case of the reaction crystallization of molecular intermediates. In the case of direct precipitation from reactants without any sparingly soluble intermediate, the situation is rather more complicated. Indeed, the surface integration and diffusion apply simultaneously to the two ionic species, provided that the electric neutrality of the crystal and the surrounding solution are respected. Concerning surface integration, numerous models have been proposed [2.1, 3.8–3.10]. The most pertinent one, which is applicable for precipitation processes, is that proposed by Chiang and Donohue [1.3]. This model is a chemical reaction engineering model, integrating several mechanisms that resemble heterogeneous catalysis steps. A growth model can be set up by writing the competition of one of the three following integration mechanisms with the diffusion of ions A^{z+} and $B^{z'-}$.

Mechanism 1 describes the individual adsorption of the ions, followed by the attainment of the insoluble component in the adsorption layer and by the integration in the crystal network:

$$A^{z+}(\text{solution}) \leftrightarrow A^{z+}(\text{adsorbed})$$
$$B^{z'-}(\text{solution}) \leftrightarrow B^{z'-}(\text{adsorbed})$$
$$xA^{z+}(\text{ads.}) + yB^{z'-}(\text{ads.}) \leftrightarrow A_xB_y(\text{ads.})$$
$$A_xB_y(\text{ads.}) \leftrightarrow A_xB_y(\text{integrated})$$

Mechanism 2 describes the individual adsorption of the ions and their direct integration in the crystal network in the ionic form:

$$A^{z+}(\text{sol.}) \leftrightarrow A^{z+}(\text{adsorbed}) \leftrightarrow A^{z+}(\text{integrated})$$
$$B^{z'-}(\text{sol.}) \leftrightarrow B^{z'-}(\text{adsorbed}) \leftrightarrow B^{z'-}(\text{integrated})$$

Mechanisms 3 have been proposed if a soluble intermediary component is existing:

- Mechanism 3a:

$$xA^{z+}(\text{sol.}) + yB^{z'-}(\text{sol.}) \leftrightarrow A_xB_y\ (\text{solution})$$

$$A_xB_y\ (\text{solution}) \leftrightarrow A_xB_y\ (\text{integrated})$$

- Mechanism 3b:

$$xA^{z+}(\text{sol.}) + yB^{z'-}(\text{sol.}) \leftrightarrow A_xB_y(\text{solution})$$

$$A_xB_y(\text{solution}) \leftrightarrow A_xB_y(\text{adsorbed}) \leftrightarrow A_xB_y\ (\text{integrated})$$

Chiang and Donohue [1.3] neglect any surface diffusion. For a given crystallization reaction, the observed mechanism is the fastest, with a kinetic limitation by the slowest step, or by external diffusion of the ionic or the molecular species. The corresponding kinetic laws can be obtained considering the growing sites as chemical entities and applying kinetics and equilibria for each of the steps of the chosen mechanism to ions and growing sites. Results in good agreement with the experiments have been reported by Chiang and Donohue with Mechanism 1 using a Langmuir adsorption isotherm for $CaCO_3$, $PbCr_4$, and $CaHPO_4{\cdot}2H_2O$.

As stated earlier, it is necessary to associate these representations of surface integrations to volumetric diffusion processes as described in Chapter 3. For reaction crystallization between two ionic species, which have to diffuse from the bulk solution to the crystal surface to be available for the surface integration, the molar fluxes of the two ions depend on their own diffusion coefficients, which may be different one from the others. Electrical neutrality has to be respected and leads to the following relation between the molar fluxes F_A and F_B of ions A^{z+} and $B^{z'-}$, respectively, as the other ions, which are not consumed, stay at constant concentration around the crystal:

$$zF_A = z'F_B \tag{3.15}$$

Using these relations, combined with the ones resulting from the relevant mechanism proposed by Chiang and Donohue, and introducing the efficiency factors from Chapter 3, it is now possible to propose a complete model of the growth mechanisms involved in the considered reaction crystallization.

For the case of reaction crystallization, the classical simple power laws between growth rate and supersaturation are not sufficient to describe the involved phenomena. Approaches such as those proposed by Chiang and Donohue allow us to take into account all the fundamental mechanisms with relatively simple equations. They lead to consider further finer mechanisms, such as the poisoning of growth sites due to impurities, and to take them into account in the growth-rate equations.

3.2.4. Agglomeration [1.2, 3.11, 3.12]

Unlike nucleation and growth, agglomeration is not a phenomenon occurring in every crystallization process. Its existence depends on the crystallizing system in terms of physical chemistry and of technology and on crystallization conditions. It arises if crystals stick together to generate new, larger particles. Three types of agglomeration processes may be distinguished:

1. If the cohesion forces are weak, the agglomeration results in fractal agglomerates, the so-called flocculation or coagulation.
2. If the supersaturation sticks the agglomerating crystals strongly together by crystal growth between the mother particles, the process is called agglomeration.
3. For intermediary processes and for processes arising without supersaturation, one will speak of aggregation.

During crystallization processes, we essentially observe agglomeration in the presence of supersaturation or sometimes aggregation without supersaturation.

To obtain agglomerates, three successive steps have to occur: (a) the collision of two particles, (b) a sufficient time interval during which the two particles stay together with the help of the flow, and (c) the adherence of the two particles caused by supersaturation. The key parameters of this process are then as follows:

1. The hydrodynamic conditions (mixing, local turbulence, etc.).
2. The nature of the solvent (viscosity, density, etc.).
3. The size and the habit of the crystals, which may have a high influence on steps (a) and (b). Thus, for small particles, the second step is facilitated and gives the third step (c) time to develop. Hence, agglomeration is likely to occur in reaction crystallization producing very small elementary particles.
4. The population density of the crystals, which has a very important direct influence on the collision frequency and, consequently, on step (a) of the agglomeration process.
5. Supersaturation and the related growth rate, which controls the adherence step (c).
6. The cohesion forces among the solvent, impurities, and the crystals, which are very important for step (b).

The agglomeration during crystallization has been less studied because it is very difficult to distinguish from the growth. It is often difficult to measure the number and size of the monocrystals in a particle. Global

approaches have been attempted sometimes rather successfully, for instance by Marchal and co-workers [3.11, 3.12] for adipic acid crystallization or by Marcant and co-workers [3.12] or Bramley and Hounslow [3.13] for the precipitation of calcium oxalate. These authors followed the crystal size distribution (CSD) and, in some cases, the supersaturation by measuring solution conductivity in perfectly mixed crystallizers operated in the batch or semibatch mode. The serious problem encountered with such a methodology including agglomeration rates is to solve the population balance equation or at least a set of equations in terms of moments of the CSD. This is necessary to obtain the constants of the kinetics laws of the different crystallization steps from the experimental data. Coagulation or flocculation without supersaturation has been, on the contrary, widely studied. The main results of these studies are the attainment of valuable models of steps (a) and (b) of the agglomeration process [3.14, 3.15]. The results of such studies are the starting point of the works of Marchal and co-workers [3.11, 3.16] and Marcant and co-workers [3.12], who used the formalism of von Smoluchowski [3.17] [i.e., treating the agglomeration like a two-particle collision mechanism (as shown in Chapter 2]. The rate of the agglomeration of two particles of size L_i and L_j in an energy dissipation field of intensity ε per unit mass is given by

$$r_{ij} = \beta(L_i, L_j, \varepsilon)N_iN_j \tag{3.16}$$

N_i and N_j are respectively the concentrations (number of particles per unit of volume) of particles of size L_i and L_j and $\beta(L_i, L_j, \varepsilon)$ is the so-called agglomeration kernel. In the general case, β is a function of mother particle sizes L_i and L_j, and ε, though the overall rate of agglomeration can appear as quasi-constant as a consequence of opposite effects of these parameters in the three steps (a–c). The agglomeration mechanism involving steps (a)–(c) and, consequently, the corresponding expression of β primarily depends on the size range of the mother particles and of the resulting agglomerate (see Ref. [3.12] and Chapter 6). Here, one should distinguish among Brownian, perikinetic, orthokinetic, and turbulent agglomerations.

The global rate of birth of particles of size L_k is finally obtained by summing up the different kinetic contributions of all the encounters combining two sizes L_i and L_j, and those contributions leading to the disappearance of crystals of size L_k by agglomeration with other particles. The total mass of the two particles in the new one of size L_k has to be conservative. This calculation combined with the difficulty of numerical solving of the population balance equation incited Marchal and co-workers [3.11, 3.12] to propose a discretization of the resulting equations. They considered the agglomeration kernel as the product of three factors representing the following:

1. The collision frequency of two particles related to hydrodynamics and, in the case of the very small particles obtained during precipitation, depending only on electrical, hydrodynamic, and van der Waals forces [3.18].
2. The probability for two particles to stay together long enough to stick. For small particles, this probability is very high, close to 1, because the particles are both small enough to stay together in a microeddy. As a matter of fact, the small eddies in turbulent-agitated vessels are described by the Kolmogorov microsale and have generally a larger size than the precipitated particles. This is not true for classical crystallization.
3. The sticking-together frequency related to the crystal growth rate and then to the supersaturation.

Although it is very difficult, it is necessary to separate the first two phenomena depending essentially on energy dissipation and not on supersaturation from the third one, which only depends on supersaturation. To develop such models, separating hydrodynamic effects from concentration effects is an absolutely necessary condition to understand the reliable phenomenon and to master the scale-up. Today, such models have to be developed not only for agglomeration but also for crystal growth and nucleation. Agglomeration is a very important process, especially during reaction crystallization, because the particles are very small and with solubilities.

3.3. Induction Time

Let us consider batch reaction crystallization with the initial homogenization of the reactants under perfect mixing conditions, which is a theoretical assumption and is very difficult to realize practically. In Figure

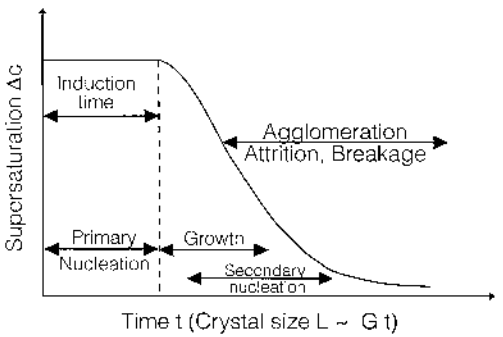

Figure 3.1. Supersaturation versus time during a batch reaction crystallization with premixed reactives, induction time, and relevant mechanisms.

3.1, the supersaturation versus time is monitored, for instance, with a conductimeter if the reactants are ions. After a certain time interval, the so-called induction time, the crystallization starts on an observable level. This initial period obviously depends on the kinetics of the different processes involved:

1. The kinetics of mixing, whose effects we consider here as negligible. This is not the general case, as explained in Sec. 4.
2. The chemical reaction kinetics.
3. The nucleation rate, which leads to the apparition of the crystals.
4. The growth rate of the formed particles. Indeed, the initial nuclei are too small and do not consume enough mass to be detectable. It is necessary for them to grow to become observable.

The induction time t_{ind} can be shared in two parts [3.19, 3.20], in the case of rapid mixing and reaction rates:

$$t_{\text{ind}} = t_n + t_g \tag{3.17}$$

where t_n is the time necessary for nucleation and t_g is the time necessary for sufficient growth. Three possibilities can be observed:

1. If $t_n \ll t_g$, it will be difficult to speak about metastability and t_{ind} will not contain any information on nucleation. t_{ind} is generally too short to be measurable and will be very dependent on mixing kinetics.
2. If t_n and t_g are of the same order of magnitude, both mechanisms of nucleation and growth have to be taken into account in the model used.
3. If $t_n \gg t_g$, t_{ind} is high enough to be measurable.

The last two cases have been studied theoretically [3.21] from the expressions of the nucleation and growth rates. These simple considerations are observed only if the reaction and mixing kinetics are very rapid. On the contrary, if mixing and reaction kinetics are not rapid, they will introduce their own timescale in the value of t_{ind}. The reaction time t_{reac} and mixing time t_m at both macroscopic and microscopic scales will influence the initial induction of the reaction crystallization process.

4. FLUID DYNAMICS, MIXING, AND PRECIPITATION

After obtaining the kinetic model including reaction and crystallization, it is necessary to characterize the crystallizer itself. Obviously, it is relatively easy to write the population, mass, and energy balances for an ideal crystallizer, either a perfect mixed vessel (continuous, semibatch, or batch) or a plug-flow

Table 4.1. Successive Steps of Mixing

Process	Size scale	Time scale
Dispersion by the velocity field (macromixing)	Macroscale	Mixing and circulation times (1–10 s)
Size reduction of eddies (mesomixing)	Taylor scale	Taylor time scale (0.1–1 s)
Stretching and swirling of eddies (micromixing)	Kolmogorov microscale	Shear time scale (0.02–0.001 s)
Diffusion (micromixing)	Batchelor microscale	Diffusion time (0.01–0.001 s)

crystallizer. The definition of a perfect mixed vessel involves a perfect homogeneity in the whole crystallizer volume of all the properties of the suspension (concentrations, temperature, pressure, energy dissipation, crystal size distribution). Then, it can be considered that all the mechanisms of the crystallization do not depend on the space coordinates in the whole volume of the vessel.

However, this assumption is no longer verified if the reaction or crystallization processes (nucleation, ripening, growth, agglomeration, breakage) are rapid with respect to mixing.

Beek and Miller [4.1] have described mixing of fresh miscible liquid feed streams in four successive steps (Table 4.1); David and Clark [4.2] have applied it to the case of water treatment and aluminum hydroxide generation:

1. Dispersion of the incoming fluid by the velocity field (macromixing)
2. Size reduction of eddies by turbulence (mesomixing, sometimes also called micromixing)
3. Stretching and swirling of eddies (micromixing)
4. Diffusion of reagents within eddies by molecular diffusion (micromixing)

The typical length and timescales of each step are summarized in Table 4.1 for aqueous solutions with low viscosities. Note that the chemical reaction (and, consequently, precipitation) may only take place when molecular contact is achieved (i.e., during the last two steps; these steps are determining for the yields and the size distribution of crystals).

4.1. Macromixing

Macromixing can be defined as the processes contributing to the uniformity of the local average value of the concentrations of all the species present in the vessel.

From the macroscopic point of view, even if agitation is provided, at least three zones have to be differentiated in a stirred precipitator.

1. A first zone, near the reactant feed point. In the case of a fast chemical reaction leading to supersaturation, this zone will be more supersaturated than the average volume of the vessel; especially, primary nucleation will occur at a higher rate in this area.
2. A second zone, in the vicinity of the stirrer or circulation pump, in which the energy dissipation is much higher than in the average volume of the vessel. Breaking, agglomeration, secondary nucleation, or diffusion-controlled growth will be influenced.
3. A third zone, the bulk of the vessel.

Industrial vessels are generally even less well mixed, because they are intermediates between mixed and plug flow reactors, in which dead zones or bypasses cannot be excluded [3.1, 3.2]. Use of the chemical reaction engineering methodologies to model the hydrodynamics of precipitators seems to be particularly suited.

A description of the macromixing state of an agitated vessel can be obtained with the help of the formulation of the residence time distributions, characterizing the hydrodynamics of the apparatus in a statistical way. A group of molecules, traveling together in the vessel and called an aggregate, can be characterized by the time elapsed between entering and exiting from the reactor, called its residence time. This residence time is a distributed parameter, because its value varies from one entity to another. Two extreme macromixing states can be obtained for a given apparatus.

1. The perfect macromixing (or maximum backmixing) for which the probability of exit for each molecule is the same at each point of the vessel. The average concentrations at each point are equal to those at the exit of the vessel: this is, for instance, the case of the mixed-suspension, mixed-product removal (MSMPR) precipitator.
2. The minimal macromixing (or zero backmixing) for which the fluid is characterized by an unique residence time equal to the ratio of the volume of the reactor to the volumetric flow rate passing through it. This case is the case of the plug flow reactor and can be represented by a tube in turbulent-flow conditions.

The modeling of a real precipitator needs an intermediate between these two extremes which has to be established for each apparatus. For the fluid flow through the reactor, applying the Navier–Stokes equations makes a rigorous description. In most cases, this type of description, especially the integration of the equations obtained, would be very difficult and would lead to much more detailed information than that needed for the process. It is much easier and convenient to use the residence time distribution (RTD) formulation introduced by Danckwerts [4.3].

4.1.1. Obtention of the macroscopic flow model

The RTD measurement is obtained on the real industrial reactor or on a representative pilot-scale model reactor. A pulse injection of a known quantity of a tracer is made at the reactor inlet. At the outlet, the tracer concentration is measured and monitored. This outlet concentration can be normalized to obtain directly the RTD function $E(t_s)$, whose integral between 0 and ∞ has to be equal to 1. $E(t_s)\,dt_s$ represents the fraction of the outlet volumetric flow rate which has a residence time between t_s and $t_s + dt_s$. In an industrial precipitator, the RTD determination has to be done under normal operation conditions in the presence of all the reactants and of the solid suspensed phase.

The key points of the measurement will be problematic:

1. During a very short time without disturbing the flow too much, it is necessary to inject a relatively large quantity of tracer in order to obtain measurable tracer concentrations at the outlet.
2. The measurement at the outlet, which is sometimes impossible on a continuous mode and has to be done by sequential sampling at a high frequency, especially at the beginning of the experiment to detect possible bypasses.
3. Sample analysis has to be very precise.
4. The tracer must fulfill several requirements:

    - Very soluble in the studied medium
    - Chemically inert with the reactants, to avoid its chemical degradation or a pollution of the production
    - Easily titrable in the low-concentrations range, to avoid the injection of too large quantities at the inlet.

An elegant solution seems to be given by the radioactive tracers, but their use in industrial conditions is sometimes rather difficult. Fluorescent dyes, especially ultraviolet (UV) dyes, should be preferred [4.4]. To avoid all of these difficulties, it is also possible to work on a model reactor fed with

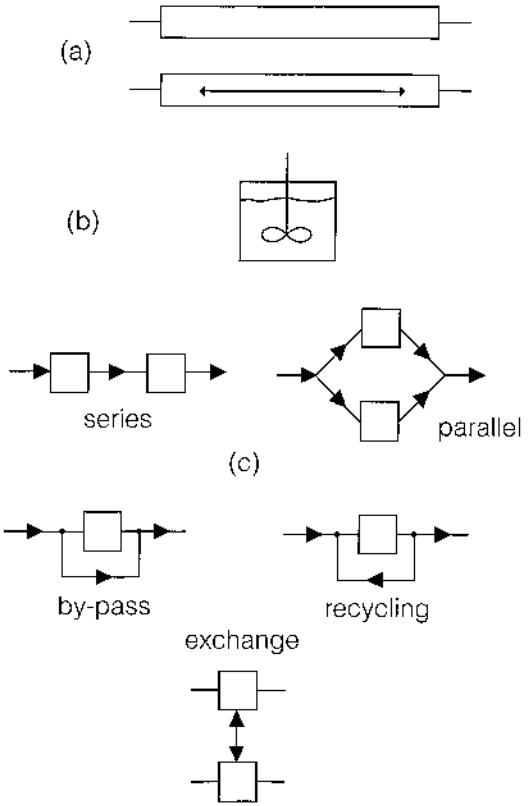

Figure 4.1. Multiparametric models: elementary patterns and binding modes.

water. Measurements in the vessel in addition to the residence time distribution are possible in this case and will lead to a better precision in the flow model.

From the experimental tracer concentration curve at the reactor outlet, the RTD can be easily obtained by normalization. A mass-balance check of the tracer has to be done in order to identify bypasses or dead zones [3.1]. It is then possible to propose a flow model according to the experimental RTD function.

A method currently used is the association of ideal zones, plug flows with or without axial dispersion (Figure 4.1a), and perfect mixed zones (Figure 4.1b) in series or in parallel, introducing, if necessary, bypasses, dead zones with or without exchanges with other zones, or recycling. A model with

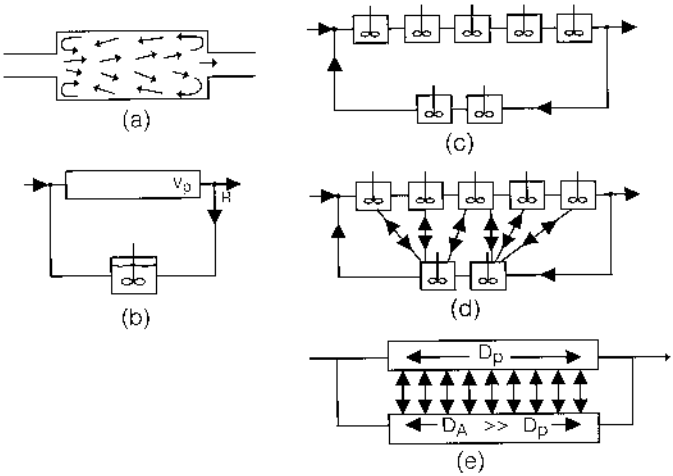

Figure 4.2. Representation of a real reactor by models of increasing complexity.

several parameters taking into account the knowledge about the internal flow in the reactor can thus be obtained.

As an example, let us examine the reactor scheme proposed in Figure 4.2a. This reactor can be described through models of increasing complexity, described in the work of Wen and Fan [4.5]. The first and simplest so-called Sinclair model represented by Figure 4.2b has two parameters: (a) the volume ratio between the plug flow and the perfect mixed zones and (b) the recycling flux ratio. This description is improved by introducing two additional parameters (e.g., J_A and J_P, the numbers of perfect mixed reactors in series in both principal and recycling flows as shown by Figure 4.2c). A physically more realistic description needs a fifth parameter in order to take into account the mass exchange between the principal and recycling flows (Clegg and Coates model, Figure 4.2d). However, five parameters are too much for the limited information contained in the measured RTD curve. It will always be possible with such a high number of parameters to fit the model on the experience, but the physical significance of the obtained set of parameters will be very poor.

For the choice of the accurate model, it is thus necessary to make a compromise between the sharpness of the model, on one hand, and the information contained in only one residence time distribution curve, on the other hand. Multiplication of the number of parameters, even if it seems to be useful physically, should be avoided.

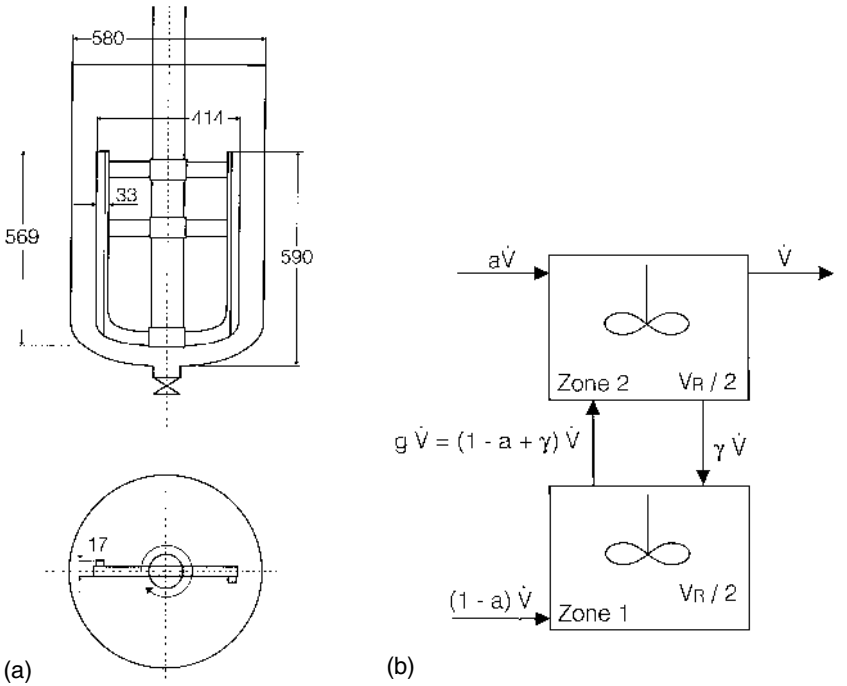

Figure 4.3. (a) Model pilot-scale representation of an industrial precipitator; (b) model of an industrial precipitator.

The problem is to only obtain an as simple as possible representative model of the physical behavior of the flow through the reactor. When a flow model is chosen, the next step is to obtain a set of parameters fitting the model on the experience by optimization on the parameters. For a reactor with several inputs or outlets or more than one physical phase, it is necessary to measure the RTD for all the phases and for all the possible inlet–outlet couples.

4.1.2. Application to an industrial precipitator [1.1]

An industrial precipitator of an organic acid from its sodium salt consists of a vessel agitated by an anchor impeller (Figure 4.3a). Reactant A (acid solution) is fed at the top and reactant B (sodium salt solution) at the bottom of the vessel. Experimental RTD measurements on the industrial reactor and on a pilot-scale model reactor resulted in modeling the precipitator with help of the well-known Cholette and Cloutier representation [3.1].

Figure 4.3b gives the characteristic parameters of this model: a is the fraction of the total flowrate arriving at the top (acid solution), γ is an internal circulation flow rate ratio between the top and the bottom parts of the vessel. $\gamma\dot{V}$ is the flow rate exchanged. For high values of γ, the model becomes equivalent to a perfect mixed vessel.

The expressions of the residence time distribution for this model have to be obtained for each inlet, using the notations of Figure 4.3b:

For the top inlet

$$E_1(t) = \frac{4ag[\exp(s_1 t) - \exp(s_2 t)]}{\tau^2} + \frac{2a[s_1 \exp(s_1 t) - s_2 \exp(s_2 t)]}{\tau(s_1 - s_2)]} \tag{4.1}$$

For the bottom inlet

$$E_2(t) = \frac{4(1-a)g\{\exp(s_1 t) - \exp(s_2 t)\}}{\tau^2(s_1 - s_2)} \tag{4.2}$$

τ is the mean residence time defined as the ratio between volume of the vessel V and total volumetric flow rate $\dot{V}$; s_1 and s_2 are obtained from the following expressions:

$$s_1 = \frac{(a - 2 - 2\gamma) + \sqrt{(a - 2 - 2\gamma)^2 - 4g}}{\tau} \tag{4.3a}$$

$$s_2 = \frac{(a - 2 - 2\gamma) - \sqrt{(a - 2 - 2\gamma)^2 - 4g}}{\tau} \tag{4.3b}$$

The two parameters of the model are the internal exchange ratio γ and the mean residence time τ. They are obtained by fitting the theoretical equations (4.1) and (4.2) to the experimental RTD curves. $\gamma = 3$ was found for the industrial reactor. This shows that this reactor cannot be considered as a perfect mixed precipitator because of the very low value of γ.

The methodology to obtain the model of the macroscopic hydrodynamics of the vessel was relatively simple because the solid had the same dynamics as the liquid, due to relatively small crystals and to a small density difference between solid and liquid. It was sufficient to measure the RTD of the liquid in real suspension conditions to obtain the representation of both the liquid and the solid. It is necessary to work in real suspension conditions because solids influence the rheology of the suspension and the hydrodynamics. In other cases, especially with bigger crystals of high solid density, the RTD of the solid may be different from that of the liquid. It is essential to measure the two residence time distributions. Overcoming this problem is not easy because the residence time distribution of the solid depends on crystal size and a representative tracer of the solid phase will be difficult to find.

During reaction crystallization, small or very small crystals are generally yielded and the two residence time distributions are practically always the same. This may not be the case for crystallizers with large, heavy crystals.

4.2. Micromixing

Let us now discuss microscopic effects or micromixing effects. The extent of a chemical reaction depends, at first, on the contact possibilities of the individual molecules. As a consequence, one has to consider the local microscopic environment of the molecules in the reactor.

The residence time distribution characterizes mean values of the concentrations at the reactor outlet. It allows the prediction of the reaction extent in the reactor only in the following two cases: (a) the reaction is a first-order reaction and the molecules decompose without any necessity of reactive collisions and (b) the residence time is the same for all molecules. In this case, the environment of the considered molecule is made of other molecules having the same mixing history. They will all be transformed with the same extent. This is the case of a plug-flow precipitator fed with premixed reactants.

Under all the other conditions, we have to consider the microscopic state in relation to local concentration fluctuations depending on the micromixing state of the reactor in addition to its macroscopic state of the reactor, characterized by the residence time distribution. A real, perfect macromixed reactor has an intermediate behavior between the two following limits: (a) the microfluid in which we have a perfect mixing at molecular level and no concentration fluctuations and (b) the macrofluid in which the molecules remain grouped in aggregates. Every aggregate can be considered as a small-batch reactor with a reaction time equal to its residence time in the vessel. Then, the extents of the chemical reactions and the selectivity are functions of the micromixing conditions.

4.2.1. Calculation of extreme micromixing states

Let us consider the reaction crystallization in a continuous MSMPR reactor represented in Figure 4.4. Agglomeration and breakage of crystals are supposed to be negligible. The space time or the mean residence time in the reactor is

$$\tau = \frac{V}{\dot{V}_A + \dot{V}_B} \tag{4.4}$$

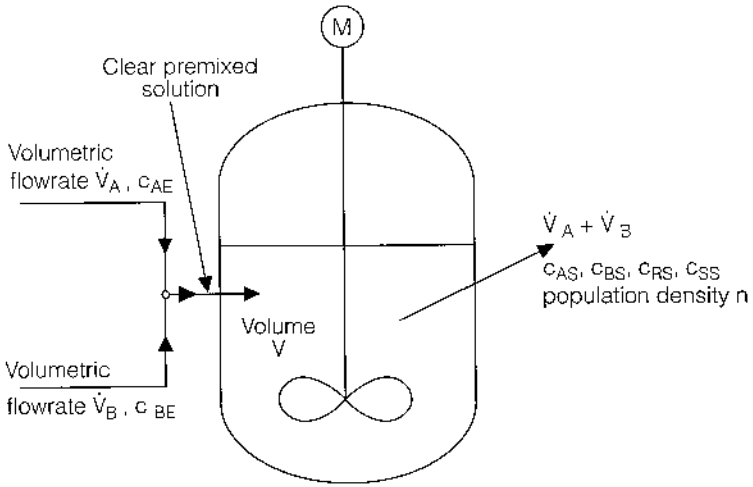

Figure 4.4. Continuous MSMPR reaction crystallizer.

Let us suppose that there is no density variation of the flow during reaction. For a microfluid, the classical MSMPR equations apply. The reaction stoichiometry can be written

$$\mathrm{A} + \mathrm{B} \leftrightarrow \mathrm{R} \qquad \text{reaction 1, rates } r_1 \text{ and } r_{-1}$$

$$\mathrm{R} \rightarrow \mathrm{S\,(solid)} \qquad \text{reaction 2, rate } r_2$$

The mass balances for components, A, B, R, and S can be written in terms of molar fluxes, with the notations of Figure 4.4:

$$\dot{V}_{\mathrm{A}} C_{\mathrm{AE}} - r_1 V + r_{-1} V = (\dot{V}_{\mathrm{A}} + \dot{V}_{\mathrm{B}}) C_{\mathrm{AS}} \tag{4.5a}$$

$$\dot{V}_{\mathrm{A}} C_{\mathrm{BE}} - r_1 V + r_{-1} V = (\dot{V}_{\mathrm{A}} + \dot{V}_{\mathrm{B}}) C_{\mathrm{BS}} \tag{4.5b}$$

$$r_1 V - r_{-1} V - r_2 V = (\dot{V}_{\mathrm{A}} + \dot{V}_{\mathrm{B}}) C_{\mathrm{RS}} \tag{4.5c}$$

$$r_2 V = (\dot{V}_{\mathrm{A}} + \dot{V}_{B}) C_{\mathrm{ss}} \tag{4.5d}$$

and the population balance is given by

$$-V \frac{d(Gn)}{dL} = (\dot{V}_A + \dot{V}_{\mathrm{B}}) n \tag{4.6a}$$

$$C_{\mathrm{ss}} = \frac{\alpha \rho_C}{\tilde{M}_S} \int_0^\infty n(L) L^3 dL \tag{4.6b}$$

The expressions obtained are generally more complicated because chemical reaction rates are defined per unit volume of liquid and not per unit volume of suspension. We are considering here the case of a negligible solid volume.

For the macrofluid, every microaggregate will react as a batch reactor, which does not exchange any mass with the other aggregates. Every aggregate reacts as long as it stays in the reactor. The outlet concentrations are obtained by integrating the evolution of all the aggregates over the residence time distribution.

For each aggregate, the mass-balance equations can be written

$$\frac{dC_A}{dt_s} = \frac{dC_B}{dt_s} = r_{-1} - r_1 \tag{4.7a}$$

$$\frac{dC_R}{dt_s} = r_1 - r_{-1} - r_2 \tag{4.7b}$$

$$\frac{dC_S}{dt_s} = r_2 \tag{4.7c}$$

with the following initial conditions for $t_s = 0$, corresponding to premixed feeds:

$$C_{A0} = \frac{C_{AE}\dot{V}_A}{\dot{V}_A + \dot{V}_B} \tag{4.8a}$$

$$C_{B0} = \frac{C_{BE}\dot{V}_A}{(\dot{V}_A + \dot{V}_B)} \tag{4.8b}$$

$$C_{R0} = C_{S0} = 0 \tag{4.8c}$$

The population balance in an aggregate is

$$\frac{\partial n}{\partial t} + \frac{\partial (Gn)}{\partial L} = B_{hom}\delta(L - L_0) \tag{4.9}$$

$\delta(L - L_0)$ is a Dirac function equal to 0 if $L \neq L_0$. Secondary nucleation is assumed to be negligible. Equation (4.6) applies for each aggregate.

The boundary conditions for the population balance in an aggregate are

$$n(0, L) = n(t_s, 0) = 0 \tag{4.10}$$

At the reactor outlet,

$$n(L) = \int_0^\infty n(t_s, L)E(t_s)\,dt_s \tag{4.11a}$$

$$C_A = \int_0^\infty C_A(t_s)E(t_s)\,dt_s \tag{4.11b}$$

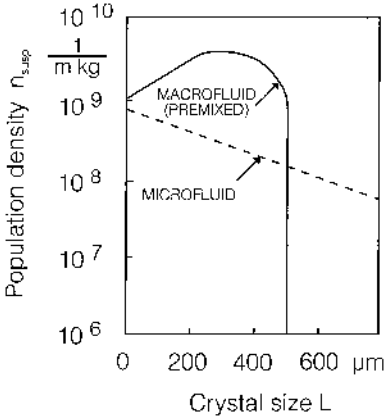

Figure 4.5. Result of the simulation of micromixing limits.

For an MSMPR crystallizer,

$$E(t_s) = \frac{\exp(-t_s/\tau)}{\tau} \tag{4.12}$$

The results obtained by Garside and Tavare [4.6] are shown on Figure 4.5 for classical reaction and crystallization kinetics. The population density is given per unit mass of suspension

$$n_{\text{susp}} = \frac{n}{\rho_{\text{sus}}} \tag{4.13}$$

where ρ_{sus} is the specific mass of the suspension. Two facts result from the simulation of Garside and Tavare:

1. For a premixed feed, an increase of the mixing quality leads to a decrease of the supersaturation. A higher nucleation rate thereby takes place under macrofluid conditions and leads to a lower mean size of the crystals. The opposite conclusion would be obtained for unpremixed feeds.
2. No local effects at the feed point are taken into account in this simulation. Such effects would increase the nucleation and simultaneously decrease the mean crystal size.

The difference between the two population densities is very important and proves that micromixing has to be considered for prediction of crystal size distribution in reaction crystallization.

4.2.2. Crystallization processes and their interaction with micromixing

Relevant crystallization processes are primary nucleation (homogeneous or heterogeneous), followed by crystal growth, secondary nucleation, agglomeration, or breakage. Among the crystallization processes, primary homogeneous nucleation is the fastest [4.7]; it is observed in the higher supersaturation range. For the sake of simplicity, one can demonstrate that primary nucleation is the main chemical process competing with the mixing process. Because for liquids with low viscosity, complete mixing of feed fractions is achieved after very few internal circulation loops following addition, mixing effects modifying the rates of nucleation, growth agglomeration, or breakage can only occur during this period. Typically, circulation times in a laboratory stirred tank are of the order of magnitude of 1 s, or a few seconds in pilot-scale tanks.

The ratio R of the crystallized mass during one circulation loop of duration t_c to the already existing solid mass is

$$R \leq \frac{3G_{\max}t_c}{L_{32}} \tag{4.14}$$

where L_{32} is the Sauter diameter and $G_{\max}$ is the maximum growth rate encountered during the loop. The calculation of R with usual values ($G_{\max} = 10^{-7}\,\mathrm{ms}^{-1}$ [4.8], $L_{32} = 10^{-5}\,\mathrm{m}$, $t_c = 1\,\mathrm{s}$) shows that it is in the order of magnitude of a few percent. The growth rate is limited by external diffusion. Of course, smaller crystals can grow faster, but the reagent depletion consecutive to this growth is negligible for small crystals. For continuous-stirred tanks (MSMPR), the equation (4.14) is written as

$$R \leq \frac{t_c}{\tau} \tag{4.15}$$

which is also very small in practice. Thus, as a first approximation, the consumption of reagents by growth can be neglected during the mixing time interval. Moreover, because primary nucleation gives negligible reagent consumption, the whole system during the first loop approximately behaves as a mixing process of inert compounds. If no crystals are initially present either in the feed streams or in the tank, induction times usually are in the order of magnitude of a few minutes [4.9–4.10].

4.2.3. Competition between mixing and primary nucleation: Modes of precipitation subject to mixing effects

The purpose of this section is not to predict the state of micromixing encountered in different precipitator types or the PSD that it generates,

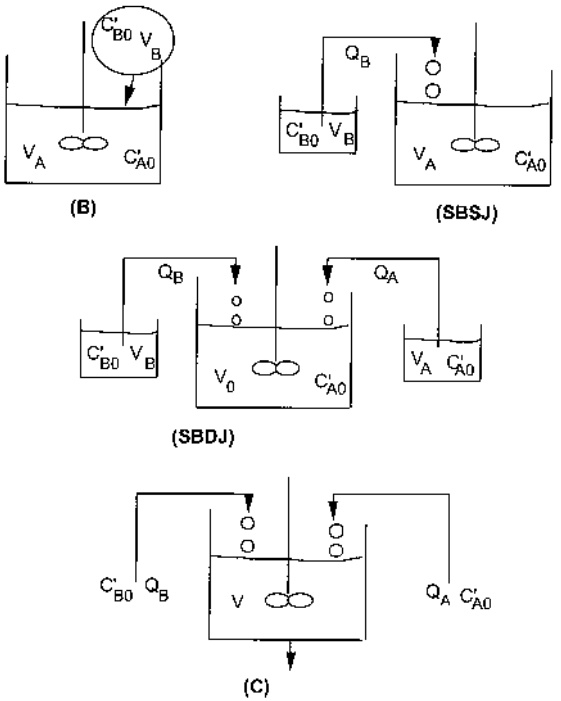

Figure 4.6. Different types of precipitators: Batch (B), semibatch single-jet (SBSJ), semibatch double-jet (SBDJ), and continuous (C).

but to forecast in which types of precipitator and under which circumstances micromixing effects are likely to occur.

We hereafter assume the simplified stoichiometry

$$A + B \rightarrow S\,(\text{solid})$$

Chemical parameters are the initial concentrations of the reagents A and B, C'_{B0} and C'_{A0}, respectively.

The generation of solids from the solutions by precipitation is generally carried out in different types of precipitator, which are classified as batch, semibatch combined with single-jet or double-jet feeding, or continuous (hereafter called precipitator types). Four types of precipitator are examined: batch, semibatch single-jet, semibatch double-jet, and continuous (Fig. 4.6). Their operating parameters are recalled in Table 4.2. When double-jet feeding is chosen, the essential difference from the point of view of mixing is that the contact of reagents may occur between the jets as well as between

Table 4.2. Parameters, Initial and Final Supersaturation in Different Precipitator Types and Operation Modes

Precipitator type	Parameters	Symmetrical (SYM) or nonsymmetrical feeding	Rapid (R) or slow (S) feed	Maximum initial Supersaturation S_{IMAX}	Final supersaturation S_F
Batch	$\alpha = \frac{V_A}{V_B}$	NSYM	R	$\frac{C'_{A0}C'_{B0}}{P_s}$	$\frac{C'_{A0}C'_{B0}}{(1+\alpha)(1+1/\alpha)P_s}$
Semi-batch single jet	$t_f, t_c, \alpha = \frac{V_A}{B_B}$ M fractions $= \frac{t_f}{t_c}$ with current fraction m: $1 \le m \le M$	NSYM	S	$\frac{C^*_A C'_{B0}}{P_s}$	$\frac{C^*_A[\alpha+(m-1)/M]\{C'_{B0}/M + C^*_B[\alpha+(m-1)/M]\}}{P_s(\alpha+m/M)^2}$
Semi-batch single jet	$t_f, t_c, \alpha = \frac{V_A}{V_B}$ M fractions $= \frac{t_f}{t_c}$ with current fraction m: $1 \le m \le M$	NSYM	R	$\frac{C'_{A0}C'_{B0}\alpha}{P_s[\alpha+(m-1)/M]}$	$\frac{C'_{A0}C'_{B0}(m/M)\alpha}{P_s(\alpha+m/M)^2}$
Semibatch double-jet separate feed	$t_f, t_c, \alpha = \frac{V_A+V_0}{V_B}$ $v = \frac{Q_A}{Q_B} = \frac{V_A}{V_B}$ M fractions $= \frac{t_f}{t_c}$ with current fraction m: $1 \le m \le M$	SYM or NSYM	S	$\frac{C^*_A C'_{B0}}{P_s}$	$\frac{\{C^*_A[\alpha-v+(1+v)(m-1)/M]+vC'_{A0}/M\}\{C'_{B0}/M + C^*_B[\alpha-v+(1+v)(m-1)/M)\}}{P_s[\alpha-v+(1+v)m/M]^2}$
Semibatch double-jet separate feed	$t_f, t_c, \alpha = \frac{V_A+V_0}{V_B}$ $v = \frac{Q_A}{Q_B} = \frac{V_A}{V_B}$ M fractions $= \frac{t_f}{t_c}$ with current fraction m: $1 \le m \le M$	SYM or NSYM	R	$\frac{C'_{A0}C'_{B0}[\alpha-v+v(m-1)/M]}{P_s[\alpha-v+(v+1)(m-1)/M]}$	$\frac{C'_{A0}C'_{B0}(\alpha-v+vm/M)(m/M)}{P_s[\alpha-v+(v+1)(m/\mathrm{M})]^2}$

Semibatch double-jet premixed feed	$t_f, t_c, \alpha = \dfrac{V_A + V_0}{V_B}$ $v = \dfrac{Q_A}{Q_B} = \dfrac{V_A}{V_B}$ M fractions $= \dfrac{t_f}{t_c}$ with current fraction m: $1 \le m \le M$	SYM or NSYM	S	$\dfrac{C'_{A0}C'_{B0}}{P_s}$	$\dfrac{\{C^*_A[\alpha - v + (1+v)(m-1)/M] + vC'_{A0}/M\}\{C'_{B0}/M + C^*_B[\alpha - v + (1+v)(m-1)/M]\}}{P_s[\alpha - v + (1+v)m/M]^2}$
Semibatch double-jet premixed feed	$t_f, t_c, \alpha = \dfrac{V_A + V_0}{V_B}$ $v = \dfrac{Q_A}{Q_B} = \dfrac{V_A}{V_B}$ M fractions $= \dfrac{t_f}{t_c}$ with current fraction m: $1 \le m \le M$	SYM or NSYM	R	$\dfrac{C'_{A0}C'_{B0}}{P_s}$	$\dfrac{C'_{A0}C'_{B0}(\alpha - v + vm/M)(m/M)}{P_s[\alpha - v + (v+1)m/M]^2}$
Continuous separate feed	$v = \dfrac{Q_A}{Q_B}, \tau, t_c$ $\alpha = \dfrac{(V + Q_A t_c)}{Q_B t_c}$ $= v + \dfrac{(v+1)\tau}{t_c}$	SYM	S	$\dfrac{C^*_A C'_{B0}}{P_s}$	$\dfrac{[C^*_A(\alpha - 2v - 1) + vC'_{A0}][C^*_B(\alpha - 2v - 1) + vC'_{B0}]}{(\alpha - v)^2 P_s}$
Continuous premixed feed	$v = \dfrac{Q_A}{Q_B}, \tau, t_c$ $\alpha = \dfrac{V + Q_A t_c}{Q_B t_c}$ $= v + (v+1)\tau/t_c$	SYM	S	$\dfrac{C'_{A0}C'_{B0}}{P_s}$	$\dfrac{[C^*_A(\alpha - 2v - 1)v + C'_{A0}][C^*_B(\alpha - 2v - 1) + vC'_{B0}]}{(\alpha - v)^2 P_s}$

each of the jets and the bulk. Thus, for semibatch double-jet and continuous precipitators, both separate and premixed feeds are considered.

Note that the batch tank as well as the semibatch single-feed tank is nonsymmetrical with respect to the flux of reagents by nature. Other types may be operated in either symmetrical (hereafter SYM) or nonsymmetrical (NSYM) ways. Either rapid (R) or slow (S) addition of reagents are considered for semibatch precipitators: The feed is divided into M fractions with $M = t_f/t_c$ (typically, $M = 100$ was used). For slow feeding, after the addition of one fraction with volume V_B/M, the system reaches an equilibrium state (C_A^*, C_B^*) before the next fraction is added and so on. For rapid feeding, the final state after one fraction is the initial state for the next fraction. From the point of view of species A and B, the system then behaves like a batch precipitator. However, nucleation, which is extremely rapid, takes place with negligible consumption of both reagents.

For each type of precipitator, an initial maximum S_{IMAX} and final supersaturation S_F are calculated in Table 4.2. Two relevant indicators of sensitivity of a given precipitator to mixing effects are (a) the maximum supersaturation ratio S_{IMAX}/S_F between the first contact of the reagents and the final mixing situation after mixing in the tank and (b) the median supersaturation $S_{AV} = (S_{IMAX} + S_F)/2$ during supersaturation decrease. S_{IMAX}/S_F is an indicator of the broadness of the range of supersaturations encountered during mixing. S_{AV} represents the order of magnitude of the average nucleation rate.

All simulations of Figures 4.7 and 4.8 have been made with $C'_{A0}/(P_S)^{0.5} = 10^3$, $M = 100$, $\tau/t_c = 100$, and under stoichiometric conditions (i.e., $C'_{B0} = \alpha C'_{A0}$ in all precipitator types excepted continuous where $C'_{B0} = \nu C'_{A0}$). S_{IMAX}/S_F and S_{AV} have been represented for the different types of precipitator. The sensitivity increases on the first diagonal toward high values of both S_{IMAX}/S_F and S_{AV}: along the x axis (small values of S_{IMAX}/S_F) there is no significant decrease of supersaturation during the mixing process; along the y axis (small values of S_{AV}), there is no sufficient supersaturation to lead to significant primary nucleation during the mixing phase.

As far as nucleation and, thus, the final particle size are concerned, the highest rates are to be observed under experimental conditions at the right-hand side of Figures 4.7 and 4.8. The results in Figures 4.7 and 4.8 merit the following additional comments:

1. The series of results appear to fall on four staged curves corresponding to four different precipitation conditions (Fig. 4.8). The upper curve is obtained for symmetrical reagent feed conditions in semibatch double-jet and continuous precipitators: The return to equilibrium is assumed

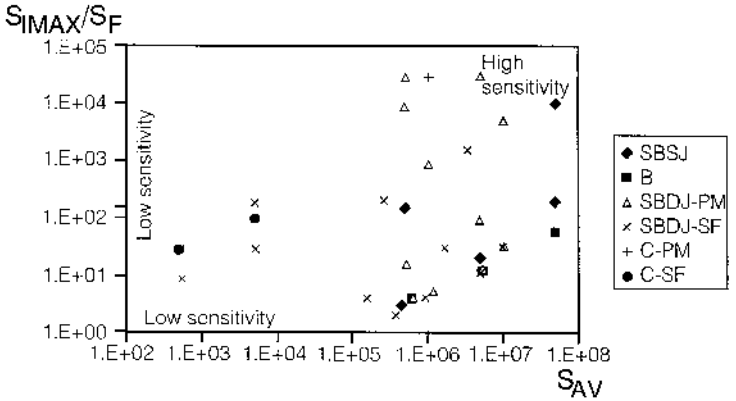

Figure 4.7. Sensitivity of different types of precipitators under stoichiometric conditions to mixing effects (B = batch; SBSF = semibatch single jet; C-SF = continuous with separate feed streams; SBDJ-SF = semibatch double jet with separate feed streams; C-PM = continuous with premixed feed streams; SBDJ-PM = semibatch double jet with premixed feed streams).

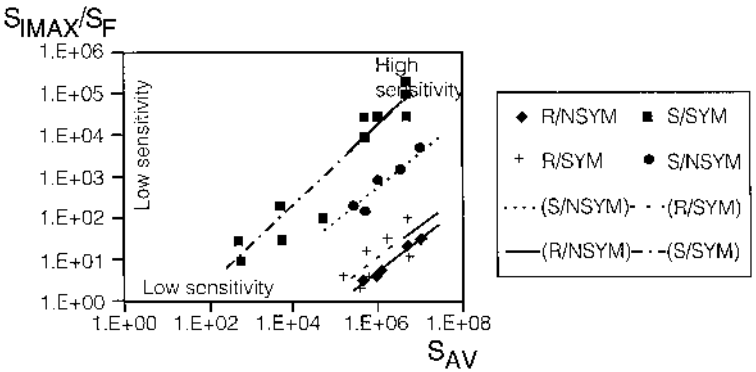

Figure 4.8. Sensitivity of different types of precipitators to mixing effects under different, stoichiometric feed conditions (SYM = symmetrical feed: stoichiometric flux of reagents and stoichiometric initial concentrations A and B; NSYM = nonsymmetrical feed; S = slow feeding; R = rapid feeding).

between two successive fractions of feed because of slow addition. The median curve corresponds to nonsymmetrical feed conditions coupled with the return to equilibrium between two successive fractions of feed. The two lower curves represent symmetrical and nonsymmetrical feed

conditions, respectively, without any return to equilibrium because of the fast feeding of the reagents.

2. For single feed, the semibatch precipitators with slow feeding always appears more sensitive to micromixing effects than the batch one (Fig. 4.7). For double feed with separate feed streams, continuous precipitators show low sensitivities. These trends are confirmed by the results from the literature [4.11, 4.12].
3. Unbalanced initial volumes ($\alpha \gg 1$) or flow rates ($\upsilon \gg 1$) enhance sensitivity in any case with a shift to the right upper corner on the corresponding curve in Figure 4.7. This has been observed among others by [4.8, 4.13] in batch precipitators.
4. Tanks with premixed feed streams are generally more sensitive to micromixing effects than those with unmixed feed streams (Fig. 4.7).

These considerations should help the engineers to select the adapted device(s) with minimum mixing effects when designing their tanks and feed modes for kinetic measurements. If a less sensitive situation to mixing is the goal (i.e., for industrial or kinetic purposes), a batch precipitator with equal volumes for single-jet case [4.8] or a continuous precipitator with separate feed streams and equal flow rates for the double-jet case [4.14] should be preferred.

Conversely, if mixing effects are sought, semibatch single-jet and semibatch premixed double-jet tanks will yield highly sensitive results to mixing. However, one should remind that these results only indicate first trends: finer tuning will depend on mixing performance and nucleation kinetics and rely on models of these. An example of this will be developed in the next section.

4.2.4. Competition between mixing and primary nucleation: A quantitative evaluation in the case of the batch tank [4.8]

At the beginning of reaction crystallization, three steps of the process are competing:

1. The micromixing step, which develops with finite kinetics, including the molecular diffusion which destroys the last concentration gradients.
2. The chemical reactions, which have their own kinetics. They can occur very rapidly, especially for ionic reactions which, practically, are always to be considered at equilibrium.
3. The primary nucleation, which is the fastest step in crystallization.

To understand the interactions between the mechanisms, let us consider the situation represented by Figure 4.7, which corresponds to the batch tank of Figure 4.4. A certain volume V_{B0} of ionic reactant B at concentration C'_{B0}

is injected in a volume V_{A0} ($V_{A0} \geq V_{B0}$) of ionic reactant A at concentration C'_{A0}. Assume the reaction crystallization of type $A + B \rightleftharpoons S$ with or without a soluble intermediary. Let us set

$$\alpha = \frac{V_{A0}}{V_{B0}} \geq 1 \quad \text{and} \quad M = \frac{C'_{B0} V_{B0}}{C'_{A0} V_{A0}}$$

After perfect mixing and before the reaction, the concentrations C_{A0} and C_{B0} can be written

$$C_{A0} = \frac{C'_{A0}}{1 + \alpha^{-1}} \tag{4.16a}$$

$$C_{B0} = \frac{C'_{B0}}{1 + \alpha} \tag{4.16b}$$

The driving force of the crystallization is given by

$$S_a = \frac{C_A C_B f_A f_B}{K_a} \tag{4.17}$$

If V_{A0} and V_{B0} had been perfectly mixed before the beginning of primary nucleation, the driving force of nucleation would have been

$$S_M = \frac{C_{A0} C_{B0} f_A f_B}{K_a} = \frac{C'_{a0} C'_{B0} f_A f_B}{K_a (2 + \alpha + \alpha^{-1})} \tag{4.18}$$

However, V_{B0} is not immediately mixed with all the volume V_{A0}, but with a fraction $V'_{A0} = \beta V_{B0}$ of it. Real concentrations after mixing of A and B in a volume $V'_{A0} + V_{B0}$ will be

$$C''_{A0} = \frac{C'_{A0}}{1 + \beta^{-1}} \tag{4.19a}$$

$$C''_{B0} = \frac{C'_{B0}}{1 + \beta} \tag{4.19b}$$

with $\beta \leq \alpha$, and the driving force of nucleation is

$$S_a = \frac{C'_{A0} C'_{B0} f_A f_B}{K_a (2 + \beta + \beta^{-1})} \tag{4.20}$$

Neglecting the variations of the activity coefficients f_A and f_B, we obtain

$$\frac{S_a}{S_M} = \frac{2 + \alpha + \alpha^{-1}}{2 + \beta + \beta^{-1}} \tag{4.21}$$

which is directly obtained by a mass balance and is a function of the quality of macromixing and micromixing. For perfect mixing, we obtain

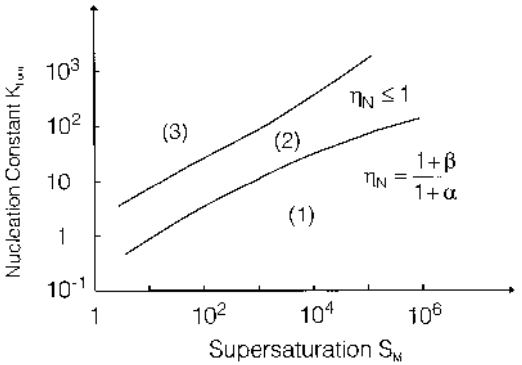

Figure 4.9. Different regions of nucleation efficiency in the (K_{hom}, S_M) plane. (From Ref. [4.8].)

$S_a = S_M$. Generally, β is much smaller than α. For values close to 1 corresponding to the mixing of two equal volumes V_{A0} and V_{B0}, the defects in mixing will lead to $S_a/S_M < 1$. On the contrary, for high values of α, S_a/S_M will be greater than 1 for every β value.

The primary homogeneous nucleation for perfect mixing develops in volume $V_{A0} + V_{B0}$ and its rate is given by

$$B_{\text{hom, th}} = A_{\text{hom}} \exp\left(-\frac{K_{\text{hom}}}{(\ln S_M)^2}\right) \tag{4.22}$$

In imperfect mixing conditions, the same expression is used, replacing S_M by S, and the primary nucleation occurs only in volume $V'_{A0} + V_{B0}$. The nucleation efficiency corresponding to the ratio between the real number of nuclei generated per unit time and the theoretical one under perfect mixing conditions will be calculated from

$$\eta_N = \frac{(V'_{A0} + V_{B0})B_{\text{hom, real}}}{(V_{A0} + V_{B0})B_{\text{hom, th}}} = \frac{(1+\beta)\exp[-K_{\text{hom}}/(\ln S)^2]}{(1+\alpha)\exp[-K_{\text{hom}}/(\ln S_M)^2]} \tag{4.23}$$

Figure 4.9 shows the result of this very simple model in the plane K_{hom} versus S_M. Three regions appear. In region 1,

$$\eta_N = \frac{1+\beta}{1+\alpha} \leq 1 \tag{4.24}$$

This corresponds to the case $B_{\text{hom}} = A_{\text{hom}}$ at very high supersaturations. In region 2, as shown in Figure 4.10b, relation (4.24) is not yet verified but η_N stays below 1. In region 3, as shown in Figure 4.10a, $\eta_N > 1$ is possible at

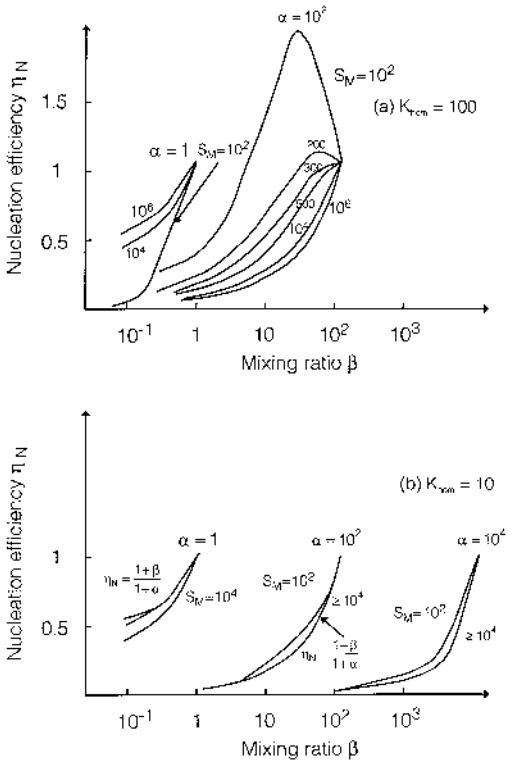

Figure 4.10. Nucleation efficiency η_N versus mixing ratio β.

high values of K_{hom} and low values of S_M. From the previous calculations, three conclusions may be drawn:

1. A small volume available for nucleation generally makes up for the high nucleation rates resulting from high intermediate local supersaturations in situations of incomplete mixing ($\beta \leq \alpha$); consequently, $\eta_N < 1$ is usually obtained. It may also be possible that ripening (see Chapter 7) of the crystals initiated under these high supersaturations occurs very rapidly. When complete and perfect mixing is achieved, supersaturation is much lower and these small crystals become thermodynamically unstable and are doomed to disappear.
2. To perform valid kinetic studies, it is necessary to operate with η_N close to 1. This can be achieved only if the local volume ratio during mixing on the molecular scale equals the overall volume ratio α. $\beta = \alpha$ certainly holds for batch precipitations with α close to 1: For such precipitations,

molecular mixing between the reactants takes place when the added fluid has been dispersed through the whole tank (in other words, with good macromixing), allowing all A to be contacted with B. In fact, in the first stages of the mixing process, the contacting of both reactants at the molecular scale is not achieved and, thus, no primary nucleation occurs. Other mixing situations, such as batch precipitations with high α volumes and semibatch single-jet precipitations, will lead to partial contact at the molecular scale between the reactants before micromixing is completed. According to Baldyga and Bourne [4.15], the local volume ratio for molecular mixing by vorticity and diffusion is about $\beta = 1$ for semibatch, single-jet stirred reactors. Thus, α is larger than β, and a segregation process at the molecular level is likely to occur.

3. Mixing effects are accentuated in precipitations having high α values. For this purpose, semibatch, single-jet precipitators may be employed, but also batch precipitations with the addition of a small volume V_{B0} of highly concentrated B into V_{A0}. In both cases, β increases from about 1 at the beginning of the diffusive mixing step up to α. Thus, nucleation efficiency is not always near 1, implying that the number of crystals produced and the final crystal size distribution differ from that obtained under perfect mixing conditions.

4.2.5. Practical interactions between mixing and the overall steps of reaction crystallization

Turbulence governs the macromixing and micromixing of the feed streams of reagents with the bulk: Macromixing is the process leading to spatial homogeneity of the average concentration in the precipitator, whereas local values of concentrations are determined by micromixing. Changing stirring speed, stirrer, or feed stream locations can modify them in a very complicated way. Pohorecki and Baldyga [4.16], Stavek et al. [4.17], and Tosun [4.11] have published this research first. Other authors have extended this research to different products and various contact modes [4.11, 4.18–4.21]. More recently, Manth et al. [4.22], van Leeuwen et al. [4.23], Houcine et al. [4.13], and Phillips et al. [4.24] have published on this subject. David has discussed many of the earlier results in a review [4.25]. These results, which are based on different precipitations (barium and strontium sulfate, calcium oxalate, benzoic acid, silver chloride, zinc oxalate), can be summarized as follows:

1. Switching to a more turbulent feed location decreases the average particle size in batch tanks [4.7], whereas it increases that size in single-jet semibatch tanks [4.13, 4.24]. The most impressive effects are obtained in single-jet semibatch tanks.

2. Increasing stirring speed decreases average particle size in batch tanks [4.8, 4.16], whereas it has miscellaneous effects in single-jet semibatch tanks [4.11, 4.12, 4.21].
3. Double-jet systems gave different results: For semibatch tanks, spectacular effects were obtained by putting the feed streams together [4.11]; the precipitations in continuous tanks are the less sensitive ones with respect to mixing effects when the stirring speed is changed [4.19].

Up to this point, we have discussed only the initial seconds of the precipitation and the micromixing process in batch or semibatch reactors. In fact, two factors are likely to affect mixing conditions during this short period: the feed point location and the stirrer speed.

The influence of the second parameter continues as long as precipitation proceeds. Thus, whereas only the primary nucleation is affected by the feed point location, the rates of primary nucleation, secondary nucleation, diffusional growth, and agglomeration vary with stirring intensity. The resulting effects of these two factors on physical values such as the number of crystals per unit volume N_c, the average diameter L of the crystals, and the overall reaction rate r are summarized in Table 4.3.

An increase of stirring speed with a fixed feed point has different effects on N_c and L, whereas r increases. On the other hand, when the stirring speed is kept constant, moving the feed addition point from one zone to another where the turbulence level is higher influences the primary nucleation only. This is because growth, agglomeration, and even secondary nucleation are slower processes, and their rates are integrated over the entire recirculation flow of the reactor. Consequently, higher values of N_c and r as well as lower values of L are expected in this situation.

Effects are revealed to be more drastic in the second case. That is why the influence of the feed addition point may be much more important than the stirring speed as far as mixing is concerned.

Therefore, changing the feed point for a constant stirring speed can be a test of the state of micromixing in a reactor. If different addition points are used and no modifications are observed in the conversion curve or the crystal size distribution, then there is no influence of micromixing on the outcome of the reaction. On the contrary, experiments of this kind with varying stirring speeds cannot be as easily interpreted, as there is competition between contradictory effects (Table 4.3). Only the first procedure leads to firm conclusions. In particular, the presence of long induction times in batch precipitation does not ensure that results do not depend on micromixing.

These conclusions are valid when primary nucleation is the only process that is sufficiently fast to be influenced by micromixing (i.e., when no sig-

Table 4.3. Influence of Mixing Increasing on Precipitation Processes

	Rapid local process primary nucleation	Slow processes averaged over the tank				
		Secondary nucleation	Growth by integration	Diffusional growth	Agglomeration	Overall effect
Same feed point; increasing stirring speed	Variable on N_C, L, r	Enhanced $N_C \uparrow, L \downarrow, r \uparrow$	No influence on N_C, L, r	Enhanced $N_C, L \uparrow, r \uparrow$	Enhanced $N_C \downarrow, L \uparrow, r \downarrow$	Related to many processes
Same stirring speed; addition in a more turbulent zone	Variable on N_C, L, r	No influence on N_C, L, r	No influence on N_C, L, r	No influence on N_C, L, r	No influence on N_C, L, r	Due to primary nucleation only

Note: N_C = number of crystals per unit volume; L = crystal mean diameter; r = overall crystallization rate.

nificant consumption of reactants takes place during the first seconds of precipitation corresponding to the mixing stage).

The first complete modeling attempts of micromixing and precipitation have been made by Pohorecki and co-workers [4.18, 4.26], Tavare [4.27] and recently Wynn et al. [4.28] and Lindberg and Rasmuson [4.29]. All of these authors consider phenomenological models of mixing coupled with kinetic equations for nucleation and crystal growth.

5. CONCLUSION: A GENERAL METHODOLOGY TO SOLVE A REACTION CRYSTALLIZATION PROBLEM

Figure 5.1 shows the complex coupling among specifications (productivity, crystal size distribution), operating conditions of the crystallizer, and process. The problem for industrial people is to design a crystallizer to obtain specifications, and this problem has no universal solution today for reaction crystallization.

Nevertheless, it is possible to propose a general methodology illustrated by Figure 5.2. After taking physical constants from the literature or after measuring them ($\rho_C, \tilde{M}_S$, solubility product, chemical equilibrium con-

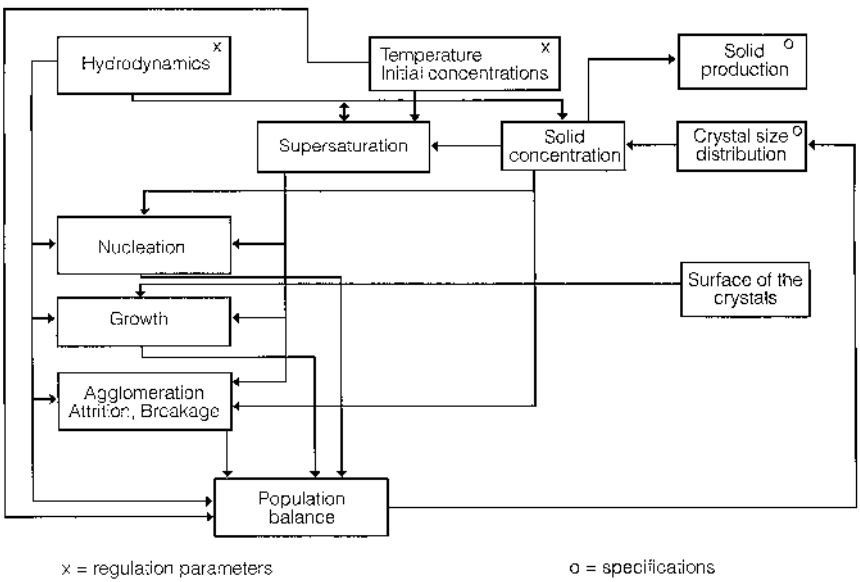

Figure 5.1. Relation between among parameters, specifications, and process steps.

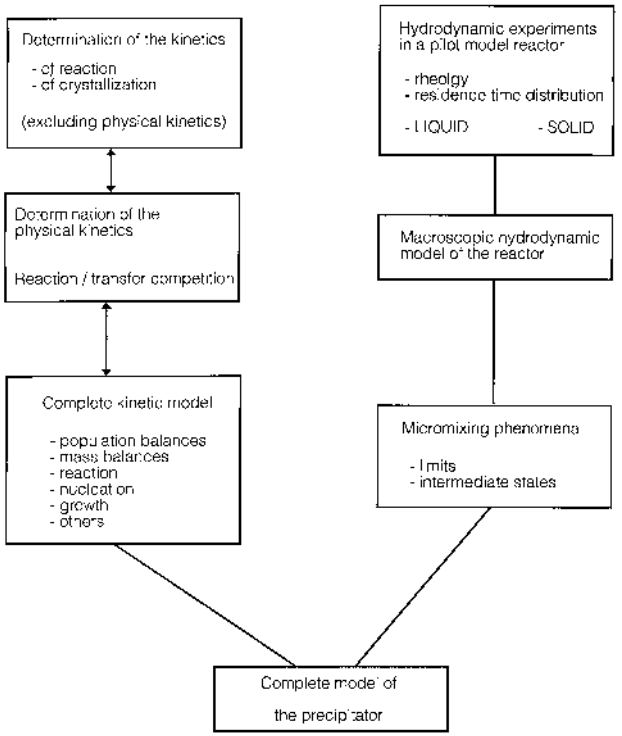

Figure 5.2. Methodology for the modeling of a reaction crystallizer.

stants, etc.), it is necessary to determine the reaction and crystallization kinetics from batch experiments, in 1-L reactors for instance. It is necessary to run these experiments in reactors, which are highly efficient in terms of mixing.

One can obtain the reaction kinetics and the kinetics of the different steps of the crystallization from these experiments by fitting theroetical models on experimental measurements of supersaturation (e.g., by conductivity for ionic reactions for example) and crystal size distribution, which are both a function of time. Varying the feed point and the stirrer speed may test the influence of micromixing.

The experimental conditions are varied (temperature, concentrations, etc.) to separate as much as possible the different steps (reaction only, nucleation, growth, agglomeration, etc.). A complete model of reaction crystallization is too complicated to be fitted on experiments, which are simultaneously influenced by all the steps.

After attainment of the kinetic model including physical limitations, it is necessary to validate it with experiments in a continuous laboratory-scale MSMPR crystallizer, with perfect mixing behavior. The industrial reactor is characterized by residence time distribution measurements, and a hydrodynamic model is established. Combining the hydrodynamic and the kinetic models, it is then possible to propose a complete model of the precipitator in order to calculate the concentrations of the reactants and solid and the population density at the reactor outlet. This can be done by writing and solving the mass-, energy-, and population-balance equations for each ideal zone of the proposed hydrodynamic model. It is also possible to simulate new situations with the aim of improving the reactor function.

Only in this way is the scale-up of the obtained kinetics to an industrial vessel possible, because mixing and hydrodynamics, in general, heavily influence reaction crystallization. Therefore, laboratory experiments under imperfect mixing conditions cannot lead to reliable kinetic models. Moreover, to run an agitated industrial vessel with the fixed aim to obtain a given crystal size distibution does not seem to be the best solution.

However, the key point in reaction crystallization is the contact between the reacting species, which generates and determines the supersaturation. Hence, developments in reaction crystallization equipment are oriented in the direction of perfectly mixed, small, continuous precipitators with a high turbulence level or jet mixing. The classical mechanically agitated industrial vessel seems to be too complicated in terms of turbulence, macromixing and micromixing to allow a reliable scale-up from laboratory experiments. Much work is still required to reach this goal, and it seems to be more efficient to work on different industrial solutions with a better homogeneity in terms of turbulence and power dissipation. Such developments have yet to be achieved in the manufacturing of pigments and silver halides.

REFERENCES

[1.1] R. Franck, R. David, J. Villermaux, and J. P. Klein, Crystallization and precipitation engineering—II: A chemical reaction engineering approach to salicyclic acid precipitation: modeling of batch kinetics and application to continuous operation, *Chem. Eng. Sci., 43*: 69 (1988).

[1.2] R. David and J. M. Bossoutrot, Crystallization and precipitation engineering: VII. The modelling of sodium tetrahydrate perborate crystallization from solution, *Chem. Eng. Sci., 51*: 4939 (1996).

[1.3] P. P. Chiang and M. D. Donohue, A kinetic approach to crystallization from ionic solution: I. Crystal growth, *J. Colloid Interf. Sci., 122*(1): 230 (1988).
[2.1] C. W. Davies and A. L. Jones, The precipitation of silver chloride from aqueous solution: Kinetics of growth of seed crystals, *Trans. Faraday Soc., 51*: 812 (1955).
[2.2] J. F. Zemaitis, D. M. Clark, M. Rafal, and N. C. Scrivner, *Handbook of Aqueous Electrolyte Thermodynamics, Theory and Applications*, American Institute of Chemical Engineering, New York (1986).
[2.3] J. A. Dirksen and T. A. Ring, Fundamentals of crystallization: kinetic effects on particle size distribution and morphology, *Chem. Eng. Sci., 46*(10): 2389 (1991).
[2.4] A. E. Nielsen, Electrolyte crystal growth mechanisms, *J. Cryst. Growth, 67*: 289 (1984)
[3.1] J. Villermaux, *Génie de la réaction chimique: conception et fontionnement des réacteurs*, Lavoisier, Paris (1985).
[3.2] G. F. Froment and K. B. Bischoff, *Chemical Reactor Analysis and Design*, John Wiley & Sons, New York (1979).
[3.3] J. P. Klein, R. Boistelle, and J. Dugua, Cristallisation: aspects théoriques, *Tech. Ing. J., 1500*: 1 (1989).
[3.4] G. Matz, Ostwald ripening: A modern concept, *Ger. Chem. Eng., 8*: 255 (1985).
[3.5] A. Mersmann and M. Kind, Chemical engineering aspects of precipitation from solution, *Chem. Eng. Technol., 11*: 264 (1988).
[3.6] H. Muhr, R. David, J. Villermaux, and P. H. Jezequel, Crystallization and precipitation engineering: V. Simulation of the precipitation of silver bromide octahedral crystals in a double-jet semi-batch reactor, *Chem. Eng. Sci., 50*: 345 (1995).
[3.7] H. Muhr, R. David, J. Villermaux, and P. H. Jezequel, Crystallization and precipitation engineering: VI. Solving population balance in the case of the precipitation of silver bromide crystals with high primary nucleation rates by using the first order upwind differentiation, *Chem. Eng. Sci., 51*: 309 (1996).
[3.8] R. H. Doremus, Precipitation kinetics of ionic salts from solution, *J. Phys. Chem., 62*: 1068 (1958).
[3.9] A. G. Walton, A theory of surface reaction controlled growth, *J. Phys. Chem., 67*: 1920 (1963).
[3.10] J. W. Mullin, *Crystallization*, 3rd ed., Butterworth-Heinemann, London (1993).
[3.11] R. David, P. Marchal, J. P. Klein, and J. Villermaux, Crystallization and precipitation engineering: III. A discrete formulation of the

agglomeration rate of crystals in a crystallization process, *Chem. Eng. Sci., 46*: 205 (1991).
[3.12] R. David, P. Marchal, and B. Marcant, The modelling of agglomeration in industrial crystallization from solution, *Chem. Eng. Technol., 18*: 302 (1995).
[3.13] A. S. Bramley and M. J. Hounslow, Aggregation during precipitation from solution: A method for extracting rates from experimental data, *J. Colloid Interf. Sci., 183*: 155 (1996).
[3.14] I. A. Valioulis, Coagulation in the aquatic environment theory and practice, *Adv. Colloid Interf. Sci., 24*: 81 (1986).
[3.15] K. Higashitani, K. Yamauchi, Y. Matsuno, and G. Hosokawa, Turbulent coagulation of particles dispersed in a viscous fluid, *J. Chem. Eng. Japan, 16*: 299 (1983).
[3.16] R. David, P. Marchal, J. P. Klein, and J. Villermaux, Crystallization and precipitation engineering: IV. Kinetic model of adipic acid crystallization, *Chem. Eng. Sci., 46*: 1129 (1991).
[3.17] M. von Smoluchowski, Versuch einer mathematischen Theorie der Koagulationskinetik kolloider Lösungen, *Z. Phys. Chem., 92*: 129 (1917).
[3.18] O. Söhnel and J. Garside, *Precipitation*, Butterworth-Heinemann, London (1992).
[3.19] J. Nyvlt, O. Söhnel, M. Matuchova, and M. Broul, *The Kinetics of Industrial Crystallization*, Elsevier, Amsterdam (1985).
[3.20] O. Söhnel and J. Mullin, Interpretation of crystallization induction periods, *J. Colloid Interf. Sci., 123*(1): 43 (1988).
[3.21] D. Kashiev, D. Verdoes, and G. M. van Rosmalen, Induction time and metastability limit in new phase formation, *J. Cryst. Growth, 110*: 373 (1991).
[4.1] J. Beek and R. S. Miller, Turbulent transport in chemical reactors, *Chem. Eng. Prog. Symp. Ser., 55*: 23 (1959).
[4.2] R. David and M. Clark, in *Mixing in Coagulation and Flocculation* (AWWA, ed.), Denver, CO, p. 170 (1991).
[4.3] P. V. Danckwerts, Continuous flow systems—Distribution of residence times, *Chem. Eng. Sci., 2*: 1 (1953).
[4.4] H. Muhr, J. P. Leclerc, and R. David, Fluorescent UV dye: A particularly well-suited tracer to determine residence time distributions of liquid phase in large industrial reactors, *Analusis, 27*: 541 (1999).
[4.5] C. Y. Wen and L. T. Fan, *Models for Flow Systems and Chemical Reactors*, Marcel Dekker, Inc., New York (1975).
[4.6] J. Garside and N. S. Tavare, Mixing, reaction and precipitation: Limits of micromixing in an MSMPR crystallizer, *Chem. Eng. Sci., 40*: 1485 (1985).

[4.7] A. Mersmann, Crystallization and precipitation, *Kona, 16*: 60 (1998).
[4.8] B. Marcant and R. David, Experimental evidence for and prediction of micromixing effects in precipitation, *AlChE J., 37*(11): 1698 (1991).
[4.9] J. Garside, Tayloring crystal products in precipitation processes and the role of mixing, *AiChE Symp. Ser., 87*: 16 (1992).
[4.10] R. H. Doremus, Crystallization of slightly soluble salts from solution, *J. Phys. Chem., 74*: 1405 (1970).
[4.11] G. Tosun, An experimental study of the effect of mixing on particle size distribution in $BaSO_4$ precipitation reaction, in *6th European Conference on Mixing*, p. 161 (1988).
[4.12] B. L. Aslund and A. C. Rasmuson, Semibatch reaction of crystallization of benzoic acid, *AIChE J., 38*: 328 (1992).
[4.13] I. Houcine, E. Plasari, R. David, and J. Villermaux, Influence of mixing characteristics on the quality and size of precipitated calcium oxalate in a pilot scale reactor, *Chem. Eng. Res. Des., 75*: 252 (1997).
[4.14] R. David and B. Marcant, Prediction of micromixing effects in precipitation: II. Case of double-jet precipitators, *AlChE J., 40*: 424 (1994).
[4.15] J. Baldyga and J. R. Bourne, A fluid mechanical approach to turbulent mixing and chemical reaction: Micromixing in the light of turbulence theory, *Chem. Eng. Commun., 28:* 243 (1984).
[4.16] R. Pohorecki and J. Baldyga, The use of a new model of micromixing for determination of crystal size in precipitation, *Chem. Eng. Sci., 38*: 79 (1983).
[4.17] J. Stavek, I. Fort, J. Nyvlt, and M. Sipek, Influence of hydrodynamic conditions on the controlled double jet precipitation of silver halides in mechanically agitated systems, in *6th European Conference on Mixing*, p. 171 (1988).
[4.18] J. Baldyga, R. Pohorecki, W. Podgorska, and B. Marcant, Micromixing effects in semibatch precipitation, in *11th Symposium on Industrial Crystallization*, p. 175 (1990).
[4.19] D. E. Fitchett and J. M. Tarbell, Effect of mixing on the precipitation of barium sulfate in a MSMPR reactor, *AlChE J., 36*: 511 (1990).
[4.20] J. Mydlarz, J. Rieber, D. Briedis, and J. A. Voigt, Kinetics of zinc oxalate precipitation in a mininucleator—MSMPR crystallizer system, *AlChE Symp. Ser., 87*: 158 (1992).
[4.21] G. Tovstiga and H. P. Wirges, The effect of mixing intensity on precipitation in a stirred tank reactor, in *11th Symposium on Industrial Crystallization*, p. 169 (1990).

[4.22] T. Manth, D. Mignon, and H. Offerman, Experimental investigation of precipitation reactions under homogeneous mixing conditions, *Chem. Eng. Sci.*, *51*: 2571 (1996).
[4.23] M. L. J. van Leeuwen, O. S. L. Bruinsma, and G. M. van Rosmalen, Influence of mixing on the product quality in precipitation, *Chem. Eng. Sci., 51*: 2595 (1996).
[4.24] R. Phillips, S. Rohani, and J. Baldyga, Micromixing in a single-feed semi-batch precipitation process, *AlChE J., 45*: 82 (1999).
[4.25] R. David, Precipitation and mixing: Review and discussion of experimental results, Delft-Bremen, in *Int. Workshop on Industrial Crystallization*, p. 74 (1993).
[4.26] R. Pohorecki and J. Baldyga, The effect of micromixing and the manner of reactor feeding on precipitation in stirred tank reactors, *Chem. Eng. Sci., 43*: 1949 (1988).
[4.27] N. S. Tavare, Mixing, reaction and precipitation: an interplay in continuous crystallizers, *Chem. Eng. Sci., 49*: 5193 (1994).
[4.28] E. J. W. Wynn, M. J. Hounslow, and D. Ilievski, Micromixing of solids and fluid in an aggregating precipitator, *Chem. Eng. Sci., 53*: 2177 (1998).
[4.29] M. Lindberg and A. C. Rasmuson, Product concentration profile in strained reacting fluid films, *Chem. Eng., Sci., 54*: 483 (1999).

12

"Tailor-Made" Additives and Impurities

I. WEISSBUCH, L. LEISEROWITZ, AND M. LAHAV
The Weizmann Institute of Science, Rehovot, Israel

1. INTRODUCTION

It has long been recognized that the presence of even minute amounts of impurities substantially affects the kinetics of crystal nucleation, growth, and dissolution [1.1–1.4]. Because of the complexity of the process, however, the exact mode of operation of these impurities on the molecular level is still, by and large, obscure. Any theory trying to explain the role played by these molecules must take into consideration structural parameters of the growing crystals, their morphologies, and the stereochemistry of the impurities. In this chapter, we present a general stereochemical correlation among the crystal structure of the substrate, the molecular structure of the additive, and the crystal faces affected [1.5]. An understanding of these stereochemical aspects provides a powerful tool for the design of useful auxiliary molecules which can deliberately be added to the solution to improve the crystallization process. We shall discuss the utilization of these additive molecules for crystal morphology engineering, crystal dissolution, and crystal etching. The role of solvent as an inevitably present impurity will be highlighted from a stereochemical point of view. Theoretical modeling, by

atom–atom potential energy computations, of the crystal morphology and of the role played by the additives is described. The mode of occlusion of additives in growing crystals and its relevance to the structure of mixed crystals are presented. Finally, the structure and function of two-dimensional self-aggregates of amphiphilic molecules at interfaces and their role as early transients in three-dimensional crystal nucleation are evaluated.

2. TAILOR-MADE ADDITIVES FOR CRYSTAL MORPHOLOGY ENGINEERING

The habit of a crystal is defined by the relative rates of its growth in different directions; the faster the growth in a given direction, the smaller the face developed perpendicular to it. Consequently, when growth is inhibited in a direction perpendicular to a given face, its area is expected to increase relative to the area of other faces of the crystal (Fig. 2.1). Differences in the relative surface area of the various faces can therefore be correlated directly to the decrease in growth rate in the various directions.

The role played by impurities on the habit modification of crystals has long attracted the attention of crystal growers. For example, Buckley [2.1] has recorded the morphological changes induced in a large variety of inorganic crystals by commercially available dyes.

A systematic study on a large variety of organic compounds crystallized in the presence of additives of molecular structure similar to that of the

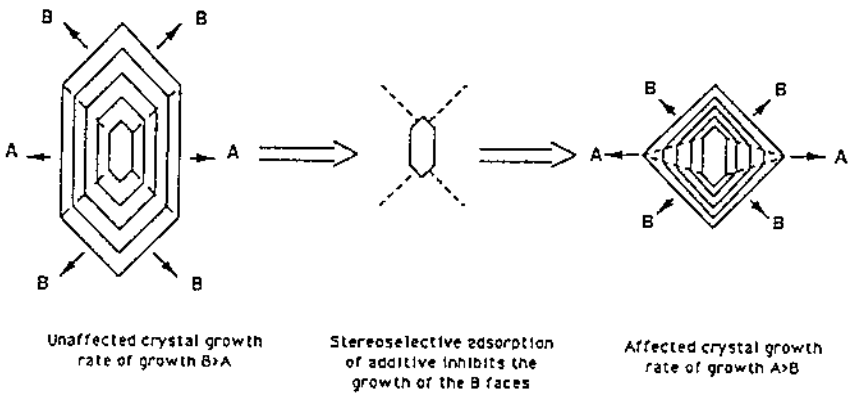

Figure 2.1. Schematic representation of the formation of crystal faces as a function of their relative growth. The change in morphology results from selective adsorption of additive. Left, normal growth; right, change in morphology by inhibition of growth on the diagonal faces.

corresponding substrate molecules has provided a stereochemical correlation between the structure of the affected surfaces and the molecular structure of the inhibitor [2.2, 2.3]. On this basis, it became possible to design tailor-made auxiliary molecules composed of two parts, one identical to that of the substrate molecules undergoing crystallization and the second part modified. When adding such molecules to a solution undergoing crystallization, they can be recognized at specific faces of the growing crystal by virtue of the moieties identical to the substrate compound. These additive molecules can then bind at the growing crystal surfaces and subsequently impede, in a stereospecific manner, further growth perpendicular to these faces, but affect slightly, if at all, the growth in other directions. Once this mechanism was established, it became possible to exploit it to modify the morphology of crystals systematically by tailoring additives that bind at preselected faces and thus inhibit growth in a predictable manner. We illustrate this methodology by some examples.*

Upon crystallization, racemic (D,L)-glutamic acid HCl (Glu·HCl), $HOOC(CH_2)_2CH(NH_3^+)COO^-$, undergoes spontaneous resolution of the enantiomers into separate enantiomorphous crystals. The crystal structure and morphology of (L)-Glu·HCl [2.4] are shown in Figure 2.2. The molecular side chains are directed along the *c* axis and form hydrogen bonds in this direction. All other α-amino acids can be regarded as tailor-made additives, as each such molecule bears the zwitterionic residue $^+H_3NC^*HCOO^-$ of the α-amino acid group while the side chain has been modified. Thus, when growing an optically resolved glutamic acid of the (L) configuration, in the presence of other (L)′-α-amino acids, the additive adsorption will take place only at the two {001} faces at which the side chains emerge. Once adsorbed, the (L′)′ additive will inhibit crystal growth in a direction perpendicular to the {001} face because it will disrupt the hydrogen-bonding along *c*. It is evident, on the other hand, that (D)′-α-amino acid molecules cannot be adsorbed at the same surface because the molecular structures of the substrate and additive are of opposite handedness. Naturally, by symmetry only a (D)′-α-amino acid can be adsorbed on a {001} face of (D)-Glu·HCl crystals. Figure 2.3 depicts the morphological changes of (L)-Glu·HCl produced by adsorption of (L)-lysine $H_2N(CH_2)_4CH(NH_3^+)COO^-$, ornithine $H_2N(CH_2)_3CH(NH_3^+)COO^-$, or other α-amino acid additives. The pure platelike crystals grow thinner and thinner and finally emerge as powder

* In many of the examples given here, we utilize various aspects of chirality, such as enantiomorphous crystal pairs or enantiotopic crystal faces related to one another by mirror symmetry or a center of inversion. When chiral additives are used, we have an internal reference system to compare.

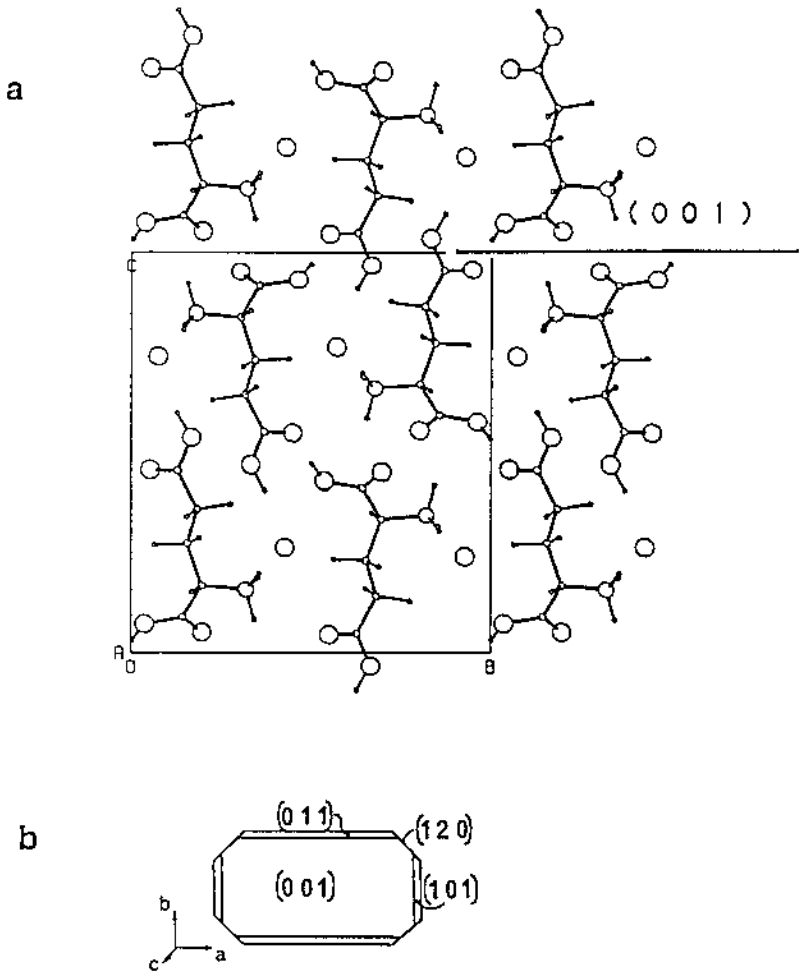

Figure 2.2. (a) Packing arrangement of (L)-Glu·HCl viewed along the *a* axis; (b) computer-drawn morphology of the pure crystals.

with increasing additive concentrations. Crystals of (D)- and (L)-Glu·HCl growth in the presence of (L) additive are shown in Figure 2.3d; the powder is the (L) enantiomer; the (D)-Glu·HCl crystals preserve their original morphology. An analogous effect by chiral-resolved glutamic acid, aspartic acid, asparagine, and other α-amino acids was observed on crystals of (D,L)-threonine, $CH_3CH(OH)CH(NH_3^+)COO^-$ [2.3, 2.4].

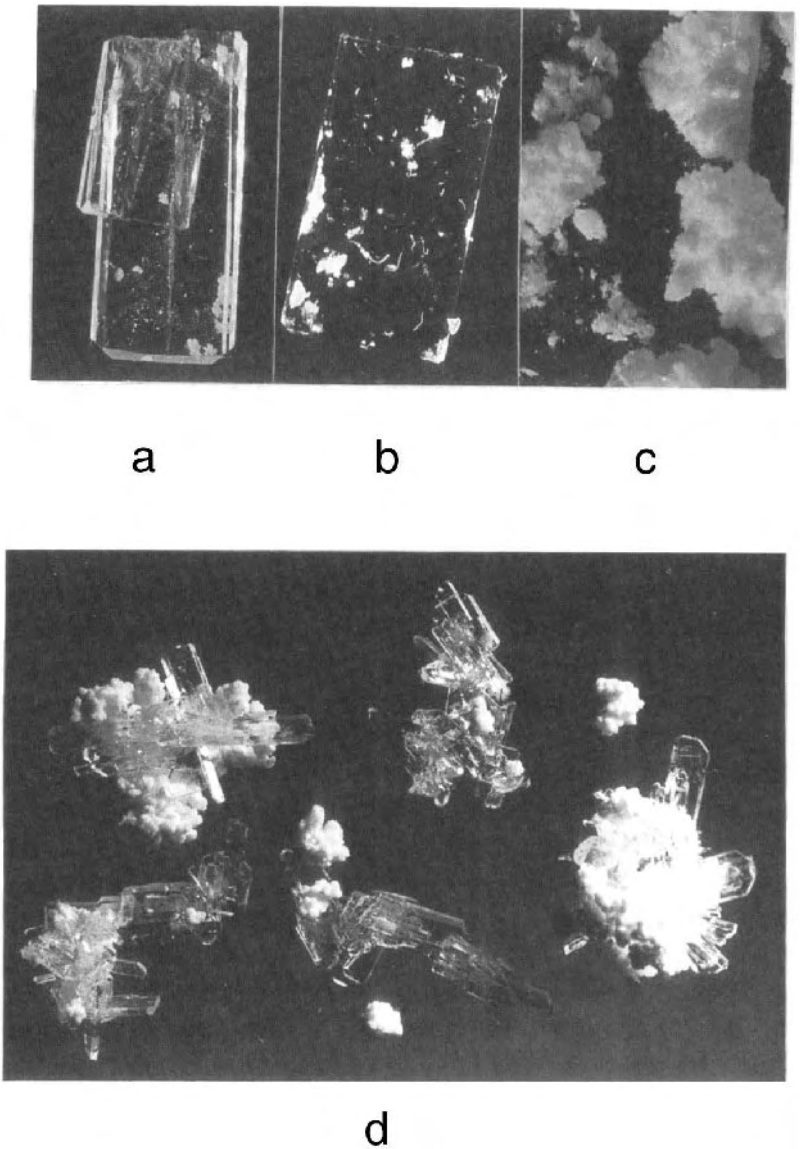

Figure 2.3. Crystals of (L)-Glu·HCl grown in the presence of an increasing amount of additive (L)-lysine: (a) no additive or (D)-lysine; (b) +2 mg/mL (L)-lysine; (c) +50 mg/mL (L)-lysine; (d) crystals of racemic Glu·HCl grown in the presence of (L)-lysine. The plates are the (D) enantiomer, whereas the powder is the (L) enantiomer.

Benzamide, $C_6H_5CONH_2$, provides a different example of how the host–additive interaction at the solid–liquid interface can be pinpointed and correlated with the change in crystal morphology [2.5]. This compound crystallizes from ethanol as plates, in the monoclinic space group $P2_1/c$. The molecules in the crystal form hydrogen-bonded cyclic dimers, further interlinked by hydrogen bonds to yield ribbons parallel to the *b* axis (Fig. 2.4a). The ribbons are stacked along the 5.6-Å *a* axis in an arrangement determined primarily by Coulomb interactions. The ribbon and stack motifs combine to form stable (001) layers. These tightly packed layers juxtapose along the *c* direction, interacting via weak van der Waals interactions between phenyl groups, thus explaining the {001} platelike shape of the crystals. Benzoic acid, C_6H_5COOH, additive, in the stable synplanar conformation, can replace a molecule of benzamide at the end of a ribbon (Fig. 2.4a); however, at the site of the additive, the attractive N—H···O bond (−25 kJ/mol) is replaced by a repulsion (4–8 kJ/mol) between adjacent oxygen lone-pair electrons of the bound additive molecule and of the oncoming benzamide molecule, leading to an overall loss in energy of 30–34 kJ/mol. As predicted, the presence of benzoic acid in solution inhibits growth of the benzamide crystals along *b*, transforming the pure platelike crystals into needles elongated along the *a* axis (Fig. 2.5b). Inhibition of growth along the *a* direction was accomplished by adding *o*-toluamide, *o*-$H_3CC_6H_4CONH_2$, to the crystallization solution. The crystals consistently grew as bars elongated in *b* (Fig. 2.5c). The additive *o*-toluamide can easily be adsorbed in the hydrogen-bonding chain without disturbing growth in the *b* direction. The *o*-methyl group emerges from the $(10\bar{4})$ side face (Fig. 2.4b) and thus interferes with growth along the *a* direction, along which the dimers are stacked. The relative orientation of benzamide at the {001} faces is shown in Fig. 2.4c. Thinner and thinner plates are obtained by adding increasing amounts of *p*-toluamide, *p*-$H_3CC_6H_4CONH_2$, whose *p*-methyl substituent perturbs the already weak van der Waals interactions between the phenyl layers in the *c* direction (Fig. 2.5d).

Sugar technologists [2.6–2.9] studied the dramatic effect played by raffinose **(1)** on the crystal growth of sucrose **(2)** during extraction of the latter from molasses. The kinetics of the crystal growth and the morphology changes observed in these crystals with raffinose and other trisaccharides follow the general mechanistic pathways discussed. The raffinose molecule can be regarded as a tailor-made additive for the crystal of sucrose because it contains a sucrose moiety, which is compatible with the host molecule, and a galactose moiety which, because it must protrude from the surface, will force raffinose to be adsorbed on a subset of crystal faces.

Tailoring of additives can also be done for inorganic single crystals using organic molecules. This can be illustrated by the changes in habit induced on

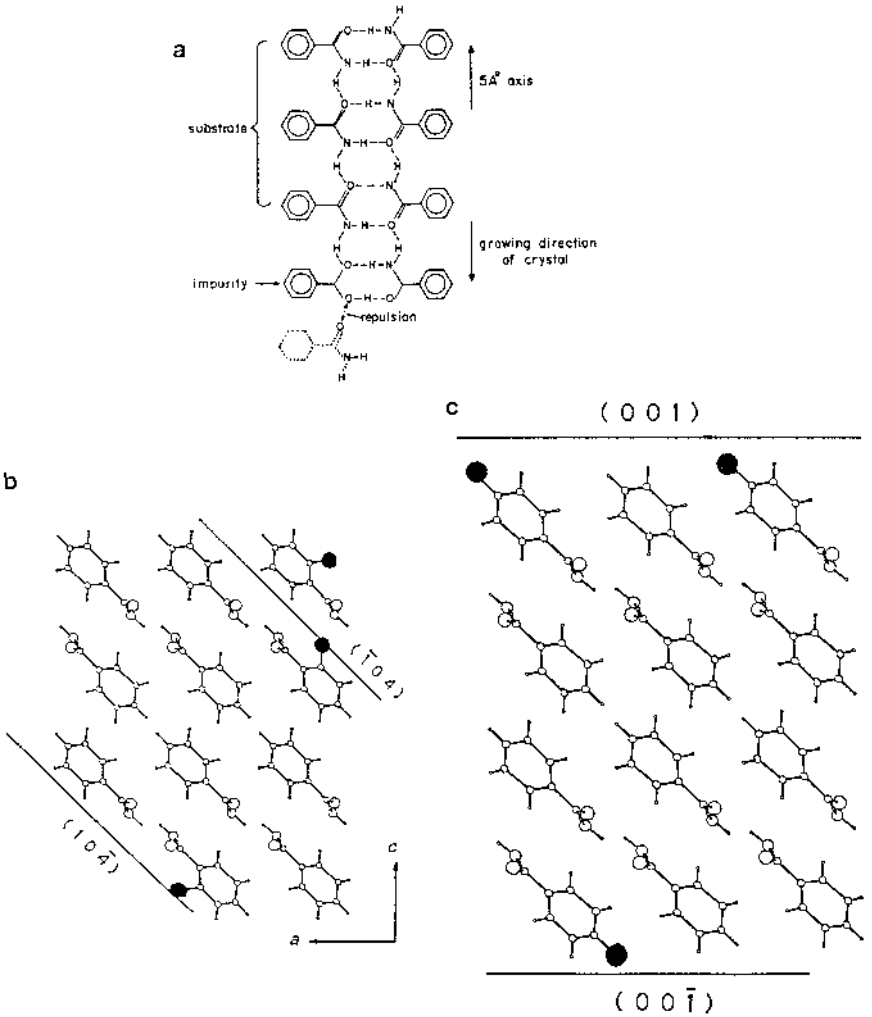

Figure 2.4. (a) Schematic representation of the ribbon motif of hydrogen-bonded dimers of benzamide molecules interlinked along the 5-Å *b* axis; (b) packing arrangement of benzamide, viewed along the *b* axis, showing the effect of *o*-toluamide inhibiting growth along the *a* direction; (c) packing arrangement of benzamide, viewed along the *b* axis, showing the effect of *p*-toluamide inhibiting growth along the *c* direction.

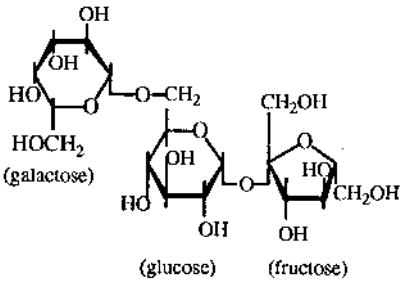

1

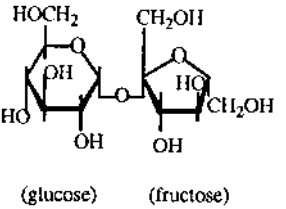

2

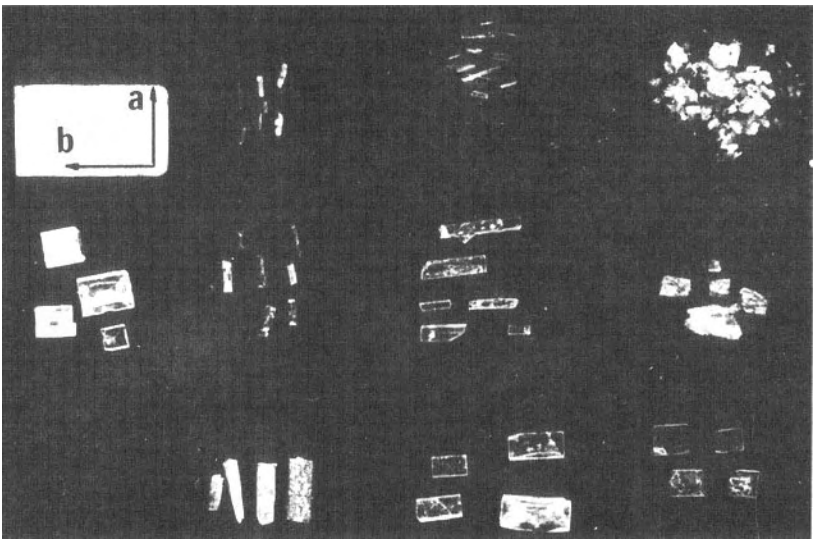

Figure 2.5. Crystals of benzamide: (a) pure and (b)–(d) grown in the presence of additives: (b) benzoic acid; (c) *o*-toluamide; (d) *p*-tolamide.

the crystals of sodium chloride [2.10] by the presence of α-amino acids. The positive (NH_3^+) and negative (CO_2^-) charge moieties of the additive fit at the {110} faces of NaCl crystal but not at the {100} or {111} crystal faces, so that the addition of a water-soluble α-amino acid induces expression of the less stable {110} face of NaCl.

Chiral habits of inorganic compounds crystallizing in centrosymmetric space groups have been reported. In 1931, Miles [2.11] demonstrated that $PbCl_2$, which normally crystallizes in centrosymmetric point group symme-

try $2/m\ 2/m\ 2/m$, assumes a chiral morphology of symmetry 222 when grown in the presence of dextrin.

More recently, interactions between organic molecules and crystals have become an important topic with relevance to biomineralized structures. Growth experiments involving the mineral gypsum ($CaSO_4 \cdot 2H_2O$) of monoclinic $2/m$ symmetry (space group $I2/a$) with optically pure α-amino acids, used as additives, were expected to demonstrate enantioselective interactions between the crystal surfaces and the additive [2.12]. Gypsum crystals grown in the presence of (L)-lysine, alanine, or histidine displayed a "right-handed modification" with well-developed {110} faces. Enantiomorphous morphology of gypsum crystals was obtained when grown in the presence of the corresponding (D)-α-amino acids. A similar but more pronounced morphological modification was produced by as little as 0.1% of the enzyme cellulase, which yielded crystals with pseudotrigonal habits. Gypsum crystals grown in the presence of the dicarboxylate α-amino acid (L)-glutamic acid displayed morphological changes at the "left side" $(1\bar{1}1\}$ faces, and (D)-glutamic acid affected the {111} faces. The results of these experiments proved the stereospecificity of the interactions between α-amino acid molecules and the gypsum crystal lattice.

In biomineralization processes, polypeptides are known to guide the growth of biological minerals such as calcium carbonate. The crystal structure of calcite is characterized by layers of calcium ions and layers of carbonate aligned perpendicularly to the *c* axis, with the planar carbonate lying in the *ab* plane. Calcite crystals in vitro generally have the morphology of the "cleavage rhombohedron" delineated by the {104} faces, in the hexagonal notation. When grown in the presence of acidic glycoproteins extracted from a sea urchin, new specific faces developed, corresponding to adsorption of the proteins on the $\{1\bar{1}0\}$ planes from which the carbonates emerge perpendicularly. In contrast to this specific behavior, the analogous proteins extracted from the shell of the mollusk *Mytilus californianus* strongly inhibit calcite crystal growth in all directions, yielding shapeless crystals, due to nonspecific adsorption. Thus, there is a clear difference in the effect on calcite crystal growth between acidic glycoproteins from two different sources even though they are associated in vivo with the same mineral [2.13].

One area of interest is in the control of mineral formation during water treatment, involving many applications from boiler descaling to desalination processes. An example is the problem of barium and calcium sulfate scale formation in offshore oil production and the use of organic compounds such as phosphonates, carboxylates, and sulfonates as inhibitors which significantly reduce the growth rate of the minerals. Thus, rhombic platelike synthetic barite, $BaSO_4$, crystals prepared under conditions chosen to mimic natural offshore oil fields were found to undergo a characteristic morpho-

logical change in the presence of diphosphonate additives [2.14]. Disklike and elliptical morphologies were obtained and shown to be consistent with binding of the diphosphonate ion, replacing two sulfates within the {011} surface.

Certain homopolymers and copolymers of maleic acid and acrylamide have been reported [2.15] to induce remarkable morphological changes as the pH of the solutions was varied. Thus, multifaceted rosettes of $BaSO_4$ crystals were obtained at high pH, long bundles of needles at pH 6, hollow fibrous cones at pH 5, and spheroids at pH 4. The solution pH controls the degree of protonation and the conformation of the polymer molecules in solution, which, in turn, changes the crystal morphology directed by the polymers.

Organic phosphonates are also known to be crystallization inhibitors and habit modifiers for gypsum, which changes from needlelike to platelike crystals.

The present approach, which is based on molecular interactions, appears to be quite general and has been applied successfully to a large class of organic [2.16–2.18], inorganic [2.14], and biological materials [2.19].

3. TAILOR-MADE ADDITIVE MOLECULES FOR CRYSTAL DISSOLUTION; STEREOSPECIFIC ETCHANTS

It has long been recognized that partial dissolution of crystals in the presence of impurities which interact with the crystal faces reduces the rate of crystal dissolution. In many cases, the addition of the impurities induces the formation of well-shaped etch pits at preselected faces of the crystal. For example, when crystals of calcite were partially dissolved in the presence of (D)- or (L)-tartaric, malic, or lactic acids, etch pits with enantiomorphous shapes were observed [3.1]. Many attempts have been made over the years to find stereochemical correlations between the structure of a given face undergoing etching, the symmetry and the geometry of the etch pit, and the structure of the etchant. Owing to the complexity of the etching mechanism, no simple model, which permits a structural correlation on the molecular level, had been evolved, so that the selection of etchants was done generally by trial and error.

It has been well established that crystal dissolution invariably begins at sites of emerging dislocations where the Burgers vector is perpendicular to the surface. At such sites, more than one type of facial surface is exposed to the solvent. In the absence of additives, the dissolution fronts of the various facets propagate from these centers in various directions at relative rates

similar to those for their growth. Under such circumstances, the overall shape of the dissolving crystal is almost preserved, although the faces become rounded. When an additive that binds selectively to a given face of the crystal is present in the solution, the crystal dissolves in different directions at rates that differ from those in the pure solution. Subsequently, etch pits are formed at the dislocation centers on those faces at which the additives are bound. The ability to design molecules that can interact stereospecifically with a given face of a crystal should, in principle, make that molecule an efficient etchant of this face. Therefore, it was anticipated that the same molecules, which act as a tailor-made growth inhibitor of a given face, operate as a tailor-made etchant of the same face when the crystal is partially dissolved. The generality of this stereochemical correlation was tested on a several substrate crystals [3.2]. We illustrate this idea by two representative examples.

Pure α-glycine, $^{-}OOCCH_2NH_3^{+}$ (space group $P2_1/n$), crystallizes from water in the form of bipyramids, with the symmetry b axis perpendicular to the base of the pyramid [3.3] (Fig. 3.1). It was observed that all natural (L)-α-amino acids apart from proline induce a dramatic morphological change

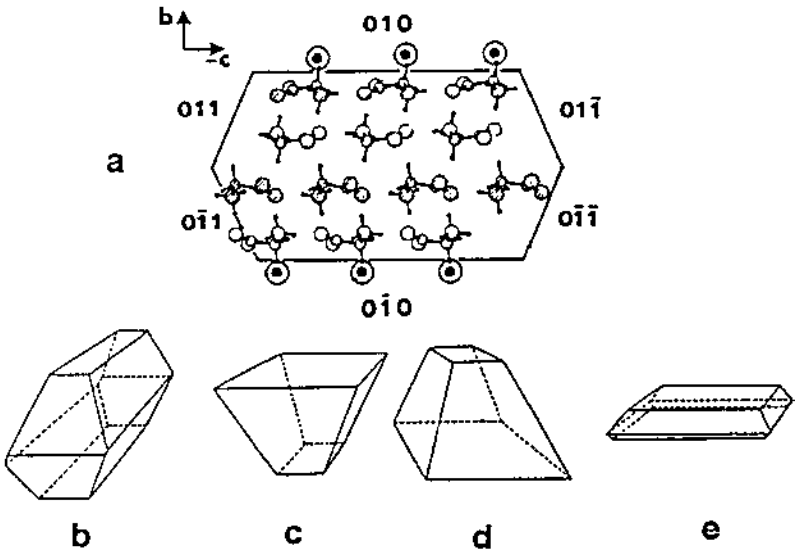

Figure 3.1. (a) Packing arrangement of α-glycine viewed along the a axis; (b)–(e) computer-drawn morphology of the crystals: (b) pure; (c) grown in the presence of (D)-α-amino acids; (d) grown in the presence of (L)-α-amino acids; (e) grown in the presence of racemic additives.

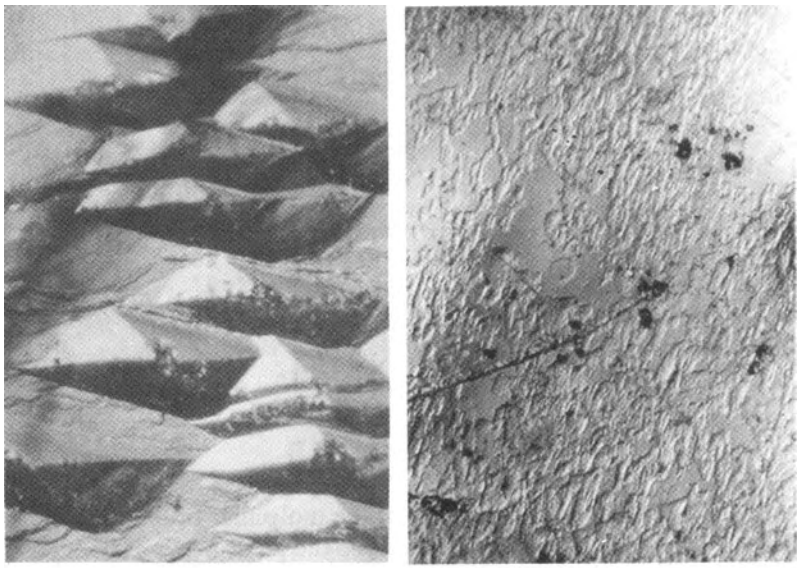

Figure 3.2. Optimal microscope pictures of the {010} faces of α-glycine crystal after partial dissolution in the presence of (D)-alanine: (a) (101) face; (b) $(0\bar{1}0)$ face.

at the $-b$ side of the crystals, with the appearance of pyramids exhibiting a dominant $(0\bar{1}0)$ face. The (D)-α-amino acids induce the formation of a pyramid of enantiomorphous morphology, thus expressing a large (010) face, whereas racemic additive causes crystallization of {010} plates.

The platelike crystals of glycine with well-developed {010} faces were submitted to partial dissolution in an undersaturated solution of glycine containing variable amounts of other α-amino acids [2.2]. When resolved (D)-alanine, $^{+}H_3NCH(CH_3)CO_2^{-}$, was present in the solution, well-developed etch pits were formed only on the (010) face (Fig. 3.2). These pits exhibit twofold morphological symmetry, with surface edges parallel to the a and c axes of the crystal. The enantiotopic $(0\bar{1}0)$ face dissolved smoothly, exactly as it does when the crystal is dissolved in an undersaturated solution of pure glycine. As expected, (L)-alanine induced etch pits on the $(0\bar{1}0)$ face. Racemic (D,L)-alanine etched both opposite {010} faces.

The same methodology holds for enantiomorphous pair of crystals dissolved in the presence of a chiral-resolved molecule [3.4]. The enantioselec-

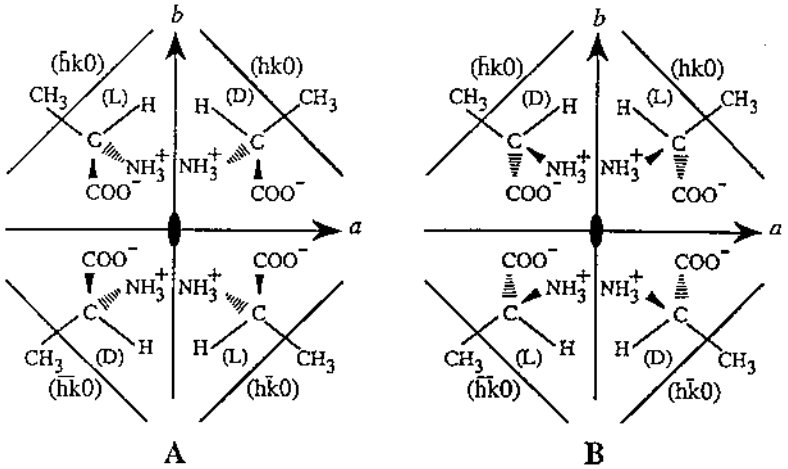

Figure 3.3. Schematic representation of the molecular orientation of the four molecules of (D,L)-alanine viewed along the polar *c* axis as delineated by the {*hk*0} symmetry-related faces; A and B represent the two possible orientations of the molecules vis-à-vis the polar *c* axis.

tive etching experiments provide a simple method of differentiating between enantiomorphous single crystals that do not express hemihedral faces. The method has been demonstrated for a class of materials, such as resolved (D)-Glu·HCl, (D)-asparagine·H_2O [3.2, 3.5], and so on.

A second example is the enantioselective etching of racemic (D,L)-alanine [3.5]. This compound crystallizes in the polar space group $Pna2_1$. In the crystal, which is needlelike, the (D) and (L) molecules are oriented with respect to the polar *c* axis so that the carboxylate CO_2^- groups are exposed at one end of the polar needle axis and the amino NH_3^+ groups at the opposite end. The crystals exhibit hemihedral end faces at opposite ends of the polar *c* axis in the sense that one is flat and the opposite capped, but conventional x-ray crystallography does not allow one to assign the absolute molecular orientation with respect to the polar axis and, thus, to establish at which ends the CO_2^- and NH_3^+ groups are exposed. Etching has been applied successfully for such an assignment by making use of the well-developed {*hk*0} side faces of the needle. The orientations of the (D) and (L) molecules vis-à-vis the four symmetry-related {210} side faces for the two possible orientations of the crystal structure with respect to the polar axis are shown in Figures 3.3A and B.

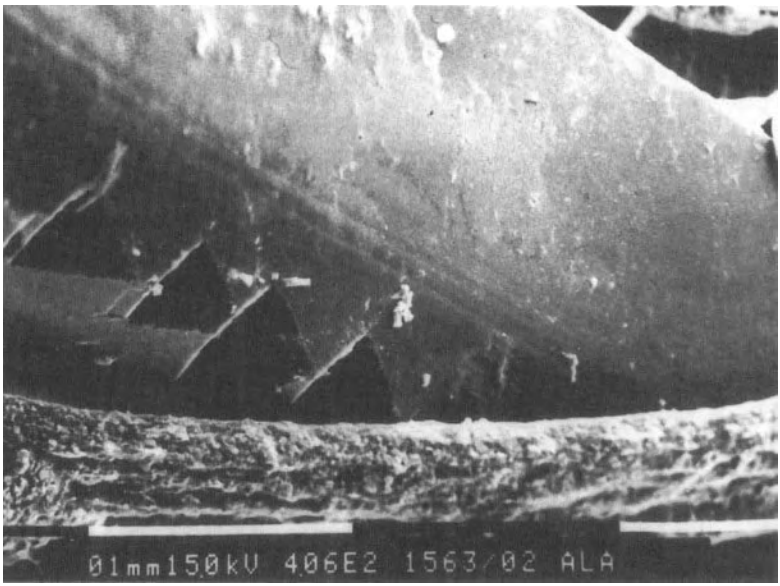

Figure 3.4. Scanning electron micrograph of the {*hk*0} side faces of (D,L)-alanine etched by (L)-threonine; only two faces are shown, one etched and the other smooth.

Once we establish these orientations in a specimen crystal, its absolute structure and thus its polarity is assigned. Growth and partial dissolution in the presence of (L)-α-amino acids such as serine, $^{+}H_3NCH(CH_2OH)CO_2^{-}$, threonine, and phenylalanine, $^{+}H_3NCH(CH_2C_6H_5)CO_2^{-}$, should replace a (L)-alanine substrate molecule at only the $(\bar{2}10)$ and $(2\bar{1}0)$ faces in Figure 3.3A but would affect the (210) and $(\bar{2}\bar{1}0)$ pair in the opposite orientation of Figure 3.3B. This expectation was demonstrated experimentally, with etch pits being formed on only one pair of side faces (Fig. 3.4), thus fixing the absolute structure of the specimen crystal and thus of all crystals grown from aqueous solution, because the crystals exhibit hemihedral end faces.

Etching is a sensitive method for studying surfaces and, by extrapolation, bulk structure and has been used successfully for detecting lamellar twinning in single crystals of (D,L)-valine [3.6]. More than two dozen compounds have been shown to display selective etching, proving the generality of the method [3.4].

3.1. Kinetic Resolution of Racemates by Dissolution with Tailor-Made Additives

As alluded to earlier, the stereospecific binding of a given tailor-made additive to a preselected face of a crystal should impede the relative rate of dissolution of this face compared to unaffected ones. This principle is illustrated here by the rate of dissolution of platelike crystals of α-glycine which were dissolved in the presence of other α-amino acids [3.7]. It was found that as little as 5% of racemic alanine already influenced dissolution. An increase in the concentration of this additive in solution to 50% reduced the rate of dissolution to less than one-third of its original value. The effect of racemic phenylalanine was more pronounced; 10% phenylalanine was as efficient as 50% alanine.

For pure bipyramidal crystals of glycine, expressing well-developed {110} and {011} faces (Fig. 3.1b), a question that arose was how such crystals would dissolve in the presence of α-amino acid additives, known to adsorb on the {010} faces. When single bipyramidal crystals were dissolved in a pure undersaturated solution, they dissolved symmetrically from all faces. However, when the crystals were dissolved in an undersaturated glycine solution containing 10–20% of a chiral-resolved α-amino acid [such as (L)-alanine], the effect was anisotropic: The $-b$ half of the bipyramid dissolved much faster than the opposite half, first yielding a ''basketlike'' shape and then a ''canoelike'' shape (Fig. 3.5). The dissolved crystal developed an $(0\bar{1}0)$ face which was not initially present, and this face exhibited etch pits that were exclusively on this surface. The partially dissolved crystal displays well-presented (011) and $(01\bar{1})$ faces, whereas the $(\bar{1}10)$ and $(\bar{1}\bar{1}0)$ faces became striated with regularly spaced steps rounded in structure. By symmetry, dissolution in the presence of a (D)-α-amino acid yielded the enantiomorphous crystal shape.

The interpretation of these results came from scanning electron microscope studies of the partially dissolved crystals. Early stages of dissolution in the presence of, say, (D)-α-amino acids indicated the formation of well-defined steps exhibiting an (010) surface. One can envisage that the exposed (010) surface of the steps can be poisoned by the presence of the (D) additive in solution. As the steps move, the (010) surface is stabilized by the adsorption of the (D)-α-amino acid; by preventing its dissolution, the $(1\bar{1}0)$ face should be enhanced in area with respect to the (110) face. This implies that the dissolution would proceed unhindered in the (110) direction rather than in the $(1\bar{1}0)$ direction. As the steps move into the bulk of the crystal, part of the $(0\bar{1}0)$ face is exposed to the solution. Dissolution of the crystal along $-b$ will take place without inhibition, because the (D)-α-amino acid does not interact with these faces, thus precluding step formation. Overall, dissolu-

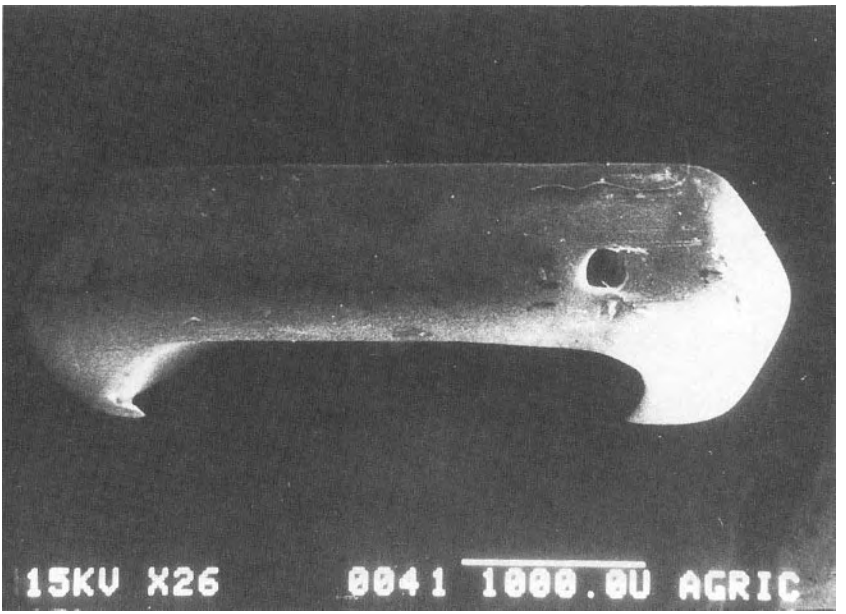

Figure 3.5. "Canoelike" crystal of α-glycine obtained after dissolution in the presence of (L)-alanine.

tion would proceed faster in the *a* than in the *c* direction, leading to the canoelike shape. As expected, when racemic α-amino acids were added, the overall dissolution of the glycine crystals remained isotropic because poisoning of both (010) and $(0\bar{1}0)$ steps occurred.

3.2. Polymeric Reagents for Stereoselective Dissolution of Conglomerates

The efficiency of the inhibitors in the dissolution of glycine crystals was markedly improved, at least by an order of magnitude, by anchoring the α-amino acids to a polymeric backbone. For example, the addition of 1–3% poly[N^{ε}-methacryloyl-(L)-lysine] (**3**) was found to be sufficient, under experimental conditions, to inhibit completely the dissolution of the $(0\bar{1}0)$ face of glycine. In this case, it is reasonable to assume that the α-amino acids side chains of the polymer bind cooperatively and nonreversibly onto the $(0\bar{1}0)$ faces of glycine.

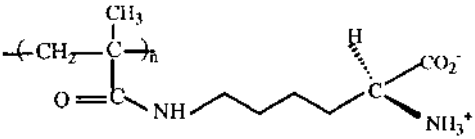

Poly[N^{ε}-metacryloyl-(L)-lysine] **3**

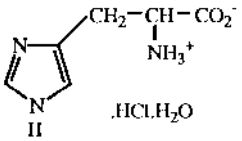

4

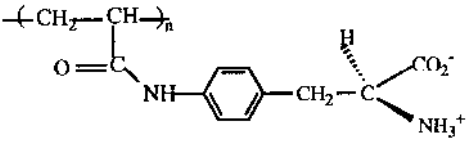

Poly[*p*-acrylamido-(L)-phenyl-alanine] **5**

In a separate series of experiments, the dissolution of conglomerate pairs [i.e., a mixture composed of chiral-resolved (L) and (D) crystals] in the presence of polymeric additives was studied [3.8]. When racemic hystidine hydrochloride monohydrate (**4**) is crystallized above 45°C, it precipitates in the form of a conglomerate mixture. It has been shown that when 1% of the polymer poly[*p*-acrylamido-(L)-phenylalanine] (**5**) was added to the crystallizing solution, it interacted enantioselectively with the {111} faces of the (L) enantiomorph of His·HCl·H_2O, thus inhibiting its growth and leading to kinetic resolution of the conglomerate. Therefore, it was expected that upon dissolution of the conglomerate in the presence of (**5**), the polymeric additive will enantioselectively bind to the same faces of the (L) crystals and delay their dissolution. This polymer will not adsorb stereoselectively onto the {111} or any other faces of the (D) enantiomorph, resulting in kinetic resolution of the conglomerate by dissolution. Some representative results of such experiments are summarized in Table 3.1. Efficient resolution is obtained with increasing amounts of polymer added to the solution.

No difference in solubility was observed when other α-amino acids such as (L)-lysine are grafted to the polymer. This polymer delays the overall rate of dissolution, but no kinetic resolution of the conglomerate could be achieved. This result implies that the imidazole ring of the histidine substrate can be replaced by the phenyl group of the polymer (**5**), but not by the lysine groups of polyl[N^{ε}-methacryloyl-(L)-lysine].

Kinetic resolution by dissolution of conglomerates was achieved in other α-amino acids systems, such as threonine and Glu·HCl, as well as other types of compounds, such as *sec*-phenethyl-3,5-dinitrobenzoate (**6**) [3.8]. Resolution of this compound was achieved by partial dissolution of the

Table 3.1. Typical Dissolution Data of (D,L)-His·HCl·H_2O Crystals (0.17 g) in an Aqueous Solution (3 mL) Containing Dissolved (D,L)-His·HCl·H_2O (0.68 g) and the Appropriate Polymer (50 mg)

Type of polymer (configuration)	Time (hs)	Amount of crystals left [mg (%)]	Enantiomeric excess [% (configuration)]
(L)-**5**	2	115 (68)	26 (L)
(L)-**5**	3	90 (53)	50 (L)
(L)-**5**	5	81 (48)	60 (L)
(L)-**5**	8	65 (38)	93 (L)
(L)-**5**	16	62 (36)	100 (L)
(D)-**5**	2	112 (66)	25 (D)
(D)-**5**	3	91 (53)	52 (D)
(D)-**5**	5	84 (49)	63 (D)
(D)-**5**	8	62 (36)	91 (D)
(D)-**5**	16	60 (35)	100 (D)
(L)-**3**	2	105 (61)	0
(L)-**3**	16	44 (26)	0
Polyacrylic acid			
(MW 2000)	2	95 (56)	0
(MW 2000)	16	39 (23)	0
Blank (no polymer)	2	93 (55)	0
Blank (no polymer)	16	42 (25)	0

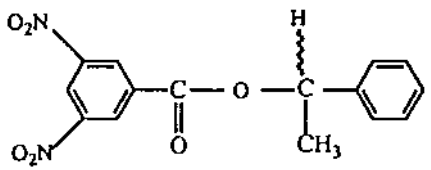

6

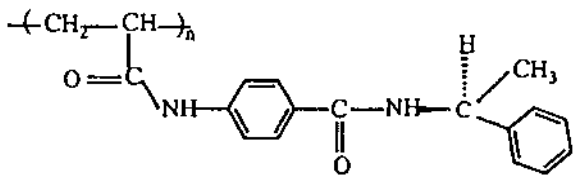

Poly[*N*-acryloyl-(*p*-aminobenzoyl)-(L)-*sec*-[phenethylamide] **7**

conglomerate mixture in the presence of poly[*N*-acryloyl-(*p*-aminobenzoyl) (L)-*sec*-phenethylamide] (**7**).

3.3. Effect of Solvent on Crystal Growth and Morphology

Although solvent has a strong influence on the habit of crystalline materials, the role played by solvent–surface interactions on the molecular level in enhancing or inhibiting crystal growth is still unclear. To date, there have been two distinct approaches to clarify this point. One theory, proposed by Bennema and others [3.9–3.12], embodies favorable interactions between solute and solvent on specific faces leading to reduced interfacial tension, causing a transition from a smooth to a rough interface and, thus, a concomitant faster surface growth. Alternatively, it has been proposed that when the solvent molecules are strongly bound to a given surface, the rate-determining step of the growth of this face will be the removal of the solvent from the face. In such an event, this face will grow more slowly than those faces at which the solvent molecules are less tightly bound [1.4, 3.13–3.16]. The studies of the role played by tailor-made additives are in keeping with the latter approach. However, can we simply extrapolate the effect of tailor-made additives to the solvent? Interactions of the latter with the crystal surface cannot, in general, be as clearly pinpointed as those between the tailor-made additives and the crystal faces. Indeed, there is also a fundamental difference; tailor-made additives are (temporarily) adsorbed at the top layer of the growing crystal surface, replacing a substrate molecule, whereas solvent may be bound to the top layer in a variety of ways.

To clarify this problem, two independent experimental approaches were adopted. Use was made of crystalline solvates where the solvent of crystallization plays the dual role of solvent and crystal solute. This is illustrated with the crystal of α-rhamnose monohydrate (**8**) [3.17] (Fig. 3.6), which contains a polar arrangement and, when grown from pure aqueous solutions, displays a bipyramidal morphology. The two O—H bonds of the

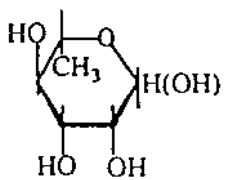

8

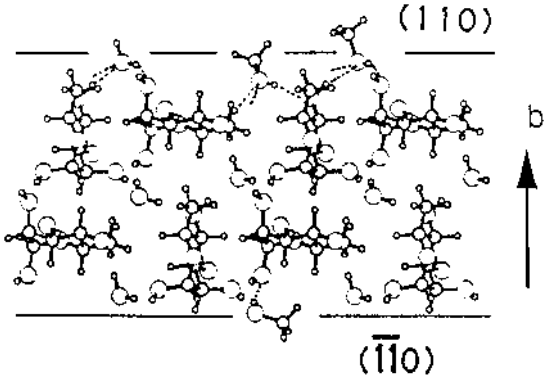

Figure 3.6. Packing arrangement of α-rhamnose monohydrate crystal viewed along the *a* axis; the OH bonds of the hydrate water molecules point toward the $+b$, but not the $-b$ direction; replacement of water by methanol on the {110} faces is depicted.

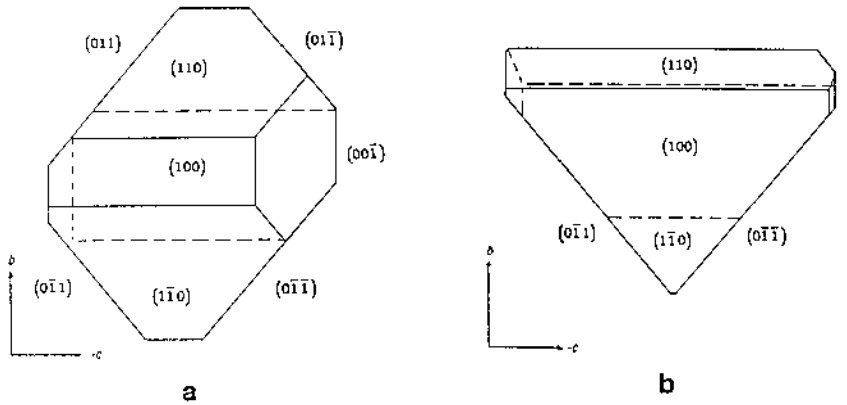

Figure 3.7. Computer-drawn morphology of α-rhamnose monohydrate crystals viewed along the *a* axis: (a) crystals grown from aqueous solution; (b) crystals grown from 9:1 methanol–water solution.

hydrate water molecules are oriented toward the $+b$, but not toward the $-b$, direction of the crystal. Thus, the addition of methanol as a cosolvent changes the morphology of the crystal, completely inhibiting growth along the $+b$ direction (Fig. 3.7). This change in morphology is in keeping with the mechanism of tailor-made additives.

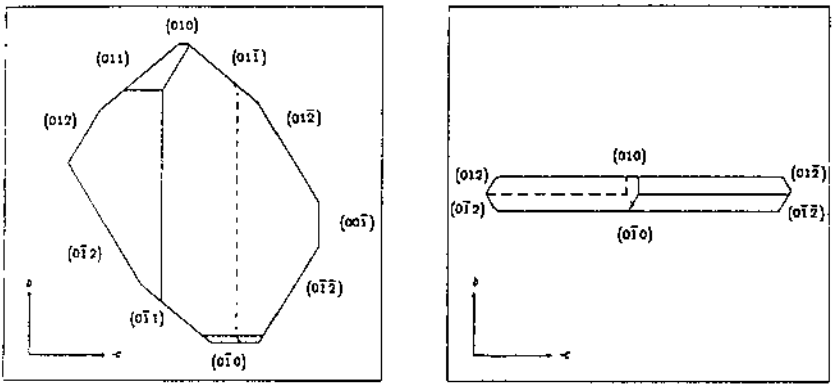

Figure 3.8. Computer-drawn morphology of (L)-asparagine crystals viewed along the *a* axis: (a) crystals grown from aqueous solution; (b) crystals grown from 3:7 methanol–water solution.

A second example is (L)-asparagine·H_2O [3.17]. When grown from pure water, it yields a crystal delineated by 18 faces (Fig. 3.8a). The packing arrangement (Fig. 3.9) shows that one of the two O—H bonds of each water molecule emerges from the {010} faces. Therefore, methanol molecules can easily be attached at these sites. Upon doing so, the methyl groups of the methanol should protrude from the {010} faces, impede growth in these directions, and thus induce expression of the {010} faces of the crystal (Fig. 3.8b). On the {011} faces, only two of the four symmetry-related molecules can be substituted by methanol, so inhibition is less dramatic. That methanol can indeed be adsorbed selectively on both the {010} and {011} faces was further demonstrated by experiments involving partial dissolution of asparagine·H_2O crystals in methanol solution, revealing etch pits, although poorly developed, on these faces only.

The role of solvent as a tailor-made inhibitor can be demonstrated in other systems where the structural correlation is less obvious. *N*-(*E*-Cinnamoyl)-(L)-alanine, C_6H_5═CHCONHCH(CH_3)COOH (**9**) crystallizes in space group $P2_1$. The packing arrangement delineated by the crystal faces as grown from methanol solution is shown in Figure 3.10. The molecules are arranged such that the carboxyl groups emerge at the {1$\bar{1}$1} faces, and the C (chiral)—H bonds are directed along the $+b$ axis. When the crystal is grown from acetic acid solution, a hydrogen-bonded cyclic dimer can be formed between the COOH group of acetic acid and of (**9**) exposed at the (1$\bar{1}$1) and

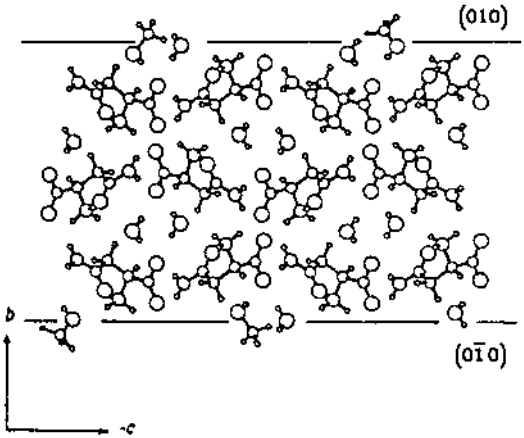

Figure 3.9. Packing arrangement of (L)-asparagine monohydrate crystal viewed along the *a* axis; the hydrate waters are oriented with one of their OH bonds emerging from the {010} faces; replacement of water by methanol on the {010} faces is depicted.

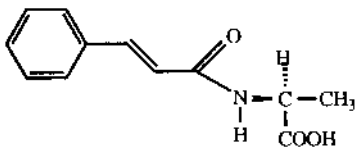

9

($\bar{1}\bar{1}\bar{1}$) faces. Moreover, acetic acid can also bind to the *$CHCO_2H$ moiety of (**9**) via a cyclic dimer, containing C—H···O and O—H···O hydrogen bonds, on the (010) face. Crystallization of (**9**) from glacial acetic acid yields crystals with the morphology shown in Figure 3.11, which is in keeping with expectation.

In the second approach, use was made of the family of platelike crystals composed of the amphiphilic chiral-resolved alkyl gluconamide molecules, which pack in layers stacked head to tail in a polar arrangement [3.18, 3.19] (Fig. 3.12). The polar platelike crystals are hydrophobic on one face and hydrophilic on the opposite face. Thus assignment of the hydrophobic–hydrophilic character of the plate faces by simple wettability measurements fixes the sense of polarity of the crystal. A pronounced difference was expected for the contact angles at the two opposite (010) and (0$\bar{1}$0) faces. The advancing contact angle was measured with three different solvents

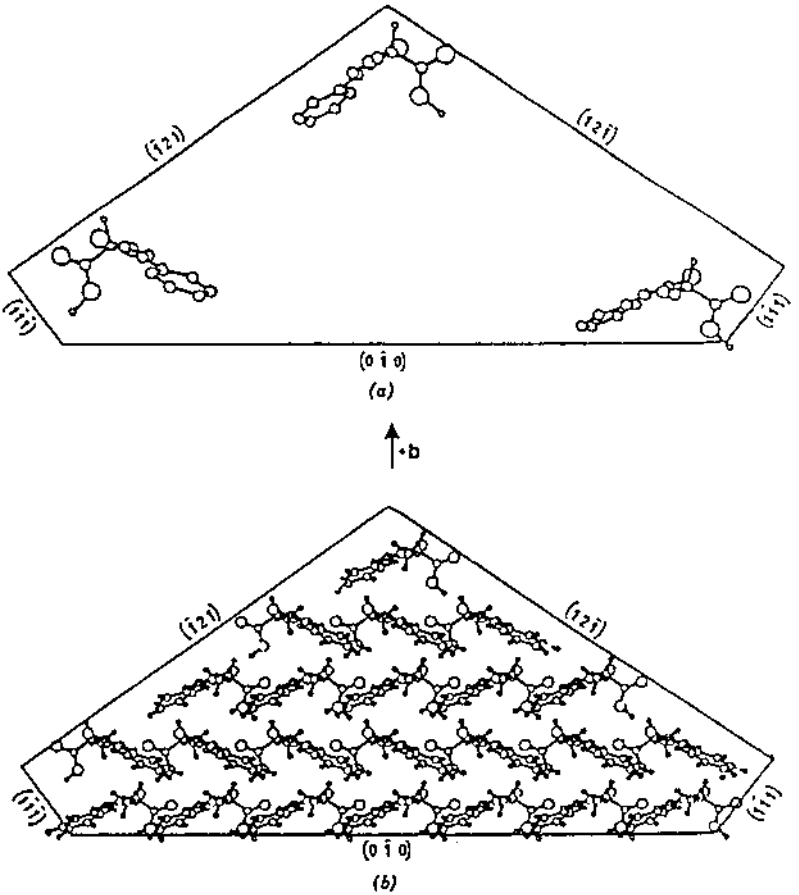

Figure 3.10. Packing arrangement of *N*-(*E*-cinnamoyl)-(L)-alanine delineated by the faces observed in the pure crystal.

(water, glycerol, and methylene glycol) and was found to be in the range 44° to 56° for the hydrophilic face and 75° to 87° for the hydrophobic face. A comparative study on the relative rates of crystal growth of the opposite hydrophobic and hydrophilic faces of the platelike crystals at room temperature showed that the hydrophobic face grows about four times faster. These experiments show once again that strong solvent–surface interactions impede crystal growth rather than enhancing it, in contradiction to the theory of surface roughening. Another example that confirms this approach is succinic acid grown from water and isopropanol solutions [3.20].

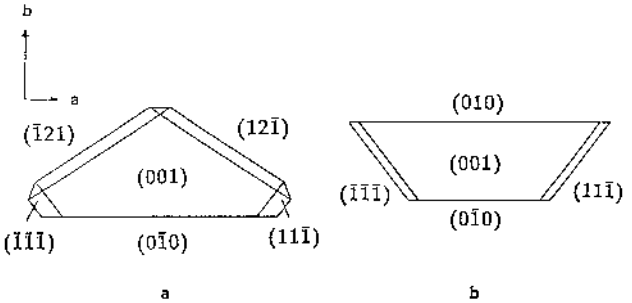

Figure 3.11. Computer-drawn morphology of the *N*-(*E*-cinnamoyl)-(L)-alanine crystals viewed along the *c* axis: (a) crystals grown from methanol; (b) crystals grown from acetic acid.

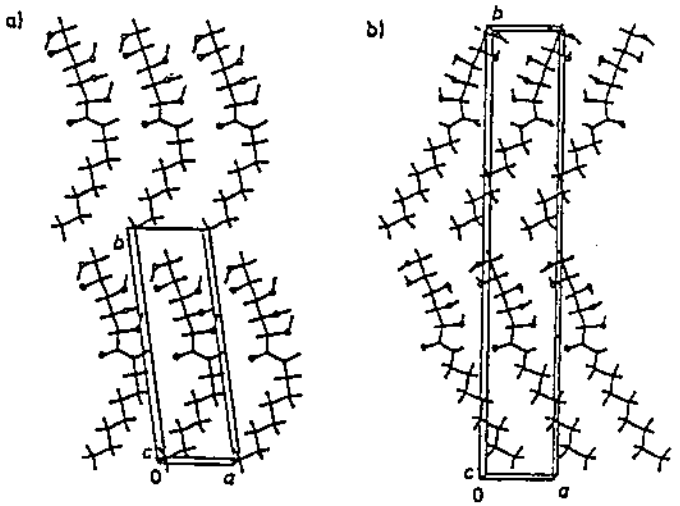

Figure 3.12. Head-to-tail packing arrangements of (a) *N*-(*n*-heptyl)-(D)-gluconamide with space group $P1$ and (b) *N*-(*n*-octyl)-(D)-gluconamide with space group $P2_1$.

An entirely different approach involved strong selective adsorption of solvent at a subset of molecular surface sites and repulsion of solvent at the remaining set of surface sites on the crystal face. It was found that such a mechanism can lead to fast growth. This has been demonstrated experimentally in two systems [3.21]. One example is provided by the growth of the polar (D,L)-alanine crystals from aqueous solution. According to the crystal

growth and etching experiments in the presence of tailor-made additives, the CO_2^- group of molecules are exposed at the $(00\bar{1})$ face, the "flat $-c$ end" of the crystal, whereas the NH_3^+ groups are exposed at the $+c$ capped end (Fig. 3.13). The crystal growth and dissolution experiments also indicated that in aqueous solutions, the $-c$ carboxylate end of the (D,L)-alanine crystals grows and dissolves much faster than the $+c$ amino end. The question remains as to which end of the crystal water molecules may bind more tightly and to correlate the macroscopic phenomena with the recognition and binding of the solvent at a molecular level.

Analysis of the packing arrangement reveals that the $(00\bar{1})$ carboxylate face is corrugated in two dimensions, containing pockets. The water molecules may be strongly bound to the outermost layer of CO_2^- groups via hydrogen bonds. In contrast, the pockets act as proton acceptors for the NH_3^+ proton-donor groups of the solute molecules. Replacement of the NH_3^+ by water within the pockets yields repulsive or, at best, weakly attractive interactions. The pockets will therefore be weakly hydrated and thus relatively easily accessible to approaching solute molecules. Conversely, the {011} and {201} faces of (D,L)-alanine, which expose NH_3^+ and CH_3 groups at the $+c$ end of the crystal, are relatively smooth and contain molecules equally accessible for water binding.

We predicted that methanol molecules could bind into the pockets of the $(00\bar{1})$ face. The methyl group of this cosolvent molecule can form weak C—H···O interactions within the pocket, and the OH group can form a hydrogen bond to the CO_2^- group at the surface. In keeping with prediction, crystals of (D,L)-alanine in an 80% methanol–water mixture grow faster at the $+c$ amino end of the crystal than at the $-c$ carboxylate end, clearly indicating that methanol is more strongly adsorbed than water at the $(00\bar{1})$ face. An analogous analysis can explain the growth and dissolution of the γ-polymorph of glycine [3.17]. In conclusion, more than a single mechanism may be operating in the description of the role played by the solvent on the growth of crystals and the fact that each class of compounds has to be considered independently.

4. THEORETICAL MODELING

A controlling factor in crystal growth is the energy of interaction between neighboring molecules. According to Hartman and Perdok [4.1, 4.2], the crucial relation is between the layer energy, E_l, which is the energy released when a new layer is formed, and the attachment energy, E_{att}, which is defined as the energy per molecule released when a new layer is attached

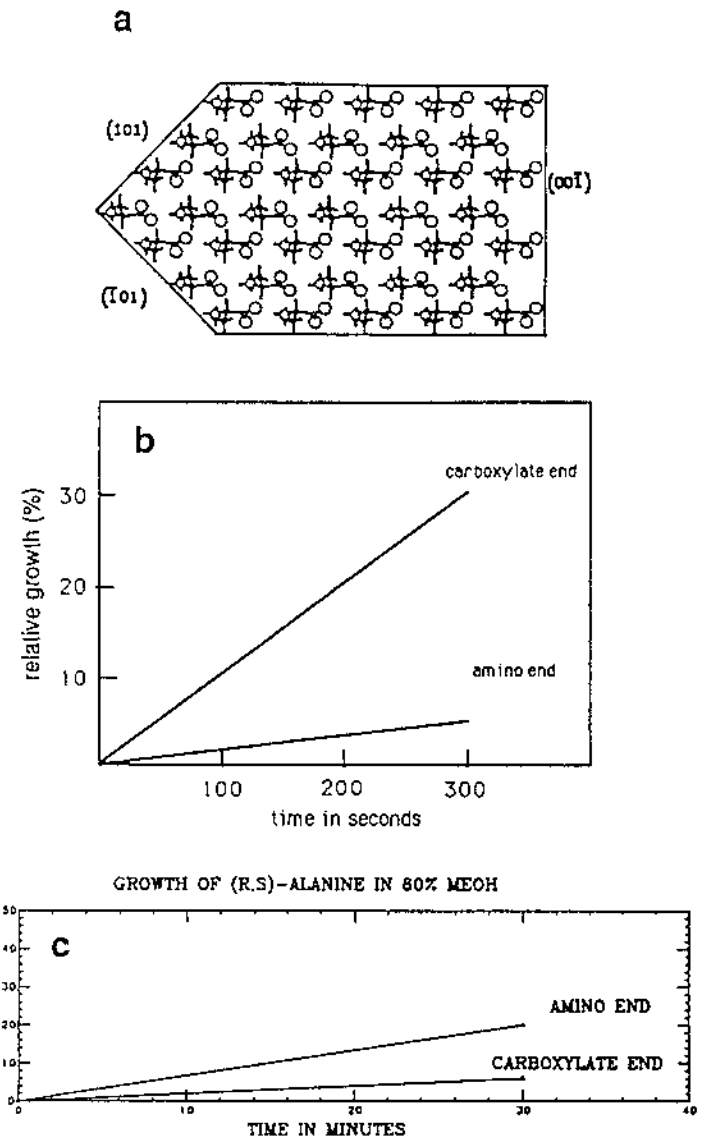

Figure 3.13. (a) Packing arrangement of (D,L)-alanine crystal delineated by the crystal faces, viewed along the *b* axis. The capped faces, {201} and {011} at the $+c$ end, expose NH_3^+ and CH_3 groups, whereas the opposite (00$\bar{1}$) face exposes the CO_2^- groups. Graph of the relative growth at the opposite poles of the polar axis of (D,L)-alanine crystals: (b) in water; (c) in 8:2 methanol–water mixture.

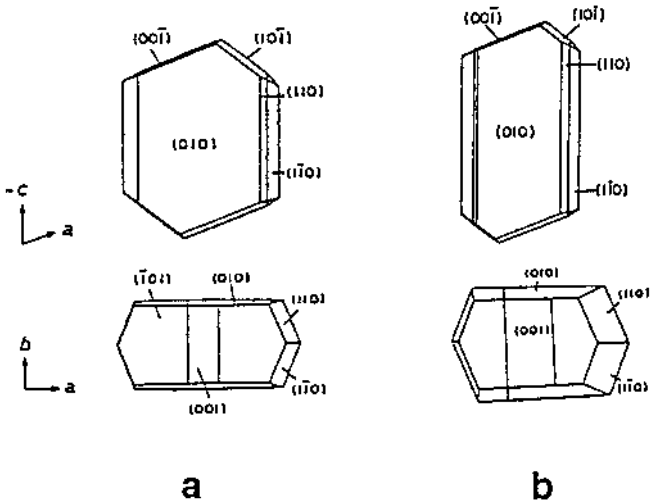

Figure 4.1. (a) Theoretical crystal form of α-glycine; (b) morphology of α-glycine crystals obtained by sublimation.

to the crystal face. E_{att} controls the growth rate perpendicular to the layer, whereas E_l measures the stability of the layer. The working hypothesis is that the morphological importance of a crystal face decreases with increasing attachment energy. Qualitative predictions of crystal morphology have recently become possible with increasing access to powerful computers. In the program developed by our group [3.14], the intermolecular interactions in the crystal were calculated from the known crystal structure using atom–atom potential energy functions which contain van der Waals and electrostatic terms. The van der Waals term is described by a number of empirical potential functions. The electrostatic term is commonly described by a coulombic interaction with parameters derived from experimental deformation electron density distributions as determined from low-temperature x-ray diffraction data [4.3]. By applying such a methodology, it became possible to calculate the values of E_l and E_{att} for various low-index faces of the crystals, from which the "theoretical crystal form" may be derived. The theoretical form of glycine [3.14] calculated by this method is in good agreement with the morphology of glycine crystals obtained by sublimation (Fig. 4.1). This morphology exhibits the well-developed {010} faces, in keeping with the dominant hydrogen-bonding energy of the molecular bilayer in the *ac* plane. However, glycine crystals grown from aqueous solution display a

distinctly different morphology, which is bipyramidal, with large {011} and {110} faces and poorly developed {010} faces. To understand these differences, substrate–solvent interactions have to be taken into account. The large {011} and {110} faces expose CO_2^- and NH_3^+ groups well oriented to have a strong affinity for water. The {010} face exposes alternating layers of C—H groups or CO_2^- and NH_3^+ groups (Fig. 5.3) and thus is less hydrophilic than the {011} and {110} faces. Moreover, if the solute glycine molecules dock at surface sites primarily as cyclic hydrogen-bonded dimers, the {010} face will essentially expose C—H groups and be less strongly bound to solvent water molecules. These qualitative ideas were expressed in a quantitative form by Coulomb energy calculations, which indicate preferential adsorption of water molecules onto the polar faces, primarily {011}, leading to a reduction in the growth rate normal to these faces relative to that of {010}, with a concomitant increase in their surface areas.

By comparison, the hydrophobic α-amino acids such as valine and leucine, which form hydrogen-bonded {010} bilayers akin to that of α-glycine, form platelike {010} crystals [4.4]. The interaction energy within the bilayer, involving both hydrogen bonds and hydrophobic contacts, are so strong that {010} plates are formed, despite the presence of solvent water–surface interactions which should enhance the appearance of faces akin to the {011} and {110} faces found in α-glycine. The theoretical morphologies of a large variety of organic molecules were computed successfully, including bezamide, cinnamide, and several α-amino acids, and a good correlation was obtained between the theoretical and measured morphologies. Differences in binding energy ($E_b = E_l + E_{att}$) of specific additive molecules relative to the substrate molecules, at each of the crystallographic sites on various crystal faces, were also computed. The highly stereoselective interactions between additive molecules and specific growing crystal surfaces were predicted from the differences in binding energy calculated in agreement with the observed changes in morphology [4.5, 4.6]. Computer programs for calculating the ''theoretical form'' of crystals are now commercially available [4.7] and have been used to predict the theoretical morphology of *p*-nitro *p*′-methyl benzylidene aniline (**10**) [4.8].

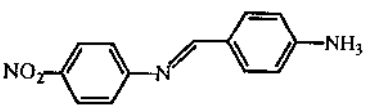

10

5. MODE OF OCCLUSION OF IMPURITIES IN CRYSTALS

Crystalization is still a commonly used process for the purification of inorganic and organic materials. Therefore, the mode of occlusion of impurities or additives inside growing crystals is of paramount technological and theoretical importance. The studies presented earlier, on the interaction of tailor-made additives with the various faces of crystals is also relevant to the general question regarding the distribution of occluded tailor-made additives within crystals.

An important concept is that crystal surfaces, although determined by the arrangement of the molecules within the crystal bulk, display surface structures different from each other and obviously from that of the bulk. Moreover, the two-dimensional symmetry relating molecules at crystal surfaces is generally lower than the three-dimensional symmetry of the bulk crystal.

One of the direct consequences of the adsorption–occlusion mechanism presented earlier is that the mode of occlusion of a tailor-made additive will depend on the structure of the faces of the growing crystal. If the crystal is delineated by faces containing structural sites at which the additives can be docked, they will be occluded inside the bulk through such faces after overgrowth by oncoming molecular layers. If the crystal expresses faces at which the additive (or impurity) cannot be strongly adsorbed, naturally no occlusion will take place. This is illustrated schematically for two different motifs in Figures 5.1 and 5.2.

According to this mechanism of selective adsorption, the additive molecules can substitute for substrate molecules at only one of the four crystallographic sites on each of the four {011} crystal faces of the motif shown in Figure 5.1. Consequently, occlusion of additive molecules through the four diagonal faces will lead to a crystal composed of four sectors, within each of which the additive molecules will be anisotropically distributed. In general, therefore, preferential occlusion through different subsets at surface sites on various faces will lead to a reduction in symmetry of the different crystal sectors, the symmetry in each sector corresponding to that of the surface through which the additives were adsorbed. Naturally, the different sectors of the whole crystal are related to each other by the point symmetry of the pure crystal.

Reduction in crystal symmetry following the foregoing principles was predicted and demonstrated experimentally in several host–additive systems by changes in crystal morphology, separation of chiral additives into separate enantiomeric islands in centrosymmetric crystals detected by high-performance liquid chromatography (HPLC), second-order nonlinear

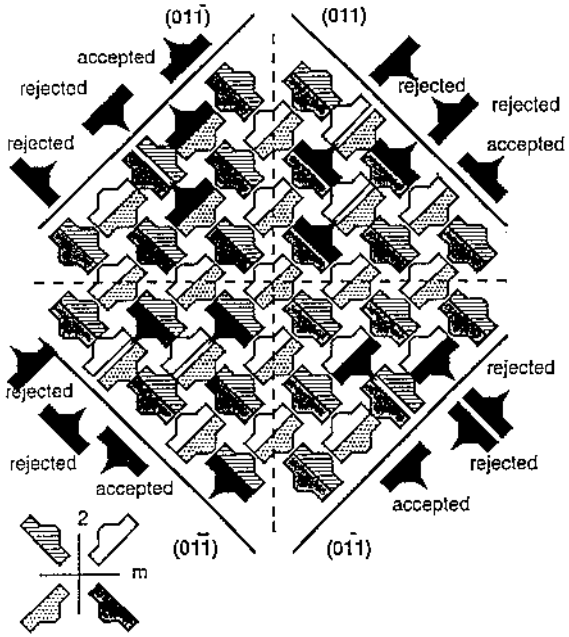

Figure 5.1. Schematic representation of adsorption and occlusion of additive molecules (in black) through the four slanted {011} faces in a centrosymmetric crystal of point symmetry $2/m$; in each of the four sectors, only one of the symmetry-related molecules can be replaced by the additive on adsorption, which means the loss of all symmetry elements. The crystal symmetry is reduced from $P2_1/c$ to $P1$.

optical effects, and crystal birefringence. Symmetry lowering has also been measured directly for some systems by x-ray and neutron diffraction techniques. We shall illustrate this reduction in symmetry with some representative examples [5.1–5.4].

Let us consider, once again, the crystal of α-glycine in which prochiral molecules pack in a layer structure of point symmetry $2/m$ (Fig. 5.3). The crystal faces of relevance for reduction in symmetry are the enantiotopic (010) and (0$\bar{1}$0) faces (see also Fig. 5.2). Of the four symmetry-related glycine molecules (1, 2, 3, 4), molecules 1 and 2 are related by twofold screw symmetry and have their C—H_{re} bonds emerging from the (010) face. By symmetry, molecules 3 and 4, related to molecules 1 and 2 by a center of inversion, have their C—H_{si} bonds emerging from the (0$\bar{1}$0) face. Consequently, only (D)-α-amino acids can substitute glycine molecules at

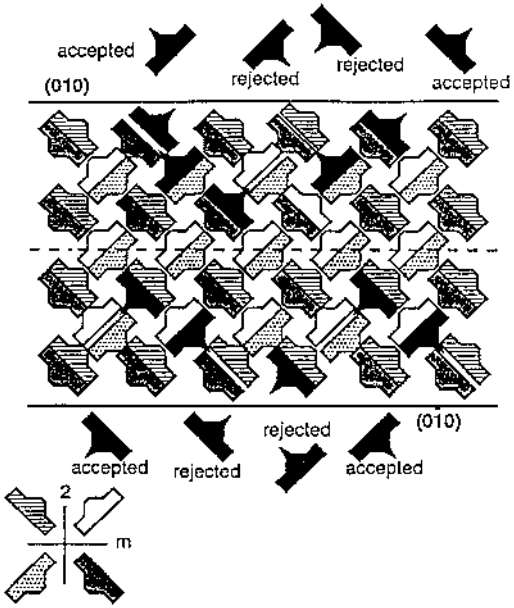

Figure 5.2. Schematic representation of adsorption and occlusion of additive molecules (in black) through the top and bottom {010} faces in a crystal of point symmetry $2/m$, resulting in the loss of the glide and inversion symmetry. The crystal symmetry is reduced from $P2_1/c$ to $P2_1$.

the 1 and 2 surface sites on face (010), whereas only (L)-α-amino acids can be adsorbed at sites 3 and 4 on the (0$\bar{1}$0) face. Following the principle that tailor-made additives can be occluded inside a growing crystal only through those surface sites in which they dock in a manner akin to the host molecule, crystallization of glycine in the presence of racemic α-amino acids would lead to spontaneous resolution of the occluded enantiomers in the bulk of the glycine crystal. The (D)-α-amino acids, which may be occluded only through the (010) face, would segregate within the $+b$ half of the crystal; by symmetry, the (L)-α-amino acids would be occluded only within the $-b$ half.

Platelike crystals of α-glycine grown in the presence of a racemic α-amino acids were found to contain 0.02–0.2% racemic additive, with the (D)-α-amino acid populating the $+b$ half and the (L)-α-amino acids populating the $-b$ half of the crystal as determined by HPLC measurements [3.3] (Fig. 5.4). In terms of the reasoning given earlier, the symmetry of each half of the crystal is lowered from centrosymmetric $P2_1/n$ (in the pure form) to chiral

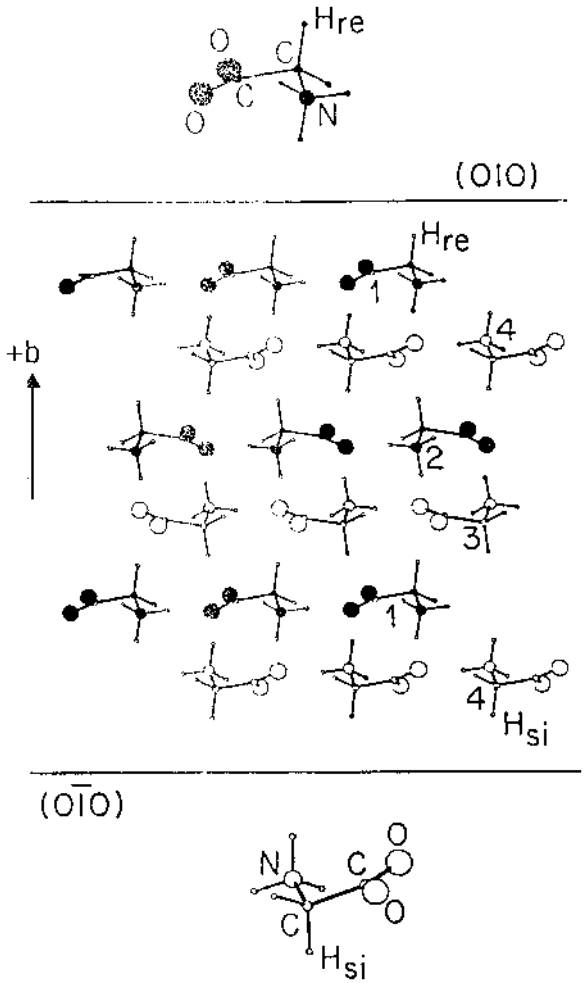

Figure 5.3. Packing arrangement of α-glycine viewed along the *a* axis showing the four symmetry-related molecules; C—H_{re} bonds of all the molecules point toward the (010) face and the C—H_{si} bonds to the (0$\bar{1}$0) face.

$P2_1$, and the two halves are enantiomorphous in accordance with the point symmetry $2/m$ of the pure crystal.

Symmetry lowering of a similar nature was demonstrated in other systems which involved enantiomeric segregation of the dipeptide glycylleucine inside growing crystals of glycylglycine, $^{+}H_3NCH_2CONHCH_2CO_2^{-}$ [4.6], and of threonine inside crystals of (D,L)-serine [4.5].

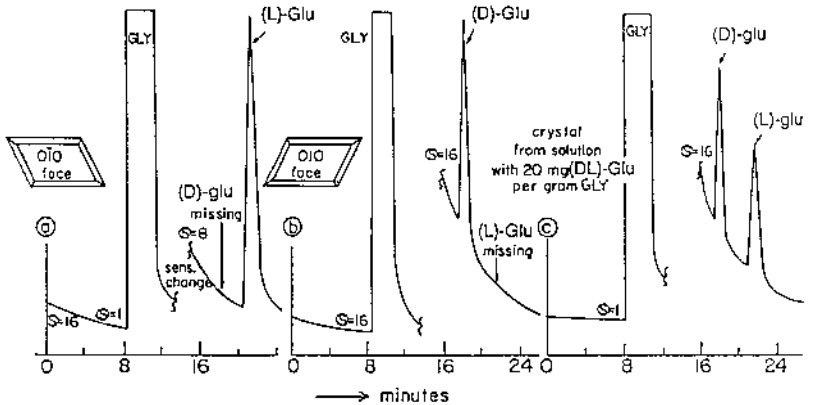

Figure 5.4. Enantiomeric distribution of (D,L)-glutamic acid occluded in {010} plate crystals of α-glycine, as measured by HPLC: (a) material taken from the $(0\bar{1}0)$ face of the crystal; (b) material taken from the (010) face; (c) whole crystal.

The symmetry lowering in all these host–additive systems involves a loss of inversion symmetry. This crystal property can be probed by nonlinear optical methods. Whereas a centrosymmetric crystal does not emit a second harmonic optical signal on irradiation with a laser beam, noncentrosymmetric crystals do. Thus, second harmonic generation (SHG) can be used as a diagnostic tool for the detection of the loss of a crystallographic center of inversion. One practical requirement is that either the host or the additive molecule have a large molecular hyperpolarizability tensor β, leading to large optical nonlinearity. A pure host crystal structure, which consists of centrosymmetric antiparallel pairs of host molecules with high β coefficients, would transform to a SHG-active crystal on site-selective occlusion of a centrosymmetric guest molecule (Fig. 5.5). Because the growth of the crystal takes place at the top exposed face, the additive is adsorbed and occluded through only one of the pair of surface sites in the growth directions leading to symmetry lowering. Naturally, symmetry lowering would occur if the additive molecules were occluded through both the top and bottom faces. Such a crystal would also be SHG active if its size were greater than the wavelength of the laser beam. We demonstrated [5.5] the potential of this approach with centrosymmetric host crystals of *p*-(*N*-dimethylamino)-benzylidene-*p*′-nityroaniline (**11**), which became acentric and SHG active on site-selective occlusion of the guest molecule *p*, *p*′-dinitrobenzylideneaniline (**12**), which is a symmetric molecule (Fig. 5.6).

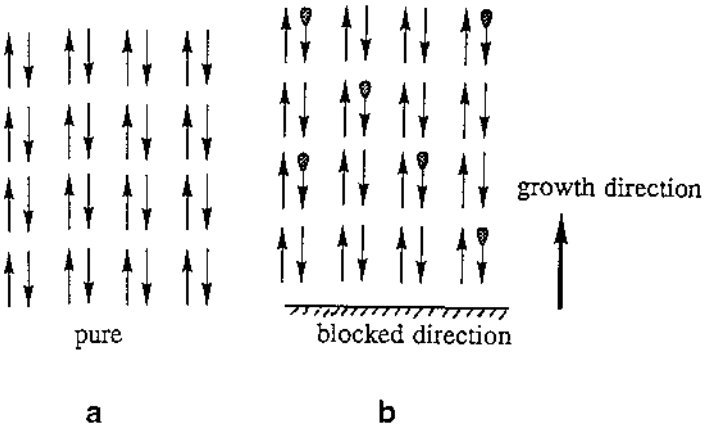

Figure 5.5. Scheme illustrating the conversion of a centrosymmetric crystal composed of host molecules with high β coefficient into an SHG-active crystal by site-selective occlusion of a symmetric guest.

The reverse situation, where only the guest has a large hyperpolarizability, is illustrated by the {010} platelike crystals of α-glycine, containing, as the additive, α-amino acids with high β coefficients, such as the *p*-nitrophenyl derivatives of lysine (**13**), ornithine (**14**), and α-γ-diaminobutyric acid (**15**) [5.5]. As discussed earlier, (D)-α-amino acid additives should be preferentially incorporated through two (sites 1 and 2) of the four symmetry-related sites on the (010) face. Such a mixed crystal should have $P2_1$ symmetry and, consequently, should not show SHG for a fundamental beam propagating along the unique *b* axis. However, the mixed crystals gave rise to SHG, implying that the overall symmetry of the mixed-crystal structure is not monoclinic $P2_1$ but, rather, triclinic $P1$. This result can be interpreted in terms of a growth mechanism of the molecular {010} layers because the additive molecules cannot be occluded at the {011} and {110} faces. If the layer growth is nucleated such that the growing ledges move in the same direction layer after layer, we may envisage that the crystal will contain guest molecules having their side chains pointing preferentially in the same direction in large domains of the crystal, leading to $P1$ symmetry.

Other systems of interest are the noncentrosymmetric orthorhombic crystals of space group symmetry $P2_12_12_1$. On symmetry grounds, such crystals are nonpolar along the three principal crystallographic axes; therefore, frequency doubling is forbidden in these directions. We anticipated that when grown in the presence of appropriate additives so as to reduce the crystal symmetry to monoclinic $P2_1$, such crystals should be SHG active along the

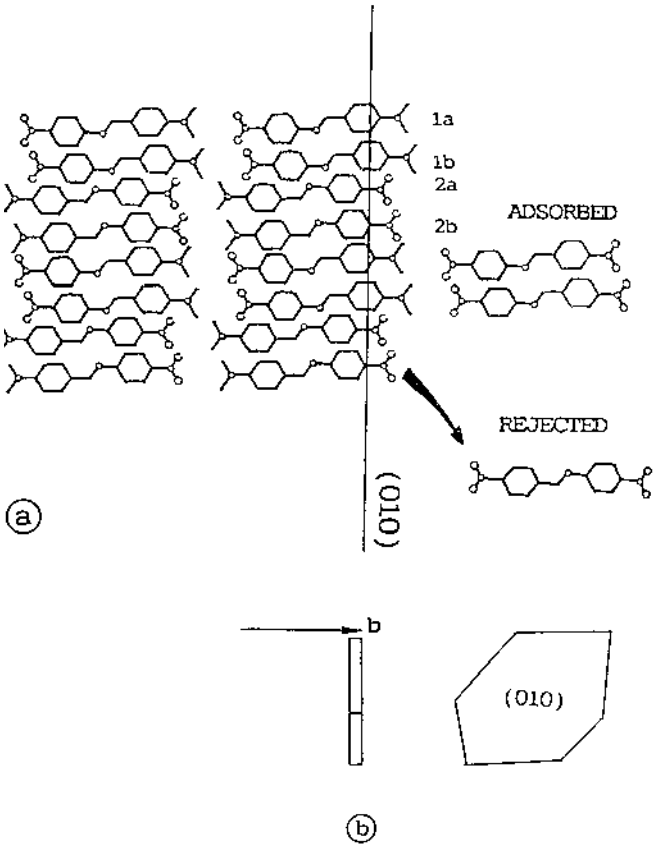

Figure 5.6. (a) Packing arrangement of a polymorph of *p*-(*N*-dimethylamino)benzylidene-*p′*-nitroaniline crystal showing how the dinitro additive may be adsorbed on the (010) face; (b) two views of the morphology of the platelike crystals.

two axes that have lost their twofold screw symmetry. In fact, single crystals of (L)-Glu·HCl grown in the presence of the additives (**13**), (**14**), and (**15**) were SHG active along all three axes, indicating symmetry lowering to *P*1, and demonstrating, again, that the guest molecules were adsorbed not on a smooth surface but, rather, on moving ledges of the growing crystal.

The property of optical birefringence in crystals has also been used to demonstrate a reduction in crystal class. McBride and Bertman [5.6] took advantage of the fact that crystals that belong to a high-symmetry class, such as tetragonal, trigonal, or hexagonal, are optically uniaxial, whereas

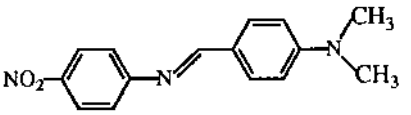

11

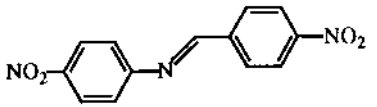

12

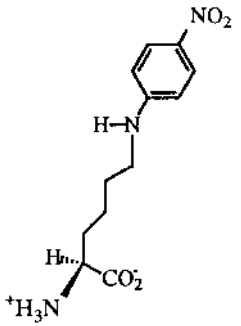

13

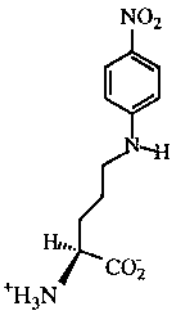

14

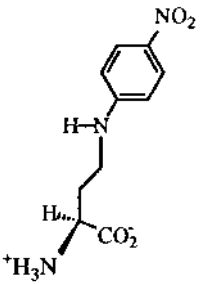

15

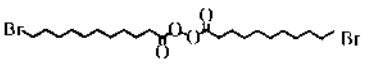

16

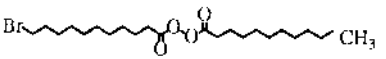

17

crystals that belong to a lower crystal class, such as triclinic, monoclinic, or orthorhombic, are optically biaxial. They studied the tetragonal crystal of di(11-bromoundecanoyl)peroxide (**16**) (denoted as Br···Br) in the presence of guest where a Br atom is replaced by CH_3 (**17**) (denoted as Br···CH_3). In the host crystal, Br···Br molecules assemble into layers that have Br atoms on both the upper and lower surfaces. Successive layers stack Br to Br atoms with 90° rotation about a fourfold screw axis in the stacking direction. These crystals, which grow as square {001} plates delineated by four {110} side faces, are not birefringent for light traveling along the fourfold screw axis perpendicular to the plate, appearing dark between crossed polarized filters. Crystals of Br···Br containing 15% Br···CH_3 are birefringent, the plate revealing four sectors under crossed polarizers. This birefringence in each sector results from unsymmetrical incorporation of the Br···CH_3 additive during crystal growth.

Other methods that have been used successfully to probe reduction in crystal symmetry are neutron and x-ray diffraction. These techniques are

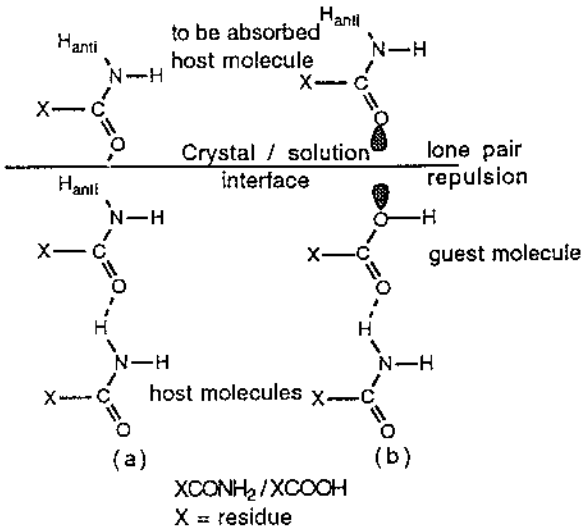

Figure 5.7. Schematic representation of the packing arrangement of primary amides ($XCONH_2$), showing carboxylic acid adsorption at the crystal–solution interface.

applicable, in particular, for systems where substantial amount of additive has been occluded into the bulk of the growing crystal. An example is solid solutions of carboxylic acids (XCO_2H) in primary amides ($XCONH_2$), where the NH_2 group is substituted by an OH moiety. Consider the N—H_{anti} bond that emerges from the crystalline surface shown in Figure 5.7. Such an amide molecule can be replaced by an acid additive. A strong inhibition of growth develops along the direction of the O═C—N—$H_{anti}\cdots$O═C hydrogen bond. Inhibition arises from repulsive O(hydroxyl)$\cdots$O(carbonyl) interactions between the lone-pair electrons of an adsorbed acid molecule and of an amide molecule at the site of an original N—H$\cdots$O hydrogen bond. Incorporation of a carboxylic acid in this orientation would substitute a 8.4-kV/mol repulsion for a 25.2-kV/mol attraction. The carboxylic acid additive would thus avoid surface sites that require the lone-pair electrons of the OH group to be oriented toward the surface and would be preferentially adsorbed at sites where the OH group emerges from the surface. Reduction in crystal symmetry has been demonstrated in the amide–carboxylic acid systems by neutron diffraction and solid-state photodimerization [5.1, 5.2]. The neutron diffraction analysis was applied to the system asparagine–aspartic acid, where as much as

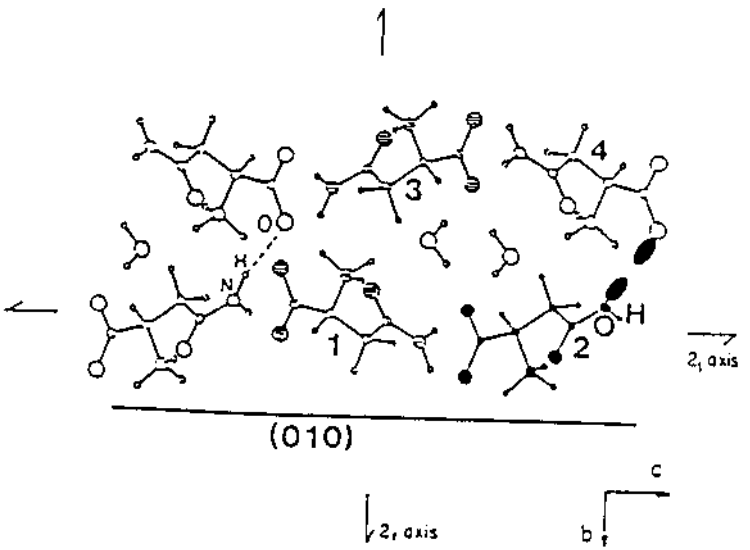

Figure 5.8. Schematic representation of the preferential adsorption of aspartic acid on the (010) surface of (L)-asparagine monohydrate crystal at sites of type 1 and 3 rather than types 2 and 4, as the crystal is growing at the (010) face.

15% additive was occluded by virtue of the numerous hydrogen bonds between guest and host.

(L)-Asparagine, $H_2NCOCH_2CH(NH_3^+)COO^-$, crystallizes from water as a monohydrate with a tight tree-dimensional net of hydrogen bonds in a $P2_12_12_1$ structure. The morphology is prismatic, with 18 developed faces. Crystallization of (L)-asparagine in the presence of (L)-aspartic acid yields {010} plates. Following the arguments given earlier for the amide–acid systems, the guest aspartic acid molecule should be more easily adsorbed at sites 1 and 3 on the growing (010) surface than at sites 2 and 4 (Fig. 5.8); naturally, the reverse situation holds for the opposite $(0\bar{1}0)$ face. If, on growth of the mixed crystal, the $(0\bar{1}0)$ face is blocked so that the amide and acid molecules would be occluded only through the (010) face, the symmetry of the mixed crystal should be reduced to $P12_11$. A low-temperature (18 K) neutron diffraction study with deuterated aspartic acid in protonated asparagine showed the expected reduction in symmetry [5.4].

E-Cinnamamide, $C_6H_5CHCHCONH_2$, has a packing arrangement along the *b* axis (Fig. 5.9) similar to that of benzamide. *E*-Cinnamic acid additive changes dramatically the morphology of the crystal [5.7] and, upon occlu-

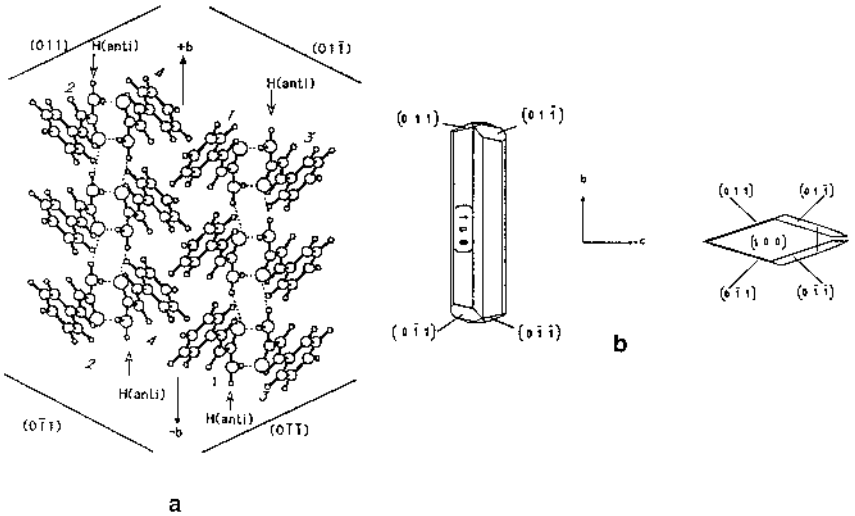

Figure 5.9. (a) Packing arrangement of *E*-cinnamamide viewed along the *a* axis delineated by the {011} faces; (b) computer-drawn morphology of *E*-cinnamamide crystals: (left) pure; (right) grown in the presence of cinnamic acid.

sion, induces a loss of the center of inversion in the crystal, which, in pure form, appears in a centrosymmetric monoclinic arrangement, space group $P2_1/c$. Reduction in symmetry could be demonstrated by performing a solid-state asymmetric photodimerization by virtue of the close-packed C═C bonds across "centers of inversion" [5.2]. When single mixed crystals were irradiated with ultraviolet light, optically active dimers of opposite handedness were found at the two poles of the *b* axis of the crystal. A comprehensive study of the reduction in crystal symmetry was done on the mixed crystal of *E*-cinnamamide/*E*-thienylacrylamide; the symmetry of different crystalline sectors were shown to be lowered from $P2_1/c$ to $P1$ by x-ray and neutron diffraction studies of the crystals cooled to low temperatures [5.3] as well as by solid-state photodimerization. The symmetry lowering arose from a replacement of attractive C—H$\cdots\pi$(electron) interactions between host molecules by repulsion between the sulfur lone-pair electrons of the guest and the π(electrons) of the host.

Crystal symmetry lowering has also been observed in inorganic crystals. Garnets where Al^{3+} ions were replaced by Fe^{3+} ions also show a reduction in lattice symmetry, from cubic down to triclinic [5.8]. Kahr and co-workers [5.9] have observed a reduction in symmetry both by optical birefrigence and

by x-ray crystallographic studies of different sectors in the mixed crystals of $NaBrO_3/NaClO_3$ and $BaNO_3/PbNO_3$.

6. TAILOR-MADE ADDITIVES FOR INHIBITION AND PROMOTION OF CRYSTAL NUCLEATION

Formation of crystals from single molecules in supersaturated solutions requires a process whereby the molecules assemble at early stages to form structured aggregates or nuclei. The driving force for the formation of these nuclei is provided by the intermolecular forces. However, these nuclei develop a surface at the interface with the environment, which is associated with positive free energy, which may destabilize them. Consequently, according to classical theory of crystal nucleation, during the growth process the nuclei must cross a critical radius above which they transform into crystals. The nuclei may assume a variety of structures, some of which are akin to that of the mature crystal. Thus, in systems displaying polymorphism, or in systems where mixtures of phases exist, the presence of aggregates of structures resembling each of the various mature phases may be expected. Close to equilibrium conditions, however, only those nuclei corresponding to the thermodynamically stable phase grow into crystals. Following this hypothesis, the structural information stored in the mature crystal may be used for the design of auxiliary molecules that can interact stereospecifically with the stable crystalline phase and selectively inhibit growth of the nuclei of this phase. If these molecules are designed so that they do not interact with the nuclei of the less stable phase, the latter phase may precipitate from the solution in a kinetically controlled process, provided that the two phases do not display too large a solubility gap.

6.1. Kinetic Resolution of Racemates by Crystallization with Tailor-Made Additives

Conglomerates are a particular case in which the two enantiomorphous phases are equienergetic. Kinetic resolution with the assistance of tailor-made inhibitors was achieved for several α-amino acids reported to undergo spontaneous resolution. These include threonine, Glu·HCl, asparagine monohydrate, and *p*-hydroxyphenylglycine-toluenesulfonate. When (D,L)-Glu·HCl was crystallized in the presence of (L)-lysine, or (D,L)-threonine was crystallized in the presence of (L)-glutamic acid, or (D,L)-asparagine in the presence of (L)-aspartic acid, a kinetic precipitation of the (D)-α-amino acid with almost 100% enantiomeric excess was obtained [6.1]. In these

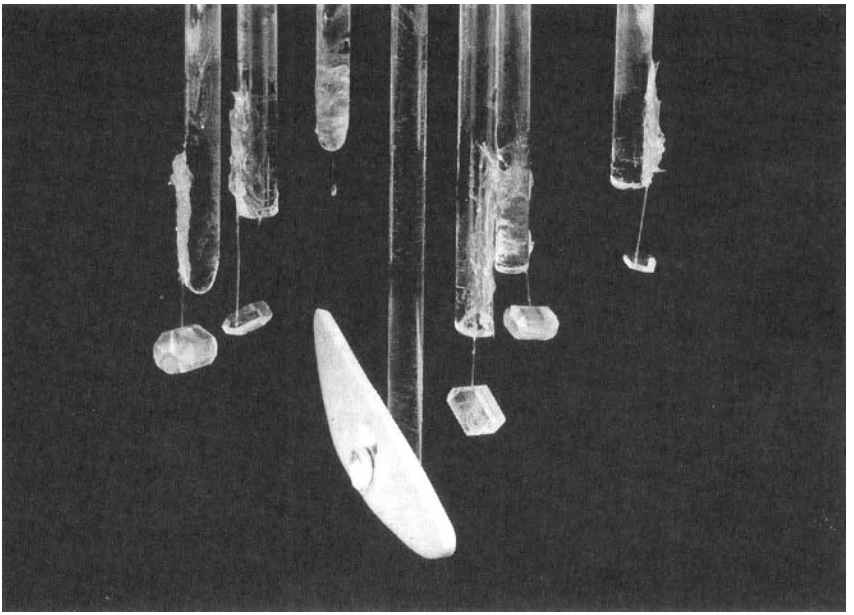

Figure 6.1. Three (D) and three (L) crystals of asparagine·H_2O grown together for 45 days under conditions close to equilibrium in the presence of (L)-serine; the large crystals are (D)-Asn·H_2O and the small ones are (L)-Asn·H_2O.

cases, the appearance and thus the growth of the affected enantiomorph were delayed up to several days with respect to that of the unaffected enantiomorphs. In the systems investigated, it could be demonstrated that the additive is occluded throughout the bulk of the affected crystals in amounts ranging typically from 0.05% to 1.5% wt/wt of substrate; in the case of asparagine–aspartic acid, a true solid–solution was formed containing up to 16% occluded aspartic acid.

The inhibition effect of the additive on the growth of the affected enantiomorph has also been demonstrated by direct comparison of the size of (L) and (D) single crystals grown in parallel from seeds, in conditions close to equilibrium [6.1] (Fig. 6.1).

A significant extension of this process has now been made by grafting the corresponding additives on a soluble polymer. These tailor-made polymers are most efficient enantioselective inhibitors, because it is sufficient to add about 1% wt/wt, or sometimes less, to the crystallizing solution to achieve

Table 6.6.1. Typical Results for the Resolution Experiments by Crystallization in the Presence of Polymeric Inhibitors

Racemic substrate	Type of polymer	Wt% of polymer	Precipitated product	Chemical yield (%)	ee (%)
Glu·HCl	(L)-**3**	0.5	(D)-Glu·HCl	20	100
Glu·HCl	(L)-**5**	1.0	(D)-Glu·HCl	21	100
Threonine	(L)-**3**	1.3	(D)-Thr	18	100
Asparagine	(L)-**3**	1.0	(D)-Asn	18	100
p-HPG pTs	(L)-**3**	1.2	(D)-*p*-HPG pTS	14	99
p-HPG pTs	(D)-**5**	1.0	(L)-*p*-HPG pTs	13	97.6
His·HCl·H_2O (45°C)	(L)-**5**	1.0	(D)-His·HCl·H_2O	12	100
	(D)-**5**	1.0	(L)-His·HCl·H_2O	11	100
His·HCl·$2H_2O$ (25°C)	(L)-**5**	3.0	(D)-His·HCl·H_2O	13	100
sec-Phenethyl 3,5 Dinitro benzoate	(D)-**7**	1.0	(L)-*sec*-Phenethyl 3,5 Dinitro benzoate	11	100

complete resolution of the enantiomers [3.8]. Such polymers have been used successfully not only for the resolution of α-amino acids but also for other materials (Table 6.1).

The method has been extended for systems where the energy gap between the racemic crystal and the mixture of resolved enantiomorphs is relatively small. For example, racemic histidine·HCl precipitates, at 25°C, as a stable racemic dihydrate crystal and a metastable conglomerate of resolved monohydrate crystals. When resolved *p*-aminophenylanine was grafted to polyacrylic acid, the addition of as little as 1% of the inhibitor induced resolution with quantitative enantiomeric yield of the desired enantiomer [6.2].

6.2. Control of Crystal Polymorphism

Molecules frequently crystallize in different polymorphic forms. Because the physical properties of a crystal depend to a large extent on its internal structure, there is, in the drug industry or for electro-optical purposes, a great interest in growing single crystals of a polymorph which may be metastable. Here, we examine how such a selective crystallization may be achieved by taking advantage of molecular packing characteristics, in the

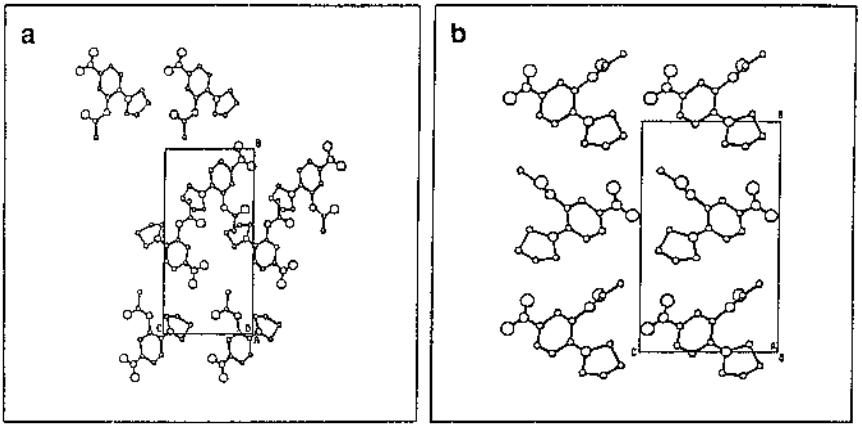

Figure 6.2. Packing arrangement of PAN crystal: (a) stable form with a pseudocentrosymmetric arrangement; (b) metastable form where the polar axis is along *b*.

case of precipitation of a polar crystal at the expense of the nonpolar polymorph. In crystals containing a polar axis, all the molecules are aligned in the same direction vis-à-vis the polar axis. In crystals with nonpolar axes, whether or not the structure is centrosymmetric, neighboring arrays of molecules along the principal axes are arranged in an antiparallel manner. An appropriate additive would inhibit growth of the nonpolar form at the opposite ends of the crystal but would inhibit growth of the polar form only at one end of its polar axis.

A system that satisfies the requirements of the foregoing concept is *N*(2-acetamido-4-nitrophenyl)pyrolidene (PAN) (**18**), the metastable polar form of which displays optical SHG [6.3] (Fig. 6.2). As little as 0.03% of the inhibitor of the polymer (**19**) induced crystallization of PAN in its meta-

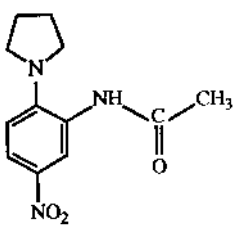

18

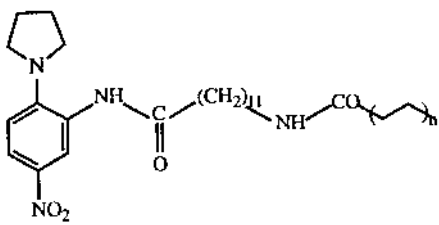

19

stable polymorph. In other systems, however, the situation may be more complex—for example, the polar form may belong to a crystal class of high symmetry, such that the host molecules adopt a variety of orientations relative to the polar size.

6.3. Tailor-Made Surfaces for Promotion of Crystal Nucleation

Crystal nucleation is generally a heterogeneous process. This means that the activation barrier for nucleation is lowered by the interaction of the embryonic nuclei with foreign surfaces. This process can happen at different levels of specificity, ranging from nonspecific adsorption to epitaxial crystal growth. Therefore, one can envisage induced nucleation of desired crystalline structures with a specific crystal orientation by designing appropriate nucleation promoters which match the structure of the crystal on a specific plane.

Several approaches have been considered. For example, self-aggregates of amphiphilic molecules had been shown to form crystallites at air–water or air–aqueous solution interfaces. The self-aggregating properties and packing arrangements of these crystallites have been determined by direct methods such as grazing incidence x-ray diffraction (GIXD) using intense synchrotron radiation [6.4, 6.5]. The self-aggregates of a variety of different amphiphilic molecules have been found to induce oriented crystallization of organic and inorganic materials at the air–water interface. Assignment of the structure and understanding of the function of these two-dimensional crystallites might throw light on the complex process of the early stages of three-dimensional crystal nucleation.

When small amounts of resolved hydrophobic α-amino acids such as valine $^{+}H_3NCH[CH(CH_3)_2]CO_2^-$, leucine, $^{+}H_3NCH[CH_2CH(CH_3)_2]CO_2^-$, and norleucine, $^{+}H_3NCH(CH_2CH_2CH_2CH_3)CO_2^-$, were added to a supersaturated solution of glycine, they induced an {010}-oriented crystallization of α-glycine at the air–solution interface [6.6, 6.7] (Fig. 6.3). The addition of (D)-α-amino acids induced the formation of α-glycine crystals oriented with their (010) face exposed to air and, by symmetry, (L)-α-amino acids induced $(0\bar{1}0)$-oriented crystals. Glycine crystals of both orientations were obtained upon the addition of the racemic mixtures of α-amino acids. Thus, we concluded that the hydrophobic α-amino acids form structured self-aggregates on the solution surface, arranged in a manner akin to the layer formed by α-glycine, and thus act as epitaxial matrices for oriented nucleation of α-glycine. There is also the possibility of a cooperative phenomenon whereby the hydrophobic α-amino acids at the aqueous solution surface and the

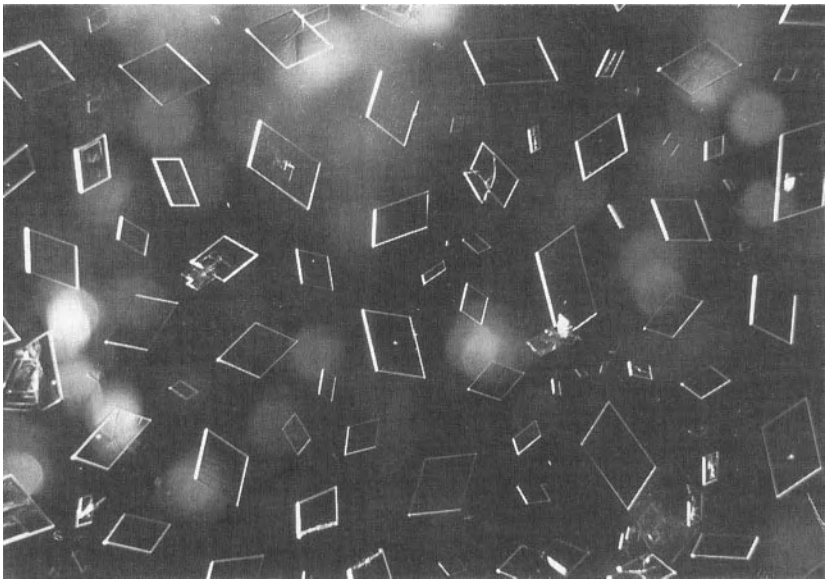

Figure 6.3. Floating crystals of α-glycine grown in the presence of 1% wt/wt (L)-leucine and 3% (D,L)-glutamic acid, exposing their $(0\bar{1}0)$ face to air.

glycine molecules from the solution form an ordered bilayer as a precursor to induced nucleation for α-glycine. Hydrophobic α-amino acids containing bulky substituents, such as *tert*-butylglycine, $^{+}H_3NC[C(CH_3)_3]CO_2^{-}$, neopentylglycine, $^{+}H_3NCH[CH_2C(CH_3)_3]CO_2^{-}$, and hexafluorovaline, $^{+}H_3NCH[CH(CF_3)_2]CO_2^{-}$, did not induce oriented nucleation of glycine crystals [4.4], perhaps because of a structural mismatch.

Oriented nucleation was also obtained in the crystallization of 4-hydroxybenzoic acid monohydrate, $4\text{-}HOC_6H_4COOH$, in the presence of additives [6.8]. Pure aqueous solutions yielded platelike crystals laying at the bottom of the dish. The addition of small amounts of 4-methoxybenzoic acid, $4\text{-}CH_3OC_6H_4COOH$, induced fast nucleation, with the crystals attached to the air–solution interface through their (401) face (Fig. 6.4). In this system, it seems unlikely that the additive 4-methoxybenzoic acid forms only two-dimensional clusters on the aqueous solution surface in an arrangement akin to that of the (401) layer of the ensuing crystal. A cooperative binding between host and additive leading to nucleation is more plausible.

From the oriented crystallization studies, we could conclude that the hydrophobic additives not only accumulate at the air–solution interface

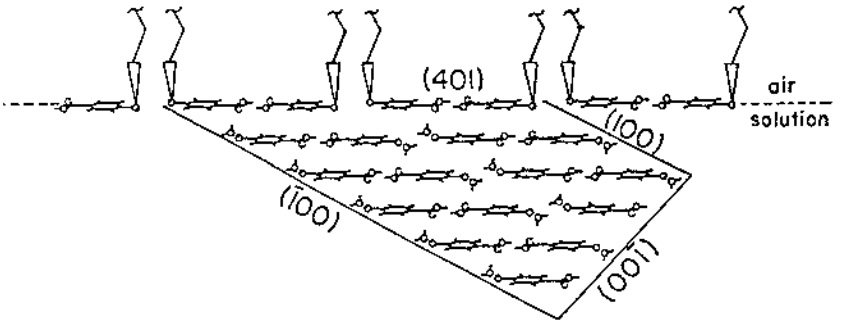

Figure 6.4. Packing arrangement of 4-hydroxybenzoic acid monohydrate crystal with the (401) face viewed edge on. The layer of molecules at the interface is the proposed model of the Langmuir film after nucleation of the crystal.

but also aggregate into structured clusters with a defined stereochemistry which interact with the substrate molecules to form the embryonic nuclei en route to crystal precipitation [4.4]. To obtain direct insight into the structures of these clusters, we carried out the same crystallizations in the presence of amphiphilic molecules bearing long hydrocarbon chains, which form Langmuir films at the air–solution interface. The advantage of these films is that they are amenable to structural analysis by analytical tools including GIXD, x-ray reflectivity, SHG from surfaces, and electron microscopy.

Langmuir monolayers of resolved α-amino acids bearing long hydrocarbon side chains were found to induce an oriented crystallization of glycine [6.9] similar to that observed with the water-soluble hydrophobic α-amino acids. The two-dimensional crystallinity of monolayers such as palmitoyl-(L)-lysine (**20**) was demonstrated by GIXD [6.10], which also confirmed that the packing arrangement (Fig. 6.5) of the polar head groups $^{+}H_3NC^{*}HCO_2^{-}$ is similar to that of the *ac* layer of α-glycine.

Several other crystals have been nucleated at the solution surface via Langmuir monolayers by virtue of either a partial structural fit or an elec-

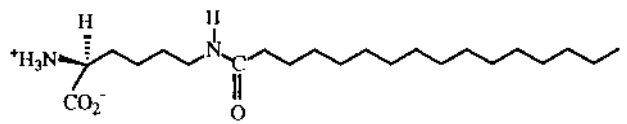

20

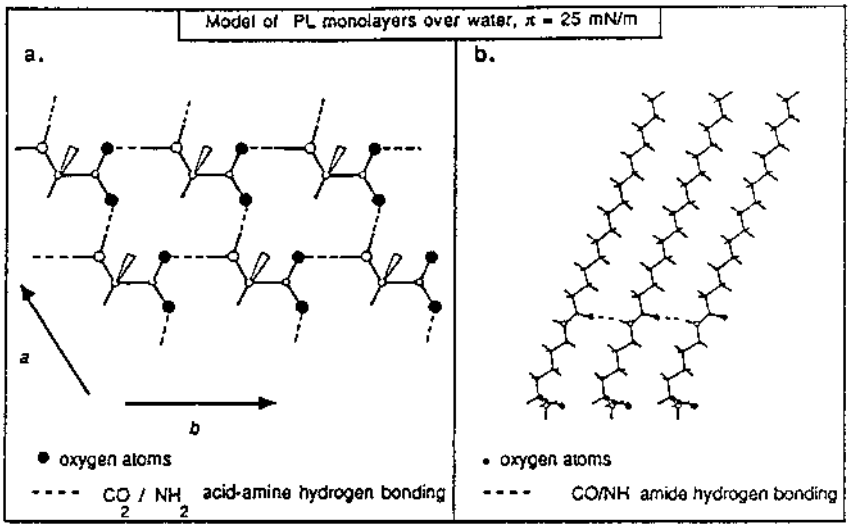

Figure 6.5. Two-dimensional structure of the monolayer of N^{ε}-palmitoyl-(D)-lysine as determined by GIXD measurements: (a) arrangement of the glycine $^{+}H_3N^{*}CHCO_2^{-}$ head groups; (b) arrangement of the molecular chain.

trostatic attraction. These include NaCl [6.11], silver propionate [6.12], calcite [6.13, 6.14], $BaSO_4$ [6.15, 6.16], and PbS [6.17]. NaCl crystallizes under monolayers of stearic acid, attached to the interface by its {111} face, whereas α-amino acids monolayers, which expose the zwitterionic $^{+}H_3NC^{*}HCO_2^{-}$ moiety to the solution, induce nucleation of NaCl from its {011} face. Induced crystallization of calcium carbonate by stearic acid monolayers and that of $BaSO_4$ by monolayers bearing sulfonate or phosphonate groups have been used as models for biomineralization. Oriented nucleation of PbS and CdSe nanocrystals by arachidic acid monolayers has interesting semiconducting properties.

Langmuir–Blodgett films deposited on solid supports have also been used as templates for oriented crystallization, giving similar results. For example, Figure 6.6 depicts crystals of α-glycine grown on a glass surface coated with resolved N^{ε}-palmitoyllysine [6.9]. Similar results were obtained for NaCl.

Recently, the presence of structured clusters at the air–solution interface and their role in promoting polymorphism has been amply demonstrated for 4-methoxy-*E*-cinnamic acid [6.18], 4-$CH_3OC_6H_4CHCHCOOH$. When crystallized from an aqueous solution with a large air–solution interface, this

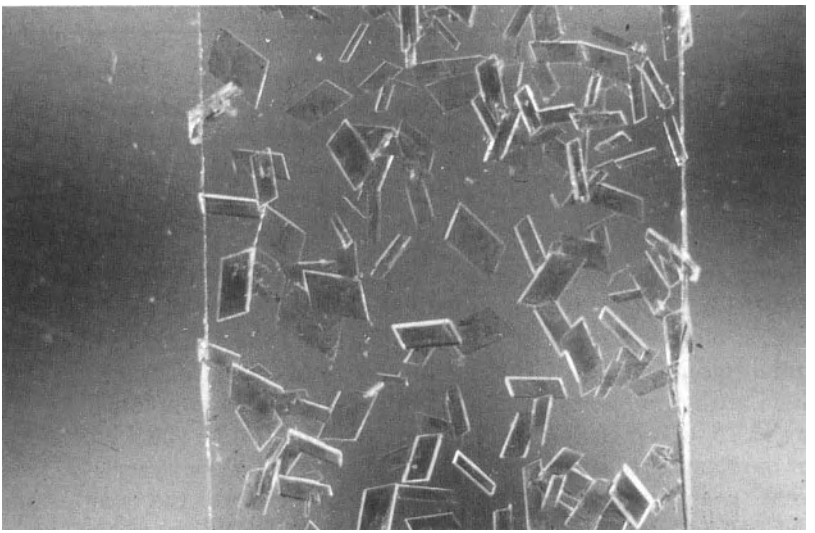

Figure 6.6. Crystals of α-glycine grown on glass surface coated with N^{ϵ}-palmitoyl-(L)-lysine.

compound yields a metastable polymorph together with the stable polymorph. The pure stable polymorph is obtained from the bulk solution when the air–aqueous solution interface is removed completely.

Nature has utilized proteins to control the morphology and the oriented crystallization of minerals. For example, proteins isolated from mollusks induced oriented crystallization of calcite [2.13]. Globular proteins act as matrices for pathological crystallization of sodium urate [6.19, 6.20] in gout. Another biological example is the induced nucleation of supercooled water by the frost bacterium *Pseudomonas syringae* [6.21]. Although the structure of its active site is still unknown, suggestions have been made that structured proteins promote the ice nucleation.

Recently, induced freezing of supercooled water drops into ice was achieved with the assistance of amphiphilic alcohols [6.22]. Water-soluble alcohols as additives generally lower the freezing point of supercooled water. On the other hand, on the basis of GIXD studies of a variety of monolayers, water-insoluble amphiphilic alcohols $C_nH_{2n+1}OH$ ($n = 23$, 30, 31) at the air–water interface form two-dimensional crystallites with coherence lengths in the range 300–1000 Å in a lattice similar to that of the *ab* lattice of hexagonal ice [6.23]. The unit cell of the crystalline monolayer of alcohols at temperatures just above 0°C may be regarded as distorted

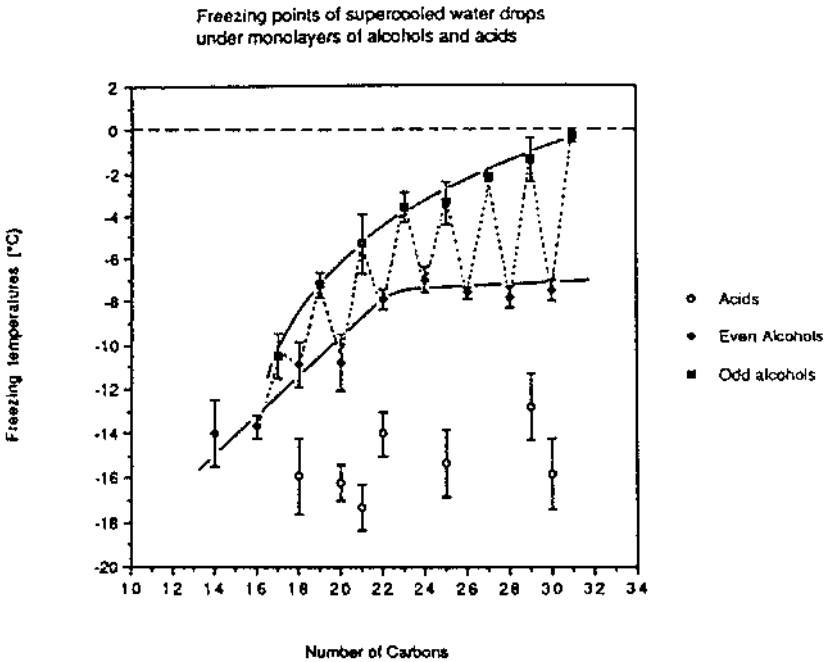

Figure 6.7. Graph summarizing the freezing point of ice as a function of the number of carbon atoms for the *n*-odd and *n*-even series of long-chain aliphatic alcohols

hexagonal with axes $a = b = 4.5$ Å, $\gamma = 113°$. Thus, the arrangement of the —OH head groups of the alcohol at the water surface would appear to mimic or complement the (001) face of hexagonal ice ($a = b = 4.5$ Å, $\gamma = 120°$) and thus might be considered as promoters of ice nucleation. This expectation was confirmed experimentally [6.24] by measuring the freezing point of supercooled water drops covered by monolayers of the aliphatic alcohols $C_nH_{2n+1}OH$, $n = 16$ to 31. The results are summarized in Figure 6.7. As seen in this figure, the freezing point is sensitive to the length and number of carbon atoms in the chain. The freezing-point curve for the *n*-odd series increases asymptotically with chain length, approaching 0°C for $n = 31$. The *n*-even series behaves differently: The freezing-point curve reaches a plateau of about −8°C for $n = 22$ to 30. The long-chain acids $C_nH_{2n+1}COOH$ are, by comparison, poor ice nucleators.

The two-dimensional structure of the uncompressed monolayers of the $C_nH_{2n+1}OH$ alcohols ($n = 23$, 30, 31) [6.25] and on the carboxylic acid, $C_{29}H_{59}COOH$ [6.26], over pure water at 5°C were determined to near atomic

resolution from an analysis of the GIXD data and by lattice energy calculations. The GIXD data of the alcohols $n = 30$ and 31 are very similar and so are their resulting structures, although it has been possible to deduce from the structure analysis together with the ice nucleating results that the arrangements of the terminal CH_2CH_2OH groups are not the same for $n = 30$ and 31. There may be a rearrangement of the head groups prior to ice nucleation, but a more detailed analysis is required to pinpoint the factors responsible for the odd–even effect. Nevertheless, the interplay between the odd–even effect on the freezing point of ice and the orientation of the alcohol groups at the air–water interface has been demonstrated unambiguously by using ester alcohols ($C_nH_{2n+1}OCOC_mH_{2m}OH$) and amide alcohols ($C_nH_{2n+1}CONHC_mH_{2m}OH$) bearing odd and even values of m. The difference in the temperature of the freezing of water drops by the ester alcohols is about 5°C. According to a GIXD study [6.25] of the ester alcohols $n = 19$ and $m = 9$ and 10, both molecules assume almost identical packing arrangements but differ in the orientation of their OH groups with respect to the water subphase; for $m = 9$, the OH bond and the two lone-pair electron lobes of the oxygen are exposed to water, whereas for $m = 10$, only the OH bond is exposed to water. How this difference in hydroxy group orientation affects the freezing point of ice is under investigation. Recently, some information on the critical size of the ice nucleus bound to the alcohol monolayer just below 0°C was obtained [6.27].

7. OUTLOOK

There is still a long way to go toward designing and manipulating molecular crystals in terms of their nucleation, growth, dissolution, morphology, and structural properties. Many of the parameters that determine the processes discussed in this chapter are still found by trial and error. The ability to design tailor-made inhibitors/promoters provides the crystal grower with a general tool and a rational way to control the crystallization process. Such a design is based primarily on understanding the interactions between the molecules at crystal faces and the solution environment; therefore, the method should be general and applicable to inorgnaic, organic, and biological crystals.

REFERENCES

[1.1] P. Hartmann, *Physics and Chemistry of Organic Solid State*, Interscience, New York, Vol. 1 (1963).
[1.2] P. Hartmann, *Crystal Growth*, North-Holland, Amsterdam (1973).

[1.3] R. Kern, *Bull. Soc. Fr. Mineral. Cristalogr.*, *76*: 391 (1953).
[1.4] A. F. Wells, *Phil. Mag.*, *37*: 180, 217, 605 (1946).
[1.5] I. Weissbuch, L. Addadi, M. Lahav, and L. Leiserowitz, *Science*, *253*: 637–645 (1991).
[2.1] H. E. Buckley, *Crystal Growth*, London (1951).
[2.2] L. Addadi, Z. Berkovitch-Yellin, I. Weissbuch, J. von Mil, L. J. W. Shimon, M. Lahav, and L. Leiserowitz, *Angew. Chem. Int. Ed. Engl.*, *24*: 466 (1985).
[2.3] L. Addadi, Z. Berkovitch-Yellin, I. Weissbuch, M. Lahav, and L. Leiserowitz, in *Topics in Stereochemistry*, *Volume 16* (E. L. Eliel, S. H. Willen, and N. L. Allinger, eds.), John Wiley & Sons, New York, pp. 1–85 (1986).
[2.4] L. Addadi, Z. Berkovitch-Yellin, N. Domb, E. Gati, M. Lahav, and L. Leiserowitz, *Nature*, *296*: 21–26 (1982).
[2.5] Z. Berkovitch-Yellin, L. Addadi, M. Idelson, M. Lahav, and L. Leiserowitz, *Angew. Chem. Suppl.*, 1336–1345 (1982).
[2.6] B. M. Smythe, *Aust. J. Chem.*, *20*: 1115 (1967).
[2.7] B. M. Smythe, *Sugar Technol. Rev.*, *1*: 191 (1971).
[2.8] G. Mantovani, G. Gilli, and F. Fagioli, *C.R. XIII Assembly*, *C115*: 289 (1967).
[2.9] A. van Hook, *Kristal. Acad. Nauk SSSR Inst. Kristallogr.*, *8*: 45 (1968).
[2.10] C. P. Fenimore and A. Thraikill, *J. Am. Chem. Soc.*, *71*: 2714 (1949).
[2.11] F. D. Miles, *Proc. Roy. Soc. London Ser. A*, *132*: 266 (1931).
[2.12] A. M. Cody and R. D. Cody, *J. Cryst. Growth*, *113*: 508 (1991).
[2.13] L. Addadi and S. Weiner, in *Biomineralizaiton: Chemicals and Biochemical Perspectives* (S. Mann, J. Webb, and R. J. P. Williams, eds.), VCH, Weinheim, Chap. 5 (1989).
[2.14] S. N. Black, L. A. Bromley, D. Cottier, R. J. Davey, B. Dobbs, and J. E. Rout, *J. Chem. Soc. Faraday Trans.*, *87*: 3409 (1991).
[2.15] W. J. Benton, I. R. Collins, I. M. Grimsey, G. M. Parkinson, and S. A. Rodger, *Faraday Discuss.*, *95*: 281 (1993).
[2.16] K. Lewtas, R. D. Tack, D. H. M. Beiny, and J. W. Mullin, *Advances in Industrial Crystallization*, Butterworth-Heinemann, London, p. 166 (1991).
[2.17] S. Skoulika, A. Michaelidis, and A. Aubry, *J. Cryst. Growth*, *108*: 285 (1991).
[2.18] P. A. Antinozzi, C. M. Brown, and D. L. Purich, *J. Cryst. Growth*, *125*: 215 (1992).
[2.19] O. Markman, D. Elias, L. Addadi, I. R. Cohen, and Z. Berkovitch-Yellin, *J. Cryst. Growth*, *122*: 344 (1992).
[3.1] A. P. Honess, *The Nature, Origin and Interpretation of the Etch Figures on Crystals*, John Wiley & Sons, New York (1927).

[3.2] L. J. W. Shimon, M. Lahav, and L. Leiserowitz, *J. Am. Chem. Soc.*, *107*: 3375 (1985).
[3.3] I. Weissbuch, L. Addadi, Z. Berkovitch-Yellin, E. Gati, S. Weinstein, M. Lahav, and L. Leiserowitz, *J. Am. Chem. Soc.*, *105*: 6613 (1983).
[3.4] L. J. W. Shimon, M. Lahav, and L. Leiserowitz, *Nou. J. Chem.*, *10*: 723 (1986).
[3.5] L. J. W. Shimon, F. C. Wireko, J. Wolf, I. Weissbuch, L. Addadi, Z. Berkovitch-Yellin, M. Lahav, and L. Leiserowitz, *Mol. Cryst. Liquid Cryst.*, *137*: 67 (1986).
[3.6] S. Grayer, Z. Berkovitch, M. Lahav, and L. Leiserowitz, *Mol. Cryst. Liquid Cryst.*, *186*: 3 (1990).
[3.7] L. J. W. Shimon, D. Zbaida, L. Addadi, M. Lahav, and L. Leiserowitz, *Mol. Cryst. Liquid Cryst.*, *161*: 138 (1988).
[3.8] D. Zbaida, I. Weissbuch, E. Shavit-Gati, L. Addadi, L. Leiserowitz, and M. Lahav, *Reactive Polym.*, *6*: 241 (1987).
[3.9] P. Bennema and G. Gilmer, in *Crystal Growth: An Introduction* (P. Hartmann, ed.), North-Holland, Amsterdam, p. 272 (1973).
[3.10] P. Bennema, *J. Cryst. Growth*, *122*: 110 (1992).
[3.11] J. R. Bourne and R. J. Davey, *J. Cryst. Growth*, *36*: 278 (1976).
[3.12] M. Elwenspock, P. Bennema, and J. P. von Eerden, *J. Cryst. Growth*, *83*: 297 (1987).
[3.13] F. C. Wireko, L. J. W. Shimon, F. Frolow, Z. Berkovitch-Yellin, M. Lahav, and L. Leiserowitz, *J. Phys. Chem.*, *91*: 472 (1987).
[3.14] Z. Berkovitch-Yellin, *J. Am. Chem. Soc.*, *107*: 3375 (1985).
[3.15] R. J. Davey, *J. Cryst. Growth*, *76*: 637 (1986).
[3.16] R. J. Davey, B. Milisavljevic, and J. R. Bourne, *J. Phys. Chem.*, *92*: 2032 (1988).
[3.17] L. J. W. Shimon, M. Vaida, L. Addadi, M. Lahav, and L. Leiserowiz, *Solvent Effect*, Oxford University Press, Oxford (1991).
[3.18] J.-L. Wang, M. Lahav, and L. Leiserowitz, *Angew. Chem. Int. Ed.*, *30*: 696 (1991).
[3.19] J.-L. Wang, L. Leiserowitz, and M. Lahav, *J. Phys. Chem.*, *96*: 15–16 (1992).
[3.20] R. J. Davey, J. W. Mullin, and M. J. L. Whiting, *J. Cryst. Growth*, *58*: 304 (1982).
[3.21] L. J. W. Shimon, M. Vaida, L. Addadi, M. Lahav, and L. Leiserowitz, *J. Am. Chem. Soc.*, *112*: 6215 (1990).
[4.1] P. Hartmann and W. G. Perdok, *Acta Crystallogr.*, *8*: 49 (1955).
[4.2] P. Hartmann, *J. Cryst. Growth*, *49*: 157, 166 (1980).
[4.3] F. L. Hirshfeld, *Theoret. Chem. Acta*, *44*: 129 (1977).
[4.4] I. Weissbuch, F. Frolow, L. Addadi, M. Lahav, and L. Leiserowitz, *J. Am. Chem. Soc.*, *112*: 7718 (1990).

[4.5] I. Weissbuch, L. J. W. Shimon, L. Addadi, Z. Berkovitch-Yellin, S. Weinstein, M. Lahav, and L. Leiserowitz, *Ist. J. Chem.*, *25*: 353–362 (1985).
[4.6] I. Weissbuch, Z. Berkovitch-Yellin, L. Leiserowitz, and M. Lahav, *Isr. J. Chem.*, *25*: 362–372 (1985).
[4.7] R. Docherty and K. Roberts, in *British Crystallography Association Spring Meeting*, Poster 39 (1987).
[4.8] S. N. Black, R. J. Davey, and T. D. McLean, *Mol. Cryst. Liquid Cryst. Inc. Nonlinear Opt.*, *161*: 283 (1988).
[5.1] M. Vaida, L. J. W. Shimon, Y. Weisinger-Lewin, F. Frolow, M. Lahav, L. Leiserowitz, and R. K. McMullan, *Science*, *241*: 1475 (1988).
[5.2] M. Vaida, L. J. W. Shimon, J. van Mil, K. Ernst-Cabrera, L. Addadi, L. Leiserowitz, and M. Lahav, *J. Am. Chem. Soc.*, *111*: 1029 (1989).
[5.3] M. Vaida, R. Popovitz-Biro, L. Leiserowitz, and M. Lahav, in *Photochemistry in Organized and Constrained Media* (V. Ramamurthy, ed.), VCH, New York, pp. 247–302 (1991).
[5.4] Y. Weisinger-Lewin, F. Frolow, R. K. McMullan, T. F. Koetzle, M. Lahav, and L. Leiserowitz, *J. Am. Chem. Soc.*, *111*: 1035–1040 (1989).
[5.5] I. Weissbuch, M. Lahav, L. Leiserowitz, G. R. Meredith, and H. Vanherzeele, *Chem. Mater.*, *1*: 14 (1989).
[5.6] J. M. McBride and S. B. Bertman, *Angew. Chem. Int. Ed. Engl.*, *28*: 300 (1989).
[5.7] Z. Berkovitch-Yellin, J. van Mill, L. Addadi, M. Idelson, M. Lahav, and L. Leiserowitz, *J. Am. Chem. Soc.*, *107*: 3111 (1985).
[5.8] F. M. Allen and P. R. Buseck, *Am. Mineral*, *73*: 568 (1988).
[5.9] P. Gopalan, M. L. Peterson, G. Crundwell, and B. Kahr, *J. Am. Chem.* Soc., *115*: 3366 (1993).
[6.1] L. Addadi, S. Weinstein, E. Gati, I. Weissbuch, and M. Lahav, *J. Am. Chem. Soc.*, *104*: 4610 (1982).
[6.2] I. Weissbuch, D. Zbaida, L. Addadi, M. Lahav, and L. Leiserowitz, *J. Am. Chem. Soc.*, *109*: 1869 (1987).
[6.3] E. Staab, L. Addadi, L. Leiserowitz, and M. Lahav, *Adv. Mater.*, *2*: 40 (1990).
[6.4] D. Jacquemain, S. Grayer Wolf, F. Leveiller, M. Lahav, L. Leiserowitz, M. Deutsch, K. Kjaer, and J. Als-Nielsen, *J. Am. Chem. Soc.*, *112*: 7724 (1990).
[6.5] D. Jacquemain, S. Grayer Wolf, F. Leveiller, M. Deutsch, K. Kjaer, J. Als-Nielsen, M. Lahav, and L. Leiserowitz, *Angew. Chem. Int. Ed. Engl.*, *31*: 130 (1992).

[6.6] I. Weissbuch, L. Addadi, Z. Berkovitch-Yellin, E. Gati, M. Lahav, and L. Leiserowitz, *Nature*, *310*: 161 (1984).
[6.7] I. Weissbuch, L. Addadi, L. Leiserowitz, and M. Lahav, *J. Am. Chem. Soc.*, *110*: 561 (1988).
[6.8] I. Weissbuch, G. Berkovic, L. Leiserowitz, and M. Lahav, *J. Am. Chem. Soc.*, *112*: 5874 (1990).
[6.9] E. M. Landau, S. G. Wolf, M. Levanon, L. Leiserowitz, M. Lahav, and J. Sagiv, *J. Am. Chem. Soc.*, *111*: 1436 (1989).
[6.10] S. G. Wolf, L. Leiserowitz, M. Lahav, M. Deutch, K. Kjaer, and J. Als-Nielsen, *Nature*, *328*: 63–66 (1987).
[6.11] E. M. Landau, R. Popovitz-Biro, M. Levanon, L. Leiserowitz, and M. Lahav, *Mol. Cryst. Liquid Cryst.*, *134*: 323 (1986).
[6.12] I. Weissbuch, J. Majewski, K. Kjaer, J. Als-Nielsen, M. Lahav, and L. Leiserowitz, *J. Phys. Chem.*, *97*: 12,848 (1993).
[6.13] S. Mann, B. R. Heywood, S. Rajam, and J. D. Birchall, *Nature*, *334*: 692 (1988).
[6.14] S. Mann, *Nature*, *332*: 119 (1988).
[6.15] B. R. Heywood and S. Mann, *Langmuir*, *8*: 1492–1498 (1992).
[6.16] B. R. Heywood and S. Mann, *J. Am. Chem. Soc.*, *114*: 4681 (1992).
[6.17] X. K. Zhao, J. Yang, L. D. McCormick, and J. H. Fendler, *J. Phys. Chem.*, *96*: 9933 (1992).
[6.18] I. Weissbuch, L. Leiserowitz, and M. Lahav, *J. Am. Chem. Soc.*, *113*: 8941 (1991).
[6.19] D. Perl-Treves and L. Addadi, *Mol. Cryst. Liquid Cryst.* 187: 1 (1990).
[6.20] M. Kam, D. Perl-Treves, and L. Addadi, *FASEB J.*, *6*: 2608 (1992).
[6.21] R. L. Green and G. J. Warren, *Nature*, *317*: 645 (1985).
[6.22] R. Popovitz-Biro, J. L. Wang, J. Majewski, E. Shanit, L. Leiserowitz and M. Lahav, *J. Am. Chem. Soc.*, *116*: 1179 (1994).
[6.23] D. Jacquemain, F. Leveiller, S. Weinbach, M. Lahav, L. Leiserowitz, K. Kjaer, and J. Als-Nielsen, *J. Am. Chem. Soc.*, *113*: 7684–7691 (1991).
[6.24] M. Gavish, R. Popovitz-Biro, M. Lahav, and L. Leiserowitz, *Science*, *250*: 973 (1990).
[6.25] J. L. Wang, F. Leveiller, D. Jacquemain, K. Kjaer, J. Als-Nilsen, M. Lahav, and L. Oleiserowitz, *J. Am. Chem. Soc.*, *116*: 1192 (1994).
[6.26] F. Leveiller, D. Jacquemain, L. Leiserowitz, K. Kjaer, and J. Als-Nielsen, *J. Phys. Chem.*, *96*: 10,380 (1992).
[6.27] J. Majewski, R. Popovitz-Biro, K. Kjaer, J. Als-Nielsen, M. Lahav, and L. Leiserowitz, *J. Phys. Chem.*, *98*: 4087 (1994).

13

Suspension Crystallization from the Melt

K. TOYOKURA AND I. HIRASAWA Waseda University, Tokyo, Japan

1. INTRODUCTION

As described in Chapters 1–4, there is no strict borderline between crystallization from the melt and crystallization from solution. As a rule, a melt contains one or, often, two or more components, and the objective of crystallization from the melt is either the simple solidification of a one-component system (cf. Chapter 14) or the purification of a multicomponent system. A single-stage crystallization of a multicomponent melt may fail to produce a pure crystalline product. The reason for this can be either an equilibrium distribution of impurities in the liquid and the crystalline phase (thermodynamics) or the incorporation of impurities into the growing crystals due to kinetic effects (cf. Chapter 3). Therefore, both the solubility and crystallization kinetics (nucleation and growth) are important parameters in crystallization from the melt. Repeated crystallization steps or recrystallization are often employed to increase crystal purity in order to obtain a pure product. If the impurities are more soluble in the solvent than in the product, most of the impurities can be removed by dissolving the crystals in a

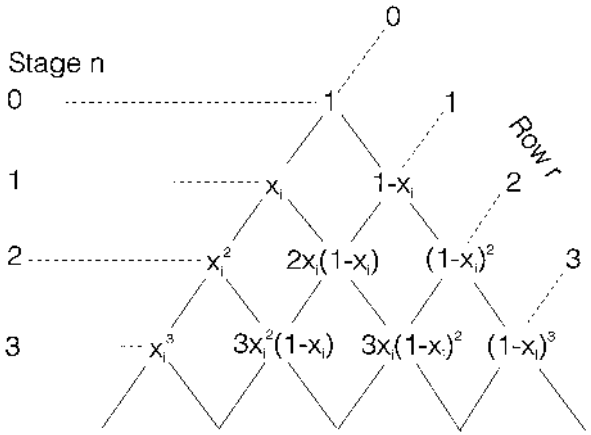

Figure 1.1. Analysis of triangular fractional crystallization.

solvent at optimal temperature. As a rule, the subsequent purification step is a cooling crystallization. Ideally, all of the impurities should be very soluble in the solvent at the temperature under consideration. If the solubility of the crystal component decreases considerably with decreasing temperature, a high yield can be expected.

Theoretically, eutectic systems can be purified by single-stage crystallization; however, solid solutions require a multistage operation, which is often carried out in column crystallizers (cf. Chapter 8). Such processes are called *fractional crystallization*. A recrystallization scheme is a suitable tool for explaining the progress of crystallization (see Fig. 1.1) [1.1]. If a constant fraction of a component is crystallized in each operation and fractions are combined as shown in Figure 1.1, the fraction x_i of the original component i which appears at any given point in the triangular scheme is given by

$$[x_i + (1 - x_i)]^n = 1 \tag{1.1}$$

where n is the number of crystallization steps.

Crystallizers for crystallization from the melt are described in Chapter 8 and in this chapter. Equipment for the crystallization of multicomponent melts may be divided into suspension crystallizers (Chapter 13) and layer crystallizers (Chapter 14). Finally, equipment used for the solidification of pure melts is dealt with in Chapter 14.

The flow of the slurry (melt and suspended crystals) in a suspension crystallizer is necessary to (a) suspend the crystals (cf. Chapter 8), (b) enhance the heat transfer between the slurry and the cooling surfaces, (c) create optimal supersaturation and rates of nucleation and growth, and (d)

produce crystals with the desired crystal size distribution (CSD) and purity. For layer crystallizers, an optimal melt velocity is recommended in order to (a) produce a compact layer of suitable morphology and sufficient purity, (b) promote heat transfer to the layer, (c) create an optimal level of supersaturation, and (d) obtain optimal rates of crystal growth.

With respect to apparatus employed in melt crystallization, layer and suspension crystallization can be distinguished. In *layer crystallization* processes, crystals generally grow on the cooled surface of a multitube or plate-type heat exchanger. The crystalline product is generally removed by mechanical separation of the crystals from the residual melt, which contains the impurities. *Suspension crystallization* from the melt is employed in various types of conventional crystallizer.

Table 1.1 shows a comparison of the main features of layer and suspension crystallizers. This comparison is based on a tube bundle with the diameter $D = 0.02\,\text{m}$ for the tubes and a volume fraction $\Psi = 0.5$ of the tubes in the bundle for layer crystallization, and on mean particle sizes $L_{32} = 1\,\text{mm}$ and $L_{32} = 0.1\,\text{mm}$ for suspension crystallization. It should be noted that the crystal growth rate is of the order of magnitude of

Table 1.1. Comparison of Layer and Suspension Crystallization

	Layer tube bundle $D = 0.02\,\text{m}$ $\Psi = 0.5$	Suspension with $\varphi_T = 0.2$ (assumption: monodisperse)	
Specific area a_T (m^2/m^3)	$a_T = \frac{4\Psi}{D}$	$a_T = \frac{6\varphi_T}{L_{32}}$	
Crystal density ρ_C (kg/m^3)	1,000	1,000	
Growth rate v (m/s)	10^{-6}	10^{-7}	10^{-8}
Mean crystal size L_{32} (m)	—	10^{-3}	10^{-4}
Specific area a_T (m^2/m^3)	100	1,200	12,000
Mass flux density $\dot{m}$ ($\text{kg}/\text{m}^2\,\text{s}$)	10^{-3}	10^{-4}	10^{-4}
Volumetric production rate $\dot{m}_V$ ($\text{kg}/\text{m}^3\,\text{s}$)	0.10	0.12	0.12
$\dot{m}_V$ ($\text{kg}/\text{m}^3\,\text{h}$)	360	432	432

$v = G/2 = 10^{-6}$ m/s in the tubular apparatus, but only $v = 10^{-7}$ m/s and 10^{-8} m/s for the suspension crystallizer.

According to the equation of Burton et al. (see Ref. [1.2]), the effective distribution coefficient $k_{\text{eff}} = x_{\text{im},S}/y^*_{\text{im},L}$ = concentration of impurity in the solid/concentration of the impurity in the liquid is given by

$$\frac{1}{k_{\text{eff}}} = 1 + \frac{y^*_{\text{im},L} - x_{\text{im},S}}{x_{\text{im},S}} \exp\left(-\frac{G}{k_d}\right) = 1 + \left(\frac{1}{K} - 1\right) \exp\left(-\frac{G}{k_d}\right) \tag{1.2}$$

In this equation, $k_{\text{eff}} = x_{\text{im},S}/y^*_{\text{im},L}$ is the distribution coefficient for equilibrium-state conditions. As can be seen, the purity of the crystals depends mainly on the growth rate. Consequently, we can expect high-purity products at the low growth rates in the suspension crystallizer. However, it is necessary to handle the solid crystals and to clean them by removing the mother liquor and washing. This is easier for layer crystallization, but the product is less pure. Sweating and recrystallization processes result in a reduction in the volumetric production rates given in Table 1.1.

During crystallization from the melt, amorphous substances are sometimes produced, depending on the operational conditions. Organic substances, in particular, quite often precipitate as amorphous material, which is generally unstable and quite often changes into the crystalline state. This process is a serious problem in industrial crystallization and has to be studied before setting up certain crystallization processes.

2. FUNDAMENTALS OF CRYSTALLIZATION FROM THE MELT

For crystallization from the melt, supersaturation, nucleation, and crystal growth are important factors (cf. Chapters 2 and 3). In contrast to crystallization from solution, the composition of the melt adjacent to the surface of growing crystals is not much changed. Therefore, the progress of crystallization is often not controlled by diffusion but by removal of the heat of crystallization. Therefore, thermal diffusion effects predominate in melt crystallization, contrary to crystallization from the solution, where heat transfer is not very important.

2.1. Phase Equilibrium and Heat of Crystallization

The composition of precipitated crystals can be read from the phase diagrams which have been discussed in Chapter 1. When the simple eutectic system shown in Figure 1.2.4a is cooled, component A crystallizes from the

melt, whose composition y is smaller than the eutectic composition. During this crystallization, pure crystals of A are theoretically precipitated and the composition of the melt increases in accordance with the equilibrium line, and finally reaches the eutectic composition. When the melt assumes the concentration of the eutectic mixture, mixed crystals of eutectic composition are produced and the composition of the melt remains constant. In real processes, the crystals include melt and/or impurities. When a pure product is desired, the mechanisms of melt crystallization and the purification of the resulting crystals should be studied (cf. Sec. 2.4) carefully.

The phase diagram designated as type I in Figure 1.2.4 is for a non-eutectic solid–mixture–melt system. During crystallization of such a system, the theoretical concentration of precipitated crystals can be read from the phase diagram for a given temperature. When a melt is gradually cooled down, the composition of the precipitated crystals as well as the concentration of the melt changes. Therefore, recrystallization in a multistage crystallizer by crystallization and melting of crystals is necessary to produce pure crystals.

As a rule, the phase diagram which is valid for atmospheric pressure (as shown in Figure 1.2.4a) is changed when the melt is compressed to high pressure. As an example, the phase diagram of the benzene–cyclohexane system of Moritoki et al. [2.1] is shown in Figure 2.1. As can be seen, the eutectic temperature and composition are affected appreciably by the pressure.

The latent heat of crystallization from the melt, ΔH^*_{CL}, can be calculated from

$$\Delta H^*_{CL} = \Re T \frac{T_0}{T_0 - T} \ln a^* \approx \Re T \frac{T_0}{T_0 - T} \ln y^* \tag{2.1}$$

In this equation, y^* is the mole fraction, T_0 is the melting point of the pure crystallizing component, and T is the temperature under discussion. ΔH^*_{CL} is also affected by the pressure, and for the crystallization of benzene from a benzene–cyclohexane mixture, this dependency can be calculated from Figure 2.1.

2.2. Kinetics

The most important kinetic parameters, the rates of nucleation and growth, have been discussed in Chapters 2 and 3. As a rule, excessive supersaturation must be avoided in order to restrict the rates of nucleation and growth. High nucleation rates lead to a fine product in suspension crystallizers. At high

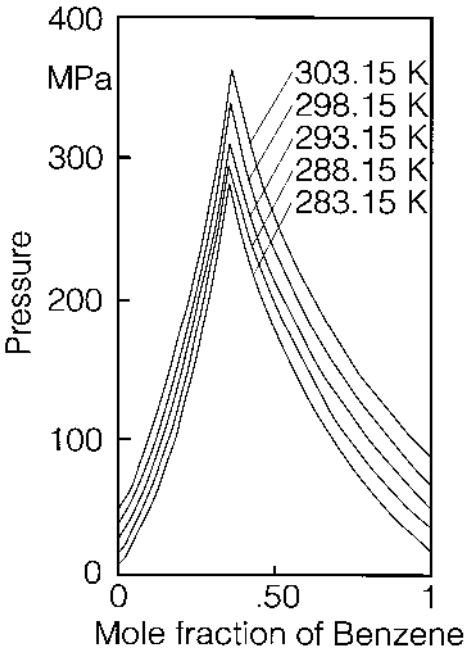

Figure 2.1. Phase diagram of the system benzene–cyclohexane.

growth rates, mother liquor and impurities may be trapped in the crystal and the product will contain inclusions.

These interrelationships will be discussed for an organic system crystallized in equipment according to Figure 2.2, where a typical batch-cooling crystallizer is shown. The data measured by Yamazaki et al. [2.2] apply to the crystallization of benzene from a benzene–cychlohexane mixture. Primary nucleation of benzene occurs in an agitated supersaturated melt by shock contact between the revolving blades of an agitator and a wire inserted into the melt. During melt crystallization of such a system, a moderate level of primary nucleation is difficult to maintain in an agitated vessel, and mechanical shock, by the method mentioned here, is an effective means of controlling nucleation. When primary nucleation takes place, the inserted wire is taken out of the vessel and the melt is further agitated to suspend the nuclei. Suspended nuclei quickly grow to visible size and the mass ratio w of benzene crystals, shown by w in Figure 2.3a, becomes almost constant after 15 min. The concentration of benzene, c_B, in the melt mixture decreases from 90% to 87.5% after 30 min of operating time and then to about 87% after 480 min. The purity of benzene crystals, c_S, simply filtered from

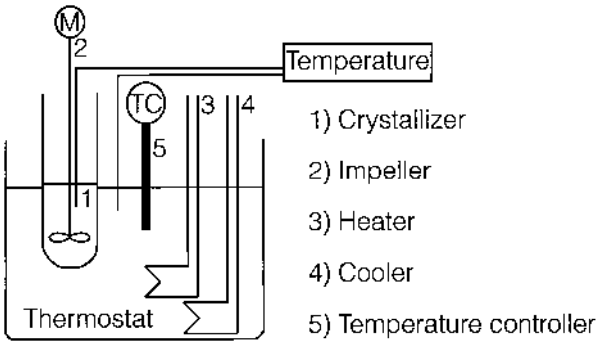

Figure 2.2. Experimental apparatus of a typical batch-cooling crystallizer.

the melt slurry gradually increases from 94% to 98%. The change of CSD and the total population of benzene crystals are shown in Figures 2.3b and 2.3c for a batch time of about 300 min. The quantity of suspended benzene crystals remains approximately constant. These results show that the behavior of suspended benzene crystals in a melt is complicated, because the crystal size increases as the number of crystals decreases. Presumably, the increase in the parity of the suspended crystals is caused by the release of mother liquor by the gradual change in crystal size. Other growth tests of suspended benzene crystals which have been kept at constant supersaturation show a further interesting phenomenon (see Ref. [2.3]). In these tests, the size distribution and total population of crystals have changed as shown in Figures 2.4a and 2.4b. During these tests, many fine crystals of relatively uniform size are suspended at the beginning of the batch and these crystals then grow, and, at the same time, the population of fines decreases. The distribution of suspended crystals becomes wider, resulting in two peaks of different size after 2 h. After this time, the population has decreased as can be seen in Figure 2.4c. The sudden increase of the total number of crystals in a melt is presumably caused by secondary nucleation. Crystal samples taken after 1.0 and 1.5 h show some large crystals of about 0.4 mm in size to be present. The reason for the decrease in the total number of crystals shown in Figure 2.4c may be the occurrence of agglomeration of fine crystals. After 4 h of operation, some large crystals of about 0.4 mm in size are observed, and the total population is almost constant. Agglomeration is correlated with the purity of the product crystals (see Chapter 6).

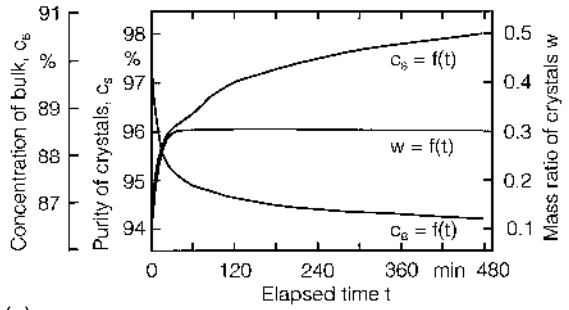

(a)

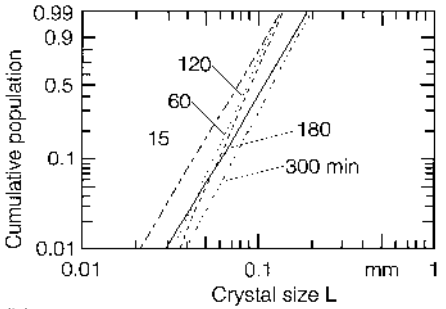

(b)

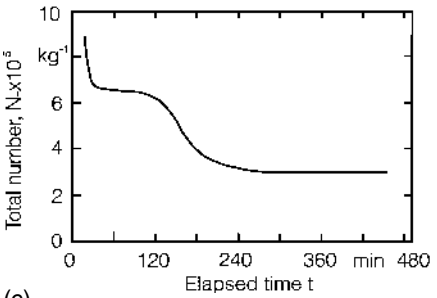

(c)

Figure 2.3. (a) Mass ratio w of crystals, bulk concentration c_B and concentration c_S of crystals against the elapsed time t; (b) crystal size distribution based on cumulative number in a Rosin–Rammler–Sperling–Bennet diagram; (c) correlation between total number of crystals, N_T, and elapsed time t.

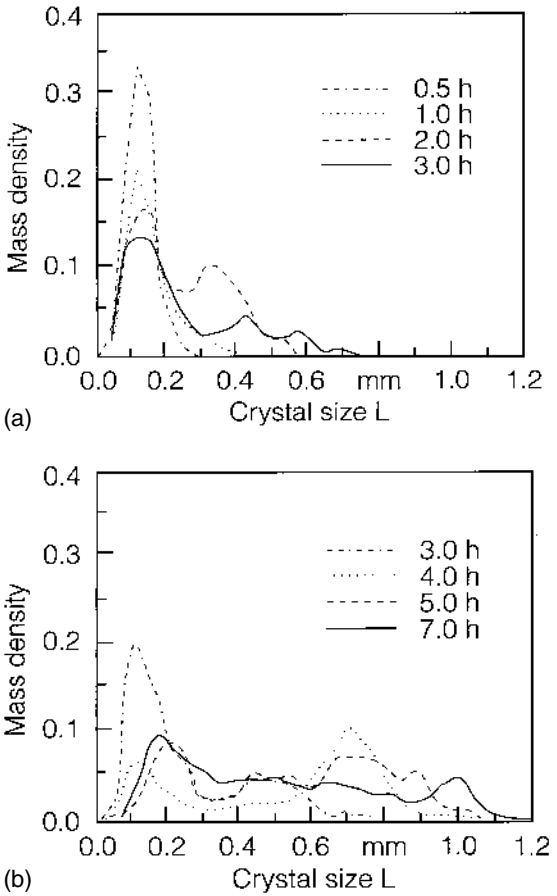

Figure 2.4. (a) Size distribution of crystals samples withdrawn after 0.5, 1, 2, and 3 h; (b) size distribution of crystal samples withdrawn after 3, 4, 5, and 7 h.

2.3. Process Choice and Design

Industrial melt crystallization processes are employed primarily for the separation of a product component from a melt. The choice of the separation by crystallization is always based on phase equilibria. The phase diagram provides the possibility of establishing material balances and defining favorable operating conditions (temperature).

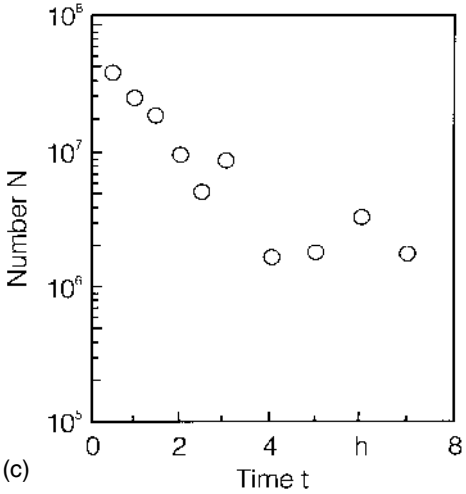

Figure 2.4. (c) Number of crystals, N, versus the crystallization time.

Besides phase equilibria, the kinetics of the crystallization process determine the purity of the crystals. The thermodynamic purity can be obtained at a very small supersaturation. During melt crystallization of some systems, it can happen that the melt remains supersaturated for a long time without crystallization, and in these cases, seeding is recommended. As a rule, reasonable operating conditions for optimal crystallization rates and/or sweating operations can only be found by laboratory studies. Recrystallization generally increases the production costs and should be avoided if possible. For suspensions, the final choice of the technical process depends on the crystals to be produced, which should be coarse, to aid crystal–melt separation.

When several components of a melt crystallize and lead to a decrease in the total volume of a melt, compressive crystallization (generally called high-pressure crystallization) should be applicable. Crystallization under high-pressure conditions may lead to a crystalline product which can be quite different from crystals produced under atmospheric pressure. At high pressure, systems that are noneutectic under atmospheric pressure sometimes change to eutectic behavior, and pure products can easily be produced.

2.4. Separation and Purification Efficiency

Layer and suspension crystallization exhibit some common features with respect to the separation and purification efficiency. According to equation

(1.2), the impurities in the crystals depend on (a) the equilibrium distribution coefficient K, (b) the growth rate $G = dL/dt$ of the layer or the suspended crystals, (c) the mass transfer coefficient k_d, and (d) the concentration of the impurities. The growth rate G may be controlled by heat transfer (heat transfer controlled) or by mass transfer (diffusion controlled). In the case of low concentrations of the impurities, low growth rates, and high mass transfer coefficients, the layer or the suspension usually contains compact and pure crystals. However, with increasing growth rates, the probability increases that melt and impurities will form inclusions in the crystals. Furthermore, growth can become dendritic and result in needlelike crystals.

If melt with a certain concentration c_i forms inclusions inside the crystal phase, this composition $c_{i,S}$ may be different from the concentration $c_{i,L}$ of this component in the melt outside. Diffusion of this component through the crystal phase will then take place. The amount I of the impurity transported by diffusion through the pores, which are assumed to be cylindrical, depends on the characteristic length l_0, the constant K_1, which specifies the property of the solid grown during the initial stage of operation, the diffusion coefficient D_{AB}, the concentrations $c_{im,S}$ and $c^*_{im,L}$, and on the diffusion time t_{dif} (see Ref. [2.4]).

$$I = \frac{c_{im,S} + c^*_{im,L}(T_C)}{2} l_0 K_1 \exp\left(\frac{c_{im,S} - c^*_{im,L}}{c_{im,S} + c^*_{im,L}} \frac{2D_{AB}}{l_0^2} t_{dif}\right) \tag{2.2}$$

In Figure 2.5, the amount of benzoic acid based on the surface of the holes in crystallized naphthalene is plotted against the time in accordance with equation (2.2). Figure 2.6 illustrates a typical example of an accumulated amount of impurity in a grown crystal according to the experimental results of Toyokura et al. [2.5]. These data refer to layer crystallization tests of naphthalene crystallized on a cooled surface from a melt with the mass fraction 0.1 of benzoic acid and 0.9 of naphthalane. A detailed, quantitative explanation is given in Section 4.

For suspension crystallization, the situation is slightly different. As described in Chapter 5, attrition fragments are generated in agitated slurries when the size of the crystals and their collision velocities exceed certain values. Many secondary nuclei are created, and some of them stick on the surface of growing crystals. This sticking phenomenon of fines affects the amount of impurities present as inclusions in the crystals. For a given supersaturation, the concentration of the impurity c_{im} depends on the size of the crystals suspended in the crystallizer. The total amount I_T of impurities is given by

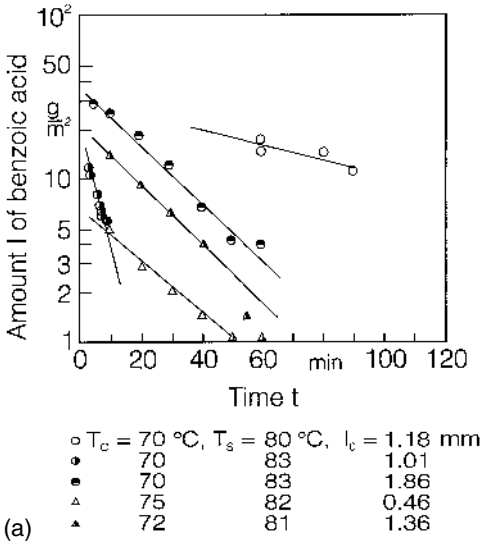

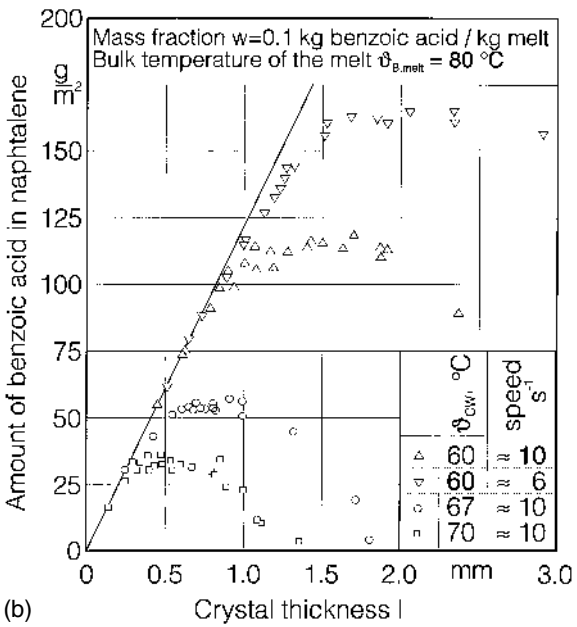

Figure 2.5. (a) Amount of benzoic acid based on the surface of the holes versus the elapsed time; (b) amount of benzoic acid in a naphthalene crystal layer versus the crystal thickness (ϑ_{cw} = temperature of cooling water).

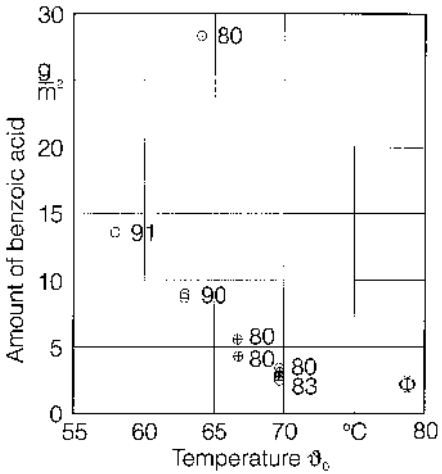

Figure 2.6. Amount of benzoic acid included in naphthalene crystals after 2 h of crystallization versus the temperature. The numbers in this figure are the bulk temperatures of the melt, and $\oplus$ and θ represent data from 10% and 5% benzoic acid melt system, respectively, Φ indicates data of blank tests.

$$I_T = \int_0^L \frac{\pi}{2} L^2 c_{\mathrm{im},L}\, dL \tag{2.3}$$

When secondary nucleation and this sticking phenomenon occur, the impurity concentration c_{im} in the crystal can be described by

$$c_{\mathrm{im}} = c_{\mathrm{im},0} \alpha L^{\beta} \tag{2.4}$$

where $c_{\mathrm{im},0}$ is the concentration that would be expected without the sticking effect for crystals of size $L < L_0$ (L_0 may be in the order of magnitude of 100 μm). In this case, beta is unity. However, for large crystals the exponent β may assume values of 2 or 3. A combination of equations (2.3) and (2.4) leads to

$$I_T = \frac{\pi}{6} L_0^3 c_{\mathrm{im},0} + \frac{\pi c_{\mathrm{im},0} \alpha}{10} (L^5 - L_0^5) \tag{2.5}$$

or

$$I_T = \frac{\pi}{6} L_0^3 c_{\mathrm{im},0} + \frac{\pi c_{\mathrm{im},0} \alpha}{12} (L^6 - L_0^6) \tag{2.6}$$

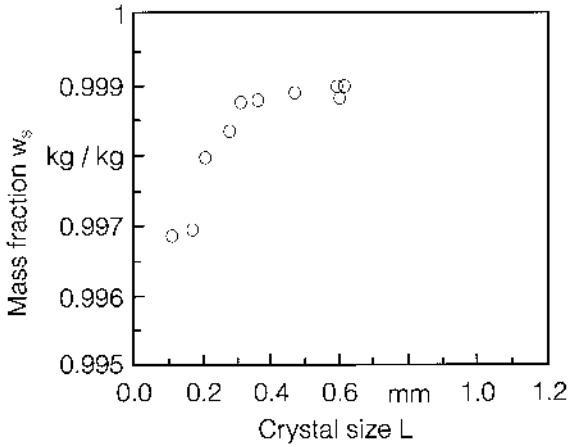

Figure 2.7. Mass fraction w_S of solid benzene crystals versus the crystal Size L. Crystals only filtered.

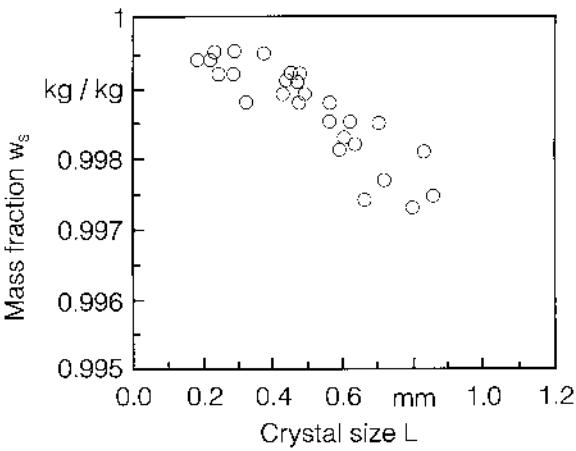

Figure 2.8. Mass fraction w_S of solid benzene crystals versus the crystal size. Residual liquid wiped off by paper.

Test data obtained by suspension crystallization of benzene from benzene-cyclohexane melt under constant supersaturation are shown in Figures 2.7 to 2.9, according to results obtained by Toyokura et al. [2.3]. The purity of benzene crystals simply filtered after crystallization increases with their size L because the volume of adjacent melt is small for large crystals (cf. Fig.

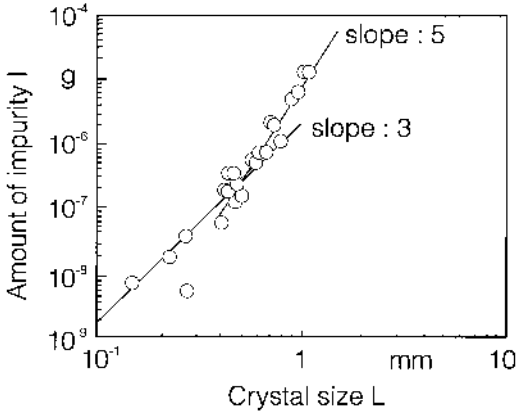

Figure 2.9. Amount of impurity (cyclohexane) versus the crystal size L.

2.7). This can be explained by Figure 9.7.7. However, when the melt on the surface of the crystals, or the occlusion impurity, is wiped off or washed with a suitable washing agent, the purity of the remaining crystals decreases with increasing crystal size (see Fig. 2.8). This can be explained by the sticking phenomena described earlier. The amount of the impurity (cyclohexane) is plotted against the size L of sieved crystals in Figure 2.9. The slope of the line is 3 for small sizes, but approaches 5 for crystals of approximately $L = 500\,\mu m$. These considerations clearly show that small crystals are favorable with respect to the sticking phenomena, but large crystals are advantageous with respect to small quantities of adjacent melt and washing efficiency (cf. Chapter 9).

2.5. Processes of Melt Crystallization

As a rule, only a part of the melt is crystallized and then separated mechanically from the crystals. In some cases, the crystals will be remelted and recrystallized to obtain a high-purity product. In all cases, it is essential to remove carefully the impure melt adjacent to the crystals by a suitable washing process. This may be sufficient when the solvent crystallizes and the impurities are dissolved in the melt or solution. This process, called *freeze crystallization*, is employed to separate water from seawater (desalination), fruit juice, or coffee extract, or to crystallize organic solvent from a liquid feed phase.

Impurities inside the crystals (inclusions) can be removed effectively by sweating, because diffusion of impurities in the solid is very slow. The

sweated melt drained from the crystals has a much higher concentration of impurities than that of the raw material.

In high-pressure crystallization, a melt is compressed and becomes supersaturated, with the result that crystals are formed. These crystals must be separated from the melt under high pressure. Subsequent depressurization initiates sweating of the crystals, which will be purified by this step in the process. Another purification process that is applied to organics, and especially to metals, is zone melting, which relies on the distribution of impurities between the liquid and solid phases. A molten zone is passed through an ingot from one end to the other. Either the heater is moved to produce a molten zone or the material is drawn slowly through a stationary heating zone.

2.5.1. Freezing

In crystallization by freezing, crystals are formed on a cooled surface or in an agitated suspension. Static or dynamic systems or fluidized beds are employed. When seawater is cooled down on a surface, an ice crust is formed and the resistance to heat transfer increases. It is therefore advisable to remove the ice by means of scrapers and to limit the supercooling ($\Delta T < 0.4\,\mathrm{K}$), because high heat flux densities lead to high supersaturation and high growth rates, with the consequence of impure crystals.

Another possibility is direct contact of the brine and a coolant (e.g., liquid propane or butane). A flow diagram for such a process is shown in Figure 2.10 [2.6]. The supercooling of the brine is less than 0.1 K. Crystals suspended in the crystallizer are transported to the bottom of the washing

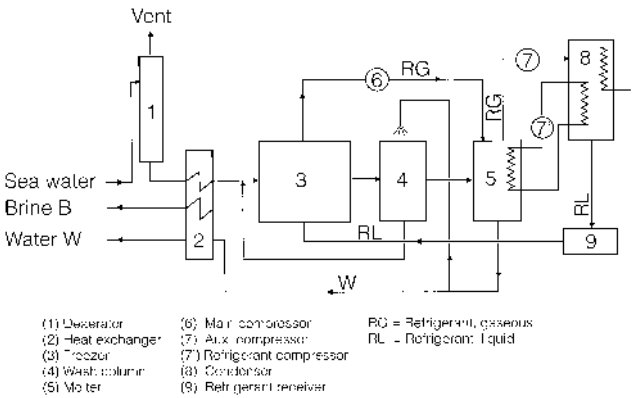

Figure 2.10. Schematic diagram of direct-contact freezing process.

column, in which the ice is floated. The brine is removed through a wire mesh located in the center of the column. The ice is chopped and melted. Most of the molten water is withdrawn as product; part of it is returned to the top of the washing column and flows over the ice to be washed. Such a countercurrent flow is very effective for purification because the final product is washed with clean water. A problem may arise when the feed pipe for the coolant is located in the brine because an ice crust will be formed. The liquid coolant should therefore be fed onto the surface of the brine in the crystallizer and mixed by rigorous agitation or forced circulation by means of a pump. A submerged nozzle developed for the desalination process shown in Figure 2.11 employs liquid natural gas as coolant.

Desalination of seawater can also be carried out by evaporative crystallization under vacuum or by vacuum freezing. By this means, scaling of the heat transfer area can be avoided. The mass fraction of seawater is approximately $w^* = 0.035\,\mathrm{kg\,salt/kg}$ brine, and 78% by mass is sodium chloride. In Figure 2.12, the melting line of the system NaCl–H_2O is shown, and in Figure 2.13, the vapor pressure is plotted against the temperature for this system. The diagrams give an approximate picture of the behavior of seawater. According to these diagrams, ice is formed at a temperature of $-1.7^\circ\mathrm{C}$ under a pressure of 512 Pa when the brine has a mass fraction of $w^* = 0.029$.

When processing natural juice, ice is the by-product and the concentrated liquid juice is the objective of the process. In some systems, the water will be frozen on the tubes of a heat exchanger. The solid crust is composed primarily of ice, but the outer layer of the crust may contain some juice ingredients that possess color and flavor. Therefore, the ice layer must be removed from the juice bath and partially melted in the atmosphere at an elevated temperature. The ice removed is colorless and tasteless.

As well as this type of batch apparatus, heat exchangers with scrapers are employed. The scrapers, made of bronze or plastic, may be in a vertical or horizontal position (cf. Fig. 2.14) and pressed against the cooling surface by means of springs. The maximum overall heat transfer coefficient for aqueous systems is approximately $1\,\mathrm{kW/m^2\,K}$ when the scraper speed is $s \approx 0.5\,\mathrm{s^{-1}}$ and the velocity of the ice slurry lies in the range 0.05–0.3 m/s [2.7].

2.5.2. High-pressure crystallization

When the solubility decreases appreciably with increasing pressure, high-pressure crystallization may be a suitable separation process. A typical high-pressure crystallization plant is composed of three major parts: the oil-pressurizing unit, the crystallization cell, and the separation cell (see Fig. 2.15

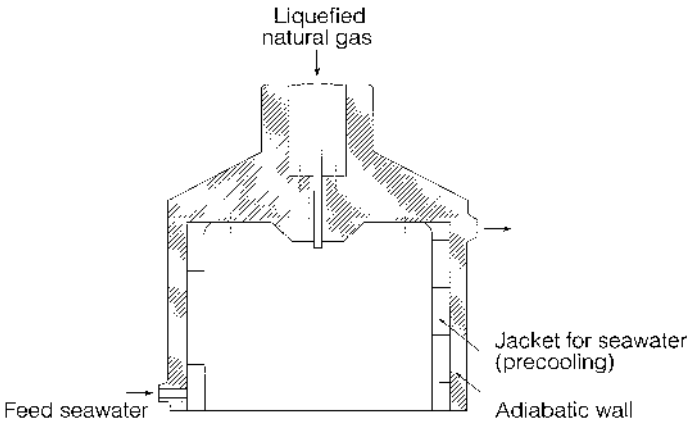

Figure 2.11. Submerged nozzle for the distribution of natural gas.

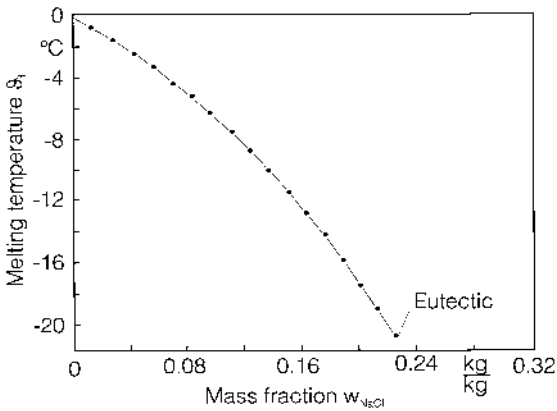

Figure 2.12. Melting temperature versus the mass fraction w_{NaCl} of the system NaCl–H_2O.

[2.8]). Raw material is fed into the crystallizer through the value V1 and compressed by the piston of a pump driven by the oil-pressure unit. The pressure is increased stepwise to approximately 20 MPa, a shown in Figure 2.16. After each pressure rise, the temperature suddenly increases (several degrees), depending on the heat of compression. After some time, the temperature of the pressurized melt again assumes the temperature of the thermostat bath. The pressure gauge also shows a sudden rise and then a decrease, as the heat of compression is removed by the thermostat bath.

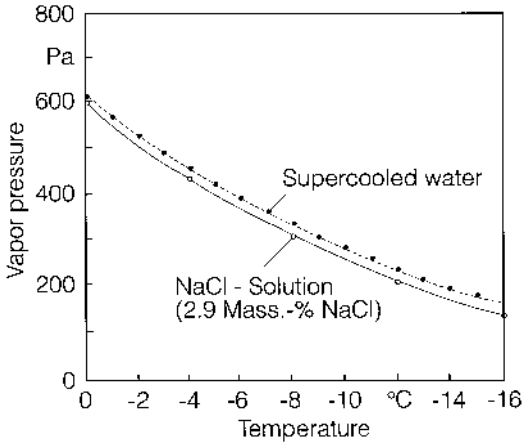

Figure 2.13. Vapor pressure of H_2O and NaCl–H_2O versus the temperature.

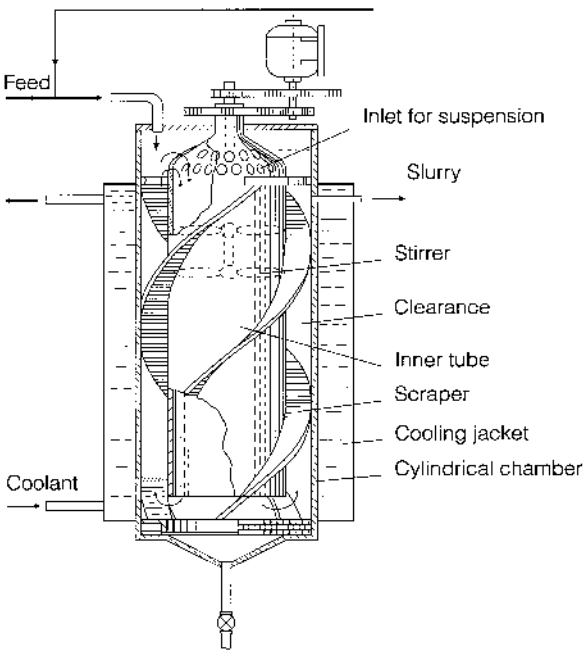

Figure 2.14. Heat exchanger with scrapers for coarse crystals.

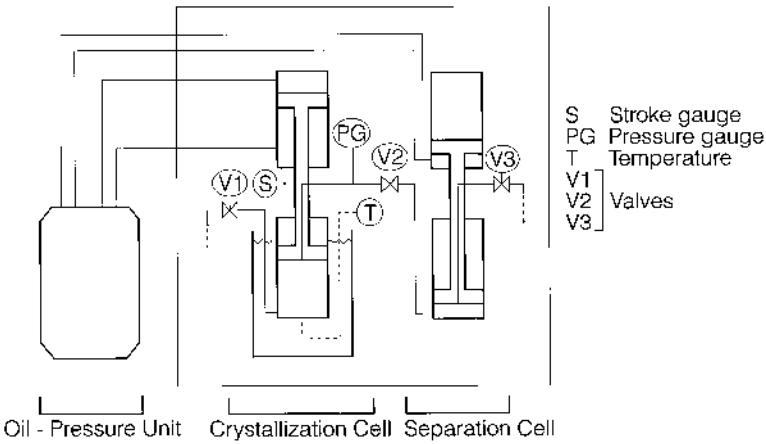

Figure 2.15. Schematic diagram of an experimental high-pressure apparatus. (From Ref. [2.8].)

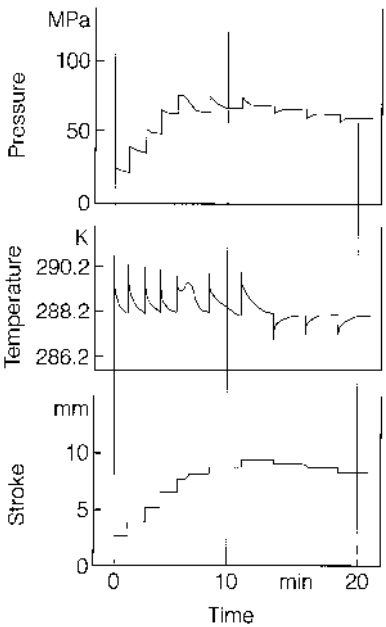

Figure 2.16. Example of changes of pressure, temperature, and stroke (benzene 98.59 mol% at 288.2 K).

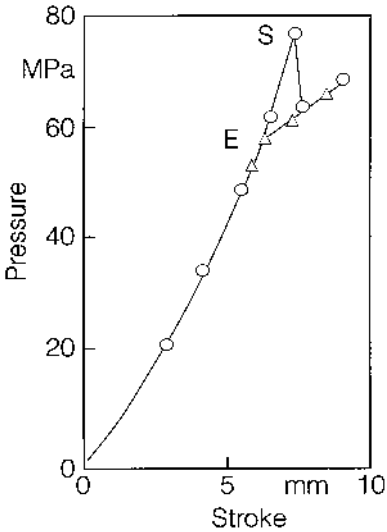

Figure 2.17. Relation between pressure and stroke (benzene 89.59 mol% at 288.2 K).

When nucleation occurs in the crystallizer, the heat of crystallization changes the direction of the lines shown in Figure 2.16. In the supersaturated melt, the nuclei formed grow to the desired product size. The pressure is then reduced stepwise to partially melt the crystals.

As a result of this sweating process, the crystals are purified. In Figure 2.17, the pressure is plotted against the displacement of the stroke. When nucleation occurs, the pressure decreases despite a small displacement of the piston, and when the pressure of the slurry is released, the pressure decreases back along the line obtained for the compression process. Point E in Figure 2.17 corresponds to the equilibrium at this temperature, at which the melt is saturated. The excess pressure range ES represents the metastable zone. For depressurization, the value V2 depicted in Figure 2.15 is gradually opened, and the remaining melt is released into the separation cell.

The advantage of high-pressure crystallization is that the pressure and, therefore, the supersaturation are constant throughout the entire crystallizer volume. In cooling and evaporative crystallizers, differences in temperature and supersaturation always exist and often lead to heterogeneous nucleation and encrustation (cf. Chapter 9).

If the melt is completely free of foreign particles, nuclei generated only by homogeneous primary nucleation (cf. Chapter 2). However, in most cases, the melt contains traces of small solid particles, and heterogeneous nuclei

will be formed. The maximum supersaturation determines the number of nuclei, whereas the average supersaturation during the growth period controls the mean growth rate and mean crystal size.

The energy consumption in high-pressure crystallization is low because the energy needed to compress the melt is low because of its small compressibility. The resulting low operating costs must be balanced against the greater investment costs for the high-pressure equipment.

Another system that may be crystallized under high pressure is mandelic acid–water, investigated by Nishiguchi [2.9]. Because the heat of crystallization of this system is lower than for benzene–cyclohexane, the irregular points depicted in Figure 2.17 are not observed.

2.5.3. Zone melting

Zone melting is described in detail by Pfann [2.10], Schildknecht [2.11], and Zief and Wilcox [2.12]. The main purpose of zone melting is the purification of organic or inorganic materials, and the purity of the final product depends greatly on the distribution coefficient K. Because the purification efficiency may be limited by this coefficient, zone melting of an ingot is repeated to obtain the final product. The purification efficiency can be described by the ratio c_S/c_L (i.e., the solid-phase concentration c_S and the solution composition c_L of the initial charge). For the case of perfect mixing in the liquid phase, negligible diffusion in the solid phase, and a constant distribution coefficient, the ratio c_S/c_L can be described for a single pass by

$$\frac{c_S}{c_L} = 1 - (1 - K)\exp\left(-K\frac{x}{l}\right) \tag{2.7}$$

The position of the melting zone x is measured from the leading edge of the ingot of length L; l is the length of the melting zone. For an infinite number of passes, the ultimate purification efficiency is given by

$$\frac{c_S}{c_L} = \frac{BL\exp(Bx)}{\exp(BL) - 1} \tag{2.8}$$

where B is a reciprocal length:

$$\frac{Bl}{\exp(Bl) - 1} = K \tag{2.9}$$

Ingot length/zone length ratios are often between 5 and 10. The zone travel velocity depends greatly on the thermal conductivity of the ingot material, and because the thermal conductivities of organics are low, the traveling rates are also low, of the order of magnitude of 10^{-6}–10^{-5} m/s. For metals, and especially for semiconductors, the travel rate and the rate of

advance of the crystal–melt interphase may be one order of magnitude larger than the values given above. For further details, see Ref. [2.12].

2.5.4. Special processes

There is a wide variety of technical processes employing melt crystallization (e.g., energy storage units) and the solidification of various inorganic and organic material. During the night, electrical energy can be utilized to freeze water, and the stored ice is then used for air conditioning during the day. Crystallization is initiated by seed crystals to avoid high supersaturation and the growth of dendritic crystals. The low temperature of 273 K can be a disadvantage of the water–ice system; and sometimes sodium acetate ($NaCH_3COO{\cdot}3H_2O$) is used as the storage agent, because it has a melting point of approximately 330 K. Traces of $Na_3PO_4{\cdot}12H_2O$ are very effective for the initiation and acceleration of nucleation (see Ref. [2.13]). Figure 2.18 illustrates the effect of seeding with this material.

Further examples of solidification are the melt crystallization of sodium and potassium hydroxide. The equipment used for these processes is described in Chapter 8. Common among industrial application is the crystallization of $NaOH{\cdot}3.5H_2O$, which contains small amounts of potassium hydroxide and sodium chloride. A typical by-product of the desalination of seawater can have the following composition: 34–40 mass% NaOH, 2–8.5 mass% KOH, and up to 1.1 mass% NaCl. An example of a pilot plant is depicted in Figure 2.19 (see Ref. [2.14]). Warm caustic solution is fed to the

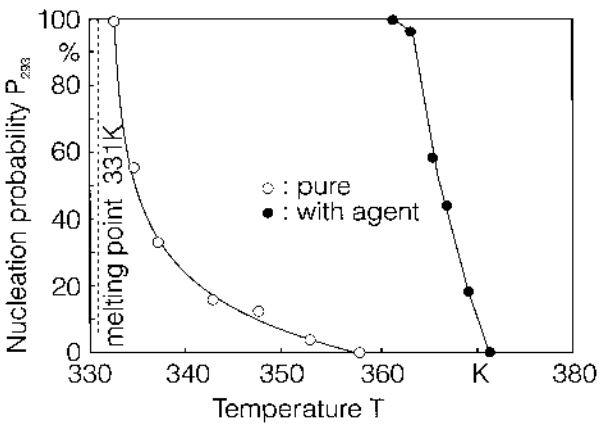

Figure 2.18. Relationship between P_{293} (nucleation probability at 293 K) and heating temperature T.

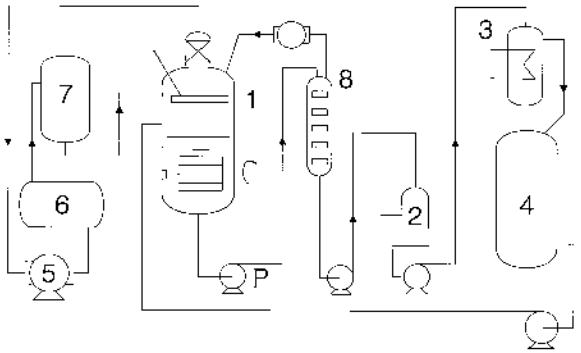

Figure 2.19. Flowsheet of pilot plant for the melt crystallization of metal hydroxides.

crystallizer and caused to run as a falling film down the wall to avoid scaling of the cold surface.

3. SUSPENSION CRYSTALLIZATION (INDIRECT HEAT TRANSFER)

As has been shown in Sec. 2, the main advantage of suspension crystallization is the high specific interfacial area between the crystals and the melt. As a consequence of the huge crystal surface area, the growth rate may be low, which aids in obtaining a certain production rate. Due to this fact, the effective distribution coefficient is favorable. In suspension crystallizers, high production rates of a very pure product can be achieved. The main disadvantage is that solid handling is necessary. When using cooling crystallizers, it may happen that the cooling surface is affected adversely by severe encrustation. This depends on heterogeneous nucleation on the wall and on the growth rate of the crust, which is favored by high heat flux densities. Frequently, the difference in the densities of the crystals and the melt is very small, and in this case, it is very easy to suspend the crystals on the basis of the information given in Chapter 8. However, in the case of countercurrent-flow crystallization columns, there may be a severe problem because the countercurrent depends on this density difference. Therefore,

the throughput of such columns may be very low when this difference is small.

3.1. Fundamentals

In suspension crystallizers, nuclei have to be formed which then grow to the required product size. The fundamentals or nucleation have been described in Chapter 2. For large product crystals, with sizes above 100 μm, it is assumed that secondary nucleation is dominant. This may also be true for small crystals which have a needlelike or platelike shape. At higher supersaturation levels, foreign particles can contribute to nucleation through the mechanism of heterogeneous primary nucleation. The size of the product crystals is proportional to the growth rate and growth time. As mentioned earlier, the growth rate may be limited by the mass transfer, the heat transfer to the crystal, or by both mechanisms. The local supersaturation depends on the temperature profile in the crystallizer. The temperatures are influenced, on the one hand, by the heating or cooling surfaces and the corresponding heat transfer coefficients and, on the other hand, by the fluid dynamics. The fluid dynamics in a crystallizer must be selected such that the crystals are suspended in the crystallizer and that sufficient mixing takes place.

3.2. Selection of the Process

The selection of the process depends on the phase equilibria of the system under discussion. It was mentioned earlier that in eutectic systems, a one-step crystallizer may be sufficient to obtain a product with a high purity. The process can be carried out in a stirred vessel or in a fluidized bed. However, for noneutectic systems, a multistep apparatus is necessary. This can be a cascade of single-step units or a horizontal or vertical crystallization column. As a rule, the crystallization process consists of three steps: the crystallization, then the mechanical separation by filtration or centrifugation, and, finally, a purification step. Quite often, separation and purification are performed simultaneously, but for the purification, it is necessary to replace the mother liquor by a pure melt.

Generally speaking, crystallizers can be operated batchwise or continuously. The main advantage of column crystallizers is that they can be operated continuously. However, the small difference in the densities between the crystals and the melt may present a problem. As has been pointed out in Chapter 2, it is very important to avoid excessive nucleation. This means that supersaturation has to be limited, often by seeding of the melt, which

can be carried out continuously in continuously operated crystallizers. Multistage operation is a useful technique for achieving high product yields and purities without recirculation of the melt. For eutectic systems, it is possible to obtain a very pure product irrespective of the operating temperature. However, in the case of industrial crystallizers, the mother liquor frequently forms inclusions in the crystals. In some industrial melt crystallization processes, crystals precipitated at the end of the recovery section in the crystallizer are moved in the direction opposite to the now uncrystallized melt (e.g., in the Brodie crystallizer and the TSK system).

3.3. Crystallizers

In all cases, the melt in the crystallizer must be supercooled or supercompressed in order to generate supersaturation and to initiate nucleation and crystal growth. For single-step crystallization, stirred vessels and fluidized beds are often employed. Certain problems may arise if a multistep crystallization is necessary because of the phase equilibria in the system. A simple solution might be a countercurrent column, which is shown in Figure 3.1. In such a column, the melt moves upward to the top countercurrent to the crystals which fall through the melt, which is produced in the melting section by a heating unit. Crystals are produced by means of a coolant in the freezing section. Figure 3.1 shows a center-fed column crystallizer in which the feed is introduced at the center of the column. The purification section is divided into the stripping section, above the feed location, and the enrichment section, below the feed. Design, operation, and scale-up of such column crystallizers can be very difficult, owing to a minute difference in the densities of the crystals and the melt and to circulation of the slurry within the column, which adversely affects the countercurrent flow of the two phases. A spiral type of conveyor or an equivalent system can be employed to avoid this circulation in the column and to establish a countercurrent flow.

Both center-fed column crystallizers and end-fed column crystallizers are used; see Figure 3.2, which shows the Brodie crystallization system. The crude melt is fed in at the center of the crystallizer and the crystals are moved in the reverse direction, against the flow of the melt. During the downward flow of the melt from the feed point, the product component in the melt is recovered by the growth of suspended crystals, and the crystals are conveyed to the refining section. The crystallizer is cooled by means of the heat exchanger located outside the wall. The suspended crystals are transported by the rotating screw conveyor through the refiner and then into the purifying section, where they are purified by countercurrent contact with the reflux flow of the melt produced from purified crystals. A fixed

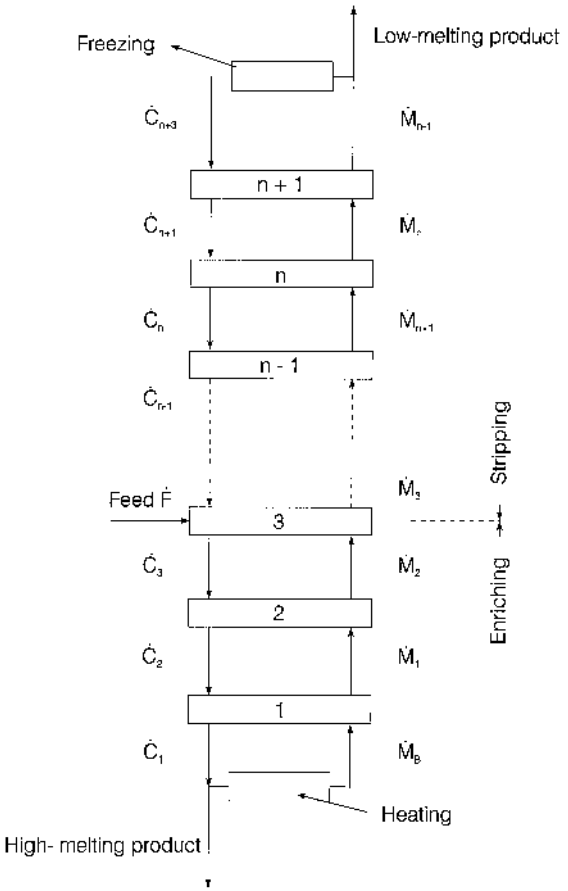

Figure 3.1. Countercurrent crystallization column.

fraction of the melt is withdrawn as product from the end of the purifier. The operation of such crystallizers is complicated, and operational conditions should be selected carefully to prevent scaling.

The TSK 4 C crystallizer (countercurrent continuous cooling) shown in Figure 3.3 is similar to the Brodie apparatus. In this crystallizer, the refining and recovery sections are replaced by multistage crystallizers equipped with scrapers, in which the behavior of the crystals and the melt can easily be controlled. In these crystallizers, crystals and melt are circulated by the double propeller and a proportion of the crystals is transported to the adjacent crystallizer as condensed slurry coming from the cyclone. The melt overflow from the cyclone returns to the original crystallizer, from

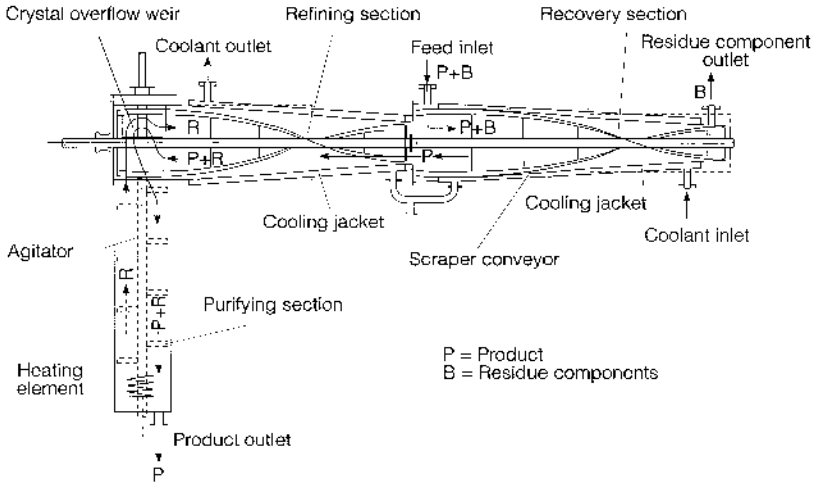

Figure 3.2. The Brodie purifier.

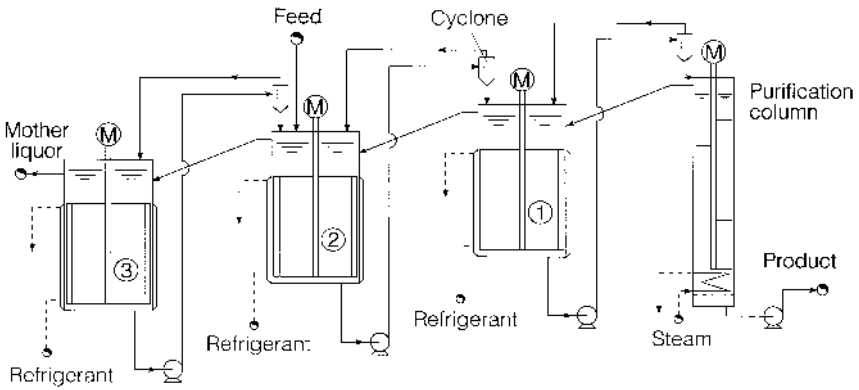

Figure 3.3. Countercurrent multistage cooling crystallizer system (crystallizers 1, 2, and 3).

which the slurry is withdrawn. Note that the slurry between the crystallizer and the purifier and between the crystallizers is conveyed by hydraulic transportation. For details, see Ref. 3.1.

The BMC column (back-mixing crystallizer) shown in Figures 3.4a and 3.4b comprises crystallization, separation, and purification sections. The agitator is rotated to keep the slurry mobile and to scrape the crystal crust from the surface of the cooled wall. Fractional crystallization of non-eutectic systems is also carried out in this type of crystallizer [3.2]. The TNO

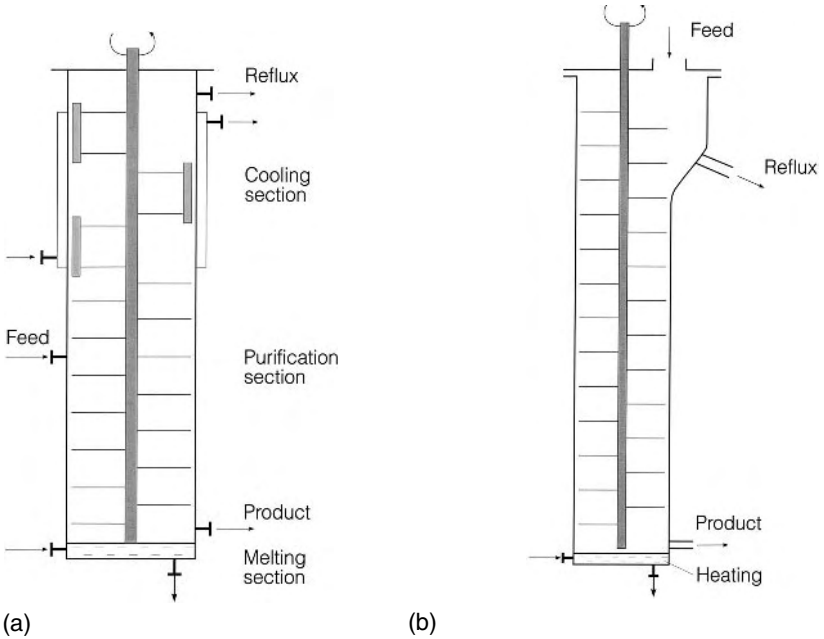

Figure 3.4. (a) Schematic diagram of a back-mixing crystallizer; (b) schematic diagram of a back-mixing column crystallizer (solid feed type).

crystallization process is characterized by concurrent flow of the solid and liquid phase. The washing section is equipped with multifilter tubes.

The KCP crystallizer uses a slightly different procedure for purification of the crystals, as shown in Figure 3.5a. In this apparatus, crystals grown in the crystallizer are separated from the slurry by the filter and transported to the bottom of the column. In the column, two vertical screws for the transport of the crystals rotate in opposite directions, and crystals fed into the column are pushed toward the top, where they are melted by the heater (see Fig. 3.5b). Most of the melt is withdrawn as product, but part of it is returned to the column and flows down over the surface of the crystals. During this process fines are melted and large crystals grow to the required product size. The falling melt collects the impurities on the crystals coming from the crystallizer. The melt withdrawn at the bottom is dirty and colored as a consequence of taking up most of the impurities.

The high-pressure crystallizer shown in Figure 3.6 is composed of the precrystallizer and the high-pressure vessel and is described in detail by Ideno et al. [3.3]. In the precrystallizer, the melt is cooled down to produce supersaturation. When the slurry is moved to the high-pressure vessel and

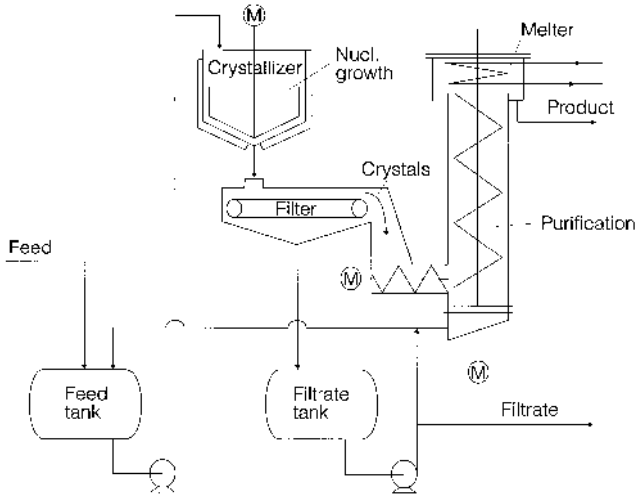

Figure 3.5. (a) Dimension of the main section of the KCP.

compressed to the desired pressure, crystals fed in with the crude melt grow rapidly, and the composition of the melt assumes equilibrium concentration. Uncrystallized melt is removed through the filter located at the outlet of the crystallizer, and the pressure on the crystal bed is reduced to atmospheric pressure. The crystals can be sweated to reduce the impurity of the crystals. High-pressure crystallizers are operated batchwise, and the entire operation, which is composed of feeding of crude melt, crystallization, filtration, and the removal of purified product, is carried out within a few minutes.

3.4. Design and Operation of Crystallizers

As discussed in Chapter 7, the main objective of a crystallizer is to produce crystals with a certain crystal size distribution, a desired crystal shape, and a certain product purity. The purity of the final crystals depends on the crystallization process as well as on the separation and purification steps. So-called separation columns are often employed to achieve an efficient crystal–liquid separation. Two types of separation columns can be distinguished: nonpacked separation columns, usually based on gravity transport of the crystals, and packed separation columns. According to Arkenbout et al. [3.4], the capacity of a nonpacked column can be estimated using the equations for hindered settling (cf. Chapter 8). The capacity of a nonpacked

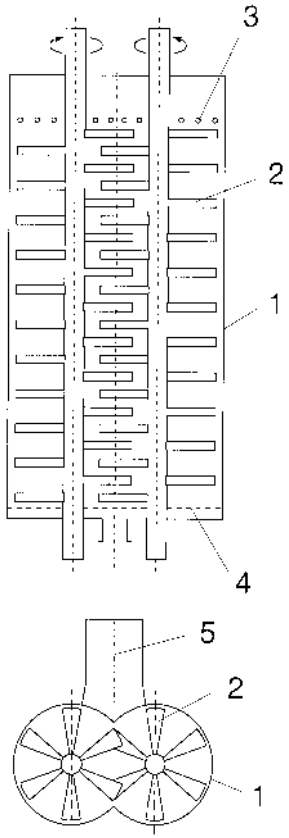

(b)

Figure 3.5. (b) Schematic diagram of a commercial KCP.

column is usually less than $1000\,kg/m^2\,h$, assuming that the crystals are spheres with diameters of at least $500\,\mu m$. For crystals of only $100\,\mu m$, a capacity of $5000\,kg$ crystals$/m^2\,h$ would appear to be feasible. The advantage of the packed-bed columns is that fluctuations in the percentage of crystals in the suspension and in the particle size distribution are easier to compensate for.

When the mother liquor forms inclusions in cylindrical holes in the crystals and the composition of the melt at the inner end of the holes corresponds to the equilibrium concentration c^* at the melt temperature, the concentration of impurity c_{im} at a distance l from the surface of crystal can be expressed by [2.4]

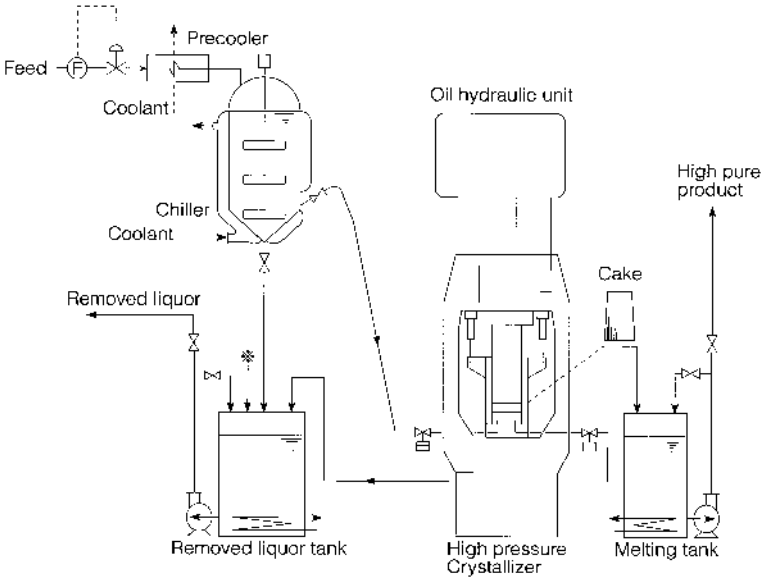

Figure 3.6. High-pressure crystallizer.

$$c_{\mathrm{im}}(l) = c^*_{\mathrm{im}}(T_C) + (c_{\mathrm{im},B} - c^*_{\mathrm{im}})\frac{l}{l_0} \tag{3.1}$$

Here, $c^*_{\mathrm{im}}(T_C)$ is the equilibrium concentration at the crystallization temperature and $c_{\mathrm{im},B}$ is the concentration of the impurity in the melt in the bulk of the purifier. Equation (3.1) is valid under the assumption that the concentration of impurity of the melt in a hole is linearly distributed. Equation (3.1) is derived from equation (2.2) for the correlation between the total amount of impurity per unit surface area of the crystals and the purification time. The terms $l_0 K_1$ and D_{AB}/l_0^2 in equation (2.2) depend on the conditions under which the crystallization and purification processes are performed. The purification time t, calculated for the desired purity of the crystals, can be used to estimate the required volume of the purifier.

4. DIRECT CONTACT COOLING CRYSTALLIZERS

In melt crystallization systems with $C^*/C_C > 0.8$, crystal growth rates G are mostly controlled by heat transfer. The rate G_h depends on the heat transfer coefficient h, the heat of crystallization Δh_{CL},

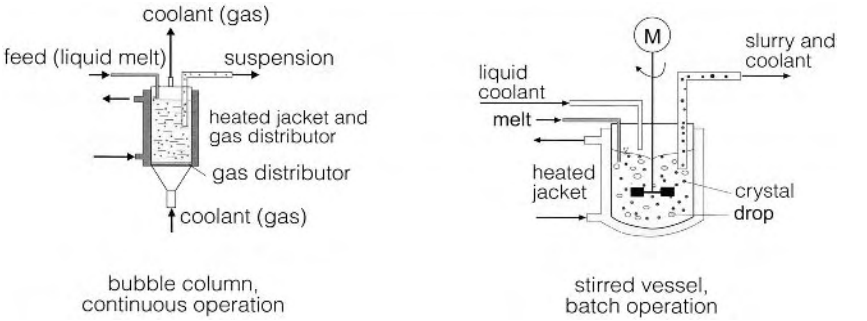

Figure 4.1. Thermostated bubble columns and a drop column for the use as a direct contact crystallizer.

$$G_h = \frac{2h\Delta T}{\rho_C \Delta h_{\mathrm{CL}}} = \frac{2hRT^2}{\rho_C \Delta h_{\mathrm{CL}}^2}\sigma = k_h \sigma \tag{4.1}$$

and the relative supersaturation σ,

$$\sigma \equiv \left(\frac{\Delta h_{\mathrm{CL}}}{RT}\right)\left(\frac{\Delta T}{T}\right) \tag{4.2}$$

With respect to economical temperature differences ΔT ($\Delta T > \Delta T_{\mathrm{met}}$), heterogeneous nucleation and growth of incrustations layers take place on the heat transfer surfaces. As a consequence, heat transfer is reduced by fouling (see Chapter 9) and the productivity $\dot{m}_V$ (in kg/m^3 s) decreases. This is the reason for the application of layer crystallization; see Chapter 14. However, the drawback of incrustation can be avoided in a direct contact cooling crystallizer (DCCC) by the introduction of a coolant (gas, eventually under pressure, liquefied gas or liquid) into the melt. In Figure 4.1, simple bubble columns are depicted. A sieve plate (or tubes with holes) can be used in order to distribute the coolant and to produce bubbles or drops which rise in the melt. The incrustation of the sieve plate and the walls can be avoided by heating of these surfaces slightly above the saturation temperature [4.1]. If the density of the coolant is higher than the density of the melt, a stirred vessel can be used instead of a column.

4.1. Experimental Results

Direct contact cooling crystallizers have been thoroughly investigated by Bartosch [4.1] for the systems *p*-/*o*-xylene, caprolactam/water, and dodecanol/decanol. The coolants have been chosen in such a way that no or nearly

Table 4.1. Recommended Liquid Coolants for the Direct Contact Cooling Crystallization Process

System	Possible liquid coolant
Dodecanol/decanol	Water, polyhydric alcohols
Caprolactam/water	Alkanes, chlorofluorcarbons
p-/*o*-Xylene	Water, polyhydric alcohols

Source: Data from Ref. [4.1].

no solubility of this substance in the melt and vice versa takes place. In Table 4.1, coolants for the three systems are given. Bartosch [4.1] describes general rules for the choice of coolants and gives recommendations for the systems named above. However, before using a direct coolant, miscibility and interactions between melt and coolant should be investigated in more detail. The maximal supersaturation occurs at the surface of the bubbles or drops where the temperature T_{cool} is lower than the temperature T_{melt} of the melt (cf. Fig. 4.2).

$$\sigma_{\max} = \frac{\Delta H_{\text{CL}}}{\Re T}\frac{T_{\text{melt}} - T}{T_{\text{melt}}} = \frac{\Delta h_{\text{CL}}}{RT}\frac{T_{\text{melt}} - T}{T_{\text{melt}}} \tag{4.3}$$

The optimal supersaturation σ_{opt} can easily be maintained by the choice of the coolant temperature T. Principally speaking, the growth rate G can be controlled by diffusion (G_{dif}), integration ($G_{\text{int}} = G_{\text{BCF}} + G_{\text{B+S}} + G_{\text{PN}}$), or heat transfer G_h; see Chap. 3:

$$G = \left(\frac{1}{G_{\text{int}}} + \frac{1}{G_{\text{dif}}} + \frac{1}{G_h}\right)^{-1} = \left(\frac{1}{G_{\text{BCF}} + G_{\text{B+S}} + G_{\text{PN}}} + \frac{1}{G_{\text{dif}}} + \frac{1}{G_h}\right)^{-1} \tag{4.4}$$

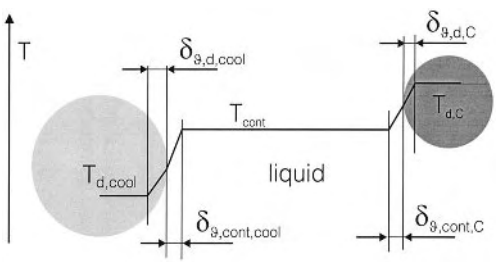

Figure 4.2. Temperature profile between dispersed coolant particle and a crystal in the liquid phase.

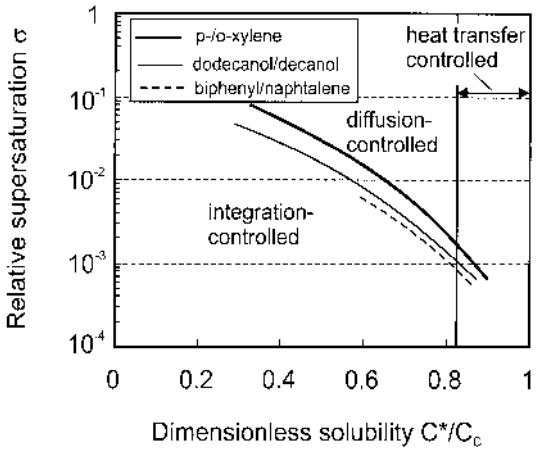

Figure 4.3. Dominant growth mechanisms in melt crystallization as a function of the dimensionless solubility and supersaturation for three different systems.

In Figure 4.3, information on the controlling step is given. Heat transfer is decisive for systems with $C^*/C_C > 0.8$. The exact value depends on the physical properties of the systems (η_L, D_{AB}).

De Goede and van Rosmalen [4.2] developed a model to calculate the contribution of heat and mass transfer resistance to the overall growth resistance. Their considerations are based on the growth-rate equations, an ideal thermodynamic phase behavior (van't Hoff), and the analogy between heat and mass transfer [cf. Equation (3.3.27)]. They assume that the growth rate limited by mass transfer can be described by

$$G = 2k_d \frac{C^*}{C_C}\sigma \tag{4.5}$$

with

$$\frac{1}{k_M} = \frac{1}{k_d}\frac{\rho_S}{\tilde{M}_S}\frac{M_L}{\rho_L}\frac{(1-x_B)}{\left\{\left[1-\left(\frac{G}{k_d}\frac{\rho_S}{\tilde{M}_S}\frac{\tilde{M}_L}{\rho_L}\right)\right]\right\}^{-1}}\left(\frac{1+\sigma}{x_B}\right) \tag{4.6}$$

as the reciprocal value of the resistance to mass transfer [4.3]. The reciprocal value of the resistance to heat transfer is defined as [4.3]

$$\frac{1}{k_h} = \frac{1}{h}\frac{\rho_S}{\tilde{M}_S}\frac{\Delta H_{CL}^2}{\Re}\left[\frac{1}{T_M} - \frac{\Re}{\Delta H_{CL}}\ln\left(\frac{x_B}{1+\sigma}\right)\right] \tag{4.7}$$

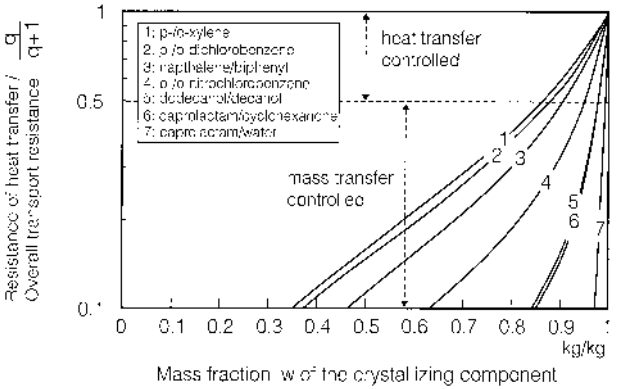

Figure 4.4. Development of heat transfer resistance q to overall transport resistance $q+1$ with the concentration of the crystallizing component for the growth of several organic systems according to a model of de Goede and van Rosmalen [4.2].

A combination of equations (4.6), (4.7), and (3.3.27) leads to the following ratio q of the kinetic coefficients k_h and k_M:

$$q = \frac{1/k_h}{1/k_M} = \frac{1}{Le^{2/3}} \frac{\Re}{c_{P,L}\tilde{M}_L} \frac{x_B}{1-x_B} \left(\frac{\Delta H_{CL}}{\Re T_f} - \ln x_B \right)^2 \tag{4.8}$$

In this equation, q is the ratio of the resistance of heat to mass transfer. In Figure 4.4, the ratio $q/(q+1)$ (e.g., the resistance of heat transfer based on the overall resistance to mass transport) is plotted against the mass fraction w of the crystallizing component for seven different systems. It can be seen that the exact concentration where the change from mass transfer to heat transfer limitation takes place is in the range $0.85 < w < 1$ but depends on the system under discussion.

In Figure 4.5, the growth rate G is plotted against the supersaturation for the system *p*-xylene/*m*-xylene in the range $0.45 < C^*/C_C < 0.86$. According to the BCF and especially the PN mechanism, the growth rate increases strongly with supersaturation. For $C^*/C_C > 0.9$, growth is controlled by heat transfer for supersaturations σ above 2×10^{-3}. These growth rates calculated from equations presented in Chapter 3 have been confirmed by experimental results.

De Goede and van Rosmalen [4.4] have measured growth rates of *p*-/*m*-xylene (Fig. 4.5) and Schreiner [4.5] determined the growth behavior of the system biphenyl/naphtalene (Fig. 4.6).

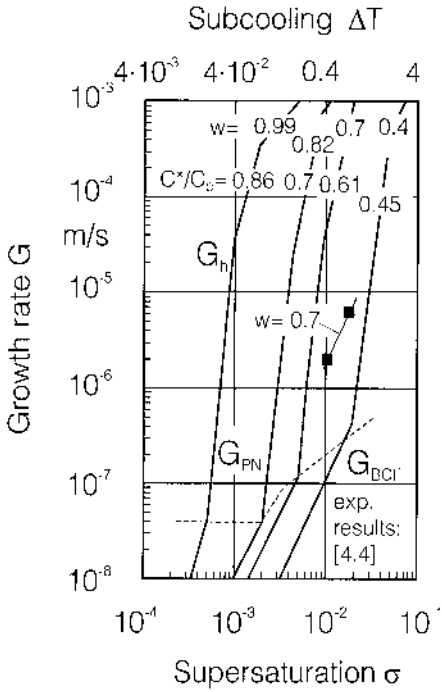

Figure 4.5. Calculated crystal growth rates of the system *p*-/*m*-xylene taking into consideration integration (BCF + PN), diffusion, and heat transfer controlled growth; data points: experimental results from literature.

Results of growth-rate calculations are depicted in Figure 4.5, where the growth rates are plotted against the relative supersaturation σ. For a given supersaturation σ (or subcooling ΔT), the growth rate increases with increasing solubility C^*/C_C. The rates of the system *p*-xylene/*m*-xylene can be described with the polynuclear model ($G = G_{PN}$), whereas the rate of biphenyl/naphthalene are controlled by integration and diffusion ($C^*/C_C < 0.95$) and heat transfer for $C^*/C_C > 0.95$ and supersaturations σ above 5×10^{-4}. The change of the growth mechanism depends also on the operating conditions (mean specific power input $\bar{\varepsilon}$ and particle size L) and has to be considered. These data and other results in the literature not reported here [4.6, 4.7] confirm the validity of models presented in Chapter 3. With respect to crystallization kinetics, it is not necessary to distinguish between solution crystallization and crystallization from the melt carried out by indirect or direct contact cooling. However, it is decisive to apply the actual supersaturation. Especially, when using direct cooling

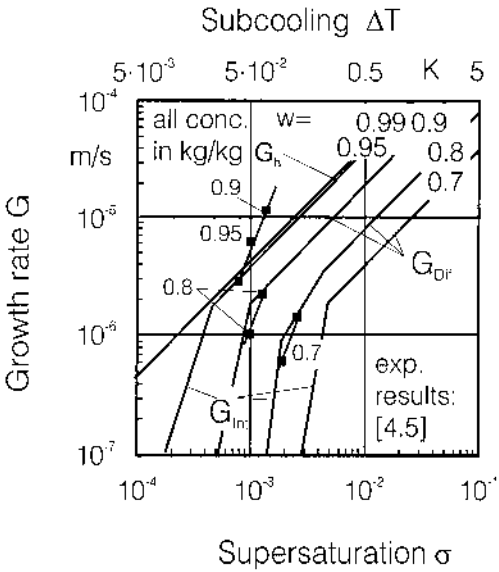

Figure 4.6. Comparison between calculated and measured growth rates for the system biphenyl/naphthalene.

techniques, it is very difficult to measure the actual supersaturation because the temperature between the dispersed coolant and the crystal changes with the rise of the coolant in the crystallizer.

Because the median crystal size depends on the kinetic parameters B_0 and G, it is necessary to limit B_0 and G, and therefore the relative supersaturation in order to match the desired mean size and crystal purity (cf. Chapter 7). This has been confirmed by Bartosch [4.1], who carried out mixed suspension, mixed product removal (MSMPR) experiments in a bubble column in which dodecanol was crystallized from dodecanol/decanol mixtures. In Figure 4.7, the nucleation rate B_0 and the growth rate G are plotted against the mean residence time τ. In Figure 4.8, the median crystal size is shown as a function of the residence time and the feed concentration. As can be seen, the kinetic data and the size are close to the results of inorganic systems of solution crystallization presented and explained in more detail in the Chapters 2–4. With $B_0/\varphi_T = 3 \times 10^8\,\mathrm{m^{-3}\,s^{-1}}$, $G = 2 \times 10^{-8}\mathrm{m/s}$, and a residence time $\tau = 3000\,\mathrm{s}$, a median crystal size $L_{50} \approx 250\,\mu\mathrm{m}$ has been obtained. These experimental results agree very well with data which can be read from Figure 4.2.2a.

The metastable supersaturation σ_{met} has been determined in the range $0.1 < \sigma_{\mathrm{met}} < 0.25$. The origin of nuclei is not very clear. It is assumed that

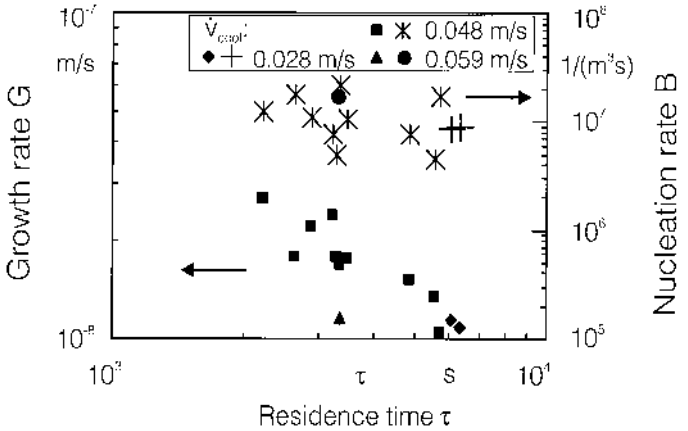

Figure 4.7. The development of nucleation and growth rates with residence time for MSMPR experiments carried out in a DCC crystallizer (system dodecanol/decanol and the direct coolant air).

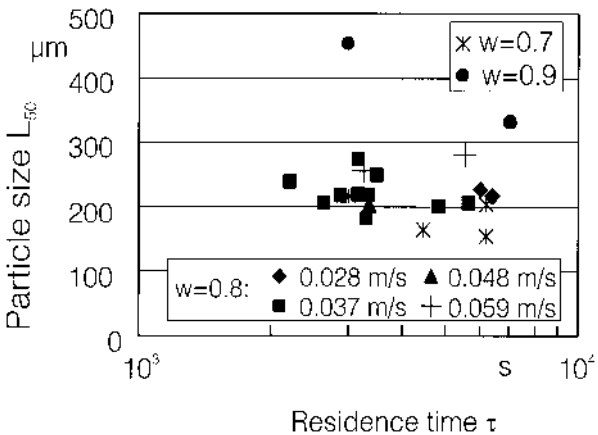

Figure 4.8. Median particle size as function of the residence time. Parameters: superficial velocity of the coolant and feed concentration, system dodecanol/decanol, MSMPR crystallizer.

secondary nucleation is dominant because the rates of primary nucleation are very low for $\sigma \approx 0.1$. Attrition may play a role; however, the models presented in Chapter 5 cannot be applied because the dodecanol crystals with a temperature near the melting point are very soft and do not show a brittle behavior.

The experiments have also shown that the heat exchange between the coolant and melt is very fast. It can be assumed that crystallization takes place only in the inlet zone of the coolant. Therefore, the MSMPR theory should only be applied with care to describe crystallization experiments with direct cooling. If the small volume of the crystallizer where the complete heat exchange and crystallization mainly takes place is used for the calculation of crystallization kinetics, nucleation rates are in the range of 10^{10} nuclei/$m^{-3}\,s^{-1}$) and growth rates are in the range of 10^{-6} m/s [4.1].

4.2. Design of DCC Crystallizers

It has been shown in the previous chapter that the crystal growth is heat transfer controlled if the solubility is very high. In this case, the mass fraction w = mass of crystals/total mass of melt results from an energy balance according to (with $\Delta T_{cool} = T_{melt} - T_{cool}$; see Fig. 4.2)

$$w = \frac{\pi T^2 \dot{v}_{cool} \rho_{cool} \tau (c_{P,cool} \Delta T_{cool} + \Delta h_{LG,cool})}{4 V_{melt} \rho_{melt} \Delta h_{CL,melt}} \tag{4.9}$$

for a crystallizer which is continuously operated and

$$w = \frac{M_{cool} (c_{P,cool} \Delta T_{cool} + \Delta h_{LG,cool})}{V_{melt} \rho_{melt} \Delta h_{CL,melt}} \tag{4.10}$$

for a batch crystallizer. These equations are only correct if the feed has the same temperature as the melt. The introduced coolant (volumetric flow density $\dot{v}_{cool}$, density ρ_{cool}) rises from the inlet temperature to the bulk temperature (difference ΔT_{cool}) during the residence time $\tau = H/w_B$ of the fluid particles with the rising velocity w_B of the fluid particles in the column with the height H and the diameter T.

The heat removed, Q, is referred to the heat of crystallization $V_{melt} \rho_{melt} \Delta h_{LC,melt}$, which is proportional to the mass $M_{melt} = V_{melt} \rho_{melt}$ of the melt and the specific heat of crystallization of the crystallizing component. Equations (4.9) and (4.10) show that the mass ratio or yield w, on the one hand, and the supersaturation σ and growth rate G_h, on the other hand, are directly proportional to the undercooling ΔT_{cool} of the incoming coolant. This means that the appropriate choice of the coolant temperature is decisive for the productivity and purity of the product. In Figure 4.9, an example for the system dodecanol/decanol is given. The yield w is plotted against the residence time τ with the volumetric flow density, $\dot{v}_{cool}$, of the coolant as parameter. Heat losses in the dispersing unit (e.g., gas dispersed from below in the melt through a thermostated sieve plate) may result in a lower yield than expected. If the coolant is introduced from above without

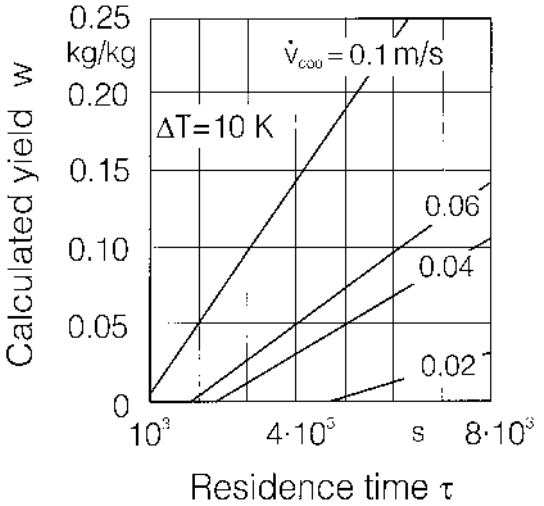

Figure 4.9. Yield w as a function of operational parameters, calculated for the system dodecanol/decanol (based on an energy balance).

any contact with the thermostated wall of the crystallizer, the calculated yield is in good agreement with experimental results [4.1].

The heat transfer coefficient h is very high, with the consequence that the fluid particles assume the temperature of the melt only after a short traveling distance. The coefficient h describes the heat transfer based on the interfacial area between the surface of the fluid particles (bubbles or drops) and the surrounding melt (volumetric area a). This coefficient h is connected with the volumetric heat transfer coefficient h_v, according to

$$h_v = ah = \frac{6(1-\Psi)}{L_{32}} h \tag{4.11}$$

with $1 - \Psi$ as the volumetric holdup of fluid particles or Ψ as the volumetric fraction of the continuous melt phase and L_{32} as the Sauter mean diameter of the bubbles or drops. In Figure 4.10, the volumetric heat transfer coefficient, h_v, is plotted against the mean superficial velocity or the volumetric flow density, $\dot{v}_{cool}$, of the coolant. With a metastable subcooling of $\Delta T_{met} \approx 2\,K$ valid for dodecanol/decanol ($w \approx 0.9\,kg/kg$), a heat transfer coefficient of $h_v = 10\,kW/m^3\,K$ would lead to a volumetric productivity of $\dot{m}_V = 0.12\,kg/m^3\,s$ for this system ($\Delta h_{CL} = 168\,kJ/kg$). As the heat transfer between coolant and melt is very fast, it was assumed that the coolant leaving the crystallizer has the temperature of the melt. The results of cal-

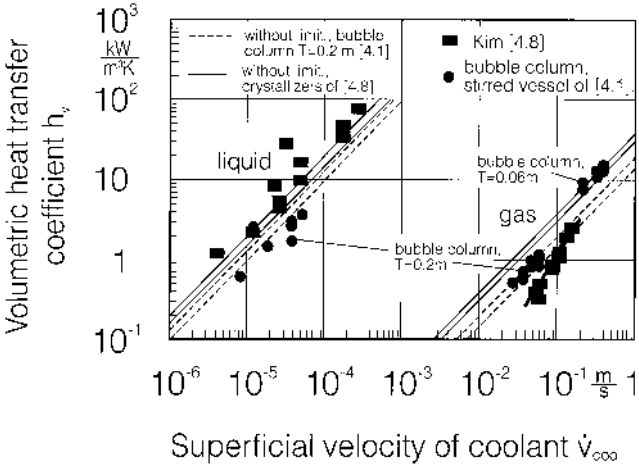

Figure 4.10. Volumetric heat transfer coefficient h_v; calculations and comparison with experimental results. (Data from Refs. [4.1] and [4.8].)

culations considering no limitations with respect to heat transfer are also illustrated in Figure 4.10. They are in good agreement with experimental results of Bartosch [4.1] and Kim and Mersmann [4.8].

This example shows that the productivity of a DCC crystallizer with a direct coolant is approximately the same or even higher (in the case of a liquid or an evaporating liquid) in comparison to the data given in Table 1.1. There are two reasons for the limitations of the maximum undercooling ΔT_{cool}:

- With respect to activated nucleation, the condition $\Delta T_{cool} < \Delta T_{met}$ holds.
- With increasing growth rates G_h controlled by heat transfer, the purity of the crystals is reduced according to equation (1.2).

4.3. Purity of Crystals

Many experiments have shown that in addition to the limitations of the growth rate, the solid–liquid separation of the suspension is a very important parameter (cf. Chapter 7). In Figure 4.11, the effective distribution coefficient, k_{eff}, is plotted versus the volumetric production rate $\dot{m}_V$ according to results of Bartosch [4.1]. Caprolactam can be produced with a high purity ($k_{eff} \approx 0.02$) when the slurry is separated by centrifugation. Vacuum

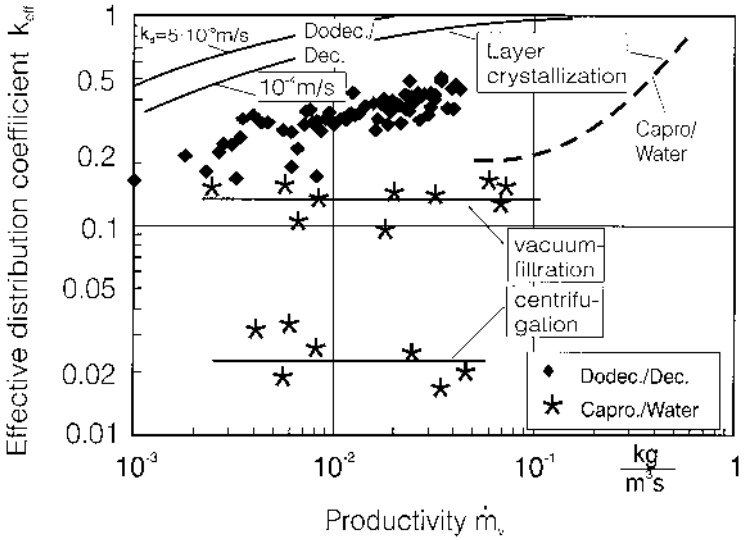

Figure 4.11. Effective distribution coefficient against productivity, systems: dodecanol/decanol and caprolactam/water; coolant: air.

filtration has been much less effective. The effective distribution coefficients of the system dodecanol/decanol are much higher ($k_{eff} \approx 0.4$ for vacuum filtration and only $k_{eff} \approx 0.15$ for vacuum filtration and washing) because the viscosity is high and, therefore, the mass transfer coefficient is small. Another reason for the low purity in the system dodecanol/decanol was a solid solubility resulting in a thermodynamic distribution coefficient K between 0.2 and 0.3. If the distribution coefficient K is considered, the measured effective distribution coefficients k_{eff} are reduced to values between 0.1 and 0.3. For the system *p*-xylene/*o*-xylene, it was possible to produce very pure *p*-xylene crystals even at temperature differences $\Delta T_{cool} = 10\,K$ and even $\Delta T_{cool} = 15\,K$ when the solid–liquid separation of the suspension was carried out by a centrifuge.

In general, the purity of the crystals produced with a gaseous coolant is higher in comparison to liquid coolants. This can be explained with low heat transfer rates and, consequently, low supersaturation and crystal growth; see Figure 4.12, in which the effective distribution coefficient is plotted against the yield for different coolants. A high effective distribution coefficient can also be the result of interactions between coolant and melt.

The combination of a direct contact cooling crystallizer operated with an appropriate coolant at the optimal temperature with a thermostated centri-

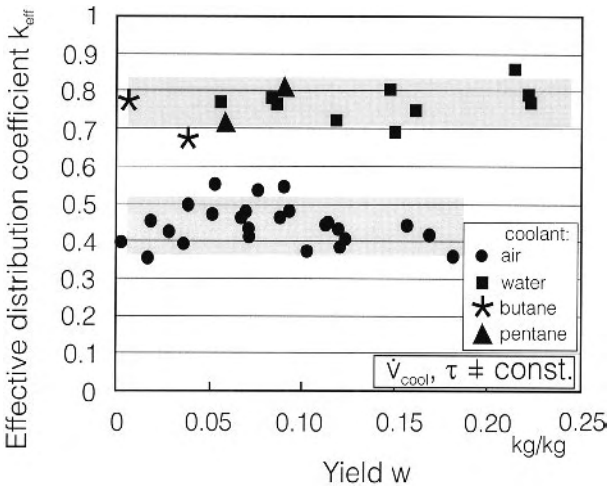

Figure 4.12. The influence of the type of coolant (gas, liquid, evaporating liquid) on the effective distribution coefficient k_{eff} in the system dodecanol/decanol.

fuge can be equal to or better than melt crystallizers presently used. The main advantages of the DCC crystallizers are as follows:

- Continuous or batch operation
- No scale-up problems
- No incrustations
- High volumetric production rates
- Easy maintenance of the optimal supersaturation
- High product purity when a centrifuge with washing is applied

REFERENCES

[1.1] J. W. Mullin, Crystallization and precipitation, in *Ullmann's Encyclopedia of Industrial Chemistry*, VCH, Weinheim (1988).

[1.2] J. A. Burton, R. C. Prim, and W. P. Slichter, The distribution of solute in crystals grown from the melt, Part I, *Chem. Phys.*, *21*: 1987–1991 (1953); Part II, *J. Chem. Phys.*, *21*: 1991–1996 (1953).

[2.1] M. Moritoki, M. Ito, T. Sawada, M. Ishiyama, Y. Yamazaki, T. Fukutomi, and K. Toyokura, Crystallizaiton of benzene by compression of the liquid phase benzene–cyclohexane, in *Industrial Crystallization '87*, pp. 485–488 (1989).

[2.2] Y. Yamazaki, Y. Watanuma, Y. Enomoto, and K. Toyokura, Formation of benzene crystals in benzene–cyclohexane in the batch agitation tank, *Kagaku Kogaku Ronbunshu*, *12*(5): 610–613 (1986).
[2.3] K. Toyokura, I. Hirasawa, S. Imada, and Y. Irie, Purity of benzene crystals obtained from a benzene cyclohexane melt by a batch cooling crystallization, in *Developments in Crystallization Engineering*, Waseda University Press, Tokyo (1992).
[2.4] K. Toyokura, N. Araki, and T. Mukaida, Purification crystallization of naphthalene from naphthalene benzoic acid, *Kagaku Kogaku Ronbunshu*, *3*(2): 149 (1977).
[2.5] K. Toyokura, H. Murata, and T. Akiya, Crystallization of naphthalene from naphthalene–benzoic acid mixtures, *AIChE Symp. Ser.*, *72* (153): 87 (1976).
[2.6] H. Futami and T. Rokkushi, Shoseki (crystallization), *Kagaku Kogyo Sha* (1973).
[2.7] G. Matz, in *Ullmanns Encyclopädie der technischen Chemie*, VCH, Weinheim, Band 2 (1972).
[2.8] K. Toyokura, M. Fukutomi, M. Ito, Y. Yamazaki, and M. Moritoki, Crystallization of benzene from benzene–cyclohexane system by high pressure, *Kagaku Kogaku Ronbunshu*, *12* (5): 622–625 (1986).
[2.9] N. Nishiguchi, M. Moritoki, K. Toyokura, M. Fukuda, and T. Ogawa, High pressure crystallization of manderic acid from aqueous solution, in *AlChE Topical Conf. on Separation Technology*, Session 18, pp. 638–643 (1992).
[2.10] W. G. Pfann, *Zone Melting*, 2nd ed., John Wiley & Sons, New York (1966).
[2.11] H. Schildknecht, *Zone Melting*, Academic Press, New York (1966).
[2.12] M. Zief and W. R. Wilcox, *Fractional Solidification*, Marcel Dekker, Inc., New York (1967).
[2.13] H. Watanabe, Effect of $Na_3PO_4 \cdot 12H_2O$ on the nucleation from $NaCH_3COO \cdot 3H_2O$, *Kagaku Kogaku Ronbunshu*, *16*(5): 875–881 (1990).
[2.14] T. Akiya, M. Owa, S. Kawasaki, T. Goto, and K. Toyokura, The operation of a $NaOH \cdot 3.5H_2O$ crystallizer by direct cooling, in *Industrial Crystallization '75*, pp. 421–429 (1976).
[3.1] K. Takegami, N. Nakamaru, and M. Morita, Industrial molten fractional crystallization, in *Industrial Crystallization '84* (S. J. Jancic and E. J. de Jong, eds.), Elsevier, Amsterdam, pp. 143–146 (1984).
[3.2] K. Sakuma and J. Ikeda, Purification of solid soluble mixtures by column crystallizer, in *Industrial Crystallization '84* (S. J. Jancic and E. J. de Jong, eds.), Elsevier, Amsterdam, pp. 147–152 (1984).

[3.3] E. Ideno, M. Moritoki, and H. Tanabe, Practical use of high pressure crystallization, *R. D. Kobe Steel Eng. Rep.*, *39*(3): 4–8 (1989).
[3.4] G. J. Arkenbout, M. Nienoord, and E. J. de Jong, On the choice of crystallization processes from melt, in *Proc. 11th Symposium on Industrial Crystallization '90* (A. Mersmann, ed.), pp. 715–720 (1990).
[4.1] K. Bartosch, The application of direct contact cooling techniques in melt suspension crystallization, Thesis, Technische Universität München (2000).
[4.2] R. de Goede and G. M. van Rosmalen, Modelling of crystal growth kinetics: A simple but illustrative approach, *J. Cryst. Growth*, *104*: 392–398 (1990).
[4.3] G. F. Arkenbout, *Melt Crystallization Technology*, Technomic Publications, Lancaster, PA (1995).
[4.4] R. de Goede and G. M. van Rosmalen, Crystal growth phenomena of paraxylene crystals, *J. Cryst. Growth*, *104*: 399–410 (1990).
[4.5] A. Schreiner, Kristallisationsverhalten von organischen Schmelzen bei der Suspensionskristallisation, Thesis, Universität Erlangen (2000).
[4.6] M. Poschmann, Zur Suspensionskristallisation organischer Schmelzen und Nachbehandlung der Kristalle durch Schwitzen und Waschen, Thesis, Universität Bremen (1995).
[4.7] P. J. Jansens, Y. H. M. Langen, E. P. G. van den Berg, and R. M. Geertman, Morphology of ε-caprolactam dependant on the crystallization conditions, *J. Cryst. Growth*, *155*: 126–134 (1995).
[4.8] K. J. Kim and A. Mersmann, Melt crystallization with direct contact cooling techniques, *Trans. IChemE*, *75*: 176–192 (1997).

14

Layer Crystallization and Melt Solidification

K. WINTERMANTEL AND G. WELLINGHOFF
BASF AG, Ludwigshafen, Germany

Layer crystallization is used as a separation process, whereas melt solidification means a phase transformation from the liquid to the solid state accompanied by product shaping.

1. LAYER CRYSTALLIZATION

Layer (or progressive) crystallization processes are characterized by the fact that an impure crude melt is selectively frozen out on cooled surfaces in the form of coherent, firmly adhering layers. The resulting heat of crystallization is removed via the crystalline layer; therefore, in contrast to suspension crystallization, the liquid phase is always at a higher temperature than the solid phase.

Due to the phase equilibrium, the crystallized layer and the residual melt can contain different concentrations of impurities. As a rule, the concentration of impurities in the solid phase will decrease while that in the liquid phase increases. As described in Chapter 13, the separation expected on a

purely thermodynamic basis is diminished by the formation of liquid inclusions during the crystallization process and by the residual melt still adhering to the solid after the solid and liquid have been separated. To obtain a high purity, it is therefore often necessary to carry out several crystallization steps, even for eutectic system [1.1].

When the layer crystallization process is carried out cyclically, the solid is separated from the liquid at the end of the freezing step simply by allowing the residual melt to drain off. The purified crystals are subsequently remelted. The advantage of this simple separation of the solid and the residual melt, which is easily performed on an industrial scale, is counterbalanced by the energetic disadvantage of the cyclic procedure. In each step, not only must the heat of crystallization be removed and then added again during the subsequent remelting process, but also the energy involved in cooling and heating the crystallizer must be removed or supplied [1.2].

These disadvantages do not occur in *continuous* layer crystallization processes, which are carried out, for example, on cooling rolls or cooling conveyor belts, because in this case the equipment is always kept at a constant temperature and the solid crystalline layer is continuously scraped off. However, such processes have not yet become established on an industrial scale.

The existing processes for melt crystallization in general are the subject of a comprehensive review by Rittner and Steiner [1.3]. In his dissertation Özoguz [1.4] has reviewed more than 300 publications specifically concerned with layer crystallization.

1.1. Theory

When designing a layer crystallization process, the aim is to perform the required separation in the smallest possible plant and with the minimum expenditure of energy. The differential distribution coefficient k_{diff} is usually used as the measure of the separation efficiency achieved in layer crystallization. It is defined as the ratio of the concentration of impurities in the crystalline layer to that in the liquid phase (Fig. 1.1):

$$k_{\text{diff}} = \frac{c_{\text{im},s}}{c_{\text{im},L}} \frac{\rho_L}{\rho_s} \tag{1.1}$$

In this connection, it is important to note that the differential distribution coefficient used is an "effective" distribution [cf. Eq. (1.2) in Chapter 13] coefficient and not the equilibrium distribution coefficient. It is calculated from the mean concentration in the crystalline layer and therefore includes the residual melt occluded in the pores. Because the system is considered

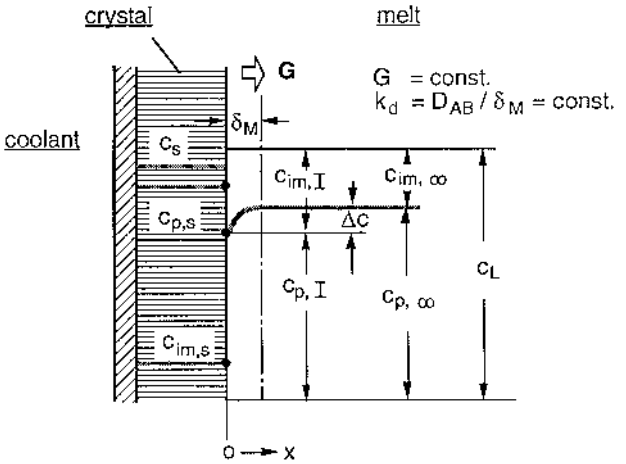

Figure 1.1. Concentrations present in layer crystallization.

from a differential point of view, the concentration in the melt is constant (i.e., $c_{\mathrm{im},L} = c_{\mathrm{im},\infty}$).

1.1.1. Boundary layer model

If the boundary layer model of Burton et al. [1.5] [cf. Eq. (1.2) in Chapter 13] is assumed, a relationship for the differential distribution coefficient can be derived in which the effect of the concentration $c_{\mathrm{im},L}$ is taken into account as well as the two parameters growth rate G and mass transfer coefficient k_d [1.6–1.8]:

$$k_{\mathrm{diff}} = f\left\{\frac{c_{\mathrm{im},L}}{\rho_L - c_{\mathrm{im},L}}\left[\exp\left(\frac{G}{k_d}\frac{\rho_s}{\rho_L}\right) - 1\right]\right\} \tag{1.2}$$

This relationship shows that when the rate of growth is low, the concentrations of impurities are low, and the mass transfer coefficient is high, compact crystalline layers can be produced which can be of very high purity under favorable conditions. On the other hand, when the growth rate is high, high concentrations of impurities are present, and the mass transfer coefficient is low, porous layers are formed to an increasing extent, which consist of large numbers of needle-shaped or dendritic crystals. In this type of layer, considerable quantities of impure residual melt are occluded initially. Therefore, k_{diff} provides information on both the purity and the structure of the layers that are frozen out.

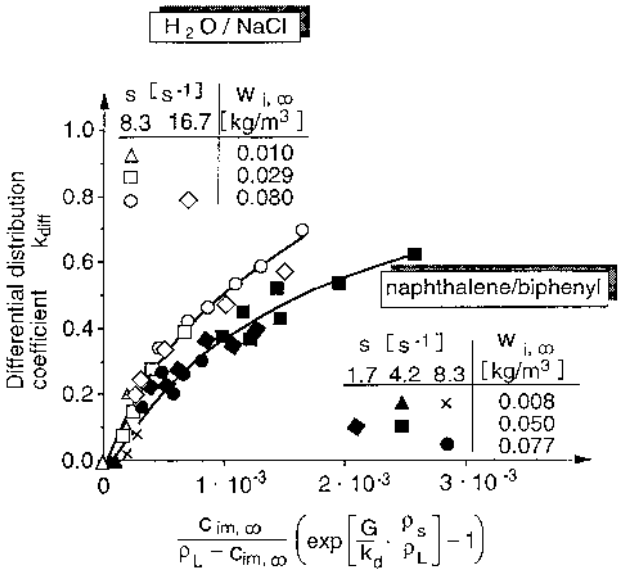

Figure 1.2. The differential distribution coefficient for the systems H_2O–NaCl and naphthalene–biphenyl. (From Ref. [1.8].)

The relationship derived has been tested for a large number of material systems and has given positive results. Figure 1.2 shows examples of the experimental results for an aqueous solution (H_2O–NaCl) and for an organic melt (naphthalene–biphenyl). The experiments were performed in a stirred vessel having a cooled base plate on which the layer is frozen out. In the following sub-section, it will be shown that the foregoing relationship enables the design and optimization of layer crystallization processes to be carried out largely by computational methods, supported by just a few laboratory experiments [1.2]. A relationship analogous to equation (1.2) can be derived to define the density of desublimed layers and it can be used for the design of corresponding processes [1.9].

1.1.2. Temperature gradient criterion

The use of the temperature gradient criterion as a basic design parameter has been discussed frequently in the literature [1.10–1.12]. This criterion shows that unstable (i.e., needle-shaped or dendritic) growth and, therefore, the formation of inclusions of residual melt occur when the real temperature profile ϑ_{real} due to the flow conditions lies below the equilibrium temperature ϑ_e determined by the concentration conditions (Fig. 1.3). This situation

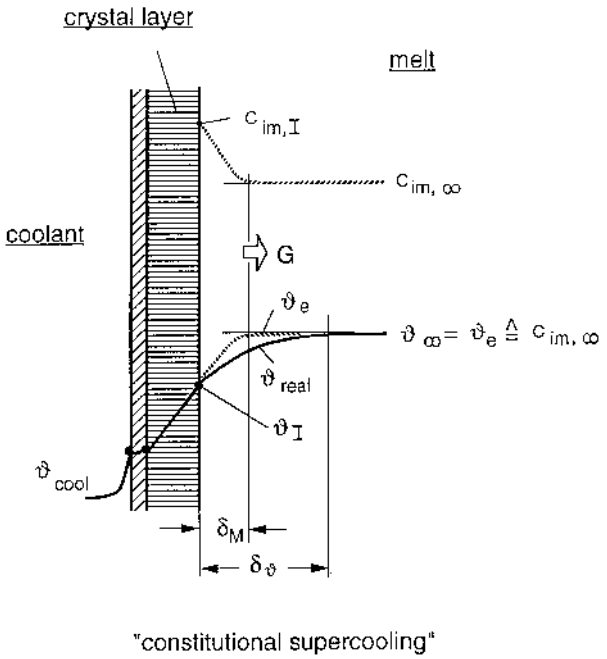

Figure 1.3. Concentrations and temperatures present in layer crystallization with constitutional supercooling.

is referred to as *constitutional supercooling*. To produce pure crystalline layers, it is therefore logical to require that the real temperature gradient must be equal to, or greater than, the gradient of the equilibrium temperature. This criterion defines a condition that is appropriate, but not necessary in all cases, for the production of layers free from inclusions. If the system does not meet this condition, it is not possible to make any quantitative statements on the structure and purity of the crystalline layers, in contrast to the case with the extended boundary layer model [Eq. (1.2)].

1.2. Layer Crystallization Processes

Layer crystallization processes that are used on an industrial scale are carried out cyclically. The operation is performed in commercially available or modified multitude or plate-type heat exchangers. The overall process can be subdivided into five individual steps:

1. Filling the crystallizer (heat exchanger) with the crude melt
2. Crystallizing the melt by reducing the temperature on the secondary side of the heat exchanger in a controlled manner
3. Draining off the highly impure residual melt
4. Further purificating the crystalline layer by *sweating* (controlled increase of the temperature on the secondary side, which at first results in highly impure fractions being melted from the crystalline layer and, subsequently, less impure fractions [1.1, 1.13, 1.14]) and/or by *washing* the layers with melt of a higher purity [4.15]
5. Melting and draining off the pure material that remains

Any combination and/or repetition of complete cycles can be selected to match this process to different materials, purity requirements, and desired yields.

In multistage processes, it is usual to feed the crystallized material into the next purification stage and to return the residue and any sweating or washing fractions to the preceding stage. However, a multistage process does not require duplication of the plant units. The individual stages are carried out at different times in the same crystallizer, and the fractions that have to be processed further are each stored in separate buffer tanks until required.

Modern layer crystallization processes are carried out completely automatically by means of a process control system. Basically, this only involves monitoring and controlling liquid levels, and operation of pump and valves, and the precise temperature control of the coolant (ϑ_{cool}).

A distinction is made between static and dynamic layer crystallization processes. In *static* processes, the crystals grow on a cooled surface in the stationary melt. Because the heat transfer and mass transport to the surface, where the deposition is occurring take place solely by natural convection, the layers formed are relatively porous (cf. Sec. 1.1), and the space-time yield is generally low. By contrast, *dynamic* layer crystallization processes depend on forced convection of the melt, which usually produces significantly more compact and, therefore, purer crystalline layers. Alternatively, for a given degree of purification, this process enables significantly higher growth rates and, therefore, higher space-time yields, than by static processes.

1.2.1. Static layer crystallization

Static layer crystallization processes are carried out in modified multitube or plate-type heat exchangers. As a consequence of their low space-time yields, the processes are used primarily when the plant capacity is low or when the concentration of impurities is very high, which frequently results in very

poorly adhering layers, which means that dynamic processes can no longer be used. The static processes are used, for example, in combination with dynamic layer crystallization processes to process residual melt streams that contain high levels of impurities from the dynamic purification stages and thus obtain very high yields. A further advantage compared with dynamic processes is that static layer crystallization requires only a relatively small temperature difference between the melt and the coolant as a result of the low growth rates (normal values: static < 5 K, dynamic < 25 K). This can be of considerable economic importance, particularly with materials having a freezing point below 0°C.

As a consequence of the very simple plant design (no moving parts in contact with the melt) and process control system, the operational safety of static layer crystallization processes is very high. There is no difficulty in scaling-up because it is only necessary to increase the number of plates or tubes in the heat exchangers. As an example, Figure 1.4 shows the layout of a static process, the PROABD refining process.

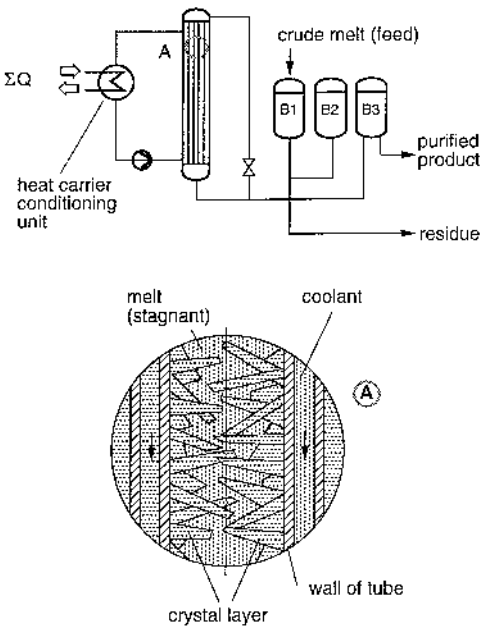

Figure 1.4. PROABD refining process (two stage). (Courtesy of BEFS Technologies, Mulhouse, France.)

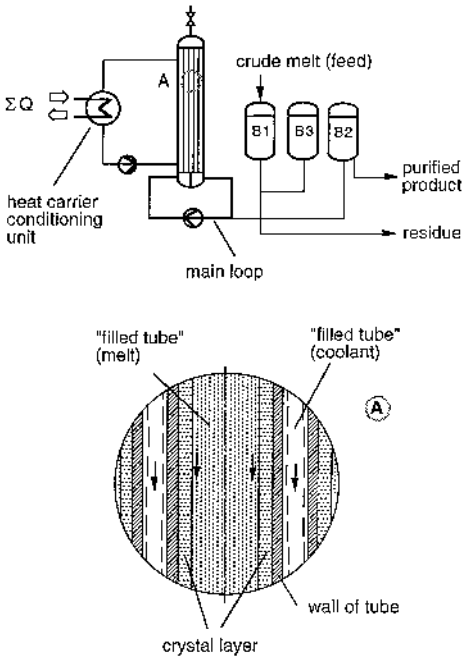

Figure 1.5. BASF process for layer crystalization (two stage). (Courtesy of BASF AG, Ludwigshafen, Germany.)

1.2.2. Dynamic layer crystallization

Dynamic layer crystallization processes are carried out in commercially available or special multitube heat exchangers. The characteristic feature of these processes is the forced convection of the melt, which is produced by the following:

1. Pump circulation of the melt through full-flow tubes (BASF process; Fig. 1.5)
2. Introduction of the melt as a falling film (Sulzer falling film process; Fig. 1.6)
3. Feeding inert gas into a tube filled with melt (bubble-column crystallizer [1.16])
4. Pulsing the melt by means of a pulsing pump [1.17]

The design of the equipment used in the dynamic layer crystallization processes is relatively simple and there are no problems involved in scaling-

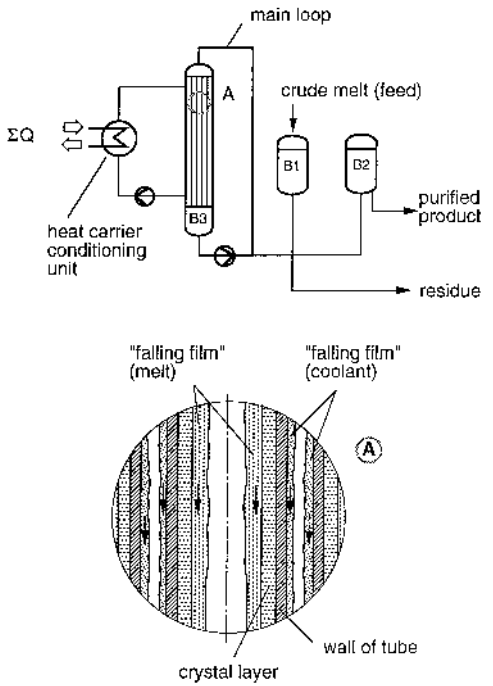

Figure 1.6. Sulzer falling film process (two stage). (Courtesy of Sulzer-Chemtech, Buchs, Switzerland.)

up by increasing the number of tubes. Dynamic layer crystallization processes have proved to be very effective in practice and they are now widely used not only for specialties but also for mass products. Multistage operation can attain very high purity and at the same time very high yields. It is possible to reduce the number of stages by, for example, sweating [1.1, 1.13, 1.14] or washing [1.15] the layers that have been frozen out.

As an example of this, Sulzer has described a seven-stage layer crystallization process, including sweating, for the purification of 90,000 metric tons per year of acrylic acid [1.18] (typical design features of multistage processes are discussed in Sec. 1.3). The feedstock already contains more than 99.5% acrylic acid and is therefore fed into stage 6. Stage 7 yields 988 kg of the acid, at a purity in excess of 99.95%, per metric ton of the feedstock. This corresponds to a product yield of about 99%. The residue from purification stages 6 and 7 is further crystallized in stages 1–5. The final residue of 12 kg then contains about 32% impurity.

1.3. Process Design

For economic reasons, industrial crystallization processes aim to achieve high crystallization ratios r_f per crystallization step, which means freezing out the maximum possible amount of solid per unit mass of the original melt. The concentration of impurities in the residual melt increases continuously during the crystallization process, and this results in a corresponding change in the local concentration of impurities in the crystalline layer. For a given differential distribution coefficient the integral distribution coefficient k_{int} can be calculated as

$$k_{\text{int}} = \frac{\bar{c}_{\text{im},s}}{c_{\text{im},\alpha}} \frac{\rho_L}{\rho_s} = \frac{1 - (1 - r_f)^{k_{\text{diff}}}}{r_f} \tag{1.3}$$

where $c_{\text{im},\alpha}$ is the concentration of impurities in the melt at the start of the crystallization process and $\bar{c}_{\text{im},s}$ is the mean concentration in the layer. k_{int} is plotted against the freezing ratio in Figure 1.7. When $r_f = 0$, $k_{\text{int}} = k_{\text{diff}}$. Whereas at low freezing ratios, the ratio of the mean concentration in the layer to the initial concentration is almost equal to the differential distribution coefficient, the mean concentration in the layer progressively approaches the initial concentration in the melt being used as the freezing

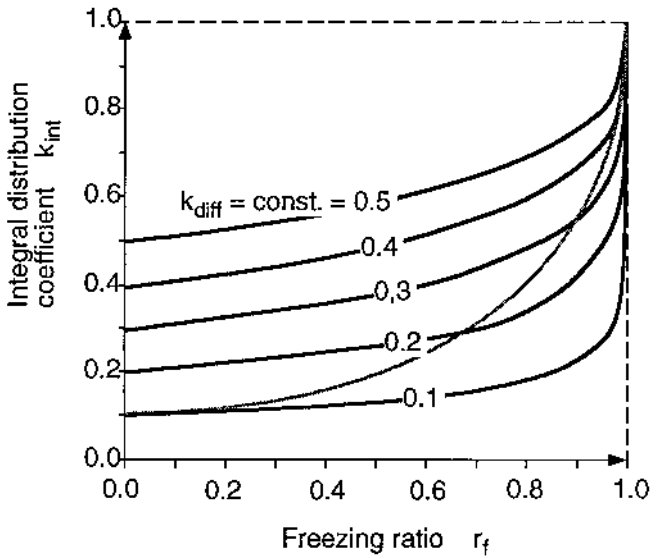

Figure 1.7. Integral distribution coefficient as a function of the freezing ratio.

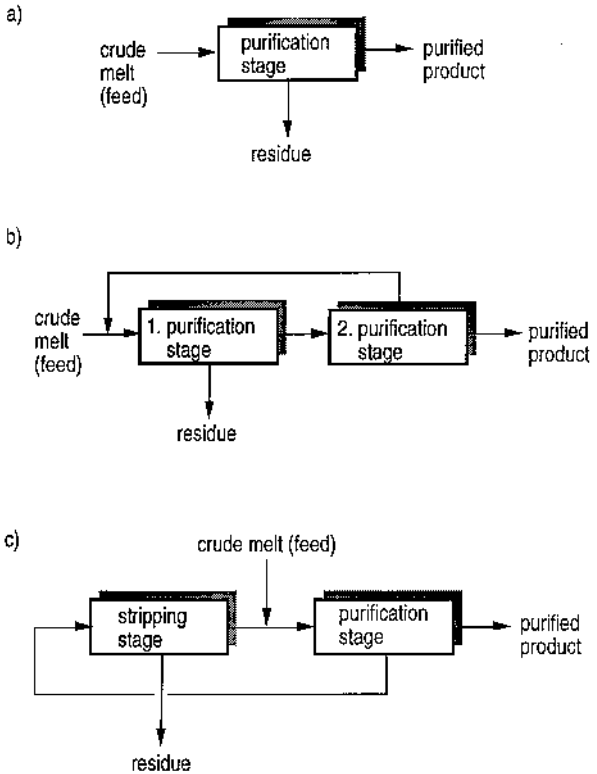

Figure 1.8. Multistage layer crystallization.

ratio increases. In the limiting case when $r_f = 1$, separation is no longer obtained on a macroscopic scale. The continuous curves apply to constant values of the differential distribution coefficient. This means that the variation of this coefficient with concentration is balanced by variations in the parameters G and k_d. However, if the ratio G/k_d is kept constant, the significantly steeper dashed line is obtained.

1.3.1. Single-stage processes

In single-stage processes (Fig. 1.8a), the distribution coefficient based on the overall process

$$k_{\text{proc}} = \frac{c_{\text{im,pp}}}{c_{\text{im,feed}}} \tag{1.4}$$

is equal to the integral distribution coefficient discussed previously. The ratio of the total amount of material crystallized to the amount of pure product is the crystallization effort E_s:

$$E_s = \frac{\sum_j \dot{M}_{s,j}}{\dot{M}_{\text{pp}}} \tag{1.5}$$

and is equal to 1 for a single-stage process. The yield Y, which is defined here as the ratio of the amount of pure product to that of the crude melt,

$$Y = \frac{\dot{M}_{\text{pp}}}{\dot{M}_{\text{feed}}} \tag{1.6}$$

is equal to the freezing ratio r_f for single-stage processes.

1.3.2. Multistage processes

In practice, single-stage processes frequently do not lead to the desired result, because either the specified product purity or the required yield is not achieved. In these cases, it is therefore necessary to use a multistage process, and the effects on the distribution coefficient for the overall process on the crystallization effort and on the yield under these circumstances are discussed below. The process distribution coefficient k_{proc} is improved considerably (Fig. 1.9A) by using two purification stages in series (Figure 1.8b). However, the crystallization effort increases at the same time, particularly at low freezing ratios (Fig. 1.9B), and the yield falls (Fig. 1.9C). Combining a purification stage with a stripping stage (Fig. 1.8c) causes almost no change in the degree of purification compared with a single-stage process (Fig. 1.9A), and the crystallization effort increases only slightly (Fig. 1.9B). On the other hand, a stripping stage can produce a considerable increase in the yield, particularly at high freezing ratios (Fig. 1.9C).

If both high purity and high yield are required, it is necessary to use a multistage process incorporating several purification and stripping stages. The resulting crystallization effort is plotted as a function of the freezing ratio in Figure 1.10. As expected, E_s increases as the required level of purity is raised (i.e., decreasing k_{proc}). The crystallization effort is high when the freezing ratio is low, because a large number of stripping stages is then necessary to obtain the required yield. At very high freezing ratios, the degree of purification obtained per crystallization stage is very low (cf. Fig. 1.7), and, as a consequence, the number of purification stages necessary increases. A minimum occurs in the crystallization effort at freezing ratios between 0.75 and 0.85.

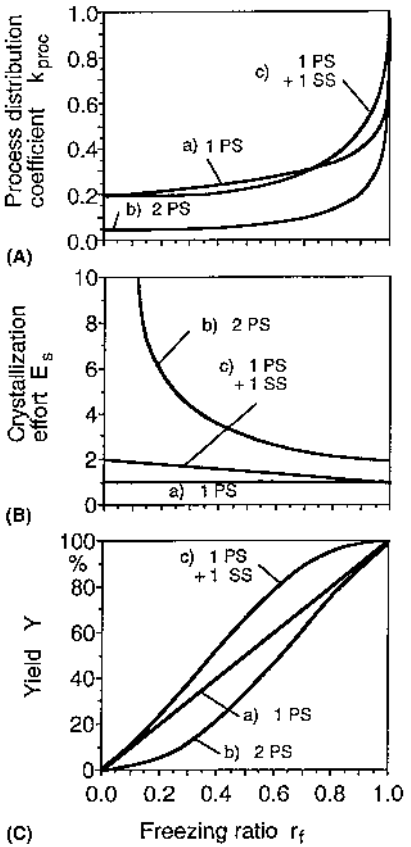

Figure 1.9. Behavior in multistage systems; $k_{\text{diff}} = 0.20 = \text{constant}$; PS, purification stage; SS, stripping stage.

It must be pointed out here that the freezing ratio relates to the volume of the entire layer crystallizer, the connecting pipes, and the pumps (for dynamic processes)]. The following conditions must be satisfied to obtain high freezing ratios based on the entire plant:

1. High freezing ratios (>0.85) in the actual crystallization zones (obtained by appropriate design of the plant and process control system)
2. A low dead volume (obtained by appropriate design)

Figure 1.11 illustrates the marked effect of the differential distribution coefficient in each stage on the crystallization effort. Halving this coefficient

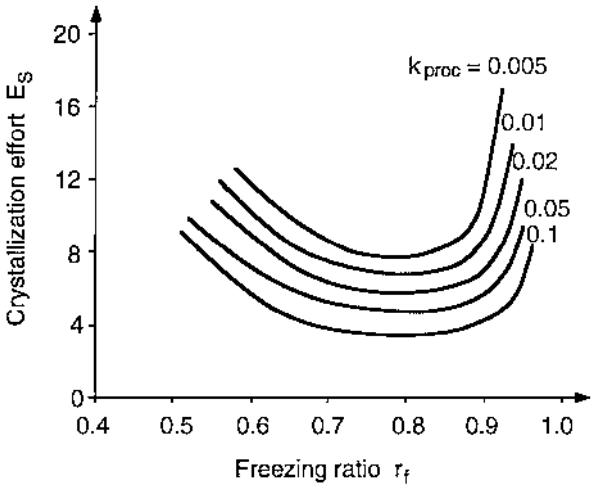

Figure 1.10. Crystallization effort as a function of the freezing ratio per stage; $k_{\text{diff}} = 0.20 = \text{constant}$; $Y = 95\% = \text{constant}$.

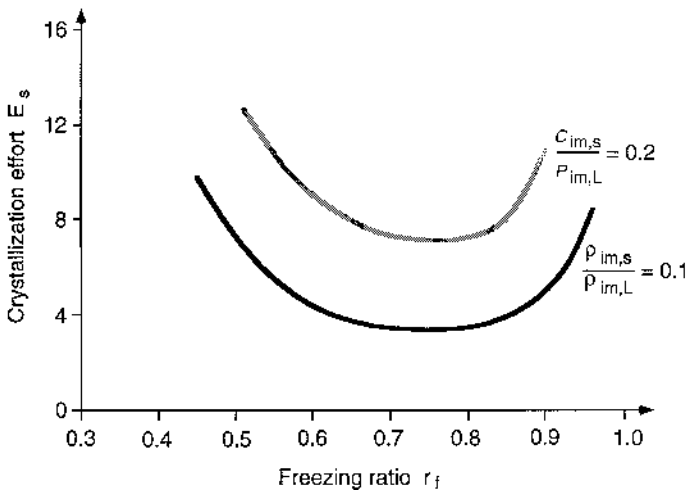

Figure 1.11. Crystallization effort as a function of the freezing ratio per stage; $k_{\text{proc}} = 0.01 = \text{constant}$; $Y = 95\% = \text{constant}$.

means, for example, that the crystallization effort is also approximately halved, as is the size of the crystallizer needed and the energy requirement. Techniques such as washing or sweating, which produce a corresponding reduction in the differential distribution coefficient, act in the same direction

and can, therefore, considerably improve the economics of a layer crystallization process.

1.3.3. Example of process design

We use as an example the design of a layer crystallization process to produce high-purity naphthalene, from which the impurity to be removed is biphenyl. The boundary conditions specified are as follows:

Capacity (pure product)	1000 kg/h
Concentration of impurity in the feed	1.0 wt%
Concentration of impurity in the purified product	0.01 wt%
Yield	90%

It follows that the concentration of impurity in the residue will be about 10 wt%.

The distribution coefficients for the individual stages were calculated on the basis of differential distribution coefficients measured in the laboratory (cf. Fig. 1.2) with the boundary conditions growth rate $G = 5 \times 10^{-6}$ m/s and mass transfer coefficient $k_d = 6 \times 10^{-6}$ m/s for a freezing ratio of $r_f = 0.65$. Two purification stages are necessary to achieve the required product purity, and one stripping stage is also needed to obtain the required value of Y = 90%. The quantitative flow diagram shown in Figure 1.12 can be derived on the basis of the foregoing values. The crystallization effort was found to be $E_s = 3.26$ by the addition of the streams $\dot{M}_{10}$, $\dot{M}_6$, and $\dot{M}_2$.

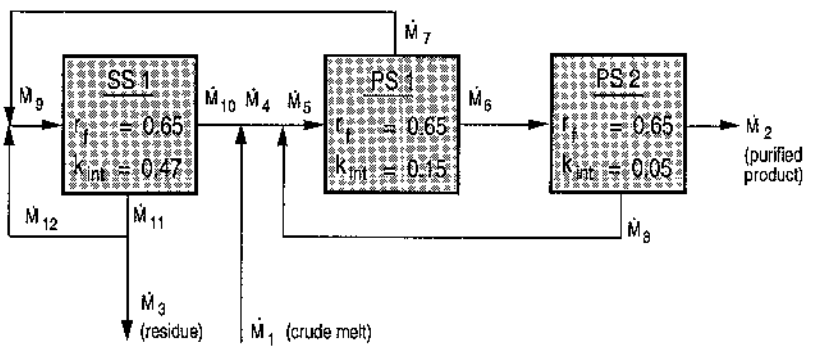

Figure 1.12. Quantitative flow diagram of a layer crystallization process for the purification of 1000 kg/h of naphthalene.

1.4. Design of Equipment for Layer Crystallization

The design of layer crystallizers is based on a quantitative flow diagram like the one in Figure 1.12. The total mass flow rate of material to be crystallized is calculated from the capacity of the system and the crystallization effort as

$$\dot{M}_s = E_s \dot{M}_{\text{pp}} \tag{1.7}$$

The time t_T needed to carry out a complete layer crystallization stage comprises the crystallization time t_s, the time for any washing or sweating steps $t_{\text{w/sw}}$, and a dead time t_d, which takes account of the filling, emptying, and melting steps:

$$t_T = t_s + t_{\text{w/sw}} + t_d \tag{1.8}$$

where

$$t_s = \frac{\delta_s}{G} \tag{1.9}$$

It is assumed that the growth rate is kept constant by appropriate control of the coolant temperature. It follows that for flat cooling surfaces the mass of crystallized material produced per second per unit area is

$$\dot{m}_s = \frac{\delta_s \bar{\rho}_s}{t_T} \tag{1.10}$$

and therefore the area of cooled surface needed in the crystallizer is

$$A_C = \frac{\dot{M}_s}{\dot{m}_s} \tag{1.11}$$

When layer crystallization is performed in multitube heat exchangers it is first necessary to calculate the rate of production of crystallized material per tube:

$$\dot{M}_{tb} = \frac{\pi}{4} \frac{[D^2 - (D - 2\delta_s)^2] L \bar{\rho}_s}{t_T} \tag{1.12}$$

The number of tubes necessary can then be calculated by analogy with equation (1.11):

$$N = \frac{\dot{M}_s}{\dot{M}_{tb}} \tag{1.13}$$

1.4.1. Example of the design of a crystallizer

On the assumption that the cooling surfaces are flat, the thickness of the crystalline layer is $\delta_s = 0.007\,\text{m}$ and the mean density of the layer is $\bar{\rho}_s = 1060\,\text{kg/m}^3$, it follows in the process illustrated in Figure 1.12 that

Equation (1.7)	$\dot{M}_s = 0.906\,\text{kg/s}\,(3260\,\text{kg/h})$
Equation (1.9)	$t_s = 1400\,\text{s}$
	$t_{w/\text{sw}} = 0\,\text{s}$
	$t_d = 1800\,\text{s}$
Equation (1.8)	$t_T = 3200\,\text{s}$
Equation (1.10)	$\dot{m}_s = 2.32 \times 10^{-3}\,\text{kg/m}^2\,\text{s}\,(8.35\,\text{kg/m}^2\,\text{h})$
Equation (1.11)	$A_C = 391\text{m}^2$

1.5. Energy Requirement for Layer Crystallization Processes

The quantity of heat that has to be removed in each freezing step in layer crystallization is the sum of the latent heat of fusion

$$Q_s = M_s h_f \tag{1.14}$$

plus the heat introduced only in the case of dynamic layer crystallization processes, by the circulating pump or other systems used to produce the forced convection

$$Q_{\text{circ}} = P_{\text{circ}} \frac{\delta_s}{G} \tag{1.15}$$

and the energy required for the cooling of all the plant units involved, including the heat transfer medium in the secondary circuit,

$$Q_{\text{app}} = \sum_j (M_{\text{app},j} c_{p/\text{app},j} \Delta\vartheta_{\text{app},j}) + (M_{\text{HC}} c_{p/\text{HC}} \Delta\vartheta_{\text{HC}}) \tag{1.16}$$

If Q_{circ} and Q_{app} are expressed as ratios of the heat of crystallization and if the multistage operation is taken into account in the crystallization effort, the total quantity of heat to be removed during the layer crystallization process is

$$\sum \dot{Q} = \dot{M}_{pp} h_f E_s \left(1 + \frac{Q_{\text{circ}}}{Q_s} + \frac{Q_{\text{app}}}{Q_s}\right) \tag{1.17}$$

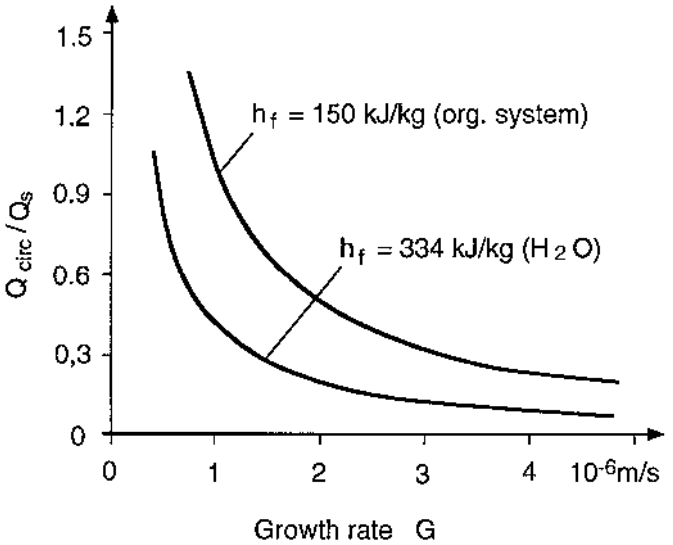

Figure 1.13. Energy input for the melt circulation as a function of the growth rate of the crystalline layer; $\delta_s = 0.008$ m.

In principle, this method of calculating the energy requirement and the resulting equation (1.17) can be applied to all layer crystallization processes.

On the basis of experience obtained with pilot plants and production-scale units employing the BASF process (cf. Fig. 1.5), values of Q_{circ} and Q_{app} have been estimated and are plotted in Figures 1.13 and 1.14 as the ratio to Q_s. For a given layer thickness, Q_{circ} decreases with an increase in the growth rate, as a consequence of the decrease in the freezing period. Over the range of growth rates of industrial importance,

$$0.1 < \frac{Q_{\text{circ}}}{Q_s} < 1.2$$

the value of Q_{app} decreases as the size of the plant is increased, since the ratio of the mass of the equipment, including the heat transfer medium, to the material content then decreases, and the following condition applies:

$$1.0 < \frac{Q_{\text{app}}}{Q_s} < 3.0$$

When a crystallizer layer is remelted, the heat needed to heat the equipment must be supplied in addition to the heat of fusion.

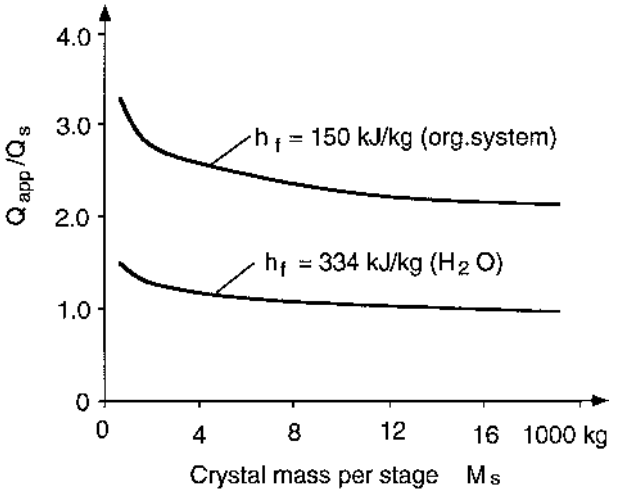

Figure 1.14. Removal of heat to cool the equipment as a function of the crystal mass per stage.

1.5.1. Example of the calculation of the energy requirement

The earlier example of the design of a layer crystallization process will now be considered in terms of the energy requirement: From Figure 1.13 it follows that $Q_{\text{circ}}/Q_s = 0.20$. The mass of crystals formed per stage is calculated from the equation

$$M_{s/\text{stage}} = A_C \bar{\rho}_s \delta_s \tag{1.18}$$

to be $M_{s/\text{stage}} = 2900\,\text{kg}$. It therefore follows from Figure 1.14 that $Q_{\text{app}}/Q_s = 2.73$, and from equation (1.17) that $\Sigma \dot{Q}/\dot{M}_{\text{pp}} h_f = 12.8$. That means that the energy requirement for the foregoing dynamic layer crystallization process for the purification of naphthalene is 12.8 times the actual heat of crystallization of the material.

The above calculations show that during the layer crystallization process, the quantity of heat that must be removed is many times greater than the heat of crystallization and that similar quantities of heat must be supplied during the melting stages. Multistage layer crystallization processes therefore compare unfavorably with distillation processes using heat recovery, owing to the limited extent to which heat recovery techniques can be used in the discontinuous layer crystallization process. The optimum with regard to overall energy consumption frequently consists of a combination of crystallization with other thermal separation processes. This approach

may also provide a solution to separation problems that cannot be solved by the application of a single physical principle. Examples of this have been described by Rittner and Steiner [1.3] and Ruegg [1.19].

Analysis of the energy requirement also demonstrates that the use of the temperature gradient criterion (Sec. 1.1) in the design and operation of layer crystallization processes would lead to uneconomic solutions [1.20, 1.21]. To be consistent, the temperature gradient criterion would have to be applied to the entire crystallizer. Therefore, a relatively high degree of overheating would be required at the inlet and the energy needed to achieve this overheating would also have to be removed. Moreover, an additional heat exchanger would have to be installed to produce the high inlet temperature. This would mean that the capital costs would be greater and that under some circumstances, it would not be possible to work at the optimum crystallization ratios (cf. Sec. 1.3). Therefore, it is always advisable to operate beyond the temperature gradient criterion considered to be sufficient and to use as a guide the physical limits derived from the boundary layer model. Only in those cases where the energy consumption is of secondary importance in terms of economic viability (e.g., single crystal growth) can the use of the temperature gradient criterion be justified, because the operation is then performed with a high level of safety.

1.6. Range of Application of Layer Crystallization Processes

Layer crystallization is used predominantly for the separation of mixtures of organic compounds; the applications range from the separation of isomers to the isolation of chemicals from tar, and the production of pure carboxylic acids to the purification of monomers. These applications frequently involve the separation of compounds whose boiling points are very close together or of azeotropic mixtures, and the purification of thermally unstable compounds.

It is possible to carry out layer crystallization processes in completely enclosed plants with almost no need for ventilation, and as in the case of distillation, solvents and other additives are generally unnecessary. However, there are some limitations to its use as a possible alternative to distillation methods, because in some circumstances, the energy consumption is very high (cf. Sec. 1.5). The range of temperatures over which it can be used extends from $-70^{\circ}C$ to $+350^{\circ}C$, although most of the applications of the process are in the range 0–$150^{\circ}C$.

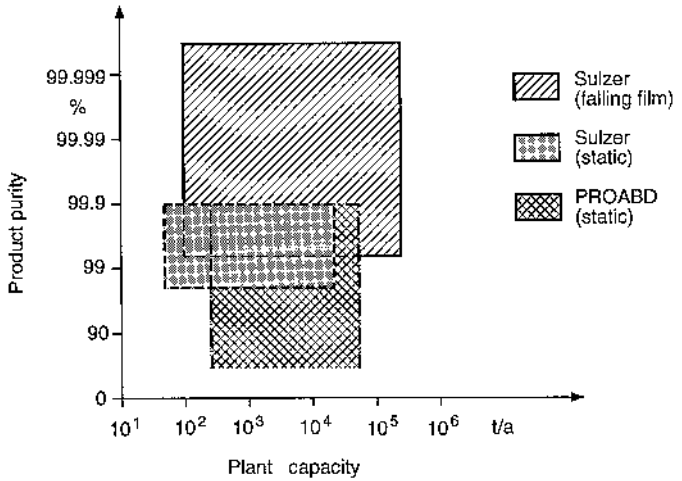

Figure 1.15. Range of application of the layer crystallization processes.

The best known commercially available processes for layer crystallization are the BEFS PROABD refining process (static) and the Sulzer falling film process (dynamic). The range of product purity and plant capacity over which the manufacturers state that their processes may be used is shown in Figure 1.15, although higher and lower limits may apply in particular cases.

2. MELT SOLIDIFICATION

Melt solidification is a product-shaping process in which it is important to control the transition from the liquid phase into the solid phase in such a way that the products are obtained in an appropriate form for their transport, storage, and subsequent use. This should be done by an economical process, one employing the smallest and simplest equipment possible. The products must normally be free-flowing and form very little dust and must retain these properties. In some cases, specific characteristics are also required in relation to the industrial use of the material (e.g., its particle size distribution). In this process, no attempt is made to obtain differences in concentration (separation of compounds) between the liquid and solid phases.

2.1. Theory

2.1.1. Phase equilibria

If an essentially pure substance is to be crystallized, solidification will occur at the melting point if kinetic effects are disregarded. At this temperature, at which all of the heat of solidification has to be removed, there is an interruption in the cooling curve (Fig. 2.1, case a), and only when all of the substance has solidified does the temperature fall with further cooling. However, in the case of an impure melt or of a mixture of compounds (Fig. 2.1, cases b and c), solidification starts below the melting point of the pure component A. It continues within a temperature range defined by the liquidus and solidus lines. When the system passes below the solidus line or reaches the constant eutectic temperature, it solidifies completely.

2.1.2. Heat transfer

In many cases, the rate at which solidification occurs is determined primarily by heat transfer and is, therefore, simple to control. For the case when a pure melt crystallizes at the melting point ϑ_s on a cooled wall [mean wall temperature $\vartheta_W(t) = \text{constant}$; Fig. 2.2), to a first approximation the solidification time t_s is proportional to the square of the layer thickness (δ_s^2):

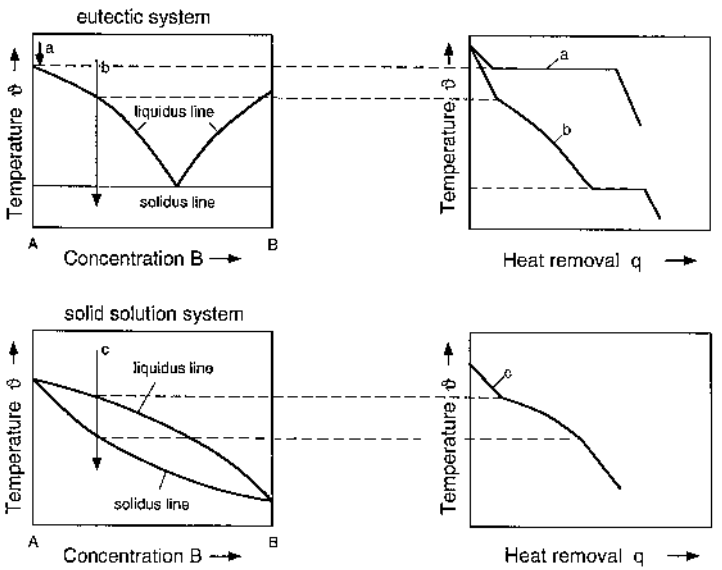

Figure 2.1. Melting diagrams and cooling curves.

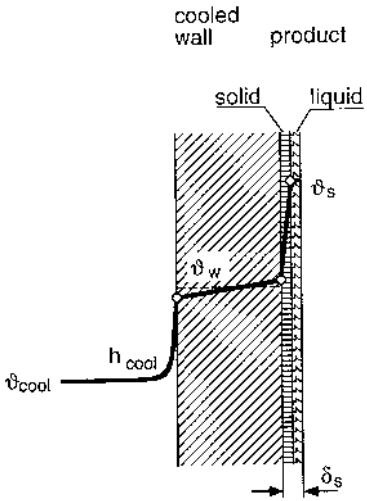

Figure 2.2. Temperature conditions during the complete solidification of a melt.

$$t_s \sim \frac{\delta_s^2}{\vartheta_s - \vartheta_W} \tag{2.1}$$

This means that, for example, halving the layer thickness theoretically reduces the crystallization time by a factor of 4. The crystallization time can also be shortened by reducing the mean wall temperature ϑ_W, which can be achieved either by using lower coolant temperatures ϑ_{cool} or by improving the heat transfer at the internal cooling surface (h_{cool}).

2.1.3. Kinetics

The measures for improving the performance described earlier will not succeed if kinetic effects are important. Figure 2.3 is a plot of the time that a 1-mm-thick layer requires to achieve complete solidification on a laboratory cooling plate at various temperatures ("unseeded" curve). As the distance from the melting point increases, the crystallization time initially decreases, as expected, because of the driving force of the higher temperature gradient. However, as a result of kinetic limitations, it passes through a minimum, and at even lower temperatures, it becomes unacceptably long for an industrial process.

The rates of nucleation and of crystal growth increase initially as the degree of supercooling is increased, as Tamman [2.1] demonstrated from

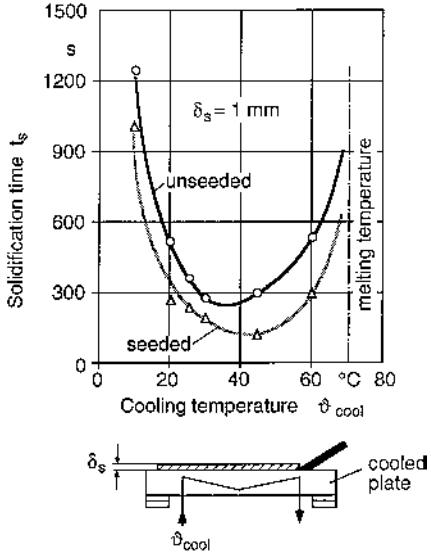

Figure 2.3. Solidification time as a function of the temperature of the cooling surface.

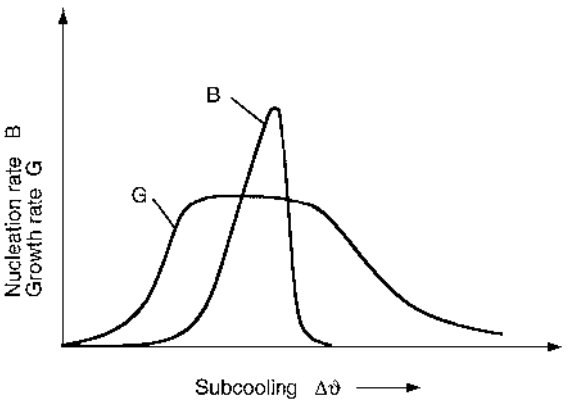

Figure 2.4. Rates of nucleation and crystal growth as a function of the degree of subcooling.

basic principles at the beginning of the twentieth century. However, as shown qualitatively in Figure 2.4, they pass through a maximum and then drop back again to zero, owing to the decreasing mobility of the molecules [2.2]. The maxima in the nucleation rate and in the rate of crystal growth can

occur at different levels of supercooling. If in an industrial process the entire temperature range is passed through so quickly that only a few nuclei are formed and can grow only very slowly, then initially the melt will be converted to a largely amorphous solid. During storage, over the course of days or weeks depending on the circumstances, postcrystallization may occur and lead to undesirable caking in the sacks and containers.

The positions of the two maxima and the number of nuclei initially present in an industrial plant determine how rapidly the crystallization process occurs. From Figure 2.3 it can also be seen that a crystallization process that is retarded by a slow rate of nucleation can be accelerated significantly at higher temperatures by "seeding" (e.g., by partial precrystallization in a scraped surface chiller or by the addition of fine crystals). At lower temperatures, the growth rate is usually reduced to such an extent that seeding will produce only a relatively small improvement.

2.2. Melt Solidification Equipment

In addition to the product-specific solidification behavior, the following are the most important criteria to be considered when selecting equipment for melt solidification: (a) the required shape of the product, (b) the proportion of fines and small crystals in the product, (c) the capital costs, and (d) the energy requirement. A variety of equipment is available to meet the various requirements of the industrial implementation of the melt conditioning process: rotary drum crystallizer, conveyor belt crystallizer, conveyor belt crystallizer with pelleting system, prilling tower, sprayed fluidized bed, and screw crystallizer.

2.2.1. Drum crystallizer

A drum crystallizer consists of a horizontally mounted, rotating cylinder that is cooled internally. The material to be crystallized is applied to the surface of the cylinder as a melt and is fully crystallized during one rotation. A scraper simultaneously removes and breaks up the solidified layer from the drum. The size and shape of the flakes are determined by the properties of the particular material (ductility/brittleness), the thickness of the crystal layer, and the angle at which the scraper blade is set.

In the case of poorly adhering materials, it can be an advantage to have grooves cut into the surface of the cylinder. When the layer of product is scraped off, some crystalline material remains in these usually dove-taillike grooves, and the new layer of crystal will grow onto it [2.3]. This technique also acts like a form of additional seeding. The adhesion characteristics of

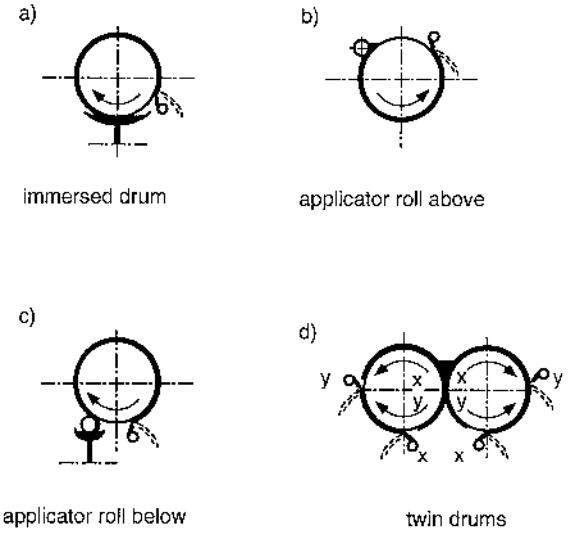

Figure 2.5. Application of material in the solidification of melts in drum crystallizers.

some substances depend on the temperature, and in many of these cases, an improvement in adhesion can result as the system approaches the melting point.

For the simplest and most frequently used drum crystallizer designs, the cylinder is partially immersed in a temperature-controlled trough filled with the melt (Fig. 2.5a). The substance crystallizes during the immersion period to form an adherent layer on the cooled surface and solidifies fully in the period between leaving the trough and reaching the point of removal. The throughput can be improved by increasing the rate of rotation of the drum (cf. Sec. 2.1), which results in a decrease in the thickness of the crystal layer δ_s. However, the residence time required for complete crystallization of the layer sets an upper limit. Moreover, it is necessary to take account of the fact that thin flakes of crystal are generally not very free-flowing, are not suitable for storage, and contain a higher proportion of fines.

Highly viscous materials can be applied to the drum by means of applicator rolls (Fig. 2.5b and 2.5c). Compared with an immersed drum, these systems have the advantage that the thickness of the crystal layer can be controlled precisely, and incrustation of the end phases can be avoided. Twin drums (Fig. 2.5d) are particularly useful for the solidification of high-temperature melts.

2.2.2. Conveyor belt crystallizer

A conveyor belt crystallizer consists of a continuously revolving steel belt that is cooled from below by a low-temperature bath or by spraying it with a coolant. The molten material applied to the belt at the start of its run solidifies along the belt and is removed at the end of the run by means of a scraper, in a manner similar to that employed in the drum crystallizer. By dividing the cooling into zones of different temperature, the process of solidification can be matched to the solidification kinetics, and the temperature dependence of the adhesion of the particular material and, therefore, the energy consumption can be optimized.

In the simplest cases, the application of material is by gravity feed, via an overflow weir or by applicator rolls (Fig. 2.6a–2.6c). With these systems, the solidified product is obtained in the form of flakes, as with drum crystallizers. In ribbon casting, the melt is applied to the belt in individual strips (Fig. 2.6d), a method of application that is frequently used for high-viscosity melts and/or when it is desired to dispense with the use of an expensive granulator at the end of the belt. It is also used for brittle products to ensure the minimum production of fines when the material is fragmented.

Seeding of the melt can be used to improve the solidification time and, therefore, the capacity of the belt crystallizer, or even to initiate the conditioning process in kinetically retarded systems. The way in which seeding

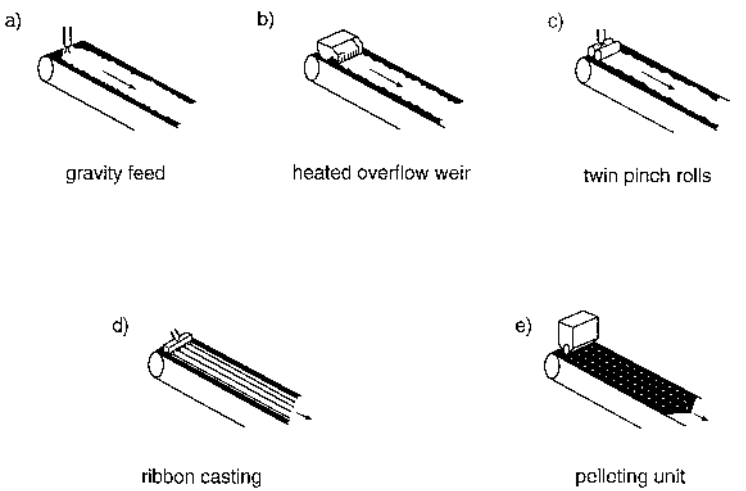

Figure 2.6. Application of material in the solidification of melts in conveyor belt crystallizers.

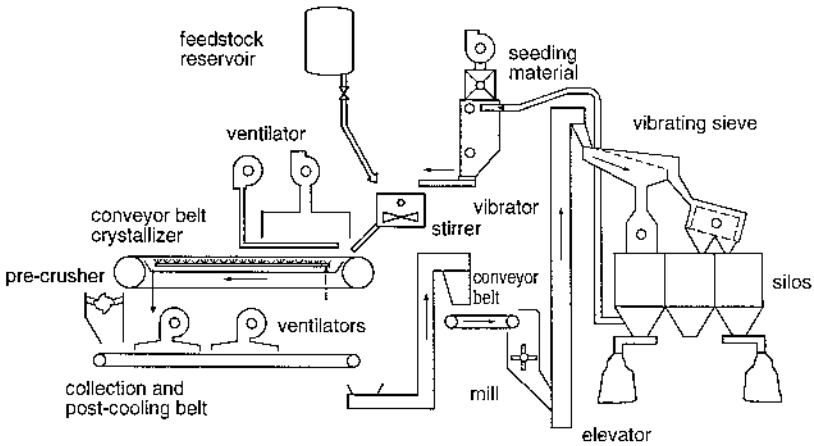

Figure 2.7. Solidification of aluminum sulfate.

may be carried out on an industrial scale is shown in Figure 2.7, which illustrates the conditioning of aluminum sulfate. In this case, the crystalline fines removed by sieving are fed back into the applicator reservoir [2.4]. Another method of seeding involves interposing a scraped surface chiller, in which a certain fraction of the feed melt crystallizes out and is mixed in with the feed. A simpler but less effective method is to install scrapers or wipers on the initial section of the belt to remove crystals that have formed and disperse them in the product layer.

2.2.3. Conveyor belt crystallizer with pelleting system

If the final product is required to be in a specified, free-flowing form containing no fines, it is best to apply the material to be conditioned by means of a pelleting system (Fig. 2.6e). This method will produce pellets ranging in shape from disks to spheres, depending on the viscosity and the surface tension of the melt, the mass of the molten drop, the wetting of the surface of the cold belt by the melt, and the speed of the belt.

The *nozzle and needle* system shown in Figure 2.8a is frequently used for low-viscosity melts [2.5]. The shape of the pellets obtained is determined by the properties of the particular melt, the geometry of the nozzle and needle system, the length of the stroke, and the frequency of the needle movement. For relatively high-viscosity melts, it is not possible to distribute the melt with a needle, although a *barrel and plunger* system can then be used, in which the plunger forces a defined volume of the melt through the outlet hole of the barrel (Fig. 2.8b).

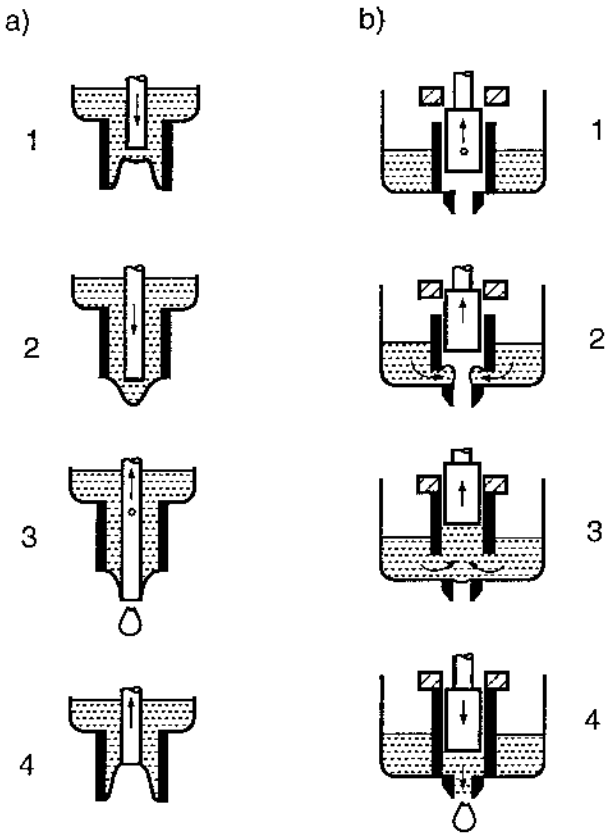

Figure 2.8. Pelleting systems: (a) nozzle and needle; (b) barrel and plunger.

In recent years, *rotor and stator* pelleting systems have become increasingly popular (Fig. 2.9), although from a manufacturing point of view, they are considerably more expensive than the systems described here. However, they permit better utilization of the cooling surface and higher throughputs. Seeding of the melt can also be used in conjunction with pelleting systems. As well as the increase in output provided by these systems, the high viscosity of the suspension can have an advantageous effect on the shape of the pellets [2.6].

2.2.4. Prilling tower

The principle of the prilling tower is already familiar, because of the analogy to spray-drying, and will not be discussed here in any detail. It is not difficult

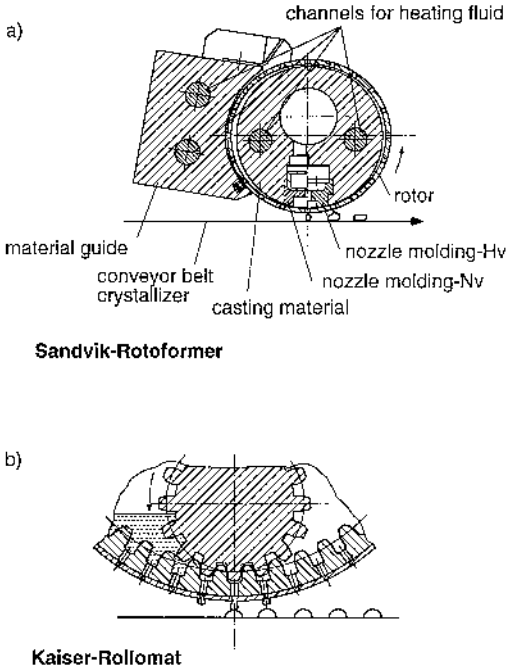

Figure 2.9. Rotor and stator systems for pelleting.

to calculate the dimensions needed for the tower, provided that kinetic effects are only of secondary importance (cf. Sec. 2.1.3) and the size of the drops produced at the top of the tower is known. Useful information on the dimensioning of prilling towers can be obtained from the literature [2.7–2.9].

The use of prilling towers for the conditioning of products in the form of a melt has diminished in recent years. The reason for this is partly the considerable cost of the plant (tower diameters up to 10 m and heights up to 40 m are common dimensions) and partly the problem caused by emissions resulting from the very high gas flow rates. The use of sprayed fluidized beds has frequently proved to be a suitable alternative (cf. Sec. 2.2.5). The prilling tower only offers advantages in a few cases which involve the production of very fine particles ($<300\,\mu m$).

A special form of prilling is *hydroprilling* [2.10, 2.11], in which the melt is dispersed in the form of individual drops in a coolant (usually water). As a result of the significantly better heat transfer compared with gaseous coolants, the material solidifies more rapidly (i.e., higher throughput rates per unit volume and time are possible). However, this process necessitates

expenditure on an additional plant to separate the particles from the liquid and for the subsequent drying.

2.2.5. Sprayed fluidized bed

In the sprayed fluidized-bed process [2.12, 2.13], the melt is sprayed into a fluidized bed consisting of previously crystallized material. The particles, which are in the vicinity of the jet for a short period, are wetted by the melt, which then crystallizes out on the cold solid. Depending on the process parameters selected and the properties of the material, the shape of the particles formed can range from shell-like spherical pellets to very irregularly shaped granules. The product is removed from the fluidized bed by means of a rotary valve, for example, and can subsequently be divided into fractions (e.g., by sieving). The oversize crystals are crushed, and together with the fines, they are returned to the fluidized bed so that they are again available as nuclei in the granulation process (Fig. 2.10). The particle size of the fraction to be used can be chosen anywhere in the range 0.2–4 mm, and by using appropriate sieves, it can be kept within very narrow limits.

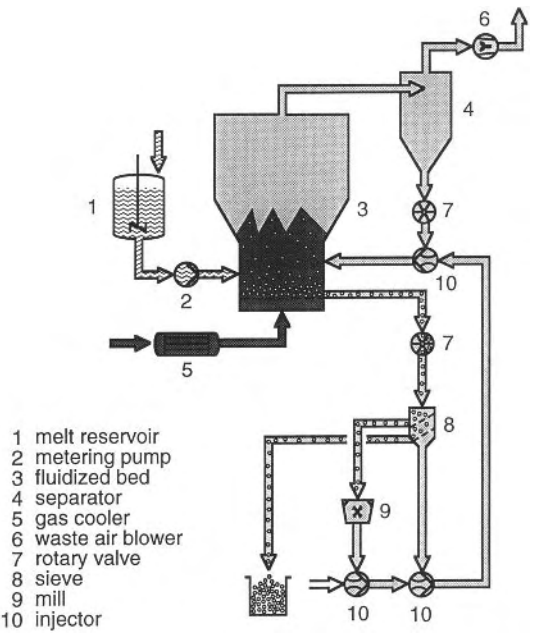

Figure 2.10. Solidification of melts in a sprayed fluidized bed.

The average residence time of a particle within the fluidized bed can be chosen over a wide range. It depends primarily on the kinetics of solidification and the tendency of the product to agglomerate and on the desired particle size. The heat removal is generally not critical; therefore, it is possible to process materials having very low nucleation rates in sprayed fluidized beds.

The air, which has to be precooled to an extent depending on the solidification temperature, acts as the fluidizing medium and, at the same time, it removes the latent heat of fusion. Because the hot exhaust air is loaded with dust particles and also, under some circumstances, with the vapor of the product, it is necessary to install suitable separators after the fluidized bed. The cost of cleaning the off-gas can be considerable, depending on the properties of the particular product and the limits to be observed for the emissions. In many cases, the cooling air is therefore recirculated and only a small fraction of it is discharged continuously.

The system described is also suitable for the granulation of dissolved solids. In this case, the air used to evaporate the solvent (usually water) has to be preheated rather than cooled. The prerequisite for using this process is that the product must exhibit good granulating properties, which, in some cases, may be achieved by suitable auxiliaries.

2.2.6. Screw crystallizer

If the vapor pressure of the melt or of the crystalline product (sublimation), or the presence of gaseous by-products that are toxic or have a noxious odor, precludes the removal of heat by convective methods (prilling tower or sprayed fluidized bed) and if very coarse and homogeneous granular material having a high bulk density is also required, the use of either an enclosed conveyor belt crystallizer with a pelleting system or of a screw crystallizer can be considered (Fig. 2.11). In the latter, the shape of the pellets obtained is determined by a die plate (usually heated) at the end of the screw. However, to be able to extrude the product, the melt must not be in a completely crystallized state at this point, or it must be remelted. In some cases, this necessitates postcooling (e.g., on a cooled belt).

In a screw crystallizer, the heat is removed by cooling the housing and the shaft. It has to be borne in mind that both the latent heat of fusion and the considerable amount of mechanical energy dissipated as heat also have to be removed. Screw crystallizers are intended primarily for the processing of high-viscosity melts. As a result of the good dispersion of nuclei formed at the cooled surfaces and the possibility of establishing different temperature zones along the screw, these crystallizers are also suited to the condi-

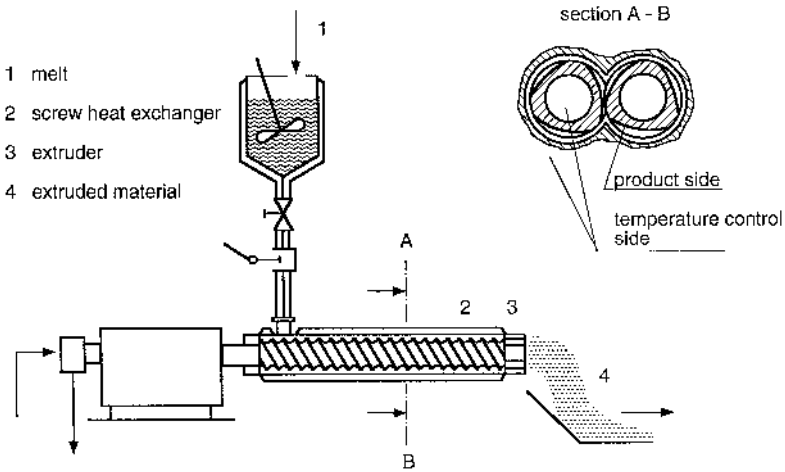

Figure 2.11. Solidification of melts in a screw crystallizer fitted with an extruder. (Courtesy of Werner & Pfleiderer Co., Stuttgart, Germany.)

tioning of kinetically retarded systems (cf. Sec. 2.1). However, overall, it is a very cost-intensive process.

2.3. Design of Equipment for Melt Solidification

The questions that must be resolved when considering the introduction of an industrial solidification process are (a) whether the crystallization kinetics can become rate determining, (b) at what cooling surface temperature a particular crystallization time is to be expected and whether there is a minimum crystallization time, and (c) whether seeding has any effect, and if so, what? These questions may be answered very easily by carrying out a basic experiment on the laboratory cooling plate previously mentioned (cf. Fig. 2.3) or by using the crystallizing trough described by Matz [2.14]. The results of this type of experiment will give some useful indications for selection of the right equipment, and for drum crystallizers and conveyor belt crystallizers, they will also enable the size of the equipment needed to be estimated.

The maximum permissible rate of rotation of the cooled drum is calculated from the measured crystallization time t_s and the ratio of the fraction of the circumference covered with crystallized material (and there-

fore being used efficiently to cool the material) to the total circumference (loading factor k_{drum}, typical value 0.7):

$$s_{\text{drum,max}} = \frac{k_{\text{drum}}}{t_s} \tag{2.2}$$

If the product is to be cooled further after solidification, t_s must be increased appropriately. To obtain the maximum output of crystalline material per unit time and cylinder area, it follows that

$$\dot{m}_{\text{drum,max}} = \rho_s \delta_s s_{\text{drum,max}} \tag{2.3}$$

To a first approximation, the relationship between the throughput and the thickness of the flake layer is given by $s_{\text{drum}} \sim \Delta\vartheta/\delta_s^2$ [cf. Eq. (2.1)]; therefore, an increase in output can be achieved by increasing the rate of rotation while decreasing the thickness of the flakes.

By analogy with equation (2.3), an estimate of the size required for a cooling belt is given by

$$\dot{m}_{\text{belt,max}} = \rho_s \delta_s \frac{k_{\text{belt}}}{t_s} \tag{2.4}$$

When the melt is applied in the form of a continuous layer (applied by gravity feed, overflow weir, or applicator roll), $k_{\text{belt}} = 1$. When a pelleting system or ribbon applicator is used, the loading factor takes account of the fact that the individual pellets or ribbons on the belt should not touch each other. Experience has shown that a realistic value for the loading factor is 0.5 when pelleting systems are employed and 0.7 for ribbon applicators.

As well as having a knowledge of the crystallization kinetics, it is necessary to know the quantities of heat that have to be removed and at what product temperature. This information can be obtained from appropriate calorimetric measurements. The example illustrated in Figure 2.12 exhibits the following feature: The product on which the measurements were made has fully crystallized at 126°C but has an additional transition point at 40°C. Bagging this product at 60°C, for example, would lead to caking, and it is therefore necessary to have an additional postcooling section in which the product is cooled to below 40°C.

To assist with the detailed design and validation of the conditioning processes described earlier, it is best to carry out trials on a pilot-plant scale. In addition to reliable data on the product throughput, these trials will provide samples of typical product material that can be characterized in terms of its particle size distribution, its behavior on storage and its flow characteristics, and other properties related to its industrial use.

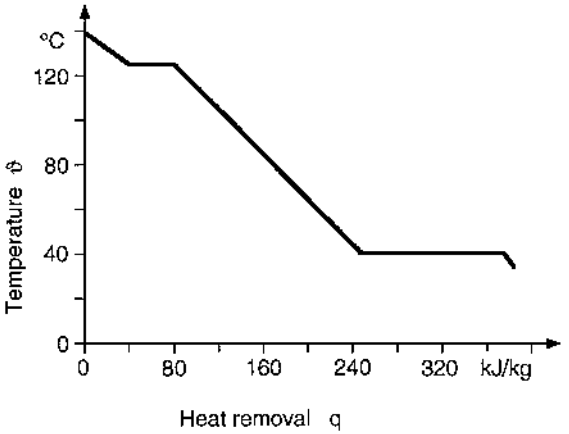

Figure 2.12. Quantity of heat to be removed as a function of the temperature.

2.4. Energy Requirement

The overall energy requirement for each of the solidification processes described in this chapter is made up of four parts:

$$\sum \dot{Q} = \dot{Q}_s + \dot{Q}_{\text{circ},p} + \dot{Q}_{\text{circ,cool}} + \dot{Q}_{\text{wa}} \tag{2.5}$$

$\dot{Q}_s$ includes the latent heat of fusion and, if appropriate, the energy used for further cooling of the solidified product. In the most favorable case, river water or air can be used, but for materials that solidify at low temperatures, it is necessary to employ energy-intensive cooling equipment (e.g., a refrigerating unit). $\dot{Q}_{\text{circ},p}$ includes the energy needed to circulate or transport the liquid or solid material. With the exception of screw crystallizers, in which considerable quantities of mechanical energy are dissipated, this term can generally be neglected.

The energy required to circulate the coolant $\dot{Q}_{\text{circ,cool}}$ can also be neglected in those processes that use indirect cooling (drum crystallizer, conveyor belt crystallizer, screw crystallizer). This also applies to the prilling tower when it can be operated under natural convection. On the other hand, this energy component is important for prilling towers using forced circulation and for the sprayed fluidized bed, in which the cooling air must overcome the resistance of the bottom plate of the fluidized bed and the layer of product on top of it.

For solidification processes carried out in drum crystallizers, conveyor belt crystallizers (with or without pelleting systems), and screw crystallizers,

the flow of waste air is generally low in comparison to the other processes. The same holds true for the associated energy consumption $\dot{Q}_{wa}$. For the prilling tower and the sprayed fluidized bed, the waste airflow is of course very high, and in these processes, the energy that has to be used to clean the waste gas is at a maximum and can be the dominant factor in some cases.

2.5. Selection of Equipment for Melt Solidification

Table 2.1 shows a qualitative comparison of the various solidification processes. A quantitative comparison would be possible only in the case of specific examples, where integration into the overall process involved can play an important part (e.g., combined cleaning of all the waste airstreams from the process, use of existing buffer tanks, etc.).

The main advantages of the pelleting system, the screw crystallizer, the prilling tower, and, to the extent that the agglomeration characteristics are satisfactory, the sprayed fluidized bed are the precisely defined form of the product and the low proportion of dust and fines in it. The crystalline materials produced in drum or belt crystallizers generally exhibit relatively poor flow properties and storage behavior, and the proportion of dust and fines is usually high. In some cases, the casting of ribbons of the melt onto a cooling belt can represent a cost-effective alternative, giving a better form of product containing a lower proportion of dust and fines.

An important boundary condition for application of the various types of solidification equipment is the solidification time. Slowly crystallizing or kinetically retarded systems cannot be processed in the prilling tower. The use of drum crystallizers is appropriate only when the solidification time is less than 2 min, although for moderately retarded systems, seeding may enable such equipment to be used. For belt crystallizers, with or without pelleting units, the solidification time should not exceed 10 min. For slowly crystallizing or kinetically retarded materials, seeding of the melt can extend the range of possible applications and/or contribute to an enhanced throughput. The residence time in screw crystallizers is usually up to 10 min, but intensive seeding and thorough dispersion of the seed crystals is ensured with this equipment; therefore, it can be used to process kinetically retarded materials. As a consequence of the long residence times in sprayed fluidized beds, the actual solidification time rarely represents a limitation for this equipment.

The capital costs of drum crystallizers and belt crystallizers are comparatively low, although pelleting units are often expensive, partly because of their costly design, and they, therefore, increase the capital expenditure compared with simple conveyor belts. This is true to a greater extent for

Table 2.1. Comparison of Solidification Processes

	Drum crystallizer	Belt crystallizer	Pelleting unit on conveyor belt	Screw crystallizer	Prilling tower	Sprayed fluidized bed
Product form	Flakes, crumbs	Strips, flakes, crumbs	Pellets	Extruded forms	Spherical particles	Spherical/ irregular particles
Proportion of dust and fines in the product	High	Medium to high	Low	Low	Low	Low to medium
Solidification time, or residence time of melt	<2 min	2–10 min	<10 min	<10 min	<15 s	<1 h
Capital costs	Low	Low	Medium to high	High	High	Medium,[a] high[b]
Energy requirement	Low	Low	Medium	Medium	Low,[a] medium[b]	Medium,[a] high[b]

[a] Low specificaiton for waste air cleaning.
[b] High specificaiton for waste air cleaning.

screw crystallizers. The capital costs for prilling towers are very high, owing to their physical size and the equipment that is generally needed to clean the high flow rates of waste air. For sprayed fluidized bed processes, a large amount of auxiliary equipment is needed in addition to the actual fluidized bed (cf. Fig. 2.10), and this means that they are more cost-intensive than the simple conditioning processes. Considerable additional investment may be needed for separators, depending on the requirements placed on the purity of the waste air.

The energy required to operate drum crystallizers or belt crystallizers is comparatively low. It will be increased if a pelleting unit is added, owing to the need to disperse the product and as a result of the lower loading density, which is equivalent to needing a larger cooling area for the same product throughput. Screw crystallizers have high-energy requirements because of the considerable dissipation of mechanical energy. The energy required to operate a prilling tower is determined mainly by the requirement to clean the waste air. This also applies to the sprayed fluidized bed, where the large number of plant units that have to be operated constitutes an additional energy demand.

To summarize, it is clear that the increasing demands placed on the quality of the product and the extra equipment needed to reduce the emissions result in plants of greater complexity and, therefore, lead to a rise in capital costs.

REFERENCES

[1.1] S. J. Jancic, Fractional crystallization, in *Proc. 10th Symp. on Industrial Crystallization* (J. Nyvlt and S. Zacek, eds.), Elsevier, Amsterdam, pp. 57–70 (1987).

[1.2] K. Wintermantel and G. Wellinghoff, Melt crystallization: Theoretical presumption and technical limits, in *Proc. 11th Symp. on Industrial Crystallization* (A. Mersmann, ed.), pp. 703–708 (1990).

[1.3] S. Rittner and R. Steiner, Die Schmelzkristallisation von organischen Stoffen und ihre grosstechnische Anwendung, *Chem. Ing. Techn.*, *57*: 91 (1985).

[1.4] M. Y. Özoguz, Zur Schichtkristallisation als Schmelzkristallisationsverfahren, Thesis, University of Bremen (1992); *Fortschr. Ber. VDI Reihe*, *3*(271) (1992).

[1.5] J. A. Burton, R. C. Prim, and W. P. Slichter, Distribution of solute in crystals grown from the melt, I. Theoretical, *J. Chem. Phys.*, *21*: 1987 (1953); II. Experimental, *J. Chem. Phys.*, *21*: 1991 (1953).

[1.6] K. Wintermantel, Wärme- und Stoffaustausch bei der Kristallisation an gekühlten Flächen, *Chem. Ing. Techn.*, *45*: 284 (1973); *45*: 728 (1973).
[1.7] S. H. Tirmizi and W. N. Gill, Experimental investigation of the dynamics of spontaneous pattern formation during dendritic ice crystal growth, *J. Cryst. Growth*, *96*: 277 (1989).
[1.8] K. Wintermantel, Die effektive Trennwirkung beim Ausfrieren von Kristallschichten aus Schmeltzen und Lösungen: eine einheitliche Darstellung, *Chem. Ing. Techn.*, *58*: 498 (1986).
[1.9] K. Wintermantel, B. Holzknecht, and P. Thomas, Density of desublimed layers, *Chem. Eng. Tech.*, *10*: 405 (1987).
[1.10] I. L. Dschu, Ausfrieren von Eis aus einer strömenden Salzlösung an gekühlten Oberflächen, *Kaltetechnik*, *19*: 278 (1967); *21*: 43 (1969).
[1.11] N. V. Lapin, D. A. Nikolaev, V. A. Malyusov, and N. M. Zhavoronkov, Occlusion of a melt during the crystallization of organic systems forming solid solutions, *Theoret. Found. Chem. Eng.* (*USSR*), *10*: 462 (1977).
[1.12] N. V. Lapin and V. A. Malyusov, Calculation of impurity distribution in crystallization of mixable melts with a cellular crystallization front, *Theoret. Found. Chem. Eng.* (*USSR*), *15*: 836 (1981).
[1.13] J. Ulrich and Y. Özoguz, Das Schwitzen: Ein Schritt zur Steigerung der Reinigung bei der gerichteten Kristallisation, *Chem. Ing. Techn.*, *61*: 76 (1989).
[1.14] J. Ulrich and Y. Özoguz, Directed crystallization and sweating: A comparison of two different approaches, in *Proc. 11th Symp. on Industrial Crystallization* (A. Mersmann, ed.), pp. 821–826 (1990).
[1.15] B. Holzknecht, H. Fuchs, E. Hetzel, K. Wintermantel, and P. Thoma, Verfahren zur Reinigung ausgefrorener Kristallschichten, German Patent DE 3708709 A 1 (March 18, 1987).
[1.16] K. Stolzenberg, Der Blasensäulenkristaller, *Chem. Ing. Techn.*, *55*: 45 (1983).
[1.17] J. Ulrich, S. J. Jancic, and A. K. Kuszlik, The effect of dissipative mixing on separating efficiency of progressive freezing of organic melts, in *Proc. 11th Symp. on Industrial Crystallization* (A. Mersmann, ed.), pp. 815–820 (1990).
[1.18] O. Fischer and A. Kuszlik, Kristallisation ohne Lösungsmittel, *Tech. Rundschau Sulzer*, *2*(92): 9 (1992).
[1.19] P. J. Ruegg, Destillation plus Kristallisation, *Chem. Ind.*, *112*(11): 83 (1989).
[1.20] G. Wellinghoff and K. Wintermantel, Schmelzkristallisation: Theoretische Voraussetzungen und technische Grenzen, *Chem. Ing. Technol.*, *63*: 881 (1991).

[1.21] K. Genthner, Trennung binärer Gemische durch Erstarren in einem Rohr bei turbulenter Strömung, *Chem. Ing. Techn.*, *44*: 587 (1972).
[2.1] G. Tamman, *Aggregatzustände*, Leopold Voss, Leipzig (1922).
[2.2] M. Volmer, *Kinetik der Phasenbildung*, Theodor Steinkopff, Dresden (1939).
[2.3] M. Preger, Anwendung und Bauformen der Kühlwalze, *Aufbereitungstechnik*, *11*: 551 (1970).
[2.4] G. Matz, Apparate für die Kristallisation, *Chem. Ing. Techn.*, *51*: 1014 (1979).
[2.5] G. Kaiser and H. Kaiser, Pastillieren, *Verfahrenstechnik*, *4*: 390 (1970).
[2.6] H.-P. Wirges, Apparate für die Kristallisation, *Chem. Ing. Techn.*, *63*: 1065 (1991).
[2.7] K. Masters, *Spray Drying Handbook*, 5th ed., John Wiley & Sons, New York (1991).
[2.8] P. Schweizer, B. Covelli, and F. Widmer, Dimensionierung eines Prillturms, *Chimia*, *29*: 78 (1975).
[2.9] L. G. Wells and I. Kern, Ein vereinfachtes Modell zur Berechnung der Abmessungen und der Leistungsdaten eines Prillturms, *Chem. Ing. Techn.*, *51*: 674 (1979).
[2.10] C. Müller and F. Widmer, Granulieren im Flüssig–Flüssig-Sprühverfahren (Hydroprilling), *Swiss Chem.*, *8*(2a): 31 (1986).
[2.11] E. Wehner and D. Voegele, Mikrokugeln-Herstellung und Eigenschaften, *Acta Pharm. Tech.*, *29*(2): 113 (1989).
[2.12] H. Uhlemann, Kontinuierliche Wirbelschicht-Sprühgranulation, *Chem. Ing. Techn.*, *62*: 822 (1990).
[2.13] S. Mortensen and S. Hovmand, Production of non-dusty granular products by fluid bed spray granulation, in *18th Chemical Engineering Exhibition Congress* (1976).
[2.14] G. Matz, *Kristallisation*, 2nd ed., Springer-Verlag, Berlin (1969).

15

Thermal Analysis and Economics of Processes

A. MERSMANN Technische Universität München, Garching, Germany

In addition to labor costs, the costs of a crystalline product are determined primarily by capital costs and energy costs. For a given production capacity, the capital costs depend on the type and volume V of the crystallizer and the heat transfer area A necessary for cooling or evaporative crystallizers and, of course, on such auxiliary equipment as circulation and vacuum pumps and ejectors. As a rule, the capital costs increase approximately to the power 2/3 (surface/volume ratio of tank diameter) of the volume V. Therefore, it is reasonable and economical to install the entire capacity in a single crystallizer, but this single unit has to operate very reliably. A prerequisite for safe operation for a long period is a good design of the crystallizer equipped with sufficient measuring and control devices and operated under slow incrustation rate. With respect to constant optimal $\Delta c_{opt} < \Delta c_{met}$, optimal crystal growth rate and low-nucleation-rate crystallizers operated continuously at constant operating parameters are superior to batch crystallizers. Of course, the operating mode may depend on the capacity of the unit. The costs of centrifuges or filters and dryers necessary for dewatering and drying are dependent on the mean crystal size L_{50} and the crystal size distribution

(CSD) of the product. This is true not only for the capital costs but also for the energy costs.

To get a better understanding of the economical situation of a crystallization process, some information on the operating parameters that influence investment and energy costs will be given. Because incrustation is decisive for the operating time and the availability of the plant, an additional short chapter is devoted to this problem. The fundamentals of incrustation have been described in Chapter 9.

1. CAPITAL COSTS OF CRYSTALLIZERS AND OPERATING PARAMETERS

In Chapter 8, the following equation for the separation index SI has been derived (valid for diffusion-controlled growth):

$$\mathrm{SI} \equiv \dot{M}_c V L_{32} = \frac{\beta}{\alpha} \varphi_T k_d \Delta c \tag{1.1}$$

The volume V necessary for the production rate $\dot{M}_c$ increases with increasing mean crystal size $L_{50} \approx L_{32}$ but decreases with rising suspension density m_T or volumetric crystal holdup φ_T. Equation (1.1) can be regrouped and simplified for $\alpha = 1$ and $\beta = 6$ according to

$$\dot{M}_c = \frac{\beta}{\alpha} \varphi_T k_d \frac{\Delta c}{L_{50}} V \approx 6 \varphi_T k_d \frac{\Delta c}{L_{50}} V \tag{1.2}$$

with $\Delta c \leq \Delta c_{\mathrm{met}}$. It is important to remember that the appropriate supersaturation is decisive not only for the crystallizer volume but also for the product quality because $L_{50} = f(\Delta c)$.

In Figure 1.1, the production rate $\dot{M}_c$ is plotted against the crystallizer volume V for the mean crystal sizes $L_{50} = 0.1\,\mathrm{mm}$ and $L_{50} = 1\,\mathrm{mm}$ and for the supersaturation $\Delta c = 1\,\mathrm{kg/m^3}$ and $\Delta c = 10\,\mathrm{kg/m^3}$. These supersaturations correspond to the metastable zone width of many systems with high solubilities $c^*/\rho_c > 0.01$, as has been shown in Chapter 8. The lines in Figure 1.1 are valid for the volumetric holdup $\varphi_T = 0.2$ and the mass transfer coefficient $k_d = 2 \times 10^{-4}\,\mathrm{m/s}$.

As can be seen from Figure 1.1, crystallizers with small volume V for a given production rate are sufficient if a fine product is produced at a high supersaturation level. However, when a coarse product is wanted by the customer, it is necessary to install a large crystallizer that is operated at low supersaturation and optimum residence time. Further increases in mean crystal size can be obtained by the reduction of attrition and dissolving of fines. Again, we see that the capital costs increase strongly with the

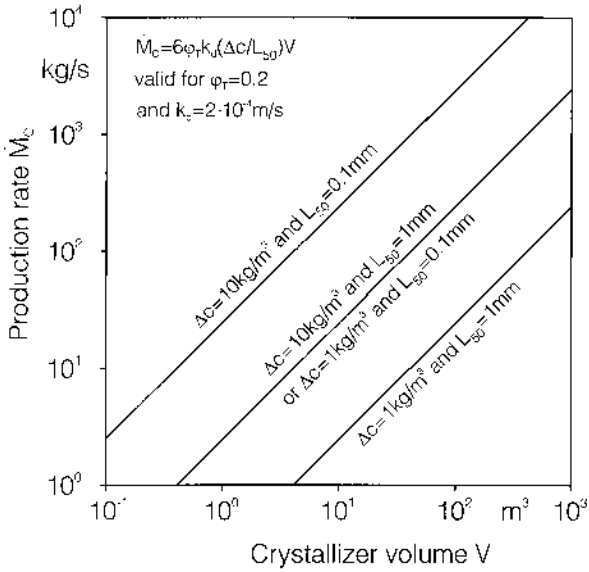

Figure 1.1. Production rate $\dot{M}_c$ versus crystallizer volume V for various supersaturations and mean crystal sizes.

crystal size wanted by the customer. This is also true for the investment costs of a heat exchanger if incrustation should be low to obtain long operating times.

The annual production of a crystallizer is the production rate $\dot{M}_c$ times the annual production period, which is reduced by the shutdown time necessary for cleaning after excessive incrustation. In the absence of removal processes, the thickness and mass of a hard crust of crystals is closely related to the local supersaturation on the heat transfer surfaces, which depends on the heat flux density $\dot{q}$. The supersaturation Δc can be expressed by the temperature difference $\Delta\vartheta$ or ΔT on the wall [ϑ(°C); T(K)] :

$$\Delta c = \frac{dc^*}{d\vartheta}\Delta\vartheta = \frac{dc^*}{dT}\Delta T \tag{1.3}$$

A combination of this equation with

$$\dot{Q} = hA(\Delta\vartheta) = hA(\Delta T) \tag{1.4}$$

for heat transfer leads to

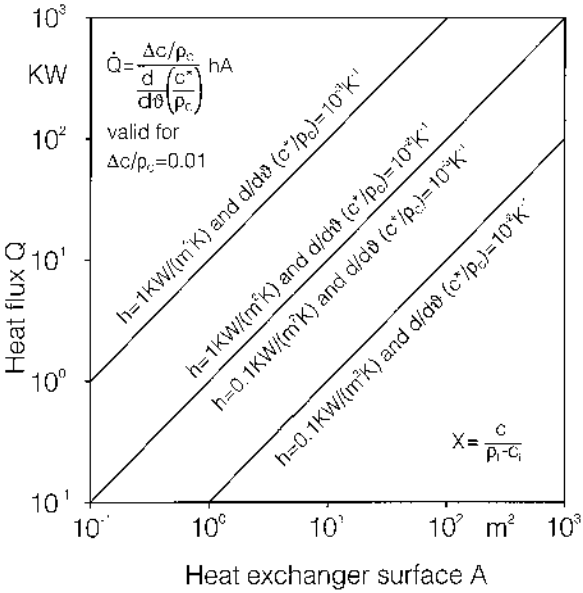

Figure 1.2. Heat flux $\dot{Q}$ versus heat transfer area A for various heat transfer coefficients and slopes of the solubility curve.

$$\dot{Q} = h\frac{\Delta c}{dc^*/d\vartheta}A = h\frac{\Delta c/\rho_C}{d(c^*/\rho_C)/d\vartheta}A = h\frac{\sigma T}{d(\ln c^*)/d(\ln T)}A \tag{1.5}$$

with $\Delta c \leq \Delta c_{\text{met}}$; compare Sec. 6 in Chapter 3. The metastable zone width for highly soluble systems with $c^*/\rho_C > 0.01$ is approximately $\Delta c_{\text{met}}/\rho_C \approx 0.01$. In Figure 1.2, the heat flux $\dot{Q}$ is plotted against the heat transfer area A for the two heat transfer coefficients $h = 0.1\,\text{kW/m}^2\,\text{K}$ and $h = 1\,\text{kW/m}^2\,\text{K}$ and for the two slopes of the solubility curve:

$$\frac{d}{d\vartheta}\left(\frac{c^*}{\rho_C}\right) = 10^{-3}\,\text{K}^{-1} \quad \text{and} \quad \frac{d}{d\vartheta}\left(\frac{c^*}{\rho_C}\right) = 10^{-2}\,\text{K}^{-1} \tag{1.6}$$

In Figure 1.3, derivatives $d(c^*/\rho_C)/d\vartheta$ for some systems are plotted against the temperature. For a given heat flux $\dot{Q}$, the heat transfer area A is small if the heat transfer coefficient is high but the solubility increases weakly with the temperature.

Figure 1.2 gives minimum heat transfer surfaces because it is valid for the highest supersaturation Δc_{met} that will lead to a certain degree of incrustation. The incrustation rate can be reduced and the operating time extended by decreasing the mean supersaturation $\Delta c < \Delta c_{\text{met}}$ in the crystallizer.

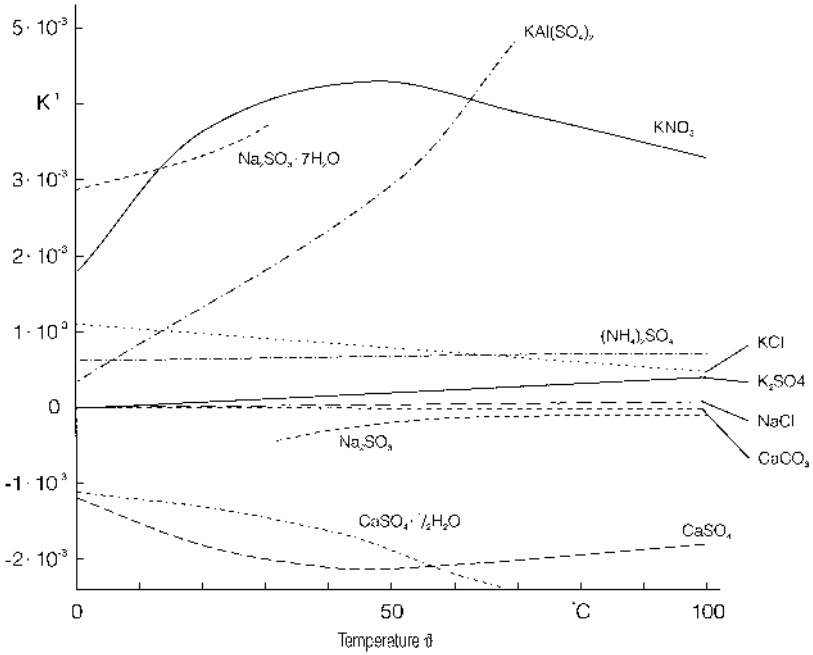

Figure 1.3. Slope of the solubility curve versus temperature for some aqueous systems.

2. ROLE OF INCRUSTATION FOR ECONOMICS

In Chapter 9, a variety of measures have been described to reduce incrustation:

- Smooth surfaces without crystal traps
- Surfaces with low affinity to nuclei
- Coated surfaces
- Ultrasonic vibrations of surfaces
- High slurry velocity to avoid settling of particles
- High wall shear stress to erode deposits and crusts
- Low superficial vapor velocity in vapor body
- Irrigation of surfaces with undersaturated liquid
- Complete insulation; heating of endangered spots
- Low bulk supersaturation and especially low wall supersaturation
- Low-temperature difference or heat flux density
- Addition of additives

Unfortunately, all these measures will increase the capital costs, the operating costs, or both. These increased costs must be balanced with the profit obtained by a reduction in incrustation and extended crystallizer running time. It is not possible to present general recommendations because the efficiency of the measures mentioned earlier is not clear, neither quantitatively nor even qualitatively in some cases. Furthermore, the design and operation of any crystallizer is embedded in a special technological and economical situation; therefore, it is difficult to present general rules with respect to incrustation. The best way is to determine the optimal value of each operating parameter under engineering and economical aspects. Some hints for this procedure are presented in the following sections.

3. MODEL OF SOLIDS PRODUCTION PROCESSES

As a rule, a solid production process consists of three different operation units: crystallization/precipitation, solid–liquid separation by centrifuges or filters, and drying of the wet crystals. Each unit will be analyzed with the objective of minimizing the energy consumption. Operating conditions, process design, and other chracteristic parameters (crystal size, porosity, and physical properties) are discussed to evaluate their influences on the process.

Figure 3.1 shows a solids production process comprising evaporation of the feed brine, crystallization, solid–liquid separation, and drying. In the case of evaporation crystallization, the feed brine is first concentrated to

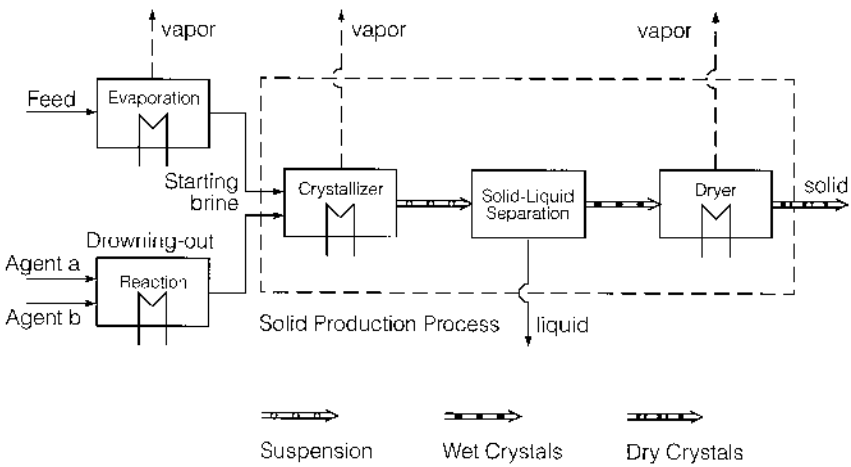

Figure 3.1. Scheme of a solids production process flow pattern.

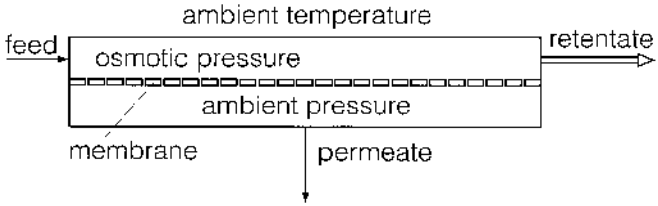

Figure 3.2. Membrane separation process.

saturation concentration c^* or mass fraction y^* by a process that separates the solvent (i.e., by evaporation).

The flowsheet shows that energy is required primarily for (a) evaporation of solvent in the crystallizer, (b) evaporation of residual mother liquor from the wet crystals, and (c) operation of centrifuges or filters. In addition, energy is needed for (d) the removal of heat during cooling crystallization and (e) the removal of heat of mixing or reaction in the case of drowning-out or reaction crystallization.

Some ideas for an optimal design of solids production processes may be found by taking a closer look at a membrane separation process (reverse osmosis) (see Fig. 3.2). To transport the solvent (permeate) through the membrane, the partial pressure of the solvent in the feed has to surpass the osmotic pressure $\Delta\Pi$ according to [3.1, 3.2]

$$\Delta\Pi = -\frac{\Re T}{V_{\text{solv}}}\ln\frac{a_{\text{solv},0}}{a_{\text{solv},1}} = -\frac{\Re T}{\tilde{V}_{\text{solv}}}\ln\left(\frac{\gamma_{\text{solv},0}y_{\text{solv},0}}{\gamma_{\text{solv},1}y_{\text{solv},1}}\right) \tag{3.1}$$

or with the mass fraction y_i of the solute,

$$\Delta\Pi = -\frac{\Re T}{\tilde{V}_{\text{solv}}}\ln(1 - Ay_i) \tag{3.2}$$

where A is a constant, a the activity, and $\tilde{V}_{\text{solv}}$ the molar volume of the solvent.

Today, the industrial technique is able to produce pressure differences of approximately 100 bar. This leads to a maximum mass fraction according to equation (3.2) of about $y_i = 0.13$. This mass fraction is achievable under the assumption that the effective pressure is equivalent to the osmotic pressure; in reality, the effective pressure has to be three times greater than the osmotic pressure to be able to obtain the theoretical maximum mass fraction.

The great advantage of reverse osmosis is the extremely low specific energy consumtion compared with that of a multistage flash evaporator. However, most of the energy is required as electric energy for the pumps to build up the necessary pressure difference.

The energy consumption of the real solids production process will be compared with the energy consumption of a theoretical membrane process. In engineering, comparisons of theoretical (but impractical) processes with real processes are common for determining the minimum energy consumption. In this case, it is assumed that this comparative membrane process separates the feed brine into solid dry crystals and solute-free solvent. The lowest osmotic pressure $\Delta\Pi$ required represents the minimum separation energy per unit volume of solution. The energy ratio

$$\frac{e_C}{e_{C,\min}} = \frac{\text{Energy of the real separation process}}{\text{Energy of the membrane separation process}}$$

will be used to evaluate the efficiency of the process. The minimum energy, $W_{\min}/M_C$, based on the mass unit of dry crystals M_C can be written as [3.3]

$$\frac{W_{\min}}{M_C} = -\frac{\Re T}{\tilde{M}_{\text{solv}}} \int_{y_0}^{y_1} \frac{\ln(1 - Ay_i)}{y_i^2}\, dy_i \tag{3.3}$$

Due to this fact, we can learn from the membrane process how the energy consumption of the solids production process can be reduced:

1. Separation should be carried out at ambient temperature.
2. Solvent has to be withdrawn from solution in the liquid state.

When evaporation crystallization must be used with respect to small slopes $dy^*/d\vartheta$ of the solubility curve $y^* = f(\vartheta)$, the energy consumption can be appreciably reduced by replacing a single-effect crystallizer by a multiple-effect crystallizer and/or by thermocompression.

4. ENERGY OF THE EVAPORATION STEP

In Figure 4.1, the flowsheet of a five-effect evaporation crystallization unit with compression of the vapor of the fifth effect is shown. The compressed vapor is used to preheat the feed brine and to heat the first evaporator. As a rule, pressures and temperatures can be chosen in such a way that solvent is released only in the liquid state, with the result that all of the heat of evaporation is consumed within the process. However, it is necessary to compress the vapor released in the final effect. Because the condensation temperature of the compressed vapor must exceed the boiling temperature of the feed brine, the final pressure p_0 has to be chosen correspondingly. The power consumption of the compressor increases with increasing pressure ratio p_0/p_5 for a given vapor flow rate. On the one hand, a low-pressure ratio p_0/p_5 results in low power consumption, but, on the other hand, it requires large heat transfer areas of the evaporators and the preheater

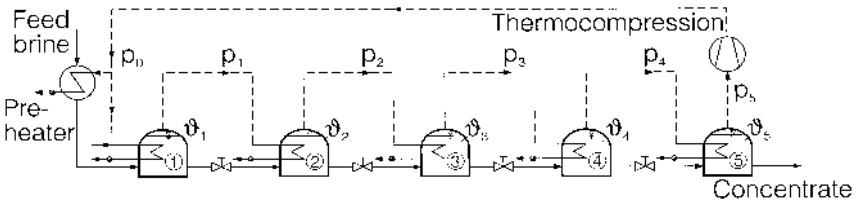

Figure 4.1. Flowsheet of a five-effect evaporation crystallizer unit with thermo compression of the vapor released from the fifth effect.

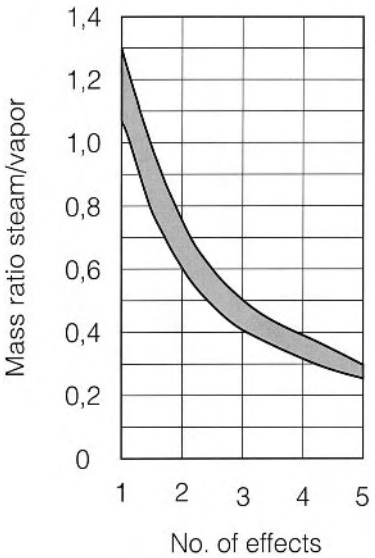

Figure 4.2. Mass ratio steam/vapor versus number of effects.

because the temperature differences $\Delta\vartheta$ are low. Energy costs can be reduced by installing a more expensive plant, which leads to higher investment costs. According to Figure 4.1, energy can be saved by (a) preheating the feed brine by waste energy, (b) multiple-effect evaporation, and (c) compression of the vapor either by thermal compression via a steam-jet ejector or by mechanical compression. With respect to low energy consumption, the number of effects should be large and the pressure ratio of the thermal or mechanical compressor should be low.

In Figure 4.2, the mass ratio kg steam/kg vapor (valid for water as solvent) is plotted against the number of effects. Energy consumption

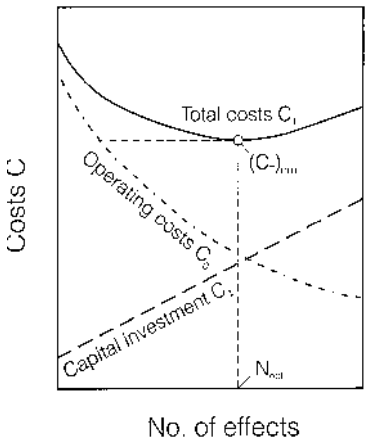

Figure 4.3. Capital investment, operating costs, and total costs versus number of effects.

decreases with the number of effects. However, capital investment increases. In Figure 4.3, capital investment, operating costs (mainly energy costs), and total costs are plotted against the number of effects. As a rule, the total costs pass through a flat minimum.

When dealing with vapor compression, the final pressure must be chosen such that the condensing temperature just exceeds the boiling temperature of the solution. In this case, energy consumption is minimal. However, a large temperature difference $\Delta\vartheta$ of the evaporator is necessary to transfer the heat. Energy consumption increases with increasing pressure ratio, but the heat transfer area A of the evaporator (capital investment) decreases (see Fig. 4.4). In Figure 4.4, capital investment, operating costs (mainly energy costs), and total costs are plotted against the pressure ratio, which can also be expressed as temperature difference $\Delta\vartheta$. The minimum temperature difference $\Delta\vartheta_{min}$ and the minimum pressure ratio $(p_5/p_0)_{min}$ depend on the boiling temperature of the solution in evaporator 1. Of course, it is possible and it may be economical to use the compressed vapor in any other evaporator.

Thermal compression is economical at low suction pressures because steam consumption decreases with an increasing ratio of motive steam pressure to suction pressure in a steam-jet ejector. Approximate values of steam consumption can be read from Figure 4.5, in which the entrainment ratio kg vapor/kg steam is plotted against the boiling temperature of aqueous solutions for the pressures 0.5 and 1 MPa of the motive steam [4.1].

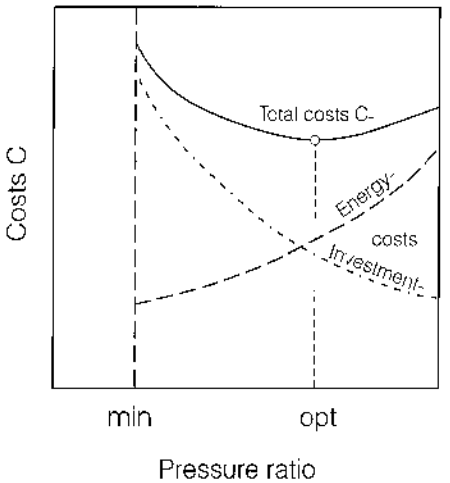

Figure 4.4. Capital investment, operating costs, and total costs versus pressure ratio.

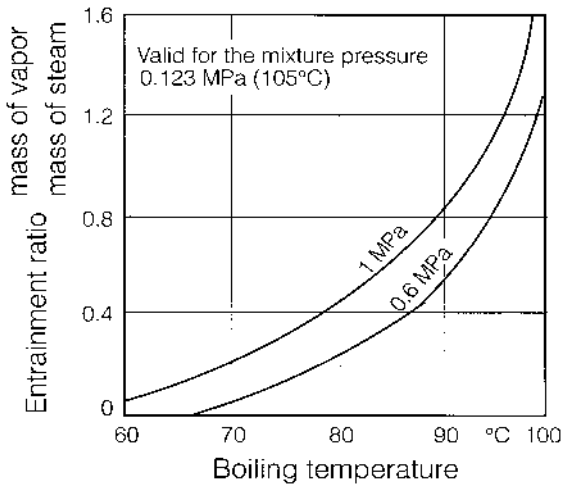

Figure 4.5. Entrainment ratio versus boiling temperature.

When dealing with mechanical compressors, incrustation and fouling of the blades and casing can become a severe problem. Average energy consumption in mechanical compression is 33 kW h/ton of vapor in single-effect evaporation, 16.5 kW h/ton in two-effect evaporation, and 11 kW h/

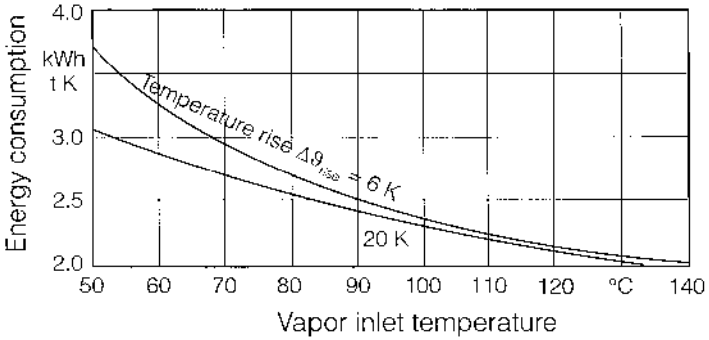

Figure 4.6. Energy consumption versus vapor inlet temperature.

ton in three-effect evaporation [4.1]. The value 33 kW h/ton of vapor is only approximate. Exact data depend on the vapor inlet temperature and the temperature rise $\Delta\vartheta_{\text{rise}}$; see Figure 4.6, in which the energy consumption based on a unit mass vapor and a unit temperature rise is plotted against the inlet temperature [4.2]. However, it is important to keep in mind that the most economical flowsheet always depends on the costs of energy (steam, electricity) at the plant site. It may be difficult to decide whether multiple-effect evaporation, mechanical or thermal compression, or a combination of these possibilities is the most economical solution. A rough guide may be that 1 ton of steam at 0.6 MPa can be considered equivalent to 150 kW h [4.1]. In any case, a careful study of the entire evaporation process is recommended.

For the following sections, it seemed reasonable to go through the production process backward, from the drying step to the crystallization step, to detect main energy losses and to develop a process of low energy consumption.

5. ENERGY OF THE DRYING STEP

When crystals with adherent mother liquor are dried by a preheated agent (hot air) that flows through the solid material, a low energy consumption is obtainable if the moist gas (air) released is nearly saturated with vapor. In this case, the flow $\dot{G}$ of the drying gas is at a minimum. With the gas concentration ratio

$$Y = \frac{\text{kg gaseous solvent}}{\text{kg gas}}$$

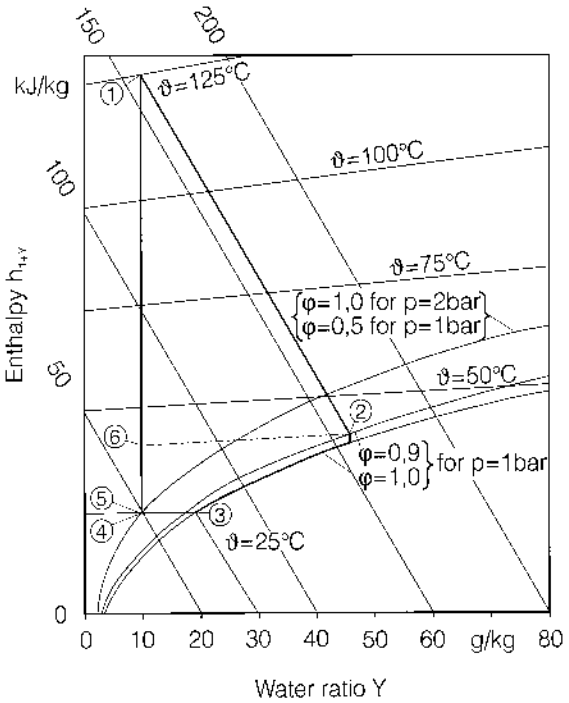

Figure 5.1. Enthalpy–concentration diagram for air–water.

the concentration ratio

$$X = \frac{\text{kg liquid solvent}}{\text{kg dry crystals}}$$

of the crystals, the enthalpy h_{1+Y} in kJ/kg gas of 1 kg dry gas $+Y$ kg gaseous solvent, and the enthalpy $\Delta h_{LG} =$ kJ/kg liquid solvent as the heat of evaporation of the solvent, the energy balance of the dryer can be written for the mass flow $\dot{M}_C$ of the crystals as

$$\dot{M}_C \Delta X \Delta h_{\mathrm{LG}} = \dot{G} \Delta Y \Delta h_{\mathrm{LG}} = \dot{G} \Delta h_{1+Y} \tag{5.1}$$

It is easy to obtain the enthalpy difference Δh_{1+Y} from the slope

$$\Delta h_{\mathrm{LG}} = \frac{dh_{1+Y}}{dY} = \frac{\Delta h_{1+Y}}{\Delta Y} \tag{5.2}$$

if an enthalpy-concentration diagram is available (see Fig. 5.1) [5.1]. (This diagram is valid for the system dry air–water at 1 bar. It is no problem to calculate such diagrams for other pressures, other carrier gases, or other

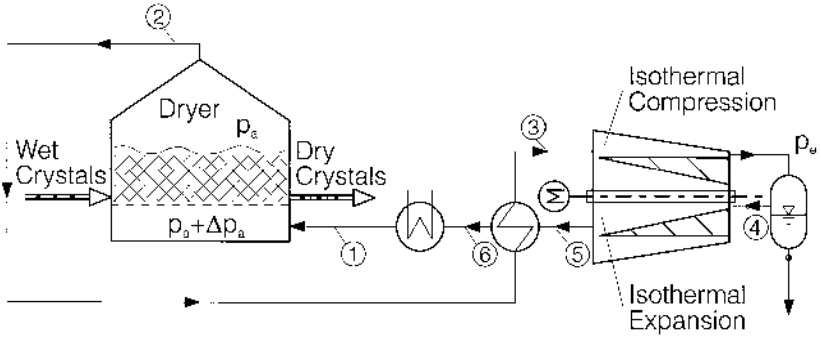

Figure 5.2. Scheme of an ideal drying process with reduced energy consumption.

solvents.) The specific energy consumption per unit mass solvent is low if the slope of the line according to the derivative dh_{1+Y}/dY is small. However, the specific energy consumption per mass unit crystals

$$e_C = \Delta X \Delta h_{\mathrm{LG}} \tag{5.3}$$

increases with the moisture difference $\Delta X = X_\alpha - X_\omega$ of the wet crystals. This consumption e_C can be reduced substantially by two measures: (a) reduction of the moisture loading ΔX (or $X_\alpha \to 0$ for $X_\omega \to 0$ for non-hygroscopic matter) and (b) release of the dried-out solvent in the liquid state ($\Delta h \to 0$). The efficiency of the first measure depends strongly on the median crystal size and, thus, on the crystallization process. With respect to the second measure, a drying process comprising an isothermal two-pressure circuit of the drying gas, with a combination of a compressor and an expansion turbine, is able to remove the moisture in the condensed or liquid phase. It is assumed that compression and expansion are carried out in the same machine and that heat of compression is immediately transferred to the expanding gas (see Fig. 5.2).

The compression of the drying gas from p_a to p_e is necessary to increase the partial pressure of the gaseous solvent, which can then be condensed by compression and withdrawn in the liquid state. In Figure 5.1, lines of constant relative humidity φ for two different total pressures are shown (air–water system, $p_a = 0.1$ MPa and $p_e = 0.2$ MPa). Such a diagram is helpful in choosing the pressure ratio p_e/p_a which depends primarily on the temperature of the cooling water and the heat transfer area. The energy consumption of such a drying process consists of the following:

1. Pressure drop $\Delta p_a + \Delta p_e$ of the gas flowing in the circuit, especially the pressure loss in the fixed or fluidized drying bed
2. Friction losses of the compressor and the turbine and deviation from isothermal compression and expansion
3. Heat loss of the entire set of equipment

This drying process has two advantages: minimum heat consumption ($h_1 - h_6$) (see Fig. 5.2) and closed circuit [i.e., no fresh air (independent of meteorological conditions) and no release of polluted air]. In addition to $\Delta h_{LG} \to 0$, another advantage is a small solvent concentration loading difference ΔX of the crystals. This can be obtained by efficient solid–liquid separation of the slurry and depends on the properties of the suspension withdrawn from the crystallizer.

6. SOLID–LIQUID SEPARATION

Because the mother liquor separated from the slurry is recycled and it is not necessary to have a solution free of small crystals, centrifuges are often used for the solid–liquid separation of crystal slurries. The residual moisture ratio X_α = kg solution/kg crystals depends on (a) the size distribution and porosity of crystals and the median crystal size L_{50}, (b) the physical properties of the liquid, such as viscosity η_L and surface tension γ_{LG}, (c) the operating conditions, such as throughput or residence time τ, and (d) the geometry and operating conditions of the centrifuge.

The residual liquid of a cake which is released by the centrifuge is shown in Figure 7.4.1. In Figure 6.1, the porosity ψ is plotted against the crystal size L. The residual liquid loading X_α is low if the following hold:

1. The median particle size L_{50} is large.
2. The porosity ψ of the crystalline cake is large.
3. The viscosity η_L and the surface tension γ_{LG} of the liquid are low.
4. The separation time τ of the solid in the centrifuge exceeds a minimum value $\tau^*_{sep,min}$ (see Fig. 7.4.1).
5. The thickness s of the solid layer in the centrifuge is low.

A cake thickness $s = 35 \times 10^{-3}$ m, a residence time $\tau = 100$ s, and an acceleration number $z = 500$ are assumed to calculate the quantity of the adhering mother liquor for further calculations. A sensitivity analysis shows that the median crystal size L_{50} is very important. Large, nearly monosized crystals with high L_{50} values exhibit the smallest residual liquid mass ratio X_α of the separated crystals. As a consequence, the crystallization process

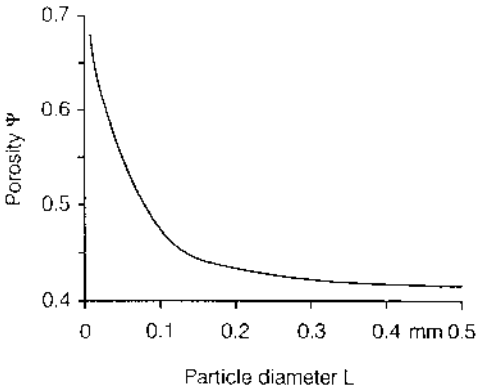

Figure 6.1. Porosity versus particle diameter.

must be carried out in such a way that a coarse crystalline product with a small coefficient of variation is obtained.

7. CRYSTALLIZATION OR PRECIPITATION STEP

From an analysis of the drying time and the solid–liquid separation unit, we can learn that the main objective of a crystallization or precipitation process is to obtain a product with (a) a large median crystal size L_{50}, (b) a small coefficient of variation of the particle size distribution, (c) a regular and compact crystal shape (nearly isometric crystals), and (d) a high degree of purity. The median crystal size is large for low nucleation rates B and high crystal growth rates G. Both kinetic parameters, B and G, depend on supersaturation Δc or on relative or dimensionless supersaturation $\sigma = \Delta c/c^*$ or $\Delta c/\rho_C$, respectively, as shown in Chapter 7.

Numerous experiments carried out in mixed suspension, mixed product removal (MSMPR) and batch-operated crystallizers have shown that the median crystal size L_{50} decreases with increasing relative supersaturation (see Fig. 7.1, in which the median crystal size L_{50} is plotted against $\Delta c/c^*$ [7.1, 7.2]. The relationship $L_{50} = f(\sigma)$ shown in Figure 7.1 is supported by experimental results on more than 40 inorganic and organic systems crystallized in laboratory and industrial crystallizers of different size and under different operating conditions; compare Figure 7.1.4. Consequently, we can learn that industrial crystallizers should be operated at the optimum relative supersaturation σ. In the case of highly soluble systems, secondary nucleation is dominant. In this case, the

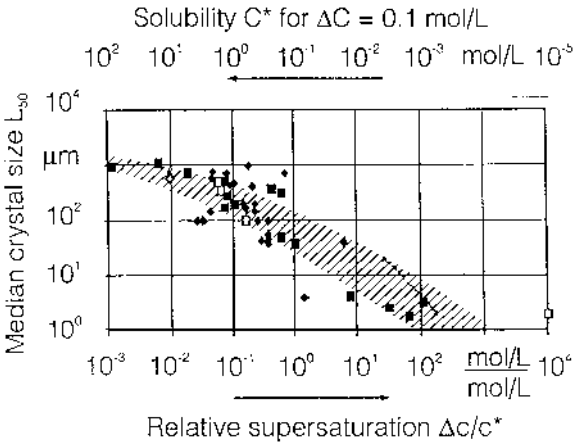

Figure 7.1. Median crystal size versus relative supersaturation: ■ inorganic systems [7.1]; □ inorganic systems; ◆ organic systems.

relationship among the rate of secondary nucleation B_0/φ_T, the mean specific power input $\bar{\varepsilon}$, and the crystal growth rate G can be expressed by

$$\frac{B_0}{\varphi_T} \sim (\bar{\varepsilon})^r G^i \tag{7.1}$$

with $r \approx 0.73$ and $1.5 < i < 2.0$ (see Chapter 5).

A general chart can be derived from these fundamental relationships that are based on experimental results and theoretical considerations. In this chart, the median crystal size L_{50}, which is based on the maximum median size $L_{50,\varepsilon_{\min}}$ valid for the minimum specific power input $\varepsilon_{\min}$ necessary to suspend the crystals, is plotted against the ratio $\varepsilon/\varepsilon_{\min}$ with the crystal growth rate $G = f(\Delta c)$ as the parameter for brittle crystals (KNO_3) (see Fig. 7.2). If plastic crystals would be used, the decrease in the median crystal size with specific power input would be less pronounced.

The main result is that a crystallizer should be operated at minimum specific power input $\varepsilon_{\min}$ [see Equation (8.6.27)] and at optimum supersaturation Δc_{opt} or crystal growth rate G, which may differ from system to system. Now we are in the position to analyze the entire solid production process thermally in order to evaluate energy consumption and the energy-saving potential.

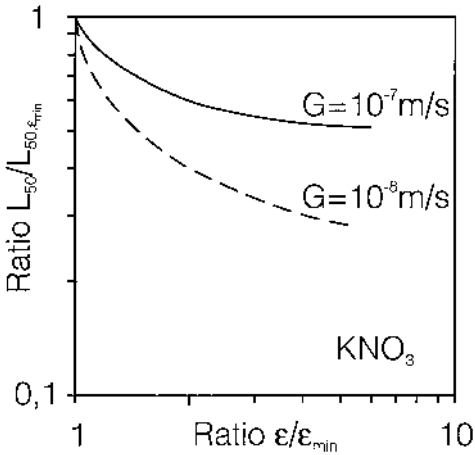

Figure 7.2. Influence of the specific power input on the median crystal size L_{50}.

8. THERMAL ANALYSIS OF THE ENTIRE PROCESS [3.3]

The total energy consumption consists of the energy required in the evaporation, crystallization, solid–liquid separation, and drying steps of the entire process. In the case of evaporation crystallization, energy costs can be kept very low by means of multiple-effect evaporation and vapor compression. Optimization calculations lead to the most economical plant (number of effects) and to the minimum energy consumption of this plant with relatively high capital investment but minimum total costs.

There is less knowledge on how to minimize the energy consumption of the entire process because the energy required for operating centrifuges (capacity and operating time) and dryers depends largely on the median crystal size L_{50} and the porosity ψ of the crystal cake. An analysis of the drying step leads to the result that energy consumption in this step can be reduced by 44% when doubling the median crystal size from 10 to 20 μm. By increasing the crystal size by a factor of 5 from 10 to 50 μm, which is possible through proper crystallizer design and operation, only 27% of the drying energy is needed (see Fig. 8.1). However, this effect slows down with increasing median crystal size. For crystals with a median size greater than 500 μm, the drying energy ratio is nearly constant.

Calculations of the energy consumption of the entire solids production process show that evaporation crystallization needs most of the energy. The

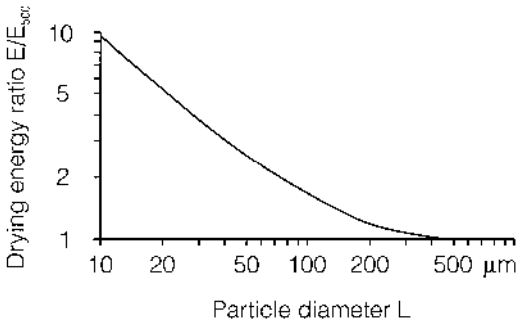

Figure 8.1. Drying energy ratio versus particle diameter.

calculated evaporation crystallization data are based on the assumption that a brine with mass fraction $y_i = 0.2$ is concentrated to $y_i = 0.33$ by a 50% evaporation of water in a five-effect evaporator. This leads to an energy consumption of about 1000 kJ/kg dry crystals for the crystallization unit. The energy consumed by centrifugation is comparatively small (28.8 kJ/kg dry crystal). The energy consumption of the drying unit depends strongly on the particle size of the product, as shown in Figure 8.1.

Calculations of the energy costs show that the separation energy per unit mass of dry crystals consumed by the real solid production process is 7.9 times higher than in the theoretical membrane separation process (see Fig. 8.2) for a median crystal size of $L_{50} = 500\,\mu m$.

In the case of a coarse product with $L_{50} = 500\,\mu m$, energy consumption in the solid–liquid separation and drying steps represents less than 10% of the total energy consumption of the solids production process. This means that approximately 90% of the total energy is consumed in the evaporation step. However, when dealing with a fine crystalline product of $L_{50} = 10\,\mu m$, 30–40% of the total energy is necessary for slurry separation and drying and only 60–70% is consumed in the evaporation step. In any case, the total energy costs per mass unit of crystalline product increase with decreasing median crystal size L_{50}.

9. OVERALL ECONOMICS

After all, the design of crystallizers and crystallization processes is a problem of economical optimization. In Figure 9.1, the capital costs, operating costs, and total costs are plotted against the investment of the entire plant. As a rule, the total costs pass through a flat minimum. The benefits of an increase

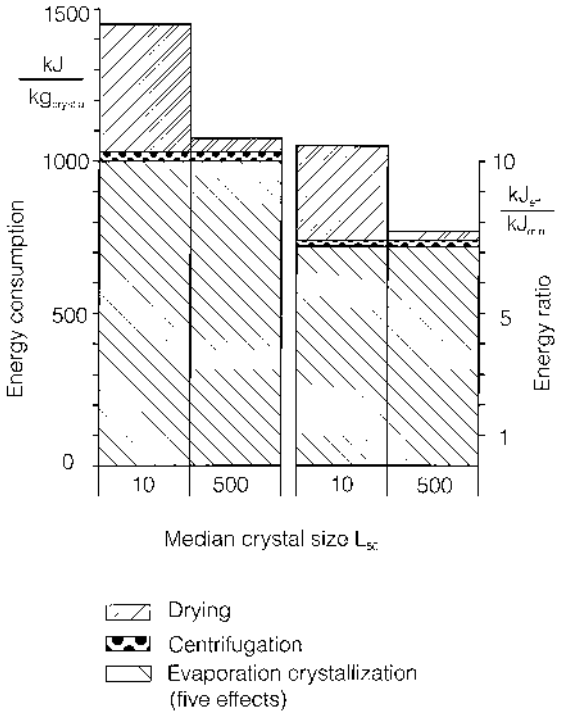

Figure 8.2. Energy consumption and energy ratio for $L_{50} = 10\,\mu m$ and $L_{50} = 500\,\mu m$.

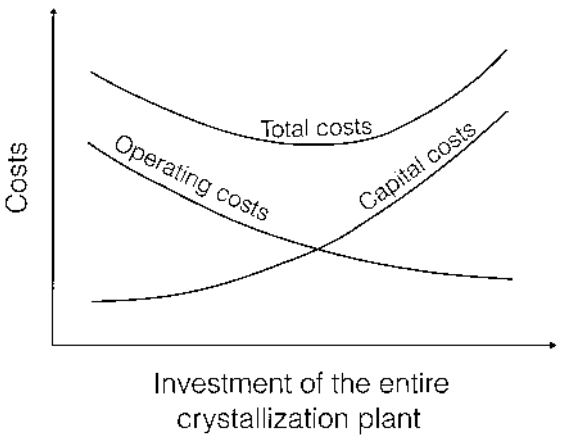

Figure 9.1. Investment, operating, and total costs versus the capital cost of the entire crystallization plant.

in investment are given by a reduction of operating costs (e.g., reduction of energy costs, cleaning costs, maintenance and repair costs, labor costs, etc.). A few examples will illustrate these relationships:

1. An increase in the number of effects of a multiple-effect evaporation plant leads to a considerable reduction in energy costs (Chapter 4).
2. An increase in heat-exchanger surface $A = \dot{Q}/h\Delta\vartheta$ results in a decrease in the temperature difference $\Delta\vartheta$ for a given heat flux $\dot{Q}$ and constant heat transfer coefficient h. Therefore, fouling of the heat exchanger and consequent costs for shutdown and cleaning will be reduced. In the case of thermal compression, the pressure ratio necessary to obtain a sufficient temperature difference $\Delta\vartheta$ between the condensing vapor and the boiling liquid can be decreased, which results in a reduction of the power consumption of the compressor.
3. An increase in the crystallizer volume $V \sim \dot{M}_C L_{50}/k_d \Delta c$ leads to an increase in the median crystal size L_{50} and/or a decrease in the mean supersaturation Δc. A reduction in supersaturation results not only in less fouling, fewer shutdowns, and less energy for cleaning but also in a decrease in nucleation rates and, therefore, in an increase in mean crystal sizes. A coarse crystalline product is beneficial with respect to capital and operating costs for centrifuges and dryers.

It is difficult to define the most economical plant exactly because of the variety of engineering and economical parameters. Furthermore, the viewpoints of various companies may be quite different. The producer of crystals is interested primarily in product quality in order to compete with the products of other manufacturers. Dealing with engineering companies, decisions are made according to the investment required for the entire plant, but a low-priced plant may be less flexible in terms of future demands. However, exploring the future is the most difficult task.

REFERENCES

[3.1] R. H. Perry and D. Green (eds.), *Perry's Chemical Engineers' Handbook*, 6th ed., McGraw-Hill, New York (1984).

[3.2] H. D. Baehr, *Thermodynamik*, 7th ed., Springer-Verlag, Berlin (1989).

[3.3] A. Mersmann and J. Franke, Thermal analysis of solid production processes, *Chem. Eng. Technol., 1*(6): 75–81 (1993).

[4.1] R. Billet, *Evaporation Technology: Principles, Applications, Economics*, VCH, Weinheim (1989).

[4.2] La compression méchanique de vapeur d'eau, *Le Courier des Établissement Neu No. 80* (1980).

[5.1] A. Mersmann, *Thermische Verfahrenstechnik*, Springer-Verlag, Berlin (1980).
[7.1] A. Mersmann and M. Kind, Parameters influencing the mean particle size of a crystalline product, *Chem. Eng. Technol., 12*: 414–419 (1989).
[7.2] M. Kind and G. Wellinghoff, *Bremer Int. Workshop for Industrial Crystallization* (J. Ulrich, ed.), pp. 18–25 (1991).

Appendix

A1. PHYSICAL PROPERTIES

A1.1. Solubilities, Densities, Heat of Crystallization, and Kinetic Information on 173 Inorganic and Organic Systems

As a rule, the solubilities are given in mass ratios W^* ($kg_{solute}/kg_{solvent}$). Data in C^* ($kmol/m^3$) require the density ρ_L of the solution which is not available for all systems. There is a variety of possibilities for measuring the solubility of a substance in a solvent. The most exact way to get the saturation temperature of a given solution is to determine stepwise the temperature at which no dissolution and no growth of an individual crystal can be observed with a microscope. Therefore, a precise temperature control and stability is necessary. A common way to produce a solution with a distinct concentration is to add accurately weighed masses of the substances under discussion. However, it is difficult to determine the exact solubility by cooling and heating and the observation of the occurrence or disappearance of solid matter, especially in the case when the solubility changes only slightly

with temperature, for instance for the NaCl–H_2O system. Therefore, it is recommended to measure the concentration of a saturated solution, which contains suspended crystals. The measurement of the concentration can be carried out by the determination of the following:

- Solution density by densitometer
- Refractive index by refractometer
- Electrical resistance by conductivity meter
- Viscosity by viscometer

For inorganic substances sparingly soluble in water, a close relationship between the ionic electrical conductivity and the concentration is given. Sometimes, ionic selective probes can be employed. When no other suitable measuring technique is available, evaporation of the solution to dryness is the easiest and most common way to measure solubility.

Note that the supersaturation can be expressed in different ways; see Chapters 1 and 2. Supersaturation

$$S_a \equiv \frac{a}{a^*} = \frac{\gamma C}{\gamma^* C^*} = \frac{\gamma(C^* + \Delta C)}{\gamma^* C^*} \tag{A1.1}$$

requires knowledge of the activity coefficients γ and γ^*. Dealing with highly soluble systems ($C^*/C_c > 0.01$), the supersaturation ΔC in industrial crystallizers is so small in comparison to the solubility C^* that $\gamma \approx \gamma^*$ and the activity coefficients can be canceled. However, in the case of sparingly soluble substances, supersaturation can assume values of $S = 100$ and higher.

Activity coefficients can be calculated from equations based on the theory of Debye–Hückel. In the case of aqueous systems, the logarithm of the activity coefficient according to Davies [A1.1] is

$$\log \gamma_\pm = 0.509|z_1 z_2|\left(\frac{\sqrt{I}}{1+\sqrt{I}} - 0.3I\right) \tag{A1.2}$$

valid for ionic strength $I < 0.1\,\text{kmol/m}^3$.

Bromley [A1.2] derived the following equation valid for $I < 6\,\text{kmol/m}^3$:

$$\log \gamma_\pm = 0.511|z_1 z_2|\frac{\sqrt{I}}{1+\sqrt{I}} + BI + |z_1 z_2|\frac{0.06 + 0.6B}{(1 + 1.5I/|z_1 z_2|)^2} \tag{A1.3}$$

z_1 and z_2 are the ionic charges. Data for the constant B are given in Table A1.1.

Data for a variety of physical properties are provided in Tables A1.2–A1.4. Following these tables is a detailed explanation of the column heads used in the tables and a key to literature citations.

Table A1.1. Data for the Constant B of equation (A1.3)

Cation	B^+	δ^+	Anion	B^-	δ^-
H^+	0.0875	0.103	F^-	0.0295	-0.93
Li^+	0.0691	0.138	Cl^-	0.0643	-0.067
Na^+	0.0000	0.028	Br^-	0.0741	0.064
K^+	-0.0452	-0.079	I^-	0.0890	0.196
Rb^+	-0.0537	-0.100	ClO_3^-	0.005	0.45
Cs^+	-0.0710	-0.138	ClO_4^-	0.002	0.79
$NH4^+$	-0.042	-0.02	BrO_3^-	-0.032	0.14
Tl^+	-0.135	-0.02	IO_3^-	(-0.04)	(0)
Ag^+	-0.058	(0)	NO_3^-	-0.025	0.27
Be^{2+}	(0.1)	(0.2)	$H_2PO_4^-$	-0.052	0.20
Mg^{2+}	0.0570	0.157	$H_2AsO_4^-$	-0.030	0.05
Ca^{2+}	0.0374	0.119	CNS^-	0.071	0.16
Sr^{2+}	0.0245	0.110	OH^-	0.076	-1.00
Ba^{2+}	0.0022	0.098	Formate (C_1)	0.072	(-0.7)
Mn^{2+}	0.037	(0.21)	Acetate (C_2)	0.104	-0.73
Fe^{2+}	0.046	(0.21)	Propionate (C_3)	0.152	(-0.7)
Co^{2+}	0.0490	0.210	Butyrate (C_4)	0.167	(-0.7)
Ni^{2+}	0.054	(0.21)	Valerate (C_5)	0.142	(-0.7)
Cu^{2+}	0.022	0.30	Caproate (C_6)	0.068	(-0.7)
Zn^{2+}	0.101	0.09	Heptylate (C_7)	-0.027	(-0.7)
Cd^{2+}	0.072	(0.09)	Caprylate (C_8)	-0.122	(-0.7)
Pb^{2+}	-0.104	0.25	Pelargonate (C_9)	-0.284	(-0.7)
UO_2^{2+}	0.079	0.19	Caprate (C_{10})	-0.459	(-0.7)
Cr^{3+}	0.066	0.15	H Malonate (C_3)	+0.005	-0.22
Al^{3+}	0.052	0.12	H Succinate (C_4)	+0.021	-0.27
Sc^{3+}	0.046	(0.2)	H Adipate (C_6)	+0.053	-0.26
Y^{3+}	0.037	(0.2)	Toluate	-0.022	-0.16
La^{3+}	0.036	0.27	CrO_4^{2-}	0.019	-0.33
Ce^{3+}	0.035	(0.27)	SO_4^{2-}	0.000	-0.40
Pr^{3+}	0.034	(0.27)	$S_2O_3^{2-}$	0.019	(-0.7)
Nd^{3+}	0.035	(0.27)	HPO_4^{2-}	-0.010	-0.57
Sm^{3+}	0.039	(0.27)	$HAsO_4^{2-}$	0.021	-0.67
Eu^{3+}	0.041	(0.27)	CO_3^{2-}	0.028	-0.67
Ga^{3+}	0.000	(0.2)	Fumarate (Trans C_4)	0.056	(-0.7)
$Co(en)_3^{3+}$	-0.089	(0)	Maleate (Cis C_4)	0.017	(-0.7)
Th^{4+}	0.062	0.19	PO_4^{3-}	0.024	-0.70
$B = B^+ + B^- + \delta^+ \delta^-$			AsO_4^{3-}	0.038	-0.78
			$Fe(CN)_6^{3-}$	0.065	(0)
B [kg/mol]			$Fe(CN)_6^{3-}$	0.054	(0)
values in parentheses are estimated			$Mo(CN)_8^{3-}$	0.056	(0)

Table A1.2. Data for some physical properties

No.	Solute	Formula	Molar mass (Anh/Hyd) $\tilde{M}$ [kg/kmol[	h_{20} [-]	Density (Hydrate) ρ_c [kg/m^3]	C_c [kmol/m^3]	Mass ratio (Hydrate) W^*_{20} [kg_{Hyd}/kg_{H2O}]	Density $\rho^*_{L,20}$ [kg/m^3]	Solubility (Hydrate) C^*_{20} [kmol/m^3]	C^*/C_c [-]	Heat of crystall. ΔH_{LC} [kJ/mol]	No.
	ALUMINIUM											
1	chloride	$AlCl_3$	133.34 241.432	6	2398	9.93	1.3068	1492	3.500	0.35	-13	1
2	hydroxide	$Al(OH)_3$	77.99	0	2420	31.03	0.00012	998	0.002	5.0E-5		2
3	sulphate	$Al_2(SO_4)_3$	342.134 630.379	16	1690	2.68	1.0017	1321 1255	0.997	0.37	-64	3
	AMMONIUM											
4	aluminium sulphate	$(NH_4)_2Al_2(SO_4)_4$	474.306 906.672	24	1640	1.81	0.1107	1050 1039	0.115	0.06		4
5	bromide	NH_4Br	97.942	0	2429	24.80	0.755	1300 1337	5.710	0.23	-15	5
6	chloride	NH_4Cl	53.491	0	1527	28.55	0.372	1076 1102	5.454	0.19	16.2	6
7	dihydrogen phosphate	$NH_4H_2PO_4$	115.025	0	1803	15.67	0.365	1160 1134	2.697	0.17		7
8	ferrous sulphate	$(NH_4)_2Fe(SO_4)_2$	284.038 392.13	6	1864	4.75	0.3798	1171 1145	0.803	0.17		8
9	hydrogen carbonate	NH_4HCO_3	79.055	0	1580	19.99	0.21	1066	2.341	0.12		9
10	nickel sulphate	$(NH_4)_2Ni(SO_4)_2$	286.908 395	6	1923	4.87		1052				10
11	nitrate	NH_4NO_3	80.043	0	1725	21.55	1.92	1310 1381	10.761	0.50	-12	11

No.	Solute	Formula	Molar mass (Anh/Hyd) $\tilde{M}$ [kg/kmol]	h_{20} [-]	Density (Hydrate) ρ_c [kg/m^3]	C_c [kmol/m^3]	Mass ratio (Hydrate) W^*_{20} [kg_{Hyd}/kg_{H2O}]	Density $\rho^*_{L,20}$ [kg/m^3]	Solubility (Hydrate) C^*_{20} [kmol/m^3]	C^*/C_c [-]	Heat of crystall. ΔH_{LC} [kJ/mol]	No.
12	sulphate	$(NH_4)_2SO_4$	132.134	0	1769	13.39	0.754	1246 1228	4.054	0.30	-6.8	12
13	thiocyanate	NH_4SCN	76.116	0	1305	17.14	1.62	1168	9.488	0.55		13
	BARIUM											
14	chloride	$BaCl_2$	208.245 244.276	2	3106	12.72	0.4468	1290 1263	1.631	0.13	-19	14
15	hydroxide	$Ba(OH)_2$	171.356 315.476	8	2180	6.91	0.0687	1034	0.211	0.03		15
16	nitrate	$Ba(NO_3)_2$	261.35	0	3222	12.33	0.092	1060 1060	0.342	0.03	-31	16
17	oxalate	BaC_2O_4	225.38	0	2658	11.79	[24]0.000024					17
18	sulphate	$BaSO_4$	233.42	0	4300	18.42	0.000002	998	8.8E-6	5.3E-7	-23	18
	BORIC											
19	acid	H_3BO_3	61.832	0	1435	23.21	0.05	1025 1013	0.789	0.03		19
	CADMIUM											
20	chloride	$CdCl_2$	183.307 228.344	5/2	3327	14.57	1.9637	1740 1862	5.049	0.35	-16	20
21	nitrate	$Cd(NO_3)_2$	236.411 308.471	4	2455	7.96	3.5	1780 1854	4.488	0.56	-33	21
22	sulphate	$CdSO_4$	208.458 256.498	8/3	3084	12.02	1.1374	1615 1560	3.236	0.27	-2.8	22
	CALCIUM											

No.	Solute	Formula	Molar mass (Anh/Hyd)		Density (Hydrate)		Mass ratio (Hydrate)	Density	Solubility (Hydrate)		Heat of crystall.	No.
			$\tilde{M}$ [kg/kmol]	h_{20} [-]	ρ_c [kg/m^3]	C_c [kmol/m^3]	W^{Hy}_{20} [kg_{Hyd}/kg_{H2O}]	$\rho^*_{1,20}$ [kg/m^3]	C^*_{20} [kmol/m^3]	C^*/C_c [-]	ΔH_{Cr} [kJ/mol]	
23	carbonate	$CaCO_3$	100.09	0	2710	27.08	0.000013	998	1.3E-4	4.8E-6		23
24	chloride	$CaCl_2$	110.987 219.077	6	1712	7.81	5.639	1430 1546	5.544	0.71	-41.5	24
25	fluoride	CaF_2	78.08	0	3180	40.73	0.00002	998	2.6E-4	6.3E-6		25
26	nitrate	$Ca(NO_3)_2$	164.091 236.151	4	1820	7.71	4.443	1579 1581	5.047	0.66	-33	26
27	phosphate	$CaHPO_4$	136.06 172.09	2	2317	13.46	$_{Anh}$0.0001	998	5.8E-4	4.3E-5		27
28	sulphate	$CaSO_4$	136.138 172.168	2	2310	13.42	0.0026	999 1000	0.015	0.001	-3	28
	COBALT											
29	chloride	$CoCl_2$	129.84 237.93	6	1924	8.09	1.7103	1434	3.802	0.47	-37	29
30	nitrate	$Co(NO_3)_2$	182.944 291.034	6	1883	6.47	3.664	1570 1582	4.238	0.66	-40	30
31	sulphate	$CoSO_4$	154.992 281.097	7	1948	6.93	0.8999	1306 1298	2.187	0.32		31
	CUPRIC											
32	chloride	$CuCl_2$	134.452 170.482	2	2514	14.75	1.1758	1524 1481	4.694	0.32	-11	32
33	nitrate	$Cu(NO_3)_2$	187.557 295.647	6	2074	7.02	7.850	1690 1849	5.070	0.72	-33	33
34	sulphate	$CuSO_4$	159.605 249.68	5	2286	9.16	0.3548	1200 1171	1.259	0.14	-14.5	34

No.	Solute	Formula	Molar mass (Anh/Hyd) $\tilde{M}$ [kg/kmol]	h_{20} [-]	Density (Hydrate) ρ_c [kg/m^3]	C_c [kmol/m^3]	Mass ratio (Hydrate) W^*_{20} [kg$_{hyd}$/kg$_{H2O}$]	Density $\rho^*_{T,20}$ [kg/m^3]	Solubility (Hydrate) C^*_{20} [kmol/m^3]	C^*/C_c [-]	Heat of crystall. ΔH_{LC} [kJ/mol]	No.
	FERROUS											
35	sulphate	$FeSO_4$	151.906 278.011	7	1899	6.83	0.6148	1225 1218	1.678	0.14	-20	35
	LEAD											
36	acetate	$Pb(CH_3COO)_2$	325.29 379.335	3	2575	6.79	0.5552	1260 1278	1.186	0.18		36
37	chloride	$PbCl_2$	278.106	0	5850	21.04	0.01	1007 1007	0.036	0.002	-25	37
38	nitrate	$Pb(NO_3)_2$	331.21	0	4535	13.69	0.57	1420 1393	1.557	0.11	-12.7	38
	LITHIUM											
39	chloride	LiCl	42.394 60.409	1	1762	29.17	1.8448	1290 1389	13.848	0.48	-8.5	39
40	iodate	$LiIO_3$	181.84	0	4500	24.75	0.745	1560 1495	3.663	0.15		40
41	sulphate	Li_2SO_4	109.94 127.955	1	2051	16.03	0.4249	1234 1179	2.747	0.17	4.8	41
	MAGNESIUM											
42	chloride	$MgCl_2$	95.212 203.302	6	1569	7.72	3.0435	1340 1375	4.961	0.64	-13	42
43	sulphate	$MgSO_4$	120.364 246.469	7	1680	6.82	1.0553	1290 1261	2.687	0.39	-22.5	43
	MANGANOUS											
44	chloride	$MnCl_2$	125.845 197.905	4	2010	10.16	2.0217	1475 1505	4.699	0.46	-23	44

No.	Solute	Formula	Molar mass (Anh/Hyd) $\tilde{M}$ [kg/kmol]	h_{20} [-]	Density (Hydrate) ρ_c [kg/m^3]	C_c [kmol/m^3]	Mass ratio (Hydrate) W^*_{20} [kg_{Hyd}/kg_{H2O}]	Density $\rho^*_{L,20}$ [kg/m^3]	Solubility (Hydrate) C^*_{20} [kmol/m^3]	C^*/C_c [-]	Heat of crystall. $\Delta H_{l,c}$ [kJ/mol]	No.
45	sulphate	$MnSO_4$	150.997 241.072	5	2103	8.72	1.6050	1490 1476	3.808	0.44	10	45
	MERCURIC											
46	chloride	$HgCl_2$	271.496	0	5440	20.04	0.0659	1050 1051	0.239	0.01		46
	NICKEL											
47	chloride	$NiCl_2$	129.617 237.707	6	1921	8.08	2.3975	1478 1510	4.483	0.56	-41	47
48	nitrate	$Ni(NO_3)_2$	182.721 290.811	6	2050	7.05	3.363	1584 1651	4.377	0.62		48
49	sulphate	$NiSO_4$	154.769 280.874	7	1948	6.94	0.9879	1330 1318	2.406	0.35	-21.5	49
	POTASSIUM											
50	aluminium sulphate	$KAl(SO_4)_2$	258.197 474.377	12	1757	3.70	0.1127	1050 1044	0.224	0.06		50
51	chrome alaun	$KAlCr(SO_4)_2$	310.207 526.387	12	1826	3.47						51
52	bromate	$KBrO_3$	167.00	0	3270	19.58	0.068	1050 1045	0.400	0.02	-36.2	52
53	bromide	KBr	119.002	0	2750	23.11	0.646	1370 1331	4.518	0.20	-14	53
54	carbonate	K_2CO_3	138.206 165.228	3/2	2155	13.04	1.6725	1559 1503	5.905	0.45		54
55	chlorate	$KClO_3$	122.549	0	2320	18.93	0.07	1050 1037	0.561	0.03	-35	55

No.	Solute	Formula	Molar mass (Anh/Hyd) $\tilde{M}$ [kg/kmol]	h_{20} [-]	Density (Hydrate) ρ_c [kg/m^3]	C_c [kmol/m^3]	Mass ratio (Hydrate) W^*_{20} [kg_{Hyd}/kg_{H2O}]	Density $\rho^*_{L,20}$ [kg/m^3]	Solubility (Hydrate) C^*_{20} [kmol/m^3]	C^*/C_c [-]	Heat of crystall. $\Delta H_{l,c}$ [kJ/mol]	No.
56	chloride	KCl	74.551	0	1989	26.68	0.34	1174 1143	3.996	0.15	-13.9	56
57	chromate	K_2CrO_4	194.19	0	2732	14.07	0.617	1380 1317	2.712	0.19	-8.3	57
58	cyanide	KCN	65.12	0	1560	23.96	0.678	1168	7.249	0.30		58
59	dichromate	$K_2Cr_2O_7$	294.184	0	2690	9.14	0.12	1070 1070	0.390	0.04	-60	59
60	dihydrogen phosphate	KH_2PO_4	136.09	0	2338	17.18	0.226	1133 1116	1.558	0.09	-17	60
61	ferricyanide	$K_3Fe(CN)_6$	329.247	0	1856	5.64	0.43	1180 1159	1.078	0.19	-40	61
62	ferrocyanide	$K_4Fe(CN)_6$	368.346 422.391	3	1853	4.39	0.3365	1150 1129	0.685	0.16	-43	62
63	hydrogen carbonate	$KHCO_3$	100.115	0	2170	21.68	0.332	1175 1154	2.872	0.13		63
64	hydrogen sulphate	$KHSO_4$	136.164	0	2350	17.26	0.514	1255 1241	3.903	0.18		64
65	hydroxide	KOH	56.106 92.136	2	2040	22.14	6.919	1546 1803	17.093	0.77	-17	65
66	iodate	KIO_3	214.001	0	3930	18.36	0.081	1060 1057	0.371	0.02	-18.5	66
67	iodide	KI	166.002	0	3123	18.81	1.44	1710 1668	6.079	0.32	-11	67
68	nitrate	KNO_3	101.103	0	2110	20.87	0.316	1170 1143	2.779	0.13	-20	68

No.	Solute	Formula	Molar mass (Anh/Hyd)		Density (Hydrate)		Mass ratio (Hydrate)	Density	Solubility (Hydrate)		Heat of crystall.	No.
			$\tilde{M}$ [kg/kmol]	h_{20} [-]	ρ_c [kg/m^3]	C_c [kmol/m^3]	W^*_{20} [kg_{Hyd}/kg_{H2O}]	$\rho^*_{L,20}$ [kg/m^3]	C^*_{20} [kmol/m^3]	C^*/C_c [-]	ΔH_{LC} [kJ/mol]	
69	nitrite	KNO_2	85.104	0	1915	22.50	3.0	1651 1557	13.726	0.61		69
70	oxalate	$K_2C_2O_4$	166.216 184.231	1	2145	11.64	0.4016	1210 1179	1.882	0.16		70
71	permanganate	$KMnO_4$	158.034	0	2738	17.33	0.063	1030 1037	0.386	0.02	-40	71
72	sulphate	K_2SO_4	174.254	0	2662	15.28	0.109	1080 1064	0.609	0.04	-21	72
73	thiocyanate	KSCN	97.176	0	1886	19.41	2.42	1419 1497	10.899	0.56	-10.5	73
74	thiosulphate	$K_2S_2O_3$	190.315 220.34	5/3	2230	10.12	2.3626	1631	5.202	0.51		74
	RUBIDIUM											
75	chloride	RbCl	120.921	0	2760	22.82	0.836	1490 1407	5.611	0.25	-12.5	75
	SILVER											
76	chloride	AgCl	143.32	0	5560	38.79	0.000002	998	1.0E-5	2.7E-7	-65	76
77	nitrate	$AgNO_3$	169.873	0	4352	25.62	2.22	2156 2130	8.644	0.34	-9.5	77
78	sulphate	Ag_2SO_4	311.794	0	5450	17.48	0.008	1005	0.026	0.002	-18	78
	SODIUM											
79	acetate	$Na(CH_3COO)$	82.035 136.08	3	1450	10.66	1.1128	1170 1194	4.528	0.43	-30	79

No.	Solute	Formula	Molar mass (Anh/Hyd) $\tilde{M}$ [kg/kmol]	h_{20} [-]	Density (Hydrate) ρ_c [kg/m³]	C_c [kmol/m³]	Mass ratio (Hydrate) W^*_{20} [kg_{Hyd}/kg_{H2O}]	Density $\rho^*_{l,20}$ [kg/m³]	Solubility (Hydrate) C^*_{20} [kmol/m³]	C^*/C_c [-]	Heat of crystall. ΔH_{Lc} [kJ/mol]	No.
80	bromide	NaBr	102.894 138.924	2	2176	15.66	1.8069	1520 1532	7.043	0.45	- 17.7	80
81	carbonate	Na_2CO_3	105.991 286.141	10	1460	5.10	0.9367	1190 1179	2.011	0.39	-58.5	81
82	chlorate	$NaClO_3$	106.441	0	2490	23.39	1.01	1430 1428	6.751	0.29	-8.7	82
83	chloride	NaCl	58.443	0	2163	37.01	0.36	1200 1164	5.435	0.15	-1.6	83
84	chromate	Na_2CrO_4	161.975 270.065	6			2.8196	1430 1316			-60	84
85	cyanide	NaCN	49.008 85.038	2	1361	16.00	1.7255	1201	8.941	0.56		85
86	dihydrogen phosphate	NaH_2PO_4	119.977 156.007	2	1910	12.24	1.4994	1390 1399	5.345	0.44		86
87	diphosphate	$Na_4P_2O_7$	265.904 446.054	10	1824	4.09	0.0878	1045 1036	0.187	0.05		87
88	hydrogen carbonate	$NaHCO_3$	84.007	0	2211	26.32	0.096	1060 1049	1.105	0.04		88
89	hydrogen phosphate	Na_2HPO_4	141.961 358.141	12	1520	4.24	0.2236	1050 1065	0.536	0.13	-75	89
90	hydroxide	NaOH	39.997 58.012	1	1750	30.17	3.091	1537 1478	19.249	0.64		90
91	iodide	NaI	149.895 185.925	2	2448	13.17	3.8321	1910 1882	8.147	0.62	6.7	91
92	nitrate	$NaNO_3$	84.995	0	2257	26.55	0.88	1380 1351	7.600	0.29	-10.5	92

No.	Solute	Formula	Molar mass (Anh/Hyd) $\tilde{M}$ [kg/kmol]	h_{20} [-]	Density (Hydrate) ρ_c [kg/m^3]	C_c [kmol/m^3]	Mass ratio (Hydrate) W^*_{20} [kg_{Hyd}/kg_{H2O}]	Density $\rho^*_{L,20}$ [kg/m^3]	Solubility (Hydrate) C^*_{20} [kmol/m^3]	C^*/C_c [-]	Heat of crystall. ΔH_{LC} [kJ/mol]	No.
93	nitrite	$NaNO_2$	68.995	0	2144	31.07	0.85	1360 1323	9.057	0.29		93
94	perchlorate	$NaClO_4$	122.44	0	2480	20.26	1.81	1670 1623	8.786	0.43	-17	94
95	phosphate	Na_3PO_4	163.943 380.123	12	1589	4.18	0.3324	1090 1100	0.715	0.17		95
96	potassium tartrate	$NaKC_4H_4O_6$	210.17 282.23	4	1790	6.34	$(Anh)^{25}$0.66	1349				96
97	sulphate	Na_2SO_4	142.039 322.189	10	1468	4.56	0.5714	1150 1130	1.298	0.29	-70.3	97
98	sulphide	Na_2S	78.041 240.176	9	2471	10.29	0.9325	1161 1401	2.815	0.27		98
99	sulphite	Na_2SO_3	126.039 252.144	7	1560	6.19	0.7184	1205 1175	1.949	0.32		99
100	tetraborate	$Na_2B_4O_7$	201.217 381.367	10	1692	4.44	0.0498	1021 1018	0.127	0.03		100
101	thiosulphate	$Na_2S_2O_3$	158.099 248.174	5	1756	7.08	1.7597	1350 1377	3.469	0.49	-50	101
	STRONTIUM											
102	chloride	$SrCl_2$	158.527 266.617	6	1954	7.33	1.3789	1380 1393	3.000	0.41	-45.5	102
103	nitrate	$Sr(NO_3)_2$	211.631 283.691	4	2249	7.93	1.2223	1440 1438	2.792	0.35	-37	103
	THALLIUM											
104	bromide	TlBr	284.28	0	7557	26.58	0.000476	999	0.002	6.3E-5	-47	104

No.	Solute	Formula	Molar mass (Anh/Hyd) $\tilde{M}$ [kg/kmol]	h_{20} [-]	Density (Hydrate) ρ_c [kg/m^3]	C_c [kmol/m^3]	Mass ratio (Hydrate) W^*_{20} [kg_{Hyd}/kg_{H2O}]	Density $\rho^*_{L,20}$ [kg/m^3]	Solubility (Hydrate) C^*_{20} [kmol/m^3]	C^*/C_c [-]	Heat of crystall. ΔH_{LC} [kJ/mol]	No.
105	sulphate	Tl_2SO_4	504.798	0	6765	13.40	0.049	1040 1040	0.096	0.01		105
	URANYL											
106	nitrate	$UO_2(NO_3)_2$	358.048 502.129	6	2807	5.59	2.316	1803 1890	2.629	0.43	-44	106
	ZINK											
107	nitrate	$Zn(NO_3)_2$	189.391 297.481	6	2067	6.95	5.839	1671 1787	5.129	0.74	-42	107
108	sulphate	$ZnSO_4$	161.439 287.544	7	1957	6.81	1.6563	1460 1437	1.780	0.47	-27	108

No.	Solute	Literature							No.
		W*, w*	ρ_L*	η_L	D_{AB}	Δc_{met}, σ_{met}	B	G	
	ALUMINIUM								
1	chloride	DAn67,Mul93,Bro81 Lan69,Nik59,Per84		Lan69					1
2	hydroxide	Lan69				Ros96	Mis71	Mis71,Kin89,Scy96	2
3	sulphate	DAn67,Mul93,Lan69 Nik59,Per84		Lan69		Rod99			3
	AMMONIUM								
4	aluminium sulphate	DAn67,Mul93,Bro81 Nik59,Per84	Mul93 Söh85	Mul93* Lan69	Lan69*,Gut90	Kin89,Mul93, Mer85	Mer85/91	Mul93,Mul80,Kin89	4
5	bromide	DAn67,Mul93,Bro81 Lan69,Nik59,Per84	Mul93 Int28	Mul93 Lan69					5
6	chloride	DAn67,Mul93,Bro81, Lan69,Nik59,Per84	Mul93 Int28	Mul93 Lan69	Lan69	Kin89,Mul93, Nyv70			6
7	dihydrogen phosphate	DAn67,Mul93,Bro81 Lan69,Nik59	Mul93 Söh85	Mul93 Lan69	Lan69,Gut90	Mul93		Mul93,Vek92,Mul67, Ben69,Kin89	7
8	ferrous sulphate	DAn67,Mul93,Bro81 Nik59	Söh85						8
9	hydrogen carbonate	DAn67,Bro81,Lan69 Nik59,Per84							9
10	nickel sulphate	Lan69	Kin89 Söh85	Mul93* Lan69	Gut90			Ang79,Mul73b,Kin89	10
11	nitrate	DAn67,Mul93,Bro81 Lan69,Nik59,Per84	Mul93 Söh85	Mul93* Lan69*	Lan69,Gut90, Mul93	Kin89,Mul93, Nyv70		Mul93,Mul80,Kin89	11
12	sulphate	DAn67,Mul93,Bro81 Lan69,Nik59,Per84	Mul93 Int28 Söh85	Mul93 Lan69	Lan69,Gut90, Mul93,Mer86	Mer85,Mul93, Kin89,Nyv68/70 Ten83ab	Kin83, Ten90, Mer85/91,San90 Kra96	Mul70/72,Wey82, Kin89,Ten83ab/90	12

No.	Solute	Literature							No.
		W*, w*	ρ_L*	η_L	D_{AB}	Δc_{met}, σ_{met}	B	G	
13	thiocyanate	DAn67,Mul93,Bro81 Lan69,Nik59,Per84		Lan69					13
	BARIUM								
14	chloride	DAn67,Mul93,Bro81 Lan69,Nik59,Per84	Mul93 Söh85	Mul93* Lan69	Lan69	Kor99			14
15	hydroxide	Bro81,Lan69,Per84						Toy84	15
16	nitrate	DAn67,Mul93,Bro81 Lan69,Nik59,Per84	Mul93 Söh85	Mul93 Lan69					16
17	oxalate	Per84			Gut90			Rei68,Kin89	17
18	sulphate	Lan69,Nik59,Per84			Gut90	Aou96, Muh96	Caf99, Che99	Dor70,Hos81,Lee89, Kin89,Nie58/79	18
	BORIC								
19	acid	Mul93,Lan69,Nik59, Per84	Mul93 Söh85			Nyv70			19
	CADMIUM								
20	chloride	DAn67,Mul93,Bro81, Lan69,Nik59,Per84	Mul93 Söh85	Mul93	Lan69				20
21	nitrate	DAn67,Mul93,Bro81, Lan69,Nik59	Mul93 Söh85	Mul93	Lan69				21
22	sulphate	DAn67,Mul93,Bro81, Lan69,Nik59,Per84	Söh85	Mul93 Lan69	Lan69				22
	CALCIUM								
23	carbonate	Lan69,Nik59			Gut90	Gom96,Kab79, Vuc96,Woj96, Oka99, Wes99	Kot90, Nak79, Tsu87, Pet84, Sch75, Ahn96	Gia88,Goo80,Kot90, Kra90,Nic79,Pet84, Sch75,Tsu87,Kin89	23
24	chloride	DAn67,Mul93,Bro81,	Mul93	Mul93	Lan69				24

No.	Solute	Literature							No.
		W*, w*	ρ_L*	η_L	D_{AB}	Δc_{met}, σ_{met}	B	G	
		Lan69,Nik59,Per84	Söh85	Lan69					
25	fluoride	Lan69,Nik59,Per84				Cli99		Ham91,Kin89	25
26	nitrate	DAn67,Mul93,Bro81, Lan69,Nik59,Per84	Mul93 Söh85	Mul93 Lan69	Lan69	Nyv70	Mer91	Pac81,Kin89	26
27	phosphate	Lan69,Nik59			Gut90	Com96,Tsu96		Mar69,Kin89	27
28	sulphate	DAn67,Mul93,Bro81, Lan69,Mar73,Nik59, Per84	Mul93		Gut90	Bad96,Elg96, Koo99,Wil99	Sik80, Wei84	Kag81,Fer90,Sik80, Lee89,Wit90,Wei84, Kin89,Amj86/88	28
	COBALT								
29	chloride	DAn67,Mul93,Bro81, Lan69,Nik59		Mul93 Lan69	Lan69				29
30	nitrate	DAn67,Mul93,Bro81, Lan69,Nik59	Mul93 Söh85	Mul93 Lan69					30
31	sulphate	DAn67,Mul93,Bro81, Lan69,Nik59	Söh85	Mul93 Lan69*					31
	CUPRIC								
32	chloride	DAn67,Mul93,Bro81, Lan69,Nik59,Per84	Söh85	Mul93 Lan69					32
33	nitrate	DAn67,Mul93,Bro81, Lan69,Nik59,Per84	Mul93 Söh85	Mul93 Lan69					33
34	sulphate	DAn67,Mul93,Bro81, Lan69,Nik59,Per84	Mul93 Söh85	Mul93 Lan69	Lan69,Gut90	Kin89,Mul93, Nyv70	Sch96	Tan64,McC51,Bra60, Kin89	34
	FERROUS								
35	sulphate	DAn67,Mul93,Bro81, Lan69,Nik59,Per84	Söh85 Hoc92			Kin89,Mul93, Nyv70			35

No.	Solute	Literature							No.
		W*, w*	ρ_L*	η_L	D_{AB}	$\Delta\sigma_{mer}$, σ_{met}	B	G	
	LEAD								
36	acetate	Mul93,Bro81,Per84	Mul93 Int28	Mul93 Lan69					36
37	chloride	DAn67,Mul93,Bro81, Lan69,Nik59,Per84	Mul93 Int28						37
38	nitrate	DAn67,Mul93,Bro81, Lan69,Nik59,Per84	Mul93 Söh85	Mul93 Lan69	Gut90				38
	LITHIUM								
39	chloride	DAn67,Mul93,Bro81, Lan69,Nik59	Mul93	Mul93 Lan69	Lan69				39
40	iodate	Lan69,Mul93	Mul93 Int28	Mul93 Lan69				Tro92	40
41	sulphate	DAn67,Mul93,Bro81L an69,Nik59	Söh85	Mul93 Lan69	Lan69				41
	MAGNESIUM								
42	chloride	DAn67,Mul93,Bro81, Lan69,Nik59,Per84	Mul93 Söh85	Mul93 Lan69	Lan69				42
43	sulphate	DAn67,Mul93,Bro81, Lan69,Nik59,Per84	Mul93 Söh85	Mul93 Lan69	Lan69,Gut90, Ada54	Mul93, Kin89	Sik76, Mer91	Liu70,Mul93,Clo72, Sik76,Ten83a,Bra60, Kin89	43
	MANGANOUS								
44	chloride	DAn67,Mul93,Bro81, Lan69,Nik59	Mul93 Söh85	Mul93 Lan69	Lan69			Mit91	44
45	sulphate	DAn67,Mul93,Bro81, Lan69,Nik59,Per84	Mul93 Söh85	Mul93 Lan69					45
	MERCURIC								

No.	Solute	Literature							No.
		W*, w*	ρ_L*	η_L	D_{AB}	Δc_{met}, σ_{met}	B	G	
46	chloride	DAn67,Mul93,Bro81, Lan69,Nik59	Mul93 Söh85	Lan69	Lan69				46
	NICKEL								
47	chloride	DAn67,Mul93,Bro81, Lan69,Nik59,Per84	Söh85	Lan69					47
48	nitrate	DAn67,Mul93,Bro81, Lan69,Nik59,Per84	Söh85		Lan69				48
49	sulphate	DAn67,Mul93,Bro81, Lan69,Nik59,Per84	Mul93 Söh85	Lan69	Gut90	Mul93, Kin89	Rey96	Mul80,Kin89	49
	POTASSIUM								
50	aluminium sulphate	DAn67,Mul93,Bro81, Lan69,Nik59,Per84	Mul93 Söh85 Int28	Mul93* Lan69	Lan69*,Gut90	Kin89,Mul93, Mer85,Shi96, Dok99,Hos99	Kar82, Mer85/91	Mul67/72/80,Gar69/ 74/76/77,Kar82, Lew74,Ben66/67/73, Den70,Liu70,Bes79, Ten 83a,Kin89	50
51	chrome alum				Gut90			Kir73,Kin89	51
52	bromate	DAn67,Mul93,Bro81, Lan69,Nik59	Mul93 Söh85	Lan69					52
53	bromide	DAn67,Mul93,Bro81, Lan69,Nik59	Mul93 Söh85	Mul93 Lan69	Lan69	Mul93,Nyv70		Bli71	53
54	carbonate	DAn67,Mul93,Bro81, Lan69,Nik59,Per84	Mul93 Söh85	Mul93 Lan69	Lan69		Mer91		54
55	chlorate	DAn67,Mul93,Bro81, Lan69,Nik59,Per84	Mul93 Söh85	Mul93 Lan69					55
56	chloride	DAn67,Mul93,Bro81, Lan69,Nik59,Per84	Mul93 Söh85 Int28	Mul93 Lan69*	Lan69,Gut90, Mul93,Mer86	Mer85,Mul93, Kin89,Nyv70/68 Ten83ab,Cek96,	Kin83, Akl91, Mer85/91San90,	Mul93,Bli71,Bot67, Kle71,Toy84,Akl91, Ulr91,Jir79,Bee82,	56

No.	Solute	Literature							No.
		W*, w*	ρ_L*	η_L	D_{AB}	Δc_{met}, σ_{met}	B	G	
						Mat96	Bee82, Lou96, Pol96	Kin89,Ten83ab,Lop99 Say96	
57	chromate	DAn67,Mul93,Bro81, Lan69,Nik59,Per84	Mul93 Söh85	Mul93 Lan69	Lan69				57
58	cyanide	DAn67,Lan69,Nik59			Lan69				58
59	dichromate	DAn67,Mul93,Bro81, Lan69,Nik59,Per84	Mul93 Söh85	Lan69*	Lan69,Gut90		Tim71, Mer91	Tim71,Kin89	59
60	dihydrogen phosphate	Lan69,Nik59	Söh85 Iloc92	Mul93	Lan69,Gut90	Mul93	Bar96	Söh77,Kin89	60
61	ferricyanide	DAn67,Mul93,Bro81, Lan69,Nik59,Per84	Mul93 Söh85	Mul93					61
62	ferrocyanide	DAn67,Mul93,Bro81, Lan69,Nik59	Mul93 Söh85	Mul93	Lan69,Ada54				62
63	hydrogen carbonate	DAn67,Mul93,Bro81, Lan69,Nik59,Per84	Söh85 Int28						63
64	hydrogen sulphate	Mul93,Bro81,Lan69 Per84	Söh85						64
65	hydroxide	DAn67,Mul93,Bro81, Lan69,Nik59,Per84	Söh85	Mul93 Lan69	Lan69				65
66	iodate	DAn67,Mul93,Bro81, Lan69,Nik59	Mul93 Söh85	Lan69	Lan69				66
67	iodide	DAn67,Mul93,Bro81, Lan69,Nik59	Mul93 Söh85	Mul93 Lan69	Lan69	Mul93,Nyv70		Bli71	67
68	nitrate	DAn67,Mul93,Bro81, Lan69,Nik59,Per84	Mul93 Söh85	Mul93 Lan69	Lan69,Gut90	Mul93,Nyv70 Mer85,Ten83ab, Nic99	Hel77, San90, Mer85/91	Mul93,Sip73,Hel77, Kin89,Ten83ab,	68

No.	Solute	Literature							No.
		W*, w*	ρ_L*	η_L	D_{AB}	Δc_{met}, σ_{met}	B	G	
69	nitrite	DAn67,Mul93,Bro81, Lan69,Per84	Söh85			Mul93,Nyv70			69
70	oxalate	Mul93,Bro81	Mul93	Mul93 Lan69					70
71	permanganate	DAn67,Mul93,Bro81, Lan69,Nik59,Per84	Mul93 Söh85	Lan69					71
72	sulphate	DAn67,Mul93,Bro81, Lan69,Nik59,Per84	Mul93 Söh85 Int28	Mul93* Lan69	Lan69,Gut90, Mer86	Kin89, Mul69/72, Mer85, Nyv70	Ran72, Mer85/91 Mul69	Mul69/72/73a/80,Gar 74/82,Ran72,Ros71, Söh77,Tav79,Ulr87, Bak82/87,Kin89	72
73	thiocyanate	DAn67,Mul93,Bro81, Lan69,Nik59,Per84	Söh85	Mul93 Lan69	Lan69				73
74	thiosulphate	DAn67,Bro81,Lan69 Per84							74
	RUBIDIUM								
75	chloride	DAn67,Mul93,Bro81, Lan69,Nik59	Mul93 Söh85	Lan69	Lan69				75
	SILVER								
76	chloride	Lan69,Nik59			Gut90			Nic79,Kin89	76
77	nitrate	DAn67,Mul93,Bro81, Lan69,Nik59,Per84	Söh85	Mul93 Lan69	Lan69				77
78	sulphate	DAn67,Mul93,Bro81, Lan69,Nik59,Per84							78
	SODIUM								
79	acetate	Mul93,Bro81,Per84	Mul93 Söh85	Mul93 Lan69	Lan69				79
		DAn67,Mul93,Bro81,		Mul93					

No.	Solute	Literature							No.
		W*, w*	ρ_L*	η_L	D_{AB}	Δc_{met}, σ_{met}	B	G	
80	bromide	Lan69,Nik59	Mul93 Söh85	Lan69	Lan69	Mul93,Nyv70			80
81	carbonate	DAn67,Mul93,Bro81, Lan69,Nik59,Per84	Mul93 Söh85	Mul93 Lan69*	Lan69	Mul93	Rol99, Shi99		81
82	chlorate	DAn67,Mul93,Bro81, Lan69,Nik59,Per84	Mul93 Söh85	Mul93 Lan69	Gut90			Ben66/67,Bli71, Lew74	82
83	chloride	DAn67,Mul93,Bro81, Lan69,Nik59,Per84	Mul93 Söh85 Int28	Mul93 Lan69*	Lan69,Gut90, Mul93,Mer86, Ada54	Kin89,Rum60, Mul93,Fer96, Mar96,Oos96	Kin83, Mer91, Mat96	Mul93/76,Kir71, Rum60,Ten83a,Yua90 Ulr91,Kin89	83
84	chromate	DAn67,Mul93,Bro81, Lan69,Nik59,Per84	Mul93 Söh85	Mul93 Lan69	Lan69	Mul93, Nyv 68/70			84
85	cyanide	DAn67,Bro81,Lan69							85
86	dihydrogen phosphate	DAn67,Mul93,Bro81, Lan69,Nik59,Per84	Mul93 Söh85	Mul93 Lan69	Lan69				86
87	diphosphate	DAn67,Mul93,Bro81, Lan69,Per84	Söh85						87
88	hydrogen carbonate	DAn67,Mul93,Bro81, Lan69,Nik59,Per84	Mul93						88
89	hydrogen phosphate	DAn67,Mul93,Bro81, Lan69,Nik59,Per84	Mul93 Söh85	Lan69	Lan69	Kin89,Mul93, Nyv68/70			89
90	hydroxide	DAn67,Mul93,Bro81, Lan69,Nik59,Per84	Söh85	Lan69	Lan69				90
91	iodide	DAn67,Mul93,Bro81, Lan69,Nik59	Mul93 Söh85	Mul93 Lan69	Lan69	Mul93,Nyv70			91
92	nitrate	DAn67,Mul93,Bro81,	Mul93	Mul93	Lan69,Gut90	Kin89,Mul93,	Gra99	Mul93/80,Sip73,	92

No.	Solute	Literature							No.
		W*, w*	ρ_L*	η_L	D_{AB}	Δc_{met}, σ_{met}	B	G	
		Lan69,Nik59,Per84	Söh85	Lan69		Nyv70		Kin89	
93	nitrite	DAn67,Mul93,Bro81, Lan69,Nik59,Per84	Mul93 Söh85	Lan69		Mul93,Nyv70		Sip73	93
94	perchlorate	Bro81,Lan69,Nik59	Hoc92 Söh85	Lan69	Lan69			Sip73	94
95	phosphate	DAn67,Mul93,Bro81, Lan69,Nik59,Per84	Mul93 Söh85						95
96	potassium tartrate	Int28	Söh85 Int28					Sip73	96
97	sulphate	DAn67,Mul93,Bro81, Lan69,Nik59,Per84	Mul93 Söh85	Mul93* Lan69	Lan69,Mer86	Kin89,Mul93, Nyv70	Shi99		97
98	sulphide	DAn67,Mul93,Bro81, Lan69,Nik59,Per84	Söh85						98
99	sulphite	DAn67,Mul93,Bro81, Lan69,Nik59,Per84	Söh85			Nyv70			99
100	tetraborate	DAn67,Mul93,Bro81, Lan69,Nik59,Per84	Söh85		Lan69	Kin89,Mul93, Nyv70			100
101	thiosulphate	DAn67,Mul93,Bro81, Lan69,Nik59	Söh85	Mul93* Lan69	Gut90	Kin89,Mul93, Nyv70		Mul93,Kin89	101
	STRONTIUM								
102	chloride	DAn67,Mul93,Bro81, Lan69,Nik59,Per84	Mul93 Söh85	Mul93 Lan69	Lan69				102
103	nitrate	DAn67,Mul93,Bro81, Lan69,Nik59,Per84	Mul93 Söh85	Mul93 Lan69	Lan69				103
	THALLIUM								
104	bromide	Lan69,Nik59			Rei68,Gut90			Rei68,Kin89	104

No.	Solute	Literature							No.
		W*, w*	ρ_L*	η_L	D_{AB}	Δe_{met}, σ_{met}	B	G	
105	sulphate	DAn67,Mul93,Bro81, Lan69,Nik59,Per84	Mul93 Int28		Lan69				105
	URANYL								
106	nitrate	DAn67,Mul93,Bro81, Nik59	Söh85	Lan69					106
	ZINC								
107	nitrate	DAn67,Mul93,Bro81, Lan69,Nik59,Per84	Söh85	Mul93 Lan69	Lan69				107
108	sulphate	DAn67,Mul93,Bro81, Lan69,Nik59,Per84	Mul93 Söh85	Mul93 Lan69	Lan69	Rey96			108

Table A1.3. Data for Some Physical Properties

No.	Solute	Formula	Molar mass (Anhydrat) $\tilde{M}$ [kg/kmol]	h [-]	Density ρ_c [kg/m^3]	C_c [kmol/m^3]	Mass ratio Water W^*_{20} [kg/kg]	Alcohol W^*_{20} [kg/kg]	Ether W^*_{20} [kg/kg]	Density ρ_L^* [kg/m^3]	No.
109	Acetamide	C_2H_5NO	59.068		999	16.91	2.3	s.	v.sl.s.		109
110	Acetanilide	C_8H_9NO	135.166		1210	8.95	0.0052	0.21	^{25}0.07		110
111	Acetylsalicylic acid	$C_9H_8O_4$	180.160		1390	7.72	^{37}0.01	s.	0.05		111
112	Adipic acid	$C_6H_{10}O_4$	146.143		1360	9.31	0.019	v.s.	^{15}0.006		112
113	Alanine(D)	$C_3H_7O_2N$	89.094				0.158				113
114	Alanine(DL)	$C_3H_7O_2N$	89.094		1400	15.71	0.157	v.sl.s.	i.		114
115	Aminophenol o-	$C_6H_5O_3N$	139.111		1290	9.27	0.02	^{0}0.043	v.s.		115
116	Aminophenol m-	$C_6H_5O_3N$	139.111		1280	9.20	0.027	s.	sl.s		116
117	Aminophenol p-	$C_6H_5O_3N$	139.111		1300	9.35	0.016	^{0}0.04			117
118	Anthracene	$C_{14}H_{10}$	178.233		1250	7.01	i.	^{20}0.015			118
119	Anthranilic acid o-	$C_7H_7O_2N$	137.138				^{14}0.0035	^{10}0.11	^{7}0.16		119
120	Benzamide	C_7H_7ON	121.139		1080	8.92	0.001	^{25}0.017	sl.s.		120
121	Benzoic acid	$C_7H_6O_2$	122.123		1266	10.37	0.0029	^{15}0.46	^{15}0.66		121
122	Cinnamic acid (trans-)	$C_9H_8O_2$	148.161		1250	8.44	0.0004	0.24	v.s.		122
123	Citric acid	$C_6H_8O_7$	192.125	1	1540	8.02	1.46	^{15}0.76	^{15}0.02	^{30}1300	123
124	Cresol o-	C_7H_8O	108.140		1047	9.68	0.025	$^{30}\infty$	$^{30}\infty$		124
125	Dicyandiamide	$C_2H_4N_4$	84.081		1400	16.65	0.032	^{18}0.013	^{18}0.0001		125
126	Ethylendiamine tartrate	$C_6H_{14}O_6N_2$	210.187	1							126

No.	Solute	Formula	Molar mass (Anhydrat) $\tilde{M}$ [kg/kmol]	h [-]	Density ρ_c [kg/m³]	C_c [kmol/m³]	Mass ratio Water W^*_{20} [kg/kg]	Alcohol W^*_{20} [kg/kg]	Ether W^*_{20} [kg/kg]	Density ρ_L^* [kg/m³]	No.
127	Fructose	$C_6H_{12}O_6$	180.158		1600	8.88	0.8	[18]0.08			127
128	Fumaric acid (trans-)	$C_4H_4O_4$	116.073		1640	14.13	0.005	0.058	[25]0.007		128
129	Glucose (alpha-D)	$C_6H_{12}O_6$	180.158	1	1560	8.66	0.92	sl.s.	i.		129
130	Glutamic acid (D)	$C_5H_9O_4N$	147.131		1540	10.47	0.0072	v.sl.s.	v.sl.s.		130
131	Glyceryl tripalmitate	$C_{51}H_{98}O_6$	807.336		875	1.08	i.	[21]0.00004	v.s.		131
132	Glyceryl tristearate	$C_{57}H_{110}O_6$	891.497		856	0.96	i.				132
133	Glycine	$C_2H_5O_2N$	75.067		830	11.06	0.225		i.		133
134	Hexamethylene tetramine	$C_6H_{12}N_4$	140.188		1331	9.49	1.67	0.03	v.sl.s.	[30]1000	134
135	Hexatriacontane	$C_{36}H_{74}$	506.984		800	1.58					135
136	Hydrochinone p-	$C_6H_6O_2$	110.112		1332	12.10	0.072	v.s.	v.s.		136
137	Hydroxybenzoic acid o-	$C_7H_6O_3$	138.123		1440	10.43	0.002				137
138	Hydroxybenzoic acid m-	$C_7H_6O_3$	138.123		1470	10.64	0.0086				138
139	Hydroxybenzoic acid p-	$C_7H_6O_3$	138.123		1470	10.64	0.0053				139
140	Itaconic acid	$C_5H_6O_4$	130.100								140
141	Lactose	$C_{12}H_{22}O_{11}$	342.300	1	1590	4.65	0.195	i.	i.		141
142	Maleic acid	$C_4H_4O_4$	116.073		1590	13.70	0.7	[30]0.7	[25]0.08		142
143	Malic acid (DL)	$C_4H_6O_5$	134.089		1600	11.93	1.26	v.s.	v.s.		143
144	Malonic acid	$C_3H_4O_4$	104.062		[15]1631		1.53	[25]0.42	[15]0.08		144
145	Maltose	$C_{12}H_{22}O_{11}$	342.300	1	1540	4.50	0.78		i.		145
146	Mannitol (D)	$C_6H_{14}O_6$	182.174		1490	8.18	0.186	[14]0.0001	i.		146

No.	Solute	Formula	Molar mass (Anhydrat) $\tilde{M}$ [kg/kmol]	h [-]	Density ρ_c [kg/m³]	C_c [kmol/m³]	Mass ratio Water W^*_{20} [kg/kg]	Alcohol W^*_{20} [kg/kg]	Ether W^*_{20} [kg/kg]	Density ρ_L^* [kg/m³]	No.
147	Melamine	$C_3H_6N_6$	126.121		1570	12.45	0.0027				147
148	Methylnaphthalene α-	$C_{11}H_{10}$	142.200		[14]1025		i.	v.s.	v.s.		148
149	Naphthalene	$C_{10}H_8$	128.174		1150	8.97	[25]0.00003	0.095	v.s.		149
150	Oxalic acid	$C_2H_2O_4$	90.035	2	1900	21.10	0.095	s.	0.013		150
151	Pentaerythritol	$C_5H_{12}O_4$	136.148		1400	10.28	0.06	v.sl.s.	i.		151
152	Phenacetin (p)	$C_{10}H_{13}O_2N$	179.219				0.0007		[25]0.016		152
153	Phenol	C_6H_6O	94.113		1070	13.03	[15]0.082	∞	∞		153
154	Phthalic acid (o)	$C_8H_6O_4$	166.133		1590	9.57	0.0056	[18]0.12	[15]0.0068		154
155	Picric acid (2-.4-.6-)	$C_6H_3O_7N_3$	229.106		1763		0.0123	0.06	[13]0.01		155
156	Pyrocatechol o-	$C_6H_6O_2$	110.112		1370	12.44	0.451	v.s.	v.s.		156
157	Raffinose	$C_{18}H_{32}O_{16}$	505.450	5	1465	2.90	0.136	0.001			157
158	Resorcinol m-	$C_6H_6O_2$	110.112		1270	11.53	1.23	v.s.	v.s.		158
159	Saccharose	$C_{12}H_{22}O_{11}$	342.300		1588	4.64	2.04	0.009	i.	[25]1350	159
160	Salicylic acid o-	$C_7H_6O_3$	138.123		1443	10.45	0.002	[15]0.49	[15]0.51		160
161	Salol (o)	$C_{13}H_{10}O_3$	214.221		1260	5.88					161
162	Sorbitol	$C_6H_{14}O_6$	182.174				2.22				162
163	Stearic acid	$C_{18}H_{36}O_2$	284.483		[69.3]847		[25]0.0003	0.02			163
164	Succinic acid	$C_4H_6O_4$	118.089		1572	13.31	0.075	[15]0.099	[15]0.012	1019	164
165	Succinimide	$C_4H_5O_2N$	99.089		1420	14.33	0.26				165
166	Sulphanilic acid (p)	$C_6H_7NO_3S$	173.193		1490	8.60	0.0112	v.sl.s.	v.sl.s.		166

No.	Solute	Formula	Molar mass (Anhydrat) $\tilde{M}$ [kg/kmol]	h [-]	Density ρ_c [kg/m^3]	C_c [kmol/m^3]	Mass ratio Water W^*_{20} [kg/kg]	Alcohol W^*_{20} [kg/kg]	Ether W^*_{20} [kg/kg]	Density ρ_L^* [kg/m^3]	No.
167	Tartaric acid (D or L)	$C_4H_6O_6$	150.088		1760	11.73	1.39	^{15}0.25	^{15}0.004		167
168	Tartaric acid (rac.)	$C_4H_6O_6$	150.088	1	1790	11.93	0.18	^{0}0.02	0.0009		168
169	Taurine	$C_2H_7O_3SN$	125.149				0.088				169
170	Thiourea	CH_4N_2S	76.122		1405	18.46	0.136	s.	sl.s.		170
171	Triglycine sulphate	$C_6H_{17}O_{10}SN_3$	323.281		1680	5.20	0.27				171
172	Urea	CH_4N_2O	60.056		1335	22.23	1.05	0.2	sl.s.	^{50}1150	172
173	Uric acid	$C_5H_4O_3N_4$	168.112		1890	11.24	0.00006	i.	i.		173

Table A1.3. (Key)

No.	Solute	Literature								No.
		W* in water	W* org. s.	ρ_L*	η_L	D_{AB}	Δc_{met}, σ_{met}	B	G	
109	Acetamide	Mul72,Lan69			Lan69	Lan69				109
110	Acetanilide	Mul72,Lan69								110
111	Acetylsalicylic acid	Lan69								111
112	Adipic acid	Mul72,DAn67,Lan69	Lan69			Gut90	Wil99		Mic60	112
113	Alanine(D)	Mul72,DAn67,Lan69			Lan69					113
114	Alanine(DL)	Mul72,DAn67,Lan69			Lan69					114
115	Aminophenol o-	Mul72,Lan69								115
116	Aminophenol m-	Mul72,Lan69								116
117	Aminophenol p-	Mul72,Lan69								117
118	Anthracene	Lan69								118
119	Anthranilic acid o-	Mul72,Lan69								119
120	Benzamide	Mul72,Lan69								120
121	Benzoic acid	Mul72,Lan69,DAn67	Lan69				Las99			121
122	Cinnamic acid (trans-)	Mul72,DAn67,Lan69	Lan69							122
123	Citric acid	Mul72,DAn67,Lan69		Kin89	Kin89, Lan69	Lan69 Gut90		Sik76	Mul72,Liu70, Sik76, Car59, Ber82/84,Kin89	123
124	Cresol o-	Lan69	Lan69							124
125	Dicyandiamide	Mul72,Lan69								125

No.	Solute	Literature								No.
		W* in water	W* org. s.	ρ_L*	η_L	D_{AB}	Δc_{met}, σ_{met}	B	G	
126	Ethylendiamine tartrate	Sko67							Boo52,Ben69	126
127	Fructose	Mul72								127
128	Fumaric acid (trans-)	Mul72,DAn67,Lan69			Lan69					128
129	Glucose (alpha-D)	Mul72,Lan69	Lan69			Lan69				129
130	Glutamic acid (D)	Mul72,DAn67,Lan69					Kit96	Kit99		130
131	Glyceryl tripalmitate		Lan69 Sko67	Kin89					Bou80,Sko67, Kin89	131
132	Glyceryl tristearate		Lan69 Sko67	Kin89					Bou80,Sko67, Kin89	132
133	Glycine	Mul72,DAn67,Lan69			Lan69					133
134	Hexamethylene tetramine	Lan69		Kin89	Lan69	Lan69 Gut90		Bou76	Bou76/80	134
135	Hexatriacontane								Bec87,Lun79, Kin89, Rub81, Sim74	135
136	Hydrochinone p-	Mul72,Lan69	Lan69			Lan69				136
137	Hydoxybenzoic acid o-	Mul72,DAn67,Lan69	Lan69		Lan69					137
138	Hydoxybenzoic acid m-	Mul72,DAn67,Lan69	Lan69		Lan69					138
139	Hydoxybenzoic acid p-	Mul72,DAn67,Lan69	Lan69		Lan69					139
140	Itaconic acid					Gut90			Car59,Liu70	140
141	Lactose	Mul72,Lan69			Lan69	Gut90	Raq99			141

No.	Solute	Literature								No.
		W* in water	W* org. s.	ρ_L*	η_L	D_{AB}	Ac_{met}, σ_{met}	B	G	
142	Maleic acid	Mul72,DAn67,Lan69			Lan69					142
143	Malic acid (DL)	Mul72,DAn67,Lan69								143
144	Malonic acid	Mul72,DAn67,Lan69			Lan69					144
145	Maltose	Mul72,Lan69			Lan69					145
146	Mannitol (D)	Mul72,Lan69	Lan69							146
147	Melamine	Mul72,Lan69								147
148	Methylnaphthalene α-									148
149	Naphthalene	Lan69					Kön99			149
150	Oxalic acid	Mul72,DAn67,Lan69			Lan69	Lan69	Zar99			150
151	Pentaerythritol	Mul72				Lan69			Kin89,Bor87	151
152	Phenacetin (p)	Mul72,Lan69								152
153	Phenol	Lan69	Lan69		Lan69					153
154	Phthalic acid (o)	Mul72,DAn67,Lan69	Lan69							154
155	Picric acid (2-.4-.6-)	Mul72								155
156	Pyrocatechol o-	Mul72,Lan69	Lan69							156
157	Raffinose	Mul72				Lan69				157
158	Resorcinol m-	Mul72,Lan69	Lan69			Lan69				158
159	Saccharose	Mul72,Lan69		Mul72	Mul72, Lan69, Per84	Lan69 Gut90	Wil99	Har80	Van69,Lew74, Kin89,Ben68, Mul72,Har80, Bro92	159

No.	Solute	Literature								No.
		W* in water	W* org. s.	ρ_L*	η_L	D_{AB}	Δc_{met}, σ_{met}	B	G	
160	Salicylic acid o-	Mul72,DAn67,Lan69	Lan69		Lan69		Bla99			160
161	Salol (o)		Lan69							161
162	Sorbitol	Mul72,Lan69								162
163	Stearic acid	DAn67,Lan69	Lan69						Bec87,Mei85	163
164	Succinic acid	Mul72,DAn67,Lan69 Mul80w	Lan69	Kin89 Mul8w	Lan69 Mul8w	Lan69 Gut90			Mul80w, Kin89	164
165	Succinimide	Mul72								165
166	Sulphanilic acid (p)	Mul72,DAn67,Lan69			Lan69	Lan69				166
167	Tartaric acid (D or L)	Mul72,DAn67,Lan69	Lan69		Lan69					167
168	Tartaric acid (rac.)	Mul72,DAn67,Lan69	Lan69							168
169	Taurine	Mul72,DAn67,Lan69								169
170	Thiourea	Mul72,Lan69			Lan69	Lan69 Gut90			Bor87	170
171	Triglycine sulphate	Mul72								171
172	Urea	Mul72,Lan69		Mul72	Mul72, Lan69	Lan69 Gut90			Nyv64	172
173	Uric acid	Mul72,DAn67,Lan69								173

Table A1.4. Conversion Table

		c_{Anh}	c_{Hyd}	ρ_L	ρ_C	W_{Anh}	W_{Hyd}	w_{Anh}	w_{Hyd}	C_{Cryst}	C_C
		$\frac{kg_{anhydrate}}{m^3_{solvent}}$	$\frac{kg_{hydrate}}{m^3_{solution}}$	$\frac{kg_{solution}}{m^3_{solution}}$	$\frac{kg_{crystal}}{m^3_{crystal}}$	$\frac{kg_{anhydrate}}{kg_{solvent}}$	$\frac{kg_{hydrate}}{kg_{free\ solvent}}$	$\frac{kg_{anhydrate}}{kg_{solution}}$	$\frac{kg_{hydrate}}{kg_{solution}}$	$\frac{kmol_{crystal}}{m^3_{solution}}$	$\frac{kmol_{crystal}}{m^3_{crystal}}$
c_{Anh}	$\frac{kg_{anhydrate}}{m^3_{solution}}$	–	$c_{Hyd}\frac{W_{Anh}}{W_{Hyd}}$	$\rho_L w_{Anh}$		$\rho_L\frac{W_{Anh}}{1+W_{Anh}}$	$\frac{\rho_L W_{Hyd}}{1+W_{Hyd}}\cdot\frac{W_{Anh}}{W_{Hyd}}$	$\rho_L w_{Anh}$	$\rho_L w_{Hyd}\frac{W_{Anh}}{W_{Hyd}}$	$C\tilde{M}_{Anh}$	–
c_{Hyd}	$\frac{kg_{hydrate}}{m^3_{solution}}$	$c_{Anh}\frac{W_{Anh}}{W_{Hyd}}$	–	$\rho_L w_{Hyd}$	–	$\frac{\rho_L W_{Anh}}{1+W_{Anh}}\cdot\frac{W_{Hyd}}{W_{Anh}}$	$\rho_L\frac{W_{Hyd}}{1+W_{Hyd}}$	$\rho_L w_{Anh}\frac{W_{Hyd}}{W_{Anh}}$	$\rho_L w_{Hyd}$	$C\tilde{M}_{Hyd}$	–
ρ_L	$\frac{kg_{solution}}{m^3_{solution}}$	$\frac{c_{Anh}}{w_{Anh}}$	$\frac{c_{Hyd}}{w_{Hyd}}$	–	–	$c_{Anh}\frac{1+W_{Anh}}{W_{Anh}}$	$c_{Hyd}\frac{1+W_{Hyd}}{W_{Hyd}}$	$\frac{c_{Anh}}{w_{Anh}}$	$\frac{c_{Hyd}}{w_{Hyd}}$	$\frac{C\tilde{M}_{Anh}}{w_{Anh}}$	
ρ_C	$\frac{kg_{crystal}}{m^3_{crystal}}$	–	–	–	–		–	–	–	–	$C_C\tilde{M}_{crystal}$
W_{Anh}	$\frac{kg_{anhydrate}}{kg_{solvent}}$	$\frac{1}{\frac{\rho_L}{c_{Anh}}-1}$	$\frac{1}{\frac{\rho_L}{c_{Hyd}}\cdot\frac{W_{Hyd}}{W_{Anh}}-1}$	$\frac{1}{\frac{\rho_L}{c_{Anh}}-1}$	–		$\frac{1}{\frac{1+W_{Hyd}}{W_{Hyd}}\cdot\frac{W_{Hyd}}{W_{Anh}}-1}$	$\frac{w_{Anh}}{1-w_{Anh}}$	$\frac{1}{\frac{1}{w_{Hyd}}\cdot\frac{W_{Hyd}}{W_{Anh}}-1}$	$\frac{1}{\frac{\rho_L}{C\tilde{M}_{Anh}}-1}$	–
W_{Hyd}	$\frac{kg_{hydrate}}{kg_{free\ solvent}}$	$\frac{1}{\frac{\rho_L}{c_{Anh}}\cdot\frac{W_{Anh}}{W_{Hyd}}-1}$	$\frac{1}{\frac{\rho_L}{c_{Hyd}}-1}$	$\frac{1}{\frac{\rho_L}{c_{Hyd}}-1}$	–	$\frac{1}{\frac{1+W_{Anh}}{W_{Anh}}\cdot\frac{W_{Anh}}{W_{Hyd}}-1}$	–	$\frac{1}{\frac{1}{w_{Anh}}\cdot\frac{W_{Anh}}{W_{Hyd}}-1}$	$\frac{w_{Hyd}}{1-w_{Hyd}}$	$\frac{1}{\frac{\rho_L}{C\tilde{M}_{Hyd}}-1}$	–
w_{Anh}	$\frac{kg_{anhydrate}}{kg_{solution}}$	$\frac{c_{Anh}}{\rho_L}$	$\frac{c_{Anh}}{\rho_L}\cdot\frac{W_{Anh}}{W_{Hyd}}$	$\frac{c_{Anh}}{\rho_L}$	–	$\frac{W_{Anh}}{1+W_{Anh}}$	$\frac{W_{Anh}}{W_{Hyd}}\cdot\frac{W_{Hyd}}{1+W_{Hyd}}$	–	$\frac{W_{Anh}}{W_{Hyd}}W_{Hyd}$	$\frac{\tilde{M}_{Anh}C}{\rho_L}$	
w_{Hyd}	$\frac{kg_{hydrate}}{kg_{solution}}$	$\frac{c_{Anh}}{\rho_L}\cdot\frac{W_{Hyd}}{W_{Anh}}$	$\frac{c_{Hyd}}{\rho_L}$	$\frac{c_{Hyd}}{\rho_L}$		$\frac{W_{Hyd}}{W_{Anh}}\cdot\frac{W_{Anh}}{1+W_{Anh}}$	$\frac{W_{Hyd}}{1+W_{Hyd}}$	$\frac{W_{Hyd}}{W_{Anh}}w_{Anh}$	–	$\frac{\tilde{M}_{Hyd}C}{\rho_L}$	–
C_{Cryst}	$\frac{kmol_{crystal}}{m^3_{solution}}$	$\frac{c_{Anh}}{\tilde{M}_{Anh}}$	$\frac{c_{Hyd}}{\tilde{M}_{Hyd}}$	$\frac{\rho_L}{\tilde{M}_{Anh}}w_{Anh}$		$\frac{\rho_L}{\tilde{M}_{Anh}}\cdot\frac{W_{Anh}}{1-W_{Anh}}$	$\frac{\rho_L}{\tilde{M}_{Hyd}}\cdot\frac{W_{Hyd}}{1+W_{Hyd}}$	$\frac{\rho_L}{\tilde{M}_{Anh}}w_{Anh}$	$\frac{\rho_L}{\tilde{M}_{Hyd}}w_{Hyd}$	–	–
C_C	$\frac{kmol_{crystal}}{m^3_{crystal}}$	–	–	–	$\frac{\rho_C}{\tilde{M}_{crystal}}$	–	–	–	–	–	–

A1.1.1. Table column annotation for Tables A1.2 and A1.3

Molar mass, $\tilde{M}_{\text{inorg}}$	Above: molar mass of the anhydrate Below: the hydrate at a temperature of 20°C, atomic masses from 1971 [DAn67, Per84]
Molar mass, $\tilde{M}_{\text{org}}$	Molar mass of 1987 by the IUPAC
$h_{20,\text{inorg}}$	Number of hydrates at 20°C [Bro81]
h_{org}	Number of hydrates [Mul72]
Density, $\rho_{C,\text{inorg}}$	Density of crystalline inorganic hydrous solids at 20°C [Nik57, Bro81, DAn67, Mul72, Kin89, Per 84]
Density, $\rho_{C,\text{org}}$	Crystal density of organic systems [Mul72]
Density, C_C	Crystal molar density, calculated with $C_C = \rho_C/\tilde{M}$
Mass ratio, W^*_{20}	Solubility of hydrated salts at 20°C in water, Anh: [Mul72, Per84]; AnhHyd: [Bro81]
Mass ratio, $W^*_{20,\text{solv}}$	Solubility of organic substances in water, alcohol, and ether at 20°C [Per84, Mul72], abb.: s., soluble; v.s., very soluble; v.sl.s., very slightly soluble; sl.s., slightly soluble; i., insoluble
Density, $\rho^*_{L,20}$	Above: density of saturated solutions at 20°C [Mul72, Kin89, Hoc92, Int28] Below: density calculated with equation (A1.9)
C^*_{20}	Calculated with $C^* = \rho_L W^*/[(1 + W^*)\tilde{M}]$
c^*/ρ_c	Dimensionless solubility
ΔH_{LC}	Heat of crystallization [Nyv82]; negative: exothermic; positive: endothermic
W^*, w^*	Solubilities
ρ^*_L	Densities of saturated solutions
η_L	Viscosities; data of saturated solutions are marked with an asterisk
agg	Agglomeration
D_{AB}	Diffusivities, data of saturated solutions are marked with an asterisk
Δc_{met}, σ_{met}	Metastable zone
B	Experimental data of nucleation rates
G	Experimental data of the growth rates
qual	(Product) quality

Author Index

Bec87	Beckmann, W. Lacmann, R.	Chem.-Ing.-Tech., 59(1): 82-83 (1987)	$C_{36}H_{74}$ $C_{18}H_{36}O_2$	*G*
Bec96	Beckmann, W. Boje, G. Rossling, G Arlt, W.	Proc. 13th Symp. Industrial Crystallization, Toulouse (1996)	$C_5H_{12}O_6$	σ
Bee82	Beer, W. F. Mersmann, A.	Industrial Crystallization 81 (S. J. Jancic, E. J. de Jong, eds.), pp. 209-215 (1982)	KCl	*B, G*
Ben66	Bennema, P.	phys. stat. sol., 17: 563-570 (1966)	$KAl(SO_4)_2$ $NaClO_3$	*G*
Ben67	Bennema, P.	J. of Crystal Growth, 1: 287-292 (1967)	$KAl(SO_4)_2$ $NaClO_3$	*G*
Ben68	Bennema, P.	J. of Crystal Growth, 3. 4: 331-334 (1968)	sucrose	*G*
Ben69	Bennema, P.	J. of Crystal Growth, 5 29-43 (1969)	$NH_4H_2PO_4$ $C_6H_{14}O_6N_2$	*G*
Ber82	Berglund, K. A. Larson, M. A.	AIChE Symp. Ser., Vol. 78 (215): 9-13 (1982)	citric acid	*G*
Ber84	Berglund, K. A. Larson, M. A.	AIChE J., Vol. 30 (2): 280-287 (1984)	citric acid	*G*
Ber99	Bernard, L. Biscans, B. Freche, M. Lacout, J. L.	Proc. 13th Symp. Industrial Crystallization, Cambridge (1999)	hydroxyapatite	*agg*
Bes79	Best, J. Brown, D. J.	Industrial Crystallization 78 (S. J. Jancic, E. J. de Jong, eds.), pp. 185-193 (1979)	$KAl(SO_4)_2$	*G*
Bla99	Blandin, A. F. Mangin, D. Nallet, V. Klein, J. P. Bossoutrot, J. M.	Proc. 13th Symp. Industrial Crystallization, Cambridge (1999)	salicylic acid	*B, G*
Bli71	Bliznakov, G. Kirkova, E. Nikolaycva, R.	Kristall u. Technik, 6: 33-38 (1971)	KCl KBr KI $NaClO_3$	*G*
Boo52	Booth, A. H. Buckley, H. E.	Nature, 169: 367-368 (1952)	EDT	*G*
Bor87	Bornhütter, K.	Diploma thesis, TU Munich (1987)	CH_4N_2S $C_5H_{12}O_4$	*G*
Bot67	Botsaris, G. D. Mason, E. A. Reid, R. C.	AIChE J., 13(4): 764-767 (1967)	KCl	*G*
Bou76	Bourne, J. R. Davey, R. J.	J. of Crystal Growth, 36: 278-296 (1969)	HMT	*G, B*
Bou80	Bourne, J. R.	AIChE Symp. Ser., 76(193): 59-64 (1980)	$C_6H_{12}N_4$ $C_{57}H_{110}O_6$ $C_{51}H_{98}O_6$	*G*
Bou96	Bouropulos, N. Santilli, N. Chianese, A.	Proc. 13th Symp. Industrial Crystallization, Toulouse (1996)	caprolactan	*quad*
Bra60	Bransom, S. H.	British Chem. Engng., 12: 838-844 (1960)	$CuSO_4$ $MgSO_4$	*G*
Bra96	Bravi, M. Chianese, A. Mazzarotta, B	Proc. 13th Symp. Industrial Crystallization, Toulouse (1996)	$Na_2B_4O_7$	*G*

Bra99	Bravi, M. Corini, C. Mazzarotta, B. Verdone, N.	Proc. 13th Symp. Industrial Crystallization, Cambridge (1999)	$CaCO_3$	*qual*
Bro81	Broul, M. Nývlt, J. Söhnel, O.	solubility in inorganic two-component systems, Physical sciences data 6, elsevier (1981)	several	W^*
Bro 92	Brown, D. J. Alexander, K.	J. of Crystal Growth, 118: 464-466 (1992)	sucrose	*B*
Caf99	Cafiero, L. M. Chianese, A. Jachuck, R. J. J.	Proc. 13th Symp. Industrial Crystallization, Cambridge (1999)	$BaSO_4$	*qual*
Car59	Cartier, R Pindzola, D. Bruins, P. F.	Ind. Engng. Chem., 51(11): 1409-1414 (1959)	citric acid itaconic acid	*G*
Cek96	Cekinski, E. Danese, M. Poco, J. G. R. Camargo, E. F. M.	Proc. 13th Symp. Industrial Crystallization, Toulouse (1996)	KCl	*qual*
Cha96	Chang, L. Y. Chen, B. D. Davey, R. J.	Proc. 13th Symp. Industrial Crystallization, Toulouse (1996)	$CaSO_4$	*qual*
Che99	Chen, P.	Proc. 13th Symp. Industrial Crystallization, Cambridge (1999)	$BaCO_3$	*qual*
Chu96	Chuvao, J. Feyodo Azevedo, S.	Proc. 13th Symp. Industrial Crystallization, Toulouse (1996)	sucrose	*B, G*
Cli96	Clifford, Y. Tai, T. M. Chen, P. C. Lee, M. S.	Proc. 13th Symp. Industrial Crystallization, Toulouse (1996)	CaF_2	*G*
Clo72	Clontz, N. A. McCabe, W. L.	Chem. Engng. Sci., 27: 307-314 (1972)	$MgSO_4$	*G*
Com96	Combes, C. Freche, M. Rey, C. Bizeans, B.	Proc. 13th Symp. Industrial Crystallization, Toulouse (1996)	$Ca_3(PO_4)_2$	*B*
Cos99	Coste, V. Gabas, N. Comtat, M. Large, C. Pavarel, J. L.	Proc. 13th Symp. Industrial Crystallization, Cambridge (1999)	potassium hydrogen tartrate	*qual*
Cou99	Couzis, A. Maldarelli, C. Hazair, S. Green, D. A	Proc. 13th Symp. Industrial Crystallization, Cambridge (1999)	$CaCO_3$	*qual*
DAn67	D'Ans, J. Lax, E.	Taschenbuch für Chemiker und Physiker, Bd. I, Springer Verlag 1967	several	W^*_{org} W^*_{inorg}
Den70	Denk, E. G. Botsaris, G. D	J. of Crystal Growth, 6: 241-244 (1970)	$KAl(SO_4)_2$	*G*
Der96	Derenzo, S. Serkler, M. M. Toste, E. M.	Proc. 13th Symp. Industrial Crystallization, Toulouse (1996)	$C_6H_{10}O_4$	*agg*
Des99	Deshpande, S. Kirwan, D.	Proc. 13th Symp. Industrial Crystallization, Cambridge (1999)	l-asparagine	L_{50}
Dix96	Dixit, A. B. Colonia, E. J. Tavare, N. S.	Proc. 13th Symp. Industrial Crystallization, Toulouse (1996)	chloro-benzoic acid	*B, G*

Dok99	Doki, N. Sato, A. Yokota, M. Kubota, N.	Proc. 13th Symp. Industrial Crystallization, Cambridge (1999)	$KAl(SO_4)_2$	*qual*
Dor70	Doremus, R. H.	The J. of Phys. Chem., 74(7): 1405-1408 (1970)	$BaSO_4$	*G*
Dug78	Dugua, J. Simon, B.	J. of Crystal Growth, 44: 265-279 (1978)	$NaBO_2 \cdot H_2O_2$	*G, B*
Elg96	Elgersma, F. Witkamp, G. J. van Rosmalen, G. M.	Proc. 13th Symp. Industrial Crystallization, Toulouse (1996)	$CaSO_4$	*qual*
Fer96	Fernandez, M.C. Avelino, A. Farelo, M. F.	Proc. 13th Symp. Industrial Crystallization, Toulouse (1996)	NaCl	*G*
Fer99	Fernandes, C.	Proc. 13th Symp. Industrial Crystallization, Cambridge (1999)	paracetamol	*qual*
Fil99	Filipescu, L. Isopescu, R. Mocioi, M. Zahanagiu, F.	Proc. 13th Symp. Industrial Crystallization, Cambridge (1999)	sodium disilicate	*B, G*
Fun96	Funakushi, K. Takiyama, H. Matsuoka, M.	Proc. 13th Symp. Industrial Crystallization, Toulouse (1996)	chloronitro-benzene	*agg*
Gab96	Gabas, N. Gerbaud, V. Costeseque, P.	Proc. 13th Symp. Industrial Crystallization, Toulouse (1996)	potassium hydrogen tart-rate	*G*
Gar74	Garside, J Mullin, J. W. Das, S. N.	Ind. Eng. Chem., Fundam., 13(4): 299-305 (1974)	K_2SO_4 $KAl(SO_4)_2$	*G*
Gar77	Garside, J.	1976 crystal growth and materials (E. Kaldis, H. J. Scheel, eds.), pp. 484-511 (1977)	$KAl(SO_4)_2$	*G*
Gar82	Garside, J. Gibilaro, L. G. Tavare, N. S.	Chem. Engng. Sci., 37(11): 1625-1628 (1982)	K_2SO_4	*G*
Gen99	Genck, W. J.	Proc. 13th Symp. Industrial Crystallization, Cambridge (1999)	$Na_2B_4O_7$	*qual*
Ger99	Gerbaud, V. Gabas, N. Canselier, J. P. Verlier, J. M.	Proc. 13th Symp. Industrial Crystallization, Cambridge (1999)	$CaCO_3$ (calcite)	*qual*
Gia88	Giannimaras, E.K. Koutsoukos, P. G.	Langmuir, 4(4): 855-861 (1988)	$CaCO_3$	*G*
Gom96	Gomez Morales, J. Rodriguez Clemente, R. Hidalgo Lopez, A. Lopez Macipe, A. Raskopf, G.	Proc. 13th Symp. Industrial Crystallization, Toulouse (1996)	$CaCO_3$	*B, G*
Gon96	Gonzalez, X. Rasmuson, A. C.	Proc. 13th Symp. Industrial Crystallization, Toulouse (1996)	C_6H_5CN	L_{50}
Goo80	Goodarz-Nia, I. Motamedi, M.	J. of Crystal Growth, 48: 125-131 (1980)	$CaCO_3$	*G*
Gra99	Granberg, R. A. Ducreux, C. Gracin, S. Rasmuson, A.	Proc. 13th Symp. Industrial Crystallization, Cambridge (1999)	paracetamol	*B*
Gra99	Graber, T. A. Taboada, M. E. Alvarez, M. N.	Proc. 13th Symp. Industrial Crystallization, Cambridge (1999)	$NaNO_3$	*G*

Gru99	Grunenberg, A. Wirges, H.-P.	Proc. 13th Symp. Industrial Crystallization, Cambridge (1999)	$CaHPO_4$	*qual*
Gun99	van der Gun, M. A. Bruinsma, O. S. L. van Rosmalen, G. M.	Proc. 13th Symp. Industrial Crystallization, Cambridge (1999)	caprolactan	*qual*
Gur96	Gurbuz, H. Bulutcu, A. N.	Proc. 13th Symp. Industrial Crystallization, Toulouse (1996)	$CaHPO_4$	*qual*
Gut90	Gutwald, S.	Internal Report, TU-Munich (1990)	several	D_{AB}
Ham91	Hamza, S. M.	J. of Crystal Growth, 113; 637-642 (1991)	CaF_2	G
Har80	Hartel, R. W. et al.	AIChE Symp. Ser., 76(193): 65-72 (1980)	sucrose	B, G
Has99	Hasegawa, K. Sano, C. Iitani, K. Miyashita, S. Sazaki, G. Nakada, T. Komatsu, H.	Proc. 13th Symp. Industrial Crystallization, Cambridge (1999)	leucine	*qual*
Hel77	Helt, J. E. Larson, M. A.	AIChE J., 23(6): 822-830 (1977)	KNO_3	B, G
Hir96	Hirasawa, I. Andoh, T. Yamaguti, Y. Kimura, K. Shimamusa, K.	Proc. 13th Symp. Industrial Crystallization, Toulouse (1996)	$Na_2B_4O_7$	*qual*
Hir99	Hirasawa, I. Katayama, A. Katayama, M. Toyokura, K.	Proc. 13th Symp. Industrial Crystallization, Cambridge (1999)	$PbSO_4$	B
Hir99	Hirasawa, I. Suzuki, T. Hosoya, S.	Proc. 13th Symp. Industrial Crystallization, Cambridge (1999)	$MgNH_4PO_4$	*qual*
Hir99	Hirasawa, I. Sata, H Yamagishi, N.	Proc. 13th Symp. Industrial Crystallization, Cambridge (1999)	hydroxyapatite	L_{50}
Hol99	Hollander, F. van de Streek, J. Boerrigter, S. Plomp, M. Meekes, H. van Enckevort, W. Bennema, P.	Proc. 13th Symp. Industrial Crystallization, Cambridge (1999)	triacylglycerol	*qual*
Hos81	Hostomský, J. Rathouský, J. Skrivánek, J.	Cryst. Res. Technol., 16(7): 759-765 (1981)	$BaSO_4$	G
Hos99	Hostomska, V. Hostomsky, J. Benes, V.	Proc. 13th Symp. Industrial Crystallization, Cambridge (1999)	$NH_4Al(SO_4)_2$	*qual*
Hou96	Housine, I. Plasari, E. David, R. Villermaux, J.	Proc. 13th Symp. Industrial Crystallization, Toulouse (1996)	CaC_2O_4	L_{50}
Ili99	Ilievski, D. Rudman, M. Metcalfe, G.	Proc. 13th Symp. Industrial Crystallization, Cambridge (1999)	gibbsite	*qual*
Ito99	Ito, T. Tsuge, H. Fujita, A. Fukatani, M.	Proc. 13th Symp. Industrial Crystallization, Cambridge (1999)	$Ni(OH)_2$	*qual*

Jir79	Jira-Arune, N.Laguerie, C.	Chem. Engng. J., 18: 47-57 (1979)	KCl	G
Jon99	Jones, A. G. Ejaz, T. Graham, P.	Proc. 13th Symp. Industrial Crystallization, Cambridge (1999)	zeolite	*qual*
Kab96	Kabasci, S. Althaus, W. Weinspack, P. M.	Proc. 13th Symp. Industrial Crystallization, Toulouse (1996)	$CuCO_3$	*qual*
Kag81	Kagawa, M. Sheehan, M. E. Nancollas, G. H.	JINC, 43:917-920 (1981)	$CuSO_4$	G
Kal96	Kalashnikowa, I. Naumov, V. Kurbakov, A. Sokolov, A. Pashkov, S.	Proc. 13th Symp. Industrial Crystallization, Toulouse (1996)	SiO_2	*qual*
Kar82	Karinsky, P. Nÿvlt, J	Cryst. Res. Technol., 17(3): 383-388 (1982)	$KAl(SO_4)_2$	B, G
Kaw99	Kawakita, T.	Proc. 13th Symp. Industrial Crystallization, Cambridge (1999)	L-glutamate	*qual*
Kel96	Kelles, T. Sayan, P. Bulutcu, A. W.	Proc. 13th Symp. Industrial Crystallization, Toulouse (1996)	H_3BO_3	G
Kim99	Kim, W. S. Kim, J. S.	Proc. 13th Symp. Industrial Crystallization, Cambridge (1999)	Yttrium oxalate	G
Kim99	Kim, H. J. Kim, W. S.	Proc. 13th Symp. Industrial Crystallization, Cambridge (1999)	NaF	L_{50}
Kim99	Kim, K. J. Kim, M.-J. Lee, J.-M.	Proc. 13th Symp. Industrial Crystallization, Cambridge (1999)	3-nitro-1,2,4-triazol	*qual*
Kin83	Kind, M. H. Mersmann, A.	Chem.-Ing.-Tech. 55(9): 720-721 (1983)	$(NH_4)_2SO_4$ KCl NaCl	B
Kin89	Kind, M. H.	Ph. D. Thesis, TU Munich (1989)	several	Ac_{met}
Kir71	Kirkova, E. Nikolaeva, R.	Kristall u. Technik, 6(6): 741-746 (1971)	NaCl	G
Kir73	Kirkova, E. Nikolaeva, R.	Kristall u. Technik, 884):463-470 (1973)	$KAl(Cr(SO_4)_2$	G
Kit96	Kitamura, M. Yamanami, T.	Proc. 13th Symp. Industrial Crystallization, Toulouse (1996)	glutamic acid	G
Kit99	Kitamura, M. Nakamura, T.	Proc. 13th Symp. Industrial Crystallization, Cambridge (1999)	glutamic acid	*qual*
Kit99	Kitamura, M. Yoshinaga, Y. Masuoka, H.	Proc. 13th Symp. Industrial Crystallization, Cambridge (1999)	sulphathiazole	*qual*
Kol99		Proc. 13th Symp. Industrial Crystallization, Cambridge (1999)	$Ca_3(PO_4)_2$	*qual*
Kön99	König, A. Steiner, R. Freund, H.	Proc. 13th Symp. Industrial Crystallization, Cambridge (1999)	biphenyle/naphthalene	*qual*

Koo99	Koopman, C. Witkamp, G. J.	Proc. 13th Symp. Industrial Crystallization, Cambridge (1999)	$CaSO_4$	*qual*
Kor96	Korolewicz, T. Wojcik, J.	Proc. 13th Symp. Industrial Crystallization, Toulouse (1996)	$Ba(NO_3)_2$	*qual*
Kor99	Korolewicz, T. Wojcik, J.	Proc. 13th Symp. Industrial Crystallization, Cambridge (1999)	$BaCl_2$	*qual*
Kot90	Kotaki, Y. Tsuge, H.	The Can. J. of Chem. Engng., 68: 435-442 (1990)	$CaCO_3$	*G, B*
Koy96	Koyoglu, A. Nasun-Sagili, G.	Proc. 13th Symp. Industrial Crystallization, Toulouse (1996)	zeolite	L_{50}
Kra90	Kralj, D. Brecevic, L. Nielsen, A. E.	J. of Crystal Growth, 104: 793-800 (1990)	$CaCO_3$	*G*
Lac96	Lacmann, R. Mayer, C.	Proc. 13th Symp. Industrial Crystallization, Toulouse (1996)	$NaClO_3$	*B*
Lan69	Landolt Börnstein	Landolt Börnstein, Springer Verlag (1966/77)	several	W^*, η D_{AB}
Las99	Lashanizadegan, A. Newsham, D. M. T. Tavare, N. S.	Proc. 13th Symp. Industrial Crystallization, Cambridge (1999)	chlorobenzoic acid	*qual*
Lee89	van der Leeden, M. van Rosmalen, G., et al	Chem.-Ing.-Tech. 61(5): 385-395 (1989)	$CaSO_4$ $BaSO_4$	*G*
Lee99	Lee, M. Parkinson, G. M. Tsukamoto, K.	Proc. 13th Symp. Industrial Crystallization, Cambridge (1999)	gibbsite	*qual*
Lew74	Lewis, B.	J. of Crystal Growth, 21: 40-50 (1974)	$KAl(SO_4)_2$ $NaClO_3$ sucrose	*G*
Lin96	Lin, G. H. Gabas, N. Canselier, J. P. Pepe, G.	Proc. 13th Symp. Industrial Crystallization, Toulouse (1996)	aminobutyric acid	*G*
Liu70	Liu, C. Y. Tsuei, H. S. Youngquist, G. R.	Chem. Engng. Prog. Symp. Ser., 67(110): 43-52 (1970)	$MgSO_4$ $KAl(SO_4)_2$ itaconic acid citric acid	*G*
Loh99	Loh, J. S. C. Parkinson, G. M. Watling, H. R.	Proc. 13th Symp. Industrial Crystallization, Cambridge (1999)	gibbsite	*qual*
Lop99	Lopes, A. Ferra, M. I. A. Farelo, F.	Proc. 13th Symp. Industrial Crystallization, Cambridge (1999)	KCl	*G*
Lou96	Louhi-Kultanen, M. Sha, Z. Shitaj, Y. Palosari, S.	Proc. 13th Symp. Industrial Crystallization, Toulouse (1996)	KCl	*B*
Lun79	Lundager Madsen, H. E. Boistelle, R.	J. of Crystal Growth, 46:681-690 (1979)	$C_{32}H_{74}$	*G*
Lyc99	Lyczko, N. Espitalier, F. Schwartzentruber, J.	Proc. 13th Symp. Industrial Crystallization, Cambridge (1999)	K_2SO_4	*B*

Mae96	Maeda, K. Kashimoto, T. Fukui, K. Hirota, S.	Proc. 13th Symp. Industrial Crystallization, Toulouse (1996)	$C_{11}H_{23}COOH$ $C_{15}H_{31}COOH$	*qual*
Mar69	Marshall, R. W. Nancollas, G. H.	The J. of Phys. Chem., 73(11): 3838-3844 (1969)	$CaHPO_4$	*G*
Mar73	Marshall, W. L. Slusher, R.	J. of Chem. Thermodyn., 5: 189-197 (1973)	$CaSO_4$	*W**
Mar96	Marrot, B. Biscans, B.	Proc. 13th Symp. Industrial Crystallization, Toulouse (1996)	NaCl	*a*
Mat96	Matsuoka, M. Takiyama, H. Otsuhata, T.	Proc. 13th Symp. Industrial Crystallization, Toulouse (1996)	KCl NaCl	*G*
Mat99	Mattos, M. Wangnick, K. Ulrich, J.	Proc. 13th Symp. Industrial Crystallization, Cambridge (1999)	benzophenone	*qual*
Mat99	Matynia, A. Wierzbowska, B. Bechtold, Z. Kuzak, E.	Proc. 13th Symp. Industrial Crystallization, Cambridge (1999)	vitamin C	*B*
McC51	McCabe, W. L. Stevens, R. P.	Chem. Engng. Prog., 47(4): 168-174 (1951)	$CuSO_4$	*G*
Mei85	Meier, J. Kämmer, S. Beckmann, W.	Chem.-Ing.-Tech., 57(11):1000-1004 (1985)	stearic acid	*G*
Mer85	Mersmann, A.	Chem.-Ing.-Tech., 57(11): 1000-1004 (1985)	K_2SO_4 KNO_3 $KAL(SO_4)_2$ KCl $NH_4Al(SO_4)_2$ $(NH_4)_2SO_4$	$B, \Delta c_{met}$
Mer86	Mersmann, A.	Stoffübertragung, Springer-Verlag, 1986	several	D_{AB}
Mic60	Michaels, A. S. Colville, A. R.	The J. of Phys. Chem., 64 (1960) 1 p. 13	adipic acid	*G*
Mis71	Misra, C. White, E. T.	Chem. Engng. Prog. Symp. Ser., 67(119):53-65 (1971)	$Al(OH)_3$	*G, B*
Mis96	Misztal, S. Verdoes, D.	Proc. 13th Symp. Industrial Crystallization, Toulouse (1996)	caprolactam	*B, G, L_{50}*
Mis99	Misztal, S. Verdoes, D.	Proc. 13th Symp. Industrial Crystallization, Cambridge (1999)	caprolactam	*L_{50}*
Mit91	Mitrovic, M. M. Ristic, R. I.	J. of Crystal Growth. 112: 160-170 (1991)	$MnCl_2$	*G*
Moc96	Mocioi, M. Ispenescu, R. Filipescu, L.	Proc. 13th Symp. Industrial Crystallization, Toulouse (1996)	$CaCO_3$	*B, G, L_{50}*
Moi99	Moizot, A. P. Neville, A. Hodgkiess, T.	Proc. 13th Symp. Industrial Crystallization, Cambridge (1999)	$CaCO_3$	*qual*
Mou99	Mougin, P. Roberts, K. Wilkinson, D. Roberts, D. Tweedie, R.	Proc. 13th Symp. Industrial Crystallization, Cambridge (1999)	urea	*qual*

Muh96	Muhr, H. Pericut, P. Plasari, E. Villermaux, J.	Proc. 13th Symp. Industrial Crystallization, Toulouse (1996)	$BaSO_4$	L_{50}
Mul67	Mullin, J. W. Garside, J.	Trans. IChemE, 45:285-290, 291-295 (1967), 46: 11-18 (1968)	$KAl(SO_4)_2$	G
Mul69	Mullin, J. W. Gaska, C.	The Can. J. of Chem. Engng., 47:483-489 (1969)	K_2SO_4	$G, B, \Delta c_{met}$
Mul70	Mullin, J. W. Chakraborty, M. Mehta, K.	J. appl. Chem., 20: 367-371 (1970)	$(NH_4)_2SO_4$	G
Mul72	Mullin, J. W.	Crystallization, 2nd ed., Butterworths, London (1972)	several	W^*, ρ_L^* $\eta_L, \Delta c_{met}$
Mul73a	Mullin, J. W. Gaska, C.	J. of Chem. Engng. Data, 18(2): 217-220 (1973)	K_2SO_4	G
Mul73b	Mullin, J. W. Osman, M. M.	J. of Chem. Engng. Data, 18(4): 353-355 (1973)	$Ni(NH_4)_2(SO_4)_2$	G
Mul80	Mullin, J. W.	Chemistry and Industry, 3 May: 372-377 (1980)	several	G
Mul80w	Mullin, J. W. Whiting, M. J. L.	Ind. Engng. Chem. Fundam., 19: 117-121 (1980)	succinic acid	G
Mul93	Mullin, J. W.	Crystallization, 3. ed., Butterworths-Heinemann, London (1993)	several	W^*, ρ_L^* $\eta_L, \Delta c_{met}$
Mum96	Mumtaz, H. S. Hounslow, M. J. Seaton, N. A. Paterson, W. R.	Proc. 13th Symp. Industrial Crystallization, Toulouse (1996)	CaC_2O_4	agg
Nag99	Nagamiya, T. Tsuge, H. Manabe, Y.	Proc. 13th Symp. Industrial Crystallization, Cambridge (1999)	$Mg(OH)_2$	$qual$
Nak79	Nakai, T. Nakamaru, H.	Proceedings on Industrial Crystallization 78 (E. J. de Jong, S. J. Jancic, eds.) (1979)	$CaCO_3$	B
Nan80	Nancollas, G. H. Koutsoukos, P. G.	Prog. Crystal Growth Charact., 3:77-102 (1980)	$Ca_5(PO_4)_3OH$	G
Nie58	Nielsen, A. E.	Acta Chem. Scand., 12(5): 951-958 (1958)	$BaSO_4$	G
Nie79	Nielsen, A. E.	Proceedings on Industrial Crystallization 78 (E. J. de Jong, S. J. Jancic, eds.) (1979)	$AgCl$ $CaCO_3$ $BaSO_4$	G
Nik57	B. P. Nikolski	Handbuch des Chemikers Bd. III, VEB Verlag Technik, Berlin (1959)	several	W^*
Nor99	Nordhoff, S. Bechtloff, B. Ulrich, J. Wagner, G. Dumpelmann, R.	Proc. 13th Symp. Industrial Crystallization, Cambridge (1999)	sodium-2-keton-L-gulonate	$qual$
Nyv64	Nývlt, J. Gottfried, J. Kricková, J.	Coll. Czechoslov. Chem. Commun., 29:161-167 (1964)	urea	G
Nyv68	Nývlt, J.	J. of Crystal Growth, 3,4: 377-383 (1968)	several	Δc_{met}
Nyv70	Nývlt, J., et al.	J. of Crystal Growth, 6:151-162 (1970)	several	Δc_{met}
Nyv82	Nývlt, J.	Industrial Crystallisation. The State of the Art, verlag chemie (1982)	several	ΔH_{LC}

Oka99	Okawa, T. Tsuge, H. Matsue, H.	Proc. 13th Symp. Industrial Crystallization, Cambridge (1999)	CaCO3	*qual*
Oos96	Oosterhof, H. Zulema, T. G. Witkamp, G. J. van Rosmalen, G. M.	Proc. 13th Symp. Industrial Crystallization, Toulouse (1996)	NaCl	L_{50}
Ozk99	Ozcan, O. Yuksel, Y. Gurlek, F. Bulutcu, A. N.	Proc. 13th Symp. Industrial Crystallization, Cambridge (1999)	$Na_2B_4O_7$	*qual*
Pac81	Pacák, P. Oesterreicherová, H.	Cryst. Res. Technol., 16(10): 1117-1121 (1981)	$Ca(NO_3)_2$	*G*
Pax99	Paxton, T. E. Sambanis, A. Rousseau, R. W.	Proc. 13th Symp. Industrial Crystallization, Cambridge (1999)	protein	*B*
Per84	Perry, R. H.	Perry's Chemical Engineer's Handbook, McGraw-Hill. (1984)	several	*W**
Pet84	Peters, R. W. Chen, P-H Chang, T.	Proceedings on Industrial Crystallization 84 (S. J. de Jon, S. J. Jancic, eds.) (1984)	$CaCO_3$	*B, G*
Pul96	Pulak, W. Sangwal, K.	Proc. 13th Symp. Industrial Crystallization, Toulouse (1996)	KCl	*B*
Pun99	Pons, M. N. Vivier, H. Faria, N. Rocha, F. de Azevedo, S. F.	Proc. 13th Symp. Industrial Crystallization, Cambridge (1999)	sugar	*qual*
Pra99	Prasad, K. V. R. Ristic, R. I. Sheen, D. B. Sherwood, J. N.	Proc. 13th Symp. Industrial Crystallization, Cambridge (1999)	paracetamol	*qual*
Pri99	Prisciandaro, M. Lancia, A. Musmarra, D.	Proc. 13th Symp. Industrial Crystallization, Cambridge (1999)	gypsum	*B*
Rag99	Raghavan, S. L. Ristic, R. I. Sheen, D. B. Sherwood, J. N.	Proc. 13th Symp. Industrial Crystallization, Cambridge (1999)	alpha-lactose	*qual*
Ran72	Randolph, A.D. Cise, M. D.	AIChE J., 18(4): 798-807 (1972)	K_2SO_4	*B, G*
Reb99	Rebello, A. M. M. J. Davey, R. J.	Proc. 13th Symp. Industrial Crystallization, Cambridge (1999)	tin(IV)oxide	*qual*
Rei96	Reitman, T. Rohani, S. Strathdee, G.	Proc. 13th Symp. Industrial Crystallization, Toulouse (1996)	K_2CO_3	*G*
Rei68	Reich, T. Kahlweit, M.	Berichte der Bunsengesellschaft, 72(1): 66-73 (1968)	BaC_2O_4 TlBr	*G*
Rey96	Reyhani, M. M. Parkinson, G. M.	Proc. 13th Symp. Industrial Crystallization, Toulouse (1996)	$NiSO_4$ $ZnSO_4$	*B*
Rin99	Ring, T. A. Dirksen, J. A. Duvall, K. N. Jongen, N.	Proc. 13th Symp. Industrial Crystallization, Cambridge (1999)	LiBr	*qual*
Rod76	Rodriguez-Clemente, R. Mullin, J. W., ed.	Proceedings on Industrial Crystallizatin 75 (J. W. Mullin, ed.) (1976)	NaCl	*G*

Rod99	Rodrigues, C. P. P. C. Rocha, F. A. N.	Proc. 13th Symp. Industrial Crystallization, Cambridge (1999)	$CaHPO_4$	*qual*
Rod99	Rodrigues, C. C. Rocha, F. A. N.	Proc. 13th Symp. Industrial Crystallization, Cambridge (1999)	$Al_2(SO_4)_3$	*qual*
Rol99	Rolfe, N. Ashcroft, M. J. Silverwood, P. R.	Proc. 13th Symp. Industrial Crystallization, Cambridge (1999)	Na_2CO_3	*qual*
Ros71	Rosen, H. N. Holburt, H. M.	Chem. Engng. Prog. Symp. Ser., 67(110): 27-31 (1971)	K_2SO_4	*G*
Ros96	Rossiter, D. S. Ilievski, D. Smith, P. G. Parkinson, G. M.	Proc. 13th Symp. Industrial Crystallization, Toulouse (1996)	$Al(OH)_3$	*B, G*
Rou96	Rousseau, R. W. Sakamoto, K.	Proc. 13th Symp. Industrial Crystallization, Toulouse (1996)	aspartame	σ_{met}
Rub81	Rubbo, M. Boistelle, R.	J. of Crystal Growth, 51: 480-488 (1981)	$C_{36}H_{74}$	*G*
Rum60	Rumford, F. Buin, J.	Trans. IChemE, 38: 10-20 (1960)	NaCl	G, Ac_{met}
Sa96	Sa, S. Guimares, L. Rocha, F. Bento, L.	Proc. 13th Symp. Industrial Crystallization, Toulouse (1996)	$C_6H_{12}O_6$	*G*
San90	Sangl, R. Mersmann, A.	Chem.-Ing.-Tech. 62(4): 346-347 (1990)	KCl KNO_3 $(NH_4)_2SO_4$	*B*
Say96	Sayan, P. Bulutcu, A. N.	Proc. 13th Symp. Industrial Crystallization, Toulouse (1996)	H_3BO_3	*B*
Say96	Sayed, S. Sultan, G. Omar, W. Mohamed, H. Ulrich, J.	Proc. 13th Symp. Industrial Crystallization, Toulouse (1996)	KCl	*G*
Sch75	Schierholz, P. M. Stevens, J. D.	AIChE Symp. Ser., 71(151): 248-256 (1975)	$CaCO_3$	*B, G*
Sch96	Schiavon, S. H. Seckler, M. M. Derenzo, S. Valarelli, J. V. Giulietti, M.	Proc. 13th Symp. Industrial Crystallization, Toulouse (1996)	$CuSO_4$	*qual*
Sey99	Seyssiecq, I. Veesler, S. Boistelle, R. Mangin, D. Klein, J. P.	Proc. 13th Symp. Industrial Crystallization, Cambridge (1999)	gibbsite	*agg*
Sey96	Seyssiecq, I. Veesler, S. Boistelle, R.	Proc. 13th Symp. Industrial Crystallization, Toulouse (1996)	$Al(OH)_3$	*agg*

Shi99	Shi, B. Rousseau, R. W.	Proc. 13th Symp. Industrial Crystallization, Cambridge (1999)	Na_2CO_3 Na_2SO_4	

Shi96	Shimizu, K Takahashi, K. Nomura, T.	Proc. 13th Symp. Industrial Crystallization. Toulouse (1996)	$KAl(SO_4)_2$	L_{50}
Sik76	Sikdar, S. K. Randolph, A. D.	AIChE J., 22(1): 110-117 (1976)	$MgSO_4$ citric acid	B, G
Sik80	Sikdar, S. K. Orό, F. Monre, J. H.	AIChE Symp. Ser., 76(193): 82-89 (1980)	$CaSO_4$	B, G
Sim74	Simon, B. Grassi, A. Boistelle, R.	J. of Crystal Growth. 26:77-89 (1974)	$C_{36}H_{74}$	G
Sip73	Sipyagin, V. V. Chernov, A. A.	Sov. Phys.-Crystallography, 17(5): 881-888 (1973)	KNO_3 $NaNO_2$ $NaNO_3$ $NaClO_4$ $C_4H_4O_6$ KNa	G
Sip99	Sipos, G. Parkinson, G. M. Kildea, J. D.	Proc. 13th Symp. Industrial Crystallization. Cambridge (1999)	$Na_2C_2O_4$	G
Sko67	Skuda, W. van den Tempel, M.	J. of Crystal Growth. 1: 207-217 (1967)	$C_{51}H_{98}O_6$ $C_{57}H_{110}O_6$	G, W^*
Söh77	Söhnel, O. Garside, J. Jancic, S. J.	J. of Crystal Growth. 39:307-214 (1977)	K_2SO_4 KH_2PO_4	G
Söh85	Söhnel, O.	densities of aqueous solutions of inorganic substances, Prague 1985	several	ρ_c, ρ_L^*
Sub96	Subra, P. Debenedetti, P. Ksibi, H	Proc. 13th Symp. Industrial Crystallization, Toulouse (1996)	caffeine	L_{50}
Tai96	Tai, C. Y. Chen, C.-S.	Proc. 13th Symp. Industrial Crystallization. Toulouse (1996)	$C_{10}H_8$	G
Tan64	Tanimoto, A. Kobayashi, K. Fujita, S.	Int. Chem. Engng., 4(1): 153-157 (1964)	$CuSO_4$	G
Tav79	Tavare, N. S. Chivate, M. R.	Trans. IChemE, 57:35-42 (1979)	K_2SO_4	G
Tei99	Teipel, U. Heintz, T. Leisinger, K. Krause, H	Proc. 13th Symp. Industrial Crystallization, Cambridge (1999)	ammonium dinitramide	*qual*
Ten83a	Tengler, T. Mersmann, A.	Ger. Chem. Eng., 7:248-259 (1984)	NaCl $MgSO_4$ $KAl(SO_4)_2$ KNO_3 KCl $(NH_4)_2SO_4$	$G, \Delta c_{met}$
Ten83b	Tengler, T. Mersmann, A.	Chem.-Ing.-Tech. 55(9):730-731 (1983)	KNO_3 KCl $(NH_4)_2SO_4$	$G, \Delta c_{met}$
Ten90	Tengler, T.	PhD Thesis, TU Munich (1990)	$(NH_4)_2SO_4$	G, B

Tho99	Thomson, G.B. Duncan, A. Roberts, K. J. Smith, L. A. Machin, D. McLeod, G.	Proc. 13th Symp. Industrial Crystallization, Cambridge (1999)	sodium dodecyl-sulfate	*qual*
Tim71	Timm, D. C. Cooper, T. R.	AIChE J., 17(2): 285-288 (1971)	$K_2Cr_2O_7$	*B, G*
Toy84	Toyokura, K. Yoshida, S Mano, T. Uchiyama, M.	Proceedings on Industrial Crystallization 84 (E.J. de Jong, S. J. Jancic, eds.) (1984)	$Ba(OH)_2$ KCl	*G*
Toy76	Toyokura, K. Yamazoe, K. Mogi, J.	AIChE Symp. Ser., 72(153): 53-60 (1976)	$KAl(SO_4)_2$	*B, G*
Tro68	Troost, S	J. of Crystal Growth, 3/4: 340-343 (1968)	$Na_5P_3O_{10}$	*G*
Tro72	Troost, S.	J. of Crystal Growth, 13/14:449-453 (1972)	$Na_5P_3O_{10}$	*G*
Tro92	Tronin, A. Y.	J. of Crystal Growth, 116: 63-74 (1992)	$LiIO_3$	*G*
Tsu87	Tsuge, H. Kotaki, Y. Hibino, S.	Ind. Cryst. 87: 611-614 (1987)	$CaCO_3$	*B, G*
Tsu96	Tsuge, H. Yoshizawa, S. Tsuzuki, M.	Proc. 13th Symp. Industrial Crystallization, Toulouse (1996)	$Ca_3(PO_4)_2$	*B, σ*
Ulr87	Ulrich, J. Stepanski, M.	Chem.-Ing.-Tech., 59(8): 680 (1987)	K_2SO_4	*G*
Ulr91	Ulrich, J. König, A.	Chem. Ing.-Tech., 63(1):55-56 (1991)	NaCl KCl	*G*
Uka96	Ukai, K. Hyodo, T. Toyokura, K.	Proc. 13th Symp. Industrial Crystallization, Toulouse (1996)	$CaCl_2$ $NaHCO_3$	L_{50}
Van69	Vanhook, A.	J. of Crystal Growth, 5: 305-311 (1969)	sucrose	*G*
Vei99	Veiga, A. R. Calimanovici, C. E. Giulietti, M.	Proc. 13th Symp. Industrial Crystallization, Cambridge (1999)	NH_4HCO_3	*qual*
Vel99	Veltmans, W. H. M. van der Heijden, A.	Proc. 13th Symp. Industrial Crystallization, Cambridge (1999)	hydraziniumnitroformate	*qual*
Vek92	Vekilov, P. G. Kuznetsov, Y. G.	J. of Crystal Growth, 119: 248-260 (1992)	$NH_4H_2PO_4$	*G*
Ver96	Verdoes, D. Nienwoord, M.	Proc. 13th Symp. Industrial Crystallization, Toulouse (1996)	caprolactan	*qual*
Viv99	Vivier, R. Muhr, H. Jamis, P. Plasari, E.	Proc. 13th Symp. Industrial Crystallization, Cambridge (1999)	Ag_2O	*qual*
Vrh99	Vrhunec, A. Livk, I. Pohar, C.	Proc. 13th Symp. Industrial Crystallization, Cambridge (1999)	$Na_2B_4O_7$	*qual*
Vuc96	Vucak, M. Pons, M. N. Vivier, H.	Proc. 13th Symp. Industrial Crystallization, Toulouse (1996)	CaC_2O_4 BaC_2O_4 SrC_2O_4	*qual*

Vuc96	Vucak, M. Peric, J. Pons, M. N.	Proc. 13th Symp. Industrial Crystallization, Toulouse (1996)	$CaCO_3$	*agg*
Wan96	Wang, J. Zhang, M. Wang, Y.	Proc. 13th Symp. Industrial Crystallization, Toulouse (1996)	penicillin	L_{50}
Was99	Wasito, B. Tavare, N. S. Prakash, O.	Proc. 13th Symp. Industrial Crystallization, Cambridge (1999)	$YBy_2Cu_3O_7$	*qual*
Wat99	Watling, H. R. Loh, J. S. C. Townsend, R.	Proc. 13th Symp. Industrial Crystallization, Cambridge (1999)	gibbsite	*qual*
Wei84	Weijnen, M. P. C. van Rosmalen, G. M.	Proceedings on Industrial Crystallization 84 (E. J. de Jong, S. J. Jancic, eds.) (1984)	$CaSO_4$	*B, G*
Wes99	Westin, K. J Rasmuson, A. C.	Proc. 13th Symp. Industrial Crystallization, Cambridge (1999)	$CaCO_3$	*qual*
Wil99	Williams- Seton, L. Davey, R. J. Lieberman, H. F.	Proc. 13th Symp. Industrial Crystallization, Cambridge (1999)	saccharin	*qual*
Wil99	Wilson, M. P. Rohl, A. L. McKinnon, A. J. Gale, J. D.	Proc. 13th Symp. Industrial Crystallization, Cambridge (1999)	gypsum	*qual*
Wil99	Williams-Seton, L. Davey, R. J. Lieberman, H. F. Pritchard, R. G.	Proc. 13th Symp. Industrial Crystallization, Cambridge (1999)	adipic acid	*qual*
Wit90	Witkamp, G. J. van der Eerden, J. P. van Rosmalen, G. M	J. of Crystal Growth. 102:281-289 (1990)	$CaSO_4$	*G*
Wey82	Wey, J. S. Jagannathan, R.	AIChE J., 28(4): 697-698 (1982)	$(NH_4)_2SO_4$	*G*
Woj96	Wojcik, J. A. Jones, A. G.	Proc. 13th Symp. Industrial Crystallization, Toulouse (1996)	$CaCO_3$	*B, G, agg*
Wuh96	Wubbolts, F. E. Buijsse, R. E. A. Brunsmn, O. S. L. de Graauw, J. van Rosmalen, G. M.	Proc. 13th Symp. Industrial Crystallization, Toulouse (1996)	poly-2,6di-methyl-1,4phenyl-ether	L_{50}
Yav96	Yavasoglu, N. Bulutcu, A. N.	Proc. 13th Symp. Industrial Crystallization, Toulouse (1996)	$Na_2B_4O_7$	*qual*
Yin99	Ying, J. Y. Wang, C. C.	Proc. 13th Symp. Industrial Crystallization, Cambridge (1999)	Ti	L_{50}
Yua90	Yuan, J. J. Stepanski, M. Ulrich, J.	Chem.-Ing.-Tech., 62(8): 645-646 (1990)	NaCl	*G*
Zah96	Zahanagiu, P. Radovici, C. Filipescu, L.	Proc. 13th Symp. Industrial Crystallization, Toulouse (1996)	Na_2SiO_5	*qual*
Zar99	ZareNezhad, B. Garside, J. Tavare, N. S.	Proc. 13th Symp. Industrial Crystallization, Cambridge (1999)	oxalic acid	*qual*

A1.2. Densities of Solutions

With the density ρ_L^0 of the pure solvent and the density ρ_C of the crystals, the mass M_L of a binary solution is the sum of the mass M_L^0 of the solvent and the mass M_C of the crystals:

$$M_L = M_L^0 + M_C \tag{A1.4}$$

or

$$V_L \rho_L = V_L^0 \rho_L^0 + V_C \rho_C \tag{A1.5}$$

The volume V_L of the solution is equal to the sum of the volume V_L^0 of the solvent and the volume V_C of the crystals and the volume difference ΔV, which accounts for volume dilatation or reduction during solving:

$$V_L = V_L^0 + V_C + \Delta V \tag{A1.6}$$

With the ratio

$$\frac{V_C}{V_L^0} = \frac{M_C \rho_L^0}{M_L^0 \rho_C} = W \frac{\rho_L^0}{\rho_C} \tag{A1.7}$$

these equations can be combined to

$$\frac{\rho_L}{\rho_L^0} = \frac{1 + W}{1 + (\rho_L^0/\rho_C) W + \Delta V^*} \tag{A1.8}$$

with $\Delta V^* = \Delta V / V_L^0$.

In Figure A1.1, the expression ΔV^* is plotted against the solubility mass ratio W^*. The data are calculated according to equation (A1.8) and based on 524 measured values of 82 inorganic aqueous systems in the temperature range from 0°C to 100°C. As a rule, the accuracy of equation (A1.8) is better than ±12% when ΔV^* is omitted according to the simplified equation

$$\frac{\rho_L}{\rho_L^0} = \frac{1 + W}{1 + (\rho_L^0/\rho_C) W} \tag{A1.9}$$

The evaluation shows that the deviation of the calculated densities from the experimental values is less than ±5% for 90% of all data.

A1.3. Viscosities

As a rule, an approximately straight line can be expected when the logarithm of the dynamic viscosity is plotted against the reciprocal of the absolute temperature; see Figure A1.2. In this diagram, the boiling temperatures at a pressure of 0.1 MPa is characterized by an asterisk. The viscosity of most

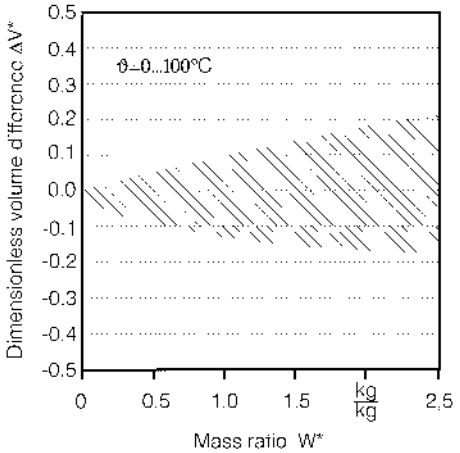

Figure A1.1. Dimensionless volume difference ΔV^* versus the solubility mass ratio W^* of 67 inorganic aqueous systems (anhydrous and hydrous).

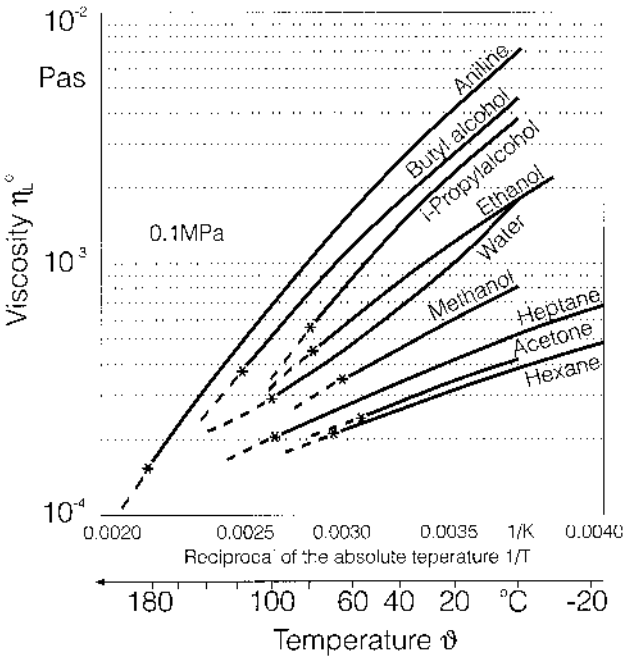

Figure A1.2. Dynamic viscosity η_L° versus the temperature for some solvents.

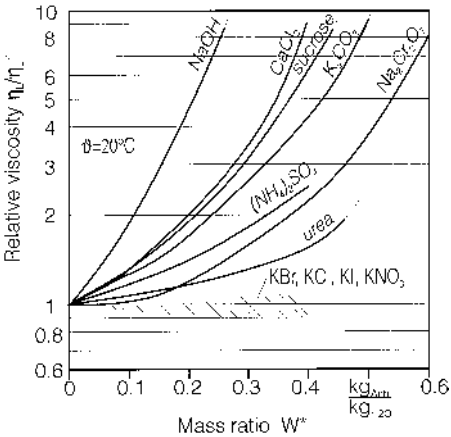

Figure A1.3. Relative viscosity η_L/η_L° versus the mass ratio W^* for some aqueous binary systems.

solvents is in the range $0.2 < \eta_L < 0.5$ mPa s at this temperature. The presence of a solute in a solvent may lead to a small decrease of the viscosity of the solvent with increasing concentration but can also increase the viscosity dramatically; see Figure A1.3. No simple rule is available in order to predict the relationship $\eta_L = f(W^*)$.

A1.4. Diffusivities

The simplest equation for the volume diffusivity is that according to Stokes–Einstein:

$$D_{\mathrm{AB}} = \frac{kT}{2\pi\eta_L d_m} \approx \frac{kT(C_C N_A)^{1/3}}{2\pi\eta_L} \tag{A1.10}$$

Figure A1.4 shows a comparison between experimental data and data calculated according to this equation. However, principally speaking, the diffusivity depends on temperature *and* concentration. In Figure A1.5, the diffusivities of the solute in some aqueous binary systems are plotted against the molar concentration C. The solubility is marked by an asterisk. It is difficult to predict the relationship $D_{\mathrm{AB}} = f(C)$. In the supersaturated range $\sigma > 0$, a decrease of diffusion coefficient accompanied by an increase in the viscosity of the solution has been observed experimentally; compare Chapter 3. The well known but not dimensionless equation of Wilke and Chang

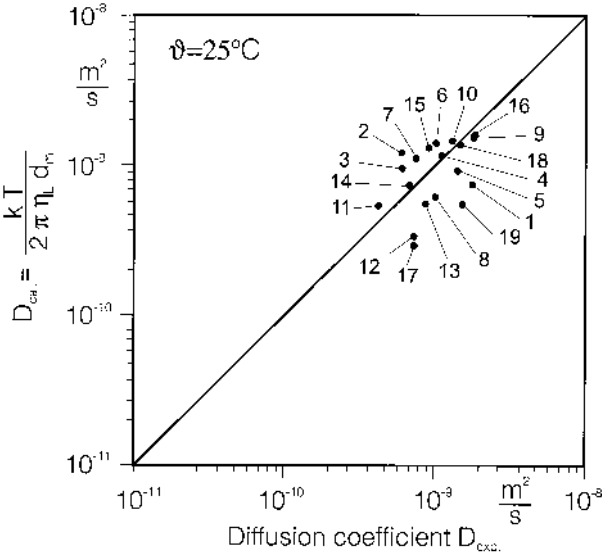

Figure A1.4. Diffusion coefficient calculated according to Stokes–Einstein versus experimental data of 18 different systems at $\vartheta = 25°C$.

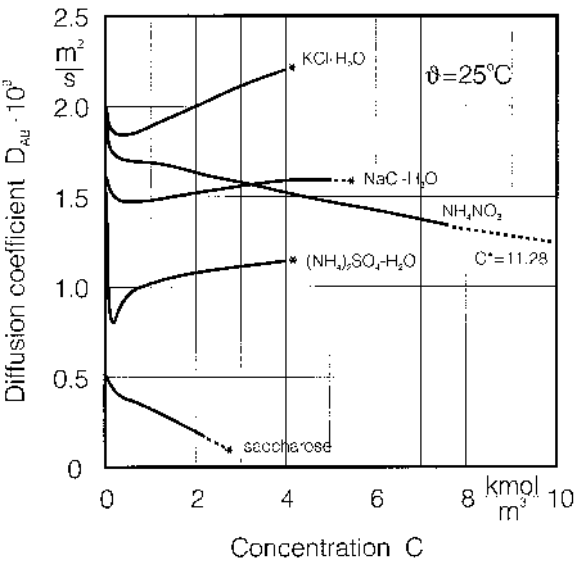

Figure A1.5. Experimental diffusivities D_{AB} of some aqueous binary system versus the concentration C.

Table A1.5. Data for Figure A1.5

No.	System	C [kmol/m³]	$D_{exp.}$ [m²/s]	$D_{sol.}$ [m²/s]	Literature
1	NH_4NO_3	0.05	1.79E-09	7.42E-10	Mul72
		1.0	1.69E-09	7.42E-10	Mul72
		7.628	1.34E-09	7.42E-10	Mul72
2	$NH_4Al(SO_4)_2*12H_2O$	0.09197	6.12E-10	1.21E-09	Lan69
3	$KAl_(SO_4)_2*12H_2O$	0.08056	6.15E-10	9.54E-10	Lan69
4	$NaNO_3$	0.00223	1.53E-09	5.50E-10	Lan69
5	$(NH_2)_2CO$ (Urea)	0.125	1.39E-09	9.18E-10	Lan69
6	K_2SO_4	0.2978	1.07E-09	1.37E-09	Lan69
7	$CuSO_4*5H_2O$	0.0028	7.47E-10	1.12E-09	Lan69
8	KH_2PO_4	0.04997	1.02E-09	6.21E-10	Lan69
9	KNO_3	0.0284	1.82E-09	1.52E-09	Lan69
10	$(NH_2)_2CS$ (Thiourea)	0.07887	1.31E-09	1.46E-09	Lan69
11	$C_{12}H_{22}O_{11}$ (sucrose)	0.2	4.26E-10	5.38E-10	Lan69
12	$MgSO_4*7H_2O$	0.0272	7.30E-10	3.34E-10	Lan69
13	$NH_4H_2PO_4$	0.4981	8.75E-10	5.54E-10	Lan69
14	$C_6H_8O_7$ (citric acid)	0.097	6.82E-10	7.59E-10	Lan69
15	$(NH_4)_2SO_4$	0.3824	9.16E-10	1.32E-09	Lan69
16	KCl	0.5	1.85E-09	1.66E-09	Mul72
		1.0	1.89E-09	1.66E-09	Mul72
		4.0	2.20E-09	1.66E-09	Mul72
17	$(CH_2)_6N_4$ (HMT)	0.0397	7.36E-10	2.93E-10	Lan69
18	NaCl	0.1	1.48E-09	1.37E-09	Mul72

[A1.3] delivers diffusivities which show approximately the same deviations from experimental data as those of equation (A1.10).

A1.5. Interfacial Tensions

A large number of interfacial tensions γ_{CL} have been determined experimentally by Nielsen and Söhnel [A1.4]. The authors have measured the rate of primary nucleation in relation to supersaturation. They derived the interfacial tensions from the statements of the classical theory of nucleation and plotted γ_{CL} against the logarithm of solubility. Another approach was published by Mersmann [A1.5]. According to this author, the dimensionless interfacial tension (compare Chapter 1)

$$\gamma^*_{CL} = \frac{\gamma_{CL} d_m^2}{0.414kT} \approx \frac{\gamma_{CL}}{0.414kT(C_C N_A)^{2/3}}$$

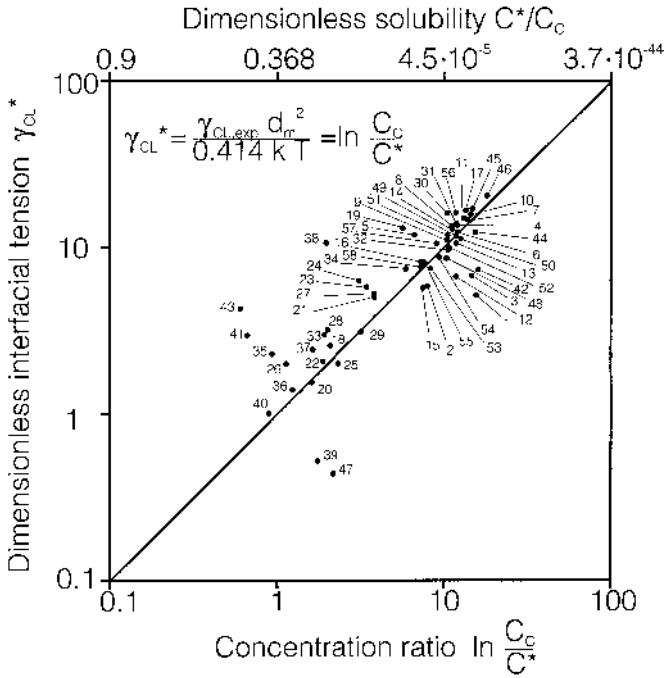

Figure A1.6. Dimensionless interfacial tension versus the concentration ratio.

is plotted against the dimensionless solubility C^*/C_C in Figure A1.6 for 58 systems. It is difficult to explain the large deviations of the systems 1, 38, 39, 41, 43, and 47.

A1.6. Thermal Conductivities

Principally speaking, the thermal conductivity depends on the temperature and the concentration of the systems. The influence of pressure is negligible. Figure A1.7 shows the thermal conductivity of some solvents. Little is known about this property for solutions. Dealing with systems which have a low solubility $W^* < 0.1$ kg solute/kg solvent, the thermal conductivity will not differ remarkably from the value valid for the solvent (see Fig. A1.8).

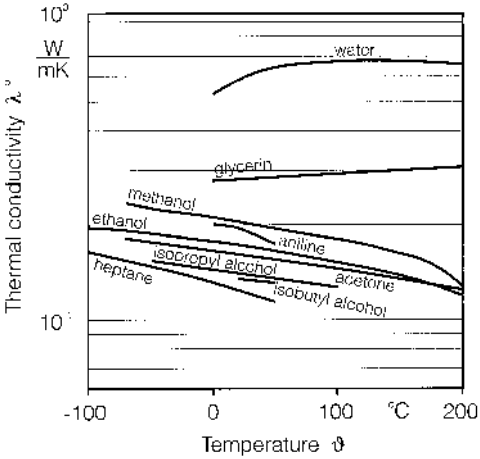

Figure A1.7. Thermal conductivity of some solvents versus the temperature.

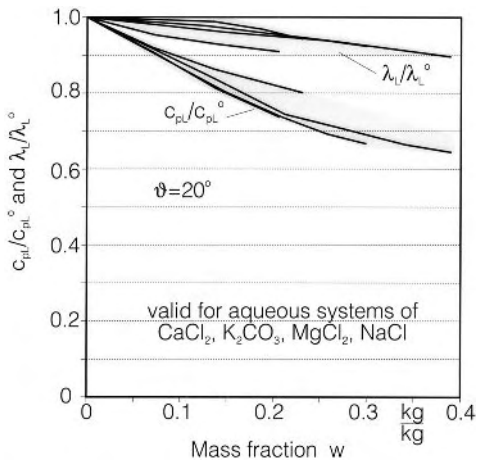

Figure A1.8. Ratio c_{pL}/c_{pL}° and $\lambda_L/\lambda_L^{\circ}$ of some aqueous systems versus the mass fraction.

A1.7. Heat Capacities

In Figure A1.9, the specific heat capacities of some solvents are plotted against temperature. It is difficult to predict the heat capacities of solutions. It is assumed that the heat capacity of a solution will not differ greatly from

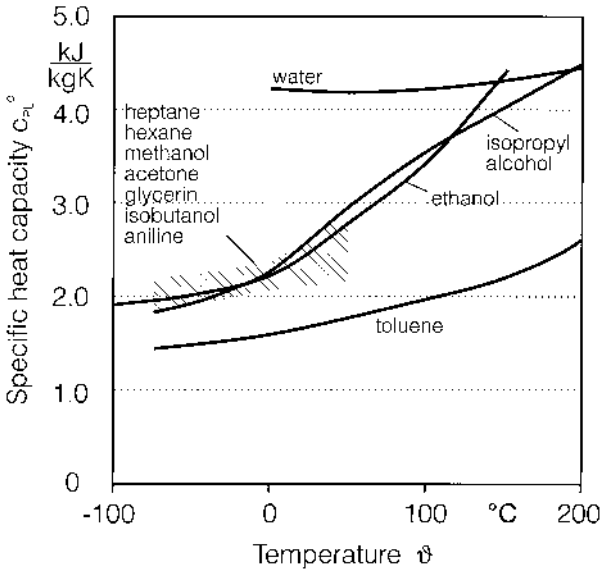

Figure A1.9. Heat capacities of some solvents versus the temperature.

the value of the solvent when the mass ratio is smaller than $W^* = 0.05\,\text{kg}$ solute/kg solvent (see Fig. A1.8).

A1.8. Shape Factors

The shape factors introduced in Chapters 3–7 are based on a characteristic length L of the crystal. The volume shape factor

$$\alpha = \frac{V_P}{L^3}$$

is derived from the particle volume V_P and the surface shape factor

$$\beta = \frac{A_P}{L^2}$$

from the particle surface A_P.

The basic orientation of a crystal is that of its greatest mechanical stability, see shapes a–h below. The length L_a is then the distance between two parallel planes perpendicular to the base, contracting the crystal in such a way to give a maximum length [24]. The width L_b is the distance between two planes which are perpendicular both to the base and to the planes

defining the length L_a and contracting the crystal on opposite corners, edges, or planes. The thickness L_c is the distance between the base and another parallel plane that contacts the crystal from above. The ratio

$$F \equiv \frac{\beta}{\alpha}$$

is called the *overall shape factor*.

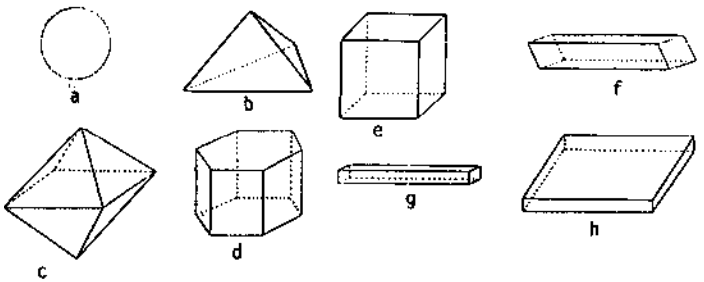

The sphericity ψ according to

$$\psi = \frac{(6\alpha/\pi)^{2/3}}{\beta/\pi}$$

is the ratio of the surface area of a sphere having the same volume as the crystal to the actual crystal surface area. The sphericity is close to 1 for isometric particles. For further detail, see Ref. [A1.6]. Some examples of shape factors are as follows

Geometric shape	α_a	β_a	F_a	α_b	β_b	F_b	ψ
(a) sphere	0.524	3.142	6.00	0.524	3.142	6.00	1.00
(b) tetrahedron	0.118	1.732	14.68	0.182	2.309	12.7	0.68
(c) octahedron	0.471	3.464	7.35	0.471	3.464	7.35	0.85
(d) hexagonal prism	0.867	5.384	6.21	2.60	11.20	4.31	0.82
(e) cube	1.000	6.000	6.00	1.000	6.000	6.00	0.81
(f) needle $5 \times 1 \times 1$	0.040	0.88	22	5	22	4.40	0.64
(g) needle $10 \times 1 \times 1$	0.010	0.42	42	10	42	4.20	0.53
(h) plate $10 \times 10 \times 1$	0.100	2.4	24	0.10	2.4	24	0.43

A2. EXAMPLES OF LARGE-SCALE INDUSTRIAL CRYSTALLIZERS

Table A2.1 presents data of large-scale industrial crystallizers. Some of the crystallizers are shown in Figure A2.1. In all cases but one, the tip speed of the rotor is less than 15 m/s and the mean specific power input does not exceed 1 W/kg. The mean residence time τ ranges between 1 and 4 h.

The growth rate G_{MSMPR} can be calculated from τ and the median crystal size L_{50}. Mass transfer coefficients k_d have been calculated according Chapter 8. Thus, it is possible to calculate the dimensionless growth rate $G_{\mathrm{MSMPR}}/2k_d$ and the crystallization parameter P_{dif} (see Fig. A2.2). Figure A2.2 allows one to calculate the supersaturation Δc which would have to be present in a MSMPR crystallizer in order to obtain the median crystal size L_{50} within the suspension residence time τ. However, processes such as agglomeration, attrition, and insufficient mixing are not taken into account. With respect to attrition, the supersaturation Δc must be larger than the data in Figure A2.2 to compensate for the negative attrition rate by a higher kinetic growth rate. Up to now, it is not possible to quantify those effects for arbitrary crystals with unknown attrition behavior. In any case, the supersaturation valid for MSMPR crystallizers can be plotted in a diagram according to the data of Chapter 2 (see Fig. A2.3).

As a rule, the effective growth rate $G_{\mathrm{eff}} = G_{\mathrm{kin}} - G_a$ is not known and depends greatly on the local and mean specific power inputs. Therefore, it is reasonable to plot the dimensionless crystal size $L_{50}/G_{\mathrm{MSMPR}}\tau$ against the relative supersaturation which is mainly responsible for nucleation (see Fig. A2.4). The ratio of the mean specific power input $\bar{\varepsilon}$ based on the minimum specific power input necessary for suspending is the parameter. At high relative supersaturation, the crystalline product is fine with respect to high nucleation rates. Attrition is less important, but agglomeration can play a certain role. In the range of $\sigma < 0.1$, nucleation is low and large crystals prone to attrition can be expected. Therefore, the median crystal size L_{50} can be remarkably reduced in comparison to the size obtained in a MSMPR crystallizer. In Figure A2.4, this effect is shown for KNO_3, which is very prone to attrition [A2.1].

The considerations discussed here lead to the following outline for designing crystallizers:

1. Process: cooling, evaporation, drowning-out, pressure, reaction
2. Crystallizer:
   (a) Batch, fed batch, continuous, single, or staged
   (b) DTB, STR, FB, FC, special

Table A2.1. Data of Large-Scale Industrial Crystallizers

No. [Ref.]	System	Volume V [m^3]	Speed of rotor n [s^{-1}]	Tip speed of rotor [m/s]	Mean spec.p.i. $\bar{\varepsilon}$ [W/kg]	Res. time τ [s]	Suspension density m_T [kg/m^3]	Medium size L_{50} [mm]	Growth rate $G_{MSMPR}=L_{50}/3{,}67\tau$ [m/s]	Temp. [°C]	c^* c_0 [kmol/m^3]	c^*/c_0 $\Delta c/c_0$ [-]	$\sigma=\Delta c/c^*$ σ_{rel} [-]	Production rate P_c [kg/h]	Circulation rate V_{circ} [m^3/h]	$\sigma_{max}=P_{c,max}/(V_{circ}\rho^*)$ [-]	$\tau_{circ}=V/V_{circ}$ [s]	τ/τ_{circ} [-]
1 [a]	$FeSO_4$	4	12.1	9.3	0.22	3540	116	0.38	$2.9A10^{-8}$	18	1.6 6.83	0.23 $1.57A10^{-3}$	$6.69A10^{-2}$ $8.7A10^{-2}$	473	240	$4.4A10^{-5}$	60	59
2 [a]	NH_4Cl	10	8.3 24.2	7.5 13.5	0.28	9800	132	0.19	$0.53A10^{-8}$	55	7.0 28.5	0.25 $0.26A10^{-3}$	$1.04A10^{-1}$ $5.3A10^{-3}$	483	300	$4.3A10^{-5}$	120	82
3 [a]	citric acid	2x6= 12	10.8	11.7	0.90	8380	226	0.41	-	60	5.0 8.67	0.58 $1.85A10^{-1}$	-	562	400	$1.5A10^{-4}$	54	161
4 [a]	Na_2SO_4	75	4.75	13.6	0.64	4040	151	0.30	$2.0A10^{-8}$	100	2.6 18.8	0.14 $0.4A10^{-3}$	$2.9A10^{-3}$ $16.4A10^{-3}$	10105	7000	$3.9A10^{-4}$	39	104
5 [d]	$CaSO_4$	200	0.27	2.9	0.22	18000	450	0.06	$0.09A10^{-8}$	55	0.012 13.4	$9.1A10^{-4}$ $4.7A10^{-3}$	$5.1A10^{-2}$	18000	22700	$3.8A10^{-4}$	32	568
6 [a]	NaCl	3x90= 270	5.0	14.1	0.55	5500	110	0.70	-	74	5.5 37.0	0.15	-	6500	7000	$2.9A10^{-5}$	46	119
7 [c]	Na_2SO_4 *) $(NH_4)_2SO_4$	3x120= 360	15.0/ 25.0	23.6/ 15.7	0.90	37000		0.12 0.65	-	93			-	5000	9600		135	274
8 [b]	NaCl	285	4	15.7	0.66	3300	140	0.50	$3.8A10^{-8}$	127	5.5 37.0	0.15 $0.4A10^{-3}$	$2.6A10^{-3}$	54000	28800	$5.8A10^{-5}$	36	94
9 [a]	KCl	7x150= 1050	3	12.2	0.39	8100	15	1.10	-	86.5	6.5 26.7	0.24		7200	105000	$1.4A10^{-4}$	36	225
10 [c]	KCl	8x350= 2800	2.72	8.2	0.16	7750	142	0.60	-	95... 30	6.9...3.9 26.7	0.26...0.15	-	140000	96000	$3.6A10^{-5}$	105	74

*) separation by wet sieving

[a] Mersmann, A., W. Wöhlk, W. Hofmann; Standard Messo, Duisburg, Germany; Large-scale industrial crystallizers, private communication

[b] Kratz, E.; Sulzer Escher Wyss AG, Zürich, Switzerland; private communication

[c] Domning, H., Die Grobkorn-Kristallisationsanlage des Werks Wintershall, Kali u. Steinsalz (1977)

[d] Rennie, F.; Du Pont, Wilmington, USA; private communication
see also: Randolph, A. D., R. Kendall, et al., Double Draw-Off Crystallizer, American Chemical Society (1990)

[e] Goatin, C.; EniChem Anic, Porto Marghera, Venezia, Italy; private communication
Gurato, G., et al., Phase Diagrams of the Na_2SO_4-$(NH_4)_2SO_4$-H_2O System, La Chimica & l'Industria, V.69, N.12, (1987)

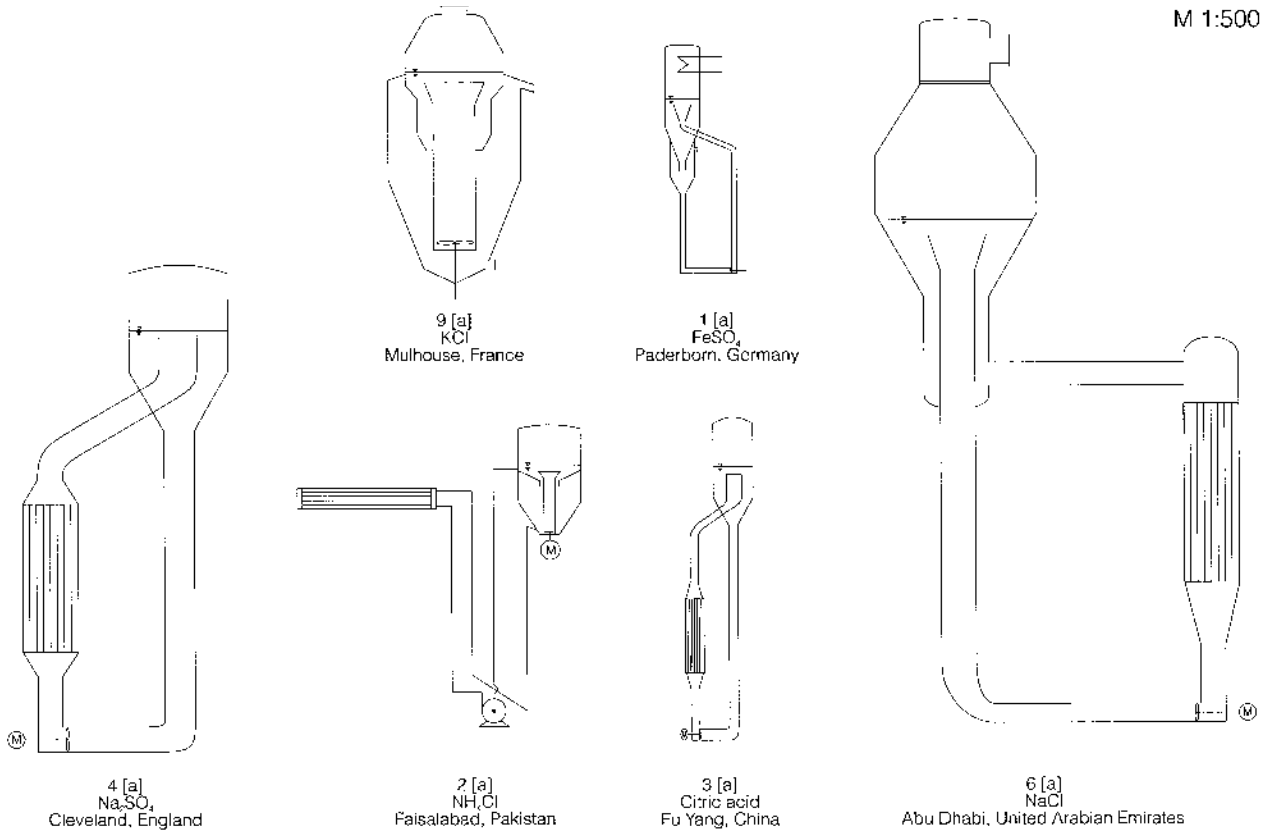

Figure A2.1. Schematic figures of industrial crystallizers. (See Table A2.1.)

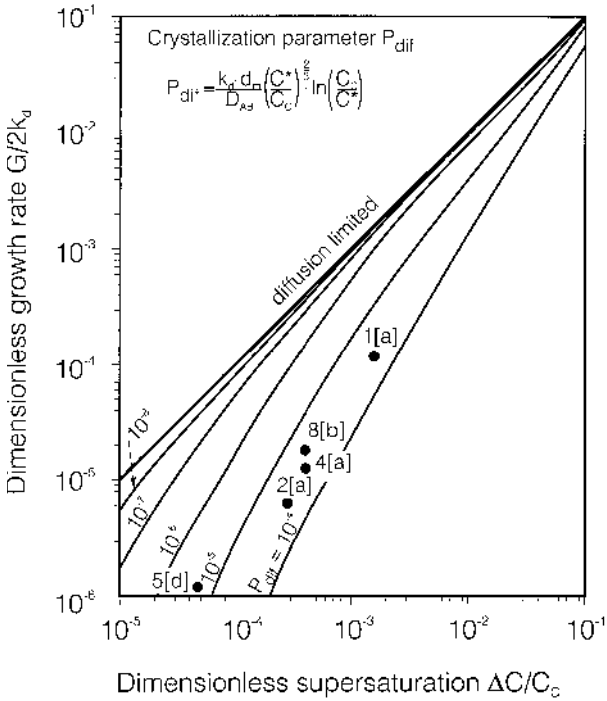

Figure A2.2. Dimensionless growth rate versus dimensionless supersaturation.

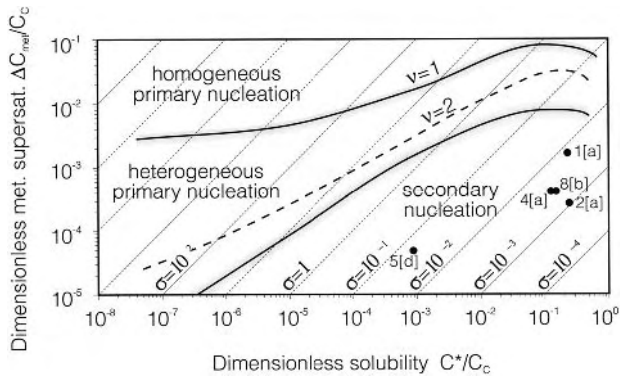

Figure A2.3. Dimensionless metastable supersaturation versus dimensionless solubility.

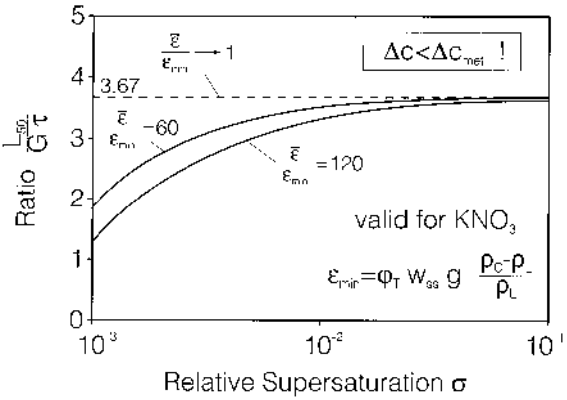

Figure A2.4. Ratio $L_{50}/G\tau$ versus relative supersaturation.

3. Fluid dynamics:
   (a) Sufficient macromixing, recirculation
   (b) Minimum local and mean specific power input
   (c) Limitation of tip speed of rotor
   (d) Minimum number of pumps with minimum power
   (e) Minimum number of valves with minimum pressure drop
4. Kinetics:
   (a) Operation at $(\Delta c)_{opt}$ in the entire crystallizer (see Fig. A2.3)
   (b) Damping of supersaturation peaks by seeding, slurry recirculation, and/or diluting
   (c) Choice of the most appropriate feed point (see Chapter 8)
5. Median crystal size L_{50}: Choose $(\Delta c)_{opt}$ from Figure A2.3, calculate the mass transfer coefficient k_d and the crystallization parameter P_{dif}, and read the growth rate G_{MSMPR} from Figure A2.2. Calculate the median crystal size from Figure A2.4.

REFERENCES

[A1.1] C. W. Davies, *Ion Association*, Butterworth, London (1962).
[A1.2] L. A. Bromley, Thermodynamic properties of strong electrolytes in aqueous solutions, *AIChE J., 19*: 313–320 (1973).
[A1.3] C. R. Wilke and P. C. Chang, Correlation of diffusion coefficients in dilute solutions, *AIChE J., 1*: 264–270 (1955).

[A1.4] A. E. Nielsen and O. Söhnel, Interfacial tensions in electrolyte crystal–aqueous solutions, from nucleation data, *J. Cryst. Growth, 11*: 233–242 (1971).
[A1.5] A. Mersmann, Calculation of interfacial tensions, *J. Cryst. Growth, 111*: 841–847 (1990).
[A1.6] J. Garside, A. Mersmann, and J. Nyvlt, *Measurement of Crystal Growth Rates*, European Federation of Chemical Engineering, Working Party on Crystallization (1990).
[A2.1] J. Pohlisch, Einfluss von mechanischer Beeinflussung und Abrieb auf die Korngrössenverteilung in Kühlungskristallisatoren, Thesis, Technical University Munich (1987).

Notation

A	constant, attachment factor
A	area, surface area (m^2)
A	Hamaker constant (J)
a	surface area per unit volume (m^2/m^3)
a	number of impeller blades, fraction
a	intermolecular distance, lattice constant, radius (m)
a	thermal diffusivity (m^2/s)
a_i	activity of component i
a_T	total interfacial area per unit volume (m^2/m^3)
B	reciprocal length (m^{-1})
B_0	nucleation rate based on volume suspension ($L \to 0$) ($m^{-3}\,s^{-1}$)
$\bar{B}_\varphi$	nucleation rate based on volume of crystals ($L \to 0$) ($m^{-3}\,s^{-1}$)
B_u	nucleation function ($m^{-3}\,s^{-1}$)
$B(L)$	birth rate ($m^{-4}\,s^{-1}$)
$B(V)$	birth rate ($m^{-6}\,s^{-1}$)

b	breadth of impeller blade (m)
b	exponent in ASL model
b	Burgers vector (m)
C	heat capacity (J/K)
C	atom–atom potential (J/m^6)
C	attrition coefficient ($m^3/J^{4/3}$)
C	constant
CV	coefficient of variation
C_{44}	shear modulus (Pa)
C	molar concentration ($kmol/m^3$)
C_i	molar concentration of component i ($kmol/m^3$)
c_p	specific heat capacity (J/kg K)
c_s	velocity of sound (m/s)
c_i	mass concentration of component i (kg/m^3)
c_{im}	mass concentration of impurity (kg/m^3)
c_w	drag coefficient
ΔC	concentration driving force or supersaturation $(= C - C^*)$ ($kmol/m^3$)
D	diameter of impeller or tube, distance (m)
$D(L)$	death rate ($m^{-4}\,s^{-1}$)
$D(V)$	death rate, disrupture rate ($m^{-6}\,s^{-1}$)
D_{AB}	diffusion coefficient (m^2/s)
d	density of absorbed units ($units/m^2$)
d	(diagonal) length (m)
d_m	molecular diameter (m)
E	energy (J)
E	Young's modulus (Pa)
$E(t)$	residence time distribution (s^{-1})
E	activation energy (J/mol)
E_{kin}	kinetic efficiency (m^{-3})
E_S	crystallization effort (kg/kg)
e	thickness of impeller blades (m)
e	specific energy (J/kg)
e	elementary electrical charge (-1.602×10^{-19} C)
F	overall shape factor
F	force (N)
F	Faraday constant (96,485 C/mol)
F	F factor ($Pa^{1/2}$)
f	natural frequency (s^{-1})
f	factor
$f\,(=\gamma)$	activity coefficient
f_c	stress (N/m^2)

G	Gibbs free energy (J/mol, J/molecule)
G	linear crystal (or layer) growth rate ($= dL/dt$) (m/s)
G_v	crystal-volume-based growth rate (m^3/s)
g	gravitational acceleration ($9.81\,m/s^2$)
g	overall order of the growth process
g	fraction, ratio
H	enthalpy (J)
H	filling height in a stirred vessel (m)
He	Henry coefficient
H_V	Vickers hardness (J/m^3)
ΔH_{CL}	enthalpy of crystallization (J/mol)
h	step height (m)
h	ratio of growth rates
h	specific enthalpy (J/kg)
h	heat transfer coefficient ($W/m^2\,K$)
h	elementary energy (J/kg)
h	Planck's constant ($6.626 \times 10^{-34}\,J\,s$)
h_f	heat of fusion (J/kg)
I	ionic strength ($kmol/m^3$)
I	impurity (kg)
I_s	degree of segregation
J	collision frequency (m^{-4}/s)
K	factor
K	equilibrium (distribution) coefficient
K	efficiency constant
K	solubility product $(kmol/m^3)^x(kmol/m^3)^y$
K_r	factor
k	rate, impact coefficient (1/s)
k	Boltzmann constant ($1.381 \times 10^{-23}\,J/K$)
k	overall heat transfer coefficient ($W/m^2\,K$)
k	reaction rate constant var.
k	loading factor
k	distribution coefficient
k_d	mass transfer coefficient (m/s)
k_g	growth-rate constant $[(kmol\text{ or }kg)^{1-g}\,m^{3\,g-2}\,s^{-1}]$
k_g'	growth-rate constant (m/s)
k_g''	growth-rate constant ($kmol/m^2\,s$)
k_n	nucleation rate constant var.
k_r	growth integration rate constant ($kmol^{1-r}\,m^{3r-2}\,s^{-1}$ or var.)
k_{reac}	reaction rate constant var.
L	length (of tube) (m)
L	particle size (m)

L_s	sieve mesh size (m)
L_{50}	mass median crystal size (m)
L_{32}	Sauter mean diameter (m)
L°	mass of pure solvent (kg)
L_0	brine (kg)
$\dot{L}^\circ$	evaporation rate (kg/s)
l	pore length, block size (m)
M	mass (kg)
$\dot{M}$	mass flow (kg/s)
$\tilde{M}$	molar mass (kg/kmol)
M_i	molality (kmol/kg)
$M(L)$	cumulative oversize mass distribution
m	mass per volume suspension (kg/m^3_{sus})
m°	mass per volume solvent (kg/m^3_{solv})
$\dot{m}$	mass flux density ($kg/m^2\,s$)
m_i	moments of population density distribution (m^{-i})
m_T	suspension density, total crystal mass per unit volume of suspension (kg/m^3)
$\dot{m}_v$	mass per unit volume and time ($kg/m^3_{sus}\,s$)
N	number of particles per unit suspension volume (m^{-3})
$\dot{N}$	molar flux (mol/s)
$\dot{N}$	particle rate per unit volume ($m^{-3}\,s^{-1}$)
N_A	Avogadro's number ($N_A = 6.023 \times 10^{23}\,mol^{-1}$)
N_V	pumping capacity
N_T	total number of particles, tubes
n	number of crystallization steps
n	amount of substance (mol)
n	population density per unit volume (m^{-4})
n	refractive index
n_v	volume-based population density (m^{-6})
$\dot{n}$	molar flux density ($mol/m^2\,s$)
n°	population density per unit mass solvent ($m^{-1}\,kg^{-1}$)
n_0	nuclei number density per unit volume (m^{-4})
$n_{0,\mathrm{eff}}$	effective nuclei number density for $L \to 0$ (m^{-4})
P	power (W)
P	probability of disruption
$p\,(= n^\circ)$	population density ($m^{-1}\,kg^{-1}$)
p	pressure (Pa)
p°	vapor pressure (Pa)
p_c	critical pressure (Pa)
p_r	reduced pressure (Pa)
Q	quantity of heat (J)

$\dot{Q}$	heat or energy flux (J/s, W)
$Q_i(L)$	cumulative undersize distribution
q	condensation coefficient
$\dot{q}$	heat flux density (W/m^2)
q	quantity of heat per unit mass (J/kg)
$q_i(L)$	undersize distribution fraction (m^{-1})
R	ratio, removal
R	radius, distance (m)
$R(L)$	cumulative oversize
R	electric resistance (Ω)
R_f	fouling factor ($m^2\,K/W$)
$\Re$	ideal gas constant ($8.314\,J/mol\,K$)
r	radius, distance (m)
r	reaction rate var.
$r(L)$	net rate of aggregation (disrupture) ($m^{-4}\,s^{-1}$)
$r(V)$	net rate of aggregation (disrupture) ($m^{-6}\,s^{-1}$)
r	order of the integration process
r_f	freezing ratio (kg/kg)
S	solid mass (kg)
S	supersaturation ratio ($S = c/c^* = \sigma + 1$)
S_a	supersaturaiton ratio ($S_a = a/a^*$)
S	surface (m^2)
s	thickness (m)
s	impeller or stirrer speed, rate of rotation (s^{-1})
s	number of overlapping dislocations
T	batch time (s)
T	tank diameter (m)
T	absolute temperature (K)
T	tensile strength (Pa)
T	period of oscillation (s)
$\dot{T}$	cooling rate (K/s)
t	time (s)
t	target extent (m)
U_s	activation energy (J)
$\bar{U}$	mean squared velocity deviation of flux (m/s)
u	fluid velocity (m/s)
u	particle volume (m^3)
u	dipole moment (C m)
u_{tip}	stirrer tip speed (m/s)
V	volume (m^3)
$\dot{V}$	volumetric flow rate (m^3/s)
v	particle volume (m^3)

v	velocity (m/s)
$\dot{v}$	superficial velocity, volumetric flux density (m/s)
$\bar{v}$	mean face growth rate, mean velocity (m/s)
v_{hkl}	face growth rate (m/s)
$\overset{>}{v}$	surface diffusion velocity (m/s)
W	work, evaporation energy (J)
W_{eff}	effectiveness factor
W_i	mass ratio of two substances ($\text{kg/kg}_{\text{solv}}$)
$W(L)$	mass distribution function (kg/m^4)
W	probability ratio
w	velocity (m/s)
w_i	mass fraction of substance i ($\text{kg/kg}_{\text{sol}}$)
w	specific work (J/kg)
w_s	surface energy (J/m^2)
w_v	volumetric energy or work (J/m^3)
X_i	mole fraction of two substances (crystal) ($\text{mol/mol}_{\text{solv}}$)
x_0	kink spacing (m)
x_i	mole ratio of substance i (crystals) ($\text{mol/mol}_{\text{sol}}$)
x_s	mean displacement (m)
Y	yield
Y	mass ratio (fluid)
Y_i	mole ratio of two substances (liquid) ($\text{mol/mol}_{\text{solv}}$)
y_i	mole fraction of substance i (liquid) ($\text{mol/mol}_{\text{sol}}$)
y_0	step spacing (m)
Z	imbalance factor
Z	degree of agglomeration
z	multiple of acceleration due to gravity
z	ionic charge
z_i	valency of component i

Greek Symbols

α	abandon rate of a cluster (s^{-1})
α	volume shape factor, fraction
α	angle (deg)
α_0	polarizability ($\text{C}^2\,\text{m}^2/\text{J}$)
β	surface area shape factor, fraction
β	angle of impeller blades (deg)
β	aggregation kernel (m^3/s)
β_R	wetting angle (deg)

γ	edge energy per molecule (J)
$\gamma\,(=f)$	activity coefficient
γ_e	edge energy (J/m)
$\gamma_{\mathrm{CL}}, \gamma_{\mathrm{LG}}$	interfacial tension ($\mathrm{J/m^2}$)
$\dot{\gamma}$	shear rate ($\mathrm{s^{-1}}$)
δ	film or layer thickness (m)
δ_H	hydrodynamic boundary layer thickness (m)
δ_M	diffusion boundary layer thickness (m)
δ_ϑ	temperature boundary layer thickness (m)
ε	porosity
ε	error signal
ε	local specific power input (W/kg)
$\bar{\varepsilon}$	mean specific power input (W/kg)
ε_0	electrical field constant (8.854×10^{-12} A s/V m)
ε_r	relative permittivity
η	dynamic viscosity (Pa·s)
η	efficiency
η	effectiveness factor for crystal growth
η_N	nucleation efficiency
η	mosaic spread
η_t, η_g, η_w	target efficiency
θ	contact angle (deg)
θ	coverage
θ	angle of tilt (deg)
θ	dimensionless particle relaxation time
ϑ	Celsius temperature (°C)
$\Delta\vartheta, \Delta T$	subcooling (K)
Γ	fracture resistance ($\mathrm{J/m^2}$)
$\Gamma\,(\Gamma^*)$	adsorption coverage ($\mathrm{mol/m^2}$) ($\mathrm{molecules/m^2}$)
Γ	frequency of disrupture ($\mathrm{m^3/s}$)
κ	reciprocal decay length ($\mathrm{m^{-1}}$)
λ	Ostwald diameter, size (m)
λ	thermal conductivity (W/m K)
λ_k	microscale of turbulence (m)
Λ	macroscale of turbulence (m)
μ	shear modulus (Pa)
μ_i	chemical potential of substance i (J/mol)
ν	number of ions
ν	frequency ($\mathrm{s^{-1}}$)
ν_c	Poisson's ratio
ν_i	stoichiometric coefficient of i

Π	osmotic pressure (Pa)
π	dimensionless tensile strength
ρ	density (kg/m^3)
ρ_C	curvature radius (m)
σ	reltive supersaturation ($= \Delta c/c^*$)
σ	tensile strength, normal stress (Pa)
σ	surface charge density (C/m^2)
τ	mean residence time, growth period (s)
τ_{CL}	surface stress (J/m^2)
τ_k	characteristic timescale (s)
τ_s	shear stress (Pa)
$\Phi, -\Delta\mu$	growth affinity (J/mol)
Ψ	porosity of voidage, sphericity
ψ	electrical potential (V)
ω	angular velocity (s^{-1})
$\Delta\phi^*$	surface energy parameter
Φ_i	volume fraction of substance i (m^3/m^3)
Φ_{ij}	binding energy (J)
ζ	reaction extent
φ	volumetric crystal holdup (m^3/m^3)
φ	interaction potential (V)
φ	relative humidity

Subscripts

A	addition, area
a	attrition, acitivity, area
accel	accelerative
ad	adsorption
adh	adherent
agg	agglomeration
anh	anhydrous
app	apparatus, apparent
AS	avoidance of settling
at	atom
att	attachment
ax	axial
B	bulk, block
BCF	Burton–Cabrera–Frank
BL	bottom lifting

B + S	birth and spread
b	boiling, breadth
belt	cooling belt
C	crystallizer, crystal
CC	crystal–crystal
CL	crystal–liquid
CLA	clear-liquor advance
c	concentration, cluster, classificaiton, critical
cal	calculated
circ	circulation, circumferential
col	collision
cool	cooling, coolant
crit	critical
cum	cumulative
cw	cooling water
D	decay
DDO	double draw of
d	dead, dominant, deposition
det	detectable
dif	diffusion
diff	differential
dis	disrupture, distribution, dissolution
dom	dominant, mode value
drum	rotating drum
e	equilibrium, elutriation, edge
eff	effective
exp	experimental
F	fines, fluid
f	feed, fine, freezing, fusion, fouling
feed	feed, crude melt
for	foreign
G	gas, vapor
g	growth, geometrical
HC	heat carrier
het	heterogeneous
hom	homogeneous
hyd	hydrous
I	interface value
i	component *i* of mixture
id	ideal
im	impeller, impurity

imp	impeded
ind	induction
int	integration, integral
k	kink, Kolmogorov number
kin	kinetic
L	liquid phase, solution, *L* dependent
LG	liquid–gas
lam	laminar
loc	local
m	molar value, value per mole, molecular
macro	macro-
max	maximum value
met	metastable
mf	minimum fluidization
micro	micro-
min	minimum value
mono	monolayer
n	nucleation, nucleus
o	overflow
opt	optimal
p	particle, product, plate, pure
par	parent
pl	plastic
pp	pure product
prim	primary
proc	process
pump	pumping
r	rotor
r	real, removal
reac	reaction
rel	relative
rep	repulsive
ripe	ripening
S	seed, solid
SG	solid–gas
s	solute, supersaturation
s	surface, semipermeable, spherical
s	sieve, step, solid, solidification
s	sinking
sat	saturation
sec	secondary
sep	separation

sett	settling
sl	slice
sol	solution
solv	solvent
sp	setting point
ss	settling in a swarm
step	step
surf	surface
sus	suspension
sw	sweating
T	total
t	target, tensile
tb	per tube
tip	tip (speed)
tot	total
turb	turbulent
u	underflow
V	Vickers, volume
v	volume
vdW	van der Waals
W	wall
w	washing
wa	waste air
α	start value (time)
φ	volumetric
ω	final value (time)
0	zero size ($L \rightarrow 0$)
0	entry (local), standard
1	withdrawal after first step (local)
∞	bulk value

Superscripts

g	kinetic order of growth
id	ideal
n	kinetic order of nucleation
$^\circ$	standard state, pure substance, based on solvent
*	equilibrium state, saturation
$\overline{}$	mean value
50	50% cumulative undersize
Δ	difference

Dimensionless Groups

Archimedes number	$\mathrm{Ar} = \dfrac{L^3 \Delta\rho g}{\nu_L^2 \rho_L}$
Crystallization parameter	$P_{\mathrm{dif}} = \dfrac{k_d d_m}{D_{\mathrm{AB}}} \left(\dfrac{C^*}{C_c}\right)^{2/3} \ln\left(\dfrac{C_c}{C^*}\right)$
Damköhler number	$\mathrm{Da} = k_r (C - C^*)^{r-1} \dfrac{1 - w_x}{k_d}$
Flow function	$\mathrm{FF} = \dfrac{\sigma_1}{\sigma_c}$
Froude number	$\mathrm{Fr} = \dfrac{\dot{v}^2 \rho_L}{L \Delta\rho g}$
Hausner ratio	HR
Importance of Morphology	IM
Lewis number	$\mathrm{Le} \equiv \dfrac{\mathrm{Sc}}{\mathrm{Pr}} = \dfrac{a_L}{D_{\mathrm{AB}}}$
Nusselt number	$\mathrm{Nu} = \dfrac{hL}{\lambda_L}$ or $\dfrac{hT}{\lambda_L}$
Power number	$\mathrm{Po} = \dfrac{P}{\rho s^3 D^5}$
Prandtl number	$\mathrm{Pr} = \dfrac{\nu_L}{a_L}$
Pumping capacity	$N_V = \dfrac{\dot{V}}{sD^3}$
Relative supersaturation	$\sigma = \dfrac{\Delta C}{C^*} = \dfrac{\Delta c}{c^*};\ S = 1 + \sigma$
Dimensionless supersaturation	$\dfrac{\Delta C}{C_c} = \sigma \dfrac{C^*}{C_c}$
Reynolds number of particle	$\mathrm{Re} = \dfrac{w_s L}{\nu_L}$
Reynolds number of stirrer	$\mathrm{Re} = \dfrac{sD^2 \rho_L}{\eta_L} = \dfrac{sD^2}{\nu_L}$
Schmidt number	$\mathrm{Sc} = \dfrac{\nu_L}{D_{\mathrm{AB}}}$
Sherwood number	$\mathrm{Sh} = \dfrac{k_d L}{D_{\mathrm{AB}}}$
Stokes number	$\mathrm{St} = \dfrac{\dot{v}_L L^2 (\rho_C - \rho_L)}{18 T \eta_L}$
Weber number	$\mathrm{We} = \dfrac{w^2 L \rho_L}{\sigma}$

Bibliography

Abegg, C. F., J. D. Stevens, and M. A. Larson, Crystal size distribution in continuous crystallizers when growth rate is size dependent, *AIChE J.*, *22*(5): 887 (1976).

Aoyama, Y., G. Kawakami, T. Mukaida, and K. Toyokura, Crystallization phenomena of alum and other substances in CEC type crystallizers, in *Proc. 8th Symp. on Industrial Crystallization '81* (S. J. Jancic and E. J. de Jong, eds.), North-Holland, Amsterdam (1982).

Arkenbout, G. F., *Melt Crystallization Technology*, Technomic Publications, Lancaster, PA (1995).

Asselbergs, C. J., and E. J. de Jong, Integral design of crystallizers as illustrated by the design of a continuous stirred tank cooling crystallizer, in *Industrial Crystallization* (J. W. Mullin, ed.), Plenum Press, New York, pp. 319–334 (1976).

Bamforth, A. W., *Industrial Crystallization*, Leonard-Hill, London (1965).

Becker, R., and W. Döring, Kinetische Behandlung der Keimbildung in übersättigten Dämpfen, *Ann. Phys.*, *24*(5): 719–752 (1935).

Bennema, P., Interpretation of the relation between the rate of crystal growth from solution and the relative supersaturation at low supersaturation, *J. Cryst. Growth*, *1*: 287–292 (1967).

Bennema, P., The importance of surface diffusion for crystal growth from solution, *J. Cryst. Growth*, *5*: 29–43 (1969).

Bennema, P., Crystal growth from solution: theory and experiment, J. Cryst. Growth, *24/25*: 76–84 (1974).

Bennema, P., and C. van Leeuven, Crystal growth from the vapour phase: confrontation of theory with experiment, *J. Cryst. Growth*, *31*: 3 (1975).

Bennet, R. A., H. Fiedelmann, and A. D. Randolph, Crystallizer-influenced nucleation, *Chem. Eng. Prog.*, *69*(7): 86–93 (1973).

Berglund, K. A., Summary of recent research on growth rate dispersion of contact nuclei, *Chem. Eng. Commun.*, *41*: 357–360 (1986).

Bernstein, J., R. J. Davey, and J.-O. Henck, Concomitant polymorphs, *Angew. Chem Int. Ed.*, *38*: 3440–3461 (1999).

Berthoud, A., Théorie de la formation des faces d'un crystal, *J. Chim. Phys.*, *10*: 624 (1912).

Boistelle, R., Survey of crystal habit modification in solution, in *Industrial Crystallization* (J. W. Mullin, ed.), Plenum Press, New York (1976).

Botsaris, G. D., Secondary nucleation: a review, in *Industrial Crystallization* (J. W. Mullin, ed.), Plenum Press, New York (1976).

Bourne, J. R., and M. Zabelka, The influence of gradual classification on continuous crystallization, *Chem. Eng. Sci.*, *35*: 533–542 (1980).

Broul, M., J. Nyvlt, and O. Söhnel, Solubility in inorganic two component systems, *Phys. Sic. Data*, *6* (1981).

Buckley, H. E., *Crystal Growth*, John Wiley & Sons, New York (1951).

Burton, W. K., N. Cabrera, and F. C. Frank, The growth of crystals and the equilibrium structure of their surface, *Phil. Trans. Roy. Soc. London*, *243*: 299–358 (1951).

Cabrera N., and D. A. Vermilyea, The growth of crystals from solution, in *Growth and Perfection of Crystals* (R. H. Doremus, B. W. Roberts, and D. Turnbull, eds.), John Wiley & Sons, London, pp. 393–410 (1958).

Chamskij, E. W., *Crystallization and Properties of Crystalline Compounds*, Nanka, Leningrad (1971) (in Russian).

Clontz, N. A., and W. L. McCabe, Contact nucleation of magnesium sulfate heptahydrate, *Chem. Eng. Prog. Symp. Ser.*, *67*(6): 110 (1971).

Davey, R. J., The effect of impurity adsorption on the kinetics of crystal growth from solution, *J. Cryst. Growth*, *34*: 109 (1976).

Davey, R. J., Industrial crystallization: new horizons, in *Proc. 10th Symp. on Industrial Crystallization* (J. Nyvlt and S. Zacek, eds.), Elsevier Amsterdam (1989).

de Jong, E. J., The one and the other, in *Industrial Crystallization '84* (S. J. Jancic and E. J. de Jong, eds.), Elsevier, Amsterdam, pp. 177–184 (1984).

de Jong, E. J., Development of crystallizers, *Int. Chem. Eng.*, *24*: 419–431 (1984).

Dirksen, J. A., and T. A. Ring, Fundamentals of crystallization: kinetic effects on particle size distributions and morphology, *Chem. Eng. Sci.*, *46*(10): 2389 (1991).

Garside, J., The concept of effectiveness factors in crystal growth, *Chem. Eng. Sci.*, *26*: 1425–1431 (1971).

Garside, J., and R. M. Davey, Secondary contact nucleation kinetics, growth and scale-up, *Chem. Eng. Commun.*, *4*: 393–424 (1980).

Garside, J., A. Mersmann, and J. Nyvlt, *Measurement of Crystal Growth Rates*, European Federation of Chemical Engineering, Working Party on Crystallization, Munich (1990).

Garside, J., J. W. Mullin, and S. N. Das, Importance of crystal shape in crystal growth rate determinations, *Ind. Eng. Chem. Process Des. Dev.*, *12*: 369–371 (1973).

Garside, J., I. T. Rusli, and M. A. Larson, Origin and size distribution of secondary nuclei, *AIChE J.*, *25*: 57–64 (1979).

Gilmer, G. H., and P. Bennema, Computer simulation of crystal surface and growth kinetics, *J. Cryst. Growth*, *13/14*: 148 (1972).

Gilmer, G. H., and K. A. Jackson, Computer simulation of crystal growth, in *Crystal Growth and Materials* (E. Kaldis and Scheel, eds.), North-Holland, Amsterdam (1977).

Griffiths, H., Crystallization, *Trans. Inst. Chem. Eng.*, *25*: xiv (1947).

Hartmann, P., *Crystal Growth: An Introduction*, Elsevier, Amsterdam (1973).

Heijden, A. E. D. M. van der, and J. P. van der Erden, Growth rate dispersion: the role of the lattice strain, *J. Cryst. Growth* (1992).

Hillig, W. B., A derivation of classical two-dimensional nucleation kinetics and the associated crystal growth laws, *Acta Met.*, *14* (1966).

Honigmann, B., *Gleichgewichts- und Wachstumsformen von Kristallen*, Steinkopf Verlag, Darmstadt (1958).

Hook, A. van, *Crystallization: Theory and Practice*, Reinhold, New York (1961).

Hulburt, H. M., and S. Katz, Some problems in particle technology: a statistical formulation, *Chem. Eng. Sci.*, *19*: 555–574 (1964).

Jackson, K. A., On the theory of crystal growth: the fundamental rate equations, *J. Cryst. Growth*, *3*: 13–18 (1969).

Jancic, S. J., and P. A. M. Grootschoolten, *Industrial Crystallization*, D. Reidel, Boston (1984).

Juzaszek, P., and M. A. Larson, Influence of fines dissolving on cyrstal size distribution in an MSMPR crystallizer, *AIChE J.*, *23*(4): 460–468 (1977).

Kaischew, R., and I. Stranski, Zur kinetischen Ableitung der Keimbildungsgeschwindigkeit, *Z. Physik. Chem.*, *B26*: 317–326 (1934).

Kossel, W., Zur Energetik von Oberflächenvorgängen, *Ann. Phys.*, *21*: 457 (1934).

Larson, M. A., Guidelines for selecting a crystallizer, *Chem. Eng.*, *13*: 90–102 (1978).

Larson, M. A., Secondary nucleation: an analysis, *Chem. Eng. Commun.*, *12*: 161–169 (1981).

Larson, M. A., Secondary nucleation: an analysis, in *Industrial Crystallization '81* (S. J. Jancic and E. J. de Jong, eds.), North-Holland, Amsterdam (1982).

Larson, M. A., and J. Garside, Crystallizer design techniques using the population balances, *Chem. Eng. J.*, 318–328 (1973).

Larson, M. A., D. C. Timm, and P. R. Wolff, Effect of suspension density on crystal size distribution, *AIChE J.*, *14*: 448–451 (1968).

McCabe, W. L., Crystal growth in aqueous solutions. I. Theory. II. Experimental, *Ind. Eng. Chem.*, *21*: 30 (1929); II. Experimental, *Ind. Eng. Chem.*, *21*: 121 (1929).

Marchal, P., *Ph.D. thesis*, Institut National Polytechnique de Lorraine, Ensic (1989).

Matz, G., *Kristallisation: Grundlagen und Technik*, Springer-Verlag, Berlin (1969).

Matz, G., Kristallisation, in *Ullmanns Enzyklopädie der technischen Chemie*, *Vol. 2*, Verlag Chemie, Weinheim, pp. 672–682 (1972).

Mayrhofer, B., and J. Nyvlt, Programmed cooling of batch crystallizers, *Chem. Eng. Process.*, *24*: 217–220 (1988).

Mersmann, A., Design of crystallizers, *Chem. Eng. Process.*, *23*: 213–228 (1988).

Mersmann, A., and M. Kind, Chemical engineering aspects on precipitation from solution, *Chem. Eng. Technol.*, *11*: 264–276 (1988).

Moyers, C. G., and A. D. Randolph, Crystal size distribution and its interaction with crystallizer design, *AIChE J.*, *19*(6): 1089–1103 (1973).

Mullin, J. W., *Industrial Crystallization*, Butterworth, London (1972) and (1993).

Mullin, J. W., Solution concentration and supersaturation units and their conversion factors, *Chem. Eng.*, 316–317 (1973).

Mullin, J. W., and M. Chakraborty, Crystal habit modification studies with ammonium and potassium dihydrogene phosphate, *J. Appl. Chem.*, *20*: 153–158 (1970).

Mullin, J. W., and S. J. Jancic, Interpretation of metastable zone widths, *Trans. Int. Chem. Eng.*, *57*: 187–193 (1979).

Myerson, A. S., *Handbook of Industrial Crystallization*, Butterworth-Heinemann, London (1993).

Nielsen, A. E., *Kinetics of Precipitation*, Pergamon Press, Oxford (1964).

Nielsen, A. E., Nucleation and growth of crystals at high supersaturation, *Krist. Tech.*, *4*: 17–38 (1969).

Nielsen, A. E., Electrolyte crystal growth mechanisms, *J. Cryst. Growth*, *67*: 289–310 (1984).

Nielsen, A. E., and O. Söhnel, Interfacial tensions in electrolyte crystal-aqueous solution, from nucleation data, *J. Cryst. Growth*, *11*: 233–242 (1971).

Nyvlt, J., *Industrial Crystallization from Solutions*, Butterworth, London (1971).

Nyvlt, J., Design of batch crystallizers, in *Industrial Crystallization* (J. W. Mullin, ed.), Plenum Press, New York, pp. 335–342 (1976).

Nyvlt, J., *Industrial Crystallization*, Verlag Chemie, Weinheim (1978, 1982).

Nyvlt, J., Kinetics of secondary nucleation with attrition and the mean size of product crystals from the continuous stirred crystallizer, *Collect. Czech. Commun.*, *46*: 79–85 (1981).

Nyvlt, J., O Söhnel, M. Matuchova, and M. Broul, *The Kinetics of Industrial Crystallization*, Chemical Engineering Monography Vol. 19, Elsevier, Amsterdam (1985).

Nyvlt, J., R. Rychly, J. Gottfried, and J. Wurzelova, Metastable zone width of some aqueous solutions, *J. Cryst. Growth*, *6*: 151 (1970).

Ohara, M., and R. C. Reid, *Modeling Crystal Growth Rates from Solution*, Prentice-Hall, Englewood Cliffs, NJ (1973).

Ottens, E. P. K., and E. J. de Jong, A model of secondary nucleation in a stirred vessel cooling crystallizer, *Ind. Eng. Chem. Fundam. 12*: 179–184 (1973).

Ramanarayanan, K. A., K. A. Berglund, and M. A. Larson, Growth rate dispersion in batch crystallizers, *Chem. Eng. Sci.*, *40*(8): 1604–1608 (1985).

Randolph, A. D., The mixed suspension, mixed product removal crystallizer as a concept in crystallizer design, *AIChE J.*, *11*: 424–430 (1965).

Randolph, A. D., How to approach the problems of crystallization, *Chem. Eng.*, *4*: 80–96 (1970).

Randolph, A. D., Design, control and analysis of crystallization processes, *AIChE Symp. Ser.*, *76* (1980).

Randolph, A., and M. A. Larson, Transient and steady state distribution in continuous mixed suspension crystallizers, *AIChE J.*, *8*(5): 639–645 (1962).

Randolph, A. D., and M. Larson, *Theory of Particulate Processes*, 2nd ed., Academic Press, San Diego, CA (1988).

Randolph, A. D., and E. T. Wright, Modeling size dispersion in the prediction of crystal size distribution, *Chem. Eng. Sci.*, *32*: 1067–1076 (1977).

Rojkowski, Z., and J. Synowiec, *Krystalizacja i krystalizatory*, Wydawnictwa Naukow Techniczne, Warsaw (1991).

Rosmalen, G. M. van, G. J. Witkamp, and H. C. de Vreugd, Additive and impurity effects in crystallization processes, in *Proc. 10th Symp. on Industrial Crystallization* (J. Nyvlt and S. Zacek, eds.), Elsevier, Amsterdam (1989).

Rousseau, R. W., and M. A. Larson, Analaysis and design of crystallization processes, *AIChE Symp. Ser.*, *72*(153) (1976).

Rousseau, R. W., K. K. Li, and W. L. McCabe, The influence of seed on nucleation rates, *AIChE Symp. Ser.*, *72*(153): 48–52 (1976).

Seidell, A., and W. F. Linke, *Solubilities of Inorganic and Metal Organic Compounds*, 4th ed., Van Nostrand, New York, Vols. 1 and 2 (1958), W. F. Linke, American Chemical Society, Washington, D.C. (1965).

Sherwood, J. N., R. I. Ristic, and T. Shripathi, The influence of mechanical deformation and fracture on crystal growth: A potential cause of growth rate dispersion, in *Proc. 11th Symp. on Industrial Crystallization* (A. Mersmann, ed.), pp. 1–9 (1990).

Söhnel, O., and J. Garside, *Precipitation*, Butterworth-Heinemann, Oxford (1992).

Stranski, I. N., Zur Theorie des Kristallwachstums, *Z. Phys. Chem.*, *136*: 259 (1928).

Strickland-Constable, R. F., *Kinetics and Mechanism of Crystallization from the Fluid phase*, Academic Press, New York (1968).

Tavare, N. S., Batch crystallizer: a review, *Chem. Eng. Commun.*, *61*: 259–318 (1987).

Toussaint, A. G., and J. M. H. Fortuin, Design criteria for DTB-vacuum crystallizers, in *Industrial Crystallization* (J. W. Mullin, ed.), Plenum Press, New York (1976).

Toyokura, K., F. Matsuda, Y. Uike, H. Sonoda, and Y. Wakabayashi, The design of a crystallizer, in *Industrial Crystallization* (J. W. Mullin, ed.), Plenum Press, New York, pp. 303–310 (1976).

Toyokura, K., M. Uchiyama, M. Kawai, H. Akutsu, and T. Ueno, in *Industrial Crystallization '81* (S. J. Jancic and E. J. de Jong, eds.), North-Holland, Amsterdam, pp. 87–96 (1982).

Toyokura, K., K. Yamazoe, and J. Mogi, Secondary nucleation rate of alum in a fluidized bed, *AIChE Symp. Ser.*, *153*(7): 53–60 (1976).

Ulrich, M., Optimierung einer diskontinuierlichen Lösungskristallisation, *Chem. Ing. Tech. 51*(3): 243–251 (1979).

Valeton, J. J. P., Wachstum und Auflösung der Kristalle, *Z. Kristallogr.*, *59*: 135 (1923); *60*: 1 (1924).

Van Hook, A., *Crystallization*, Reinhold, New York (1961).

Villermaux, J., Precipitation reaction engineering, in *Proc. 11th Symp. on Industrial Crystallization* A. Mersmann, ed.), pp. 157–162 (1990).

Volmer, M., and A. Weber, Keimbildung in übersättigten Lösungen, *Z. Phys. Chem.*, *119*: 277–301 (1926).

Walton, A. G., *The Formation and Properties of Precipitates*, Interscience, New York (1967).

White, E. T., and P. G. Wright, Magnitude of size dispersion effects in crystallizers, *Chem. Eng. Prog. Symp. Ser.*, *67*(110): 81 (1971).

White, E. T., and P. G. Wright, in *Proceedings of the Queensland Society of Sugar Cane Technology*, *36th Conference*, 299 (1969).

Wöhlk, W., and G. Hofmann, Types of crystallizers, *Int. Chem. Eng.*, *27*(2): 197–204 (1987).

Wöhlk, W., G. Hofmann, and E. J. de Jong, Crystallization theory in crystallization practice, in *Proc. 11th Symp. on Industrial Crystallization* (A. Mersmann, ed.), pp. 349–354 (1990).

Zumstein, R. C., and R. W. Rousseau, Experimental and theoretical analysis of growth rate dispersion, in *Industrial Crystallization '87* (J. Nyvlt and S. Zacek, eds.), Elsevier, Amsterdam, pp. 211–214 (1989).

Substance Index

I. Inorganic Compounds

ALUMINIUM chloride	$AlCl_3$	Table A1.2
hydroxide	$Al(OH)_3$	Table A1.2, 20
sulphate	$Al_3(SO_4)_3$	Table A1.2, 14
AMMONIUM aluminium sulphate	$(NH_4)_2Al_3(SO_4)_4$	Table A1.2, Figure A1.4, 130, 132, 341, 707
bromide	NH_4Br	Table A1.2, Figure A1.6
chloride	NH_4Cl	Table A1.2, A1.6, Figure A1.6, 8, 130, 132, 782
dichromate	$(NH_4)_2Cr_2O_7$	Figure A1.6
dihydrogen phosphate	$NH_4H_2PO_4$	Table A1.2, Figure A1.4, A1.6, 122, 124, 130, 133
ferrous sulphate	$(NH_4)_2Fe(SO_4)_2$	Table A1.2
fluoride	NH_4F	304
hydrogen carbonate	NH_4HCO_3	Table A1.2
iodide	NH_4I	Figure A1.6
nickel sulphate	$(NH_4)_2Ni(SO_4)_2$	Table A1.2
nitrate	NH_4NO_3	Table A1.2, Figure A1.4, A1.5, A1.6, 8, 130, 133, 337
sulphate	$(NH_4)_2SO_4$	Table A1.2, A1.6, Figure A1.3, A1.4, A1.5, 30, 124, 130, 133, 160, 163, 176, 198, 200, 221, 229, 288, 338, 362, 404, 412, 782
thiocyanate	NH_4SCN	Table A1.2, Figure A1.6
BARIUM carbonate	$BaCO_3$	Figure A1.6
chloride	$BaCl_2$	Table A1.2
chromate	$BaCrO_4$	Figure A1.6
fluoride	BaF_2	304
hydroxide	$Ba(OH)_2$	Table A1.2
nitrate	$Ba(NO_3)_2$	Table A1.2, 602
oxalate	BaC_2O_4	Table A1.2

sulphate	$CuSO_4$	Table A1.2, Figure A1.4, 130, 133, 337
FERROUS sulphate	$FeSO_4$	Table A1.2, Table A1.6, 9, 130, 133, 342, 782
LEAD acetate	$Pb(CH_3COO)_2$	Table A1.2
carbonate	$PbCO_3$	Figure A1.6
chloride	$PbCl_2$	Table A1.2, 570
chromate	$PbCrO_4$	Figure A1.6, 526
fluoride	PbF_2	118
nitrate	$Pb(NO_3)_2$	Table A1.2, Figure A1.6, 602
oxalate	PbC_2O_4	Figure A1.6
sulphate	$PbSO_4$	Figure A1.6
sulphide	PbS	609
selenate	$PbSeO_4$	Figure A1.6
LITHIUM chloride	LiCl	Table A 1.2
fluoride	LiF	17
iodate	$LiIO_3$	Table A1.2
sulphate	Li_2SO_4	Table A1.2, 448
MAGNESIUM chloride	$MgCl_2$	Table A1.2, Figure A1.8
hydroxide	$Mg(OH)_2$	Figure A1.6, 448
fluoride	MgF_2	Figure A1.6
sulphate	$MgSO_4$	Table A1.2, Figure A1.4, 15, 16, 30, 101, 130, 133, 198, 200, 342
MANGANOUS carbonate	$MnCO_3$	Figure A1.6
chloride	$MnCl_2$	Table A1.2
sulphate	$MnSO_4$	Table A1.2
MERCURIC chloride	$HgCl_2$	Table A1.2
NICKEL chloride	$NiCl_2$	Table A1.2

II. Organic Compounds

Acetamide	C_2H_5NO	Table A1.3
Acetanilide	C_8H_9NO	Table A1.3
Acetic acid	$C_2H_4O_2$	13
Acetylsalicylic acid	$C_9H_8O_4$	Table A1.3
Acrylic acid	$C_3H_4O_2$	671
Adipic acid	$C_6H_{10}O_4$	Table A1.3, 310, 444
Alanine	$C_3H_7O_2N$	Table A1.3, 22, 575, 583, 586
Aminophenol	$C_6H_5O_3N$	Table A1.3
Anthracene	$C_{14}H_{10}$	Table A1.3, 9, 310
Anthranilic acid	$C_7H_7O_2N$	Table A1.3
Asparagine	$C_4H_8O_3N_2$	410, 566, 583, 600, 602
Aspartic acid	$C_4H_7O_4N$	566
Benzamide	C_7H_7ON	Table A1.3, 568, 590, 600
Benzene	C_6H_6	621pp, 630, 637
Benzoic acid	$C_7H_6O_2$	Table A1.3, 552, 628
Biphenyl	$C_{12}H_{10}$	651, 666, 677
Caprolactam	$(CH_2)_5CONH$	650
Cinnamic acid	$C_9H_8O_2$	Table A1.3, 609
Cinnamide	C_9H_9ON	609
Citric acid	$C_6H_8O_7$	Table A1.3, A1.6, Figure A1.4, 30, 110, 198, 221, 288, 337, 782
Cresol	C_7H_8O	Table A 1.3, 13
Cyclohexane	C_4H_8	621pp, 652
Cyclohexanone	C_4H_6O	652
Decanol	$C_{10}H_{20}O$	649pp
p-/o-Dichlorobenzene	$C_6H_4Cl_2$	652
Dodecanol	$C_{12}H_{24}O$	649pp
Dextrin	$(C_6H_{10}O_5)x$	571
Dicyandiamide	C_2H_4N4	Table A1.3
Dinitrobrombenzene	$C_6H_3Br(NO_2)_2$	11
Dinitrochlorbenzene	$C_6H_3Cl(NO_2)_2$	11

Dinitroanisol	$C_7H_6O(NO_2)_2$	11
Ethylendiamine tartrate	$C_6H_{14}O_6N_2$	Table A1.3
Fructose	$C_6H_{12}O_6$	Table A1.3, 570
Fumaric acid	$C_4H_4O_4$	Table A1.3
Galactose	$C_6H_{12}O_6$	568pp
Glucose	$C_6H_{12}O_6$	Table A1.3, 570
Glutamic acid	$C_5H_9O_4N$	Table A1.3, 410, 565, 596pp
Glyceryl tripalmitate	$C_{51}H_8O_6$	Table A1.3
Glyceryl tristearate	$C_{57}H_{110}O_6$	Table A1.3
Glycine	$C_2H_5O_2N$	Table A1.3, 85, 573, 577, 587, 590, 592, 596, 606, 608
Hexamethylene tetramine	$C_6H_{12}N_4$	Table A1.3, Figure A1.4, 88
Hexatriacontane	$C_{36}H_{74}$	Table A1.3
Histidine	$C_6H_9O_2N_3$	579pp, 604pp
Hydrochinone	$C_6H_6O_2$	Table A1.3
Hydoxybenzoic acid	$C_7H_6O_3$	Table A1.3
Itaconic acid	$C_5H_6O_4$	Table A1.3
Lactic acid	$C_3H_6O_3$	572
Lactose	$C_{12}H_{22}O_{11}$	Table A1.3
Leucine	$C_6H_{13}O_2N$	590, 608pp
Lysine	$C_6H_{14}O_2N_2$	566pp, 578pp, 604pp
Maleic acid	$C_4H_4O_4$	Table A1.3, 572
Malic acid	$C_4H_6O_5$	Table A1.3
Malonic acid	$C_3H_4O_4$	Table A1.3
Maltose	$C_{12}H_{22}O_{11}$	Table A1.3
Mannitol	$C_6H_{14}O_6$	Table A1.3
Melamine	$C_3H_6N_6$	Table A1.3
Methylnaphthalene	$C_{11}H_{10}$	Table A1.3
Naphthalene	$C_{10}H_8$	Table A1.3, 628pp, 651, 659pp, 666, 670pp, 677
p-/o-Nitrochlorobenzene	$C_6H_4O_2ClN$	652
Ornithine	$C_5H_{12}N_2O_2$	566, 596
Oxalic acid	$C_2H_2O_4$	Table A1.3

Pentaerythritol	$C_5H_{12}O_4$	Table A1.3
Phenacetin	$C_{10}H_{13}O_{22}N$	Table A1.3
Phenol	C_6H_6O	Table A1.3
Phenylalanine	$C_9H_{11}O_2N$	574pp, 604pp
Phthalic acid	$C_8H_6O_4$	Table A1.3
Picric acid	$C_6H_3O_7N_3$	Table A1.3
Proline	$C_5H_8O_2N$	573
Pyrocatechol	$C_6H_6O_2$	Table A1.3
Raffinose	$C_{18}H_{32}O_{16}$	Table A1.3, 568–570
Resorcinol	$C_6H_6O_2$	Table A1.3
Rhamnose	$C_6H_{14}O_6$	581pp
Salicylic acid	$C_7H_6O_3$	Table A1.3, 339
Salol	$C_{13}H_{10}O_3$	Table A1.3
Serine	$C_3H_7O_3N$	594, 597pp
Sorbitol	$C_6H_{14}O_6$	Table A1.3
Stearic acid	$C_{18}H_{36}O_2$	Table A1.3, 611
Succinic acid	$C_4H_6O_4$	Table A1.3, 304, 585
Succinimide	$C_4H_5O_2N$	Table A1.3
Sucrose	$C_{12}H_{22}O_{11}$	Figure A1.3, A1.4, A1.5, 568–570
Sulphanilic acid	$C_6H_6NO_3S$	Table A1.3
Tartaric acid	$C_4H_6O_6$	Table A1.3, 30, 198pp, 221, 572
Taurine	$C_2H_6O_3SN$	Table A1.3
Terephthalic acid	$C_8H_6O_4$	339
Thiourea	CH_4N_2S	Table A1.3, Figure A1.4, 30, 201, 221, 288, 337
Threonine	$C_4H_9O_3N$	566, 579, 602
Toluamide	C_8H_9ON	568pp
Triglycine sulphate	$C_6H_{17}O_{10}SN_3$	Table A1.3
Urea	CH_4N_2O	Table A1.3, Figure A1.3, A1.4, 337, 362
Uric acid	$C_5H_4O_3N_4$	Table A1.3
p-/o-Xylene	C_8H_{10}	650pp
Valine	$C_5H_{11}O_2N$	85, 576, 590

III. Solvents

Acetic acid	$C_2H_4O_2$	13, 586
Acetone	C_3H_4O	Figure A1.2, A1.7, A1.9
Aniline	C_6H_7N	Figure A1.2, A1.7, A1.9
Butyl alcohol	$C_4H_{10}O$	Figure A1.2, A1.7, A1.9
Ethanol	C_2H_6O	Figure A1.2, A1.7, A1.9
Glycerol/glycerin	$C_3H_8O_3$	Figure A1.7, A1.9
I-leptane	C_7H_{16}	Figure A1.2, A1.7, A1.9
Hexane	C_6H_{14}	Figure A1.2, A1.9
Isopropanol	C_3H_8O	587
Methanol	CH_4O	Figure A1.2, A1.7, A1.9, 180
Propanol	C_3H_8O	Figure A1.2, A1.7, A1.9
Toluene	C_7H_8	Figure A1.9
Water	H_2O	Figure A1.2, A1.7, A1.9